Brush-painted Silver Nanoparticle UHF RFID Tags on Fabric Substrates

Johanna Virkki, Toni Björninen, Lauri Sydänheimo, and Leena Ukkonen
Department of Electronics and Communications Engineering
Tampere University of Technology, P. O. Box 692, FI-33101 Tampere, Finland

Abstract— Due to an increasing interest to wearable electronics, versatile electronics manufacturing methods are needed for numerous applications. Brush-painting is a simple and fast additive manufacturing method for electronics, which involves only two process steps: painting and sintering. In our study, passive UHF RFID tag antennas were brush-painted through a stencil on two different fabric substrates by using only one layer of silver nanoparticle ink. According to our measurements, the tags on Fabrics 1 and 2 showed peak read ranges of over 8 meters and of 2 meters, respectively, both on top of the fabric and while embedded between two layers of fabric. The brush-painted tags also showed suitable on-body read ranges. However, the characteristics of the fabric substrate had a significant effect on the tag performance.

1. INTRODUCTION

A new generation of clothing will be able to sense, communicate data, and harvest energy in a nonintrusive way. These innovations in the area of wearable electronics are paving the way toward ambient intelligence and the internet of things [1, 2]. Wearable passive UHF (ultra high frequency) RFID (radio-frequency identification) tags, for instance, have enormous potential in future welfare and healthcare applications. This growing interest to wearable electronics has created a need for versatile antenna manufacturing methods that are needed for numerous applications. Screen and inkjet printing of metal nanoparticle inks, embroidery with metal-coated sewing thread and patterning of metallized fabrics are examples of technologies used to produce textile conductors [3–6].

Brush-painting is a simple and fast method, which enables mass production in the future. The manufacturing process involves only two process steps: painting and sintering, and it is possible to fabricate antennas with only one brushed layer on porous and fibrous fabric substrates. The brushing-method not only reduces process-steps, but also minimizes the amount of deposited conductive material (ink), because it is dispensed directly to the brush, and from the brush directly to the antenna area in the substrate. Brush-painting is also possible without a stencil. This novel fabrication method offers great competitiveness in future wearable RFID tag manufacturing and an appealing alternative to screen printing.

2. BRUSH-PAINTED UHF RFID TAGS

In our study, we brush-painted antennas for passive UHF RFID tags through a stencil on two different fabrics. The conductive material we used was Harima NPS-JL silver nanoparticle ink [7] which was deposited on both fabrics in a single brush. Fabric 1 was a mix of polyester and viscose used in pants and Fabric 2 was 100 % cotton used in coveralls. The stencil was patterned from 50 µm thick polyimide film. Figure 1 shows the geometry of the studied antenna and Figure 2 illustrates the manufacturing process steps.

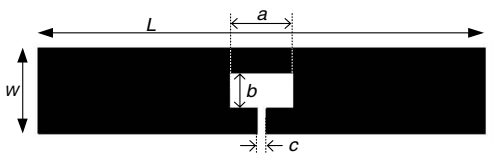

Geometrical parameters in millimeters.

L	W	a	b	c
100	20	14.3	8.125	2

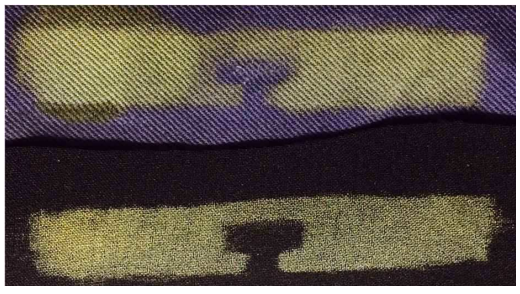

Figure 1: Antenna geometry and samples of brush-painted antennas.

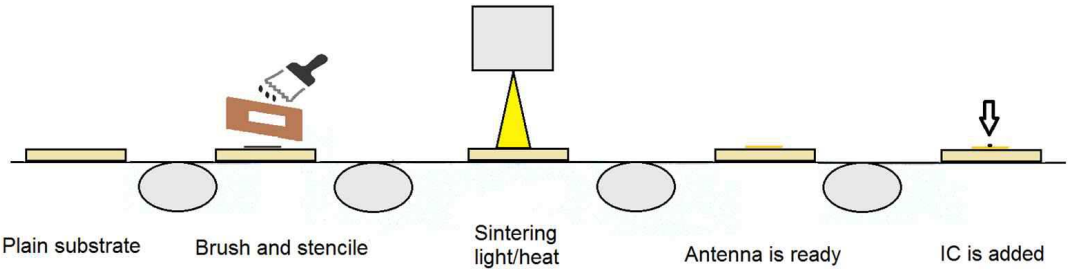

Figure 2: Brush-painting process.

After brushing the ink through the stencil, the tag antennas were sintered with two different methods: by Xenon photonic sintering system and by heat sintering in an oven. The parameters for the photonic sintering were found by experimenting while manufacturer recommendations were used in heat sintering. In photonic sintering we used a single flashpulse mode, but it was used 3 times with a break of 1.5 seconds between the flashes. The used voltage for Fabrics 1 and 2 was 2800 V and 3000 V, respectively. In heat sintering, the antennas weresintered in 150°C for 1 hour. The prototype antennas are shown in Figure 1.

The tag IC utilized in this study is NXP UCODE G2iL series IC with the wake-up power of −18 dBm (15.8 µW) [8]. The manufacturer had mounted the chip on a strap (copper on a plastic film). After sintering, we attached the pads of the strap to the antenna using a conductive silver epoxy resin. In this study, we did not concentrate on IC bonding process, but the main goal was to investigate the novel additive manufacturing method on fabric substrate.

3. TAG PERFORMANCE EVALUATION

Normally, the read range of passive tags is limited by the forward link operation [9], i.e., the efficiency of the wireless power transfer from the reader to the tag IC. Assuming free-space conditions for site-independent comparison, the attainable tag read range in the directions ϕ and θ of a spherical coordinate system centered at the tag is given by [9]

$$d_{tag}(\phi,\theta) = \frac{\lambda}{4\pi}\sqrt{\frac{\chi_{pol}(\phi,\theta)\ ,\tau\, e_{r,tag} D_{tag}(\phi,\theta)\, EIRP}{P_{ic0}}}; \quad \tau = \frac{4\mathrm{Re}(Z_{tag})\,\mathrm{Re}W(Z_{ic})}{|Z_{tag}+Z_{ic}|^2}, \tag{1}$$

where τ is the antenna-IC power transfer efficiency determined by the antenna and IC impedances Z_{tag} and Z_{ic}, resepectively, λ is the wavelength of the reader's carrier signal, $EIRP$ is the regulated equivalent isotropic radiated power, P_{ic0} is the wake-up power of the tag IC, χ_{pol} is the mutual polarization power efficiency between the tag and reader antennas, $e_{r,tag}$ is the tag antenna radiation efficiency and D_{tag} is the tag antenna directivity.

Equation (1) show explicitly how the electromagnetic properties of the tagantenna and tag IC determine the attainable read range of the tag. However, the measurement of small antennas and accurate characterization of the non-linear IC frontend is problematic [10, 11]. Thus, the required measured data to evaluate (1) is difficult to obtain. Moreover, uncertainties may accumulate from the radiation pattern, antenna impedance, and tag IC measurements. Hence, the performance evaluation of fully assembled RFID tags based on the reader-to-tag communication threshold is advantageous. This can be with using readers with adjustable output power and RFID testers [12]. Weused Voyantic Tagformance RFID measurement system.

During testing, the lowest transmission power (threshold power: P_{th}) at which the tag remains responsive is recorded. Here wedefined P_{th} as the lowest power at which the identification code can be read from the tag's memory based on ISO 18000-6C communication standard. In addition, the wireless channel from the reader antenna to the location of the tag under test was characterized using a system reference with known properties. As detailed in [13], we computed the attainable read range of the tag under testbased on the measured threshold power from

$$d_{tag} = \frac{\lambda}{4\pi}\sqrt{\frac{EIRP}{\Lambda}\frac{P_{th*}}{P_{th}}}, \tag{2}$$

where P_{th} is the measured threshold power of the tag under test, Λ is a constant provided by the system manufacturer to describe the sensitivity of the reference tag at each frequency, and P_{th*} is the measured threshold power of the reference tag. In this article, we report the results under the European RFID emission regulation: $EIRP = 3.28$ W.

4. RESULTS AND DISCUSSION

The measurement results obtained in an anechoic chamber are presented in Figure 3. In our measurements, the RFID tags with heat sintered antennas did not respond. Thus, heat sintering was found to be unsuitable method for sintering this nanoparticle ink on the studied fabrics. However, the RFID tags with photonic sintered antennas on Fabric 1 showed a peak read range close to 9 meters. Also, the photonic sintering process was much faster than the heat sintering process; only a few seconds. As in practice the antenna pattern would not likely be exposed at the outer fabric layer, we used normal textile glue join the two fabric layers so that the antenna is embedded in between the two layers of fabric. This did not affect the tag performance significantly: the peak read range remained close to 8.5 meters with a slight 10 MHz downward shift in frequency. In contrast, tags on Fabric 2 showed much smaller read ranges of 1.5-to-2 meters both on top of the fabric and embedded in between two layers of fabric. Thus, in addition to the chosen sintering method, the characteristics of the fabric substrate have a huge effect on the characteristics of the brush-painted RFID tag antennas. Similar results have been found in case on screen-printed antennas on different fabric substrates [14]: the uneven fabric surface caused discontinuities and breaks, making the tag very poorly matched to the IC and hence reducing the realised gain and read range.

We also compared the performance of the brush-painted tag against two other types of textile-based tags with the same antenna (described in Figure 1) fabricated using screen printing and patterned from a metallized fabric. The screen-printed antenna was fabricated from polymer thick film silver ink on stretchable fabric substrate with the same ink and process described in [14]. The electro-textile tag was cut from Less EMF Stretch Conductive Fabric (Cat. #321), which is silver plated stretchable fabric made of nylon (76%) and elastic fibers (24%) [15]. As seen from Figure 3, the measured peak read range of the brush-painted tag on Fabric 1 is very close to that of the screen-printed tag and nearly three meters higher than that of the electro-textile tag. It is worth noticing that unlike the screen-printed and electro-textile antennas, the brush-painted antenna did not exhibit accurately defined edges (see Figure 1). Still, the performance of the brush-painted tag on Fabric 1 operated very similar to the screen-printed one, suggesting that the studied antenna geometry is not sensitive toward edge roughness.

Finally, we measured the practical on-body read range of the tags on Fabric 1, as it was a more suitable substrate to be used with the chosen silver nanoparticle ink and brush-painting method. The measurement was conducted in an office room with some absorbers placed to reduce scattering. The tag is separated 3–4 mm from the body only with a shirt layer. During the measurements,

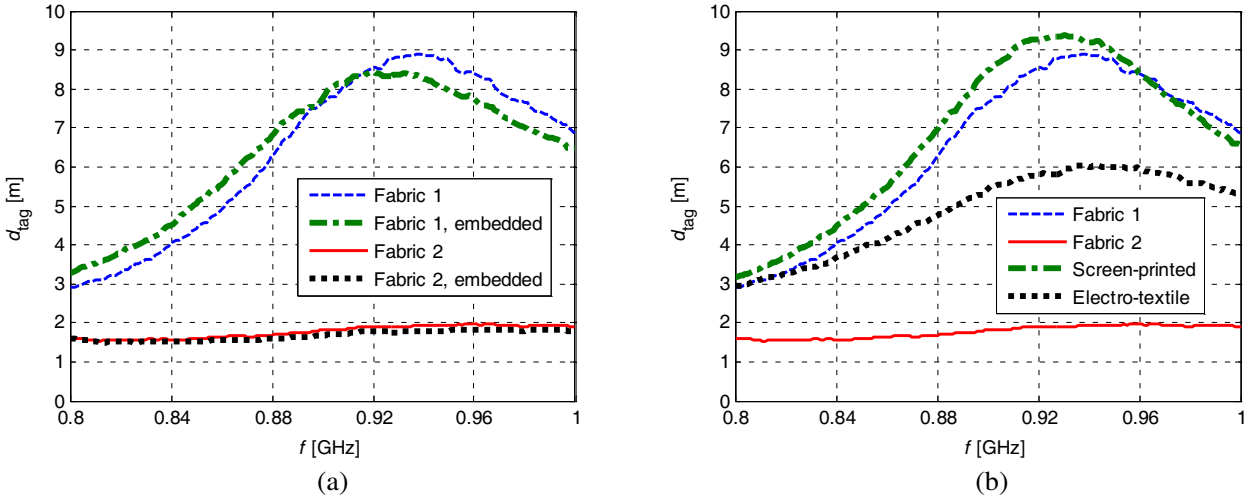

Figure 3: (a) Maximum read ranges for brush-painted tags on top of the fabric and while embedded between two layers of fabric and (b) maximum read ranges of brush-painted, screen-printed, and electro-textile UHF RFID tags.

the tag was attached to the body on the right arm and was measured from 3 different directions, as shown in Figure 4. The tags achieved the best read ranges, 3–5 meters, when measured from direction 1. However, also read ranges from directions 2 and 3, which were 1.5-to-2.5 meters and 2-to-3 meters, respectively, can be considered suitable for many applications. The fluctuations seen in the graph are manifestation of the scattering, which was not completely compensated from the results via the system reference tag measurement. This was because the presence of the human body changed the environment.

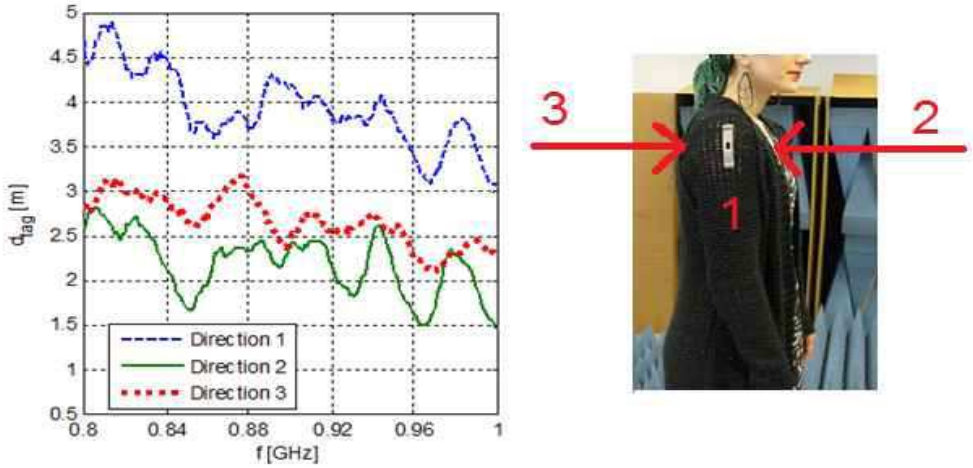

Figure 4: Measurement results for on-body read ranges from 3 different directions.

5. CONCLUSIONS

According to our results, brush-painted silver nanoparticle passive UHF RFID tags have great potential for future wearable applications. Brush-painted tags on fabric substrate achieved maximum read ranges of over 8 meters, also when embedded inside two layers of fabric. In addition, the measured on-body read ranges were found to be suitable for many future applications. It should be noted that the characteristics of the fabric substrate have a huge effect on the tag performance and the right sintering parameters for each substrate have to be studied individually. Future work will include finding the best manufacturing parameters for different types of fabric substrates and testing different types of nanoparticle inks.

ACKNOWLEDGMENT

This research work was funded by the Academy of Finland and the Finnish Funding Agency for Innovation (Tekes).

REFERENCES

1. Swan, M., "Sensor mania! The internet of things, wearable computing, objective metrics, and the quantified self 2.0," *Journal of Sensor and Actuator Networks*, Vol. 3, No. 1, 217–253, 2012.
2. Yoo, H. J., "Your heart on your sleeve: Advances in textile-based electronics are weaving computers right into the clothes we wear," *IEEE Solid-State Circuits Mag.*, Vol. 5, No. 1, 59–70, 2013.
3. Merilampi, S., T. Björninen, V. Haukka, P. Ruuskanen, L. Ukkonen, and L. Sydänheimo, "Analysis of electrically conductive silver ink on stretchable substrates under tensile load," *Microel. Reliab.*, Vol. 50, No. 12, 2001–2011, 2010.
4. Chauraya, A., W. G. Whittow, J. C. Vardaxoglou, L. Yi, R. Torah, Y. Kai, S. Beeby, and J. Tudor, "Inkjet printed dipole antennas on textiles for wearable communications," *IET Microw. Antennas Propag.*, Vol. 7, No. 9, 760–767, 2013.
5. Post, E. R., M. Orth, P. R. Russo, and N. Gershenfeld, "E-broidery: Design and fabrication of textile-based computing," *IBM Syst. J.*, Vol. 39, Nos. 3–4, 840–860, 2000.
6. Kaufmann, T., I.-M. Fumeaux, and C. Fumeaux, "Comparison of fabric and embroidered dipole antennas," *Proc. EuCAP*, 1662–1666, 2013.

7. Harima NPS-JL Silver Nanoparticle, Ink:https://www.harima.co.jp/en/products/electronics/pdf/brochure14e_21.pdf.
8. NXP UCODE G2iL IC, http://www.nxp.com/documents/data_sheet/SL3S1203_1213.pdf.
9. Marrocco, G., "The art of UHF RFID antenna design: Impedance-matching and size-reduction techniques," *IEEE Antennas Propag. Mag.*, Vol. 50, No. 1, 66–79, 2008.
10. Icheln, C., J. Krogenius, and P. Vainikainen, "Use of balunchokes in small-antenna radiation measurements," *IEEE Trans. Instrum. Meas.*, Vol. 53, No. 2, 498–506, 2004.
11. Grosinger, C., C. Mecklenbräuker, and A. L. Scholtz, "UHF RFID transponder chip and antenna impedance measurements," *Proc. EURASIP Workshop on RFID Technology*, 43–46, 2010.
12. Nikitin, P., K. V. S. Rao, and S. Lam, "UHF RFID tag characterization: Overview and state-of-the-art," *Proc. AMTA Symp.*, 6 p, 2012.
13. Virkki, J., T. Björninen, S. Merilampi, L. Sydänheimo, and L. Ukkonen, "Manufacturing and applications of screen-printed RFID tags on paper substrate," *PIERS Proceedings*, 562–566, Stockholm, Aug. 12–15, 2013.
14. Kellomäki, T., J. Virkki, S. Merilampi, and L. Ukkonen, "Towards washable wearable antennas: Acomparison of coating materials for screen-printed textile-based UHF RFID tags," *Intl. J. Antennas Propag.*, Vol. 2012, Article ID 476570, 11 p, 2012.
15. Less EMF Stretch Conductive, Fabric:http://www.lessemf.com/321.pdf.

On Coordinated Multi-Point Transmission for Cellular Environments

Mário Marques da Silva[1,2], **Américo Correia**[1,3], **Rui Dinis**[1,4], **and Paulo Montezuma**[1,4]

[1]Instituto de Telecomunições, Portugal
[2]Universidade Autónoma de Lisboa, Portugal
[3]ISCTE-IUL, Portugal
[4]DEE-FCT-UNL, Portugal

Abstract— Current and emergent services are demanding higher data rates, improved spectral efficiency and increased network capacity. To face these new requirements, it is important to find schemes able to reduce the effects of fading and to exploit new types of diversity.

Coordinated Multi-Point transmission (CoMP) comprises the coordinated transmission of signals from adjacent base stations (BS), and the corresponding reception from user equipments (UE). CoMP transmission is an important technique that can mitigate inter-cell interference, improve the throughput, exploit diversity and, therefore, improve the spectrum efficiency.

This paper performs a comparison between different multi-antenna techniques that can be employed in CoMP to achieve the requirements of the Fourth Generation Cellular Systems (4G).

1. INTRODUCTION

An important requirement of 4G systems is the ability to deliver a homogenous service, regardless the users' positions. Users located at the cell edge may experience a degradation of the Signal-to-Noise Ratio (SNR) due to inter-cell interference, additional path loss or limited BS transmit power. In these scenarios, Coordinated Multi-Point Transmission plays an important role, as it allows the exploitation of additional diversity or the delivery of a high and constant throughput, regardless the users' positions.

The basic concept of Multiple Input Multiple Output (MIMO) relies on the transmission of signals through multiple paths, between multiple transmit and multiple receive antennas.

Multi-antenna systems are used in order to push the performance or capacity/throughput limits as high as possible without an increase of the spectrum bandwidth, although at the cost of an obvious increase of complexity. In the case of frequency selective fading channel, different symbols suffer from interference from each other, whose effect is usually known as Intersymbol Interference (ISI). This effect tends to increase with the used bandwidth. By exploiting diversity, multi-antenna systems can be employed to mitigate the effects of ISI.

Instead of representing an additional interference level, the multiple paths of MIMO signals can be used as an advantage. Moreover, while in MIMO the multiple transmit or the multiple receive antennas are co-located, advanced cellular network architectures may also achieve the same level of diversity, but using antennas belonging to different base stations or relay nodes. Nevertheless, a certain level of synchronization or coordination is normally required between those stations.

The various multi-antenna configurations are referred to as Single Input Single Output (SISO), Multiple Input Single Output (MISO), Single Input Multiple Output (SIMO) or MIMO. The SIMO and MISO architectures are forms of receive and transmit diversity schemes, respectively. MIMO architectures can be used for combined transmit and receive diversity, for the parallel transmission of data or for spatial multiplexing. When used for spatial multiplexing, MIMO technology promises high bit rates in a narrow bandwidth. Therefore, it is of high significance to spectrum users. In this case, MIMO system considers the transmission of different signals from each transmit antenna element so that the receiving antenna array receives a superposition of all transmitted signals.

Most common CoMP techniques present the following configurations [1–3]:

- Space-Time Block Coding (STBC)
- Multi-layer Transmission

Although STBC is essentially a MISO system, the use of receive diversity makes it a MIMO, which corresponds to the most common configuration for this type of diversity. STBC based schemes focus on achieving a performance improvement through the exploitation of additional diversity,

while keeping the symbol rate unchanged [2, 4]. On the other hand, multi-layer transmission and Space-Division Multiple Access (SDMA) belong to another group, entitled Spatial Multiplexing (SM), whose principles are similar but whose purposes are quite different. The goal of the MIMO based on multi-layer transmission scheme relies on achieving higher data rates in a given bandwidth, whose increase rate corresponds to the number of transmit antennas [1]. In this case, the number of receive antennas must be equal or higher than the number of transmit antennas. The increase of symbol rate is achieved by logically "steering" the receive antennas to each one (separately) of the transmit antennas, in order to receive the corresponding data stream [5, 6]. This is achieved through the use of the nulling algorithm.

1.1. Single-User MIMO and Multi-User MIMO

The MIMO techniques previously exposed are typically employed in the concept of Single-User MIMO (SU-MIMO). SU-MIMO considers data being transmitted from a single user into another individual user. An alternative concept is the Multi-User MIMO (MU-MIMO) where multiple streams of data are simultaneously allocated to different users, using the same frequency bands.

The approach behind MU-MIMO is similar to Space-Division Multiple Access (SDMA). Nevertheless, while SDMA is typically employed in the uplink (because the nulling algorithm requires higher number of antennas), the MU-MIMO can also be implemented in the downlink. This allows sending different data streams into different UE. In this case, instead of performing the nulling algorithm at the receiver side, the nulling algorithm is performed using a pre-coding approach at the transmitter side (BS). This is possible because the BS can accommodate a high number of transmit antennas and the UE can only accommodate a single or reduced number (lower) of receive antennas. In the downlink of a MU-MIMO configuration, the number of transmit antennas must be higher than the number of multiple data streams that is sent to multiple users, at the same time and occupying the same frequency bands (the opposite of the SDMA approach). In this configuration, the nulling algorithm is implemented at the transmitter side using a pre-processing algorithm such as Zero Forcing (ZF), Minimum Mean Square Error (MMSE), dirty paper coding, etc.. Alternatively, instead of implementing the above described spatial multiplexing principle, the MU-MIMO can be performed using the beamforming algorithm. In any case, MU-MIMO requires accurate downlink Channel State Information (CSI) at the transmitter side. Obtaining CSI is trivial using Time Division Duplexing (TDD) mode, being more difficult to be achieved when Frequency Division Duplexing (FDD) is employed. In FDD mode, CSI is normally obtained using a feedback link in the opposite direction.

Note that when the aim relies on achieving a performance improvement, a SU-MIMO is normally employed using an algorithm such as STBC. On the other hand, when the aim is to achieve higher through puts using a constrained spectrum, we have two options: in the downlink, the MU-MIMO is typically the solution; in the uplink, SDMA is normally employed.

It is worth noting that users located at the cell edge, served by MU-MIMO, may experience a degradation of the SNR due to inter-cell interference, inter-user interference[1], due to additional path loss or due to limited BS transmit power (which results from the use of a pre-coding). A mechanism that can be implemented to mitigate such limitation relies on employing a dynamic MIMO system, where MU-MIMO is employed everywhere, except at the cell edge. In this location, the BS switches into SU-MIMO using STBC, translating in a performance improvement [7] at the cost of a reduced throughput. Alternatively, base station cooperation is known as an effective mechanism which improves the performance at the cell edge, resulting in a more homogenous service quality, regardless the users' positions.

This paper is organized as follows: different MIMO systems possible for CoMP use are described in Section 2; in Section 3, a description about coordinated multipoint transmission is presented, while Section 4 presents a set of performance results; finally, Section 5 summarizes this paper.

2. MIMO CHARACTERIZATION

This section describes different multi-antenna techniques which can be used to improve the performance, spectral efficiency or to achieve an increased network capacity in CoMP.

2.1. Space-Time Block Coding

Although Space-Time Block Coding (STBC) is essentially a MISO system, the use of receiver diversity makes it a MIMO, which corresponds to the most common configuration for this type of

[1] Users that share the spectrum and that are separated by the MU-MIMO spatial multiplexing.

diversity. Transmit diversity (TD) techniques are particularly interesting for fading channels where it is difficult to have multiple receive antennas (as in conventional receiver diversity schemes). A possible scenario is the downlink transmission where the base station uses several transmit antennas and the mobile terminal only has a single one [2].

STBC based schemes focus on achieving a performance improvement through the exploitation of additional diversity, while keeping the symbol rate unchanged [2, 3]. Symbols are transmitted using an orthogonal block structure, which enables simple decoding algorithm at the receiver [2, 3].

2.1.1. Open Loop Techniques

Open Loop Transmit Diversity schemes are performed without previous knowledge of the channel state by the transmitter. Space Time Block Coding, also known as the Alamouti scheme, is the most known open loop technique [2].

If we employ Alamouti's transmit diversity we need some processing at the transmitter. The Alamouti's coding can be implemented either in the time domain or in the frequency domain. In this paper we consider time-domain coding (the extension to frequency domain coding is straightforward). By considering the STBC with two transmit antennas, the lth time-domain block to be transmitted by the mth antenna ($m = 1$ or 2) is $s_l^{(m)}$, with [2, 8]

$$s_{2l-1}^{(1)} = a_{2l-1} \qquad s_{2l-1}^{(2)} = -a_{2l}^* \qquad s_{2l}^{(1)} = a_{2l} \qquad s_{2l}^{(2)} = a_{2l-1}^* \tag{1}$$

where a_l refers to the symbol selected from a given constellation, to be transmitted in the lth time domain block. Considering the matrix-vector representation, we define $\mathbf{s}_l^{[1,2]}$

$$\mathbf{s}_l^{[1,2]} = \begin{bmatrix} a_{2l-1} & a_{2l} \\ -a_{2l}^* & a_{2l-1}^* \end{bmatrix} \tag{2}$$

where different rows of the matrix refer to transmit antenna order and different columns refer to symbol period orders. The Alamouti's post-processing for two antennas comes [8],

$$\tilde{A}_{2l-1} = \left[Y_{2l-1}H_l^{(1)*} + Y_{2l}^* H_l^{(2)}\right]\beta \qquad \tilde{A}_{2l} = \left[Y_{2l}H_l^{(1)*} - Y_{2l-1}^* H_l^{(2)}\right]\beta \tag{3}$$

where $\beta = [\sum_{m=1}^{M} |H_l^{(m)}|^2]^{-1}$. Defining $\mathbf{Y}_l^{[1,2]} = \begin{bmatrix} Y_{2l-1} & Y_{2l}^* \\ Y_{2l} & -Y_{2l-1}^* \end{bmatrix}$ and $\mathbf{H}_l^{[1,2]} = \begin{bmatrix} H_l^{(1)*} & H_l^{(2)} \end{bmatrix}^T$, (3) can be expressed in matrix-vector representation as $\tilde{\mathbf{A}}_l^{[1,2]} = [\mathbf{Y}_l^{[1,2]} \times \mathbf{H}_l^{[1,2]}] \times \beta$, where $\tilde{\mathbf{A}}_l^{[1,2]} = \begin{bmatrix} \tilde{A}_{2l-1} & \tilde{A}_{2l} \end{bmatrix}^T$.

Finally, the decoded symbols come

$$\tilde{A}_{2l-j} = \overbrace{A_{2l-j}\sum_{m=1}^{M}\left|H_l^{(m)}\right|^2\beta}^{\text{Desired Symbol}} + \overbrace{N_{2l-j}^{eq}}^{\text{Noise Component}} \qquad j = 0, 1 \tag{4}$$

where $N_{k,l}^{eq}$ denotes the equivalent noise for detection purposes.

Orthogonal code of rate 1 using more than two antennas does not exist. Schemes with 4 and 8 antennas with code rate one only exist in the case of binary transmission. If orthogonality is essential (fully loaded systems with significant interference levels), a code with $R < 1$ should be employed for such cases.

The signal processing for non-orthogonal 4 and 8 transmit antennas is defined in [8] and in the references therein. In both cases, the decoding does not achieve the maximum possible path diversity since in the decoding of all symbols there is always inter-symbolic interference from one symbol in the case of 4 antennas (c_0), and from 3 symbols in the case of 8 antennas (c_0, c_1, c_2).

It is worth noting that although the described STBC scheme is a MISO, by adopting receive diversity, this can be viewed as a MIMO system.

2.1.2. Closed Loop Techniques

In the case of the downlink, the space diversity provided by the Selective Transmit Diversity (STD) scheme presents a low rate feedback link from the receiver (UE) informing the transmitter (BS)

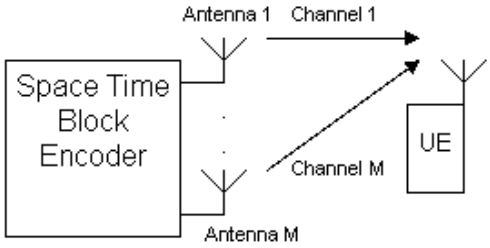

Figure 1: Generic block diagram of an open loop transmitter scheme.

which antenna should be employed for transmission. There is a common or dedicated pilot sequence being transmitted. Different antennas with specific pilot patterns/codes enable antenna selection. Once the UE sends back to the transmitter the information about the M link qualities (number of transmit antennas), the BS transmits a single symbol stream over the best antenna. The receiver is supposed to re-acquire the carrier phase $\theta_k(t)$ after every switch between antennas. Moreover, the Antenna Switch (AS) has the capability to switch every slot duration. Note that STD can be viewed as a type of CoMP, using a scheduling technique.

2.2. Spatial Multiplexing

Multi-layer Transmission and SDMA belong to group entitled Spatial Multiplexing (SM), whose principles are similar but whose purposes are quite different. As long as the antennas are located sufficiently far apart, the transmitted and received signals from each antenna undergo independent fading.

The primary goal of the MIMO based on multi-layer transmission scheme relies on achieving higher data rates in a given bandwidth, whose increase rate corresponds to the number of transmit antennas [1, 3]. An example of a receiving algorithm employed in multi-layer transmission is the Vertical — Bell Laboratories Layered Space-Time (V-BLAST) algorithm. In the Multi-Layer MIMO, the number of receive antennas N must be equal or higher than the number of transmit antennas M. The increase of symbol rate is achieved by logically "steering" the receive antennas to each one (separately) of the transmit antennas, in order to receive the corresponding data stream. This is achieved through the use of the nulling algorithm [3].

As depicted in Figure 2, two different Multi-Layer MIMO schemes are considered: scheme 1 and scheme 2 [3]. Scheme 1 directly allows an increase of the data rate whose increase rate corresponds to the number of transmit antennas. Scheme 2 allows the exploitation of diversity, without achieving an increase of data rate. The transmit diversity combining is achieved using any combining algorithm, namely the Mean-Square Error (MSE) based or the Maximum Ratio Combining (MRC). In the case of scheme 2 (depicted in Figure 2(b))), the antenna switching is performed at a symbol rate, where the red dashed lines represent the signal path at even symbol periods, in case of two transmit antennas. The diversity is achieved because each symbol is transmitted by different antennas, at different symbol periods. Output signals are then properly delayed and combined to

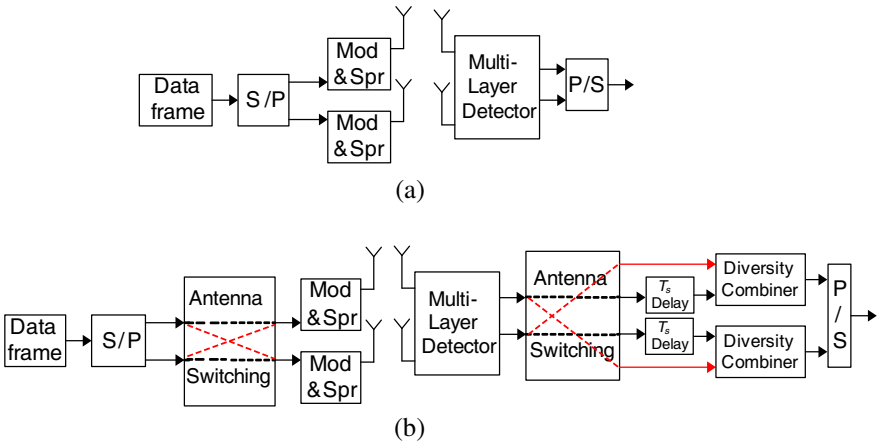

Figure 2: Generic diagram of the 2×2 multi-layer MIMO, (a) scheme 1 and (b) scheme 2.

provide diversity.

In Multi-Layer MIMO, the symbol with the highest SNR is first detected using a linear nulling algorithm such as zero forcing (ZF) or minimum mean square error (MMSE) [1, 9]. The detected symbol is regenerated, and the corresponding signal portion is subtracted from the received signal vector using typically a Successive Interference Cancellation (SIC) algorithm. This cancellation process results in a modified received signal vector with fewer interfering signal components left. This process is repeated, until all symbols from different transmit antennas are detected. [1] provides the signal description for the V-BLAST receiver, while in [5] it is proposed an advanced receiver for the Multi-Layer MIMO scheme applied to Wideband Code Division Multiple Access (WCDMA) signals.

3. COORDINATED MULTI-POINT TRANSMISSION

Using CoMP transmission, independent antenna elements of different BSs are grouped together, forming a cluster, and the UEs can experience a throughput increase or performance improvement. A pre-processing is typically employed at the BSs side such that the signals that reach the UE do not require any type of post-processing.

In case each BS uses the MIMO scheme, the resulting MIMO can be viewed as a "giant MIMO", consisting of a combination of independent antenna elements from different BSs (see Figure 3).

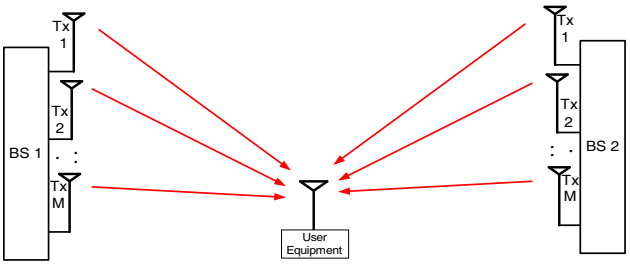

Figure 3: CoMP implemented as a downlink MIMO.

Coordinated multi-point transmission comprises the coordinated transmission of signals from adjacent BSs, and the corresponding reception from a UE. The signal received at the UE side consists of the sum of independent signals sent by different BSs.

CoMP transmission is an important technique that can mitigate inter-cell interference, improve the throughput, exploit diversity and, therefore, improve the spectrum efficiency. Note that CoMP transmission allows a spectrum efficiency improvement, even at the cell edge. CoMP transmission can be viewed as a special type of MU-MIMO.

Similar to MU-MIMO, a pre-processing such as beamforming, ZF, MMSE or dirty-paper coding is employed, in order to assure that the UE receives a combined signal coming from multiple BSs. In this case, the UE commonly employs a low-complexity and regular detector. Alternatively, a single-user like MIMO detector can be employed at the receiver (UE) or a coordinated scheduling can also be employed. In the latter case, CoMP transmission can be associated to carrier aggregation, activating or de-activating some carriers in order to optimize the performance.

Similar to MU-MIMO, accurate downlink CSI is typically required at BSs side, which consists of an implementation difficulty. In case of TDD, obtaining CSI is trivial, as the uplink and downlink channels are almost the same. Nevertheless, in case of FDD, obtaining CSI at the transmitter side is a complex task.

Depending on the way the coordination between different BSs is performed, and the way CSI is obtained (in FDD mode), two different architectures can be implemented:

- Centralized architecture: in this architecture there is a central Control Unit (CU) which decides about the transmission scheme and resources allocation to be used by different BSs. In this case, the CU is connected to different BSs of the cluster. Each UE estimates the downlink CSI of the signals received from each BS. Then, the CSI is sent back to the corresponding BS. At a third stage, CSI is sent from different BSs of the cluster to the CU through backhaul links. Based on CSI, the CU decides about the transmission scheme and resources allocation to be used by each BS, and sends this information to different BSs of the cluster. A major limitation of this architecture relies on the latency, whose factor may result in performance degradation due to fast CSI variations [10].

- Distributed architecture: in this architecture, each BS is associated to a different CU, and the decision about the transmission scheme and resources allocation is performed independently at the BS level. Then, this information is exchanged between the cluster's BSs. In this case, each UE estimates the downlink CSI to different BSs and sends this joint data back not only to the BS of reference, but to all BSs. This way the CU associated to each BS has information about different downlink CSI and makes the decision accordingly. An advantage of this architecture relies on the fact that latency is much reduced, and there is no need to use backhaul links for the purpose of exchanging CSI. Nevertheless, this architecture is more subject to errors caused by the uplink transmission [11].

4. PERFORMANCE RESULTS

In this section we present a set of performance results concerning the proposed CoMP using different configurations, namely with one and two receive antennas, for a regular single carrier transmission (that is, without any advanced transmission technique such as multi-carrier or CDMA), and for the Pedestrian A and Vehicular A propagation environments (corresponds to a rich multipath propagation). Uncoded Bit Error Rate (BER) performance is considered, which is expressed as a function of the bit signal-to-noise ratio E_b/N_0, employing the QPSK constellation under a Gray mapping rule. Concerning the system level simulation, a total of four mobile terminals were considered in the cell. Different multi-antenna systems were considered in the simulations: the "no CoMP" corresponds to the SISO, that is, using a single BS (CoMP is not employed), where the receiver comprises a single receive antenna; the CoMP STBC and CoMP STBC 2×2 correspond to the Alamouti-like scheme with two transmit antennas and a single or two receive antennas, respectively; the CoMP STD corresponds to the closed loop technique, that is, corresponds to two BS's and a single receive antenna; finally, CoMP SPATIAL MUX 2×2 corresponds to spatial multiplexing with two transmit and two receive antennas (see Figure 2 for layers 1 and 2).

Figure 4 shows the performance results concerning the Pedestrian A propagation environment, and assuming a single receive antenna. As can be seen, through the exploitation of diversity the CoMP STBC and CoMP STD allows a performance improvement relating to the "No CoMP". Note that the STD performs better than the STBC for E_b/N_0 below 12 dB. Since the Pedestrian A presents a propagation environment close to the single path (flat fading), the selective diversity allows selecting the antenna that presents less instantaneous frequency selectivity, leading to good results even under noisy conditions. Nevertheless, since the STBC always transmits the signals by the two antennas (antenna diversity), and since the corresponding channel presents low level of multipath diversity, it is only able to perform better than the STD for low levels of noise, that is, for high E_b/N_0 levels.

Figure 5 presents the performance for the Pedestrian A, but with two receive antennas. As expected, the performance obtained with the layer 2 is better than that of layer 1 due to its ability to exploit diversity, but the throughput is not duplicated. Moreover, the CoMP based on the Alamouti-like MIMO scheme (CoMP STBC 2×2) achieves a performance improvement relating to the layer 2, achieving the best overall performance.

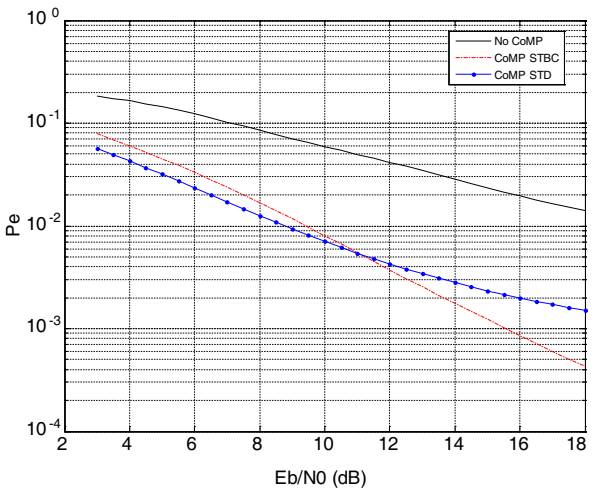

Figure 4: Pedestrian A propagation model (single receive antenna).

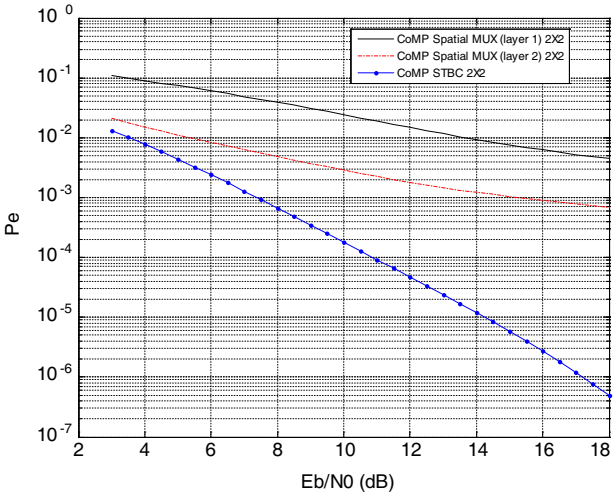

Figure 5: Pedestrian A propagation model (two receive antennas).

Figure 6 corresponds to the results plotted in Figure 4 but concerning the Vehicular A, which is a rich multipath propagation. In this case, the best overall performance is achieved by CoMP STBC for all levels of E_b/N_0.

Figure 7 corresponds to Figure 5 but for the Vehicular A propagation environment. As before, the best overall performance is achieved by CoMP STBC 2×2. Nevertheless, comparing the results of Vehicular A against those of Pedestrian A, it is viewed that the difference of performance between CoMP MUX layer 2 and CoMP STBC is reduced.

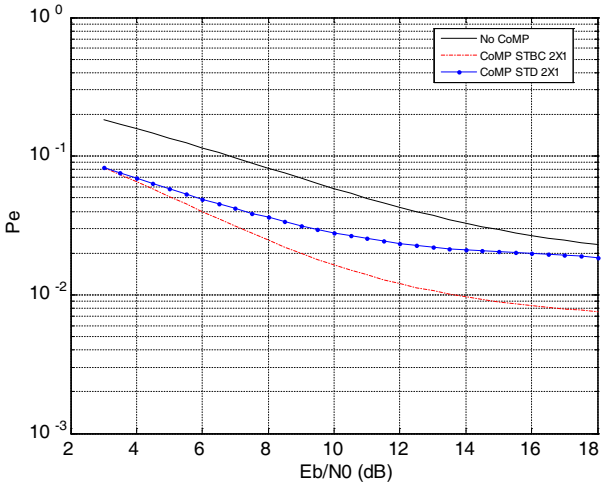

Figure 6: Vehicular A propagation model (single receive antenna).

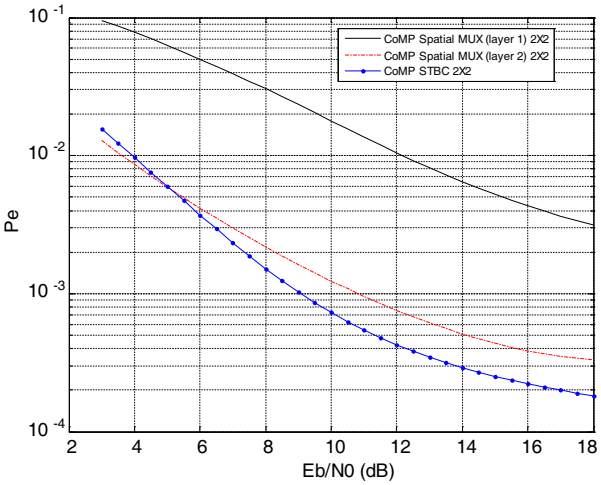

Figure 7: Vehicular A propagation model (two receive antennas).

5. CONCLUSIONS

This paper performed a comparison between different coordinated multi-point transmission techniques. It was shown that the best overall performance tends to be achieved by the CoMP using the Alamouti-like scheme (STBC). Naturally, when the aim is the increase of throughput, instead of performance improvement, CoMP implementing spatial multiplexing (layer 1) should be viewed as an option.

ACKNOWLEDGMENT

This work was supported by the FCT (Fundação para a Ciência e Tecnologia) via projects PEst-OE/EEI/LA0008/2013, GLANC EXPL/EEI-TEL/1582/2013, and EnAcoMIMOCo EXPL/EEI-TEL/2408/2013.

REFERENCES

1. Foschini, G. J., "Layered space-time architecture for wireless communication in a fading environment when using multiple antennas," *Bell Laboratories Technical Journal*, Vol. 1, No. 2, 41–59, Autumn, 1996.
2. Alamouti, S. M., "A simple transmitter diversity scheme for wireless communications," *IEEE JSAC*, 1451–1458, Oct. 1998.
3. Marques da Silva, M. and F. Monteiro, *MIMO Processing for 4G and Beyond — Fundamentals and Evolution*, 1st Edition, CRC Press, FL, USA, May 2014, Accepted for Publication,
4. Tarokh, V., et al., "Space-time block codes from orthogonal designs," *IEEE Trans. Inform. Theory*, 1456–1467, Jul. 1999.
5. Marques da Silva, M., R. Dinis, and A. Correia, "A new V-BLAST detector approach for W-CDMA signals with frequency selective fading," *PIMRC 2005*, Berlin, Germany, Sep. 2005.
6. Marques da Silva, M., *Multimedia Communications and Networking*, 1st Edition, CRC Press, ISBN: 9781439874844, FL, USA, Mar. 2012.
7. Liu, L., R. Chen, S. Geirhofer, K. Sayana, Z. Shi, and Y. Zhou, "Downlink MIMO in LTE-advanced: SU-MIMO vs. MU-MIMO," *IEEE Communications Magazine*, Vol. 50, No. 2, 140–147, Feb. 2012.

8. Marques da Silva, M. and R. Dinis, "Iterative frequency-domain detection and channel estimation for space-time block codes," *European Transactions on Telecommunications*, Vol. 22, No. 7, 339–351, John Wiley & Sons, Ltd., Nov. 2011.
9. Marques da Silva, M., et al., *Transmission Techniques for 4G Systems*, CRC Press Auerbach Publications, ISBN: 9781439815939, FL, USA, Nov. 2012, http://www.crcpress.com/product/isbn/9781466512337.
10. Diehm, F., P. Marsch, and G. Fetweeis, "The FUTON prototype: Proof of concept of coordinated multi-point in conjunction with a novel integrated wireless/optical architecture," *Proc. IEEE WCNCW'10*, 1–4, Sydney, NSW, Apr. 2010.
11. Papadogiannis, A., E. Hardouin, and D. Gesbert, "Decentralising multicell cooperative processing: A novel robust framework," *EURASIP J. Wireless Communications and Networking*, Vol. 2009, 1–10, Aug. 2009.

Path Loss Model with Multiple-antenna

Hae-Gyu Park[1], **Hongsik Keum**[2], **and Heung-Gyoon Ryu**[1]

[1]Department of Electronic Engineering, Chungbuk National University, South Korea
[2]ElectroMagnetic Wave Technology Institute, RAPA, South Korea

Abstract— In this paper, we propose a path loss model with the multiple antennas using diversity effect. Currently wireless communication systems use the multiple antennas in order to improve the channel capacity or diversity gain. However, until recently, many researches on path loss model only consider geographical environment between the transmitter and the receiver. There is no study about path loss model considering diversity effect. Nowadays wireless communication use the multiple antennas and we in common find examples using diversity scheme that is method in order to enhance a channel capacity. Moreover we anticipate that it work harder in future researches. But in this communication system, path loss model isn't established that predict strength of received signal. So, in order to predict strength of received signal, we take changing SNR by diversity gain. When exceeding the number of antennas of receiver are 7 in proposed model, diversity effect is saturated. Therefore we consider the number of antenna of receiver until 10. We find RMSE between proposed model and value of calculation is 1. We calculate the diversity gain by conventional BER curve. Proposed model can predict loss of received signal in system using multiple antennas system using multiple antennas.

1. INTRODUCTION

With the rapid development of technology and human civilization, in the downtown area, it is easy to find a high structure. Due to the effect of various objects, multi path effect is occurred and it has brought the fading effect.

For this reason, we can use diversity to raise the lowering of transmission quality and meet maximally the users' needs that desire the high quality. In the diversity mechanics, there are several methods, such as space diversity using two antennas that are separated in two or more, polarization diversity receiving horizontal polarization and vertical polarization separately, frequency diversity using two or more frequencies at the same time.

In this paper, we used the space diversity which utilizes multiple antennas. We used this, because of techniques that improve the communication capacity proportional to the number of antennas such as MIMO. MIMO is currently being used in the fourth generation movement communication, besides we can easily find the case that using multi-antenna like MRC (Maximal Ratio Combining) [1] technique, STBC (Space-Time Block Code) [2]. At present, there are many models for analyzing the loss of the current path, but some models have difficulty in order to apply the variety of environment comprehensively Representative such as Hata model [3, 4] which is path loss model, the research about the model for predicting the path loss of receiver's and transmitter's in an environment of urban and suburban which is urbanized and open area, has been proceeded [5, 6]. However, studies in a system environment using multiple antennas, has been considered relatively less. Therefore, it is necessary to model the path loss model by analyzing diversity gain accurately using multiple antennas. In this paper, we will explain the receive diversity and general loss model which is basis of this study. If there are 10 or more antennas, the effect of diversity converges to a constant value, in the proposed path loss models we take into account 10 antennas. Also, we consider the BER of the received signal, from to which is guaranteed the guarantee QoS (Quality of Service). In Rayleigh channels, we analyze the proposed model by divided into two environments that the case of using modulation schemes of BPSK (Binary Phase Shift Keying) and QPSK (Quadrature Amplitude Modulation). It modeled the path loss model using interpolation and curve fitting.

2. RECEIVE DIVERSITY

Using receiver has many antennas; receiver diversity scheme has a diversity gain. That is to say it is system using one transmit antenna and multiple receive antennas [7]. When non-selective fading channel, SIMO (single input multiple output) channel is given by

$$H = [h_1 \ h_2 \ \ldots \ h_{N_R}]^T \tag{1}$$

When transmit signal is, reception signal is given by

$$y = \sqrt{E_s}Hx + z \tag{2}$$

Here, y is reception signal vector of $N_R \times 1$, z is AWGN having characteristic of $E\{zz^H\} = N_0 I_{N_R}$. There are several main synthesis scheme which is a SC (selection combining), MRC (maximal ratio combining) and EGC (Equal gain combining). MRC scheme apply independent superposition to all branch [7]. Superposition value is calculated by SNR of each branch. When superposition value of each branch is and receive signal is from each branch.

$$y_{\mathrm{MRC}} = \sum_{i=1}^{N_R} G_i y_i \tag{3}$$

Here, transmit signal is $y_i = h_i x_i + n_i$, $E\{|x_i^2|\} = 2E$. n_i has of power spectrum, which is noise component from each branch. So we present as follows

$$y_{\mathrm{MRC}} = \sum_{i=1}^{N_R} G_i h_i x_i + \sum_{i=1}^{N_R} G_i n_i \tag{4}$$

After applied MRC scheme, power spectrum is given by

$$S_v = 2N_0 \sum_{i=1}^{N_R} |G_i|^2 \tag{5}$$

And momentary signal power is given by

$$P = 2E_s \left| \sum_{i=1}^{N_R} |G_i h_i|^2 \right| \tag{6}$$

Calculated average SNR of each branch based on the result is given by

$$\rho_{\mathrm{MRC}} = \frac{E_s \left| \sum\limits_{i=1}^{N_R} |G_i h_i|^2 \right|}{N_0 \sum\limits_{i=1}^{N_R} |G_i|^2} \tag{7}$$

Equation (8) is Cauchy-Schwartz's theorem.

$$\left| \sum_{i=1}^{N_R} |a_i b_i|^2 \right| \leq \sum_{i=1}^{N_R} |a_i|^2 \sum_{i=1}^{N_R} |b_i|^2 \tag{8}$$

When we exactly recognize channel information, the SNR of each branch is given by

$$\rho_{\mathrm{MRC}} = \frac{E_S}{N_0} \sum_{i=0}^{N_R} |G_i| \tag{9}$$

3. PATH LOSS MODEL WITH MULTIPLE-ANTENNA

Structure of array receiver's antenna is Figure 1 in this paper. Path Loss Model with multiple-antenna is modeled by target BER, the number of receive antennas and SNR that is connected with mutual characteristic. A Theoretical calculation of proposed model is simulated by MATLAB. Table 1 shows equation parameter in MATLAB.

Using MRC scheme in BPSK and QPSK at Rayleigh channel, non-selective fading channel, BER is calculated by a under processing.

$$P_b = \frac{1}{k} \left(\sum_{i=1}^{M/2} \left(w_i' \right) P_i \right) \tag{10}$$

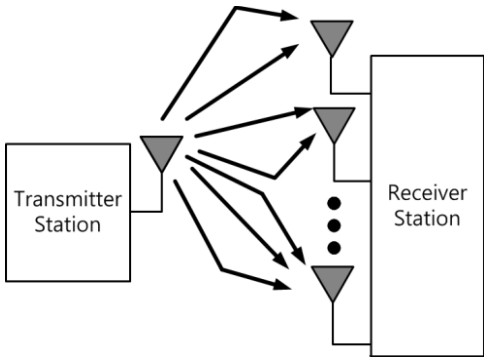

Figure 1: Structure of array receiver's antenna.

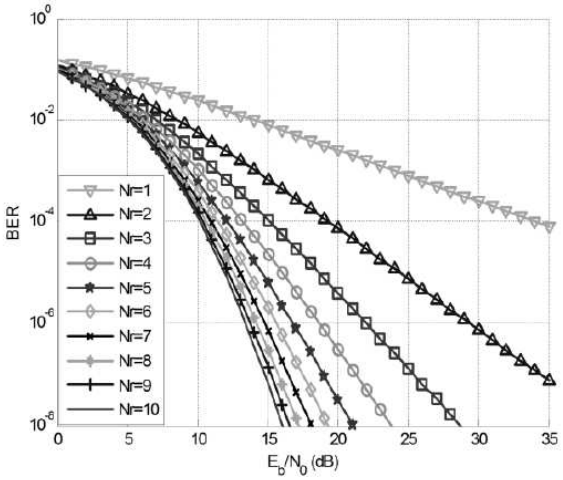

Figure 2: BER curve by the number of N_R.

Table 1: Parameter in equation.

Size of modulation constellation	M
Number of bits per symbol	k
Bit error rate	P_b
Power of the fading amplitude r	$\Omega = E[r^2]$, where $E[\cdot]$ denotes statistical expectation
Number of diversity branch	L
SNR per symbol per branch	$\overline{r_l} = (\Omega_l)\frac{kE_b}{N_0}/L$
Moment generating function for each diversity branch	$M_{r_l}(s) = \frac{1}{1-s\overline{r_l}}$

where, $w_i' = w_i + w_{M-i}$, $w_{M/2} = w_{M/2}$, w_i is a Hamming weight assigned symbol i.

$$P_i = \frac{1}{2\pi}\int_0^{\pi(1-(2i-1)/M)}\prod_{l=1}^{L} M_{r_l}\left(-\frac{kE_b}{N_0}\frac{\sin^2\left[(2i-1)\pi/M\right]}{\sin^2\theta}\right)d\theta - \frac{1}{2\pi}\int_0^{\pi(1-(2i+1)/M)}\prod_{l=1}^{L} M_{r_l}\left(-\frac{kE_b}{N_0}\frac{\sin^2\left[(2i+1)\pi/M\right]}{\sin^2\theta}\right)d\theta \quad (11)$$

We use Figure 2 shows BER calculated by Equation (10) and Equation (11) in BPSK and QPSK ($M = 2$ or 4) at Rayleigh fading channel.

When target BER, P_b is 10^{-4}, Figure 3 shows errors comparing $G(N_R)$ by curve fitting with theoretical calculation values. Table 4 shows $G(N_R)$ defined by curve fitting depending on each target BER, $P_bG(N_R)$ showing at Table 4 can presents $G(N_R) = a/N_R^b \cdot \log_{10}(N_R) + c$ using three coefficient. And the coefficient a, b, c is changed by target BER. We can analyze that three coefficients is result of function like $a, b, c = f(\text{BER})$ and the coefficient is estimated by an interpolation. Table 5 shows results estimated varying coefficient depending on target BER by interpolation.

We can find that path loss is changed by target BER and the number of antennas and finally, proposed path loss model with both elements is given by

$$G(N_R, \text{BER}) = \frac{13.2525\,|\log_{10}(\text{BER})| - 9.115}{N_R^{-0.005|\log_{10}(\text{BER})|+0.37}} 10\log_{10}(N_T) + 0.323(|\log_{10}(\text{BER})| - 0.34)^{1.75} + 0.357\,|\log_{10}(\text{BER})| - 0.326 \quad (12)$$

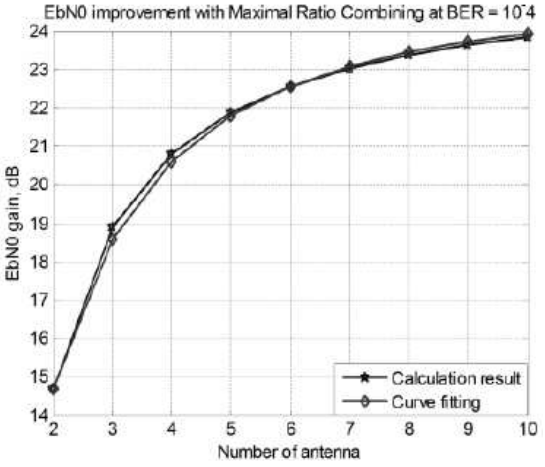

Figure 3: Curve fitting at BER $= 10^{-4}$.

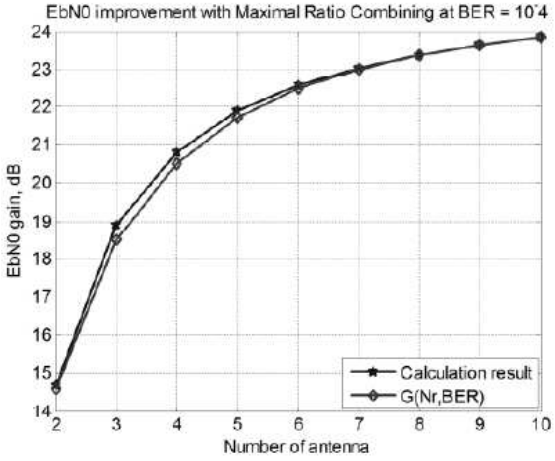

Figure 4: Curve fitting at $G(N_R, \mathrm{BER})$.

Table 2: Gain of signal strength by the number of N_R.

N_R	E_b/N_0	Gain of signal strength
1	33.981	0
2	19.284	14.697
3	15.082	18.899
4	13.174	20.807
5	12.103	21.878
6	11.419	22.562
7	10.948	23.033
8	10.603	23.378
9	10.34	23.641
10	10.133	23.848

Table 3: Gain of signal strength at target BER.

N_R	$P_b = 10^{-2}$	$P_b = 10^{-3}$	$P_b = 10^{-4}$	$P_b = 10^{-5}$	$P_b = 10^{-6}$
1	0	0	0	0	0
2	5.389	9.861	14.697	19.631	24.612
3	6.916	12.643	18.899	25.383	31.965
4	7.624	13.91	20.807	27.995	35.308
5	8.032	14.633	21.878	29.445	37.207
6	8.296	15.094	22.562	30.383	38.396
7	8.481	15.414	23.033	31.019	39.211
8	8.618	15.649	23.378	31.485	39.803
9	8.723	15.829	23.641	31.837	40.251
10	8.806	15.972	23.848	32.114	40.602

4. SIMULATION AND ANALYSIS

Table 6 shows parameter of simulation in order to confirm an accuracy of proposed model.

Figure 4 shows errors compared theoretical calculation result with proposed the path loss model in BPSK and QPSK using the Equation (12). When the target BER is $P_b = 10^{-6}$, each coefficient of $G(N_R, \mathrm{BER})$ is $a = 43.893$, $b = 0.35$, $c = 402302$. So $G(N_R, \mathrm{BER})$ is $\frac{43.895}{N_R^{-0.35}} 10\log_{10}(N_T) + 4.2302$. Biggest error of $G(N_R, \mathrm{BER})$ is 0.411 dB at three antennas and we can conform RMSE is not up

Table 4: $G(N_R)$ by curve fitting.

Target BER	Equation by curve fitting
$P_b = 10^{-2}$	$G(N_R) = \frac{15.41}{N_R^{0.36}} \log(N_R) + 1.52$
$P_b = 10^{-3}$	$G(N_R) = \frac{15.41}{N_R^{0.36}} \log(N_R) + 1.52$
$P_b = 10^{-4}$	$G(N_R) = \frac{15.41}{N_R^{0.36}} \log(N_R) + 1.52$
$P_b = 10^{-5}$	$G(N_R) = \frac{15.41}{N_R^{0.36}} \log(N_R) + 1.52$
$P_b = 10^{-6}$	$G(N_R) = \frac{15.41}{N_R^{0.36}} \log(N_R) + 1.52$

Table 5: Estimating coefficient by interpolation.

Coefficient	Estimating Coefficient by Interpolation
a	$13.2525\lvert\log_{10}(\text{BER})\rvert - 9.115$
b	$-0.005\lvert\log_{10}(\text{BER})\rvert - 0.37$
c	$0.323(\lvert\log_{10}(\text{BER})\rvert - 0.34)^{1.75} + 0.357\,\lvert\log_{10}(\text{BER})\rvert - 0.326$

Table 6: Simulation parameters.

Parameters	Value
Diversity type	Maximal Ratio Combining
Modulation	BPSK or QPSK/16-QAM
Channel	Rayleigh fading channel

to 1. Previous results confirm that we can calculate path loss of communication system with multiple-antenna in BPSK and QPSK using the target BER and the number of receiver antennas.

5. CONCLUSION

In this paper, we propose the path loss model that result from the diversity gain in order to predict path loss of communication system with multiple-antenna. We define using the characteristic of the target BER, SNR, and diversity gain and calculate a change of path loss using the proposed model. The errors are under 1 dB at each number of receiver antennas. The proposed path loss model could be had difference of measured path loss in real practical environment because this model is modeled by the theoretical curve fitting and interpolation. But, this model can predict the path loss of communication system using with multiple-antenna and henceforward this model is a theoretical standard of comparison with measured path loss in real practical environment.

ACKNOWLEDGMENT

This research was supported by Basic Science Research Program through the National Research Foundation of Korea (NRF) funded by the Ministry of Education, Science and Technology (No. 2013 017339).

REFERENCES

1. Lo, T. K. Y., "Maximum ratio transmission," *IEEE International Conference on Communications, 1999, ICC'99*, Vol. 2, 1999.
2. Alamouti, S. M., "A simple transmit diversity technique for wireless communications," *IEEE Journal on Selected Areas in Communications*, Vol. 16, No. 8, 1451–1458, 1998.
3. Okumura, Y., E. Ohmori, T. Kawano, and K. Fukuda, "Field strength and its variability in VHF and UHF land-mobile radio service," *Rev. Elec. Commun. Lab.*, Vol. 16, No. 9, 825–873, 1968.
4. Hata, M., "Empirical formula for propagation loss in land mobile radio services," *IEEE Transactions on Vehicular Technology*, Vol. 29, No. 3, 317–325, 1980.
5. Traveset, J. V., G. Caire, E. Biglieri, and G. Taricco, "Impact of diversity reception on fading channels with coded modulation. I. Coherent detection," *IEEE Transactions on Communications*, Vol. 45, No. 5, 563–572, 1997.

6. Tarokh, V., N. Seshadri, and A. R. Calderbank, "Space-time codes for high data rate wireless communication: Performance criterion and code construction," *IEEE Transactions on Information Theory*, Vol. 44, No. 2, 744–765, 1998.
7. Cho, Y. S., J. Kim, and W. Y. Yang, *MIMO-OFMD Wireless Communications with MATLAB*, 1st Edition, John Wiley & Sons, Inc., 2008.
8. Friis, H. T., "A note on a simple transmission formula," *Proc. IRE*, Vol. 34, No. 5, 254–236, May 1946.
9. Simon, M. K. and M. S. Alouini, *Digital Communication over Fading Channels — A Unified Approach to Performance Analysis*, 1st Edition, Wiley, 2000.
10. Lee, P., "Computation of the bit error rate of coherent M-ary PSK with Gray code bit mapping," *IEEE Transactions on Communications*, Vol. 34, 488–491, 1986.
11. Cho, K. and D. Yoon, "On the general BER expression of one-and two-dimensional amplitude modulations," *IEEE Transactions on Communications*, Vol. 50, No. 7, 1074–1080, 2002.

Coordinated Multi-Point MIMO Processing for 4G

C. Reis[1], **A. Correia**[1,2], **N. Souto**[1,2], **and M. Marques da Silva**[2,3]

[1]ISCTE-Instituto Universitário de Lisboa, Portugal
[2]Instituto de Telecomunicações, Portugal
[3]Universidade Autónoma de Lisboa, Portugal

Abstract— The concept of cooperative Multiple-Input-Multiple-Output (MIMO), also referred to as network MIMO, or as Coordinated Multi-Point Transmission (CoMP), was standardized in 3GPP Release 11. The goal of CoMP is to improve the coverage of high data rates and cell-edge throughput, and also to increase system throughput. In this paper we analyze only the latter scenario, using system level simulations in accordance with 3GPP guidelines. It is shown that the use of joint coordinated multipoint transmission achieves additional throughput gains. However, the gains depend on the scheduling type. This paper also indicates that the criterion of fairness is an important parameter when the number of users is high.

1. INTRODUCTION

4G networks are gaining momentum, and mobile data traffic is growing exponentially with new multimedia applications on smart mobile devices. This new paradigm is putting more stringent demands on the quality of service. In addition to supporting efficiently the signaling and traffic from interactive video and gaming applications, 4G networks also need to handle the signaling and traffic from a multitude of machine-type communication devices.

Heterogeneous networks comprising macrocells and low-power nodes are gaining importance. Macrocells are essential for provision of wide-area coverage and support of high-mobility. The addition of small cells is the mechanism for providing exponential capacity growth to match demand. These and others features are also among the key requirements that have driven the development of LTE Release 11 [1–3]. Features such as CoMP transmission/reception, machine type communication and energy saving are among the new features introduced in Release 11.

This paper presents system level simulations for CoMP transmission considering various 3GPP scenarios. In Section 2, CoMP is introduced, while Section 3 provides a description of the system level simulations. Numerical results and conclusions are then presented in Sections 4 and 5.

2. COORDINATED MULTI-POINT TRANSMISSION

Using CoMP transmission, independent antenna elements of different BSs are grouped together, forming a cluster, and the User Equipments (UE) can experience a throughput increase or performance improvement. A pre-processing is typically employed at the BSs side such that the signals that reach the UE do not require any type of post-processing.

In case each BS uses the MIMO scheme, the resulting MIMO can be viewed as a "giant MIMO", consisting of a combination of independent antenna elements from different BSs (see Figure 1).

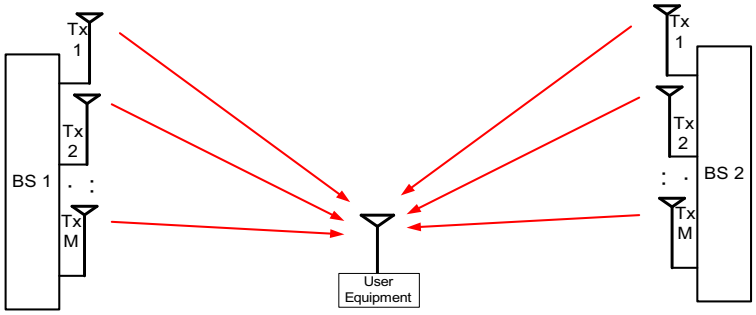

Figure 1: CoMP implemented as a downlink MIMO.

Coordinated multi-point transmission comprises the coordinated transmission of signals from adjacent BSs, and the corresponding reception from a UE. The signal received at the UE side consists of the sum of independent signals sent by different BSs.

CoMP transmission is an important technique that can mitigate inter-cell interference, improve the throughput, exploit diversity and, therefore, improve the spectrum efficiency. Note that CoMP transmission allows a spectrum efficiency improvement, even at the cell edge. CoMP transmission can be viewed as a special type of Multi-User MIMO (MU-MIMO).

Similar to MU-MIMO, a pre-processing such as beamforming, Zero Forcing (ZF), Minimum Mean Square Error (MMSE) or dirty-paper coding is employed, in order to assure that the UE receives a combined signal coming from multiple BSs. In this case, the UE commonly employs a low-complexity and regular detector. Alternatively, a single-user like MIMO detector can be employed at the receiver (UE) or a coordinated scheduling can also be used. In the latter case, CoMP transmission can be associated to carrier aggregation, activating or de-activating some carriers in order to optimize the performance.

Similar to MU-MIMO, accurate downlink Channel State Information (CSI) is typically required at BSs side, which consists of an implementation difficulty. In case of Time Division Duplexing (TDD), obtaining CSI is trivial, as the uplink and downlink channels are almost the same. Nevertheless, in case of Frequency Division Duplexing (FDD), obtaining CSI at the transmitter side is a complex task.

Depending on the way the coordination between different BSs is performed, and the way CSI is obtained (in FDD mode), two different architectures can be implemented:

- Centralized architecture: in this architecture there is a central Control Unit (CU) which decides about the transmission scheme and resources allocation to be used by different BSs. In this case, the CU is connected to different BSs of the cluster. Each UE estimates the downlink CSI of the signals received from each BS. Then, the CSI is sent back to the corresponding BS. At a third stage, CSI is sent from different BSs of the cluster to the CU through backhaul links. Based on CSI, the CU decides about the transmission scheme and resources allocation to be used by each BS, and sends this information to different BSs of the cluster. A major limitation of this architecture relies on the latency, whose factor may result in performance degradation due to fast CSI variations [4].
- Distributed architecture: in this architecture, each BS is associated to a different CU, and the decision about the transmission scheme and resources allocation is performed independently at the BS level. Then, this information is exchanged between the cluster's BSs. In this case, each UE estimates the downlink CSI to different BSs and sends this joint data back not only to the BS of reference, but to all BSs. This way the CU associated to each BS has information about different downlink CSI and makes the decision accordingly. An advantage of this architecture relies on the fact that latency is much reduced, and there is no need to use backhaul links for the purpose of exchanging CSI. Nevertheless, this architecture is more subject to errors caused by the uplink transmission [5].

The primary difference between standard MIMO and CoMP is that, for the latter, the transmitters are not physically co-located. In the case of downlink CoMP there is, however, the possibility of linking the transmitters at baseband to enable sharing of payload data for the purposes of coordinated precoding. For the standard network topology in which the BSs are physically distributed, the provision of a high capacity and low latency baseband link is challenging and would probably require augmentation of the inter-BSs interface bandwidth using fiber. However, a cost-effective solution for inter-BSs connectivity is offered by a network architecture in which the baseband and RF transceivers are located at a central site with distribution of the RF to the Remote Radio Heads (RRH) via fiber. Four downlink deployment scenarios were defined for the feasibility study in Release 11 [6]:

- CoMP scenario 1 corresponds to a homogeneous macro network (all cells have the same coverage area) with intra-site CoMP. This is the least complex form of CoMP and is limited to BSs sharing the same site.
- CoMP scenario 2 is also a homogeneous network but with high Tx-power RRHs. This is an extension of scenario 1 in which the six sites adjacent to the central site are connected via fiber optic links to enable baseband cooperation across a wider area than is possible with scenario 1.
- CoMP scenario 3 is a heterogeneous network in which low power RRHs with limited coverage are located within the macro cell coverage area.

- CoMP scenario 4 is a heterogeneous network in which low power RRHs with limited coverage are located within the macro cell coverage area. The transmission/reception points created by RRHs have the same cell identity as the macro cell scenarios 3 and are expected to be used in metropolitan areas, where network deployment is dense and RRHs of different transmission power levels coexist.

3. SYSTEM LEVEL SIMULATIONS

For the System Level Simulations (SLS), a nineteen cell network topology was used as the baseline network topology, as defined in [7]. In the simulations, only the downlink scenario has been considered. The system is modeled as a network of 7 clusters. Each cluster has 19 hexagonal cells with six cells in the first tier and twelve cells in the second tier surrounding the central cell of each cluster. Each cell has three sectors. To save simulation time the mobile users are only located on the seven cells at the center of the scenario, as illustrated in Figure 2. Mobiles are randomly assigned channel models, following a uniform distribution inside the system. The sector with best path to the user, taking into account slow fading characteristics (path loss, shadowing, and antenna gains) is chosen as the serving sector. Fading signal and fading interference are computed from each mobile station into each sector and from each sector to each mobile for each simulation interval. Moreover, users with a required traffic class shall be modeled according to the traffic models defined in this paper. Finally, packets are scheduled with a packet scheduler using the required scheduling technique. When a packet is lost, a retransmission process is carried out.

Another general description of a SLS is presented in [8].

The ITU-R IMT-Advanced MIMO channel model for SLS is a geometry-based stochastic model. It can also be called double directional channel model. It does not explicitly specify the locations of the scatters, but rather the directions of the rays, like the well-known Spatial Channel Model (SCM) [9]. Geometry-based modeling of the radio channel enables separation of propagation parameters and antennas.

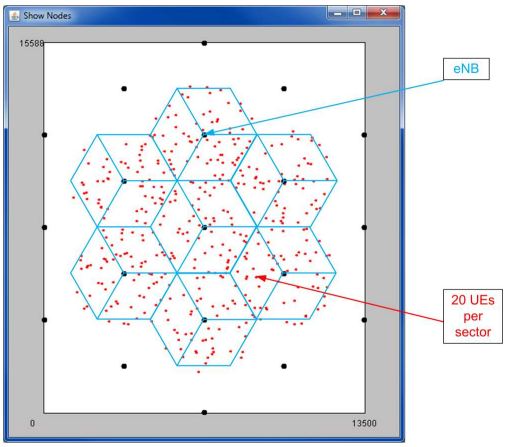

Figure 2: Users distribution inside the scenario.

Several different scenarios will be evaluated, considering different traffic services in Point-to-point (PtP) mode. The single-user SU-MIMO and CoMP scenarios [10] will be evaluated in the next section.

4. NUMERICAL RESULTS

In PtP scenario, every UE is served individually, and the link established by any given UE. If a user does not receive a packet properly, there is the option to retransmit the lost packet. Therefore, in this type of system the coverage is assured. In this scenario, service delay or outage can be experienced (e.g., due to large waiting times when scheduling), being outage one of the aspects that is analyzed here. Another important aspect to study is the overall system capacity, that is, the maximum number of users per cell that the system serves.

Since every UE is individually allocated with resources, and once these are finite, some sort of scheduling mechanism is necessary. Different scheduling mechanisms are tested, using different numbers of UEs in the system to better understand how every scheduling algorithm performs [11].

The scheduler Maximum Carrier-Interference (MCI), also referred to in the literature as 'Maximum SINR', or simply as 'Max C/I', is a channel aware scheduling algorithm where it is given more priority to users with good channel conditions (users located closer to the base-station). The scheduler chooses the user k with maximum Signal-to-Interference plus Noise Ratio (SINR) at instant t. The measurement of SINR is performed via constant periodic Channel Quality Indicator (CQI) feedback by every single user. It is commonly stated that the MCI is not fair because the scheduling decisions do not allocate resources to more delayed users. In this context, there are three 'fair' schedulers: the simple Round Robin (RR), the Proportional Fair (PF), and the Largest Delay First (LDF). In RR, users form a circular queue and the scheduler allocates equal timeslots for each and every user in the queue. PF is channel aware. In fact, we can look at PF as a less aggressive version of Max C/I scheduling algorithm. PF uses CQI feedback sent by users to determine the instantaneous possible data rate a user k can achieve at a given instant t, and also the average throughput a user k had until instant t. This way, users that have instantaneous throughputs higher than their average throughput are scheduled first. LDF takes into consideration first the users experiencing the largest overall delay in packets [13]. This delay is measured using time-stamps that indicate the time of packet creation and/or arrival at the transmission queue for each user. Because users at the cell edge typically experience worst SINR than users at the center of the cell, they can only use lower modulation schemes and coding rates, generally transmitting with lower throughputs than users at the center of the cell, and therefore having longer transmission queues. Consequently, the packets accumulate the highest delays. When LDF is used these users with lower SINR will be scheduled more often than users with high SINR and fairness can be achieved.

The following results cover two traffic models. The File Transfer Protocol (FTP) traffic model emulates the traffic generated by FTP applications. This type of traffic is characterized by having sequences of packet transfers separated by reading times where the receiver checks the data received and decides to request more data to be sent. In FTP traffic, delay is not an important concern (it is not delay sensitive) but overall large waiting times can deteriorate the user experience. The FTP traffic model obeys the characteristics of the model described by 3GPP in [12], and the average load offered to each UE is around 925 kbps. On the other hand, the Constant Bit Rate (CBR) traffic model, as the name indicates, generates always the same amount of data, with exactly the same time intervals between consecutive data. This is the traffic model that comes closer to type of traffic generated in real sector transmissions. CBR traffic model generates a packet of 37,800 bits every 1 ms (millisecond). This represents a traffic generator offering a load of 37,800 kbps per UE and a maximum spectral efficiency per user of 3.7 bps/Hz in a 10 MHz band with MIMO 4×4 [1]. The influence of the type of used scheduling technique and the cell loading are here evaluated.

Figure 3 and Figure 4 show the Cumulative Distribution Function of throughput (CDF(x)) as a function of the throughput, for SU-MIMO 4×4, with eleven CQIs QPSK modulated (Quadrature Phase Shift Keying), and five CQIs 16QAM modulated (Quadrature Amplitude Modulation). The CDF(x) is the probability of the random variable % of UEs with throughput value less than or equal to x. The SU-MIMO considered in this paper refers to the multi-layer transmission initially

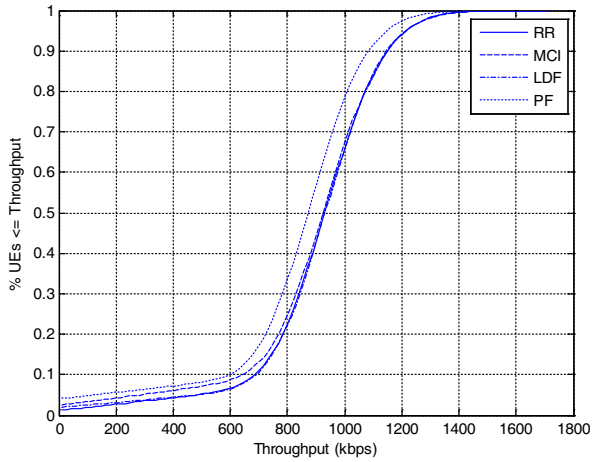

Figure 3: CDF Throughput for 5 users FTP traffic.

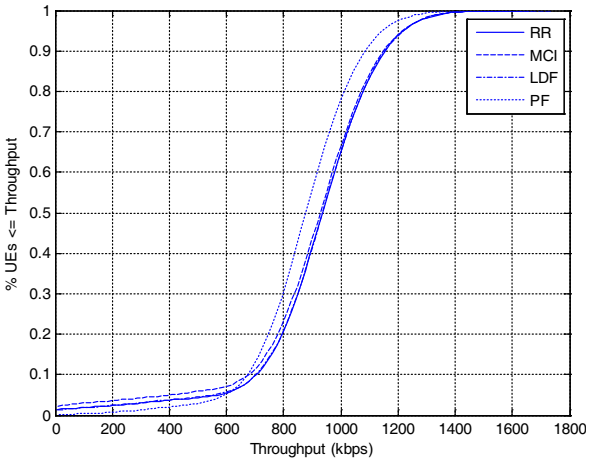

Figure 4: CDF Throughput for 20 users FTP traffic.

proposed by Foschini. The receiver considers a MMSE detector to perform the nulling algorithm, alongside with a Successive Interference Cancellation (SIC) algorithm, to perform the detection of different transmit antennas by their received power descending order.

The FTP traffic and the four different schedulers are considered, where the number of users per sector is 5 and 20, respectively. As can be observed, there is no difference between the schedulers performance with 5 and 20 users because the average load per user is only 925 kbps and SU-MIMO 4×4 offers much higher capacity. For such a traffic load, the CDF(x) is almost independent of the scheduling mechanism.

Figure 5 and Figure 6 depict the CDF(x) of throughput for SU-MIMO 4×4, with the CBR traffic, where the number of users per sector is 5 and 20, respectively. It is obvious the difference between the performance of the schedulers specially with 20 users, because the average load per user is 7,560 kbps and 1,890 kbps for 5 and 20 users, respectively. LDF presents the best performance for 50% of users with 6,500 kbps and 1,750 kbps for 5 and 20 users, respectively. MCI assures throughput values above 8,000 kbps for more than 30% of 5 users and above 6,750 kbps for more than 10% of 20 users. However, for 50% of users, MCI performance is very low. The throughput performance of RR and PF schedulers is between the two extreme cases of LDF and MCI schedulers. For such traffic source with high load, it does matter what the scheduling technique is chosen by the operator in order to assure adequate quality of service.

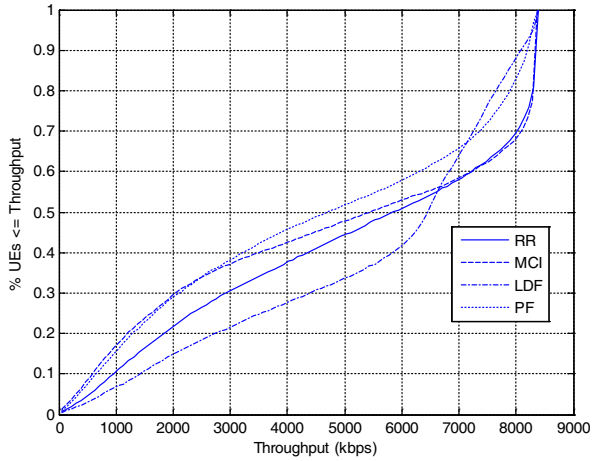

Figure 5: CDF Throughput for 5 users CBR traffic.

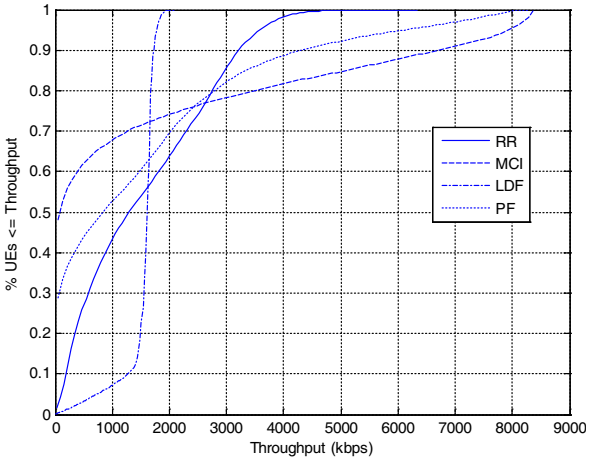

Figure 6: CDF Throughput for 20 users CBR traffic.

Data to a UE is simultaneously transmitted (joint transmission) from multiple points to coherently improve the received signal quality or data throughput. A combination of SU-MIMO with CoMP is employed. We take the simplification of assuming that the quality of CSI is very good (perfect estimation).

Figure 7 depicts the CDF(x) of throughput results for CoMP with SU-MIMO 4×4 (with $M = 4$ transmitting antennas per site), with the same adaptive modulation and coding schemes as before. The same four different schedulers are analyzed, where the number of users per sector is 20. LDF and RR present the best performance for 50% of users with 2,200 kbps for 20 users, followed by PF with 2,000 kbps. MCI assures throughput values above 7,800 kbps for more than 10% of 20 users but for 50% of users the throughput is bellow 1,000 kbps. There is a throughput gain due to CoMP but its computation is not straightforward because it depends on the scheduler. For LDF, the gain for 50% of users is 2,150/1,750 = 1.23, around 23%. For the cell edge users corresponding to the worse 5% of users, the gain is 1,500/750 = 2, around 100%. For RR, there is also throughput gain for 50% and 5% of the users due to CoMP and the way it operates.

Figure 8 depicts the throughput distribution versus the geometry factor of CoMP with SU-MIMO, $M = 4$ per site, and for $Nu = 20$ users per sector. Note that this corresponds to CDF(x) results in the environment of previous Figure 7. The geometry factor was the term used in UMTS to indicate the ratio of the wanted signal relating to the interference plus noise. This corresponds to SINR. Users located closer to the base-station have higher geometry than users located at the cell borders with lower geometry. LDF presents an almost constant throughput independently of the location of the mobiles. The opposite is MCI with a high linear increase of throughput for

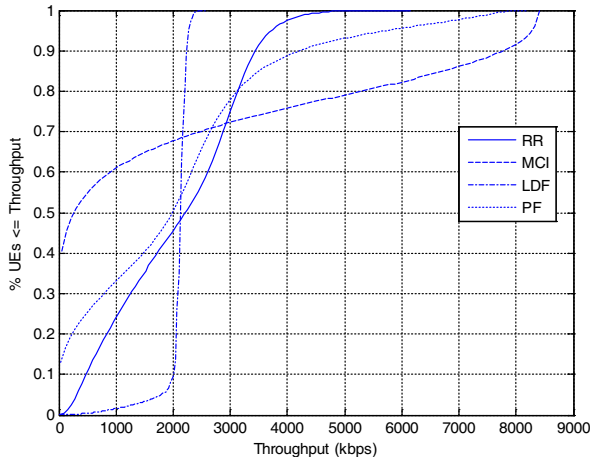

Figure 7: CDF Throughput for 20 users, CBR, CoMP.

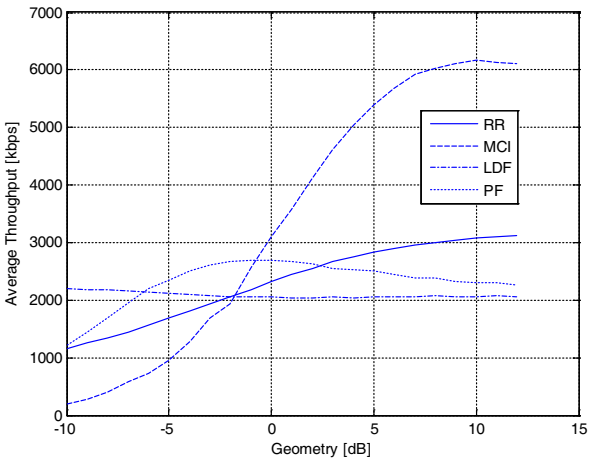

Figure 8: Throughput vs geometry, CoMP, $Nu = 20$.

users moving towards the base station site. RR provides a small linear increase of throughput for increasing geometry values. PF behavior is explained as a mix of MCI and LDF. Consequently, it presents a nonlinear throughput increase with increasing throughput value.

5. CONCLUSIONS

This paper analyzed the influence of the scheduler type and of the cell loading. It was viewed that there is no difference between the schedulers performance when the average load per user is small compared to the higher capacity of MIMO 4×4 transmission scheme. For such a traffic load it does not matter what the chosen scheduler is. In order to increase the spectral efficiency on average and/or at the cell borders, or when the number of users is increasing, CoMP with fair scheduling should be employed.

The use of joint CoMP transmission achieves additional throughput gains. Nevertheless, these gains depend on the scheduling type. The performance results indicate that the criterion of fairness giving priority to users at the cell border is important when the number of users is increasing and CoMP is employed.

ACKNOWLEDGMENT

This work was supported by the FCT (Fundação para a Ciência e Tecnologia) via projects PEst-OE/EEI/LA0008/2013, GLANC EXPL/EEI-TEL/1582/2013, and EnAcoMIMOCo EXPL/EEI-TEL/2408/2013.

REFERENCES

1. 3GPP, "Requirements for further advancements of E-UTRA (LTE-Advanced)," TR 36.913 V11.0.0.
2. 3GPP, "Evolved Universal Terrestrial radio Access (E-UTRA) and evolved Universal Terrestrial Radio Access Network (E-UTRAN); Overall Description; Stage 2," TR 36.300 V11.3.0.
3. 3GPP, "Further advancements for E-UTRA physical layer aspects," TS 36.814, V9.0.0, 2010.
4. Diehm, F., P. Marsch, and G. Fetweeis, "The FUTON prototype: Proof of concept of coordinated multi-point in conjunction with a novel integrated wireless/optical architecture," *Proc. IEEE WCNCW'10*, 1–4, Sydney, NSW, April 2010.
5. Papadogiannis, A., E. Hardouin, and D. Gesbert, "Decentralising multicell cooperative processing: A novel robust framework," *EURASIP J. Wireless Communications and Networking*, Vol. 2009, 1–10, August 2009.
6. 3GPP, "Coordinated multi-point operation for LTE physical layer aspects," TS 36.819, V11.1.0, 2011.
7. ITU-R, "Guidelines for evaluation of radio interface technologies for IMT-Advanced," M.2135, 2008.
8. Marques da Silva, M., A. Correia, R. Dinis, N. Souto, and J. C. Silva, *Transmission Techniques for 4G Systems*, 1st Edition, CRC Press Auerbach Publications, ISBN: 9781466512337, FL, USA, November 2012

9. 3GPP, "Requirements for Evolved UTRA (E-UTRA) and Evolved UTRAN (E-UTRAN)," TR 25.913 v9.0.0, December 2009.
10. Lee J., B. Ng, and D. Mazzarese, "Coordinated mutipoint transmission and reception in LTE-advanced systems," *IEEE Communications Magazine*, 44–50, November 2012.
11. Gomes, P. S., "Scheduling techniques to transmit multi-resolution in E-MBMS services of LTE-advanced," PhD. Thesis, ISCTE-IUL, September 2010.
12. 3GPP, "Feasibility study for orthogonal frequency division multiplexing (OFDM) for UTRAN enhancement (Release 6)," Technical Report TR 25.892 v6.0.0, June 2004.
13. Entrambasaguas, J. T., M. C. Aguayo-Torres, G. Gómez, and J. F. Paris, "Multiuser capacity and fairness evaluation of channel/QoS-aware multiplexing algorithms," *IEEE Network*, Vol. 21, No. 3, 24–30, May–June 2007.

Multiple Input Multiple Output System with Multi User Support Based on Directive Information Transmission

Paulo Carvalho[1, 2, 3], **Mario Marques da Silva**[2, 4], **and Rui Dinis**[1, 2]

[1]DEE, FCT Universidade Nova de Lisboa, Portugal
[2]IT, Instituto de Telecomunicações, Av. Rovisco Pais, Lisboa, Portugal
[3]Uninova, Instituto de Desenvolvimento de Novas Tecnologias
Quinta da Torre, Caparica, Portugal
[4]Universidade Autonoma de Lisboa, Portugal

Abstract— Low interference and privacy are crucial requirements for system reliability and security. Present and further mobile communication systems must support multiple users achieving at same time low interference levels. Several solutions can be adopted to reduce interference between users, such as spreading codes or beam forming. For very high bit rates first solution must be discarded. On the other hand, in environments with a very high number of users beamforming can impose demanding hardware requirements in mobile devices, which is undesirable. Transmitters with directivity introduced at information level where the transmitted constellation is only optimized in the desired direction can also be used to assure low interference. Under this approach, power efficiency on amplification can be also improved, due to the fact that constellations are decomposed into several BPSK (Bi Phase Shift Keying) or QPSK components (Quadri-Phase Shift Keying), being each one separately amplified and transmitted independently by an antenna. Therefore, several users can coexist since each user must know the configuration parameters associated to the constellation configuration, i.e., the direction in which the constellation is optimized, otherwise receives a degenerated constellation with useless data. The simulation results show the effectiveness in user data stream separation of the proposed approach.

1. INTRODUCTION

Performance of wireless communication systems can be compromised by interference. Normally, interference among users is minimized by orthogonalizing the channel so that the BS (base station) communicates with each user in separate time-frequency resources. This reduces overall efficiency and throughput and higher data rates can only be achieved when the BS communicates with several users using same time-frequency resource [1, 2].

MIMO (Multiple-input multiple-output) systems can increase throughput in modern wireless networks and reduce interference [3–5]. One advantage of MIMO systems is the reduction of the transmitted power. On the other hand, the use of multilevel modulations in modern wireless standards leads to high peak-to-average power ratios and further drives the costs of power amplifiers while reducing their efficiency. This problem can be avoided with this new transmission scheme, where the constellations are decomposed into several BPSK, QPSK or OQPSK components (Offset QPSK), being each component amplified and transmitted independently by an antenna. Furthermore, power efficiency can be also improved adopting nonlinear (NL) amplifiers in such operation, which can maximize the power efficiency of the transmission system [6, 7]. Now the coefficients associated to each array element are the coefficients associated to the elementary sub-constellations and each antenna transmits uncorrelated signals. Obviously, in the desired direction of transmission we have the optimized multilevel constellation, otherwise the constellation signal is degenerated. Since the directivity is introduced in the transmitted information, this can be viewed as a scheme where the directivity is implicitly on the constellation's symbols arrangement associated to each transmission direction.

Current MIMO transmitters require a separate RF (Radio frequency) — chain including a power amplifier for each antenna element [8]. Therefore, the transmission scheme resembles to MIMO transmitter structures, since we still have several RF-chains in parallel. However there is a key difference in the concept since each RF chain is associated to a BPSK component of the multilevel constellation that is transmitted. Obviously, the receiver must know the constellation coefficients, associated to the amplification stage as well as the array configuration, otherwise will receive a degenerated signal. Therefore, interference among users can be avoided when the transmissions are only optimized for the directions θ_j associated to the several users.

SC-FDE schemes (Single-Carrier with Frequency-Domain Equalization) [9] are excellent transmission schemes for broadband wireless systems, with low cost transmitters and efficient power amplification when constant or quasi constant envelope modulations are employed. Another drawback of multilevel constellations is their sensitivity to imperfect channel compensation effects (particulary when we have a linear equalizer optimized under the MMSE (Minimum Squared Mean Error)). Additional performance improvements can be achieved by a IB-DFE receiver (Iterative Block Decision Feedback Equalization) [9–11], where both the feedforward and the feedback filters are implemented in the frequency domain. Obviously, IB-DFE receivers should be optimized for multilevel constellations to minimize the residual ISI and IQI (In phase Quadrature Interference) interferences associated to multilevel Offset modulations [12, 13].

This paper is organized as follows: A brief characterization of the theoretical principles behind the structure of the transmitter with directivity at constellation level is made in Section 2. Section 3 characterizes the receivers. A set of performance results is presented in Section 4. Section 5 resumes this paper.

2. CONSTELLATION DECOMPOSITION

Let us consider two OQPSK signals, $x_p(t)$ and $x_{p'}(t)$, with complex envelope given by

$$x_p(t) = \sum_{n'} b_{n'}^{(p)} x^{(p)}(t - n'T), \tag{1}$$

and

$$x_{p'}(t) = \sum_{n'} b_{n'}^{(p')} x^{(p')}(t - n'T). \tag{2}$$

Without loss of generality, we assume the same pulse shape for both signals, i.e., $x^{(p)}(t) = k_p r(t)$ and $x^{(p')}(t) = k_{p'} r(t)$, where $r(t)$ represents a pulse shape that guarantees null ISI at the matched filter's output and k_p and $k_{p'}$ are real coefficients. Combining the signals results for each sampling instant

$$k_p b_{n'}^{(p)} + k_{p'} b_{n'}^{(p')} = s'_{n'}, \tag{3}$$

where s'_n can assume the values $\pm k_p \pm k_{p'}$, $\pm jk_p \pm k_{p'}$, $\pm k_p \pm jk_{p'}$ and $\pm jk_p \pm jk_{p'}$, which correspond to the four sub-sets of 4 symbols from a 16-OQAM (Offset Quadrature Amplitude Modulation) constellation.

Since OQPSK or QPSK constellations are a sum of two BPSK components in quadrature, it turns obvious that the symbols of multilevel constellations can be expressed as function of the corresponding bits as follows[1]:

$$s_n = g_0 + g_1 b_n^{(1)} + g_2 b_n^{(2)} + g_3 b_n^{(1)} b_n^{(2)} + g_4 b_n^{(3)} + \ldots = \sum_{i=0}^{M-1} g_i \prod_{m=1}^{\mu} \left(b_n^{(m)}\right)^{\gamma_{m,i}} = \sum_{i=0}^{M-1} g_i b_n^{eq(m)}, \tag{4}$$

with $b_n^{eq(m)} = \prod_{m=1}^{\mu} (b_n^{(m)})^{\gamma_{m,i}}$. For each $s_n \in \mathfrak{S}$, where $(\gamma_{\mu,i}\, \gamma_{\mu-1,i} \ldots \gamma_{2,i}\, \gamma_{1,i})$ is the binary representation of i and $b_n^{(m)} = 2\beta_n^{(m)} - 1$ where $\beta_n^{(m)}$ denotes the mth bit of the n constellation point. Since we have M constellation symbols in $\mathfrak{S}$ and M complex coefficients g_i, (4) is a system of M equations that can be used to obtain the coefficients g_i, $i = 0, 1, \ldots, \mu - 1$.

Since power-efficient constellations have zero mean, $g_0 = 0$ and are only necessary $M - 1$ BPSK signals to generate a given constellation. Moreover, M-QAM constellation's symbols can be characterized with only $\log_2(M)$ BPSK signals, with all the remaining g_i coefficients null. For instance, the 16-OQAM with Gray mapping only needs four BPSK signals (associated to the set of non-zero complex coefficients $g_2 = 2j$, $g_3 = j$, $g_8 = 2$ and $g_{12} = 1$) or two QPSK or OQPSK constellations.

Let us to use (4) to describe the transmitted signal $x(t)$ as

$$x(t) = \sum_{n=0}^{N-1} \sum_{m=0}^{M-1} g_i b_n^{eq(m)} r(t - nT). \tag{5}$$

[1] It should be noted that s_n denotes the nth constellation point and not the nth transmitted symbol.

This means that any M-OQAM constellation can be decomposed as the sum of several components with quasi-constant or constant envelope, that can be separately amplified with an non-linear amplifier. The transmitter will have in parallel M RF branches, each one with a NL amplifier followed by an antenna, that transmit the M BPSK uncorrelated signals (i.e., the components of multilevel constellation), as shown in Figure 1. It is also assumed that each succeeding element has a $\alpha_i = 2\pi i \cos(\frac{\pi}{2} + \Theta)\frac{d}{\lambda}$ has a progressive phase of the supply current relative to the previous element. We have equal spaced isotropic antennas with $d/\lambda = 1/4$ (it should be noted that the current magnitudes at different antennas depend on the amplification coefficients associated to the constellation decomposition). Obviously the BPSK components in the amplification branches are uncorrelated, which means that the resulting radiation pattern is still omnidirectional. Therefore, the directivity is only introduced at the transmitted information through a rearrangement of the constellation symbols according to the direction θ. It is possible to define an equivalent Array Factor (AF) GA as

$$G_A = \sum_{i=1}^{M} g_i \exp\left(j\alpha_i\right), \tag{6}$$

From (6) it becomes obvious that each sub-constellation suffers a different rotation that depends on the antenna position in the array. By changing the phase of each RF branch, α_i, the directivity

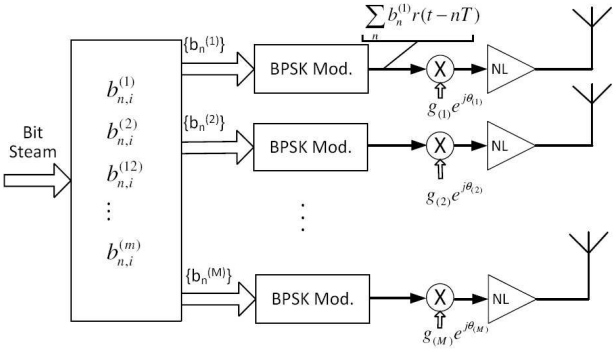

Figure 1: Structure of constellation directive transmitter.

Table 1: Gain values for Sort=LINEAR.

Sort=LINEAR			Sort=CENTER		
Gain	QAM	VORONOI	Gain	QAM	VORONOI
g_0	2j	$0.717 + j0.546$	g_0	0	$-0.100 + j0.075$
g_1	2	$-0.588 + j0.572$	g_1	0	$-0.014 - j0.124$
g_2	j	$0.359 + j0.273$	g_2	0	$-0.014 - j0.124$
g_3	1	$-0.186 + j0.273$	g_3	0	$0.086 - j0.199$
g_4	0	$-0.201 + j0.149$	g_4	0	$0.086 - j0.199$
g_5	0	$0.029 + j0.248$	g_5	0	$-0.201 + j0.149$
g_6	0	$0.086 - j0.199$	g_6	j	$0.359 + j0.273$
g_7	0	$0.086 - j0.199$	g_7	2j	$0.717 + j0.546$
g_8	0	$0.086 - j0.199$	g_8	2	$-0.588 + j0.572$
g_9	0	$0.086 - j0.199$	g_9	1	$-0.186 + j0.273$
g_{10}	0	$-0.014 - j0.124$	g_{10}	0	$0.029 + j0.248$
g_{11}	0	$-0.100 + j0.075$	g_{11}	0	$0.086 - j0.199$
g_{12}	0	$-0.014 - j0.124$	g_{12}	0	$0.086 - j0.199$
g_{13}	0	$-0.100 + j0.075$	g_{13}	0	$-0.100 + j0.075$
g_{14}	0	$-0.100 + j0.075$	g_{14}	0	$-0.100 + j0.075$
g_{15}	0	0.000	g_{15}	0	0.000

can be increased and the constellation can be optimized for the desired direction. This leads to a directivity in the transmitted information since the constellation will be only optimized in the desired direction. It should be mentioned that there isn't a fixed arrangement of the several BPSK components in the transmitter. However, here we consider two possible arrangements for the BPSK components of 16 QAM and 16-Voronoi constellations whose sort order along the RF branches are presented in Table 1. The transmitter's structure is similar to the MIMO's structure where M uncorrelated data streams for M users are sent at same time. However, here the bit rate do not increases by a factor of M, since the signals from the different branches are components of the multilevel constellation transmitted to a user.

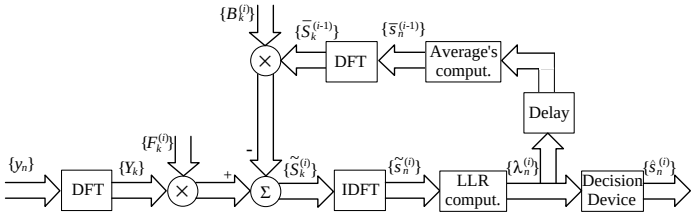

Figure 2: IB-DFE receiver with soft decisions.

3. RECEIVER

At receiver's side we may have a similar structure with M antennas in parallel, followed by a combiner that reconstructs the transmitted constellation symbol. Obviously at each branch the coefficients compensate the phase rotation due to channel's delay and the phase rotations associated to the array configuration of the transmitter. The combiner is followed by a IB-DFE receiver whose structure is depicted in Figure 2. We assume an ideal linear transmitter (this can be achieved with the transmitter structure of Figure 1, with constant envelope signals in each amplification branch). The signal associated to a given block is

$$s(t) = \sum_{n=-N_G}^{N-1} s_n h_T(t - nT_S), \tag{7}$$

with T_S denoting the symbol duration, N_G denoting the number of samples at the cyclic prefix, N denoting the number of samples at the useful part of the block and $h_T(t)$ denoting the adopted pulse shape. The nth transmitted symbol[2] s_n belongs to a given size-M constellation $\mathfrak{S}$. As usual, the cyclic prefix corresponds to a periodic extension of the useful part of the block, i.e., $s_{-n} = s_{N-n}$ with a length higher than the overall channel impulse response.

At the receiver the samples associated to the cyclic prefix are discarded, which means null IBI (Inter Block Interference) and reduces the impact of a time-dispersive channel to a scaling factor for each frequency. Thus, the corresponding frequency-domain block is $\{Y_k; k = 0, 1, \ldots, N-1\} = \text{DFT}\,\{y_n; n = 0, 1, \ldots, N-1\})$, where

$$Y_k = S_k H_k + N_k, \tag{8}$$

with H_k denoting the channel frequency response for the kth subcarrier and N_k the corresponding channel noise.

For a given iteration the output samples are given by

$$\tilde{S}_k = F_k Y_k - B_k \bar{S}_k, \tag{9}$$

where $\{F_k; k = 0, 1, \ldots, N-1\}$ and $\{B_k; k = 0, 1, \ldots, N-1\}$ denote the feedforward and the feedback coefficients, respectively, and $\{\bar{S}_k; k = 0, 1, \ldots, N-1\}$ is the DFT of the block $\{\bar{s}_n; n = 0, 1, \ldots, N-1\}$, with $\bar{s}_n$ denoting the average value of s_n conditioned to the FDE output associated to the previous iteration. It can be shown that the optimum coefficients F_k and B_k are given by (see [14, 15])

$$F_k = \frac{\kappa H_k^{\circ}}{E[|N_k|^2]/E[|S_k|^2] + (1-\rho^2)|H_k|^2}, \tag{10}$$

[2]It should be pointed out that we have a slight abuse of notation, since in this section s_n designates the nth transmitted symbol of the block, while in Section 2 s_n designates the nth symbol of the constellation.

and

$$B_k = F_k H_k - 1, \tag{11}$$

respectively, with κ selected to ensure that $\sum_{k=0}^{N-1} F_k H_k / N = 1$. The correlation coefficient ρ [15], is given by

$$\rho = \frac{E[\hat{s}_n s_n^{\circ}]}{E[|s_n|^2]} = \frac{\sum_{i=0}^{M-1} |g_i|^2 \prod_{m=1}^{\mu} \left(\rho_n^{(m)}\right)^{\gamma_{m,i}}}{\sum_{i=0}^{M-1} |g_i|^2}, \tag{12}$$

where $\rho_n^{(m)} = |\tanh(\frac{\lambda_n^{(m)}}{2})|$ represents the reliability of the mth bit of the nth transmitted symbol. $\lambda_n^{(m)}$ is the log-likelihood ratio of the mth bit for the nth transmitted symbol given by

$$\lambda_n^{(m)} = \log\left(\frac{\sum_{s\in\Psi_1^{(m)}} \exp\left(-\frac{|\tilde{s}_n - s|^2}{2\sigma^2}\right)}{\sum_{s\in\Psi_0^{(m)}} \exp\left(-\frac{|\tilde{s}_n - s|^2}{2\sigma^2}\right)}\right), \tag{13}$$

where $\Psi_1^{(m)}$ and $\Psi_0^{(m)}$ are the constellation's subsets associated to the symbols with the m(th) bit at 1 or 0, respectively. $\{\tilde{s}_n;\ n = 0,\ 1,\ \ldots,\ N-1\}$ denotes the IDFT of $\{\tilde{S}_k;\ k = 0,\ 1,\ \ldots,\ N-1\}$, i.e., the $\tilde{s}_n$ are the time-domain samples at the FDE output. In (13) σ^2 denotes the variance of the noise at the FDE output, i.e.,

$$\sigma^2 \approx \frac{1}{2N} \sum_{n=0}^{N-1} E\left[\left|\hat{s}_n - \tilde{s}_n\right|^2\right], \tag{14}$$

where $\hat{s}_n$ denotes the hard decisions associated to s_n.

Since we have uncorrelated BPSK components, according to [15] we may write

$$\bar{s}_n = \sum_{i=0}^{M-1} g_i \prod_{m=1}^{\mu} \left(\tanh\left(\frac{\lambda_n^{(m)}}{2}\right)\right)^{\gamma_{m,i}}. \tag{15}$$

4. PERFORMANCE RESULTS

In simulations we considered a SC-FDE modulation with blocks of $N = 256$ useful symbols plus a cyclic prefix of 32 symbols longer than overall delay spread of the channel. The modulation symbols belong to a M-QAM or M-Voronoi constellation (dimensions of $M = 16$ and $M = 64$ are considered) and the transmitted data is mapped on constellation's symbols to optimize energy efficiency. The antennas are equal spaced by $d/\lambda = 1/4$ and the amplifiers gains of the antennas follow the sort order of Table 1 for linear and centered arrangements, respectively (under these conditions the directivity in the transmitted constellation is assured by phase rotations of the BPSK components). AWGN channel and a severely time-dispersive channel are considered. The second is characterized by an uniform PDP (Power Delay Profile), with 32 equal-power taps, with uncorrelated rayleigh fading on each tap. For both channels it is assumed a scenario with several users where each user only knows the transmission parameters regarding his data stream. Thus, each user is able to configure the receiver with the correct coefficients $g_i \alpha_i'$ to compensate the information directivity inherent to the transmitted constellation.

It is also assumed linear power amplification at the transmitter, perfect synchronization and channel estimation at the receiver. Performance results are expressed as function of $\frac{E_b}{N_0}$, where N_0 is the one-sided power spectral density of the noise and E_b is the energy of the transmitted bits.

To have a clear idea of the impact on performance of angle errors against the direction in which the constellation is optimized we start with the AWGN channel. Figures 3 and 4 refer the results for constellations with 16 and 64 symbols, respectively. As we can see the impact of constellation's directivity on system's performance increases significantly with the size of the constellation and, as expected, a higher directivity is assured by Voronoi constellations with a linear arrangement (as we can see from figures the impact of any angle error against θ is higher in Voronoi constellation and grows with the size of the constellations). Obviously, the impact of those angle errors is higher for constellations that are decomposed in a higher number of sub-constellations, which is the case of Voronoi constellations. This means that by increasing the spectral efficiency of the system we can

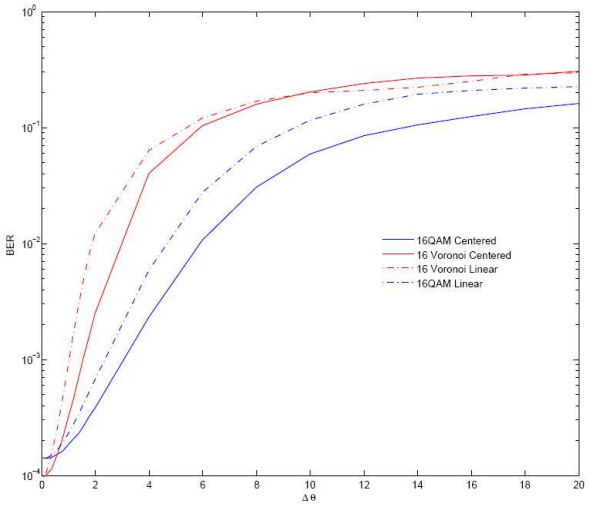

Figure 3: Impact of an angle error regarding the transmission direction θ in BER performance of size-16 constellations using linear and centered arrangements. ($E_b/N_0 = 12\,\text{dB}$ for both constellations types.

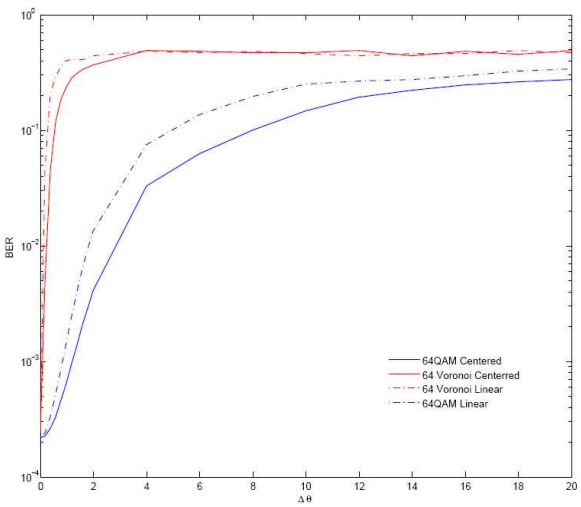

Figure 4: Impact of an angle error regarding the transmission direction θ in BER performance of size-64 constellations using linear and centered arrangements. ($E_b/N_0 = 16\,\text{dB}$ for both constellations types.

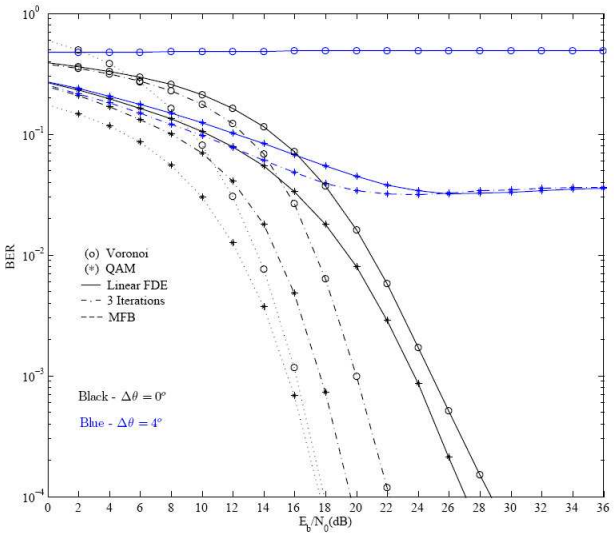

Figure 5: Linear array: BER performance for size-64 constellations with a frequency selective channel and an angle error regarding to transmission direction θ.

assure a better separation of the data streams transmitted for the different users. For that reason, in the following results we only consider constellations' sizes of 64.

Figure 5 shows the BER (Bit error rate) performance results for both constellations types with 64 symbols for a severely time-dispersive channel and a linear arrangement. As we can see from this figure, when the angle error is null for 3 iterations the performance is close to the matched filter bound (MFB). This means that the degradation on system's performance is mainly due to errors on the angle estimation in which the constellation is optimized. It becomes clear that due directivity other users are unable to decode efficiently the transmitted data to the user i when they do not know the direction θ_i, despite the power level of the sent signal. We can compare this scenario to a CDMA (Code Division Multiple access) case, where all the users transmit orthogonal data streams with the same power, but now the separation is assured by constellation directivity instead orthogonal spreading sequences. From the results, it becomes obvious that the best choice are Voronoi constellations since the system directivity is higher due to higher number of RF branches needed to decompose these constellations. Obviously, this leads to a more sensitive system to the direction θ associated to each user and achieves a lower interference among users.

5. CONCLUSIONS

In this paper we considered a transmission system comparable with MIMO that allow independent transmissions among several users by using directivity at information level. The results showed that due to the directivity in the transmitted constellations any angle error against the desired direction θ in which the information is optimized has a major impact in system performance and the ability to decode the information. This means that other users are unable to decode with success data streams belonging to other users. Moreover, the separation between users can increase with higher spectral efficiencies. Besides the aspects already mentioned, this approach assures also better power efficiency given that the decomposition of multilevel constellations into constant envelope signals.

ACKNOWLEDGMENT

This work was supported in part by CTS multi-annual funding project PEst-OE/EEI/UI0066/2011, IT multi-annual funding project PEst-OE/EEI/LA0008/2013, GALNC EXPL/EEI-TEL/1582/2013, EnAcoMIMOCo EXPL/EEI-TEL/2408/2013 and CoPWIN PTDC/EEI-TEL/1417/2012 GALNC (EXPL/EEI-TEL/1582/2013).

REFERENCES

1. Andrews, J. G., "Interference cancelation for cellular systems: A conterporary overview," *IEEE Wireless Comm.*, Vol. 12, No. 2, 19–29, Ap. 2005.
2. Yan, X., X. Wang, G. Leus, G. Yue, and J. Jiang, "Interference management in wireless communication systems: Theory and applications," *EURASIP Journal on Wireless Communications and Networking*, Vol. 2010, Hindawi Publishing Corp., New York, NY, United States, Jan. 2010.
3. Goldsmith, A., S. A. Jafar, N. Jindal, and S. Vishwanath, "Capacity limits of MIMO channels," *IEEE J. Select. Areas Commun.*, Vol. 21, No. 5, 684–702, 2003.
4. Gesbert, D., M. Kountouris, R. W. Heath, Jr., C. B. Chae, and T. Slzer, "Shifting the MIMO paradigm: From single user to multiuser communications," *IEEE Signal Processing Magazine*, Vol. 24, No. 5, 36–46, Oct. 2007.
5. Marques da Silva, M. and F. A. Monteiro, *MIMO Processing for 4G and Beyond: Fundamentals and Evolution,* CRC Press Auerbach Publications, FL, USA, May 2014, ISBN: 9781466598072, http://www.crcpress.com/product/isbn/9781466598072.
6. Montezuma, P. and A. Gusmão, "Design of TC-OQAM schemes using a generalised nonlinear OQPSK-type format," *IEE Elect. Letters*, Vol. 35, No. 11, 860–861, May 1999.
7. Astucia, V., P. Montezuma, R. Dinis, and M. Beko, "On the use of multiple grossly nonlinear amplifiers for higly efficient linear amplification of multilevel constellations," *Proc. IEEE VTC2013-Fall*, Las Vegas, NV, US, Sep. 2013.
8. Tse, D. N. C. and P. Viswanath, *Fundamentals of Wireless Communications,* Cambridge University Press, Cambridge, UK, 2005.
9. Benvenuto, N. and S. Tomasin, "Block iterative DFE for single carrier modulation," *IEE Elect. Letters*, Vol. 39, No. 19, 1144–1145, Sep. 2002.
10. Dinis, R., R. Kalbasi, D. Falconer, and A. Banihashemi, "Iterative layered space-time receivers for single-carrier transmission over severe time-dispersive channels," *IEEE Comm. Letters*, Vol. 8, No. 9, 579–581, Sep. 2004.
11. Benvenuto, N. and S. Tomasin, "Iterative design and detection of a DFE in the frequency domain," *IEEE Trans. on Comm.*, Vol. 53, No. 11, 1867–1875, Nov. 2005.
12. Luzio, M., R. Dinis, and P. Montezuma, "On the design of linear receivers for SC-FDE schemes employing OQPSK modulation," *Proc. IEEE VTC2010-Fall*, Ottawa, Sep. 2010.
13. Luzio, M., R. Dinis, and P. Montezuma, "On the design of iterative FDE receivers for OQAM modulations," *IEEE GLOBECOM'10 — BSCFDC Workshop*, Miami, Apr. 2010.
14. Gusmão, A., P. Torres, R. Dinis, and N. Esteves, "A turbo FDE technique for reduced-CP SC-based block transmission systems," *IEEE Trans. on Comm.*, Vol. 55, No. 1, 16–20, Jan. 2007.
15. Dinis, R., P. Montezuma, N. Souto, and J. Silva, "Iterative frequency-domain equalization for general constellations," *IEEE Sarnoff Symposium*, Princeton, USA, Apr. 2010.

Channel Capacity Experiment of a Polarization Controlled MIMO Antenna for Wearable Applications

Kun Li, Kazuhiro Honda, and Koichi Ogawa
Graduate School of Engineering, Toyama University
3190 Gofuku, Toyama-shi, Toyama 930-8555, Japan

Abstract— This paper presents a preliminary experiment for evaluating the channel capacity of a 2×2 polarization-controlled MIMO antenna that takes the variation of the radio wave propagation environment and the antenna inclination angle into consideration simultaneously. Firstly, the radiation pattern of a 2×2 polarization-controlled MIMO antenna was measured in an anechoic chamber. Then, the MIMO channel capacity measurement has been carried out under different use scenarios using an OTA apparatus. From an agreement between the measured data and analytical results, the effectiveness of the proposed antenna was confirmed.

1. INTRODUCTION

A Small Cell era is coming for realizing ultra-high-capacity mobile communications using multiple-input multiple-output (MIMO) technique as a result of the development of LTE, LTE-Advanced and Beyond 4G cellular systems. Since mobile terminals are used close to base stations in the urban area, the cross polarization power ratio (XPR) will increase and vary significantly. Further, a polarization mismatch will also occur easily due to the variation in the inclination angle of an antenna caused by the operator's dynamic motions. In order to solve such difficulties, we proposed a 3-axis weighted-polarization active antenna that can realize a large-capacity transmission in wearable radio applications in an analytical way [1].

For the purpose of confirming the validity of the proposed antenna, this paper presents a preliminary experiment for evaluating the channel capacity of a polarization-controlled MIMO antenna. Firstly, the configuration of the proposed 3-axis weighted-polarization active antenna is introduced. Then, the radiation pattern of the 2×2 polarization-controlled MIMO antenna was measured in an anechoic chamber. Finally, the MIMO channel capacity measurement has been carried out under different use scenarios using an OTA apparatus. From an agreement between the measured data and analytical outcomes, the effectiveness of the proposed antenna is verified, demonstrating that the proposed antenna is useful for realizing the gigabit mobile communications in forthcoming high-speed and wearable mobile applications.

2. 3-AXIS WEIGHTED-POLARIZATION ACTIVE ANTENNA

Figure 1 shows the configuration of the 3-axis weighted-polarization active antenna [1]. The proposed antenna is comprised of three orthogonal dipole antennas (A_x, A_y, A_z). When the antenna is rotated by the operation of a user, two of the three dipole antennas are selected using two switches (SW_1, SW_2). The received signals (vertical polarization s_V and horizontal polarization s_H) from two selected antennas are combined using the weight function created based on the variation of XPR and the variation due to the antenna inclination angle (α). As shown in Fig. 1, the received signals (s_V, s_H) are multiplied by the weight functions (W_V, W_H). Consequently, the signal at an output port (a) of the proposed antenna is expressed by the following equation:

$$a = W_V s_V + W_H s_H \tag{1}$$

where the weight functions (W_V, W_H) are calculated by the allotment of signals under the XPR, and are given by:

$$W_V = \sqrt{\frac{XPR}{1+XPR}}, \tag{2}$$

$$W_H = \sqrt{\frac{1}{1+XPR}}, \tag{3}$$

Figure 2 shows the situation that the proposed antenna (see Fig. 1) is mounted on a tablet handset. The holding angle α of the tablet handset is changed by an operator, which will cause the

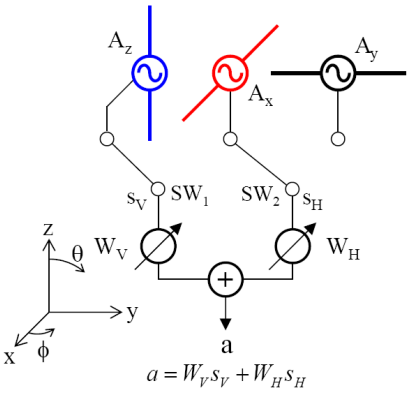

Figure 1: 3-axis weighted-polarization active antenna.

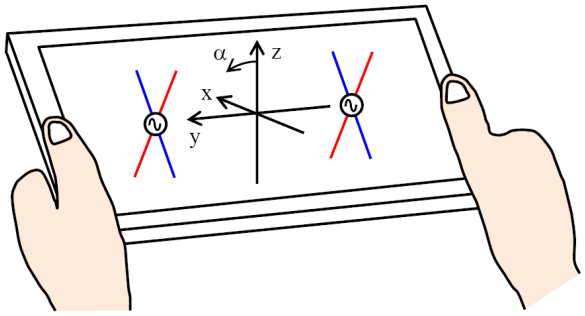

Figure 2: Holding angle α in a tablet handset.

variation of antenna polarization. Therefore, the weight functions (2), (3) are not appropriate for the situation in Fig. 2 where the antenna is inclined. Thus, the following equations are presented:

$$a = W'_V s_V + W'_H s_H e^{j\frac{\pi}{2}} \tag{4}$$

$$W'_V = W_V \left|\cos\alpha\right| + W_H \left|\sin\alpha\right| \tag{5}$$

$$W'_H = W_V \left|\sin\alpha\right| + W_H \left|\cos\alpha\right|, \tag{6}$$

where the weight functions (W'_V, W'_H) are provided considering both the weight functions defined by the Equations (2), (3) (W_V, W_H) and the variation of holding angle (α). A quadrature phase shift appearing in the last term in Equation (4) is needed because there is a cancellation between the vertically or horizontally polarized component of the vertical antenna and that of the horizontal antenna when the proposed antenna is inclined, as shown in Fig. 2. As described in this manner, the Equation (5), (6) present a method of signal combination in consideration of the antenna polarization characteristics caused by the variation of holding angle.

In order to confirm the validity of the proposed method, a preliminary measurement using a 2×2 polarization-controlled MIMO antenna has been carried out, as will be introduced hereafter.

3. RADIATION PATTERN

Firstly, the radiation pattern of a 2×2 polarization-controlled MIMO antenna was measured in an anechoic chamber. Fig. 3 shows the structure of the 2×2 MIMO array antenna comprised of two dipole antennas. The two orthogonal half-wavelength dipole antennas were arranged as a MIMO array antenna in the y-direction. The space between the two array elements was set to 18 cm. The array antenna is attached to a jig that can change the antenna inclination angle as we need. The frequency for the design is 950 MHz.

The attenuator was used to represent the weight function mentioned in Section 2. Table 1 shows an example of the setup of the attenuators A_v and A_H indicate the actual attenuation in the attenuators while W'_v and W'_H indicate the analytical weight functions illustrated by the

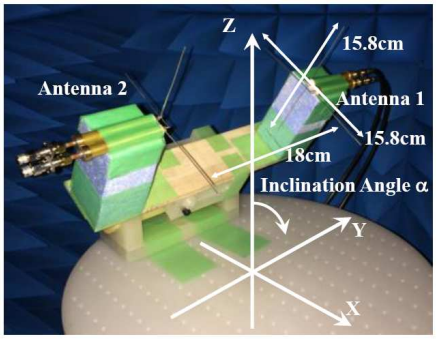

Figure 3: Configuration of the 2×2 MIMO antenna.

Table 1: Setup of attenuators.

XPR [dB]	α [deg]	A_V	A_H	$\frac{A_V}{A_H}$	W'_V	W'_H	$\frac{W'_V}{W'_H}$
0	0	1.00	1.00	1.0	0.50	0.50	1.0
10	0	1.00	0.10	10	0.90	0.10	10
20	0	1.00	0.01	100	0.99	0.01	100
20	30	1.00	0.42	2.4	0.71	0.29	2.4
20	45	1.00	1.00	1.0	0.50	0.50	1.0

Equations (5) and (6). The power ratio of A_v and A_H was adjusted to set the ratio of W'_v and W'_H for realizing the proposed polarization-controlled method in different use scenarios For example, when the XPR is set to 0 dB and α is fixed at 0 degree, the weight functions W'_v and W'_H have the same value because there is no polarization distribution in this situation. Therefore, the attenuators that are connected to the vertical and horizontal antennas will be set to unity (0 dB) for both cases. However, when the XPR is set to 20 dB and α is fixed at 30 degree, a polarization mismatch will occur so that we set the values of the attenuators to be $A_v = 1$ (0 dB) and $A_H = 0.42$ (-3.77 dB). This allows the ratio of A_v and A_H to be 2.4 (3.77 dB) to achieve the same power ratio as in the theoretical weight functions W'_v and W'_H. The method of setting the attenuators in the antenna side will also be applied to the measurement of MIMO channel capacity, as will be presented in Section 4.

Figures 4 and 5 present the measured and analytical results of the radiation patterns for the polarization controlled 2×2 MIMO antenna in the horizontal plane. The XPR was set to two values: XPR = 0 dB and 20 dB, as shown by Figs. 4(a) and (b), respectively. In Fig. 4, the antenna inclination angle (α) was fixed at 0 degree while, in Fig. 5, α was set to 30 degrees. The blue lines indicate the E_θ while the red lines indicate the E_ϕ, which denote the electric field directivity of the antenna element for the θ and ϕ components, respectively.

As shown by Figs. 4(a) and (b), when α was fixed at 0 degree, with an increase in XPR from 0 to

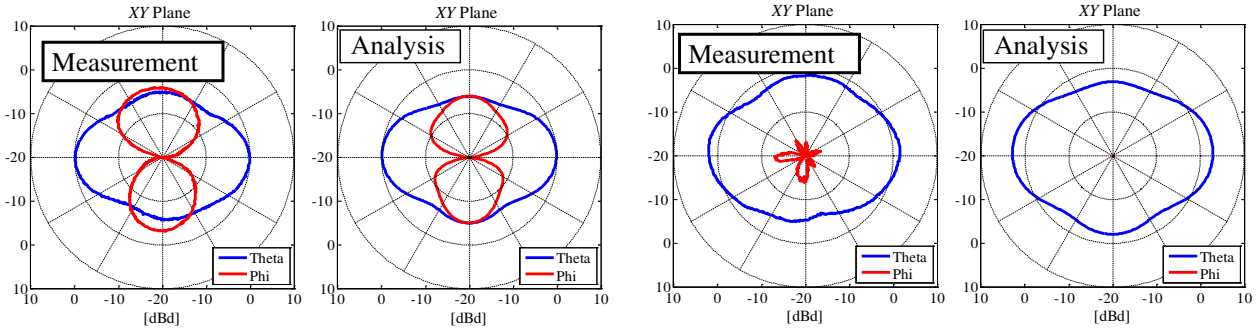

(a) XPR=0 dB (b) XPR=20 dB

Figure 4: Measured and analyzed results of the radiation pattern with different XPRs ($\alpha = 0$ deg).

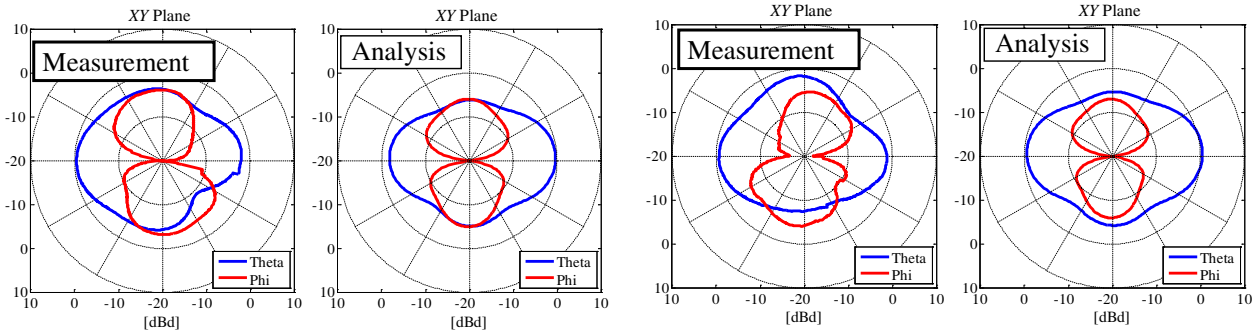

(a) XPR=0 dB (b) XPR=20 dB

Figure 5: Measured and analyzed results of the radiation pattern with different XPRs ($\alpha = 30$ deg).

20 dB, the vertically polarized component in the radiation pattern is large whereas the horizontally polarized component disappears. This is a desirable characteristic for an antenna operated in a radio propagation environment with a large XPR of 20 dB because a strong vertical polarization appears in that environment. This fact indicates that the weight function works well according to the change of the XPR.

In Fig. 4(a) and Fig. 5(a), when the XPR was 0 dB, similar radiation patterns can be observed even when α was changed from 0 to 30 degrees. This characteristic is also desirable for an antenna in a propagation environment with XPR = 0 dB because almost the same radiation intensity of E_θ and E_ϕ, as shown in Figs. 4(a) and 5(a), means that an optimum combination of θ and ϕ polarized incident waves can be achieved due to the identical amplitude of the two polarized incident waves. This particular nature of the proposed antenna is originated from the fact that the weight function W_v' and W_H' derived from Equations (5) and (6) are unchanged when XPR = 0 dB, leading to a similar radiation pattern regardless of the antenna inclination angle α. Consequently, our intention to design the proposed antenna is successfully satisfied.

However, when we compare Fig. 4(b) with Fig. 5(b), where XPR = 20 dB, a large E_ϕ component can be seen in Fig. 5(b) in the case of $\alpha = 30$ deg. This is an undesirable characteristic because a ϕ-polarized incident wave is not dominant when XPR = 20 dB. This observation can be attributed to the fact that only the amplitude-controlled operation was considered in the proposed weighting method, so that an undesired polarization component generated by an increased α cannot be suppressed sufficiently. This viewpoint can be supported by Fig. 8, where there is a slight degradation in the MIMO channel capacity when α is 30 degrees and XPR is 20 dB, as indicated by the position Q_1. Despite this drawback, the channel capacity still maintains at a high level compared with the position Q_2 where α is 0 degree, indicating that the effectiveness of proposed weight function according to the simultaneous variation of the XPR and α.

4. MIMO CHANNEL CAPACITY

After the weight function was confirmed by the measurement of the radiation patterns, the MIMO channel capacity of a 2×2 polarization-controlled MIMO antenna was measured by an OTA apparatus.

The spatial fading emulator for the MIMO-OTA testing is shown in Fig. 6(a) The 2×2 MIMO antenna mentioned in Section 3 was set at the center of the fading emulator. The fading emulator has 7 scattering units located at equal intervals around a circle with 2.4 m in diameter surrounded by electromagnetic absorbers Each unit is comprised of two orthogonal half-wavelength dipole antennas to create the cross-polarized fading signals Fig. 6(b) shows the microwave circuit that controls the signals radiated from the scatterers. The circuit is comprised of 14 sets of phase shifters and attenuators, which is divided by two groups of vertical and horizontal polarization components for creating the XPR as needed Using this OTA apparatus, the MIMO channel capacity of a 2×2 polarization-controlled MIMO antenna under different use scenarios (XPR and α) was measured.

Figure 7 shows the measured results of 2×2 MIMO channel capacity as a function of the XPR when the antenna inclination angle (α) was fixed at 0 degree. Fig. 8 shows the measured results of 2×2 MIMO channel capacity as a function of the antenna inclination angle (α) when the XPR was fixed at 20 dB. The SNR of incident wave was set to 30 dB. In Figs. 7 and 8, the black line shows

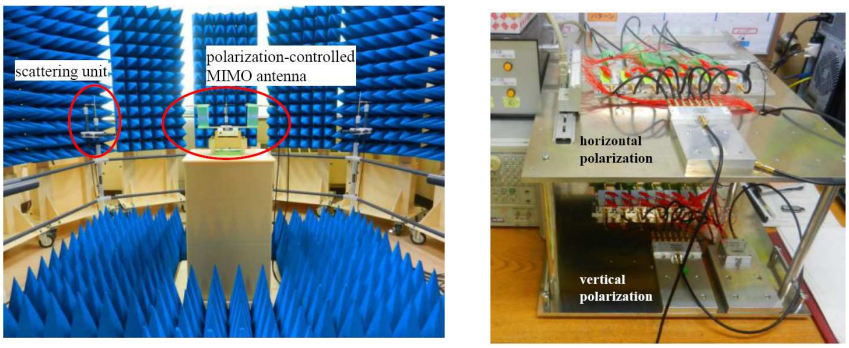

(a) Spatial fading emulator (b) Control circuit

Figure 6: Spatial fading emulator and control circuit.

the measured results obtained from the fading emulator while the red line indicates the analytical outcome calculated by the Monte Carlo simulation [2].

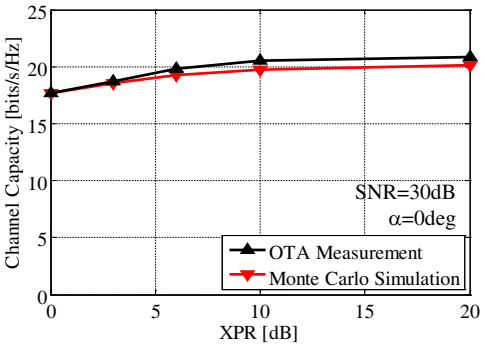

Figure 7: MIMO channel capacity vs. XPR.

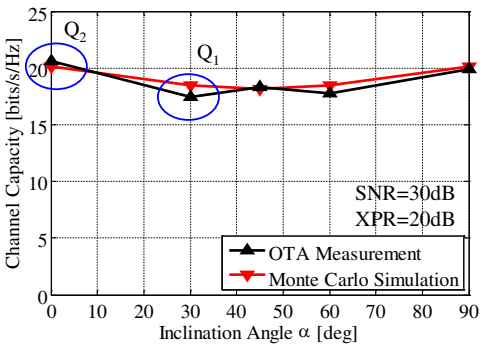

Figure 8: MIMO channel capacity vs. inclination angle α.

As can be seen in Fig. 7, in different propagation environments (XPR), the measured results agree well with the analytical outcome, indicating that a stable channel capacity can be observed. Therefore, in propagation environments where XPR is changed in a great extent a high level of channel capacity can be obtained and maintained using the proposed polarization-controlled antenna.

In Fig. 8, a good agreement between the measured results and the analytical outcome can be observed, indicating that in different antenna inclination angle (α), the same level of channel capacity can be obtained and maintained using the proposed antenna.

Therefore, the validity of the proposed weighted-polarization method is confirmed by the experiments for radiation pattern and MIMO channel capacity using the 2×2 polarization-controlled MIMO antenna.

5. CONCLUSION

This paper presents a preliminary experiment for evaluating the channel capacity of the proposed MIMO antenna. The measured radiation pattern and channel capacity of a 2×2 MIMO weighted-polarization antenna coincide well with the analytical results, indicating the effectiveness of the weight functions used in the propose antenna. The realization of gigabit mobile communications using the proposed antenna are anticipated in forthcoming high-speed and wearable cellular applications, and this will be addressed in our future works.

ACKNOWLEDGMENT

This work was supported in part by the SCOPE 2013 grant number 135005102.

REFERENCES

1. Honda, K., K. Li, and K. Ogawa, "An 8×8 MIMO 3-axis weighted polarization active antenna for wearable radio applications," *31th URSI General Assembly and Scientific Symposium*, Beijing, China, Aug. 2014, to be Presented.
2. Ogawa, K., H. Iwai, A. Yamamoto, and J. Takada, "Channel capacity of a handset MIMO antenna influenced by the effects of 3D angular spectrum, polarization, and operator, " *IEEE AP-S Intl. Symp. Digest*, 153–156, Jul. 2006.

Non-stationarity Characterization for Vehicle-to-vehicle Channels Using Correlation Matrix Distance and Shadow Fading Correlation

Ruisi He[1, 2], **Olivier Renaudin**[2], **Veli-Matti Kolmonen**[3], **Katsuyuki Haneda**[4], **Zhangdui Zhong**[1], **Bo Ai**[1], **and Claude Oestges**[2]

[1]State Key Laboratory of Rail Traffic Control and Safety, Beijing Jiaotong University, Beijing, China
[2]Institute for Information and Communication Technologies, Electronics and Applied Mathematics Université Catholique de Louvain, Louvain-la-Neuve, Belgium
[3]Philips Medical Systems, MR, Finland
[4]Department of Radio Science and Engineering, Aalto University, Aalto, Finland

Abstract— Vehicle-to-Vehicle (V2V) radio channels have been considered as non-stationary due to the dynamic scatterers in V2V environments. To characterize its stationarity is of great importance as it determines the time-variant V2V channel statistics. Therefore, we analyze the non-stationarity of V2V radio channels using two metrics: the correlation matrix distance (CMD) and the shadow fading correlation. The analysis is based on the measurements conducted in a suburban area of Finland at 5.3 GHz. We use the Aalto channel sounder and a 30×4 MIMO system. The power delay profile (PDP), CMD, and shadowing are estimated from the measured channel impulse responses. The equivalent stationarity distance is found to be around 6 m, and it is observed that regions with large delay spreads correspond to smaller stationarity regions. The shadow fading auto-correlation coefficient is found to follow an exponential decay model and the decorrelation distance is considered as the shadowing-based equivalent stationarity distance. Based on the comparison of the equivalent stationarity distances estimated by the two metrics, it is found that the CMD metric is more sensitive to the changes of direction-of-arrival/departure, whereas the shadowing metric takes only into account the power variations over time. We also note that the estimation of shadowing metric is close to the results from CMD. This shows that the shadow correlation can also be used to characterize the non-stationarity of radio channels.

1. INTRODUCTION

Vehicle-to-vehicle (V2V) communication networks will potentially improve the efficiency and safety of Intelligent Transportation Systems (ITS). Since ITS applications imply strict packet delay constraints, a dependable connectivity is crucial. Accurate V2V radio channel models are therefore required. Owing to the rapidly changing environment when both link ends move, vehicular radio channels have been found to be non-stationary. Characterizing the non-stationary is therefore important for V2V channel modeling.

A number of papers have already investigated the non-stationarity of V2V channels. In [1] and [2], the correlation matrix distance (CMD) was employed to characterize the non-stationarity of V2V MIMO channels. In [3], the spectral divergence was used to analyze the non-stationarity of vehicular channels, and in [4], the complexity of spectral divergence was investigated based on V2V measurements.

A more traditional measure of the changes in channel statistics is the shadow fading correlation [5], which was so far not considered for V2V channels. Shadowing represents the variability of the received power around its expected value. The spatial autocorrelation function of shadowing is a measure of how fast the local shadowing evolves as the two mobile terminals (i.e., V2V) move along a certain route: the decorrelation distance of shadowing dictates how rapidly the environment changes, and can thus be considered as an equivalent stationarity distance.

Summarizing, the existing works have several limitations. In particular, a comparison of the stationarity evaluations from the CMD and shadowing correlation is currently lacking. It is still unclear whether the two metrics lead to similar evaluations or not. Therefore, we conduct the V2V channel measurements in suburban environments and introduce a shadowing-correlation based stationarity distance to characterize the non-stationarity of V2V channels. The estimated stationarity distances using the two metrics are compared.

The remainder of the paper is organized as follows. Section 2 shows the measurement campaign. Section 3 introduces the two metrics to investigate the non-stationarity of channels. Section 4 presents the results. Finally, Section 5 concludes the paper.

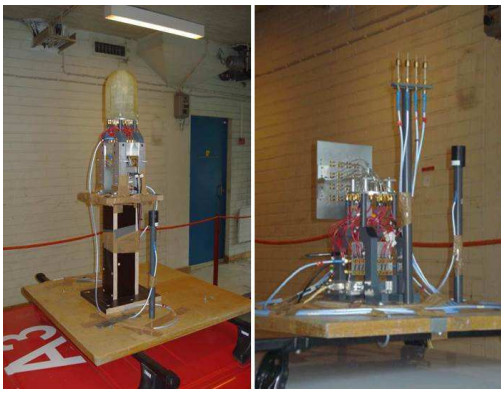

(a) (b)

Figure 1: Antenna arrays. (a) Semi-spherical antenna array of Rx. (b) Uniform linear array of Tx.

2. MEASUREMENTS

The Aalto channel sounder [6], which is based on the switched-array principle, was used in the measurements. The measurements were conducted at 5.3 GHz, with a bandwidth of 60 MHz. The snapshot time (i.e., the time required to measure all antenna pair channels) was set at 1.632 ms, whereas the snapshot repetition rate was set at 66.7 Hz. The transmit power was 36 dBm. A dual-polarized semi-spherical antenna array was used at the receive (Rx) side. The antenna arrays consist of 15 dual-polarized (horizontal and vertical) elements (i.e., 30 feeds), which are arranged in a spherical geometry. A Uniform Linear Array (ULA) with 4 vertically polarized antenna elements was used at the transmit (Tx) side. The antenna arrays are shown in Fig. 1. In the measurements, the Tx car was always traveling ahead of the Rx car. We thus cluster the antenna elements at Rx by defining the "front" and "back" elements. The "front" case has pure line-of-sight (LOS), whereas the LOS path is blocked by the Rx array for the "back" case (since these elements are hidden from the Tx side, owing to the geometry of the Rx antenna array). This grouping enables us to evaluate the impacts of different array configurations on the channel stationarity.

The measurement campaign was conducted in suburban (Tapiola) area, which mostly consist of small detached houses, parking lots, and an average tree density of roughly 5 m high. There are large sidewalks and road signs sparsely distributed on both sides of the two-lane road. In the measurements the cars were driving in the same direction (convoy), mainly under LOS conditions. 6800 snapshots were recorded. The inter-vehicle distance varied between 10 and 500 m, due to the medium traffic conditions.

3. METRICS

We use two metrics to analyze the stationarity: CMD and shadowing correlation. The CMD between the two correlation matrices $\mathbf{R}(it_{\text{rep}})$ and $\mathbf{R}(jt_{\text{rep}})$ measured at times it_{rep} and jt_{rep} is defined by

$$d_{\text{corr}}(i,j) = 1 - \frac{\text{tr}\left\{\mathbf{R}(it_{\text{rep}}) \cdot \mathbf{R}(jt_{\text{rep}})\right\}}{\left\|\mathbf{R}(it_{\text{rep}})\right\|_f \cdot \left\|\mathbf{R}(jt_{\text{rep}})\right\|_f}, \tag{1}$$

where i and j are the time indices, $t_{\text{rep}} = 15$ ms is the snapshot time interval and $\text{tr}\{\cdot\}$ and $\|\cdot\|_f$ denotes the trace and Frobenius norm of a matrix. The CMD is zero if the correlation matrices are equal up to a scaling factor and one if they are completely uncorrelated. In this paper, the CMD is computed with full channel correlation matrix, defined as

$$\mathbf{R}_{\text{Full}}(it_{\text{rep}}) = \frac{1}{W} \sum_{k=i}^{i+W-1} \text{vec}\left[\mathbf{G}(kt_{\text{rep}})\right] \cdot \text{vec}[\mathbf{G}(kt_{\text{rep}})]^{\text{H}}, \tag{2}$$

where W is the averaging interval to remove the impact of the small-scale fading, $(\cdot)^{\text{H}}$ denotes hermitian transpose, and $\text{vec}\,[\cdot]$ operator stacks a matrix into a vector columnwise. The complex MIMO channel matrices $\mathbf{G}(kt_{\text{rep}})$ are obtained from the $N_{\text{Rx}} \times N_{\text{Tx}}$ impulse response matrices $\mathbf{H}(\tau, kt_{\text{rep}})$, as

$$\mathbf{G}(kt_{\text{rep}}) = \sum_{\tau} \mathbf{H}(\tau, kt_{\text{rep}}), \tag{3}$$

where τ denotes delay. W was set to 54, which corresponds to a 40 wavelengths window at 5.3 GHz with an average speed of 10 km/h in the measurements.

For the shadowing metric, the auto-correlation coefficient of shadow fading is employed, expressed as

$$\rho(\Delta k t_{\text{rep}}) = \left| \frac{E\left\{X(kt_{\text{rep}})X(kt_{\text{rep}} + \Delta k t_{\text{rep}})\right\}}{\sigma} \right| , \tag{4}$$

where $E\{\cdot\}$ denotes the expected value of $\{\cdot\}$. $X(kt_{\text{rep}})$ is the shadow fading component measured at time index k, and σ is the standard deviation of shadow fading. The procedure for obtaining $X(kt_{\text{rep}})$ is as follows: i) we first estimate the path gain $P_G(kt_{\text{rep}})$ from the channel impulse response, averaged over Tx/Rx and the 40 wavelengths window; ii) then we use the delay of the LOS component in power delay profile (PDP) to estimate the Tx-Rx distance, and conduct least-square (LS) fit to get the distance-dependent path gain; iii) finally we remove the distance-dependent path gain out of the corresponding $P_G(kt_{\text{rep}})$ to get $X(kt_{\text{rep}})$. The decorrelation time, which depends on the scenario, is defined to be the time at which the auto-correlation coefficient drops to $1/e$. By multiplying it by the speed, we obtain the decorrelation distance, which is considered as the shadowing-based equivalent stationarity distance.

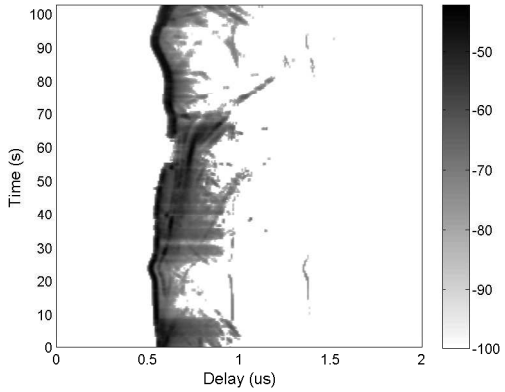

Figure 2: APDPs of the measurements in suburban.

4. RESULTS

The averaged PDPs (APDPs) (over the 40 wavelengths window) of the measurement route are presented in Fig. 2. We can see that in APDPs there are two regions (10–25 s and 70–95 s) with a small number of scattering components after the LOS component. These two regions correspond to the open areas in the beginning and the end of the route. For the other regions of APDPs, there are relatively rich scattering components after the LOS path, which are mostly caused by the surrounding large tree densities and heavy traffic conditions. For the two regions with few scattering components, the corresponding RMS delay spreads are very small with a mean value of 25.41 ns; while the mean value of the RMS delay spreads in other regions is 51.64 ns.

Figure 3 shows the plot of the estimated CMD between arbitrary times of the example route for the "front" case. It is observed that there are generally two stationarity regions in CMD plots, corresponding to the regions of 10–25 s and 70–95 s. This means that the region with a large delay spread corresponds to a reduced stationarity of channels. For the CMD, the time-variant stationarity time is defined as the maximum period over which the CMD remains below a certain threshold, and the stationarity distance is the product of the stationarity time and average speed. In our analysis, the threshold for CMD was set at 0.2, as suggested by [1] for V2V channels.

The estimated auto-correlation coefficient of shadowing is found to follow an exponential decay [5]

$$\rho(\Delta d) = \exp\left(-\frac{\Delta d}{d_{\text{cor}}}\right), \tag{5}$$

where Δd denotes the equivalent distance difference, and d_{cor} denotes the equivalent decorrelation distance (also the shadowing-based equivalent stationarity distance). Fig. 4 shows the estimated auto-correlation coefficient and the exponential decay model. It is found that Eq. (5) offers a good fit to the measurements.

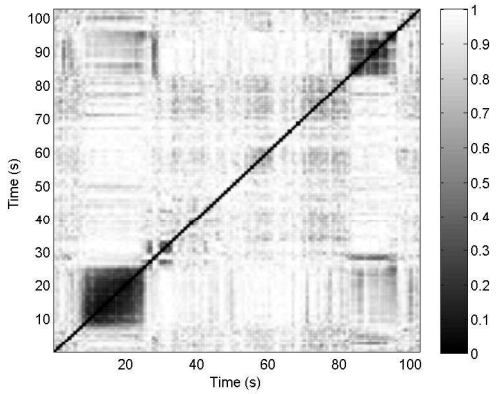

Figure 3: Estimated CMD for the "front" case in the measurements.

The results of CMD and shadowing correlation are summarized in Table 1. From the CMD metric we find that the "front" case has a larger stationarity distance than the "back" case. This is because the "front" array has a strong and stable LOS component that dominates the radio wave propagation. While for the "back" case, the broadside of most antenna elements points towards opposite direction to the Tx, and there is no LOS so that weaker components have more importance in the radio wave propagation. Since these components are likely to appear/disappear rapidly on small time scales, the structure of the MIMO channel will change faster than in the "front" case. From shadowing metric, it is found that the "front" and "back" cases are relatively close to each other. This is because the shadowing correlation takes only into account the power variations over time. Hence, if the power of the LOS and of the roadside components vary both similarly over time, then same shadowing correlation can be obtained. On the other hand, the direction-of-arrival/departure of the LOS component are more or less constant over time (as long as the relative orientation of the Tx and Rx vehicles doesn't change), while it is obviously not the case for the roadside scatterers.

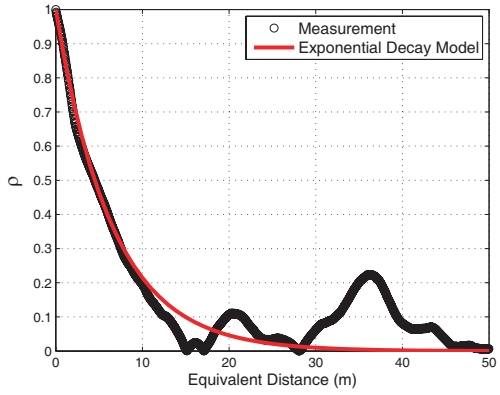

Figure 4: Exponential decay model of the shadow fading correlation.

The estimated stationarity distances using the shadowing metric is generally close to the estimations of CMD using full channel correlation matrix. This shows that the shadowing metric can be used for characterization of the non-stationarity of V2V channels. As the estimation of shadow fading does not require MIMO measurements, it thus has a more wide application range.

Table 1: Estimated equivalent stationarity distance.

CMD, Front	Shadowing, Front	CMD, Back	Shadowing, Back
6.03 (m)	6.50 (m)	3.21 (m)	6.84 (m)

5. CONCLUSION

In this paper, we employed two metrics, correlation matrix distance (CMD) and shadow fading correlation, to characterize the non-stationarity of V2V radio channels based on data measured with a 30×4 MIMO sounder at 5.3 GHz in suburban environment. The equivalent stationarity distance is found to be around 6 m. It is found that: i) the region with a large delay spread leads to a reduced size of stationarity region; ii) CMD metric is more sensitive to the changes of direction-of-arrival/direction-of-departure; and iii) the shadowing metric offers a good performance for the non-stationarity characterization. As the measurements of shadowing do not require MIMO system and are easier to be conducted, the shadowing correlation metric might have a wider application range in the analysis of channel non-stationarity.

ACKNOWLEDGMENT

The authors would like to thank P. Vainikainen, J. Koivunen, and M. Olkkonen for their contributions in the measurement campaign.

REFERENCES

1. Renaudin, O., V. Kolmonen, P. Vainikainen, and C. Oestges, "Non-stationary narrowband MIMO inter-vehicle channel characterization in the 5-GHz band," *IEEE Transactions on Vehicular Technology*, Vol. 59, No. 4, 2007–2015, 2010.
2. Renaudin, O., V. Kolmonen, P. Vainikainen, and C. Oestges, "Car-to-car channel models based on wideband MIMO measurements at 5.3 GHz," *Proceedings of EuCAP*, 635–639, Berlin, Germany, March 2009.
3. Bernado, L., T. Zemen, A. Paier, G. Matz, J. Karedal, N. Czink, C. Dumard, F. Tufvesson, M. Hagenauer, and A. F. Molisch, "Non-WSSUS vehicular channel characterization at 5.2 GHz-spectral divergence and time-variant coherence parameters," *Proceedings of XXIXth URSI General Assembly*, 9–16, Chicago, USA, 2008.
4. Bernado, L., T. Zemen, A. Paier, and J. Karedal, "Complexity reduction for vehicular channel estimation using the filter divergence measure," *Proceedings of the Forty Fourth Asilomar Conference on Signals, Systems and Computers*, 141–145, Pacific Grove, California, 2010.
5. Gudmundson, M., "Correlation model for shadow fading in mobile radio systems," *Electronics letters*, Vol. 27, No. 23, 2145–2146, 1991.
6. Kolmonen,, V., J. Kivinen, L. Vuokko, and P. Vainikainen, "5.3-GHz MIMO radio channel sounder," *IEEE Transactions on Instrumentation and Measurement*, Vol. 55, No. 4, 1263–1269, 2006.

On Effective Gain Variability with Antenna Orientation

Hassan El-Sallabi, Mohamed Abdallah, and Khalid Qaraqe
Electrical and Computer Engineering Department, Texas A&M University at Qatar, Qatar

Abstract— Antenna pattern for both vertical and horizontal polarization varies with antenna's orientation angle. Varying antenna orientation is a common practice with advanced portable wireless devices such as smart phones. This orientation variability affects its effective gain, which has impact on performance of wireless communication system. In this work, we address effective gain variability with antenna orientation. We present the well-known mean effective gain (MEG), instantaneous effective gain (IEG) and stochastic effective gain (SEG). The data series of IEG and SEG is used to extract their statistics as function of the orientation angle.

1. INTRODUCTION

Antenna characteristics, in particular its gain,have major impact on link quality and performance of wireless communication system. Antenna gain is a crucial parameter in design of communication systems where direct line-of-sight (LOS) exists between transmitter and receiver such as in microwave links, where both transmitter and receiver are fixed. Such communication links require maximum gain of antenna in pointing direction to the other communications end. For such applications, the maximum antenna gain is a useful parameter to characterize and improve communications link quality. However, in other applications such as mobile communications, the mobile terminal could be in any direction relative to the main pointing direction of maximum gain of the fixed station (e.g., base station) antenna. The position of mobile terminal could be in LOS or non-line-of-sight (NLOS). In LOS, direct signal may arrive to a fixed antenna from directions other than that of maximum antenna gain and similarly with NLOS propagation conditions. It is well known that in multipath environment, the effective gain of antennas cannot be characterized by directive gain with sufficient accuracy. In multipath channel, the maximum directive gain can be used to increase coverage in particular geographical regions but it does not maximize the gain in a specific direction. Mean effective gain (MEG) has been introduced in literature [1–4] as a more descriptive parameter for multipath propagation environment that accounts for mutual relationship between antenna radiation pattern and strength of multipath components from different directions. MEG is a statistical average measure over a series of measurements along a "route" that is considered as environment measure. The MEG of antenna is usually given in a single number for fixed antenna orientation. This fixed number could be acceptable in in fixed antenna orientation but not for variable orientation. Communication systems based on reconfigurable antenna adopt switching between different antenna states in order to enhance its performance. Hence, neither directive gain nor MEG are anymore good metrics that are needed for switching decisions. Switching between antenna states has to be based on instantaneous information. This leads to the concept of instantaneous effective gain (IEG) [5], which is based on instantaneous signal power distribution. The IEG is more suitable than MEG to applications, where antenna pattern switching takes place.

In this work, we present variability of MEG with average cross polarization ratio (XPR) and antenna orientation in order to find the critical angle for half-wavelength dipole antenna, where the MEG is independent of XPR and find parameters that affect the critical angle. We also present variability of IEG with orientation angle for fixed and random parameters of vertical plane angle of arrivals in terms of cumulative distribution function (CDF). The statistics of IEG in terms of its mean are also presented as a function of inclination angle of dipole antenna. Then, we discuss our investigations on the statistics and variability of SEG in order to provide more insight in its variability with instantaneous XPRs and azimuthal and elevation angle of arrivals. We present how the CDF and statistics of the SEG vary with antenna orientation angles.

2. EFFECTIVE ANTENNA GAIN

The advance in handheld wireless terminals such as smart phones and portable devices require more care in antenna design due to dynamic variation of device's orientations. The match between directional radio channel response with polarization state and radiation pattern of antenna has significant role in performance of wireless devices. Handling of smart phones and portable wireless devices could have different orientation at dynamic convenience of a user. This makes it to have

different angles relative to directional information of multipath components. This is reflected in the interplay between the antenna pattern and multipath components for different polarizations. This interplay can be characterized in the average sense by MEG of antenna, or in instantaneous sense by IEG. However, both parameters are obtained from stochastic nature of the interaction of antenna and arrived radio wave signals from different directions and polarizations. The MEG as a commonly used statistical measure can be written as [1]

$$MEG = \frac{P_{rec}}{P_\theta + P_\phi} \tag{1}$$

where P_{rec} is the average received power that is given as

$$P_{rec} = \oint\!\!\oint \left\{ P_\theta \Im_\theta \left(\Omega, \Psi\right) P_\theta \left(\theta, \phi\right) + P_\phi \Im_\phi \left(\Omega, \Psi\right) P_\phi \left(\theta, \phi\right) \right\} \sin\theta d\theta d\phi \tag{2}$$

and P_θ and P_ϕ are the average received power of electric field of θ- and ϕ-polarization states, since any incident wave can be decomposed into two polarized components, E_θ in vertical plane and E_ϕ in the horizontal plane, $\Im_\theta(\Omega, \Psi)$ and $\Im_\phi(\Omega, \Psi)$ are the θ- and ϕ-components of radiation gain pattern of antenna with orientation angle, $\Psi\left(\alpha, \beta\right)$, of inclination angle (α) and tilt angle (β), Ω is direction of arrivals of radio waves in elevation plane θ, relative to z-axis and ϕ in azimuthal plane, relative to x-axis. The average cross polarization ratio (XPR) is given as $XPR = P_\theta / P_\phi$, $P_\theta(\theta, \phi)$ and $P_\phi(\theta, \phi)$ are the weighted probability density function of angle of arrivals of the stochastic components angular power densities. The MEG as a function of XPR is commonly used as this ratio combines both P_θ and P_ϕ. It is given as [1]

$$MEG = \int_0^{2\pi} \int_0^{\pi} \left\{ \frac{XPR}{1+XPR} \Im_\theta \left(\Omega, \Psi\right) P_\theta \left(\theta, \phi\right) + \frac{1}{1+XPR} \Im_\phi \left(\Omega, \Psi\right) P_\phi \left(\theta, \phi\right) \right\} \sin\theta d\theta d\phi \tag{3}$$

It has been shown by many measurement campaigns [6] that XPR has a lognormal distribution for different indoor and outdoor environments. Hence, the MEG for fixed orientation angle, Ψ, can be written to include of being a function of χ as a random variable of XPR as follows

$$MEG = \int_0^{2\pi} \int_0^{\pi} \int_0^{\infty} \left\{ \frac{\chi}{1+\chi} \Im_\theta(\Omega, \Psi) P_\theta(\theta, \phi) + \frac{\chi}{1+\chi} \Im_\Phi(\Omega, \Psi) P_\Phi(\theta, \phi) \right\} \sin\theta d\chi d\theta d\phi \tag{4}$$

This formulation may be extended further assuming that Ψ has a random distribution, which makes it to have more integration levels, one is over random variable inclination angle (α) and other integration is over random variable tilt angle (β). The weighted probability density function of angle of arrivals has to satisfy

$$\int_0^{2\pi} \int_0^{\pi} P_\theta \left(\theta, \phi\right) \sin\theta d\theta d\phi = \int_0^{2\pi} \int_0^{\pi} P_\phi \left(\theta, \phi\right) \sin\theta d\theta d\phi = 1 \tag{5}$$

and can be given as [1]

$$\int_0^{2\pi} \int_0^{\pi} P_\theta \left(\theta, \phi\right) \sin\theta d\theta d\phi = \int_0^{2\pi} \int_0^{\pi} P_\phi \left(\theta, \phi\right) \sin\theta d\theta d\phi = 1 \tag{6}$$

$$P_\theta \left(\theta, \phi\right) = A_\theta \exp\left(-\frac{\left\{\theta - (\pi/2 - \mu_\theta)\right\}^2}{2\sigma_\theta^2} \right) \tag{7}$$

$$P_\phi \left(\theta, \phi\right) = A_\phi \exp\left(-\frac{\left\{\theta - (\pi/2 - \mu_\phi)\right\}^2}{2\sigma_\phi^2} \right) \tag{8}$$

where μ_θ and μ_ϕ, are the mean elevation angle of each θ- and ϕ-wave distribution, respectively, observed from horizontal direction and σ_θ and σ_ϕ are their corresponding standard deviation of

wave distribution, A_θ and A_ϕ are selected to satisfy the above mentioned conditions in Eq. (5). For IEG, the following parameters has to be instantaneous values, $P_{rec}(t)$, $P\theta(t)$ and $P_\phi(t)$ {i.e., $XPR(t)$}. The formulation to compute ISG is same as MEG but the values are instantaneous values instead of average ones [5]. The IEG parameter combines the instantaneous interaction of radiation pattern of antenna under test with propagation characteristics of the environment relative to a reference antenna (e.g., isotropic) antenna. The impact of antenna on IEG depends on antenna characteristics such as antenna pattern, polarization, orientation, etc.. The IEG is a measure how a partial radiation gain interacts with a realization of a stochastic channel that varies with varying directional informations and matching angles. It is shown in [4] that IEG is maximized when antenna coefficients are equal to the complex conjugates of the expansion coefficients of the incoming field of the spherical vector waves.

The formulation in (3) shows that the MEG is a mathematical averaging of the random functions [6]:

$$G_{eff}^{\theta} \sim \frac{XPR}{1+XPR}\Im_\theta(\Omega,\Psi) \tag{9}$$

$$G_{eff}^{\phi} \sim \frac{1}{1+XPR}\Im_\phi(\Omega,\Psi) \tag{10}$$

This leads to definition of stochastic effective gain (SEG), which can be formulated as

$$SEG = G_{eff}^{\theta} + G_{eff}^{\phi} \tag{11}$$

The mean of SEG can be expressed as

$$MSEG = E\{SEG\} \tag{12}$$

where $E\{\cdot\}$ is the mean operator. The CDF of SEG as a function of antenna orientation angle Ψ can be obtained by Monte-Carlo method. The process is based on repeatedly generating large number of multipath components with arrival angles (θ_i, ϕ_i) and cross-polarization of each path is characterized by χ_i. Super-resolution analysis of multi-antenna measurement indicated that XPR multipath components can be modeled with lognormal distribution as shown [7] for different propagation environments. The SEG can also be characterized with second order statistics to a measure to fluctuation of antenna effective gain. This detailed knowledge of effect of antenna is also important for multiple antenna channels [8, 9].

3. NUMERICAL RESULTS

In this work, the antenna orientation is simulated with antenna orientation angle, Ψ, of antenna pattern of a half-wave dipole of a mobile device with varying inclination angle of the antenna (α) and assumed tilting angle (β) be zero, which makes $\Im_\theta(\Omega,\alpha) = \Im_\theta(\Omega,\Psi)$ and $\Im_\phi(\Omega,\alpha) = \Im_\phi(\Omega,\Psi)$. The θ-component of antenna pattern, $\Im_\theta(\Omega,\Psi)$ and ϕ-component of antenna pattern, $\Im_\phi(\Omega,\Psi)$, can be written as [1]:

$$\Im_\theta(\Omega,\alpha) = 1.64\left(\cos\theta\cos\phi\sin\alpha - \sin\theta\cos\alpha\right)^2 \frac{\cos^2(\pi\zeta/2)}{\left(1-\zeta^2\right)^2} \tag{13}$$

and

$$\Im_\phi(\Omega,\alpha) = 1.64\sin^2\phi\sin^2\alpha\frac{\cos(\pi\zeta/2)^2}{\left(1-\zeta^2\right)^2} \tag{14}$$

where $\zeta = \sin\theta\cos\phi\sin\alpha + \cos\phi\cos\alpha$ and the angle α is the inclination angle of the antenna element from z-axis in the vertical zx-plane, ϕ is the azimuth angle relative to x-axis, θ is the elevation angle relative to z-axis, the coefficient 1.64 corresponds to the directivity of the half-wavelength dipole antenna.

The presented simulation results are for indoor environment. It is assumed that the distribution of azimuth angle of arrival is uniform distribution within angular range of $(0, 2\pi)$ for both polarizations. The distribution of elevation angle of arrivals is assumed Gaussian with mean angle of arrival μ_θ and μ_ϕ for both θ- and ϕ-polarizations with standard deviation of σ_θ and σ_ϕ, respectively. We assume in the simulation that both polarization have same values of μ and σ (i.e., $\mu_\theta = \mu_\phi$ and

$\sigma_\theta = \sigma_\phi$), though they may not be same in reality. Figure 1 shows the commonly known behavior of MEG for different values of average XPR and antenna inclination angle, when $\mu_\theta = \mu_\phi = 30°$ and $\sigma_\theta = \sigma_\phi = 30°$. The 0° inclination angle has lowest MEG with lowest tested XPR value. At this angle, the MEG increases as XPR increases. The MEG in channels with negative average XPR values varies in a slower rate as inclination angle moves from 0°. The MEG varies slowly generally with inclination angle for positive average XPR values when compared to negative values of XPR. Measurement data for indoor propagation showed that XPR values are generally positive. Figure 1(b) shows a critical inclination angle that the MEG is independent of XPR, which is close to (±60°). Detailed investigation showed that the critical inclination angle is a function of both mean and standard deviation of angle of arrivals. Figure 2 shows the this critical inclination angles as a function of both μ and σ. We can see that space of critical angles is dominated by mainly two degree, i.e., 60° and 55° at which the antenna patterns for both polarization are quite similar. Figure 3 depicts behavior of IEG generated by large number of channel realizations where IEG is computed for every channel realization. Each channel realization is generated by large number of multipath components. Each signal is characterized by $(\theta_i, \phi_i, \chi_i)$, where θ_i, ϕ_i, χ_i are elevation angle of arrival, azimuth angle of arrival, and XPR value of radio wave signal i, respectively. The χ_i, instantaneous XPR, has lognormal distribution with mean of 8.7 dB and standard deviation

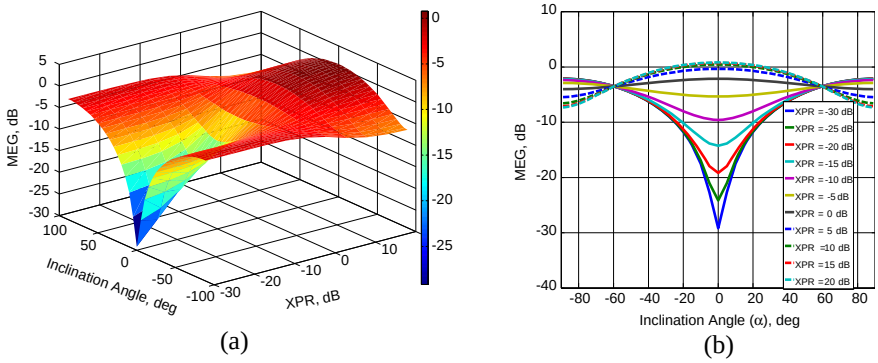

Figure 1: Behavior of MEG when $\mu_\theta = \mu_\phi = 30°$ and $\sigma_\theta = \sigma_\phi = 30°$.

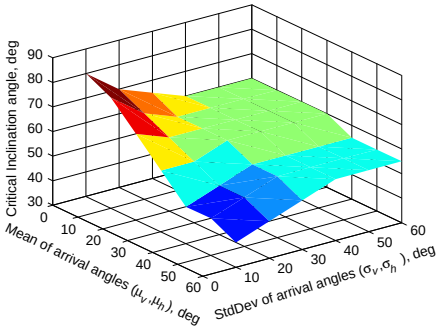

Figure 2: Critical inclination angles.

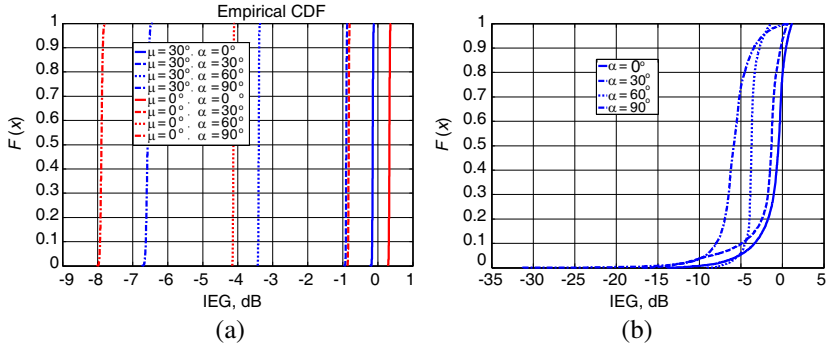

Figure 3: CDF of IEG. (a) Fixed $\mu_\theta = \mu_\phi$ and $\sigma_\theta = \sigma_\phi$, (b) random $\mu_\theta = \mu_\phi$ and $\sigma_\theta = \sigma_\phi$.

5.2 dB. In order to investigate IEG, two different Monte-Carlo experiments have conducted; 1) Fixed $\mu_\theta = \mu_\phi$ and $\sigma_\theta = \sigma_\phi$ for all realizations; and 2) Random $\mu_\theta = \mu_\phi$ and $\sigma_\theta = \sigma_\phi$ that differ from realization to other. Figure 3(a) depicts CDF of variability ofIEG with inclination angles for two fixed parameters $\mu_\theta = \mu_\phi = 0^\circ$ for horizontal plane propagation and $\mu_\theta = \mu_\phi = 30^\circ$ for oblique propagation. Both data sets are generated for $\sigma_\theta = \sigma_\phi = 30^\circ$. We can see clearly that the mean offset increases with inclination angle of antenna but also depends on mean direction of elevation angle of arrival. The shape of CDF curves is still the same for different values of α but differ in offset values. Figure 3(b) shows the CDF of variability IEG as a function of α for random $\mu_\theta = \mu_\phi$ and $\sigma_\theta = \sigma_\phi$ where offset value and shape of CDF curves change. The estimated mean of IEG as a function of α for the three different sets of IEG realizations are depicted on Figure 4. The horizontal propagation makes higher mean IEG for low values of α and lower gain than that of oblique propagation at higher values of α. The mean of IEG for random $\mu_\theta = \mu_\phi$ and $\sigma_\theta = \sigma_\phi$ is lowest for small values α but is higher for large α. The SEG realizations are generated by assuming large number of arriving radio wave signals that follow particular statistical distributions in azimuth and elevation planes as described earlier. Figure 5 shows CDF of SEG for different values

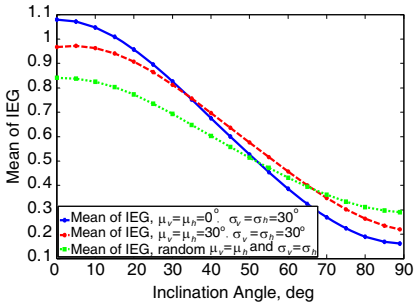

Figure 4: Mean of IEG.

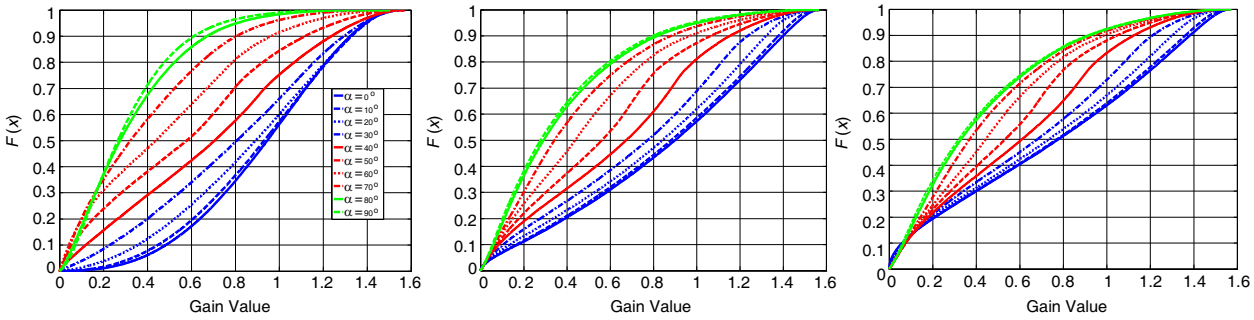

(a) $\sigma_V = \sigma_H = 15^o$ (b) $\sigma_V = \sigma_H = 30^o$ (c) $\sigma_V = \sigma_H = 45^o$

Figure 5: CDF of SEG for different inclination angles and direction spread of elevation angle of arrival.

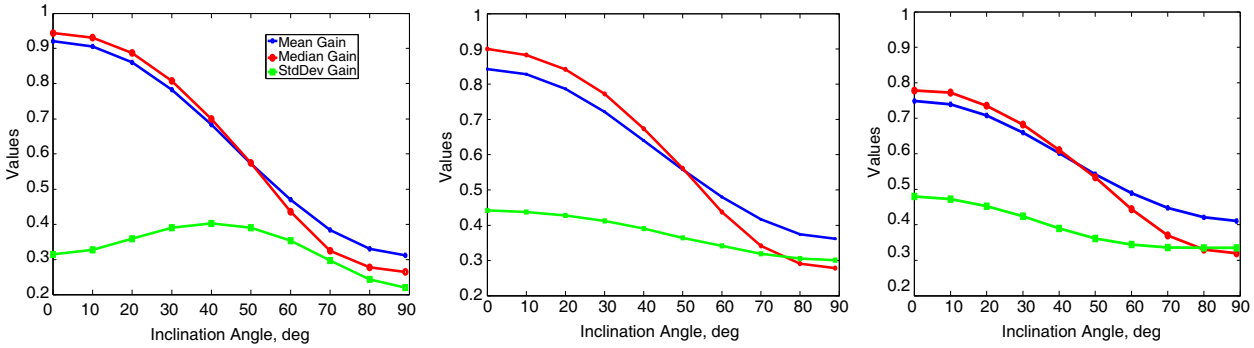

(a) $\sigma_V = \sigma_H = 15^o$ (b) $\sigma_V = \sigma_H = 30^o$ (c) $\sigma_V = \sigma_H = 45^o$

Figure 6: Mean, median and StdDev of SEG for different inclination angles and direction spread of elevation angle of arrival.

of inclination angles for different values of standard deviation of elevation angle of arrivals (i.e., $\sigma_V = \sigma_H = 15°$, $\sigma_V = \sigma_H = 30°$, $\sigma_V = \sigma_H = 45°$) as indicated on the figure. The curves are obtained for $\mu_V = \mu_H = 30°$ and instantaneous XPR has same parameters of lognormal distribution stated earlier. The range of inclination angles are shown in Figure 4(a) (i.e., 0°, 10°, 20°, 30°, 40°, 50°, 60°, 70°, 80°, and 90°). This different inclination angles cause different antenna patterns for vertical and horizontal polarizations, which lead to different levels of interplay between multipath components of different values of $(\theta_i, \phi_i, \chi_i)$. The variability ranges of SEG with increasing inclination angles reduces with increasing σ for fixed μ. The $MSEG$ (given as mean gain on figure), median and standard deviations of SEG of the CDF curves as function of inclination angles are presented in Figure 5. The MSEG and median of SEG reduces with inclination angle for different values of $\sigma_V,\ \sigma_H$. The fluctuation of SEG around its MSEG increases with inclination angle with higher $\sigma_V,\ \sigma_H$.

4. CONCLUSION

This work has presented investigation resultson the critical inclination angle of half-wavelength dipole antenna and showed that, based on Monte-Carlo simulation, it is a function of mean and standard deviations of elevation direction of arrival. The common critical angle is close to 55° and 60°, where radiation pattern of both vertical and horizontal polarization are similar. Other critical inclination angles are also observed. Statistical analysis of Monte-Carlo simulation of both IEG and SEG have been presented. The mean of IEG reduces with increasing inclination angle of antenna for fixed $\mu_\theta = \mu_\phi$ and $\sigma_\theta = \sigma_\phi$ and keep same IEG distribution, however, though the mean reduces for random $\mu_\theta = \mu_\phi$ and $\sigma_\theta = \sigma_\phi$ but the shape of the IEG statistical distribution also changes. The mean, median of SEG reduces with inclination angle. The standard deviation of fluctuations of SEG increases with inclination angles. The statistical results are for different values of angular spread of elevation angle of arrival.

ACKNOWLEDGMENT

This publication was made possible by NPRP grants #: NPRP 5-653-2-268 from the Qatar National Research Fund (a member of Qatar Foundation). The statements made herein are solely the responsibility of the authors.

REFERENCES

1. Taga, T., "Analysis for mean effective gain of mobile antennas in land mobile radio environments," *IEEE Trans. Veh. Technol.*, Vol. 39, 117–131, May 1990.
2. Glazunov, A., A. Molisch, and F. Tufvesson, "Mean effective gain of antennas in a wireless channel," *IET Microw., Antennas Propag.*, Vol. 3, No. 2, 214–227, 2009.
3. Kalliola, K., K. Sulonen, H. Laitinen, O. Kivekas, J. Krogerus, and P. Vainikainen, "Angular power distribution and mean effective gain of mobile antenna in different propagation environments," *IEEE Trans. Veh. Technol.*, Vol. 51, No. 5, 823–838, 2002.
4. Glazunov, A., M. Gustafasson, and A. Molisch "On physical limitations of the interaction of a spherical aperture and a random field," *IEEE Trans. on Antennas and Propagt.*, Vol. 59, 119–128, Jan. 2011.
5. Zhao, X., D. C. K. Lee, Z. Pan, N. Boubaker, and R. S. K. Cheng, "Modified antenna effective gain in multiple-cluster 3D channel model," *IEEE Sarnoff Symposium*, Nassau Inn, Princeton, NJ, Apr. 30–May 2, 2007.
6. Carro, P. L., P. G. Ducar, and J. de Mingo, "Analysis of the antenna stochastic effective gain in mobile environments," *Proc. IEEE 69th Vehicular Technology Conference, VTC 2009*, 1–5, Spring, 2009.
7. El-Sallabi, H., D. S. Baum, P. Zetterberg, P. Kyosti, T. Rautiainen, and C. Schneider, "Wideband spatial channel model for MIMO systems at 5 GHz in indoor and outdoor environments," *Proc. IEEE 63rd Vehicular Technology Conference, VTC 2006*, Spring, Vol. 6, 2916–2921, 2006.
8. Wang, S., et al., "Time-varying MIMO channels: Parametric statistical modeling and experimental results," *IEEE Trans. Vehicular Technology*, Vol. 56, No. 4, 1949–1963, 2007.
9. Salo, J., et al., "Some insights into MIMO mutual information: The high SNR case," *IEEE Trans. on Wireless Communications*, Vol. 5, No. 11, 2997–3001, Nov. 2006.

Broadband Channel Measurements inside Metro Station

Ke Guan[1], **Zhangdui Zhong**[1], **Cesar Briso-Rodríguez**[2], **Carlos Rodríguez-Sanchez**[3], **Juan Moreno**[3], **Sergio Perez**[2], **and Bi Ai**[1]

[1]State Key Laboratory of Rail Traffic Control and Safety
Beijing Jiaotong University, Beijing 100044, China
[2]Radio Communications Research Group (GRC)
Universidad Politécnica de Madrid, Madrid 28031, Spain
[3]Metro de Madrid, Madrid 28013, Spain

Abstract— This paper presents a set of broadband channel measurements conducted in a real metro station in Madrid at 2.45 GHz and 1 GHz, respectively. The power delay profile (PDP) of broadband channels at these two frequencies are obtained. Based on the PDPs, two preliminary tapped delay line models are established. The measured results and corresponding models provide the first-hand information of broadband channel and, therefore, are useful to design and assess the next generation of broadband communication systems in the metro environment.

1. INTRODUCTION

Nowadays, the traditional widespread narrowband standard railway communication system — Global System for Mobile Communications-Railway (GSM-R) — cannot meet the requirements such as real time video or other high capacity data transmissions. It has been widely acknowledged that the next generation of broadband communication systems will require high quality video for the trains' control and surveillance. For instance, such kind of system is mandatory for the automated driving of trains scheduled for the year 2020 in many modern subways.

In order to support the design and assess of new railway communication systems in the metro environment, it is crucial and essential to get the insight into the channel characteristics. Currently, 900 MHz and 2.4 GHz are the two potential choices of carrier frequencies for the next generation of broadband train communication systems [1, 2], such as Long Term Evolution for Railway (LTE-R) [3], CBTC (Communication Based Train Control System), etc.. A common idea in the engineering implementation is that a better coverage could be realized by using the lower frequency because of the lower propagation loss. However, the metro station is a specific indoor scenario, in which the propagation characteristics could differ from the cases in the other common railway scenarios, such as viaduct [4], cutting [5], train station [6, 7], crossing bridge [8], etc.. Moreover, for the broadband systems, a good coverage is not the only precondition for a high data rate. Besides the propagation loss and fading characteristics which have been systematically investigated in literature, such as [9–11], etc., time delay spread is another factor influencing the system performance as well. To some extent, the delay profile is more critical than the loss characteristics for the broadband systems. However, as far as the authors know, the power delay profile in the metro station has been rarely investigated. In order to characterize the broadband channel in such scenario, a set of measurements are conducted in a real metro station in Madrid at 2.45 GHz and 1 GHz, respectively.

1.1. Measurement Environment

The measurements are carried out in a metro station named "Ciudad de los Angeles" in the Line 3 of Metro of Madrid. Figs. 1(a) and 1(b) show the side view and the front view the metro station in the study. Corresponding geometrical information is included in the figures as well.

1.2. Test System

A channel sounder developed by Radio Communications Research Group (GRC), Universidad Politécnica de Madrid, is utilized in the measurements. The sounder is composed by a suit of transmitter (Tx) and receiver (Rx), and each side assembled by a baseband subsystem and a radio frequency (RF) subsystem. Details of this channel sounder can be found in [12]. In the measurements, both Tx and Rx are synchronized by using the baseband pulse generated on the transmitting side, and the received signal is demodulated by the logarithmic amplifier with a sensitivity of 25 mV/dB. The PDPs which are included in the following sections are extracted from the channel impulse response (CIR) captured by the oscilloscope. Table 1 provides the main parameters of the test system. Radiation patterns of antennas are measured in an anechoic chamber and given by Fig. 2.

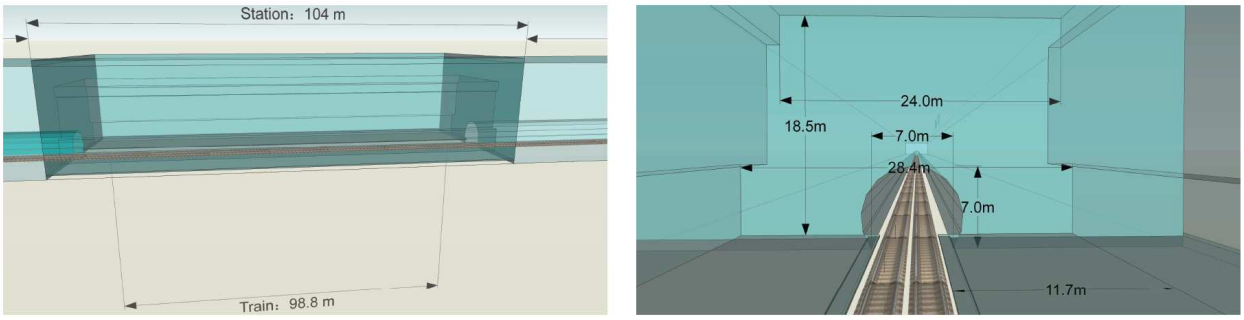

(a) (b)

Figure 1: (a) Side view and (b) front view the metro station in the study.

Table 1: Main parameters of the test system.

Frequency	Transmitted power	Pulse width	Time delay resolution	Tx/Rx antennas
2.45 GHz	38 dBm	47 ns	200 MHz	HG2414P
1 GHz	40 dBm	47 ns	200 MHz	HG908P

2. MEASUREMENTS AND PROPAGATION

The sketch and geometrical parameters of the measurement campaign are shown in Fig. 3. Tx and Rx are separated from each other by 20 m. Both antenna systems are oriented towards the same wall (in the upper left of Fig. 3) in order to avoid the overload in the measurements. The train is located in the middle of the station, at the track which is closer to the RF equipments used for broadband measurements.

Figures 4(a) and 4(b) illustrate the PDP and corresponding taps of the tapped delay line (TDL) models in the cases of 2.45 GHz and 1 GHz, respectively. It can be seen that the RMS delay of the channel at 1 GHz is 428.8 ns, which is much larger than its value (75.7 ns) in the case of 2.45 GHz. This is because that the station is widely covered with steel that improves reflections at lower frequencies. Moreover, the propagation loss in the free space at 1 GHz is much smaller than the case of 2.45 GHz. Each multiple path experiences smaller propagation loss. Thus, more multi-path components are retained and finally received. On the other hand, the channel of 2.45 GHz has a much smaller time delay spread, which could be more beneficial to the broadband system performance. Table 2 gives the preliminary TDL models. The number of the taps L are obtained by [13]:

$$L = \lceil \sigma_\tau / T_c \rceil + 1 \tag{1}$$

where σ_τ is the RMS delay spread, T_c is the pulse width in this study.

Table 2: TDL models of channels in metro station at 2.45 GHz and 1 GHz.

Parameter	2.45 GHz			TDL model of channel in metro station at 1 GHz										
Tap index	1	2	3	1	2	3	4	5	6	7	8	9	10	11
Gain [dB]	−8.0	−26.2	−39.8	0	−23.1	−31.0	−44.0	−37.2	−51.4	−59.3	−57.7	−61.2	−63.0	−64.7
Delay [ns]	0	150	300	0	160	320	480	640	800	960	1120	1280	1440	1600

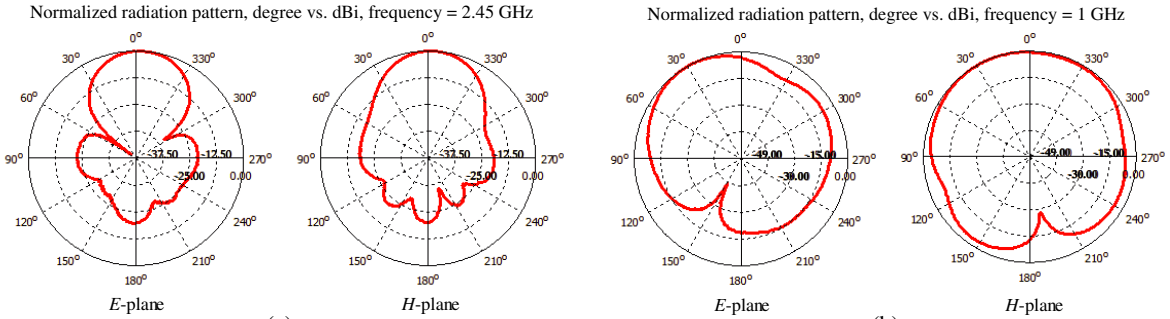

(a) (b)

Figure 2: Radiation patterns of antennas used in the study.

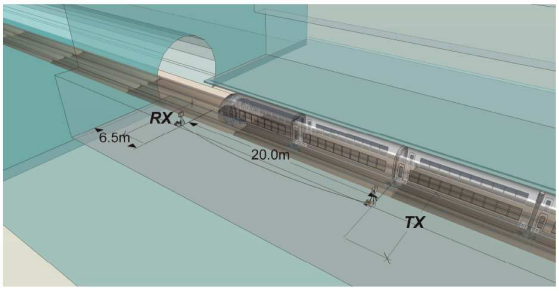

Figure 3: Sketch and geometrical parameters of the measurement campaign.

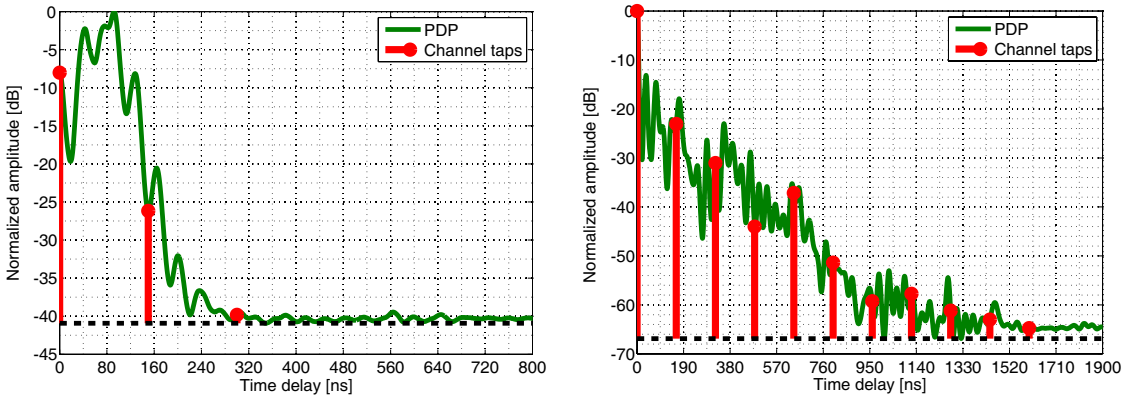

Figure 4: PDP and taps of the channel at (a) 2.45 GHz, and (b) 1 GHz.

3. CONCLUSION

A set of broadband channel measurements in a real metro station are reported. The RMS delay spreads are 75.7 ns and 428.8 ns in the channels at 2.45 GHz and 1 GHz, respectively. Preliminary TDL models are presented to give the first impression of the broadband channel in the metro station. The measurement campaign and results are useful for the broadband communication system design, modeling, and simulation tools validations.

ACKNOWLEDGMENT

This work is supported by the NNSF under Grant U1334202, NNSF under Grant 61222105, Project of State Key Lab under Grant RCS2012ZT013, RCS2011ZZ008, RCS2014ZT11, and INNPACTO TECRAIL research project IPT-2011-1034-37000 funded by the Spanish Ministry of Economy and Competitiveness.

REFERENCES

1. Briso, C., J. M. Cruz, and J. I. Alonso, "Measurements and modeling of distributed antenna systems in railway tunnels," *IEEE Trans Veh. Technol.*, Vol. 56, 2870–2879, Sept. 2007.
2. Guan, K., Z. Zhong, C. Briso, and J. I. Alonso, "Measurement of distributed antenna systems at 2.4 GHz in a realistic subway tunnel environment," *IEEE Trans Veh. Technol.*, Vol. 61, 834–837, Feb. 2012.
3. Guan, K., Z. Zhong, and B. Ai, "Assessment of LTE-R using high speed railway channel model," *Proc. Third International Conference on Commnunications and Mobile Computing*, 461–464, Qingdao, 2011.
4. He, R., Z. Zhong, B. Ai, G. Wang, J. Ding, and A. F. Molisch, "Measurements and analysis of propagation channels in high-speed railway viaducts," *IEEE Trans. Wirel. Comm.*, Vol. 12, No. 2, 794–805, Feb. 2013.
5. He, R., Z. Zhong, B. Ai, J. Ding, Y. Yang, and A. F. Molisch, "Short-term fading behavior in high-speed rail cutting scenario: Measurements, analysis, and statistical models," *IEEE Trans. Antennas Propag.*, Vol. 10, 808–812, 2011.
6. Guan, K., Z. Zhong, B. Ai, and T. Kurner, "Propagation measurements and analysis for train stations of high-speed railway at 930 MHz," *IEEE Trans Veh. Technol.*, to appear, 2014.

7. Guan, K., Z. Zhong, B. Ai, and T. Kürner, "Empirical models for extra propagation loss of train stations on high-speed railway," *IEEE Trans. Antenna. Propagat.*, to appear, 2014.
8. Guan, K., Z. Zhong, B. Ai, and T. Kürner, "Propagation measurements and modeling of crossing bridges on high-speed railway," *IEEE Trans. Veh. Technol.*, Vol. 63, 502–517, Feb. 2014.
9. Guan, K., Z. Zhong, B. Ai, R. He, B. Chen, Y. Li, and C. Briso, "Complete propagation modeling in tunnels," *IEEE Antennas Wireless Propag. Lett.*, to appear, 2013.
10. Guan, K., Z. Zhong, B. Ai, R. He, B. Chen, Y. Li, and C. Briso, "Complete propagation model structure inside tunnels," *Progress In Electromagnetics Research*, Vol. 141, 711–726, 2013.
11. Guan, K., Z. Zhong, B. Ai, R. He, and C. Briso, "Five-zone propagation model for large-size vehicles inside tunnels," *Progress In Electromagnetics Research*, Vol. 138, 389–405, 2013.
12. http://tecrail.lcc.uma.es/.
13. Sen, I. and D. W. Matolak, "Vehicle-vehicle channel models for the 5-GHz band," *IEEE Trans. Intell. Transp. Syst.*, Vol. 9, No. 2, 235–245, 2008.

Impact of Shadowing Correlation on Microdiversity and Marcodiversity of Cellular System in High-speed Railway Environments

Bei Zhang, Zhangdui Zhong, Bo Ai, and Ruisi He
State Key Laboratory of Rail Traffic Control and Safety, Beijing Jiaotong University, China

Abstract— Outage probabilities in shadow fading channels of high-speed railway (HSR) scenarios are evaluated when macro-diversity and micro-diversity techniques are considered. First, the power density function of signal-to-noise ratio (SNR) is derived in order to obtain a close form of outage probability for the narrow-strip-shaped cells in HSR. It is noteworthy that a Rice distribution is more realistic for modeling small-scale fading in HSR environments, a log-normal distribution is adopted to model the shadowing component. Then, the outage probabilities on the assumption of micro-diversity with maximal ratio combining and macro-diversity with selection combining are deduced, considering correlation property of shadow fading among base stations. It is calculated as a function of the shadowing cross-correlation coefficient, which is defined as correlations of links between one mobile station and two different base stations. Finally, the attenuation of signal amplitude caused by carriage passing loss in outage analysis for HSR is investigated.

1. INTRODUCTION

The characterization of radio wave propagation for wireless system in high-speed railways (HSRs) has attracted a lot of interests recently [1]. There are great differences for wireless channel between the HSR scenario and the typical scenario, especially in fading behaviors. The HSR channel has a location-based fading characteristics due to high mobility and dynamic propagation environment. One of the most powerful techniques to improve the reliability of communication over the wireless channels is diversity combining [2]. One approach is to choose either one or a combination of two different diversity techniques, namely, micro-diversity and macro-diversity. Performance of diversity is significantly affected by the propagation channels, especially by the correlation of shadow fading [3–5]. The performance of diversity receivers has been studied extensively in the literature for some well-known fading models, such as Rayleigh, Rice, Nakagami-m and Nakagami-q, for both independent and correlated fading channel [6]. The average output signal-to-noise ratio (SNR), the amount of fading, and the outage probability were investigated for dual receivers operating in correlative log-normal fading in [7]. Outage probability for the most general case, where multiple correlated base stations are involved in macro-diversity and correlation also exists among the multiple channels at the microlevel, was evaluated in [8].

In HSR environments, correlated shadowing has been widely observed [11], mainly because the signals from two neighboring base stations (BSs) are likely to be shadowed by the same obstacles. The outage probability analysis with the effect of correlated shadow fading has not been addressed as far as the authors know. The main motivation of our work is to confirm the impact of shadowing correlation on outage probability of wireless networks with marco-diversity and micro-diversity techniques in HSR environment.

The paper is organized as follows. The probability density function (PDF) of instantaneous SNR as well as local mean SNR and outage probability are introduced in Section 2. In Section 3, an exponential shadowing correlation model based on experimental data fitting in HSR environments is briefly described. In Section 4, numerical results for different shadowing correlation coefficients. In Section 5 conclusions are drawn.

2. OUTAGE ANALYSIS

In this paper, we consider a cellular mobile radio system with micro-diversity achieved by using multiple antennas at the base station and macro-diversity provided through two base stations that are used to serve each cell. We address the downlink direction only. It is assumed that a number of transmitting BSs are distributed over a narrow-strip-shaped railway cell. One single receiving station which has several antennas to achieve micro-diversity gain is located at the roof of a train. Shadowing can be modeled by a log-normal distribution for HSR environments based on empirical measurements [7–9]. To investigate the small scale fading behavior, we use Rice distribution since

the HSR scenario is considered as a typical line-of-sight (LOS) condition. It is also assumed that a maximal ratio combining (MRC) is used at the micro level, and selective combining (SC) is used at the macro level. Each port has a L-branch micro-diversity combiner. Let R_{i1}, R_{i2}, ..., R_{iL} $(i = 1, 2, \ldots, N)$ denote the envelopes of the received signals at the ith port. Consider a macro-diversity system of N-fold ports with time division multiple address (TDMA), i.e., there is no co-channel interference. The instantaneous SNR at the MRC output of the ith port is $\gamma_i = (E_b/N_0)\sum_{k=1}^{L} R_{ik}^2$, where E_b is the transmitted signal energy per bit and N_0 is the single side power spectral density of the additive white Gaussian noise. Then, the pdf of the instantaneous SNR, conditioned on the local mean SNR Ω_i per port is given by [4]

$$f(\gamma_i|\Omega_i) = \frac{K+1}{\Omega_i}\exp\left(-\frac{(K+1)\gamma_i}{\Omega_i} - KL\right)\left(\frac{(K+1)\gamma_i}{KL}\right)^{(L-1)/2} I_{L-1}\left(2\sqrt{\frac{KL(K+1)\gamma_i}{\Omega_i}}\right), \quad (1)$$

where $I_{L-1}(\cdot)$ is the modified Bessel function of the first kind of order $(L-1)$, K is Rice factor defined as the ratio of the average fading power of the dominant multipath component and the average fading power received over the non-dominant paths. The Rice K-factor is modeled as a piecewise-linear function of distance in HSR environments [9]. When K goes to zero, the channel statistics becomes Rayleigh, whereas, if K goes to infinity, the channel becomes a nonfading channel. Here, it is expected that the short term fading is averaged so perfectly that the fluctuation of local mean received power at fixed port is only caused by shadowing after MRC process, and therefore the local mean SNR of each port has a pdf given by the standard log-normal expression. The local mean SNR of the whole macro-diversity combiner is $M = \max\{\Omega_1, \Omega_2, \ldots, \Omega_N\}$.

The outage probability p_{out} is defined as the probability that the instantaneous SNR of the system exceeds a threshold SNR value, say M_t. The outage threshold is a protection value of the SNR above which the quality of service (QoS) is satisfactory. The outage probability can be obtained by

$$p_{out}(\gamma_i|\Omega_i) = \int_0^{M_t} f(\gamma_i|\Omega_i)d\gamma_i, \quad (2)$$

then the average outage probability after selective combine can be expressed as [7]

$$P_{out} = \int_0^{\infty}\int_0^{\infty},\ldots,\int_0^{\infty}\prod_{i=1}^{N} p_{out}(\gamma_i|\Omega_i)f(\Omega_1,\Omega_2,\ldots,\Omega_N)d\Omega_1 d\Omega_2,\ldots,d\Omega_N, \quad (3)$$

A power correlation coefficient $\rho_{ij} = Cov(X_i, X_j)/\sigma_i\sigma_j$ of received signal X_i, X_j is adopted to study the effects of correlated shadow fading with a standard deviation given by σ. Recall that for a pair of random variables X and Y, their covariance is defined as

$$Cov[X,Y] = E[(X - E[X])(Y - E(Y))] = E[XY] - E[X]E[Y], \quad (4)$$

Since a lognormal pdf is used to model shadow fading component, the joint pdf of the local mean SNR $\Omega = \{\Omega_1, \Omega_2, \ldots, \Omega_N\}^T$ is given by

$$f(\Omega;\mu,D) = \frac{1}{(2\pi)^{(N/2)}|D|}\exp\left(-\frac{1}{2}(\Omega-\mu)^T D^{-1}(\Omega-\mu)\right), \quad (5)$$

with a mean and a positive semi-definite covariance matrix of shadow fading given by μ, D. As a consequence, it is shown that the outage probability of the MRC-SC diversity system in HSR environment can be written as a function of shadowing correlation.

3. CROSS CORRELATION MODEL FOR SHADOW FADING IN HSR ENVIRONMENT

In this section, an exponential shadowing cross-correlation model is described based on empirical measurement in HSR environments. In order to find the influence of the separation distance on the cross-correlation property of shadow fading, the cross-correlation coefficient of shadow fading received from two BSs with different separation distances is calculated as shown in Fig. 1. The measurement campaign was performed in China along a dedicated passenger railway line from Xingyang to Luoyang using the high speed train at the center frequency of 930 MHz. In total,

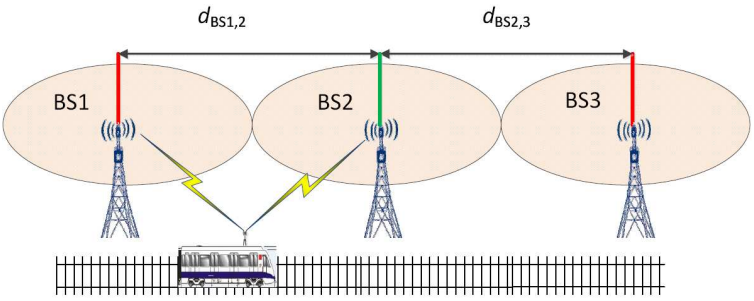

Figure 1: A schematic diagram of shadow fading measurements.

over 90 km of measurements were taken mainly in typical HSR scenarios including viaduct, cutting, countryside, etc.. The real base stations of global system mobile communications for railway (GSM-R) was used as the transmitters (Tx). The receiver (Rx) is composed of a Willtek 8300 Griffin fast measurement receiver, a distance sensor, and GPS. The received power was averaged over local areas of 40λ (12.9 m at 930 MHz) to exclude small-scale fading effects. A more detailed analysis of the measurement system can be found in [9, 10]. An example for the received power for the 980 MHz band is shown in Fig. 2. In the data fitting model, shadow fading correlation is proposed as a function of separation distance d between the base stations as [12]

$$\rho(d) = 1.362 \cdot \exp(-1.397 \cdot \lg(d/d_0)) - 0.362. \tag{6}$$

This specific statistical shadow fading correlation model can be used to evaluate the macrodiversity performance to test out how to achieve optimal diversity gain by determining different BSs location and separation distance.

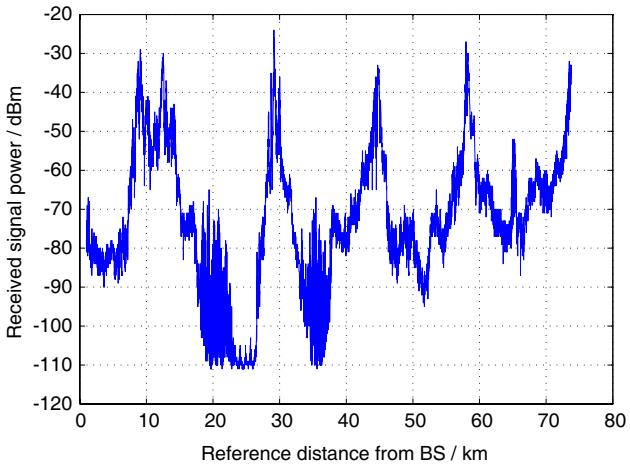

Figure 2: The instantaneous received power as a function of distance from base station.

4. RESULTS AND DISCUSSION

In this section, the outage probability by numerically evaluating the derived expressions for the system employing micro- and macrodiversity is presented in a Rician fading channel with Rice factor $K = 5$ dB. Set the number of macrodiversity port $N = 2$, the number of microdiversity branch $L = 2$. In this case, the joint pdf of the local mean SNR has the form [7],

$$f(\Omega_1, \Omega_2) = \frac{\varepsilon^2}{2\pi\sigma_1\sigma_2\sqrt{1-\rho^2}\Omega_1\Omega_2} \times \exp\left\{ -\frac{1}{1-\rho^2}\left[\frac{(10\log\Omega_1 - \mu_1)^2}{2\sigma_1^2} + \frac{(10\log\Omega_2 - \mu_2)^2}{2\sigma_2^2} \right.\right.$$
$$\left.\left. -2\rho\left(\frac{10\log\Omega_1 - \mu_1}{\sqrt{2}\sigma_1}\right)\left(\frac{10\log\Omega_2 - \mu_2}{\sqrt{2}\sigma_2}\right)\right]\right\}, \tag{7}$$

where $\varepsilon = 10/\ln 10$, $\Omega_1 \geq 0$, $\Omega_2 \geq 0$. Set the mean μ_1, μ_2 of lognormal shadow fading is assumed to be 0 dB, moreover, all the ports are also assumed to experience equally severe shadowing, i.e., $\sigma_1 = \sigma_2 = 5$ dB. The threshold SNR $M_t = 1$ dB. A simple general method supposed in [13] is used to approximate the sum of log-normal and Rice distribution via Gauss-Hermite integration, since the use of a log-normal distribution to model the average power to account for shadowing does not lead to a closed form solution for the PDF of the SNR at the output of a macrodiversity system. Fig. 3 shows the effect of correlated lognormal shadowing on outage probability with $N = 2$, $L = 2$. Outage probabilities were calculated in MRC-SC systems for different shadowing correlation values 0, 0.3, 0.6, 0.9. As expected, higher values of the correlation lead to high values of outage probabilities. It is observed that as the correlation coefficient increases, the system performance deteriorates. As the correlation coefficient tends to unity, the performance obtained coincides with that with no macrodiversity. In real Chinese HSRs, the separate distance between two BSs is 3 km, i.e., the cross-correlation coefficient of shadow fading is 0.34 according to the exponential model in [12].

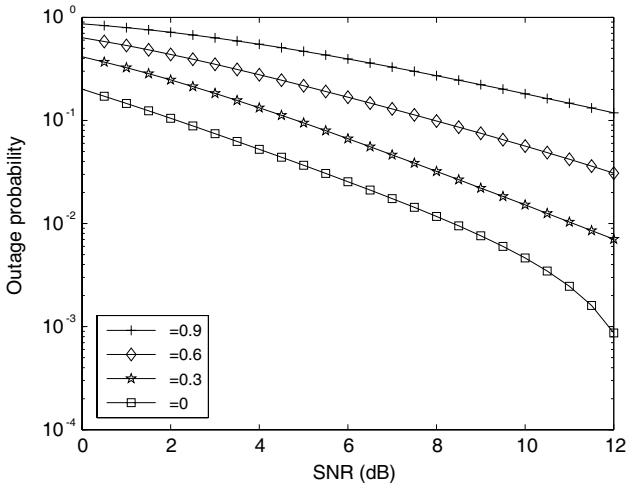

Figure 3: Outage probabilities versus SNR in HSRs with different shadowing cross-correlation coefficients.

5. CONCLUSION

In this paper, the impact of correlated lognormal shadowing on outage probability for a system with micro- and macrodiversity reception is studied in HSR environments, using L-branch MRC and N-port SC. The received signal envelop has a Rician distribution and it also suffers lognormal shadowing. It should be noted that when the base stations in HSR wireless communication system are very closely spaced, the correlation coefficient tends to 1, therefore, the effect of correlated shadowing on system performance cannot be ignored. It is also noted that performance can be improved by using macrodiversity and microdiversity techniques based on shadowing cross-correlation between different BSs.

ACKNOWLEDGMENT

This work is supported by State Key Laboratory of Rail Traffic Control and Safety project (RCS2014 ZZ03), Beijing Jiaotong University, the National Natural Science Foundation of China (Grant No. U1334202) and the National 863 Project Granted No. 2014AA01A706.

REFERENCES

1. Ai, B., et al., "Challenges towards wireless communications for high-speed railways," *IEEE Transactions on Intelligent Transportation Systems*, Vol. TBD, No. TBD, 1–16, DOI:10.1109/TITS.2014.2310771, 2014.
2. Rappaport, T. S., *Wireless Communications Principles and Practice*, 2nd Edition, Prentice Hall, 2001.
3. Wang, L.-C., G. Stuber, and C.-T. Lea, "Effects of Rician fading and branch correlation on a local-mean-based macrodiversity cellular system," *IEEE Trans. Veh. Technol.*, Vol. 48, No. 2, 429–436, Mar. 1999.

4. Zhang, J. and V. Aalo, "Effect of macrodiversity on average-error probabilities in a Rician fading channel with correlated lognormal shadowing," *IEEE Trans. Commun.*, Vol. 49, No. 1, 14–18, Jan. 2001.
5. Mukherjee, S. and D. Avidor, "Effect of microdiversity and correlated macrodiversity on outages in a cellular system," *IEEE Trans. Wireless Commun.*, Vol. 2, No. 1, 50–58, Jan. 2003.
6. Simon, M. K. and M.-S. Alouni, *Digital Communication over Fading Channels: A Unified Approach to Performance Analysis*, Wiely, New York, 2000.
7. Alouini, M.-S. and M. K. Simon, "Dual diversity over correlated log-normal fading channels," *IEEE Trans. Commun.*, Vol. 50, 1946–1959, Dec. 2002.
8. Shankar, P. M., "Macrodiversity and microdiversity in correlated shadowed fading channels," *IEEE Trans. Veh. Technol.*, Vol. 58, No. 2, 727–732, 2009.
9. He, R., Z. Zhong, B. Ai, G. Wang, J. Ding, and A. F. Molisch, "Measurements and analysis of propagation channels in high-speed railway viaducts," *IEEE Trans. Wireless Commun.*, Vol. 12, No. 2, 794–805, 2013.
10. He, R., Z. Zhong, B. Ai, and J. Ding, "An empirical path loss model and fading analysis for high-speed railway viaduct scenarios," *IEEE Antennas Wireless Propag. Lett.*, Vol. 10, 808–812, 2011.
11. Kyosti, P., et al., WINNER II channel models, WINNER II Public Deliverable 5.4, Sep. 2007.
12. Zhang, B., Z. Zhong, B. Ai, and R. He, "Measurements and modeling of cross-correlation property of shadow fading in high-speed railways," *IEEE VTC 2014 Fall*, accepted.
13. Mehta, N. B., J. Wu, A. F. Molisch, and J. Zhang, "Approximating a sum of random variables with a lognormal," *IEEE Trans. Wireless Commun.*, Vol. 6, No. 7, 2690–2699, 2007.

A Novel 3D Ray-tracing Acceleration Technique Based on Kd-tree Algorithm for Radio Propagation Prediction in Complex Indoor Environment

Xiaowei Mei, **Yong Zhang**, **and Hai Lin**
State Key Laboratory of CAD&CG, Zhejiang University, Hangzhou, Zhejiang, China

Abstract— This paper presents a new 3D ray tracing acceleration technique based on the kd-tree algorithm for predicting the radio coverage in complex indoor environment. For each ray emitted from the transmitter, all the valid ray propagation paths can be searched for by the hybrid ray tracing model which combines the shooting and bouncing ray (SBR) and the image method. The kd-tree algorithm is mainly used to accelerate the intersection test of ray tracing. In addition, the receiver power strength can be calculated based on geometrical optics (GO) and uniform theory of diffraction (UTD). As expected, the proposed method performs higher superiority than the conventional ray tracing model in terms of computational efficiency. Meanwhile, it also shows good agreement with measurements and the Winprop's simulated results with respect to computational accuracy.

1. INTRODUCTION

With the rapid spread of wireless communication technology, the efficient and accurate indoor propagation model becomes a topic of most concern in designing and deploying communication systems.

Many radio propagation models were developed over the past decades for indoor environments, particularly site-specific models [2], which are based on electromagnetic wave propagation theory. Among of those site-specific models, the ray tracing models are the most widely used, such as the image method [2, 3], shooting and bouncing ray (SBR) method [1, 2] and the hybrid method (SBR/image) [2, 4, 5]. The image method is accurate, but suffers from inefficiency when the environment is complex. The SBR method is efficient but the accuracy is not stable. Because it needs to introduce a receiving sphere, while the size of it is of great importance to the calculation accuracy. Hybrid method combines the image and SBR method, performing both the advantages of such two methods. However, when applied to the complex and convoluted indoor environment, ray tracing models still face the problem of computational inefficiency.

The purpose of this study is to introduce a new three dimensional (3D) ray tracing acceleration technique based on kd-tree algorithm [6, 7] for predicting radio coverage in complex indoor environment. The proposed method is based on the hybrid ray tracing model and the kd-tree technique. In addition, the precedence of the proposed acceleration method is proved by comparing with the measured data, commercial maturity software Winprop and the conventional ray-tracing technique in terms of computational accuracy and efficiency.

2. THE IMPLEMENTATION OF PROPOSED METHOD

Ray tracing models are vastly applied in radio propagation prediction. One of the biggest challenges of ray tracing is the computational burden of overload ray-object intersection test. Therefore, to overcome this drawback, the proposed method introduces a well-known acceleration intersection technique, namely, kd-tree algorithm. The following subsections focus on describing the details of how to search for the radio propagation paths and finally the whole ray tracing procedure is presented.

2.1. Searching for Propagation Paths

The highly important step of ray tracing is to search for the valid radio propagation paths between transmitter and receiver, which is the most time consuming and the most challenging part. In order to improve the efficiency of finding propagation paths, both the hybrid ray tracing model and kd-tree technique are adopted.

2.1.1. The Hybrid Ray Tracing Model

The hybrid model which combines SBR and image method is recommended as follows. The SBR method is used to quickly identify all possible propagation paths from transmitter to receiver.

Each propagation path is composed of a series of face ID intersecting with the ray and the type of propagation mechanism (reflection or transmission) on this face. Tracking each ray, when it intersects with an obstacle, it will be transmitted and reflected generating two new rays. For the new ray, continue to search for the intersected face. The above process is repeated until it reaches the set maximum reflection, transmission times. So far all propagation paths corresponding to the ray have been obtained and recorded. Among of these paths attained by the SBR model, there exist some paths through which it cannot reach the receiving point from the emitter. Therefore, it is necessary to apply the image method to determine the effectiveness of propagation paths. For each possible path, on the basis of recorded information, all the mirror points relevant to every interacted face are calculated respectively. Based on these mirror points, we can search for the exact point of intersection and judge whether the path is legal. At this point, all valid propagation paths have been acquired via the hybrid model.

2.1.2. Acceleration Technique — Kd-tree Algorithm

Traditional intersection test needs to judge whether the ray intersects with all the faces one by one in the whole scene space. For ease of understanding, a simple 2D scenario is illustrated in Figure 1(a), the a, b, c, d, e triangles represent different faces of obstacles and a signal ray is plotted as red line. Traditional way requires to test all the a, b, c, d, e faces whether intersecting with the ray. When the simulated environment is complex, it takes plenty of time.

The kd-tree algorithm can get through such inefficiency of above traditional intersection test. The implementation of kd-tree [6] is described as follows with the help of illustration in Figure 1. The symbols s_0, s_1, s_2, s_3 denote the space related to internal node and n_0, n_1, n_2, n_3, n_4 denote the smallest subspace related to leaf node in the tree.

2.1.2.1. Construction of Kd-tree

The construction of kd-tree is based on space partition. Firstly, a bounding box representing the whole original space is generated for the goal scenario. It is corresponding to the root node in the tree as s_0 in Figure 1(b). Then the best split plane can be selected based on ray tracing costs estimation model, the most widely used greedy surface area strategy (SAH) [6]. As plotted in Figure 1(a), the split_plane0 is namely the best split plane corresponding to the space s_0. According to the split plane, the original space s_0 is divided into two subspace s_1, s_2 (in Figure 1(a)) and at the same time the root node s_0 generates two child nodes s_1, s_2 (in Figure 1(b)). For the new subspace, we go on to search for its optimal split plane and then generate new child nodes. The above operation is recursive until it meets construction terminal condition, then there is no need to continue space subdivision directly generating a leaf node. After all, the complete and optimal kd-tree can be constructed corresponding to the simulated environment, as illustrated in Figure 1(b). It must emphasize that the kd-tree is only constructed once for a given scenario and it is independent of the position of transmitter and receiver, so it is ease of application.

2.1.2.2. Traversing of Kd-tree

After the kd-tree is constructed, starting from the root node to traversal the tree. For internal node of kd-tree as s_0 in Figure 1(b), according to the position relationship between the ray and the split plane split_plane0 (in Figure 1(a)) of space s_0, the nearer child node s_1 to the ray is acquired to continue traversing while the faster child node s_2 is recorded and pushed back into stack. If the current node is not a leaf node, it is required to keep searching for its child node. For the finally

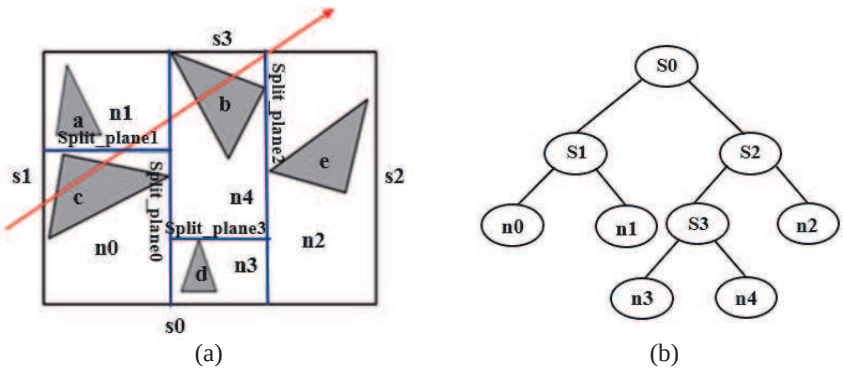

Figure 1: (a) The space division of 2D scene. (b) The corresponding constructed kd-tree.

obtained leaf node n_0, the ray is just only to test whether intersecting with faces in it. Generally it can find a valid intersection face. Otherwise, the traversal procedure is repeated by pushing up the top node in stack.

After fully understanding the features of kd-tree algorithm, based on its spatial division and traversal criterion, we can generally find a smaller subspace of the scene which is the nearest to the ray and then it is only to judge whether the ray intersects with faces in this subspace. As a result, the number of intersection test dramatically reduces. As illustrated in Figure 1, for the emitted geometrical-optics ray, it needs five times of intersection test by the means of traditional way but only one time by applying the kd-tree algorithm. It adequately shows the advantage of kd-tree algorithm in terms of acceleration intersection test for ray tracing.

2.2. Ray Tracing Procedure

In Figure 2, a general flowchart of the proposed method is presented. It is composed of three important phases: modeling, searching for path and calculating.

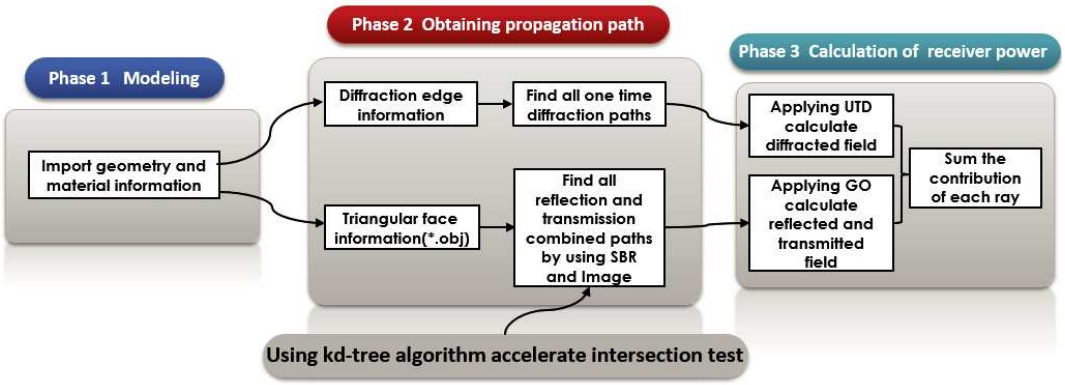

Figure 2: Procedure of the proposed ray tracing model.

Firstly, the original input geometry and material information files are converted and combined to generate the edge information file and triangular face information file conformed to requirement. Secondly, all possible reflection and transmission combined propagation paths are searched for by using the SBR method and then all the valid paths can be picked out by applying the image method. Furthermore, one time diffraction propagation paths must be considered for the indoor object edge. Lastly, after all the paths are determined, tracking the path and employing the GO and UTD theoretical formulas [8, 9] to calculate the final receiver power strength. Moreover, it is valuable to note that the introduction of kd-tree algorithm is used to accelerate the intersection test of ray tracing.

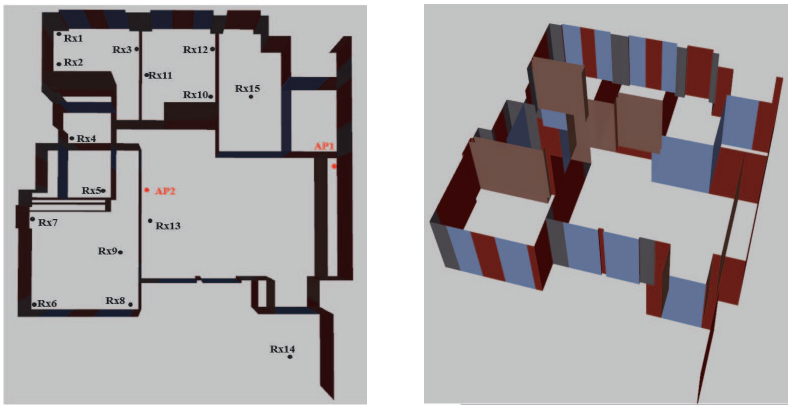

(a) (b)

Figure 3: Illustration of simulated house environment. (a) 2D diagram. (b) 3D contour structure.

3. COMPARISON OF NUMERICAL RESULTS

In order to demonstrate the accuracy and efficiency of the proposed acceleration ray tracing model, the simulated results is not only compared with the measurements and the commercial software Winrpop but also the conventional ray tracing model. A complex indoor simulated environment, a household room, is total of about 140 square meters and composed of three bedrooms, two halls and two bathrooms, as illustrated in Figure 3. Figure 3(a) is two dimension (2D) simplified diagram of the simulated household environment, while Figure 3(b) is three dimension (3D) graphic of the house contour structure. In Figure 3(a), symbol AP1, AP2 represent transmitters (Tx) and Rx1, Rx2, ..., Rx15 represent receivers (Rx). The result are taken by moving one Tx to two different position (AP1 (12.1, 9.5, 0.5), AP2 (5.3, 8.5, 0.4)) while keeping 15 Rx steady in the simulation household environment. Different Tx represents different scenarios and they all use a same transmitting antenna, which is isotropic, the power is 18 dBm and the frequency is 2.4 GHZ.

The simulation has been separately done for 2 scenarios as presented in Figure 3(a). The received power obtained by the proposed method is compared to the measurements and Winprop in terms of computational accuracy, which are plotted in Figure 4. It can be observed that the proposed method shows good performance and agreement not only with measurements but also the Winprop simulated result. However, there still exists slight difference in a certain receiver points. By analysis, it may be primarily caused by the subtle difference between simulation and actual measurement environment. Because the simulation modeling environment actually skips some difficult-to-model indoor objects which make a non-negligible contribution to the overall computed field strength at the receiver. Furthermore, in order to demonstrate the efficiency, the proposed technique has also been compared with the conventional ray tracing (CRT), which in this paper is namely the hybrid model as stated in Section 2.1.1 but without any acceleration technique. Figure 5 shows a comparison, which is one Tx corresponding to one Rx based on computational time, considering 15 different receiver points in 2 different scenarios as presented in Figure 3(a). Hence, it can be

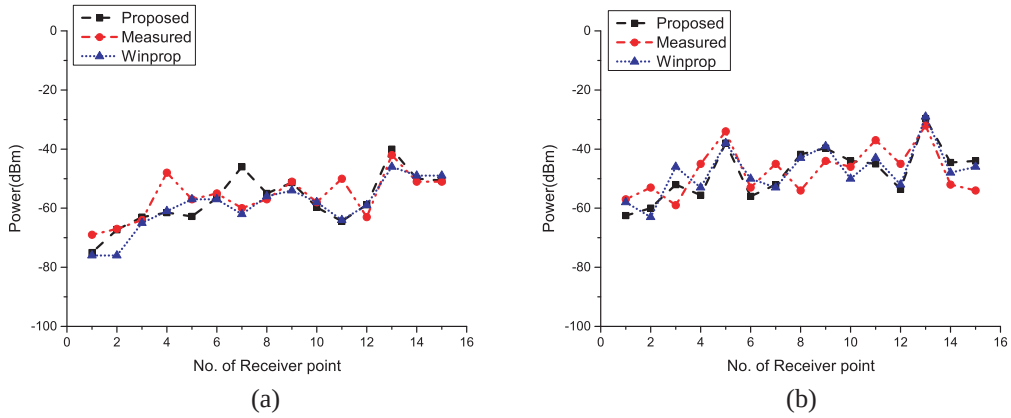

Figure 4: Comparison of measured data, Winprop and the proposed method. (a) AP1. (b) AP2.

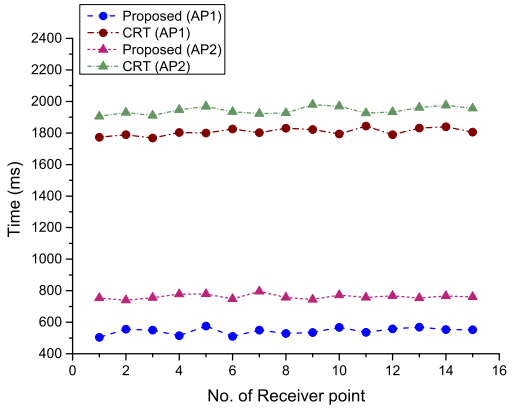

Figure 5: Comparison between the proposed method and conventional ray tracing model based on computational time in terms of 15 receiver points in 2 different scenarios (AP1, AP2).

found that the proposed method gives obviously higher computational efficiency than the CRT. Therefore, it can be summarized that the proposed acceleration ray-tracing technique based on the kd-tree algorithm shows high superiority in terms of both computational accuracy and efficiency.

4. CONCLUSION

In this study, a sophisticated 3D ray tracing acceleration technique based on kd-tree algorithm has been implemented and can be applied to complex indoor environment radio prediction. The proposed method is based on the hybrid ray tracing model and the kd-tree technique. The kd-tree algorithm is applied to accelerate the intersection test of ray tracing by tremendously reducing the number of intersection test. The precedence and reliability of the proposed acceleration method are confirmed by comparing the simulated results with measurements, commercial maturity software Winprop in terms of computational accuracy and at the same time comparing with the the conventional ray-tracing technique in terms of computational efficiency, respectively. The achievement of this study will facilitate the deployment of personal communication systems in complex indoor environment. Moreover, our future work will be concentrated on applying the proposed method to outdoor or indoor-outdoor collaboration radio coverage prediction.

ACKNOWLEDGMENT

This work was supported in part by the National Natural Science Foundation of China under Grant 61171035.

REFERENCES

1. Mohtashami, V. and A. A. Shishegar, "Efficient shooting and bouncing ray tracing using decomposition of wavefronts," *IET Microwaves Antennas and Propagation,* Vol. 4, No. 10, 1567–1574, 2010.
2. Iskander, M. F. and Z. Yun, "Propagation prediction models for wireless communication systems," *IEEE Transactions on Microwave Theory and Techniques*, Vol. 50, No. 3, 662–673, 2002.
3. Tan, S. Y. and H. S. Tan, "A microcellular communications propagation model based on the uniform theory of difraction and multiple image theory," *IEEE Transactions on Antennas Propagation,* Vol. 44, No. 10, 1317–1326, 1996.
4. Chen, S. H. and S. K. Jeng, "SBR image approach for radio wave propagation in tunnels with and without traffic," *IEEE Transactions on Antennas and Propagation*, Vol. 3, No. 45, 570–578, 1996.
5. Chen, S. H., "An SBR/image approach for radio wave propagation in indoor environments with metallic furniture," *IEEE Transactions on Antennas and Propagation*, Vol. 1, No. 45, 98–106, 1997.
6. Pharr, M. and G. Humphreys, *Physically Based Rendering: From Theory to Implementation,* Har/Cdr Edition, Morgan Kaufmann, 2004.
7. Tao, Y. B., H. Lin, H. J. Bao, "Kd-tree based fast ray tracing for rcs prediction," *Progress In Electromagnetics Research*, Vol. 81, 329–341, 2008.
8. Seidel, S. Y. and T. S. Rappaport, "Site-specific propagation prediction for wireless in-building personal communication system design," *IEEE Trans. Veh. Technol.*, Vol. 43, 879–891, 1994.
9. El-Sallabi, H. M. and P. Vainikainen, "Improvements to diffraction coefficient for non-perfectly conducting wedges," *IEEE Trans. Antennas Propag.* Vol. 53, 3105–3109, 2005.

Similarity Measure of Fading Profiles of Different Antenna States of Reconfigurable Antennas

Hassan El-Sallabi, Mohamed Abdallah, and Khalid Qaraqe
Electrical and Computer Engineering Department, Texas A&M University at Qatar, Qatar

Abstract— Design of antenna states in reconfigurable antenna based wireless communication system require careful characterization process based on interplay between pattern of an antenna state and directional impulse response of propagation channel. This work introduces similarity and distance (i.e., dis-similarity) measures that are used in other field of science for characterizing interaction of antenna pattern and propagation channel. The distance/similarity measures are presented in cumulative distribution functions that characterize the interplay of different antenna states with propagation channels and show which antenna states that behave similarly. The presented approach may help in devising a design process to select the antenna state that may enhance the performance of wireless communication systems.

1. INTRODUCTION

Smart antenna research has been well explored and investigated based on array signal processing theories [1]. It was considered that at least two antennas are needed to achieve a performance gain from array signal processing theories. However, this research field assumed that the antenna pattern of each antenna element is assumed to be fixed. Reconfigurable antenna is a field that adds one more degree of freedom for wireless communications. It is based on possibility of altering some of antenna characteristics such as antenna pattern, pointing direction, polarization and resonance frequency [2]. This makes wireless system based on either a single antenna or a multiple antennas to be more flexible than conventional antenna technology. Reconfigurable antennas usually have several antenna states, where each state defines some particular antenna characteristics. The interplay between each antenna state with multipath component of propagation environment results in different fading profiles. For similar directional radio channel response, there will be different fadinglevels with different antenna states.

In this work, we present methods to characterize the similarity and dis-similarity measures [3, 4] between fading profiles that correspond to their responses of different antenna states for same directional impulse channel response. The dissimilarity measures indicate the amount of differences between fading profiles by providing information onhow much we can gain from diversity of antenna states. While the similarity index refers to amount of similar behavior of different fading profiles. The results might be used as input to design of antenna states process to know which antenna states that behave differently from others and may provide a frontier to the receiver for better channel conditions. The presented results are for dissimilarity (or distance) measures named as Sorenson coefficient and Canberra distance. The Canberra distance is normalized to feature vector length to transform it to Canberra coefficient. The presented results for similarity measure are for Jaccard coefficient [4].

2. RADIO CHANNEL MODEL AND RECONFIGURABLE ANTENNA

This work adopts physics based radio channel model for LOS propagation conditions. The multipath components are based on specular reflection mechanism that results from interaction of radio waves with reflection surfaces. Each ray is characterized with multi-dimensional parameters in delay and direction domain in terms of its delay, azimuth and co-elevation angle of arrival, azimuth and co-elevation angle of departure. The amplitude is computed with free space electromagnetic formulation and interaction with surface via the known Fresnel coefficient based on angle of incidence on wall and electrical properties of the surface. These parameters are given in explicit mathematical expression for cubical indoor environment such as a corridor, office, lecture hall, convention center, etc.. The mathematical forms are derived based on image theory. It is based on same essence as in [5, 6] but extending it for RF propagation indoor environment. The simulated propagation characteristics are determined by the input parameters to the model a communications link setup. The input parameters to the channel model include operating frequency, system bandwidth, antenna's polarization and the heights of transmitter and receiver, antennas' field pattern, electrical properties of scatterers, etc.. The communication link setup includes the locations of transmitter

and receiver antennas with respect to the scatterers and reflecting surfaces such as ceiling, side and opposite walls, etc.. The complex signals arrive receiver antenna in multipath channels interact and combined together that results in constructive and destructive interference based on their amplitudes and phases. The multi-domain RF characteristics depend on the dispersion patterns in their corresponding domain such as delay, direction and Doppler. The impulse response of the LOS radio multipath channel is obtained as a linear superposition of $N+1$ individual rays, and it can be represented as follows:

$$h(t) = \frac{\lambda}{4\pi r_{los}} \sqrt{G_{tx}(\varphi_{los}, \vartheta_{los})\, G_{rx}(\phi_{los}, \theta_{los})} \times \delta(t - \tau_{los})\, e^{-jk(r_{los} - \mathbf{V}\cdot\mathbf{\Psi}_{los}t)} + \sum_{n=1}^{N} \frac{\lambda}{4\pi r_n} \sqrt{G_{tx}(\varphi_n, \vartheta_n)\, G_{rx}(\phi_n, \theta_n)} \prod_{p=1}^{P_n} \Gamma_p e^{-jkd_{n,p}} \times \delta(t - \tau_n)\, e^{jk(\mathbf{V}\cdot\mathbf{\Psi}_n)t}$$

where λ is the wavelength of operating frequency, Γ_p denotes the Fresnel reflection coefficient for the p-th wave-interface intersection, k is the wave number expressed as $k = \frac{2\pi}{\lambda}$, $\mathbf{\Psi}_n$ stands forthearrival direction vector defined for ray n as

$$\mathbf{\Psi}_n = \cos(\phi_n)\sin(\theta_n)\,\vec{x} + \sin(\phi_n)\sin(\theta_n)\,\vec{y} + \cos(\theta_n)\vec{z}$$

$\mathbf{V}$ is the velocity (speed and direction) of the mobile terminal, which is assumed as the receiver in this notation, and defined by $\mathbf{V} = v_x\vec{x} + v_y\vec{y} + v_z\vec{z}$ and $d_{n,p}$ denotes the distance traversed by the specular wave between the $(p-1)$ and p-th boundary intersections, r_{los} is the length of LOS path and r_n is the specular reflection path length, $G_{tx}(\varphi_n, \vartheta_n)$, $G_{rx}(\phi_n, \theta_n)$ are the transmitter and receiver reconfigurable antenna (RA) gain, respectively, where ϕ_n and θ_n are the horizontal and co-elevation arrival angles of ray n (or LOS ray when subscript is *los*) relative to the x-axis and z-axis, respectively.

The RA can altercharacteristics of its field pattern such as resonance frequency,polarization and pointing direction. The main idea in gaining benefit from RA is based on understanding the interplay between directional impulse response of multipath components of radio channel, three dimensional antenna patterns, and velocity of mobile terminal. This interplay would affect channel characteristics in RF propagation domains, i.e., delay, direction and Doppler domains. This is reflected in impact on their corresponding correlation parameters such as coherence spectra (i.e., frequency correlation), spatial correlation and coherence time, respectively. In this work, RA pattern of a mobile device is simulated in terms of reconfiguringinclination angle (α) of the antenna, which modifies antenna gain pattern for vertical polarization that can be written as [7]

$$G_v(\theta, \phi) = 1.64\,(\cos\theta\cos\phi\sin\alpha - \sin\theta\cos\alpha)^2\, \frac{\cos^2(\pi\zeta/2)}{(1-\zeta^2)^2}$$

and its antenna gain pattern for horizontal polarization is

$$G_h(\theta, \phi) = 1.64\sin^2\phi\sin^2\alpha \frac{\cos(\pi\zeta/2)^2}{(1-\zeta^2)^2}$$

where the angle α is from z-axis in the vertical zx-plane, $\zeta = \sin\theta\cos\phi\sin\alpha + \cos\phi\cos\alpha$ and, ϕ, the coefficient 1.64 corresponds to the directivity of the half-wavelength dipole antenna. Impact of orientation angle on multi antenna radio channels [9, 10] can also be studied and investigated using this RA model to characterize the dis-similarity between different sub-channels.

3. SIMILARITY MEASURE OF FADING CHANNEL PROFILES

A similarity measure is a function that assigns a number to a pair of patterns that describe quantitatively level of resemblanceof how close two objects are [3, 4]. For the same multipath propagation channel, radio channels supported with RA may have different interplay results for different antenna states of RA. This difference in interplay results comes from different weighting of multipath components due to different antenna states. In order to measure the similarity of different fading profiles due to different antenna states, we need a metric that describe the similarity or dis-similarity (i.e., distance) between different fading patterns. There are already different measures in literature that are used to measure the distance between two features. The selection of dis-similarity/similarity

Table 1: L_1 Dis-similarity and inner product similarity measure families [4].

L_1 Dis-similarity Measure	Sorensen	$D_{sor} = \frac{\sum_{i=1}^{n} \lvert\mathcal{M}_i - \aleph_i\rvert}{\sum_{i=1}^{n} \lvert\mathcal{M}_i + \aleph_i\rvert}$
	Canberra	$D_{Can} = \frac{1}{n} \sum_{i=1}^{n} \frac{\lvert\mathcal{M}_i - \aleph_i\rvert}{\lvert\mathcal{M}_i + \aleph_i\rvert}$
Inner Product Similarity Measure	Jaccard	$S_{Jac} = \frac{\sum_{i=1}^{n} \mathcal{M}_i \cdot \aleph_i}{\sum_{i=1}^{n} \mathcal{M}_i^2 + \sum_{i=1}^{n} \aleph_i^2 - \sum_{i=1}^{n} \mathcal{M}_i \aleph_i}$

metric depends on measurement type of features [8]. The most widely measure is the Euclidian distance. It is justified in maximum likelihood perspective when the feature has Gaussian distribution. The other commonly used is the Manhattan distance, which is justified when the feature has exponential (or double exponential) distribution. In many applications, the assumption as either Gaussian or Exponential is invalid. However, these two measures are members of L_P Minkowski family. The generalized formula for Minkowski distance measure family can be written as $d_{MK} = \sqrt[P]{\sum_{i=1}^{n} |\mathcal{M}_i - \aleph_i|^P}$ where $P = 1$ for Manhattan (aka city block, taxicab rectilinear) distance and $P = 2$ for Euclidean distance, where $\mathcal{M}$ and $\aleph_i$ are vectors of features. Different normalization forms are available for Manhattan Distance measure that are combined in L_1 family. The other similarity measure family incorporates inner product, $(\mathcal{M}_i \cdot \aleph_i)$ in their definition. The inner product refers to number of matches or overlap between $\mathcal{M}_i$ and $\aleph_i$ in case of binary vectors. This work presents (dis)-similarity measures that are presented in the Table 1.

4. NUMERICAL RESULTS

The radio channel model is used to generate radio channel realizations for different antenna states that represent different inclination angles (i.e., 0°, 20°, 60°, 80°). The simulation results assume vertical polarization with operating frequency of 5 GHz. Access point antenna is placed at ceiling of the indoor environment at height of 10 m. Receiver antenna height is 1.7 m. Maximum specular reflection order is 6 from every reflection surface (i.e., four walls, ceiling and floor). Relative Permittivity of each reflection surface is set 6. Two distance measures and one similarity have been selected for presentation in this work. Sorensen and Canberra distance coefficients measure dis-similarity between two fading profiles, while Jaccard coefficient measures the similarity between fading profiles. Jaccard similarity measure was originally developed for binary data but we extend its application in this work. They are proportion coefficients expressed as proportions of maximum distance possible. Figure 1 shows samples of fading profiles of received powers and their corresponding Jaccard Sorensen and Canberra coefficients. The results are given in terms of similarity and dis-similarity ratios. For Jaccard similarity index, when it is equal to one, then, the two profiles are identical and when it is zero, they are completely different. The opposite scale takes place with Sorensen distance measure (i.e., when it is zero, it means that there is no distance difference). The radio channel model has been used to generate 13026000 channel samples for every antenna states. Channel samples have organized into channel vectors of 1040 samples that correspond to a time duration of 40 ms, which is considered as two word codes of 20 ms length. The similarity and dissimilarity coefficient for each block of power offast fading signals of 1040 samples have been computed for different states as shown on legend of Figure 2. The number of computed (dis)-similarity blocks is 12525 for every antenna state versus other received power blocks of other antenna states.

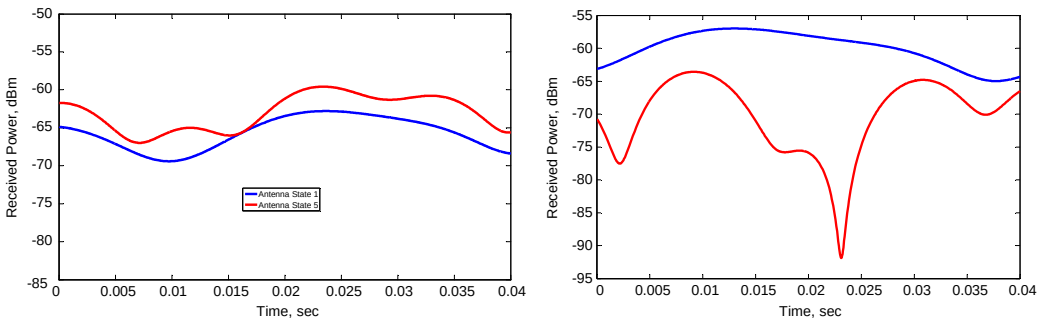

Figure 1: (a) $S_{Jac} = 0.9663$, $D_{sor} = 0.0816$, $D_{Can} = 0.0941$. (b) $S_{Jac} = 0.0747$, $D_{sor} = 0.8466$, $D_{Can} = 0.8137$.

The computed coefficients are presented in cumulative distribution curves (CDF) as presented in Figure 2. The CDF curves are for thetwo selected different dis-similarity measures (i.e., as Sorenson and Canberra distance measures) and one similarity measure, (i.e., Jaccard similarity measure). The presented (dis)-similarity coefficients are ranged from zero to one. The zero values for Sorenson and Canberra distances correspond to the one value of Jaccard similarity, which indicate to very similar or identical vectors and vice versa for other extreme value. The statistics of the three tested (dis)-similarity measures are presented in Table 2. The closer values to zeros for Sorenson and Jaccard coefficients indicate the closer to each other fading profiles from different antenna states. Fading profiles of antenna state 1 and antenna state 5 have largest dis-similarity. The second largest

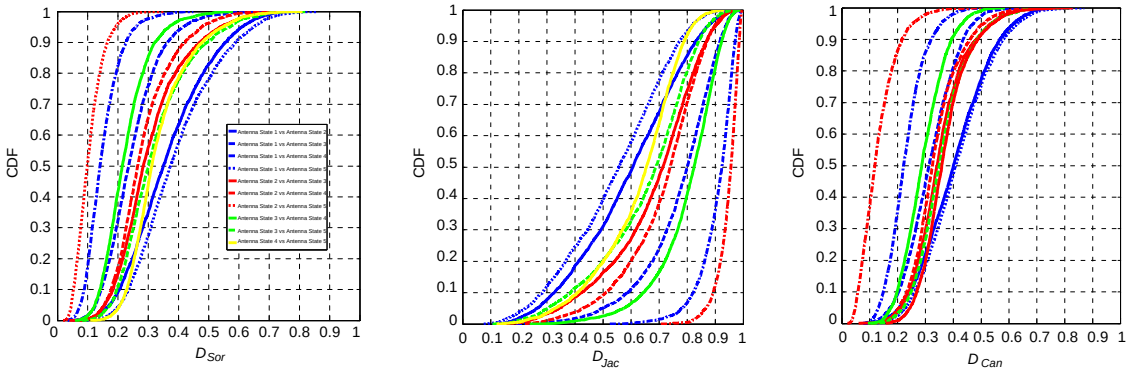

Figure 2: Cumulative distribution functions of (dis)-similarity measures of fading profiles for different antenna states. (a) Sorenson Coefficient. (b) Jaccard Coefficient. (c) Canberra Coefficient.

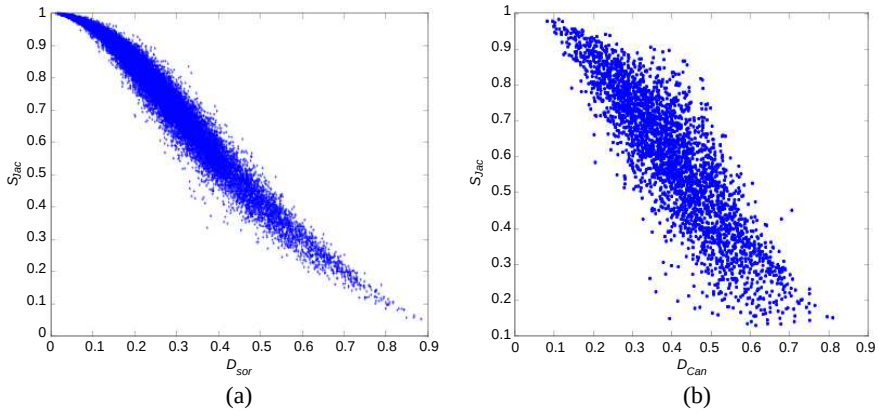

Figure 3: Scatter plot of similarity measure versus dis-similarity measures for fading profiles of antenna state 1 and that of antenna state 2. (a) Jaccard Coeff. vs Sorenson Coeff. (b) Jaccard Coeff. vs Canberra Coeff.

Table 2: Statics of tested (dis)-similarity measures for different combinations of antenna states.

	Sorenson Measure		Canberra Measure		Jaccard Measure	
	Mean	StdDev	Mean	StdDev	Mean	StdDev
Antenna 1 vs Antenna 2	0.3656	0.1336	0.4038	0.1240	0.5917	0.1874
Antenna 1 vs Antenna 3	0.2476	0.0901	0.3175	0.0910	0.7723	0.1340
Antenna 1 vs Antenna 4	0.1510	0.0587	0.2299	0.0679	0.9065	0.0653
Antenna 1 vs Antenna 5	0.3935	0.1355	0.4164	0.1225	0.5421	0.1834
Antenna 2 vs Antenna 3	0.3074	0.1145	0.3518	0.0962	0.6784	0.1681
Antenna 2 vs Antenna 4	0.2839	0.0978	0.3365	0.0907	0.7118	0.1422
Antenna 2 vs Antenna 5	0.1053	0.0456	0.1302	0.0658	0.9458	0.0395
Antenna 3 vs Antenna 4	0.2259	0.0771	0.2930	0.0771	0.8005	0.1162
Antenna 3 vs Antenna 5	0.3243	0.1186	0.3593	0.0956	0.6493	0.1737
Antenna 4 vs Antenna 5	0.3349	0.1028	0.3700	0.0890	0.6250	0.1481

dis-similar coefficient is between fading profiles of antenna state 1 and antenna state 2. However, the dis-similarity measure between fading profiles of antenna state 2 and antenna state 5 is quite low to indicate that they are quite similar. This indicate in a setup of antenna states, 1, 2 and 5, there will be effectively two antennas that cause different fading profiles. If the design requires two antenna states, then, it is easy to select the best two antenna states that generates diversity in fading profiles so the RA system can switch between them. However, the situation becomes more complicated if three antenna states are needed due to similar behavior of some of antenna states. According to our simulation results, the following combination sets may be a good choice, a) antenna states 1, 2, and 3. b) Antenna states 1, 3 and 5. It is shown that Sorenson and Canberra coefficients results in similar behavior in their distance measure between different fading profiles of different antenna states. Jaccard coefficient has a strong negative correlation with both Sorenson and Canberra coefficients as shown in Figure 3.

5. CONCLUSION

This work presents results of different distance and similarity measure that describe the resemblance between different fading profiles. The similarity of measures are already being used in other field of science but we introduce them here for fading radio channels of different antenna states. These measures help in design of best selection antenna states technique that enhance performance of RA based wireless communication systems. Both Sorenson and Canberra coefficient shows similar behavior as distance measure, while Jaccard coefficient shows strong negative correlation with both Sorenson and Canberra coefficient. For three antenna states design, the simulation results show that two different sets may work well for enhancement of RA based wireless communications; i.e., a) antenna states 1, 2, and 3. b) Antenna states 1, 3 and 5.

ACKNOWLEDGMENT

This publication was made possible by NPRP grants #: NPRP 5-653-2-268 from the Qatar National Research Fund (a member of Qatar Foundation). The statements made herein are solely the responsibility of the authors.

REFERENCES

1. Chang, D.-C. and C.-N. Hu, "Smart antennas for advanced communication systems," *Proceedings of the IEEE*, Vol. 100, No. 7, 2233–2249, Jul. 2012.
2. Bernhard, J. T., "Reconfigurable antennas," *Synthesis Lectures on Antennas*, 65, Morgan & Claypool Publishers, 2007.
3. Santini, S. and R. Jain, "Similarity measures," *IEEE Trans. of Pattern Analysis and Machine Intelligence*, Vol. 21, No. 9, 871–883, Sep. 1999.
4. Cha, S.-H., "Comprehensive survey on distance/similarity measures between probability density functions," *International Journal of Mathematical Models and Methods in Applied Sciences*, Vol. 1, No. 4, 300–307, 2007.
5. El-Sallabi, H. M. and P. Vainikainen, "Physical modeling of line-of-sight wideband propagation in a city street for microcellular communication," *Journal of Electromagnetic Waves and Applications*, Vol. 14, No. 7, 905–927, 2000.
6. El-Sallabi, H. M. and P. Vainikainen, "Radio wave propagation in perpendicular streets of urban street grid for microcellular communications. Part I: Channel modeling," *Progress In Electromagnetics Research*, Vol. 40, 229–254, 2003; *Journal of Electromagnetic Waves and Applications*, Vol. 17, No. 8, 1157–1158, 2003.
7. Taga, T., "Analysis for mean effective gain of mobile antennas in land mobile radio environments," *IEEE Trans. Veh. Technol.*, Vol. 39, 117–131, May 1990.
8. Yu, J., J. Amores, N. Sebe, P. Radeva, and Q. Tian, "Distance learning for similarity estimation," *IEEE Trans. of Pattern Analysis and Machine Intelligence*, Vol. 30, No. 3, 451–462, Mar. 2008.
9. Wang, S., et al., "Time-varying MIMO channels: Parametric statistical modeling and experimental results," *IEEE Trans Vehicular Technology*, Vol. 56, No. 4, 1949–1963, 2007.
10. Salo, J., et al., "Some insights into MIMO mutual information: the high SNR case," *IEEE Trans. on Wireless Communications*, Vol. 5, No. 11, 2997–3001, November, 2006.

Algorithms for Indoor Localization on WLAN Networks Applications

S. Helhel and A. Kocakusak
Department of Electrical and Electronics Engineering, Akdeniz University, Turkey

Abstract— A locating system for indoors has been tried to develop by using WLAN systems (protocol number: IEEE 802.11). Wireless modems using IEEE 802.11 protocol installed all around 4 corners of corridor were used as RF transmitters as well as laptop computer was used as RF receiver. A computer software generated by EMUMAM software group was used in order to calculate RSS, and 672 different measurement data were collected. Each location measurement was repeated by 7 times. 100% location success rate is achieved within the ±10% deviation and ±5% deviation in exact location is achieved with 75% success.

1. INTRODUCTION

Increased popularity of locating technologies requires that development of a proper indoor propagation model is essential for obtaining precise indoor location. Use of a proper model is not only required for indoor localization but also Body Area Network (BAN) systems and personal tracking systems in in forest areas [1–3].

This paper proposes algorithms for location applications for indoor scenarios over Wireless Local Area Networks (WLAN). We compare the use of radio frequency (RF) power levels based on ray-tracing as detection methods to estimate the localization of a set of mobile station using the fingerprint technique. Wi-Fi (802.11x) and Wi-Max (802.16x) standards play an important role in applications of high frequencies techniques for locations as a detection method. The proposed algorithm computes the Euclidean distance between the samples of signals received from each known source position and radio-map obtained using EMUMAM's simulation tool. The Euclidean distance has been compared with others similarity distance measures. Experimental results show that more precision can be obtained at same level instead of different floor location of transmitter and receiver. An effect of increasing the number of transmitters has also been investigated and compared. Proposed algorithm allows to obtain very precise indoor localization over WLAN networks. WiFi systems using IEEE 802.11 procols have been used for generating indoor locating algorithms that they use RSS measurements [4, 5].

2. INDOOR PATH LOSS MODEL

Friis uqaution is basically used for calculating path loss between tranciever couples operating line-of-sight, and let us to calculate distance between those couples. Instead varying indoor propagation models are valid in the literature [6–8], very common model used for indoor path calculation using Radio Signal Strength (RSS) is given in Equation (1).

$$P(d) = P(d_0) - 10 \times n \times \log\left(\frac{d}{d_0}\right) + \zeta \tag{1}$$

where $P(d)$is the signal strength obtained by the receiver at a distance of d and $P(d_0)$ is the received signal strength at 1 m distance (means referance signal) both in dBm, n is the path loss index for indoors, and ζ is the random variable describing shadowing factor [6, 9].

3. DERIVATION OF n AND MEASUREMENT CAMPAIGN

At first glance, it seems that it had better to use values of n given in the literature rather than calculating new one; however, n value is a value strictly depend on interested campaign. Figure 1 gives measurement campaign, and there are 6 WiFi transmitters located around the corridor which are shown as red stars. Given corridor is 7.2 m wide and 50 m length, and measurement points are aligned by 60 cm apart from each other that we determine 120 different locations. It has to be noted that each transmitter has its own "n" value that is going to be used in path loss.

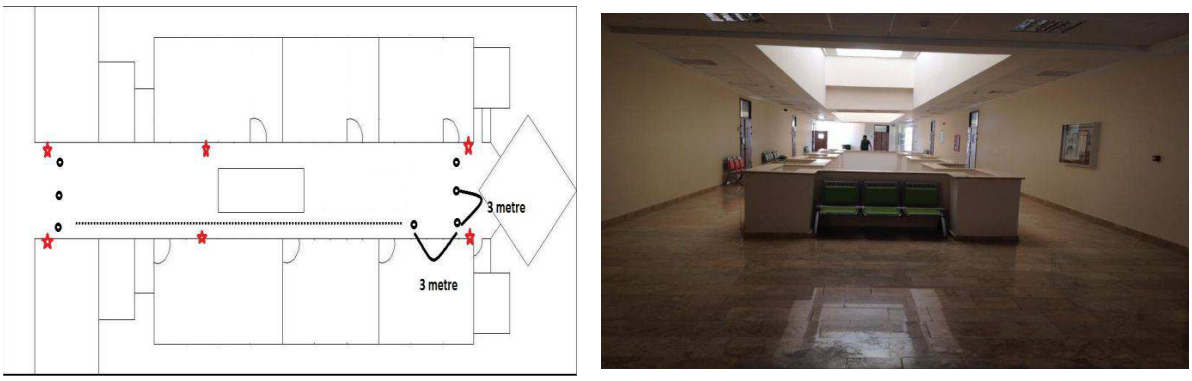

Figure 1: Second floor of engineering faculty.

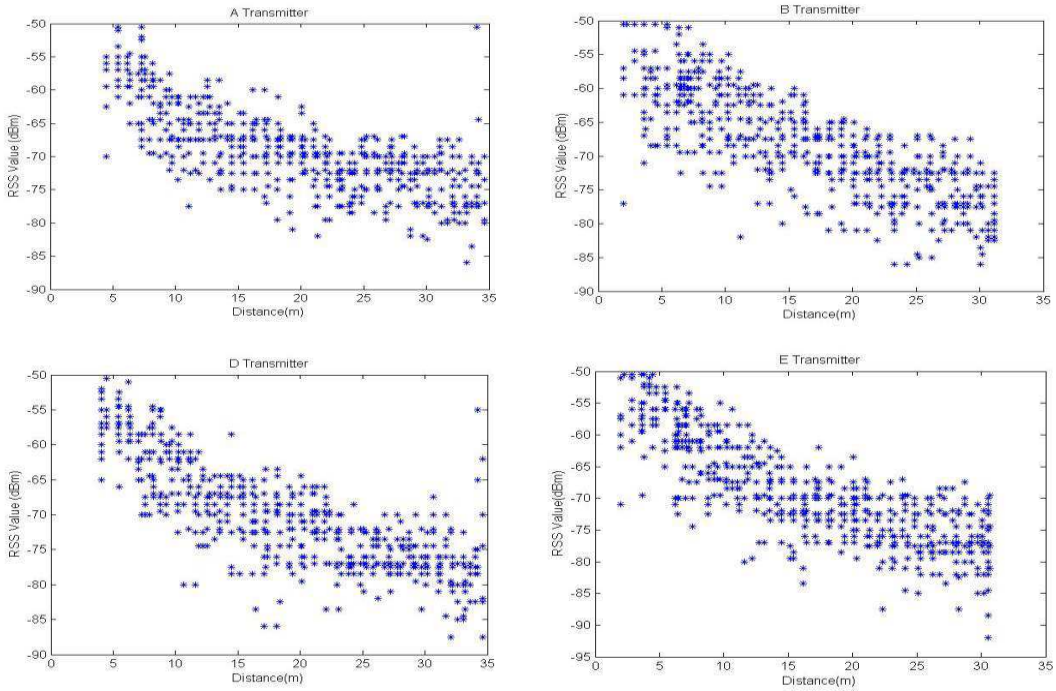

Figure 2: Obtained RSS values related to 4 different WiFi transmitters.

4. RESULTS AND CONCLUSIONS

Figure 2 shows measured RSS values at pre-determined locations which are used for calculating "n" values of each transmitter. Since the path loss equation is basically given by Eq. (2a) in draft, logarithmic form of n is given by Eq. (2b).

$$path\ loss \propto \left(\frac{d}{d_0}\right)^{-n} \tag{2a}$$

$$n = 10\log_{10}\left(d/d_0\right) \tag{2b}$$

For those given locations calculated "n" values are calculated as shown in Figure 3.

Figure 4 shows predicted locations and real measured locations. As easily seen from the figures that 100% location success rate is achieved within the ±10% deviation and ±5% deviation in exact location is achieved with 75% success.

Predicted results at initial step of current project shows that very preceise indoor location estimation has been achived in case of small distance between Rx and Tx. 100% location success rate is achieved within the ±10% deviation and ±5% deviation in exact location is achieved with 75% success rate.

The Smart Locater a software which is currently being developed in our group will have a

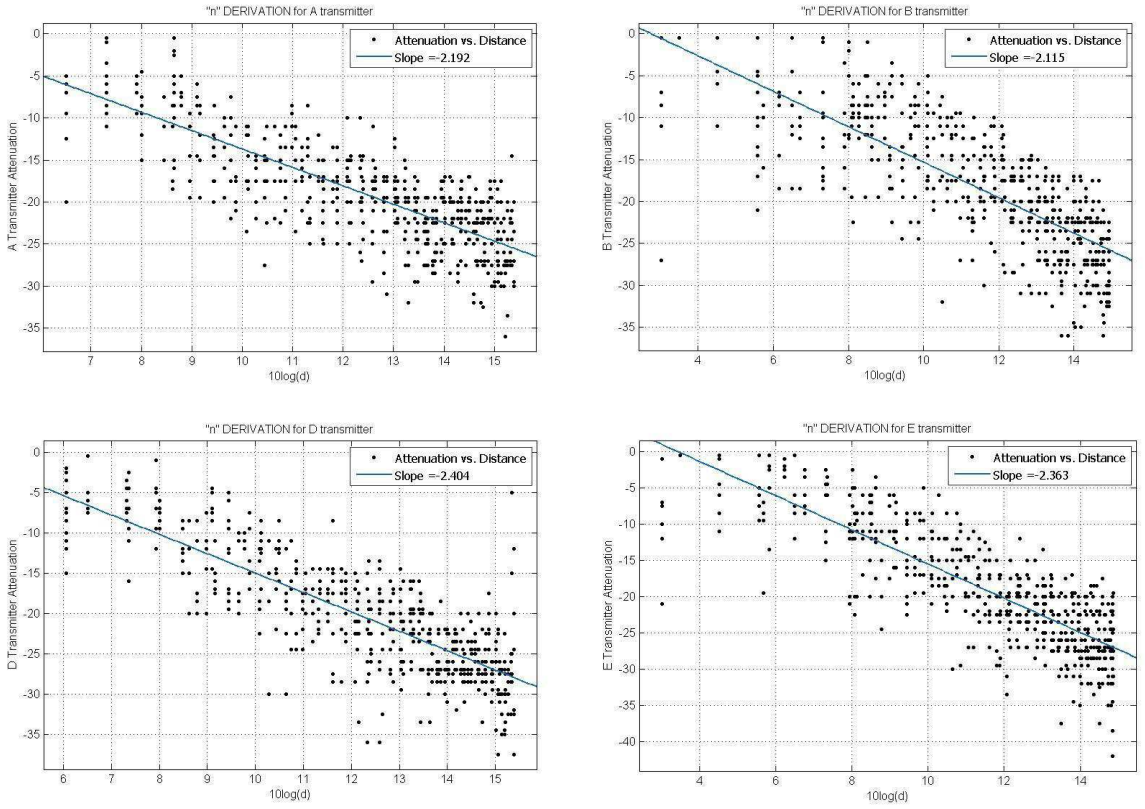

Figure 3: Calculated n values.

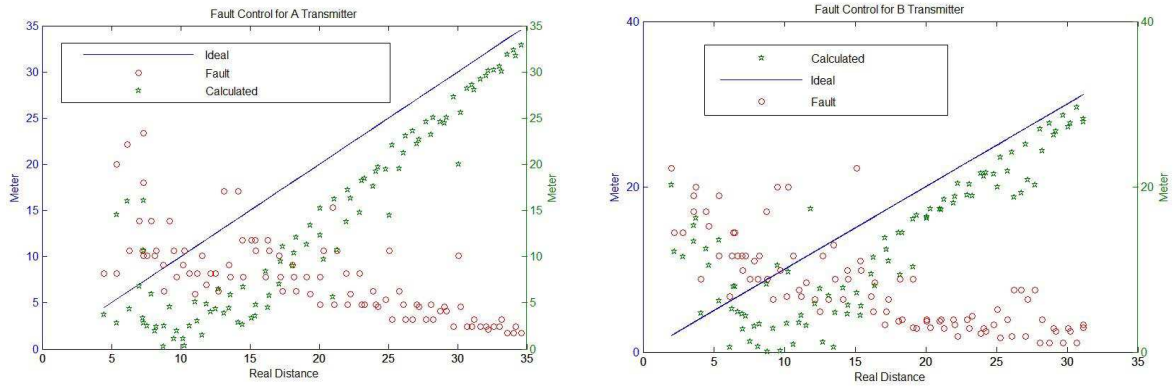

Figure 4: Measured and predicted distance.

capability to decide which "n" value need to be selected in a certain location will improve the system's preceise. Up to know, our group did not concenrate on location update time duration or locating speed of system, and this will be another subject that will be taken into accout in near future.

EMUMAM group is also working on ultrasonic and acustic indoor systems as well as high frequency indoor systems, and aimed to design hybrid indoor systems.

ACKNOWLEDGMENT

This project was granted by TÜBİAK 2209-A (PN: 1919B011303278) and Akdeniz University, Scientific Research Projects Supporting Unit (BAPYB).

REFERENCES

1. Helhel, S., "Comparison of 900 MHz and 1800 MHz indoor propagation deterioration," *IEEE Trans. Antennas and Propagation*, Vol. 54, 3921–3924, Dec. 2006.

2. Helhel, S., S. Ozen, I. B. Basyigit, O. Kurnaz, Y. E. Yoruk, M. Bitirgan, and Z. Colak, "Radiated susceptibility of medical equipments in health care units: 2G and 3G mobile phones as an interferer," *Microwave and Optical Technology Letters*, Vol. 53, 2657–2661, Nov. 2011.
3. Kurnaz, O. and S. Helhel, "Near ground propagation model for pine tree forest environment," *AEU — International Journal of Electronics and Communications*, in Press, http://dx.doi.org/10.1016/j.aeue.2014.04.019.
4. Kocakuşak,A., "Bina içi ve ormanlık alanda konum tespiti," Lisans Bitirme Projesi, Elektrik Elektronik Mühendisliği Bölümü, Mühendislik Fakültesi, Akdeniz Üniversitesi, Haziran, 2014.
5. Kaemarungsi, K., "Distribution of WLAN received signal strength indication for indoor location determination," *Proc. First Int'l Symp. Wireless Pervasive Computing*, 6–11, Jan. 2006.
6. Zhao, Y., M. Li, and F. Shi, "Indoor radio propagation model based on dominant path," *Int. J. Communications, Network and System Sciences*, Vol. 3, 330–337, Blished Online, Mar. 2010, Doi: 10.4236/ijcns.2010.33042.
7. Celik, S., Y. E. Yoruk, M. Bitirgan, O. Kurnaz, B. Basyigit, S. Helhel, and S. Ozen, "Indoor to outdoor propagation model improvement for GSM900/GSM1800/CDMA-2100," *2011 XXXth URSI General Assembly and Scientific Symposium*, 1–4, 2011.
8. Çelik, S., O. Kurnaz, Y. Albayrak, M. Bitirgan, I. Basyigit, and S. Helhel, "An indoor to outdoor propagation model at GSM900 GSM1800 and CDMA2100," *International Journal of Engineering & Applied Sciences (IJEAS)*, Vol. 5, No. 2, 9–17, 2013.
9. Lin, Y. S., R. C. Chen, and Y. C. Lin, "An indoor location identification system based on neural network and genetic algorithm," *2011 3rd International Conference on Awareness Science and Technology (iCAST)*, 193–198, Sep. 27–30, 2011.

Three Dimensional (3D) Electromagnetic Field Distributions in the Air and Relative Diversity Gain

Selçuk Helhel[1, 2], Şükrü Özen[2], Yalcın Albayrak[2, 3], and I. Bahadir Basyigit[4]

[1]Tübitak National Observatory, Akdeniz University Campus, Antalya, Turkey
[2]Engineering Faculty, Department of EE, Akdeniz University, Antalya, Turkey
[3]Engineering Faculty, Department of EE, Sakarya University, Adapazarı, Turkey
[4]School of Distance Education, S. Demirel University, Isparta, Turkey

Abstract— There exists 3-dimensional (3D) electromagnetic field distribution (EMFD) in the air and its components can be used for polarization discrimination (XPD) or equivalently diversity improvement. Measurements were carried out through shore roads and hillsides. The results show that the lowest XPD is obtained for hill side road area, and very high signal cross-correlation is achieved through shore road. Calculated values point out that 30 dB extra relative gain can be obtained by using suitable 3 dimensional antenna design at shore sides, while 4.6 dB by hill-side roads.

1. INTRODUCTION

Polarization discrimination (XPD) or equivalently polarization diversity is commonly used to improve quality in wireless communication systems such as mobile equipments' applications, LAN and WLAN applications. MIMO antennas have very big applications in wireless communications especially for broadening channel capacity. With similar reasons, people started to focus on designing new antennas having three dimensional (3D) electric field sensing capability for varying applications. Diversity reception especially polarization diversity, for mobile communication systems results in decreasing transmitting power as well as in receiving power which allows to control interfering signals [1, 2]. Space diversity applications basically require 10λ antenna separation, and that much of space requirement (equals to 3 m at 900 MHz) results in increased installation budget. In this case, de-correlation of polarized signal components become an attractive alternative for space diversity. It is noted that, environment as an obstacle affects the polarization diversity scheme performances [3, 4], and polarization discrimination (XPD) or equivalently the polarization diversity can also be applied to mobile equipments instead of BSS receivers. The partial evaluation of the possibility of usage of polarization diversity can be achieved by analyzing 3D EMF components. There are studies in the literature [3, 5, 6] focusing on the cross polarization discrimination and/or cross-correlation with horizontally or vertically polarized varying antenna configurations. Scattering of signals from different scatters rotates the polarization of waves through multipath fading, and it allows deriving cross-polarization diversity gain. A relationship between XPD and polarization diversity gain is evaluated experimentally by using cross polarized reception data at the base-station (BS) end. 5 dB to 15 dB XPD is reported in their study, and reported those varying values are depending on the scattering environment and on the radio propagation path between the BS and mobile station. Propagation path can be either line-of-sight (LOS) or non-line-of-sight (NLOS) [7].

Lotse et al. [8] and Jaana et al. [9] proposed a study for estimating polarization diversity gain, and NARDA SRM3000 with a type 18 isotropic E-field probe is used the studies [3, 4] for performing measurements. Jaana et al. [3] demonstrates that polarization diversity archives a gain performance comparable with the horizontal space diversity in urban and suburban environments. In this paper, discussion takes place on the distribution of 3D EMF radiated from a horizontally polarized BS transmitting antenna instead of two dimensional (horizontal and vertical) electromagnetic field distributions. The measurements were performed at The Antalya Gulf. Aim is to get RF planners' attention on how sea surface and mountain based reflections affect polarization diversity gain, and increasing their background and confidence about aforementioned subjects.

2. MEASUREMENT ENVIRONMENTS

The measurements were performed at the Antalya Gulf in 1800 MHz network. A Type-18 isotropic electric field probe compatible with NARDA SRM300 is preferred during the measurement. Aforementioned probe includes three mutually located perpendicular dipoles inside, and the head of each

Figure 1: Measurement path through shore side road.

Figure 2: Measurement path at hillside (Kemer intercity R).

dipoles connected to the basic unit through three channel switches and a coaxial cable. There are three high impedances fed by three sensor voltages down to the rod into the instrument to avoid distortion in the field. No measurement error is expected as a result of switching from one axis to the next, since the blind time is 20 milliseconds between switching one axis to the next. Given blind time is several orders of magnitude less than the blind time of classical spectrum analyzers.

An avoiding Rayleigh fading during measurements requires having enough samples over the wavelength, and thus a vehicle speed was kept as 30 km/h. Thus, results have a good correspondence on slow-moving equipment [7]. BSS transmitting antenna tower height is 30 m. The first measurement set was conducted in a cell which is serving a road next to shore demonstrated in Fig. 1. The second measurement set was conducted in a cell which is serving a part Antalya-Kemer road. It is also assumed as Hill Side road that south of road is Antalya Gulf (Calticak Bay) and north side is 1000 m height Taurus Mountains. Driving area is illuminated from the other side of bay which is shown in Fig. 2. Illumination angle of transmitting antenna is 30 degree in order to overcome escaping signals to the city of Antalya.

3. EXPERIMENTAL RESULTS

The signal mean level difference between 3D polarized components specifies the value of XPD. The propagation environment has an influence on the calculated XPD, and thus, the area-type description is important [8]. XPD can be approximated as in Eq. (1a), Eq. (1b) and Eq. (1c). Cross polarization discrimination values are relative to one another, and given in Table 1.

$$\mathrm{XPD}_{xy} = 20\log\left(\frac{E_x}{E_y}\right) \tag{1a}$$

$$\mathrm{XPD}_{xz} = 20\log\left(\frac{E_x}{E_z}\right) \tag{1b}$$

$$\mathrm{XPD}_{yz} = 20\log\left(\frac{E_y}{E_z}\right) \tag{1c}$$

An average XPD values and standard deviation are presented in Table 1. Through shore side road average XPD value is about 23 dB which extremely high than expected values, and 4.69 dB through hillside road is also important value for solving communication problems. Fig. 3 and Fig. 4 both plot relative gain value variation with respect to distance from transmitting antenna. As represented in Fig. 3, relative gain varies between 0–30 dB and there is about 25 dB relative gain on the average. Compared to Fig. 3, Fig. 4 represents that relative gain at hill side road varies between 0–10 dB and relative gain average obtained at hill side is about 10 dB. Relative gain plots both at shore road and hillside road has their own fading-like values.

Table 1: Environment dependent XPD values.

Propagation Environments	**Calculated Average XPD Values (dB)**	**Standard Deviation**
Shore Through Road	23.16	6.19
Hillside	4.69	2.72

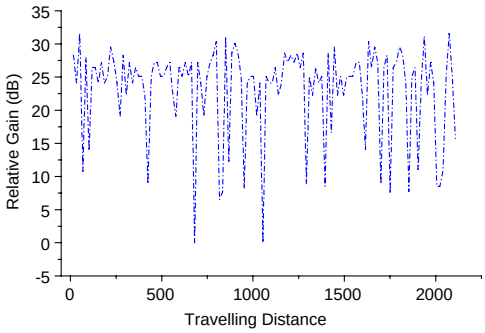

Figure 3: Relative gain through shore road.

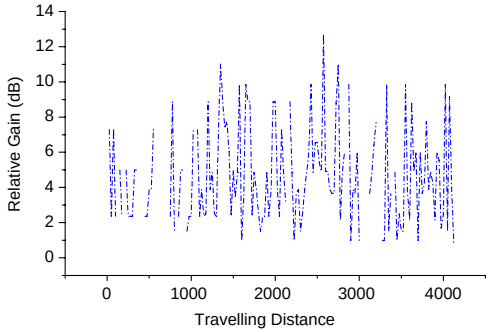

Figure 4: Relative gain through hillside intercity road.

4. CONCLUSIONS

The relationship between XPD assumed as 3D polarization diversity gain at 1800 MHz has been investigated. The results show that the lowest XPD is obtained for hill side road area, and very high signal cross-correlation is achieved through shore road. Since antennas are generally preferred to be placed below rooftops in dense urban area, multiple wall reflections [10–12] are occurred. As a result, propagated waves are strongly affected by street structures wall reflectivity, and diffraction at the vertical edges of street corners. Obtained XPD from such an environment depicts that 3 dimensional antennas may allow to obtain better diversity gain and resolves quality problems especially in such kind of shore area/shore roads. Thus, cross polarization discrimination gain depends mostly on the signal mean difference between two receiver branches, and it offers a good choice for radio frequency design engineers by not requiring additional space between two antennas and extra bandwidth [13]. 30 dB relative XPD/gain on the average can be achieved by suitable antenna design.

ACKNOWLEDGMENT

This project has been supported by Akdeniz University Scientific Research Project Support Unit (BAPYB).

REFERENCES

1. Kozono, S., T. Tsuruhara, and M. Sakamoto, "Base station polarization diversity reception for mobile radio," *IEEE Transactions on Vehicular Technology*, Vol. 33, No. 4, 301–306, Nov. 1984.
2. "RF engineering continuing education and training, propagation modeling, traffic planning and link budgets," *Agilent Technologies Course Book*, Melbourne FL 32904, USA, 2000.
3. Laiho-Steflens, J., J. Lempiainen, M. Salmenkaita, J. Siltaniemi, and O. Jukarainen, "Experimental evaluation of polarization diversity gain at the base station end in a GSM900 network," *IEEE Vehicular Technologies, IEEE VTC'98*, 16–20, 1998.
4. Helhel, S., H. Goksu, and S. Ozen, "Investigation of 3D electromagnetic field distribution for dynamic polarization diversity," *IEEE Antennas and Wireless Propagation Letters*, Vol. 7, 171–174, 2008.
5. Turkmani, A. M. D., A. A. Arowojolu, P. A. Jefford, and C. J. Kellett, "An experimental evaluation of the performance of two-branch space and polarisation diversity schemes at 1800 MHz," *IEEE Transactions on Vehicular Technology*, Vol. 44, No. 2, 318–326, May 1995.
6. Lemieux, J. F., M. S. El-Tanany, and H. M. Hafez, "Experimental evaluation of space/frequency/polarization diversity in the indoor wireless channel," *IEEE Transactions on Vehicular Technology*, Vol. 40, No. 3, 569–574, Aug. 1991.
7. Lempiainen, J. J. A. and J. K. Laiho-Steffens, "The performance of polarization diversity schemes at a base station in small/micro cells at 1800 MHz," *IEEE Transactions on Vehicular Technology*, Vol. 47, No. 3, 1087–1092, Aug. 1998.
8. Lotse, F., J.-E. Berg, U. Forssen, and P. Idahl, "Base station polarization diversity reception in microcellular systems at 1800 MHz," *IEEE Vehicular Technology Conference Record*, 1643–1646, 1996.

9. Laiho-Steffens, J. and J. Lempiznen, "Impact of the mobile antenna inclination on the polarization diversity gain in a DCS 1800 network," *1997 International Symposium on Personal, Indoor and Mobile Radio Communications Proceedings*, 580–583, 1997.
10. El-Sallabi, H. and P. Vainiakainen, "Physical modeling of line-of-sight wideband propagation in a city street for microcellular communications," *Journal of Electromagnetic Waves and Applications*, Vol. 14, No. 17, 904–927, 2000.
11. Helhel, S., "Comparison of 900 MHz and 1800 MHz indoor propagation deterioration," *IEEE Transactions on Antennas and Propagation*, 3921–3924, Dec. 2006.
12. Ozen, S., S. Helhel, and O. H. Colak, "Electromagnetic field measurements of radio transmitters in urban area and exposure analysis," *Microwave and Optical Technology Letters*, 1572–1578, Jul. 2007.
13. Lemieux, J.-F., M. S. El-Tanany, and H. M. Hafez, "Experimental evaluation of space/frequency/polarization diversity in the indoor wireless channel," *IEEE Transactions on Vehicular Technology*, Vol. 40, No. 3, 569–574, Aug. 1991.

Analysis and Design of Beam-scanning Reflectarray with Circular Polarization

Zuoxing Dai[1], **Yuanbo Shang**[1], **Fengwei Yao**[2], **and Xiaobo Xuan**[1]

[1]Shanghai Radio Equipment Research Institute, Shanghai, China
[2]Science and Technology on Electromagnetic Scattering Laboratory, Shanghai, China

Abstract— The design of a beam-scanning reflectarray with circular polarization is presented. The element allows tuning of the reflected signal's phase over a 360 range, and the spiral antenna is adopted as the feed of the reflectarray. By full-wave commercial simulation software HFSS, the model of the antenna is simulated and optimized. Two reflectarray prototypes with different compensate methods for phase delays are designed and proceed, of which one is with different length of stubs, the other is with different rotated angle.

1. INTRODUCTION

A microstrip reflectarray antenna [1, 2], being the mixture of a reflector antenna and a planar phased array antenna, uses a suitable phasing scheme for its elements to convert a spherical wave produced by its feed into a plane wave.

Printed reflectarrays consist of an array of microstrip elements illuminated by a primary radiator, typically represented by a horn antenna. The printed elements, giving a flat reflecting surface, are designed to reradiate the incident field with a planar phase front in a prescribed direction. The use of microstrip technology gives significant improvements, in terms of low-cost, less-weight, and easy installation, with respect to standard parabolic reflectors. On the other hand, the feeding mechanism inherited from reflector antennas avoids the disadvantages, in terms of complexity and losses, due to the feeding networks usually adopted in phased arrays.

Various configurations of passive printed reflectarrays, adopting different tuning mechanisms, have been introduced in literature [3]. Dynamic phase control techniques have been also investigated for the design of active reflectarrays [4], and significant achievements have been obtained in the improvement of bandwidth performances [5]. Analysis methods based on different approaches, such as that assuming an infinite array model [6] or that considering each radiator as an isolated element on a grounded dielectric substrate [7], have been considered in literature, and various numerical methods have been implemented for both single-layer and multilayer reflectarrays. A very efficient synthesis technique based on the intersection approach [8] and properly taking into account both the amplitude and the phase of the field reflected by the reflectarray unit cell, has

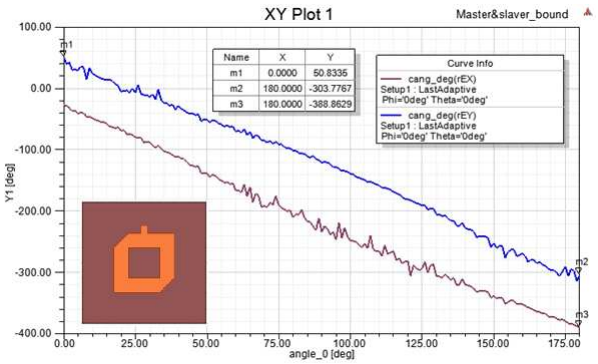

Figure 1: Top view of reflectarray element configuration and simulation reflection phase with different rotate angle.

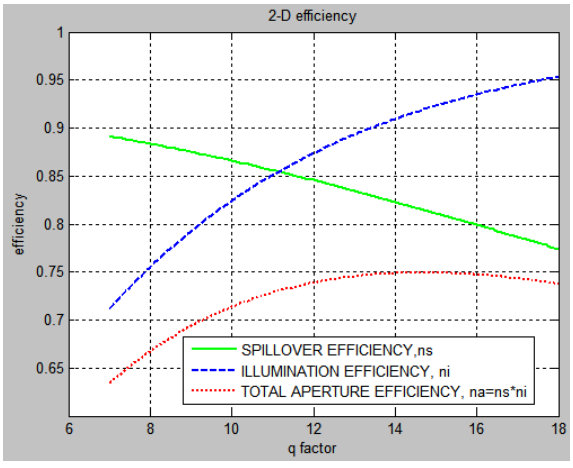

Figure 2: Microstrip reflectarray spillover and illumination efficiencies versus feed pattern shape.

been developed and applied in [9]. Experimental methods alternative to the standard waveguide simulator approach [10] have been developed, with the adoption of open resonator [11] and near field [12] techniques for the characterization of both passive and active reflectarray unit cell.

In this paper, the design of beam-scanning reflectarray with circular polarization is presented. A quadrilateral ring microstrip patch is chosen as reconfigurable reflectarray element, which allows tuning of the reflected signal's phase over a 360 range, and the spiral antenna is adopted as the feed of the reflectarray. Three fixed-beam reflectarray prototypes with different rotated angle for compensate phase delays is designed and proceed.

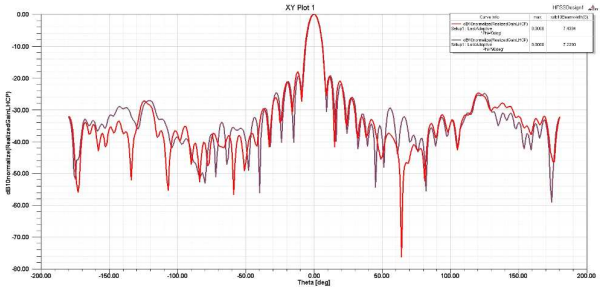

Figure 3: Simulation plane pattern of reflectarray at $\theta = 0°$ and $\theta = 90°$.

Figure 4: Photograph of the reflectarray prototype into the anechoic chamber.

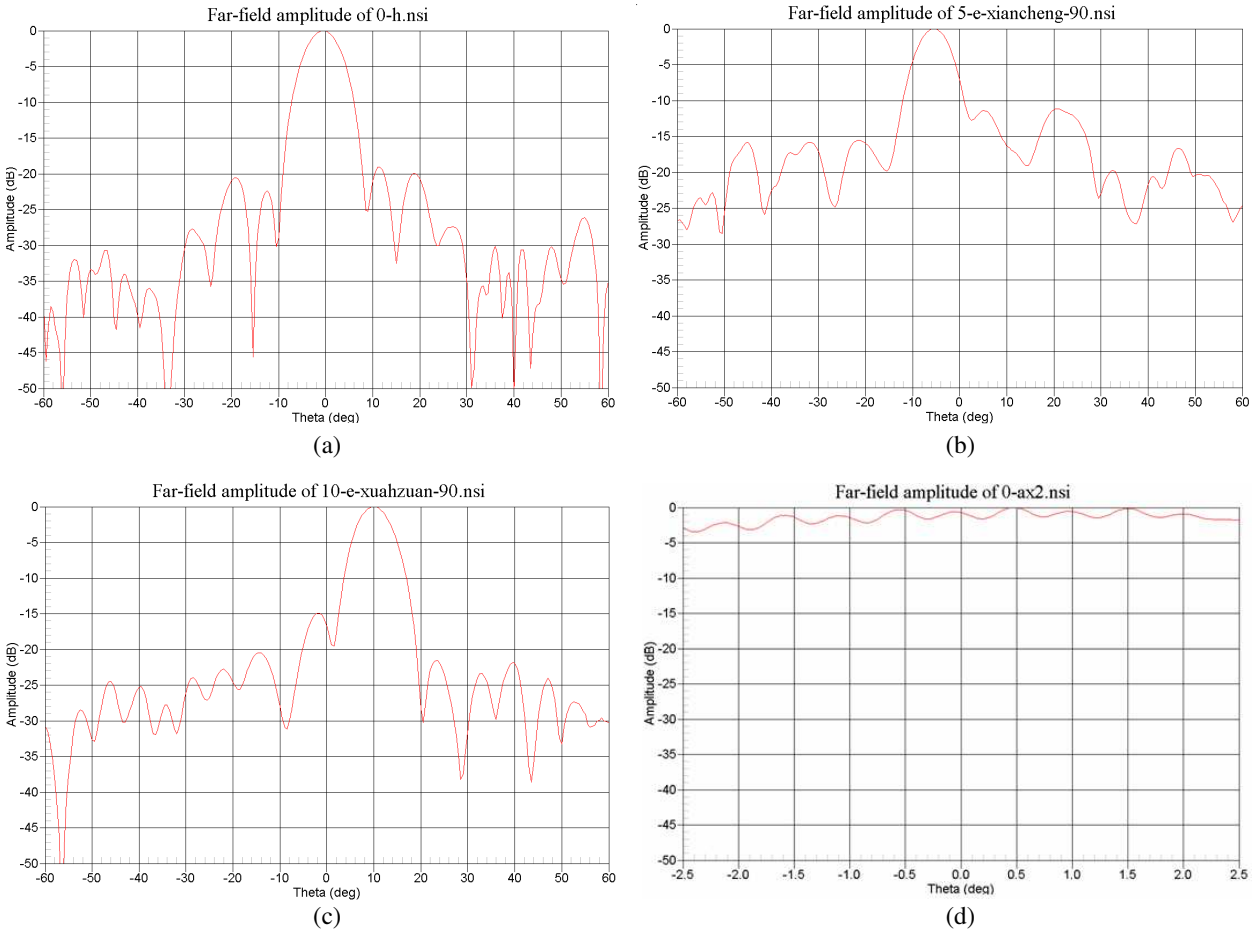

Figure 5: Measured radiation patterns for various beam direction, (a) 0°, (b) 5°, (c) 10°, (d) axial ratio.

2. ANALYSIS AND SIMULATION

In a circularly polarized microstrip reflectarray, the circular polarization can be achieved by many types. Considering connecting with the phase shifts, we chose the quadrilateral ring microstrip patch with short stub which is shown in Fig. 1. By the software HFSS, the performance of circular polarization and impedance matching can be optimized.

To each patch element is rotated its angle in Z axis to compensate for the phase delay over the path from the illuminating feed. In theory, the reflection phase is 36 degree when the element is rotated by 180 degree from its initial position; the phase curve of the X component of E field is parallel to that of Y component and the difference of each other is 90 degree or 270 degree. The simulation results in general accord with above conclusions, which are shown in Fig. 1.

The two primary factors that govern the efficiency of the microstrip reflectarray are very similar to those for the parabolic reflector. These are the aperture illumination efficiency and the feed spillover efficiency [13]. The efficiencies are plotted against the feed pattern shapes in Fig. 2 with a given reflectarray diameter of 130 mm at 21 GHz and an f/D ratio of 0.85.

The model of reflectarray antenna with phase-delay compensation by rotation of identical elements and a spiral antenna as feed is shown in the upper left corner of the Fig. 3. Simulation plane pattern of reflectarray at $\theta = 0^\circ$ and $\theta = 90^\circ$ are also shown in Fig. 3. The gain 3 dB beam width and axial ratio are 25.3 dB, 7.3° and 0.9 dB respectively.

3. REFLECTARRAY PROTOTYPE AND MEASUREMENT

Photograph of the reflectarray prototype into the anechoic chamber is shown in Fig. 4. Three microstrip reflectarray prototypes by rotated angle for compensate phase delays form the feed is proceed and measured, of which with different beam directivity (0° 5° 10°). Two methods are adopted to achieve beam deviation, one is changing the length of stub and the other is rotation of identical elements. For the approximate simulation of two bits phase shifts, the phase difference between elements is set to 0° 90° 180° and 270°. So the first sidelobe of scanning antenna is relative high.

Measured radiation patterns for three reflectarray antennas are shown in Fig. 5. Relative good agreement are found between simulation and measured results.

4. CONCLUSION

The design of circular polarization reflectarray consists of an quadrilateral ring microstrip patch, printed on the TLY-5 substrate is analysis, simulated and measured. For the approximate simulation of two bits phase shifts, two reflectarray prototypes with different compensate methods for beam-scanning are proceed, of which one is with different length of stubs, the other is with different rotated angle. Due to the four states of the switch phase shifter, the first sidelobe of antenna is high, up to −11.5 dB when beam scanning to 5°.

ACKNOWLEDGMENT

This work was supported by the national Nature Science Fund of China under Grant No. 61201116.

REFERENCES

1. Malagasi, C. S., "Microstrip disc element reflectarray," *Electron. Aerospace Syst. Conv.*, Sep. 1978.
2. Kelkar, A., "FLAPS: Conformal phased reflecting surfaces," *Proc. IEEE National Radar Conf.*, 58–62, Los Angeles, CA, Mar. 1991.
3. Pozar, D. M. and T. A. Metzler, "Analysis of a reflectarray antenna using microstrip patches of variable size," *Electronics Letters*, Vol. 29, No. 8, 657–658, 1993.
4. Hum, S. V., M. Okoniewski, and R. J. Davies, "Realizing an electronically tunable reflectarray using varactor diode-tuned elements," *IEEE Microwave and Wireless Components Letters*, Vol. 15, No. 6, 422–424, 2005.
5. Encinar, J. A., "Design of two-layer printed reflectarrays using patches of variable size," *IEEE Transactions on Antennas and Propagation*, Vol. 49, No. 10, 1403–1410, 2001.
6. Pozar, D. M., "Microstrip reflectarrays: Myths and realities," *Proceedings of the International Symposium on Antennas (JINA'04)*, 175–179, Nice, France, 2004.

7. Venneri, F., G. Angiulli, and G. Di Massa, "Design of microstrip reflectarray using data from isolated patch analysis," *Microwave and Optical Technology Letters*, Vol. 34, No. 6, 411–414, 2002.
8. Bucci, O. M., G. Franceschetti, G. Mazzarella, and G. Panariello, "Intersection approach to array pattern synthesis," *IEE Proceedings H*, Vol. 137, No. 6, 349–357, 1990.
9. Costanzo, S., F. Venneri, G. Di Massa, and G. Angiulli, "Synthesis of microstrip reflectarrays as planar scatterers for SAR interferometry," *Electronics Letters*, Vol. 39, No. 3, 266–267, 2003.
10. Tsai, F. C. E. and M. E. Bialkowski, "An equivalent waveguide approach to designing of reflect arrays with the use of variablesize microstrip patches," *Microwave and Optical Technology Letters*, Vol. 34, No. 3, 172–175, 2002.
11. Costanzo, S., G. DiMassa, and O. H. Moreno, "Improved open resonator technique for dielectric characterization," *Proceedings of the 6th European Conference on Antennas and Propagation (EuCAP'12)*, 2127–2129, 2012.
12. Costanzo, S. and G. Di Massa, "Far-field reconstruction from phaseless near-field data on a cylindrical helix," *Journal of Electromagnetic Waves and Applications*, Vol. 18, No. 8, 1057–1071, 2004.
13. Rudge, A. W., K. Milne, A. D. Olver, and P. Knight, *The Handbook of Antenna Design*, Vol. 1, 169–172, London, England, Peter Peregrinus Ltd., 1982.

A Novel Hybrid Reconfigurable Antenna for Portable Wireless Terminal Applications

Wenxing Li, Lei Bao, Si Li, and Yingsong Li
College of Information and Communications Engineering
Harbin Engineering University, Harbin, Heilongjiang 150001, China

Abstract— In this paper, a dielectric embedded antenna with hybrid reconfigurable characteristics is proposed for portable wireless terminal applications, which is used as frequency or radiation reconfigurable antenna. The proposed hybrid reconfigurable antenna consists of a driven element, two parasitic elements and eight switches. By controlling the ON/OFF states of these switches set on the driven element, the proposed antenna can operate at two different frequencies, namely, 0.85 GHz and 1.9 GHz. The radiation reconfigurable characteristic is achieved by switching six switches installed on the parasitic elements. The proposed antenna has three modes of the radiation patterns at each frequency, has the potential to reduce noisy interference, and hence can improve the performance of the wireless systems. The simulation results demonstrated that the proposed antenna with flexible frequency and radiation pattern reconfigurable function is small in size and is promising for portable wireless devices.

1. INTRODUCTION

With the rapid development of communication technology, the reconfigurable antenna emerges as one of the most important research topics and has broad applications for various communication devices. A good reconfigurable antenna has the potential to improve the overall performance of a wireless communication system and can enable these systems to avoid noisy environments, to maneuver away from electronic jamming and to save energy via adjusting directing signals toward intended users [1]. Moreover, reconfigurable properties are usually realized by integrating electronic switches, capacitors or phase shifters into antenna structure. In [2, 3], a kind of wide slot antenna with frequency reconfigurable characteristics for ultra-wideband (UWB) communication systems has been proposed and investigated deeply. The designed antennas can be used as an UWB antenna, a multi-band antenna and a band-notched UWB antenna though controlling the states of the switches. In addition, a lot of Yagi antennas with pattern reconfigurable characteristics have been proposed [4–8] and widely studied. However, the radiation patterns of the proposed antennas can only scan in the upper-half space. In [9], a reconfigurable antenna with independently reconfigurable operating frequency, radiation pattern and polarization has been reported. Unfortunately, this antenna is large in size and has too many switches. In this paper, a novel hybrid reconfigurable antenna which has frequency and radiation reconfigurable functions was proposed for portable wireless devices. The proposed antenna integrated with eight switches, which controlled the current paths for providing frequency and pattern reconfigurable behaviors. The designed antenna can change the frequency band via adjusting its resonance length and meanwhile maintain the coincident radiation patterns, while the radiation pattern is also reconfigurable at each operating frequency band. In comparison with the previous reported antennas mentioned above, the proposed antenna with small size can not only provide the directional radiation, but also has the omni-directional radiation characteristic in the reconfigurable bands. In the simulation, ideal switches are employed to verify the proposed antenna [2, 3].

2. DESIGN OF THE PROPOSED HYBRID RECONFIGURABLE ANTENNA

Figure 1 shows the physical structure of the proposed hybrid reconfigurable antenna, where S1∼S8 are switches. It can be seen that the proposed antenna consists of a driven element, two parasitic elements and eight switches. Additionally, the antenna and these switches are embedded in the dielectric substrate, whose dielectric constant is 4.4 and the loss tangent is 0.002. The driven element, which is realized by using a meandered line dipole, is approximately a quarter wave length at the resonance frequency of 0.85 GHz in free space. Furthermore, two parasitic elements are set along the driven element at each side. The driven element is fed via a 50 Ω coaxial probe, which lies in the center of the proposed antenna. On the one hand, when the two switches, namely S4 and S5, on the driven element are OFF, the proposed antenna operates at 1.9 GHz, while when these two switches are ON, the antenna works at 0.85 GHz. On the other hand, when the switches on

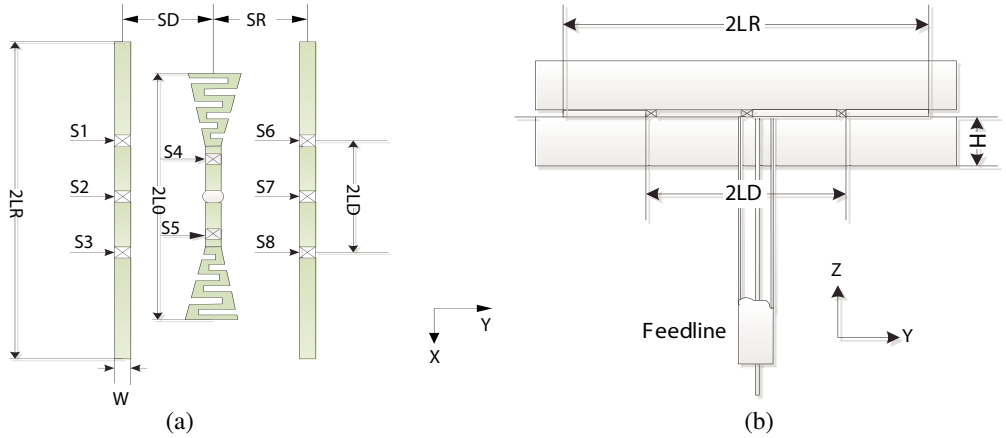

Figure 1: Physical structure of the proposed hybrid reconfigurable antenna. (a) Top view of the antenna. (b) Side view of the antenna.

the parasitic elements are ON, the parasitic element can be regarded as reflectors, while they act as directors when the switches on the parasitic element are OFF. When the left parasitic element works as a director and the right parasitic element works as a reflector, the H-plane radiation pattern tilts to the negative y axis. Conversely, the H-plane radiation pattern tilts to the positive y axis with left parasitic element working as a reflector and the right parasitic element working as a director. When both of the parasitic elements are used as directors, the proposed antenna has omni-directional radiation characteristic.

3. RESULTS AND DISCUSSIONS

To verify the performance of the proposed hybrid reconfigurable antenna, high-frequency structure simulator (HFSS) is employed to obtain the VSWR and the radiation patterns. The optimized dimensions of the proposed antenna are: $H = 3\,\text{mm}$, $W = 2\,\text{mm}$, $2L0 = 0.26\lambda_0$, $2LR = 0.34\lambda_0$, $2LD = 0.142\lambda_0$, $SD = SR = 0.06\lambda_0$, where λ_0 is the wavelength in the free space at the resonance frequency of 0.85 GHz. Since the impedance of the utilized switches is very low, metal strips of size $2 \times 2\,\text{mm}$ are adopted for the proof of the ideal switch concept [2, 3]. The states of the eight switches at each mode are listed in Table 1. The simulated VSWR is shown in Fig. 2. It can be seen that the proposed antenna can operate from 0.78 GHz to 0.87 GHz at mode-1, mode-2 and mode-3. When the proposed antenna works at modes 4–6, it can cover the bandwidth of 1.79 GHz–1.92 GHz with VSWR under 2.5. The radiation patterns are described in Fig. 3. It can be seen from Fig. 3 that the proposed antenna can be used as an omni-directional antenna at mode-1 and mode-4. In other modes, the antenna has Yagi-like radiation patterns. The simulated peak gain for the mode-2, mode-3, mode-5 and mode-6 are 3.95 dBi, 3.85 dBi, 6.6 dBi and 6.63 dBi.

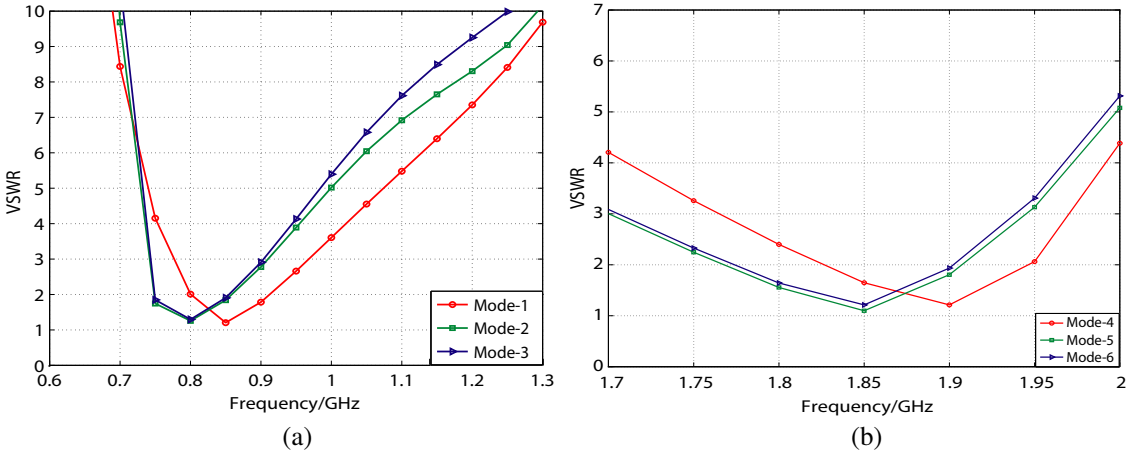

Figure 2: VSWR of the proposed hybrid reconfigurable antenna.

Table 1: Modes of the proposed hybrid reconfigurable antenna.

Modes	S1	S2	S3	S4	S5	S6	S7	S8
Mode-1	OFF	OFF	OFF	ON	ON	OFF	OFF	OFF
Mode-2	ON	ON	ON	ON	ON	OFF	OFF	OFF
Mode-3	OFF	OFF	OFF	ON	ON	ON	ON	ON
Mode-4	OFF	OFF	OFF	OFF	OFF	OFF	OFF	OFF
Mode-5	ON	ON	ON	OFF	OFF	OFF	OFF	OFF
Mode-6	OFF	OFF	OFF	OFF	OFF	ON	ON	ON

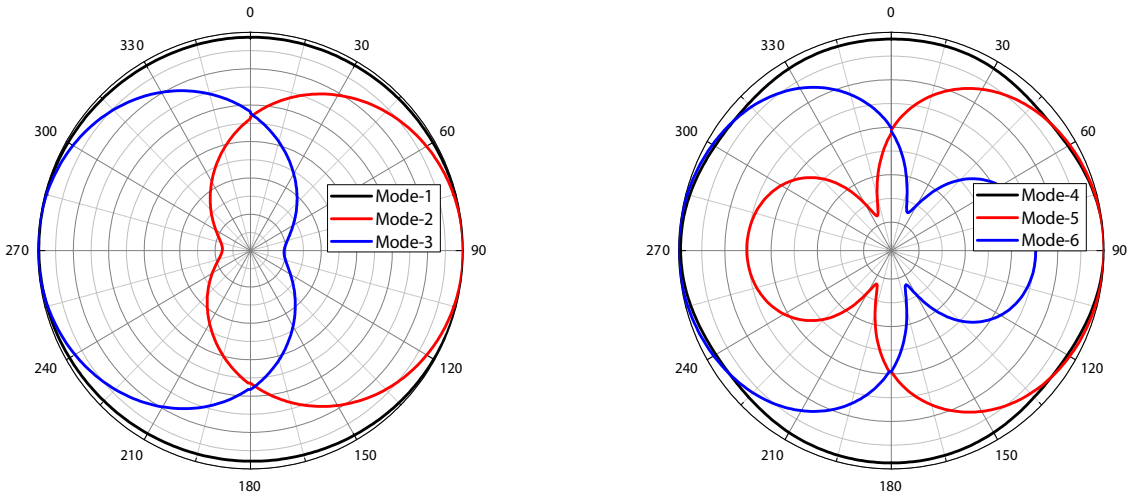

Figure 3: Radiation pattern of the hybrid reconfigurable antenna.

4. CONCLUSION

A dielectric embedded antenna with frequency and pattern reconfigurable characteristics for portable terminals has been investigated. The simulation results demonstrated that the proposed antenna can operate at 0.85 GHz and 1.9 GHz, while the radiation patterns are directional or omnidirectional. The antenna is small in size. In the future, we will fabricate and measure the proposed antenna by using the PIN diodes.

ACKNOWLEDGMENT

This paper is supported by Pre-Research Fund of the 12th Five-Year Plan (No. 4010403020102).

REFERENCES

1. Zhang, S., G. H. Huff, J. Feng, and J. T. Bernhard, "A pattern reconfigurable microstrip parasitic array," *IEEE Trans. Antennas Propagat.*, Vol. 52, No. 10, 2273–2776, 2004.
2. Li, Y., W. Li, and Q. Ye, "Compact reconfigure UWB antenna integrated with SIRs and switches for multimode wireless communications," *IEICE Electronics Express*, Vol. 9, No. 9, 629–635, 2012.
3. Li, Y., W. Li, and W. Yu, "A switchable UWB slot antenna using SIS-HSIR and SIS-SIR for multi-mode wireless communications applications," *Applied Computational Electromagnetics Society Journal*, Vol. 27, No. 4, 340–351, 2012.
4. Yang, X. S., B. Z. Wang, W. Wu, and S. Xiao, "Yagi patch antenna with dual-band and pattern reconfigurable characteristics," *IEEE Trans. Antennas Propagat.*, Vol. 6, No. 10, 168–171, 2007.
5. Huang, J. and A. C. Densmore, "Microstrip Yagi array antenna for mobile satellite vehicle application," *IEEE Trans. Antennas Propagat.*, Vol. 39, No. 10, 1024–1030, 1991.
6. Padhi, S. K. and M. E. Bialkowski, "Parametric study of a microstrip Yagi antenna," *Proc. 2000 Asia-Pacific Microw. Conf.*, 715–718, Sydney, Australia, 2000.

7. Huff, G. H., J. Feng, S. Zhang, and J. T. Bernhard, "A novel radiation pattern and frequency reconfigurable single turn square spiral microstrip antenna," *IEEE Microwave Wireless Components Lett.*, Vol. 13, No. 10, 57–59, 2003.
8. Wahid, P. F., M. A. Ali, and B. C. DeLoach, "A reconfigurable Yagi antenna for wireless communications," *Microw. Opt. Tech. Lett.*, Vol. 38, No. 2, 140–141, 2003.
9. Rodrigo, D., B. A. Cetiner, and L. Jofre, "Frequency, radiation pattern and polarization reconfigurable antenna using a parasitic pixel layer," *IEEE Trans. Antennas Propagat.*, Vol. 62, No. 2, 3422–3427, 2014.

Novel Hepta-band Coupled-fed Antenna for WWAN/LTE Metal-ring-frame Smartphone Applications

Li-Wan Zhang and Yong-Ling Ban
Institute of Electromagnetics, University of Electronic Science and Technology of China
2006 Xi-Yuan Avenue, Western High-Tech District, Chengdu, Sichuan 611731, China

Abstract— A novel hepta-band coupled-fed antenna is presented for WWAN/LTE metal-ring-frame (MRF) smartphone applications in this paper. Unlike the conventional solutions simply removing the redundant resonances generated by the metal ring, A creative couple-fed scheme is utilized in this proposed antenna to take full advantage of the metal ring resonances. With compact size occupation and wide band coverage, the proposed antenna for smartphones enhances the bandwidth coverage, as well as user experience of cosmetic appearance and mechanical strength.

1. INTRODUCTION

The metal-ring frame embracing the samrtphone can enhance the user experience of cosmetic appearance and mechanical strength, but also impede the effective radiation of the internal mobile phone antennas. When the mobile antenna is embraced by a full metal frame in the vicinity of antenna, the coupling between the antenna and the adjacent metal ring would be very intensive to excite multiple additional resonances and set up a negative feedback to the antenna's original radiation.

Concerning the antenna design problem for MRF smartphones, a effective option [1] is to push the multiple metal-ring resonances out of the working band so as to eliminate the adverse effects on the performance of the original antenna. To make better use of radiation generated by the metal ring, a $15 \times 56.5\,\mathrm{mm}^2$ planar slot antenna operated under surroundings of an unbroken metal ring is introduced in [2].

While the problem of the designed antennas for the mental-ring-frame smartphones should be addressed on their large size and failure to cover the LTE2300/2500 operation.

In this paper, an innovative hepta-band couple-fed antenna for WWAN/LTE MRF smartphone applications is presented, which has a compact layout of a printed monopole and the metal-ring frame. By applying the coupled-fed technique [3–8] in a creative way, the sections of the disjointed metal-ring frame are capacitively fed by the printed monopole to generate a dual-resonance mode at the GSM850/900 operation and a higher-order resonant mode at LTE2300/2500 operation. With multiband operation, metal-ring frame, and small size occupation, the proposed scheme might initiate a new antenna design for MRF smartphone applications coving GSM/1800/1900/UMTS2100/LTE2300/2500 (1710–2690 MHz) banding operation.

2. PROPOSED ANTENNA

The geometry of the proposed antenna integrated with a notched system ground plane for WWAN/LTE operation in the MRF smartphone is shown in Fig. 1. Embraced by a metal ring frame with close proximity, the system circuit board is a 0.8-mm thick FR4 substrate of relative permittivity 4.4, loss tangent 0.0245, and size of $120 \times 60\,\mathrm{mm}^2$. The directly feeding monopole is deposed at the bottom corner of the system circuit board with no-ground portion of $10 \times 40\,\mathrm{mm}^2$. At the bottom side of the system circuit board, there is a protruded ground of size $20 \times 10\,\mathrm{mm}^2$ extending from the main ground plane, which can be used to accommodate associated electronic elements in the smartphones.

As shown in Fig. 1, a 0.3-mm-thick brass sheet with two cuts encloses the main circuit board as the metal ring frame, which has a distance of 2 mm to the substrate. Two slits and two grounding patches divide the metal ring into four sections, which are Section 1, Section 2, Section 3 and Section 4 respectively. The length of each section is well tuned for good impedance matching. Unlike the design in iphone4 which cuts slits on the length side of mobile phone, the two slits filled with engineering plastic of Polyoxymethylene (POM) are etched on bottom of the metal ring in our proposed scheme, which can reduce the possibility to be covered by hand at the talk mode. To realize slim smartphone design, the height of the metal ring is only 5 mm. To achieve good artistic appearance of the metal ring, S_2 (inserted slit 2) is etched on the bottom edge with the same distance of S_1 (inserted slit 1) to its nearby bending corner which creates a symmetrical image for

the users. Besides the ornamental function, the metal ring also play an important role to enhance the antenna radiation.

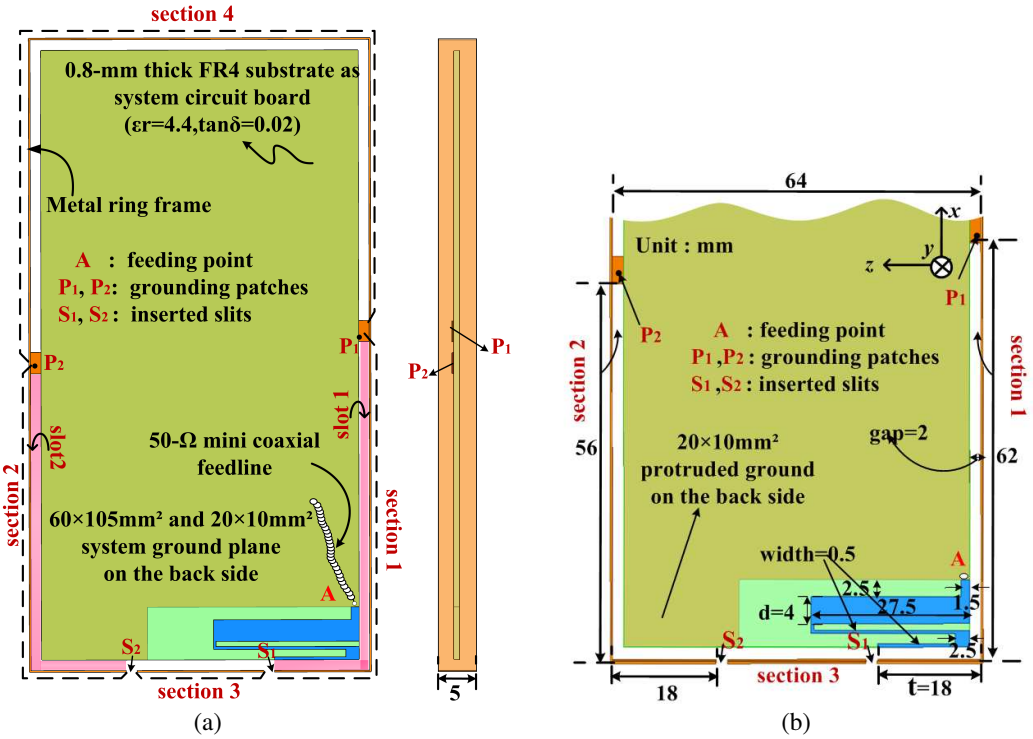

Figure 1: Configuration of the proposed antenna. (a) Geometry of the small size hepta-band antenna with a metal ring frame. (b) Detailed dimensions of the proposed antenna (Unit: mm).

The detailed dimensions of the proposed antenna has be given clearly in Fig. 1(b). The printed part of antenna is composed of a driven meandering monopole, with length of 76 mm, and occupies a small area of $10 \times 27.5\,\text{mm}^2$. The meandering monopole is directly fed by a 50 Ω mini coaxial feeding line and acts as the primary radiator for the upper band while the metal ring is couple-fed by the monopole and works as a parasitic radiator. Shorted by grounding patch P_1, Section 1 and the ground plane forms an open Slot 1 with length of 78 mm, which excites its fundament resonant mode as $\lambda/4$ monopole slot at 850 MHz and its third-order at 2450 MHz. While Section 2 and the ground plane shorted by patch P_2 forms the other open Slot 2 with length of 74 mm, about 0.237 wavelength at 950 MHz, which also generates a $\lambda/4$ monopole slot at 950 MHz. The lower band operation(GSM850/950) could be successfully covered by these two $\lambda/4$ resonant modes. And the impedance matching of the upper band (1710–2690 MHz) is also enhanced by the fundament resonant mode of driven monopole and the higher-order resonant mode of monopole slot 1.

Compared with the traditional couple-fed antennas [6–10] that have a compact structure of the primary radiator and the parasitic radiator, our design has presented a distributed couple-fed layout achieving wide band coverage and miniaturization.

3. RESULTS

The proposed coupled-fed antenna for hepta-band MRF smartphone applications is fabricated to measure. Results of the measured and simulated return loss are presented in Fig. 2. The simulated result is obtained by Ansoft HFSS version 12, while the measured result is tested by using an Agilent N5247A vector network analyzer. The impedance matching for frequencies more over the desired lower band of 824–960 MHz and upper band of 1710–2690 MHz are better than 3 : 1 VSWR or 6 dB return loss, which is widely accepted as the design specification for the WWAN/LTE mobile phone antennas.

The antenna peak gain and radiation efficiency of the proposed mobile phone antenna is also measured in Satimo chamber as seen in Fig. 3. Over the lower band of GSM850/900 (824–960 MHz), the antenna gain varies from about −1.7 to 0.9 dBi. For the upper band operation which includes DCS1800/PCS1900/UMTS 2100/LTE2300/2500, the antenna gain ranges from about 0.2 to 5 dBi.

Measured radiation efficiency is about 47%–82% in the lower band and 65%–91% in the upper band. The result demonstrates an high total radiation efficiency of the proposed antenna, which is suitable for the practical WWAN/LTE MRF smartphone antenna applications.

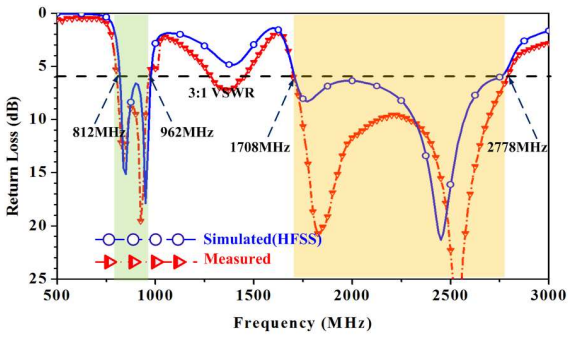

Figure 2: Measured and simulated return loss.

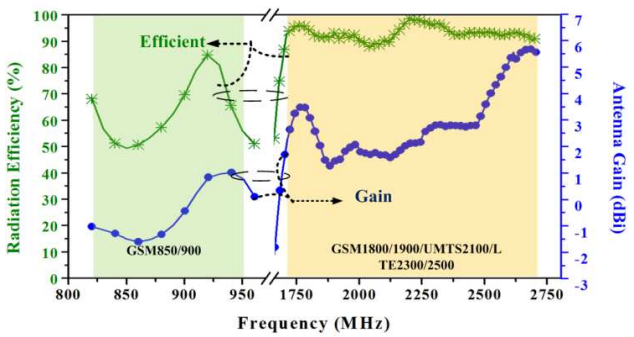

Figure 3: Measured gain and radiation efficiency.

4. CONCLUSION

A novel hepta-band antenna for WWAN/LTE MRF smartphone applications is proposed, which presents a distributed couple-fed layout achieving wide operating bands of 824–960 and 1710–2690 MHz. The disjointed metal-ring frame is capacitively fed by a printed meandering monopole according to the couple-fed mechanism, and generates a dual-resonance mode of GSM850/900 operation and a higher-resonance mode of LTE 2300/2500 operation. By effectively applying the metal-ring resonances, the proposed antenna achieves size reduction and wider bandwidth for MRF smartphone applications. The obtained measured results including return loss, antenna peak gain, and radiation efficiency indicate that the proposed antenna is promising for practical wide band MRF smartphone applications with excellent aesthetic consideration and enhanced mechanic sturdiness.

REFERENCES

1. Guo, Q., R. Mittra, F. Lei, et al., "Interaction between internal antenna and external antenna of mobile phone and hand effect," *IEEE Trans. Antennas Propag.*, Vol. 61, No. 2, 862–870, 2013.
2. Yuan, B., Y. Z. Cao, G. F. Wang, and B. Cui, "Slot antenna for metal-rimmed mobile handsets," *IEEE Antennas Wireless Propag. Lett.*, Vol. 11, No. 1, 1334–1337, 2012.
3. Ban, Y. L., J. H. Chen, S. Yang, et al., "Low-profile printed octaband LTE/WWAN mobile phone antenna using embedded parallel resonant structure," *IEEE Trans. Antennas Propag.*, Vol. 61. No. 7, 3889–3894, 2013.
4. Chen, S. C. and K. L. Wong, "Low-profile, small-size, wireless wide area network handset antenna close integration with surrounding ground plane," *Microw. Opt. Technol. Lett.*, Vol. 54, No. 3, 623–629, 2012.
5. Ban, Y. L., C. L. Liu, L. W. Li, et al.,"Small-size coupled-fed antenna with two printed distributed inductors for seven-band WWAN/LTE mobile handset," *IEEE Trans. Antennas Propag.*, Vol. 61. No. 11, 5780–5784, 2013.
6. Chu, F. H. and K. L. Wong, "Internal coupled-fed dual-loop antenna integrated with a USB connector for WWAN/LTE mobile handset," *IEEE Trans. Antennas Propag.*, Vol. 59, No. 11, 4215–4221, 2011.
7. Chen, Z., Y. L. Ban, J. H. Chen, et al., "Novel surface-mounted antenna with a chip capacitance embedded for LTE/WWAN wireless USB dongle applications," *Electromagnetics*, Vol. 33, No. 3, 221–233, 2013.
8. Hsu, C. K. and S. J. Chung, "Compact antenna with U-shaped open-end slot structure for multi-band handset applications," *IEEE Trans. Antennas Propag.*, Vol. 62, No. 2, 929–932, 2014.
9. Ban, Y. L., J. H. Chen, L. W. Li, et al., "Small-size printed coupled-fed embedding two inductors in radiating strips for internal mobile phone LTE/WWAN operation," *IET Microw. Antennas Propag.*, Vol. 7, No. 6, 399–407, 2013.

10. Anguera, J., I. Sanz, J. Mumbrú, and C. Puente,"Multiband handset antenna with a parallel excitation of PIFA and slot radiators," *IEEE Trans. Antennas Propag.*, Vol. 61, No. 8, 4358–4363, 2013.

A Hepta-band WWAN/LTE Antenna Design for Metal-rimmed Smartphone Applications

Yun-Fei Qiang and Yong-Ling Ban
Institute of Electromagnetics
University of Electronic Science and Technology of China
2006 Xi-Yuan Avenue, Western High-Tech District, Chengdu, Sichuan 611731, China

Abstract— A simple direct-fed dual-loop antenna capable of providing hepta-band WWAN/LTE operation under surroundings of an unbroken metal rim in smartphone applications is proposed. The greatest highlight of this proposed antenna is that it provides a simple and effective solution for an unbroken metal-rimmed smartphone. The unbroken metal rim with 5 mm in height embraces the system circuit board of $130 \times 70\,\text{mm}^2$. Two no-ground portions of $10 \times 70\,\text{mm}^2$ and $5 \times 70\,\text{mm}^2$ are set on the top and bottom edge of the system circuit board, respectively. In-between the two separate no-ground portions, there is a system ground of $115 \times 70\,\text{mm}^2$ connected with the unbroken metal rim by a small grounded patch. This proposed dual-loop antenna is capable of covering GSM850/900/DCS/PCS/UMTS2100/LTE2300/2500 operating bands. Detailed design considerations of the proposed antenna are described and both experimental and simulation results are also presented and discussed.

1. INTRODUCTION

In recent years, smartphones have entered into a rapid development period and have gradually become the main communication tools. Furthermore, a smartphone with an unbroken metal rim has become an obvious trend. The metal rim can not only provide sufficient mechanical strength to extend the service life of the smartphone, but also can possess a wonderful appearance, which is very desirable for consumers.

Recently, several promising solutions have been demonstrated which can resolve the effects of the metal rim [1, 2]. For example, reported in [1], it has shown a method to reduce the effects of the metal rim by inserting three gaps and two grounded patches. By judiciously choosing the locations of the gaps and the grounded patches, this method can alleviate the effects of the metal rim. However, the radiation efficiency will be dramatically reduced if these gaps are directly touched by fingers or hands. By adding several grounded patches between the bottom system ground and the unbroken metal rim, a compact slot antenna is proposed in [2]. The two slots are fed by the same feeding strip, which can cover five WWAN bands of GSM850/900/DCS/PCS/UMTS2100 operation. Seen from the above discussion, none of them can provide enough bandwidth to cover WWAN/LTE operating bands.

To alleviate this problem, a simple direct-fed dual-loop antenna capable of providing hepta-band WWAN/LTE operation under surroundings of an unbroken metal rim in smartphone applications is proposed. The unbroken metal rim, which is directly fed by a 50-Ω mini coaxial feed line, is connected to the system ground by a small grounded patch. The biggest merit of the proposed antenna is that it keeps the integrity of the metal rim and provides sufficient bandwidth to cover hepta-band WWAN/LTE operation, which makes it very promising for metal-rimmed smartphone applications.

Compared with some other promising antennas [3–5] whose bandwidth is widened by utilizing matching network requiring additional board area and cause insertion loss, the proposed simple dual-loop antenna structure without any matching network not only can simplify the difficulty of antenna tuning in the final optimization process, but also can guarantee its low fabrication cost and high radiation efficiency.

2. PROPOSED ANTENNA CONFIGURATION

Figure 1(a) shows the geometry of the proposed dual-loop antenna formed by an unbroken metal rim for WWAN/LTE smartphones, whose detailed structure and optimized dimensions are given in Fig. 1(b). As illustrated in Fig. 1(a), a 0.8-mm thick FR4 substrate of relative permittivity 4.4 and loss tangent 0.024 is used as the system circuit board. The system circuit board of $130 \times 70\,\text{mm}^2$ is embraced by an unbroken metal rim whose height is of 5 mm and thickness is of 0.3 mm. The distance between the system circuit board and the metal rim is 2 mm [2]. Two no-ground portions

of $10 \times 70\,\text{mm}^2$ and $5 \times 70\,\text{mm}^2$ are set on the top and bottom edge of the system circuit board, respectively. In-between the two separate no-ground portions, there is a system ground plane with the length of 115 mm and the width of 70 mm.

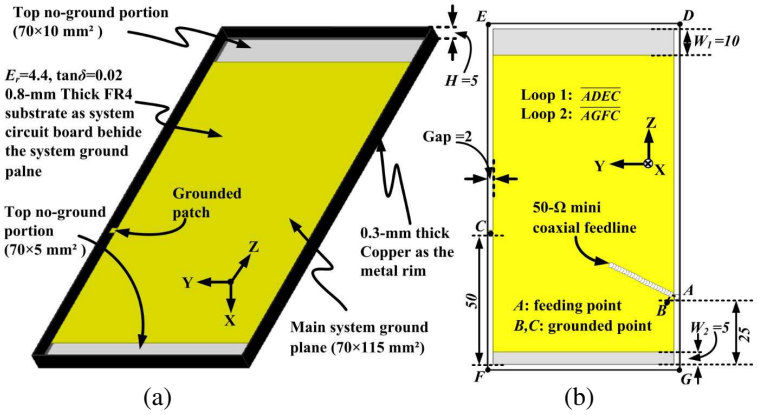

Figure 1: Proposed antenna configuration: (a) Geometry of the metal-rimmed antenna for hepta-band operations in smartphone applications; (b) Detailed dimensions of the proposed antenna (Unit: mm).

Seen from the Fig. 1(b), a 50-Ω mini coaxial feed line is employed to excite the antenna connected to the feeding point (point A) and the grounded point (point B). The distance between the feeding point and the bottom edge of the system circuit board is 25 mm. The unbroken metal rim is divided into two loops by a small grounded patch which has a distance of 50 mm away from the bottom edge of the system circuit board.

3. RESONANT MODES AND CURRENT DISTRIBUTION

To fully comprehend the excited modes of the proposed dual-loop antenna, two reference antennas (Ref-1 and Ref-2) are introduced. Fig. 2(a) shows the simulated input reactance of the proposed antenna and the reference antennas, the case with Loop 1 only (Ref-1) and the case with Loop 2 only (Ref-2). The modes generated by the Ref-1 (Loop 1 only) and the Ref-2 (Loop 2 only) are marked as $M_{0.5n\lambda,\,L_1}$ and $M_{0.5n\lambda,\,L_2}$, respectively, where n represents the n-th order modes. Seen from the Fig. 2, the proposed dual-loop has five resonant modes ($M_{0.5\lambda,\,L_1}$, $M_{0.5\lambda,\,L_2}$, $M_{1\lambda,\,L_2}$, $M_{2\lambda,\,L_1}$, $M_{1.5\lambda,\,L_2}$ or $M_{2.5\lambda,\,L_1}$). Seen from Fig. 2(a), two modes of Ref-1 $M_{1\lambda,\,L_1}$, $M_{1.5\lambda,\,L_1}$ are not appeared in the proposed antenna. This is explained as follows: the resonant frequency of the $M_{1\lambda,\,L_1}$ is very closed to the resonant frequency of the $M_{0.5\lambda,\,L_2}$. Around the resonant frequency of the $M_{1\lambda,\,L_1}$, the inductive reactance of the $M_{1\lambda,\,L_1}$ is compensated by the larger capacitive reactance of the $M_{0.5\lambda,\,L_2}$. Finally, in the proposed antenna, only one resonant mode is appeared in the proposed antenna. The above theory can also be used to explain the behavior of the $M_{1.5\lambda,\,L_1}$. Fig. 2(b) shows the corresponding simulated return loss of the Fig. 2(a). The multi-resonant character for

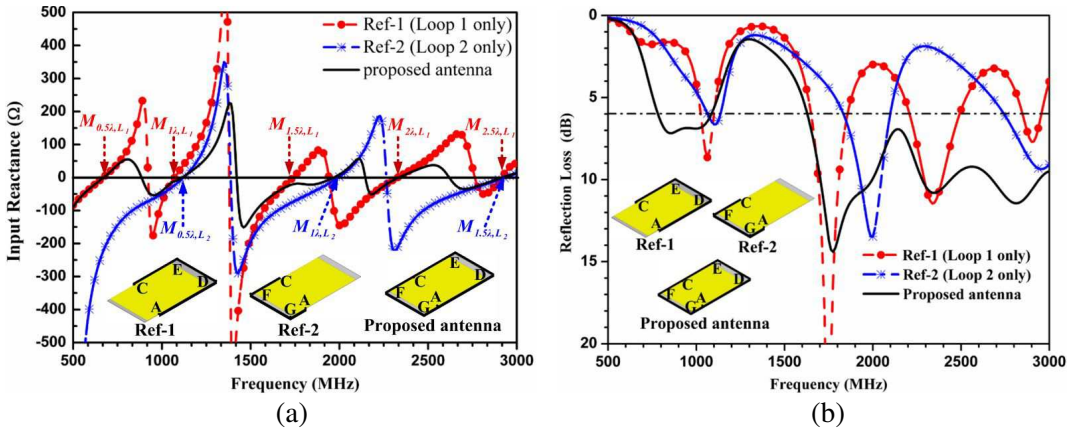

Figure 2: (a) Simulated input reactance and (b) simulated return loss, respectively, of the proposed antenna and the case with Loop 1 only (Ref-1), and the case with Loop 2 only (Ref-2).

both Ref-1 and Ref-2 can be easily seen from Fig. 2(b). The bandwidth for each resonant mode of Ref-1 and Ref-2 is very narrow. However, by employing the multi-resonant modes provided by the Ref-1 and Ref-2, the proposed antenna can provide two wide operating bands of 824–960 MHz and 1710–2690 MHz, respectively.

In order to distinguish these resonant modes, simulated surface vector current distributions of the proposed antenna at frequencies of 0.67 GHz, 1.13 GHz, 1.98 GHz, 2.35 GHz and 2.93 GHz, which corresponds to the modes of $M_{0.5\lambda,L_1}$, $M_{0.5\lambda,L_2}$, $M_{1\lambda,L_2}$, $M_{2\lambda,L_1}$, $M_{1.5\lambda,L_2}$ (or $M_{2.5\lambda,L_1}$), are plotted in Figs. 3(a), (b), (c), (d) and (e), respectively. It can be clearly seen that the simulated surface current has a null point along the Loop 1 at 0.67 GHz. This indicates that the proposed antenna operates in the $M_{0.5\lambda,L_1}$ which is the fundamental mode of the Loop 1. The other modes of $M_{0.5\lambda,L_2}$, $M_{1\lambda,L_2}$, $M_{2\lambda,L_1}$ can be analyzed easily from Fig. 2 and the surface current distributions of the corresponding resonant frequencies in Figs. 3(b), (c), (d).

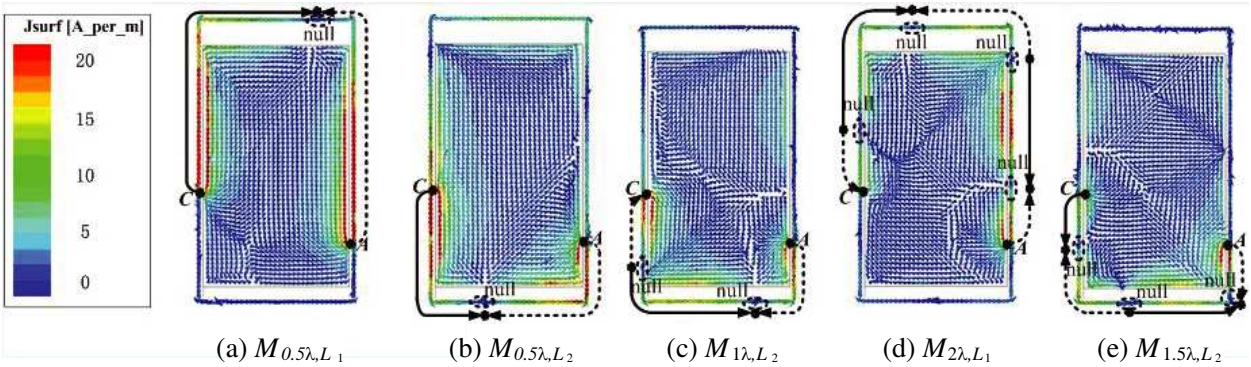

Figure 3: Simulated surface current distributions in the proposed antenna at the corresponding resonant frequencies of (a) 0.67 GHz; (b) 1.13 GHz; (c) 1.98 GHz; (d) 2.35 GHz; (e) 2.93 GHz.

4. RESULTS AND DISCUSSION

The simulated results are gained by Ansoft HFSS version 13, while the measured results are tested by using an Agilent N5247A vector network analyzer. Fig. 4 presents the measured and simulated return losses for the prototype, which are in with good agreement.

The measured total efficiency and antenna gain of the fabricated antenna are presented in Fig. 5. For the lower band of GSM850/900 (824–960 MHz), the antenna gain varies from about 1.2 to 2.0 dBi and the total efficiency is about 62–79%, which are acceptable for practical application. For the desired upper bands of DCS/PCS/UMTS2100/LTE2300/2500 (1710–2690 MHz), the obtained antenna gain is 1.0–3.9 dBi and the corresponding total efficiency is larger than 54%. As a result, the measured radiation characteristics of the proposed antenna within the operating band are suitable for meeting the requirement for smartphone systems [6, 7].

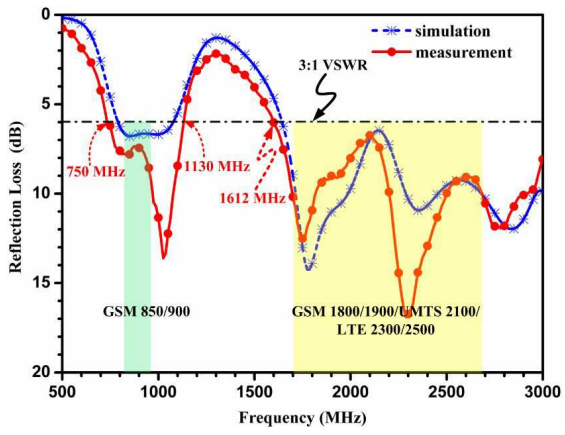

Figure 4: Measured and simulated S parameters.

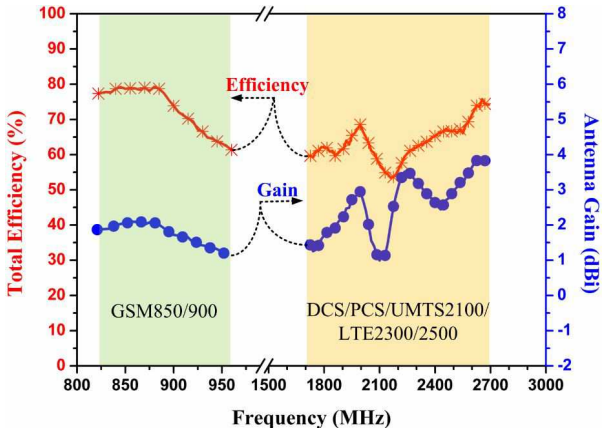

Figure 5: Measured radiation efficiency.

5. CONCLUSION

A simple direct-fed dual-loop antenna capable of providing hepta-band WWAN/LTE operation under surroundings of an unbroken metal rim in smartphone applications is proposed and studied in this paper. The obtained measured results including return loss and total efficiency are presented, which can meet the requirements for smartphone systems. The greatest highlight is that the proposed antenna can keep the integrity of the metal rim, which is very novel for metal-rimmed smartphone applications.

REFERENCES

1. Guo, Q. X., R. Mittra, F. Lei, and Z. R. Li, "Interaction between internal antenna and external antenna of mobile phone and hand effect," *IEEE Trans. Antennas Propag.*, Vol. 61, No. 2, 862–870, 2013.
2. Yuan, B., Y. Cao, G. F. Wang, and B. Cui, "Slot antenna for metal-rimmed mobile handsets," *IEEE Antennas Wirel. Propag. Lett.*, Vol. 11, 1334–1337, 2012.
3. Valkonen, R., M. Kaltiokallio, and C. Icheln, "Capacitive coupling element antennas for multi-standard mobile handsets," *IEEE Trans. Antennas Propag.*, Vol. 61, No. 5, 2783–2791, 2013.
4. Zheng, M., H. Y. Wang, and Y. Hao, "Internal hexa-band folded monopole/dipole/loop antenna with four resonances for mobile device," *IEEE Trans. Antennas Propag.*, Vol. 60, No. 6, 2880–2885, 2012.
5. Ban, Y. L., Y. F. Qiang, Z. Chen, K. Kang, and J. L. W. Li, "Low-Profile narrow-frame antenna for seven-band WWAN/LTE smartphone applications," *IEEE Antennas Wirel. Propag. Lett.*, Vol. 13, 463–466, 2014.
6. Ban, Y. L., J. H. Chen, S. Yang, J. Li, and Y. Wu, "Low-profile printed octaband LTE/WWAN mobile phone antenna using embedded parallel resonant structure," *IEEE Trans. Antennas Propag.*, Vol. 61, No. 7, 3889–3894, 2013.
7. Ban, Y. L., C. L. Liu, and L. W. Li, "Small-size coupled-fed antenna with two printed distributed inductors for seven-band WWAN/LTE mobile handset," *IEEE Trans. Antennas Propag.*, Vol. 61, No. 11, 5780–5784, 2013.

Printed Multi-band Slot Antenna Surrounded by a Metal Ring for WWAN Smartphone Applications

Peng-Peng Li and Yong-Ling Ban
Institute of Electromagnetics
University of Electronic Science and Technology of China
2006 Xi-Yuan Avenue, Western High-Tech District, Chengdu, Sichuan 611731, China

Abstract— A printed monopole slot antenna for WWAN metal-ring frame (MRF) smartphone applications is presented and studied in this paper. The greatest highlight of the proposed antenna is that the band of 824–960 MHz scarcely affected by the modified MRF and achieves great stability. The MRF resonance is also utilized to enhance the bandwidth of the upper band of 1710–2170 MHz. With small size of $8 \times 40\,\text{mm}^2$ occupation and wide band coverage, the proposed antenna is a promising candidate for the MRF smartphone applications.

1. INTRODUCTION

Recently, more and more phone manufactures incline to use a metal ring frame embracing the smartphone for mechanical strength or aesthetic feelings. Inevitably, The coupling between the antenna and the adjacent MRF is very intensive which excites multiple additional resonances and sets up a negative feedback to the antenna's original radiation. So, The MRF usually deteriorate the performance of the antenna. For this reason, it becomes a tremendous challenge to modify the MRF to achieve the desired performance of the antenna.

The study of the antenna design surrounded by metal ring have been reported [1]. A $15 \times 56.5\,\text{mm}^2$ planar slot antenna operated under surroundings of an unbroken metal ring is also introduced in [2]. By applying the coupled-fed technique, slot and band-stop matching circuit were also adopted to design the antenna embraced by the MRF [3–8].

In this study, The advantage of this proposed antenna is that the band of 824–960 MHz scarcely affected by the modified MRF and achieves great stability. The MRF resonance is also utilized to enhance the bandwidth of the upper band of 1710–2170 MHz. Moreover, the antennas are planar, printed, small size according to the requirement of the modern smartphone.

In this paper, a novel compact monopole slot is utilized for metal-ring frame smartphone applications. As the main radiator, the slot occupy a small size nearly $8 \times 40\,\text{mm}^2$ on the system circuit board corner. The dual-band band-stop matching circuit in this article can generate two separate parallel resonances and lead to two dual-resonance excitations of the quarter-wavelength and higher-order resonant modes of the monopole slot antenna to apparently enhance the bandwidths of both the antenna lower and upper bands. This proposed antenna can cover the WWAN operation in the 824–960 and 1710–2170 MHz bands.

2. PROPOSED ANTENNA CONFIGURATION

Figure 1(a) shows the geometry of the proposed monopole slot antenna with dual-band band-stop matching circuit at the bottom corner of the system circuit board, and the dimensions of the antenna metal pattern are given in Fig. 1(b). In this study, a 0.8-mm thick FR4 substrate of relative permittivity 4.4, loss tangent 0.02, and size $50 \times 115\,\text{mm}^2$ is used as the system circuit board of the practical smartphone applications. The system circuit board is embraced by an almost negligible thickness metal ring, which has a height of 5 mm in the design and the distance between the circuit board and the metal ring is 2 mm. By means of splitting two symmetrical slits whose length is 3 mm and height is 5 mm near the bottom of the rectangle metal ring, connecting the ground of circuit board to the rectangle metal ring through metallic patch whose size is $2 \times 2\,\text{mm}^2$ in the top right of the circuit board, the metal-ring frame is divided into three sections, which are Section 1, Section 2 and Section 3 as depicted in Fig. 1(a). The distance of the slit to the top of the metal ring is 7 mm.

Detailed dimensions of the proposed antenna are shown in Fig. 1(b). The proposed antenna consists of a shorter feeding strip and a longer coupling monopole slot seen from its functions. The monopole slot is folded to achieve a compact antenna configuration and consisted of two parallel slot sections in the upper and down location respectively. The upper slot section have a length of 33 mm and a width of 2.5 mm and the down slot section have a length of 37 mm and a width of

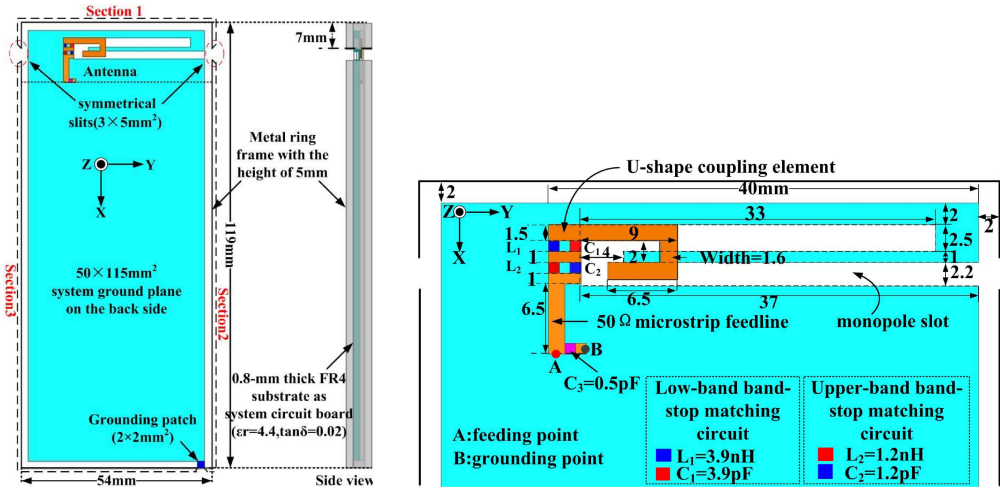

(a) (b)

Figure 1: (a) Geometry of the proposed WWAN monopole slot antenna disposed at the system ground plane. (b) Dimensions of the antenna's metal pattern (Unit: mm).

2.2 mm in the ground plane. So, the monopole slot have a length of about 72 mm in total. The feeding strip consisted of the U-shape coupling element, the dual-band band-stop matching circuit and the 50-Ω microstrip feedline. The U-shape coupling element has an overall length of 20.5 mm and is adjusted to extend from the upper slot section to the down slot section. the 50-Ω microstrip feedline has a length of 6.5 mm. To achieve good impedance matching of the antenna, a 0.5-pF chip capacitor is displaced parallel to the microstrip feedline at the feeding point.

3. RESULTS AND DISCUSSION

The simulated results are gained by Ansoft HFSS version 13, while the measured results are tested by using an Agilent N5247A vector network analyzer. The results of the measured and simulated reflection coefficient are shown in Fig. 2. The desired operating bands (824–960 and 1710–2170 MHz) are shown in the shaded regions in the figure. Based on 3 : 1 VSWR definition, the obtained bandwidths cover the desired operating bands. Good agreement between the measurement and the simulation obtained is also seen. the measured antenna peak gain and radiation efficiency for the proposed smart-phone antenna. Over the desired lower band of GSM850/900 (824–960 MHz), the antenna gain is varied from about −1.9 to 0.7 dBi, and the radiation efficiency is generally larger than 50%. For the desired upper band of DCS1800/PCS1900/UMTS2100 (1710–2170 MHz), the antenna gain is varied from about 0.2 to 2.4 dBi, and the radiation efficiency is larger than about 55%.

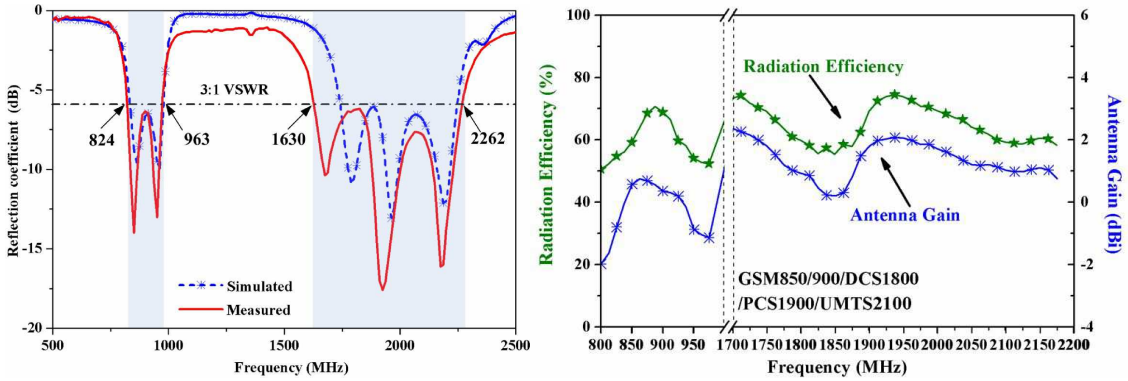

(a) (b)

Figure 2: (a) Measured and simulated S parameters. (b) Measured antenna gain and radiation efficiency.

4. CONCLUSION

A monopole slot antenna printed on a FR4 substrate of $50 \times 115\,\mathrm{mm}^2$ surrounded by a rectangle MRF is presented. In this paper, by means of splitting two symmetrical slits near the bottom of the rectangle metal ring ,connecting the ground of circuit board to the metal ring through metallic patch in the top right corner of the circuit board and a dual band band-stop matching circuit in the 50-Ω micro-strip line which feeds the monopole slot, both the bandwidths of the antenna's lower and upper bands can be covered. The obtained measured results including reflection coefficient, antenna peak gain, and radiation efficiency are presented, which indicate that the proposed antenna is promising for the smartphone applications.

REFERENCES

1. Guo, Q., R. Mittra, F. Lei, et al., "Interaction between internal antenna and external antenna of mobile phone and hand effect," *IEEE Trans. Antennas Propag.*, Vol. 61, No. 2, 862–870, 2013.
2. Yuan, B., Y. Z. Cao, G. F. Wang, and B. Cui, "Slot antenna for metal-rimmed mobile handsets," *IEEE Antennas Wireless Propag. Lett.*, Vol. 11, No. 1, 1334–1337, 2012.
3. Ban, Y. L., J. H. Chen, S. Yang, et al., "Low-profile printed octaband LTE/WWAN mobile phone antenna using embedded parallel resonant structure," *IEEE Trans. Antennas Propag.*, Vol. 61. No. 7, 3889–3894, 2013.
4. Chen, S. C. and K. L. Wong, "Low-profile, small-size, wireless wide area network handset antenna close integration with surrounding ground plane," *Microw. Opt. Technol. Lett.*, Vol. 54, No. 3, 623–629, 2012.
5. Ban, Y. L., C. L. Liu, L. W. Li, et al., "Small-size coupled-fed antenna with two printed distributed inductors for seven-band WWAN/LTE mobile handset," *IEEE Trans. Antennas Propag.,* Vol. 61. No. 11, 5780–5784, 2013.
6. Chu, F. H. and K. L. Wong, "Internal coupled-fed dual-loop antenna integrated with a USB connector for WWAN/LTE mobile handset," *IEEE Trans. Antennas Propag.*, Vol. 59, No. 11, 4215–4221, 2011.
7. Chen, Z., Y. L. Ban, J. H. Chen, et al., "Novel surface-mounted antenna with a chip capacitance embedded for LTE/WWAN wireless USB dongle applications," *Electromagnetics*, Vol. 33, No. 3, 221–233, 2013.
8. Hsu, C. K. and S. J. Chung, "Compact antenna with U-shaped open-end slot structure for multi-band handset applications," *IEEE Trans. Antennas Propag.*, Vol. 62, No. 2, 929–932, 2014.

Tunable Antenna Introductions, Challenges and Opportunities

Guangli Yang[1], **Hao Wang**[1], **and Li Yang**[2]

[1]Shanghai University, China
[2]Northeastern University, China

Abstract— In this paper we systematically summarized tunable technologies in mobile terminal applications with various aspects, including the advantages, popular applications techniques, tunable switch and capacitor selections, closed and open loop tunable system architecture as well as the future opportunities and challenges.

1. INTRODUCTION

With the rise of the 4G mobile technology, LTE (long term evolution) technology has been adopted in modern mobile terminal for the better broadband and multimedia service than traditional WWAN mobile network, which means that, in addition to GSM850 (824–894 MHz), GSM900 (880–960 MHz), DCS1800 (1710–1880 MHz), PCS1900 (1850–1990 MHz), UMTS (1920–2170 MHz), the LTE antenna also need to support LTE700 (704–787 MHz) and LTE2600 (2500–2690 MHz) for global applications. This is a big challenge for slim phones with limited space for antenna. On the other hand, more and more carriers require not only free space TRP and TIS, but also phantom head, head+hand performance. Because the head, hand could detune antenna resonance, traditional passive antenna is getting very difficult to balance performances at all these conditions. Fig. 1(a) showed the head and hand position defined in the CTIA standard. Our study showed that head and hand could shift low band frequency significantly at the tight grip situation in Fig. 1(b) which could cause 4 dB efficiency reduction.

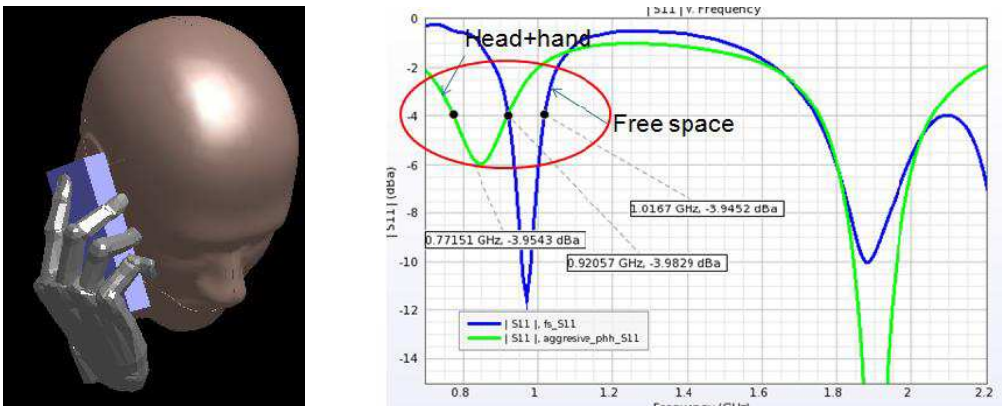

(a) (b)

Figure 1: Head and hand (a) position defined in the CTIA standard, (b) detuned antenna S_{11}.

Tunable antenna is the trend to overcome the passive antenna limitations to support (1) more bandwidth and bands and (2) minimize the head and hand or the user environment impacts. In this paper, we will briefly introduce tunable antenna technologies in application, element selection, antenna design and system integration etc..

Tunable antenna can be used for any antennas such as WAN, WLAN, RFID, mobile TV etc.. In this paper we only focus on the WAN antenna because it is the most challenge we are facing. The other antenna applications will be similar.

2. TWO COMMON TUNING TECHNIQUES

Tunable matching is to put switch (connected with inductor or capacitor, or grounded) or tunable capacitor in series or shunt to the antenna feeding structure as indicated in Fig. 2(a). At each stage, a different inductance or capacitance can be applied to the antenna impedance matching therefore shifted frequency to what we planned, for example, from GSM 850 to LTE 700. To reduce the

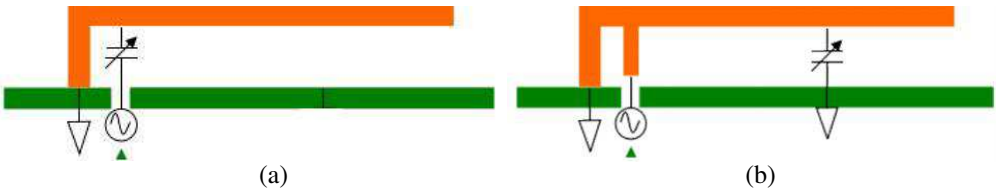

Figure 2: Two common tunable methods, (a) at matching, (b) at antenna structure.

additional loss, usually shunt element positioning is preferred. The antenna matching can improve S_{11} and system efficiency accordingly but do not improve the antenna radiation efficiency because antenna structure is not changed. Tuning antenna structure, for example, Fig. 2(b), is to put tunable component on antenna structure (connect or disconnect an arm when Switch is ON and OFF) or between PCB and antenna grounded leg to change the antenna radiation principle. If used properly, in experiment we saw less loss than tunable matching and could improve antenna radiation efficiency. Which method to select is totally depending on user's practical situation, including tunable frequency required range, tunable element increased loss to system, tunable element harmonics, ease of manufacturing, cost etc..

3. TUNABLE SWITCH AND CAPACITOR

After decided the methods to tune antenna, the next important thing is to select proper tuning element, RF switch or tunable capacitor. Thanks to the global R&D from different companies, we have options to use digital tunable capacitor, BST varactor diode, RF switch, MEMS etc.. Which company solution to use varies depending on the application requirements as shown in Table 1. According our experience, most switch and tunable capacitor can support frequency up to 3 GHz and support power more than 35 dBm with physical size of 2×2 or 3×3 mm. Usually the claimed loss is 0.5 dB or less, but be careful that the loss could be much higher if not used properly. For tunable capacitor, the typical tuning range is from 1 to 5 pF.

Table 1: Tunable switch or capacitor selection parameters.

Parameters	Target	Parameters	Target
Insertion loos (dB)	0.2–0.3	Harmonics (LB/HB) fREQ 2xf. (dBm)	< -40
Capacitor tunable range (pF)	1–5	Supply Voltage	3
IP3 (dBm)	$> +65$	Switching time (µs)	
Operation Freq (GHz)	> 3	Size (mm)	2×2
Power Handling (dBm) (Low Band/Hi band)	35/32	Q	

4. OPEN LOOP AND CLOSED LOOP

In terminal system level, tunable component can be controlled by so called open loop or closed loop. What we saw in the market is typically open loop tunable antenna. The simplest case of open loop is like a switch with ON and OFF two stages. more advanced open loop antenna has a look-up table with pre-measured data installed in the device to react at defined situation, such as that at free space the tunable capacitor set value at 1 pF and at head+hand case to set value to 3 pF etc.. The main limitation is that it only works at the pre-defined situation and can't be adjusted dynamically. Closed loop will be much better, means that at anytime whenever antenna is detuned, the system will noticed it and tune the antenna resonance to normal, it will be more complicated in terms of return loss S_{11} detection and system level support.

Figure 3 showed our proposed closed loop including tunable capacitor, coupler, power detector and CPU/microcontroller. The Coupler is used to detect the incident and reflected RF power and give to power detector to convert to DC respectively, then microcontroller is used to calculate the return loss S_{11} and decide how to change the tunable capacitor value to optimize S_{11}. Based on this concept, we have developed a cellular phone WAN antenna supporting 6 bands

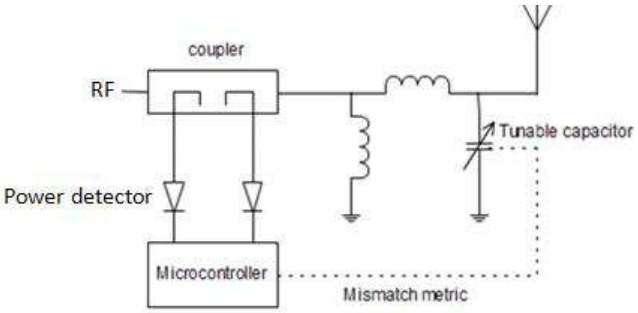

Figure 3: Proposed closed loop structure.

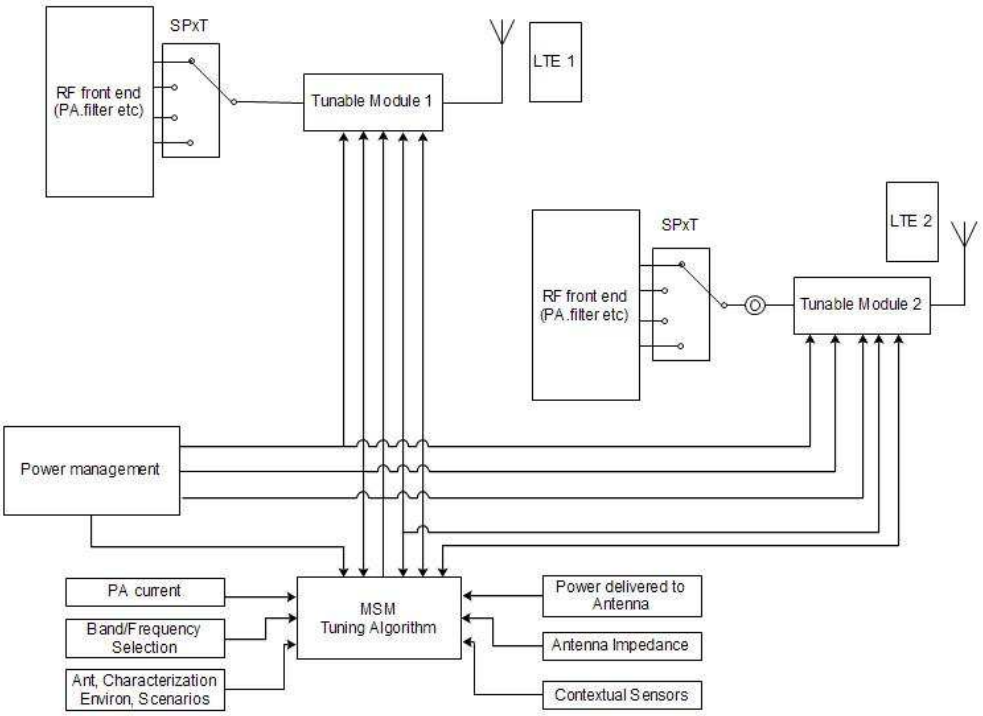

Figure 4: Closed loop antenna architecture for LTE MIMO system.

(700/850/900/1800/1900/2100) for global LTE application. This prototype includes antenna, tunable capacitor, coupler, power detector, microcontroller, filter and other RF and EE component. Given any hand, head, or environment changes causing antenna frequency shift, the system can adjust the antenna resonance back to original condition with milliseconds. The design details and video will be demoed in the conference presentation.

After proving the closed loop concept, our next step is to develop a RF tunable module to integrate the closed loop tuning circuits within a 2×2 mm size so that it can be used in more convenient and powerful ways. For example, the LTE MIMO system can be designed as a smart tuning system as shown in Fig. 4. In this system each antenna is connected with a tunable module. How tunable module will operate is based on the calculation results from MSM, where it is connected and determined by many input information like PA current, phone operation band, power to antenna, sensors etc. we are working with cellular phone company at platform level to implement this breakthrough technology. The outcome of this research will completely change the terminal device design principle and users experience to prevent drop call and better voice and data signal quality experience.

5. CONCLUSIONS

Smart tunable antenna is the trend to support more bandwidth and bands, minimize antenna size, and reduce user condition like hand, hand effects. With the maturity of the RF switch and tunable capacitor and proper integration to antenna, it becomes possible and is already started to implement on mobile terminals. Currently antenna tuning is mainly used as open loop to support different bands. Next big thing will be closed loop tunable solution to dynamically optimize antenna performance, it will come soon when more mobile terminal developers are developing new solutions.

REFERENCES

1. "Tunable switch and capacitor public information from different venders like Peregrine," Skywork, Sony, Wistry, Agile.
2. Qualcomm publich QFE1510 information.
3. Samsung Galaxy II and HTC ONE public information.
4. Allen, W. N. and D. Peroulis, "Bandwidth-optimal single-tunable-element matching network for antenna tuning in mobile handsets," *IEEE MTT-S International Microwave Symposium Digest (MTT)*, Baltimore, Jun. 2011.
5. Liu, P. and A. Springer, "Tunable antenna impedance matching for 4G mobile communications," *Proceedings of the International Symposium on ISAP*, Vol. 2, 863–866, 2013.
6. Koga, Y., T. Yamagajo, and M. Shimizu, "Frequency tunable antenna design technique with MEMS switches for mobile phone," *Proceedings of the Asia-Pacific Microwave Conference*, Dec. 2011.
7. Koga, Y., A. S. Andrenko, T. Yamagajo, and M. Snimizu, "Compact frequency-tunable antenna with a GaAs switch for mobile handset," *IEEE-APS Topical Conference on APWC*, 736–739, Torino, Sep. 2013.
8. Morris, A. S., Q. Gu, S. P. Natarajan, and J. R. Deluis, "High performance tuners for handsets," *IEEE MTT-S International Microwave Symposium Digest (MTT)*, Baltimore, Jun. 2011.
9. Ramachandran, P., P. Annamaa, R. Gaddi, P. Tornatta, L. Morrell, and C. Schepens, "Reconfigurable small antenna for mobile phone using MEMS tunable capacitor," *Loughborough Antennas & Propagation Conference*, Loughborough, UK, Nov. 2013.
10. Virga, K. L. and Y. Rahmat-Samii, "Low-profile enhanced-bandwidth PIFA antennas for wireless communications packaging," *IEEE Trans. on MTT*, Vol. 45, 1879–1888, Oct. 1997.
11. Takemura, N., "Tunable inverted-L antenna with split-ring resonator structure for mobile phones," *IEEE Trans. on AP*, Vol. 61, 1891–1897, Apr. 2013.
12. Hu, Z., P. S. Hall, P. Gardner, and Y. Nechayev, "Wide tunable balanced antenna for mobile terminals and its potential for MIMO applications," *Loughborough Antennas & Propagation Conference*, Loughborough, UK, Nov. 2011.
13. Song, C. T. P., Z. H. Hu, J. Kelly, and P. S. Hall, "Wide tunable dualband reconfigurable antenna for future wireless devices," *Loughborough Antennas & Propagation Conference*, 601–604, Loughborough, UK, Nov. 2009.

A RFID Tag Based on MIT Technology

Y. F. Hou, J. W. Yu, J. Zhang, F. Cheng, and X. Q. Lin
EHF Key Laboratory of Science, School of Engineering
University of Electronic Science and Technology of China, Chengdu 611731, China

Abstract— In this paper, a new chipless RFID tag is designed based on the concept of metamaterials induced transparency (MIT). By inserting an arc slot on the circular loop and adjusting the length of the slot, a narrow transmission windows will appear in the stopband when the resonance frequency of circular loop is similar to the resonance frequency of arc slots. Such transmission windows has high Q factor and each transmission pole comes along two transmission zeros on its side, so the resonant frequencies can be brought very close. To make high density coding, four arc slots are added on the circular loop to generate multiple zero and pole distributions in a relatively narrow frequency band. By locating some stubs along the slot, the relevant codes are deleted because the resonators are nulled. Then four-bit chipless RFID tag is finally finished. The design concept is verified well by the full-wave simulation.

1. INTRODUCTION

Today, there is a growing demand for the application of chipless RFID tags with simple structure and high-density identification data [1–3]. In many resonant-based RFID designs, resonant frequencies can't be brought too close or they will merge into one broadband frequency response. Metamaterial induced transparency (MIT), which has a narrow transmission window in a wide absorpting band and provides an extremely large group delay, was firstly reported in Ref. [4]. It was realized by using fish-net pattern and can generate an EIT-like phenomenon. Now, the MIT-effect has attracted a lot interests in different regions [5–7].

In this paper, we propose a new chipless RFID tag design using the concept of MIT. The transmission windows in MIT has high Q factor and each transmission pole comes along two transmission zeros on its side, so the resonant frequencies can be brought very close thus achieve high density data coding. By inserting an arc slot on the circular loop and adjusting the length of the slot, a narrow passband will appear in the stopband when the resonance frequency of circular loop is similar to the resonance frequency of arc slots. Four-bit chipless RFID tag is detailed designed and verified well by the full-wave simulation.

2. MIT REALIZED BY ARC SLOT ETCHED ON RING RESONATOR

In this section, we first analyze the characteristics of our novel MIT structures. Single circular loop structure is first presented in Fig. 1(a), where periodic boundary condition is set all around the structure and floquet port is used for inputting and outputting the signal. From the simulated S_{21}

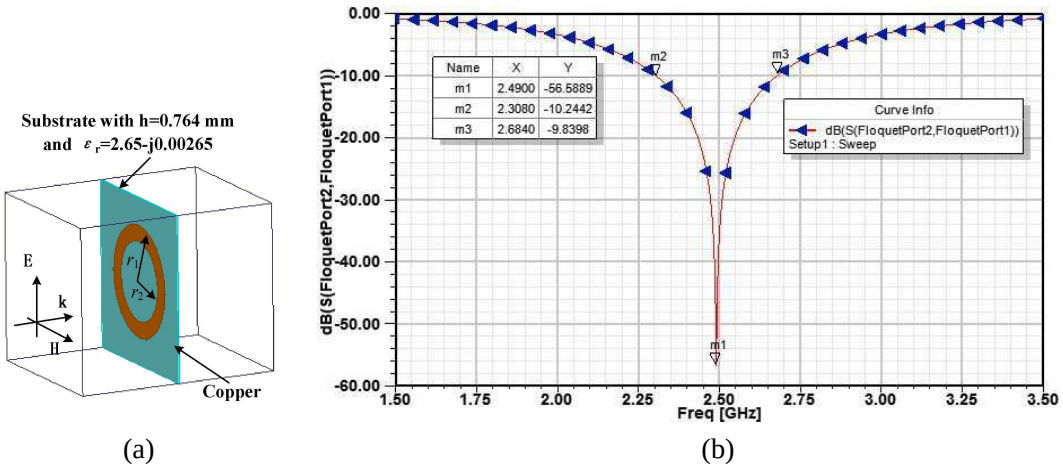

(a) (b)

Figure 1: Schematic structure and resonant response of a circular loop with $r_1 = 27\,\text{mm}$ and $r_1 = 19.2\,\text{mm}$. (a) Schematic Structure. (b) Simulated S_{21}.

results in Fig. 1(b), we notice that, a −10 dB stop band is obtained from 2.306 GHz to 2.683 GHz with relative bandwidth of 15.11%.

In order to realize a MIT effect, an arc slot is then added as shown in Fig. 2(a). Changing the length of arc slot (referred to different angles), the transmission window is varied. Fig. 2(b) gives the simulated results of two examples where two angles of $\theta = 50°$ and $60°$ is chosen, two transmission windows with center frequency of 2.206 GHz and 2.608 GHz are obtained, respectively. This means that when more arc slots are etched on the circular loop, more transmission windows

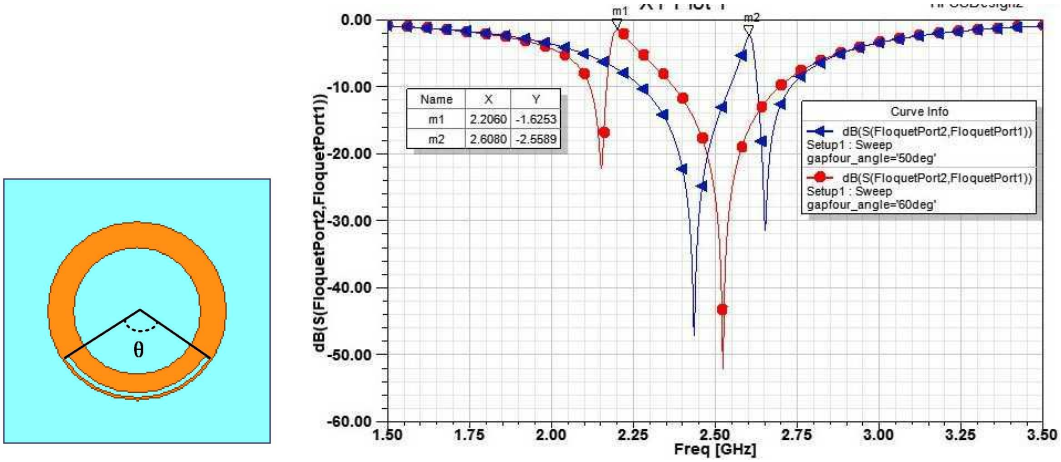

(a) (b)

Figure 2: Schematic structures and transmission responses of EIT structures with $\theta = 50°$ and $\theta = 60°$, respectively. (a) Schematic Structure. (b) Simulated S_{21}.

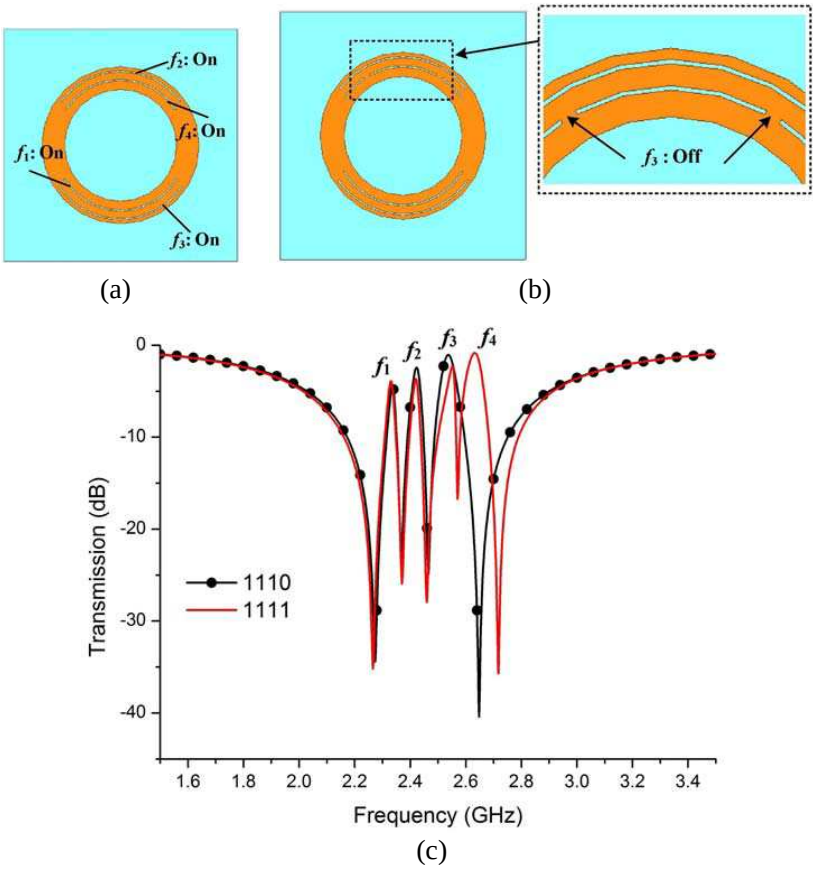

(a) (b)

(c)

Figure 3: Chipless RFID based on MIT-effect. (a) Structure of 1111-code. (b) Structure of 1110-code. (c) Transmission responses of two codes.

are hoped to be achieved.

3. CHIPLESS RFID TAG DESIGN

In this section, we would like to use the proposed MIT structure to design a chipless RFID tag. As a sample, we add four arc slots on the circular loop as shown in Fig. 3(a). Two slots are etched on the top part of the loop and resonant at the center frequencies of f_1 and f_3, respectively. The other two slots are etched on the bottom part of the loop and resonant at the center frequencies of f_2 and f_4, respectively. In order to form different codes, two stubs are suggested to add to the slot as shown in Fig. 3(b). We can image that when the stub is added, the relative transmission windows will be closed.

In order to verify our design concept, two situations are detailed designed with their responses in Fig. 3(c). From Fig. 3(c), we notice that when four slots are presented at the same time, four transmission windows are presented with each center frequency of 2.332 GHz, 2.424 GHz, 2.552 GHz and 2.632 GHz. This situation is marked as the code of 1111. When we add two stubs to the inner slot on the top part. The transmission window of 2.632 GHz is disappeared which refers to the code of 1110. Only 0.3 GHz-band is occupied by four-bit coding which is narrower than many other published results. If wanted, more situations can be achieved just by adding or deleting the stub to or from relative slots.

4. CONCLUSION

we propose a new chipless RFID tag designed using the concept of MIT. The MIT structure is discussed in detail. By inserting an arc slot on the circular loop and adjusting the length of the slot, a narrow transmission window appears in the stopband when the resonance frequency of circular loop is similar to the resonance frequency of arc slots. Each transmission pole comes along two transmission zeros on its sides, so the resonant frequencies can be brought very close thus achieve high density data coding in our RFID tag design. Four-bit chipless RFID tag is finally proposed, and only 0.3 GHz-band is occupied which is narrower than many other published results. If wanted, more bit codes can be further achieved by adding more arc slots in one circular loop. Such RFID tag is easy to be designed and can be used in many real regions.

ACKNOWLEDGMENT

This work was supported in part by the State Key Laboratory of CEMEE Foundation under Grant No. CEMEE2014Z0201A, in part by the Fundamental Research Funds for the Central Universities under Grant Nos. ZYGX2010J021 and ZYGX2012YB002, in part by the Program for New Century Excellent Talents in University under Grant No. NCET-13-****.

REFERENCES

1. Preradovic, S. and N. C. Karmakar, "Chipless RFID: Bar code of the future," *IEEE Microwave Magazine*, Vol. 11, No. 7, 87–97, 2010.
2. Vena, A., E. Perret, and S. Tedjni, "A depolarizing chipless RFID tag for robust detection and its FCC compliant UWB Reading system," *IEEE Microwave Magazine*, Vol. 61, No. 8, 2982–2994, 2013.
3. Karimi, G. and S. Majidifar, "A novel chipless RFID tag using spiral resonator to achieve the pentamerous data encoding form," *Journal of Electromagnetic Waves and Applications*, Vol. 28, No. 1, 13–27, 2014.
4. Papasimakis, N., V. A. Fedotov, and N. I. Zheludev, "Metamaterial analog of electromagnetically induced transparency," *Physical Review Letters*, Vol. 101, No. 25, 2593, 2008.
5. Tassin, P., L. Zhang, T. Koschny, et al., "Planar designs for electromagnetically induced transparency in metamaterials," *Optics Express*, Vol. 17, No. 7, 5595–5605, 2009.
6. Meng, F. Y., Q. Wu, D. Erni, et al., "Polarization-independent metamaterial analog of electromagnetically induced transparency for a refractive-index-based sensor," *IEEE Transactions on Microwave Theory and Techniques*, Vol. 60, No. 10, 3013–3022, 2012.
7. Park, J. W., P. Van-Tuong, J. Y. Rhee, et al., "Multi-band metamaterial absorber based on the arrangement of donut-type resonators," *Optics Express*, Vol. 21, No. 8, 9691–9702, 2013.

Design of Robust UHF RFID Tag Antenna for Free-space and Metal Surface

Ye Qi[1], **Yuan Yao**[1], **Hongbin Ge**[1], **Junsheng Yu**[1], **and Xiaodong Chen**[2]

[1]School of Electronic Engineering, Beijing University of Posts and Telecommunications, Beijing, China
[2]School of Electronic Engineering and Computer Science, Queen Mary, University of London, London, UK

Abstract— Here, we present a robust RFID tag antenna with an appropriate structure that would operate adequately as a dipole in free space and as a relatively efficient microstrip antenna when placed on a metal surface. Good impedance matching is achieved by the use of a T-matching network in the both cases. For low-cost fabrication and simple structure, the antenna is printed on a single-layer substrate without a ground plane or shorting. The measured results show that the half-power bandwidth is 1 GHz (730 MHz–1.7 GHz) and 110 MHz (845 MHz–955 MHz) when in free space and on the metal surface, and the both reading distances are about 8 m measured by using a commercial measurement system.

1. INTRODUCTION

Radio frequency identification (RFID) is a rapidly developing technology which uses RF signals for automatic identification of objects. And the UHF RFID system operates at the bands of North and South America (902–928 MHz, FCC band), China (840–845 MHz and 920–925 MHz) and Europe (866–869 MHz). A typical RFID system consists of transponders and transceivers such as tag and reader. In a passive back-scattered RFID system, the reader transmits a modulated signal to the tag and the tag backscatters a signal with identification data to reader at the same time. A passive UHF RFID tag usually includes an antenna and a RF chip which has a memory to store identification data [1].

UHF RFID system has been widely used in many areas such as supply chains, airport luggage management and animal tracking. However, most normal tags are very sensitive to the working environment [2], especially the metal objects, reflecting and loss make the reading distance decreased [3]. When the tag placed on the metal surface, the electromagnetic boundary condition that there is no tangential electric field component on a metal surface brings some obstacles to detect metallic items by RFID tags, as most tag antenna's excitation significantly depends on a tangential electric field. Of course, some solutions for metallic item identification have been presented in the previous papers. Among existing solutions, the earliest is to insert a one quarter wavelength (about 82 mm around 915 MHz) spacing between an antenna and a metallic object making the whole structure suffer from being bulky and easily damaged. And some metal-friendly tags including an inserted ground plane have also been proposed. These antennas adequately operate on various dielectrics as well as metallic objects, because the inserted ground plane can properly eliminate influence from underlying objects. However, its bulky, complicated geometry and hemisphere radiation pattern not only limit their application in some cases but also increases both cost and difficulty in mass production.

A new type of antenna as a dipole or microstrip with the classical features is proposed in [4], while its size is very large. Here, we will have a further research on this type tag antenna with a novel structure in this paper. The presented antenna works as a dipole in the free space or placed on some dielectric objects such as paper, glass and foam, and when attached on the metal surface, has a good performance as a microstrip using the metallic object surface as its ground plane.

2. ANTENNA DESIGN

The structure of the proposed robust RFID tag antenna for free space and metal surface is illustrated as Figure 1. For low-cost fabrication and simple structure, the antenna is printed on a single-layer substrate without a ground plane or shorting. Here we use a FR4 substrate with thickness 0.3 mm, relative permittivity 4.4, and loss tangent 0.02. When the tag antenna placed on the metal surface as a microstrip antenna, there is a layer of foam between the tag and the metal surface. The proposed tag antenna can't be placed on the metal surface directly because of the poor performance. There is an air-layer between the tag and the metal objects in the simulation.

Here, we choose the Impinj Monza^{TM} 4 QT as the tag chip, which exhibits an impedance of $11 - j143\,\Omega$ at 915 MHz. In order to deliver the maximum power between the antenna and chip,

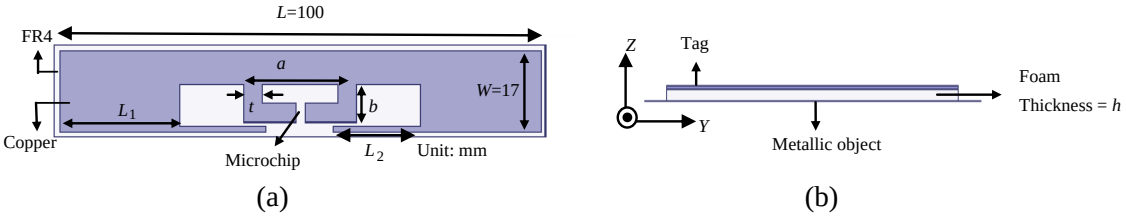

Figure 1: Detailed geometry of the proposed tag antenna. (a) Top view. (b) Side view when placed on the metal surface.

the input impedance of the antenna needs to be $11 + j143\,\Omega$. The T-matching network is normally used to decrease the resistance and to increase the reactance to provide conjugate impedance to the IC impedance [5, 6]. We have known that, it is able to use a T-match to effectively modify the impedance of dipole antenna and simultaneously to feed and provide an impedance match for a microstrip antenna. So the proposed antenna can use a T-matching network to achieve impedance matching.

For the antenna's structure, we choose the W and L according to the classical formula so that the antenna, as a microstrip, has a resonant frequency of approximately 920 MHz. But the calculated theoretical values are too large for many practical applications. So the folded element can be beneficial to realize the antenna miniaturization [6]. The parameters ($a = 23.7$, $b = 8$, $t = 4$) are modified until a suitable tradeoff between the dipole's and microstrip's impedance is achieved. And we choose the $L_1 = 25$ and $L_2 = 18$, when the both resonant frequency close to 920 MHz and the structure is small.

3. SIMULATED AND MEASURED RESULTS

The simulated results of the antenna are carried out from HFSS, which is a full wavelength numeric electromagnetic simulation tool. To validate the performance of the designed antenna, a prototype, shown in Figure 2, was fabricated to do some experiments in a partially anechoic environment.

We have already mentioned that there will be a layer of foam between the tag and metallic object, Figure 3 shows that the s_{11} features with changing foam's thickness h, we can see that there is a small frequency deviation and so we can believe that the antenna can have a good performance

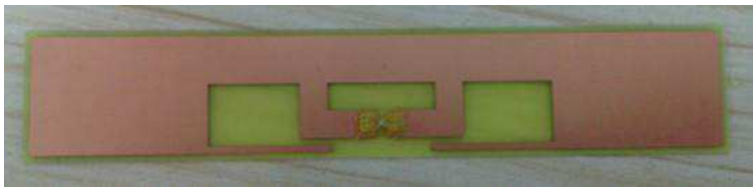

Figure 2: Picture of the fabricated robust tag antenna.

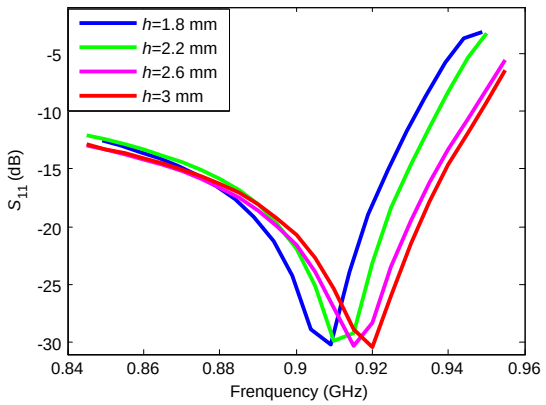

Figure 3: The S_{11} characteristic when placed on the metal with the varying thickness h.

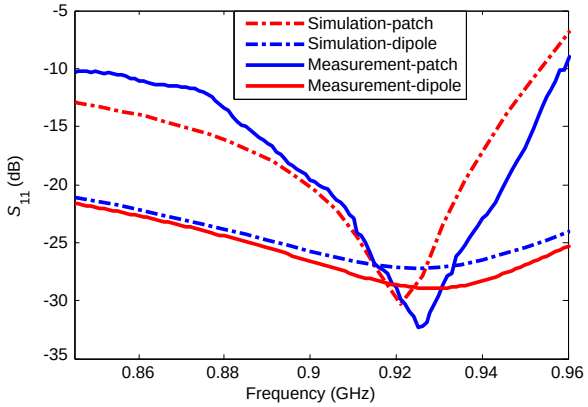

Figure 4: The comparison of simulated and measured S_{11} of the proposed antenna.

with the thickness changing from 2 mm to 3 mm, clearly, when the thickness is 3 mm or greater, the performance will be better. This about 3 mm foam is used in the actual measurement.

Figure 4 shows the simulated and measured s_{11} in both cases. From the figure we can see that both the measured results agree with the simulated ones with a slight deviation. The -10 dB bandwidth of the antenna, as a dipole, is very wide from 730 MHz to 1.7 GHz, not fully shown in this figure, and ranges from 845 MHz to 955 MHz when as a microstrip, the band both can cover the Chinese RFID UHF band (920–925 MHz).

Figure 5 shows the simulated resistance R and reactance X of the antenna when in free space behaving as a dipole, and when on the metal behaving as a microstrip. In free space, there is no much change in impedance over the band, however, as a microstrip, the reactance has a significant increase following the frequency and the resistance is little bit small, but can be accepted. Obviously, there is not a very perfect impedance matching when the antenna works as a microstrip, while the power transfer coefficient is effective.

Since it is difficult that the tag antenna matches to a coaxial line, the measurement of testing radiation patterns is hard to implement, here we just give the simulated data. Figure 6 shows the radiation patterns in YOZ plane. We can see that both have a good gain. A 2 dB enhancement in gain could be achieved when the proposed tag antenna placed on a $150 \times 150\,\text{mm}^2$ metal plate.

In addition, we measured the tag sensitivity and reading distance of the fabricated tags in an anechoic chamber in the both cases, using a commercial measurement system, Tagformance Lite of Voyantic Corporation. Figure 7 presents the reading characteristic when the tags are mounted in free space (on the foam) and on the metal surface. As shown in Figure 7, although the measured results show the operating frequency offset, especially in free space, according with the measured return loss, such small deviation is not enough for affecting practical application. We have got that, there is a higher gain when the tag placed on the metallic surface at 920 MHz, which is why the red curve in Figure 7 shows a farther reading distance in the band 920 MHz–925 MHz, however, the

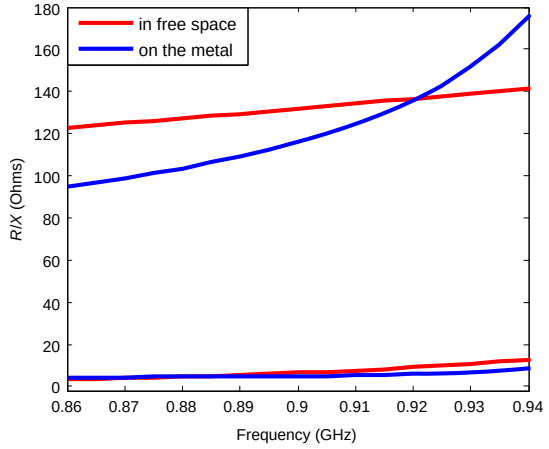

Figure 5: The simulated impedance of the proposed antenna at 920 MHz.

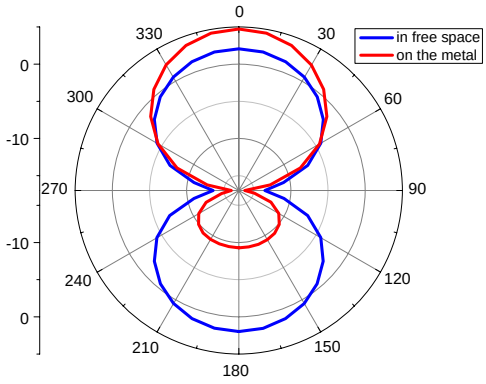

Figure 6: The simulated radiation pattern of the proposed antenna at 920 MHz in YOZ.

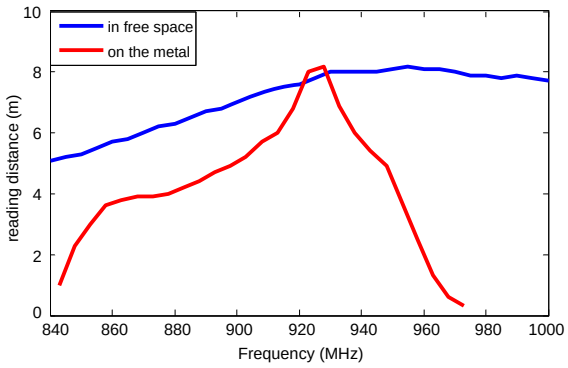

Figure 7: The reading distance of the proposed tag measured by Tagformance Lite.

not very perfect impedance matching when as a microstrip explains why the distance on the metal only a bit bigger than that in free space.

4. CONCLUSION

A robust tag antenna is proposed in the UHF band which can be applied as a dipole in free space, and as a microstrip on the metal surface. Good impedance matching is achieved by geometrically adjusting the size of the T-matching network, which is a classical impedance matching to a dipole, and when attached to metal surface, operates as a microstrip antenna with balanced edge feeds. The tag antenna has half-power bandwidth of 1 GHz and 110 MHz, in free space and on the metal, respectively. We got that the expected reading distance on both cases is about 8 m by a Tagformance Lite. The proposed tag antenna would be suitable for practical applications dealing with free-space and metallic objects.

ACKNOWLEDGMENT

This work is supported by the National Natural Science Foundation of China under Grant No. 61201-026, and Beijing Higher Education Young Elite Teacher Project (Grant No. YETP0438).

REFERENCES

1. RSO, K. V. S., P. V. Nikitin, and S. F. Lam, "Antenna design for UHF RFID tags: A review and a practical application," *IEEE Trans. Antennas and Propag.*, Vol. 53, No. 2, 3870–3876, 2005.
2. Dobkin, D. M. and S. M. Weigand, "Environmental effects on RFID tag antennas," *IEEE Int. Microwave Symp.*, Jun. 2005.
3. Zhang, Y., "Effect of metallic objects and liquid supplies on RFID links," *IEEE Digital Object Identifier*, 1–4, 2009.
4. Mohammed, N. A., "An RFID tag capable of free-space and on-metal operation," *IEEE Digital Object Identifier*, 63–66, 2009.
5. Marrocco, G., "The art of UHF RFID antenna design: Impedance matching and size-reduction techniques," *IEEE Antennas and Propag. Magazine*, Vol. 50, No. 1, 66–79, 2008.
6. Choo, J. and J. Ryoo, "T-matching networks for the efficient matching of practical RFID tags," *Proc. 39th Eur. Microw. Conf.*, 5–8, Rome, Italy, 2009.

Modified Miniature Tri-band CPW-fed Antenna for RFID Applications

Huihui Li[1], **Yongjin Zhou**[2], **and Lei Wang**[1]

[1]Shenzhen Institutes of Advanced Technology, Chinese Academy of Sciences, China
[2]Shenzhen University, China

Abstract— A modified tri-band CPW-fed antenna is designed on a PCBoard with $\epsilon_r = 4.4$ for RFID applications. The design is optimized to operate at 0.915 GHz, 2.45 GHz, 3.50 GHz using the finite element method. In this design, two U-shaped branches are added as additional resonators to achieve multi-band operation based on our previous design. Simulation shows that the $30 \times 30\,\text{mm}^2$ antenna achieves less than -10 dB return loss at the targeted frequencies. Furthermore, the antenna achieves less than -8 dB of S_{11} at 5.8 GHz. Simulated current distribution and radiation patterns are given in the paper.

1. INTRODUCTION

Radio frequency identification (RFID) is a contactless automatic identification technology [1]. It has been used extensively in a variety of applications, such as supply chain management, logistics tracking, access control, electronic toll collection (ETC) and public transportation card. RFID can be classified into low frequency (LF), high frequency (HF), ultrahigh frequency (UHF), and microwave RFID systems, according to its use in different frequency bands [2]. UHF RFID frequency band extends from 840 to 960 MHz divided into four world regions: China (840–845 MHz, 920–925 MHz), Europe (865–868 MHz), US (902–928 MHz), and Japan (950–956 MHz) [3]. Furthermore, microwave RFID operation is assigned at 2.45 or 5.8 GHz. Therefore, more and more wireless communications and RFID systems require dual or multi-band antenna designs. Some multi-band antennas have been designed for RFID, such as dual-band antenna with Tree-like fractal structure [4] (842/922 MHz), triband fractal tree antenna (3.6/5.8/8.2 GHz) [5], planar inverted F-antenna (PIFA) (433 MHz/912 MHz/2.45 GHz) [6] and meandered dipole antenna [7]. However, most of these antennas are in large size.

In this paper, we propose a modified tri-band CPW-fed antenna which is based on our previous design [8]. Two U-shaped patches are added in the antenna. This paper is organized as follows. Section 2 presents the structure of antenna. Simulated results and discussions are shown in Section 3 and Section 4 concludes this paper.

2. ANTENNA CONFIGURATION

Proposed antenna is implemented on a low-cost FR-4 substrate with dielectric constant $\varepsilon_r = 4.4$, loss tangent $\tan\delta = 0.02$ and thickness $h = 1.6$ mm (Fig. 1). The antenna's size is limited to $30 \times 30\,\text{mm}^2$ ($L \times W$). A 50 Ω CPW transmission line is used for feeding patch element with a fixed strip $S = 2.6$ mm and a gap distance $G = 0.2$ mm between the feeding line and ground. In order to achieve multi-band performance, the designed symmetric antenna has two U-shaped, four L-shaped and two F-shaped branches. The six branches function as additional resonators to resonate the antenna at multiple frequency bands. Two L-shaped branches ($L_{11} \times W_{13}$) are used to lower the resonant frequencies to the lower bands (0.915 GHz and 2.45 GHz) and two other L-shaped branches ($L_{10} \times W_9$) and two L-shaped branches ($L_1 \times W_3$) are designed for the higher bands (3.50 GHz and 5.8 GHz). Two F-shaped branches are used for compact antenna characteristic. The geometric dimensions for the proposed antenna are given in Table 1.

3. SIMULATED RESULTS

The proposed antenna is simulated by the finite element method (FEM), and the resulting reflection coefficients within the targeted frequency bands are shown in Figs. 2(a)–(d) using the FEM. The proposed antenna achieves less than -10 dB return loss at the targeted frequencies (0.915 GHz, 2.45 GHz, 3.50 GHz). The bandwidths (VSWR ≤ 2) are 11 MHz (908 MHz to 919 MHz), 35 MHz (2.435 GHz to 2.470 GHz), 100 MHz (3.50 GHz to 3.60 GHz) respectively. Furthermore, the antenna achieves less than -8 dB of S_{11} at 5.8 GHz.

Table 1: Geometric dimensions of proposed antenna

Parameter	Dimension (mm)	Parameter	Dimension (mm)
W_1	0.5	L_1	8.7
W_2	11.6	L_2	0.5
W_3	4.8	L_3	0.5
W_4	0.6	L_4	0.5
W_5	5.4	L_5	2.3
W_6	13	L_6	1.4
W_7	0.6	L_7	4
W_8	5	L_8	1.5
W_9	2.5	L_9	2
W_{10}	3.8	L_{10}	4
W_{11}	4	L_{11}	4
W_{12}	9	L_{12}	1.5
W_{13}	12.5	W_{14}	8
W_{15}	9		

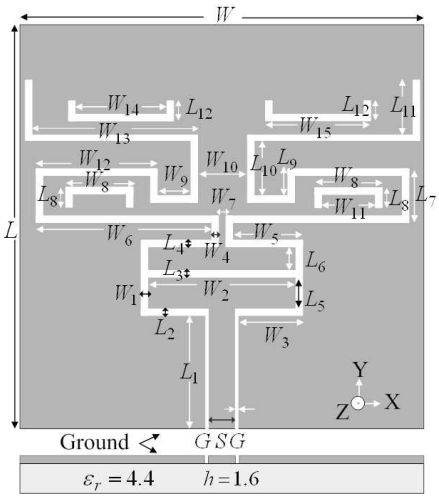

Figure 1: Antenna architecture.

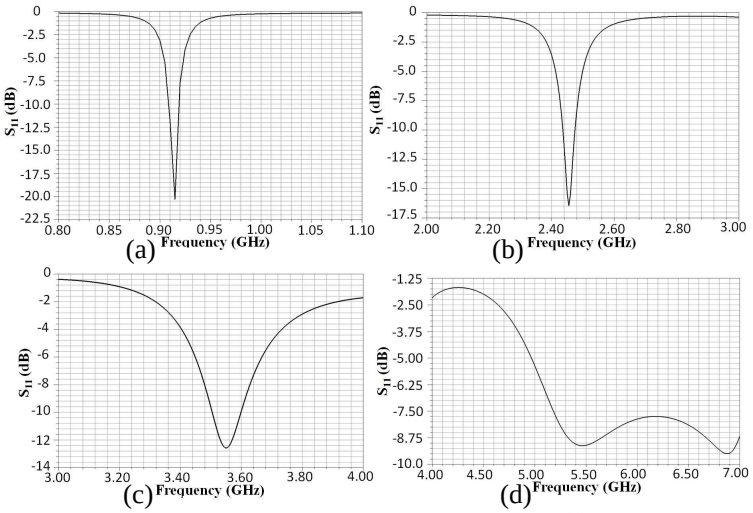

Figure 2: Simulated S_{11} of proposed antenna at four bands obtained by FEM. (a) First band (0.915 GHz); (b) Second band (2.44 GHz); (c) Third band (3.55 GHz); (d) Fourth band (5.80 GHz).

The simulated surface current distributions were analyzed and shown in Fig. 3 for the proposed antenna and antenna without U-shaped branches at operational frequencies of 0.915 GHz, 2.45 GHz, 3.50 GHz and 5.80 GHz respectively. It can be seen in Fig. 3 that antenna with added U-shaped branches has stronger surface current along the meander line at 0.915 GHz and 2.45 GHz respectively, which means that the radiations would be strengthened at these two frequencies. As for the higher two frequency (3.50 GHz and 5.8 GHz), surface current seems to be the same for both antennnas with and without U-shaped branches. It also can be seen that a relative strong surface current is formed along the meander line over L-shaped branches ($L_{11} \times W_{13}$ and $L_{10} \times W_9$) at 0.915 GHz, while most of the surface current concentrates on the two L-shaped branches ($L_7 \times W_6$) and branches (W_7) at 2.45 GHz, and surface current is strong at two L-shaped branches ($L_1 \times W_3$) and slot S at 3.50 GHz. Furthermore, two F-shaped branches ($L_6 \times W_5$) have a relative strong current at 5.8 GHz. Therefore, L-shaped branches ($L_{11} \times W_{13}$) affect the lowest resonant frequency band at 0.915 GHz. With length L_{11} increasing, the lower frequency band will shift to lower frequency with fine-tuning.

Simulated radiation patterns of the proposed antenna in the xz plane ($\phi = 0°$) and the yz ($\phi = 90°$) plane at four targeted frequencies are shown in Fig. 4 (E_θ and E_ϕ). It can be observed

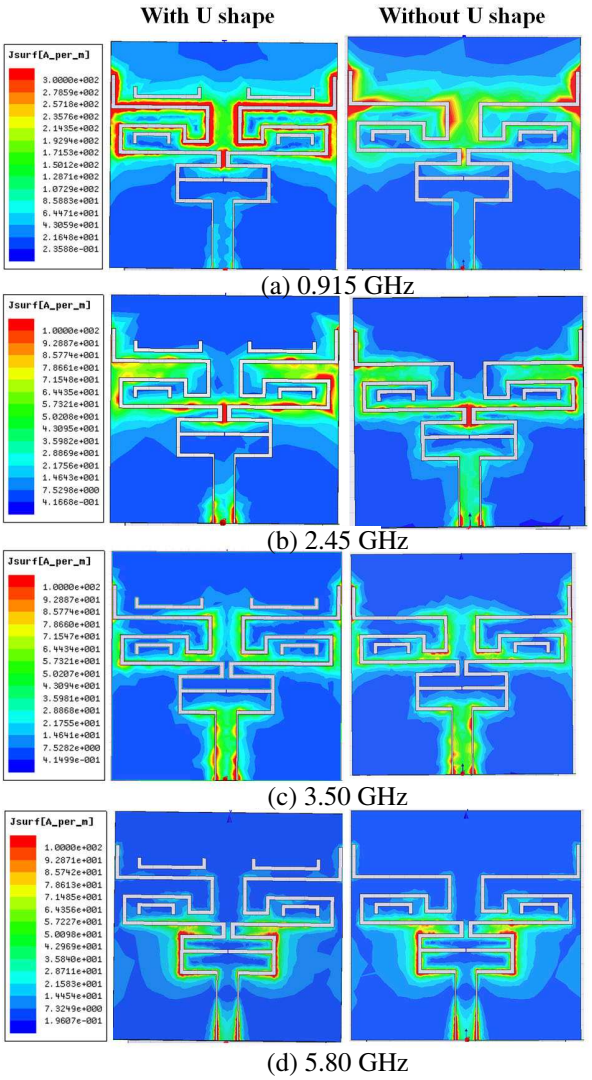

Figure 3: Simulated S_{11} of proposed antenna at four bands obtained by FEM. (a) First band (0.915 GHz); (b) Second band (2.44 GHz); (c) Third band (3.55 GHz); (d) Fourth band (5.80 GHz)

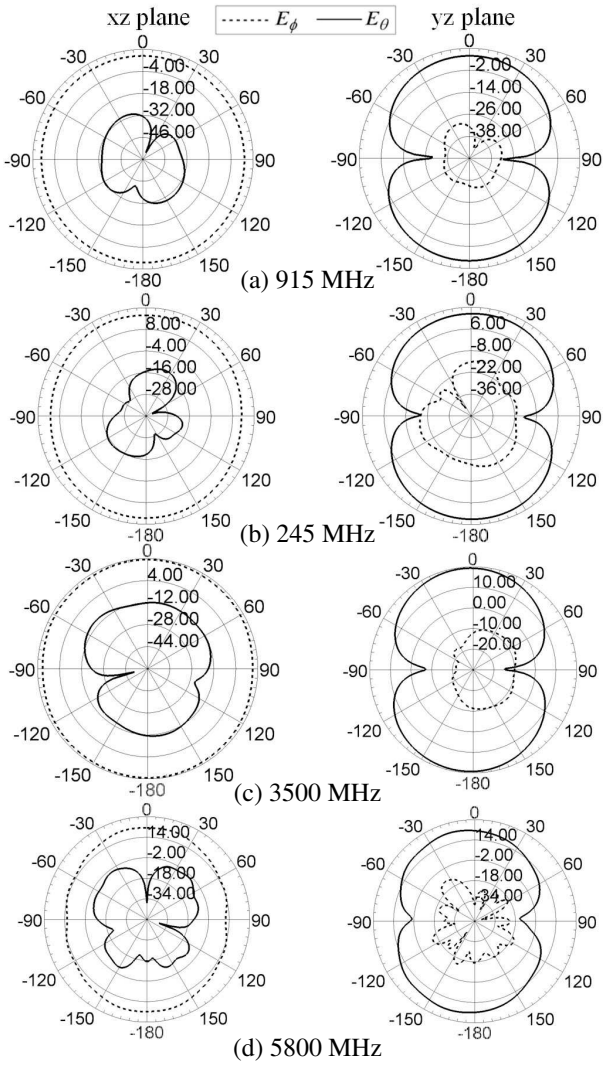

Figure 4: Simulated radiation patterns of proposed antenna at four bands obtained by FEM. (a) First band (0.915 GHz); (b) Second band (2.45 GHz); (c) Third band (3.50 GHz); (d) Fourth band (5.80 GHz).

that radiation patterns of the antenna at 0.915 GHz, 2.45 GHz and 3.50 GHz are omnidirectional in xz plane and quasi-dipole in yz plane. These characteristics may be suitable for RFID applications. Moreover, the simulated peak antenna gains appear to be -11.6 dBi at 0.915 GHz, -1.08 dBi at 2.45 GHz, 2.09 dBi at 3.50 GHz and 5.69 dBi at 5.80 GHz respectively.

4. CONCLUSION

A modified tri-band RFID tag antenna is reported in this paper. Two U-shaped branches are utilized as additional resonators in order to achieve multi-band operation and strengthen the radiation at 0.915 GHz and 2.45 GHz. In the future, by adjusting parameter L_{11}, the designed antenna would be suitable for the combination of the triple-band RFID applications and the multi-band WiMAX/WLAN applications in a single system.

ACKNOWLEDGMENT

The project is supported partially by National Natural Science Foundation of China (Grant No. U12 01256), the Guangdong Innovative Research Team Program (2011S013, GIRTF-LCHT), the next generation communication technology Major project of National S&T (2013ZX03005013), the 'Low-

cost Healthcare' Programs of Chinese Academy of Sciences, International Science and Technology Cooperation Program of Guangdong Province (2012B050200004).

REFERENCES

1. Finkenzeller, K., *RFID Handbook: Fundamentals and Application in Contactless Smart Cards and Identification*, John Wiley and Sons Inc., UK, 2003.
2. Wu, T. Q., H. Su, L. Y. Gan, H. Z. Chen, J. Y. Huang, and H. W. Zhang, "A compact and broadband microstrip stacked patch antenna with circular polarization for 2.45-GHz mobile RFID reader," *IEEE Antennas and Wireless Propagation Letters*, Vol. 12, 623–626, 2013.
3. Santiago, A. G., J. R. Costa, and C. A. Fernandes, "Broadband UHF RFID passive tag antenna for near-body applications," *IEEE Antennas and Wireless Propagation Letters*, Vol. 12, 136–139, 2013.
4. Liu, G., L. Xu, and Z. S. Wu, "Dual-band microstrip RFID antenna with tree-like fractal structure," *IEEE Antennas and Wireless Propagation Letters*, Vol. 12, 976–978, 2013.
5. Varadhan, C., J. K. Pakkathillam, M. Kanagasabai, R. Sivasamy, R. Natarajan, and S. K. Palaniswamy, "Triband antenna structures for RFID systems deploying fractal geometry," *IEEE Antennas and Wireless Propagation Letters*, Vol. 12, 437–440, 2013.
6. Ko, J. H., K. T. Kim, D. H. Kim, H. B. Lee, and H. S. Kim, "A practical approach to robust design of a RFID triple-band PIFA structure," *IEEE Trans. Magnetics*, Vol. 46, No. 8, 3333–3336, 2010.
7. Ni, J., S. Yan, and M. Z. Zhang, "A triple-band meandered dipole antenna with bandwidth improved for RFID tag," *Proceedings of International Conference on Electronics, Communications and Control*, 1857–1859, Ningbo, China, Sep. 2011.
8. Li, H. H., X. Q. Mou, Z. Ji, H. Yu, Y. Li, and L. Jiang, "Miniature RFID tri-band CPW-fed antenna optimised using ISPO algorithm," *Electronics Letters*, Vol. 47, No. 3, 161–162, 2013.

Study of CO_2Z Hexaferrite Magnetodielectric Material as Substrate for RFID Reader Antenna

Haiyang Yu[1], **Yuan Yao**[1], **Junsheng Yu**[1], **Xiaodong Chen**[2], **and Xiaoming Liu**[1]

[1]School of Electronic Engineering, Beijing University of Posts and Telecommunications, China
[2]School of Electronic Engineering and Computer Science, Queen Mary, University of London, UK

Abstract— In this paper, Co_2Z material as the substrate is applied to design a microstrip patch antenna at 920 MHz for UHF RFID reader antenna application with simulation software CST. The simulation and measurement results show that this innovative magnetodielectric material is useful in antenna miniaturization, beneficial to achieve greater bandwidth, and there will have more performance optimizations in the design.

1. INTRODUCTION

The antenna's miniaturization is one of the challenges for antenna design. Due to the advantages such as planar structure, small volume, light weight, microstrip patch antennas have become increasingly sophisticated. Typically, patch antenna miniaturization can start from structure or substrate materials. Structurally, innovation and improvement are mainly for the resonance characteristics of the antenna design. In substrate material, according to the antenna design theory, the material with specific permeability and permittivity has a significant help for miniaturization. When using a single high dielectric constant substrate material, although the size of the antenna is reduced, but the antenna's radiation efficiency and bandwidth will be affected so that the difficulties of the antenna design increase. In antenna design, remarkably, a low loss substrate material with high permittivity and magnetic permeability is both possible to achieve antenna miniaturization and to ensure the improvement of radiation efficiency and bandwidth.

In this article, an UHF RFID reader antenna is simulated and designed with a low-loss Co_2Z material with high dielectric constant and magnetic permeability as substrate material. According to the theory and practical simulation, we can observe that Co_2Z material as a new material is beneficial to bandwidth and significantly reduces the dimension.

2. ANTENNA DESIGN

Normally, the length and width dimension of the antenna is considered first. According to experience in the design [1], the value of the width **W** should be designed with reference to the final dimension of the length **L** in order to generate the circular polarization effect. According to the equation $\mathbf{L} = \frac{\mathbf{c}}{2\mathbf{f}\sqrt{\boldsymbol{\varepsilon\mu}}}$, there is an estimate of the length dimension **L** of the antenna. And $\boldsymbol{\varepsilon}$ is the permittivity of the dielectric substrate, $\boldsymbol{\mu}$ is the magnetic permeability of the substrate material. The parameter $\sqrt{\boldsymbol{\varepsilon\mu}}$ is Miniaturization factor [2]. The permittivity of the substrate material and the magnetic permeability influence the antenna length dimension at the same time [3]. In order to meet the performance of the circular polarization, it keeps the length and width of the antenna

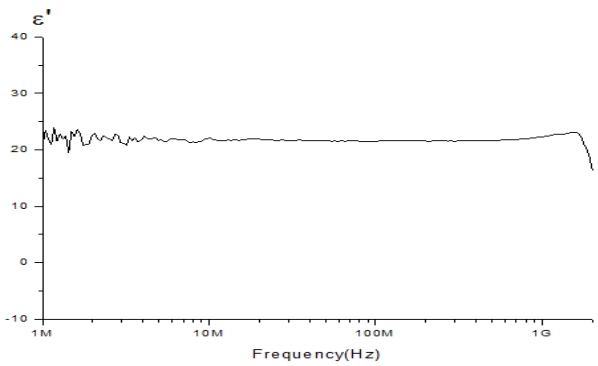

Figure 1: Permittivity of Co_2Z.

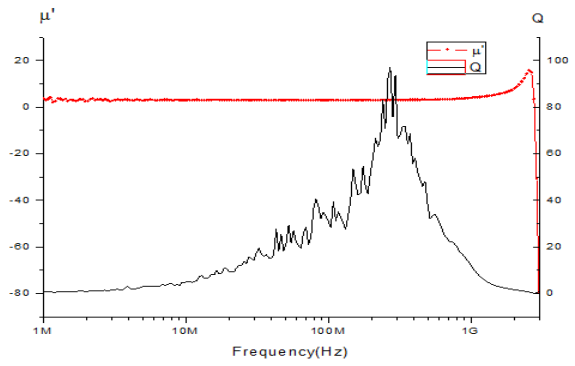

Figure 2: Permeability of Co_2Z.

as the same size. Here the dimension of the dielectric substrate is set as an experimental value, the length of the substrate will be set as $\mathbf{LG} = \mathbf{L} + 0.2\boldsymbol{\lambda}_\mathbf{g}$, where $\boldsymbol{\lambda}_\mathbf{g} = \boldsymbol{\lambda}_0\sqrt{\boldsymbol{\varepsilon\mu}}$. Figure 1 and Figure 2 show the measured values in preliminary tests on the material properties. At 900 MHz, the permittivity is 22, the permeability is 3. So the value of the miniaturization factor is approximately 8. According to the characteristic of the substrate material and the resonance frequency of the proposed antenna designed at 920 MHz, therefore the valuation of the length is 21 mm.

Meanwhile, in order to achieve circular polarization, an additional degeneracy separation unit $\boldsymbol{\Delta S}$ is needed. According to the existing confirmed formula, with additional degeneracy separation unit $\boldsymbol{\Delta S}$, the resonance frequencies of orthogonal polarization mode driven by the patch antenna generate separation. The separation depends on the value of $\boldsymbol{\Delta S}/\mathbf{S}$. Therefore, the effective value of $\Delta\mathbf{S}$ can make the antenna produce circularly polarized radiation. A simplified equation: $|\boldsymbol{\Delta S}/\mathbf{S}|\mathbf{Q}_0 = 1/2$, where $\mathbf{Q}_0$ is unload quality factor of the antenna. This formula can be used when the position of the feeding point is on the X-axis or Y-axis direction. So the valuation of the degeneracy separation unit $\boldsymbol{\Delta S}$ is 4 mm^2.

Emulated and debugged with software CST, simulation dimensions of the patch antenna are obtained with the antenna length and width of 23.9 mm, degeneracy separation unit length of 2.3 mm, substrate length of 45 mm, and substrate thickness of 3 mm. Figure 3 shows the simulation geometry of the patch antenna.

Notably, the substrate thickness affects the bandwidth, radiation and other indicators [4, 5]. When the size of the antenna is fixed, a reasonable thickness of the substrate provided for the patch antenna is critical. How to make the patch antenna get enough bandwidth and good radiation performance should be concerned by setting the thickness of magneto-dielectric material as substrate.

3. SIMULATION RESULTS

Figure 4 shows the simulated S_{11} parameters.

In order to verify the effects of the magnetic permeability of Co_2Z material on the antenna dimension, a hypothetical high-k material is simulated to compare with Co_2Z material. The high-k material has same permittivity as Co_2Z, but its permeability value is 1. Compared with the high-k

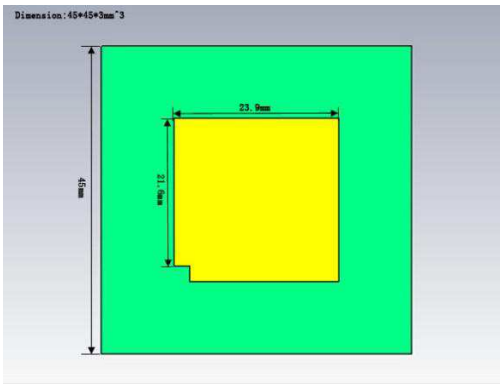

Figure 3: Geometry of the proposed antenna.

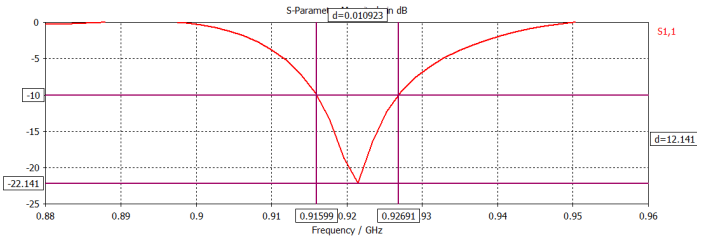

Figure 4: Simulated S_{11} of the proposed antenna.

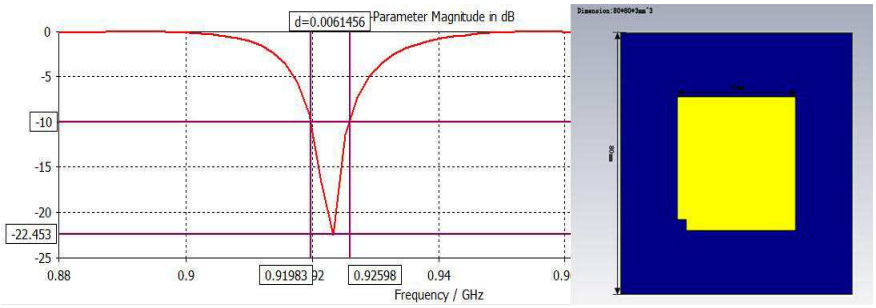

Figure 5: Geometry of high-K antenna and simulated S_{11} parameters.

Table 1: Performance of compared simulation antennas.

Material	Property	Dimension	Bandwidth ($S_{11} \leq 10\,\mathrm{dB}$)
Co_2Z	$\varepsilon = 22,\ \mu = 3$	$45 * 45 * 3\,\mathrm{mm}^3$	915.9–926.9 MHz
High-K	$\varepsilon = 22,\ \mu = 1$	$80 * 80 * 3\,\mathrm{mm}^3$	919.8–925.9 MHz

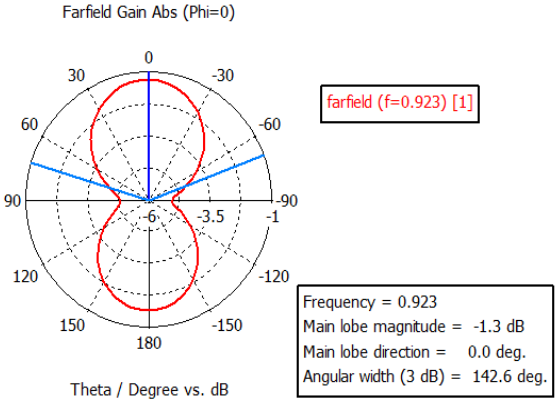

Figure 6: Farfield gain of the proposed antenna.

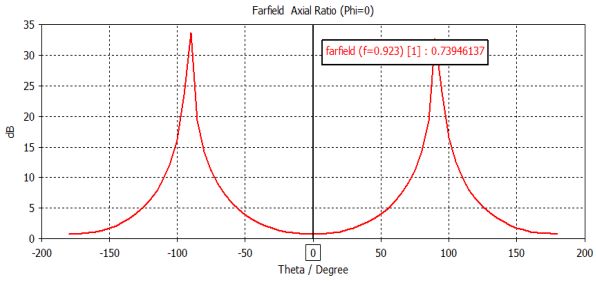

Figure 7: Axial ratio of the proposed antenna.

material antenna, the dimension of the Co_2Z antenna has been significantly reduced. And the bandwidth of Co_2Z antenna is wider than high-K antenna. Figure 5 shows the simulation geometry of high-K antenna and simulated S_{11} parameters. Table 1 shows the different performance between two simulation antennas with different material as substrate.

The Co_2Z antenna's radiation efficiency does not play a distinct advantage in the simulation, which will be focused and improved in the subsequent measurement. Figure 6 shows the antenna simulated Farfield gain.

Simulation antenna achieved circular polarization at 920–925 MHz. Figure 7 shows the antenna axial ratio.

4. CONCLUSION

In this paper, an UHF RFID reader antenna with Co_2Z magneto-dielectric material as substrate is designed and simulated. This antenna exhibited a more excellent property on miniaturization, bandwidth performance and circular polarization characteristic. In the simulation, the radiation characteristic receives some limit, which will be optimized and improved in the subsequent experiment. At the time of this writing, the antenna is being machined. The measurement results and data will be complemented before this article published. Overall, Co_2Z magneto-dielectric material has a sufficient development space in antenna design.

ACKNOWLEDGMENT

This work is supported by the National Natural Science Foundation of China under Grant No. 61201-026, and Beijing Higher Education Young Elite Teacher Project (Grant No. YETP0438).

REFERENCES

1. Balanis, C. A., *Antenna Theory: Analysis and Design,* Wiley, New York, 1997.
2. Mosallaei, H. and K. Sarabandi, "Magneto-dielectric materials in electromagnetic: Concept and applications," *IEEE Transactions on Antenna and Propagation*, Vol. 52, No. 6, 1558–1567, Jun. 2004.
3. Hansen, R. C. and M. Burke, "Antennas with magneto-dielectric materials," *Microwave Opt. Tech. Letter*, Vol. 26, No. 2, 75–78, Jul. 2000.
4. Mossallaei, H. and K. Sarabandi, "Magneto-dielectrics in electromagnetic: Concept and applications," *IEEE Transactions on Antenna and Propagation*, Vol. 52, 1558–1567, 2004.
5. Brown, A. D., J. L. Volakis, L. C. Kempel, and Y. Botros, "Patch antennas on ferromagnetic substrates," *IEEE Transactions on Antenna and Propagation*, Vol. 47, No. 1, 26–32, Jan. 1999.

A Novel Fully Printed 28-bits Capacity Chipless RFID Tag Based on Open Conical Resonators

Raji Nair[1], **Marvin Barahona**[1], **Diego Betancourt**[1], **Georg Schmidt**[2], **Maxi Bellmann**[2], **Daniel Höft**[2], **Dirk Plettermeier**[3], **Arbed Hübler**[2], **and Frank Ellinger**[1]

[1]Circuit Design and Network Theory, TU Dresden, Dresden, Germany
[2]Institute for Print and Media Technology, TU Chemnitz, Chemnitz, Germany
[3]RF Engineering, TU Dresden, Dresden, Germany

Abstract— A novel fully printed 28-bits capacity chipless RFID tag using conical resonators is proposed here. The angle of aperture of these resonators is adjusted to suppress high order modes allowing an efficient use of the UWB frequency bandwidth. By using 12 resonators within a reduced dimension of $4.2 \times 3\,\mathrm{cm}^2$, a coding capacity of 28 bits is achieved, which is the highest coding capacity reported for a fully printed chipless tag. Several chipless tags are printed on flexible substrate and validated experimentally.

1. INTRODUCTION

Printed Chipless RFID owing to the elimination of both batteries and silicon chip provides a feasible method to obtain a wireless identification solution to the conventional barcode cost. Researchers all over the world have added numerous features to the chipless tags like, polarization diversity, tag detuning, coding capacity comparable to barcode, etc. [1, 2]. Even though it is easy to find "fully printable" tags on flexible substrate, most of the tags are developed using the conventional photolithography process and a "fully printed" passive chipless tag with high coding capacity can be seldom found. Besides the design of the chipless tag could be done without any surface mounted devices (SMD) on it, but simply using some conductive strips so as to reduce the cost and simplify its fabrication.

The highest reported coding capacity of a chipless tag comparable to the barcode is 49 bits [1], where multiple circular ring patch resonators are used. However, the chipless tags are developed on Rogers's substrate using conventional photolithography process. The same authors have also developed printed chipless tags on paper substrate using the high speed flexography process [3]. Here, 19 bits are achieved within a reasonable size of $7 \times 3\,\mathrm{cm}^2$.

A fully printed chipless tag on flexible substrate can be seen in [4], where a prototype of the tag is printed on a photo paper. Several capacitive discontinuities are placed at different distances and the reflected signals from these discontinuities are used for encoding. Nevertheless, it uses some discrete localized components and the conductivity of the metallic strips is approximately $3 \times 10^6\,\mathrm{S/m}$ due to the metallic thickness ($\approx 1\,\mu\mathrm{m}$). In order to rectify this, a linear tapered microstrip line is used which in turn increases the overall size of the tag, achieving a final coding capacity of 10 bits. Moreover, the prototype demands the use of external antennas and SMA connectors.

Thus, in short a fully printed passive chipless tag with coding capacity higher than 19 bits has not yet been developed. In this paper, a novel fully printed 28-bits capacity chipless tag based on open conical resonators is proposed. The chipless tag is developed on flexible substrate using screen-printing process which enables the fabrication of low cost tags for mass production applications. The proposed chipless tag can encode 28 bits within a compact size ($4.2 \times 3\,\mathrm{cm}^2$). The Radar Cross Section (RCS) of the chipless tag is encoded using the frequency shift generated by changing the physical length of each resonator.

2. CHIPLESS TAG DESIGN

The classical way of encoding in chipless tag is to create some resonance peaks or dips in the backscattered signal from the tag 1. To do so, the RCS of the tag is exploited. The proposed chipless tag is based on multiple open conical resonators which are able to produce RCS with sharp peaks at particular frequencies corresponding to the physical dimension of the resonator. Basically two different types of conical resonators can be seen, one with open end and the other with short circuited end. Figure 1 shows the simulated RCS of these two types for a given length 'l' and a cone angle 'φ'. CST Microwave Studio is used as the simulation tool. PET with 100 μm thickness is chosen as the substrate which has an effective permittivity of 2.9 and loss tangent of 0.0025.

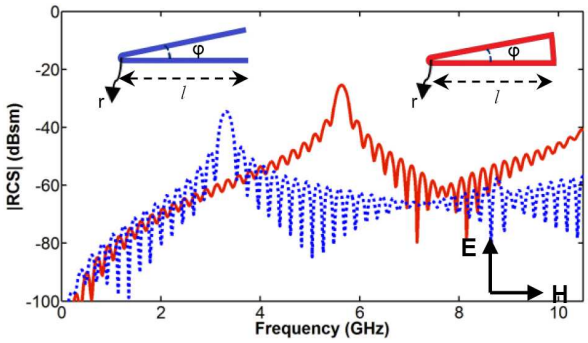

Figure 1: |RCS| of open and short circuit conical resonators along with the design parameters. 'l' is the length, 'φ' is the cone angle and 'r' is the radius of the curvature nose edge. In this example $l = 24\,\text{mm}$, $r = 1\,\text{mm}$ and $\varphi = 10°$.

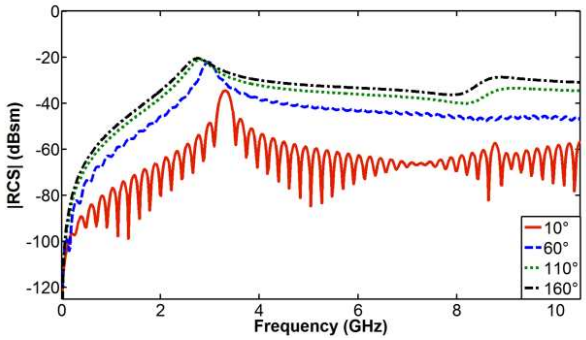

Figure 2: Simulated |RCS| of open conical resonator for different aperture angles φ and $l = 24\,\text{mm}$.

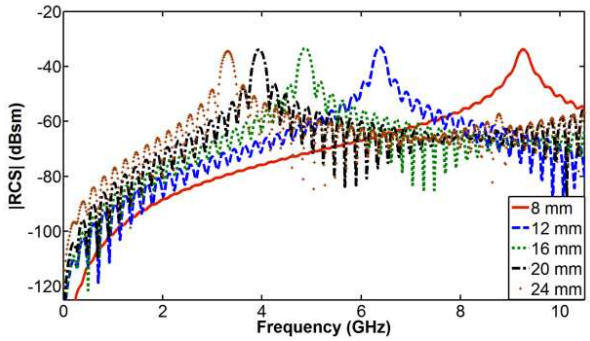

Figure 3: Simulated |RCS| of open conical resonator for different lengths l and $\varphi = 10°$.

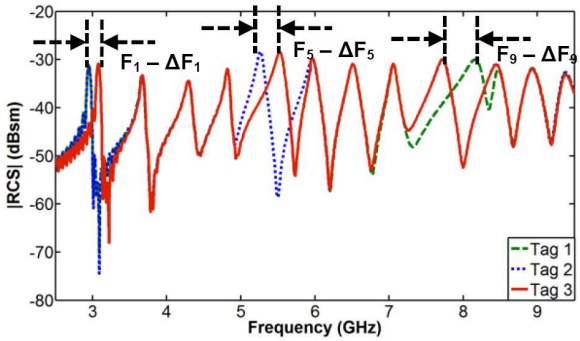

Figure 4: Simulated |RCS| response of different chipless tag combinations with 12 resonators.

When a vertically polarized electromagnetic wave is impinged on the surface of the resonator, it can backscatter energy peaks at certain resonance frequencies depending upon the physical length of the resonator. Even though the short circuited conical resonator produces better RCS, the open conical resonator can achieve a more compact size and better frequency selectivity ($\sim 25\%$). Since we are interested in high coding capacity, better selectivity allows increasing the number of resonators. Thus, a choice can be taken depending on the application and open resonators is chosen for this particular tag design.

Simulations have been done in order to verify the effect of each design parameter. One of the significant design parameter which determines the performance of the conical resonator is the cone angle 'φ'. It has been found that while decreasing the cone angle, the frequency peaks become highly selective with suppression in the even mode, while generating an odd mode. This suppression allows an efficient use of the frequency bandwidth. The reason for highly selective RCS is due to the increase in coupling between the two arms while cone angle is decreasing. Several simulations were done and it has been found that both 'l' and 'φ' influences the frequency of operation. The simulation results are shown in Figures 3 and 4.

A 10° cone angle 'φ' is chosen in order to have highly selective RCS peak. Several tag combinations are designed by changing the number of resonators in order to have the proof of concept. The designs are made on a single layer and no ground plane is included in the proposed case. Tags are simulated using 12 resonators. It has been found that when several resonators are used, third order modes can be observed which may be due to the coupling produced between the resonators. Hence the frequency of operation has been limited between 3.1 GHz and 9.3 GHz, since an odd mode is observed at 9.4 GHz; this means that for the used UWB frequency range, one resonator could be placed per almost 500 MHz bandwidth. Figure 2 shows the simulated RCS response of different tags with 12 resonators.

Frequency shift coding is implemented here, as explained in [1], and in order to assess the tag

encoding capacity for the selected bandwidth of 6.2 GHz, the number of possible frequency slots needs to be determined. For this purpose, the 3 dB bandwidth of each peak is considered. With this, the amount of frequency slots per resonator can be calculated by simple dividing the resonator's assigned bandwidth by its 3 dB peak bandwidth.

Furthermore, the total chiplesstag combinations without repetition 'N' in the case that the resonators are being able to take any frequency slot can be calculated using the following equation [5],

$$N = \frac{n_s!}{(n_s - n_r)!} * \frac{1}{n_r!} \tag{1}$$

where n_s is the number of slots and n_r is the number of resonators. The capacity of coding can be calculated as [6],

$$C = \log_2(N) \tag{2}$$

3. RESULTS AND PRINCIPLE OF ENCODING

In order to validate the design, the simulated chipless tags are fabricated on flexible PET substrate with a thickness of 100 µm. Screen printing with silver particle based ink is used for printing the metallic strips. The printed tags have a metallic thickness of approximately 8 to 10 µm and are able to produce a conductivity of 2×10^6 S/m. The width of the strip is chosen as 1 mm and the cone angle as 10°. Several tag combinations are printed and a bi-static measurement set-up is used for the tag characterization as shown in Figure 5. The tests are conducted in an anechoic chamber. An Agilent Performance Network Analyzer (PNA E8364B) is used to record the backscattered electromagnetic response from the tag. Two horn antennas with an average gain of 10 dBi in the frequency band from 1 GHz to 18 GHz and separated a distance of 45 cm from each other are connected to the two ports of the network analyzer.

The horn antennas are horizontally polarized, since this polarization provides the best radiation pattern to measure the higher frequencies components of the backscattered signal from the tag at shorter distances. In this case, the chipless tags are placed vertically in order to be interrogated with the horizontally polarized wave. Due to the antenna limitations, in order to efficiently extract the RCS high frequency peaks with a reduced noise level, the power delivered by VNA is set to 6 dBm and thechipless tags are placed at a distance of 50 cm from the horn antennas. In the practical case, the FCC and ETSI regulated power can be used to interrogate the tag [7] and it will also be detectable. A complex S_{21} has been measured using this configuration with the technique explained in 1. In order to validate the concept, 7 different chipless tag combinations are measured. The RCS of each chipless tag has been calculated using the formula explained in 1.

The measured |RCS| for chipless tags with 12 resonators is shown in Figure 6. All the 12 peaks are easily detectable in the figure but the |RCS| level is less than the simulation which may be due to the poor conductivity of the printed chipless tag. A simulation has been conducted with a conductivity of 2×10^6 S/m and it has been found that the |RCS| level decreased as in the case of measurement.

Even though simulations results permit more number of peaks and therefore bits, coding capacity is calculated based on the obtained measurement results since the measured RCS peaks have a wider

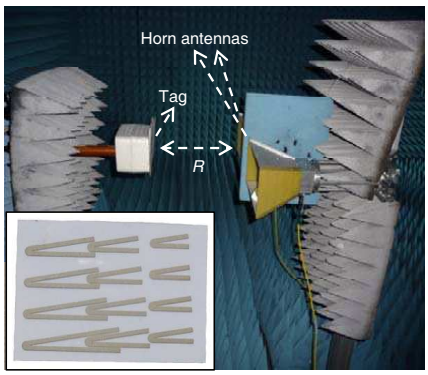

Figure 5: The bi-static measurement set-up used. The horn antennas are horizontally polarized. Inset: chipless tag with 12 resonators printed on transparent PET. The dimension of the tag is $4.2 \times 3\,\text{cm}^2$.

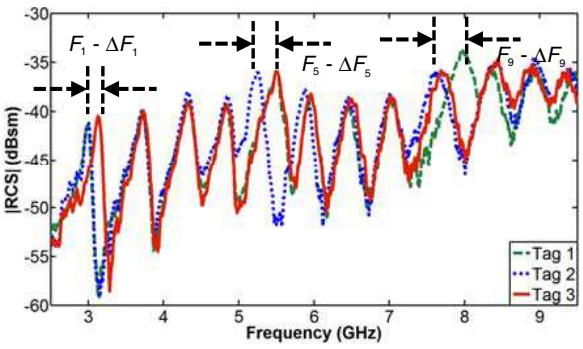

Figure 6: Measured |RCS| response of different tag combinations with 12 resonators.

bandwidth. As explained previously, the 3 dB peaks generate a total of 32 frequency slots for the 12 resonators tag and the given bandwidth as shown in Table 1. Thus for 12 resonators (n_s) with 32 slots (n_r), the capacity (C) of coding is calculated using (1) and (2) as 28 bits.

Table 1: 3 dB bandwidth and number of frequency slots per resonators.

Resonator	Frequency Range (GHz)	3 dB Bandwidth (MHz)	Frequency Slots per Resonator
1	3.1–3.6	100	5
2	3.6–4.2	150	4
3	4.2–4.8	150	4
4	4.8–5.4	150	4
5	5.4–5.8	200	2
6	5.8–6.2	200	2
7	6.2–6.6	200	2
8	6.6–7.0	200	2
9	7.0–7.6	300	2
10	7.6–8.2	300	2
11	8.2–8.8	300	2
12	8.8–9.3	500	1

4. CONCLUSION

In this paper, a novel fully printed chipless tag with high coding capacity is proposed. The tag consists of open conical resonators and the RCS of each resonance peak is used for encoding. A coding capacity of 28 bits is achieved within the unlicensed UWB from 3.1 GHz to 9.3 GHz, which is the highest coding capacity reported yet for a fully printed tag. The tag is printed on flexible PET substrate with a thickness of 100 µm using screen printing process and has a compact dimension of $4.2 \times 3\,\text{cm}^2$. The proposed design is validated experimentally and the obtained results proved the concept.

ACKNOWLEDGMENT

The research leading to these results has received funding from the European Union's Seventh Framework Program (FP7/2007-2013) under grant agreement No. 313161, eVACUATE. The authors are grateful to P. K. Wolf for his enthusiastic and valuable support during the chipless tags measurement.

REFERENCES

1. Vena, A., E. Perret, and S. Tedjini, "High capacity chipless RFID tag insensitive to the polarization," *IEEE Transactions on Antennas and Propagation*, Vol. 60, No. 10, 2012.
2. Islam, M. A. and N. C. Karmakar, "A novel compact printable dual-polarized chipless RFID system," *IEEE Transactions on Microwave Theory and Techniques*, Vol. 60, No. 7, 2142–2151, Jul. 2012.
3. Vena, A., E. Perret, S. Tedjini, G. E. P. Tourtollet, A. Delattre, F. Garet, and Y. Boutant, "Design of chipless RFID tags printed on paper by flexography," *IEEE Transcations of Antennas and Propagation*, Sep. 2013, DOI: 10.1109/TAP.2013.2281742.
4. Shao, Q. Chen, Y. Amin, R. Liu, and L. R. Zheng, "Chipless RFID tags fabricated by fully printable of metallic inks," *Annals of Telecommunications*, Jun. 2013, DOI 10.1007/s12243-013-0378-3.
5. Hays, W., *Statistics*, Harcourt Brace College Publishers, Florida, 1994.
6. Proakis, J. and M. Salehi, *Digital Communications*, 5th Edition, McGraw-Hill, New York, 2008.
7. Nair, R. S., E. Perret, and S. Tedjini, "A novel temporal multi-frequency encoding technique for chipless RFID based on C-sections," *Progress In Electromagnetics Research B*, Vol. 49, 107–127, 2013.

FEM Analysis of Conical Type Coaxial Open-ended Probe for Dielectric Measurement

H. Arab and C. Akyel
Ecole Polytechnique of Montreal, Canada

Abstract— This paper deals with a numerical modelling technique based on finite elements method (FEM) in microwave frequency for computing the dielectric constant and loss factor of a homogeneous dielectric material by using conical-type coaxial probe. This sort of probe can be easily inserted into a wide range of biological tissue types and semi-rigid materials like rubber, some plastics, and organic materials (ex: dairy, butter, etc. for measuring moisture content). Where his feature is considered to be very important in biological and industrial applications. The measuring principle is based on detecting conductance and capacitance change with respect to the dielectric mass movement in the fringe electrical field. A three-dimensional finite-element formulation is employed in the dielectric material region and a small neighbouring region of the probe structure on which it is mounted. The electrical input admittance as well as the reflection coefficient are found from the finite-element analysis. From this, the conductance and capacitance related to the conical probe and fringing field are calculated and consequently the dielectric constant and loss factor are determined. In contrast to many other modelling techniques used for coaxial probe which are approximate and hence limited, the finite-element model is more exact and is applicable to complicated geometries. To demonstrate the accuracy of the numerical model, a parallel experimental study was carried out in the laboratory for the same geometric dimensions. The two results are compared and show excellent agreement, and also demonstrating that finite-element modelling is a good approach for optimized conical coaxial probe design.

1. INTRODUCTION

Measurement of dielectric properties of materials at microwave frequencies has been the subject of many literatures [1–4]. The dielectric constant is an unique and essential property of dielectric materials to characterize the interaction between an electric field and matter. Accurate measurements of these properties can provide scientists and engineers with essential and valuable information to properly incorporate the materials into their intended applications. For example, this information is useful in the area of aerospace, automotive, agriculture, food engineering, bioengineering, medical treatments, and electronics applications, etc.. There are many techniques that have been developed to material characterization like the Transmission/Reflection Line, Open-ended coaxial probe, Free space and resonator method (cavity method) [3–5]. The open-ended coaxial probe has been widely researched over the years as a way to effectively and quickly characterize material properties in a wide frequency spectrum (200 MHz to near 50 GHz). Many models have been built to analyze open ended coaxial probes terminated by semi-infinite homogeneous materials [6–8]. There are four typical models (Capacitive model, Antenna model, Virtual line model, Rational function model,etc.). However, there is an undiscovered area in this field, the study of conical type open ended coaxial line which is a coaxial line ending in a conical shape geometry. The advantage of this kind of probe is the possibility of placing the probe into the solid materials which are difficult for dielectric measurement. In this research, The characteristic impedance of probe are calculated in the different frequencies for various materials by using finite element method, and then antenna model is chosen to relate the conical type coaxial probe characteristic impedance to the dielectric constant and loss factor of the material under test. The sensitivity and accuracy of the models in measuring lossy dielectric or biological material in compare to experimental results are investigated.

2. BASIC EQUATIONS

The problem of electromagnetic field analysis on a macroscopic level is fully described by Maxwell equations subject to certain boundary condition. The conical probe is assumed to be uniform along its longitudinal z axis; therefore maxwell curl equations for time harmonic fields are:

$$\nabla \times \mathbf{E} = -j\omega\mu\mathbf{H} \tag{1}$$

$$\nabla \times \mathbf{H} = -j\omega\epsilon\mathbf{E} \tag{2}$$

By taking the curl of (1) and (2), we have the following curl-curl equation for E:

$$\nabla \times \left(\frac{1}{\mu}\nabla \times \mathbf{E}\right) - k_0^2 \epsilon \mathbf{E} = 0 \quad \text{in } \Omega \tag{3}$$

where k_0 is the free-space wave number and Ω is the probe cross section. An Neumann and Dirichlet boundary condition must be applied by the field vectors in all boundary and interface between two materials. The Galerkin method is chosen for finding numerical solutions to differential equations where the solution residue is minimized giving rise to the well-known weak formulation of problems. The basic idea of this method is to approximate the solution to a differential equation by very simple functions. The residual associated with the PDE Equation (3) is given by:

$$\partial F(\mathbf{E}) = 0 \tag{4}$$

where

$$R(\mathbf{E}) = \frac{1}{2}\iint_{\Omega}\left(\frac{1}{\mu}(\nabla \times \mathbf{E}) \cdot (\nabla \times \mathbf{E})^* - k_0^2 \epsilon \mathbf{E} \cdot \mathbf{E}^*\right) d\Omega \tag{5}$$

suppose that E can be approximated by the expansion

$$E(x, y, z) = \sum_{j=1}^{n} N_j^e(x, y, z) E_j^e \tag{6}$$

where $N_j^e(x, y)$ denotes the basis function defined over the entire domain, M is the number of elements in the domain, and n is the number of edge in the element, and E_j^e is constant coefficients to be determined. By substituting Equation (6) in (5), we can obtain the generalized matrix form eigenvalue problem. More detail about this part can be find in [9] and [10]. This method is used to calculate dielectric field in the aperture of the conical probe and then the reflection coefficient and characteristic impedance of probe at measurement port (which is shown in Fig. 1). Consequently, antenna model is chosen to relate the conical type coaxial probe characteristic impedance to the dielectric constant and loss factor of the material under test. The 2-dimensional electromagnetic structure of conical-type open-ended coaxial probe is shown in Fig. 2 is considered. And the global constant related to structure and martial property are presented in Table 1.

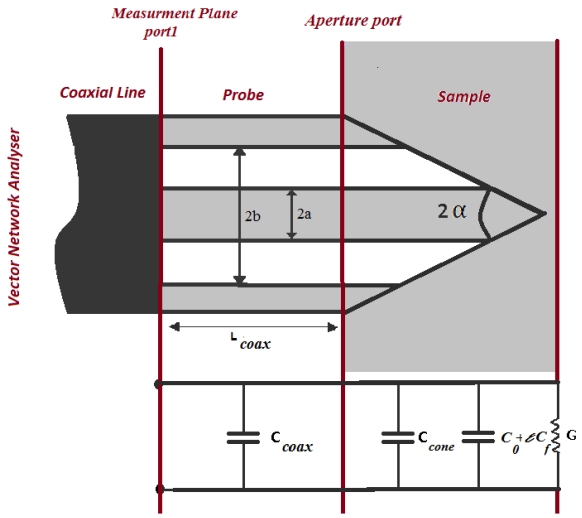

Figure 1: Conical-type coaxial probe geometry and equivalent circuit.

Figure 2: Handmade probes and network analyzer.

In antenna model, the probe is modelled by tow capacitance C_f and C_{cone}, while the material under test (MUT) is modelled by a capacitance $\epsilon^* C_m$ and a conductance G connected in parallel to capacitance for modelling the radiation in MUT. The admittance of this equivalent circuit is given by:

$$\frac{Y}{Y_0} = j\omega C_f Z_0 + j\omega C_{\text{cone}} Z_0 + j\omega C_m Z_0(\omega, \epsilon_0) + Z_0 G(\omega, \epsilon_0) \tag{7}$$

Table 1: Global constant for electromagnetic model.

Name	Expression	Description
a	0.455 [mm]	Coax inner radius
b	1.49 [mm]	Coax outer radius
L_{coax}	250 [mm]	Length of conical coax probe
f	300 [MHz]–3 [GHz]	Frequency
α	30	Cone Angle

For coaxial line whose dimensions are small compared to a wavelength, C_f and C_{cone} are frequency independent, while C_m and G are dependent on frequency. For coaxial probe immersed in a lossy medium it has been shown in [7] that

$$Y\left(\omega, \epsilon^*\right) = \sqrt{\epsilon^*} Y\left(\sqrt{\epsilon^*}\omega, \epsilon_0\right) \tag{8}$$

Hence Equation (7) may be written

$$\frac{Y}{Y_0} = j\omega C_f Z_0 + j\omega C_{\text{cone}} Z_0 + j\omega \epsilon^* C_m Z_0 + Z_0 G \epsilon^{*5/2} \tag{9}$$

Two unknown parameters, C_f and C_0, are estimated accurately by using two material with known properties (air and water). Analytical computation of C_{cone} part is complicated due to the different size of two conductors and their irregular locations. However, dividing the aperture into many thin layer and each layer can be approximated constant radius provides an elegant way to calculate it accurately. Results for different frequencies are shown in Table 2.

Table 2: Capacitances of probe and fringe field (C_f and C_{cone}).

freq	G	C_{cone}	C_{coax}	C_0	C_f
300000000	$3.12E-04$	$1.28E-13$	$2.44E-11$	$3.79376E-14$	$1.2763E-13$
600000000	$4.29E-04$	$1.28E-13$	$2.44E-11$	$3.88725E-14$	$7.49492E-14$
900000000	$6.11E-04$	$1.28E-13$	$2.44E-11$	$3.95339E-14$	$6.85539E-14$
1200000000	$9.67E-04$	$1.28E-13$	$2.44E-11$	$4.07336E-14$	$8.74826E-14$
1500000000	0.001200643	$1.28E-13$	$2.44E-11$	$4.34477E-14$	$8.3988E-14$
1800000000	0.00130072	$1.28E-13$	$2.44E-11$	$4.69067E-14$	$6.81714E-14$
2100000000	0.001568596	$1.28E-13$	$2.44E-11$	$5.0166E-14$	$6.88041E-14$
$2.40E+09$	0.001915157	$1.28E-13$	$2.44E-11$	$5.52373E-14$	$7.18766E-14$
$2.70E+09$	0.002068937	$1.28E-13$	$2.44E-11$	$6.48864E-14$	$5.72198E-14$
$3.00E+09$	0.002208294	$1.28E-13$	$2.44E-11$	$7.79847E-14$	$3.9359E-14$

3. RESULTS AND DISCUSSION

The reflection coefficient factor, electromagnetic field at the probe aperture and permittivity of different materials were analyzed in different frequencies (300 MHz to 3 GHz). Fig. 3 shows the measured reflection coefficient of Air, Water, Methanol and Butanol at 20 degree with conical type open ended coaxial probe. Fig. 4 shows relative permittivity and conductivity for three different materials (Ethanol, Methanol, and Butanol) with conical type open ended coaxial probe. These permittivity are calculated from the reflection coefficient measured at port 1 in Fig. 1. The use of such model is a good approximation for large band of permittivity at radio and microwave frequencies.

The results show that open-ended conical coaxial probes can be successfully used especially at low frequencies with the advantage of increased accuracy and sensitivity. Moreover, it is less effected by unavoidable temperature variation when compared to standard at-plan open-circuit coaxial-probe. An additional advantage of the conical-type probe is that it does not have the problem of flat coaxial probe with solid surface.

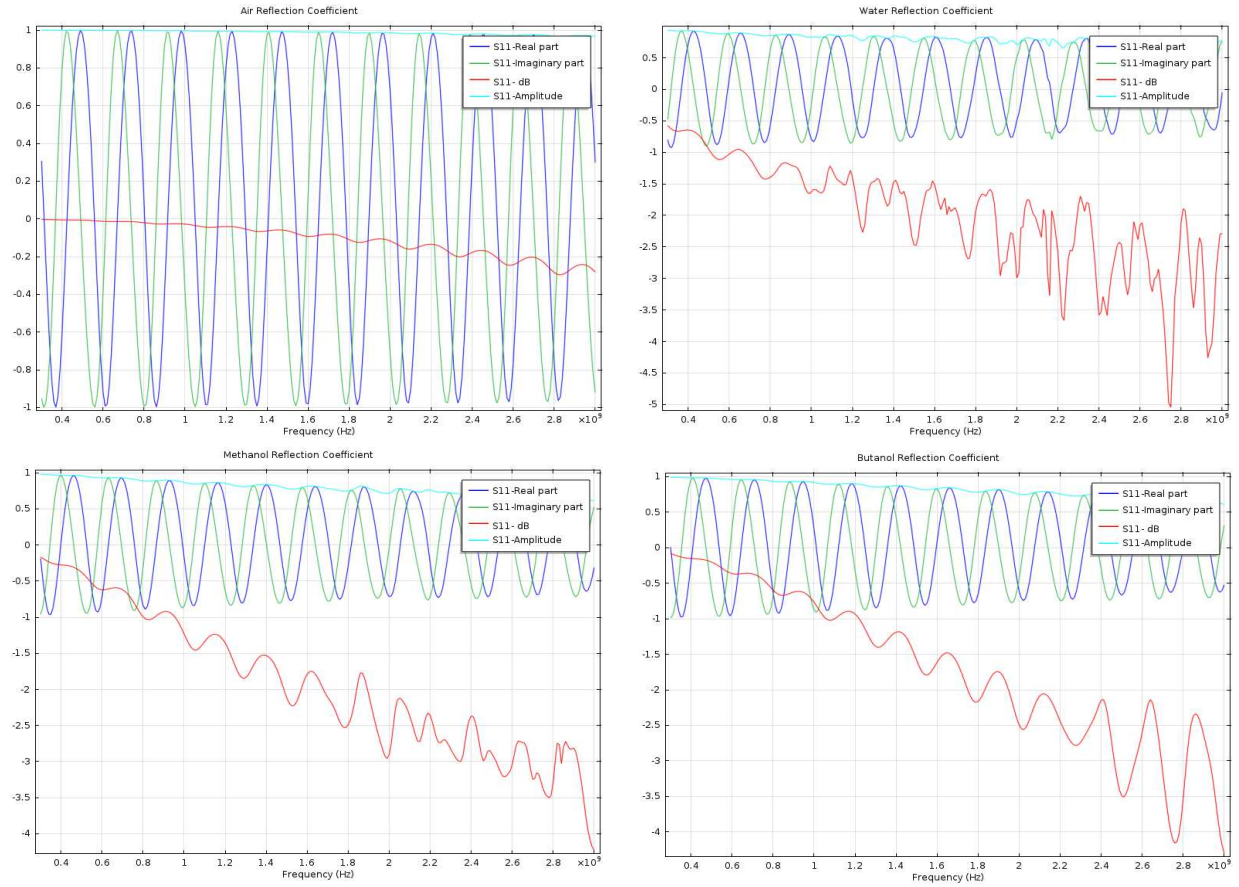

Figure 3: Reflection coefficient for Air, Water, Methanol and Butanol.

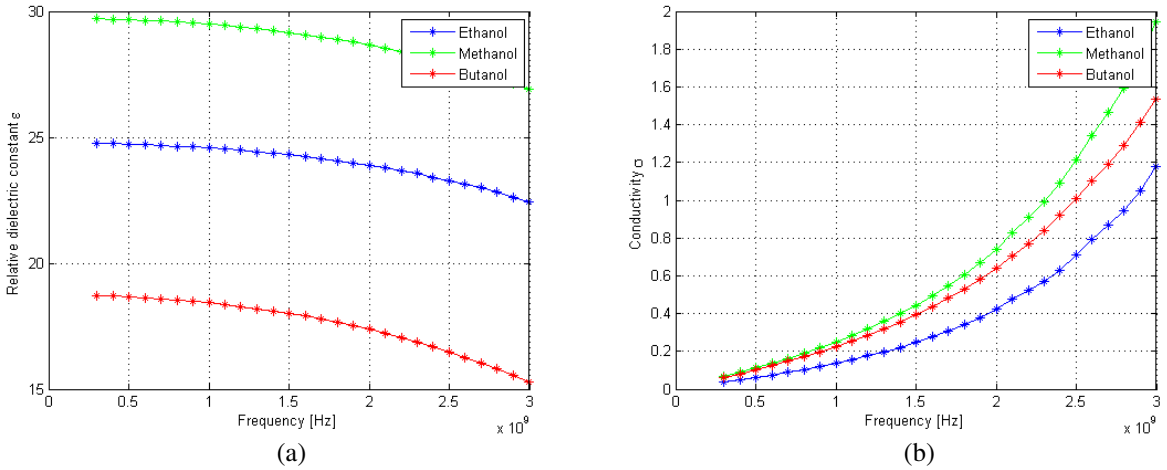

Figure 4: (a) Relative permittivity. (b) Conductivity for open ended conical coaxial probe (cone angle 30 degree).

4. CONCLUSION

In this work, dielectric constant and loss factor of a homogeneous dielectric material by using conical-type coaxial probe are studied and reported. The advantages of the conical coaxial probe is not only in its easy insertion in material and biological application, but it can be successfully used especially at low frequencies with the advantage of increased accuracy and sensitivity.

REFERENCES

1. Bao, J. Z., C. Davis, and M. Swicord, "Microwave dielectric measurements of erythrocyte suspensions," *Biophys. Soc. All Rights Res. Biphys. J.*, Vol. 66, No. 6, 2173–2180, Jun. 1994.
2. Athey, T. W., M. A. Stuchly, and S. S. Stuchly, "Measurement of radio frequency permittivity of biological tissues with an open-ended coaxial line," *IEEE Transactions on Microwave Theory and Techniques*, Vol. 30, No. 1, 82–86, 1982.
3. Sheen, J., "Microwave dielectric properties measurements using the waveguide reflection dielectric resonator," *IEEE Instrumentation and Measurement Technology Conference Proceedings, 2007, IMTC 2007*, 1–4, 2007.
4. Dankov, P. I., "Two-resonator method for measurement of dielectric anisotropy in multi-layer samples," *IEEE Transactions on Microwave Theory and Techniques*, Vol. 54, No. 4, 1534–1544, 2006.
5. Popovic, D. and M. Okoniewski, "Precision open-ended coaxial probe for dielectric spectroscopy of breast tissue," *IEEE Antennas and Propagation Society International Symposium*, Vol. 1, 815–818, 2002.
6. Marsland, T. and S. Evans, "Dielectric measurements with an open-ended coaxial probe," *IEE Proceedings H (Microwaves, Antennas and Propagation)*, Vol. 134, No. 4, 341–349, 1987.
7. Wagner, N., M. Schwing, and A. Scheuermann, "Numerical 3-D FEM and experimental analysis of the open-ended coaxial line technique for microwave dielectric spectroscopy on soil," Vol. 52, No. 2, 1064–1076, 2014.
8. Lan, F., C. Akyel, et al., "A six-port based on-line measurement system using special probe with conical open end to determine relative complex permittivity at radio and microwave frequencies," *Proceedings of the 16th IEEE Instrumentation and Measurement Technology Conference, 1999, IMTC/99*, 1999.
9. Keam, R. B. and J. R. Holdem, "Complex dielectric permittivity measurement using a coaxial-line conical-tip probe," *Asia Pacific Microwave Conference*, 1996.
10. Jin, J., *The Finite Element Method in Electromagnetics*, Wiley, New York, 1993.
11. Arab, H., F. Afshar, et al., "Edge element and second-order nodal analysis for arbitrary shaped waveguides," *Comsol Conference*, Boston, 2013.

FDTD Analysis of Digitally-modulated Electromagnetic Wave Propagation in Human Head

T. Wuren[1], **Y. Tanaka**[1], **M. Fujii**[2], **K. Kamiyama**[2], **A. Ando**[2], **and F. Costen**[3]

[1]Kurume National College of Technology, Japan
[2]University of Toyama, Japan
[3]The University of Manchester, UK

Abstract— Numerical analysis has been performed regarding the propagation and scattering of digitally modulated electromagnetic waves in human head. It is found that waveform distortion and noises are caused unsystematically by the interaction between the wide frequency components of the digital signals and the complicated dielectric structure of the human head. It is also found that pulse shaping to the digital base-band waveform, which limits the band width of the digital signals, reduces the noise in the waveform.

1. INTRODUCTION

Wireless digital communication systems prevail rapidly in our life environment. The influence of the electromagnetic wave to the human body has been carefully evaluated so that they will not impair human health [1, 2]. However, there still exist a number of uncertainties in accessing the influence quantitatively, in particular, inside the complicated dielectric structure of the human bodies. The digitally-modulated electromagnetic waves have a distinctive feature compared to the continuous harmonic waves; e.g. the widely used phase shift keying (PSK) signals have a sudden phase shift, which typically results in a wide frequency spectrum of the transmitted signals.

In this paper, an interaction is investigated numerically between the digitally-modulated electromagnetic waves and the human head in which the distribution of the dielectric permittivity is complicated and even considered random from the electromagnetic point of view. We analize the influence of the phase-shifting modulation, without the loss of generality, associated with the typical binary phase shift keying (BPSK). Other phase-shift schemes such as the quaternary phase shift keying (QPSK) and its modifications basically have the same principle of the phase shifting, thus can be treated in the same context. Although specific communication systems that comprise sophisticated waveform shaping techniques are not considered, the influence of basic waveform shaping effects is investigated using simple trapezoidal digital waveforms. Other modulation techniques such as the frequency shift keying (FSK) and the minimum shift keying (MSK) will be our future topic of research.

Our analysis has been performed with the finite-difference time-domain (FDTD) method. The numerical human phantom used in our analysis was developed in the National Institute of Information and Communications Technology (NICT), Japan, by the nuclear magnetic resonance computer tomography (NMR-CT) of actual human bodies [3], and is anatomically accurate. The measured tissue properties [4] have been modeled in the FDTD method as multi-pole Debye media [5]. Our FDTD code has a capability of dealing with the frequency dependent permittivity and conductivity of 50 different tissues over a frequency range as wide as 1 MHz to 20 GHz [6]. To the best of authors' knowledge, such a numerical analysis has not been performed elsewhere including the geometrical and the material complexity at the same time. This paper attempts to elucidate the behavior of the digitally-modulated electromagnetic waves in the human head.

2. RANDOM NATURE OF THE ELECTRICAL PROPERTY OF HUMAN HEAD

The configuration of the head model is shown in Fig. 1, which has been implemented in our FDTD analysis. The size of the FDTD analysis space is 320 mm in x, 300 mm in y, and 310 mm in z-direction, in which the head model is situated; the height is 270 mm from the neck to the top of the head. The FDTD space is terminated by the PML absorbing boundary conditions, and 20 mm air spaces are inserted both under and over the head model. The whole region is discretized with $\Delta = 1$ mm Yee cell cubes, while the spatial resolution of the head model is 2 mm cube. The electromagnetic wave is illuminated from the front of the face as a plane wave with E_z polarization. The maximum instantaneous field strength is $E_0 = 27.4\,\mathrm{V/m}$, which makes the time-averaged illumination intensity $\bar{P}_0 = 1\,\mathrm{W/m^2}$.

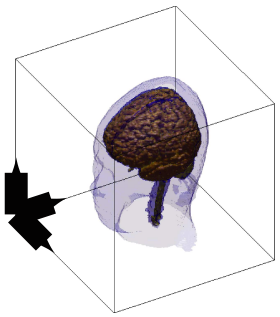

Figure 1: Configuration of the male human head model analyzed in this paper. The shape of the cerebrospinal system is emphasized, while other organs, bones and fluid are all included in the model.

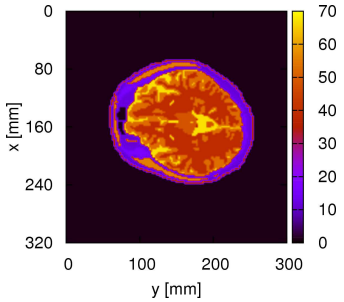

Figure 2: Distribution of the relative dielectric permittivity ε'_r (color bar) of the male human head model at 2000 MHz on a horizontal cross section 100 mm down from the top of the head.

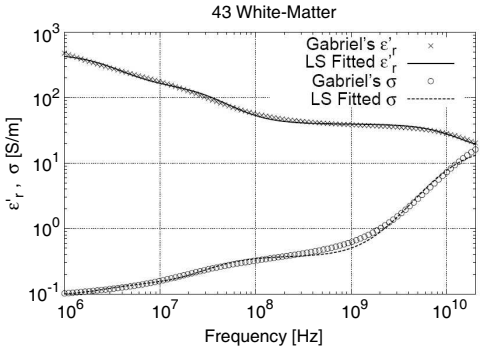

Figure 3: Frequency dependency of the dielectric permittivity ε_r and conductivity σ of white matter for the head model. Gabriel's original experimental data [4] and their fit by Debye dispersion [6] are shown.

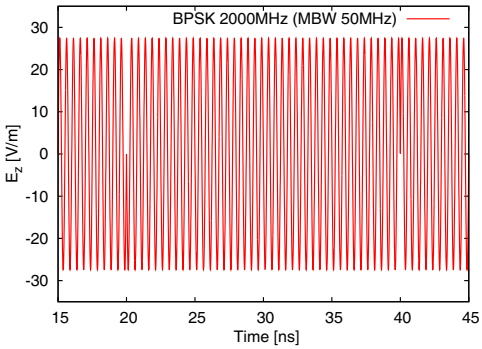

Figure 4: Input BPSK time data for 2000 MHz carrier wave and 50 MHz MBW with no pulse shaping.

The human head has a complicated dielectric structure as shown in the cross section of Fig. 2, regarded even as random electromagnetic media. For example, the skull consists of bone cortical, of which complex relative permittivity at 1 GHz is $\dot{\varepsilon}_r \equiv \varepsilon'_r - i\varepsilon''_r = 12 - i2.7$; the brain consists of white matter ($\dot{\varepsilon}_r = 39 - i11$), gray matter ($\dot{\varepsilon}_r = 52 - i18$), cerebrospinal fluid ($\dot{\varepsilon}_r = 68 - i43$) and so on, which all intricately intermingle.

The human tissues also have frequency dispersion in the permittivity, which varies significantly in the microwave frequency range of our interest. The frequency dependencies of the 50 kinds of the human tissues are modeled by the multi-pole Debye functions [6], which have been implemented into the FDTD method for the effective frequency range from 1 MHz to 20 GHz. An example of the white matter as a part of the brain is shown in Fig. 3; the real part of the relative permittivity decreases by an order of magnitude and the conductivity σ, which relates to the imaginary part of the permittivity by $\varepsilon''_r = \sigma/(\omega\varepsilon_0)$ with ω the angular frequency and ε_0 the permittivity of vacuum, increases by two orders of magnitudes in this frequency range. The strong frequency dispersion, common to the most human tissues, leads to random scattering and propagation of electromagnetic waves in human body, particularly inside the human head as is expected from the layered shell structure of skin, skull and fluid.

3. NUMERICAL ANALYSIS OF DIGITAL ELECTROMAGNETIC WAVE PROPAGATION IN HUMAN HEAD

A plane wave was illuminated with the BPSK time signal from the front of the face at the carrier frequency of 2000 MHz. The digital signals shift the phase every 40, 20, 10 and 5 periods of the carrier wave, i.e., the modulation band width (MBW) of 50 MHz, 100 MHz, 200 MHz and 400 MHz were tested to study their effects to the digital signal propagation. The input BPSK time signal for 50 MHz MBW is plotted in Fig. 4, where the sudden phase shifting is observed at time 20 ns

and 40 ns. The resulting time signals and the Fourier spectra observed at the center of the head are plotted in Fig. 5 for the BPSK without pulse shaping, and in Fig. 6 for the BPSK with a trapezoidal pulse shaping.

For the results shown in Fig. 5(a), large noise-like spikes appear at the instant when the BPSK signal switches the phase. The noise has its peak height nearly three times as large as the CW part of the signal. Comparison to the results of other MBWs in Fig. 5(b) shows that the noise waveform is independent of the MBW. This is because the noise is associated with the sudden phase change

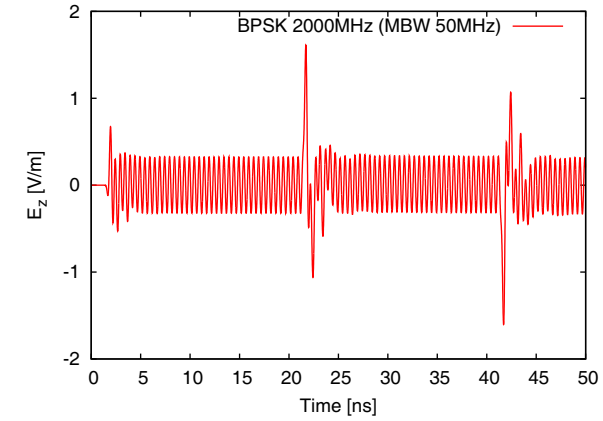

(a)

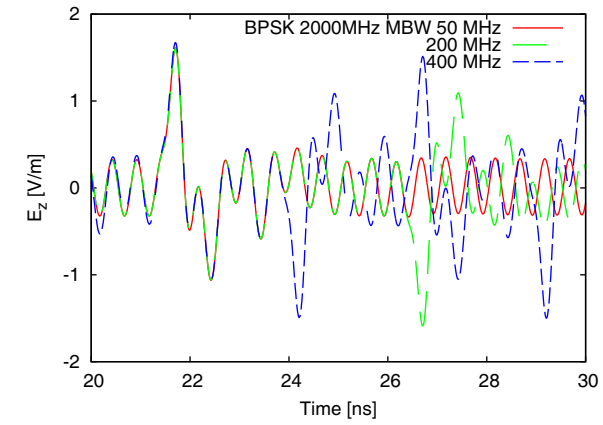

(b)

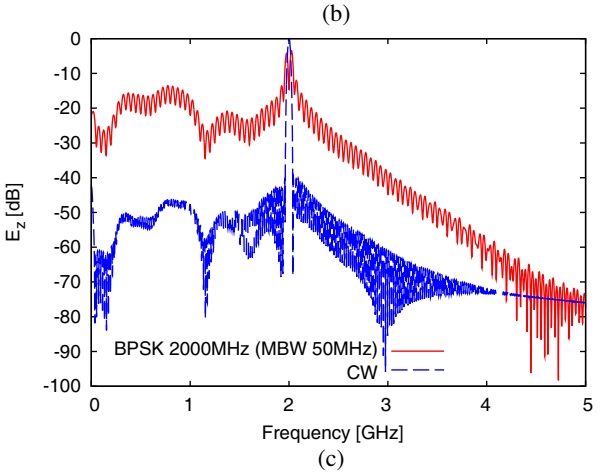

(c)

Figure 5: Time data and Fourier spectrum for 2000 MHz wave observed at the center of the male head without pulse shaping. (a) Time data inside the human head. (b) Expanded waveform of (a) for the comparison of spike noise for various MBWs. (c) Normalized fourier spectrum of (a).

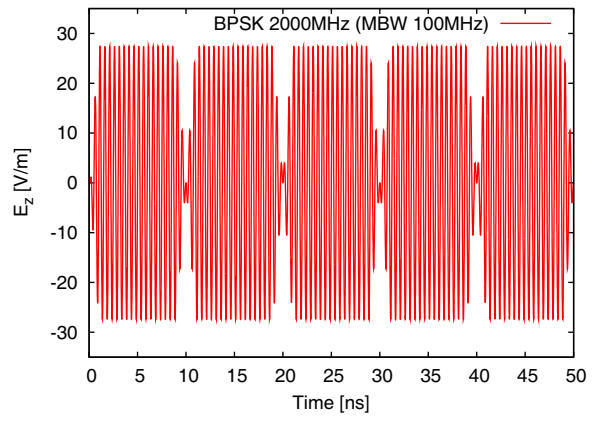

(a)

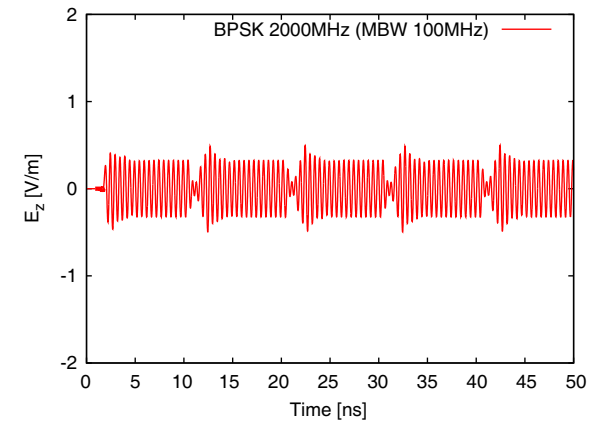

(b)

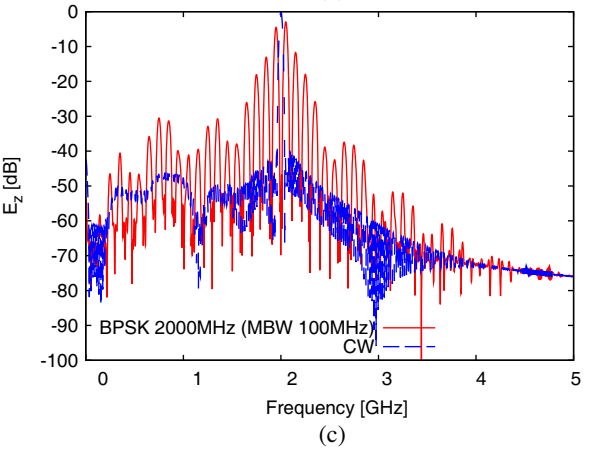

(c)

Figure 6: Time data and Fourier spectrum for 2000 MHz wave observed at the center of the male head with trapezoidal pulse shaping. (a) Input BPSK time data processed with trapezoidal pulse shaping. (b) Time data inside the human head. (c) Normalized Fourier spectrum of (b).

of the digital modulation. The reason for it is also seen in their spectrum in Fig. 5(c); the spectrum widely spreads over approximately 5 GHz range and interacts with the frequency dispersion of the human tissues, typically varies over an order of magnitude in the same frequency range as seen in Fig. 3. Our preliminary analysis showed that a number of high-order resonances occur in the human head over the frequency range from approximately 300 MHz to 2000 MHz due to the round shape of the head (not shown in this paper). It is also presumed that the noise is enhanced as the frequency components happen to come closer to those resonances.

The input signal is then modulated with a digital base-band signal having a trapezoidal waveform. The resulting BPSK signal exhibits gradual phase shifting as shown in Fig. 6(a). The signal observed at the center of the head is shown in Fig. 6(b). Obviously, the spike noise at the time of phase shift has decreased significantly. The Fourier spectrum in Fig. 6(c) shows a limited bandwidth of the digital signal after pulse shaping. More practical pulse shaping techniques such as the raised-cosine filter will have the same effect.

It has been also observed in our additional analyses, using a female head model and similar models reduced in size as infants (not shown), that the head, with its round shape, tends to focus the electromagnetic wave onto the center region of the head. The focal point is not obvious due to the complicated distribution of the human tissues, but strongly depends on the individual configuration of the head, brain, and skull, as well as the frequency, the location, and the polarization of the illuminating source. The signal is not always but occasionally enhanced as in Fig. 6. Such randomness may well cause individual variation in their permissible level against electromagnetic exposure.

4. CONCLUSIONS

Scattering and propagation of electromagnetic waves in the human head have been investigated for the wireless digital signals using the numerical human phantom and the frequency dispersion tissue models. It has been observed that the BPSK signal without pulse shaping exhibits large noise-like signals, which is reduced significantly when the digital signal is processed with a pulse shaping technique. Such enhanced scattering of digital waves has been observed randomly in the human head models under various conditions, which may cause a certain level of individual variation in the perceptiveness to electromagnetic exposure.

ACKNOWLEDGMENT

Authors would like to thank the National Institute of Information and Communication Technology (NICT), Japan, for providing us with the numerical human body phantom.

REFERENCES

1. International Commission on Non-ionizing Radiation Protection, "Guidelines for limiting exposure to time-varying electric, magnetic, and electromagnetic fields (up to 300 GHz)," *Health Phys.*, Vol. 74, 494–522, 1998.
2. Institute of Electrical and Electronic Engineers, "Standard for safety levels with respect to human exposure to radiofrequency electromagnetic fields, 3 kHz to 300 GHz," Tech. Rep., IEEE Std C95.1, 1999 Edition, 1999.
3. Nagaoka, T., S. Watanabe, et al., "Development of realistic high-resolution whole-body voxel models of Japanese adult male and female of average height and weight, and application of models to radio-frequency electromagnetic-field dosimetry," *Physics in Medicine and Biology*, Vol. 49, 1–15, 2004.
4. Gabriel, C., "Compilation of the dielectric properties of body tissues at RF and microwave frequencies," Tech. Rep., Brooks Air Force Technical Report AL/OE-TR-1996-0037, 1996.
5. Fujii, M., R. Fujii, R. Yotsuki, T. Wuren, T. Takai, and I. Sakagami, "Exploration of whole human body and UWB radiation interaction by efficient and accurate two-Debye-pole tissue models," *IEEE Trans. Antennas Prop.*, Vol. 58, No. 2, 515–524, Feb. 2010.
6. Fujii, M., "Maximum frequency range limit of multi-pole Debye models of human body tissues," *IEEE Microwave and Wireless Components Lett.*, Vol. 22, No. 2, 73–75, Feb. 2012.

Microwave Technology Based Medical Imaging and Diagnostics

Jan Vrba, Jr. and David Vrba
Department of Biomedical Technique, Faculty of Biomedical Engineering
Czech Technical University in Prague, Kladno, Czech Republic

Abstract— Future trends in medical applications of microwave technique and technology can be seen in development of new diagnostic and imaging methods based on high frequency EM field. A significant importance for the future can be identified for the following methods: Microwave tomography, Microwave radiometry, Measurement of complex permittivity, Imaging in the Terahertz waves band and Microwave diagnostic radars.

1. INTRODUCTION

Recent trends in microwave medical applications are to study the possibilities to develop new diagnostics based on EM field resp. on microwace technique. A significant importance for the future can be identified for the next methods:

- Magnetic resonance,
- Microwave tomography,
- Microwave radiometry,
- Measurement of complex permittivity,
- Imaging with terahertz waves,
- Microwave diagnostic radar.

We will not talk here about magnetic resonance, as it is just well known and broadly used application of EM field in medical diagnostics. We will focus here on other above mentioned methods (excluding microwave diagnostics radars).

2. MICROWAVE APPLICATORS FOR MEDICAL IMAGING AND DIGNOSTICS

Since 1981 we develop microwave thermotherapeutical applicators working in frequency band from 27 MHz up to 2450 MHz. These applicators were used for the treatment of more then 1000 patients with superficial or sub-cutaneous tumors (up to the depth cca 4–6 cm). Now, following new trends in this field, we continue our research in the important directions of deep local and regional applicators. We have found, that quite similar applicators are optimal to be used for medical imaging and diagnostics.

3. MICROWAVE TOMOGRAPHY

Microwave tomography [1] is in general application of basic CT principals but by utilization of microwave band. Scattering of EM waves in non-homogeneous human body is however much more complicated than simple attenuation of ionising radiation. Therefore development of microwave tomography is conditioned by new theoretical approach, optimization of evaluation algorythms and more efficient computer technique.

An experimental setup is schematically shown on Figure 1. Studied object will be placed in water phantom. It will be irradiated by transmitting antenna while scattered EM field will be monitored by receiving antenna and evaluated by a network analyser. Receieving antenna will be scanning around studied object and/or it will be possible to move/rotate the studied object.

Microwave tomography represents applications of CT known principals to microwave frequency band, where in general situation is more complicated because of much more complicated propagation of EM waves. Therefore mathematical model should be created and optimized evaluation algorithms are needed and last but not least — powerful computers are necessary for the calculations.

4. MICROWAVE RADIOMETRY

Microwave radiometry is based on measurement of a very weak EM signal, which radiate any object (e.g., people), whose temperature is superior to absolute zero [1]. It is based on utilization of so-called Planck radiation law. Interest in microwave radiometry is given by possibility of its utilization at diagnostics of cancer and also of inflammatory disorder (e.g., appendicitis, arthritis,

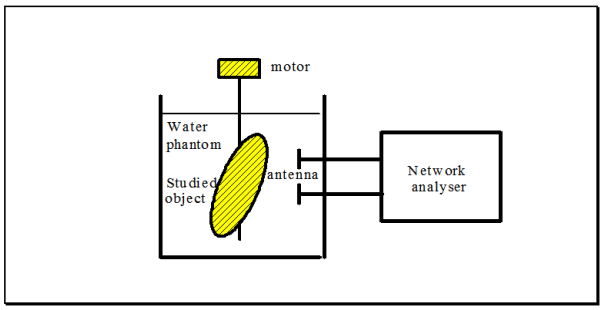

Figure 1: Schematics of experimental setup of microwave tomograph for biomedical imaging.

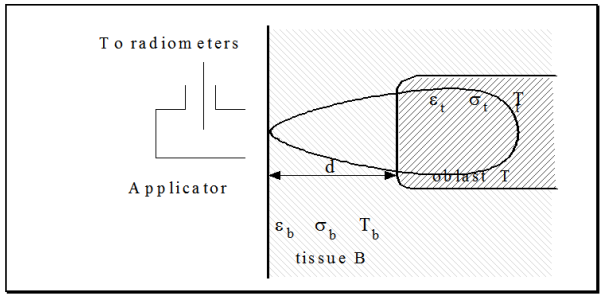

Figure 2: Principals of imaging by a microwave radiometer.

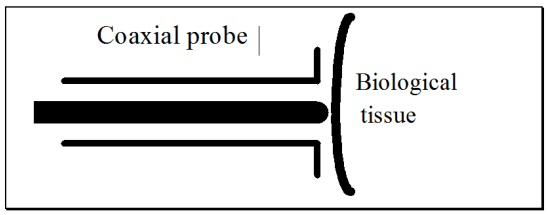

Figure 3: Coaxial probe for measurement of ???.

atp.) because tumors and inflammatory processes causes temperature rise. Microwave radiometer as a tool for biomedical imaging applications has the possibility to "monitore" a thermal noise produced by objects with the temperature over absolute zero. Figure 2 gives a basic idea about experimental setup. Advantage of microwave radiometer is ability to "see" the temperature increase under the surface of human body. Therefore wee need to scan studied area of the tissue with a sensor and to evaluate the results of temperature measurements.

Let us suppose, that applicator (antenna of the radiometer) is situated on the layer B of the monitored biological tissue. Thicknes of this layer is d and it temperature T_b. Its dielectric parameters will be ε_b and σ_b.

5. MESUREMENTS OF COMPLEX PERMITTIVITY

Measurements of complex permittivity "in vivo" could be a suitable for biomedical imaging applications [1]. Usually an open end of coaxial line is used as a very suitable sensor for this measurement. Scanning the studied object by a such probe can bring us a map of the permittivity — we can then evaluate symmetry resp. unsymmetry of the measurement results and from this information we can make hypothesis about possible medical problems.

Characteristic impedance is Z_o, C_o and C_f are fringing.

ACKNOWLEDGMENT

This research is supported by Grant Agency of the Czech Republic, project: "Microwave Imaging for Biomedical Applications" (102/05/0959) and by the research program MSM6840770012 "Transdisciplinary Research in the Area of Biomedical Engineering II" of the CTU in Prague, sponsored by the Ministry of Education, Youth and Sports of the Czech Republic.

REFERENCES

1. Vrba, J., *Medical Applications of Microwaves*, 1st Edition, 168, Issued by CTU, Prague, 2003, ISBN 80-01-02705-8.
2. Semenov, S. Y., et al., "Three-dimensional microwave tomography, initial experimental imaging of animals," *IEEE Transactions on BME*, Vol. 49, No. 1, 55–63, Jan. 2002.
3. Gabriel, S., R. W. Lau, and C. Gabriel, "The dielectric properties of biological tissue — II. measurements in the frequency range 10 Hz to 20 GHz," *Phys. Med. Biol.*, Vol. 41, 2251–2269, 1996.
4. Fear, E. C. and M. A. Stuchly, "Microwave detection of breast cancer," *IEEE Trans. Microwave Theory Tech.*, Vol. 48, 1854–1863, 2000.

5. Vrba, J., et al., "Technical aspects of microwave thermotherapy," *RF Interaction with Humans: Mechanisms, Exposures and Medical Applications, IPEM Meeting*, Institute of Physics, London, Feb. 2003.
6. Vrba, J., C. Franconi, F. Montecchia, and I. Vanucci, "Evanescent mode applicators for subcutaneous hyperthermia," *IEEE Trans. on Biomedical Engineering*, Vol. 40, No. 5, 397–407, May 1993.
7. Franconi, C., J. Vrba, and F. Montecchia, "27 MHz hybrid evanescent-mode applicators with flexible heating field for deep hyperthermia," *International Journal of Hyperthermia*, Vol. 9, No. 5, 655–673, 1993.

Using Functional Near-infrared Spectroscopy to Investigate Frontal Cortical Response to Joint/non-joint Attention in Children

Jun Li, **Zhifang Zhu**, **and Huilin Zhu**
Centre for Optical and Electromagnetic Research
South China Normal University, Guangzhou 510006, China

Abstract— Functional near-infrared spectroscopy (fNIRS) is an optical technique for non-invasively investigating brain functional activity. It measures cerebral hemodynamic parameters that are closely associated with the neural activity. Previous study has demonstrated that individuals with autism are very poor in joint attention skills. In this work, fNIRS was used to access cerebral hemodynamic response to joint and non-joint attention stimuli in children classified as of high and low autistic traits. The stimuli were given by a video that engenders an experience of joint or non-joint attention in observers. 49 channels of oxygenated hemoglobin (HBO) time series were recorded from the frontal cortex when subjects were watching the video. The HBO activation pattern was obtained and the functional connectivity was determined for the two conditions. Results show there are significant differences between children with high and low autistic traits, in both the HBO response and the functional connectivity for each condition. Our data suggest that fNIRS may provide imaging-based objective evaluation on autistic traits.

1. INTRODUCTION

Functional near-infrared spectroscopy (fNIRS) is a promising technique for cost effective and non-invasive brain imaging [1–8]. It uses near-infrared light to measure cortical activity through intact scalp and skull.

Similar to functional magnetic resonance imaging (fMRI), fNIRS measures cerebral hemodynamic parameters closely related to the neuronal activity through neurovascular coupling. fNIRS has high temporal resolution (∼ms), reasonable spatial resolution (∼cm), and is compatible with other commonly used imaging modalities, such as fMRI, EEG and MEG. It is also possible for fNIRS to map the entire cortical surface.

Joint attention is a process whereby two individuals share the focus on the same object, as one is checking and following the attention focus of the other [9]. This cognitive skill emerges very early even in one's infancy, for example, infants can follow the direction of other's gaze in the first year after birth [10]. It is of high social implication, since the only goal of joint attention is to share thoughts, ideas, memories, observations and experiences with another individual.

Previous studies have demonstrated impairment in joint attention is one of the characteristics of autism spectrum disorder (ASD) [11]. fMRI study has shown there is distinct activation pattern in the frontal cortex between joint and non-joint attention stimuli [9]. In this study, we used fNIRS to record HBO signal from the frontal cortex of children classified as of high and low autistic traits during joint and non-joint attention tasks. The HBO response and the functional connectivity in the frontal cortex were determined and compared between children with high and low autistic traits.

2. METHOD

2.1. Participants and Protocol

Seventeen right-handed children (9 boys) participated in this study. They were all recruited from a kindergarten. The average age was 5 ± 0.9 years old (4–6 years old).

Before fNIRS measurement, the social and communication disorders checklist (SCDC) was used to evaluate children's autistic traits. A child with high score in SCDC implies he/she has ASD-like traits. After the SCDC evaluation, Seventeen children were divided into two groups with approximate equal size of group; namely, eight children were classified as of relative high (SCDC > 15), and the other nine as of relative low autistic traits. During the experiment, the child sat in a comfortable chair in a dark room and watched successively 8 video clips for 8 minutes in total. The video clip was made that can engender an experience of joint or non-joint attention in observer [9]. Each video clip consisted of 30 s black screen (control) followed by 30s task (joint or non-joint attention stimuli). The 8 video clips consisted of 4 joint and 4 non-joint attention stimuli, with a random presentation order across subjects.

Prior to the experiment, children and their parents were informed on the measuring procedure and written consents were obtained from the parents. The experiment protocol was approved by the Institutional Review Board of South China Normal University.

2.2. Experimental Setup

Measurements were performed with a commercial continuous-wave fNIRS system (FOIRE-3000, Shimadzu Corporation, Kyoto, Japan) working at three wavelengths, 780 nm, 805 nm and 830 nm. FOIRE-3000 is equipped with sixteen fiber sources and sixteen fiber detectors, building up to 52 detecting channels with a fixed source-detector distance of 3.0 cm. The absorptions of the three wavelengths of near infrared light were measured and then transformed into concentration of HBO based on the modified Beer-Lambert law.

The optical sensors were secured on the scalp by a headgear to ensure good sensor-scalp contact. The measured area and the locations for optical channels are schematically shown in Fig. 1.

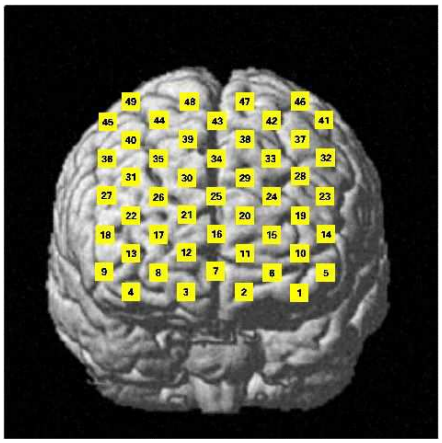

Figure 1: The sketch for positions of the 49 optical channels over the frontal cortex.

2.3. Data Analysis

The 8-min HBO time series data were first filtered with a band-pass (0.004–0.08 Hz) filter to get rid of the very low frequency drift and the systemic components, such as those from cardiac cycles (∼1 Hz), respirations (∼0.2 Hz) and Mayer waves (∼0.1 Hz). After the data were filtered, the block average was performed for the two conditions (joint attention and non-joint attention stimuli), separately.

For the HBO activation pattern, the late 20 s HBO data were averaged in each block, and then averaged across all blocks for the two conditions, separately.

To determine the functional connectivity during the task period, the 30s block averaged HBO data were used for computing the Pearson correlation coefficients between a seed channel and the all other channels.

To visualize the activation pattern, a false color map is made where the color value for each pixel represents the HBO activation value. While for the connectivity map, in the false color map each pixel value is a correlation coefficient between this pixel (channel) and the seed pixel (channel).

3. RESULT

The mean HBO activation map is shown in Fig. 2 for joint and non-joint task, and for children with low and high autistic traits. Distinct activation pattern can be observed: in the condition of joint attention, children with low autistic traits show stronger activation than children with high autistic traits in both hemispheres. However, for the non-joint attention condition, the opposite activation pattern can be observed.

Since both in joint and non-joint attention conditions, right hemisphere (specially the middle frontal gyrus) shows relative strong HBO activation, a seed in the right hemisphere is selected (channel 35 in Fig. 1) to generate connectivity (or correlation) map, as shown in Fig. 3. Children with low autistic traits show stronger intra- and inter-hemispheric connectivity than children with high autistic traits, in both joint and non-joint conditions.

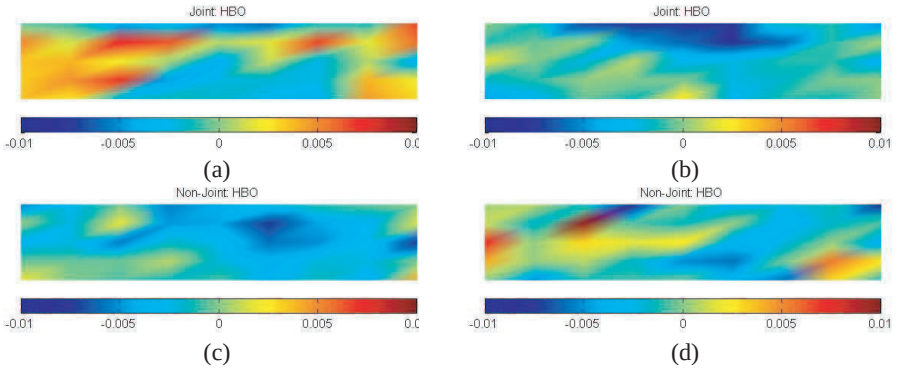

Figure 2: The HBO response for (a), (b) joint and (c), (d) non-joint attention conditions, and for children with (a), (c) low and (b), (d) high autistic traits.

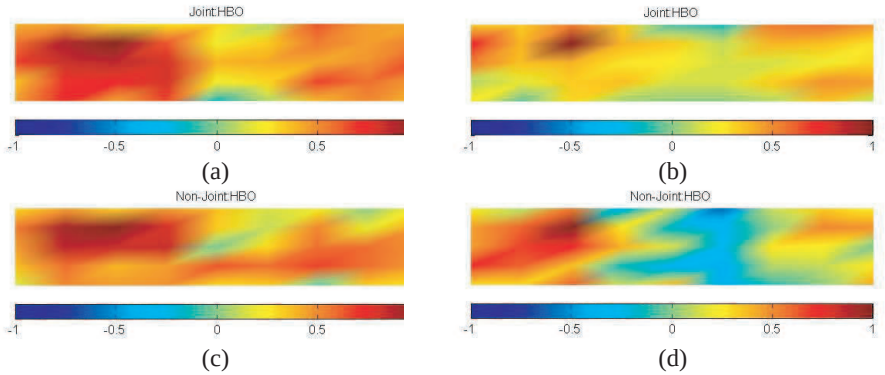

Figure 3: The functional connectivity map in (a), (b) joint and (c), (d) non-joint (bottom row) attention conditions, for children with =(a), (c) low and (b), (d) high autistic traits. In each case, the seed (channel 35) is selected in the right hemisphere, can be visually identified with the largest color value.

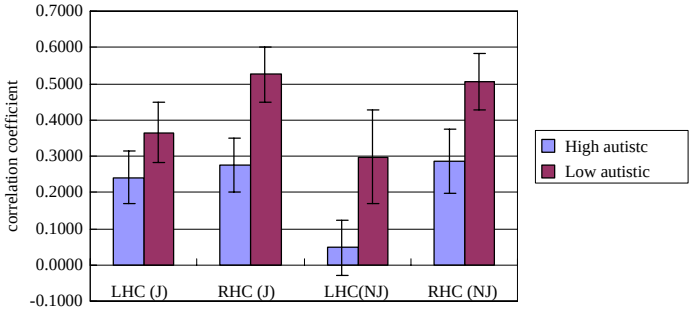

Figure 4: The average connectivity (or correlation coefficients) in the left and the right hemisphere for the two conditions, and two groups of children with low and high autistic traits. The correlations are calculated with respect to the seed (channel 35 located in the right hemisphere). The error bar was calculated across each group for each condition. LHC: left hemisphere correlation, RHC: right hemispheric correlation, J: joint attention, NJ: non-joint attention.

To quantitatively compare the connectivity in the left and the right hemisphere between children with low and high autistic traits, the average correlation coefficients for the left and right hemisphere are calculated for the two conditions, and for the two groups. The result is illustrated in Fig. 4.

The functional connectivity is stronger for children with low than with high autistic traits in both hemispheres, and for both conditions. Statistical analysis shows the difference in the connectivity is more significant ($p < 0.05$) in the right hemisphere for joint attention condition.

4. DISCUSSION

In the past twenty years fNIRS has been rapidly developed and now is becoming an effective tool for investigating functioning brain in a verity of areas ranging from basic neuroscience, psychology to numerous clinical applications.

In this study we used fNIRS to study frontal cortical response to joint and non-joint attention stimuli in children. Previous study with fMRI [9] has demonstrated that both joint and non-joint attention stimuli induce activation in the right middle frontal gyrus. Our HBO activation pattern revealed by fNIRS is in line with this observation. This fMRI study also shows during joint attention task, a large region in the left frontal gyrus is activated, including the left medial, the left superior and the left inferior frontal gyrus. Our data show the HBO activation in the similar region are also observed, but pronouncedly for children with low autistic traits.

Before this work, fNIRS was used to study the frontal response of children to join and non-joint stimuli [12]. However, in their study only a few optical channels were used, with two sources and four detectors, which is hard to make image for cortical response. Their study showed, compared to the resting state, there was a decrease in HBO for both joint and non-joint attention conditions. Our HBO response maps also show there are indeed some region in the frontal cortex where slightly decreased HBO is observed, especially in the anterior prefrontal cortex (Brodmann area 10), as seen in Fig. 2.

Recent studies on autism with fMRI [13] and fNIRS [14] have demonstrated that children with autism show poor synchronization of bilateral cortical (spontaneous) activity. These studies imply that the connectivity in the functional network of children with autism is weaker than children of typical development. Our data reveal the connectivity in the functional network is different between children with high and low autistic traits. Children with high autistic traits have weaker connectivity in the network than children with low autistic traits, which is similar to the comparison between children with autism and children of typical development. Our result may imply that in the view of the spectrum, an individual with high autistic traits is somehow 'closer' to the typical autism than an individual with low autistic traits.

5. CONCLUSION

In summary, we use fNIRS to investigate response in the frontal cortex to joint and non-joint attention stimuli for children. Our data show the HBO activation pattern and the functional connectivity are distinct between children with high and low autistic traits, and between joint and non-joint attention conditions. These results imply fNIRS might be able to provide imaging-based objective evaluation on autistic traits.

ACKNOWLEDGMENT

This work was supported by Guangdong (China) Innovative Research Team Program (No. 201001D-0104799318).

REFERENCES

1. Jöbsis, F. F., "Noninvasive, infrared monitoring of cerebral and myocardial oxygen sufficiency and circulatory parameters," *Science*, Vol. 198, 1264–1267, 1977.
2. Chance, B., Z. Zhuang, C. UnAh, et al., "Cognition-activated low-frequency modulation of light absorption in human brain," *Proceedings of the National Academy of Sciences*, Vol. 90, 3770–3774, 1993.
3. Villringer, A. and B. Chance, "Non-invasive optical spectroscopy and imaging of human brain function," *Trends in Neurosciences*, Vol. 20, 435–442, 1997.
4. Hillman, E. M. C., "Optical brain imaging in vivo: Techniques and applications from animal to man," *Journal of Biomedical Optics*, Vol. 12, 051402, 2007.
5. Hoshi, Y., "Functional near-infrared optical imaging: Utility and limitations in human brain mapping," *Psychophysiology*, Vol. 40, 511–520, 2003.
6. Ehlis, A. C., S. Schneider, T. Dresler, et al., "Application of functional near-infrared spectroscopy in psychiatry," *Neuroimage*, Vol. 85, 478–488, 2014.
7. Fallgatter, A. J., M. Roesler, L. Sitzmann, et al., "Loss of functional hemispheric asymmetry in Alzheimer's dementia assessed with near-infrared spectroscopy," *Cognitive Brain Research*, Vol. 6, 67–72, 1997.

8. Kita, Y., A. Gunji, Y. Inoue, et al., "Self-face recognition in children with autism spectrum disorders: A near-infrared spectroscopy study," *Brain and Development*, Vol. 33, 494–503, 2011.
9. Williams, J. H. G., G. D. Waiter, O. Perra, et al., "An fMRI study of joint attention experience," *Neuroimage*, Vol. 25, 133–140, 2005.
10. Scaife, M. and J. S. Bruner, "The capacity for joint visual attention in the infant," *Nature*, Vol. 253, 265–266, 1975.
11. Dawson, G., S. Webb, G. D. Schellenberg, et al., "Defining the broader phenotype of autism: Genetic, brain, and behavioral perspectives," *Dev. Psychopathol.*, Vol. 3, 581–611, 2002.
12. Zhu, B., N. Yadav, G. Rey, et al., "Diffuse optical imaging of brain activation to joint attention experience," *Behavioural Brain Research*, Vol. 202, 32–39, 2009.
13. Dinstein, I., K. Pierce, L. Eyler, et al., "Disrupted neural synchronization in toddlers with autism," *Neuron*, Vol. 70, 1218–1225, 2011.
14. Zhu, H., Y. Fan, H. Guo, et al., "Reduced interhemispheric functional connectivity of children with autism spectrum disorder: Evidence from functional near infrared spectroscopy studies," *Biomedical Optics Express*, Vol. 5, 1262–1274, 2014.

Tunable S-band RF Front End Receiver for LEO Mission

Geetanjali Sharma, Viral Degarwala, and M. R. Tripathy
Department of Electronics and Communication Engineering
ASET, Amity University, Noida, U.P., India

Abstract— This paper presents the design strategy, simulation results and final schematic of Radiofrequency front end (receiver) block level designing with a flexible centre frequency for S-band (2025–2110 MHz). The idea behind this is basically a planning for communication such as data, voice and video communication. In this study, with a Radio-frequency (different channel frequencies) the required specifications were achieved such as gain < 130 dB, noise figure 2 dB, bandwidth 6 MHz which is targeted for LEO mission. This design is having very low noise figure, high gain and low spurious levels and RF-Front end circuit includes low noise amplifier, filter, mixer and local oscillator. To obtain proper output frequency and determination of a system performance, the measured data including gain, noise figure and S parameter agree well with the simulation results on ADS Software.

1. INTRODUCTION

S-band is very popular band for the mobile satellite system (MSS). The receiver front end architecture is a part of ground terminal which is connected with the s-band satellite for the data-reception and transmission. The function of receiver front-end is to provide the gain to the very weak signal without adding of much noise and convert it to the Intermediate-Frequency (IF). Low noise, high gain and the low spurious output with the compact size are the main advantage of the developed unit. The Radio frequency (RF) front end receiver needed because of amplification to compensate for the transmission loss, selectivity to separate the desired signal from others and tenability to select the desired signal [1].

At the receiver input, diplexer will give direction to the different channel frequency to be tuned at same input, the suppression of transmitted signal is very important because over received signal is 2025–2110 MHz. To make the system compatible and in order to meet the (PFD) constraints, Code division multiple access (CDMA) which is a spread spectrum technique is used for communication and it also fulfil the standard spreading of 6 MHz bandwidth requirement. A two-stage LNA allows achieving extremely good receiver sensitivity. This paper describes the flexible s-band front end receiver in which frequency are tuned to different channel frequencies.

2. RECEIVER CONCEPT

Receiver design is started by selecting Local-Oscillator (LO) and IF so that no significant spurious and harmonics will fall in opposite frequency band or near this band. Gain is distributed in RF and IF frequency. Figure 1 shows the block level designing of the receiver front end with sub-blocks such as; LNA, BPF, HPF, LPF, Single balanced mixers, IF-amplifiers and Circulators.

2.1. Low Noise Amplifier

It is the first component in any RF part. The fundamental goal of LNA is to amplify a very weak signal received from the antenna, while adding as little noise as possible. An ideal amplifier increases the desired signal without adding distortion or noise. It requires low noise, high gain, good return loss, low power dissipation and high reliability as well as compact size. In a receiver chain the first amplifier after the antenna contributes most to the system's noise-figure. Since LNA is a first gain stage in a receiver system, its noise-figure dominants that of the entire system. LNA purposes are many, it provides the isolation between the LO or mixer stages and the antenna, it improves the image frequency selection and lastly; provides some selectivity. Four LNA blocks are placed in the designing in which three of them having 38 dB as an input gain and one is put in a variable namely; x for varying its input gain according to the flexibility requirement [3].

2.2. Circulator

The 3-port device is terminated by a resistor of 50 ohms to make it perform as an isolator because it absorbs the power for propagation in one direction and thus; provides lossless transmission in the opposite direction. In general case, isolator is used to improve frequency stability. It's typical performance is about 0.1 dB loss and 1.05 VSWR.

2.3. Filters

Filter circuits are the key components in any high frequency wireless systems. In modern trends the implementation of filter using Digital Signal Processing (DSP) is replacing analog filtering. The background and the tools for designing filter circuits at microwave frequencies begins with the review of two-port circuits and definition of gain, attenuation and return-loss (RL). The various filters are described such as; BPF, LPF, HPF in order to show how these affects the roll-off of the gain response [4, 6].

2.3.1. Bandpass Filter (BPF)

Apart from received signal, this filter is purposed for the rejection of the transmitted signal 2025–2110 MHz. The resultant rejection of 20 dB is first achieved at the given transmitted signal. Filter's passband is 2028.6–2062.6 MHz and the insertion loss (IL) is 0.4 dB [2].

2.3.2. Lowpass Filter (LPF)

LPF is used here for harmonic rejection. It exists in many forms and passes all the frequencies lower than its cutoff which is 70 MHz which is kept as an IF output for 2nd mixer [2].

2.3.3. Highpass Filter (HPF)

HPF passes all the higher frequencies and attenuates the signal with the frequency lower than the cutoff frequency. In the designing of Receiver, HPF acts as a blocker of DC and having a cutoff frequency of 200 MHz. It will pass all the frequencies more than its cutoff value that is 200 MHz.

2.4. Mixer

RF mixer is an essential part of the wireless communication system. In order to optimize the overall system performance and compromises between figure of merit such as linearity gain, dynamic range, noise figure and port to port isolation is limited by first down conversion mixer. It perform frequency translation by multiplying two signals (and possibly their harmonics). The RF frequency is 2025–2110 MHz, the RF rejection which is given to the mixer is 20 dB. The LO frequency is tunable on the frequencies like 1828.6, 1835.6, 1842.6, 1849.6, 1856.6. The flexibility for s-band in LEO-mission comes from these frequencies at 6 MHz bandwidth each. Since the frequency translation process will generate some unwanted spurious signal to degrade signal to noise ratio (SNR), the linearity becomes an important factor in mixer design. In most of the front-end receiver, the linearity of mixer affects overall linearity. This design architect proposes a reasonably good conversion loss and also a good isolation from LO-RF. Whereas in architecture, mixer translate all the channel frequencies in which bandwidth and frequency both are vary for good simulation [7].

3. RECEIVER SPECIFICATION

S. No.	1	2	3	4	5	6
Parameter	RF-frequency	IF-Frequency	Nominal Input Power	Nominal Output Power	Noise-Figure	Gain Stability
Unit	MHz	MHz	dBm	dBm	dB	dBp-p
Values	2025–2110	70	−130	0	2	1.5
S. No.	7	8	9	10	11	
Parameter	Gain Flatness over any channel	Gain Flatness overall	Translation Frequency	Channel Frequency	Centre-Frequency; F_c	
Unit	dB	dB	MHz	MHz	GHz	
Values	1	2	1828.6 1835.6 1842.6 1849.6 1856.6	2031.6 2038.6 2045.6 2052.6 2059.6	2.045	

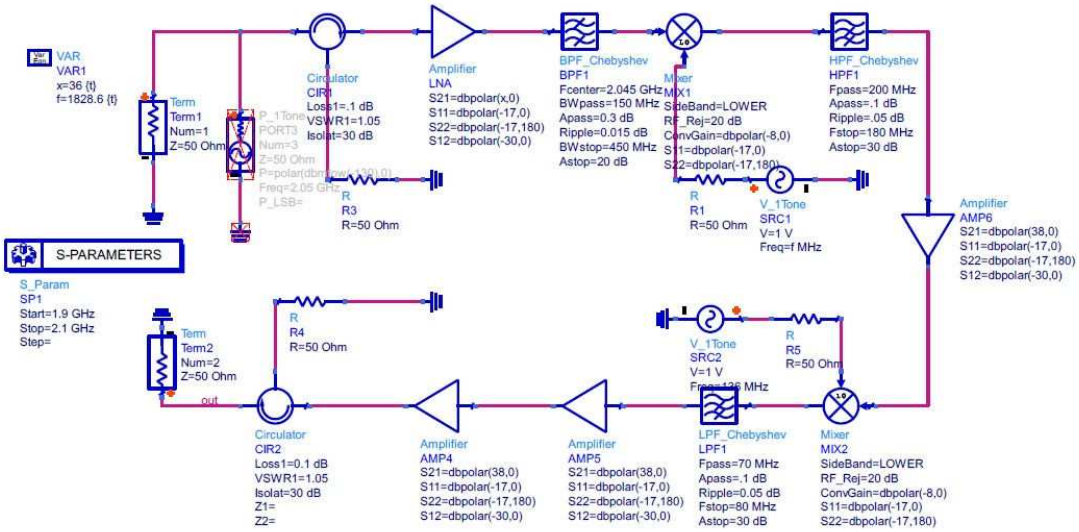

Figure 1: Schematic level diagram of RF-front end.

4. SIMULATION RESULTS

In this paper, the following scenarios are considered: Noise figure and Gain, for each translation frequencies. By changing the value of LO frequency of first mixer (f_1) in MHz, it shows the result

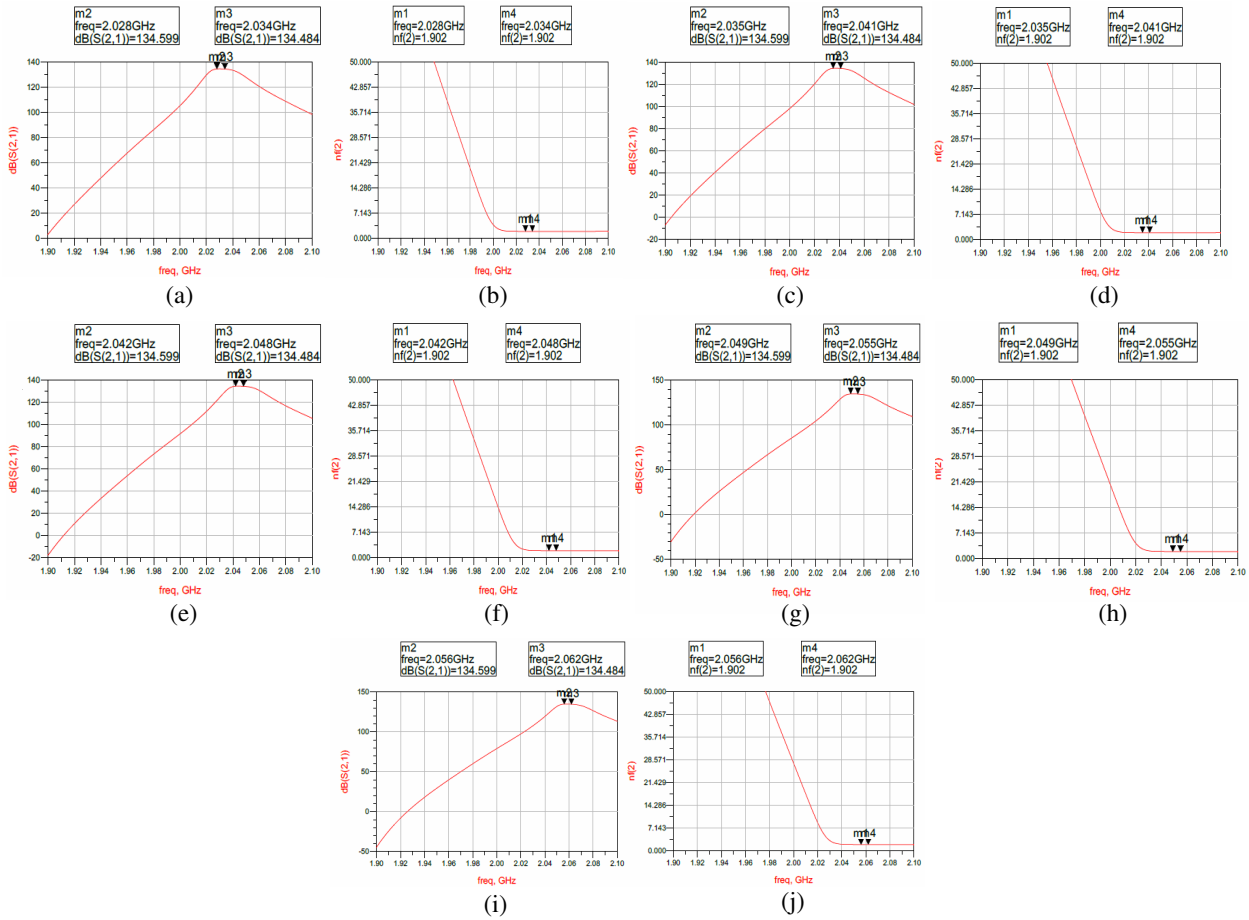

Figure 2: Shows (a) 134.59 dB gain and (b) 1.9 dB noise figure for $f_1 = 1828.6$ MHz; (c) 134.59 dB gain and (d) 1.9 dB noise figure for $f_1 = 1835.6$ MHz; (e) 134.59 dB gain and (f) 1.9 dB noise figure for $f_1 = 1842.6$ MHz; (g) 134.59 dB gain and (h) 1.9 dB noise figure for $f_1 = 1849.6$ MHz; (i) 134.59 dB gain and (j) 1.9 dB noise figure for $f_1 = 1856.6$ MHz.

of tuning of center frequency with the same output. The expected output has been realized during simulation. Fig. 2 shows the spectrum of s-band in which the different channel frequencies and their translation frequencies are seen. The analysis result shows that if we tune or vary center frequency or if relocate the satellite in the define spectrum for communication. We can have same gain and noise figure throughout the defined band.

5. CONCLUSION

According to the fixed noise figure, i.e., 2 dB, nominal input power is decided while designing an system block level designing of Receiver for s-band. It shows optimize performance in terms of gain and noise figure. Dealing with all translation frequencies in the system design, output can be seen at different channel frequencies which show a good gain and a fixed low noise figure which can purposely make an effective use for communication. A good agreement is achieved between simulated and targeted data.

ACKNOWLEDGMENT

Authors are great thankful to Mr. D. K. Singh, Group Director, RFSG/SNPA, ISRO-SAC for the valuable support and suggestions. Authors are also thankful to Richa Chakravarty, Sci/Engr, ISRO-SAC for the encouragement and for providing valuable suggestions.

REFERENCES

1. Jain, S. K., J. Raval, D. K. Singh, and S. Singh, "S-band receiver front-end design for portable satellite ground terminal," *IEEE International Conference on Devices, Circuits and Systems (ICDCS)*, 666–669, 2012.
2. Lee, H.-M. and C.-M. Tsai, "Dual band filter design with flexible pass band frequency and bandwidth selections," *IEEE Transactions on Microwave Theory and Techniques*, Vol. 55, No. 5, 1002–1009, 2007.
3. Gonzalez, G., *Microwave Transistor Amplifiers Analysis and Design*, Prentice Hall, 1997.
4. Mattaei, G., L. Young, and E. M. T. Jones, *Microwaves Filters, Impedance-matching Networks and Coupling Structure*, Artech House, Norwood, 1980.
5. Deng, Y. and K. Wu, "Reconfigurable and tunable filters with flexible frequency and bandwidth response characteristics for wireless handsets and mobile terminal," *IEEE International Wireless Symposium (IWS)*, 1–4, 2013.
6. Hong, J.-S. and M. J. Lancaster, *Microstrip Filters for RF/Microwave Applications*, John Wiley & Son, Inc., 2001.
7. Mass, S., *Microwave Mixers*, 2nd Edition, Artech House, 1993.

Dual Band Rectangular Dielectric Resonator Antenna Design

Raghuraman Selvaraju[1, 2], **Mohsen Khalily**[1], **Muhammad R. Kamarudin**[1], **Mohd H. Jamaluddin**[1], **and Jamal Nasir**[1]

[1]Wireless communication center (WCC), Universiti Teknologi Malaysia, Malaysia
[2]Department of Electronics and Communication Engineering, Periyar Maniammai University, India

Abstract— A Dual band rectangular dielectric resonator antenna (RDRA) capable of frequency tunings at two different resonant modes is presented and investigated. In this design two rectangular dielectric resonators with different permittivity situated on top of the substrate are employed. The antenna is fed by 50 Ω microstrip feedline etched on the top of the Fr-4 epoxy printed circuit board (PCB) with a total size of $80 \times 50 \times 1.6\,\text{mm}^3$ and $\varepsilon_{rs} = 4.6$ (loss tangent = 0.02). In order to excite two resenant frequencies, two RDRA with relative permittivity of $\varepsilon_{r1} = 10$ and $\varepsilon_{r2} = 30$ are chosen to operate at 2.4 GHz and 3.8 GHz. From the parametric study the lower permitivity DRA resonates at 3.8 GHz whereas the higher permitivity DRA resonates at 2.4 GHz. Ansoft HFSS v14 has been used for the simulation of the proposed dual-band antenna. The simulation results show that the 3.8 design can efficiently perform in both frequency bands.

1. INTRODUCTION

Dielectric resonators antenna (DRA) was first proposed by professor Long in 1983, the DRAs have been an active research area for the last two decades due to the several characteristics such as high radiation efficiency, small in size, light weight and low profile. Antennas that use dielectric resonators experience very low loss, so they ensure higher efficiency without conductor loss [1]. DRAs are able to perform with different performance such as wide-band [2], ultra-wideband [3], dual-band [4], and multi-band [5]. In adittion DRAs can produce circular polarized field by exiting orthogonal modes [6–9]. There are three major dielectric resonator shapes; Hemispherical, Cylindrical, Rectangular which rectangular one has more advantages rather than two others because of having two aspect ratios and simplicity of fabrication. Furthermore various types of feeds can be employed to excite DRAs such as Microstrip feedline, coaxial probe, aperture coupling, and coplanar waveguides (CPWs). Today, dual-band systems are commonly found in the modern wireless communications, because we have different wireless systems, WiFi, Wimax, LTE, etc., each systems operates at different frequencys so all the wireless device should be able to operate at different frequencys, this motivating the study of the dual-band DRA. In this paper, dual band DRA for 2.4 GHz and 4 GHz is investigated and presented. The configuration and design guidelines of the proposed antenna structures are presented in the Section 2. Parametric study is present in the Section 3. Simulation and experimental results are presented in Section 4. Finally, a conclusion is given in Section 5.

2. ANTENNA DESIGN AND CONFIGURATION

The proposed dual band rectangular DRA is shown in the Fig. 1, it consists of two layers, the first layer is a feed-line structure which is seen in the Fig. 1(a). This layer is printed on top of FR-4 epoxy substrate with the relative permittivity of 4.6 and dimension of $50 \times 80 \times 1.6\,\text{mm}^3$. It must be noted that this feeding structure has no resonance and only it is used to excite DR radiation elements. In order to excite two resonance frequency, two rectangular dielectric resonators with the different relative permittivity of $\varepsilon_{r1} = 10$ and $\varepsilon_{r2} = 30$ are employed on the top of the feed-line which can be shown in Fig. 1(b). The dimensions of both rectangular dielectric resonator are $15 \times 15 \times 8\,\text{mm}^3$, the distance between these dielectrics and the top edge of the substrate is optimized and fixed at 17.5 mm. Finally, a rectangular with 20 mm × 2 mm slot is introduced in the center of the ground plane to improve the impedance matching. All optimal dimensions can be shown in Figs. 1(a) and (b).

3. PARAMETRIC STUDIES AND DISCUSSIONS

In this study the performance of the proposed with and without dielectric resonator is considered. The proposed antenna is simulated by High frequency structural simulator software (HFSS). First, the feed-line structure is studied. The important parameter of the feed-line structure is three

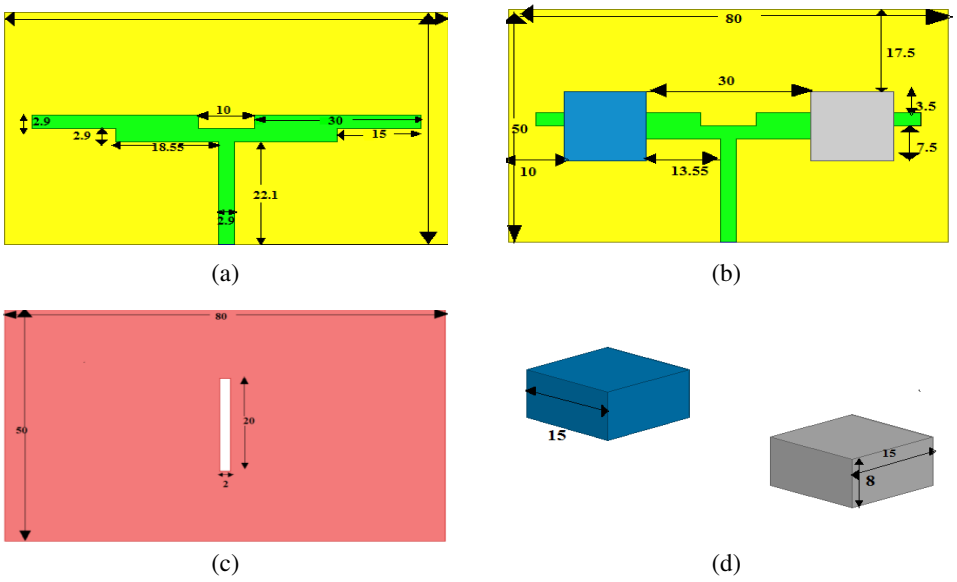

Figure 1: (a) Top view without DR. (b) Top view with DR. (c) Bottom view of the presented antenna. (d) DR side view.

rectangular notches at two top corners of the patch and one at top center of the patch which their dimension are seen in the Fig. 1(a). Fig. 2 clearly shows the return loss of the modified microstrip feed-line. In this case there is not any resonance and it will be shown that dual-band operation is only related to both DRA. In order to achieve dual-band operation, two RDRAs with different permitivities are introduced in the structure.

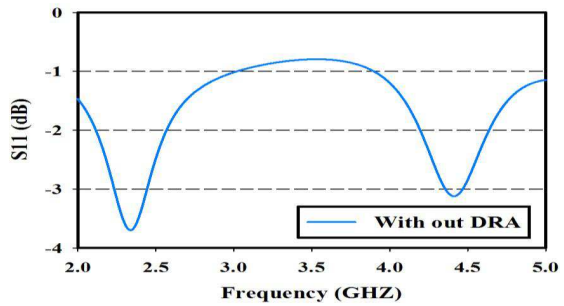

Figure 2: Simulated Return loss of the proposed antenna without DRs.

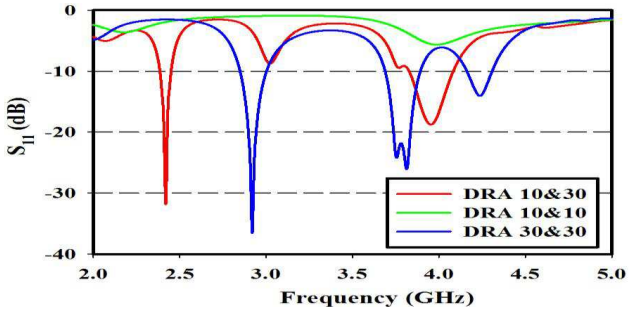

Figure 3: Simulated return loss of the proposed antenna with different permitivities.

After introducing the dielectric radiators, the performance of the antenna is verified by varying the relative permittivity of the DRA. When same permittivity either 10 or 30 are chosen simultaneously, dual-band cant be achieved. Fig. 3 shows the return loss of the proposed antenna with different radiator permittivities.

4. SIMULATION AND EXPERIMENTAL RESULTS

The rectangular dielectric resonators are the main components in this design. By employing two DRs with different dielectric constants dual band operation has been achieved. In fact, both the DRs have the same dimensions, the one with high permittivity resonates at lower frequency band and the other with low permittivity resonates at the high frequency band. Therefore the antenna can support two wireless systems which are 2.4 GHz-WLAN and 3.82-4.08-C-band. Fig. 4 illustrates the prototype of the proposed dual-band DRA. Fig. 5 provides a comparison of simulated and measured return loss results of the proposed antenna. The discrepancy between the simulated and measured results may be due to the effect of fabrication errors and the use of glue for pasting the DRs. As it can be seen that from this figure dual band antenna is archived.

Figure 5 shows the simulated H- and E-plane radiation patterns for proposed antenna at 2.4 GHz and 3.8 GHz. It must be noted that gain of the designed antenna is 1.22 dB at 2.4 GHz and 1.86 at

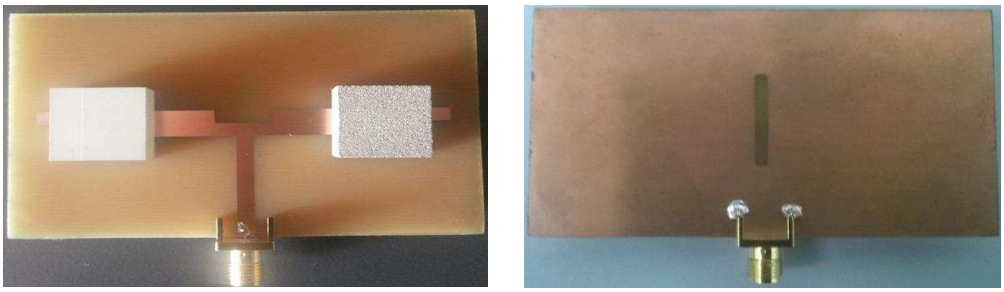

(a) (b)

Figure 4: Prototype of the proposed DR antenna. (a) Top view. (b) Bottom view.

3.8 GHz.

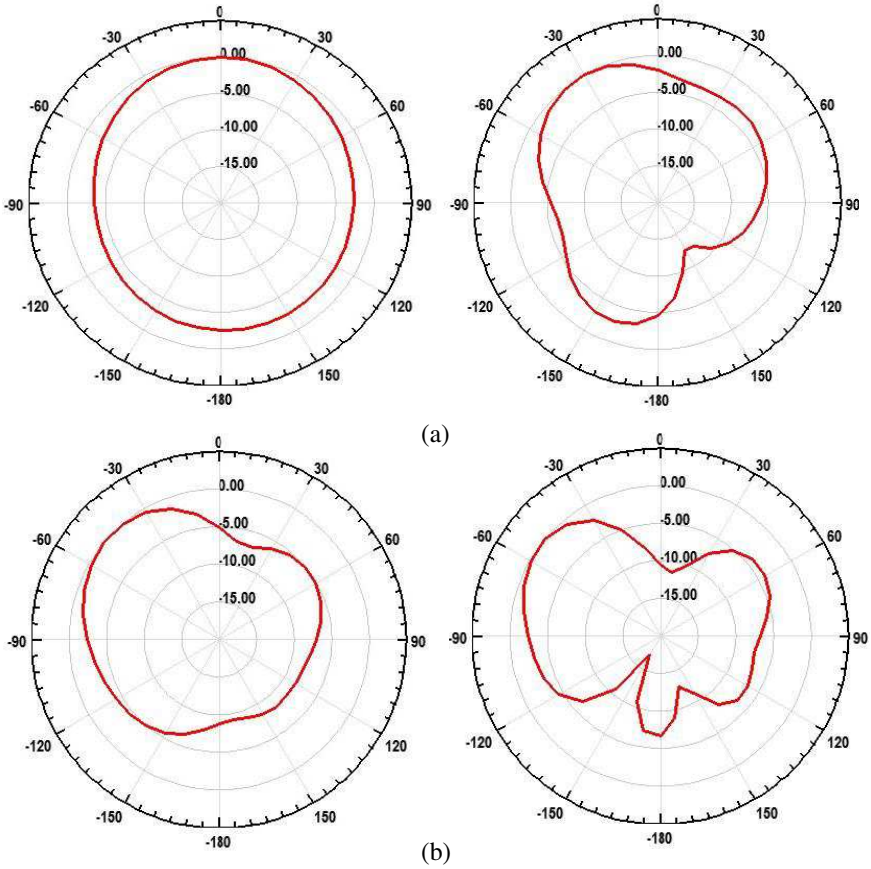

(a)

(b)

Figure 5: Simulated radiation patterns H-plane and E-plane at (a) 2.4 GHz and (b) 3.8 GHz.

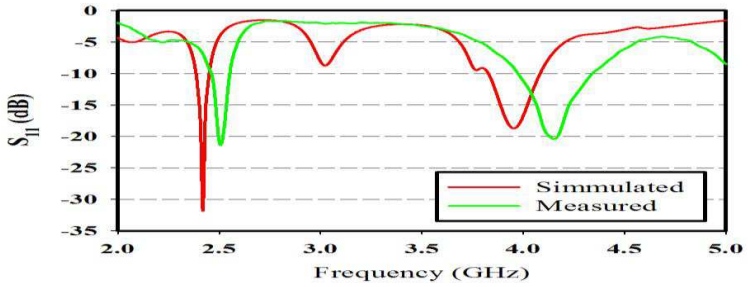

Figure 6: Simulated and measured reflection coefficient magnitudes of the proposed antenna.

5. CONCLUSION

In this paper, a dual band rectangular dielectric resonator antenna has been presented. In this design, a modified monopole antenna and two different relative permittivity rectangular dielectric resonators antenna has been employed. By using these design the antenna can support two wireless systems 2.4 GHz-WLAN and 3.8–4.4 GHz-C-band. Simultaneously. The proposed antenna was fabricated and tested, the good agreement between the measured and simulated (HFSS) results was presented. As a results the proposed antennas has excellent characteristics that makes them good candidates for two various wireless applications.

ACKNOWLEDGMENT

The authors wish to thank Ministry of Higher Education (MOE) and Universiti Teknologi Malaysia (UTM) for providing some funding through GUP (Vote 05H34) and FRGS (Vote 4F283) to enable this work to be completed.

REFERENCES

1. Mongia, R. K. and A. Ittipiboon, "Theoretical and experimental investigations on rectangualr dielectric resonator antennas" *IEEE Transactions on Antennas And Propagation*, Vol. 45, 1348–1356, 1997.
2. Khalily, M., M. K. A. Rahim, A. A. Kishk, and S. Danesh, "Wideband P-shaped dielectric resonator antenna," *Radioengineering*, Vol. 22, 281–285, 2013.
3. Abedian, M., S. K. A. Rahim, and M. Khalily, "Two-segments compact dielectric resonator antenna for UWB application," *IEEE Antennas and Wireless Propagation Letter*, Vol. 11, 1533–1536, 2012.
4. Khalily, M. and M. K. A. Rahim, "A novel hybreid design of printed hemi-cylindrical dielectric resonator monopole antenna with multi-bands operation," *Progress In Electromagnetics Research C*, Vol. 15, 175–186, 2010.
5. Khalily, M., M. K. A. Rahim, N. A. Murad, N. A. Samsuri, and A. A. Kishk, "Rectangular ring-shaped dielectric resonator antenna for dual and wideband frequency," *Microwave and Optical Technology Letters*, Vol. 55, 1077–1081, 2013.
6. Khalily, M., M. K. A. Rahim, and A. A. Kishk, "Planar wideband circularly polarized antenna design with rectangular ring dielectric resonator and parasitic printed loops," *IEEE Antenna and Wireless Propagation Letters*, Vol. 11, 905–908, 2012.
7. Khalily, M., M. R. Kamarudin, and M. H. Jamaluddin, "A novel square dielectric resonator antenna with two unequal inclined slits for wideband circular polarization," *IEEE Antenna and Wireless Propagation Letters*, Vol. 12, 1256–1259, 2013.
8. Danesh, S., S. K. A. Rahim, and M. Khalily, "A wideband trapezoidal dielectric resonator antenna with circular polarization," *Progress In Electromagnetics Research Letters*, Vol. 34, 91–100, 2012.
9. Khalily, M., M. R. Kamarudin, M. Mokayef, and M. H. Jamaluddin, "Omnidirectional circularly polarized dielectricresonator antenna for 5.2-GHz WLAN applications," *IEEE Antenna and Wireless Propagation Letters*, Vol. 13, 443–446, 2014.

Gain Enhanced UWB Dielectric Resonator Antenna

Mohsen Khalily[1], **Jamal Nasir**[1], **M. R. Kamarudin**[1], **Raghuraman Selvaraju**[1,2], **and M. H. Jamaluddin**[1]

[1]Wireless communication centre (WCC), Universiti Teknologi Malaysia, Malaysia
[2]Periyar Maniammai University, India

Abstract— An ultra-wideband dielectric resonator antenna (DRA) with enhanced gain is presented and investigated for wireless applications. The antenna has a compact shape with UWB characteristics. The radiator's structure is a split Z-shaped DRA with dielectric constant (ε_r) of 10. The antenna is mounted on a copper ground plane of size $75 \times 90\,\text{mm}^2$ and is fed by a split bevel-shaped strip to improve the impedance matching. Also, an air gap has been introduced between DR and ground plane to reduce the Q factor and dielectric constant, which in turn improves the impedance bandwidth. Extensive parametric studies have been carried out on different parameters in order to achieve an optimum structure. Ansoft HFSS v14 has been used for the simulation of the proposed antenna. The simulated results show that the antenna can efficiently operate over the frequency range from 2.5 GHz to 10.6 GHz covering the entire UWB range.

1. INTRODUCTION

In the last two decades, antennas using high-permittivity dielectric materials as radiation elements have received extensive attention due to several attractive features such as high radiation efficiency, low profile, considerable bandwidth and low temperature coefficient [1]. Also, Dielectric Resonator Antennas (DRAs) can be designed with various shapes [2] and excited by different feeding methods such as microstrip feed-line [3], coaxial probe [4], and etc.. In addition, DRAs have been used for dual-band [5], and multi-band [6] applications. DRAs are able to produce circularly polarized wave by exciting orthogonal modes [7, 8]. Over the last decades, researchers have focused on the bandwidth enhancement and various techniques have been developed for DRAs. Besides, ultra-wideband antennas have received lots of consideration due to the facility and mobility wireless communications. These antennas generally strive to be compatible with the Federal Communications Commission (FCC), which supports an impedance bandwidth of 7.5 GHz, i.e., from 3.1 to 10.6 GHz [9, 10]. This paper presents an UWB DRA with enhanced gain with impedance bandwidth of 8.1 GHz.

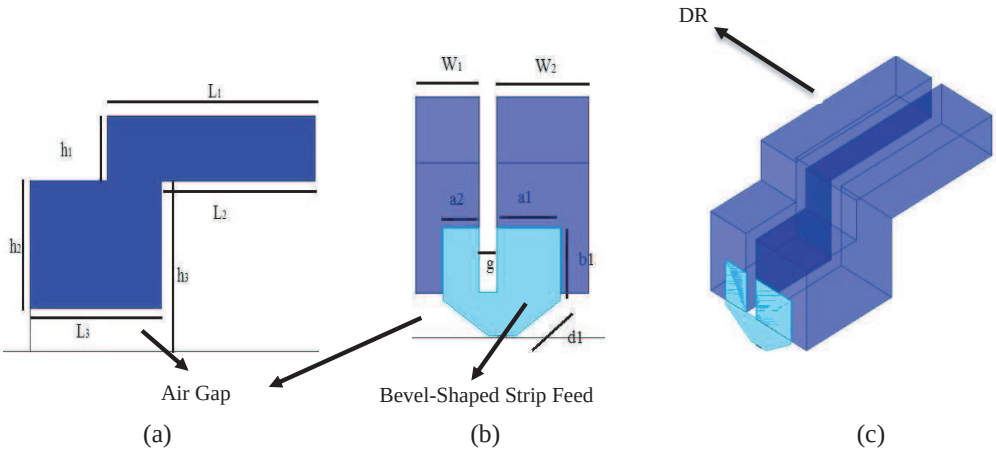

Figure 1: Geometry of the proposed UWB DRA: (a) Side view, (b) front view, and (c) 3-D view.

2. ANTENNA DESIGN AND CONFIGURATION

Figure 1 shows the geometry of the proposed UWB DRA. As it can be seen that from Figure 1(a) two split Z-shaped DR have been used as radiator elements. DRs are mounted on top of the ground

plane and excited by split bevel-Shaped strips from one side of DRs as it shown in Figure 2(b). Figure 1(c) illustrates the 3-D view of the proposed UWB DRA. The DRA is lifted above the ground plane by an air gap. The reason for using the split Z-shaped DRA is to improve the electric field distribution inside the DRA over the whole UWB frequency range. It is noted that, the split bevel shaped feeding structure has been employed to provide a smooth transition from one mode to another to widen the bandwidth. Also, using air gap between DRA and ground plane will reduce the effective permittivity, hence impedance bandwidth will be enhanced. Dielectric constant of 10 has been chosen for DR radiator elements by thickness of 5.12 mm. The final dimensions of the DR are $L_1 = 27\,\text{mm}$, $L_3 = 17\,\text{mm}$, $h_1 = 6.3\,\text{mm}$, $h_2 = 12.6\,\text{mm}$, $h_3 = 16.6\,\text{mm}$, $W_1 = 7\,\text{mm}$, $W_2 = 10.1\,\text{mm}$, $g = 2\,\text{mm}$ mounted on a $75 \times 90\,\text{mm}^2$ ground plane. The best matching is achieved when the parameters of the feed line are as follows: $a_1 = 4\,\text{mm}$, $a_2 = 7\,\text{mm}$, $b_1 = 6.9\,\text{mm}$, and $d_1 = 6\,\text{mm}$.

3. PARAMETRIC STUDIES AND DISCUSSIONS

For a better understanding of the behaviour of the designed UWB DRA, parametric study is performed to see the effect of variation of some parameters on the impedance bandwidth. For this purpose, the Ansoft HFSS v14, which is based on the finite element method, is used for the parametric analysis. Figures 2 and 3 illustrate the effect of d and dielectric constant on the reflection coefficient.

4. SIMULATIOMN RESULTS

By using optimal DR, air gap, and feed line dimensions, UWB DRA can cove frequency range from 2.5 GHz to 10.6 GHz. Figure 2 presents simulated return loss of the presented antenna. UWB frequency range of coverage is obtained because of exciting different modes by using bevel-shaped feeding structure, an air gap and using split Z-shaped DRAs.

Figure 5 shows the simulated 3D radiation patterns for proposed antenna at 5.2 GHz and 8 GHz. It must be noted that H-plane patterns are symmetrical and patch-like across the operating frequency range for presented antenna. However, the E-plane patterns are not as symmetrical as in the H-plane. In addition, gain values of the presented UWB antenna varied between 7 dB at 3 GHz and 10 dB at 10.6 GHz which is greater than gain value in [8, 9].

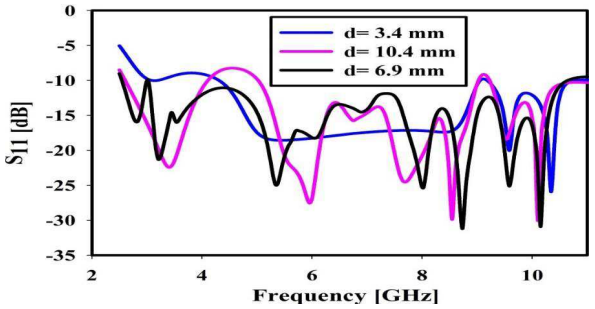

Figure 2: Simulated S_{11} with different value of d (length of bevel-shaped feed line).

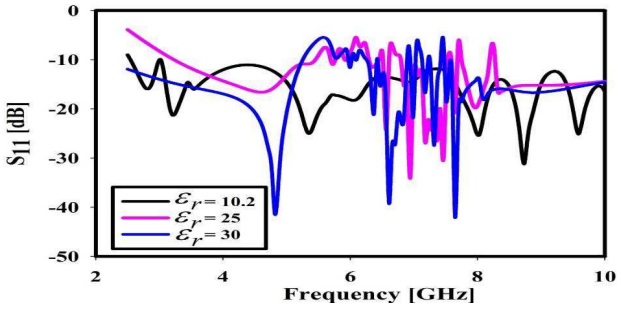

Figure 3: Simulated S_{11} with different value of ε_r.

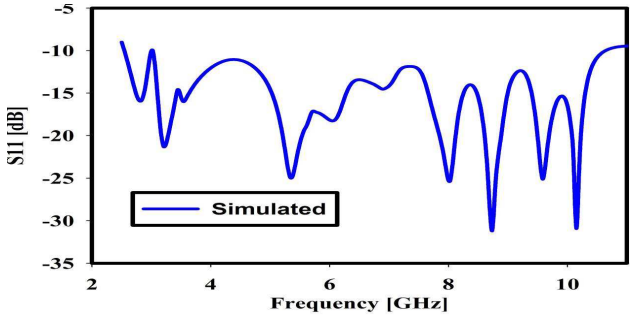

Figure 4: Return Loss of the proposed UWB DRA.

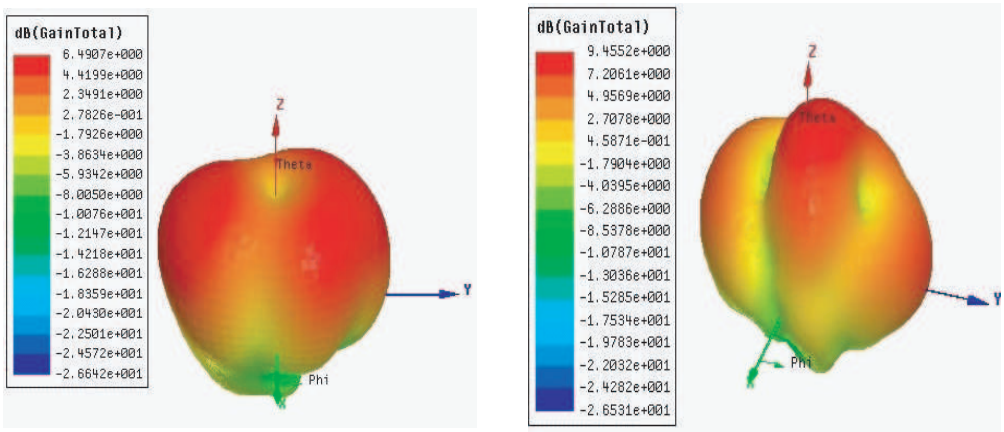

(a) (b)

Figure 5: Simulated 3-D radiation patterns at (a) 5.2 GHz and (b) 8 GHz.

5. CONCLUSION

An UWB DRA with a good radiation characteristics has been proposed in this paper. The antenna consist of two Z-shaped dielectric resonators mounted on a copper plane fed by a bevel shaped feed. There is also an air gap between radiator elements and ground plane to reduce Q-factor, hence improving the impedance bandwidth. It is found that the proposed antenna is able to operate in the UWB frequency range covering from 2.5 GHz to 10.6 GHz. The gain of the antenna is 7 dB to 10 dB and the efficiency is more than 85% throughout the UWB frequency range. Simulated results prove that the proposed enhanced gain UWB DRA is a good candidate for UWB wireless applications.

ACKNOWLEDGMENT

The authors wish to thank Ministry of Higher Education (MOE) and Universiti Teknologi Malaysia (UTM) for providing some funding through GUP (Vote 05H34) and FRGS (Vote 4F283) to enable this work to be completed.

REFERENCES

1. Mongia, R. K. and A. Ittipiboon, "Theoretical and experimental investigations on rectangular dielectric resonator antennas," *IEEE Trans. Antennas Propag.*, Vol. 45, No. 9, Sep. 1997.
2. Khalily, M., M. K. A. Rahim, A. A. Kishk, and S. Danesh, "Wideband P-shaped dielectric resonator antenna," *Radioengineering*, Vol. 22, No. 1, Apr. 2013.
3. Khalily, M., M. K. A. Rahim, and A. A. Kishk, "Planar wideband circularly polarized antenna design with rectangular ring dielectric resonator and parasitic printed loops," *IEEE Antennas and Wireless Propagation Letters*, Vol. 11, 905–907, 2012.
4. Khalily, M., M. R. Kamarudin, and M. H. Jamaluddin, "A novel square dielectric resonator antenna with two unequal inclined slits for wideband circular polarization," *IEEE Antennas and Wireless Propagation Letters*, Vol. 12, 1256–1259, 2013.
5. Khalily, M., M. K. A. Rahim, N. A. Murad, N. A. Samsuri, and A. A. Kishk, "Rectangular ring-shaped dielectric resonator antenna for dual and wideband frequency," *Microwave and Oprical Technology Letters*, Vol. 55, No. 5, May 2013.
6. Khalily, M. and M. K. A. Rahim, "A novel hybreid design of printed hemi-cylindrical dielectric resonator monopole antenna with multi-bands operation," *Progress In Electromagnetics Research C*, Vol. 15, 175–186, 2010.
7. Danesh, S., S. K. A. Rahim, and M. Khalily, "A wideband trapezoidal dielectric resonator antenna with circular polarization," *Progress In Electromagnetics Research Letters*, Vol. 34, 91–100, 2012.
8. Khalily, M., M. R. Kamarudin, M. Mokayef, and M. H. Jamaluddin, "Omnidirectional circularly polarized dielectric resonator antenna for 5.2-GHz WLAN applications," *IEEE Antennas and Wireless Propagation Letters*, Vol. 13, 443–446, 2014.
9. Denidni, T. A., Z. Weng, and M. Niroo-jazi, "Z-shaped dielectric resonator antenna for ultra-wideband applications," *IEEE Trans. Antennas Propag.*, Vol. 58, No. 12, 4059–4062, Oct. 2010.

10. Abedian, M., S. K. A. Rahim, and M. Khalily, "Two-segments compact dielectric resonator antenna for UWB application," *IEEE Antennas and Wireless Propagation Letters*, Vol. 11, 2012.

Electromagnetic Modeling and Simulation for Packaging Structures with Lossy Conductors

Y. Q. Zhang, G. Z. Yin, X. W. Zhang, J. Zhang, and M. S. Tong
Department of Electronic Science and Technology
Tongji University, Shanghai, China

Abstract— Accurate electromagnetic (EM) analysis for interconnect structures requires to consider the finite conductivity of involved conductors. The conductor loss could be accounted for through an approximate surface impedance when the skin depth of current is small. However, this approximation may not be valid for large skin depth caused by low frequencies or small conductivities. In this work, we treat the lossy conductors as homogeneous dielectric media and use electric field integral equations (EFIEs) to describe the problem. The EFIEs are solved with the method of moments (MoM) in which the Rao-Wilton-Glisson (RWG) and dual basis functions are used to represent the electric and magnetic current densities, respectively. A numerical example is presented to demonstrate the approach.

1. INTRODUCTION

Accurate electromagnetic (EM) analysis based on numerical modeling and simulation is essential for the optimal design of electronic devices or systems [1]. For interconnect and packaging structures, the conductors are usually lossy and we have to account for the skin effect in numerical solutions. In the integral equation approach for solving the problem, one may use the volume-filament method like the partial equivalent electric circuit (PEEC) solver or surface integral equation (SIE) approach with an approximate surface impedance [2–7]. However, they are only efficient to model interconnect conductors which are usually long and thin and cannot handle the conductors with irregular shape such as bends and junctions [8]. The SIE approach is preferred whenever available because it only discretizes the boundaries or interfaces of media, resulting less number of unknowns [1].

To treat arbitrarily-shaped structures with lossy conductors by the SIE approach, the generalized impedance boundary condition (GIBC) approach was proposed by formulating the problem in two regions [8]. The approach treats the lossy conductors as general dielectric media and uses the electric field integral equations (EFIEs) to describe the exterior region of conductors and the magnetic field integral equations (MFIEs) to formulate the interior region of conductors. In this work, we use the EFIEs to describe both the exterior region and interior region of conductors and consider the structural mixture of dielectrics and conductors which were not considered previously. The EFIEs are solved with the method of moments (MoM) in which the the Rao-Wilton-Glisson (RWG) basis function [9] is used to represent the electric current density while the dual basis function is employed to expand the magnetic current density [10]. The two basis functions are also used as testing functions to wisely test the EFIEs so that the conditioning of resulting system matrix can be improved. We present the numerical example for analyzing a typical interconnect structure to illustrate the approach and good results can be observed.

2. SURFACE INTEGRAL EQUATIONS

The interconnect structures include both dielectric substrates and conducting signal lines and ground (conductors). We label the conductors as Region 1, the substrate as Region 2, and the surrounding medium (free space) as Region 0, and the subscripts of parameters indicate the corresponding regions. Consider the EM scattering by a general dielectric object labeled as Region i, the EFIEs can be written as [1]

$$\hat{n} \times [\mathcal{L}_0(\mathbf{J}_i) + \mathcal{K}_0(\mathbf{M}_i)] = -\hat{n} \times \mathbf{E}^{inc}, \quad \mathbf{r} \in S_i \tag{1}$$

$$\hat{n} \times [\mathcal{L}_i(\mathbf{J}_i) + \mathcal{K}_i(\mathbf{M}_i)] = 0, \quad \mathbf{r} \in S_i \tag{2}$$

where $\hat{n}$ is the unit normal vector at the object surface S_i, $\mathbf{J}_i$ and $\mathbf{M}_i$ are the equivalent electric current density and magnetic current density at the object surface, respectively, and $\mathbf{E}^{inc}$ is the

incident electric field. Also, $\mathcal{L}$ and $\mathcal{K}$ are the operators which are respectively defined as

$$\mathcal{L}(\mathbf{A}) = i\omega\mu \int_{S_i} \left(\bar{\mathbf{I}} + \frac{\nabla\nabla}{k^2}\right) g(\mathbf{r},\mathbf{r}') \cdot \mathbf{A}(\mathbf{r}')\, dS' \tag{3}$$

$$\mathcal{K}(\mathbf{A}) = \frac{1}{2}\hat{n} \times \mathbf{A} + \int\!\!\!\!\!\!\diagup_{S_i} \mathbf{A}(\mathbf{r}') \times \nabla g(\mathbf{r},\mathbf{r}')\, dS' \tag{4}$$

where $\mathbf{A}$ represents a current density, k is the wavenumber, and $g(\mathbf{r},\mathbf{r}') = e^{ikR}/(4\pi R)$ is the scalar Green's function in which $R = |\mathbf{r} - \mathbf{r}'|$ is the distance between an observation point $\mathbf{r}$ and a source point $\mathbf{r}'$. The above EFIEs can also be applied to a lossy conductor with a finite conductivity when we treat it as a generalized dielectric object. For an interconnect structure, we apply the above EFIEs to both the conductor region and substrate region to yield the following integral equations.

$$\hat{n} \times [\mathcal{L}_0(\mathbf{J}_1) + \mathcal{K}_0(\mathbf{M}_1) + \mathcal{L}_0(\mathbf{J}_2) + \mathcal{K}_0(\mathbf{M}_2)] = -\hat{n} \times \mathbf{E}^{ex}, \quad \mathbf{r} \in S_1 \tag{5}$$

$$\hat{n} \times [\mathcal{L}_1(\mathbf{J}_1) + \mathcal{K}_1(\mathbf{M}_1)] = 0, \quad \mathbf{r} \in S_1 \tag{6}$$

$$\hat{n} \times [\mathcal{L}_0(\mathbf{J}_1) + \mathcal{K}_0(\mathbf{M}_1) + \mathcal{L}_0(\mathbf{J}_2) + \mathcal{K}_0(\mathbf{M}_2)] = 0, \quad \mathbf{r} \in S_2 \tag{7}$$

$$\hat{n} \times [\mathcal{L}_2(\mathbf{J}_2) + \mathcal{K}_2(\mathbf{M}_2)] = 0, \quad \mathbf{r} \in S_2 \tag{8}$$

where S_1 and S_2 are the surface of the substrate and conductors, respectively, and $\mathbf{E}^{ex}$ is a delta-gap source. From the above equations, we can solve the current densities and then find the needed parameters for circuit analysis.

3. THE METHOD OF MOMENTS SOLUTION

The above EFIEs can be solved with the MoM. Since we have both unknown electric current density and unknown magnetic current density on each medium interface, we need to use two basis functions to represent them, respectively. To improve the conditioning of resulting system matrix, we use the RWG basis function to represent the electric current density and the dual basis function to expand the magnetic current density, i.e.,

$$\mathbf{J}_i(\mathbf{r}') = \sum_{n=1}^{N_i} a_n^{(i)} \mathbf{\Lambda}_n(\mathbf{r}') \tag{9}$$

$$\mathbf{M}_i(\mathbf{r}') = \sum_{n=1}^{N_i} b_n^{(i)} \tilde{\mathbf{\Lambda}}_n(\mathbf{r}') \tag{10}$$

where N_i $(i = 1, 2)$ is the number of RWG triangle pairs at the surface of Region i after discretization. The definitions of RWG basis function and dual basis function can be found in [9, 10], respectively. The two basis functions are also used as testing functions to test the above integral equations and we can obtain the following matrix equation

$$\sum_{n=1}^{N_1} \left\{ a_n^{(1)} \langle \mathbf{\Lambda}_m, \mathcal{L}_0(\mathbf{\Lambda}_n)\rangle + b_n^{(1)} \langle \mathbf{\Lambda}_m, \mathcal{K}_0(\tilde{\mathbf{\Lambda}}_n)\rangle \right\} + \sum_{n=1}^{N_2} \left\{ a_n^{(2)} \langle \mathbf{\Lambda}_m, \mathcal{L}_0(\mathbf{\Lambda}_n)\rangle + b_n^{(2)} \langle \mathbf{\Lambda}_m, \mathcal{K}_0(\tilde{\mathbf{\Lambda}}_n)\rangle \right\}$$
$$= -\langle \mathbf{\Lambda}_m, \mathbf{E}^{ex}\rangle, \quad m = 1, 2, \ldots, N_1 \tag{11}$$

$$\sum_{n=1}^{N_1} \left\{ a_n^{(1)} \langle \tilde{\mathbf{\Lambda}}_m, \mathcal{L}_1(\mathbf{\Lambda}_n)\rangle + b_n^{(1)} \langle \tilde{\mathbf{\Lambda}}_m, \mathcal{K}_1(\tilde{\mathbf{\Lambda}}_n)\rangle \right\} = 0, \quad m = 1, 2, \ldots, N_1 \tag{12}$$

$$\sum_{n=1}^{N_1} \left\{ a_n^{(1)} \langle \mathbf{\Lambda}_m, \mathcal{L}_0(\mathbf{\Lambda}_n)\rangle + b_n^{(1)} \langle \mathbf{\Lambda}_m, \mathcal{K}_0(\tilde{\mathbf{\Lambda}}_n)\rangle \right\} + \sum_{n=1}^{N_2} \left\{ a_n^{(2)} \langle \mathbf{\Lambda}_m, \mathcal{L}_0(\mathbf{\Lambda}_n)\rangle + b_n^{(2)} \langle \mathbf{\Lambda}_m, \mathcal{K}_0(\tilde{\mathbf{\Lambda}}_n)\rangle \right\}$$
$$= 0, \quad m = 1, 2, \ldots, N_2 \tag{13}$$

$$\sum_{n=1}^{N_2} \left\{ a_n^{(2)} \langle \tilde{\mathbf{\Lambda}}_m, \mathcal{L}_2(\mathbf{\Lambda}_n)\rangle + b_n^{(2)} \langle \tilde{\mathbf{\Lambda}}_m, \mathcal{K}_2(\tilde{\mathbf{\Lambda}}_n)\rangle \right\} = 0, \quad m = 1, 2, \ldots, N_2. \tag{14}$$

Note that the wavenumber is $k \approx (1 + i)/\delta$ where $\delta \approx \sqrt{2/\omega\mu\sigma}$ is the skin depth for a lossy conductor.

4. NUMERICAL EXAMPLES

To demonstrate the approach, we consider the EM analysis for a typical interconnect structure, i.e., two conducting signal lines on a one-layer dielectric substrate with a ground as sketched in Fig. 1. The dielectric substrate is lossless but the conducting signal lines and ground are lossy. The geometry are characterized with $l = 10.0$, $w = 5.0$, $h = 0.3$, $d = 0.1$, $s = s_1 = s_2 = 0.2$, and $t_1 = t_2 = 0.05$, all in millimeter (mm). Here l is the length that the ground, substrate, and signal lines commonly have, w is the width that the ground and substrate commonly have, h is the height of the substrate, d is the thickness of the ground, s is the spacing between the two signal lines whose widths are s_1 and s_2, and thicknesses are t_1 and t_2, respectively. The relative permittivity of the dielectric substrate is $\epsilon_r = 4.0$ and the conductivity of conductors is $\sigma = 5.8 \times 10^7$ S/m (the relative permeability $\mu_r = 1.0$ for both substrate and conductors). Fig. 2 shows the solutions of S parameters (magnitude) for the structure with a comparison to the result from a finite element method (FEM) solver.

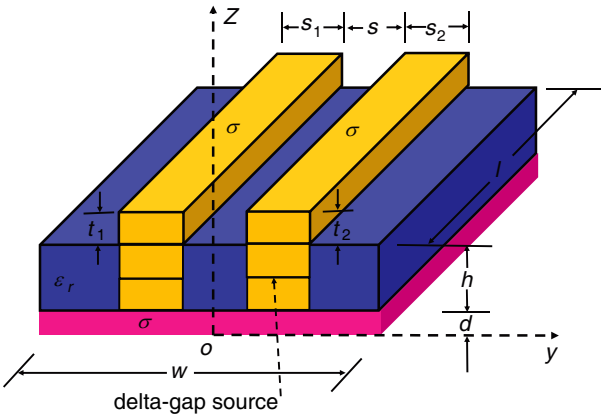

Figure 1: Geometry of a typical interconnect and packaging structure. A conducting signal line is at the top of a one-layer dielectric substrate with a ground.

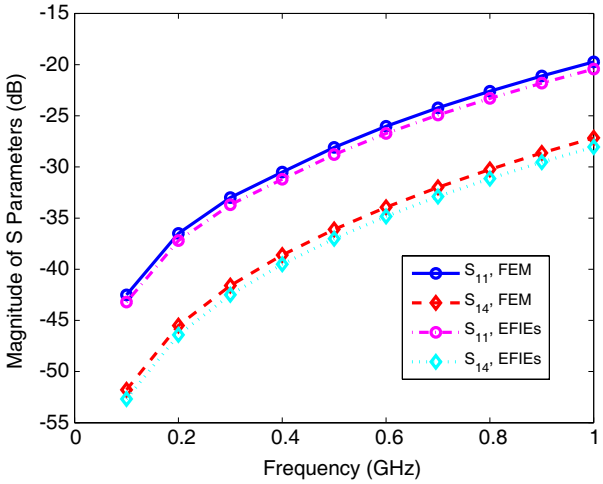

Figure 2: S parameter for the interconnect and packaging structure including a signal line and a one-layer dielectric substrate. The geometry is defined with $l = 10.0$, $w = 5.0$, $d = 0.1$, $s = 0.2$, $t = 0.05$, and $h = 0.3$, all in millimeters, and the substrate has a relative permittivity $\varepsilon_r = 4.0$.

5. CONCLUSION

In this work, we consider the lossy conductors in the EM analysis for interconnect structures. The conductors are treated as general homogeneous dielectric media and we use the two-region EFIEs to formulate both conductor region and dielectric substrate region together. The EFIEs are solved by the MoM in which the electric and magnetic current densities at region boundaries are represented with the RWG and dual basis functions, respectively. The basis functions are also used as testing functions to alternatively test the EFIEs so that the conditioning of system matrix can be improved. We present a typical numerical example to illustrate the approach and good results have been observed.

ACKNOWLEDGMENT

This work was supported by the Specialized Research Fund for the Doctoral Program of Higher Education of China with Project No. 20120072110044.

REFERENCES

1. Chew, W. C., M. S. Tong, and B. Hu, *Integral Equation Methods for Electromagnetic and Elastic Waves*, Morgan & Claypool, San Rafael, CA, 2008.
2. Ruehli, A. E., "Equivalent circuit models for three dimensional multiconductor systems," *IEEE Trans. Microw. Theory Tech.*, Vol. 22, No. 3, 216–221, Mar. 1974.

3. Heeb, H. and A. E. Ruehli, "Three-dimensional interconnect analysis using partial element equivalent circuits," *IEEE Trans. Circuits Syst. I*, Vol. 39, No. 11, 974–982, Nov. 1992.
4. Coperich, K. M., A. E. Ruehli, and A. Cangellaris, "Enhanced skin effect for partial-element equivalent-circuit (PEEC) models," *IEEE Trans. Microw. Theory Tech.*, Vol. 48, No. 9, 1435–1442, Sep. 2000.
5. Morsey, J. D., V. I. Okhmatovski, and A. C. Cangellaris, "Finite thickness conductor models for full-wave analysis of interconnects with a fast integral equation method," *IEEE Trans. Adv. Packag.*, Vol. 27, No. 1, 24–33, Feb. 2004.
6. Rong, A. and A. C. Cangellaris, "Comprehensive broadband electromagnetic modeling of on-chip interconnects with a surface discretization-based generalized PEEC model," *IEEE Trans. Adv. Packag.*, Vol. 28, No. 3, 434–444, Aug. 2005.
7. De Zutter, D., H. Rogier, L. Knockaert, and J. Sercu, "Surface current modelling of the skin effect for on-chip interconnects," *IEEE Trans. Adv. Packag.*, Vol. 30, No. 2, 342–349, May 2007.
8. Qian, Z. G. and W. C. Chew, "Generalized impedance boundary condition for conductor modeling in surface integral equation," *IEEE Trans. Antennas Propagat.*, Vol. 55, No. 11, 2354–2364, Nov. 2007.
9. Rao, S. M., D. R. Wilton, and A. W. Glisson, "Electromagnetic scattering by surfaces of arbitrary shape," *IEEE Trans. Antennas Propagat.*, Vol. 30, 409–418, 1982.
10. Chen, Q. L., "Electromagnetic modeling of three-dimensional piecewise homogeneous material bodies of arbitrary composition and geometry," Ph.D. Dissertation, University of Houston, 1990.

A Numerical Study on 2D Photonic Crystal Devices for Millimeter and Terahertz Wave Applications

T. Kato[1], **K. Kamata**[1], **C. P. Chen**[1], **T. Anada**[1], **Steve Greedy**[2], **and Trevor Benson**[2]

[1]Kanagawa University, 221-8686, Japan
[2]University of Nottingham, NG7 2RD, UK

Abstract— Novel terahertz functional devices based on photonic crystals are proposed in this paper. The photonic crystal band gap of metal/dielectric rods in an air background is computed using the plane wave expansion method. For metallic rods in air, the frequency dependent dielectric function is described by the Drude model. By adjusting the positions and radii of the metallic and dielectric rods, and their alignment with the lattice, a compact PhC bandpass filter, and T-junction switching circuits are demonstrated.

1. INTRODUCTION

As the demand for greater bandwidth increases alongside the development of the next and future generations of wireless communication systems, the extension of the operating frequency of these systems into the upper-millimeter wave or terahertz region (100 GHz–3 THz) of the electromagnetic spectrum is inevitable [1]. Standardization and regulation activities for THz communications began in 2008 when the IEEE 802.15 Terahertz Interest Group was established to explore wireless systems operating at 300 GHz and beyond [1]. Therefore technologies that enable electronic devices to work in the terahertz region are required, technologies that perform the operations provided by traditional passive circuits; switches, splitters and filters for example. One technology that has shown promise for the realization of such devices is that of silicon (Si) based photonic crystals (PhC) [2].

To date many studies have considered point defect resonators and line defect waveguides in dielectric photonic band gap (PBG) crystals. However, there have been very few studies concerning guided modes in metallic PBG crystals [3]. Nevertheless, it has been suggested that periodic metallic structures have important applications. Recently, planar substrate integrated waveguides (SIW) using metallic via holes have been developed. However, as THz waveguides demand lower loss and higher levels of device integration, some drawbacks become apparent. Recent developments in nanofabrication allow the fabrication of nano-scale 2D arrays of silicon pillars, or holes, resulting in materials with a periodic refractive index that may be utilized as a basis for PhCs. These 2D PhCs can provide a bandgap in every direction of propagation in the lattice's plane of periodicity [3]. In this work, we propose new and compact electromagnetic circuits by embedding the photonic crystal structure into current SIW and non-radiative dielectric (NRD) structures. Through the introduction of point or line defects in the PhCs, the electromagnetic (EM) wave can be controlled, i.e., confined, guided, or localized. Such photonic band gap structures also provide a promising tool for controlling the signal-flow within integrated EM circuits.

In order to design a metallic/dielectric photonic crystal line defect waveguide and point defect high-Q microcavity, the dispersion relations of photonic bandgap are initially calculated using the plane wave expansion method [4]. The frequency characteristics of THz functional devices using photonic crystal line defect waveguides and point-defect resonators are then numerically studied by the finite difference time domain (FDTD) method.

2. 2D METALLIC/DIELECTRIC PHOTONIC CRYSTAL STRUCTURES AND BANDGAP

We consider 2D metallic PhCs consisting of metallic/dielectric rod arrays in air; the PhCs have a square lattice and are embedded inside a parallel-plate metal waveguide, as shown in Figure 1. Compared with dielectric photonic crystals, metallic photonic crystals have the following promising characteristics:

1) Structures composed of metallic photonic crystals may have more compact sizes than those of dielectric PhCs. Since metals are more reflective than dielectrics at few terahertz frequencies, less photonic crystal columns are required to establish band gaps.

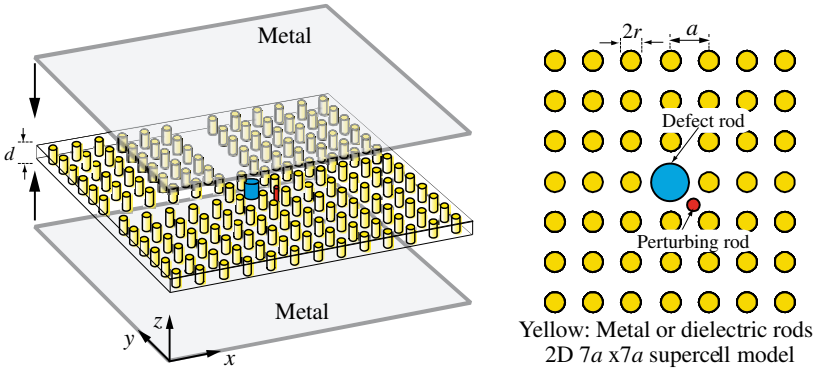

Figure 1: Typical 2D metallic/dielectric photonic crystal model in parallel plate waveguide. R_d is dielectric defect rod (blue) and r_p is perturbing dielectric rod (red).

2) Metallic photonic crystals may enlarge the band gaps, which leaves more margins to the applications. Especially, metallic PhCs operating with E-polarization have a global bandgap that covers the frequency range from zero to cut-off frequency.

The band structure depends on the PhCs geometric and constitutive parameters such as the lattice radius r, lattice constant a and the frequency dependent dielectric constant $\varepsilon(\omega)$. In order to introduce a frequency dependent dielectric function for the metal, time-dependent Maxwell's equations can be written in the following form,

$$\frac{\partial \mathbf{H}}{\partial t} = -\frac{1}{\mu(r)}\nabla \times \mathbf{E} \qquad \frac{\partial \mathbf{E}}{\partial t} = -\frac{1}{\varepsilon(r)}\nabla \times \mathbf{H} - \frac{\sigma(r)}{\varepsilon(r)}\mathbf{E} \tag{1}$$

where $\varepsilon(r)$, $\mu(r)$, and $\sigma(r)$ in above Equation (1) are the position dependent permittivity, permeability, and conductivity of the material, respectively. In the case of M-PhC, we use the frequency dependent Drude model to describe the dielectric constant of metal as follows:

$$\varepsilon_r(\omega) = \left(\varepsilon_\infty - i\frac{\sigma}{\omega\varepsilon_0}\right) = \left(\varepsilon_\infty - \frac{\omega_p^2}{\omega_\tau^2+\omega^2}\right) + j\frac{\omega_p^2\omega_\tau}{\omega\omega_\tau^2+\omega^3}, \quad \omega_p = \sqrt{\frac{Ne^2}{m_e}} \quad \text{(Plasma frequency)} \tag{2}$$

where N is the electron density, e is the electron charge, m_e is electron mass, $\omega_\tau/2\pi$ is the damping frequency, and $\omega_p/2\pi$ is the plasma frequency. ε_∞ is the permittivity at infinite frequency. The Drude model parameters used in the calculations for the metal (copper) are $\omega_p/2\pi = 1914\,\text{THz}$ and $\omega_\tau/2\pi = 8.34\,\text{THz}$ [3].

The damping frequency is neglected because it is small compared to the plasma frequency. Thus a simple Drude model is obtained in which the imaginary part of (2) is neglected. Figure 2 shows the computed values of the band gaps obtained by using the standard plane wave expansion (PWE) method. The metallic photonic crystal in Figure 2(a) has a global band-gap for the E polarized field, in the frequency range of a/λ $(= \omega a/2\pi c)$ from 0 to 0.528 (a/λ), the height of metal rods is $d = 0.5a$ and the ratio of the rod's radius to the lattice is $r/a = 0.2$, respectively. While TE modes

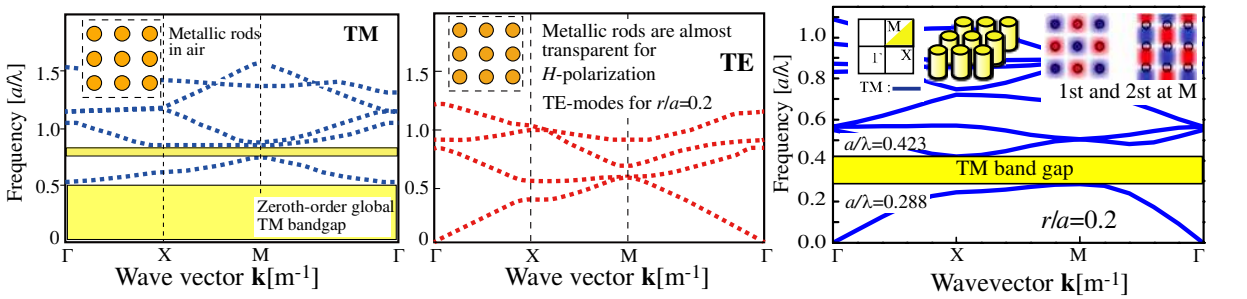

(a) Metal square lattice in air (r/a=0.2) (b) Dielectric square lattice in air (r/a=0.2)

Figure 2: Typical photonic band gap diagrams for metallic and dielectric models.

do not have a cutoff frequency as shown in Figure 2(a). Moreover, a typical dielectric PhC has an index of refraction of $n = 3.40$, which corresponds to high-resistivity and high-purity silicon which is transparent at THz frequencies. Figure 2(b) shows the D-PhC band gap for TM mode obtained by using the standard plane wave method.

3. SIMULATION RESULTS

The validity of our approach is justified through application to examples of a PBG straight waveguides, right angled bend for metallic band-gap waveguides, T-junction power splitter circuits, and PhC narrowband bandpass filters using the double degenerate modes of microcavities.

3.1. Propagation Properties of a Line Defect Straight and Right Angled Bend Waveguide

A PhC right-angled waveguide bend formed within a 2D square lattice of metallic cylinders is considered. Its ability to confine and guide a THz wave, polarized parallel to the PhC rod-axis, i.e., the transverse magnetic (TM) mode, is examined and its performance assessed by considering its transmission characteristics. Propagation loss is a key factor in designing a PhC based waveguide and it is related to the confinement of the guided mode. Figure 3(a) shows the propagation constant of dominant guided mode in metallic PhC line defect waveguide with a conventional metal waveguide of width $W = 1.82a$. They are in a good agreement except upper high frequency region. Figure 3(b) and Figure 3(c) show the frequency response and electric field distributions of a PhC right-angled bend with perfect conductor and Drude models of the metal (copper) conductors. Metallic loss is taken into account with a frequency dependent dielectric constant achieved by the Drude model. Here, the radius of rods and the lattice constant are $r = 11.7\,\mu\text{m}$ and $a = 58.5\,\mu\text{m}$, respectively. From the electric field distributions at increasing frequencies it is observed that the dominant mode couples into the higher-order mode and the bending loss increases rapidly as the range of the confinement, determined by the PBG, is exceeded, and the electromagnetic field is radiated away from the line defect waveguide.

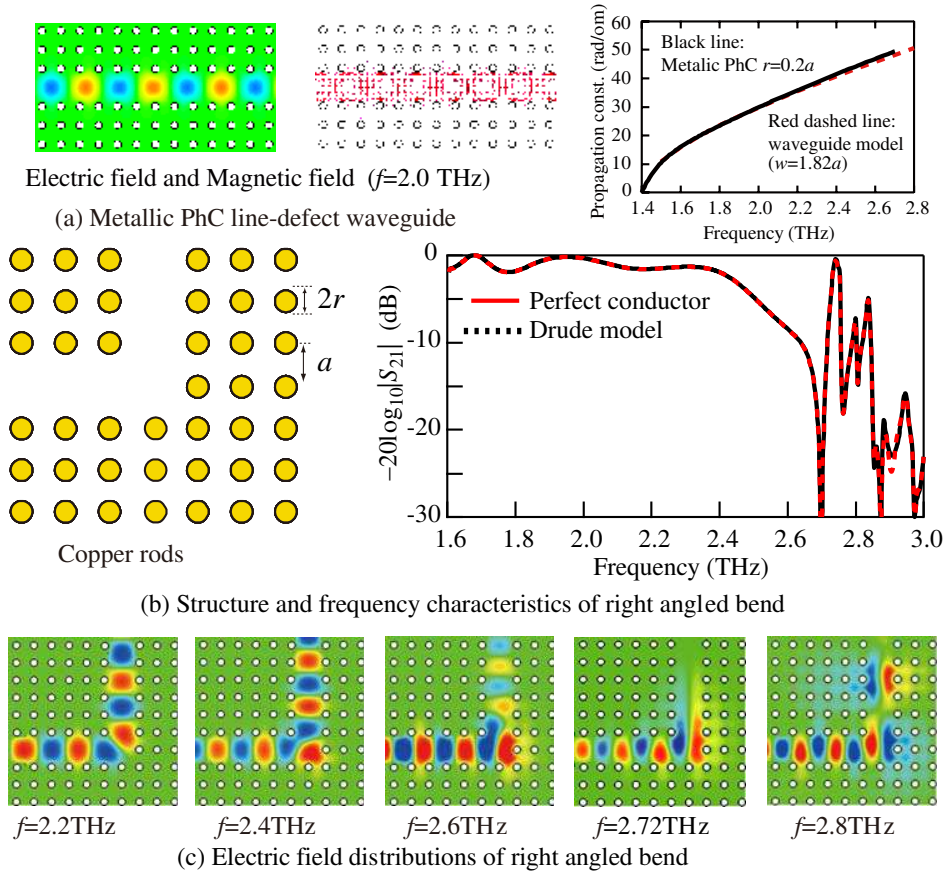

Figure 3: Structure, frequency characteristics and electric field distributions of right angled bend.

3.2. A Metallic Photonic Crystal Switch Created by Inserting a Small Dielectric Perturbing Rod within a T-shaped Waveguide Branches

A novel T-shaped PhC switch is proposed here that can control the direction of an EM-wave that propagates along a line defect waveguide. As shown in Figure 4, the selectivity of the direction is determined by the insertion of a small dielectric rod. The two positions considered for the dielectric perturbing rod (r_p) in the T-junction are $(dx, dy) = (0.0, 0.6a)$ and $(dx, dy) = (-0.65a, 0.65a)$.

(a) When a single rod is placed at $(x, y) = (-0.65a, +0.65a)$, the power, at a frequency $f =$ 2.15 THz, fed into port 1 is coupled only to port 3.

(b) When a single rod is placed at $(x, y) = (0, 0.6a)$, at an operating frequency $f = 2.25$ THz, a TM wave incident at port 2 is coupled only to port 3.

(c) When two rods are introduced, Figure 4(c), power at a frequency of $f = 2.10$ THz fed into port 3 couples to only port 4. As shown in Figures 4(c), (d), more complicated network configurations such as interconnects that may contain many branches can be achieved by combining the situations described by (a) and (b) above. The power transmission efficiency is seen to be near 95% at frequency $f = 2.10$ THz. Figures 4(c) and (d) show the almost same frequency response.

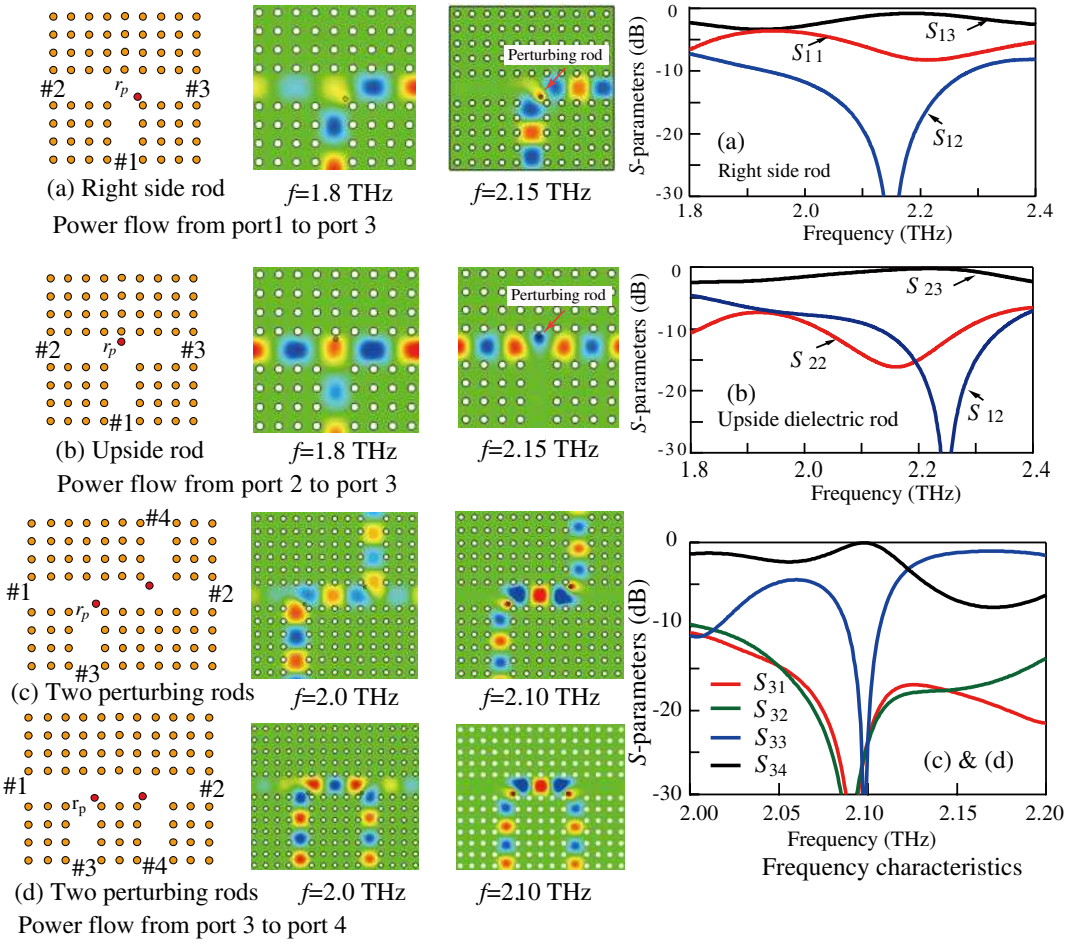

Figure 4: Metallic photonic crystal T-junction power splitter with perturbing dielectric rod. Yellow: metallic PhC and red: dielectric perturbing rod ($r_p = 0.55r$).

As was expected, the EM waves give rise to a **"pull-in" phenomenon** with a small dielectric perturbation rod resulting in a switching function. The PhC switch function is realized by changing the index of the PhC by MEMS, changing the conductance of the semiconductor in the PhC structure, etc..

3.3. A Novel Inductive Window-type Bandpass Filter Using PhC Degenerate Modes

We consider PhC bandpass filter with an additional large dielectric rod of radius R_d and a small dielectric-perturbing rod of radius r_p as shown in Figure 5. By laying out the input/output ports orthogonally (90°), both of the degenerate modes are excited and coupled to each other due to the small perturbing rod within the point defect microcavity. When a small perturbing dielectric rod

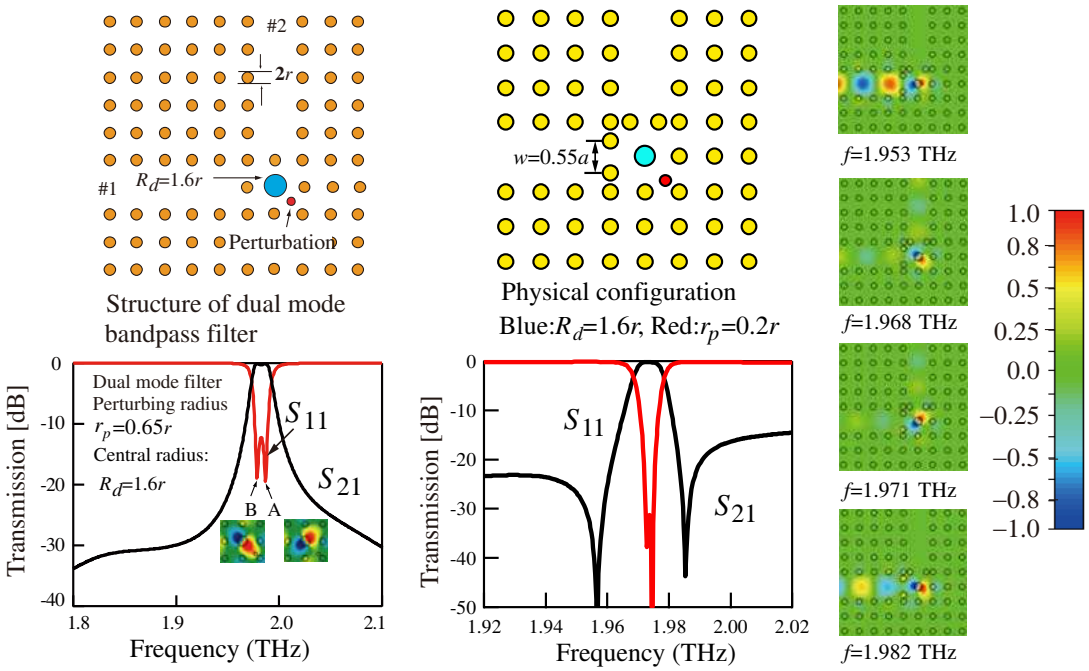

(a) Structure of dual mode bandpass filter

(b) Structure of Pseudo-eliptic function bandpass filter, frequency characteristics, and *Ez* field distributions.

Figure 5: Structure and its properties of proposed photonic crystal bandpass filter.

is added to the dual-mode cavity, as shown in Figure 5(a), the field and resonant frequency will be the sum (= "TM_{210} + TM_{120}") and difference (= "TM_{210} − TM_{120}") of the modes as shown here. By utilizing input-output coupling windows as shown in Figure 5(b), two transmission zeros are created to improve the performance of the filter. Furthermore, two transmission zeros can be simultaneously placed below or above the passband. The input/output coupling structure is inductive with an optimum gap of about $0.5r$. Simulation results show that the resulting bandpass filter exhibits a quasi-elliptic response with two transmission zeros at finite frequencies near the passband as depicted in Figure 5. The filter shows a very good response with a return loss of about 25 dB and a fractional bandwidth of about 5% at a frequency of 1.97 THz. Two identical dual-mode cavity resonators are coupled through inter-coupling rods to achieve the desired frequency response with high selectivity as well as a high-level of compactness.

4. CONCLUSION

The applicability of metallic PhC planar circuits to control signal-flow has been demonstrated in the THz regime. A process of design and simulation has shown that the PhC T-junction type switch can control the direction of propagation of THz waves with specified frequencies. We have also designed bandpass filters consisting of point defect resonators with additional dielectric rods. From these results, we can conclude that the photonic crystal planar circuit shows promise as a key technology for constructing high density integrated electromagnetic circuits. In the near future, the PhC devices proposed here will be applied to EM wave propagations in practical photonic crystal circuits.

REFERENCES

1. Siegel, P. H., "Terahertz technology," *IEEE Trans. Microwave Theory Tech.*, Vol. 50, 910–928, 2002.
2. Johnson, S. G., "MIT applied mathematics photonic crystals: A crash course in designer electromagnetism," http://ab-initio.mit.edu/photons/tutorial/spie-course-2012.pdf.
3. Sigalas, M. M., C. T. Chan, K. M. Ho, and C. M. Soukoulis, "Metallic photonic band gap materials," *Phys. Rev. B*, Vol. 52, 11744–11751, 1995.
4. Kuzmiak, V., A. Maradudin, and F. Pincemin, "Photonic band structures of two-dimensional systems containing metallic components," *Phys. Rev. B*, Vol. 50, 16835–16844, 1994.
5. Fan, S., P. R. Villeneuve, J. D. Joannopoulos, and H. A. Haus, "Channel drop tunneling through localized states," *Physical Review Letters*, Vol. 80, No. 5, 950–963, 1998.

Advance of Research on Coaxial Relativistic Backward Wave Oscillator

Yan Teng, Jun Sun, Zhimin Song, Changhua Chen, and Zhaoyu Du
Northwest Institute of Nuclear Technology, P. O. Box 69-13, Xi'an, Shaanxi 710024, China

Abstract— Coaxial relativistic backward wave oscillator (CRBWO) is a new type of high power microwave (HPM) generator remarked by the conversion efficiency higher than 35%. It is found that in CRBWO the promotion of the beam quality, the synchronous harmonic distribution, and the collection of the spent electron on the inner conductor of the coaxial slow wave structure (SWS) accounts for the high efficiency which is confirmed by experiments. According to the special structure and distinguishing physical mechanism, a series of important improvements of the coaxial reflector and the structure with coaxial dual annular cathodes has been developed to enhance both the output power and the conversion efficiency up to 3.63 GW and 45%. And making full use of the both rippled conductors of CRBWO by installing an additional set of SWS into the inner conductor results in the generation of the beating wave with the average output power 5.88 GW and conversion efficiency 41.5%.

1. INTRODUCTION

As high power microwave (HPM) technology matures gradually, relativistic backward wave oscillator (RBWO) attracts more and more attention due to its compact structure and the capacity of repetitive operation [1–4]. The conversion efficiency has been considered to be very important [5]. The coaxial relativistic backward wave oscillator (CRBWO) as shown in Figure 1 developed in recent years presents a practical approach to achieve high output efficiency [6–9]. The numerical simulation [6] and the theoretical calculation [7] on CRBWO predicted its output efficiency up to 35%, which is validated by experiment [8, 9].

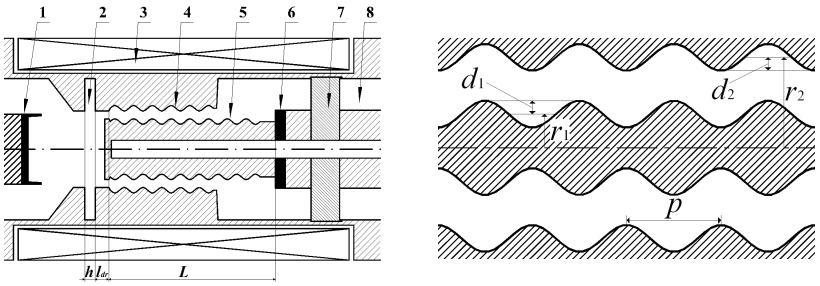

Figure 1: (a) Structure of coaxial RBWO. 1-annular cathode; 2-resonant reflector; 3-guide magnet solenoid; 4-outer SWS; 5-inner SWS; 6-fluting electron collector; 7-equipotential support; 8-output waveguide. (b) Coaxial SWS.

Compared with the hollow slow wave structure (SWS), coaxial SWS reduces the space-charge effect, which makes the electron beam more energetic to amplify the microwave [7]. The synchronous harmonic distribution in coaxial SWS benefits the wave-beam interaction [10]. And the electron dump on the inner conductor ensures the wave-beam interaction efficiently till the electron is collected by the inner conductor [11]. These distinguishing physical characteristics result in the high conversion efficiency.

In recent year, much progress has been made on the development of CRBWO. This paper summarizes the present advance of research on CRBWO and provides suggestion for the development and practical application of this new type of HPM generator.

2. ANALYSIS ON PHYSICAL MODEL

The dispersion with consideration of annular electron beam of CRBWO is demonstrated in Figure 2. The fast space charge wave interacts with the electron beam without energy exchange, while the slower space charge wave and the structure wave merge into a complex conjugate pair with the

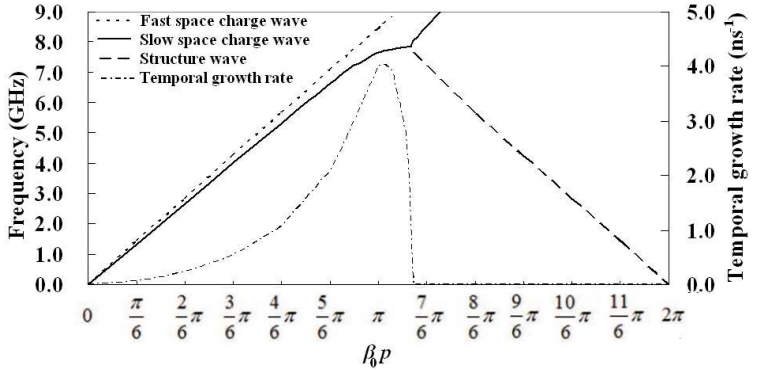

Figure 2: Dispersion of coaxial SWS with the consideration of annular electron beam with energy of 500 keV and current of 400 kA.

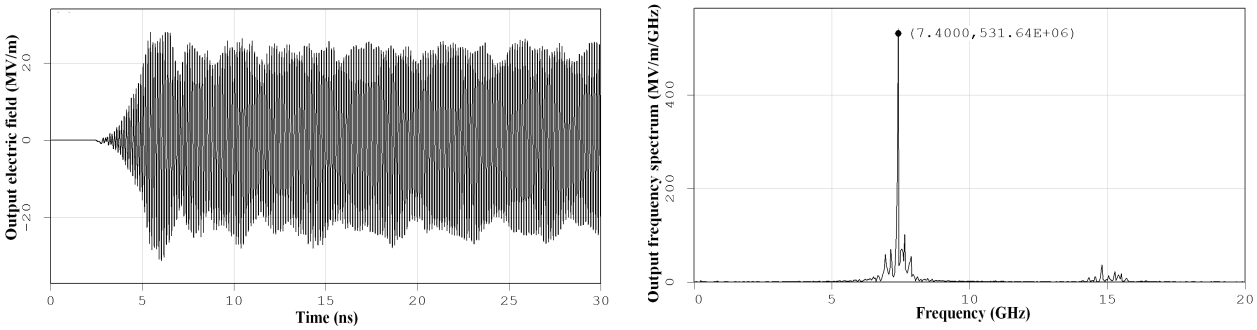

Figure 3: Numerical simulation of CRBWO. (a) Output electric field. (b) Output frequency.

nontrivial temporal growth rate from $\beta_0 p = 0$ to π. The largest temporal growth rate occurs on the branch of the fundamental harmonics.

The starting current of CRBWO as shown in Figure 1(a) is analytically expressed as

$$I_{st} = \frac{\varepsilon_0 \omega_s m_0 \gamma_0^3 v_0^3 \sqrt{\left[(\omega_s^2 - \omega^2)/\omega\omega_s\right]^2 + Q^{-2}}}{e\omega E_h hl \left[\sin\left(\omega h/2v_0\right)/\left(\omega h/2v_0\right)\right] \left|\int_L e^{-j\omega z/v_0} E_{sz}\left(r_b, z\right) dz\right|}, \tag{1}$$

where ε_0 and μ_0 are the vacuum permittivity and permeability, ω_s is the eigen frequency of the finitely long coaxial SWS, m_0 is the electron rest mass, γ_0 is the electron relativistic factor, v_0 is the electron velocity, ω is the operation frequency, Q is the external quality factor of finitely long coaxial SWS, e is the electron charge, E_h is the average modulating electric field in the resonant cavity, E_{sz} (r_b, z) is the normalized electric field in the coaxial SWS, r_b is the radius of the annular beam, $l = -h/2 - l_{dr}$. The result calculated from (1) is in good agreement with those obtained by numerical simulation. It is found that during the startup of oscillation CRBWO is suffering from mode competition, which will be more severely when the electron kinetic energy becomes higher. Therefore, CRBWO should be driven by electron beam of the medium kinetic energy about 400 keV–500 keV [12].

The physical model of the wave-beam interaction in CRBWO, which is described by the self-consistent equations of the electromagnetic field and the electron movement equation, is established for the conversion efficiency prediction [13]. The electron relativistic factors at both ends of SWS are $\gamma_0 = 1.92$ and $\gamma_L = 1.57$ at the stable state, which indicates the conversion efficiency is $(\gamma_0 - \gamma_L)/(\gamma_0 - 1) = 0.38$ [14]. In numerical simulation, the microwave pulse of 754 MW at 7.33 GHz is generated under 508 kV and 3.97 kA with the conversion efficiency 36% as shown in Figure 3.

3. EXPERIMENTAL RESEARCH

In experiments, some important technical improvement has been made. First, the components of CRBWO are surface-treated shown in Figure 4(a), because the problem of the power capacity became more serious due to the introduction of the inner conductor [7]. Second, the equipotential

(a) (b)

Figure 4: Important technical improvement in experiments. (a) Outer and inner ripples coated with the TiN film. (b) Close-up view of equipotential support in Figure 1.

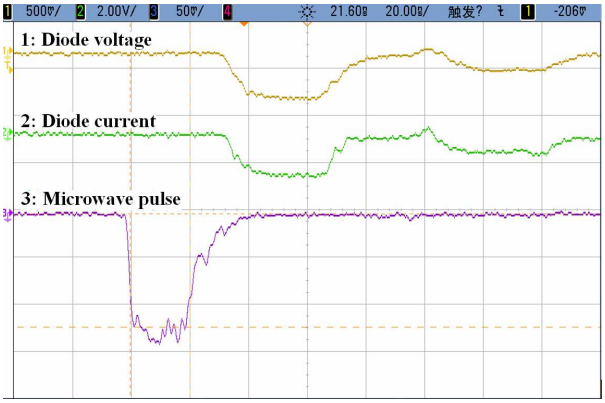

Figure 5: Typical experiment results of CRBWO. Resolution is 20 ns/div on horizontal axis. 1: diode voltage, 505 kV; 2: diode current, 4.26 kA; 3: microwave pulse, 733 MW.

support in Figure 1(a) has been developed as shown in Figure 4(b) to make sure the inner and outer conductors are well coaxial. The equipotential support is carefully designed and optimized for the maximum microwave transmission coefficient so that the electromagnetic wave can propagate through with little reflection.

With these improvements, the output power higher than 730 MW and the pulse duration 20 ns were obtained in the experiment under the diode voltage 500 kV and current 4.3 kA as shown in Figure 5. The conversion efficiency is about 34%, and the output frequency measured by the heterodyne method is 7.4 GHz close to the simulation prediction. This is the first experimental research on CRBWO which has confirmed its high efficiency close up to 35% as the theoretical and numerical expectation. When the diode voltage was up to 560 kV, the output power and efficiency increase 1.01 GW and 36%, but the pulse duration fell to 16 ns. It can be tentatively indicated that beyond the limitation of the power capacity, the output power and the conversion efficiency of CRBWO can be enhanced further [9].

4. FURTHER ENHANCEMENT OF OUTPUT POWER AND CONVERSION EFFICIENCY

4.1. New Type of Coaxial Reflector

The coaxial reflector, which is different from the traditional reflector in Figure 1(a), is developed specialized for CRBWO. Two types of resonant reflector are illustrated in Figure 6, and bunches of the electron beams are compared in Figure 7. It can be concluded that the ratio of the difference between the maximum and minimum modulated velocities to the initial one is 0.13 in the resonant reflector in Figure 1(a), while that is 0.17 in the coaxial reflector [15]. The improvement of the electron modulation results in increasing of the conversion efficiency. In numerical simulation, the conversion efficiency 43% and output power 1.0 GW at 7.3 GHz are obtained under the diode voltage 530 kV and current 4.4 kA [15].

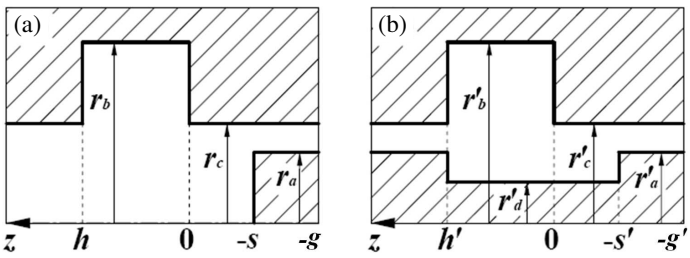

Figure 6: (a) Traditional and (b) improved resonant reflector for CRBWO.

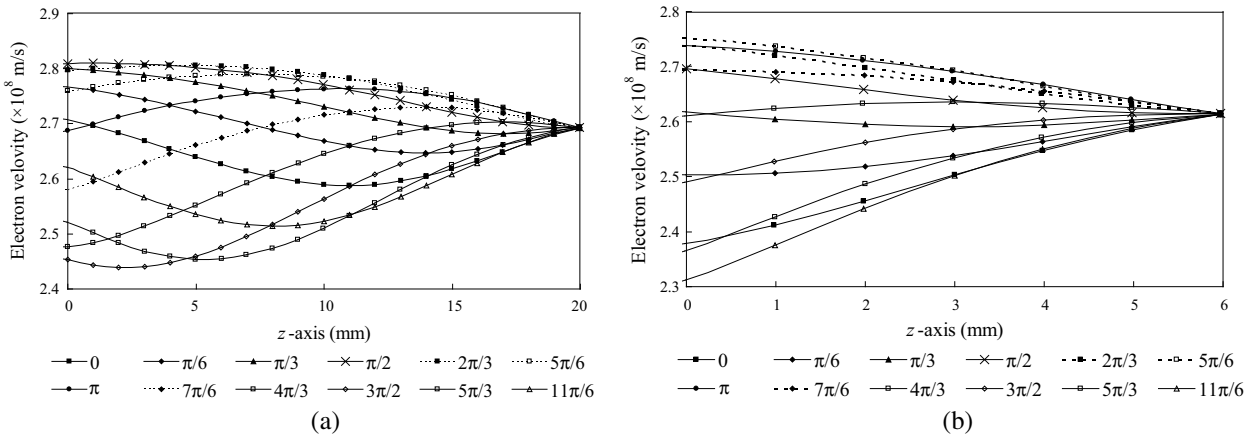

Figure 7: Bunches of electron beam in (a) traditional reflector and (b) coaxial reflector.

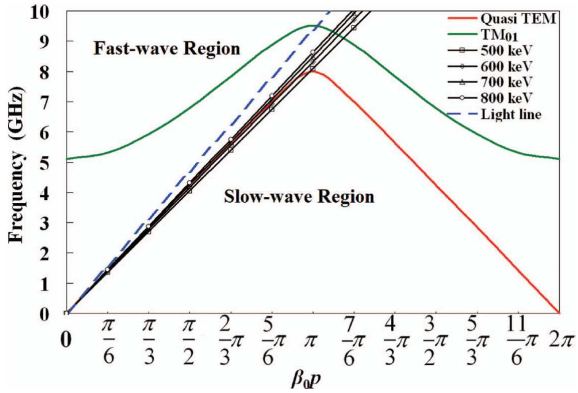

Figure 8: Dispersion of quasi-TEM mode in coaxial SWS and TM_{01} mode in traditional hollow SWS with the same outer average radius, the same ripple depth and the same ripple period.

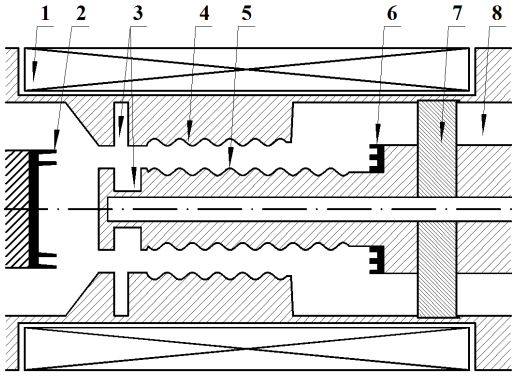

Figure 9: CRBWO with coaxial dual annular cathodes. 1-guide magnet solenoid; 2-coaxial annular cathodes; 3-coaxial reflector; 4-outer SWS; 5-inner SWS; 6-fluting electron collector; 7-coaxial transmission supporter; 8-cylindrical waveguide.

4.2. CRBWO with Coaxial Dual Annular Cathodes

It is found that raising the diode voltage can hardly increase the output power with high conversion efficiency [7]. This can be qualitatively explained by the comparison of dispersion between the coaxial and traditional hollow SWSs as shown in Figure 8, which is divided into fast-wave and slow-wave regions by the light line. The fundamental harmonic branch of the TM_{01} mode in the traditional hollow SWS is located in the fast-wave region and the -1st harmonic branch is located in the slow-wave region. The beam lines are under the light line in any case. Therefore, the operating point determined approximately by the intersection of the wave structure with the beam lines can be found obviously, no matter how high the diode voltage becomes. However, in the coaxial SWS, both the fundamental and the -1st harmonic branches of the quasi-TEM mode in the coaxial SWS lie in the slow-wave region [12]. Thus an electron beam with too large kinetic energy will deviate seriously from the π point of the quasi-TEM mode as shown in Figure 8. This deviation may result in inefficient wave-beam interactions with low conversion efficiency in the coaxial SWS.

However, the double rippled conductors of the coaxial SWS provide a feasible way to increase the output power with high conversion efficiency by the interaction with coaxial dual annular beams. Thus CRBWO with coaxial dual annular cathodes is devised as illustrated in Figure 9. In numerical simulation, the microwave generation is up to 3.63 GW with the conversion efficiency 45% under a diode voltage 659 kV and current 12.27 kA at 8.97 GHz as shown in Figure 10. The currents of the inner and outer annular beams with the same kinetic energies are $I_i = 3.72$ kA and $I_o = 8.55$ kA, respectively.

4.3. HPM Beating Wave Generator

Owing to the special structure and physical characteristics CRBWO also offers the efficient approach to compactly generate the beating-wave HPM pulse, which is proved to be able to decrease the injury threshold of the electronic devices and cause more serious damage [16]. In order to make full use of the inner conductor, the multi-coaxial relativistic backward wave oscillator (M-CRBWO) which produces HPM beating wave is developed as shown in Figure 11, in which one inner cathode feeds the annular beam into the inner RBWO while the two outer cathodes feed the outer CRBWO. The coaxial transmission supporter as illustrated in Figure 12(a) fixes the inner RBWO into the outer CRBWO. It also converts TEM mode in the coaxial waveguide into TM_{01} mode in the cylindrical one with little reflection as shown in Figure 12(b) for the sake of the incoherent combination of the generations of the inner RBWO and outer CRBWO.

In numerical simulation M-CRBWO generates HPM beating wave with the average power 5.88 GW under the diode voltage 724 kV and current 19.57 kA with the conversion efficiency 41.5%.

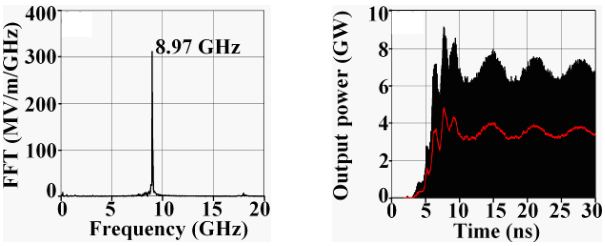

(a) (b)

Figure 10: (a) Output spectrum. (b) Instantaneous waveform and envelope of output power.

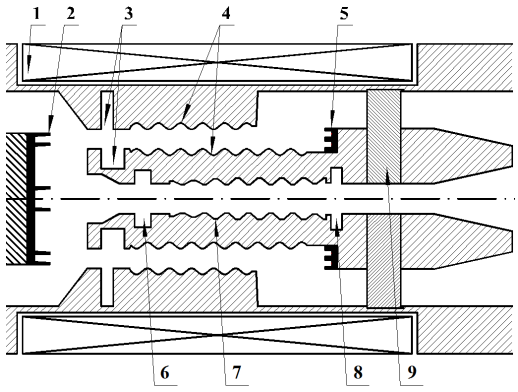

Figure 11: Configuration of M-CRBWO. 1-guide magnet solenoid; 2-coaxial annular cathodes; 3-coaxial reflector; 4-coaxial SWS; 5-fluting electron collector; 6-inner reflector; 7-inner SWS; 8-abstracting cavity; 9-coaxial transmission supporter.

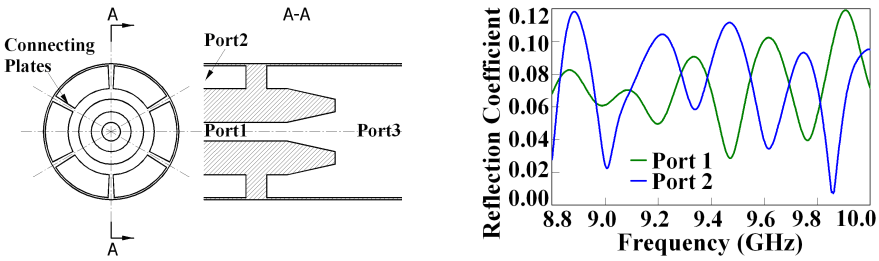

(a) (b)

Figure 12: (a) Schematic of coaxial transmission supporter in Figure 11. (b) Reflection coefficients of electric field.

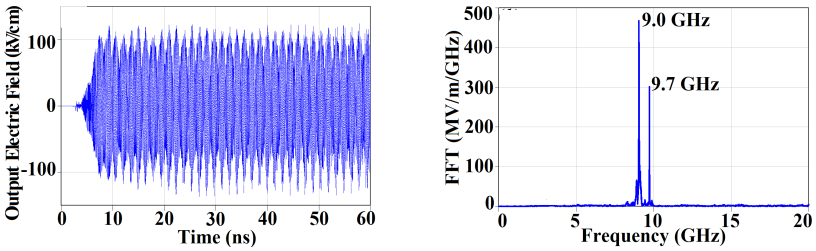

(a) (b)

Figure 13: Beating wave of HPM pulse generated by M-CRBWO. (a) Instantaneous waveform of electric field. (b) Spectrum of electric field.

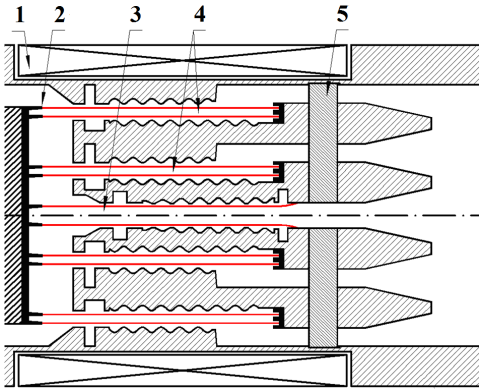

Figure 14: Expanded M-CRBWO. 1-guide magnet solenoid; 2-coaxial annular cathodes; 3-inner RBWO; 4-middle CRBWO and outer CRBWO; 5-coaxial transmission supporter.

The HPM pulse consists of two frequency components 9.0 GHz and 9.7 GHz as shown in Figure 13, corresponding to 2.23 GW and 3.65 GW, respectively [17].

The proposal of M-CRBWO not only puts up a compact generator of HPM beating wave, but also provides a practical method and platform of organizing multiple source devices to realize the synchronous composite HPM output of several narrow-band pulses at one shot. Therefore, M-CRBWO can be expanded into the configuration as shown in Figure 14. As a result, HPM generation combining different frequency components, or different output powers, or different pulse widths, will be obtained.

5. SUMMARY AND CONCLUSION

Since CRBWO with two rippled conductors was put forward in 2002, its notable merit of high efficiency is validated primarily through experiments and the reasons accounting for its high conversion efficiency has been investigated and analyzed. Moreover, a series of important improvements including the coaxial reflector, the coaxial dual annular cathodes, and the beating wave generator, has been made in order based on the special structure and the physical characteristics. However, the further study indicates two key points which are important for the development of CRBWO. First, the physical mechanism of the wave-beam interaction in CRBWO which is remarkably distinguished from that in the traditional hollow RBWO should be researched totally to make full use of its potential of the high efficiency. Second, the technological problems especially such as coaxiality and power capacity should be well considered and optimized delicately to make sure the experimental structure is identical to the physical model.

ACKNOWLEDGMENT

Acknowledgement is made to National Natural Science Foundation of China for the support of this research through Grant No. 11305130.

REFERENCES

1. Nation, J. A., "On the coupling of a high-current relativistic electron beam," *Appl. Phys. Lett.*, Vol. 17, 491–494, 1970.
2. Parker, R. K., R. H. Abrams, B. G. Danly, et al., "Vacuum electronics," *IEEE Tran. Microwave Theory Tech.*, Vol. 50, 835–845, 2002.
3. Wright, E., K. Nguyen, J. Pasour, et al., "Modeling and design of high-power single-beam and multiple-beam inductive output tubes," *Proceedings of IEEE 10th International Vacuum Electronic Conference*, 103–104, 2009.
4. Agee, F. J. and J. A. Gaudet, "Progress in high-power microwave basic research at the Air Force Research Laboratory," *Proceedings of SPIE*, Vol. 4031, 1–6, 2000.
5. Swegle, J. A. and J. N. Benford, "High-power microwaves at 25 years: The current state of development," *Proceedings of 12th International Conf. on High-power Particle Beams*, Vol. 1, 149–152, Jun. 1998.
6. Liu, G. Z., "Numerical simulation research on a relativistic high power microwave device with coaxial slow wave structure," *Proceedings of 5th High Power Microwave Conf.*, 2–6, 2002.

7. Liu, G. Z., C. H. Chen, H. Shao, Y. M. Hu, et al., "A Cerenkov generator with coaxial slow wave structure," *J. Appl. Phys.*, Vol. 103, 093303, Feb. 2008.
8. Teng, Y., R. Z. Xiao, Z. M. Song, et al., "High-efficiency coaxial relativistic backward wave oscillator," *Rev. Sci. Instrum.*, Vol. 82, 024701, 2011.
9. Teng, Y., C. H. Chen, H. Shao, et al., "Design and efficient operation of a coaxial RBWO," *Laser Part. Beams*, Vol. 31, 321–331, 2013.
10. Teng, Y., R. Z. Xiao, Z. M. Song, et al., "Wave-beam interaction in coaxial relativistic backward wave oscillator," *High Power Laser and Particle Beams*, Vol. 24, 175–180, 2012.
11. Teng, Y., Z. M. Song, J. Sun, et al., "Efficiency enhancement of RBWO by introduction of rippled inner conductor," *Proceedings of 25th Asia-Pacific Microwave Conference*, 215–218, 2011.
12. Teng, Y., G. Z. Liu, C. X. Tang, et al., "Starting current of coaxial relative backward wave oscillator," *Phys. Plasmas*, Vol. 17, 063108, 2010.
13. Levush, B., T. M. Antonsen, Jr., A. Bromborsky, et al., "Theory of relativistic backward-wave oscillators with end reflections," *IEEE Trans. Plasma Sci.*, Vol. 20, 263–280, 1994.
14. Huang, F., D. Wang, and Q. Z. Xing, "Study on the region of instable beam-wave interaction in a relativistic backward wave oscillator," *High Power Laser and Particle Beams*, Vol. 17, 1547–1552, 2005.
15. Teng, Y., G. Z. Liu, H. Shao, et al., "A new reflector designed for efficiency enhancement of CRBWO," *IEEE Trans. Plasma Sci.*, Vol. 6, No. 37, 1062–1068, 2009.
16. Fang, J. Y., G. Z. Liu, P. Li, et al., "Experimental study of the high power microwave pulse width effect," *High Power Laser and Particle Beams*, Vol. 5, 639–642, 1999.
17. Teng, Y., T. Z. Liang, and J. Sun, "Generation of beating wave by multi-coaxial relativistic backward wave oscillator," *Laser Part. Beams*, Vol. 31, 703–714, 2013.

Reduction of Bend Losses at Sharp Bend in Post Wall Waveguide

Ken'ichiro Yashiro[1] **and Ning Guan**[2]

[1]Chiba University, Japan
[2]Fujikura Ltd., Japan

Abstract— In this paper, we consider some techniques to reduce the bend losses. We apply the method of moments to analyse the reflection of millimeter waves from the right-angle bend. The global basis functions were used to reduce the number of unknowns per metal post and the necessary computer memory is also reduced. Furthermore, the Galerkin method was used to obtain a sytem of linear equations. Therefore, the resulting matrix is symmetric. Since the objects were confined to circular metallic posts, the elements of matrix were calculated in closed form and no numerical integration is needed.

It will be shown that only a few additional posts are set at appropriate positions in the post wall waveguide, almost all incident waves go around the corner and the bend losses are minimized. Especially, only one additional metallic post is enough to minimize the bend losses.

1. INTRODUCTION

A post wall waveguide is a promising candidate for the development of low cost circuits in the millimetre-wave region. Recently, the integrated-waveguide scheme was proposed by Hirokawa et al. and the feed waveguide for a parallel-plate slot array antenna was composed of densely arrayed posts on the same layer as the parallel plates [1]. The integrated-waveguide filter was demonstrated by using the post-wall waveguide technique [2].

The post-wall waveguide consists of two rows of metal posts sandwiched between two parallel metal plates as shown in Figure 1. In some instances, the post-wall waveguide may be bent to fabricate millimeter-wave integrated circuits. Various bend geometries was introduced [3]. These geometries include the right-angle bend with a via, chamfered bend and rounded bend. The influence of the geometry of the chamfered bends was investigated by HFSS and the transmission coefficients S_{21} were determined [4].

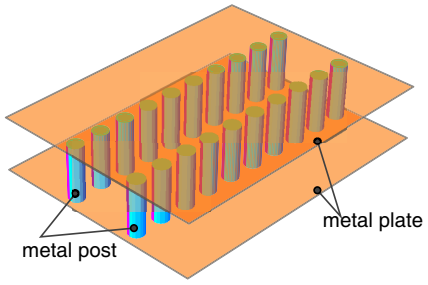

Figure 1: Post-wall waveguide.

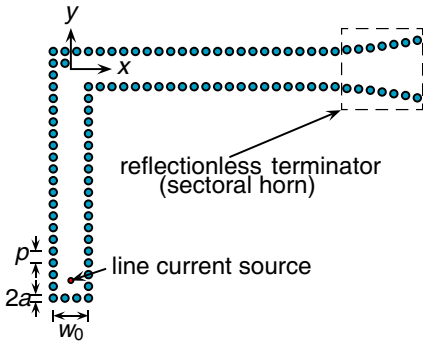

Figure 2: Geometry of problem.

In this paper, we consider some geometries of bends to reduce the bend losses. We will analyse the reflections from the right-angle bend. The method of moments (MoM) with global base [5] is used to obatin the distribution of electromagnetic fields. The global basis functions were used to reduce the number of unknowns per metal post and the necessary computer memory is also reduced. Furthermore, the Galerkin method was used to obtain a sytem of linear equations. Therefore, the resulting matrix is symmetric. Since the objects were confined to circular metallic posts, the elements of matrix were calculated in closed form and no numerical integration is needed. The standing waves will be computed and the reflections from the bends are evaluated from the voltage standing wave ratio (VSWR).

2. FORMULATION

The geometry of the problem consists of N posts as illustrated in Figure 2. Suppose that the incident plane wave is a cylindrical wave radiated from a line current source located at (x_0, y_0). One end of the waveguide is short-terminated behind the line source and the other end is connected to a H-plane sectoral horn, which works as reflectionless terminator.

The electromagnetic fields are assumed to be uniform along z-axis. A time dependence $e^{j\omega t}$ is assumed and suppressed throughout. Then the incident wave is assumed to be expressed as

$$E_z^i(\vec{\rho}) = \frac{E_0}{j4} H_0^{(2)}(k_0|\vec{\rho} - \vec{\rho}_0|) \tag{1}$$

where $H_0^{(2)}(x)$, k_0 and $\vec{\rho}_0$ are the Hankel function of the second kind of 0-th order, the wave number and a location of source, respectively. Let $J_z^\nu(\vec{\rho})$ be the current density on the ν-th cylinder of which cross-section has a circumference C_ν with a radius a_ν. Then the scattered wave is described by

$$E_z^s(\vec{\rho}) = -\frac{k_0\zeta_0}{4} \cdot \sum_{\nu=1}^{N} \int_{C_\nu} H_0^{(2)}(k_0|\vec{\rho} - \vec{\rho}'|) J_z^\nu(\vec{\rho}')d\rho' \tag{2}$$

where $\zeta_0 (= \sqrt{\mu_0/\varepsilon_0})$ is the intrinsic impedance of free space. The total tangential component of electric fields vanishes on every post surface. Hence,

$$E_z^s(\vec{\rho}) = -E_z^i(\vec{\rho}), \quad \vec{\rho} \in C_\nu \ (\nu = 1, 2, \ldots, N) \tag{3}$$

Equation (3) give a system of boundary integral equations.

Here we introduce a local polar coordinate system (r_ν, θ_ν) of which origin is the center of C_ν, i.e., $\vec{\rho}_\nu$. Then $\vec{\rho} = \vec{\rho}_\nu + \vec{r}_\nu$. Since the current density should be periodic along C_ν, each current is expanded in terms of a set of global basis functions $e^{-jn\theta_\nu}$ as

$$J_z^\nu(\vec{\rho}') = E_0 \sum_{n=-N_\nu}^{N_\nu} \chi_n^\nu e^{-jn\theta'_\nu} \tag{4}$$

Substituting (4) into (2) and using Graf's addition theorem [6]

$$H_n^{(2)}(k_0 R) \begin{matrix}\cos \\ \sin\end{matrix} n\psi = \sum_{m=-\infty}^{\infty} H_{n+m}^{(2)}(k_0 R_\nu) J_m(k_0 a_\nu) \begin{matrix}\cos \\ \sin\end{matrix} m\varphi \tag{5}$$

we integrate the resulting equation to obtain

$$E_z^s(\vec{\rho}) = -E_0 \frac{\pi k_0 \zeta_0}{2} \sum_{\nu=1}^{N} \sum_{n=-N_\nu}^{N_\nu} \chi_n^\nu a_\nu J_n(k_0 a_\nu) H_n^{(2)}(k_0 R_\nu) e^{-jn\theta_\nu} \tag{6}$$

where $R_\nu = |\vec{\rho} - \vec{\rho}_\nu|$, θ_ν is an angle between $\vec{\rho} - \vec{\rho}_\nu$ and x-axis. Three points $\vec{\rho}$, $\vec{\rho}'$, $\vec{\rho}_\nu$ form a triangle with sides, $\vec{\rho} - \vec{\rho}'$, $\vec{\rho} - \vec{\rho}_\nu$, $\vec{\rho}' - \vec{\rho}_\nu$, and ψ and φ are vertex angles opposite to $\vec{\rho}' - \vec{\rho}_\nu$ and $\vec{\rho} - \vec{\rho}'$, respectively.

We take an inner product of (3) with a set of weighting functions to obtain a matrix equation. The basis functions are also chosen as weighting functions. In other words, the Galerkin's method is used. By using Graf's addition theorem, the right side of the inner product of (3) with $e^{jm\theta_\mu}$ yields

$$-\int_{C_\mu} E_z^i(\vec{\rho}) e^{jm\theta_\mu} d\rho = -\frac{\pi}{j2k_0} E_0 (-1)^m k_0 a_\mu J_m(k_0 a_\mu) H_m^{(2)}(k_0 R_{\mu 0}) e^{jm\alpha_{\mu 0}} \tag{7}$$

where $R_{\mu 0} = |\vec{\rho}_\mu - \vec{\rho}_0|$, and $\alpha_{\mu 0}$ is an angle between $\vec{\rho}_\mu - \vec{\rho}_0$ and x-axis.

The left side of the inner product of (3) with $e^{jm\theta_\mu}$ does not depend on the incident wave except χ_n^ν. Hence its integration is carried out in the same way as the case of incident plane wave in [5].And the resulting matrix equation is given by

$$\begin{bmatrix} A_{11} & A_{12} & \ldots & A_{1N} \\ A_{21} & A_{22} & \ldots & A_{2N} \\ \cdot & \cdot & \ldots & \cdot \\ A_{N1} & A_{N2} & \ldots & A_{NN} \end{bmatrix} \begin{bmatrix} X_1 \\ X_2 \\ \cdot \\ X_N \end{bmatrix} = \begin{bmatrix} B_1 \\ B_2 \\ \cdot \\ B_N \end{bmatrix} \tag{8}$$

where $A_{\nu\nu}$ and $A_{\mu\nu}$ are $(2N_\nu+1)\times(2N_\nu+1)$ diagonal matrix and $(2N_\mu+1)\times(2N_\nu+1)$ matrix, respectively, and X_ν and B_ν are $2N_\nu+1$ column vectors, and their elements are given as follows:

$$a_{mn}^{\nu\nu} = -\frac{\pi^2\zeta_0}{k_0}(k_0a_\nu)^2 J_n(k_0a_\nu)H_n^{(2)}(k_0a_\nu)\delta_{mn} \tag{9}$$

$$a_{mn}^{\mu\nu} = -\frac{\pi^2\zeta_0}{k_0}k_0a_\mu k_0a_\nu J_m(k_0a_\mu)J_n(k_0a_\nu)H_{n-m}^{(2)}(k_0R_{\mu\nu})e^{-j(n-m)\alpha_{\mu\nu}} \tag{10}$$

$$b_m^\mu = -\frac{\pi}{j2k_0}(-1)^m k_0a_\mu J_m\left(k_0a_\mu\right)H_m^{(2)}\left(k_0R_{\mu0}\right)e^{jm\alpha_{\mu0}} \tag{11}$$

where δ_{mn} is the Kronecker delta, $R_{\mu\nu}=|\vec{\rho}_\mu-\vec{\rho}_\nu|$, and $\alpha_{\mu\nu}$ is an angle between $\vec{\rho}_\mu-\vec{\rho}_\nu$ and x-axis.

The magnetic fields can be calculated from the Maxwell equation.

$$H_x^i(\vec{\rho}) = -\frac{E_0}{4\zeta_0}H_1^{(2)}(k_0|\vec{\rho}-\vec{\rho}_0|)\frac{y-y_0}{|\vec{\rho}-\vec{\rho}_0|} = -\frac{E_0}{4\zeta_0}H_1^{(2)}(k_0|\vec{\rho}-\vec{\rho}_0|)\sin\theta_0 \tag{12}$$

$$H_y^i(\vec{\rho}) = \frac{E_0}{4\zeta_0}H_1^{(2)}(k_0|\vec{\rho}-\vec{\rho}_0|)\frac{x-x_0}{|\vec{\rho}-\vec{\rho}_0|} = \frac{E_0}{4\zeta_0}H_1^{(2)}(k_0|\vec{\rho}-\vec{\rho}_0|)\cos\theta_0 \tag{13}$$

$$\begin{aligned} H_x^s(\vec{\rho}) = -E_0\frac{\pi}{2}\sum_{\nu=1}^{N}\Bigg\{&\cos\theta_\nu\sum_{n=-N_\nu}^{N_\nu}\chi_n^\nu k_0a_\nu J_n(k_0a_\nu)e^{-jn\theta_\nu}\frac{n}{k_0R_\nu}H_n^{(2)}(k_0R_\nu)\\ &+j\sin\theta_\nu\sum_{n=-N_\nu}^{N_\nu}\chi_n^\nu k_0a_\nu J_n(k_0a_\nu)e^{-jn\theta_\nu}H_n^{(2)'}(k_0R_\nu)\Bigg\}\end{aligned} \tag{14}$$

$$\begin{aligned} H_y^s(\vec{\rho}) = -E_0\frac{\pi}{2}\sum_{\nu=1}^{N}\Bigg\{&-j\cos\theta_\nu\sum_{n=-N_\nu}^{N_\nu}\chi_n^\nu k_0a_\nu J_n(k_0a_\nu)e^{-jn\theta_\nu}H_n^{(2)'}(k_0R_\nu)\\ &+\sin\theta_\nu\sum_{n=-N_\nu}^{N_\nu}\chi_n^\nu k_0a_\nu J_n(k_0a_\nu)e^{-jn\theta_\nu}\frac{n}{k_0R_\nu}H_n^{(2)}(k_0R_\nu)\Bigg\}\end{aligned} \tag{15}$$

3. NUMERICAL RESULTS

For numerical computation, all the lengths are normalized by the wavelength in free space. The following values are used: $a=0.05\lambda$, $p=0.2\lambda$ and $w_0=0.6\lambda$, where λ is the wavelength in free space.

If the reflection at the open end of the post wall waveguide is large, it is difficult to evaluate qualitatively the reflected wave from the bend. Therefore, an H-plane sectoral horn is connected to the open end of the waveguide in order to reduce the reflected waves there. It is known [7] that a family of hyperbolic horns have the cross-sectional area S related to the distance x through the hyperbolic functions. Hence, the width w of horn can be given by

$$w = w_0\left(\cosh\alpha x + T\sinh\alpha x\right) \tag{16}$$

where w_0 is the width of waveguide, and α and T are constants. For $T=1$, the horn is an exponential horn.

The electric field distributions in the straight waveguide excited by a line current source are shown in Figure 3. Figure 3(a) shows the amplitude distribution of electric field in the post wall waveguide terminated with open end. It is seen from Figure 3(a) that some part of the enegy is reflected at the open end and standing waves are created. A horn is connected to the open end of waveguide so that the change in impedance at the end of a waveguide is gradual. Figure 3(b) shows the amplitude distribution of electric field in the post wall waveguide terminated with horn. We can see from the figure that almost no standing waves are formed.

Here, the horn is adopted as a reflectionless terminator. So the type of horn used is chosen according to the voltage standing wave ratio (VSWR). The length of horn is set to be 6λ long. Figure 4 shows the VSWR as a function of the parameter α with $T=0.2$. The VSWR for the waveguide terminated with open end is also shown in Figure 4. For the waveguide terminated with open end, the VSWR is 2.193 and the reflection coefficient $|\Gamma|=(VSWR-1)/(VSWR+1)$ is 0.374. However, the reflections at the end of waveguide is suppressed by terminating the horn.

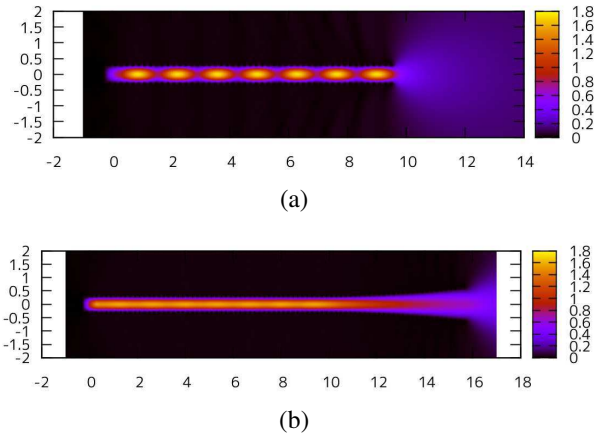

Figure 3: Electric field distribution in terminated post wall waveguide. (a) Waveguide terminated with open end. (b) Waveguide terminated with horn.

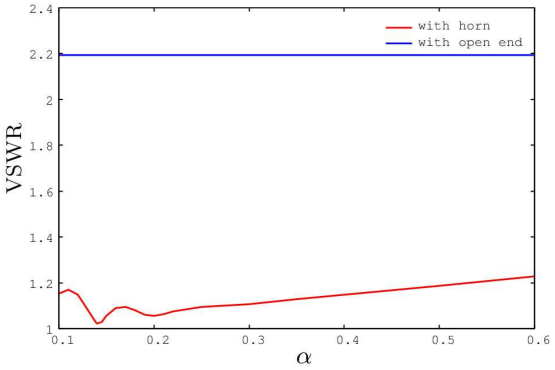

Figure 4: VSWR for post wall waveguide terminated by hyperbolic horn.

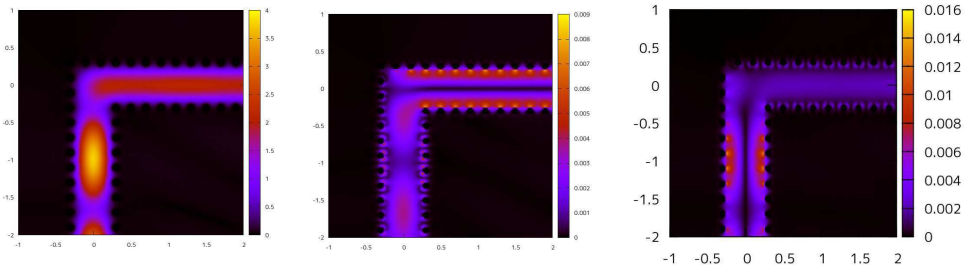

Figure 5: Amplitude distributions of electromagnetic fields near right-angle bend.

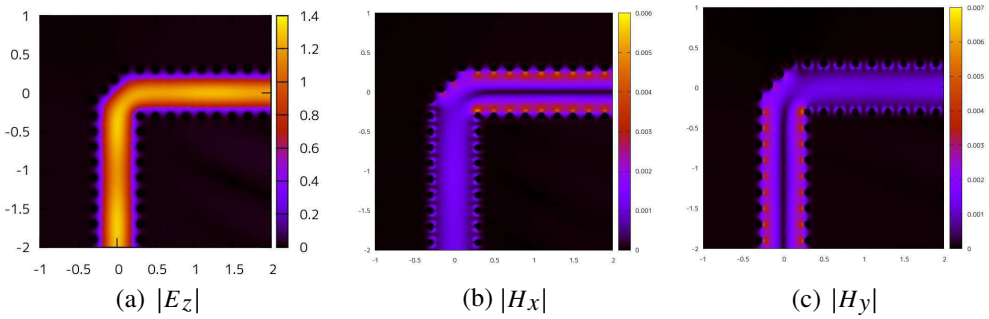

Figure 6: Amplitude distributions of electromagnetic fields near the type A of the bend.

The VSWR is 1.055 for horn with $\alpha = 0.2$ and then $|\Gamma| = 0.0268$. The amplitude distribution in Figure 3(b) is corresponding to this case. These values are used in the following computations.

Figures 5(a)–(c) show the amplitude distributions of the electromagnetic fields near the bend. The waveguide is only just bent without any sorts of devices. In this case, it is seen that the bend causes reflections and produces standing waves of which the VSWR is 3.26.

To suppress the reflections from the bend, the two types of bends are considered. In one type A of the bend, odd number of posts are removed from the corner of the outer sidewall and a straight array of posts are added to close the resulting aperture. Figures 6(a)–(c) show the amplitude distribution of the fields in the type A of bend in case of replacement of three posts. The bend prevents the reflections and the VSWR is 1.12.

The other type B of the bend has an additional post near the corner as shown in Figure 7. Figure 8 shows the VSWR as a function of position x of an addtional post. The right-angle bend with a post located at appropriate position does not cause reflections. The amplitude distributions of the electromagnetic fields near the bend with an additional post at $x = -0.09\lambda$ are shown in Figure 9. It is seen from the figures that almost all incident wave goes around the corner and the bend losses are minimized.

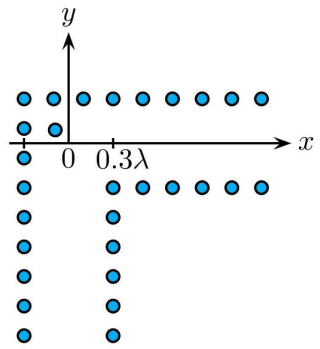

Figure 7: The type B of the bend.

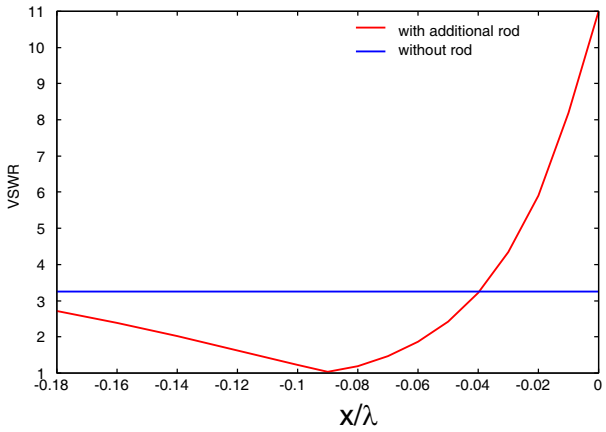

Figure 8: The VSWR for type B of the bend.

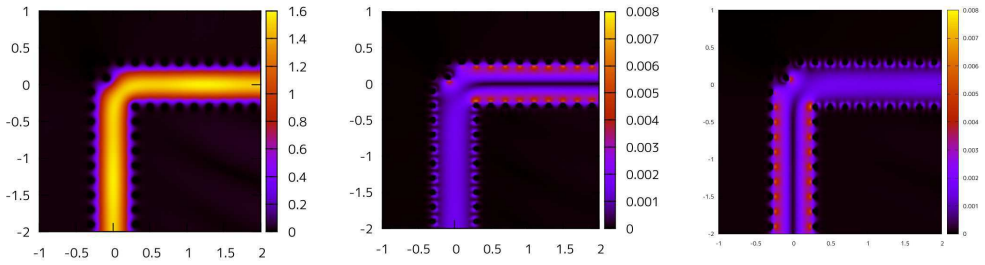

(a) $|Ez|$ (b) $|Hx|$ (c) $|Hy|$

Figure 9: Amplitude distributions of electromagnetic fields near the type B of the bend. The additional post is located at $(-0.09\lambda, 0.09\lambda)$.

4. CONCLUSION

The reflection of the guided mode at waveguide bend was examined by the mehod of moments with global basis functions. Only a few additional posts are set at appropriate positions in the post wall waveguide to reduce the bend losses. Especially, only one additional metallic post is enough to minimize the bend losses.

REFERENCES

1. Hirokawa, J. and M. Ando, "Single-layer feed waveguide consisting of posts for plane TEM wave excitation in parallel plates," *IEEE Trans. Antennas Propagat.*, Vol. 46, No. 5, 625–630, 1998.
2. Deslandes, D. and K. Wu, "Single-substrate integration technique of planar circuits and waveguide filters," *IEEE Trans. Microwave Theory Tech.*, Vol. 51, No. 2, 593–596, 2003.
3. Suntives, A. and R. Abhari, "Design and characterization of the EBG waveguide-based interconnects," *IEEE Trans. Adv. Packag.*, Vol. 30, No. 2, 163–170, 2007.
4. Bochra, R., F. Mohammed, and J. Tao, "Design of optimal chamfered bends in rectangular substrate integrated waveguide," *Int. J. Comp. Sci. Iss.*, Vol. 8, No. 2, 376–379, 2011.
5. Yashiro, K., "Global base approach to scattering by conducting circular cylinders," *Proceedings of ICEAA*, 1453–1456, Torino, Italy, September 2013.
6. Abramowitz, M. and I. A. Stegun, *Handbook of Mathematical Functions with Formulas, Graphs, and Mathematical Tables*, 363, Dover, New York, 1972.
7. Lesniewski, P., "Discrete component equivalent circuit for Webster's horns," *Appl. Acoust.*, Vol. 44, No. 2, 117–124, 1995.

The Squarax Amplifier: An Electromagnetic and Thermo-mechanical Innovation

Alberto Leggieri, **Davide Passi**, **and Franco Di Paolo**
Dipartimento di Ingegneria Elettronica, Università degli Studi di Roma "Tor Vergata"
Via del Politecnico, 1, Roma 00133, Italy

Abstract— This paper describes a novel broad band Spatial Power Combiner (SPC) Amplifier based on Square Coaxial (Squarax) Transmission Line (TL), able to tolerate the Thermo-Mechanical effects due to the transistor heating. In the proposed SPC, Fin Line to microstrip transitions (FLuS) are inserted into the Squarax TL, in order to connect many Monolithic Microwave Integrated Circuit (MMIC) Solid State Power Amplifier (SSPA) while maintaining an easy integration. The proposed structure has some advantages over the traditional SPC's. The Squarax SPC geometry allows the feeding of a higher number of MMIC than in a Waveguide SPC, and its straight profile allows to connect simple and low-cost square or rectangular heat-sink devices with high thermal dissipation attitude. Conversely, coaxial SPC needs apposite circular heat-sinkers that requires expensive custom production. Squarax structure ensures high power outputs and small sizes, together with theoretical DC frequency cut-off. In this work, a 16 cards Squarax SPC in the operative bandwidth 4–18 GHz has been designed, able to account for 32 MMIC SSPA's. The design Electromagnetic and Thermo-structural simulation of the proposed device are shown.

1. INTRODUCTION

Spatial power amplifiers (SPA) are high power amplifiers based on the Spatial Power Combining approach. In this case, power dividing and combining is performed in a parallel way. Actually, high power levels are obtained by Travelling Wave Tube Amplifiers. In comparing with such tubes, SSPA's based amplifiers offers short warm-up time, low standby mode power consumption and a reduced size [1]. The traditional approach to obtain a significant power output with SSPA's is the binary combining of many transistors through microstrip Transmission Lines [2, 3].

Binary combining of many transistors through microstrip Transmission Lines is limited to the losses which each printed transmission-line combiner inserts. Binary combining, in addition, limits the number of devices to a power of two.

In comparing to the binary combining, SPC approach offers high device compactness, low combining losses, higher available power outputs and losses are rather independent with the number of used PA's. In SPC the independent coupling of individual devices within the TL makes a little sensitivity to single-point failures, ensuring graceful degradation of output power. With a constant target output power, combining many devices by using the spatial approach allows to reduce size, weight, power draw, and cost [1, 4–10]. Since the loss is rather constant to the number of amplifiers, their size limits the combiner area with both the contributions of the active devices, the bias distribution and heat sink systems, which are especially important in order to avoid performance degradation and even device failure.

In this paper an innovative solution for SPC PA is shown. The proposed system is based on a Squarax TL [11], and use a Fin-Line [12] to microstrip (FLuS) transition to convert the energy of a square coaxial TEM fundamental mode to a microstrip quasi-TEM mode, which is then amplified by a SSPA. Many SSPA's outputs are recombined by the same principle. In order to maximize the useful space for energy dividing and combining in the SPC, the Squarax TL configuration has been adopted. Since the FLuS cards can be placed all around the inner conductor of Squarax TL, a high number of such structures can be driven: This provide a high power output when MMIC PA's will be employed. In order to hold up the inner conductor of the Squarax several metal cards are used, each one holding FLuS transitions, as will be shown later. A practical important aspect is the straightness of the Squarax SPC profile, which allows to be connected to a simple square or rectangular heat-sink devices, easily available in the market: it is completely different from the case of a Circular Coaxial SPC which needs apposite circular heat-sinker that require a custom production. Similarly, using a Circular Coaxial SPC there is the need of FLuS cards with a circular section of the lateral profile and with not planar faces, more expensive than simple rectangular cards as in the case of Squarax SPC.

Several circuital and technological solutions have been adopted. In order to reduce the combining loss and size, exponential FLuS transitions have been considered, using antipodal configuration. In order to improve the operative band, a parasitic void has been implemented by inserting an anti-resonance metal in the antipodal FLuS transitions [13]. Since electromagnetic characteristics depend on various factors, such as the FLuS shape and the number of cards, a computational electromagnetic model has been developed using HFSS version 15. The power dissipation of the MMIC SSPA's produces a considerable temperature increase and induces a thermal expansion of both the PA's and the connected structure. Transistor damage or an alteration of the desired electromagnetic behavior may occur. In order to inquire about these multiple aspects, a Thermo-mechanical model has been implemented on Comsol Multiphysic Version 4.

2. THE SQUARAX AMPLIFIER

In TL active SPC architecture each amplifier is connected to a probe, in order to couple its input port mode with the energy of the TL propagating mode. Several amplifiers, usually MMIC's, are mounted in metallic cards containing their related functional circuitry, like probes, transitions, biasing: such cards are placed in parallel inside the TL. Input probes, printed on each card, receive a portion of the input power so that many lower amplitude signals are obtained, which are then amplified by PA's and routed to output probes [11]. As much, these outputs are recombined coherently in an output TL by using the same principle, so the circuit consists of a back-to-back configuration of splitting and combining structure used as through elements.

In TL SPC architecture, the energy is distributed in low loss electromagnetic modes and combined in the TL dielectric, for example in a closed waveguide and, above all, using a single stage of power combining; this reduces the ohmic combining losses and makes it quite independent to the number of devices [9].

The Squarax TL is a coaxial line having square inner and outer conductors [14]. In order to maximize the useful space of mode combining of the SPC, the same FLuS structures can be implemented to couple a quasi TEM mode driven by a microstrip to a portion of the TEM mode of the Squarax. Circular Coaxial Transmission Lines (CCTL's) have been used extensively in the past, but square coaxial lines may be preferable since the presence of flat rather than circular surfaces offers mechanical advantages [15]. The Squarax constant ratio of the outer to inner conductors was chosen to $3:1$ so that the characteristic impedance of the SCTL is as close as possible to the $50\,\Omega$ that is $61\,\Omega$ [15, 16]. An example of an 8 carriers, each with two FLuS's, inside the central part of the SCTL is depicted in Figure 1. The two pyramidal tapers allows for the connection with N type connectors.

Electromagnetic design of the Squarax SPC Amplifier proposed in this work is widely described in [11], we report only a briefly description of its main features. In this paper we mostly provide useful details on the thermo mechanical features of such device.

A microstrip taper has been used as a broad-band impedance transformer between the tapered-slot antenna and MMIC amplifier, since the characteristic impedance at the taper end of the probe can be different to the impedance required by the PA input port matching condition [10]. In order to reduce the combining loss, the shape of the antenna taper has to be chosen properly so that return loss can be minimized within the frequency band of interest. Several spatial profiles of FL can be implemented: exponential, parabolic, sine, sine squared, cosine and cosine squared taper [12]. The former is chosen to ensure the smoothness of the taper, whereby very good matched-load is readily available for the Squarax, because this transition indeed reflects a small amount of incident power. From Riccati's equation it is possible to find the reflection coefficient trend with respect the

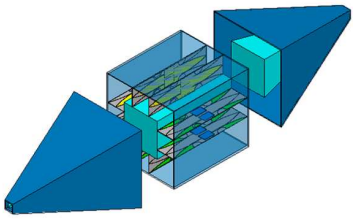

Figure 1: Example of an 8 carriers, each with two FLuS's, inside the central part of the Squarax SPC.

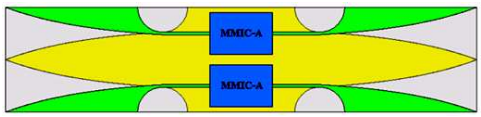

Figure 2: The carrier, holding FLuS's and two MMIC-PA's.

product βl is given by (1) [17] and Microstrip Lines were designed following Hammerstad formulas reported in [18].

$$\Gamma = \frac{1}{2} e^{-j\beta l} \ln\left(\frac{z_1}{z_2}\right) \frac{\sin(\beta l)}{\beta l} \tag{1}$$

In order to obtain great system integration, Antipodal configuration of Fin-Line to microstrip transition is an attractive solution [13], but presents evanescent modes inducing resonances. In order to solve this problem, the Fin-Line discontinuities can be designed so as to break the slot electric field lines. An useful solution has been applied; it consists to model a circular section through the metal sheet in the area where the parasitic slot might create [13].

In order to improve the return loss, a dielectric Quarter Wave Transformer (QWT) has also been provided.

More cards can be inserted by proper impedance matching between the central section and the input/outputs ports. Each cards is composed with input and output dual FLuS transitions, two MMIC's, together with their bias circuitry, and a carrier holding all these components. The carrier is made with copper, to assure high thermal conductivity, and an interface sheet composed with CuMo compound, is placed under the MMIC to assure thermo-mechanical compatibility between GaAs MMIC and the carrier. A picture of the carrier is reported in Figure 2.

In the actual case, FLuS uses the rigid Al_2O_3 substrate, brazed on Cu carrier. The square profile of the Squarax determines the defined plane of polarization and the wave can travel down to the FLuS transitions to coherently couple their energy to the microstrips. Since such transitions can be placed all around the inner conductor of the Squarax, a higher number of FLuS transitions can be illuminated than in other TL, for example a rectangular WG [1, 8, 10]. Therefore a high power output can be reached, because the power output of a SPC amplifier increases with the number of its internal coupled active devices.

In order to have high power output, in every SPC, SSPA's may be employed at maximum efficiency and they produce significant power dissipations. A thermo-mechanical modification of the carrier shape, induced by such power dissipation, may induce significant modification on the electromagnetic behavior of the guiding and combining SPC structures. For this reason a good heat-sinking subsystem is recommended.

Due to the straightness of its profile, the Squarax SPC can be connected to a simple square or rectangular heat-sink devices, which is easily available with a low cost. A classical circular CCTL needs a heat-sink with a semicircular cross section which has to be specially designed, requiring higher cost. Moreover, when using a CCTL as a SPC, cards with a circular section of the lateral profile of the substrate are required; this further increases the manufacturing costs.

In a Squarax TL, in addition to the TEM fundamental mode, higher order modes can propagate. The higher order mode spectrum of circular coaxial lines is very well known and, as described in [15], a SCTL can be used alternatively to a CCTL with its technological advantages, maintaining great wave-guiding properties as for the CCTL. However, when the CCTL is loaded with the FLuS, ε_r changes, and a numerical optimization is mandatory.

3. COMPUTATIONAL DESIGN AND SIMULATIONS OF A 16 CARDS SQUARAX SPC

3.1. Computational Electromagnetic Model and Analysis

Return loss characteristic of the passive structure SPC depends also on the number of inserted cards. In order to meet the operating power goals with the fewest possible devices, to minimize the insertion loss and to maximize the return loss, the better configuration can be found selecting the profile shape of the FLuS (including the microstrip transformer and the anti-resonance circular section) which allows to accommodate the optimum number of cards and the number of devices per card to insert in the target Squarax. A 16 cards Squarax SPC in the operative bandwidth 4–18 GHz has been designed, able to account for 32 MMIC SSPA's. The inner part has the cross sections $a = 13.524\,\text{mm}$ $b = 33.524\,\text{mm}$, while the tapered transition from coaxial input and output sections to the inner part is 60 mm long. Exponential tapered FL transitions are mounted on 16 cards placed at each side of the Squarax. The FLuS are made on Al_2O_3 substrate, with a thickness of 0.254 mm. Each card contains two FLuS connected back to back with double asymmetrical QWT sections. The Squarax conductors have been considered as copper, which has excellent thermal conductivity. The simulation of the proposed device has been performed, using HFSS version 15 of Ansys-Ansoft. The 3D simulated structure is shown in Figure 3. Simulation setup has been

developed in order to reach the desired high performances which distinguish the proposed device from the classical spatial power combiner-dividers.

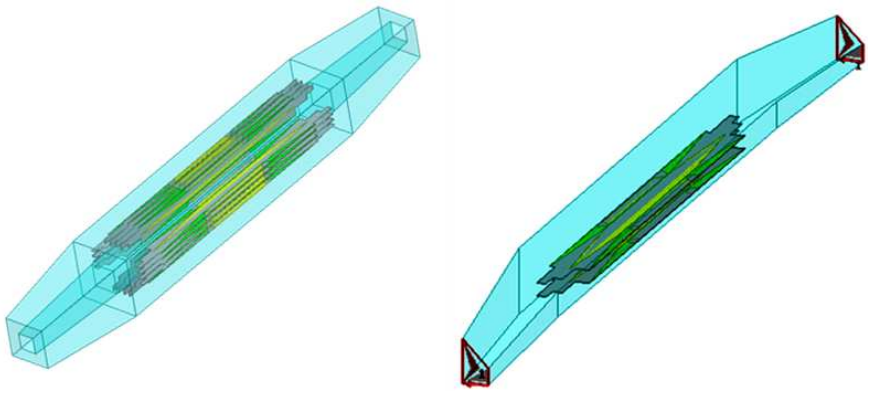

(a) (b)

Figure 3: (a) 3D view of the 16 Cards-32 MMIC's designed Squarax and (b) the simulated octave of the device.

Figure 4: Reflection coefficient, in dB, of the Squarax SPC. Return losses are better than 10 dB in the whole bandwidth.

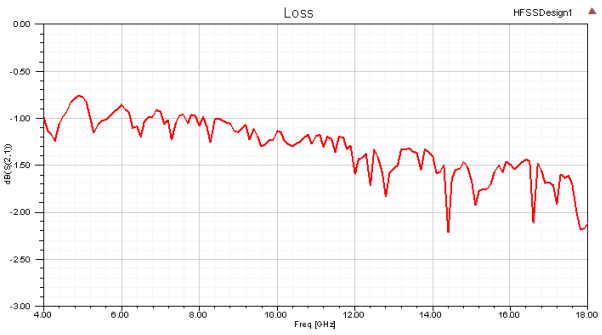

Figure 5: Transmission coefficient, in dB, of the Squarax SPC. Insertion losses are less than 2.5 dB.

Since the Squarax SPC is willing to be interfaced with external devices, such as front-end, back end modules or phase shifter, isolator and other passive devices, commonly with circular coaxial ports, two wave ports with such shape have been needed. Circular coaxial ports have been assigned to the Squarax model by defining two integration lines: one for each port, like a circular coaxial. Since the Squarax is a TEM structure, ports are introduced by employing an Electric Filed Arrow, from inner conductor to outer one. Ports have been assumed as matched with interconnected outer devices, thus a port renormalization hasn't been necessary. Losses of copper waveguide walls and gold metallization of the micro-strip lines and dielectric losses on the alumina slabs have been considered. The Squarax internal volume is filled by air, in such medium the stationary solution of the wave equation in the frequency domain (2) [17] has been solved with HFSS.

$$\nabla \times \mu_r^{-1}(\nabla \times \bar{E}) - k_0^2 \left(\varepsilon_r - \frac{j\sigma}{\omega\varepsilon_0}\right)\bar{E} = 0 \tag{2}$$

where μ_r is the magnetic permeability, ε_r the electrical permittivity and σ the electrical conductivity of the material; ε_0 is the electrical permittivity of the vacuum, k_0 the wave number in free space, ω the wave angular frequency and $\bar{E}$ the electric field.

Driven modal analysis has been performed with a 18 GHz solution frequency and a standard 0.02 Maximum Delta S has been adopted. In the adaptive options tab a 20% maximum refinement per pass has been choice, in order to reduce probability to get an unneeded large amount of tetrahedrons. Moreover, in order to ensure a good solution quality, a minimum converged passes has been set to 2 and an iterative solver with mixed order basis function has been employed. The simulated S-parameters are given in Figure 4 for s_{11}, and Figure 5 for s_{21}.

We note that the Squarax SPC ensures a maximum insertion loss of 2.3 dB and a minimum Return Loss of 10 dB in the whole 4–18 GHz. Several problems were solved, such as a large amount of tetrahedrons in meshing steps and several resonance occurrences. At last about 980 thousands tetrahedrons versus 8 million ones have been obtained, resulting in a reliable modeling which has ensured correct results. This improvement was achieved by defining two Perfect Magnetic Conductors (PMC) within the Squarax SPC. Furthermore, since a good discretization of the Fin taper profile was of fundamental importance, the exponential profile was approximated with a discrete number of points such that the different segment obtained were smaller than $\lambda/20$ at the highest frequency of the operative band. In this way the discretization doesn't affect the performance but reduces the computational complexity. By adopting these strategies and by enabling the Iterative Solver of HFSS, 9.7 GB of memory have been employed, instead of 32 GB ones necessary without this reduction. A dimensioning optimization of the Squarax SPC length has been needed to cut out the resonances. In order to improve the lower band return loss and to extend the operative bandwidth, longer FLuS can be used, with negligible insertion loss degradation. A group QWT's, tuned to different frequencies from the actual, can be a preferable solution. A triple QWT's may be also designed. In Figure 6 we report the result of the electromagnetic simulation of the Squarax SPC, obtained by using COMSOL Multiphysics Version 4: this is a front view of the central section of a quarter of the structure depicted in Figure 3, representing the intensity of the electric field at the microstrips after the FLuS.

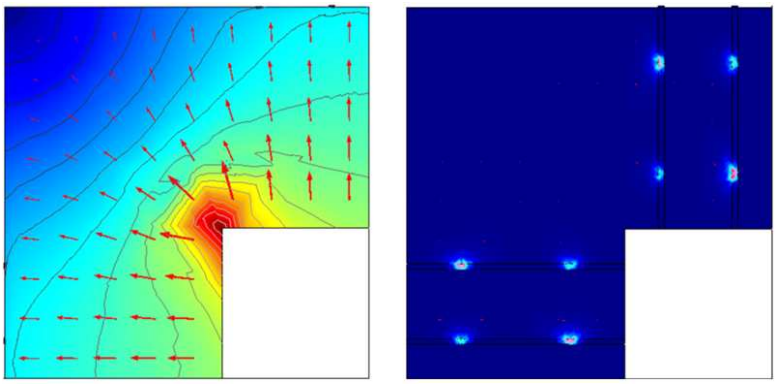

Figure 6: E-field intensity (a) at the TEM interfaces and (b) at the microstrips between the FLuS's. The blank part is the inner conductor.

3.2. Thermo-structural Model and Simulation

The power dissipation of the MMIC SSPA's produces a considerable temperature increase and induces a thermal expansion of both the PA's and the connected structure. If the SSPA's temperature exceeds the maximum allowed value (specified by the SSPA's vendor), an amplification failure or device damage may occur. After the main electromagnetic design, a thermo-structural analysis has been performed in order to define the carrier profiles and its proper materials. As for the electromagnetic simulation, since the structure is doubly symmetric respect two longitudinal orthogonal planes, one quarter of the complete structure has been simulated.

To inquire about the Heat Management Capability of this new SPC, we have performed a Thermal Simulation step linked to a Structural Mechanics analysis totally dependent. This analysis has been performed by supposing to use one of the most powerful GaAs MMIC available on the market, i.e., the TGA9083 produced by Triquint. For such simulation we have used the software Comsol Multiphysic Version 4. The Squarax has been supposed to be held at a constant temperature at its outside, equal to 27°C.

An innovation respect to the Thermo-mechanical simulation approach is represented by the proposed approach, described below. Many MMIC SSPA's are composed by a driver stage and a final stage FET's, but quite often thermal analysis are performed considering the amplifiers as a unique heat sources, which dissipate the total power in all their volumes [6, 10]. The problem of this thermal approach is that it doesn't allow understanding if a determined area of the integrated circuit exceeds the maximum rated temperature, as the channel temperature. The total power dissipation can be evaluated by the ratio between the maximum power output and the Power

Added Efficiency of the MMIC. The driver devices are smaller than the final, and have typical power dissipation P_{Driver} which is generally estimated, when the exact values are not available, as the total power dissipation P_{outMax} multiplied for the ratio of the driver volume V_{Driver} and the final volume V_{Final}: the remaining one is dissipated by the final stage. The power dissipation of the driver is expressed in (6). The Heat power density related to such dissipation can be expressed by the (7).

$$P_{Driver} \approx P_{outMax} \frac{V_{Driver}}{V_{Ended}}, \tag{3}$$

$$Q_{Driver} \approx \frac{P_{Driver}}{V_{Driver}} \tag{4}$$

The difference of heat power distributions between the two active stages determines a different path of the heat generated by the driver and the heat generated by the final transistor. These energies, in the form of heat, combine and induce heat in several points of the material, and only with this driver-final dedicated analysis is possible to determine if the transistor channels can be cooled. The specific heat flux paths determine specific thermal expansion of the materials in different portions of the SSPA volume, which induce specific compressive forces distribute in the subjected areas. Stresses and strains are thus applied to the device, and need to be computed, because consequent displacement of the guiding and combining structures may alter the desired electromagnetic behavior of the structure in different manners, depending on these heat paths. WG walls are intended as in a stationary temperature regime, cooled by the external environment, so they are non deformable by thermal stress and consists in virtual fixed constraints. Solid model is isotropic and the structural transient behavior is quasi-static. For this analysis we have considered the temperatures dependent of the displacements and a coupled computation has been adopted. The Comsol TS module is employed to solve the system of steady state Equation (3) [19]:

$$-\nabla \cdot \sigma = \bar{F}_V \qquad \rho C_p \bar{u} \cdot \nabla T = \nabla \cdot (k \nabla T) + Q \tag{5}$$

where σ is the stress and $\bar{F}_V$ is the force per unit volume; ρ is the density, Cp the heat capacity

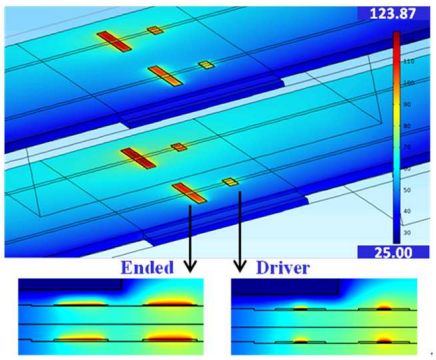

Figure 7: Simulated temperature (°C) inside the GaAs FET channels.

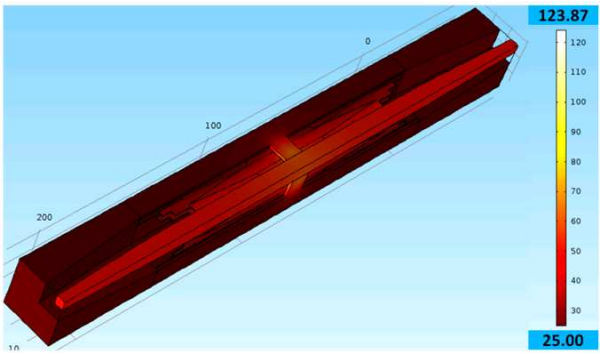

Figure 8: Simulation of the temperature (°C) inside the Squarax volume.

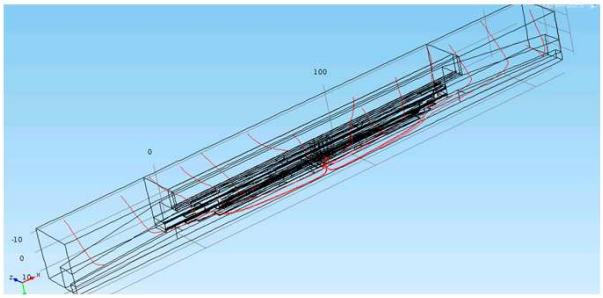

Figure 9: Heat flux streamlines described in a quarter of the SPC.

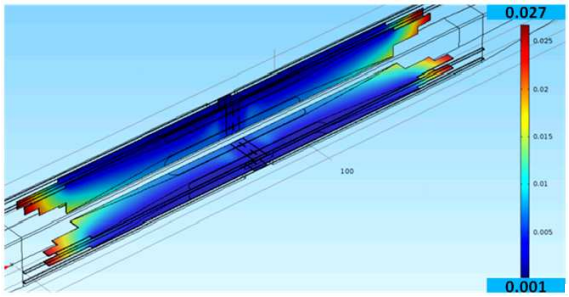

Figure 10: Total displacement (mm) in the Squarax SPC volume, due to heat generation inside the MMIC SSPA's.

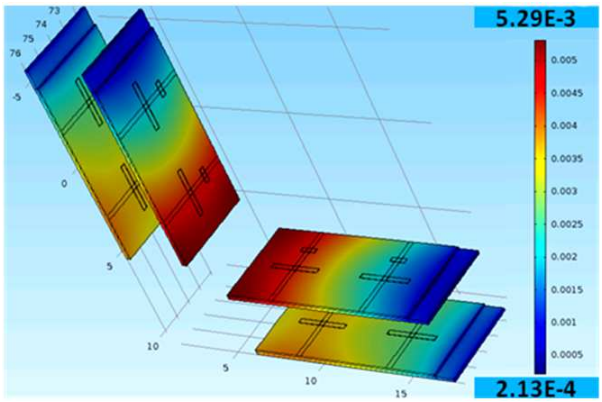

Figure 11: Representation of the displacement (mm) on the SSPA's.

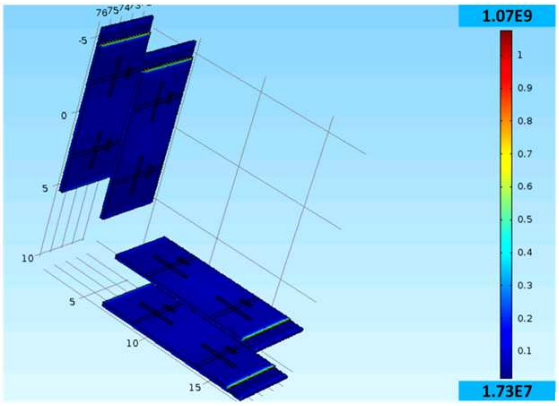

Figure 12: Representation of the Stress (N/m^2) suffered by the SSPA's.

and k the thermal conductivity of the material. Q is the heat source, $\bar{u}$ is the spatial displacement vector.

We have evaluated the thermo-mechanical features of the 16 cards Squarax SPC, where 32 MMIC SSPA's type TGA 9083 are used. We have imposed a total power dissipation of 23 W distributed in the driver and final transistors of each MMIC. Heat power densities have been evaluated, as explained above, basing on the volumes of the transistors. In Figure 7 we have the result of the thermal simulation of the transistors and Figure 8 we report the temperature distribution inside the whole structure.

Driver channels reach 107°C and Final 124°C. We note that Maximum temperature is perfectly respecting the maximum ratings reported by the SSPA vendor. In Figure 9 we report the total Heat Flux Streamlines derived in a quarter of the SPC structure. Heat Flux is directed towards the Sqaurax TL walls, ensuring the correct heat sinking. In Figure 10 the result we obtained for the total displacement, due the thermal stress induced by the heat dissipation is described. We can note, by observing this result, that the maximum displacement is about 27 µm. From Figure 10 we note that the displacement maximum due to temperature, which is obviously obtained at the end of the QWT, is in any case negligible due to low Temperature Expansion Coefficient of the Alumina substrate. The Maximum displacement on the whole SPC surfaces is 27 µm and, since is located on the end of the QWT, is in any case negligible. However, on the MMIC surface we have a maximum displacement of 5.3 µm, as shown in Figure 11: The problem is that GaAs is not very resistant to this displacement values. For this reason, CuMo or CuW layers can be inserted between the back of the GaAs MMIC and the copper carrier. We have adopted the following solution: The carrier is made with copper, to assure high thermal conductivity, and an interface sheet composed with CuMo compound, is placed under the MMIC to assure thermo-mechanical compatibility between GaAs MMIC and the carrier. In Figure 12 we report the Stress on the MMIC devices. Maximum stress, which is less than 1.1 GN/m^2, is located on the GaAs SSPA near the connection between the copper carrier and the Squarax walls.

4. CONCLUSIONS

The Squarax SPC technology has been studied and several circuital and technological solutions have been adopted. The Squarax SPC represents an innovative solution, in order to increase available power outputs and low cost.

By using this solution, optimal results have been achieved. A 16 cards Squarax SPC has been designed with great performance: The model presents gain variation of ±0.4 dB, and 10 dB minimum for Return Loss for the whole 4–18 GHz.

The average insertion Loss of the whole SPC is $IL = 1.5$ dB and, by taking into account such losses, and considering that each TGA9083 can reach a maximum power of 37.4 dBm, the proposed SPA can reach a maximum power output of 51 dBm.

The structure offers 14 GHz of Operative Band with about 230 cm^3 of volume. A thermo-structural simulation has been also performed, showing good results in term of heat management and structural stability.

The maximum power dissipation of the transistors produces a maximum temperature of 124°C

locally on the ended transistors and induces a maximum displacement of about 27 µm. According to this study, the appropriate materials have been chosen in order to ensure the correct operation of the device in thermal stress affected working conditions.

REFERENCES

1. Than, H. T., G. W. Sun, G. S. Cuellar, J. Zeng, N. T. Schultz, M. E. Moya, Y. Chung, B. C. Deckman, and M. P. DeLisio, "Design and Performance of a 600-W-band amplifier using spatially combined GaAs FETs for satellite communications," *IEEE Journal of Solid-State Circuits*, Vol. 47, No. 10, Oct. 2012.
2. Russel, K. J., "Microwave power combining techniques," *IEEE Trans. on MTT*, Vol. 27, No. 5, 472–478, May 1979.
3. Chang, K. and C. Sun, "Millimeter-wave power combining techniques," *IEEE Trans. on MTT*, Vol. 31, No. 2, 91–107, Feb. 1983.
4. Courtney, P. G., T. Tran, C. Bartak, S. Behan, and P. Jia, "High efficiency 80 W X-band power amplifier using coaxial waveguide spatial power combining technique," *International Microwave Symposium Digest*, 1396–1399, Anaheim, CA, USA, May 23–28, 2010.
5. Russo, I., L. Boccia, G. Amendola, and G. Di Massa, "Parametric analysis of grid amplifiers," *Proceedings of European Microwave Week*, 1326–1329, Amsterdam, 2008.
6. An, D., X. Li, J. Mou, and X. Liv, "A new type of Ka-band waveguide-based power combining structures," *Proceedings of ICMMT*, 1–4, Nanjing, China, Apr. 21–24, 2008.
7. Russo, I., L. Boccia, G. Amendola, and H. Shumacher, "Compact hybrid coaxial achitecture for 3–10 GHz UWB quasi-optical power combiner," *Progress In Electromagnetic Research*, Vol. 122, 77–92, 2012.
8. Lopz, D., L. Bortoli, J.-P. Fraysse, D. Langrez, J. F. Villemazet, J. L. Cazaux, G. Soubercaze-Pun, and L. Lapierre, "HPA module for active antenna applications," *Proceedings of 5th European Microwave Integrated Circuit Conference*, 404–407, Paris, Sep. 27–28, 2010.
9. DeLisio, M. P. and R. A. York, "Quasi-optical and spatial power combining," *IEEE Transactions on Microwave Theory and Techniques*, Vol. 50, No. 3, Mar. 2002.
10. Cheng, N.-S., P. Jia, D. B. Rensch, and R. A. York, "A 120-W X-band spatially combined solid-state amplifier," *IEEE Transactions on Microwave Theory and Techniques*, Vol. 47, No. 12, Dec. 1999.
11. Leggieri, A., G. Orengo, D. Passi, and F. Di Paolo, "The Squarax spatial power combiner," *Progress In Electromagnetics Research C*, Vol. 45, 43–55, 2013.
12. Bhat, B. and S. K. Koul, *Analysis, Design and Optimization of Fin Lines*, Artech House, 1987.
13. Ponchak, G. E. and A. N. Downey, "A new model for broadband waveguide to microstrip transition design," *NASA Technical Memorandum*, 88905, Lewis Research Center Cleveland, Ohio, Dec. 1986.
14. Wadell, B. C., *Transmission Line Design Handbook*, Artech House, ISBN 0-89006-436-9, 1991.
15. Gruner, L., "Higher order modes in square coaxial lines," *IEEE Transactions on Microwave Theory and Techniques*, Vol. 31, No. 9, Sep. 1983.
16. Kang, T.-W., C. Christopoulos, and J. Paul, "A square coaxial transmission line with a thin-wire inner conductor to measure the absorbing performance of electromagnetic absorbers," *Journal of the Korea Electromagnetic Engineering Society*, Vol. 4, No. 1, JKEES 2004-4-1-08, Mar. 2004.
17. Pozar, D. M., *Microwave Engineering*, John Wiley & Sons, ISBN 0-471-44878-8, 1998.
18. Di Paolo, F., *Networks and Devices Using Planar Transmission Lines*, CRC Press LLC, ISBN 0-8493-1835-1, 2000.
19. COMSOL Structural Mechanics Module User's Guide, Version 4.3, May 2012.

Injection Phase-locking of a High-power Transit-time Oscillator

Lin Lian, Juntao He, Junpu Ling, Zumin Qi, and Yi Hu
College of Optoelectronic Science and Engineering, National University of Defence Technology, China

Abstract— The enhancement of microwave power density at a certain extent is one of the most significant problems in the development and application of the high power microwave (HPM) sources. Limited by the power capacity and radio frequency (RF) breakdown issues, a single HPM device can hardly achieve high output power. The spatial power combining among several HPM sources is a feasible method. A transit-time oscillator (TTO) with advantages of stability, simple structure, and high beam-wave interaction efficiency, is one candidate for spatial power combining. To lock the phases of the output microwaves of different TTOs, a Ku-band coaxial transit-time oscillator with an injection structure is presented. Between the independent input cavity and the trinal-cavity buncher, a reflector with reflection efficiency of 99.9% is introduced to prevent the leakage power propagating to the input cavity. The RF signal is injected into the input cavity through a coaxial waveguide along the guiding magnet, which avoids separating the magnet coils, and suppresses the asymmetric modes excited in the device. Particle-in-cell (PIC) simulation results indicate that when the injection power ratio ρ ($\rho^2 = P_{in}/P_{out}$, where P_{in} is the injection power, and P_{out} is the output power of the oscillator) is large ($\rho \sim 0.1$), the phase-locking is achieved for a frequency difference of 67 MHz. When the injection power ratio is small ($\rho \sim 0.01$), the phase of the device with the same frequency can be locked ($\Delta f \sim 2$ MHz). It has also been found that the injected signal of high power results in higher output power and earlier saturation than that of a TTO without the injection structure. Moreover, a wider locking bandwidth is expected by the results than that obtained by the Adler's condition.

1. INTRODUCTION

Enhancing the operation frequency and the output power of high power microwave (HPM) sources is the developing trend of HPM technologies [1]. At present, a gigawatt-level output power of microwave sources has been achieved at the relative low frequency bands, such as P-band, L-band, C-band and X-band [2]. However, at the higher frequency band, like Ku-band which is widely used in the broadcasting and communications, the microwave sources mostly can only obtain a megawatt-level output power. This is mainly limited by the decreasing power handling capacity of smaller structure dimensions. An alternative approach is to combine the power of several HPM sources spatially. Many investigations have indicated that combining the power of several phase-locking HPM oscillators is a logical and promising approach for enhancing the output power [3–5]. In order to combine the output power of multiple HPM sources in an antenna array efficiently, the sources must be phase-locked at the same frequency.

The microwave source is a significant part of the combining system. The transit-time oscillator (TTO) has been intensely investigated recently due to its merits such as simple structure, pure frequency and high power [6]. In addition, the coaxial TTO is low impedance, high power capacity and needs a low guiding magnetic field, which make it an ideal HPM source for power combining. Due to above virtues, a coaxial TTO with an injected signal to lock its phase is proposed in this paper. An input cavity and a resonant reflector are designed to increase the injection efficiency and suppress the TEM mode leakage to the input cavity, which will be demonstrated in Section 2. Section 3 show the phase-locking results under different conditions, and the locking bandwidth for different injection power ratios will be presented. A short summary is given in Section 4.

2. STRUCTURE MODEL

The schematic structure of the coaxial TTO with an injected signal is shown in Figure 1, mainly consisting of eight parts: a cathode, an input cavity, a resonant reflector, a modulation trinal-cavity, a dual-cavity extractor, a beam collector, a sloping wedge, a coaxial waveguide and a coaxial injection structure. An independent input cavity with injection efficiency of 98% is designed. The injected signal propagates through a coaxial waveguide which avoids separating the magnet coils, and then reaches the input cavity through a sloping wedge which connects the waveguide and the input cavity. A resonant reflector is located between the input cavity and the modulation trinal-cavity to suppress the communications between them, namely, to reduce the influence of the leakage power from the modulation trinal-cavity on the normal operation of the input cavity. By optimizing

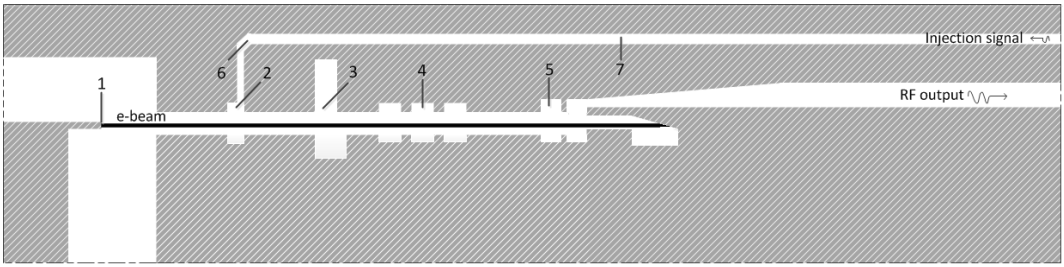

Figure 1: Schematic diagram of the coaxial TTO. 1 cathode, 2 input cavity, 3 resonant reflector, 4 modulation trinal-cavity, 5 dual-cavity extractor, 6 sloping wedge, 7 coaxial waveguide.

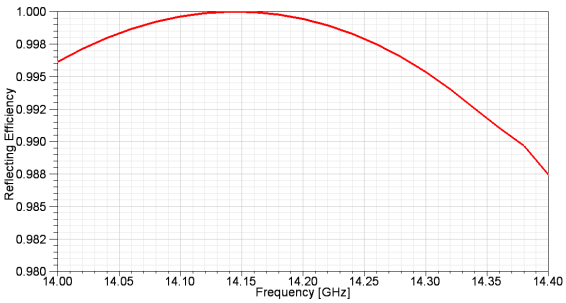

Figure 2: The reflection efficiency of TEM mode of the resonant reflector.

the distribution of the electric field and distances between the three types of cavities, the reflection efficiency of the TEM mode is made above 99.8% in the frequency range of 14.04–14.25 GHz, which is shown in Figure 2. The remainder of the structure has the similar function with that of the coaxial TTO proposed in Ref. [7].

3. SIMULATION RESULTS

A PIC code KARAT [8] has been used to demonstrate the phase-locking process of TTO.

To observe the phase control process of the output signal, the injected signal is defined as the reference signal. The phase-locking characteristics of the output signal can be confirmed by comparing the relative phase of the output signal and the reference signal.

Assuming the frequency of the reference signal is f_r, the initial phase of the reference signal is φ_0, which are equal to that of the injected signal. f and φ are the frequency and the initial phase of the output signal, respectively. Then the relative phase can be given by:

$$\Delta\varphi = 2\pi\left(f - f_r\right)t + \left(\varphi - \varphi_0\right) \tag{1}$$

From Eq. (1), one can ascertain that the relative phase keeps at $\varphi - \varphi_0$ when $f = f_r$.

The operation frequency and output power of the proposed structure are 14.164 GHz and 900 MW, respectively when there is no injected signal. The relative phases for different injection power and different initial phase of the injected signal are illustrated in Figure 3 when the injection frequency is identical with the free-running frequency ($f_r = 14.164$ GHz).

As shown in Figure 3(a), when the injection power is low (∼10 kW, ρ∼0.003), the relative phases between the injected signal and the output signal levels off with a fluctuation of 6° with different initial phases of the injected signal (0°, 45°, 90°), which means the frequencies of the output signals is almost consistent with the free-running frequency. And the phase-locking is achieved.

Figures 3(b) and 3(c) illustrate that when the injection power increases (∼100 kW, ρ∼0.01: ∼1 MW, ρ∼0.03), both of the relative phases show an ascending trend, indicating that there should be a frequency excursion ($f > f_r$, due to Eq. (1)) between the frequency of the output signal and the injected signal. Figure 4 further confirms it. While injecting signals of 100 kW or 1 MW power, the average frequencies of the output signals are both higher than the free-running frequency of the TTO. The variety of the injection power results in the changes of the intrinsic field of the cavity in TTO, leading to a frequency drift [8]. An injection power of 10 kW is too low to obtain a visible frequency drift, therefore the average frequency of the output signal is approximately equal to the free-running frequency ($f - f_r \approx 0$), as shown in Figure 4. The relative phases with different initial

phase of the injected signal are nearly identical in Figures 3(b) and 3(c), which means the initial phase of output signal can be still controlled. In this case, if the frequency of the injected signal is equal to the virtual operation frequency of the TTO, phase-locking can be achieved.

When the injection power reaches 10 MW (ρ∼0.1), the relative phase is constant after about 27 ns as shown in Figure 3(d). The average frequency of the output signal is consistent with the injection frequency (Figure 4), which means that not only the initial phase but also the frequency of the output signal can be locked under a condition of a 10 MW injection power. And the relative phases for different injection frequencies are illustrated in Figure 5, indicating that in the frequency range of 14.125–14.192 GHz, each relative phase difference fluctuates less than 8°.

With an injection frequency of 14.164 GHz and an injection power of 10 MW, the relative phase is investigated when the injected signal is stopped after operating for 60 nanoseconds as presented in Figure 6. After the injected signal is stopped, both the phase and the frequency fail being locked. It can be concluded that the phase-locking process needs a consecutive injected signal.

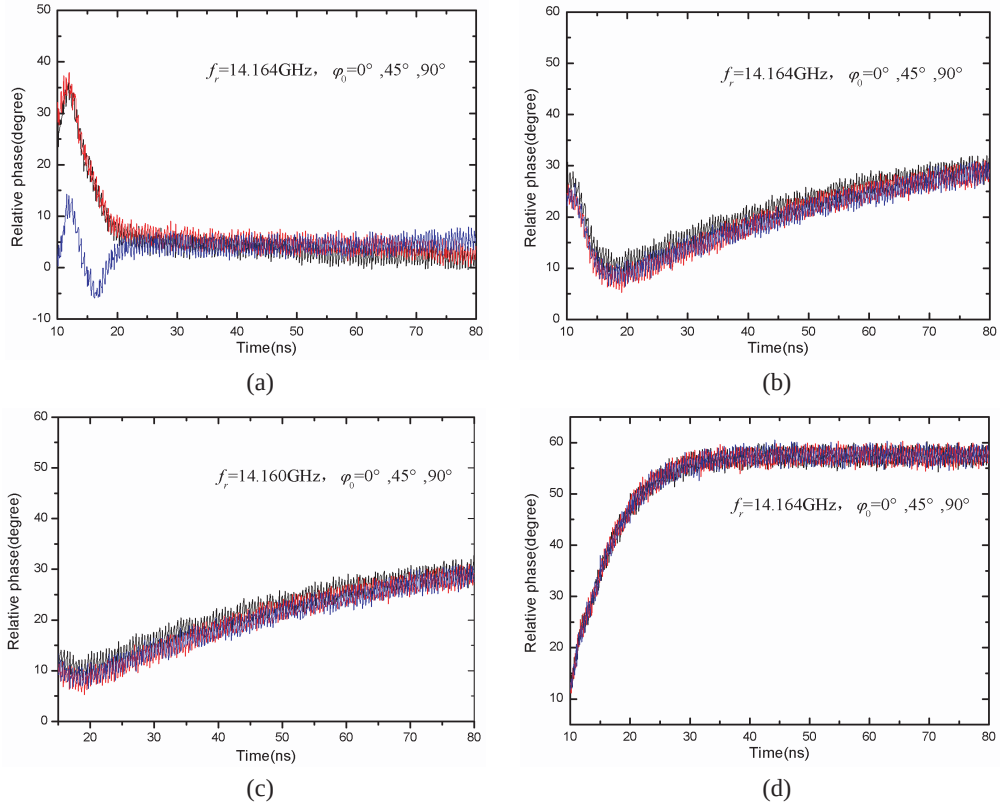

Figure 3: Relative phases for different injection power and different initial phases of the injection signal. (a) 10 kW. (b) 100 kW. (c) 1 MW. (d) 10 MW.

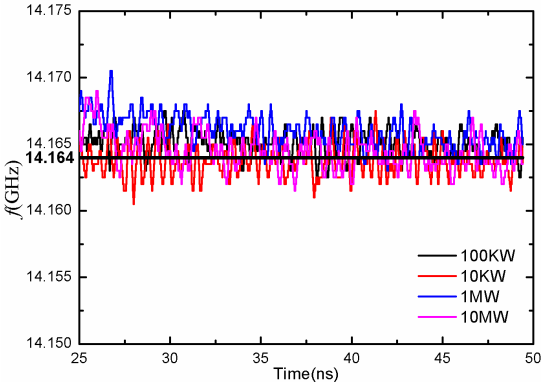

Figure 4: Frequency vs simulation time for different injection power.

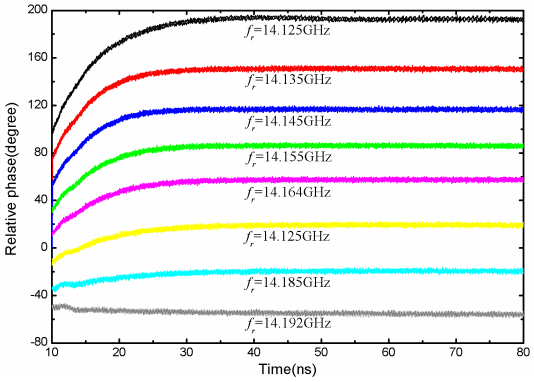

Figure 5: Relative phase for different injection frequency. Here, $\varphi_0 = 0°$.

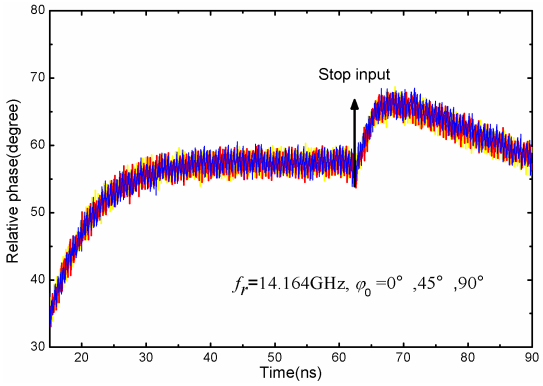

Figure 6: The relative phase under condition of an injected signal stopped after 60 ns.

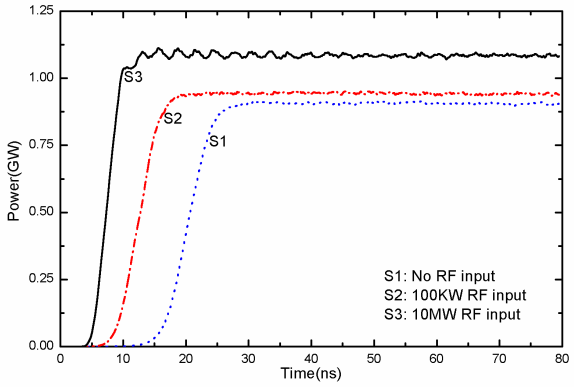

Figure 7: The output power for different injection power.

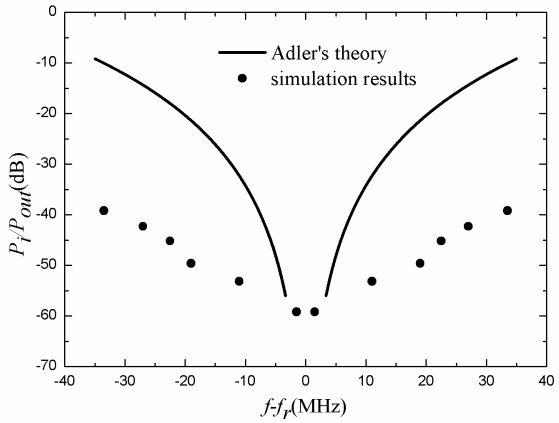

Figure 8: Comparison of the locking bandwidth for different injection power ratios. Solid dots: the condition proposed in this communication, solid line: the conventional phase locking theory. Here, $Q = 1600$, $f_r = 14.164$ GHz.

It can be seen from Figure 7 that the increasing injection power can enhance the output power and accelerate the saturation, which suggests the feasibility that the injected signal can greatly improve the output capacity of the microwave source.

The phase-locking bandwidth as a function of the power ratio between the injection power and output power is shown in Figure 8. It can be seen that the injection power needed to achieve phase-locking is much lower than that predicted by Adler's theory [9] for the same phase-locking bandwidth. When the frequency difference between the injected signal and the output signal is 19 MHz, an injection power of 3 MW is sufficient to lock the phase of a 1 GW output microwave.

4. CONCLUSION

A coaxial TTO with an injected signal is investigated in this article. In the device, an independent input cavity and a resonant reflector are designed before the modulating trinal-cavity to increase the injection efficiency and to decrease the leakage power respectively. The simulation results demonstrate that a high-power injected signal can lock the frequency and phase of the proposed device and improve the output capacity. When the frequency mismatch between the injected signal and the free-running coaxial TTO is ±33.5 MHz, an injection power of 10 MW can lock the phase of 1.1 GW microwave. Moreover, although a small injected signal can hardly lock the operation frequency of the device, the phase of output microwave can be controlled. Simulation results also show that the injection power needed to achieve phase-locking is much lower than that predicted by Adler's theory.

REFERENCES

1. Jiang, W.-H. and C. Zhang, *High Power Microwave*, 2nd Edition, National Defense Industry Press, Beijing, 2009.
2. Gunin, A. V., "Relativistic three-centimeter backward-wave tube with 3 GW pulse power," *Russian Physics Journal*, Vol. 39, No. 12, 1996.
3. Benford, J., H. Sze, W. Woo, et al., "Phase locking of relativistic magnetrons," *Phys. Rev. Lett.*, Vol. 65, No. 12, 5185–5189, 1989.
4. Fazio, M. V., J. Kinross-Wright, B. Haynes, et al., "The virtual cathode microwave amplifier experiment," *J. Appl. Phys.*, Vol. 66, No. 6, 2675–2677, 1989.
5. Teng, Y., W. Song, J. Sun, et al., "Phase locking of high power relativistic backward wave oscillator using priming effect," *J. Appl. Phys.*, Vol. 111, 043303(1–4), 2012.
6. Cao, Y. B., et al., "A low-impedance transit-time oscillator without foils," *Phys. Plasmas*, Vol. 16, 083102(1–6), 2009.
7. Tarakanov, V. P., *User's Manual for Code KARAT*, Berkeley Research Associate, Springfield, 1998.
8. Cao, Y. B., "Investigation of a foilless transit radiation oscillator with low-impedance," Master's Thesis, 9–16, National University of Defense Technology, Changsha, 2008.
9. Adler, R., "A study of locking phenomena in oscillators," *Proc. IRE*, Vol. 34, 351–357, 1946.

Optimization of Nanostructured Lüneburg Lens Based on the Transformation Optics Method

Yinghui Cao[1, 2], **Yongmin Liu**[3, 4], **and Zhenyu Liu**[1]

[1]Changchun Institute of Optics, Fine Mechanics and Physics
3888 East Nanhu Road, Changchun, Jilin 130033, China
[2]College of Computer Science and Technology, Jilin University
2699 Qianjin Street, Changchun, Jilin 130021, China
[3]Department of Mechanical and Industrial Engineering, Northeastern University
360 Huntington Avenue, Boston, MA 02115, USA
[4]Department of Electrical and Computer Engineering, Northeastern University
360 Huntington Avenue, Boston, MA 02115, USA

Abstract— In this work, we present the design of the nanostructured Lüneburg lens by using the electromagnetic field simulation and gradient optimization method that based on Transformation Optics (TO) technique. In the proposed method, the nanostructured Lüneburg lens is simulated with an equivalent model, in which the original dielectric rods with varying size are transformed into uniform and fixed sized rods, with parameterized permittivity and permeability distributions, and then the nanostructured Lüneburg lens is optimized with the gradient optimization method. By using the TO modeling method, mesh refinement around the smaller rods can be avoided, and repetitions of regenerating the geometry and mesh grids during the optimization iterations can be eliminated, thus the computation efficiency is improved. The proposed design method opens up a new avenue to design and optimize a variety of photonic and optical devices with large number of complex structures.

1. INTRODUCTION

Lüneburg lens [1] is a spherical lens with gradient refractive index (GRIN) structure, it can focus incoming plane wave from any direction into a focal point at the surface of the lens on the opposite direction. However, as a GRIN device, Lüneburg lens is difficult to be fabricated at optical wavelengths. In recent years, nanostructured Lüneburg lens [2–4] that composed of Graded Photonic Crystals (GPC) has been proposed. The nanostructured Lüneburg lens can be designed using the homogenization method of periodic structures [2], the ray tracing method [3], and the effective medium theory [4]. In our previous work [5], we used the electromagnetic field simulation and optimization method that based on Transformation Optics (TO) [6, 7] to design Photonic Crystal (PhC) devices, including the PhC coupler and PhC waveguide bend that consists of dielectric rods with varying sizes. In this work, we use the TO-based simulation and optimization method to design the nanostructured Lüneburg lens, and compare the optimized nanostructured Lüneburg lens with the GRIN Lüneburg lens.

2. DESIGN OF NANOSTRUCTURED LÜNEBURG LENS

Figure 1(a) shows a nanostructured Lüneburg lens which contains 95 dielectric rods in circular lattice. The radius of the lens is $R = 6a$, where a is the lattice constant. In this work, we set the lattice constant as $a = 0.25\ \mu\text{m}$. The nanostructured Lüneburg lens is modeled with the TO method, namely, the original dielectric rods with varying sizes are transformed into an equivalent model that consists of uniform and fixed sized rods, with parameterized permittivity and permeability distributions [5]. The permittivity and permeability of the transformed model can be calculated with the TO formulae. By using the TO modeling method, mesh refinement around the smaller rods can be avoided, and repetitions of regenerating the geometry and mesh grids during the optimization iterations can be eliminated, thus the computation efficiency is improved [5, 8].

The nanostructured Lüneburg lens is optimized with a gradient optimization package minConf [9], The optimization object is defined as the average electric field intensity around the focal point as

$$E_{obj} = \frac{\iint_{\Sigma} |\mathbf{E}|\, \mathrm{d}x\, \mathrm{d}y}{\iint_{\Sigma} \mathrm{d}x\, \mathrm{d}y} \tag{1}$$

where Σ is a small "observation" zone that enclosing the focal point. For nanostructured Lüneburg lens in Fig. 1(a), the "observation" zone Σ is defined as a rounded region of radius a, with its center at $(x, y) = (6a, 0)$. The wavelength of incident light is set as $\lambda = 1.55\,\mu\text{m}$, and the refractive index of the dielectric rod is $n_{rod} = 3.4$. To ensure the symmetry of the optimized nanostructured Lüneburg lens, the gradient of rods at the same distance from the center of the lens are averaged. In addition, to mimic the gradual change of refractive index of the GRIN material, a constraint is applied in the optimization that the sizes of the inner rods of the nanostructured lens should be larger than the outer rods. At the begining of the optimization process, the initial rods radii are set as

$$r_j = r_0\left(1 - \alpha\frac{R_j}{R}\right) \tag{2}$$

where r_j is the initial radius of the jth rod, r_0 is the initial radius of the rod at lens center, α is a parameter to control the inital size of rods, R_j is the distance of the jth rod from the lens center, R is the radius the lens. For nanostructured Lüneburg lens of $R = 6a(\sim \lambda)$, we set the initial value parameter as $r_0 = 0.16a$ and $\alpha = 0.5$. The incident light is set as a plane wave propagating along x axis, polarized along z axis. After 21 steps of optimization iterations, the average electric field intensity around the focal point converges to $E_{obj} = 2.432$, the program running time is 857.8 seconds on a computer with Xeon E5645 CPU (2.4 GHz). The optimized structure and electric field distribution is shown in Fig. 1(b).

As a comparison, the GRIN Lüneburg lens of radius $R = 1.5\,\mu\text{m}$ is simulated, the calculated field distribution is shown in Fig. 1(c). The averaged field intensity around focal point is 2.238, which is a bit lower than the optimized nanostructured Lüneburg lens. Comparing Figs. 1(b) and 1(c), the focal spot of the GRIN Lüneburg lens is a bit larger than the optimized nanostructured Lüneburg lens.

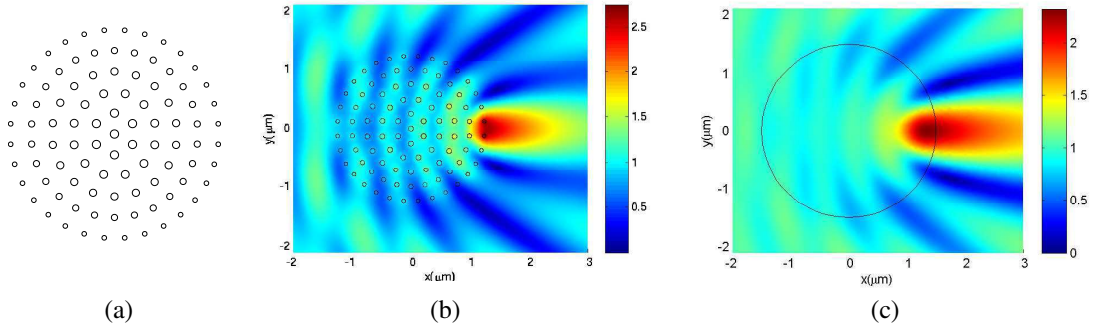

Figure 1: (a) Schematic diagram of the nanostructured Lüneburg lenses in circular lattice, with lens radius of $R = 6a$. (b) The structure and field distribution of the optimized nanostructured Lüneburg lenses. (c) The field distribution of GRIN Lüneburg lens of $R = 1.5\,\mu\text{m}$.

3. CONCLUSIONS

In this work, the design of the nanostructured Lüneburg lens using the TO-base simulation and optimization method is presented. The proposed TO-base simulation and optimization method is an effective and efficient method for graded photonic crystal devices, it opens up a new avenue to design and optimize a variety of photonic and optical devices with large number of complex structures.

REFERENCES

1. Luneburg, R. K., *Mathematical Theory of Optics*, University of California, Berkeley and Los Angeles, 182–188, 1964.
2. Vasić, B., G. Isić, R. Gajić, and K. Hingerl, "Controlling electromagnetic fields with graded photonic crystals in metamaterial regime," *Opt. Express*, Vol. 18, No. 19, 20321–20333, 2010.
3. Gao, H., B. S. Takahashi, L. Tian, and G. Barbastathis, "Aperiodic subwavelength Lüeburg lens with nonlinear Kerr effect compensation," *Opt. Express*, Vol. 19, No. 3, 2257–2265, 2011.

4. Gao, H., B. Zhang, S. G. Johnson, and G. Barbastathis, "Design of thin-film photonic metamaterial Lüneburg lens using analytical approach," *Opt. Express*, Vol. 20, No. 2, 1617–1628, 2012.
5. Cao, Y., J. Xie, Y. Liu, and Z. Liu, "Modeling and optimization of photonic crystal devices based on transformation optics method," *Opt. Express*, Vol. 22, No. 3, 2725–2734, 2014.
6. Pendry, J. B., D. Schurig, and D. R. Smith, "Controlling electromagnetic fields," *Science*, Vol. 312, No. 5781, 1780–1782, 2006.
7. Liu, Y. M. and X. Zhang, "Recent advances in transformation optics," *Nanoscale*, Vol. 4, No. 17, 5277–5292, 2012.
8. Ozgun, O. and M. Kuzuoglu, "Software metamaterials: Transformation media based multiscale techniques for computational electromagnetics," *J. Comput. Phys.*, Vol. 236, 203–219, 2013.
9. Schmidt, M., http://www.di.ens.fr/~Emschmidt/Software/minConf.html.

670 W Single-frequency Retrievable Multi-tone All-fiber MOPA

X. L. Wang, P. Zhou, R. M. Tao, R. T. Su, and X. J. Xu
College of Optoelectronic Science and Engineering
National University of Defense Technology (NUDT), Changsha, China

Abstract— We demonstrated a single-frequency retrievable multi-tone all-fiber laser in master-oscillator power-amplification (MOPA) configuration with the highest recorded power of 670 W. The seed laser runs in multi-tone regime by phase modulating a single-frequency fiber laser using a sine wave signal. Power amplification of the multi-tone master oscillator is then implemented by four cascaded all-fiber power amplifier and a power scaling up to 670 W is achieved. A proof-of-concept experiment for retrieving single-frequency laser from the high power multi-tone laser is carried out by implementing a demodulation signal, which is π phase shift of the modulation signal, on the output laser at a relative low power level. Results indicated that the single-frequency laser can be retrieved with a sideband suppression of more than 20 dB at the power level of 670 W. This method may provide a feasible way for power scaling of single-frequency laser over the SBS limitation in fiber amplifier.

1. INTRODUCTION

High-power single-frequency fiber lasers are widely used in a lot of fields, including nonlinear frequency conversion, remote sensing and coherent beam combining [1, 2]. Nevertheless, restricted in terms of thermal load, fiber damage and nonlinear effects, especially the stimulated Brillouin scattering (SBS) effects [3], the ultimate output power of the single-frequency fiber amplifier has been limited to the several hundred watts level [4, 5]. Moreover, the highest reported single-frequency all-fiber laser is about 203 W [6]. In order to suppress SBS and increase the output power in fiber amplifier, various techniques for SBS suppression, including stress, large-mode area (LMA) fibers, thermal gradients [7] and gain competition [6] have been proposed. Broadband linewidth [8] and multi-tone single-frequency [3, 9] master oscillator is also helpful for SBS suppression. But the linewidth is somewhat broad in a lot of applications such as coherent beam combining. Special assistant technique (such as fine optical path control using optical delay line in coherent beam combining) should be implemented and the system becomes bulk and complex. If the amplified broadband linewidth laser could be converted back to be a single-frequency one, high power single-frequency laser over the SBS limitation would be achieved. There are a lot of solutions to get broadband or multi-tone single-frequency master oscillator, such as built a broadband linewidth laser, generating broadband linewidth laser by phase modulation with a noise signal [10], or a regular signal [11]. Of the three methods mentioned above, modulating the single-frequency laser by a sine wave signal is a simple way. Furthermore, this type of broadband linewidth laser is multi-tone one and can be converted to single-frequency laser by a special demodulation signal [12]. In previous work, Rhein et al. [11] has demodulated an amplified phase modulated single-frequency signal laser at the power of 10 W. Here in this paper, we will report our experiment demonstration of a 670 W single-frequency retrievable multi-tone amplifier. Experiment for retrieving single-frequency laser from the high power multi-tone laser is carried out by implement a demodulation signal has a π phase shift of the modulation signal on the output laser. Results indicated that the single-frequency laser can be retrieved with sideband suppression by more than 13 dB at the power level of 670 W. The feasibility of demodulation a phase modulated single-frequency laser in high power level is demonstrated.

2. EXPERIMENT SETUP

The experimental setup is shown in Fig. 1. A linearly polarized single-frequency laser generating 40 mW of power at a wavelength of 1064 nm with a linewidth of about 200 kHz [13] is phase modulated a modulator (PM1). A function generator (FG) which can produce sine wave signal is used to driven PM1. The multi-tone master oscillator (MO) is then amplified by a four stages power amplifier chain.

The first pre-amplifier (AI) is based on a single-mode Yb^{3+} doped fiber (YDF, core/cladding diameter 6/125 μm, 0.12 NA), which scale the seed laser from 10 mW to more than 200 mW. The second and third pre-amplifier are both based on double cladding YDF with core/inner diameter of 15/130 μm, 0.08/0.46 NA. In the second amplifier (AII), a 4 meter long YDF is pumped by a 9 W

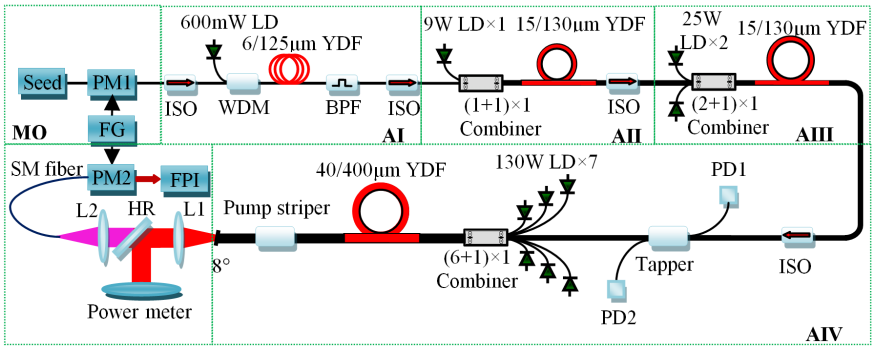

Figure 1: Experimental setup of the single-frequency retrievable fiber laser in MOPA configuration. PM1 and PM2-phase modulator, FG-function generator, ISO-isolator, WDM-wavelength division multiplexing, LD-laser diode; YDF-Yb^{3+} doped fiber, BPF-band pass filters, PD1 and PD2-photodetector, L1-collimated lens, HR-high reflection mirror, L2-focus lens, FPI-Fabry-Perot interferometer, AI, AII, AIII and AIV-amplifiers in different stages.

fiber pigtailed laser diode (LD) and scale the power up to 5 W. In third amplifier (AIII), a 6 meter long YDF is pumped by two 25 W LDs and can scale the power up to 30 W. The main amplifier bases on a $\sim$ 7.5 meter long LMA double clad YDF with core diameter of 40 μm ($NA = 0.06$), inner cladding diameter of 400 μm ($NA = 0.46$), absorption coefficient of $\sim$ 5.5 dB/m at 975 nm wavelength. Six 130 W multimode fiber pigtailed 976 nm LDs are coupled into the gain fiber through a $(6 + 1) \times 1$ signal/pump combiner. The output end of the delivery fiber is angle cleaved at 8° to suppress spurious lasing. Between the third pre-amplifier and the main power amplifier (AIV), a tap coupler cooperated with two photodetedtor (PD1, PD2) are used to detect the output power of the third amplifier and especially to monitor the backward signal of the main amplifier. A control circuit is built to protect devices by turning off power supply of LDs when nonlinear increasing of the backward signal is observed. As the power handle ability of the tap coupler is lower than 20 W, the third pre-amplifier is operated at a lower power of 15 W. The output laser is first collimated by a lens (L_1), and then reflected by a high reflection mirror (HR). The reflected beam which contains main power ($> 99\%$) of the laser is sent to a power meter. The transmitted beam that contains less than 1% power of the laser is first focused by a lens (L_2) with a focus lens of 150 mm, and then coupled into a single-mode (SM) fiber. The signal in the SM fiber is sent to a phase modulator (PM2) for demodulation. A Fabry-Perot interferometer (FPI) is located after PM2 to measure the linewidth of the laser in different case. When PM2 is driven by a signal which is π phase shift of the modulation one, single-frequency laser could be retrieved.

3. RESULTS AND ANALYSIS

In experiment, when the single-frequency laser $E(t) = E_0 e^{-j\omega_0 t}$ is phase modulated by a sine wave phase signal $\varphi_m(t) = \psi_0 \cos(\omega_m t)$, multi-tone signal with expression $E_{md}(t) = \sum_{n=-\infty}^{\infty} j^n J_n(\psi_0)$ $e^{-j(\omega_0 + n\omega_m)t}$ will generate. In experiment, the single-frequency laser is modulated by a sine wave signal with a frequency of 100 MHz, amplitude of 5 V. When the first two pre-amplifier is work at the full power, the output power and backward power of the main amplifier changes with the pump power is measured and shown in Fig. 2. The output power reaches as high as 670 W at the limited pump power of 765 W, with a power efficiency of about 86%. The monitored maximum backward power is less than 0.6 W. As the single-frequency laser is broadened by the phase modulation, SBS effect is suppressed, therefore, there are no nonlinearly increasing is observed in the measured backward power even at the highest power. In experiment, we coiled the fiber with a diameter less than 10 cm and used high-index gel to strip the high-order mode as well as residual pump in inner cladding of the large mode fiber to make the amplifier working in the lower mode. The measured beam quality M_2 is about 1.7 when the output power is 670 W. The beam profile of the amplifier at the highest power level is also inserted in Fig. 2.

The output power spectrum at the highest power is measured and shown in Fig. 3. We can see that the residual pump light is 25 dB less than of the signal. No ASE (Amplified Spontaneous Emission) is observed, which indicates the output power of the main amplifier can be further

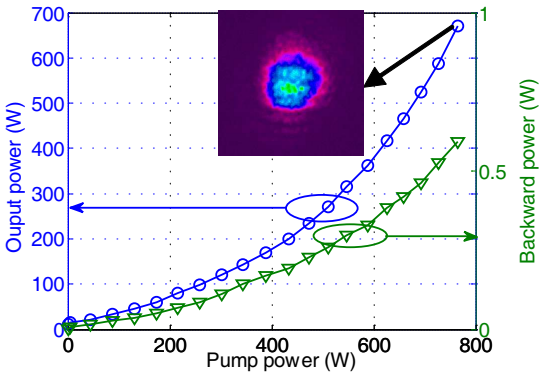

Figure 2: Output power and beam profile of the main amplifier in different pump power.

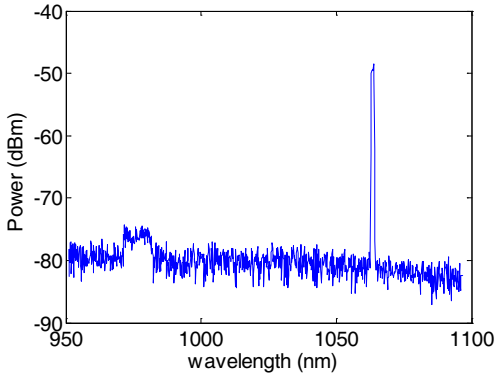

Figure 3: Spectrum of the main amplifier at 670 W output.

increased by only increase pump power.

To confirm the linewidth broadened and the feasibility of demodulation of the modulated single-frequency laser, we use an FPI (FPI100, FSR = 4 GHz, fineness ∼ 10 MHz, Toptica inc.) to measure the linewidth before and after the modulation and demodulation. Fig. 4(a) shows the measured linewidth before and after demodulation when the main power amplifier (AIV) is off. When the modulation is on, the single-frequency laser is broadened to be a multi-tone signal with a full measure linewidth of about 1.8 GHz. When the demodulation signal is on, a single-frequency like signal with only two sidebands are obtained with a side bands suppression of about 22 dB. When the main power amplifier is operated at the full power, the amplified signal is recorded and shown in Fig. 4(b), compared with Fig. 4(a), there is no obvious difference between before and after the main power amplifier. When the demodulation signal is applied, the retrieved single-frequency laser in full power operation is also generated with a sideband suppression of more than 20 dB. The residual demodulation error can be mainly attributed to the mismatch of the frequency, phase and amplitude between the modulation and demodulation signal. In the demodulated signal, only two sidebands are measured, which validated that the amplitude of the generated full wave mixing (FWM) is so small that it can't be recorded by the FPI. In multi-tone amplifier, FWM may appear, but as the power is much less than the signal power in each tone, the influence on the frequency retrieving can be neglected, this will be studied in theory latter.

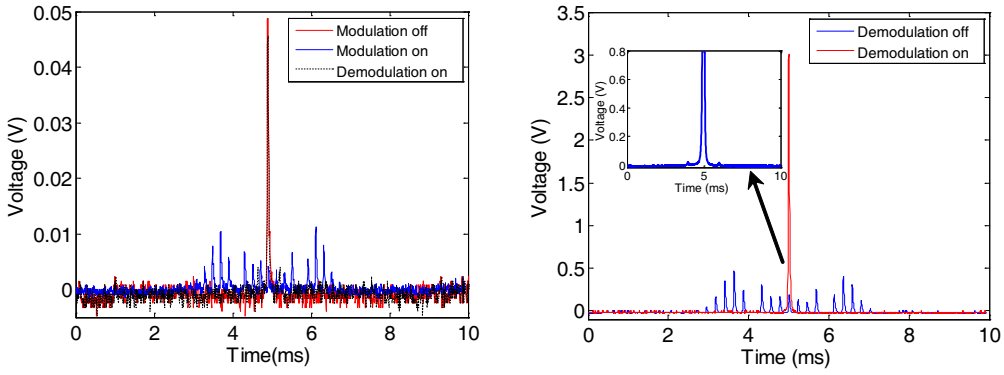

Figure 4: Oscilloscope trace of the over a Fabry-Perot interferometer (a) without and (b) with main power amplifier.

In theory, the power of the FWM sideband (with frequency of $\omega_{pps} = 2\omega_p - \omega_s$) produced by pump laser (with frequency of ω_p) and signal laser (with frequency of ω_p) can be calculated by $P_{PPS} = \eta\gamma^2 P_p P_s^2 L_{eff}^2$ [14–16]. Here η is conversion efficiency, for a signal positioned close to the pump, $\eta = 1$ [15]. P_p, P_s are the powers of pump and signal laser. γ is the nonlinear parameter, it can be calculated as $\gamma = n_2\omega/(cA_{eff}) = 2\pi n_2/(\lambda A_{eff})$ [17]. Here n_2 is the nonlinear index coefficient, λ is the wavelength of the laser and A_{eff} is the effective core area of the fiber. L_{eff} is the

effective interaction length [17]. For a Silicon-based fiber, $n_2 = 3 \times 10^{20}\,\mathrm{m}^2/\mathrm{W}$ at the wavelength of 1.064 µm [17]. In our experiment, the core diameter of the fiber is 40 µm, then γ is calculated to be $\gamma = 2.5 \times 10^{-4}\,\mathrm{m}^{-1}\mathrm{W}^{-1}$. There is 7.5 m active fiber delivery a non-uniform power and a 0.5 m passive fiber delivery a power up to 670 W. The effective interaction length at the full power of 670 W can be estimated to be less than 3 m. In experiment, there are 17 sidebands amplifier (see Fig. 5(a)) which contains a total power of 670 W, therefore the minimum power of the lowest signal is calculated to be 1.5 W. The FWM sidebands can be calculated and shown in Fig. 5(b), the maximum power of the FWM sideband is less than 0.25 W, and the total power of the 61 FWM sidebands is less than 7 W. In Fig. 4(b), a voltage of 3.0 V represent a power of 670 W, therefore, the maximum response voltage of FWM sideband in the FPI is less than 1.1 mV, which can't be recorded effectively by the oscillograph. To conclude, the influence of the FWM sidebands on the single-frequency retrieving can be neglected.

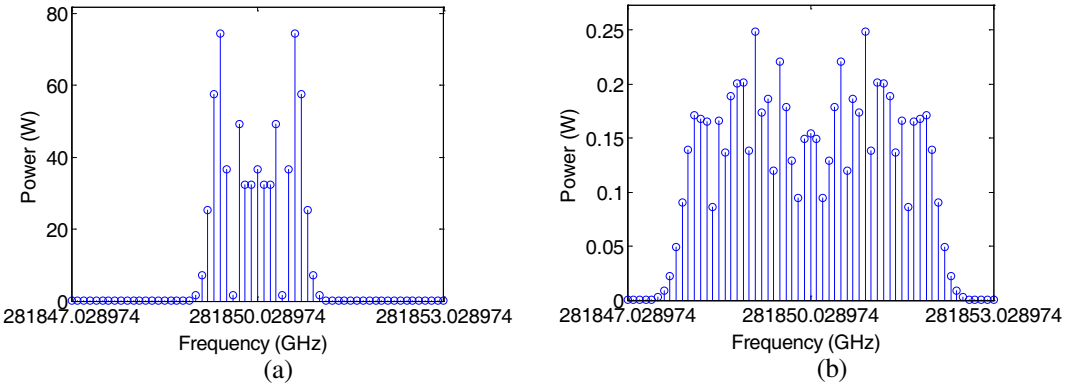

Figure 5: (a) Estimated power distribution and (b) FWM sidebands in amplifier.

4. SUMMARY

In conclusion, we have demonstrated a single-frequency retrievable laser with a record power of 670 W. The full linewidth is less than 1.8 GHz, and it's possible to be converted back to a single-frequency laser. Compared a with 25 GHz broad linewidth [18], this laser can be used for coherent beam combining directly without phase demodulation. It is should be note that we didn't retrieve single-frequency laser in a high power level for the damage threshold of the available phase modulator is less than 100 mW. Up to now, the damage threshold of commercially available free space KTP phase modulator is $20\,\mathrm{W/mm}^2$ [19], the power handle ability of this type of phase modulator is about 60 W. Although high power (up to 600 W) phase modulator is not available yet, as the development of material and relative technology such as resonant phase modulator [19], we believe that high threshold, high bandwidth and relative low half-wave voltage phase modulator will be available in the future. Therefore, if a high power phase modulator is available, a single-frequency laser with much higher power than that of so far reported can be retrieved. This may be a feasible way for power scaling up of single-frequency laser over the SBS limitation in fiber amplifier.

ACKNOWLEDGMENT

This work is supported by scientific research project in National University Defense of Technology of China.

REFERENCES

1. Fermann, M. E. and I. Hartl, "Fiber laser based hyperspectral sources," *Laser Physics Letters*, Vol. 6, No. 1, 11–21, 2009.
2. Andres, M. V., J. L. Cruz, A. Diez, P. Perez-Millan, and M. Delgado-Pinar, "Actively Q-switched all-fiber lasers," *Laser Physics Letters*, Vol. 5, No. 2, 93–99, 2008.
3. Dajani, I., C. Zeringue, and T. Shay, "Investigation of nonlinear effects in multitone-driven narrow-linewidth high-power amplifiers," *IEEE J. Sel. Top. Quantum Electron.*, Vol. 15, No. 2, 406–414, 2009.

4. Gray, S., A. Liu, D. T. Walton, J. Wang, M. Li, X. Chen, A. R. Boh, J. A. Demeritt, and L. A. Zenteno, "502 Watt, single transverse mode, narrow linewidth, bidirectionally pumped Yb-doped fiber amplifier," *Opt. Express*, Vol. 15, No. 25, 17044–17050, 2007.
5. Goodno, G. D., L. D. Book, and J. E. Rothenberg, "Low-phase-noise, single-frequency, single-mode 608 W thulium fiber amplifier," *Opt. Lett.*, Vol. 34, No. 8, 1204–1206, 2009.
6. Zeringue, C., C. Vergien, and I. Dajani, "Pump-limited, 203 W, single-frequency monolithic fiber amplifier based on laser gain competition," *Opt. Lett.*, Vol. 36, No. 5, 618–620, 2011.
7. Liu, A., "Suppressing stimulated Brillouin scattering in fiber amplifiers using nonuniform fiber and temperature gradient," *Opt. Express*, Vol. 15, No. 3, 977–984, 2007.
8. Engin, D., W. Lu, and M. Akbulut, "1 kW CW Yb-fiber-amplifier with < 0.5 GHz linewidth and near-diffraction limited beam-quality for coherent combining application," *Proc. of SPIE*, Vol. 7914, No. 791407, 2011.
9. Weßels, P., P. Adel, M. Auerbach, D. Wandt, and C. Fallnich, "Novel suppression scheme for Brillouin scattering," *Opt. Express*, Vol. 12, No. 19, 4443–4448, 2004.
10. Khitrov, V., K. Farley, R. Leveille, J. Galipeau, I. Majid, S. Christensen, B. Samson, and K. Tankala, "kW level narrow linewidth Yb fiber amplifiers for beam combining," *Proc. of SPIE*, Vol. 7686, No. 76860A, 1–8, 2010.
11. Rhein, S., O. Schmidt, H. Zimer, T. Schreiber, R. Eberhardt, and A. Tünnermann, "High average power optical demodulation of a fiber amplified phase modulated single-frequency signal," *Proc. of SPIE*, Vol. 7914, No. 791430, 1–6, 2011.
12. Massey, G. A., M. K. Oshman, and R. Targ, "Generation of single-frequency light using the FM laser," *Appl. Phys. Lett.*, Vol. 6, No. 1, 10–11, 1965.
13. Xu, S., Z. Yang, W. Zhang, X. Wei, Q. Qian, D. Chen, Q. Zhang, S. Shen, M. Peng, and J. Qiu, "400 mW ultrashort cavity low-noise single-frequency Yb^{3+}-doped phosphate fiber laser," *Opt. Lett.*, Vol. 36, No. 18, 3708–3710, 2011.
14. Hill, K. O., D. C. Johnson, B. S. Kawasaki, and R. I. Macdonald, "CW three-wave mixing in single-mode optical fibers," *J. Appl. Phys.*, Vol. 49, No. 10, 5098–5106, 1978.
15. Shibata, N., R. Braun, and R. Waarts, "Phase-mismatch dependence of efficiency of wave generation through four-wave mixing in a single-mode optical fiber," *IEEE Journal of Quantum Electronics*, Vol. 23, No. 7, 1205–1210, 1987.
16. Brès, C., S. Zlatanovic, A. O. J. Wiberg, and S. Radic, "Continuous-wave four-wave mixing in cm-long Chalcogenide microstructured fiber," *Opt. Express*, Vol. 19, No. 26, B621–B627, 2011.
17. Agrawal, G. P., *Nonlinear Fiber Optics*, 367, Beijing World Publishing Corporation, Beijing, 2005.
18. Goodno, G. D., S. J. Mcnaught, J. E. Rothenberg, T. S. Mccomb, P. A. Thielen, M. G. Wickham, and M. E. Weber, "Active phase and polarization locking of a 1.4 kW fiber amplifier," *Opt. Lett.*, Vol. 35, No. 10, 1542–1544, 2010.
19. Newport, "DC-250 MHz electro-optic phase modulators," EB/OL, 2007, http://search.newport.com/?q=*&x2=sku&q2=4063-M.

The Frequency Gap and SNR Improvement for Self-seeded Multi-wavelength Brillouin-Erbium Fiber Laser

Pinghe Wang and Feng Gao
School of Opto-Electronic Information
University of Electronic Science and Technology of China, Chengdu 610054, China

Abstract— We demonstrate a self-seeded multi-wavelength brillouin-erbium fiber laser with double-brillouin-frequency gap. First, the factor that induces the double frequency gap is investigated. The twice channel gap is induced by the gain difference in different directions. Then, a self-seeded multi-wavelength brillouin-erbium fiber laser with high signal to noise ratio (SNR) is reported. 44 stable output channels (above −25 dBm) with 20 GHz frequency spacing is obtained when the 980 nm pump power is 300 mW.

1. INTRODUCTION

Stimulated Brillouin scattering (SBS) is a nonlinear process in optical fiber resulted from the interaction between a pump wave and an acoustic wave [1]. When a light wave launched into an optical fiber exceeds SBS threshold, a backward stokes wave with a Brillouin frequency shift f_B is generated. SBS in optical fiber has wide application in many fields, such as optical communication [2–4], optical sensor [5, 6], slow and fast light [7–9], optical storage [10], micro-wave photonics [11, 12].

Brillouin-Erbium fiber lasers (BEFL), which integrates the nonlinear gain of single mode fiber and the linear gain of erbium doped fiber, is first demonstrated by G. J. Cowle, et al. [13]. The BEFL has drawn a lot of interest in recent years because of its unique properties-narrow linewidth and high output power [14–16]. Multiwavelength BEFL can be generated by cascaded stimulated brillouin scattering effect [17]. 150 lines are generated by enhanced four wave mixing effect in the cavity [18]. In 2005, Song, et al. reported the self-seeded BEFL that generated 120 lines [19]. A little later, a self-seeded BEFL with 200 lines was report by the same group [20]. The low SNR is one of the main disadvantages of the self-seeded BEFL [18].

The frequency gap of the multiwavelength is equal to the Brillouin frequency shift f_B which depends on the fiber material. For single mode fiber (SMF) based on silica, it is about 10 GHz (~ 0.08 nm) [1]. The narrow frequency gap limits the applications of the multiwavelength BEFL in system implementation. Some researchers are interested in expanding the channel spacing. In reference [21], a BEFL with 10 and 20 GHz frequency gap was reported. The odd-and even-odd Stokes lines are outputting from different arm in the cavity. In reference [22], the multiwavelength BEFL contains two cavities, the multiwavelength comb with 20 GHz frequency gap can be produced in one of the cavities. Recently, Y. G. Shee, et al. reported a multiwavelength BEFL with 20 GHz frequency spacing [23]. A four ports circulator is used to combine two cavities. The light output from the unidirectional cavity has the 20 GHz frequency gap. All the multiwavelength BEFLs above are the traditional BEFLs with the Brillouin pump. To the best knowledge of us, there is no self-seeded BEFL with 20 GHz frequency gap reported.

In this paper, we propose a self-seeded multiwavelength BEFL with 20 GHz frequency gap. The relation between the pump power and the spectra is investigated. The factor that induces the double frequency gap is investigated and proved. 44 output channels with 20 GHz gap are generated when the pump power is 300 mW. The SNR of the multi-wavelength comb is more than 20 dBm.

2. EXPERIMENTAL AND PRINCIPLES

The experimental setup of the multi-wavelength brillouin-erbium fiber laser is shown in Figure 1. The 50 : 50 coupler is the core component in the ring cavity: port a works as the output port, port b and port d form a ring cavity, port c connects to a Sagnac loop. In the ring cavity there are a 980/1550 wavelength division multiplexing (WDM), 980 nm pump laser, 11 m L-band erbium-doped fiber (EDF), 12 km single mode fiber (SMF). The EDF is produced by OFS, its absorption coefficient at 1530 nm is 28.81 dB/m. The 12 km SMF is produced by Yangtze Optical Fibre and Cable Company. Its mode field diameter at 1550 nm is $9.9 \sim 10.9$ μm and the dispersion at 1550 nm is 18 ps/(ns · km). The Sagnac loop filter consists of a 50 : 50 coupler, 10 cm and 18 cm long PMFs and two polarization controllers. The intensity transfer function of the Sagnac loop filter can be expressed as $T = [\sin\theta\cos(\frac{\pi l\Delta n}{\lambda})]^2$ [24], where θ is the initial polarization angle, l is the length

of the PM fiber, and Δn represents the effective refractive index difference between the slow and fast axes of the PMF. In our case, the Sagnac loop filter serves as a reflective filter. A two-section Sagnac loop filter is used in the cavity because it has better performance for gain-flatten of the EDFA [25]. An AQ6370 optical spectrum analyzer (OSA) with resolution of 0.02 nm was used to measure the output spectra of the laser. The mechanism of the laser is shown in reference [19]: when a lasing mode is established, its linewidth is narrowed by the Rayleigh scattering in the SMF, the narrow linewidth mode becomes the pump for the SBS effect in the SMF.

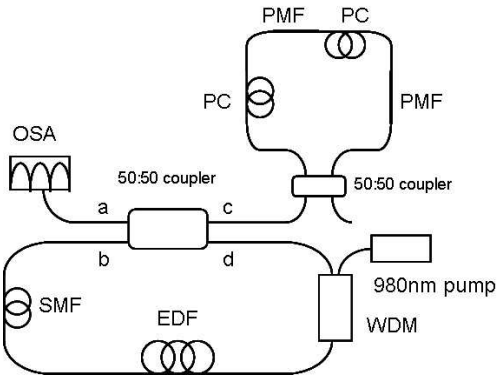

Figure 1: The experimental setup of the multi-wavelength brillouin-erbium fiber laser, EDF: Erbium-doped fiber, OC: optical coupler, OSA: optical spectrum analyzer, SMF: Single mode fiber, PC: polarization controller, PMF: polarization maintaining fiber.

3. RESULTS AND DISCUSSION

In this experiment, the multi-wavelength comb is observed when the power of 980 nm pump laser is above 200 mW. The spectra are shown in Figure 2 when the power varies from 200 mW to 300 mW with the 20 mW interval. When the pump power is less than 240 mW, there appears multi-wavelength comb, but it is not strong enough to suppress the mode competition in the cavity. When the pump power is 260 mW, there appears stable multiwavelength comb. The number of the lines increases with the pump power. In our experiment, the maximum pump power is 300 mW, there are 36 peaks above -20 dBm.

In order to check the frequency gap, the fine spectra from 1597 nm to 1599 nm in Figure 2 at 300 mW pump power are shown in Figure 3. There are 12 peaks in 2 nm. It indicates that the frequency gap between adjacent peaks is 20 GHz.

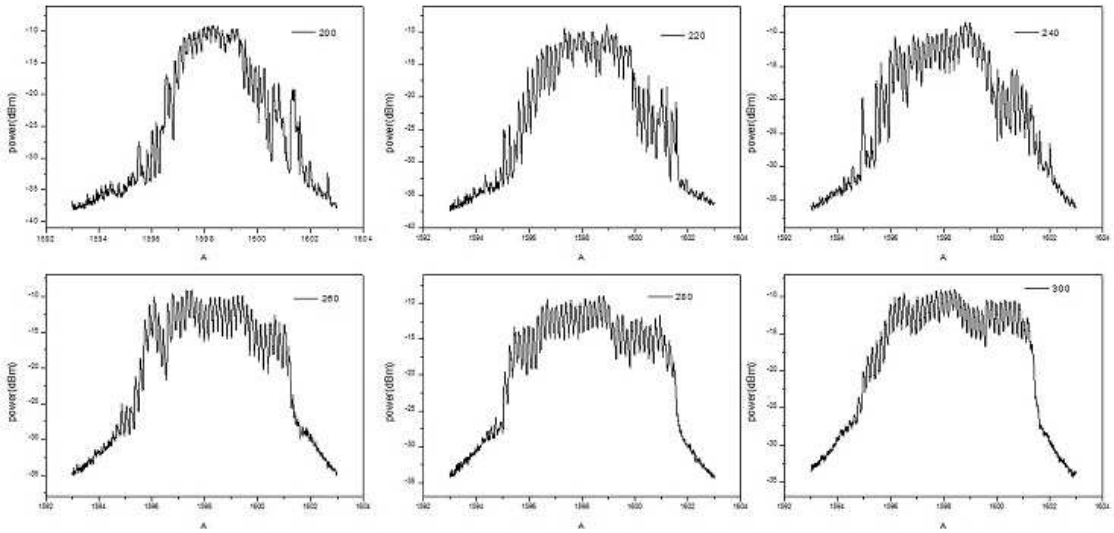

Figure 2: The spectra of multi-wavelength combs when 980 nm pump power varies from 200 mW to 300 mW.

The reason why the frequency gap is 20 GHz is the different paths that the lights at different directions go through. In the cavity, the path of the output light at clockwise direction is the

SMF-port b-port c-port a, the path of the other part light at clockwise direction is the SMF-port b-port d-EDF-the SMF; the path of the output light at anti-clockwise direction is the SMF-EDF-port d-port a, the path of the other part light at anti-clockwise direction is the SMF-EDF-port d-port b-the SMF. In BEFL, the location of the EDFA has big effect on the output characteristics of the laser [26]. Before output, the light at anti-clockwise direction is amplified by the EDFA, but the light at clockwise direction is not. So the output lights at different directions have big power difference, the output spectrum only shows the light from anti-clockwise direction. It induces that the frequency gap becomes 20 GHz.

In the previous results, the light at clockwise direction can't be shown because it is not amplified before output. In order to equalize the power, another EDFA that consists of a 980 nm pump, a WDM and 11 meters long EDF is inserted into the left side of the ring cavity. In the new structure, the light at clockwise direction can be amplified before output. It can compensate the power difference of the light at different direction.

There is stable multiwavelength output when the 980 nm pump power at left side is 130 mW and the 980 nm pump power at right side is 126 mW. Figure 4 shows the output multiwavelength comb. The small figure at the right top in Figure 5 shows the fine spectra at the range from 1601 nm to 1602 nm. There are 12 peaks in 1 nm. It indicates that the frequency gap is 10 GHz. It proves that the reason of double frequency gap is the lack of the amplifier at left side.

From Figure 2 to Figure 4, the SNR of the output is less than 5 dB. It is not good enough for application. In order to improve the SNR, the EDF in the cavity is changed. The new 10-meter-long EDF is produced by Nufern, whose absorption coefficient at 1530 nm is 25.0 ± 2.0 dB/m. The

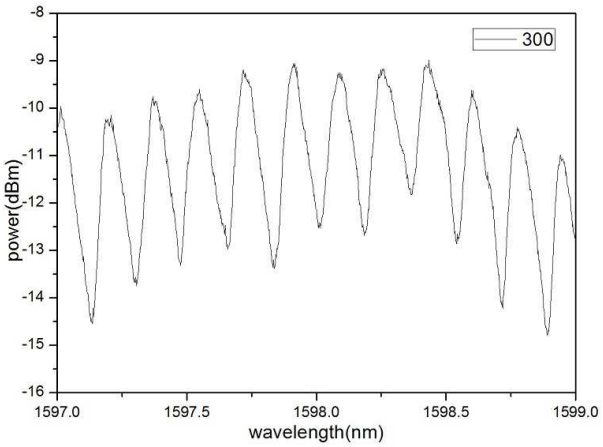

Figure 3: The fine Spectra of multi-wavelength combs when 980 nm pump power fixed at 300 mW.

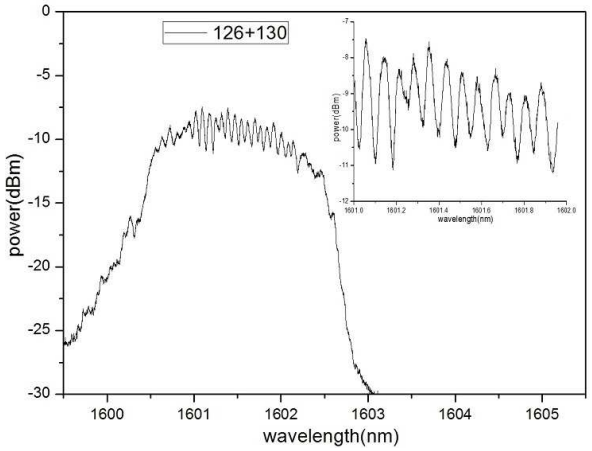

Figure 4: The spectra of the laser with two amplifiers.

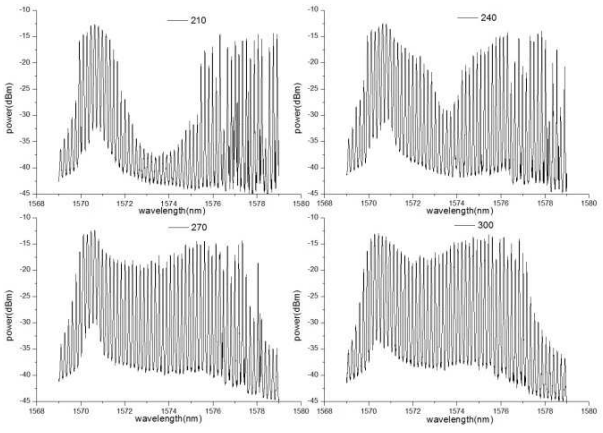

Figure 5: The spectra of multi-wavelength combs when 980 nm pump power is 210 mW, 240 mW, 270 mW, 300 mW.

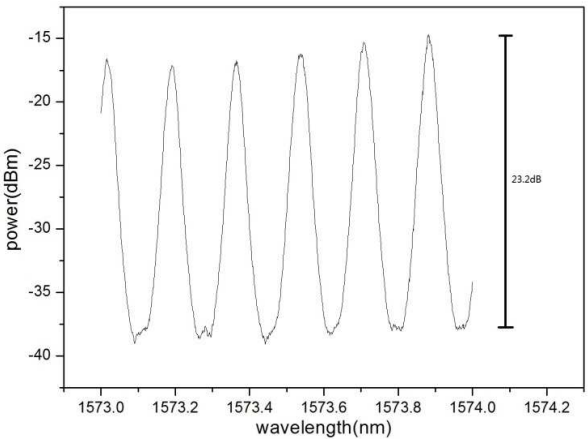

Figure 6: The fine spectra from 1573 nm to 1574 nm when the pump power is 300 mW.

relationship between the multi-wavelength comb and the power of 980 nm pump laser is shown in Figure 5. The power varies from 210 mW to 300 mW with the 30 mW interval. When pump power is 300 mW, there are 44 peaks above −25 dBm.

In order to check the SNR of the multi-wavelength comb, the fine spectra from 1573 nm to 1574 nm in Figure 5 at 300 mW pump power are shown in Figure 6. There are 6 peaks. The biggest SNR is 23.2 dB. The SNR of the lines in figure 6 is more than 20 dB.

4. CONCLUSION

We have successfully demonstrated a self-seeded multi-wavelength brillouin-erbium fiber laser with double frequency gap. The influence of the pump power on the multiwavelength output is investigated. The reason of the double-frequency-gap is the gain difference in different directions. When the amplifier is balanced in both sides of the SMF, the frequency gap becomes normal. At the same time, the method to improve the SNR of the multiwavelength comb is reported. The multi-wavelength comb with 44 double-brillouin-frequency stokes lines is obtained when the pump power is 300 mW. The multiwavelenghth BEFL can be used for potential applications in DWDM and optical sensor systems.

REFERENCES

1. Agrawal, G. P., *Nonlinear Fiber Optics*, 4th Edition, 329, Academic, San Diego, CA, 2007.
2. Song, Y. J., L. Zhan, S. Hu, et al., *IEEE Photon. Technol. Lett.*, Vol. 16, 2015–2017, 2004.
3. Nasir, M. N. M., Z. Yusoff, M. H. Al-Mansoori, et al., *Opt. Exp.*, Vol. 17, 12829–12834, 2009.
4. Zhao, J., T. Liao, X. Yang, et al., *J. Opt.*, Vol. 12, 115202, 2010.
5. Bernini, R., A. Minardo, and L. Zeni, *Opt. Lett.*, Vol. 29, 1977–1979, 2004.
6. Dong, Y., L. Chen, and X. Bao, *Opt. Lett.*, Vol. 36, 277–279, 2011.
7. Song, K. Y., M. González Herráez, and L. Thévenaz, *Opt. Exp.*, Vol. 13, 82–88, 2005.
8. Wu, Y. L. Zhan, Y. Wang, S. Luo, and Y. Xia, *J. Opt. Soc. Am. B*, Vol. 28, 2605–2610, 2011.
9. Zhang, L., L. Zhan, K. Qian, et al., *Phys. Rev. Lett.*, Vol. 107, 093903, 2011.
10. Zhu, Z., D. J. Gauthier, and R. W. Boyd, *Science*, Vol. 318, 1748–1750, 2007.
11. Sancho, J., N. Primerov, S. Chin, et al., *Opt. Exp.*, Vol. 20, 6157–6162, 2012.
12. Liu, J., L. Zhan, P. Xiao, et al., *IEEE Photon. Technol. Lett.*, Vol. 24, 22–24, 2012.
13. Cowle, G. J. and D. Y. Stepanov, *Opt. Lett.*, Vol. 21, 1250–1252, 1996.
14. Harun, S. W., S. Shahi, and H. Ahmad, *Opt. Lett.*, Vol. 34, 46–48, 2009.
15. Wang, G., L. Zhan, J. Liu, et al., *Opt. Lett.*, Vol. 38, 19–21, 2013.
16. Chen, M., Z. Meng, X. Tu, and H. Zhou, *Opt. Lett.*, Vol. 38, 2041–2043, 2013.
17. Cowle, G. J. and D. Yu. Stepanov, *IEEE Photon. Technol. Lett.*, Vol. 8, 1465–1467, 1996.
18. Al-Alimi, A. W., M. H. Yaacob, A. F. Abas, et al., *IEEE Photonics J.*, Vol. 5, 1501010, 2013.
19. Song, Y. J., L. Zhan, J. H. Ji, Y. Su, Q. H. Ye, and Y. X. Xia, *Opt. Lett.*, Vol. 30, 486–488, 2005.
20. Huang, Y., L. Zhan, J. Ji, S. Luo, and Y. Xia, *Opt. Commun.*, Vol. 281, 452–456, 2008.
21. Oh, W. Y., J. S. Ko, D. S. Lim, and W. Seo, *Opt. Commun.*, Vol. 201, 399–403, 2002.
22. Abd-Rahman, M. K., M. K. Abdullah, and H. Ahmad, *Opt. Commun.*, Vol. 181, 135–139, 2000.
23. Shee, Y. G., M. H. Al-Mansoori, A. Ismail, et al., *Opt. Exp.*, Vol. 19, 1699–1706, 2011.
24. Fang, X., H. Ji, C. T. Allen, et al., *IEEE Photon. Technol. Lett.*, Vol. 9, 458–460, 1997.
25. Li, S., K. S. Chiang, and W. A. Gambling, *IEEE Photon. Technol. Lett.*, Vol. 13, 942–944, 2001.
26. Hambali, N. A. M. A., M. A. Mahdi, et al., *Opt. Exp.*, Vol. 17, 11768–11775, 2009.

Product Trends of Optical *E*-field Sensor

Yoshikazu Toba[1], **Jun Ichijoh**[1], **Takehiro Morioka**[2], **Masanobu Hirose**[2], **and Satoru Kurokawa**[2]

[1]SEIKOH GIKEN Co., Ltd. 296-1, Matsuhidai, Matsudo, Chiba 270-2214, Japan
[2]National Institute of Advanced Industrial Science and Technology
1-1-1, Umezono, Tsukuba, Ibaraki 305-8563, Japan

Abstract— We have developed the Optical Electric Field Sensor utilizing the Pockels effect of lithium niobate ($LiNbO_3$), and proposed it for EMC measurement.

This sensor can measure not only *E*-field strength but also frequency and phase. The feature of this sensor are: mitigating disturbance of the surrounding *E*-field, high-accuracy, elimination of common noise, small sensor head, measurement ability of any kinds of modulations such as AM, FM, CDMA and so on and wide frequency range such as 100 kHz to 10 GHz.

In this paper, we introduce some applications of the optical electric field sensor. And we describe the efforts of some of the future.

1. INTRODUCTION

In recent years, the damage to other electronic devices by electromagnetic radiation has becomes a problem depending on spread to wireless devices. Therefore, Measurement technique which can accurately measure the electromagnetic wave is required.

We have developed Optical *E*-field Sensor and measurement technology using RoF (Radio over Fiber) technology. And we have introduced them for EMC (electro-magnetic compatibility) field [1–3]. Features of this sensor utilizing Pockels effect of lithium niobate are shown below:

a. Passive acquisition of signals, mitigating disturbances of the surrounding *E*-field.
b. Precise measurements of Frequency, Phase, and *E*-field.
c. High sensitivity and linear response over a broad frequency range.
d. Miniaturized sensor heads.
e. Elimination of common noise.

In the measurement of the Free-space *E*-field strength, the conventional method of using antenna had been degraded accuracy of *E*-field measurement by feed line (coaxial cable). Namely, the coaxial cable induce disturbance of the surrounding *E*-field. This Optical *E*-field Sensor with above features can be expected accuracy of *E*-field measurement improvement.

The radio waves are shortened by the high frequency of wireless device, so the sensor is required to minute spatial resolution. The conventional method could not increase the resolution of the measurement. Optical *E*-field Sensor is formed antenna elements on the LN substrate, so sensor head can be reduced the dimension.

In this paper, we introduce some applications of the Optical *E*-field Sensor. And I describe the efforts of some of the future.

2. OPTICAL *E*-FIELD SENSOR

2.1. Structure of the Optical *E*-field Sensor

As shown in Fig. 1, the Optical *E*-field Sensor consists of a sensor head, controller, single-mode optical fibers for signal transfer, and spectrum analyzer for signal analysis.

The controller consists of an optical source unit, optical circulator, optical fiber amplifier, O/E converter, and control circuit. Here, optical fiber amplifier compensate the fluctuation of the optical power due to optical fiber bending or contact.

Un-modulated light emitted from the optical source unit (optical wavelength: 1550 nm) passes through the optical circulator, and is guided to the sensor head. This sensor head consist of a $3(W) \times 13(L) \times 0.5(t)$ mm LN (x-cut) crystal substrate, on which a 6 µm-wide optical waveguide, reflector, and optical fiber are formed via Ti diffusion.

Figure 2 shows an external view of sensor head. The sensor head uses interferometric branched optical modulators that branch the incoming light, and then combine it again. The LN crystal exhibits the Pockels effect. If an *E*-field is applied to this crystal, its refractive index is modulated. This modulation caused the speed of optical wave on the wave-guide to go faster or slower. The Mach-Zehnder interferometer converts this optical wave speed modulation to amplitude modulation.

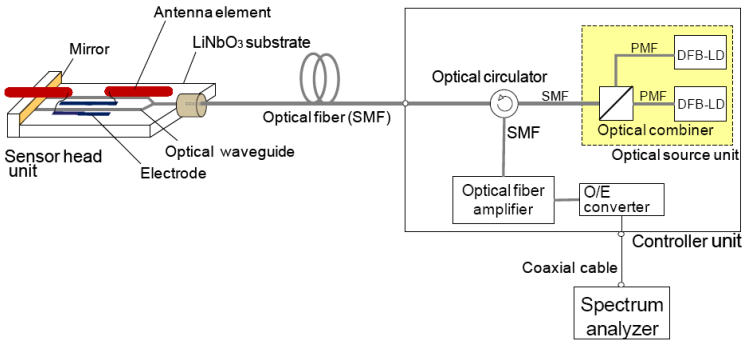

Figure 1: System diagram of the optical E-field sensor.

The light which has been amplitude modulated via a spatial E-field, returns again to the optical circulator, and is guided to the O/E converter. It is possible to measure the output on after O/E conversion with a spectrum analyzer, and measure the E-field strength near the sensor head.

In order to detect weak electric fields, this sensor uses an optical source with low relative intensity noise (RIN) and high light intensity, and it uses a reflective structure [4] that has about twice the round-trip sensitivity as a transmission type with the same modulation electrode length. The reflective structure only requires one optical fiber, which is an effective for miniaturizing the sensor head.

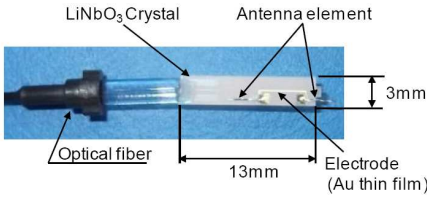

Figure 2: External view of sensor head.

2.2. Isotropic Composition

E-field sensor is required isotropic. So these three LN optical modulators are arranged onto the three sides of a triangle prism, obtaining isotropy as shown in Fig. 3 [5]. In other words, the three LN optical modulators are arranged so that they are at right angles to each other, and their maximum radiation angle from the optical waveguide is 54.7 deg., thus achieving isotropy. It is possible to measure the output on each axis, and measure the E-field strength (E) by applying the following formula.

$$E = \sqrt{E_x^2 + E_y^2 + E_z^2} \tag{1}$$

Here, E_x is the E-field strength on the X axis; E_y is the E-field strength on the Y axis; and E_z is the E-field strength on the Z axis.

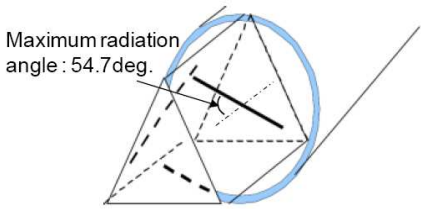

Figure 3: Structure of isotropic sensor head.

2.3. Product Family

Figure 4 shows the dynamic range of Isotropic Optical E-field Sensor which is commercialized. These sensors obtain wide frequency response (100 kHz–10 GHz) and wide dynamic range.

SH-10EL has miniaturized a sensor head by forming an electric field-detection antenna pattern on an LN crystal substrate. It is used to SAR (Specific Absorption Rate) measurement.

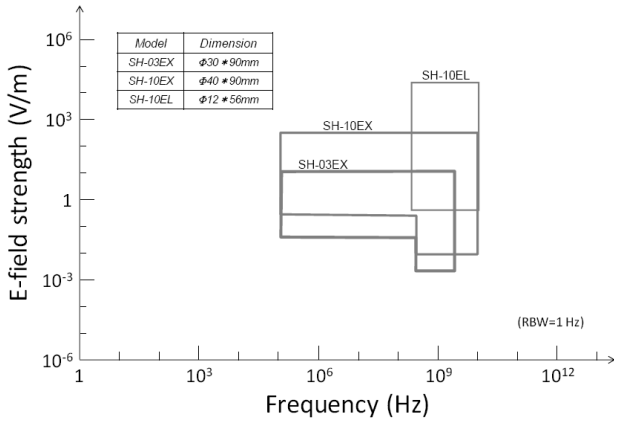

Figure 4: Dynamic range of isotropic optical E-field sensor.

3. PROPOSAL TO FIELD TRANSFER PROBE

The standard E-field is ordinary generated in an anechoic chamber or a TEM (transverse electromagnetic) cell. Since usable frequency and scale of the system, these methods are usually used for the primary standard field generation. In contrast to these methods, a G-TEM (Gigahertz-TEM) cell can realize a compact and wide frequency range E-field generation system. However, a field transfer probe is necessary for the E-field strength calibration of the G-TEM. So we expect that Optical E-field Sensor is adopted a field transfer probe from its features.

We studied the factors of output-power fluctuation of the optical E-field sensor. As a result, the output-power fluctuation factors are optical interference due to the cross talk of the optical circulator in addition to input optical power of the O/E converter. Improving the factors, this sensor obtained excellent performance of output-power fluctuation of 0.01 dB (Fig. 5). Uncertainty in E-field measurement using optical E-field sensor will be improved by it.

There is possibility that it will be adapted applications of standard E-field strength.

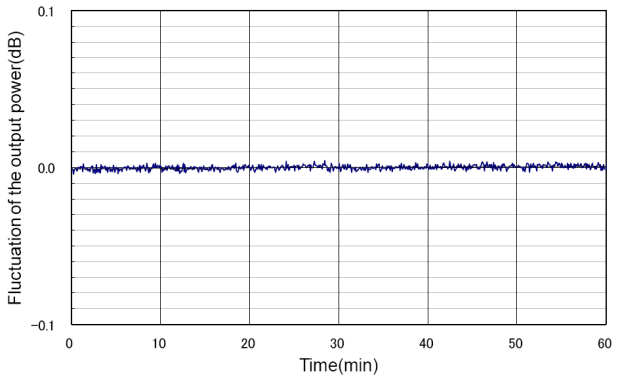

Figure 5: Stability of Optical E-field Sensor (25deg.) .

4. CONCLUSION

We described the structure and features of the optical E-field sensor using a Pockels effect of LN crystal. In the future, we will improve the uncertainty of the optical E-field sensor and establish of E-field measuring techniques in EMC field. In addition, we will propose to simple optical fiber link using RoF technologies for the improvement of disturbances of the surrounding E-field. We expect that it will find a wide variety of applications, including field distribution and high E-field measurement of transmission antennas and the like.

REFERENCES

1. Torihata, S., et al., "A high accuracy optical electric field sensor for an EMC application," *IEEJ Technical Report*, IM-00-54 58, 25–29, 2000.
2. Toba, Y., et al., "Development of micro isotropy optical electric field sensor," *IEICE(C)*, Vol. J91-C, No.1, 84–92, 2008.
3. Kurokawa, S., et al., "Optical fiber link for antenna measurement system," *IEICE(C)*, Vol. J91-C, No. 1, 64–74, 2008.
4. Kondo, M., et al., "Reflection type electro-optic electric field sensor with $LiNbO_3$ optical waveguide," *EMC SYMPOSIUM'94 SENDAI*, 19P606, 1994.
5. Loader, B. G., et al., "An optical electric field probe for specific absorption rate measurement," *15th International Zurich Symposium on Electromagnetic Compatibility*, 57–60, Zurich, 2003.

Ultrabroadband Infrared Spectroscopy by Chirped Pulse Upconversion

Takao Fuji, Yutaka Nomura, and Hideto Shirai
Institute for Molecular Science, Japan
(*Invited Paper*)

Abstract— We have demonstrated ultrabroadband infrared pump-probe spectroscopy using chirped pulse upconversion technique with a nonlinear mixing in a gas medium. Ultrafast pump-probe spectroscopy in a full mid-infrared region (200–5000 cm^{-1}) at high speed has been realized with the technique. By using the system, we have measured ultrafast carrier dynamics in Ge in the range of 200–5000 cm^{-1}.

1. INTRODUCTION

Supercontinuum in the mid-infrared spectral region (MIR, 500–4000 cm^{-1}) is a highly attractive light source for studies in molecular science and solid state physics since a number of molecular and lattice vibrations have resonance in this wavelength region. The light source can be applied to various advanced molecular and solid state spectroscopies, such as frequency comb spectroscopy for the molecular fingerprint region [1], pump-probe spectroscopy to trace ultrafast structural dynamics [2], real-time molecular imaging of biological tissues [3], etc.. For such applications, ultrabroadband MIR continuum generated by using four-wave mixing of two-color femtosecond pulses in gases is one of the most promising light sources. The MIR pulse generation by using this scheme was firstly demonstrated in 2007 [4], and the technique has been improved by several groups [5–11]. Recently, the light source has started to be used for a femtosecond pump-probe spectroscopy [12–14].

Single-shot detection of the entire MIR supercontinuum (500–4000 cm^{-1}) with reasonable resolution has been required for the above mentioned advanced molecular and solid state spectroscopies. It would be straightforward to measure the MIR spectrum with a dispersive MIR spectrometer consisting of a grating and a multichannel MIR detector. However, the bandwidth of this method has been limited to $\sim 500\,\mathrm{cm}^{-1}$ due to the low sensitivity and the high cost of the multichannel MIR detectors [15]. Moreover, overlapping diffraction orders from the grating would prevent simultaneous detection of multi-octave MIR supercontinuum spectra. One has to change the gratings in the spectrometer several times to record the multi-octave MIR spectra even though a multichannel MIR detector is used.

An alternative approach to detect the MIR supercontinuum with single-shot is optically converting the spectra into visible region and recording them with a visible spectrometer, which has much higher performance than the MIR spectrometers. In [16, 17], upconversion methods of MIR pulses with narrow band visible pulses were reported. An upconversion method with spectrally dispersed MIR pulses was also reported [18]. In [19–21], chirped pulses were used for upconversion of MIR pulses. However, the bandwidths of these upconversion methods have still been limited to $\sim 600\,\mathrm{cm}^{-1}$ because of the limited phase matching bandwidth of the nonlinear solid crystals for the upconversion [20].

Recently, we have demonstrated the chirped pulse upconversion (CPU) by using a gas as a nonlinear medium [22]. The detection bandwidth dramatically broadens to more than $5000\,\mathrm{cm}^{-1}$ due to the wide transmission range and the broadband phase matching condition of the gas medium. Although the low frequency conversion efficiency due to the low nonlinearity of the gas media is the large drawback of the method, it was possible to measure spectra over the range of MIR region, specifically 200–5500 cm^{-1} with $\sim 2\,\mathrm{cm}^{-1}$ resolution on a single-shot basis.

In this paper, we report the application of the gas-based CPU technique for ultrabroadband infrared pump-probe spectroscopy to study ultrafast dynamics in Ge (germanium). By using the system, we have measured ultrafast carrier dynamics in Ge in the range of 200–5000 cm^{-1}.

2. EXPERIMENTAL SETUP

The ultrabroadband infrared pump-probe spectroscopy with CPU was realized with the system shown in Fig. 1(a). The light source was based on a Ti : sapphire multi-pass amplifier system (800 nm, 30 fs, 0.85 mJ at 1 kHz, Femtopower compactPro, FEMTOLASERS). The output pulse

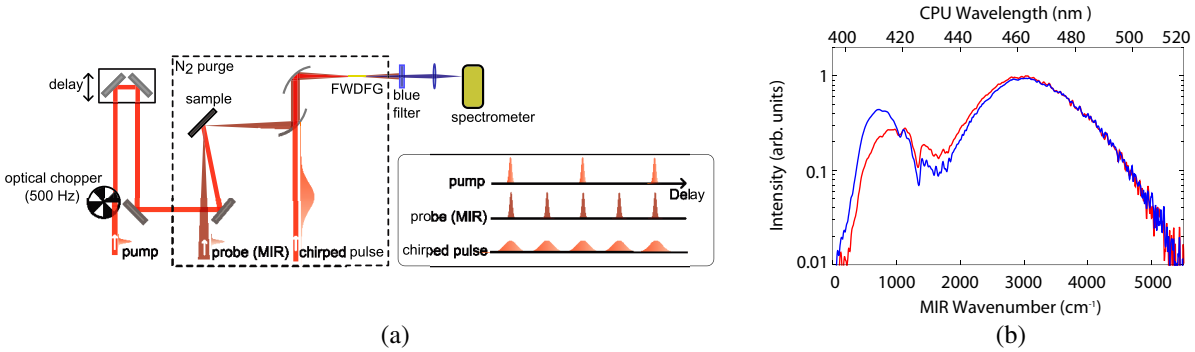

(a) (b)

Figure 1: (a) Schematic illustration of the experimental setup. (b) Typical upconverted spectra of the MIR pulse reflected by the sample (Ge) with (blue curve) and without (red curve) the pump pulse, respectively.

was split into three, the first pulse (595 μJ) was for infrared generation, the second pulse (255 μJ) was the pump pulse for the pump-probe spectroscopy, and the third pulse (128 μJ) was used as a chirped pulse for CPU.

The ultrabroadband infrared pulse for the probe pulse at the pump-probe spectroscopy was generated by using four-wave mixing of fundamental and second harmonic of Ti : sapphire amplifier output through filamentation in nitrogen [11]. The pulse duration and spectral range of the infrared pulse were ~ 7 fs and 200–5000 cm^{-1}, respectively. The infrared pulse was reflected by three BK7 substrates coated with indium tin oxide ($t = 300$ nm), which reflect the infrared pulse without adding any chirp and transmit the residual visible beam along the infrared pulse. The infrared pulse was focused onto a sample, a Ge substrate, by using a concave mirror ($f = 0.75$ m). The angle of the incidence of the beam was $\sim 45°$, and the polarization of the infrared pulse was p-polarization. The diameter of the infrared beam on the sample was ~ 0.4 mm.

The pump pulse (800 nm, 30 fs) was collimated down to 4 mm diameter and overlapped to the infrared pulse on the sample. The spot size of the pump pulse is much larger than that of the probe pulse so that the pump pulse excites the sample with homogeneous intensity in the whole region where the probe pulse was focused. For shot-to-shot data acquisition of reflectivity-change signals, every second pump pulse was blocked by using a mechanical chopper, which is synchronized with a half-frequency of the repetition rate of the laser pulse train.

The power of the infrared pulse reflected by the sample was much smaller than that in our previous gas-based CPU experiment [22]. To achieve reasonable signal-to-noise ratio with such condition, we had to make the pulse duration of the chirped pulse much shorter than that in the previous experiment. The pulse duration of the chirped pulse which passed through one ZnSe ($t = 3$ mm) and four BK7 ($t = 8$ mm) substrates was ~ 0.4 ps. The frequency resolution of the spectroscopy becomes 41 cm^{-1} with such a chirped pulse. Although it is 20 times worse than that in our previous experiment, the resolution is enough for our current experiment. The chirped pulse was combined with the infrared pulse reflected by the sample through a mirror with a hole. The combined beam was focused into nitrogen with a parabolic mirror ($f = 50$ mm) and upconverted into a visible beam (ω_2, 400–500 nm) through four-wave difference frequency generation (FWDFG, $\omega_1 + \omega_1 - \omega_0 \rightarrow \omega_2$) of the chirped pulse ($\omega_1$) and the infrared pulse (ω_0).

The FWDFG signal generated at a fixed delay between the infrared and chirped pulses was sent to a ~ 0.3 m focal length spectrometer with a 300 grooves/mm grating in combination with a 1600 × 400 pixel EMCCD camera (SP-2358 with ProEM+1600, Princeton Instruments) with spectral resolution of ~ 0.2 nm. The upconverted spectrum was obtained by accumulating 100 pairs of with/without-pump infrared spectra at each delay time between the pump and probe pulses to achieve a reasonable signal-to-noise ratio. Figure 1(b) shows a pair of with/without-pump infrared spectra after removing cross-phase modulation due to CPU [23].

3. RESULTS

Figures 2 and 3 show the ultrafast reflectivity-change signal, $\Delta R = R$, of Ge for the excitation density of 202 $\mu\mathrm{J/cm}^2$, 135 $\mu\mathrm{J/cm}^2$ and 67 $\mu\mathrm{J/cm}^2$. One trace can be obtained within 20 minutes. The sensitivity of the method is ~ 10 mOD in the region from 300 cm^{-1} to 4000 cm^{-1}. A large increase ($\Delta R/R \sim 2$ at 202 $\mu\mathrm{J/cm}^2$ excitation density) in reflectivity with the peak at ~ 300 cm^{-1} was observed, on the other hand, some decrease of the reflectivity was observed in the rather

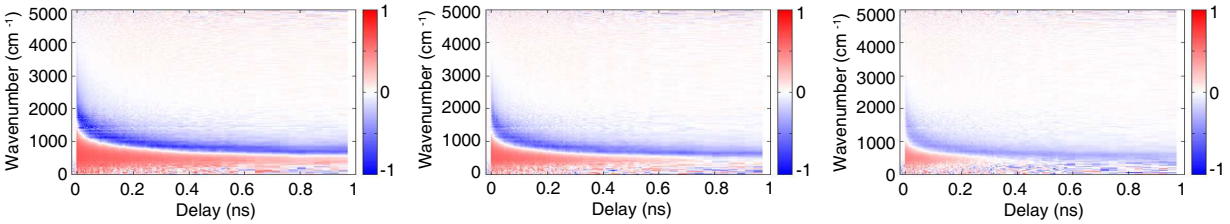

Figure 2: Ultrafast reflectivity-change signal $\Delta R/R$ of Ge under variable excitation density: (a) 202 μJ/cm^2, (b) 135 μJ/cm^2, (c) 67 μJ/cm^2.

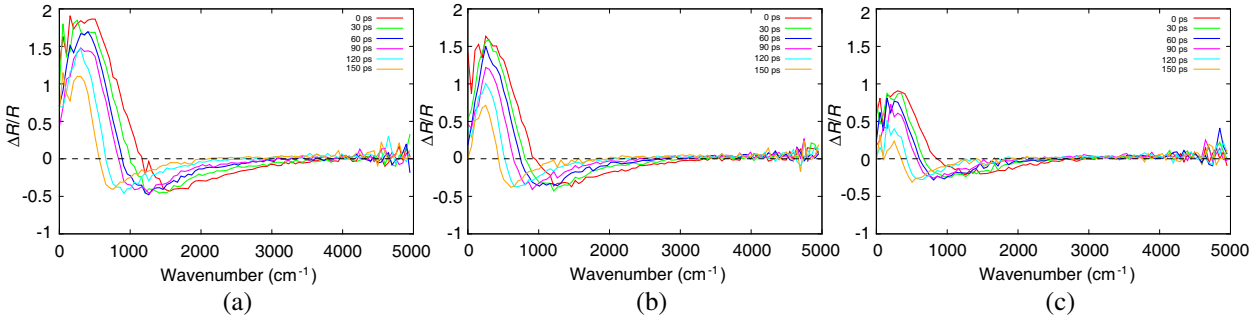

Figure 3: Ultrafast reflectivity-change signal $\Delta R/R$ of Ge under variable excitation density at several delay times: (a) 202 μJ/cm^2, (b) 135 μJ/cm^2, (c) 67 μJ/cm^2.

high frequency region (500–3000 cm^{-1}). The frequency of the reflectivity reduction shifts to lower frequency by increasing the delay time. Even though increase and decrease of the reflectivity was observed in the broad spectrum region, such reflectivity change can be explained as induced absorption due to free-carrier absorption.

4. CONCLUSION

In conclusion, we described ultrabroadband infrared pump-probe spectroscopy using gas-based CPU technique. We have applied the gas-based CPU technique for femtosecond infrared pump-probe spectroscopy to study ultrafast carrier dynamics in Ge. By using the system, we have measured several hundred picosecond recovery of the induced absorption due to the free-carrier absorption in the range of 200–5000 cm^{-1}.

ACKNOWLEDGMENT

This work was supported by NINS Program for Cross-Disciplinary Study, the Joint Studies Program (2012–2013) of the Institute for Molecular Science, MEXT/JSPS KAKENHI (24360030), and SENTAN, JST (Japan Science and Technology Agency).

REFERENCES

1. Schliesser, A., N. Picque, and T. W. Haensch, "Mid-infrared frequency COMBS," *Nature Photon.*, Vol. 6, No. 7, 440–449, 2012.
2. Bakker, H. J. and J. L. Skinner, "Vibrational spectroscopy as a probe of structure and dynamics in liquid water," *Chem. Rev.*, Vol. 110, No. 3, 1498–1517, 2010.
3. Barth, A., "Infrared spectroscopy of proteins," *Biochem. Biophys. Acta*, Vol. 1767, No. 9, 1073–1101, 2007.
4. Fuji, T. and T. Suzuki, "Generation of sub-two-cycle mid-infrared pulses by four-wave mixing through filamentation in air," *Opt. Lett.*, Vol. 32, 3330–3332, 2007.
5. Théberge, F., M. Châteauneuf, G. Roy, P. Mathieu, and J. Dubois, "Generation of tunable and broadband far-infrared laser pulses during two-color filamentation," *Phys. Rev. A*, Vol. 81, No. 3, 033821, 2010.
6. Petersen, P. B. and A. Tokmakoff, "Source for ultrafast continuum infrared and terahertz radiation," *Opt. Lett.*, Vol. 35, No. 12, 1962–1964, 2010.

7. Thomson, M. D., V. Blank, and H. G. Roskos, "Terahertz white-light pulses from an air plasma photo-induced by incommensurate two-color optical fields," *Opt. Express*, Vol. 18, No. 22, 23173–23182, 2010.
8. Lassonde, P., F. Théberge, S. Payeur, M. Châteauneuf, J. Dubois, and J. C. Kieffer, "Infrared generation by filamentation in air of a spectrally shaped laser beam," *Opt. Express*, Vol. 19, No. 15, 14093–14098, 2011.
9. Cheng, M., A. Reynolds, H. Widgren, and M. Khalil, "Generation of tunable octave-spanning mid-infrared pulses by filamentation in gas media," *Opt. Lett.*, Vol. 37, No. 11, 1787–1789, 2012.
10. Nomura, Y., H. Shirai, K. Ishii, N. Tsurumachi, A. A. Voronin, A. M. Zheltikov, and T. Fuji, "Phase-stable sub-cycle mid-infrared conical emission from filamentation in gases," *Opt. Express*, Vol. 20, No. 22, 24741–24747, 2012.
11. Fuji, T. and Y. Nomura, "Generation of phase-stable sub-cycle mid-infrared pulses from filamentation in nitrogen," *Appl. Sci.*, Vol. 3, No. 1, 122–138, 2013.
12. Calabrese, C., A. M. Stingel, L. Shen, and P. B. Petersen, "Ultrafast continuum mid-infrared spectroscopy: Probing the entire vibrational spectrum in a single laser shot with femtosecond time resolution," *Opt. Lett.*, Vol. 37, No. 12, 2265–2267, 2012.
13. De Marco, L., K. Ramasesha, and A. Tokmakoff, "Experimental evidence of fermi resonances in isotopically dilute water from ultrafast broadband IR spectroscopy," *J. Phys. Chem. B*, Vol. 117, No. 49, 15319–15327, 2013.
14. Stingel, A. M., C. Calabrese, and P. B. Petersen, "Strong intermolecular vibrational coupling through cyclic hydrogen-bonded structures revealed by ultrafast continuum mid-IR spectroscopy," *J. Phys. Chem. B*, Vol. 117, No. 49, 15714–15719, 2013.
15. Cho, M., *Two-dimensional Optical Spectroscopy*, CRC Press, Boca Raton, 2009.
16. Heilweil, E. J., "Ultrashort-pulse multichannel infrared spectroscopy using broadband frequency conversion in $LiIO_3$," *Opt. Lett.*, Vol. 14, No. 11, 551–553, 1989.
17. Dougherty, T. P. and E. J. Heilweil, "Dual-beam subpicosecond broadband infrared spectrometer," *Opt. Lett.*, Vol. 19, No. 2, 129–131, 1994.
18. De Camp, M. F. and A. Tokmakoff, "Upconversion multichannel infrared spectrometer," *Opt. Lett.*, Vol. 30, No. 14, 1818–1820, 2005.
19. Kubarych, K. J., M. Joffre, A. Moore, N. Belabas, and D. M. Jonas, "Mid-infrared electric field characterization using a visible charge-coupled-device-based spectrometer," *Opt. Lett.*, Vol. 30, No. 10, 1228–1230, 2005.
20. Baiz, C. R. and K. J. Kubarych, "Ultrabroadband detection of a mid-IR continuum by chirped-pulse upconversion," *Opt. Lett.*, Vol. 36, No. 2, 187–189, 2011.
21. Zhu, J., T. Mathes, A. D. Stahl, J. T. M. Kennis, and M. L. Groot, "Ultrafast mid-infrared spectroscopy by chirped pulse upconversion in 1800–1000 cm^{-1} region," *Opt. Express*, Vol. 20, No. 10, 10562–10571, 2012.
22. Nomura, Y., Y. T. Wang, T. Kozai, H. Shirai, A. Yabushita, C. W. Luo, S. Nakanishi, and T. Fuji, "Single-shot detection of mid-infrared spectra by chirped-pulse upconversion with four-wave difference frequency generation in gases," *Opt. Express*, Vol. 21, No. 15, 18249–18254, 2013.
23. Lee, K. F., P. Nuernberger, A. Bonvalet, and M. Joffre, "Removing cross-phase modulation from midinfrared chirped-pulse upconversion spectra," *Opt. Express*, Vol. 17, No. 21, 18738–18744, 2009.

Analysis and Design of the Dielectric Yagi-Uda Nanoantenna with a Double Driven Element

Thanatcha Satitchantrakul and Rardchawadee Silapunt
Department of Electronic and Telecommunication
King Mongkut's University of Technology Thonburi, Bangkok, Thailand

Abstract— The Yagi-Uda silicon nanoantenna with the double driven element and 4 directors is proposed here. The simulation of single Si nanoparticles with a diameter between 40 and 53 nm shows an increasing of the directivities for all emitter locations. The trend of the directivity appears to be random as the nanoparticle dimension and emitter distance increase. For the double driven element, the directivity profiles as a function of the radius appears to be wave-like forms. The directivity is clearly determined by two competing factors that are particle coupling and dimension. The directivity of the Yagi-Uda Si nanoantenna can be improved with more number of directors. The maximum directivity of the proposed structure with optimized geometric parameters is 11.42. The preliminary numerical model for predicting the directivity of this antenna is determined. The directivity can be further improved to 12.52 by reducing the gap between the double driven element and the first director.

1. INTRODUCTION

The diffraction limit issue has significantly impeded the development of silicon photonic waveguides for nanoscale interconnect integration in integrated circuits. Currently, many researchers propose a variety of subwavelength scale methods to overcome this problem [1–3]. However, most of them still suffer from high absorption loss during guided-transmission when compared to the silicon (Si) photonic waveguide. Optical wireless nano interconnects using metallic antennas have later been explored. It is found that the plasmonic scheme can potentially reduce such loss [4–8]. However, the absorption loss can be further reduced by the introduction of Si nanoparticles antennas [8, 9]. This dielectric material possesses promising optical and radiation properties at the optical frequency. As the interconnect, the Si nanoparticles antenna can remarkably enhance the transfer data rate in an intrachip link. With a proper design, its performance can certainly be improved.

In this paper, we propose a design and simulation of the Si Yagi-Uda nanoantenna array with a double driven element, for optical transmission. We will determine radiation properties including directivity and radiation patterns for different antenna structures, using computer-aided simulation. Section 2 presents the design approach and simulation parameters and Section 3 presents results and discussion. The conclusion is described in Section 4.

2. DESIGN APPROACH AND SIMULATION PARAMETERS

All model structures consist of Si nanoparticles embedded in SiO_2 to minimize the loss associated with signal refraction. A dipole source is used as an emitter to excite the antenna and placed at the left end of a structure. The process of designing the Yagi-Uda nanoantenna array is as follows. First, the antenna directivity and radiation pattern of single Si nanoparticles with the radius between 40–80 nm are investigated [10]. The exciting wavelength of 660 nm (455 THz) is selected. Note that, this wavelength is simply chosen to demonstrate radiation properties of Si nanoparticles in the visible region. Next, the directivity, radiation pattern, and return loss of the double driven element are studied for different gap sizes at the same exciting wavelength. The Yagi-Uda structures with the double driven element with 1 and 4 directors respectively, are then investigated. The Lorentzian 4 parameters are applied to determine the correlation of geometric

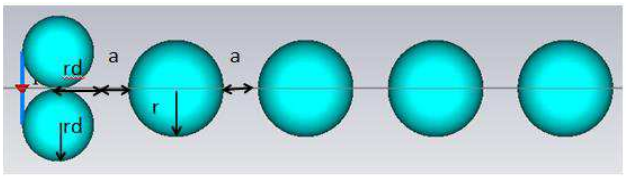

Figure 1: The Yagi-Uda silicon nanoantenna with the double driven element and 4 directors.

parameters. The Finite Integrated Method (FIT) has been used in all simulations. The proposed antenna with 4 directors is shown in Figure 1. The radii of the driven element and director are denoted at rd and r respectively, the side-to-side gap is denoted as d, the emitter distance is denoted as a, and the vertical gap between driven elements is denoted as g.

3. RESULTS AND DISCUSSION

3.1. Single Si Nanoparticles

In this study, the emitter is placed at the distance a, from the Si nanoparticle as shown in Figure 2(a). Figure 2(b) shows the directivity as a function of the emitter location, for different sizes of Si nanoparticles. It can be seen that directivities increase monotonically with the radius only from 40 to 53 nm and start to oscillate after that. The trend of the directivity as a function of the emitter location is also random. The maximum directivity of 4.4 is obtained from the $r = 80$ nm particle and $a = 5.3$ nm. It is believed that the directivity can be further increased with larger particle sizes. However, they may be out of range for magnetic resonance support [10]. The inset shows the radiation pattern associated with the specified particle. We found that the return loss

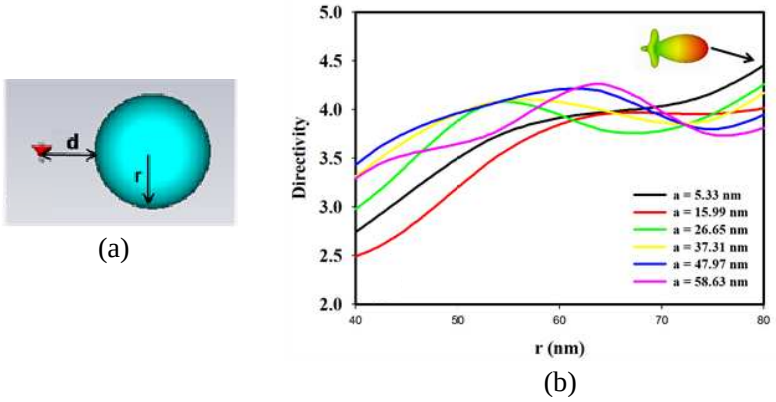

Figure 2: (a) A silicon nanoparticle and (b) directivity as a function of the emitter location.

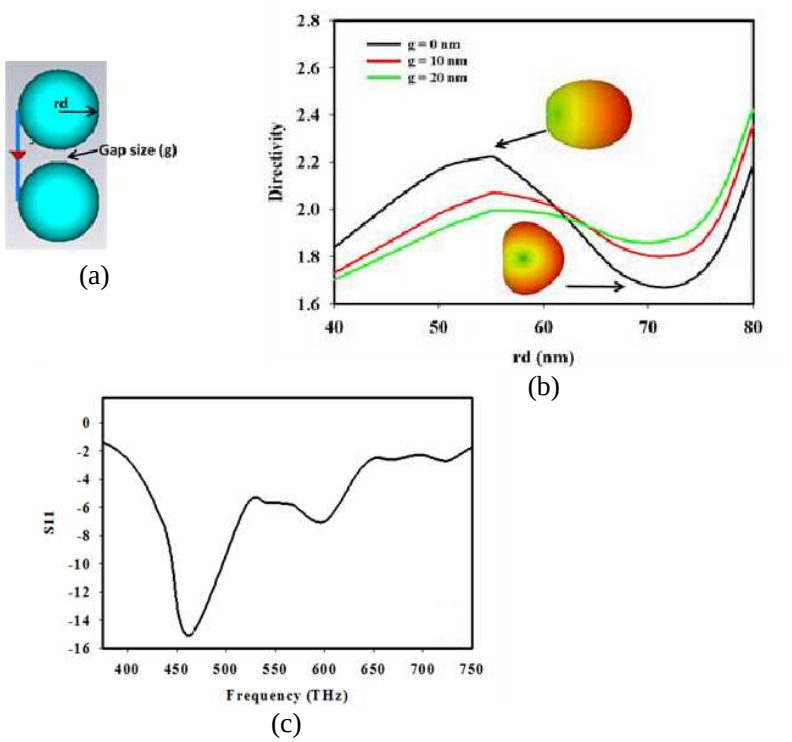

Figure 3: (a) Two silicon nanoparticles aligned vertically, (b) forward directivity as a function of rd for different gap sizes, and (c) insertion loss of the $rd = 54.5$ nm and $g = 0$ structure.

of the single Si nanoparticle, regardless of its dimension, is extremely high (the result is not shown here), suggesting very poor antenna efficiency.

3.2. Double Driven Element

Next, we consider two particles aligned vertically as shown in Figure 3(a). This study is performed in order to measure radiation properties of the double driven element. The emitter is placed on the left end of the elements. The exciting wavelength is 660 nm. Figure 3(b) shows the directivity as a function of the radius for $g = 0$, 10, and 20 nm. All directivity profiles exhibit wave-like forms. The directivity increases as the gap decreases up to $r = 62$ nm. The relation of the two parameters is clearly inversed after that. The insets show associated radiation patterns at $g = 0$, and $rd = 54.5$ and 72 nm, respectively. The result suggests that the directivity is likely product of two competing factors, i.e., rd and g. Note again that, the directivity can be further increased with larger particle sizes; however, they will be out of the magnetic resonance support range. Therefore, we instead consider the double driven element with $rd = 54.5$ nm that generates the maximum directivity of around 2.24 at $g = 0$. The insertion loss vs. the frequency of the mentioned structure is shown in Figure 3(c). The reflection coefficient $|\Gamma|$ at the wavelength of interest is calculated. We find that approximately, 96.9% of power can be transmitted through the double driven element.

3.3. Yagi-Uda Silicon Nanoantenna

The Yagi-Uda nanoantenna structure with the double driven element is created. The antenna with the double driven element and 1 director is first investigated followed by the proposed structure with 4 directors. The relationships of geometric parameters from both cases are considered for optimization of the antenna directivity. The optimized director and driven element parameters include $r = 74.6$ nm, $rd = 54.5$ nm, and $g = 0$, respectively. Figure 4 illustrates the directivities as a function of the wavelength for 1- and 4-director structures for different side-to-side gap distances. For the 1-director structure, the directivity profiles are fairly similar for all gap distances. The maximum directivity is around 5 and achieved at $\lambda = 650$ nm. The improvement of the directivity can be realized using the 4-director structure, as shown in Figure 5(b). We obtain the maximum directivity of around 11.42. The wavelength at maximum directivity slightly shifts up to 665 nm. Profiles are more similar as a increases. The result suggests the number of directors as one of the important design factors to improve the antenna performance.

From the result of the Yagi-Uda nanoantenna with the double driven element and 4 directors, we can derive the correlation among geometric parameters and directivity by Lorentzian 4 parameters. The preliminary numerical model of the directivity is shown in Equation (1). Note that, this equation can be used in the 400–800 nm range.

$$D = \left(2.549 + \frac{8.546}{1 + \left(\frac{\frac{rd}{r} - 0.805}{0.173} \right)^2} \right) - a, \tag{1}$$

where D is the nanoantenna directivity.

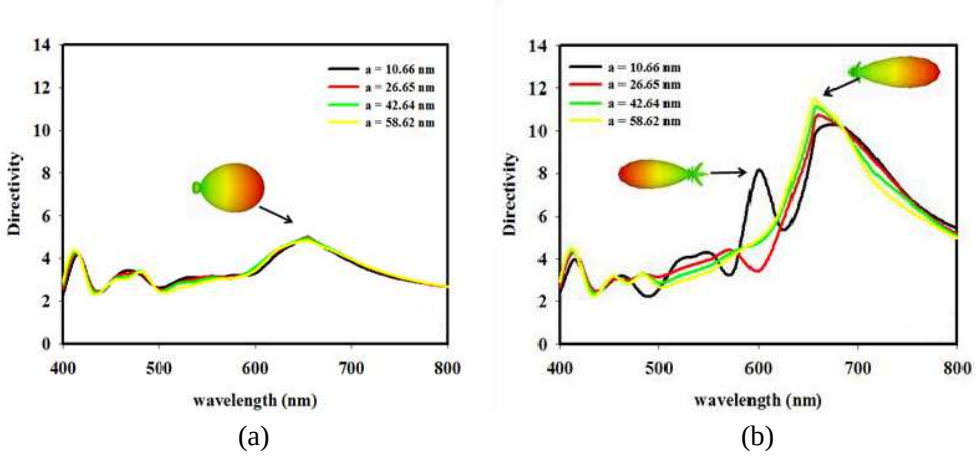

Figure 4: Directivity profile comparison between Yagi-Uda nanoantenna with (a) 1 director and (b) 4 directors.

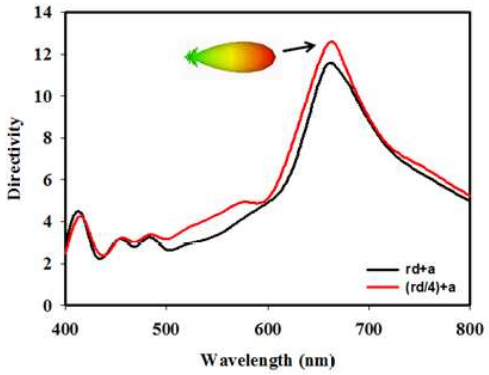

Figure 5: Directivity profiles for structures with distances $rd + a$ and $(rd/4) + a$.

We find that the directivity can be further improved by decreasing the distance between the double driven element and the first director. By simply reducing it from $rd + a$ to $(rd/4) + a$, the directivity can be slightly raised up to 12.52, found at $\lambda = 660\,\text{nm}$. Figure 5 compares the directivities for $rd + a$ and $(rd/4) + a$ structures. Inferred from this result, we believe that coupling between particles strongly affect the radiation properties of the antenna.

4. CONCLUSIONS

Overall, we have discussed the silicon optical nanoantenna as the transmitter for optical wireless link. Our proposed Yagi-Uda Si nanoantenna is made of Si particles and embedded in SiO_2. It is found that the directivity generated by the single Si particle only increases with the particle for $r = 40$–$53\,\text{nm}$, and the profiles become quite random after that. The directivity of two vertically-aligned particles used as the driven element increases as the gap decreases up to $rd = 62\,\text{nm}$. The relation of the two parameters is clearly inversed after that. The result suggests that the directivity is determined by competing effects between particle coupling and particle dimension. Geometric parameters are optimized for the Yagi-Uda with the double driven element structure to enhance directivity and antenna efficiency. The maximum directivity of 11.42 is achieved for the proposed 4-director structure. In addition, we derive the analytical expression for predicting the directivity of this nanoantenna in 400–800 nm range. We finally find that the directivity can be further improved by reducing the gap between the double driven element and the first director. The result suggests strong influence of coupling between particles.

REFERENCES

1. Bozhevolnyi, S. I., *Plasmonic Nanoguides and Circuits*, Pan Stanford Publishing Pte. Ltd., Singapore, 2009.
2. Dionne, J. A., E. Verhagen, A. Polman, and H. A. Atwater, "Are negative index materials achievable with surface plasmon waveguides? A case study of three plasmonic geometries," *Optical Society of America*, Vol. 16, No. 23, 2008.
3. Ctyroky, J., J. Homola, and M. Skalsky, "Modelling of surface plasmon resonance waveguide sensor by complex mode expansion an propagation method," *Optical and Quantum Electronics*, Vol. 29, No. 2, 301–311, Feb. 1997.
4. Alù, A and N. Engheta, "Wireless at the nanoscale: Optical interconnects using matched nanoantennas," *Physical Review Letters*, Vol. 104, 213902, 2010.
5. Novotny, L. and N. V. Hulst, "Antenna for light," *Natural Photonics*, Vol. 5, 83–90, 2011, Doi: 10.1038/nphoton.2010.237.
6. Taminiau, T. H., F. D. Stefani, and N. F. V. Hulst, "Enhanced directional excitation and emission of single emitters by a nano-optical Yagi-Uda antenna," *Optics Express*, Vol. 16, 10858–10866, 2008.
7. Solis, D. M., J. M. Taboada, F. Obelleiro, and L. Landesa, "Optimization of an optical wireless nanolink using directive nanoantennas," *Optics Express*, Vol. 21, No. 2, 2377, Jan. 28, 2013.
8. Maksymov, I. S., I. Staude, A. E. Miroshnichenko, and Y. S. Kivshar, "All-dielectric optical nanoantennas," *Physics Optics*, Jun. 25, 2012.

9. Krasnok, A. E., A. E. Miroshnichenko, P. A. Belov, and Y. S. Kivshar, "Optical Yagi-Uda nanoantennas," *Nanophotonic*, Vol. 1, No. 1, 65–81, Jun. 2012, Doi: 10.1515/nanoph-2012-0005.
10. Evlyukhin, A. B., C. Reinhardt, A. Seidel, B. S. Lukyanchuk, and B. N. Chichkov, "Optical response features of Si-nanoparticle arrays," *Phys. Rev. B*, Vol. 82, 045404, 2010.

Using Multiple-precision Arithmetic to Prevent Low-frequency Breakdowns in the Diagonalization of the Green's Function

Ö. Ergül and B. Karaosmanoğlu
Department of Electrical and Electronics Engineering
Middle East Technical University, Ankara, Turkey

Abstract— Multiple-precision arithmetic (MPA) is used to prevent low-frequency breakdowns in the diagonalization of the Green's function that is required to implement the multilevel fast multipole algorithm (MLFMA). The breakdown problem is considered at a numerical level, where rounding errors are reduced by increasing the precision as much as required. Using MPA seems to provide a direct solution to low-frequency breakdowns of the standard diagonalization, which may lead to straightforward implementations of broadband MLFMA.

1. INTRODUCTION

The multilevel fast multipole algorithm (MLFMA) is a powerful method for the solution of electromagnetic problems discretized with large numbers of unknowns [1–4]. However, conventional implementations of MLFMA are not efficient for low-frequency problems, where dense discretizations with respect to wavelength are used locally or globally on structures. Specifically, box sizes in MLFMA cannot be very small with respect to wavelength [5], and solutions of such problems involving dense discretizations lead to many interactions that must be calculated directly. It is well known that the diagonalization of the Green's function, i.e., expansion of spherical waves in terms of plane waves [6, 7], is responsible for low-frequency breakdowns. Therefore, in the literature, alternative implementations of MLFMA, such as using explicitly multipoles [8–12] and/or evanescent waves [13–16] at short distances, are suggested to solve low-frequency problems, as well as multiscale problems involving large objects with dense discretizations.

In this work, we approach low-frequency breakdowns from a different direction and prevent them by using multiple-precision arithmetic (MPA), which has recently become popular in the scientific computation area [17, 18]. Considering breakdowns from a numerical point of view, the standard diagonalization of the Green's function fails to provide accurate subwavelength interactions due to insufficient numbers of digits used in computations. Even when using the double-precision arithmetic, plane waves can be insufficient to represent radiation and receiving patterns of small sources. In addition, translations at short distances may involve addition and subtraction of large numbers due to spherical Hankel functions. Increasing the number of digits by means of MPA, it becomes possible to improve all these computations and perform such critical interactions with a desired level of accuracy using the conventional diagonalization. MPA may easily be used in the existing implementations of MLFMA and convert them to broadband implementations via relatively simple modifications.

2. LOW-FREQUENCY BREAKDOWNS IN THE DIAGONALIZATION OF THE GREEN'S FUNCTION

Consider the truncated form of the Gegenbauer's addition theorem, i.e.,

$$g\left(\mathbf{r},\mathbf{r}'\right)=\frac{\exp(ik|\mathbf{r}-\mathbf{r}'|)}{4\pi|\mathbf{r}-\mathbf{r}'|}=\frac{\exp(ik|\mathbf{w}+\mathbf{v}|)}{4\pi|\mathbf{w}+\mathbf{v}|}=\frac{ik}{4\pi}\sum_{t=0}^{\tau}(-1)^t(2t+1)j_t(kv)h_t^{(1)}(kw)P_t(\hat{\mathbf{v}}\cdot\hat{\mathbf{w}}), \quad (1)$$

where k is the wavenumber, $\mathbf{r}-\mathbf{r}'=\mathbf{w}+\mathbf{v}$, $\mathbf{w}=\hat{\mathbf{w}}w$, $\mathbf{v}=\hat{\mathbf{v}}v$, and $w>v$. In the above, $h_t^{(1)}$ is the spherical Hankel function of the first kind, j_t is the spherical Bessel function of the first kind, and P_t represents Legendre polynomials. The truncation number τ is usually determined by heuristic approaches, such as excess bandwidth formulas [19]. MLFMA and similar fast algorithms are based on the diagonalization of the factorization in (1). For example, expanding spherical waves in terms of plane waves as

$$j_t(kv)P_t\left(\hat{\mathbf{v}}\cdot\hat{\mathbf{w}}\right)=\frac{1}{4\pi i^t}\int d^2\hat{\mathbf{k}}\exp(ik\hat{\mathbf{k}}\cdot\mathbf{v})P_t(\hat{\mathbf{k}}\cdot\hat{\mathbf{w}}), \quad (2)$$

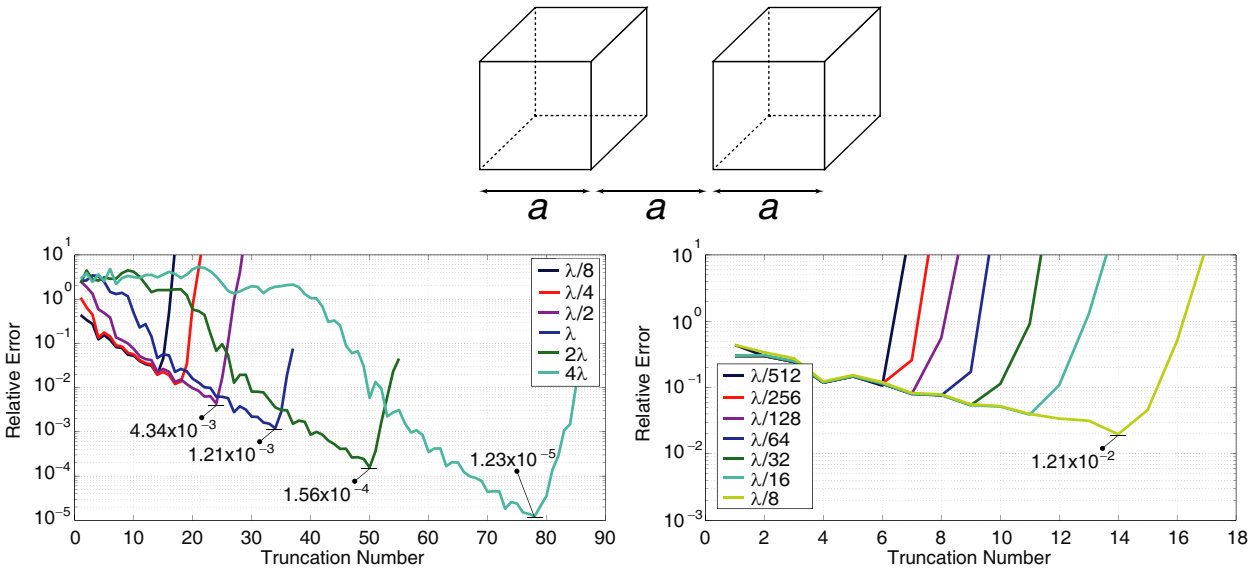

Figure 1: Maximum relative error in the diagonalized Green's function considering the worst-case scenario according to a one-box-buffer scheme for different box sizes. The standard double-precision arithmetic is used.

one can obtain

$$g\left(\mathbf{r},\mathbf{r}'\right)=\frac{ik}{(4\pi)^2}\sum_{t=0}^{\tau}i^t(2t+1)h_t^{(1)}(kw)\int d^2\hat{\mathbf{k}}\exp(ik\hat{\mathbf{k}}\cdot\mathbf{v})P_t(\hat{\mathbf{k}}\cdot\hat{\mathbf{w}}) \tag{3}$$

or

$$g\left(\mathbf{r},\mathbf{r}'\right)=\frac{ik}{(4\pi)^2}\int d^2\hat{\mathbf{k}}\exp(ik\hat{\mathbf{k}}\cdot\mathbf{v})\alpha_\tau(k,\hat{\mathbf{k}},\mathbf{w}), \tag{4}$$

where

$$\alpha_\tau(k,\hat{\mathbf{k}},\mathbf{w})=\sum_{t=0}^{\tau}i^t(2t+1)h_t^{(1)}(kw)P_t(\hat{\mathbf{k}}\cdot\hat{\mathbf{w}}) \tag{5}$$

represents the translation operator. We emphasize that (4) is typically used in MLFMA, while even the expression in (3) suffers from low-frequency breakdowns when $kw\ll 1$.

Figure 1 depicts a set of experiments, where we compute the relative error using the expression in (4) with respect to the direct evaluation of the Green's function. As also depicted in the figure, we consider cubic clustering (that is a standard in the conventional implementations of MLFMA [5]) and the worst-case scenario according to a one-box-buffer scheme. The box size (as well as the distance between boxes) is changed from 4λ to $\lambda/8$ and then from $\lambda/8$ to $\lambda/512$, whereas the truncation number (τ) is increased for each box size until a clear breakdown is observed. In these experiments, angular integrations are carried out by using $2(\tau+1)$ regular samples in the ϕ direction and $\tau+1$ Gauss-Legendre points in the θ direction [6]. For each case (box size and truncation number), we select the maximum error encountered in $15\times 15=225$ different scenarios considering different source and observation locations (including box centers, face centers, and corners). Given a box size, the error increases dramatically after an obvious breakdown, which occurs earlier for smaller boxes. It is remarkable that even 1% error cannot be achieved when the box size is smaller than $\lambda/8$, verifying that such box sizes are not suitable in MLFMA using the standard double-precision arithmetic.

There are many studies in the literature for solving low-frequency breakdowns in MLFMA. Two popular methods are using multipoles directly [8–12] and changing integration branches to complex angular values such that evanescent waves are included in subwavelength interactions [13–16]. Unfortunately, both types of methods require reimplementations of MLFMA in more complicated forms. In this study, we attack the low-frequency breakdown problem at a numerical level that leads to a straightforward solution to this important limitation. This new approach may also enable a direct implementation of a broadband MLFMA.

3. USING MPA TO PREVENT LOW-FREQUENCY BREAKDOWNS

MPA is well known in various areas [17], but is recently introduced in the computational electromagnetics community [18]. Using MPA, it is possible to use different precisions for representing different numbers. This is particularly useful when the double-precision arithmetic is not sufficient for accurate results. Low-frequency breakdowns in MLFMA can be interpreted as numerical problems due to disastrous effects of rounding errors. The spherical Hankel functions in (5) are very large when $kw \ll 1$ leading to difficult computations as new harmonics are added to achieve a convergence. In addition, radiation and receiving patterns of subwavelength boxes may not be expanded accurately via plane waves using the double-precision arithmetic. With more digits, how-

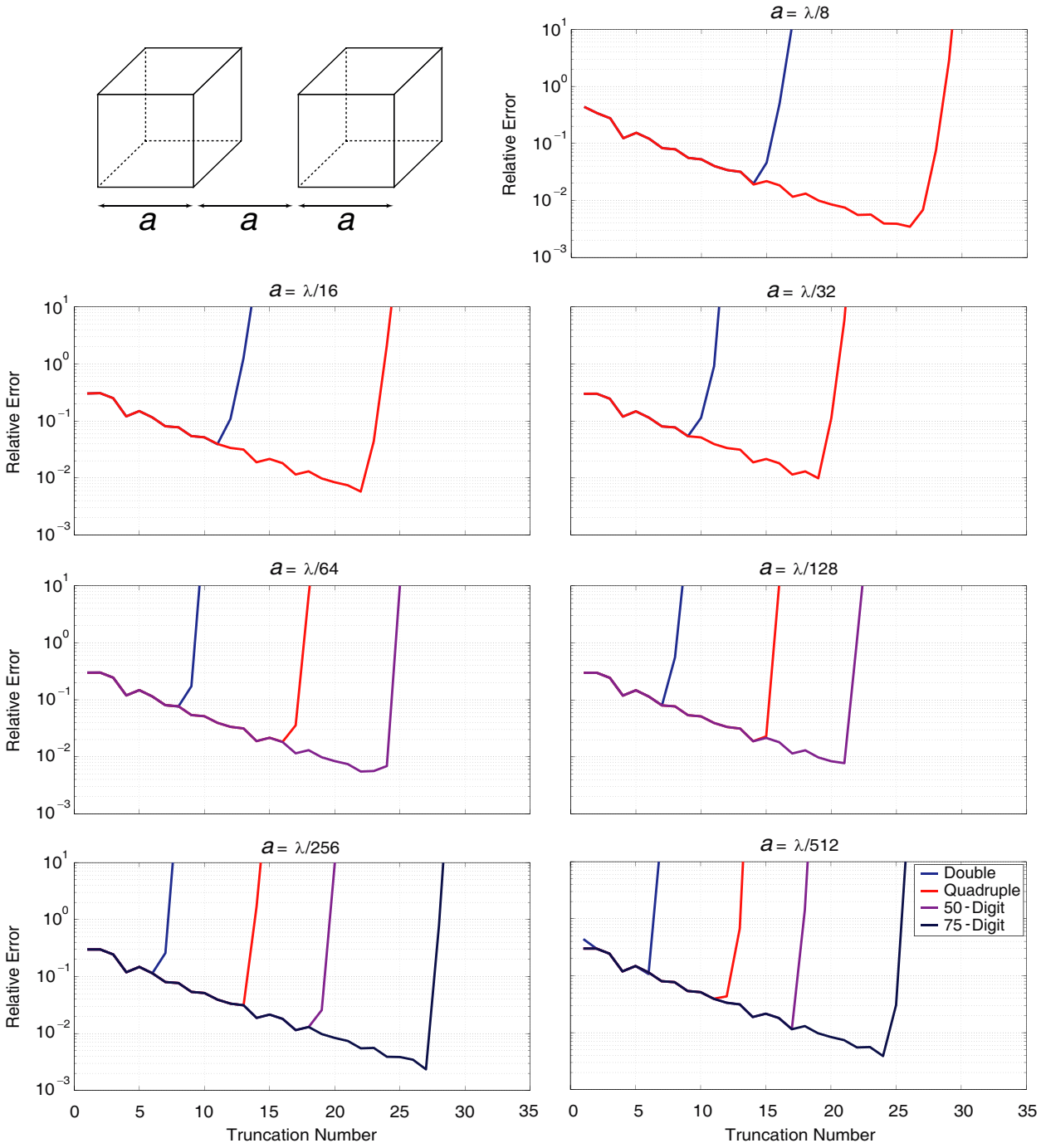

Figure 2: Maximum relative error in the diagonalized Green's function considering the worst-case scenario according to a one-box-buffer scheme. The box size is in the $\lambda/512 - \lambda/8$ range, while various precision arithmetics are used.

ever, it becomes possible to accurately represent patterns and add sufficient harmonics to achieve any desired level of accuracy.

As an example, Fig. 2 presents the results obtained when the box size is in the $\lambda/512 - \lambda/8$ range, while considering the worst case scenario according to a one-box-buffer scheme. We again select the maximum relative error encountered in $15 \times 15 = 225$ different cases as the truncation number increases from 1 to 35. It can be observed that using higher precision arithmetics delays the breakdown of the diagonalization. Specifically, the number of harmonics that can be used increases proportionally to the number of digits used in the computations, whereas the convergence rate is unaffected. By delaying the breakdown, we are able to use more harmonics to reduce the error and to improve the accuracy of the diagonalization.

Based on our experiments on the diagonalization of the Green's function using MPA, we are able to determine the number of harmonics as well as the precision required for a given box size and error criteria. As an example, Table 1 lists truncation numbers and precisions (number of digits) to achieve 1% maximum error for different box sizes from 4λ to $\lambda/512$. Maximum errors encountered in these measurements are also given in the fourth column. These values are again found by considering the worst case for boxes (see Figs. 1 and 2) and taking the maximum error out of 225 cases. We note that, in a typical solution using MLFMA, most of the interactions would require fewer harmonics and lower precisions, depending on locations of source and observation points in boxes. The following observations can be made in Table 1.

1. Double-precision arithmetic is sufficient only for boxes larger than $\lambda/4$ (shown with D in the third column), whereas smaller boxes require higher precisions to achieve 1% error.
2. For smaller boxes requiring higher precisions, halving the box size needs almost a constant increase in the number of digits to achieve the same diagonalization error. For 1% error, this corresponds to 5–6 digits.
3. For smaller boxes using higher precisions, the number of harmonics can be fixed, similar to low-frequency implementations using multipoles. For 1% diagonalization error, the truncation number can be fixed to 19.

Table 1: Truncation numbers and precisions required to obtain maximum 1% error in the diagonalization of the Green's function.

Box Size	Truncation Number	Precision (Digits)	Maximum Error
4λ	52	D	0.0095
2λ	30	D	0.0081
λ	23	D	0.0098
$\lambda/2$	20	D	0.0097
$\lambda/4$	19	19	0.0086
$\lambda/8$	19	24	0.0099
$\lambda/16$	19	29	0.0098
$\lambda/32$	19	34	0.0098
$\lambda/64$	19	40	0.0097
$\lambda/128$	19	46	0.0097
$\lambda/256$	19	52	0.0097
$\lambda/512$	19	57	0.0097

Numerical results, some of which are listed in Table 1, show that using MPA in the diagonalization of the Green's function provides a straightforward solution to low-frequency breakdowns. Hence, using MPA may extend the applicability of the conventional diagonalization, as well as MLFMA implementations, to multiscale problems. Using higher numbers of digits increases the cost, i.e., processing time and memory; but, the resulting solvers can still be efficient compared to other broadband implementations in the literature.

4. CONCLUSION

We use MPA to prevent low-frequency breakdowns in the diagonalization of the Green's function. This way, subwavelength interactions can be calculated accurately using the standard diagonal-

ization without resorting to alternative factorization and diagonalization methods. A systematic selection of precisions and their usage may be used to convert conventional MLFMA implementations to broadband solvers for solving multiscale problems.

ACKNOWLEDGMENT

This work was supported by the Scientific and Technical Research Council of Turkey (TUBITAK) under the Research Grant 113E276 and by a BAGEP Grant from Bilim Akademisi (The Science Academy, Turkey).

REFERENCES

1. Song, J., C.-C. Lu, and W. C. Chew, "Multilevel fast multipole algorithm for electromagnetic scattering by large complex objects," *IEEE Trans. Antennas Propag.*, Vol. 45, No. 10, 1488–1493, Oct. 1997.
2. Taboada, J. M., M. G. Araujo, J. M. Bertolo, L. Landesa, F. Obelleiro, and J. L. Rodriguez, "MLFMA-FFT parallel algorithm for the solution of large-scale problems in electromagnetics," *Progress In Electromagnetics Research*, Vol. 105, 15–30, 2010.
3. Ergül, Ö., "Solutions of large-scale electromagnetics problems involving dielectric objects with the parallel multilevel fast multipole algorithm," *J. Opt. Soc. Am. A.*, Vol. 28, No. 11, 2261–2268, Nov. 2011.
4. Ergül, Ö. and L. Gürel, "Fast and accurate analysis of large-scale composite structures with the parallel multilevel fast multipole algorithm," *J. Opt. Soc. Am. A.*, Vol. 30, No. 3, 509–517, Mar. 2013.
5. Chew, W. C., J.-M. Jin, E. Michielssen, and J. Song, *Fast and Efficient Algorithms in Computational Electromagnetics*, Artech House, Boston, MA, 2001.
6. Coifman, R., V. Rokhlin, and S. Wandzura, "The fast multipole method for the wave equation: A pedestrian prescription," *IEEE Antennas Propag. Mag.*, Vol. 35, No. 3, 7–12, Jun. 1993.
7. Koc, S., J. M. Song, and W. C. Chew, "Error analysis for the numerical evaluation of the diagonal forms of the scalar spherical addition theorem," *SIAM J. Numer. Anal.*, Vol. 36, No. 3, 906–921, 1999.
8. Zhao, J.-S. and W. C. Chew, "Three dimensional multilevel fast multipole algorithm from static to electrodynamic," *Microw. Opt. Technol. Lett.*, Vol. 26, No. 1, 43–48, Jul. 2000.
9. Zhao, J.-S. and W. C. Chew, "Applying LF-MLFMA to solve complex PEC structures," *Microw. Opt. Technol. Lett.*, Vol. 28, No. 3, 155–160, Feb. 2001.
10. Chu, Y.-H. and W. C. Chew, "A multilevel fast multipole algorithm for electrically small composite structures," *Microw. Opt. Technol. Lett.*, Vol. 43, No. 3, 202–207, Nov. 2004.
11. Jiang, L. J. and W. C. Chew, "A mixed-form fast multipole algorithm," *IEEE Trans. Antennas Propag.*, Vol. 53, No. 12, 4145–4156, Dec. 2005.
12. Ergül, Ö. and L. Gürel, "Efficient solutions of metamaterial problems using a low-frequency multilevel fast multipole algorithm," *Progress In Electromagnetics Research*, Vol. 108, 81–99, 2010.
13. Greengard, L., J. Huang, V. Rokhlin, and S. Wadzura, "Accelerating fast multipole methods for the Helmholtz equation at low frequencies," *IEEE Comput. Sci. Eng.*, Vol. 5, 32–38, Jul.–Sep. 1998.
14. Jiang, L. J. and W. C. Chew, "Low-frequency fast inhomogeneous plane-wave algorithm (LF-FIPWA)," *Microw. Opt. Technol. Lett.*, Vol. 40, No. 2, 117–122, Jan. 2004.
15. Bogaert, I., J. Peeters, and F. Olyslager, "A nondirective plane wave MLFMA stable at low frequencies," *IEEE Trans. Antennas Propag.*, Vol. 56, No. 12, 3752–3767, Dec. 2008.
16. Bogaert, I. and F. Olyslager, "A low frequency stable plane wave addition theorem," *J. Comput. Phys.*, Vol. 228, No. 4, 1000–1016, Mar. 2009.
17. Smith, D. M., "Using multiple-precision arithmetic," *Computing in Science and Engineering*, Vol. 5, No. 4, 88–93, Jul.–Aug. 2003.
18. Stefanski, T. P., "Electromagnetic problems requiring high-precision computations," *Antennas Propag. Mag.*, Vol. 55, No. 2, 344–353, Apr. 2013.
19. Ohnuki, S. and W. C. Chew, "Truncation error analysis of multipole expansions," *SIAM J. Sci. Comput.*, Vol. 25, No. 4, 1293–1306, 2003.

Properties of the Gram Matrices Associated with Loop-flower Basis Functions

Yibei Hou and Gaobiao Xiao
Key Laboratory of Ministry of Education of Design and Electromagnetic Compatibility of High-Speed Electronic Systems, Shanghai Jiao Tong University, Shanghai, China

Abstract— In this paper, loop-flower basis functions are addressed to solve the electric field integral equation (EFIE) in electromagnetic scattering issues that rise from perfectly conducting objects. A loop basis function and a flower basis function are both defined as the sum of a set of modified RWG basis functions associated with a node in triangular meshes. Moreover, they could also be represented by node based Lagrange interpolation polynomials. A flower basis function, which also resembles the star basis function, is named after its shape. In contrast to all previous quasi-Helmholtz decomposition, loop-flower decomposition holds several good characteristics. First, loop-flower decomposition can be used to cure low-frequency breakdown of EFIE spectrum. Second, it can also be directly used to implement Calderón preconditioners for EFIE. Last but not least, the unknown number corresponding with loop-flower basis functions reduces to approximately two thirds of the one associated with RWG. Given that the property of a Calderón preconditioner is largely affected by the Gram matrix that links the range and domain of EFIE operator, this paper will focus on the properties of Gram matrices associated with loop-flower basis function. Analysis shows that the Gram matrices associated with loop-flower basis functions are invertible, and their condition numbers are approximately of the order of (h^{-2}), in which h is the characteristic dimension of a triangular mesh. The theoretical analysis will be demonstrated by several numerical examples.

1. INTRODUCTION

Surface integral equations (SIEs) have been widely used for solving electromagnetic radiation and scattering problems from perfect electric conductors (PEC). To numerically solve SIEs with method of moment (MoM) requires surface to be discretized as simple elements such as triangles and quadrilaterals. Rao-Wilton-Glisson (RWG) basis functions are popular to expand surface electric and magnetic currents among divergence-conforming vector basis functions. However, the use of RWG basis functions for the electric field integral equation (EFIE) exhibits low frequency breakdown, that is to say, at very low frequencies, the EFIE discretized system matrix is highly ill-conditioned and hence is difficult to be solved accurately and efficiently. The quasi Helmholtz decomposition, expanding current with loop-tree or loop-star basis functions [1–3], has been proposed to overcome the low frequency breakdown. The use of loop-tree and loop-star basis functions can provide an effective approach to scale the solenoidal currents and the non-solenoidal ones properly at low frequencies, hence, both the two parts of the currents can be handled correctly. However, the quasi Helmholtz decomposition does not improve the spectrum property of the electric field integral operator. Recently, a Calderón multiplicative preconditioner [4] has been proposed to solve the above problem, which largely improves the characteristics of the spectrum of EFIF operator. The main difficulty in implementing the Calderón preconditioner is to find a well conditioned Gram matrix which links the domain and range of the EFIE operators. The Buffa-Christiansen basis functions are approximately orthogonal to the standard RWG basis functions [5], consequently, the resultant Gram matrix of these two basis functions is well conditioned. However, it is necessary to divide the combined operator into four parts and discarding the most hypersingular term, otherwise, the Calderón preconditioner with BC basis functions may fail at very low frequency. Loop-flower basis functions [6] are proposed to implement Calderón preconditioner directly, which work well to overcome the low frequency breakdown. Loop and flower basis functions are both defined on nodes, which lower the degree of freedom compared with RWG basis functions. This work will analyze the condition number of the Gram matrices associated with loop-flower basis functions. Theoretic analysis and numerical results show that the conditioning of loop-flower Gram matrices will become worse with the decreasing of mesh length. In addition, this work will also present numerical results to demonstrate the practical effectiveness of loop-flower basis functions in solving electromagnetic scattering issues.

2. LOOP-FLOWER BASIS FUNCTIONS

Loop-flower basis functions arise from the need to perform quasi Helmholtz decomposition. Loop basis functions are used to expand the solenoidal current, whereas flower basis functions are for the irrotational part. A loop basis function is defined on each interior vertex v_n, which is shown in Fig. 1(a). Explicit representation of loop basis function is as follows

$$\mathbf{\Lambda}_j(\mathbf{r}) = \sum_{i=1}^{N_j} \bar{\bar{\mathbf{\Lambda}}}_{i,j} \mathbf{f}'_j \tag{1}$$

where N_j is the number of the surrounding triangles, $\bar{\bar{\mathbf{\Lambda}}}$ is the loop to RWG transformation matrix, $\mathbf{f}'_i$ is the standard RWG basis function divided by the common edge length.

It is very interesting to find that the loop basis function that we use in the MoM community maintains a direct relationship with the piecewise linear Lagrange basis function [3] (or the nodal basis function) associated with vertex in the FEM community. Consequently, loop basis function can be also expressed by

$$\mathbf{\Lambda}_p(\mathbf{r}) = \nabla \times \hat{\mathbf{n}}_r \lambda_p(\mathbf{r}) = \hat{\mathbf{n}}_r \times \nabla \lambda_p(\mathbf{r}) \tag{2}$$

in which $\hat{\mathbf{n}}_r$ denotes the outward normal unit vector and $\lambda(r)$ denotes piecewise linear Lagrange basis function.

A flower basis function is also defined on the node v_n, like a loop basis function, as depicted in Fig. 1(b). Its support covers all the RWG bases that share the reference node v_n as one free vertex. It can be explicit expressed by

$$\mathbf{f}_j^{\text{flower}}(\mathbf{r}) = \sum_{i=1}^{N_j} \bar{\bar{\boldsymbol{F}}}_{i,j} \mathbf{f}'_i \tag{3}$$

in which, $\bar{\bar{\boldsymbol{F}}}$ stands for the flower to RWG transformation matrix. The reference direction of flower basis function points away from the reference node.

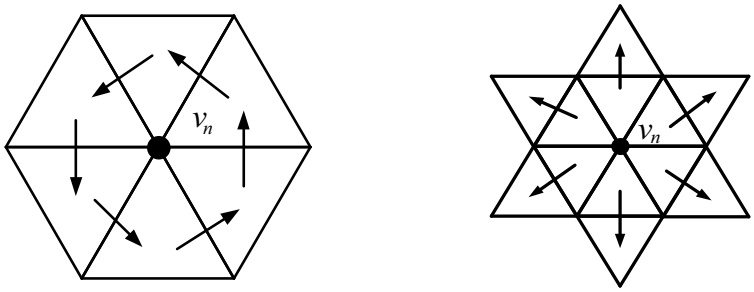

Figure 1: (a) Loop and (b) flower basis function.

3. LOOP-FLOWER GRAM MATRIX

The Gram matrix of RWG bases

$$\left(\bar{\bar{\mathbf{G}}}\right)_{i,j} = \langle \mathbf{f}'_i, \mathbf{f}'_j \rangle \tag{4}$$

is well-conditioned [1], namely, $\bar{\bar{\mathbf{G}}} \asymp \bar{\bar{\mathbf{I}}}$, where $\bar{\bar{\mathbf{I}}}$ is the identity matrix.

When the loop-flower bases are used, the loop-flower to RWG transformation matrix can be written as $\bar{\bar{\mathbf{H}}}^{\Lambda F} = [\bar{\bar{\mathbf{\Lambda}}}, \bar{\bar{\boldsymbol{F}}}]$, whose columns are the coefficients of the loop-flower functions when expressed as linear combinations of RWG functions. Since coefficients of loop and flower functions are orthogonal and RWG Gram matrix is well conditioned, thereby loop-flower Gram matrix meets the following relations

$$\bar{\bar{\mathbf{G}}}^{\Lambda F} = \bar{\bar{\mathbf{H}}}^H_{\Lambda F} \bar{\bar{\mathbf{G}}} \bar{\bar{\mathbf{H}}}_{\Lambda F} \asymp \bar{\bar{\mathbf{H}}}^H_{\Lambda F} \bar{\bar{\mathbf{H}}}_{\Lambda F} = \begin{pmatrix} \bar{\bar{\mathbf{\Lambda}}}^H \bar{\bar{\mathbf{\Lambda}}} & \bar{\bar{\mathbf{0}}} \\ \bar{\bar{\mathbf{0}}} & \bar{\bar{\mathbf{\Sigma}}}^H \bar{\bar{\mathbf{\Sigma}}} \end{pmatrix} \asymp \begin{pmatrix} \bar{\bar{\mathbf{\Lambda}}}^H \bar{\bar{\mathbf{G}}} \bar{\bar{\mathbf{\Lambda}}} & \bar{\bar{\mathbf{0}}} \\ \bar{\bar{\mathbf{0}}} & \bar{\bar{\boldsymbol{F}}}^H \bar{\bar{\mathbf{G}}} \bar{\bar{\boldsymbol{F}}} \end{pmatrix} = \begin{pmatrix} \bar{\bar{\mathbf{G}}}^{\Lambda} & \bar{\bar{\mathbf{0}}} \\ \bar{\bar{\mathbf{0}}} & \bar{\bar{\mathbf{G}}}^{F} \end{pmatrix} \tag{5}$$

where

$$\left\{\bar{\bar{\mathbf{G}}}^{\Lambda}\right\}_{i,j}=\left\{\bar{\bar{\mathbf{\Lambda}}}^{H}\bar{\bar{\mathbf{G}}}\bar{\bar{\mathbf{\Lambda}}}\right\}_{i,j}=\left\langle\bar{\bar{\mathbf{\Lambda}}}_i,\bar{\bar{\mathbf{\Lambda}}}_j\right\rangle\quad\text{and}\quad\left\{\bar{\bar{\mathbf{G}}}^{F}\right\}_{i,j}=\left\{\bar{\bar{\boldsymbol{F}}}^{H}\bar{\bar{\mathbf{G}}}\bar{\bar{\boldsymbol{F}}}\right\}_{i,j}=\langle\bar{\bar{\boldsymbol{F}}}_i,\bar{\bar{\boldsymbol{F}}}_j\rangle \tag{6}$$

From (5), it is clear to find that, instead of analyzing the conditioning of the block diagonal loop-flower Gram matrix directly, we can analyze the loop and Gram matrices separately to get the total conditioning.

Substitute (2) into (6), the loop Gram matrix [7] can be rewritten as

$$\left\{\bar{\bar{\mathbf{G}}}^{\Lambda}\right\}_{i,j}=\langle\nabla\times\hat{\mathbf{n}}_r\lambda_i,\,\nabla\times\hat{\mathbf{n}}_r\lambda_j\rangle=\langle\nabla_s\lambda_i,\,\nabla_s\lambda_j\rangle \tag{7}$$

Consider that in a Sobolev space $H^1(\Omega)$, which is the space of functions defined on the Ω that are square integrable and whose gradient is also square integrable Poincare Inequality and Inverse Inequality for piecewise polynomials hold true [8]. Since piecewise linear Lagrange basis function λ meets above requirements, so we have

$$\|\lambda\|_2^2\lesssim\|\nabla\lambda\|_2^2\quad\text{and}\quad\|\nabla\lambda\|_2^2\lesssim\frac{1}{h^2}\|\lambda\|_2^2\quad\text{with}\quad\forall\lambda:\lambda=\sum_i\upsilon_i\lambda_i \tag{8}$$

Assume that $\lambda=\sum\limits_i\upsilon_i\lambda_i$, $\|\lambda\|_2^2$ and $\|\nabla\lambda\|_2^2$ can be further expressed as

$$\|\lambda\|_2^2=\bar{\mathbf{v}}^{H}\bar{\bar{\mathbf{G}}}^{\lambda}\bar{\mathbf{v}}\quad\text{and}\quad\|\nabla\lambda\|_2^2=\bar{\mathbf{v}}^{H}\bar{\bar{\mathbf{G}}}\bar{\mathbf{v}} \tag{9}$$

Since the Rayleigh Quotient of a matrix is bounded by the maximum and minimum signular values, combing (7), (8) and (9) yields

$$\bar{\bar{\mathbf{G}}}^{\lambda}\lesssim\bar{\bar{\mathbf{G}}}^{\Lambda}\lesssim\frac{1}{h^2}\bar{\bar{\mathbf{G}}}^{\lambda} \tag{10}$$

With the help of $\bar{\bar{\mathbf{G}}}^{\lambda}\asymp h^2\bar{\bar{\mathbf{I}}}$ (readers can refer to [8] and references therein for detail discussion), we can get

$$h^2\bar{\bar{\mathbf{I}}}\lesssim\bar{\bar{\mathbf{G}}}^{\Lambda}\lesssim\bar{\bar{\mathbf{I}}} \tag{11}$$

In result, the condition number of loop Gram matrix satisfies

$$\mathrm{cond}\left(\bar{\bar{\mathbf{G}}}^{\Lambda}\right)\asymp\frac{1}{h^2} \tag{12}$$

When analyze the flower Gram matrix, we will the use the BC basis function as auxiliary tool. In fact, the BC Gran matrix $(\bar{\bar{\mathbf{G}}}_{\mathrm{BC}})_{i,j}=\langle\mathbf{f}_i^{\mathrm{BC}},\,\mathbf{f}_j^{\mathrm{BC}}\rangle$ is well conditioned [5], so that we can get

$$\left(\bar{\bar{\mathbf{G}}}^{F}\right)=\bar{\bar{F}}^{T}\bar{\bar{\mathbf{G}}}\bar{\bar{F}}\asymp\bar{\bar{F}}^{T}\bar{\bar{\mathbf{G}}}_{\mathrm{BC}}\bar{\bar{F}}=\left\langle\nabla_s\lambda^{\mathrm{bar}},\,\nabla_s\lambda^{\mathrm{bar}}\right\rangle \tag{13}$$

where λ^{bar} is the piecewise linear, cell-centered function similar to the linear Lagrange basis function. Replacing λ with λ^{bar} in the analysis of loop Gram matrix yields

$$\mathrm{cond}\left(\bar{\bar{\mathbf{G}}}^{F}\right)\asymp\frac{1}{h^2} \tag{14}$$

From Equations (5), (12) and (14), it is clear to find that the loop-flower Gram matrix have a condition number which will be growing with mesh refinement as $1/h^2$.

4. APPLICATION OF LOOP-FLOWER BASIS FUNCTIONS

Consider a electromagnetic wave scattering problem by an PEC object with surface Ω whose normal is denoted as $\hat{\mathbf{n}}$. The relationship between incident electric field $\mathbf{E}^{inc}$ and scattered filed $\mathbf{E}^{sca}$, which is produced by an equivalent current $\mathbf{J}(r)$ on the Ω, can be expressed as

$$\hat{\mathbf{n}}\times\mathbf{E}^{sca}=\mathcal{T}(\mathbf{J})=-\hat{\mathbf{n}}\times\mathbf{E}^{inc} \tag{15}$$

in which, the EFIE operator $\mathcal{T}(\mathbf{J}) = \mathcal{T}_s(\mathbf{J}) + \mathcal{T}_h(\mathbf{J})$ with

$$\mathcal{T}_s(\mathbf{J}) = iw\mu\hat{\mathbf{n}}_r \times \int_S \frac{e^{ik|\mathbf{r}-\mathbf{r}'|}}{4\pi|\mathbf{r}-\mathbf{r}'|}\mathbf{J}(\mathbf{r}')ds' \tag{16}$$

$$\mathcal{T}_h(\mathbf{J}) = -\frac{1}{i\omega\varepsilon}\hat{\mathbf{n}}_r \times \nabla \int_S \frac{e^{ik|\mathbf{r}-\mathbf{r}'|}}{4\pi|\mathbf{r}-\mathbf{r}'|}\nabla'_S \cdot \mathbf{J}(\mathbf{r}')ds' \tag{17}$$

where k stands for the free-space wave number, the subscript "s" and "h" stand for "singular" (vector potential) and "hyper-singular" (scalar potential), respectively. Current density $\mathbf{J}$ is expanded with loop-flower bases as

$$\mathbf{J} = \sum_{n=1}^{N_{\text{loop}}} I_n^l \mathbf{f}_n^{\text{loop}} + \sum_{n=1}^{N_{\text{flower}}} I_n^f \mathbf{f}_n^{\text{flower}} \tag{18}$$

The degree of freedom of loop and flower basis functions can be determined according to [6] and reference therein. Given that the ill-conditioning of impedance matrix is rooted in the spectral property of the EFIE operator, Calderon identity is used to modify the spectrum distribution of EFIE operator. The Calderon identity

$$\mathcal{T}^2(\mathbf{J}) = -\frac{\mathbf{J}}{4} + \mathcal{K}^2(\mathbf{J}) \tag{19}$$

where $\mathcal{K}$ is the magnetic field integral equation operator

$$\mathcal{K}(\mathbf{J}) = \hat{\mathbf{n}} \times \int_S \nabla g(\mathbf{r}, \mathbf{r}') \times \mathbf{J}dS \tag{20}$$

Based on the discussion above, the solution of EFIE can be achieved by solving the preconditioned system

$$\mathcal{T}^2(\mathbf{J}) = \mathcal{T}\left(\hat{\mathbf{n}} \times \mathbf{E}^{inc}\right) \tag{21}$$

Assume that the inner and the outer operator are both discretized with $\mathbf{f}_n^{\text{loop}}$, $\mathbf{f}_n^{\text{flower}}$ and tested with $\hat{\mathbf{n}} \times \mathbf{f}_n^{\text{loop}}$, $\hat{\mathbf{n}} \times \mathbf{f}_n^{\text{flower}}$, then the corresponding Gram matrix $\bar{\bar{\mathbf{G}}}$ can be expressed by

$$\bar{\bar{\mathbf{G}}} = \begin{bmatrix} \bar{\bar{\mathbf{G}}}^{LL} & \bar{\bar{\mathbf{G}}}^{LF} \\ \bar{\bar{\mathbf{G}}}^{FL} & \bar{\bar{\mathbf{G}}}^{FF} \end{bmatrix} = \begin{bmatrix} \langle \hat{\mathbf{n}} \times \mathbf{f}^L, \mathbf{f}^L \rangle & \langle \hat{\mathbf{n}} \times \mathbf{f}^L, \mathbf{f}^F \rangle \\ \langle \hat{\mathbf{n}} \times \mathbf{f}^F, \mathbf{f}^L \rangle & \langle \hat{\mathbf{n}} \times \mathbf{f}^F, \mathbf{f}^F \rangle \end{bmatrix} \tag{22}$$

The preconditioned system can be rewritten as

$$\bar{\bar{\mathbf{Z}}}\bar{\bar{\mathbf{G}}}^{-1}\bar{\bar{\mathbf{Z}}} \cdot \bar{\mathbf{J}} = \bar{\bar{\mathbf{Z}}}\bar{\bar{\mathbf{G}}}^{-1} \cdot \bar{\mathbf{V}} \tag{23}$$

where $\bar{\bar{\mathbf{Z}}}$ is impendence matrix concerning with loop flower basis functions, $\bar{\mathbf{J}}$ is coefficient vector of current, $\bar{\mathbf{V}}$ is excitation vector. It is clear that $\bar{\bar{\mathbf{Z}}}\bar{\bar{\mathbf{G}}}^{-1}$ is the preconditioner of initial EFIE discretized system. The preconditioner introduced in (23) is rather simpler than previous ones, because the two matrices associated with the left and right operator are the same.

5. NUMERICAL RESULTS

In this section, the theoretical analysis of Gram matrices will be verified on a sphere discretized with quasi-uniform meshes of different mesh size h, and in addition, the effectiveness of loop flower basis functions will be demonstrated on a PEC conesphere.

5.1. Gram Matrices Associated with Loop-flower Basis Functions

We first analyze the conditioning of Gram matrices on a PEC sphere with a radius of 1 m. Fig. 3(a) shows that the condition number of the RWG Gram matrix maintains the same level versus the mesh size. It is clear to find that the standard RWG Gram matrix is well-conditioned. Similar to RWG basis functions, Fig. 3(b) shows that the condition number of the BC Gram matrix also remains very small, slightly bigger than that of RWG. Fig. 3(c) shows that the condition number of the loop-flower Gram matrix reduces against the increment of mesh size. It is clear that the condition number of the loop-flower Gram matrix has the theoretically predicted growth of $1/h^2$. Fig. 3(d) shows that the condition number of the Gram matrix of loop-flower basis functions in the Calderon preconditoner also has a growth of $1/h^2$.

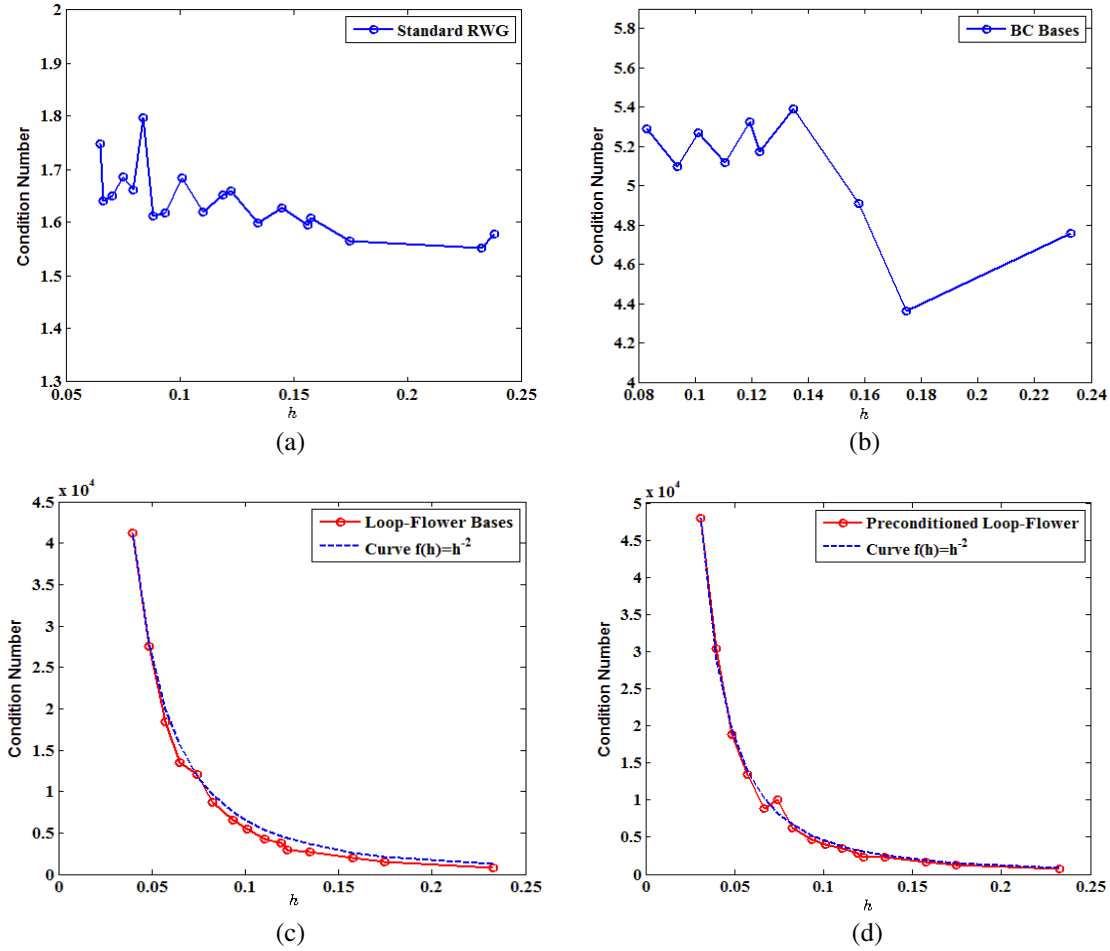

Figure 2: Condition Numbers of Gram matrices associated with different basis functions versus different values of mesh size. (a) Gram matrix of standard RWG basis functions. (b) Gram matrix of BC basis functions. (c) Gram matrix of loop-flower basis functions. (d) Gram matrix of loop-flower basis functions with Calderon preconditioner.

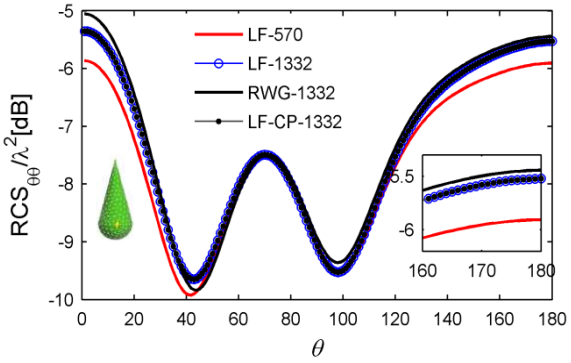

Figure 3: BiRCSs of the PEC cone-sphere at 0.3 GHz.

5.2. Calculate RCS Using Loop-flower Basis Functions

A PEC cone-sphere is analyzed as an example. The height of the cone is 1 m and the radius of the hemi-sphere is 0.25 m. The cone-sphere is analyzed twice on a coarse mesh (570 RWGs) and a fine mesh (1332 RWGs), respectively. The biRCSs are shown in Fig. 3. It can be seen that the accuracy can be improved using finer mesh structures.

In the case of PEC cone-sphere, there exists a sharp tip. The discrepancies between the results

obtained by using loop-flower basis and those by using RWG basis or loop-star basis functions are larger than that in the PEC sphere with smooth surface. Careful examination shows that the currents near the sharp tip tend to have larger errors than currents on smooth surfaces. This can be explained from the fact that in a flower basis function, the currents are assumed to flow away from the reference node almost uniformly in all directions. However, at sharp edges, tips and corners, this approximation is acceptable only when the mesh structure is sufficiently fine.

6. CONCLUSION

In this paper, a theoretical analysis of the conditioning of loop-flower Gram matrix has been presented. The analysis shows that condition number of loop-flower Gram matrix has a growth of $1/h^2$. In addition, numerical example shows that loop-flower basis functions are effective for solving electromagnetic scattering problems.

REFERENCES

1. Vecchi, G., "Loop-star decomposition of basis functions in the discretization of the EFIE," *IEEE Transactions on Antennas and Propagation*, Vol. 47, No. 2, 339–346, 1999.
2. Zhao, J.-S. and W. C. Chew, "Integral equation solution of Maxwell's equations from zero frequency to microwave frequencies," *IEEE Transactions on Antennas and Propagation*, Vol. 48, No. 10, 1635–1645, 2000.
3. Lee, J.-F. and R. J. Burkholder, "Loop star basis functions and a robust preconditioner for EFIE scattering problems," *IEEE Transactions on Antennas and Propagation*, Vol. 51, No. 8, 1855–1863, 2003.
4. Andriulli, F. P., K. Cools, H. Bagci, F. Olyslager, A. Buffa, S. Christiansen, and E. Michielssen, "A multiplicative Calderon preconditioner for the electric field integral equation," *IEEE Transactions on Antennas and Propagation*, Vol. 56, No. 8, 2398–2412, 2008.
5. Buffa, A. and S. Christiansen, "A dual finite element complex on the barycentric refinement," *Mathematics of Computation*, Vol. 76, No. 260, 1743–1769, 2007.
6. Xiao, G., "Applying loop-flower basis functions to analyze electromagnetic scattering problems of PEC scatterers," *International Journal of Antennas and Propagation*, Vol. 2014, Article ID 905935, 2014.
7. Andriulli, F. P., "Loop-star and loop-tree decompositions: Analysis and efficient algorithms," *IEEE Transactions on Antennas and Propagation*, Vol. 60, No. 5, 2347–2356, 2012.
8. Quarteroni, A., A. M. Quarteroni, and A. Valli, *Numerical Approximation of Partial Differential Equations*, Springer, Berlin, 2008.

Intelligent Channel Assignment for WI-FI System Based on Reinforcement Learning

R. Urban and P. Drexler
Department of Theoretical and Experimental Electrical Engineering
Brno University of Technology, Technicka 12, Brno 612 00, Czech Republic

Abstract— This paper focuses on enhanced channel planning for WI-FI systems. Based on a real measurement of the frequency spectrum background, the quality of each channel has been classified. Machine learning algorithms are used to process these data and control the system. Reinforcement learning (a special example of machine learning) is used due to its complexity as a test-trial agents system. In the proposed system punishment and reward schema are utilized making it possible to change channels during the transmission and use the one with minimal interference. The promising increase of SINR up to 5% for outdoor scenarios and up to 30% for indoor scenarios should be applied to improve modulation schemas and increase data throughput.

1. INTRODUCTION

WI-FI has recently become a dominant wireless technology for local area networks (LAN) and personal area networks (PAN) worldwide. All modifications of IEEE 802.11 [1] became extremely popular over recent decades and WI-FI modules are now installed in various types of devices such as laptops, mobile phones, smart TVs, digital cameras etc. Even intelligent buildings need to be connected to the common, domestic, network devices such as laundry machines and fridges. The ISM frequency bands (2.4 GHz and 5 GHz) used for WI-FI systems are quite narrow resulting in a lack of the capacity for all the devices. Another issue which has to be solved is the demand for high transmission speed. To provide higher than 100 Mbit connectivity between the receiver and transmitter, new modulation schemes and connections between several consecutive channels (channel aggregation) have to be used. These solutions require high Signal-to-Noise-Ratio (SNR) and precise spectrum planning. Cognitive radio [2] ideas should solve the following frequency spectrum problems: low SNR, overfilled frequency spectrum and channel assignment. Cognitive radio is an intelligent autonomous system with the ability to change its parameters according to the environment (radiation power, modulation, and channel). In this paper we introduce intelligent channel allocation for a single-channel WI-FI system as well as an aggregated-channel WI-FI system (802.11n) [3]. Based on real measured data [4] from the spectrum survey, the entire WI-FI band is investigated in detail and channels are prioritized according to its occupancy. Each channel receives a score (the higher the score, the less suitable the channel) given by a weigh function from the reinforcement learning algorithms. Afterwards, this score is updated over time and the temporarily used channel should also decrease its score as a consequence of subsequent time steps. The learning is in continuous action.

2. SCENARIO DESCRIPTION

The data in the simulation are based on a real measurement of spectrum background which is described in [2]. The data are collected by a fast and sensitive energy detector, an omni-directional antenna and post-processed in Matlab environment. Firstly, systematic errors are removed from the measured data via calibration. Secondly, we assume that the data (mdata) are structured as in (1):

$$m_{data} = m_{signal} + m_{noise}, \tag{1}$$

where m_{signal} stands for any signal at a particular frequency/frequency band. m_{noise} is an additive noise from the environment and the measurement system which is eliminated in calibration.

The measurements were performed in carefully chosen outdoor and indoor locations as depicted in Fig. 1. Indoor scenarios were measured in a university building to provide data from a heavily used wireless environment. The measurements ran during lectures and night hours to cover the difference in usage of the shared spectrum. The same parameters were chosen for outdoor measurements. For this paper we used data from the roof of the university building which covers a large geographical area occupied by numerous public and private wireless services.

(a) (b)

Figure 1: Measurement setup for indoor and outdoor locations.

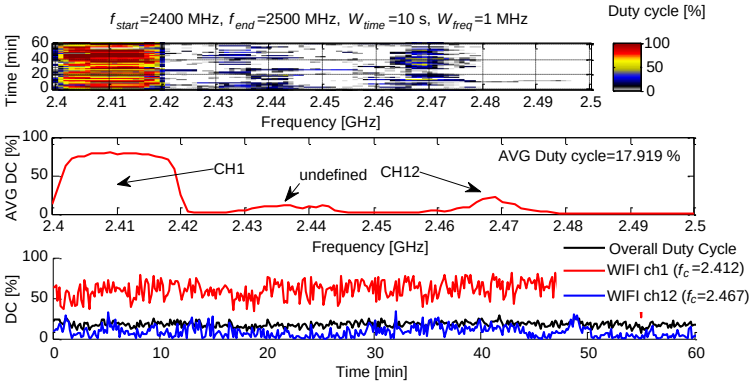

Figure 2: Occupation of the WI-FI band for an indoor scenario.

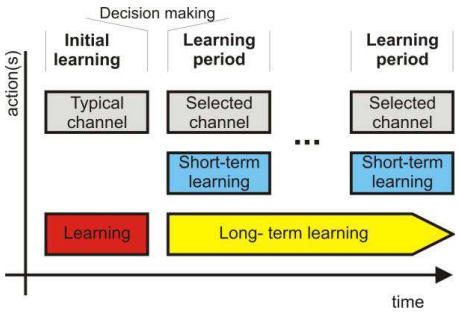

Figure 3: System description in time.

Energy detection for spectrum monitoring [3, 4] is sometimes called semi-blind because the decision threshold needs to be carefully estimated. For the measured data we chose a threshold level 12 dB over the baseline based on [5], where the calculation was made using the Q-function. Baseline was calculated as an absolute value of the measured data m_{data} and the calibration data m_{cal}. For the calibration we used the average value of 100 measured samples for each frequency point. This calibration reduced all noise created by the measurement system. All peaks detected over the threshold level (12 dB) were counted as "interference count" and they brought additional noise to the transmission.

The main indicator of spectrum utilization is not the level of the signal, but the *Duty Cycle* which is defined as the number of detected peaks over the threshold divided by the number of total frequency and time points in the measurement. These results for the WI-FI band are presented in Fig. 2.

The whole system works as depicted in Fig. 3. At the beginning of the communication, the connection starts normally. Clients are connected to a specific SSID (Service Set Identifier). During the communication, the initial learning is performed and the vector of suitable channels is picked up. We focused on the five best channels to have more choices. When several channels had the same score, the one with lowest number was chosen. Secondly, the wireless channel should be changed after the initial learning or kept the same if the currently used channel is listed in the five best channels. Otherwise, AP informs the clients about changing the transmission channel and the communication is transformed to a different channel.

3. SIMULATION RESULTS

The crucial parameter of the whole system is the machine learning [6] output — the vector of all channels with its scores. The scores are obtained from a reinforcement learning algorithm. That is a technique using an agent to learn from direct interaction with the environment to maximize its reward and perform a specific action [6]. Generally, the agent has no additional information and it needs to discover which available action yields the highest performance of the system. Reinforce-

ment learning has 2 main features: test-and-trial and delay of reward. In our example, the reward gains the channel when there is interference on an investigated frequency point. The channel received punishment when the frequency point was used. The output of the algorithm is presented in Fig. 4.

Our reinforcement learning algorithm used the overlapping windows with window size (SW) set to 2. This value was set to increase the influence of consecutive interference for a particular channel (2). Each channel in our system had its own weight value (WR_{ch}). The state from the previous iteration ($W_{ch,t-1}$) is updated with a new reward/punishment (RP) score of a particular channel.

$$[WR_{ch} = W_{ch,t-1} + RP. \tag{2}$$

Our proposed system worked with restrictive punishment (3). Moreover, to disable the accumulating reward, due to several consecutive samples, we decided that RP needed to be zero or a positive number.

$$RP = \sum_{i=1}^{S_W} P_i + R_i = \sum_{i=1}^{S_W} \left(\sum_{y_i}^{n_i} 5^n - \sum_{z_i}^{m_i} 2^n \right) \quad \text{if} \quad P_i < R_i, \quad P_i + R_i = 0, \tag{3}$$

where SW is the number of samples in the window. R_i and P_i stand for total reward and punishment in the window. In each window, we were detecting n_i sub-windows containing interference where n is the number of consecutive samples with the same condition. When there is no interference detected we user m and m_i respectively instead of n.

Learning time needs to be discussed as well. We found the optimal learning time for initial learning to be two minutes. In the simulations, we compared initial learning with the results from all the measured dataset. By this calculation we are able to evaluate the accuracy of initial learning, see Fig. 5, where it is clearly proved that two minutes is the shortest initial learning time period.

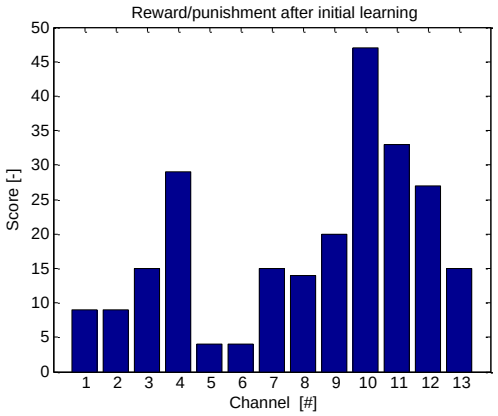

Figure 4: Scores from learning after 2 minutes.

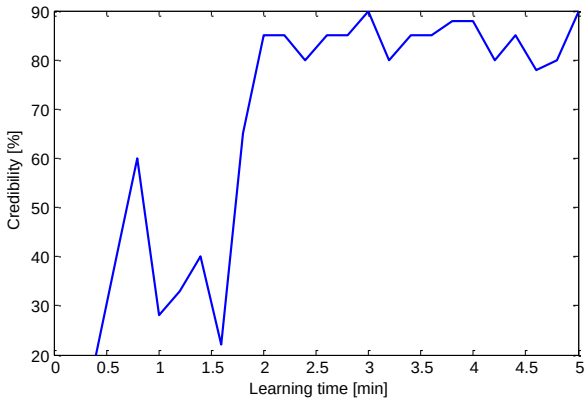

Figure 5: Credibility of the initial learning.

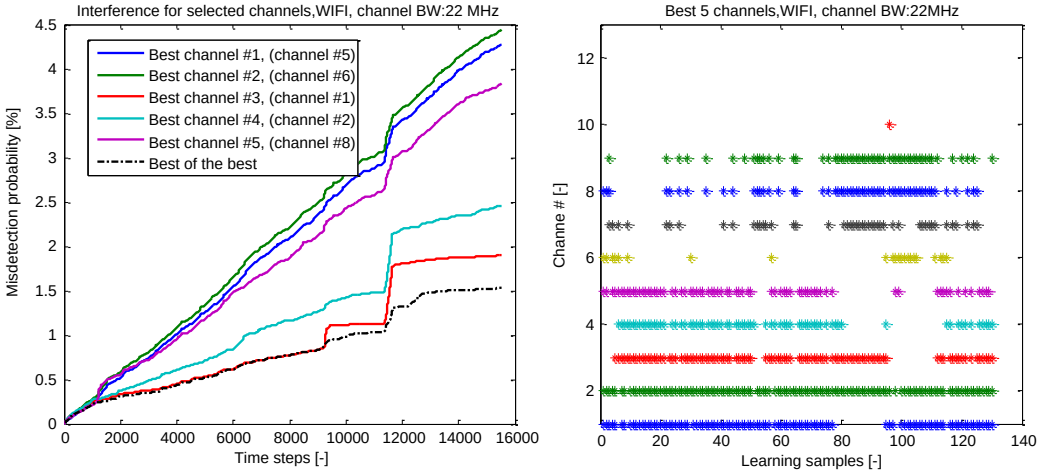

Figure 6: The best channel selection for outdoor heavily used system.

After initial learning we chose the best channel, then every 10 minutes (this time was chosen and verified with the same principle as the initial learning time) the scores were updated. Fig. 6 shows the misdetection probability, representing the total number of the interference count, which actually influences our system. This figure also presents the distribution of the five best channels in the system.

4. CONCLUSION

The preliminary results for channel selection for WI-FI were presented. We assume that modern WI-FI access points are continuously sensing the spectrum. These data are processed by a novel machine learning system and the vector of the available channels is created and updated over the whole transmission period. The presented system brings a significant improvement in WI-FI channel planning and interference noise of the chosen channel. Compared to traditional channel assignment, we improved the system by 2%–10% for outdoor systems and up to 30% for indoor systems. The improvement rate was calculated by counting the interference occurrences based on measured data.

ACKNOWLEDGMENT

This work was supported by the project CZ.1.07/2.3.00/30.0005 of Brno University of Technology.

REFERENCES

1. IEEE, "Part 11: Wireless LAN medium access control (MAC) and physical layer (PHY) specifications," *Amendment 4: Further Higher Data Rate Extension in the 2.4 GHz Band*, The Institute of Electrical and Electronics Engineers, Inc., 2003.
2. Urban, R., T. Korinek, and P. Pechac, "Broadband spectrum survey measurements for cognitive radio applications," *Radioengineering*, Vol. 21, 2012, ISSN: 1210-2512.
3. Datla, D., A. M. Wyglinski, and G. J. Minden, "A spectrum surveying framework for dynamic spectrum access networks," *IEEE Transactions on Vehicular Technology*, Vol. 58, 4158–4168, 2009.
4. Islam, M. H., C. L. Koh, S. W. Oh, X. Qing, Y. Y. Lai, C. Wang, Y.-C. Liang, B. E. Toh, F. Chin, G. L. Tan, and W. Toh, "Spectrum survey in Singapore: Occupancy measurements and analyses," *3rd International Conference on Cognitive Radio Oriented Wireless Networks and Communications (CrownCom 2008)*, 1–7, 2008.
5. Urban, R. and E. Hutova, "Rapid channel assignment for intelligent indoor scenarios," *European Conference on Antennas and Propagation, EUCAP 2014*, The Hague, 2014.
6. Sutton, R. S. and A. G. Barto, *Reinforcement Learning: An Introduction,* The MIT Press, 1998, ISBN: 9780262193986.

Analysis of Conditions on the Boundary between Layers

R. Kadlec and P. Fiala
Department of Theoretical and Experimental Electrical Engineering
Brno University of Technology, Technická 3082/12, Brno 616 00, Czech Republic

Abstract— The authors report on an analysis of conditions on the boundary between layers having varied electromagnetic properties. The research is performed using consistent theoretical derivation of analytical formulas, and the underlying problem is considered also in view of multiple boundaries, including the effect of the propagation of electromagnetic waves exhibiting different instantaneous speed.

The paper includes a theoretical analysis and references to the generated algorithms. The main algorithm was assembled to enable simple evaluation of all components of the electromagnetic field in relation to the speed of the wave propagation in a heterogeneous environment. The proposed algorithms are compared by means of different numerical methods for the modelling of electromagnetic waves on the boundary between materials; moreover, electromagnetic field components in common points of the model are also subject to comparison.

When in conjunction with tools facilitating the analysis of material response to the source of a continuous signal, the algorithms constitute a supplementary instrument for the design of a layered material. Such design enables the realization of, for example, recoilless plane, recoilless transition between different types of environment, and filters for both optical and radio frequencies. This phenomenon occurs in metamaterials.

1. INTRODUCTION

Inhomogeneities and regions with different parameters generally appear even in the cleanest materials. During the passage of an electromagnetic wave through a material, we can observe amplitude decrease and wave phase shift. These phenomena are due to the concrete material characteristics, such as conductivity, permittivity, or permeability [1]. If a wave impinges on an inhomogeneity, there occurs a change in its propagation. The change manifests itself in two forms, namely in reflection and refraction. In addition to this process, polarisation and interference may appear in these waves [2].

In the Matlab program, algorithms were created that simulate reflection and refraction in a lossy environment on the boundary between two dielectrics. The reflection and refraction are in accordance with Snell's law for electromagnetic waves, as shown in Fig. 1(a).

The interpretation of the propagation of electromagnetic waves on a layered heterogeneous medium is expressed by the formula

$$\mathbf{E}_{\mathrm{r}l} = \mathbf{E}_{\mathrm{i}l}\rho_{\mathrm{E}l} \cdot \mathrm{e}^{-\mathrm{j}\mathbf{k}_l \mathbf{u}_{\mathrm{nr}l} \times \mathbf{r}_l}, \quad \mathbf{E}_{\mathrm{t}l} = \mathbf{E}_{\mathrm{i}l}\tau_{\mathrm{E}l} \cdot \mathrm{e}^{-\mathrm{j}\mathbf{k}_l \mathbf{u}_{\mathrm{nt}l} \times \mathbf{r}_l}, \tag{1}$$

where $\mathbf{E}_{\mathrm{r}l}$ and $\mathbf{E}_{\mathrm{t}l}$ are the reflection and refraction of the electromagnetic waves on the boundary line ($l = 1, \ldots, \max$) according to Fig. 1(a), $\mathbf{E}_{\mathrm{i}l}$ is the amplitude electric field strength on the boundary line l, $\rho_{\mathrm{E}l}$ and $\tau_{\mathrm{E}l}$ are the reflection coefficient and transmission factor on the boundary line l, $\mathbf{k}_l$ is the wave number of the layer, $\mathbf{r}_l$ is the electromagnetic wave positional vector on the boundary line l, $\mathbf{u}_{\mathrm{nt}l}$ and $\mathbf{u}_{\mathrm{nr}l}$ are the unit vectors of the propagation direction.

2. OBLIQUE INCIDENT WAVE ON A LAYERED MEDIUM

The Matlab-based analysis using Equation (1) was performed in the planar layers. Figs. 2 and 3 show the response of the environment of 5 layers with the same thickness $d = 20\,\mathrm{mm}$. During the transmission, the wave at the frequency of 1.5 GHz passes through a material 1 with parameters $\varepsilon_{r1} = 1$, $\mu_{r1} = 1$ and $\gamma_1 = 1 \cdot 10^{-9}\,\mathrm{S/m}$, where the wave is reflected and refracted. Furthermore, the wave propagates through material 2 with parameters $\varepsilon_{r2} = 81.6$, $\mu_{r2} = 0.999991$, and $\gamma_2 = 4.405 \cdot 10^{-9}\,\mathrm{S/m}$. The incidence of the wave on boundary 1 is at the angle of θ_0. The described configuration is according to Fig. 1(a). The selection of the material parameters is only of testing character, and thus it does not have any special meaning.

Figure 2 presents the response of the separate layers to the primary refraction electromagnetic wave. The response of the material is the response to an electromagnetic wave of the pulse source.

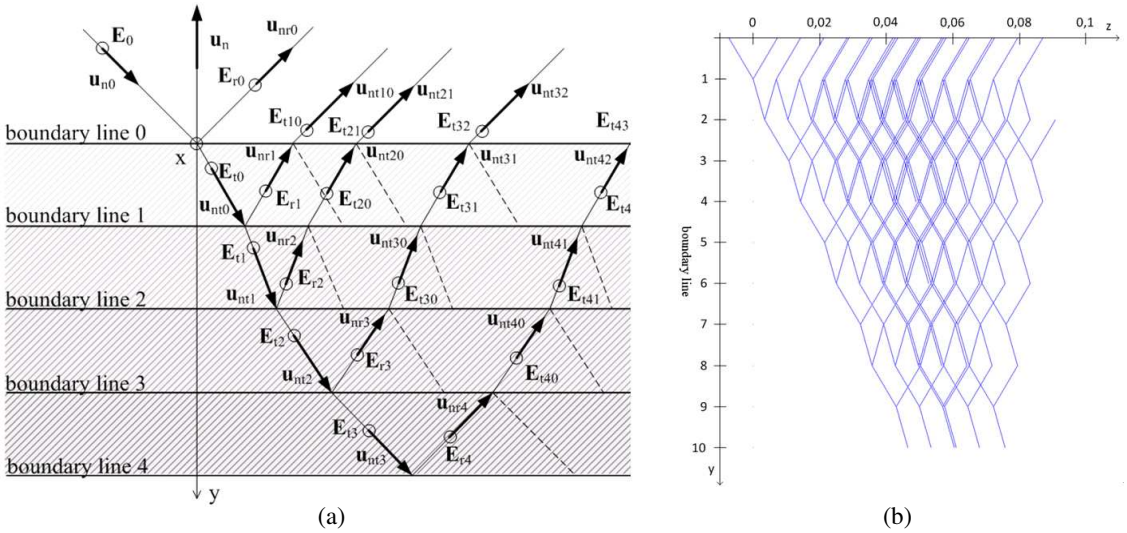

Figure 1: The reflection and refraction of the electric component of an electromagnetic wave on a layered medium: (a) layout, (b) Matlab for 2000 cycles.

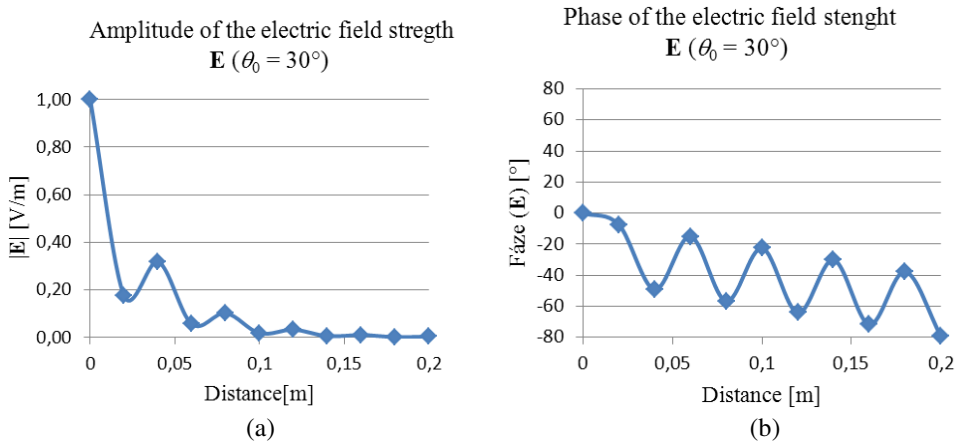

Figure 2: The strength of the electric component of the TE wave on a layered medium at the angle $\theta_0 = 30°$.

Fig. 2, however, does not show the interferences for a more descriptive interpretation of the attenuation of the electromagnetic waves. However, the algorithm evaluates all of the reflected and refracted waves.

The results of the analysis shown in the images consist in the modules of the electric field strength **E** along the boundary between the first layer and the external environment. To a certain extent, these values can be compared with already known methods for the analysis of the electromagnetic field. The analysis of the response to the incidence of an EMG wave on the surface of a multilayered environment within the given time interval is presented in Fig. 3; here, the module of the electric field strength **E** is introduced depending on the plane leading from the center of the model towards its edge. The distribution of the modules of the electric field strength **E** on the surface of the material is obvious from the waveform of the EMG waves propagating through and reflecting from a multilayered material, as shown in Fig. 1(b).

3. FEM MODEL OF A LAYERED MEDIUM

In order to verify the properties of the analytical model of an accurate evaluation of wave propagation in a layered environment, we used another model. This numerical approach utilised the finite element method (FEM) and exhibited the same properties as the previous model. As the mathematical expression, we applied the enhanced wave equation for a lossy environment:

$$\nabla^2 u + f\frac{\partial u}{\partial t} + g\frac{\partial^2 u}{\partial t^2} - f_c\left(x, y, z, t\right) = 0 \;\forall g\left(x, y, z\right) \neq 0,\; \forall f\left(x, y, z\right) \neq 0,\; \text{in}\,\Omega \tag{2}$$

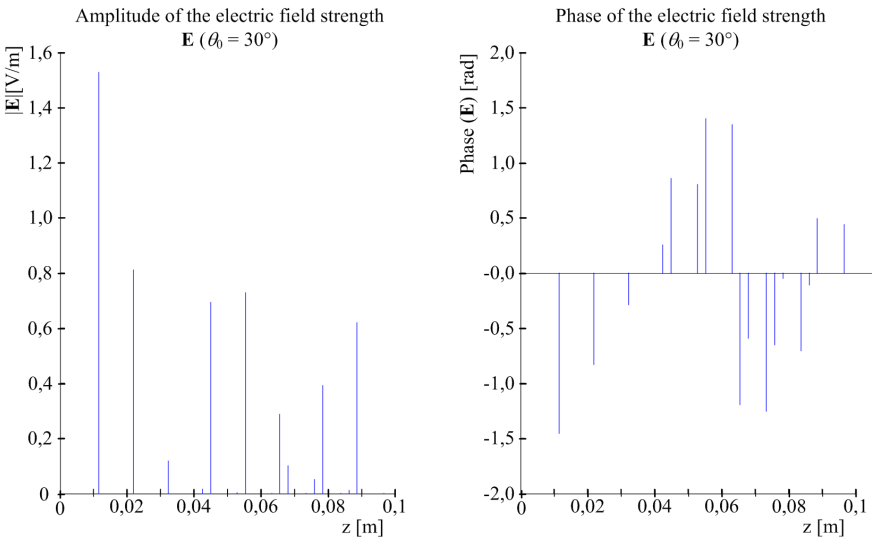

Figure 3: The strength of the electric component of the TE wave on a layered medium at the angle $\theta_0 = 30°$.

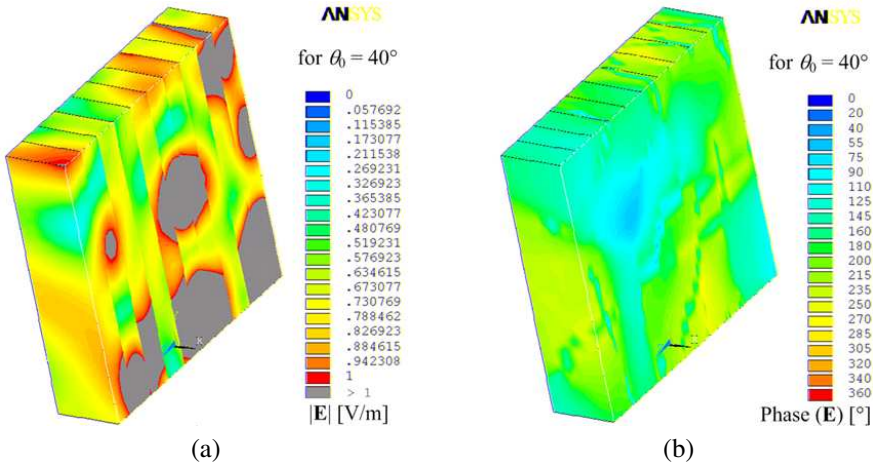

Figure 4: The distribution of the electric field strength **E**: (a) amplitude, and (b) phase for $\theta_0 = 40°$.

where u is the searched functional, f a function of the electromagnetic wave damping, g a function of the electromagnetic wave excitation, f_c a function of the lossy environment, Ω the defining domain of variables and functions.

The distribution of the electric field **E** and its phase ϕ are both shown in Fig. 4. The characteristics in Fig. 4 correspond to the axis direction perpendicular to the layer plane.

4. COMPARISON OF BOTH MODELS

Direct comparison of the different analysis results obtained via the applied methods can be performed only with substantial difficulty. For this reason, we designed algorithms to evaluate the selected time intervals in the ray-tracing model. The evaluation of the module of the electric field strength **E** on the surface of the material at these time intervals is indicated in Fig. 3. A continuous electromagnetic wave was generated by the source. A suitably selected time interval of the medium response expressed by the maximum values of the electromagnetic field strength facilitates verification by the instantaneous values obtained via the applied finite element method. Fig. 5 shows that the results acquired through both analyses are comparable.

The EMAG module of ANSYS is not a convenient tool for the evaluation of either the pulse process or the maximum values of an electromagnetic wave in a heterogeneous environment. This drawback stems from the fact that the EMAG module is characterised by multiple interferences and various wave propagation velocities; consequently, the behaviour of the electromagnetic field strength phase is not uniform. And if already used parameters are set, the number of the discretisa-

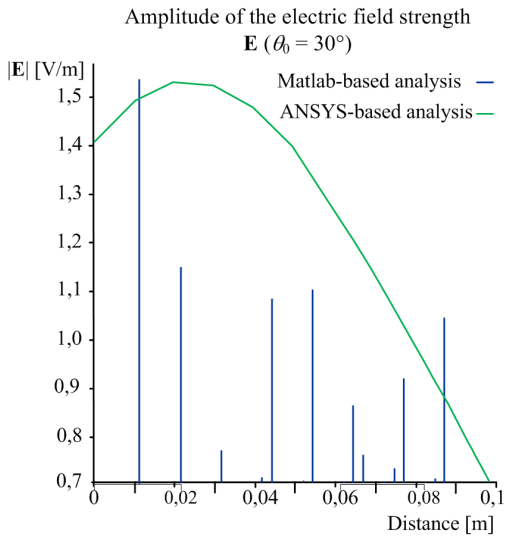

Figure 5: The diagram of the distribution of the electric field strength **E**: for $\theta_0 = 30°$, on the surface of the material, and in the plane of incidence.

tion mesh divisions in the ANSYS-based model will be unfavourable with respect to the wavelength of the propagating wave. For comparison purposes, however, this negative effect is still acceptable. Consequently, the resulting values (and thus also comparison possibilities) are restricted.

5. CONCLUSION

The article presents a comparison of two approaches to the analysis of wave propagation in a layered material structure. The first of these techniques is based on of the propagation of electromagnetic waves as defined by analytical formulas (1) and was solved in the Matlab program. The second approach exploits the FEM applied to the wave equation. The FEM-based solution was conducted using the ANSYS system. The actual comparison of the results provided by both approaches cannot be performed directly.

Numerical modelling carried out by means of the wave equation and ANSYS produces a continuous source of electromagnetic waves. Interference effects between the reflected and refracted waves arise on the boundary between the layers. Moreover, the interference process is also entered by the time-delayed waves from the source and by interface reflections [4].

A complex form of the angle of reflection and refraction is considered in the case of the analytical approach, which allows accurate determination of the size and intensity of the reflected and refracted waves. In order to determine the direction of the constant phase propagation in a lossy medium, we consider only real parts of the wave number. The analytical solution and its algorithms process the time-varying phenomena of the pulsed source. The analytical solution includes the effect of time-dependent propagation of electromagnetic waves in a heterogeneous medium, and it results in the distribution of the electromagnetic field at the boundaries during certain moments of time.

The results of the ANSYS-based analysis of the propagation of electromagnetic waves in a material in the time-domain corresponds to the resulting distribution of the superimposed field intensities on individual boundaries of the analytical model. The approach using the finite element method in ANSYS is limited to spatial distribution of quantities with distributed parameters. This solution, despite being very robust in the time domain, is not suitable for multiple layers due to the method of the element mesh division. In FEM-based numerical models, the number of divisions of the discretised mesh can be determined only with difficulty (considering the wavelength of the propagating wave), and the solution of a large model by currently available means is almost impossible. Importantly, this drawback can be eliminated via the proposed method. The analysis of the pulsed source of the electromagnetic wave by means of an analytical model provides expectable results in heterogeneous structures since the behavior of phase change is uniform. The analytical solution allows us to analyze the response of the material in detail for the individual parts.

ACKNOWLEDGMENT

The research described in the paper was financially supported by Czech Science Foundation (13-09086S), a project of the BUT science fund, No. FEKT-S-14-2545/2014, and a project from the Education for Competitiveness Operative Programme, No. CZ.1.07.2.3.00.20.0175 (Electro-researcher).

REFERENCES

1. Roubal, Z., M. Steinbauer, and Z. Szabó, "Modeling of saturation characteristic of an aspiration condenser," *PIERS Proceedings*, 216–220, Xi'an, China, Mar. 22–26, 2010.
2. Roubal, Z. and V. Smejkal, "Determination of parameters in the Jiles-Atherton model for measured hysteresis loops," *Proceading Measurement 2013*, 127–131, SAV, Smolenice, 2013, ISBN: 9788096967254.
3. Schmidt, E., *Optické vlastnosti pevných látek*, 1, vyd, Státní pedagogické nakladatelství, 200, Praha, 1986.
4. Drexler, P. and R. Kubásek, "Pulsed magnetic field fiber optic sensor based on orthoconjugate retroreflector," *Proceedings of SCS 2009 International Conference on Signals, Circuits and Systems*, 52–57, Tunisia, 2009, ISBN: 978-1-4244-4398-7.

Fast Calculation of T_2 Relaxation Time in Magnetic Resonance Imaging

J. Mikulka[1] **and P. Dvořák**[2]

[1]Department of Theoretical and Experimental Electrical Engineering
Brno University of Technology, Technická 12, Brno 616 00, Czech Republic
[2]Academy of Science of the Czech Republic, Institute of Scientific Instruments
Královopolská 147, Brno 612 64, Czech Republic

Abstract— The main parameters displayed by means of magnetic resonance include, for example, relaxation times T_1 and T_2 or diffusion parameters. This paper presents the computation of relaxation time T_2 measured indirectly with the Spin Echo method. The sensing coil of the tomograph provides a signal in which the important factor is the location of the peaks from individual measurements. These points must be interleaved with an exponential function. The relaxation time T_2 can be directly determined from the exponential shape. The described process has to be repeated for each pixel of the sensed tissue, and this requirement makes the processing of larger images very demanding in terms of both the actual computation and the time needed for the entire operation. More concretely, if we assume the common resolution of 256×256, 20 slices, and five measurements with different times T_E, it is necessary to reconstruct $1.3 \cdot 106$ exponential functions in total, which requires the processing of more than 6 MB of data. At present, such computation lasts approximately 3 minutes if performed by means of a regular PC. The author discusses various approaches to the parallelization of the given problem. In the described context, the time required for the processing of the applied three-dimensional image was shortened to 300 ms thanks to simple interpolation approach. The final section of the paper comprises a detailed comparison of the computation times characterizing both the sequential and the parallel solutions.

1. INTRODUCTION

The imaging of biological tissues carried out via magnetic resonance (MR) currently constitutes one of the most advanced diagnostic techniques [1, 2]. A large number of imaging sequences are available, and each of them finds its application in the imaging of a particular set of tissue properties [3, 4]. The most common tomographically acquired parameters include relaxation times T_1 and T_2. In this context, it is possible to point out that the higher the number of known tissue parameters, the better their discernibility (or the concrete pathology diagnosis) [5]. The relaxation time T_2, whose reconstruction is discussed within this paper, can be acquired via a number of sequences, and one of the techniques most widely used for the purpose is the Spin Echo (SE) method. In magnetic resonance, a spin echo is a pulse sequence comprising two radio frequency pulses with the phases of 90° and 180°. After the first pulse, the magnetization vector is flipped into the xy plane, and the T_2^* relaxation begins; this means that while some protons precess with slightly higher frequencies, others perform the same with lower ones. Subsequently, dephasing occurs. However, if there follows a 180° refocusing pulse, which will flip the individual spins in the xy plane, then the spins are in phase again, and the receiver coil detects a signal. The amplitude of the signal depends on the T_2 of the tissue. This process is repeated with the increasing time T_E, where $T_E/2$ is the time between the above-mentioned pulses with the phases of 90° and 180°. The time progression of the SE sequence is displayed in Figure 1.

The relaxation time T_2 is determined from the exponential function, which passes through the maximum values of the individual echoes. This function can be expressed as

$$E = e^{-\frac{T_E}{T_2}}, \tag{1}$$

where E is the envelope of the spin echoes, and T_E is the time of the echo arrival from the first excitation pulse. This time is given by double the time between the arrivals through the first and the second excitation pulses [6].

The determination of the relaxation time T_2 therefore comprises the following steps: acquisition of several images via the SE sequence with different times T_E; exponential regression at points located in the maxima of the individual echo signals; computation of the T_2 relaxation. The

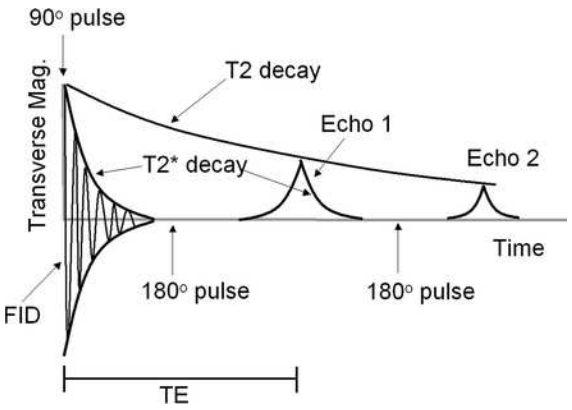

Figure 1: The time progression of the Spin Echo sequence and the T_2 exponential decay.

process is repeated for all pixels in the image. In the applied image having the size of 256×256 pixels and depth of 20 slices, this corresponds to $1.3 \cdot 106$ exponential regressions, and there are 5 points from which the exponential is reconstructed. It follows from the above-indicated facts that the computational problem is very extensive with respect to the data size. Generally, two solution options are available to eliminate the drawback. In the first approach, the problem is solved sequentially, and we have to perform (within each step) exponential regression from the five measurements for each voxel individually; the second option is based on the parallelization of the problem. The computation of the value of the relaxation time T_2 of each voxel depends only on the values obtained from the five measurements carried out with the SE technique, and therefore the regression can be performed for all voxels simultaneously.

The investigation of methods for the reconstruction of T_2 images has been described and discussed in a large number of papers, for example [7, 8]. Importantly, the most prominent disadvantage of the techniques can be identified in the computational speed, as suggested above. Recently, however, the drawback has been markedly suppressed by the application of high-speed graphic processors, which enable us to realize the computational process in a parallel — and very fast — manner [9, 10].

2. IMAGE DATABASE, HARDWARE & SOFTWARE

In order to test the proposed parallel processing method, we used a three-dimensional image of a brown rat; this image had been acquired via a Bruker Biospec 94/30 tomograph having the elementary magnetic field intensity of 9.4 T. The images exhibited the resolution of 256×256 pixels, and 20 slices were applied. Each voxel was measured five times using the SE method. The echo times T_E were selected as follows: 15 ms, 45 ms, 75 ms, 105 ms, 135 ms.

The actual comparison of the sequential and parallel variants of the computation of T_2 maps was performed with a PC comprising an Intel Core2 Quad 2.66 GHz, 4 GB RAM processor. The applied software included Windows 7 64-bit and Matlab R2013a. The parallel computing was carried out utilizing the CUDA platform containing the following graphics card: nVidia GeForce GTX 770 (1024 threads per block, max thread block size $1024 \times 1024 \times 64$, 4 GB of total memory at the frequency of 7 GHz, 1 GHz GPU).

3. METHODS

The aim of the processing is to obtain a T_2 map of the relaxation times of the tissues imaged during the tomographic measurement. In this respect, the paper describes two processing methods, namely a) sequential computation, and b) parallelized computation.

3.1. The Sequential Approach

The described reconstruction of the T_2 map from an MR set of images was implemented in the Matlab environment. Here, the computation proceeds in a single for cycle. Within each step of the program, the exponential regression of one pixel is performed from 5 measured values of the maximum intensity of the echo. The number of cycles is 1 310 720. The exponential regression initially employed the function fit, whose syntax is as follows:

$$\text{fitobject} = \text{fit}\ (x,\ y,\ \text{'exp1'});$$

where x is the vector of the times of the arrival of the echoes T_E, and y is the vector of the measured values of the maximum intensity of the echoes.

At the following stage, we implemented the method described and used in the parallel computation.

3.2. The Parallel Approach

The implementation of this option was also performed in the Matlab environment. In this approach, the computation is carried out in a single step, namely by calling the computational core of the graphics card. The computation of the value of each pixel is assigned one thread of the process.

In this experiment, the actual regression computation was performed using the conversion of exponential regression to linear regression. The measured values are assumed to approximately correspond to the functional dependence in the form

$$y = a \cdot e^{bx}. \tag{2}$$

If this formula is logarithmized, we obtain the linear equation

$$\ln y = \ln 1 + \ln e^{bx}. \tag{3}$$

After applying the method of least squares, we obtain the following relation for the calculation of the coefficient b:

$$b = \left[n \cdot \sum_{i=1}^{n} x_i \cdot \ln y_i - \sum_{i=1}^{n} x_i \cdot \sum_{i=1}^{n} \ln y_i \right] \Bigg/ \left[n \cdot \sum_{i=1}^{n} x_i^2 - \left(\sum_{i=1}^{n} x_i \right)^2 \right], \tag{4}$$

where the vector x represents individual times to the echoes T_E, the vector y denotes the measured values of the echoes, and n is the number of measurements. By comparing formulas (1) and (2) and through substituting the coefficient b from Equation (4), we obtain the relaxation time T_2 in the form

$$T_2 = -\frac{1}{b}. \tag{5}$$

The parallel computation always runs with only one slice of the 3-D image, whose resolution is 256×256 pixels (this value corresponds to 65536 threads of the graphics processor). The computation of the three-dimensional T_2 map is then carried out in a series-parallel manner.

4. RESULTS AND DISCUSSION

The comparison of the approaches to the computation of T_2 is realized with respect to both the time required by the process and the accuracy of the obtained values. In view of the large difference between the sequential and the parallel execution of the program, the comparison of the time requirements is carried out using a three-dimensional image, which exhibits the resolution of 256×256 pixels and where the total number of slices is 20. The comparison targeting the accuracy of the obtained values is materialized via subjective revision of the computed images and by means of the computation and analysis of the differential image.

For quick reference, the time requirement values are quoted in Table 1.

Table 1: Sequential and parallel computation: Values of the time required.

Computation	Time required per 1 slice	Time required per 20 slices
Sequential (the *fit* function)	41 min	$\approx$ 14 h
Sequential (function according to formula (8))	10.3 s	$\approx$ 210 s
Parallel	8.8 ms	167 ms

The correctness of the computation is verified by means of a difference image and its analysis. Figure 2 shows (a) the selected T_2 map in the 9th slice of the volume from the sequential computation using the fit function, and (b) displays the result of the parallel computation. Figure 3 presents the difference image which appears after the sequentially computed image is subtracted from the image obtained via the parallel computation.

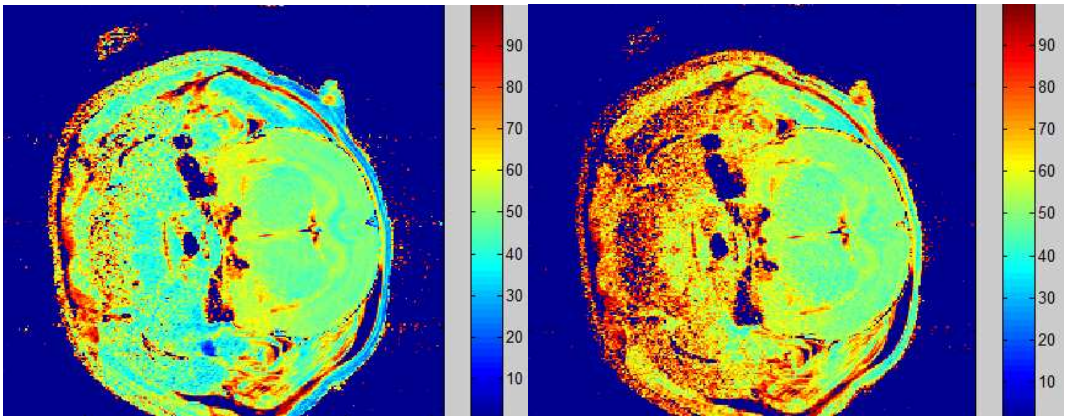

(a) (b)

Figure 2: The resulting T_2-map obtained from the sequential and parallel computation. (a) Sequential computation result. (b) Parallel computation result.

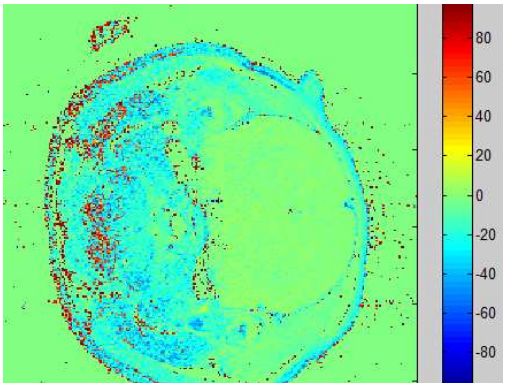

Figure 3: The image resulting from the difference between the results of the sequential and the parallel computation.

A subjective comparison of the images from Figures 2(a) and 2(b) will show agreement between the two methods of T_2 computation. Further, an analysis of the map obtained via parallel processing will indicate a higher sensitivity to noise, which is a factor that affects SE-based images already at the time of their making. This effect manifests itself mainly in the left portion of the image; such distribution of the problem is caused by a weak response of the examined tissues stemming from the fact that the image was produced using a surfaced coil located on the right-hand side. Principally, however, the above-described disadvantage cannot be ascribed to parallel image processing, and its origins should be sought in the applied exponential regression method.

The correctness of the result can be demonstrated also on the difference image displayed in Figure 3. Here, too, a higher error rate appears in regions exhibiting a lower level of the SE signal. The image background was subtracted before the actual computation of the T_2 map, and therefore the computational error is zero. Before subtraction of the background, the error rate in these regions is at its highest level, and the map can be displayed only with difficulty. In its left section, the differential image again exhibits a higher error rate caused by the location of the surface coil.

5. CONCLUSION

The article presents a solution enabling fast computation of images of the relaxation time T_2; such images are very often analyzed in the diagnostics and description of tissues performed within magnetic resonance tomography. In the given context, two computational methods are described. The first of these techniques consists in the standard sequential approach, where the value T_2 of the relaxation time is (in each pixel) computed within one step of the cycle of the common process thread. This technique requires a significant amount of time to perform a complete reconstruction (the process lasts 14 hours if the embedded m-function fit is applied, but it takes up less than 4 minutes with a simple regression function). Conversely, the parallel approach employing the

CUDA platform and utilizing effective computation performed by means of an nVidia graphics card requires approximately 200 ms to reconstruct a three-dimensional T_2 map having the size of $256 \times 256 \times 20$ pixels. The specified time can be even lower, and its concrete values then differ according to the graphics card used (the number of physically allocated CUDA cores), speed of the graphics processor, and memory. As shown in Figures 2, and 3, the images provided by both methods exhibited an identical structure of the displayed tissues. The results differ in the sensitivity to noise, mainly in regions with a low level of the SE signal. Such low level is caused by the location of the sensing surface coil of the tomograph. In the computation of T_2 relaxation times, the sensitivity to noise is a critical factor, and therefore the noise in the images has to be eliminated. This paper comprises a description of the exponential regression method converted to a linear problem. For future applications, the analysis of exponential regression results via other methods is assumed; one of related possibilities consists in the pre-processing of SE images to facilitate the suppression of noise or motion artefacts already in source images. The problems thus specified would then affect the resulting T_2 map only minimally.

ACKNOWLEDGMENT

This work was supported in part by the Grant GAČR 102/12/1104 and by the project CZ.1.07/2.3.-00/30.0039 of Brno University of Technology.

REFERENCES

1. Mikulka, J., E. Gescheidtova, and K. Bartusek, "Soft-tissues image processing: Comparison of traditional segmentation methods with 2D active contour methods," *Meas. Sci. Rev.*, Vol. 12, No. 4, 153–161, 2012.
2. Mikulka, J., E. Gescheidtova, and K. Bartusek, "Perimeter measurement of spruce needles profile using MRI," *PIERS Proceedings*, 1128–1131, Beijing, China, Mar. 23–27, 2009.
3. Marcon, P., K. Bartušek, E. Gescheidtová, and Z. Dokoupil, "Diffusion MRI: Magnetic field inhomogenieties mitigation," *Meas. Sci. Rev.*, Vol. 12, No. 5, 205–212, 2012.
4. Marcon, P., K. Bartušek, R. Korínek, and Z. Dokoupil, "Correction of artifacts in diffusion-weighted MR images," *34th International Conference on Telecommunications and Signal Processing (TSP)*, 391–397, Budapest, 2011.
5. Marcon, P. and K. Bartusek, "Multiparametric data collection of animal tissues in magnetic resonance imaging," *2012 35th Int. Conf. Telecommun. Signal Process. TSP*, 566–569, 2012.
6. Yan, H., *Signal Processing for Magnetic Resonance Imaging and Spectroscopy*, CRC Press, 2002.
7. Iwaoka, H., T. Hirata, and H. Matsuura, "Optimal pulse sequences for magnetic resonance imaging-computing accurate T_1, T_2, and proton density images," *IEEE Trans. Med. Imaging*, Vol. 6, No. 4, 360–369, 1987.
8. Singh, M., K. Oshio, and R. R. Brechner, "Iterative estimation of T_2 to correct echo planar magnetic resonance images," *IEEE Trans. Nucl. Sci.*, Vol. 37, No. 2, 795–799, 1990.
9. Karantza, A., S. L. Alarcon, and N. D. Cahill, "A comparison of sequential and GPU-accelerated implementations of B-spline signal processing operations for 2-D and 3-D images," *2012 3rd International Conference on Image Processing Theory, Tools and Applications (IPTA)*, 74–79, 2012.
10. Keceli, A. S. and A. B. Can, "GPU based brain segmentation method," *2011 IEEE 19th Conference on Signal Processing and Communications Applications (SIU)*, 258–261, 2011.

Measuring and Application of NIR Light Absorption Coefficient of Bacteria

Pavel Krepelka[1], **Fernando Camara Martos**[2],
Guiomar Denisse Posada-Izquierdo[2], **and Fernando Pérez-Rodríguez**[2]

[1]Department of Theoretical and Experimental Electrical Engineering
Brno University of Technology, Technická 12, Brno 616 00, Czech Republic
[2]Departamento de Bromatología y Tecnología de los Alimentos, Ed. Darwin-Anexo
Campus Rabanales s/n, Universidad de Córdoba, Córdoba 14014, Spain

Abstract— Near infrared spectroscopy is a widespread technique in analytical chemistry. However, recently, there has been a growing interest in the usage of the NIR spectroscopy in microbiological analysis. Due to the improvement of the experiment setup and an increase in the efficiency of the evaluation methods, the knowledge of the absorption coefficient of a sample can be very beneficial. The purpose of this study is to introduce problems that relate to the measurement and handling of absorption coefficients.

The molecular bonds presented in the examined sample cause absorption of the incident light. When the energy quantum from a source of light equals the energy necessary for the transition of a bond to a higher vibration level, the light is absorbed. Considering this effect, it is possible to identify the chemical composition of a sample. Recent studies [1] have proved that the chemical composition of different bacteria species is sufficiently diverse, and thus the bacteria can be identified using a NIR spectrum. The absorption coefficient is mostly used in the Lambert-Beer-Bouguer law. This equation expresses how the optical intensity of a light wave is exponentially reduced along the beam's path through the sample. In the case of NIR spectroscopy, the output light intensity is measured. The multiplicative scatter and other unwanted influences of the incoming radiation make direct measurement difficult. For correct computing of the absorption coefficient, it is necessary to separate the physical light-scattering effect from the chemical light absorbance constituted by vibrations of a molecule's bonds. The absorption coefficient is a function of the energy of photons (wavelength), and its value depends on the position and amplitude of the fundamental, overtone, and combination types of molecular bond absorption.

Knowledge of the absorption coefficient is important due to optimizing the measurement technique and statistics methods. Because any straightforward measuring of bacteria cells requires a special approach, prior knowledge of the absorption coefficient can help to reduce costs in terms of money and time.

1. INTRODUCTION

The growing demand for rapid methods of bacterial identification accelerates the development of alternative techniques including Near infrared spectroscopy. Traditional methods are mostly based on immunoanalysis, gram staining, mass spectroscopy, DNA sequencing, and other biochemical testing approaches. In contrast with the above-listed common methods, Near infrared spectroscopy is a cheap, fast, and simple technique.

The ability to determine bacterial species is based on their different chemical composition, which leads to different ratio between IR active molecule bonds (C-H, N-H, O-H). The membrane structure of a bacterial cell and the ratio of lipids, proteins, and polysaccharides depend on the bacterial species. Unlike the mid-IR spectrum, the NIR spectrum is difficult to interpret because of the wide and overlapping combination and overtone peaks. Therefore, multivariate statistics need to be performed to provide information from the NIR spectrum. Applied procedures for signal preprocessing, classification and validation exert essential influence on the final identification efficiency.

The determination of a NIR absorption coefficient is a non-trivial procedure because of light scattering, spurious absorption, non-homogeneous sample, and other effects. To suppress these factors, the statistical parameters and experiment setup must be optimized.

2. ABSORPTION COEFFICIENT

The relation between the sample concentration and light absorption is described by the Lambert-Beer-Bouguer Law. The equation defines the amount of light absorbed by specific component in a

sample. The law assumes that the absorbances of multiple components are of additive character (at the same wavelength) and the samples are homogeneous and nonscattering

$$-\frac{dI_x}{I_x} = \frac{\sigma C S dx}{S}. \tag{1}$$

Consider the light incident on a material with a pre-determined sample concentration (C). The incoming light with intensity I_x illuminates $CSdx$ molecules, where S expresses the size of the illuminated area and dx is the light path length. The above-shown formula (1) expresses the probability of beam absorption in a material with thickness dx. The Lambert-Beer-Bouguer Law arises from integration of the Equation (1)

$$\int_{I_0}^{I} -\frac{dI_x}{I_x} = \int_0^x \sigma C dx \tag{2}$$

$$I = I_0 e^{-\sigma C x}. \tag{3}$$

The light intensity decreases exponentially with the length of penetration. To simplify the equations, linear attenuation coefficient (Eq. (4)) and absorbance (Eq. (5)) are used. Absorbance is defined as the inversed ratio of light intensity in front of and behind the sample

$$\mu = \sigma C \tag{4}$$

$$A = \log\left(\frac{I_0}{I}\right). \tag{5}$$

The extinction coefficient is defined as $\varepsilon = \log(e)\sigma$. The coefficient is used for expressing the light absorbance unit — see Eq. (6). In electromagnetic theory, extinction coefficient can be derived from the imaginary part of complex refractive index

$$A = \varepsilon C x. \tag{6}$$

Absorbance is linearly dependent on the concentration, pathlength, and absorption (extinction) coefficient of the investigated sample. The advantage of this notation lies in the possibility of summing up the absorption effects from particular components.

3. MATERIAL AND METHODS

In the first experiment, the absorption spectrum of bacteria in an aqueous solution was measured. Three different common food pathogen bacteria (*Listeria ivanovii, Escherichia coli, Salmonella*) were grown in tryptic soy broth, shaken, and measured in a saline solution. The near infra-red spectra were acquired via a diffuse-reflectance integrating sphere within the region of 1100 nm–2500 nm using a PerkinElmer Spectrum One NTS instrument. Figure 1(a) shows the setup of the design. In most cases, spectra variations caused by the investigated component are negligible; thus, multivariate statistics need to be performed. In chemistry, statistics is called chemometrics and comprises three main parts: Exploratory analysis (Principal component analysis), Regression (Partial least square regression), and Classification (Soft Independent Modeling of Class Analogy; Canonical variate analysis). Generally, bacterial identification is a classification task. The spectrum-processing techniques were carried out using Mathworks Matlab 8.1a. It is clear from Figure 1(b) that the peaks caused by water are dominant and the spectra variations caused by the bacteria are negligible. The absorption coefficient of the solution varies from 0–120 cm^{-1}. From the known bacteria concentration verified by a laboratory method, it is possible to compute the number of bacteria in the measured area. Approximately 17 10^5 bacteria were placed on the mirror.

Despite the application of advanced statistics, the validated correct classification rate is low (see Table 1). It follows from this level of accuracy that the analysis of bacteria in an aqueous solution is impossible to perform. A proof based on the absorption coefficient will be introduced later.

The total of 60 samples were included in the second experiment. To remove the effect of the supernatant, the samples were centrifuged and resuspended in distilled water. Further, the samples were filtered with a glass fiber filter and dehydrated to eliminate the absorption effect of water. On each filter, five measurements were carried out at different places. To ensure the same level of concentration, the sample absorbance of wideband (420 nm–580 nm) light was maintained at

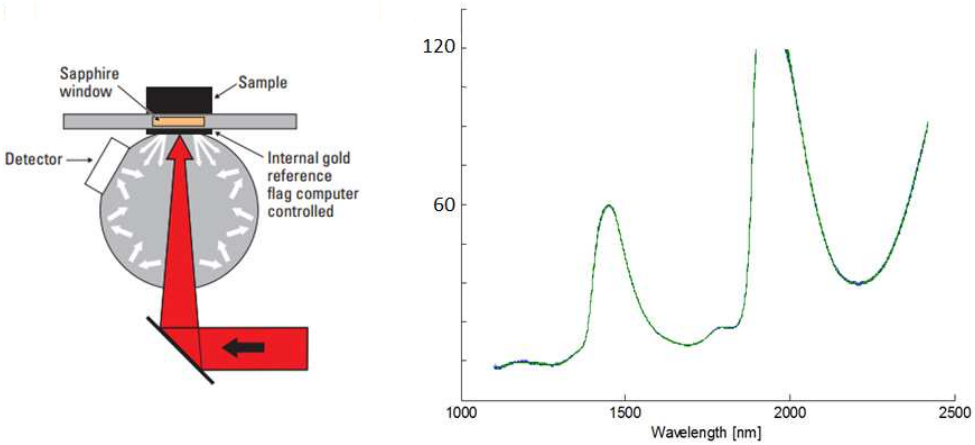

Figure 1: Design of the first experiment and the NIR spectrum of aqueous solution.

Table 1: The models performed in the first (first raw) and the second (second raw) experiment. Performance is expressed correct classification rate. CVA — canonical variate analysis, PLS-DA — partial least square-discriminant analysis, SIMCA — soft independent modeling class analogy, ANN — artificial neural network.

CVA	PLS-DA	SIMCA	ANN
40	45	34	35
100	90	100	95

approximately 0.85 (concentration aprox. 10^7 CFU/ml). The whole experimental design is shown in Figure 2. By this procedure, the pure spectrum of bacteria can be acquired. Although the spectra variations are more pronounced, we have to apply suitable statistics to facilitate correct computation of the absorption coefficient. For separate chemical absorption and light scattering, the EMSC algorithm [3] (Extended Multiplicative Scatter Correction) was performed. This algorithm can modify the NIR spectrum and make it applicable to the Lambert-Beer-Bouguer law, which considers only chemical light absorption (see Eq. (7)).

$$Z_i = a_i I + b_i m + h_i p + d_i \lambda + e_i \lambda^2 + \varepsilon_i, \tag{7}$$

where I is the identity matrix, m is the mean spectrum, p constitutes the first canonical component, and is the vector of the wavelengths. This equation is minimized using the method of least squares. Table 1 presents the high correct classification rates of the models. It is clear that the identification of highly concentrated bacteria suspensions was successful.

Approximately 10^{10} bacteria were placed on the filter. We can compute the corresponding volume of the highly concentrated solution of bacteria, which is necessary for correct identification.

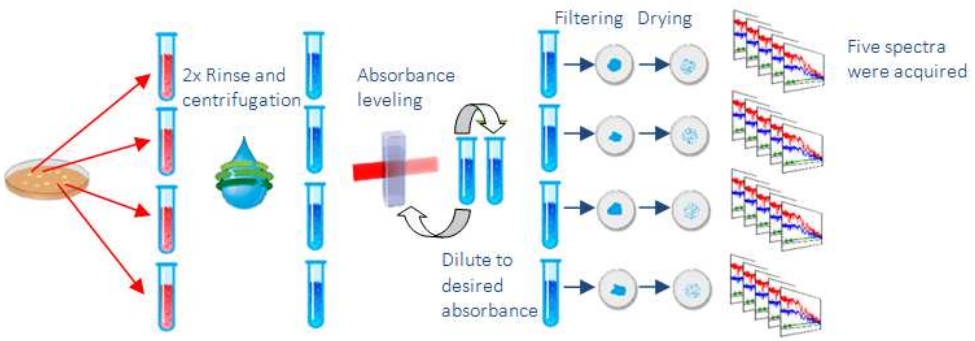

Figure 2: Design of the second experiment.

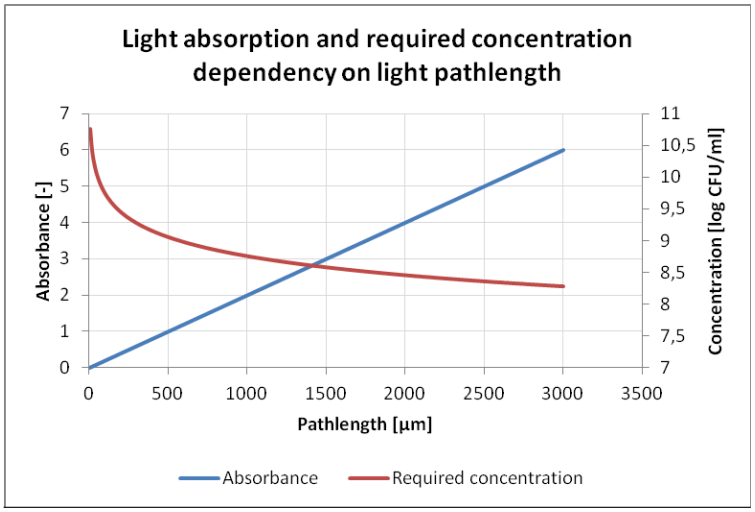

Figure 3: Graph of light absorption and required concentration dependency on light pathlength.

Since the absorption coefficient of the solution is known, a graph expressing the relation between the absorption of bacteria and the solution can be constructed.

4. CONCLUSION

In the first experiment, the impossibility of bacteria strain identification in the suspension was proven. In some cases, the composition of the sample can be predicted based on secondary chemical changes, but the biomass volume is not sufficient to facilitate determination. All the performed models exhibit very low correct classification rates.

The following experiment showed the ability of NIR spectroscopy to identify bacteria strains. A method for examining the pure spectrum of bacteria was developed. A bacteria suspension was placed on a glass fibre filter, and the water was evaporated. The samples prepared in this manner were identifiable via NIR using advanced statistical methods.

If the absorption coefficients of the bacterial cells and water are known, it is possible to define the minimal sample path length. Therefore, the possibilities of measurement in water can be theoretically determined, and the experiment setup can be optimized.

ACKNOWLEDGMENT

The research described in the paper was financially supported by project of the BUT science fund, No. FEKT-S-14-2545, and a project from the Education for Competitiveness Operative Programme, No. CZ.1.07.2.3.00.20.0175 (Electro-researcher).

REFERENCES

1. Boyer, A. E., M. G. Candela, R. C. Lins, Z. Kuklenyik, A. Woolfitt, H. Moura, S. Kalb, C. P. Quinn, and J. R. Barr, "Quantitative mass spectrometry for bacterial protein toxins — A sensitive, specific, high-throughput tool for detection and diagnosis," *Molecules*, Vol. 16, 2391–2413, ISSN 1420-3049, 2011.
2. Thermo Scientific, Smart NIR Integrating Sphere, Product Datasheet, online: http://www.thermo.com/eThermo/CMA/PDFs/Product/productPDF_7545.pdf.
3. Thennadil, S. N., H. Martens, and A. Kohler, "Physics-based multiplicative scatter correction approaches for improving the performance of calibration models," *Appl. Spectrosc.*, Vol. 60, 315–321, 2006.

Using Diffusion-weighted Images to Identify Brain Tumors

P. Marcon[1], **K. Bartusek**[2], **and A. Sprlakova**[3]

[1]Department of Theoretical and Experimental Electrical Engineering
Brno University of Technology, Technicka, Brno 3082/12, Czech Republic
[2]Institute of Scientific Instruments of the ASCR, v.v.i
Kralovopolska 147, Brno 612 64, Czech Republic
[3]Radiological Clinic, The University Hospital Brno, Jihlavska 20, Brno 625 00, Czech Republic

Abstract— The paper presents an evaluation of the magnetic resonance images of a pathology in the human brain. The experiment involved patients with high-grade glioma tumors in the brain, and an MR tomograph operated by the University Hospital Brno-Bohunice was utilized in the related examinations.

In our investigation, we measured images weighted by diffusion. A very interesting technique is diffusion-weighted imaging (DWI), where the measurement sequence comprises a table with 32 vectors of the b-factor orientation. The goal is to perform signal processing in the measured diffusion-weighted images. We proposed a special algorithm for the processing of the DWI image signal. The next step in the procedure was the statistical evaluation of DWI images of healthy and diseased human tissues. We also calculated the brain white matter images, such as those of the fraction anisotropy, RA (relative anisotropy), and VR (volume ratio).

1. INTRODUCTION

The research of pathology of human tissues is currently very interesting [1, 2]. Development of the magnetic resonance imaging represent very significant step because this technique provides images with excellent soft tissues contrast [3, 4]. We used methods for diffusion weighted images (DWI). In this method the pixels are weighted by diffusion coefficients D. This coefficient constitutes a random translational motion of molecules given by their thermal energy without requiring mass volumes motion. During diffusion time [5], the molecules may pass through regions having different diffusion coefficients D, by which means there occurs time dependence of the coefficient The most commonly used method for measurement of diffusion coefficient is The Pulsed Field Gradient Spin Echo (PFGSE). It is Spin echo methods, with two diffusion gradients [6].

Diffusion is often an anisotropic quantity (the D-value differs depending on the direction), and therefore coefficient D turns into tensor $\mathbf{D}$, which can be obtained minimally through measurement in six independent directions. From the tensor $\mathbf{D}$, we can calculate also these diffusion weighted images: Mean of all B0s, Mean of all DWIs, Tensor, Color Map, Anisotropy FA, Anisotropy RA, Anisotropy VR, $K2$, $K3$, $R1$ [5]. The goal of this paper is comparing these methods and finding the best method for diagnosing a tumor in the brain tissue.

2. EXPERIMENT

In our experiment we used a MR tomograph at the University Hospital Bohunice. The MR tomograph dispose of static field flux density $B_0 = 1.5\,\mathrm{T}$. Method of measurement and processing was tested on the patient with tumor in brain area.

We defined the area of tumor, tumor vicinity — edema and healthy tissue. The statistic analysis was made in these selected areas of the tissues. The value of maximum, minimum, means and standard deviation was obtained. With the knowledge of the individual tissues statistical quantities, the particular tissues can be automatically searched by using a special proposed algorithm.

In our experiment we measured diffusion coefficient — anisotropy quantities. We used 32 direction gradient system (better SNR [7–11]), and therefore coefficient D turns into tensor $\mathbf{D}$. From the tensor $\mathbf{D}$, we calculate also these diffusion weighted images: Mean of all B0s, Mean of all DWIs, Tensor, Color Map, Anisotropy FA, Anisotropy RA, Anisotropy VR, $K2$, $K3$, $R1$ [5].

- **Mean of all B0s** — this image is weighted by mean value of all images measured without diffusion gradient pulse.
- **Mean of all DWIs** — image weighted by mean value of all measured DWI images.
- **Tensor** — image weighted by diffusion tensor [5].

- **Color Map** — Color-coded orientation map. In the color-coded map, red, green and blue value represent fibers running along the right-left, anterior-posterior, and superior-inferior axes, respectively are scaled between 0 and 1.
- **Anisotropy FA (Fractional Anisotropy)** — refers to how restricted diffusion is. So anisotropy means "not the same in all directions", which is what we are trying to find out about the diffusion of water molecules in each voxel. The ADC and eADC just communicate information about the diffusion in a voxel, where as anisotropy maps go one step further and communicate information about the orientation of the underlying structure of the fiber tracts in the brain.
- **Anisotropy RA (Relative Anisotropy)** — is similar to FA, but it is a slightly different calculation (like FA it uses the scalar values from the tensor eigenvectors, but never mind about that now). FA gives better detail.
- **Anisotropy VR (Volume Ratio)** — is another calculated measure of anisotropy. The SNR and detail of VR is lower than FA and RA. The one thing VR has going for it is that the

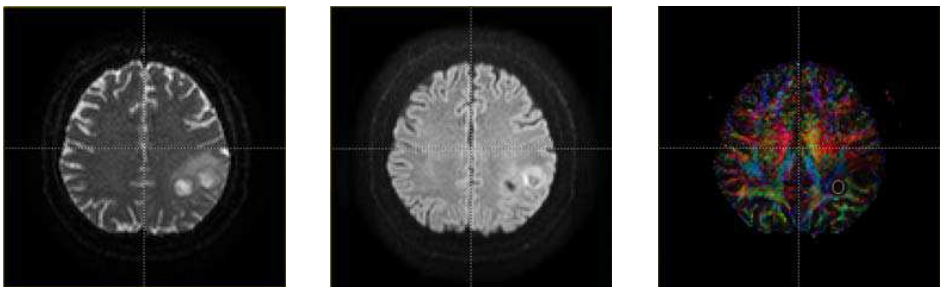

Figure 1: Transversal slices with 2D imaging of the brain with tumor; images from the left hand side: Mean of all B0s, Mean of all DWIs and Color Map.

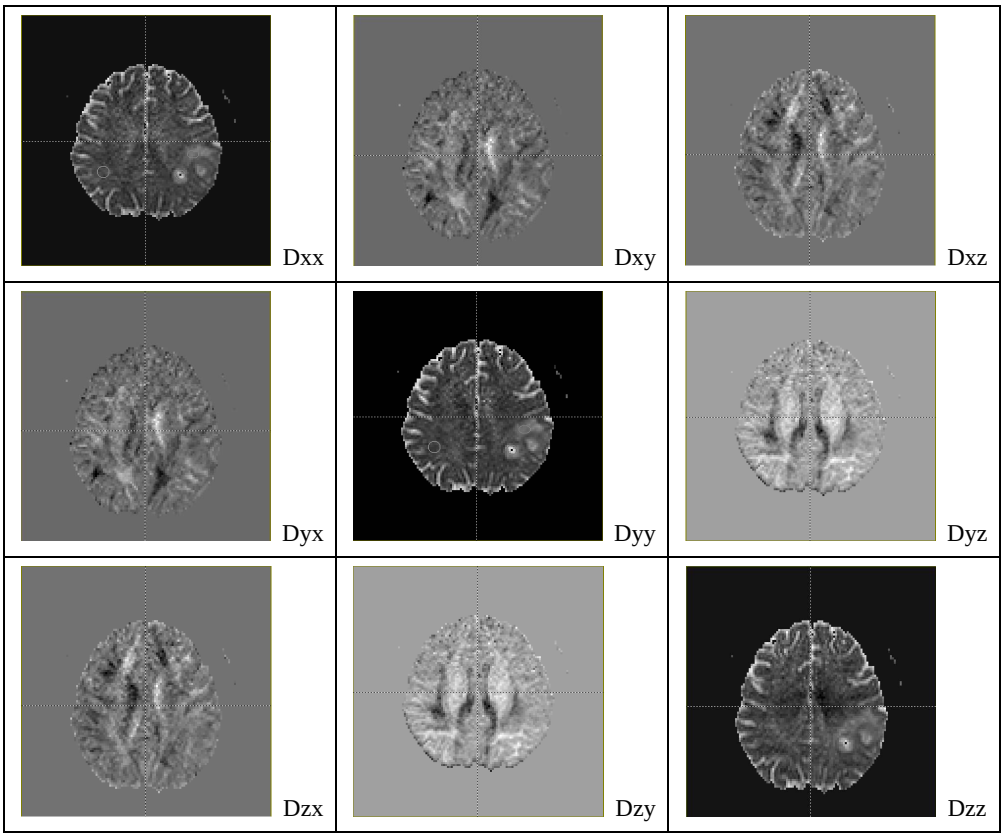

Figure 2: Tensor weighted images of the brain with tumor.

contrast between regions of low and high anisotropy is stronger than FA or RA.

- **K2** — represents the magnitude of anisotropy (by analogy to a polar cylindrical coordinate system $K2$ is the radial component and $K3$ is the azimuthal component)
- **K3** — represents the mode of anisotropy, is defined on interval $[-1, 1]$, where $K3 = 0$ indicates an orthotropic tensor, and $K3 = 1$ indicates a linear anisotropic tensor (one large diffusion tensor eigenvalue and two small eigenvalues).
- **R1** — a mutually orthogonal invariant set containing fractional anisotropy as a member. For symmetric, positive-definite tensor $R1$ is defined on the interval $[0, +\infty]$. $R1$ is a measure of tensor magnitude.

3. RESULTS

First we obtained 32 images of each slice. In a next step we processed these images and calculated different types od diffusion weighted images, as you can see in Figure 1–Figure 3. Figure 1 shows three measured images (Mean of all B0s, Mean of all DWIs and Color Map) of brain with tumor.

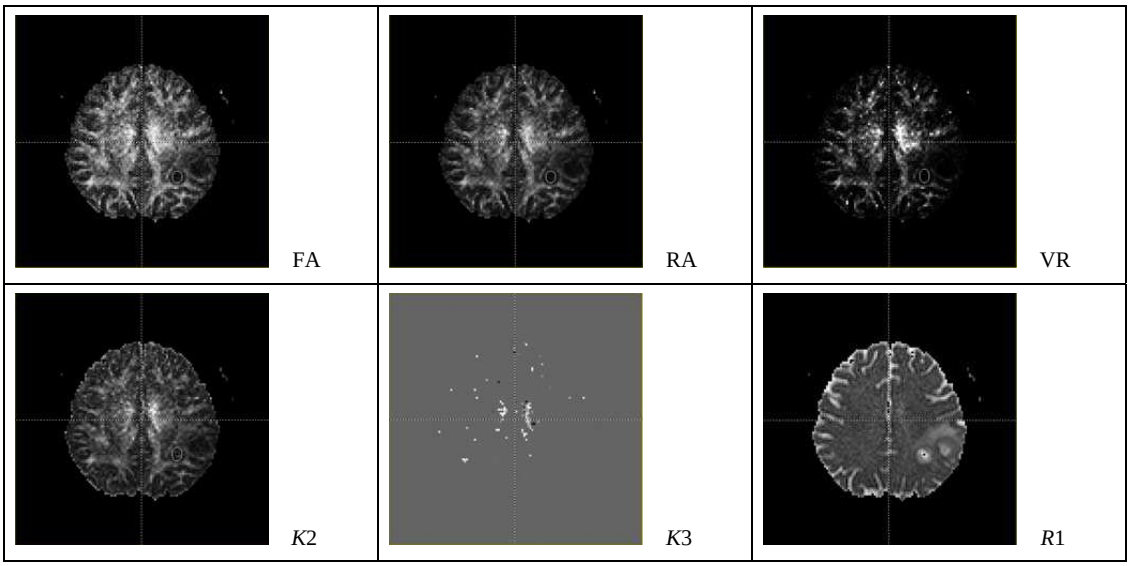

Figure 3: Images weighted of FA, RA, VR, $K2$, $K3$ and $R1$.

Table 1: The evaluate parameters from multi-contrast images.

Contrast	Tumor		Edem		Healthy tissue	
	Mean	s.d.	Mean	s.d.	Mean	s.d.
Mean DWIs	23.47	6.88	25.60	1.52	24.70	1.69
Mean B0s	**144.52**	**22.74**	**108.34**	**4.17**	**53.00**	**5.51**
Tenzor_Dxx	1.84e-003	5.88e-004	1.66e-003	1.31e-004	1.98e-004	8.81e-004
Tenzor_Dyy	1.75e-003	5.78e-004	1.44e-003	1.32e-004	8.32e-004	1.35e-004
Tenzor_Dzz	1.77e-003	5.30e-004	1.31e-003	1.10e-004	6.74e-004	2.13e-004
Tenzor_Dxz	1.11e-005	5.62e-005	8.57e-005	6.64e-005	−1.53e-005	8.68e-005
Tenzor_Dxy	−3.56e-005	6.98e-005	4.44e-006	1.07e-004	3.01e-005	1.10e-004
Tenzor_Dyz	−1.73e-005	5.36e-005	1.27e-005	6.28e-005	−5.10e-005	1.66e-004
Color Map	-	-	-	-	-	-
FA	0.09	0.04	0.17	0.05	0.36	0.10
RA	0.07	0.03	0.14	0.04	0.32	0.10
VR	9.90e-003	8.70e-003	0.03	0.02	0.16	0.11
$K2$	2.36e-004	1.11e-004	3.61e-004	1.14e-004	4.23e-004	1.08e-004
$K3$	2.36e-004	1.11e-004	3.61e-004	1.14e-004	4.23e-004	1.08e-004
R1	**3.11e-003**	**9.63e-004**	**2.57e-003**	**1.45e-004**	**1.45e-003**	**1.83e-004**

Figure 2 displays individual diffusion weighted images from which it is possible to calculate the diffusion tensor weighted image.

Figure 3 shows images weighted of Fractional Anisotropy — FA, Relative anisotropy — RA, Volume Ratio — VR, and $K2$, $K3$ and $R1$. The evaluated statistical parameters of measured and processed images are shown in Table 1.

4. CONCLUSIONS

This work is focused on the measurement of diffusion-weighted imaging (DWI), where the measurement sequence comprises a table with 32 vectors of the b-factor orientation. The goal is to perform signal processing in the measured diffusion-weighted images of brain tumors. We proposed a special algorithm for the processing of the DWI image signal. The next step in the procedure was the statistical evaluation of DWI images of healthy and diseased human tissues. We also calculated the brain white matter images, such as those of the fraction anisotropy, RA (relative anisotropy), and VR (volume ratio).

To the classification and segmentation of tissues are very interesting obtained data from MeanB0s and R1 weighted images. The values in Table 1 are very important for selection of segmentation methods such as thresholding, edge analysis by Sobel mask, watershed and very interesting method based on region-based level set approach or active contour [12]. The segmentation can play an important role in determining pathology in animal tissues even in human tissues.

ACKNOWLEDGMENT

This work was supported in part by the Grant GAČR 102/12/1104 and the programme FEKT-S-14-2545 and Education for Competitiveness Operative Programme CZ.1.07.2.3.00.20.0175 (Electro-researcher).

REFERENCES

1. Mikulka, J., E. Gescheidtova, and K. Bartusek, "Processing of MR slices of human liver for volumetry," *PIERS Proceedings*, 202–204, Xi'an, China, Mar. 22–26, 2010.
2. Wapler, M. C., J. Leupold, I. Dragonu, D. Elverfeld, M. Zaitsev, and U. Wallrabe, "Magnetic properties of materials for MR engineering, micro-MR and beyond," *Journal of Magnetic Resonance*, Vol. 242, 233–242, 2014.
3. Mikulka, J., E. Gescheidtova, and K. Bartusek, "Soft-tissues image processing: Comparison of traditional segmentation methods with 2D active contour methods," *Measurement Science Review*, Vol. 12, No. 4, 153–161, 2012.
4. Marcon, P., K. Bartusek, and M. Cap, "Multiparametric data collection and data processing of animal tissues in MRI images," *PIERS Proceedings*, 358–362, Moscow, Russia, Aug. 19–23, 2012.
5. Mori, S., *Introduction to Diffusion Tensor Imaging*, Elsevier, China, 2009.
6. Marcon, P. and K. Bartusek, "Errors in diffusion coefficients measurement," *PIERS Proceedings*, 1035–1039, Cambridge, USA, Jul. 5–8, 2010.
7. Andris, P. and I. Frollo, "Measurement of magnetic field with background using a low-field NMR scanner," *Measurement Science Technology*, Vol. 23, 2012.
8. Gogola, D., A. Krafcik, O. Strbak, and I. Frollo, "Magnetic resonance imaging of surgical implants made from weak magnetic materials," *Measurement Science Review*, Vol. 13, No. 4, 165–168, 2013.
9. Marcon, P., K. Bartusek, R. Korinek, and Z. Dokoupil, "Correction of artifacts in diffusion-weighted MR images," *34th International Conference on Telecommunications and Signal Processing (TSP)*, 391–397, Budapest, 2011.
10. Marcon, P., K. Bartusek, E. Gescheidtova, and Z. Dokoupil, "Diffusion MRI: Magnetic field inhomogeneities mitigation," *Measurement Science Review*, Vol. 12, No. 5, 205–212, 2012.
11. Marcon, P., K. Bartusek, M. Burdkova, and Z. Dokoupil, "Magnetic susceptibility measurement using 2D magnetic resonance imaging," *Measurement Science and Technology*, Vol. 22, 2001.
12. Tsai, J. Z., S. J. Peng, Y. W. Chen, K. W. Wang, H. K. Wu, Y. Y. Lin, Y. Y. Lee, C. J. Chen, H. J. Lin, E. E. Smith, P. S. Yeh, and Y. L. Hsin, "Automatic detection and quantification of acute cerebral infarct by fuzzy clustering and histographic characterization on diffusion weighted mr imaging and apparent diffusion coefficient map," *Hindawi: BioMed Research International*, 1–6, Vol. 2014, 2014.

Partial Discharge Detection and Localization System

M. Cap, P. Drexler, and P. Fiala
Department of Theoretical and Experimental Electrical Engineering
Brno University of Technology, Technicka 3082/12, Brno 616 00, Czech Republic

Abstract— This article describes the partial discharges (PD) detection and localization system. Localization can be performed on the basis of measured UHF waveforms analysis during activity of the partial discharges. The time-shifts of the waveforms related to transient process occurrence in the signals are the main input parameters for localization methods. In order to estimate the position of the signal source in the 3D space a minimum of four antennas has to be used, since the time of the PD is unknown. Analysis of the PD starts with visual investigation of the signals present inside of the power oil transformer. PD signal level is in comparison to other signals inside the transformer very low. Therefore, signal line contains, except amplifiers, also controlled attenuators to reach required trigger conditions. Detailed investigation of all signals inside transformer is provided in memory mode in which system store defined number of signals for offline diagnosis a localization. Continual and memory mode of the system also contain discrimination method for non PD signals removing. Discrimination method is based on simultaneous detection of the signal inside and outside of the transformer with aim to acquire only signal which comes from inside of the transformer. Localization of the PD origin is based on TDOA and matrix algorithm. Resulting position are visualized as point in transformer 2D and 3D scheme.

1. INTRODUCTION

Partial discharges (PD) in the high voltage transformer could cause risk of the transformer damage. Detection of the discharge presence is possible by several methods based on sound, electromagnetic signal measurement or gas chromatography. This work is focused on measurement and evaluation of the UHF (Ultra High Frequencies) electromagnetic signal. Partial discharge is detected as a signal in range from hundreds of megahertz to units of gigahertz. Propagation delay of the signal from the place of the PD to the each detector can be used for spatial localization of the PD. Goal of this work to design software for detection, analysis and localization of the partial discharges.

2. MEASUREMENT SYSTEM AND LOCALIZATION METHODS

2.1. Diagnostic System

PD signal is detected by the special measuring system. Whole system contains 4 specially designed sensing heads (Figs. 1, 2), central unit (Fig. 3) and software for PD analysis and localization. Sensing heads are mounted in to the front wall of the transformer. Heads are connected by triaxial cables for simultaneous RF signal transmission and DC powering. Signal preprocessing part of each head includes conical antenna, controllable attenuators, amplifiers, high pass filter and RF limiter. Data are acquired by Agilent data acquisition system which uses a four-channel, 10 bit high speed cPCI digitizer. Signal is preprocessed by sensing heads and digitalized with 2GSa sampling frequency. Because of strong electromagnetic interference, diagnostic system is mounted in a shielded

Figure 1: Sensing head.

Figure 2: Sensing heads mounted on the transformer.

Figure 3: Assembly of the diagnostic system in shielded box.

box. This two stage box contains all required powering, data acquisition and communication parts, Fig. 3.

2.2. Localization Methods

2.2.1. Time of Arrival

Method of the partial discharge location is based on the time differences of signal arrival (TDOA). Signal arrival time is determined from energy accumulation curve EAC given by equation [1, 2]:

$$w_i = \frac{t_s}{Z_0} \sum_{k=0}^{i} u_k^2, \quad k = 1 \ldots N \tag{1}$$

Selection of the signal arrival time could be done by two methods. Point could be marked as the time of signal arrival when energy accumulation curve or its first derivation reach threshold value. Method and threshold values for each channel are selected manually before localization algorithm starts. Precise detection of the signal arrival time is crucial point of signal spatial localization. Due to small dimensions of the transformer and short time of propagation cause small errors in arrival time detection big errors in spatial localization [3].

2.2.2. TDOA

Due to given antenna arrangement shown in Fig. 2 the localization results lies on circle which plane is perpendicular to the straight line join of antennas. Therefore, solution can be found only in 2D space as an intersection of the circle with relevant part of tested transformer. The initial equation system defines source position towards three antennas

$$x^2 + y^2 = v^2 t_0^2, \tag{2}$$

$$x^2 + (y - y_2)^2 = v^2 (t_0 + t_{12})^2, \tag{3}$$

$$x^2 + (y - y_3)^2 = v^2 (t_0 + t_{13})^2, \tag{4}$$

Solution of Equations (2)–(3) leads to definition solution for t_0, x, y as

$$t_0 = \frac{v^2 \left(y_2 t_{13}^2 - y_3 t_{12}^2\right) + y_3 y_2^2 - y_2 y_3^2}{2v^2 (y_3 t_{12} - y_2 t_{13})}, \tag{5}$$

$$y = \frac{y_2}{2} - \frac{v^2 \left(y_2 t_{13}^2 - y_3 t_{12}^2\right) + \left(y_3 y_2^2 - y_2 y_3^2\right)}{2y_2 (y_3 t_{12} - y_2 t_{13})} t_{12} - \frac{v^2 t_{12}^2}{2y_2}, \tag{6}$$

$$x = \sqrt{v^2 \left(\frac{v^2 \left(y_2 t_{13}^2 - y_3 t_{12}^2\right) + y_3 y_2^2 - y_2 y_3^2}{2v^2 (y_3 t_{12} - y_2 t_{13})}\right)^2 - \left(\frac{y_2}{2} - \frac{v^2 \left(y_2 t_{13}^2 - y_3 t_{12}^2\right) + \left(y_3 y_2^2 - y_2 y_3^2\right)}{2y_2 (y_3 t_{12} - y_2 t_{13})} t_{12} - \frac{v^2 t_{12}^2}{2y_2}\right)^2}. \tag{7}$$

Results of PD localization are calculated as a mean value from three partial solution obtained from different combination of channels.

2.2.3. Matrix Method

Due to high sensitivity of TDOA to precision of the signal arrival time determination is useful to use results accumulation. This method use matrix of propagation times from defined points in transformer to all sensing heads. Calculated time differences of signal propagation are compared to matrix values and points which are in tolerance interval are with defined neighborhood marked as a potential source of the signal. Each detected point increase value in $50 \times 50 \times 50$ cm cube around signal potential origin. Space surrounding the signal origin will increase its value after each detected signal. Localization results are defined as a points with value higher than 50% of maximal value.

3. PARTIAL DISCHARGE DIAGNOSTIC AND LOCALIZATION SOFTWARE

PD localization software application is designed as a multithread application. Basic function concept of this application is to split measurement and visualization into separate threads in order to achieve maximal possible computer performance for both application parts.

3.1. Acquisition Settings and Attenuators Control

3.1.1. Settings

Basic acqusition setting is shown in Fig. 5. These parameter are setted up with regard to signal parameters. Possibillity of changing of acqusition parameters is crucial especially in case of first examination of signals in continual aqusition mode.

3.1.2. Attenuators

Controable attenuators regulate transmition path output power. Attenuator attenuation depend on controll voltage which is set by usb controlled hardware in range 3–40 dB, see Fig. 4.

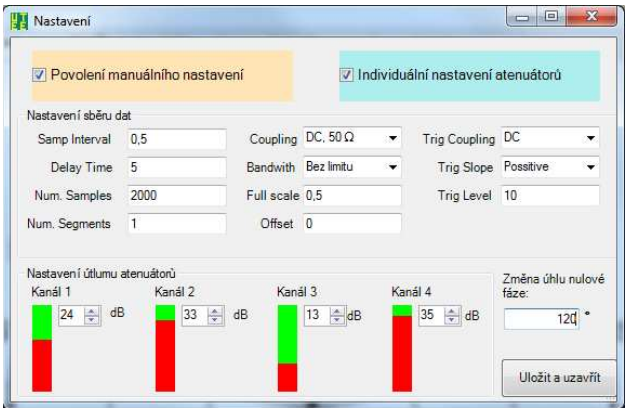

Figure 4: Settings.

3.1.3. Trigger

Detection of the partial discharge is provided on all digitizer channels. Detected signal energy depends on the place of origin of the PD. If the PD will occur on the left or right side of the transformer winding the energy of detected signal will be biggest on the first or fourth channel. Therefore, trigger input is configured as a multichannel trigger so the trigger input is used all four input channels.

3.2. Application Modes

3.2.1. Continual and Memory Mode

Diagnostic of partial discharge could be split into the two modes. Firs mode works in loop in order to acquire and visualize data continuously. This mode is to a certain extent similar to the basic function of the traditional oscilloscope. Second mode could be described as "acquire and wait". In this case program will acquire 300 of data packets and stops acquisition. Both modes use two types of acquired signal visualization, phase chart and time graphs of all four channels which shows position of the acquired data to the zero supply voltage point, Fig. 5. Chart uses two values, first is angle 0°–360° calculated as the position of data to the time of the supply voltage zero time, Fig. 6. Actual angle need to be additionally corrected with power and transformer angle difference. Second parameter is mean value calculated from maximal voltage values in all channels [4, 5].

3.2.2. Calibration Mode

Determination of the system hardware and software correct functionality is provided by detection of signal injected into the third sensing head space. Calibration could be done with or without synchronization of the signal source and digitizer trigger. In case of synchronous trigger is the signal source and digitizer triggered at the same time. Therefore, only injected signal is measured [6, 7].

3.2.3. Interference Signal Discrimination

Detection of presence of the partial discharge is because of strong interference relatively difficult. Huge amount of signals is getting into transformer thru high and low voltage bushing. Moreover, interference signals are in its principle of creation similar to the partial discharges. Difference between the interference signal and partial discharges is in propagation distance. Resulting interference signal have longer duration time and narrower bandwidth [8]. One of the key part of this work is to detect partial discharges and suppress number of detections of the interference signals.

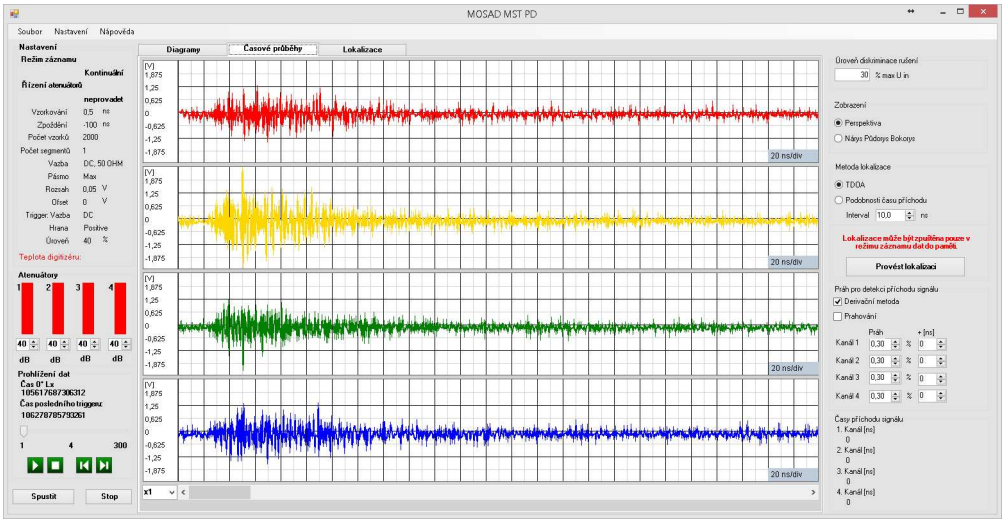

Figure 5: Visualization of the signal in time domain.

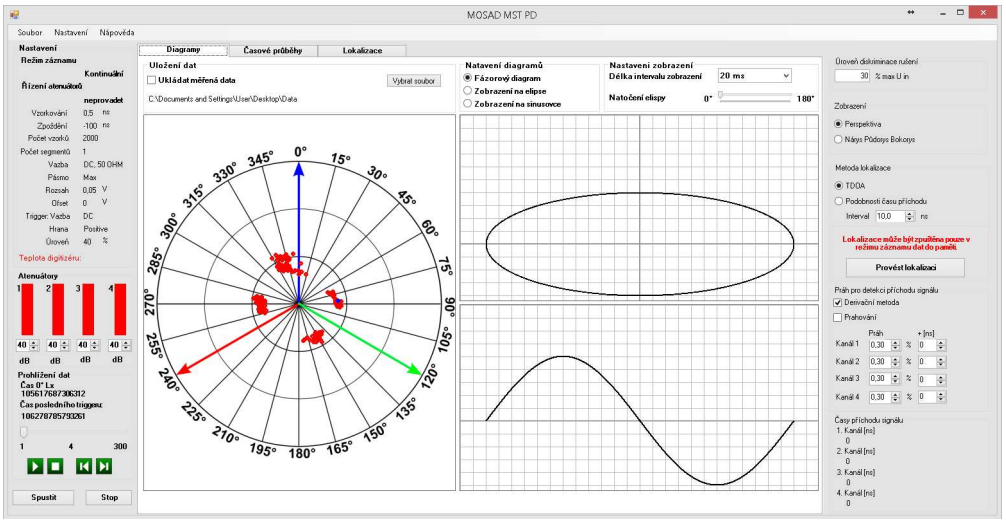

Figure 6: Main window with phase chart.

Assuming that the origin of the interference signal is outside of the transformer itself we can use external sensing head for detection of the interference presence outside of the transformer. In case of interference we can say that signal will be present inside and outside of the transformer. In case of partial discharge the signal will be present only inside of the transformer. Discrimination criteria is the amplitude on the third channel which is used for external antenna. If the signal in third channel exceed defined threshold (defined as % from other channels signal maximum) is signal marked as an interference and deleted. Interference discrimination is available for continual and memory mode.

3.3. Partial Discharge Location

Partial discharge location uses TDOA and matrix method. Localization is because of large amount of processed data in online mode available only in memory mode. Use of four antennas allows us to locate position of partial discharge in three dimensions. Unfortunately, transformers in nuclear power plant Dukovany has all antenna plug-in points placed on the front side in line (see Fig. 2). Hence, results of the localization lies on the circle with center on sensing head line and with diameter calculated from localization algorithm.

Signal origin is from TDOA and matrix algorithm visualized in perspective and front, side and top view of the transformer. In case of TDOA is signal visualized as a circle, for matrix method are used points with 10 cm distance. Localization of the signal source mounted in third sensing head space is shown in Fig. 7.

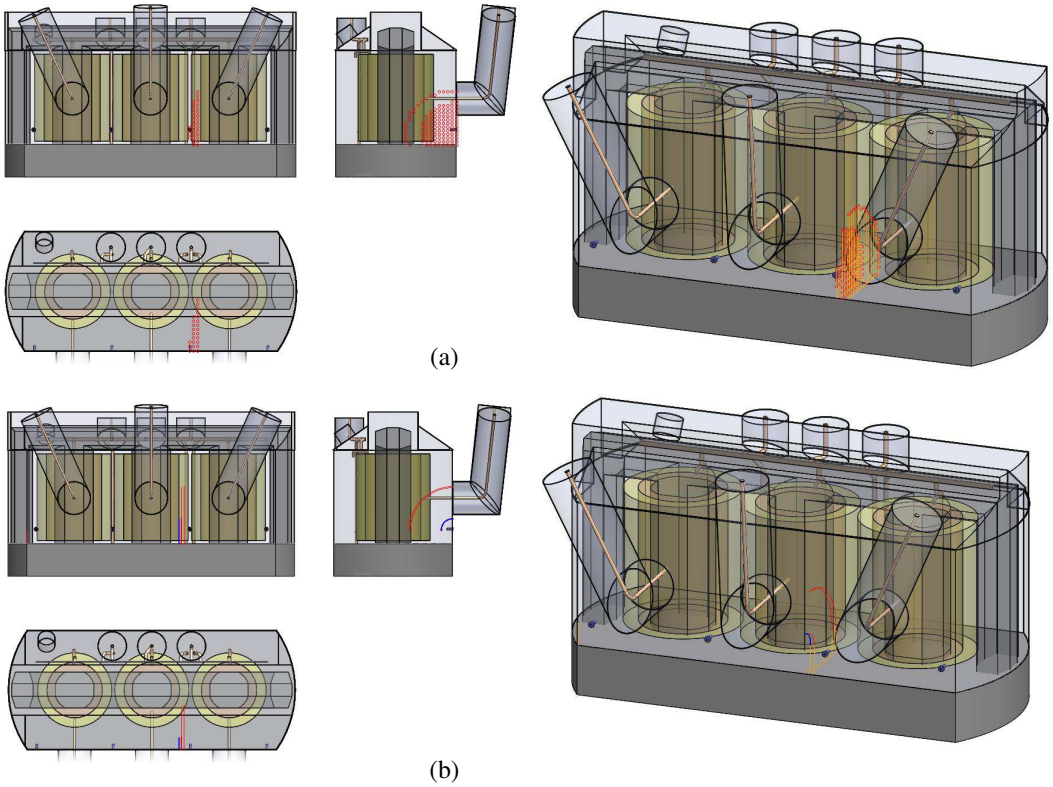

Figure 7: Injected signal localization results of (a) Matrix and (b) TDOA algorithm.

4. CONCLUSION

Basics of the partial discharge detection is analysis of the signal shape and its time position in supply voltage waveform. For correct localization is necessary to process large amount of signals. Setting of the variable attenuators and trigger conditions allows with interference signal discrimination reduction the amount of interference signals. If mentioned settings reduce number of detected interference signal then the special localization of the signal origin will give us more accurate results. Other factor affecting accuracy of the spatial localization are signal to noise ratio and signal shape itself. In case of low SNR and long propagation length will be difficult to correctly detect the signal arrival time and calculate position of the signal origin.

ACKNOWLEDGMENT

The research described in the paper was financially by project of the BUT science fund, No. FEKT-S-14-2545/2014, and a project from the Education for Competitiveness Operative Programme, No. CZ.1.07.2.3.00.20.0175 (Electro-researcher).

REFERENCES

1. Fiala, P., T. Jirku, P. Drexler, and P. Dohnal, "Detection of partial discharge inside of HV transformer, modeling, sensors and measurement," *PIERS Proceedings*, 1013–1016, Cambridge, USA, July 5–8, 2010.
2. Myška, R. and P. Drexler, "Simulation and verification of methods for partial discharge source localization," *PIERS Proceedings*, 704–708, Kuala Lumpur, Malaysia, March 27–30, 2012.
3. Dalarsson, M. and M. Norgren, "First-order perturbation approach to elliptic winding deformations," *Proceedings of International Symposium on Electromagnetic Theory*, 13–16, Hiroshima, Japan, 2013.
4. Dalarsson, M., A. Motevasselian, and M. Norgren, "Using multiple modes to reconstruct conductor locations in a cylindrical model of a power transformer winding," *International Journal of Applied Electromagnetics and Mechanics,* Vol. 41, No. 3, 279–291, 2013.
5. Fiala, P., "Pulse-powered virtual cathode oscillator," *IEEE Trans. Dielectr. Electr. Insul.*, Vol. 18, No. 4, 1046–1053, 2011.

6. Szabo, Z., J. Sedlacek, and M. Hadinec, "Optimization method of EMI power filters and its measurement," *PIERS Proceedings*, 1085–1088, Hangzhou, China, March 24–28, 2008.
7. Marcon, P., P. Fiala, M. Steinbauer, and M. Cap, "Special high voltage function generator," *PIERS Proceedings*, 1000–1003, Suzhou, China, September 12–16, 2011.
8. Szabo, Z. and P. Fiala, "Characterisation and testing shielding fabrics," *PIERS Proceedings*, 1273–1276, Moscow, Russia, August 18–21, 2009.

Numerical Model of a Large Periodic Structure

R. Urban, P. Drexler, P. Fiala, and D. Nešpor
FEEC, BUT, UTEE, Technická 12, Brno 616 00, Czech Republic

Abstract— The aim of this paper is to present the particulars of new research in special numerical models of structures used for nanoapplications. These models can be advantageously used in the evaluation of electromagnetic parameters, thus helping researchers and designers to solve problems related to nanoelements and nanotechnology. The first numerical model of large periodic structure is designed to test electromagnetic wave propagation in a graphene composite structure. According to the interpretation of the results, the basic design will be prepared for experimental fabrication of the functional sample.

1. INTRODUCTION

It is obvious from the research presented in papers [1, 3] that the periodic structure of graphene should exhibit certain interesting electrical and electromagnetic properties regarding the propagation of an electromagnetic wave. Thus, new horizons could be opened for the use of graphene in electrical engineering (EMG) and electronics. The referenced articles nevertheless do not provide a clear conclusion that would facilitate prospective application of periodic structures with extreme properties in the field of electromagnetic wave propagation; these structures can be based on either natural or artificial materials.

The authors of this paper have developed the idea to set up a simple numerical model and to propose an experiment suitable for the related verification. Fig. 1 shows the known concepts of carbon nanostructures [2, 3] and layered polymer. The numerical model enables us to evaluate the propagation of an electromagnetic wave along the surface consisting of a periodic structure (such as graphene or metamaterial) and the surrounding dielectric environment The aim of the model is to evaluate the components of both the EMG wave and the power flux density in the time domain; thus, based on our knowledge of today's manufacturing technologies, it would be easily possible to define the applicability of the periodic structure for specific purposes in electrical engineering and electronics. Examples of periodic structure arrangements can be found in several studies, for instance in the referenced paper [2], Fig. 2.

The proposed analysis has to be based on a specific numerical model; this model should respect the character of the Telegrapher‘s equations as well as the multiplicity of the repeating periodic structure element.

2. MODEL OF A PERIODIC STRUCTURE

The geometrical model designed to provide a simple comparison between classic materials and those based on a periodic structure with a large number of repeated elements could be identified with the body shown in Fig. 3. The presented drawing shows the concept of a macroscopic approach to the model combined with a quantum-mechanical model, both of which are described by concentric

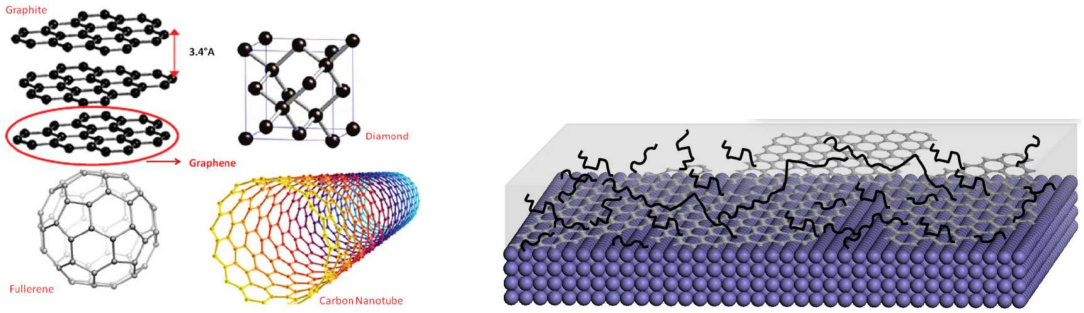

(a) (b)

Figure 1: Structures of carbon nanomaterials [2, 3]: (a) known arrangement of carbon structures; (b) graphene-polymer composite.

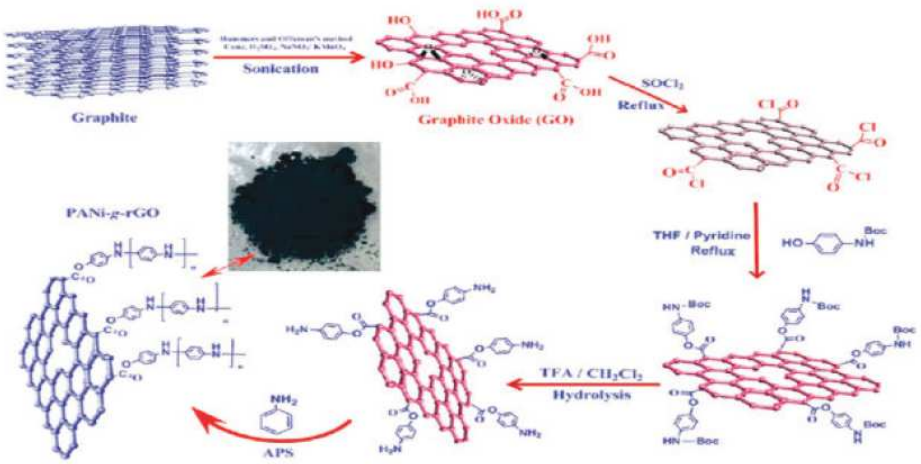

Figure 2: Formation of a special graphene-polymer structure (composite) [2].

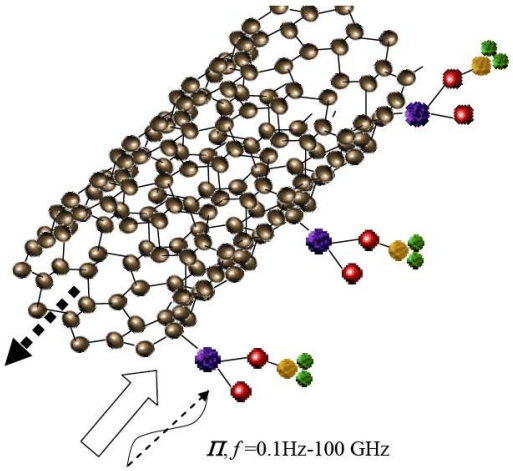

Figure 3: Geometrical structure of the numerical analysis of surface wave propagation.

particles. In a radial coordinate, the model will assume dimensions in the order of nanometers, and in the longitudinal axis the dimensions will be more than several tens of millimeters.

For any case of analysis of transient processes in the conditions of quantum physics particle position shift, the model according to formula (1) is suitable for the description of transient processes of dynamically assumed particles. The model with a higher order of the time variation of functional u, namely the model described by the Telegrapher's equation, is expressed in the form

$$\Delta u = C_{t0}\frac{\partial^2 u}{\partial t^2} + C_{t1}\frac{\partial u}{\partial t} + C_{t2}u + C_{t3} \tag{1}$$

This model represents precisely the dynamics of the system of moving particles, and the simplified form of the model is the well-known wave equation in the form

$$\Delta u = C_{w0}\frac{\partial^2 u}{\partial t^2} \tag{2}$$

The above-described hypothesis based on formula (1) and coupled with relation (2) offers an easier solution — albeit of a more complicated model — using the numerical apparatus. The solution consists in a periodic damped wave written generally as

$$u = C_{tv1}e^{F(t)}e^{F(\Omega)} \tag{3}$$

where Ω is the space for which relation (1) was formulated. As a result of the proposed model, there occurs a shift in the field of quantum physics. Based on relations (1) and (2), it is possible to assume that the elementary phenomenon of the quantum physics solution is an electromagnetic wave. A particle (plasmon), according to the hitherto used quantum physics hypothesis, is the result of the waves' interference effect. It is assumed that the basic elements of matter are an electric charge and its motion. The fundamentals of this hypothesis have been already described in papers and reports [5, 7], proposing that

$$\rho_e^2 = \rho_g \tag{4}$$

where ρ_e is the electric charge volume density and ρ_g is the volume density of matter.

The model (1), (2) enables us, using the well-known numerical methods, to simulate the behaviour of the individual basic types and geometries of elements of nanomaterial and periodic structures.

The proposed numerical model is based on the formulation of partial differential equations for the electromagnetic field, known as reduced Maxwell's equations; according to Heaviside's notation, we have the following formula for the magnetic field strengths and flux densities:

$$\mathrm{rot}\mathbf{E} = -\frac{\partial \mathbf{B}}{\partial t} + \mathrm{rot}\left(\mathbf{v} \times \mathbf{B}\right), \quad \mathrm{rot}\mathbf{H} = \mathbf{J}_T + \frac{\partial \mathbf{D}}{\partial t} + \mathrm{rot}\left(\mathbf{v} \times \mathbf{D}\right) \tag{5}$$

$$\mathrm{div}\,\mathbf{B} = 0, \quad \mathrm{div}\,\mathbf{D} = \rho, \tag{6}$$

where $\mathbf{H}$ is the magnetic field strength, $\mathbf{B}$ is the magnetic field flux density, $\mathbf{J}_T$ is the total current density, $\mathbf{D}$ is the electric field displacement, $\mathbf{v}$ is the instantaneous velocity of the moving element. Respecting the continuity equation

$$\mathrm{div}\,\mathbf{J}_T = -\frac{\partial \rho}{\partial t}, \tag{7}$$

the vector functions are expressed by means of the scalar electric potential ϕ_e and the vector magnetic potential $\mathbf{A}$, and, after Coulomb calibration [8], the relationship between the quantities is expressed as

$$\mathbf{E} = -\mathrm{grad}\phi_\mathrm{e} - \frac{\partial \mathbf{A}}{\partial t}, \tag{8}$$

$$\mathbf{B} = r\mathrm{ot}\mathbf{A}. \tag{9}$$

Considering the velocity of moving electrically charged particles $\mathbf{v}$ in the magnetic field, the total current density $\mathbf{J}_T$ from formula (5) is

$$\mathbf{J}_T = \gamma\left(\mathbf{E} + \mathbf{v} \times \mathbf{B}\right) - \frac{\partial\left(\varepsilon \mathbf{E}\right)}{\partial t} + \frac{\gamma}{q}\left(\frac{m\mathrm{d}\mathbf{v}}{\mathrm{d}t} + l\mathbf{v} + k\int_t \mathbf{v}\mathrm{d}t\right), \tag{10}$$

where m is the particle mass, considering the formula

$$m = m_0\left(1 - \frac{v^2}{c^2}\right)^{-\frac{1}{2}}, \tag{11}$$

where m_0 is the quiescent mass of the particle, q is the electric charge of the moving particle, γ is the specific conductivity of the environment from the macroscopic perspective, l is the damping coefficient, k is the stiffness coefficient of the surrounding environment. The material electromagnetic relations for the macroscopic part of the model are represented by the terms of symbolically isotropic properties

$$\mathbf{B} = \mu_0\mu_r\mathbf{H}, \quad \mathbf{D} = \varepsilon_0\varepsilon_r\mathbf{E}, \tag{12}$$

where the quantity indexes of the permeabilities and permittivities r denote the relative quantity value and 0 denotes the value of the quantity for vacuum. The relationship between the macroscopic and the microscopic parts of the model (particle dynamics in the electromagnetic field) is described by the formulas defining the force acting on individual electrically charged particles of

the electromagnetic field in their gravity centre, and the effect is considered of the motion of the electrically charged particles on the surrounding electromagnetic field:

$$m\frac{\mathrm{d}\mathbf{v}}{\mathrm{d}t} + l\mathbf{v} + k\int_t \mathbf{v}\mathrm{d}t = q\ (\mathbf{E} + \mathbf{v}\times\mathbf{B}) - \frac{q}{\gamma}\frac{\partial\left(\varepsilon\mathbf{E}\right)}{\partial t}. \tag{13}$$

The relationship between the macroscopic model of the geometrical part of the electromagnetic field and the quantum-mechanical model of bound particles is expressed via the application of current density (10) and by the formula (5) as follows:

$$\mathrm{rot}\mathbf{H} = \gamma(\mathbf{E} + \mathbf{v}\times\mathbf{B}) - \frac{\partial(\varepsilon\mathbf{E})}{\partial t} + \frac{\gamma}{q}\left(\frac{m_0\left(1-\frac{v^2}{c^2}\right)^{-\frac{1}{2}}\mathrm{d}\mathbf{v}}{\mathrm{d}t} + l\mathbf{v} + k\int_t \mathbf{v}\mathrm{d}t\right) + \frac{\partial\mathbf{D}}{\partial t} + \mathrm{rot}\left(\mathbf{v}\times\mathbf{D}\right). \tag{14}$$

With respect to the fact that the model comprises not only the electric and the magnetic components of the electromagnetic wave but also the space of the motion of the electrically charged particles, including the action of interacting forces, it is necessary to solve the model as a designed system (1) characterised by the Telegrapher's equations.

By applying the Galerkin method to find the functional minimum (as described in, for example, reference [9]) and considering the boundary conditions, we obtain the numerical model as a system of non-linear equations to be solved by standard methods. The model is designed for the ANSYS software, where the solution is carried out with finite numerical methods [10].

3. THE STRUCTURE MODEL

As indicated above, the basic model is built in a system based on the finite element method, namely the ANSYS tool, and enables us to find the geometry and parameters of the target structure with respect to its chemical survivability. The elementary structure according to Fig. 2 was chosen and solved as the basis of the numerical model according to formula (14).

The geometry of a large system incompatible both in its dimensions and the number of included elements is solved with the known condition of periodicity and also as a partially stochastic model Certain problems occur in modelling the bond between the polymer and the graphene basis. The mathematical-numerical model consists of basic elements characterising the ANSYS software, namely HF119, HF120 and others, and it is complemented with the proper code of the model according to formula (14). Currently, the model solution process is at the stage of tuning and the related verification of the gradually obtained analytical result is being performed Considering the robustness of the model, it is necessary to point out that the making and analysis of the model are time-intensive activities.

ACKNOWLEDGMENT

The research described in the paper was financially supported by research plan project of the BUT Grant Agency, No. FEKT-S-14-2545/2014 an GACR 13-09086S supervised by Czech Science Foundation. It was supported by the project CZ.1.07/2.3.00/30.0005 of Brno University of Technology.

4. CONCLUSION

We designed the numerical model of a large periodic structure to analyse the propagation of an electromagnetic wave in such a structure. The model is currently under testing, and analyses of the results are being carried out. Simultaneously, we are designing an experiment to verify and compare the results obtained via examination of the model.

REFERENCES

1. Castro Neto, A. H., F. Guinea, K. S. Novoselov, and A. K. Geim, "The electronic properties of graphene," *Reviews of Modern Physics*, Vol. 81, The American Physical Society, January–March 2009.
2. Yan, C., K.-S. Kim, S.-K. Lee, S.-H. Bae, B. H. Hong, J.-H. Kim, H.-J. Lee, and J.-H. Ahn, "Mechanical and environmental stability of polymer thin-film-coated graphene," *ACS NANO*, Vol. 6., No. 3, 2096–2103, 2012.

3. Singh, K., A. Ohlan, and S. K. Dhawan, "Polymer-graphene nanocomposites: Preparation, characterization, properties, and applications," INTECH, ©, 2012, http://dx.doi.org/10.5772/50408.
4. Lincoln Vogel, F., "The electrical conductivity of graphite intercalated with superacid fluorides: Experiments with antimony pentafluoride," *Journal of Materials Science*, Vol. 12, No. 5, 982–986, 1997.
5. Van Vlaenderen, K. J. and A. Waser, "Electrodynamics with the scalar field," *Physics*, Vol. 2, 1–13, 2001.
6. Kikuchir, H., *Electrohydrodynamics in Dusty and Dirty Plasmas, Gravito-electrodynamics and EHD,* Kluwer Academic Publishers, Dordrecht/Boston/London, 2001.
7. Van Vlaenderen, K. J., "A charge space as the orogin of sources, fields and potentials," *Physics*, 1–13, October 1999, arXiv:physics/9910022 v1 16.
8. Stratton, J. A., *Teorie Elektromagnetického Pole*, 51–60, Czech Republic, SNTL, Praha, 1985.
9. Fiala, P., "Modeling and design of pulsed power generator," Habilitation Thesis, No. 13, VUT FEKT, Brno, Czech Republic, August 2005, ISBN 80-214-1346-8.
10. www.ansys.com.

Optimization of the Particle Swarm Algorithm

J. Chytil
Department of Theoretical and Experimental Electrical Engineering
Brno University of Technology, Technicka 12, Brno 616 00, Czech Republic

Abstract— Particle Swarm Optimization is a swarm intelligence based and stochastic algorithm to solve the optimization problem. This paper presents the Multidimensional Particle Swarm algorithm with non-equidistant discrete input data such as E-Series or Renard numbers for circuit design. The authors describe the optimization of this method for different circuit designs, agent recycling, and omission of already computed points. The problem of omission of already computed points is to determinate when it is faster to omit the points than compute them. The personal omission history can be used for agent recycling or trajectory corrections. There is also described effect of recycled agents with corrected parameters on the convergence of optimalization. Parameters corrections are based on the principles of genetic algorithms in the other words inheritance from the best rated agents. System of agents rating is described briefly.

1. INTRODUCTION

This paper presents problems related to the need of implementing the method of Particle Swarm Optimization in purpose-built software for circuit design. A substantial portion of circuit components can be computed using analytic equations. The results, however, are only rarely accurate within E-Series values [1]. The algorithm based on Particle Swarm Optimization (also referred to as PSO) should choose the best design out of the set of E-series components, considering their tolerance. Another aspect to be assessed by the algorithm consists in the results of multicriterial circuit evaluation. With respect to the implementation of Particle Swarm Optimization [2, 3], substantial effort has been made to accelerate this method to the highest posssible degree.

2. THE PROBLEM OF OMISSION OF ALREADY COMPUTED POINTS

The very first way to make PSO faster is right decision when is faster to compute already computed value of the function or when is better to omit the computing. That problem can be resolved by programmer or can be set by selfevaluating methode. Self evaluating methode used measurement of function computing timeconsumtion and compare it with timeconsumption of omitting algorythm. The selfevaluating algorythm is hard to set and it is depended on a lot of parameters like agent count, maximum runs and last but not least on the shape of function. And it also afected by size of space.

Limiting size of space is on of most importat thing to do for speed up PSO alogorythm. The first borders have to be based on physical properties. For example and for simlicity: If we are going to design resistor consist of two serial connected resistors we definitely know that the each of resistors must have lower or equal resistance like searched resistor.

Empiricaly was shown that there is better to compute the function rather then trying to omit the computing if there are an analitical equations. And counter it, there is prefered trying to omit the computing if there is simulation necessary to obtain value of the criterial function. And there is still the selfevaluating algorythm that can be used.

This algorythm measure the time of computing criterial function for each agent and compare this time with measured time of looking for possibility of duplical computing in pregenerated artifical set of used position. And considering the results the method will be choosen.

3. OCCASION OF AGENT TERMINATING OR RECYCLING

The only reason to terminate an agent or his recyclation is that this agent haven't got the benefits for algorythm. The benefits of agent is assessed by evaluating function. An example of evaluated properties and it's score or penalization are in Table 3.

If the agent evaluating function is determined. It is necessary to determine decision function which decide which agent will be terminated or recycled.

This task can by resolved by triggering level. In the other words if the evaluation function of Agent goes under the triggering level the Agent will be recycled or terminated. Or it can by resolved by probabilities of termination or recyclation. So the agent with lower value of evaluation function has got greater probability of termination or recyclation.

Table 1: Example of evaluated properties and its score or penalization.

Evaluated property	**score**
Found global best result	+100
Found personal best result	+20
Occurance on already computed point	−15
Criterial function Order of magnitude higher	−10 per order of magnitude
No benefit for algorythm	−5per run
Stayed in global best	−50 each run
Occurance on already computed points near global best	−25

Table 2: Example of agent setting.

Agent's property	**value**
Own speed	0.82
Global best attraction	0.3
Personal best attraction	0.15
Group best attraction	0.23
Randomize of Global best attraction Standard deviation	0.3
Randomize of Personal best attraction Standard deviation	0.3
Randomize of Own speed Standard deviation	0.3
Probability of affecting by random speed	0.05
Velocity increase based on high value of criterial function	0.1

There is demand to preset agent new score after recyclation. Is not wise to set it on constant value. The better way is used average or median score value of agent's population.

4. WAYS OF AGENT'S RECYCLING

There are countless ways of agent's recycling and here is only small enumeration out of it's general principles.

1. New position and speed
   - Simple generation of new random position or speed or both
   - Pre-computed new speed and position
2. New agent's setting
   - The same as all of agnets
   - New random
   - Inherited from the best agents (better Agent has got greater probability of refering of his setting)
   - Inheritance based on genetic algorithm
3. Agent's acquired information (for example personal best position and value)
   - Forgetting of all the informations
   - Forgetting of selected informations
   - Modifying of chosen informations
   - Keep all the information
4. Agent's shared values (for example global best position and value)
   - Unchanged system (values all shared with each of all agents)

- Shared between agent generations
- Exponential moving average

The tested methods are all based on simple generation of new random position and speed, forgetting of all personaly acquired informations and global values shared over all of the Agents. So the only instrument which is varied is modifying of agent's setting. The method of bare recyclation (the same setting as all of Agnets), random generation of setting, the method of inheritance from the best Agents and also the methods based on genetic algorithms will be compared with methods without recyclation.

5. NEW AGENT'S SETTING BASED ON PROBABILITY AND GENETIC ALGORITHM

The method used to obtain new Agent's setting based on probability is quite easy to implement. The Agent will be choosen to refer it's setting to the new Agent with certain probability. This probability is determined by the score of Agents (obtained by evalution function). The Agents with better score have greater probability of to be choosen.

Modified method of obtaining new Agent's setting is based on Genetic algorythm (search heuristic that mimics the process of natural selection). During each successive generation, a proportion of the existing population is selected to breed a new generation [4, 5]. The new parameters are obtain by some of Crossover techniques from two or more parents.

There are used method called Three parent crossover. But it can be easily replaced by another genetic algorithm.

6. METHODIC AND RESULTS OF TESTING

For testing were used four corrected functions for testing of multidimesional optimalization methods in E-Serie's space. There are used Sphere function, Rosenbrock function, Styblinski Tang function and Rastrigin function. Futher can be used Shekel function.

Sphere function and it's minimun

$$f(x) = \sum_{i=1}^{n} x_i^2, f(x_1, \ldots, x_n) = f(0, \ldots, 0) = 0 \tag{1}$$

Rosenbrock function and it's minimun

$$f(x) = \sum_{i=1}^{n-1} 100(x_{i+1} - x_i^2)^2 + (x_i - 1)^2, f(x_1, \ldots, x_n) = f(1, \ldots, 1) = 0 \tag{2}$$

Rastrigin function and it's minimun

$$f(x) = An + \sum_{i=1}^{n} (x_i^2 - Acos(2\pi_i)), f(x_1, \ldots, x_n) = f(0, \ldots, 0) = 0 \tag{3}$$

Styblinski Tang function and it's minimun

$$f(x) = \frac{\sum_{i=1}^{n} x_i^4 - 16x_i^2 + x_i}{2}, f(x_1, \ldots, x_n) = f(-2.903534, \ldots, -2.903534) = -39.16599n \tag{4}$$

Shekel function and it's minimun

$$f(x) = \sum_{i=1}^{m} \frac{1}{c_i + \sum_{j=1}^{n} (x_j - a_{ij})^2}, \quad \textit{given by matrix } A \tag{5}$$

Functions are corrected for usage with E-Series components. Working area is limited by 6 decades of E-Series. And every optimalization process run ten-thousand times for obtain the average duration.

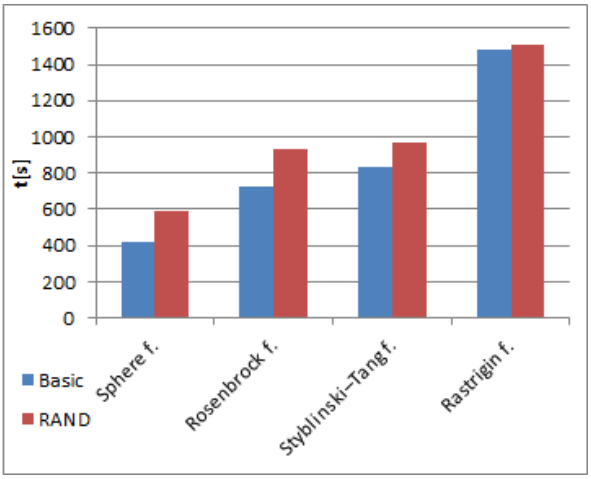

Figure 1: Comparison of the basic PSO and PSO with random setting of recycled Agents.

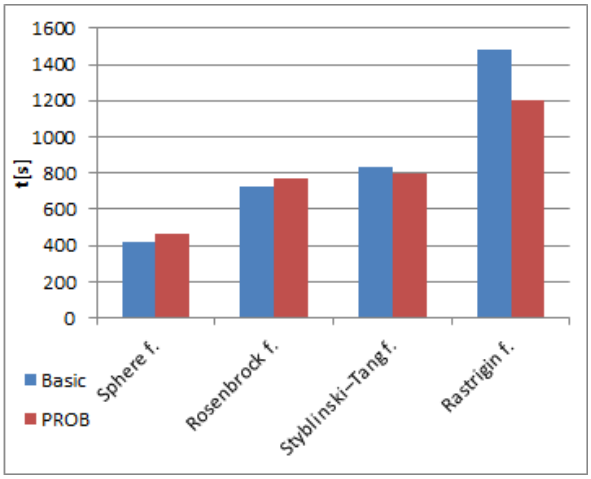

Figure 2: Comparison of the basic PSO and PSO with setting of recycled Agents generated considering probability.

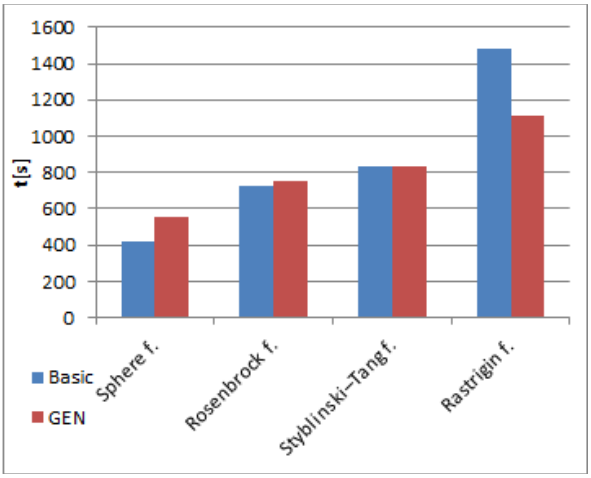

Figure 3: Comparison of the basic PSO and PSO with new Agents setting based on genetic algorith.

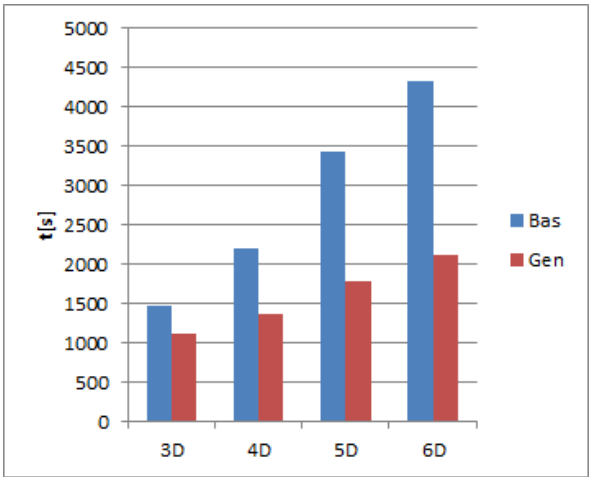

Figure 4: Ilustration of benefits of recyclation Agents with setting inheritance based on genetic algorith versus dimensions.

7. CONCLUSION

Generally, applicable results for the PSO are difficult to obtain because of a large number of the degrees of freedom (the number of Agents, number of dimensions, the Agent setting which cannot be modified by the pre-set function, and other aspects). In the given context, it is also important to point out the lack of test functions for multidimensional optimization in comparison with the count of such functions for one or two dimensions. Although the acquired results are not accurate, they show certain regularities in the behaviour of different settings of the PSO.

It is clear that a correctly set PSO without recycling surpasses PSOs with recycling in case of simple functions, such as the sphere or Rosenbrock ones. However, the more complex - for example, Rastrigin - functions were solved faster by the algorithm with recyclation.

By further extension, we can also point to the fact that, when used with the more complicated functions (the Rastrigin function), the genetic algorithm provides significant benefit; this aspect becomes even more obvious with increasing dimension of the solved function. This state occurs because the genetic algorithm needs enough iterations of the PSO to express itself.

8. GLOSSARY OF TERMS

Agents generation — group of agent with the same generation number of agent's recyclation).

Agents goupe — group of agent whom sharing some parameters or values.

ACKNOWLEDGMENT

The research described in the paper was financially supported by a grant of the BUT science fund, no. FEKT-S-11-5/1012, and the authors also received assistance from projects within the Education for Competitiveness Operative Programme, nos. CZ.1.07.2.3.00.20.0175.

REFERENCES

1. Ibrahim, I., Z. M. Yusof, S. W. Nawawi, M. A. A. Rahim, K. Khalil, H. Ahmad, and Z. Ibrahim, "A novel multi-state particle swarm optimization for discrete combinatorial optimization problems," *Computational Intelligence, Modelling and Simulation*, 18–23, 2012.
2. Zhang, H. and H. Qing, "Hybrid multiagent swarm optimization: Algorithms, evaluation, and application," *Decision and Control*, 5699–5704, 2012.
3. Anantathanavit, M. and M. A. Munlin, "Radius particle swarm optimization," *Computer Science and Engineering Conference*, 126–130, 2013.
4. Pratiwi, L., Y.-H. Choo, N. A. Muda, and A. K. Muda, "Improving ant swarm optimization with embedded vaccination for optimum reducts generation," *Hybrid Intelligent Systems*, 448–454 2011.
5. Wu, X., "A density adjustment based particle swarm optimization learning algorithm for neural network design," *Electrical and Control Engineering*, 2829–2832, 2011.

Sensitivity Improvement in NQR Based Detection Methods

M. Steinbauer, J. Segiňák, and P. Dohnal
Department of Theoretical and Experimental Electrical Engineering
Brno University of Technology, Technická 12, Brno 616 00, Czech Republic

Abstract— This article presents an approach to sensitivity improvement in a detection method based on nuclear quadrupole resonance (NQR); this technique is widely applied in, for example, the detection of explosives. We have an experimental pulsed NQR apparatus equipped with a 250 W pulse power rf amplifier with the working frequency range from 0.5 to approximately 50 MHz. This range can be employed in detecting the isotopes ^{14}N and ^{35}Cl. The article will describe certain improvements in the circuitry of the NQR system proposed by the authors and then experimentally verified on the existing system. These modifications lead to an increased signal-to-noise ratio (SNR), thus also increasing the sensitivity of the system during the detection of substances. The main improvements are in the rf blocking circuit, which prevents the power rf pulse from reaching the preamplifier of the receiver. In this position, some impedance transformers with switched coils have been tested. The appropriate quenching circuit further reduces the penetration of the excitation pulse to this sensitive preamplifier and thus shortens the recovery time.

1. INTRODUCTION

The principles of NQR spectroscopy can be found in [1, 2]. The experimental NQR spectrometer installed in our laboratory uses a SpinCore radioprocessor for signals in the range of 0–100 MHz. The board has two analog I/O channels and four digital outputs. The sampling rate is up to 75 MSPS with 14-bit resolution; the converter utilizes quadrature detection. The DDFS generator provides a signal with the resolution of 14 bits at a frequency of up to 300 MSPS with the baseband bandwidth of 10 MHz. The best achievable time resolution of the radioprocessor is 13.3 ns.

The block diagram of the spectrometer is shown in Figure 1. The 250 W rf amplifier is keyed to reduce the noise in the phase of FID acquisition. An active damping circuit is employed to shorten the time between the excitation and signal acquisition due to the decay of the LC probe.

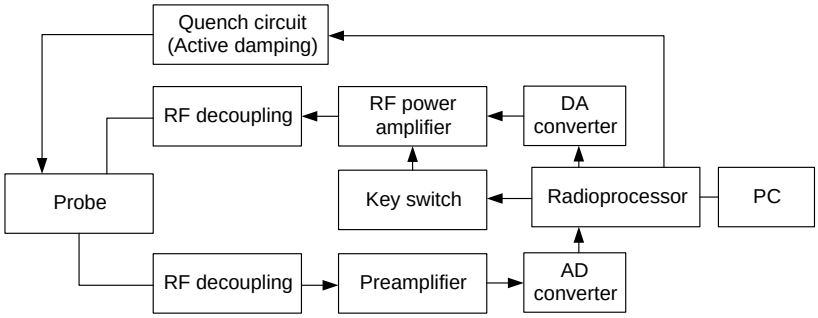

Figure 1: The block diagram of the NQR experimental spectrometer with a radioprocessor.

2. RF DECOUPLING

We decided to compare the properties of two different concepts of rf decoupling on our experimental NQR system.

2.1. LC Filter

To separate the sensitive input of the rf preamplifier from the power circuitry, an LC filter is normally used; this filter is often formed as π-match, see Figure 2 or source [3]. During the operation of the power amplifier, which two pairs of antiparallel diodes will open, and the filter behaves like an impedance divider with high attenuation (L_1 impedance vs input impedance of the preamplifier including protection diodes). At the time of the FID signal acquisition, this circuit acts as a low-pass frequency filter, limiting the undesirable spectral components and thus improving the SNR. The filter is tuned to the desired center frequency with the declared bandwidth.

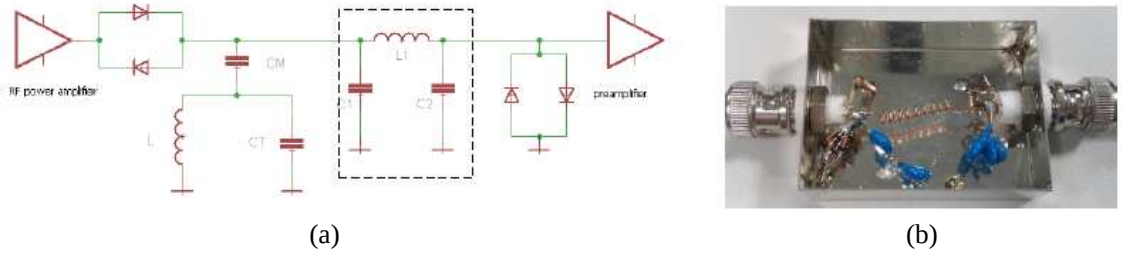

(a) (b)

Figure 2: (a) The basic diagram of the parallel resonance NQR detector (L is the coil of the probe). (b) The π-match implementation for 28 MHz center frequency.

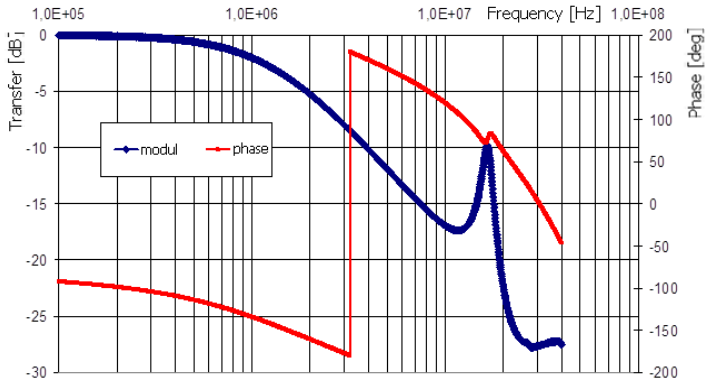

Figure 3: The measured transmission characteristics of the π-match circuit from Figure 2.

One of the filters used in our experimental NQR spectrometer is a π-match with the cut-off frequency of 28 MHz. In the passband, it has an acceptable insertion loss of about 7 dB. Since this filter is narrowband, it is advisable to have one of these circuits for each frequency band and change it when tuning to another spectral region. In NQR detection, we can universally employ π-match filters with the central frequencies of 1; 3.5; 5; 12; 28 MHz or higher.

2.2. Impedance Transformer

Another solution how to isolate the rf preamplifier from the power amplifier consists in the use of an impedance transformer (Figure 4); this approach is described in reference [4]. If no current flows through the lower winding (which is disconnected), the upper winding of the transformer acts as an inductor and exhibits high impedance for the rf signal. If the transistor is turned on, the switching diodes open and short-circuit the lower winding of the transformer; then, the upper coil also exhibits low impedance, and the rf signal passes to the preamplifier.

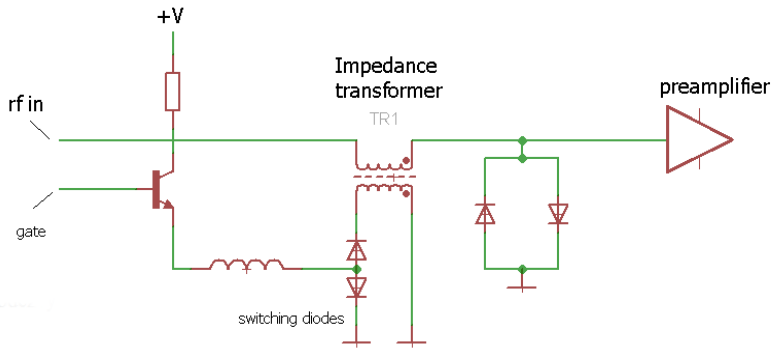

Figure 4: The decoupling of the rf preamplifier pulses performed by the transformer.

3. RESULTS AND DISCUSSION

We designed and experimentally built the circuit according to Figure 4. The transformer 1 : 1 was wound bifilarly from a R174 coaxial cable having the characteristic impedance of 50 Ω. In terms of shielding, the outer wire of the coaxial cable is used as the switched winding and the internal wire as the rf winding. A very important parameter consists in the core material, which must correspond to the particular frequency and have high permeability. The number and distribution of the threads is especially significant with respect to the parasitic capacity and influences the behavior of the transformer. Some of the cores have been tested: the T106-2 with 7 turns (A), the T5020 with 21 turns (B) based on the CF195 material, and the FT140-43 with 30 turns (C).

First, the properties of the actual transformers were measured via simple short-circuiting and opening of the primary winding. The measured results for the transformers (A) and (C) are shown in the graphs in Figures 5 and 6.

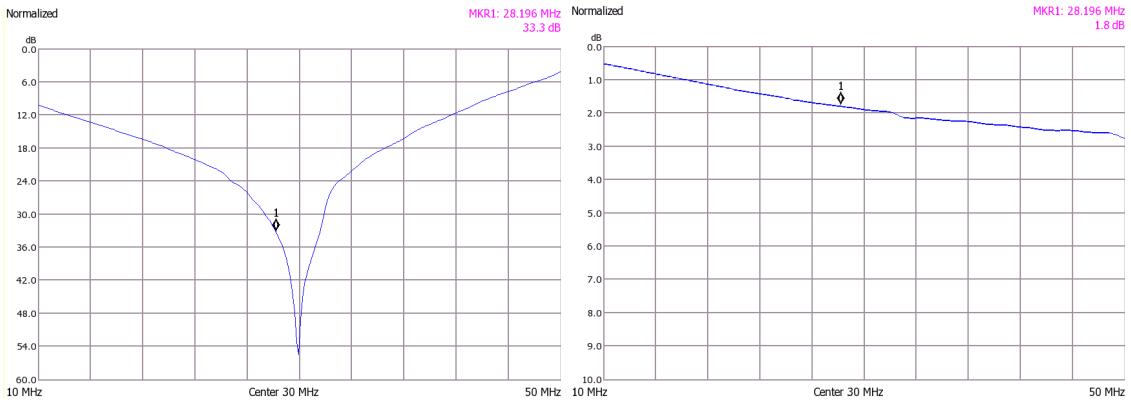

(a) (b)

Figure 5: The attenuation of the impedance transformer (A) with the (a) primary winding opened and (b) short-circuited; the attenuation achieves up to 54 dB at 30 MHz, while the insertion loss is 1.8 dB.

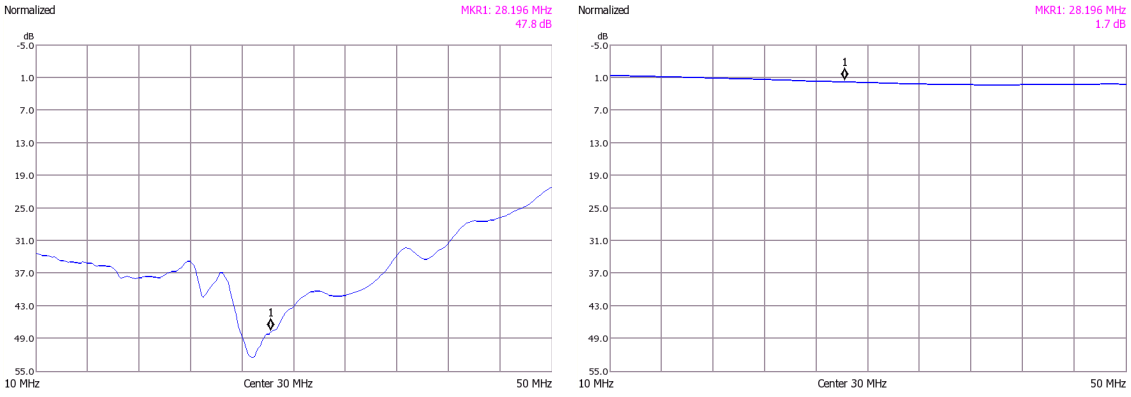

(a) (b)

Figure 6: The attenuation of the impedance transformer (C) with the (a) primary winding opened and (b) short-circuited; the attenuation achieves up to 47.8 dB at 28.1 MHz, while the insertion loss is 1.7 dB.

The transformer (C) was used for the implementation of the circuit according to Figure 7. During the experiments, it was proved that the attenuation of the circuit decreases with the increasing power of the rf signal. This fact is mainly caused by the parasitic capacitance of the diodes in the circuit switch. High-frequency current is transformed to the primary winding and flows through the parasitic capacitance of the diodes; this lowered impedance of the primary winding is then transformed into the secondary one, thus reducing the attenuation. It is therefore appropriate to improve the circuitry and use diodes with minimal parasitic capacitances.

Finally, the response of the entire circuit at the operating frequency of 28 MHz has been tested. The reached switch-off and switch-on times are shown in the oscilloscope images in Figure 7. Here,

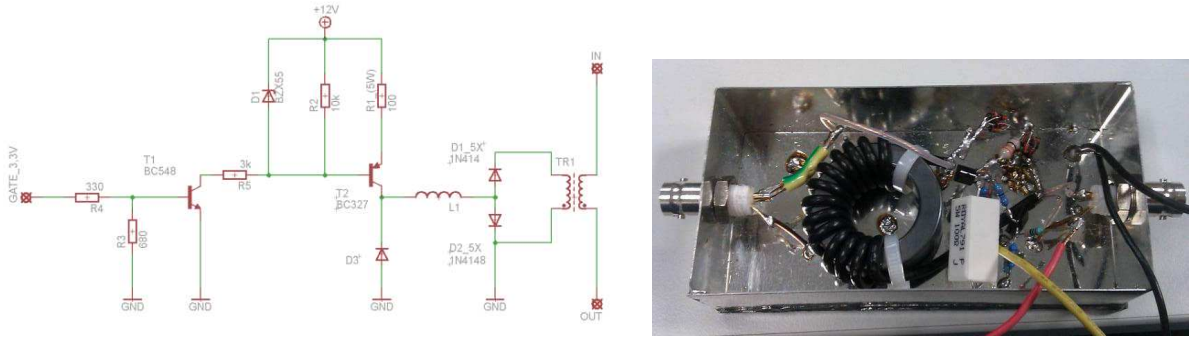

Figure 7: The circuit diagram and photograph of the implemented switch circuit with the impedance transformer.

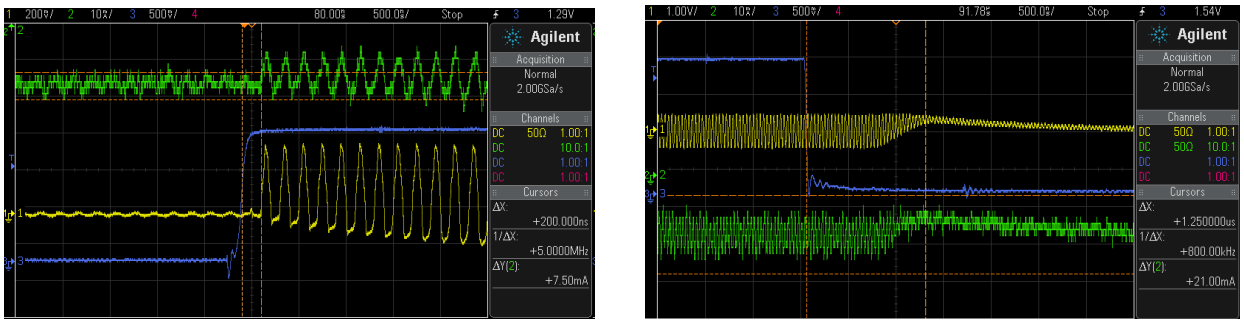

Figure 8: The measured voltage and current waveforms during the transition in the circuit from Figure 7.

the blue curve indicates the keying pulse from the radioprocessor, the yellow curve represents the voltage on the 50 Ω load, and the green curve represents the current flowing through the windings of the transformer. It is obvious from these oscillograms that the delay between the keying pulse and the current flowing through the transformer is about 200 ns when switching on and approximately 1.25 µs when switching off.

4. CONCLUSION

The implementation of the above-described decoupling circuit reduces the attenuation of the measured FID signal and also shortens the dead time between the sample excitation with an rf pulse and the beginning of the signal acquisition.

The planned sensitivity improvement will be based on the suppression of false signals interchangeable with the FID response; such signals are caused by external rf sources. This could be performed either by a differential method with a reference external antenna or via a switched magnetic field in the sample. The latter option results in the loss of NQR signals in the sample when a magnetic field is applied, and therefore differential measurement with and without a static magnetic field affecting the sample can dramatically highlight the NQR peaks in the spectrum of the detected signal.

ACKNOWLEDGMENT

The presented activities were supported by the project No. FEKT-S-14-2545/2014, Brno University of Technology internal science fund. Further, the research utilized financial assistance from the project No. CZ.1.07.2.3.00.20.0175 within the Education for Competitiveness Operative Programme.

REFERENCES

1. Suits, B. H., "Nuclear quadrupole resonance spectroscopy," *Handbook of Applied Solid State Spectroscopy*, D. R. Vij, Springer, Physics Department, Michigan Technological University, Houston, USA, Jul. 2006, ISBN-10: 0387324976.
2. Sathyanarayana, D. N., *Introduction to Magnetic Resonance Spectroscopy ESR, NMR, NQR*, I.K. International Publishing House, 2009, ISBN-13: 978-9380026251.

3. Hiblot, N., B. Cordier, M. Ferrari, A. Retournard, D. Grandclaude, J. Bedet, S. Leclerc, and D. Canet, "A fully homemade ^{14}N quadrupole resonance spectrometer," *Comptes Rendus Chimie*, Vol. 11, 568–579, Methodologie RMN, Nancy-Universite, Universite Henri-Poincare, France, 2008.
4. Ostafin, M. and B. Nogaj, "^{14}N-NQR based device for detection of explosives in landmines," *Measurement*, Vol. 40, No. 1, 43–54, Elsevier, Department of Physics, Adam Mickiewicz University of Poznan, Umultowska 85, Poznan 61-614, Poland, 2007.

A Dark Matter Model to Unify Gravity and Electromagnetism

Michael J. Underhill
Underhill Research Ltd, Lingfield, UK

Abstract— All fields and potentials in space have energy. The gravitational field and potential are no exceptions. Such energy is a 'super-liquid' having a non-particulate continuous distribution. It is not quantised. Field energy is thus defined as 'dark matter'. Any 'dark' matter has gravitational mass density proportional to energy density according to $E = mc^2$. But dark matter has low inertia. Its inertial mass is deduced to be $< 1/(2\pi)^2 =\sim 1/40$ of its gravitational mass. The gravitational potentials from any two or more objects combine at any point according to newly discovered RSS (Root-Sum-of-the-Squares) 'process capture' rules. This means that the stronger potential partially 'suppresses' the weaker potential. The weaker energy is thus partially suppressed and becomes 'excluded' in the region of stronger energy density from a dominant source. Total energy is reduced and gravitational attraction is thereby created. The 'lost' energy increases according to the inverse square law of two sources. This is the source of gravitational attraction of sources and masses. The gravitational field of a light particle terminates at a finite distance when it drops below the Zero-Point-Energy density of free space. These rules can be shown to apply both to gravity and to electromagnetic energy of any spectral distribution. Gravity and Electromagnetism thus become 'unified'.

1. INTRODUCTION

In previous papers feasible electromagnetic structures for all particles have been proposed [1–4]. These support the propositions that 'Everything is Electromagnetic' and there is 'An Electromagnetic Theory of Everything'. The prime basis for the 'Physical Electromagnetic Model' is the discovery of Electromagnetic (EM) Coupling [1–8]. Paper [9] suggested how this model could explain the ratio of measured stable masses of all the sub-atomic particles in the Standard Model [10].

Paper [8] also proposed that *any* form of energy has a *gravitational* mass in accordance with $E = mc^2$. We should note that this included the energy in fields and distributed potentials of low density particles such as photons and neutrinos [1, 8]. All forms of energy can be expressed as $E = \Phi \times \Psi$, where Φ is potential and Ψ is *substance* (charges, currents and matter-substance). This definition is common to both Gravity and Electromagnetism and therefore is itself a unifying concept.

In paper [8] an EM coupling mechanism was given for the *inertial* mass of particles having a dense central core. In this case inertial mass is defined to be equal to gravitational mass. The 'core-atmosphere' particle model in [8] is assumed as the basis for finding particle stability conditions [9]. The core consists of concentrated 'substance' which creates the surrounding 'atmosphere'.

Low density forms of energy such as heat, light and electromagnetic and gravitational fields are considered to be *dark matter* having a low inertia but with gravitational mass defined by $E = mc^2$. Thus even the fields created by and emanating from any form of 'substance', such as any type of charge, current, matter, or mass, do themselves have energy and mass and therefore are defined also as *dark matter* having full gravitational mass but low inertial mass. Note that particles are predicted to have line spectra with each spectral component having energy E_n and frequency f_n, given by $E_n = hf_n$. By contrast heat and in general dark matter have continuous broadband spectra. (Frequency is regarded as 'the fifth dimension').

Electromagnetic Coupling is now defined both as a trans-impedance $Z_{12}e^{-j\omega\tau}$ with delay τ and as a trans-conductance $Y_{21}e^{-j\omega\tau}$ with the same delay. The delay value is a (new) fundamental physical constant and can be shown to be the origin of the 'inertial mass of any particle [8]. These definitions also apply to mass and gravity as a result of the common definitions: Energy, $E = mc^2 =$ Potential, $\Phi \times$ Substance, Ψ.

This 'dark matter model of gravitation' is based on the observation of 'process capture' where the fields from two sources overlap. When applied to either EM or gravitational fields, the process capture RSS (Root-Sum-of-the-Squares) rule in general causes a reduction in total field energy, and in total mass when two particles (having mass) are brought together. It is this diminution of energy that is the root cause of gravitational attraction. This concept can be extended to further cases, such as small particles in a large (gravitational) field, self-attraction of dark matter, and black holes.

2. PARTICLES IN NORMAL MATTER COMPARED WITH DARK MATTER

Normal (ordinary) matter exists in solid, liquid and gaseous forms. All these are assemblies of particles, atoms and molecules. Figure 1, taken from Figure 2 of [8], shows why any matter made up of particles has inertial mass equal to gravitational mass. Whereas dark matter has no dense particle cores and as a consequence has much lower inertial mass but the same gravitational mass for the same energy. On the basis that electromagnetic self-coupling is $1/2\pi$ dark matter inertial mass cannot be higher than $1/(2\pi)^2 =\sim 1/40$ of its gravitational mass in the case of a dominant spectrum line type particle [8]. For heat energy with a wideband 'white-noise' spectrum the inertial mass can be expected to be less with a guessed limit of $1/(2\pi)^4 =\sim 1/1600$ of its gravitational mass.

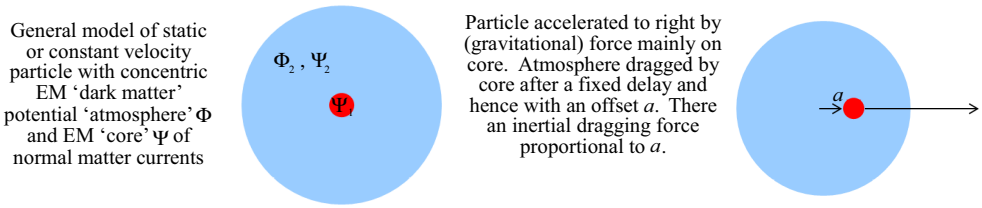

Figure 1: General model of a particle with an explanation for the inertia of normal matter.

In summary, 'dark matter' is any energy that is diffuse and continuous with 'soft' boundaries and contains no dense particles. It inertial mass is much lower than its gravitational mass. The energy of all potentials and fields qualifies as 'dark matter'.

3. PARTICLE GRAVITATIONAL FIELD TERMINATED AT ZERO POINT ENERGY LEVEL BY PROCESS CAPTURE

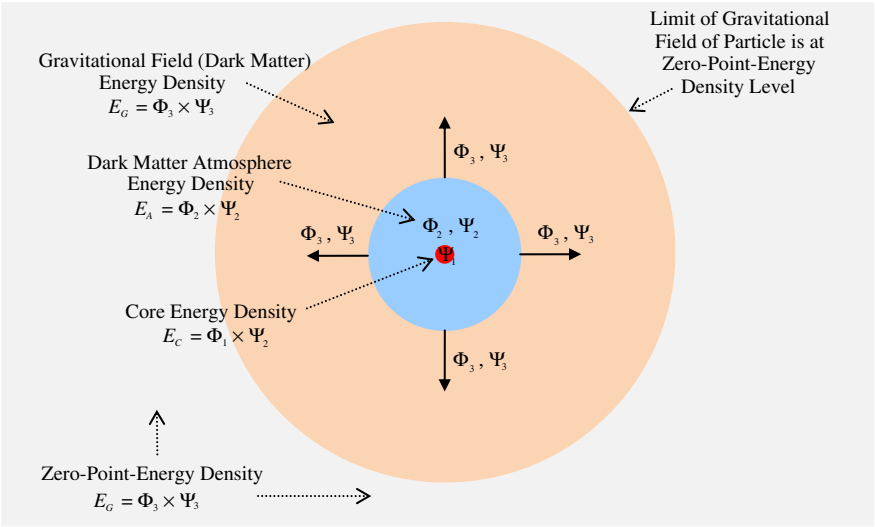

Figure 2: Isolated particle consisting of dense core with finite diffuse atmosphere and surrounded by its own gravitational field energy, extending in density as the inverse square law. The field terminates when it drops below the Zero-Point-Energy (ZPE) level. Both the Atmosphere and the Gravitational Field are Dark Matter. The diagram is not to scale — the radial scale is approximately logarithmic. Ψ is 'substance' density. Φ is potential. E is energy density.

4. PROCESS CAPTURE FOR OVERLAPPING GRAVITATIONAL POTENTIALS

Process capture is a fundamental effect that exists throughout all physics. It was first discovered in measurements of the radiation and loss resistances of the multiple radiation modes of small tuned loop antennas [11] are thereafter exploited in [1–9] and [12–15]. The key feature is that coupled processes overlapping and occupying the same space combine according to the Root-Sum-of-the-Squares (RSS) energy conserving law. It is a 'combination and capture' law where the

stronger process 'captures' and suppresses the weaker process. In some cases the energy conservation requirement may involve the conversion of energy to a different type or form [14].

A gravitational potential or field is a 'process' that fills space with energy usually with an inverse square law of distance from its source. For two spaced sources there is an overlap boundary at which the gravitational energy densities A and B are equal. Either side of this boundary the stronger energy density suppresses the weaker according to the Root-Sum-of-the-Squares (RSS) 'process combination and capture rule'. Essentially it is a power/energy conserving process. Two unequal ($A > B$) energy densities coupling in a finite volume are combined by the Root-Sum-of-the-Squares (RSS) rule as shown in (1) and where RSS combination is indicated by the symbol $\oplus$:

$$A \oplus B = \sqrt{\left(A^2 + B^2\right)} \approx A + B^2/A \to A \tag{1}$$

Thus 'process capture' causes the weaker component to be 'suppressed' by the ratio of the weaker component to the stronger. On the other side of the boundary A and B in (1) are interchanged. The excluded energy E_X is

$$E_X = A + B - \sqrt{\left(A^2 + B^2\right)} \tag{2}$$

At the boundary $A = B$ and E_X has a maximum value of $A(2 - \sqrt{2})$ or a 29.3% exclusion of energy.

At a short distance either side of the boundary either A or B is substantially suppressed and energy of the weaker component becomes almost totally excluded. For large masses this exclusion of energy process becomes the classical gravitational force law. This analysis was originally used for the energy coupling of the spurious components that can appear in an oscillator spectrum [15].

5. ATTRACTION BY EXCLUSION OF GRAVITATIONAL ENERGY AND ZERO-POINT-ENERGY LIMIT

Figure 3 shows four examples where two particles are attracted to each other whenever some of their overlapping gravitational energy becomes 'excluded'. The amount of excluded energy is

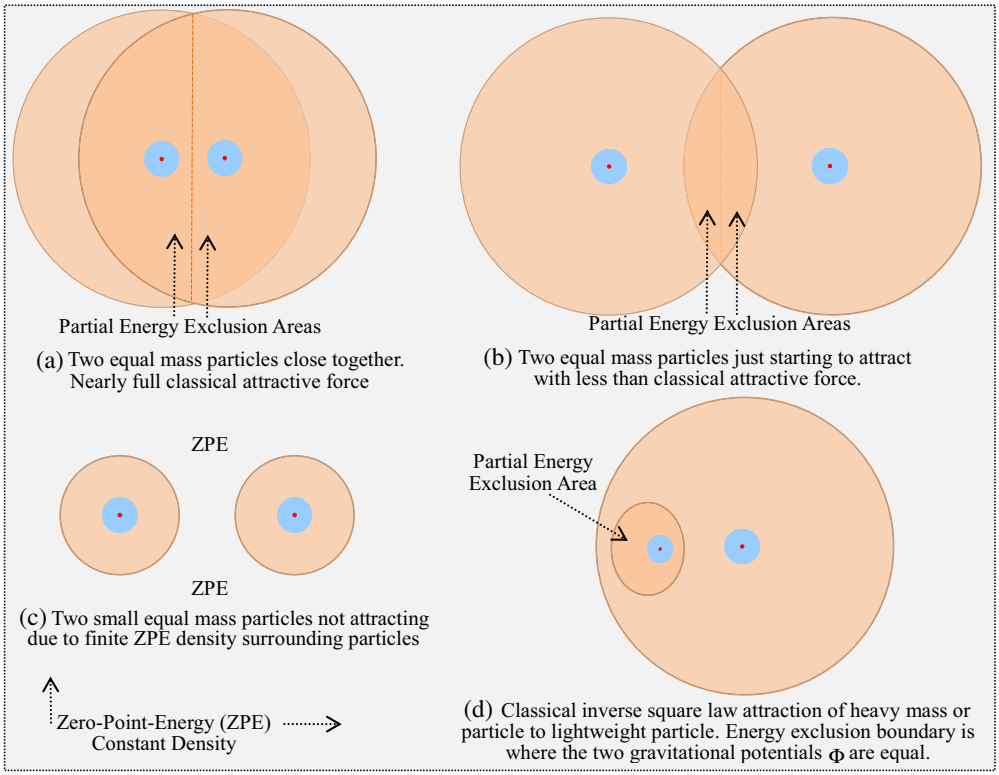

Figure 3: Four cases of gravitational attraction. The attractive force is from energy exclusion where two gravitational potentials/fields try to occupy the same volume in space. The reduced energy is translated into a force. 'Process capture' causes energy exclusion. The weaker energy is suppressed according to the RSS rule.

proportional to a force between the two particles of a pair. The classical 'work done by a force' principle can be used to calculate the force. The amount of energy 'excluded' can also be estimated by integrating the RSS combination Equation (2) to a sufficient distance either side of the 'equal energy boundary' line. Because the RSS process capture and suppresses the weaker component, the required integration distance is not excessive. In many cases exact analytic solution is feasible. This is always much faster than a Finite Element numerical solution [16].

Of particular note in Figure 3 is the use of the novel proposition that the Zero-Point-Energy (ZPE) of (the ether of) free space is a lower limit of the gravitational potential and field and therefore to the gravitational attraction of particles. See for example (c) in Figure 3. It would be a nice experiment to try to measure and confirm this directly.

6. CONCLUSIONS

Fields and potentials in space have energy. This energy is in the form and nature of 'dark matter'. Gravity and Electromagnetics (EM) both comply with these two propositions/assertions. In this way gravity and EM may be 'joined up'.

Energy exclusion where gravitational potentials from different sources overlap is what creates gravitational attraction. The magnitude of the excluded energy at any point can be calculated from suppression/reduction of total energy in accordance with the RSS (Root-Sum-of-the-Squares) process combining rule.

The existence of the Zero-Point-Energy (ZPE) of (the ether of) free space provides a distance limit to gravitational attraction (of small particles).

REFERENCES

1. Underhill, M. J., "The phase noise spectrum and structure of photons?," *Proc. 16th EFTF-2010*, 8 pages, Noordwijk, Netherlands, Apr. 13–16, 2010.
2. Underhill, M. J., "A physical model of electro-magnetism for a theory of everything," *PIERS Online*, Vol. 7, No. 2, 196–200, 2011.
3. Underhill, M. J., "Maxwell's transfer functions," *PIERS Proceedings*, 1766–1770, Kuala Lumpur, Malaysia, Mar. 27–30, 2012.
4. Underhill, M. J., "A local ether lens path integral model of electromagnetic wave reception by wires," *PIERS Proceedings*, 1005–1008, Moscow, Russia, Aug. 19–23, 2012.
5. Underhill, M. J., "Antenna pattern formation in the near field local ether," *PIERS Proceedings*, 1009–1012, Moscow, Russia, Aug. 19–23, 2012.
6. Underhill, M. J., "Wideband small loop-monopole HF transmitting antenna with implications for Maxwell's equations and the Chu criterion," *PIERS Proceedings*, 764–768, Taipei, Mar. 25–28, 2013.
7. Underhill, M. J., "Coupled electromagnetic wave propagation in space and around surfaces and interfaces," *PIERS Proceedings*, 394–398, Stockholm, Aug. 12–15, 2013.
8. Underhill, M. J., "Electromagnetic structures and inertias of particles including the Higgs boson," *PIERS Proceedings*, 401–405,, Taipei, Mar. 25–28, 2013.
9. Underhill, M. J., "The stability of EM particles and predicted mass ratios," *PIERS Proceedings*, 399–404, Stockholm, Aug. 12–15, 2013.
10. http://en.wikipedia.org/wiki/Standard_Model.
11. Underhill, M. J. and M. Harper, "Small antenna input impedances that contradict the Chu-Wheeler Q criterion," *Electronics Letters*, Vol. 39, No. 11, May 23, 2003.
12. Underhill, M. J. and M. Harper, "Simple circuit model of small tuned loop antenna including observable environmental effects," *Electronics Letters*, Vol. 38, No. 18, 1006–1008, 2002.
13. Underhill, M. J. and M. J. Blewett, "Unidirectional tuned loop antennas using combined loop and dipole modes," *8th Int. Conf. on HF Radio Systems and Techniques, 2000*, No. 474, IEE Conf. Publ., 2000.
14. Underhill, M. J., "Discovery and theory of small antenna near-field dissipation and frequency conversion with implications for antenna efficiency, beverage antenna noise reduction, Maxwell's equations and the Chu criterion," *Progress In Electromagnetics Research Symposium*, Guangzhou, Aug. 25–28, 2014.
15. Underhill, M. J., "Coupling theory for fluctuating spurs in oscillators," *IEEE International Frequency Control Symposium 2014*, 596–599, Taipei, Taiwan, May 20–22, 2014.
16. Underhill, M. J., "Novel analytic EM modelling of antennas and fields," *PIERS Proceedings*, 1771–1775, Kuala Lumpur, Malaysia, Mar. 27–30, 2012.

Interactive Segmentation of Hip Joint Cartilage

Pavel Dvorak[1, 2], **Vladimir Juras**[3], **Wolf-Dieter Vogl**[4], **and Jiri Chytil**[2]

[1]Institute of Scientific Instruments of the ASCR
v.v.i., Královopolská 147, Brno 612 64, Czech Republic
[2]Faculty of Electrical Engineering, Brno University of Technology
Technická 12, Brno 612 00, Czech Republic
[3]High Field MR Center, Department of Biomedical Imaging and Image-guided Therapy
Medical University of Vienna, Waehringer Guertel 18-20, Vienna A-1090, Austria
[4]Computational Image Analysis and Radiology Lab, Department of Radiology
Medical University of Vienna, Lazarettgasse 14, Vienna A-1090, Austria

Abstract— This work deals with hip joint cartilage segmentation, which is an important task in joint diseases diagnosis. Since the manual segmentation commonly used nowadays, is a tedious and lengthy task, this work brings a new idea into its automation and simplification of the medical expert work. The proposed method is an interactive algorithm for hip joint cartilage segmentation, and hence it requires some user interaction, which is common and usually desired in medical image processing. The first step of the method is a selection of several points in several slices lying inside the cartilage. The purpose is a rough delimitation of the cartilage area. This delimitation is based on the assumption that the femoral head has approximately circular shape. The cartilage is then segmented using the combination of Graph Cut segmentation and K-means clustering techniques. The algorithm was tested on 3D isotropic True-FISP volumes of patients with femoroacetabular impingement and the results were evaluated by commonly used Dice Similarity Coefficient (0.62). The results of the segmentation will be prospectively used for the segmentation of quantitative MR maps (T1 and T2) in femoro-acetabular impingement (FAI) investigation.

1. INTRODUCTION

This work deals with hip joint cartilage segmentation, which is an important task in joint diseases diagnosis. Since the manual segmentation commonly used nowadays, is a tedious and lengthy task, this work brings a new idea into its automation and simplification of the medical expert work.

General image segmentation is still an unsolved problem, therefore specific methods have to be applied for particular types of images. A general method that could be applied for all kinds of images has not been developed so far and in the near future the situation will probably remain the same. For MR image segmentation, the classic techniques such as thresholding, region growing, active contour, etc. can be used [1]. Another type of segmentation used in MRI is pixel classification into several classes. This can be either supervised using algorithms such as SVM [2] used e.g., in [3], or unsupervised using clustering algorithms. Such algorithms can be based on data space division such as k-means algorithm [4] or they can respect the noise distribution such as Gaussian Mixture Model using the Expectation-Maximization algorithm for determination of model parameters [5]. Since tissues of a user's interest may reach similar intensities as other tissues present in image, more sophisticated algorithm has to be used.

Only few algorithms were proposed for hip joint cartilage segmentation task. Sato et al. [6] proposed a method based on automatic determination of approximate center of femoral head and subsequent determination of cartilage using a radial directional derivatives. The method proposed by Khanmohammadi et al. [7] is based on automatic determination of femoral center by Hough transform. Femoral head and acetabulum are detected, and segmented and the cartilage is found as the space between these two bones.

The method proposed in this paper is semi-automated and expects manual determination of several starting points lying inside the hip joint cartilage. Users have higher control on the segmentation process since they can manually correct the partial segmentation, which can improve the overall result of the segmentation process. Even though this leads to higher demands on users, it can achieve the accuracy according the user's expectation.

2. PROPOSED METHOD

The flow diagram of the proposed method is depicted in Figure 1. The algorithm is based on 2D segmentation of selected axial slice and subsequent propagation in both directions with possible

manual correction. It uses graph cut segmentation algorithm with subsequent automatic correction by Bayesian Quadratic Discriminant Analysis (Bayesian QDA) for the segmentation of selected slice. In propagation, only Bayesian QDA is employed.

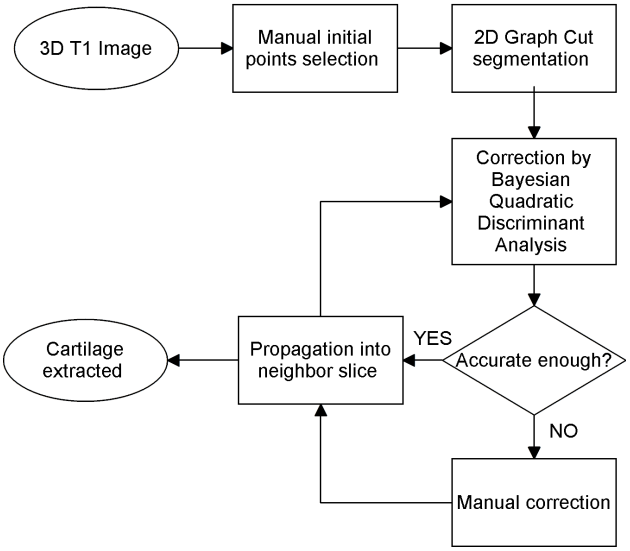

Figure 1: Flow diagram of the proposed method.

2.1. ROI Delimitation

The first step of the method is a manual selection of several points not lying in a plane. The purpose is a rough delimitation of the cartilage area using a sphere fitting to these points. This delimitation is based on the assumption that the femoral head has approximately a circular shape. The next step consists of the manual selection of the suitable axial slice and the subsequent several reference point selection. These points are interpolated by a cubic spline in clock-wise order with respect to the center of the circle that best fits the points. The spline creates the foreground mask for subsequent segmentation. The background mask is created as inverted morphological dilation of the spline with particular dilation size dependent on the image resolution.

2.2. Graph Cut Segmentation

The labels for points in between foreground and background are computed by Graph Cut segmentation technique [8]. The input of this method, except the image itself, is a map of labels. Each pixel is labeled as foreground, background or unknown. The optimal border between foreground and background is found in the area of unknown labels.

2.3. Correction

The result of the Graph Cut segmentation is corrected by Bayesian Quadratic Discriminant Analysis (Bayesian QDA) [9], where the training data consists of pixels inside and outside the segmentation result with respect to their label in the mask. The new label is assigned again to the pixels with previously unknown label and isolated ones are eliminated.

Bayesian QDA is a supervised classification technique using a Gaussian distribution for modeling the likelihood of each class. The Gaussian parameters are estimated by maximum likelihood estimation from training points.

As a next step, the segmentation result can be corrected or confirmed by user and it is used as reference segmentation for neighbor slices.

2.4. Propagation

The resulting mask of 2D segmentation is used as a reference segmentation in the propagation process into the neighbor slices.

The points from the neighbor slice lying inside the dilated reference mask are classified by Bayesian Quadratic Discriminant Analysis, where pixels from the previous slice are used for training. Isolated pixels are eliminated and the result can be again corrected by user, because its precision plays a significant role in the subsequent segmentation in further slices. The result is again used as a reference for the next slice segmentation.

3. EXPERIMENTS AND RESULTS

3.1. Evaluation Criteria

The results were evaluated by commonly used Dice Coefficient (DC) and Accuracy Coefficient (AC), where only the space inside the bounding box for enlarged fitted sphere was considered. If the whole volume had been considered, the DSC would reach the same value, but the accuracy would be very close to 1 and would not reflect the algorithm performance. No interaction or manual correction was performed during this testing procedure.

The Dice Coefficient (DC), in some works called Similarity Index, is computed according to the equation

$$\mathrm{DC} = \frac{2\,|A \bigcap B|}{|A| + |B|}, \tag{1}$$

where A and B denotes the ground truth and the result masks of the segmentation, respectively. This criterion compares the intersection of two sets with their union. The range of values of DC is $\langle 0; 1\rangle$, where the value 1 expresses the perfect segmentation. According to [10], the DC > 0.7 indicates an excellent similarity.

Another measure widely employed for segmentation evaluation is Accuracy (A), used e.g., in [3] and defined by the equation:

$$A = \frac{TP + TN}{TP + FP + TN + FN}, \tag{2}$$

where TP, FP, FN and TN stand for "True Positive", "False Positive", "False Negative", and "True Negative", respectively. Both measures are in the same range as DC and the higher value indicates the better performance as well.

3.2. Results

The algorithm was tested on 20 3D isotropic True-FISP volumes of patients with femoroacetabular impingement. All MR images were obtained using a 1.5 T system (Avanto, Siemens Healthcare, Erlangen, Germany) with the voxel size of $0.63 \times 0.63 \times 0.63$ mm and the volume size of $512 \times 512 \times 321$ px. The ground truth performed by a medical expert was available. More information about the data can be found in [11]. The results are summarized in Table 1 using the both coefficients for initial selected slice and the whole 3D volume. For each of 20 cases, the algorithm was repeated three times with different initial slice, where 10 points were chosen in the initial slice. An average example of the result for an initial slice is shown in Figure 2.

Table 1: Segmentation evaluation by dice coefficient and accuracy for both planes.

	DC	Accuracy
Initial slice	0.81 ± 0.05	0.94 ± 0.02
3D volume	0.62 ± 0.07	0.96 ± 0.01

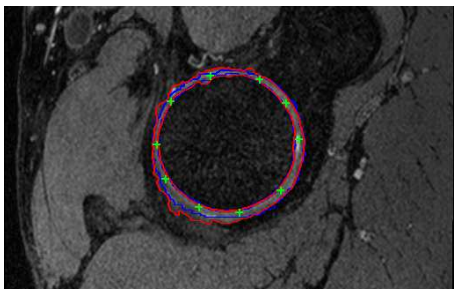

Figure 2: Average result (DC = 0.82) of an initial slice segmentation (red) compared to ground truth (blue) for manually selected 10 points (green).

4. CONCLUSION AND FUTURE WORK

This work describes the initial research in the automation of the hip joint cartilage segmentation task. The result of this work is a tool for the automated interactive segmentation, which speeds

up this tedious task in the diseases diagnosis and research. There are only a few papers dealing with this particular problem (e.g., [6]), and these do not contain quantitative results; therefore the proposed method cannot be compared with them. The future research will focus on improving the accuracy of the automated segmentation of the hip cartilage, especially in the most problematic area of femoral neck, and will be prospectively used for the segmentation of quantitative MR maps (T1 and T2) in femoro-acetabular impingement (FAI) investigation.

ACKNOWLEDGMENT

The described research is funded by the projects CZ.1.07/2.3.00/20.0094, GACR 102/12/1104, SIX CZ.1.05/2.1.00/03.0072 and COST CZ LD14091.

REFERENCES

1. Zhang, H., J. E. Fritts, and S. A. Goldman, "Image segmentation evaluation: A survey of unsupervised methods," *Computer Vision and Image Understanding*, Vol. 110, No. 2, 260–280, 2008, [Online] Available: http://www.sciencedirect.com/science/article/pii/S1077314207001294.
2. Cortes, C. and V. Vapnik, "Support-vector networks," *Mach. Learn.*, Vol. 20, No. 3, 273–297, Sep. 1995, [Online] Available: http://dx.doi.org/10.1023/A:1022627411411.
3. Mikulka, J. and E. Gescheidtova, "An improved segmentation of brain tumor, edema and necrosis," *PIERS Proceedings*, 25–28, Taipei, Mar. 25–28, 2013.
4. MacQueen, J. B., "Some methods for classification and analysis of multivariate observations," *Proceedings of 5th Berkeley Symposium on Mathematical Statistics and Probability*, Vol. 1, 281–297, 1967.
5. McLachlan, G. and D. Peel, *Finite Mixture Models*, John Wiley & Sons, Inc., 2000.
6. Sato, Y., K. Nakanishi, H. Tanaka, N. Sugano, T. Nishii, H. Nakamura, T. Ochi, and S. Tamura, "A fully automated method for segmentation and thickness determination of hip joint cartilage from 3d MR data," *International Congress Series*, Vol. 1230, No. 0, 352–358, Computer Assisted Radiology and Surgery, 2001, [Online] Available: http://www.sciencedirect.com/science/article/pii/S0531513101000292.
7. Khanmohammadi, M., R. Zoroofi, Y. Sato, T. Nishii, K. Nakashi, N. Suguro, H. Yoshikawa, H. Nakamara, and S. Tamura, "Automated segmentation of the hip cartilage in multi-slice mr data," *Proc. Cairo Int. Biomed. Eng. Conf.*, 2006.
8. Boykov, Y. and V. Kolmogorov, "An experimental comparison of min-cut/max- ow algorithms for energy minimization in vision," *IEEE Transactions on Pattern Analysis and Machine Intelligence*, Vol. 26, No. 9, 1124–1137, Sep. 2004.
9. Krzanowski, W. J., *Principles of Multivariate Analysis: A User's Perspective*, Oxford University Press, New York, 1988.
10. Zijdenbos, A. and B. Dawant, "Brain segmentation and white matter lesion detection in MR images," *Critical Reviews in Biomedical Engineering*, Vol. 22, 401–465, 1994.
11. Stelzeneder, D., T. Mamisch, I. Kress, S. Domayer, S. Werlen, S. Bixby, M. Millis, and Y.-J. Kim, "Patterns of joint damage seen on mri in early hip osteoarthritis due to structural hip deformities, osteoarthritis and cartilag," *Osteoarthritis Cartilage*, Vol. 20, No. 7, 661–669, 2012.

PIERS: Progress In Electromagnetism — Relativity Superseded

Piers Hutchinson
MA Oxon, 485 Hilson Ave, Ottawa K1Z 6C6, Canada

Abstract— In the conflict between probabilistic Quantum Mechanics and deterministic Relativity, this paper sides with QM and explains free will. Einstein wrote, "Everything is determined, the beginning as well as the end, by forces over which we have no control; human beings, vegetables, or cosmic dust, we all dance to a *mysterious* tune, intoned in the distance by an *invisible piper*". In fact only time past is determined; time future is open.

The basic idea of this paper is not new. It is Maxwell's medium for electromagnetism, which Einstein rejected following the null result of the Michelson-Morley experiment conducted in 1887 when he was 8 years old. But the null result actually came from the fact that Maxwell's medium revolves with the earth, like the atmosphere. If the experiment is repeated on a *moving* platform — for example on a high-speed train — it shows a positive result, as in the experiment of D. Wang et al. [1]. Maxwell was able to predict the speed of light (680,000,000 mph) from the permeability μ and permittivity ε of its medium via the formula $1/\sqrt{\mu\varepsilon}$ just as we can predict the speed of sound in its various media using the same formula.

The new idea is that Maxwell's medium is made of basic particles of Plank length and mass, here called 'evrons', of which all matter (all particles) are made. This is the missing 'Dark Matter' which rotates with a galaxy keeping the outer stars up to the speed of the inner stars. The four forces are made of pressure waves of different wavelengths in the medium. This is the missing 'Dark Energy'. The evrons carry the forces as molecules carry sound. The waves are polarized like those of sound passing through steel. The medium allows any number of radio telephone conversations to pass through every small spot in a room at the same time. The new idea is that the so-called relativistic effects are actually drag effects of the medium that follow Lorentz's drag formula, $\sqrt{1-(v/c)^2}$: the mass increase of a speeding electron is the build-up of evrons ahead of the electron; the slowing of clocks on speeding GPS satellites is caused by evronic pressure.

The medium allows us to be rid of many anomalies of modern physics while explaining the strange data of some of its experiments. We can be rid of unexplained 'singularities' like the Big Bang and explain the Red-shift and the Cosmic Microwave Background by the spreading, in the evrons, of light waves from stars in an endless universe. This in turn explains the existence of clusters of galaxies that took far longer to form than the 13.8 billion years allowed by Big Bang theory and the recent discovery of mature galaxies, needing billions of years to form, existing 12 billion years ago [2].

Standard physics has matter pulling other matter with an unexplained negative force called 'Gravity'. The new idea is that gravity is positive evronic pressure which is stronger near massive structures owing to the diminution of counteracting pressure, as when clocks on GPS satellites are slowed when closer to the earth.

The new idea is that energy is always a pressure wave and never a particle; so we can be rid of any inexplicable change of matter into energy in a nuclear bomb. Instead, the bomb releases the binding evronic energy according to $e = mc^2$ while the nucleons are conserved. The new idea is that Electricity is not made of electrons (matter) but is pressure in the evrons (energy), which accounts for the electrical field surrounding a live wire. Atoms are not solar-systems, which would knock each other's electrons out of orbit when sodium met chlorine, but nucleons projecting pressure patterns into the evrons described by the Schrodinger *wave* equation.

Unification comes in the understanding that particles are spinning collections of evrons (nearly 100 billion in a proton and 50 million in an electron) [3], with antiparticles spinning in the opposite direction. This explains particles appearing out of, and disappearing into, the so-called vacuum in the Hadron Collider, with more mass in the products of a hadron collision than were put into the experiment [4]. The photoelectric effect is the creation of an electron. The strange finding of the two-slit experiment of a particle seeming to go through two slits at the same time is explained by the fact that, however weak, light is always a wave in the evrons (which can go through both slits at the same time) and never a particle. The so-called 'non-locality' (statistical) experiments are explained by reflections of waves affecting the waves that follow.

The medium allows the development of life epigenetically [outside the genes rather than by 'selfish' genes], from the lighter elements H, C, O, N, P or S. The missing 'variation' of Darwin's 'variation and natural selection' comes from the recombination of genes at conception — this is the reason for sexual reproduction instead of the less energetic cloning which only takes place in the absence of competition — and not through random mutation which is generally deleterious. Human creativity mirrors natural creativity [5]. The management of an organism is through waves — for example the wave structure of an antibody is complementary to part of the wave structure of an antigen.

The major confirmation of evrons comes from their explanation of consciousness. Evrons fill the three parts of the nervous system — sensory, autonomic and motor. Perception is explained by waves from the environment resonating with similar wave patterns perceived earlier reverberating in the sensory nervous system. [If sensation were transmitted to the brain in nervous impulses moving at only 100 mph, virtually all the data arriving at 680,000,000 mph would be lost.] Waves allow the perception of a wide angle of a scene in a single fixation, unlike a digital camera which has to scan the scene. Waves allow the blending of fixations. Waves allow the blending of present with past so that a table can be seen as similar to other tables. Waves allow the blending of the senses which all produce data in waves, including smell [6] and the magnetic sense of birds and the infrared sense of snakes. The speed of light allows a touch to the toe to be perceived as simultaneous to a simultaneous touch to the nose [7]. Waves allow the combination of sensation in the sensory nervous system with *feeling* in the autonomic nervous system; behavior mediated by waves in the motor system can be influenced by mood; music can be an international language.

Waves bridge the time needed to build long term memory structures; and they mediate, through resonance, the retrieval of memory from those structures, coordinating the two sides of the brain at light speed. Waves dissipate, allowing short-term memory to fade (unlike the memory of a computer), to give a sense of the passage of time. Waves explain the ability of a rat to remember a maze when its brain has been sectioned [8]. Anyone can understand these words as he reads them through the coexistence in his brain in wave form of a lifetime of experience. Reverberating waves allow a savant to draw New York in detail after a short helicopter ride [9], and explain how anyone can recognize each scene in a movie he saw last week. If light were made of photons one would not be able to distinguish between one piece of furniture and another with all the reflected light in the room. If light were made of photons, the photons from distant galaxies would spread out and miss earthbound telescopes.

Above all, waves allow a blending of past and present to give a sense of where things will be in the future — for instance when trying to cross a busy intersection — and hence a chance to intervene to change that future. This is in opposition to Einstein, Stephen Hawking, Richard Dawkins and Steven Pinker who have all said that free will is an illusion. Through superposition, waves allow us to see the world in perspective — we are not bound, as Einstein said, to one frame of reference. The Uncertainty Principle says that we cannot measure the position and the momentum of a particle at the same time, but any particle does have a fixed position and momentum at any one time — Schrodinger's cat is either alive or dead. Waves even allow us the perspective to alter what we want — the addict can resist his temptation; the hunger-striker can overcome his hunger and the suicide bomber can overcome his will to live.

String Theorists following Einstein have been searching for the last four decades for a grand design (a set of equations) that would predict everything. They have not found one. There is a basic conflict between smooth Relativity, which works as if everything were predetermined by a mathematician, and bitty Quantum Mechanics, which works on the Uncertainty Principle. The new idea is that nothing is predetermined and that there was no *design* before animals like us. Each of our bodies is built from scratch using a set of genes that allowed our parents to survive, so that in a single generation completely new organisms like conjoint-twins are produced. Each of our lives is built from scratch, with the freedom to make unpredictable changes. We are not predetermined. The superposition of waves allows all the uniquely human things — the love of solving problems, vicarious enjoyment, laughter on seeing a joke, the correction of error and the working towards long-term goals.

REFERENCES

1. Wang, R., et al., *Physics Letters A*, Vol. 312, 7–10, 2003.
2. *Astrophysics Journal*, Mar. 2014.
3. Enrique, M.-R., "Reconstructing modern physics," 2009.

4. Hadron, C., "Proton-proton runs," Dec. 2010.
5. Adrian, B., *Shape and Structure, from Engineering to Nature*, 2000.
6. Luca, T., "The science of scent," *TED Conference*, 2006.
7. David, M. E., "What's next?," 155, 2009.
8. Karl, S. L., *Symposium of Society of Experimental Biology*, Vol. 4, 454–482, 1950.
9. Stephen, W., Panorama, New York, 2009.

PO-GO/ECM for Bistatic RCS Modeling of Complex Objects over Rough Sea Surface

Y. Bennani[1] **and R. Talhi**[1, 2]

[1]Department of EECS, University of Tours, Avenue Monge, Tours 37200, France
[2]CNRS/LPC2E, 3A Avenue de la Recherche Scientifique, Orleans Cedex 2 45071, France

Abstract— The work summarized in this paper fits well in the field of remote sensing of the marine environment. It shall include, firstly, the study of interaction of an electromagnetic wave with a sea surface in the presence of a complex target observed in bi-static configuration. On the other hand, the work is completed by the study and analysis of the influence on this electromagnetic (EM) interaction of various parameters related to both the target and also to the environment. The proposed model has been validated by comparing theoretical results to experimental measurements obtained in the anechoic chamber, and then it was applied to a marine scene by considering the sea surface and the target as a single complex object.

1. INTRODUCTION

The prediction of scattering from a complex target over sea surface is a subject of recent interest in the radar target recognition field [1]. The computation of the Radar Cross Section (RCS) of a complex target involves several kinds of scattering mechanisms, such as multiple scattering, specular reflection, diffraction by edges [9]. To take into account these effects we have used asymptotic methods [6]. These methods can be divided into two types. The first one called asymptotic methods of rays based on the asymptotic expression for the scattered field such as Geometrical Optic (GO) [6] completed by the Uniform Theory of Diffraction (UTD) [6]. The other family called asymptotic methods of currents that are based on the asymptotic expression of surface current distributed on the illuminated surface of the target, where the scattered field is calculated as the scattering of these currents. So, surface reflection is calculated by Physical Optics (PO) method and edge diffraction is computed by the Equivalent Currents Method (ECM) [7]. The aim of this paper deals with modelling of interaction between electromagnetic (EM) wave and the complex target over sea surface. The RCS is computed using a combination based on PO-GO [10] and ECM [7] approximations.

In order to introduce the influence of the sea surface on the electromagnetic response of the target in its environment, we opted for a representation of the scene (target + sea surface) by a set of triangular facets. Within this framework, the target discretized by a triangular mesh is generated using a CAD — Computer Aided Design — tool (CATIA, V5); as regards the sea surface, it is generated using the Elfouhaily sea spectrum [3] (and the Debye model [11] to take into account the dielectric parameters of seawater).

2. GEOMETRICAL MODELLING OF COMPLEX TARGETS

The first step in RCS computation [6] is to define the target in a global system coordinates as shown in Figure 1(a). We have chosen to represent the target by a collection of triangular facets, because they allow to obtain a good representation of complex targets and allow to achieve an accurate estimated contribution. When an EM wave intercepts a complex target, it gives rise to different scattering mechanisms.

Figure 1(b) illustrates some scattering mechanisms. In this paper, we consider different types of effects such as shadowing effects [5], direct scattering [6], multiple scattering [10], diffraction by edges [8]. The first step before computation of the RCS is to determine the real surface illuminated by the incident EM wave.

2.1. Shadowing Effect

When an incident EM wave is intercepted by a target, a portion of its surface is illuminated and the rest remains dark. In addition, portions of the target can be hidden by other parts. As exposed above, it is assumed that the RCS takes into account only this visibility phenomenon. According to the propagation direction towards the target, the test of visibility is based on the algorithm of Trumbore et al. [5]. The main idea is to check if the ray passing through a predetermined point of the first facet intersects with the second facet. The visibility test is applied on a boat example

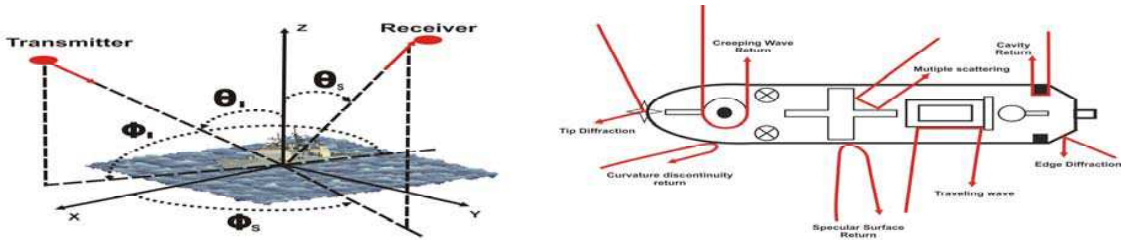

(a) Global system coordinates for marine scene (b) Scattering mechanisms for a marine target

Figure 1: Global system coordinate and scattering mechanisms.

for some radar viewpoints. Figures 2(a) and (b) show the visible facets with green colour for two positions of the radar ($\theta = \varphi = 0°$) and ($\theta = \varphi = 45°$). Another example is given in [4]. Now, as part of the illuminated target by the incident wave is determined, we apply PO approximation in order to calculate the contribution of direct scattering (specular reflection).

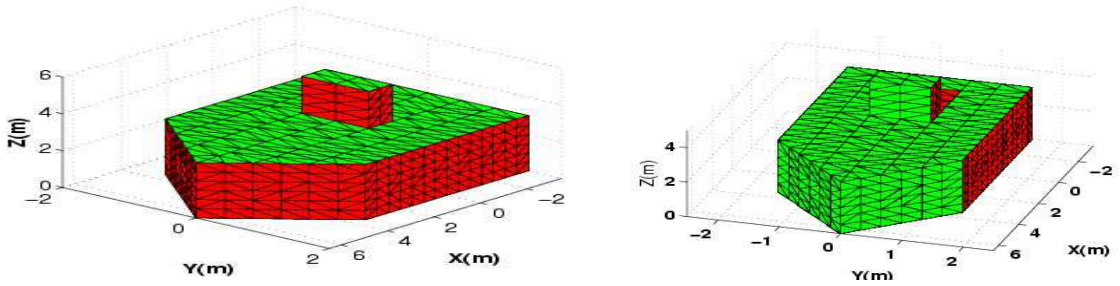

(a) Radar viewpoint (θ=φ=0 °) (b) Radar viewpoint (θ=φ=45 °)

Figure 2: The visibility test for a generic boat.

2.2. Direct Scattering (Physical Optics)

The specular reflection of each facet is obtained from PO method. The current is used in the radiation integrals to compute the scattered far field [6]. The simplified expression of the electrical scattered far field is given by the following equation:

$$\vec{E}_s = -\frac{jke^{-jkR}}{4\pi R} \int\limits_S Z_0 \vec{k}_s \times \left[\vec{k}_s \times \vec{J}\right] - \left[\vec{k}_s \times \vec{M}\right] \; e^{-jk\,\vec{k}_s \cdot \vec{r}}\, dS \tag{1}$$

where $\vec{J}$ and $\vec{M}$ represent respectively the electric and magnetic current on the surface, their expressions are $\vec{J} = \hat{n} \times (\vec{H}_i + \vec{H}_r)$ and $\vec{M} = -\hat{n} \times (\vec{E}_i + \vec{E}_r)$, where $\vec{E}_i$, $\vec{E}_r$ and $\vec{H}_i$, $\vec{H}_r$, represent respectively the electric and magnetic incident and reflected fields. This is valid for r in S_i, where S_i is the illuminated surface, k is the wave number, R is the distance between the illuminated surface and the receiver, $\vec{k}_s$ is the unit vector in the direction of the receiver, and Z_0 is the impedance of free space. For more accuracy of our model, we present in the next section, the multiple scattering contribution.

2.3. Multiple Scattering

Treatment of multiple scattering is not a trivial topic and requires careful implementation. Multiple interactions are approximated very well by GO approach [10]. The combination GO-PO technique is developed in [10], which uses the PO to calculate contribution at the last reflexion at the surface of the object. However, describing the complex target in terms of facets and edges reduces significantly the problem. The multiple scattering contributions are primarily expressed in terms of facet-facet. So, to take into account the contribution of double reflection [10] to the RCS of a complex target, we must find the facets candidates to the double reflection. To do so, we take the first facet intercepted by an incident EM wave and we select all facets oriented towards this facet as shown in Figure 3(a). The double reflection is expressed in terms of triangle-triangle.

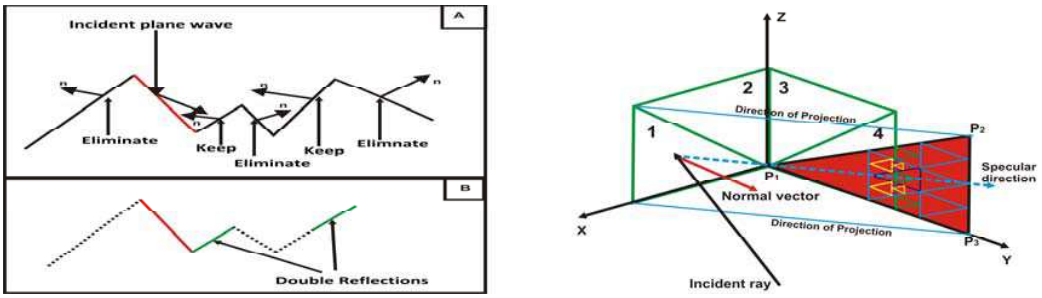

(a) (b)

Figure 3: Multiple scattering contribution. (a) Detection of facets candidates for a double reflection contribution. (b) Real surface for double reflection contribution.

2.4. Diffraction by Edge (Equivalent Currents Method)

The ECM [8] is a technique involving integrals of radiation. The source of diffracted field is attributed to the fictitious equivalent currents, both electric and magnetic, which flowing along the edge. The expressions given by Michaeli [7, 8] are used to determine the diffracted far-field by an edge, and are based on the fringe currents existing on the edge. These currents are calculated assuming the straight edge locally around each point of the considered contour. The diffracted field is then calculated by linear integration of the equivalent currents on the contour L of the edge:

$$\vec{E}_d \approx jk \int_L \left[Z_0 \vec{I} \vec{k}_s \times \left(\vec{k}_s \times \vec{t} \right) + \vec{M} \vec{k}_s \times \vec{t} \right] \frac{e^{-j\vec{k}\,\vec{r}}}{4\pi r}\, dl \tag{2}$$

where $\vec{t}$ is the unit vector tangent to the edge, $\vec{I}$ and $\vec{M}$ are respectively the electric and the magnetic currents given in [6].

3. MARINE TARGET OVER SEA SURFACE

The purpose of this section is to study the RCS of a complex target located in a rough sea surface [2]. The complexity of the target and multiple interactions between the target and a rough surface, as shown in [2], make the model more difficult to handle. So, before computing RCS of marine target, we must characterize and generate 2D sea surface. The 2D sea surface has been generated using Elfouhaily spectrum [3]. Then we generated a surface mesh with triangular facets and we made a projection of this surface to obtain a sea surface meshing on triangular facets as shown in Figure 4(a). Finally, a target will be introduced over this sea surface to obtain a global complex target (Sea+Target); an example of sea surface and its corresponding discretized surface is given in Figure 4(b).

(a) Triangular representation of sea surface (b) Target over sea surface

Figure 4: Example of marine scenario.

3.1. Geometrical and Physical Characterization of Sea Surface

The scattering of EM waves by sea surface requires knowledge of the physical and geometrical characteristics of seawater [2]. The physical parameters that characterize the sea surface are the magnetic permeability and dielectric constant. The relative magnetic permeability is unitary because we assume that the sea surface is not magnetic. The dielectric constant is calculated from the Debye model [11] and depends on frequency f, temperature T and salinity S of seawater. The

geometrical characterization of the sea surface can be done by the slopes distribution of rough surface. We chose in this work to characterize the surface by the Elfouhaily spectrum [3], established in 1997 from a synthesis of all works done since the 70 s. This model is semi-empirical and takes into account the fetch, speed and wind direction and the gravity and capillary waves.

4. NUMERICAL RESULTS AND VALIDATION

In order to validate our method, mono-static RCS of a Perfectly Conducting (PEC) plate is presented here. Then a PEC dihedral illustrates multiple scattering contributions. The model has been validated by measurement results only in the mono-static case. For the bi-static case, our results are also rather good compared to those published in the literature [2]. Another complex case as a box over a flat surface and a box target over sea surface are presented below in mono-static and bi-static configurations.

4.1. Rectangular Plate and Dihedral

Mono-static RCS of a square plate is calculated at $f = 10$ GHz and compared with measurements (in anechoic chamber) results for a square conducting plate with dimensions 15 cm $\times$ 15 cm in Figure 5(a), and a square perfectly conducting dihedral with the same dimensions is shown in Figure 5(b). Measurements and theoretical values provided by PO method are normalized to compare measurement results with the theoretical model. When the dihedral plate is normal to the axis of reception ($\pm 45°$), we find the main lobes of the RCS of a flat plate. Moreover, we observe that the level of the reflected signals of these lobes is more important than the multiple reflections occurring within the dihedral, while the theoretical model contradicts this finding.

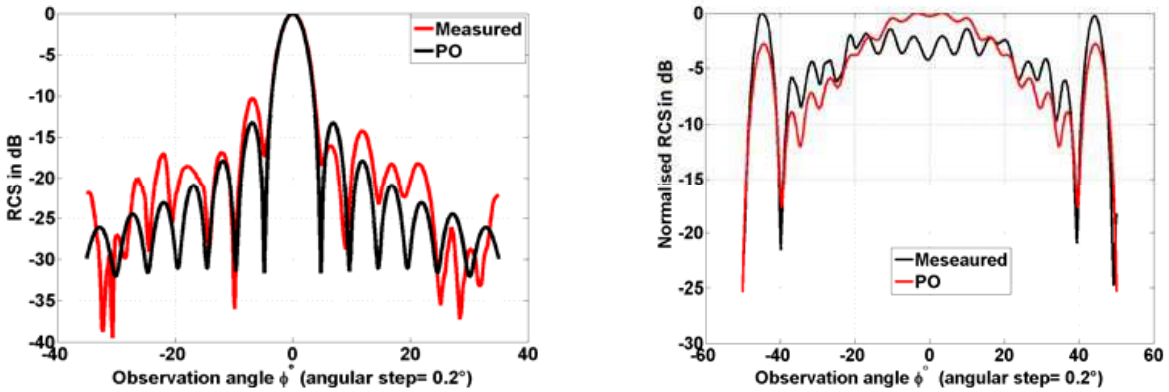

(a) (b)

Figure 5: Theory and measurements of normalized RCS for the square plate and dihedral. (a) Mono-static RCS of a square plate (PO and measurements). (b) Mono-static RCS of a square dihedral (GO-PO and measurements).

The computational time is not addressed in detail in this work, but as an example, for a dihedral of 5λ side, the mono-static RCS was calculated for a large number of facets (roughly 10^5) at a frequency of 10 GHz, and the cost time estimated with the method of moments is more than 3 hours against 1 minute with our model. All numerical calculations are carried out on a computer platform with a Microsoft Windows server 2003 operating system and Intel processor with a clock speed of 3 GHz, and a total memory of 4 GB.

4.2. Box Target over Plane Surface

As it is mentioned in [2], changes in the RCS of a complex target caused by a rough sea surface can be taken into account by studying the RCS of a target located in a flat surface. Indeed the surface of the sea at the local level in vicinity of the target tends to look like a flat plane [2]. Here, for monostatic RCS, we consider, a simple block of target of 1 m high by 1 m wide placed on positive x-axis extremity of rough sea surface of 5 m wide in y direction, and 20 m length in x direction as shown in Figure 6(a). Figure 6(b) illustrates another configuration for the computation of RCS in bistatic case. Mono-static and Bi-static RCS results are shown in Figures 7(a) and 7(b) respectively; as seen in these figures, the presence of target on the surface affects the scattered field, mostly in mono-static case for low elevation angles for which the scattering from sea clutter is small. These

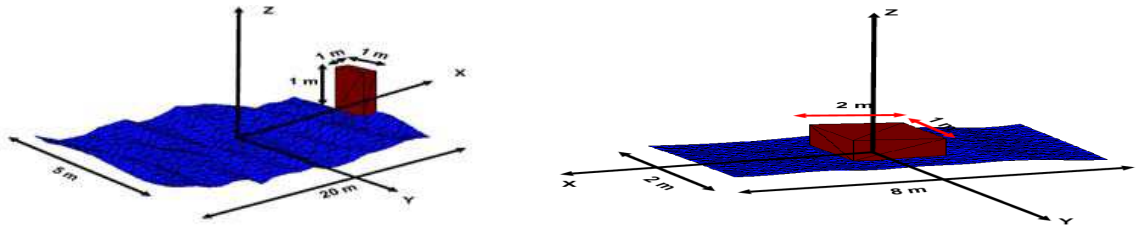

(a) (b)

Figure 6: Geometrical configuration (box over sea surface).

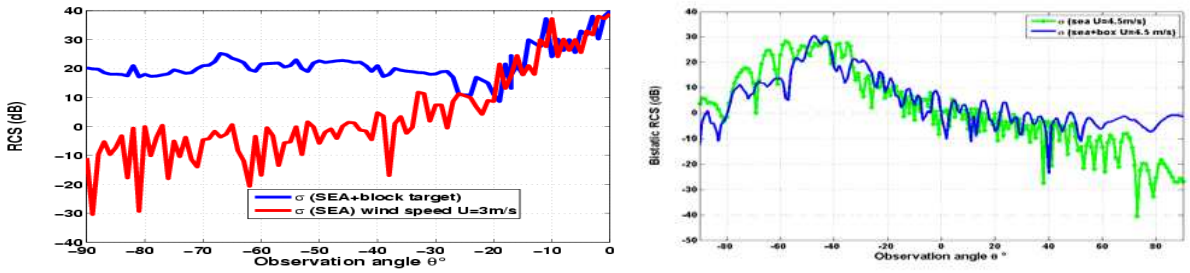

(a) (b)

Figure 7: (a) Mono-static and (b) Bi-static RCS of PEC box over rough sea surface at $f = 1\,\text{GHz}$.

simulations show a good agreement when compared with those performed by R. J. Burkholder et al. [2].

A more complex scene is presented by a generic boat Figure 8(a), and consists of boat of 10 m length in x direction, 3 m wide in y direction, and 5 m height in z direction, centered on a rough sea surface of 50 m length in x direction and 50 m wide in y direction. The physical characteristics of sea are temperature $T = 20°\text{C}$, salinity $S = 35$ ppt (part per thousand), and wind speed $U = 5\,\text{m/s}$. Bi-static RCS results are shown in Figure 8(b). The black curve shows the RCS of the generic boat only obtained with our model, compared to the blue curve obtained using EM simulation (FEKO software) [13]. Finally, the curves with red and green colours show respectively, the RCS of sea surface alone and the RCS of the marine scene composed with the generic boat and sea surface. We find that the RCS of the sea surface is predominant, and this is due to the choice of the sea surface dimensions which are quite large compared to those of the boat.

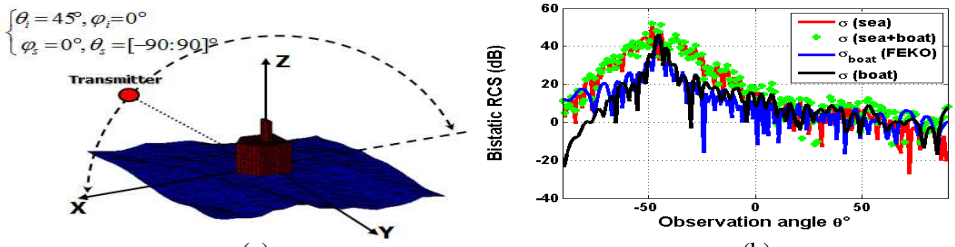

(a) (b)

Figure 8: Bi-static RCS of a PEC generic boat over 2D sea surface at $f = 10\,\text{GHz}$.

5. CONCLUSION

Combination of PO-GO and ECM methods for modelling the bi-static RCS of a complex target provides rather good results when compared with FEKO software (in bi-static configuration) and experimental measurements (in mono-static case), by taking into account the shadowing effects, double reflection and diffraction by edges. Total scattering, including multiple interactions between PEC target and rough sea surface, was computed using the PO-GO based approach where the Fresnel reflections coefficients are considered in the PO formulation to account for the dielectric aspect of sea surface. The computational time is not addressed in detail in this work, knowing

that the choice of asymptotic methods is justified by their ease of application and by reducing the computational time. Therefore it would be necessary to optimize the model in order to reduce this time.

The presented model provides a good estimation of the RCS. However, it seems possible to improve it by taking into account more scattering mechanisms such as the triple reflections contribution, to make the model more reliable, and by including the diffraction by dielectric edges. Other phenomena could be incorporated in the computational process such as edge-edge interactions, edge-surface and creeping waves on the target. Moreover, other applications of our method could be the radar imagery in bi-static representation and 3-D imagery representation.

REFERENCES

1. Xu, F. and Y. Q. Jin, "Bidirectional analytic ray tracing for fast computation of composite scattering from electric-large target over a randomly rough surface," *IEEE Transactions on Antennas and Propagation*, Vol. 57, 1495–1505, 2009.
2. Burkholder, R. J., P. Janpugdee, and D. Colak, "Development of computational tools for pre-decting the radar scattering from target on a rough sea surface," Tech. Rep., Ohio State University, 2001.
3. Elfouhaily, T., B. Chapron, and K. Katsaros, "A unified directional spectrum for long and short wind-driven waves," *Journal of Geophysical Research*, Vol. 102, 15–781, 1997.
4. Bennani, Y., F. Comblet, and A. Khenchaf, "RCS of complex targets: Original representation validated by measurements — Application to ISAR imagery," *IEEE Transactions on Geoscience and Remote Sensing*, Vol. 50, 3882–3891, Oct. 2012.
5. Moller, T. and B. Trumbore, "Fast, minimum storage ray-triangle intersection," *Journal of Graphics Tools*, Vol. 2, No. 1, 21–28, 1997.
6. Knott, F., F. Shaeffer, and T. Tuley, *Radar Cross Section*, Artech House, Boston, London, Sep. 1992.
7. Michaeli, A., "Elimination of infinities in equivalent edge currents Part 2: Fringe current components," *IEEE Transactions on Antennas and Propagation*, Vol. 34, No. 7, Jul. 1986.
8. Michaeli, A., "Equivalent edge currents for arbitrary aspects of observation," *IEEE Transactions on Antennas and Propagation*, Vol. 32, No. 3, Mar. 1984.
9. Youssef, N. N., "Radar cross section of complex targets," *Proceeding of the IEEE*, Vol. 77, No. 5, May 1989.
10. Griesser, T. and C. Balanis, " Backscatter analysis of dihedral corner reflectors using physical optics and the physical theory of diffraction," *IEEE Transactions on Antennas and Propagation*, Vol. 35, 1137–1147, 1987.
11. Cox, C. and W. Munk, "Measurement of the roughness of the sea surface from photographs of the suns glitter," *Measurement*, 1954.
12. Debye, P. J. W., *Polar Molecules*, 1929.
13. Available: http://www.feko.info.

Study on the Variation Characteristics of Land Desertification in Ebinur Lake Basin

L. S. Sun[1], **Y. T. Ma**[1, 2], **and H. Ding**[1]

[1]School of Civil Engineering, Shenyang Jianzhu University, Shenyang, China
[2]School of Resource & Civil Engineering, Northeastern University, Shenyang, China

Abstract— Desertification is one of the most serious problems of environment and social economy in the world today, which threats to human survival safety directly. In this paper, based on MODIS-NDVI data and dimidiate pixel model, we analyzed space distribution and change characteristics of desertification in Ebinur Lake Basin. Study results indicated the sandy desertification in most parts of Ebinur Lake Basin was mild and moderate desertifications which were always over the 60 percent of total area, the area of micro and non-desertification had been still transforming to the area of the severe, moderate and mild desertification.

1. INTRODUCE

Desertification refers to the land degradation in the arid, semi-arid and dry sub-humid areas due to various factors, including climatic variations and human activities. It has potentially impacted on 40% of global land area and 32% of population (United Nations Environment Agency, 1997), traveled over more than 100 countries on six continents in Asia, Africa, Australia, Europe, North America and South America. Global desertification area has added up to $3.56 \times 109\,\mathrm{km}^2$ and the economic losses due to desertification every year have amounted to \$42.308 billion (Lixian Wang, 1994) [1]. This showed that the monitoring and control of desertification has become a pressing problem. Desertification monitoring using satellite remote sensing research abroad began in 1970s, when people mostly adopted soil salinization and land retirement represented by the NVDI to indicate desertification [2–5]. For instance, the status of land desertification was evaluated by remote sensing method in Argentina. In the early 80s, China has started to do a survey of resource on land desertification by using remote sensing technology. Zhu et al. did a research on the dynamics desertification in Khorchin region by the aerial photo in 1975 and the TM images of 1987–1988 [6]. During 1984–1986, the Ministry of Water Resources Center organized a national survey of soil erosion by remote sensing. Based on MODIS-NDVI data in August 2006, 2009 and 2012 and dimidiate pixel model [7], the vegetation coverage was estimated in this paper. Furthermore, the land sandy desertification in Ebinur Lake Basin was also processed to reflect the dynamic changes of desertification in last 6 years, which offered decision support for regional ecological environment assessment and sustainable development.

2. DATA AND PROCESSING

2.1. Investigation Area

Xinjiang Ebinur Lake wetland is located in the border between China and kazakhstan, nest to the international port of ala mountain running from east longitude $79^\circ 53'$ to $85^\circ 02'$ and north latitude $43^\circ 37'$ to $45^\circ 55'$. It covers 2800 square kilometers of wetland around Ebinur. Ebinur Lake wetland is the lowest bottomland depressions of southwestern margin of the Junggar Basin and salt water collection center, is the largest salt water lake in Xinjiang. Because of particular geographical location and characteristics of topography various types of desertification exist in the region. Taking into account the specific characteristics of desertification, the integrity of the study area and the resolution of image, we determined that the scope of the study area covers the entire Bortala Mongol Autonomous Prefecture including Jing he, Bole and Wenquan counties.

2.2. Data

In this paper, the data of NDVI (MOD13A3) come from NASA Earth Observation System (EOS) at a time resolution of the month and a space resolution of 1 km. The time was respectively in August in 2006, 2009 and 2012. The range was from east longitude $79^\circ 53'$ to $85^\circ 02'$ and north latitude $43^\circ 37'$ to $45^\circ 55'$.

2.3. Data Processing

Through image projection conversion, subsetting, mosaicing, stacking and other steps, NDVI data were acquired. Then we calculated the vegetation coverage by the following formula:

$$f_g = (\mathrm{NDVI} - \mathrm{NDVI}_{\min}) / (\mathrm{NDVI}_{\max} - \mathrm{NDVI}_{\min})$$

Among them: f_g is vegetation coverage, NDVI is Normalized Difference Vegetation Index, $\mathrm{NDVI}_{\min}$ is the smallest vegetation index in images, generally which is the minimum value of bare land pixels. $\mathrm{NDVI}_{\max}$ is the maximum vegetation index in images, generally which is the maximum value of pure vegetation cover pixels.

3. RESEARCH RESULT

3.1. Spatial Distribution of Land Desertification

According to the standard of soil erosion and desertification indicator developed by Z. D. Zhu and others, the study area in this paper was in line with the prerequisite of standard developed by them, so we applied the desertification indicator to classify land in Ebinur areas (Table 1).

According to the indicator of desertification, the desertification thematic figures were shown in Figure 1 and percents of desertification level were listed in Table 2 in 2006, 2009 and 2012 respectively.

It could be seen that from the figure and table, the desertification in the study area mainly were mild, moderate and not desertification. During 2006 and 2012, moderate and micro desertification land area were in a case of reduction followed by increase. There was a larger proportion of moderate

Table 1: Remote monitoring indicators of desertification in Ebinur Lake area (Bole).

Table 1 Remote monitoring indicators of desertification in Ebinur Lake area (Bole)

Desertification grades [legend]	Not [ ]	Micro-degree [ ]	Mild [ ]	Moderate [ ]	Serious [ ]
Vegetation coverage	Water or vegetation cover > 80%	60%–80%	30%–60%	10%–30%	10%

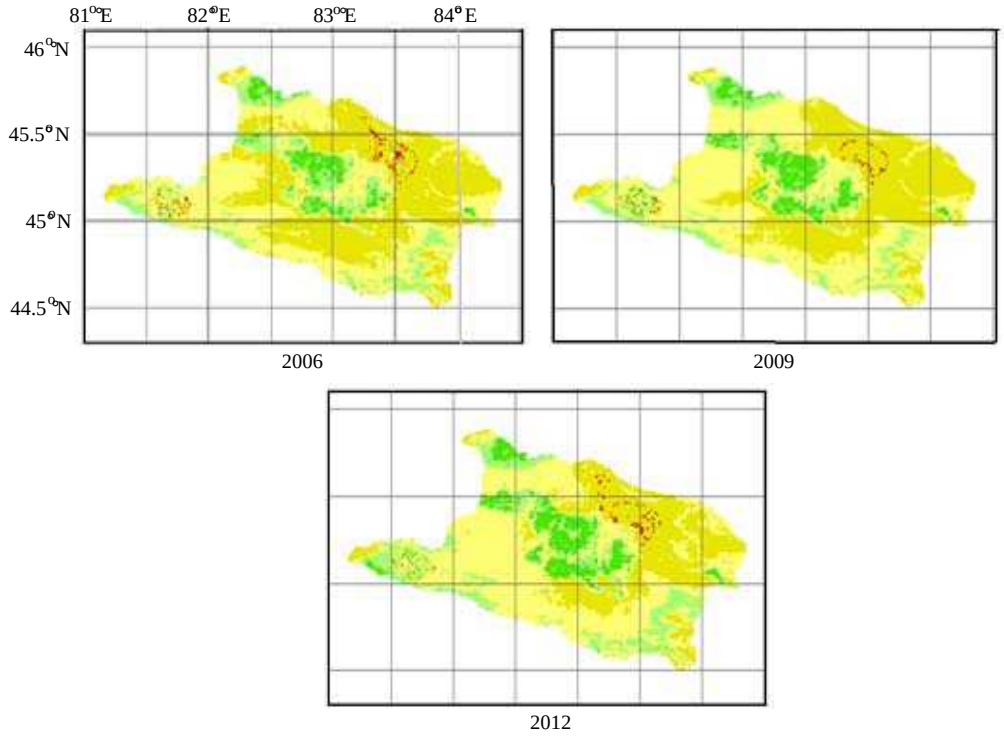

Figure 1: Spatial distribution of land desertification (legend in Table 1).

and mild desertification land in the research area indicating that the difficulty of desertification control in the Ebinur Lake region was still very great.

3.2. Land Desertification Type Transformation

In order to study the construction of land desertification transformation in Ebinur Lake (Bole) region, two phases of RS classification diagram were performed the operation of subtract in ERDAS, generating the distribution figure of desertification type changes and desertification conversion degree tables. Because of limited space, only statistics of desertification conversion types in 2006 and 2009 was listed in Table 3.

It could be perceived from Table 3 that between 2006 and 2009 there were 51.358% of the land turning from micro-desertification to not desertification, 4.3011% converting from micro-desertification into mild desertification, 1.5697% transforming from mild desertification to moderate desertification, 1.0119% truning from mild desertification to micro-desertification, 1.358% switching from moderate desertification to serious desertification, 15.4541%, 17.6742%, 4.1512% and 1.9026% of the land respectively remaining the original micro, mild, moderate and serious desertification degree with no change.

3.3. Annual Variation Rate of Land Desertification Change

This study described the rate of change of land desertification in the Ebinur region on the method of calculating the variation rate of land use and compute the variation and the annual variation

Table 2: Statistics of desertification grades.

Desertification grades	2006		2009		2012	
	Pixel numbers	Percentage	Pixel numbers	Percentage	Pixel numbers	Percentage
Severe Desertification	1090	2.4060	680	1.4991	990	2.1846
Moderate Desertification	23402	51.5917	20592	45.3965	17453	38.4771
Mild Desertification	10937	24.1116	9252	20.3968	10282	22.6675
Micro-degree Desertification	2827	6.2302	1555	3.4281	1905	4.1977
Not Desertification	7104	15.6605	13281	29.2795	14730	32.4731

Table 3: Statistics of desertification conversion types from 2006 to 2009.

Conversion types	Pixel gray value	Pixel numbers	Percentage	Desertification types	Pixel gray value	Pixel numbers	Percentage
Severe-Not	16	1	0.0022	Micro-degree -Mild	126	1951	4.3011
Moderate-Not	24	5	0.011	Severe- Moderate	240	91	0.2006
Mild-Not	28	11	0.0243	Moderate	248	1883	4.1512
Micro-degree-Not	30	23296	51.358	Mild-Moderate	252	712	1.5697
Moderate-Micro-degree	56	15	0.0331	Micro-degree-Moderate	254	40	0.0882
Mild-Micro-degree	60	459	1.0119	Severe	496	863	1.9026
Micro-degree	62	7010	15.4541	Moderate-Severe	504	616	1.358
Severe-Mild	112	7	0.0154	Mild-Severe	508	53	0.1168
Moderate-Mild	120	307	0.6768	Micro-degree-Severe	510	23	0.0507
Mild	124	8017	17.6742				

Table 4: Comparison of desertification area in different grades.

Desertification grades	2006 (km^2)	2012 (km^2)	Variation (km^2)	Annual Rate (%)
Not Desertification	12844.270	12815.739	−28.531	−0.037%
Micro-degree Desertification	4894.678	3108.166	−1786.512	−6.083%
Mild Desertification	5077.987	6002.824	924.837	3.035%
Moderate Desertification	1551.071	1922.220	365.149	3.924%
Severe Desertification	527.994	1045.059	517.065	16.322%
Total	24896	24894.008	−1.992	

rate of different desertification area amount in different study periods from 2006 to 2012, a positive value indicating the level of desertification area increase and a negative value indicating decrease. Results as shown in Table 4.

As was very clear from Table 4 that compared with 2006, in 2012, severe, moderate and mild desertification area was increasing while micro-desertification and not desertification was decreasing, of which serious desertification area was the most significant change that the area added 517.065 square kilometers in six years in an annual rate of 16.332%. In the meantime, micro-desertification area decreased 1786.512 square kilometers in the annual rate of −6.083% and the not desertification area had slight decrease. These showed that not desertification and micro-desertification was developing in the direction of mild, moderate and serious desertification. So from an overall point of view, the degree of desertification in the Ebinur Lake region was increasing.

4. CONCLUSIONS

In this thesis, during the process of desertification monitoring in the Ebinur Lake region, we found that the land desertification of Ebinur Lake region (Bole) region mainly dominated by moderate and mild desertification whose sum is always more than 60% of the total land area per year. More than 50% land converted from micro-desertification to not desertification from 2006 to 2009 and 2009 to 2012. Comparing with 2006, in 2012, serious, moderate and mild desertification area is increasing while micro-desertification and not desertification is decreasing, of which serious desertification area is the most significant change that the area added 517.065 square kilometers in six years in an annual rate of 16.332%. In the meantime, micro-desertification area decreased 1786.512 square kilometers in the annual rate of −6.083% and the not desertification area had slight decrease. These show that not desertification and micro-desertification is developing in the direction of mild, moderate and serious desertification. Overall study results indicate that the area of desertification land is on the decline but the type conversion structure shows that the strength of desertification is in the constant development stages. Thus, these prevention and treatment recommendations are provided in this thesis as follows: 1. Ensure the Ebinur Lake area of the waters. 2. Comprehensive management of Ebinur Lake wetland nature reserve. 3. Firm control the blind expansion of arable land and mining digging. 4. Reasonable irrigation and water conservation.

REFERENCES

1. Wang, L. X., "The state of control and tendency of development of the global desertification," *World Forestry Research*, Vol. 1, 10–17, 1994.
2. Li, X. Y., B. Zhang, and Z. B. Jin, "Dynamic monitoring of vegetation coverage based on MODIS-NDVI in Hedong area of Gansu Province," *Research of Soil and Water Conservation*, Vol. 20, No. 1, 16–58, 2013.
3. Tian, J. Q. and X. J. He, "Progress vegetation index advances in earth science," *Advances in Earth Science*, Vol. 13, No. 4, 327–333, 1998.
4. Sheng, Y. W., W. Y. Chen, and Q. G. Xiao, "Macroscopic classification of vegetation in China by vegetation index from weather satellite," *Chinese Science Bulletin*, Vol. 40, No. 1, 68–71, 1995.
5. Xiong, L., K. Q. Yan, L. Wu, and W. J. Huang, "Vegetation cover variation analysis of NDVI sequence image in growing season of Urumqi region," *Desert and Oasis Meteorology*, Vol. 5, No. 6, 54–58, 2011.
6. Zhu, Z. D., "The concept, causes and prevention of desertification in China," *Quaternary Sciences*, Vol. 2, No. 6, 145–155, 1998.
7. Lin, Z. R., Y. G. Feng, and G. J. Yang, "Estimation method commentary of vegetation coverage based on remote sensing," *Remote Sensing Technology and Application*, Vol. 24, No. 6, 233–258, 2009.

Analysis of EVI and NDVI Characteristics in Different Land Cover Types in Liaoning Province

J. L. Wang[1], **Y. T. Ma**[1, 2, *], **and L. S. Sun**[1]

[1]School of Civil Engineering, Shenyang Jianzhu University, Shenyang, China
[2]School of Resource & Civil Engineering, Northeastern University, Shenyang, China

Abstract— For four types of land cover in Liaoning province, the variations of their EVI and NDVI basing on MODIS data in time series were studied in this paper. The result can offer a method of monitoring land cover types. The characteristics of EVI and NDVI from four kinds of land cover, including woodland, cropland, water and urban area, were analyzed by the data statistics method whose data were from 16 regions of interest in Liaoning province basing on 2012 MODIS data. In the woodland coverage areas, the shape of their NDVI and EVI in time series looked like a bell-shaped curve in the period of forests turning green and growing, NDVI was prone to become saturated, and could not show the growth process of trees while EVI could better do that. In the cropland coverage area, the shape of their NDVI and EVI in time series looked like an inverted V-shaped curve in the period of crops growing season. In the water coverage areas and urban areas, the values of their NDVI and EVI were slightly higher in the summer than other seasons, and the annual variation range of their NDVI and EVI was small. In the cropland coverage areas, both NDVI and EVI could well show the process of vegetation growth. In the water coverage areas and urban areas, NDVI sensitively was influenced by noise, while EVI could overcome this shortcoming. The curves shape of NDVI and EVI under different land cover types is of great significance for vegetation classification and extraction in Liaoning province. The figures characteristics of NDVI and EVI indicate that EVI can well monitor the growth of forest in the woodland coverage areas, both NDVI and EVI can monitor the growth of crops in the cropland coverage area, and EVI can well monitor the growth of vegetation in the water coverage areas and urban areas.

1. INTRODUCE

The vegetation information on remote sensing image can be reflected by vegetation indexes, EVI and NDVI are two of those vegetation indexes wide used. At present, those two vegetation indexes are applied to a variety of fields, such as vegetation classification, crop yield estimation, land cover change, relationship of the soil moisture content and the rainfall, ecological environment monitoring, foreign scholars early started to study the vegetation information by vegetation indexes and had got a lot of achievements. After Huete et al. studied vegetation index product, they found that EVI and NDVI of the biotic formation in different regions were sensitive to seasonal change, land cover change and biophysical parameters change [1]. Huiqing Liu and Huete demonstrated that NDVI was highly relevant to EVI and the value of NDVI was always bigger than EVI when the soil background and the atmospheric aerosol vary less. Domestic research on those two vegetation indexes is in the beginning. Wang Zhengxing and Liu Chuang et al. demonstrated that EVI overcame drawbacks of NDVI and improved linear relation between vegetation index and vegetation density [2]. Cheng Qian and Huang Jingfeng et al. analyzed the vegetation indexes based on MODIS in Zhejiang Province and Xianju County, and the result showed that comparing to NDVI, EVI was prone to lower value, normal distribution, uneasy to be saturated and suitable for monitoring high biomass groups [3].

The vegetation indexes are often affected by a lot of factors such as climate, geographic positions, soil, atmospheric reflectance, sensors etc. Therefore, it is necessary to choose the vegetation indexes which are less affected by those factors in application. In this paper the characteristics of two vegetation indexes in time series and the relationship of them in different land cover types in Liaoning Province were studied. The result could provide a method of monitoring dynamically vegetation in Liaoning Province.

2. DATA AND PROCESSING

2.1. Research Area

Liaoning Province locates in the east coast of Eurasia and belongs to temperate continental monsoon climate zone. Because of the complicated terrain, including mountain land, plain, hills area

*Corresponding author: Yuntao Ma (mayuntao7@163.com).

and coastal land, each region has its own climate in Liaoning Province. The general climate characteristics are: long cold period, strong plain wind, wet east and dry west, concentrated rainfall, abundant sunshine, four distinctive seasons. In order to study the characteristics of NDVI and EVI in different land covers, four types of typical land cover (woodland, plowland, water and urban area) were chose to study with four regions as samples respectively. The distribution and types of land cover were showed in Table 1.

Table 1: Sample area.

land cover type	Sample area
woodland	Qingshan gou, Toudao gou, Daheishan, Bingyu gou
plowland	Beisijiazi, Beiwanzi, Houliu cun, Zhaojiawo bao
water	Baishi reservoir, Hunhe river, Gadalou reservoir, fengchengyulong lake
Urban area	Shenyang, Liaoyang, Dalian, Huludao

2.2. Data

Vegetation index consists of red and infrared light reflectance in accordance with spectral reflectance characteristics of green plants, and it is simple and effective to monitor vegetation cover and its growth conditions. NDVI is dimensionless data by operation among spectral channels and is empirical or semi empirical index on vegetation. Its expression is as follow:

$$\mathrm{NDVI} = \frac{\rho_{nir} - \rho_{red}}{\rho_{nir} + \rho_{red}} \tag{1}$$

For MODIS data, ρ_{nir} and ρ_{red} are the 2nd and 1st MODIS spectral reflectance data respectively [4–7]. According to the statistics of NDVI, the areas of low vegetation cover are more sensitive and the areas of high vegetation cover are prone to be saturated. Moreover, NDVI is easily affected by atmospheric noise and soil background. However, EVI corrected the surface reflectance to be more sensitive to high biomass and took advantages of coupling canopy background signal as well as reducing atmospheric influence to improve the precision of vegetation monitoring. Its expression is as follow:

$$\mathrm{EVI} = 2.5 \times \frac{\rho_{nir} - \rho_{red}}{L + \rho_{nir} + C_1\rho_{red} - C_2\rho_{blue}} \tag{2}$$

ρ_{blue} is the reflectance of blue band referring to 3rd band reflectance of MODIS. L is the parameter of soil regulating, its value is 1. C_1 is the calibration parameter of red light, its value is 6. C_2 is the calibration parameter of blue light, its value is 7.5 [8, 9].

In this paper, the data were MODI13A2 at a time resolution of 16 days and a space resolution of 1 km in 2011. There were 23 periods of processed vegetation index data.

2.3. Processing

Through image projection conversion, subsetting, mosaicing, stacking and other steps, NDVI and EVI data in Liaoning Province were acquired, and were spotted together in time series. The correlations of NDVI and EVI in woodland, plowland, water and urban area were counted and analyzed.

3. RESULT ANANLYSIS

Linear correlation between NDVI and EVI were shown in Table 2, R^2 represents correlation coefficient of two vegetation indexes. Seasonal time sequence of vegetation index were studied and only one of each kind (woodland, cropland, water, urban) was shown in Figures 1, 2, 3, 4, where the horizontal axis and the vertical axis represent time and two vegetation indexes values respectively. From Table 2, we could find that linear correlation of between NDVI and EVI in woodland and cropland higher, while in urban area and water lower.

3.1. Features of Vegetation Indexes in Woodland

Figure 1 showed that the value of NDVI was higher than EVI in woodland of Liaoning, both reflected responsively the vegetation growth condition in woodland with seasons change and were in a same trend and looked like bell-shaped curve that were changed with the season obviously. In the 97th day to the 129th day, that EVI and NDVI grew rapidly indicated that the process of

Table 2: The linear correlation of two vegetation index.

sample	correlations	R^2	Land cover types
Qingshangou	$y = 0.921x + 0.279$	0.888	Woodland
Toudaogou	$y = 1.328x + 0.112$	0.923	Woodland
Daheishan	$y = 1.251x + 0.173$	0.932	Woodland
Bingyugou	$y = 1.189x + 0.164$	0.951	Woodland
Beisijiazi	$y = 1.488x + 0.014$	0.973	Plowland
Beiwanzi	$y = 1.636x + 0.032$	0.980	Plowland
Houliucun	$y = 1.528x + 0.061$	0.941	Plowland
Zhaojiawobao	$y = 1.416x + 0.016$	0.966	Plowland
Baishireservoir	$y = 3.963x - 0.004$	0.602	Water
Hunhe river	$y = 1.774x - 0.043$	0.612	Water
Gedalou reservoir	$y = 1.781x - 0.041$	0.799	Water
Fengchengyulong lake	$y = 2.686x - 0.003$	0.583	Water
Shenyang	$y = 2.185x + 0.023$	0.874	Urban area
Liaoyang	$y = 1.739x + 0.027$	0.872	Urban area
Dalian	$y = 0.839x + 0.104$	0.528	Urban area
Huludao	$y = 1.533x + 0.026$	0.847	Urban area

vegetation re-becoming green was obvious. In the 129th to the 273th day, that EVI and NDVI were stable comparatively indicated that the woodland was in the period of flourishing. In the 177th day to the 193rd day, there was a peak of EVI while the transition of NDVI was smooth without fluctuation, the phenomenon indicated that in the period of woods flourishing, NDVI was easy to be saturated and could not reflect the growth situation of vegetation significantly, while in other time NDVI was sensitive and fluctuated more evidently than EVI.

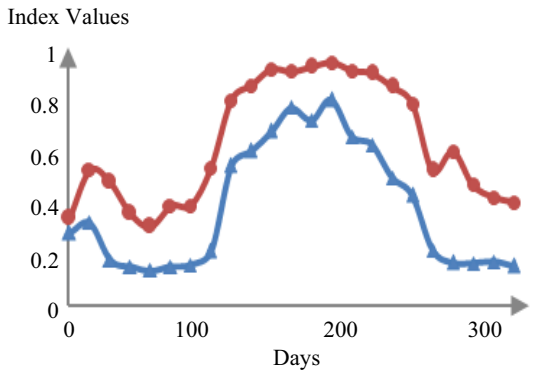

Figure 1: Qingshan gou woodland.

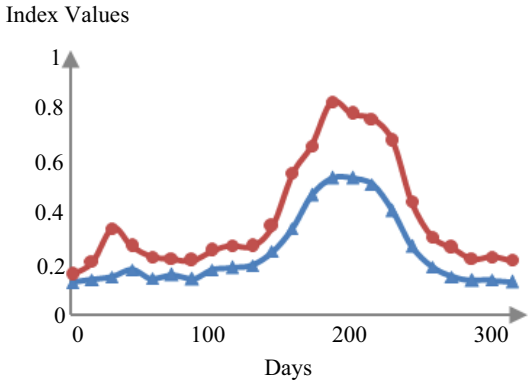

Figure 2: Beisijiazi farmland.

3.2. Features of Vegetation Indexes of Cropland

From Fig. 2, we could find that: In the croplands of Liaoning province, the value of NDVI was always higher than EVI; Both of the two vegetation indexes were V-shaped curve and had same variation tendency; Both of the two vegetation indexes reflected the process of vegetation growth compared to the woodland, EVI and NDVI of croplands increased rapidly one month later. In the 129th to the 193rd the increase of EVI and NDVI were comparatively rapid but gentle compared to the woodland. It indicated that the corps was in the period of growth. When EVI and NDVI reach to the peak, then they decreased rapidly rather than fall slowly. It indicated that the corps had a short period of flourishing

3.3. Features of Vegetation Indexes of Water

From Fig. 3, we could find that in the 129th day to the 257th day, both of the two vegetation indexes were higher than any other time and the values of them were positive. It indicated that the values

had something with water chlorophyll at that time in the period, NDVI fluctuated dramatically at some points. It indicated that NDVI was greatly affected by noise, but EVI was comparatively gentle and less affected by noise. In the other time, the value of EVI and NDVI fluctuated around zero and most of the values were negative.

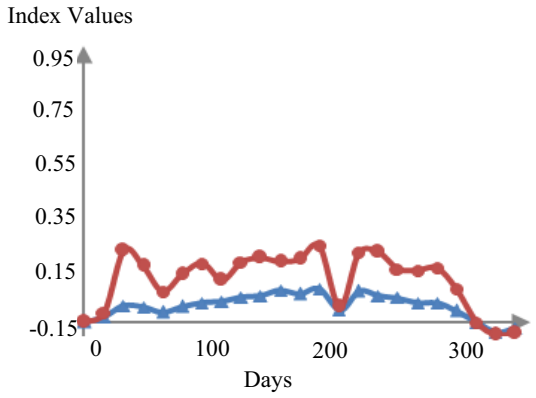

Figure 3: Baishi reservoir.

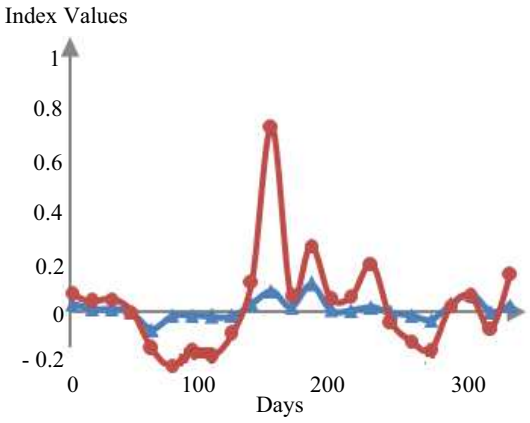

Figure 4: Shenyang.

3.4. Features of Vegetation Indexes of Urban Area

From Fig. 4, we could find that both of the vegetation indexes were lower than plowland and woodland. At some points NDVI fluctuated dramatically, it indicated that when detecting urban area, NDVI was affected by noise greatly, while EVI overcame the shortcoming well.

4. CONCLUSIONS

1. In Liaoning province, NDVI and EVI of woodland show bell-shaped curve, NDVI and EVI of plowland show inverted V-shaped curve, NDVI and EVI of water don't show specific curve, while NDVI and EVI of urban area show arc curve. So the curve shape of NDVI and EVI in different land cover is of significant importance for vegetation classification and extraction.

2. In Liaoning province, the period of trees turned green is in early April to early May, the period of trees flourishing is in early May to early October. The period of corps growing is in early May to middle of July and the period of corps flourishing is short.

3. In the period of trees flourishing, NDVI is prone to be saturated while EVI can overcome it well so as to monitoring the growth of trees. In the period of corps growth, both of the vegetation indexes can reflect the process of corps growth well. In the water and urban area, NDVI is easy to be affected by noise while EVI can overcome it and monitor the growth of vegetation well.

REFERENCES

1. Huete, A., K. Didan, and T. Miura, "Overview of the radiometric and biophysical performance of the MODIS vegetation indices," *Remote Sensing of Environment*, Vol. 83, No. 1, 195–213, 2002.
2. Wang, Z. X., C. Liu, and A. Huete, "From AVHRR-NDVI to MODIS-EVI: Advances in vegetation index research," *Acta Ecologica Sinica*, Vol. 23, No. 5, 979–987, 2003.
3. Cheng, O., J. F. Huang, and Wang R. C., "Preliminary analysis of difference between MODIS and NOAAI AVHRR vegetation indices," *Bulletin of Science and Technology*, Vol. 21, No. 2, 205–209, 2005.
4. Matsushita, B., W. Yang, and Chen J., "Sensitivity of the enhanced vegetation index (EVI) and normalized difference vegetation index (NDVI) to topographic effects: A case study in high-density cypress forest," *Sensors*, Vol. 7, No. 11, 2636–2651, 2007.
5. Schucknecht, A., S. Erasmi, and I. Niemeyer, "Assessing vegetation variability and trends in north-eastern Brazil using AVHRR and MODIS NDVI time series," *European Journal of Remote Sensing*, Vol. 46, No.1, 40–59, 2013.
6. Caroline, P., M. Lewis, and D. White, "Monitoring temporal dynamics of Great Artesian Basin wetland vegetation, Australia, using MODIS NDVI," *Ecological Indicators*, Vol. 34, No. 11, 41–52, 2013.

7. Cui, X. L., J. Zhang, and H. H. Y. Bai, "Analysis of vegetation cover change in Shanxi Province based on modis NDVI," *Journal of Northwest A&F University: Natural Science*, Vol. 41, No. 5, 1–7, 2013.
8. Nicholas, C., J. Rogana, and Z. Christman, "Modelling dry season deciduousness in Mexican Yucatán forest using MODIS EVI data," *GIScience & Remote Sensing*, Vol. 50, No. 1, 26–49, 2013.
9. Yudi, S. and K Yoshino, "Detecting land-use change from seasonal vegetation dynamics on regional scale with MODIS EVI 250-m time-series imagery," *Journal of Land Use Science*, Vol. 1, No. 7, 243–248, 2012.

Minkowski Fractal Antenna Design with DMS-SRR and DGS-SRR Structure for WLAN Application

H. Nornikman[1,2], F. Malek[1], M. H. F. Mohd Fakri[1], M. Z. A. Abd Aziz[2], and B. H. Ahmad[2]

[1]School of Computer and Communication, Universiti Malaysia Perlis, Perlis, Malaysia
[2]Center for Telecommunication Research and Innovation (CeTRI)
Faculty of Electronics and Computer Engineering
Universiti Teknikal Malaysia Melaka, Durian Tunggal, Melaka, Malaysia

Abstract— Nowadays, the high gain and compact antennas are the most common issue that commonly considered by many researchers in the telecommunication area, especially in antenna design. There are many types of microstrip patch antenna had been researching to cater this problem. This paper is focused on the combination of defected microstrip structure of split ring resonators (DMS-SRR) and defected ground structure of split ring resonators (DGS-SRR) on the ground plane. The proposed DMS-SRR structure effect to wider the bandwidth and also increase the gain of the Minkowski fractal patch antenna. The other technique used in this design is a double layer substrate of FR-4 to improve the gain of the antenna. This double layer effect to increase the Minkowski fractal antenna gain to 3.827 dB, but it shifted the resonant frequency to 2.634 GHz. The DGS-SRR structure used to shift back the resonant frequency to 2.4 GHz region. Other parameters that had been considered in this work are return loss, radiation pattern and surface current. The first work is started by designing a normal Minkowski patch antenna. Then, three units of DMS-SRR had been added to the front side of the Minkowski fractal antenna. After that, a pair of DGS-SRR had been added to the ground plane of the antenna. The resonant frequency of this antenna is 2.4 GHz used for wireless LAN (WLAN) application. The proposed antenna capability to improve the antenna gain from 2.445 GHz to 3.650 GHz while the bandwidth is improving from from 69.00 MHz (2.368 GHz to 2.437 GHz) to 129.90 MHz (2.407 GHz to 2.537 GHz).

1. INTRODUCTION

In the recent day, the high gain and miniaturize patch antennas are the most common issue that had been focusing by many researchers in the telecommunication sector. There are many techniques can matter this problem such as using array patch, slots, dielectric resonator, metamaterial and fractal geometry structure in their design. In 1968, Veselago had been introduced the combination of the conducting wire and split ring resonator structure into his design [1]. This theory had been applied by Pendry work in 1999 [2] and Smith work in 2000 [3]. In literature, the metamaterial is the artificial material that had been implemented to miniaturize the patch antenna size by reducing the resonant frequency. Split ring resonator (SRR) [4, 5] is an example of a left handed material (LHM) in a metamaterial structure group beside photonic band gap (PBG) [6], electronic band gap (EBG) [7] and artificial magnetic conductor (AMC) [8]. There are many works that apply the defected microstrip structure (DMS) [9, 10] , defected ground structure (DGS) [11, 12] and defected stripline structure (DSS) [13, 14] on their work.

The term of fractal was originally introduced by Mandelbrot [15]. Fractals are generally composed of multiple copies of the similarity structure with different scale and size. Minkowski design is one of the popular fractal that had been used. The other examples of fractal geometry that use in antenna design are Koch, Sierpinski, Hilbert. This fractal design such as Minkowski can provide a multiband effect and also significantly can miniaturize the patch antenna design by reducing the resonant frequency [16]. The Minkowski design is based on a square, rectangular or triangular generator structure [17].

2. ANTENNA DESIGN

The complementary structure of defected microstrip structure SRR (DMS-SRR) had been attached at the upper part of the FR-4 substrate. It consists a combination of two main parts — straight line part and spiral part. The location of this complimentary DMS-SRR is at the center of the modified Minkowski patch antenna, based on this paper [18]. Figure 1(a) shows the single unit and the DMS-SRR structure. The dimensions of the DMS-SRR are SRR width, $W_{s1} = 1.13$ mm, SRR length, $L_{s1} = 1.78$ mm while SRR gap, $G_s = 0.16$ mm. Figure 1(b) and Table 1 shows the first

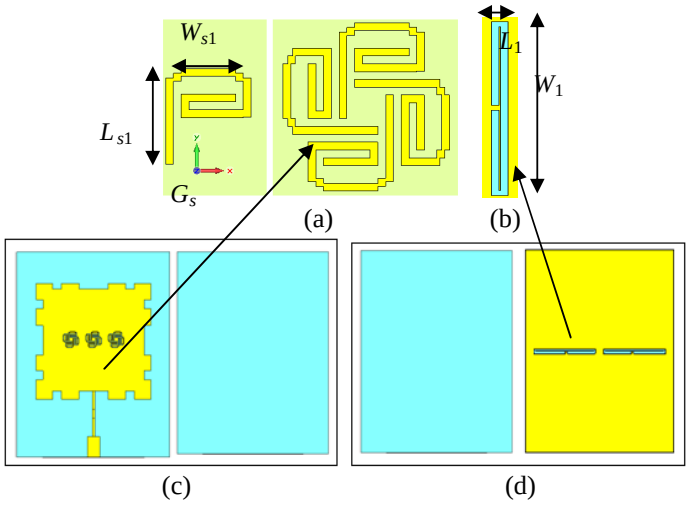

Figure 1: (a) DMS-SRR structure. (b) DGS-SRR structure. (c) 3-N DMS-SRR Minkowski antenna (first layer). (d) 3-N DMS-SRR Minkowski antenna with DGS-SRR structure on the ground (second layer).

layer of proposed antenna that contain Minkowski patch antenna with feedline. The dimension of this antenna is patch width, W_p and patch length, $L_p = 28.866$ mm, feedline width, $W_f = 2.81$ mm and feedline length, $L_f = 14.5$ mm. Figure 1(c) shows the second layer of antenna that contain a defected ground structure SRR (DGS-SRR). Figure 1(d) represents the DGS-SRR with dimension of 14 mm width, $W_1 \times 1.9$ mm length, L_1.

There are five stages of development of the proposed antenna, the initial stage (S_0) is a single layer of the Minkowski antenna without any SRR structure. The first stage (S_1), second stage (S_2) and third stage (S_3) is the addition of 1-N DMS-SRR, 2-N DMS-SRR and 3-N DMS-SRR. All three design is single layer with ground plane at the back. The fourth stage (S_4) is the double layer 3-N DMS-SRR antenna with ground plane while the fifth stage (S_5) is the double layer 3-N DMS-SRR with a pair DGS-SRR at the ground plane.

3. RESULT

Figure 2(a) and Table 1 compare the return loss of Minkowski patch antenna (S_0) and the DMS-SRR Minkowski patch antenna design (S_1, S_2, and S_3) in CST Microwave Studio simulation software. The resonant frequency, f_r for this normal Minkowski antenna is 2.402 GHz with -47.990 dB of return loss performance. The bandwidth of this antenna is 69.0 MHz in the frequency range between lower frequency limit, f_L and higher frequency limit, f_H. The value of $f_L = 2.368$ GHz while the $f_H = 2.437$ GHz. The return loss of the DMS-SRR Minkowski antenna had been worst the return loss value to -26.761 dB, -31.106 dB and -26.072 dB respectively. This DMS-SRR structure had been functioning to shifting the frequency into the lower frequency tan the normal Minkowski antenna. It shows that, the addition of 2-N DMS-SRR structure can be shifted to the resonant frequency from 2.402 GHz to 2.392 GHz. This is can be a potential technique to reduce the size

Table 1: Minkowski patch performance with different number of QPS-SRR.

Antenna Design	**Resonant frequency (GHz)**	**Return loss (dB)**	**Bandwidth (MHz)**	**Gain (dB)**
Normal Minkowski	2.402	−47.990	69 (2.368–2.437)	2.445
1-N DMS-SRR	2.404	−26.761	66 (2.372–2.438)	2.573
2-N DMS-SRR	2.392	−31.106	65 (2.359–2.424)	2.536
3-N DMS-SRR	2.394	−26.072	65 (2.362–2.427)	2.540
3-N DMS-SRR (double layer, without DGS-SRR)	2.634	−21.013	120.3 (2.575–2.695)	3.827
3-N DMS-SRR (double layer, with DGS-SRR)	2.410	−23.695	129.90 (2.407–2.537)	3.650

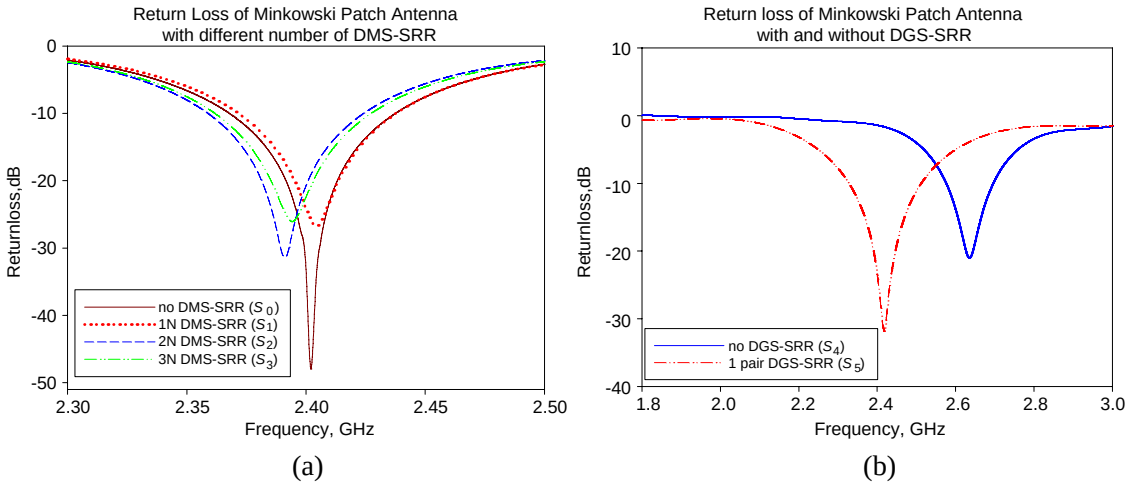

Figure 2: (a) Return loss of Minkowski patch antenna with different number of QPS-SRR. (b) Return loss of Minkowski patch antenna with different number of SF-SRR at the ground plane.

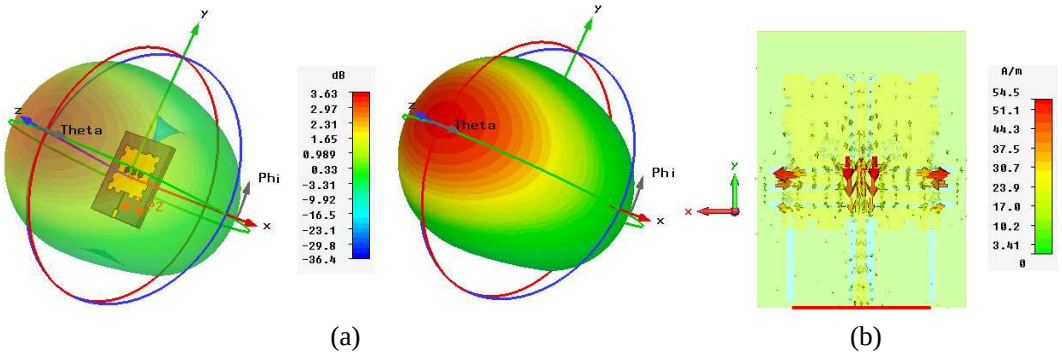

Figure 3: (a) The gain performance of the 3-N DMS-SRR Minkowsi patch antenna with a pairs DGS-SRR at the ground. (b) The surface current flow of the 3-N DMS-SRR Minkowsi patch antenna with a pairs DGS-SRR.

of the antenna. It also can improve the gain performance from 2.445 dB for normal Minkowski antenna to 2.573 dB.

In Figure 2(b), the fourth stage and fifth stages of the antenna had been compared its return loss performance. This double layer technique potentially to improve significantly the gain of the antenna from 2.445 GHz to 3.827 GHz. The problem a is the resonant frequency had been shifted from 2.402 GHz to 2.634 GHz. So, it had settled up by adding the DGS-SRR at the ground plane. It shows that the frequency had been shifted back to the 2.410 GHz by adding of DGS-SRR structures.

Figure 3 shows the performance gain of the 3-N DMS-SRR Minkowsi patch antenna with a pairs DGS-SRR at the ground while Figure 9 shows the surface current flow of the 3-N DMS-SRR Minkowsi patch antenna with 6 pairs DGS-SRR.

4. CONCLUSION

From the simulated results, it shows that the split ring resonator can be functioned to increase the gain and miniaturized the size of the Minkowski patch antenna. A different number of the DMS-SRR and DGS-SRR also can affect the resonant frequency, gain, return loss and bandwidth of the Minkowski antenna performances.

ACKNOWLEDGMENT

The authors would like to thank Universiti Teknikal Malaysia Melaka (UTeM) and the MyBrain15 program from the Government of Malaysia for sponsoring this study. The authors would also like to thank UTeM for sponsoring this work under the PJP grant.

REFERENCES

1. Vselago, V. G., "The electromagnetics of substances with simultaneously negative value ε and μ," *Soviet Physics Uspekhi*, Vol. 10, 509–514, 1968.
2. Pendry, J. B., A. J. Holden, D. J. Robbins, and W. J. Stewart, "Magnetism from conductors and enhanced nonlinear phenomena," *IEEE Transactions Microwave Theory Techniques*, Vol. 47, No. 11, 2075–2084, 1999.
3. Smith, D. R., W. J. Padilla, D. C. Vier, S. C. Nemat-Nasser, and S. Schultz, "Composite medium with simultaneously negative permeability and permittivity," *Physical Review Letters*, Vol. 84, No. 18, 4184–4187, 2000.
4. Powell, D. A., K. Hannam, I. V. Shadrivov, and Y. S. Kivshar, "Interaction of twisted split ring resonators," *2011 Conference on and 12th European Quantum Electronics Conference*, 1, 2011.
5. Majid, H. A., M. K. A. Rahim, and T. Masri, "Left handed metamaterial design for microstrip antenna application," *IEEE International RF and Microwave Conference (RFM 2008)*, 218–221, 2008.
6. Goswami, K., A. Dubey, G. C. Tripathi, and B. Singh, "Design and analysis of rectangular microstrip antenna with PBG structure for enhancement of bandwidth, global," *Jouranl of Research Engineering*, Vol. 11, No. 2, 2011.
7. Zhu, S. and R. Langley, "Dual-band wearable textile antenna on an EBG substrate," *IEEE Transactions on Antennas and Propagation*, Vol. 57, No. 4, 926–935, 2009.
8. Abu, M., M. K. A. Rahim, O. Ayop, and F. Zubir, "Triple-band printed dipole antenna with single-band AMC-HIS," *Progress In Electromagnetics Research B*, Vol. 20, 225–244, 2010.
9. Zakaria, Z., M. A. Mutalib, M. I. M. Sa'ari, N. A. Zainuddin, S. W. Yik, and A. R. Othman, "Design of microstrip bandpass filter with defected microstrip structure (DMS)," *Australian Journal of Basic & Applied Sciences*, Vol. 8, No. 4, 2013.
10. Ariffin, M. M., H. Nornikman, W. Y. Sam, A. M. M. Fareq, A. A. M. Z. Abidin, Z. Zahrialdha, and O. M. Azlishah, "Patch antenna design with defected microstrip structure (DMS) of quadruple C-slot at WiMAX application," *Australian Journal of Basic & Applied Sciences*, Vol. 7, No. 11, 2014.
11. Hadi, M. H., B. H. Ahmad, P. W. Wong, and N. A. Shairi, "An overview of isolation improvement techniques in RF switch," *Journal of Engineering & Applied Sciences*, Vol. 9, No. 3, 2014.
12. Hadi, M. H., B. H. Ahmad, N. A. Shairi, and P. W. Wong, "Effect of a discrete PIN diode on defected ground structure," *2013 IEEE Symposium on Wireless Technology and Applications (ISWTA 2013)*, 333–337, 2013.
13. Zakaria, Z., M. A. Mutalib, A. R. Othman, M. M. Ismail, M. S. M. Isa, and N. A. Zainuddin, "Suspended stripline structure (SSS) microwave bandpass filter with defected stripline structure (DSS)," *Advanced Science Letters*, Vol. 20, No. 2, 469–472, 2014.
14. Zakaria, Z., M. A. Mutalib, M. S. M. Isa, A. A. Md Isa, N. A. Zainuddin, and W. Y. Sam, "Design of generalized Chebyshev lowpass filter with defected stripline structure (DSS)," *2013 IEEE Symposium on Wireless Technology and Applications (ISWTA)*, 230–235, 2013.
15. Voldman, J., B. Mandelbrot, L. W. Hoevel, J. Knight, and P. Rosenfeld, "Fractal nature of software-cache interaction," *IBM Journal of Research and Development*, Vol. 27, No. 2, 164–170, 1983.
16. Lee, E. C., P. J. Soh, M. B. M. Hashim, G. A. E. Vandenbosch, G. A. E. Vandenbosch, V. Volski, I. Adam, H. Mirza, and M. Z. A. A. Aziz, "Design and fabrication of a flexible Minkowski fractal antenna for VHF applications," *5th European Conference on Antennas and Propagation (EUCAP)*, 521–524, 2011.
17. Lee, E. C., P. J. Soh, N. B. M. Hashim, G. A. E. Vandenbosch, H. Mirza, I. Adam, and S. L. Ooi, "Design of a flexible Minlowski-like pre fractal (MLPF) antenna with different ground planes for VHF LMR," *2011 International Workshop on Antenna Technology*, 298–301, 2011.
18. Nornikman, H., B. H. Ahmad, M. Z. A. Abd Aziz, and A. R. Othman, "Effect of single complimentary split ring resonator structure on microstrip patch antenna design," *2012 IEEE Symposium on Wireless Technology and Applications (ISWTA 2012)*, 239–244, 2012.

Equivalent Circuit Model of Different Configurations of Loop Elements Using Vector-fitting

Payal Majumdar, Zhiya Zhao, Yutao Yue, Chunlin Ji, and Ruopeng Liu
State Key Laboratory of Meta-RF Electromagnetic Modulation Technology
Kuang-Chi Institute of Advanced Technology, Shenzhen, Guangdong 518000, China

Abstract— The analysis and modeling of different configurations of loop elements based FSS, with resonant unit cells adopting an efficient vector-fitting is proposed. The elements studied are — 1) Square loop, 2) Double Square loop and 3) Gridded Square loop. The simulations of microstructure are performed with full wave simulation tool CST Microwave Studio on single-substrate for different physical parameters, oblique incidence and effect of TE/TM polarization. Then circuit models are extracted and developed using the vector fitting tool and implemented in a circuit simulator enabling both time and frequency analyses along with effect of polarization and angle of incidence. ADS SPICE generator is used for verifying circuit models developed. The developed models are within 1% of average deviation against reference data.

1. INTRODUCTION

There is a growing demand for developing an accurate circuit model for FSS so that one can synthesize a desired frequency response by an optimization method and can quickly predict the response of the structure in a reasonably short time using a circuit simulator [1]. Unlike traditional microwave filters, the frequency response of FSS are not only functions of frequency, but also functions of incident angle and polarizations of EM waves. Consequently, it is necessary that an excellent FSS should provide stable performances for both various incidence angles and different polarizations within its operating frequencies [2].

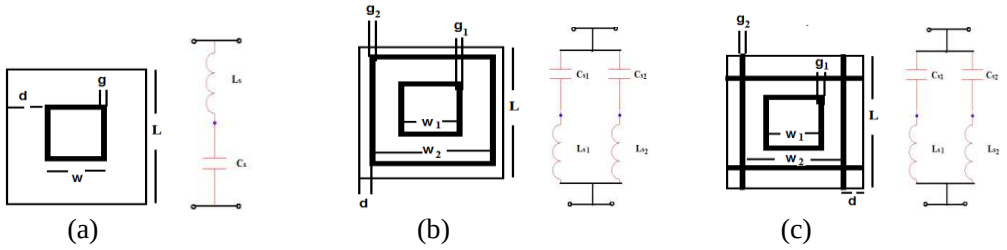

Figure 1: Layout of different configurations of loop elements FSS and its equivalent circuit. (a) Square loop. (b) Double square loop. (c) Gridded square loop.

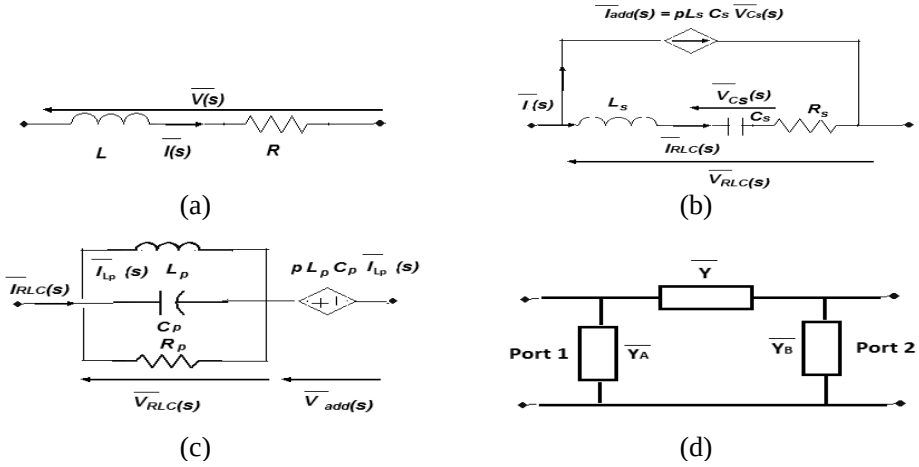

Figure 2: (a) Equivalent RL circuit for real pole synthesis; (b) equivalent series RLC circuit; (c) equivalent parallel RLC circuit for complex pole pair synthesis, and (d) equivalent Π circuit.

In this paper, we present the analysis and equivalent circuit modeling of three different configurations of loop elements based FSS, with resonant unit cells. The elements studied are 1) Square loop [2–4], 2) Double square loop [2, 5] and 3) Gridded square loop [2, 5], which are shown in Figure 1 along with equivalent circuits traditionally used to model them. For modeling purpose, vector fitting (VF) technique [6] is used for determination of poles and residues from simulated S-parameters obtained from full wave simulation tool CST Microwave Studio [7]. Then the SPICE-compatible equivalent circuit model [8] of frequency-domain responses approximated by rational functions are developed. The transmission and reflection properties are evaluated through a simple and accurate circuit approach. The developed models are within 1% of average deviation against reference data.

2. EQUIVALENT CIRCUIT MODELING BY VECTOR FITTING

VF method is a general fitting methodology which gives unconditional stability by forcing real terms of poles to become negative and is represented by the rational function approximation [6] as shown in Equation (1).

$$f(s) = \sum_{n=1}^{N} \frac{c_n}{s - a_n} + d + sh \tag{1}$$

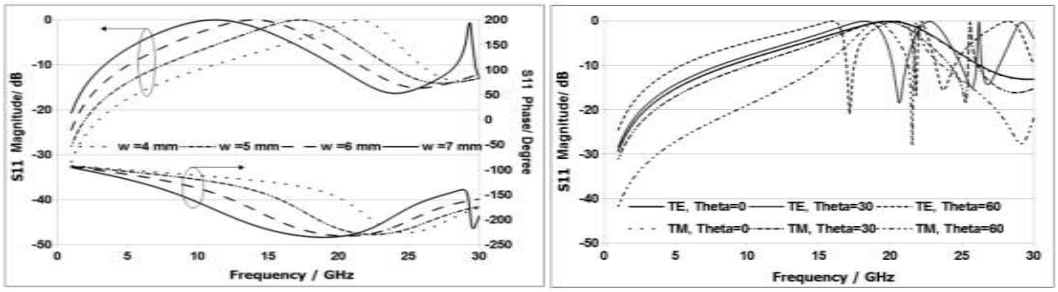

w = 4.5 mm, g = 0.9 mm, d = 2.25 mm and L = 9 mm

(a) (b)

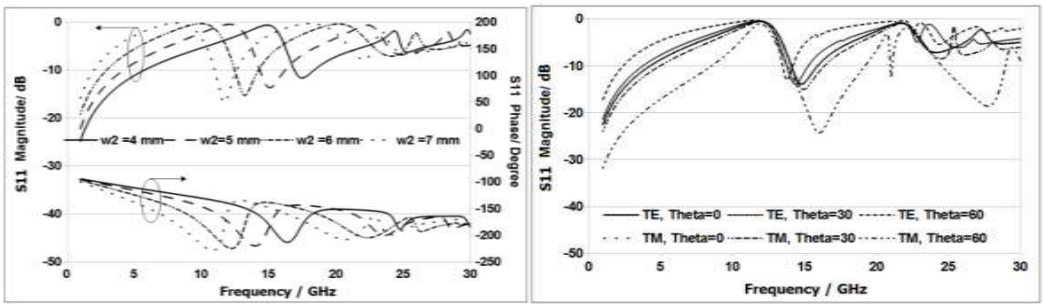

w_1 = 2.5 mm, g_1= 0.25 mm, w_2 = 5 mm, g_2= 0.5 mm, d = 1.5 mm and L = 9 mm

(c) (d)

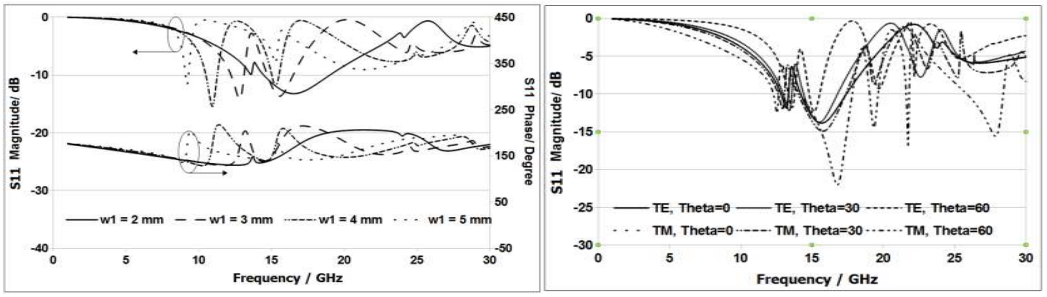

w_1= 2.5 mm, g_1= 0.25 mm, w_2 = 6.5 mm, g_2= 0.25 mm, d = 1 mm and L = 9 mm

(e) (f)

Figure 3: Plane-wave reflection response for different configurations of loop elements in FSS. (a) Square Loop — normal incidence. (b) Square Loop — oblique incidence. (c) Double Square Loop — normal incidence. (d) Double Square Loop — oblique incidence. (e) Gridded Square Loop — normal incidence. (f) Gridded Square Loop — oblique incidence.

The residues c_n and poles a_n are either real quantities or come in complex conjugate pairs, while d and h are real. It gives the fractional terms that directly lead to fixed forms of R, L and C.

In this section, circuit representations for complex pairs obtained from VF and synthesis approach are presented briefly for the generation of SPICE [8] compatible equivalent circuits enabling both time and frequency analyses of square loop, double square loop from three-dimensional models. The detailed synthesis of a complex pole pair by means of RLC elements with only one controlled source, allowing rational approximation of impedances or admittances to be implemented in a circuit simulator along with the equations can be obtained from [8].

The following synthesis approach has been used in this work to achieve the SPICE-compatible equivalent circuits of loop elements based FSS microstructure:

Step 1) S-parameter extraction by means of simulation of FSS microstructure in CST Microwave Studio;

Step 2) $ABCD$ parameters evaluation;

Step 3) Building of the equivalent circuit as shown in Figure 2(d);

Step 4) Residues and poles extraction of admittances $\bar{Y}_A$, $\bar{Y}_B$ and $\bar{Y}$;

Step 5) SPICE-compatible equivalent circuit synthesis [8].

The VF technique has been adopted to extract poles and residues of admittances $\bar{Y}_A$, $\bar{Y}_B$ and $\bar{Y}$, which have been synthesized in the equivalent circuit, as shown in Figures 2(a)–2(c), of FSS

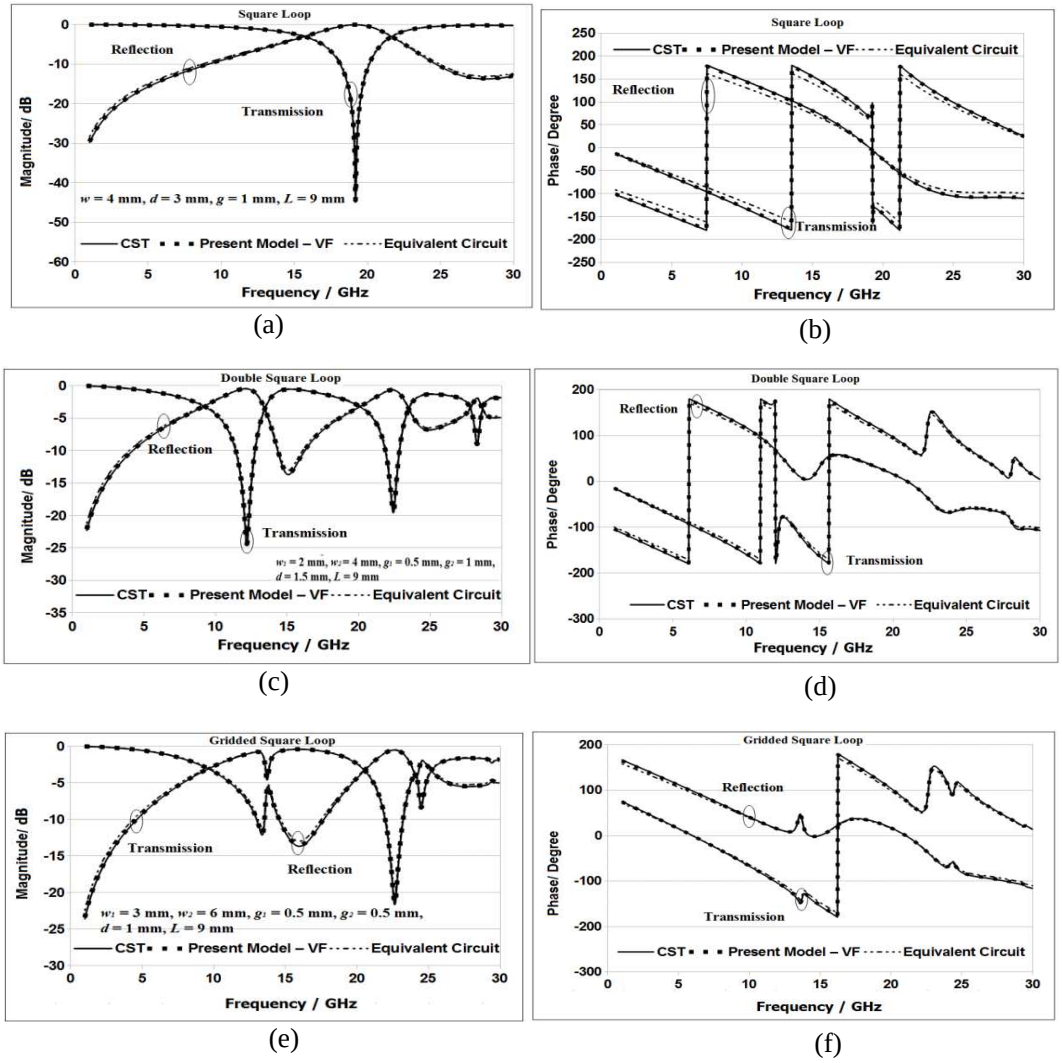

Figure 4: Comparison of VF based equivalent circuit model against CST and traditional circuit model for different configurations of loop elements based FSS (Substrate: $\varepsilon_r = 4.4$, $\tan\delta = 0.025$ and $h = 1\,\text{mm}$).

microstructure and simulated in a ADS SPICE [9] environment enabling both time and frequency analyses.

3. PARAMETRIC STUDY AND MODEL VALIDATION

This section is dedicated to the validation of the presented equivalent circuit models for three different configurations of loop elements in FSS. Firstly, different configurations of loop elements based FSS structures are studied and investigated on single-substrate for different physical parameters using CST Microwave Studio [10]. The effects of oblique incidence and TE/TM polarization are also studied. All the FSS designs are simulated on FR4 substrate with permittivity $\varepsilon_r = 4.4$, loss tangent $\tan\delta = 0.025$ and substrate thickness $h = 1\,\text{mm}$. For the sake of brevity, few results are shown here.

Figure 3 shows the reflection characteristics at normal incidence for different loop sizes and the effect of oblique incidence and TE/TM polarization on its magnitude of square loop, double square loop and gridded square loop respectively. It has been observed in all the three configurations of FSS that by increasing loop size there is shift in resonance towards lower frequency and by increasing substrate thickness, there is shift in resonance towards lower frequency.

Figure 4 shows the compared results of magnitude and phase of reflection and transmission characteristics at normal incidence obtained from the developed circuit model using VF tool, circuit model available from literature and CST simulations for square loop, double square loop and gridded square loop respectively. The reflection and transmission coefficients of square loop have been fitted by using 10 poles (two real poles and four complex pairs); double square loop and gridded square loop using 12 poles (two real poles and five complex pairs) respectively [6]. The extracted pole pairs obtained using fitting procedure can be synthesized in ADS SPICE generator using repeated equivalent circuit units shown in Figure 2.

The results of the developed equivalent circuit model showed good agreement, up to the propagation of high-order Floquet modes. Thus proposed synthesis allows a satisfactory approximation of all the considered FSS being the percentage errors on magnitude and phase of the order of 1%. While the equivalent circuits available in literature have the percentage errors on magnitude and phase of the order of 1.5%. All the equivalent circuits are designed and simulated using ADS SPICE generator. In future work, this approach will be extended to multilayer substrates.

4. CONCLUSIONS

The present work reports development of vector-fitting based equivalent circuit model of three different configurations of loop elements based FSS, with resonant unit cells. The elements studied are — 1) Square loop, 2) Double square loop and 3) Gridded square loop. The simulations are performed with CST Microwave Studio on single-substrate for different physical parameters, oblique incidence and effect of TE/TM polarization. The VF tool is employed to extract equivalent circuits from S-parameters of FSS microstructure to use in circuit simulators to avoid time consuming 3D simulations. Then ADS SPICE generator is used for verifying circuit models developed using simulated results. All the models are within 1% of average deviation against reference data.

ACKNOWLEDGMENT

This research work has been supported by Shenzhen Key Laboratory of Meta-RF Fabrication and Packaging (No. CXB201109210102A), Guangdong Natural Science Funds for Distinguished Young Scholar (No. S20120011253) and the introduction of innovative R&D team program of Guangdong Province (No. 2011D024).

REFERENCES

1. Costa, F., A. Monorchio, and G. Manara, "Efficient analysis of frequency-selective surfaces by a simple equivalent-circuit model," *IEEE Antennas and Propagation Magazine*, Vol. 54, No. 4, 35–48, 2012.
2. Munk, B. A., *Frequency-selective Surfaces: Theory and Design*, Wiley, New York, 2000.
3. Chung, Y.-C., K.-W. Lee, I.-P. Hong, M.-G. Lee, H.-J. Chun, and J.-G. Yook, "Simple prediction of FSS radome transmission characteristics using an FSS equivalent circuit model," *IEICE Electronics Express*, Vol. 8, No. 2, 89–95, 2011.
4. Lee, C. K. and R. J. Langley, "Equivalent-circuit models for frequency-selective surfaces at oblique angle of incidence," *IEE Proc.*, Vol. 132, No. 6, 395–399, 1985.

5. Singh, D., A. Kumar, S. Meena, and V. Aggarwal, "Analysis of frequency selective surfaces for radar absorbing materials," *Progress In Electromagnetics Research B*, Vol. 38, 297–314, 2012.
6. Gustavsen, B. and A. Semlyen, "Rational approximation of frequency domain responses by vector fitting," *IEEE Trans. Power Delivery*, Vol. 14, 1052–1061, 1999.
7. CST Studio Suite, CST GmbH — Computer Simulation Technology, 2011, www.cst.com.
8. Antonini, G., "SPICE equivalent circuits of frequency-domain responses," *IEEE Trans. on Electromagnetic Compatibility*, Vol. 45, 502–512, 2003.
9. Agilent Advanced Design System, 2011.
10. Majumdar, P., Z. Zhao, and R. Liu, "Parametric analysis of different configurations of loop elements in frequency-selective surfaces," *Advance in Electronic and Electric Engineering*, Vol. 4, No. 2, 161–168, 2014.

Antenna Reconfiguration Using Metasurfaces

Hailiang Zhu, S. W. Cheung, and T. I. Yuk
Department of Electrical and Electronic Engineering
The University of Hong Kong, Hong Kong

Abstract— The paper describes the designs of a frequency-reconfigurable, polarization reconfigurable and pattern reconfigurable antennas using metasurfaces (MS). The frequency-reconfigurable and polarization reconfigurable antennas are composed of a simple circular patch antenna or slot antenna as the source antenna and a circular MS with the same diameter, with both source antenna and MS implemented using planar technology. The pattern reconfigurable antenna is composed of a circular patch antenna as the source antenna and a semicircular MS with the same diameter. In all these reconfigurable antennas, the MS is placed directly atop of the source antenna, making the antenna very compact and low profile with a thickness of only $0.05\lambda_0$. By rotating the MS around the center with respect to the source antenna, the frequency, polarization or pattern of the reconfigurable antenna can be reconfigured.

1. INTRODUCTION

In general, operating frequency, polarization and radiation pattern are the three major characteristics in the design of antennas. As the growing demand for integrating multiple wireless standards into a single wireless platform, it is highly desirable if one or more of the above mentioned performance characteristics in an antenna can be reconfigured. Thus substantial research work has been carried out to reconfigure these characteristics for antennas.

The mechanism used to reconfigure the operating frequency, polarization and radiation pattern of an antenna can be mechanical or electrical. Electrically reconfigurable antennas are far more popular and can be achieved by using PIN-diode switches or varactor diodes. In the design of these antennas, direct-current (DC) source and biasing circuits are needed to bias the PIN or varactor diodes. These electronic components and circuits may have adverse effects on the antennas performances such as efficiencies and radiation pattern. Moreover, the antenna performance depends on the reliability of the electronic components and the DC sources [1]. Mechanically reconfigurable antennas usually require adjusting some movable parts to achieve reconfiguration [2]. The main drawback is that the actuator used to produce the mechanical movements is very complicated and usually occupies much space, making it bulky and expensive. In fact, change of size and/or shape is the common problem for most mechanically reconfigurable antennas. To overcome these shortcomings, we propose to use metasurfaces to design reconfigurable antennas.

Metasurface (MS) is a two-dimensional equivalent of metamaterial and essentially a surface distribution of electrically small scatterers [3]. Due to its succinct planar structure and low cost, MS provides a good option for the movable part of mechanically reconfigurable antennas and can be easily integrated with printed planar antennas.

In this paper, we describe the use of MS to design three different types of reconfigurable antennas, namely, frequency-reconfigurable, polarization-reconfigurable and pattern-reconfigurable antennas. The frequency-reconfigurable and polarization reconfigurable antennas have been introduced in our previous papers [6, 7] in details and the idea of pattern reconfigurable antenna using MS is first time presented.

2. ANTENNAS DESIGN

2.1. Frequency-reconfigurable Antenna

The frequency-reconfigurable metasurfaced (FRMS) antenna described here, as shown in Fig. 1, consists of a patch antenna (as the source antenna) and a MS which uses a rectangular loop as the unit cell [6]. The patch antenna and MS are designed to have a circular shape with same diameter. The patch antenna is designed on a double-sided substrate using planar technology as shown in Fig. 1(a), while the MS is designed on a single-sided substrate, as shown in Figs. 1(b) and (c). The frequency reconfigurability of the antenna is achieved by rotating the MS around the center relative to the patch antenna. The rotation angle θ_R is measured from the y-axis as shown in Fig. 1(b). Due to the horizontal and vertical symmetries of the MS, $\theta_R = -\theta_R$ and the maximum rotation angle without repeating is 90°. In assembling the FRMS antenna, the non-copper side of the MS is

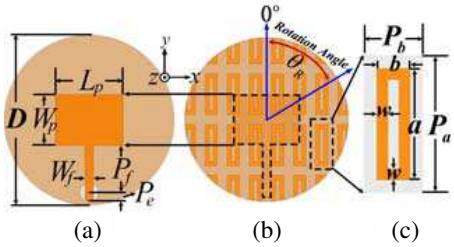

Figure 1: Geometries of (a) patch antenna, (b) MS and (c) unit cell.

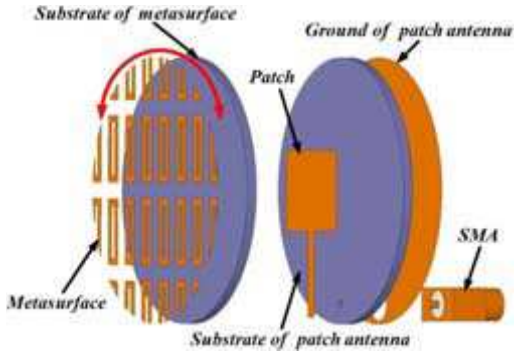

Figure 2: Assembly schematic of FRMS antenna.

Table 1: Dimensions of FRMS antenna (Unit: mm).

$\mathbf{P_a}$	$\mathbf{P_b}$	**a**	**b**	**w**	$\mathbf{L_p}$	$\mathbf{W_p}$	$\mathbf{W_f}$	$\mathbf{P_f}$	$\mathbf{P_e}$	**D**
12.4	5.4	10	3	1	16	12	2	11	2	40

placed in direct contact with the radiator of the patch antenna as shown in Fig. 2, leading to a very compact and low profile structure. The antenna is designed on the Rogers substrates RO4350B, having a thickness of 1.524 mm and a relative permittivity of $\varepsilon_r = 3.48$. The optimized dimensions are listed in Table 1.

2.2. Polarization Reconfigurable Antenna

The polarization-reconfigurable metasurfaced (PRMS) antenna, as shown in Fig. 3, consists of a slot antenna (as the source antenna) and a metasurface (MS) [7]. The MS is composed of corner-truncated square unit cells as shown in Fig. 3(a) on a single-sided substrate. The polarization reconfigurablity of the antenna is accomplished by rotating the MS around the center relative to the slot antenna. The rotation angle θ_R is measured from the y-axis as shown in Fig. 3(a). Studies have shown that with $\theta_R = 0°$ and 90°, the operation of the antenna is left-hand circular polarization (LHCP) and right-hand circular polarization (RHCP), respectively. With $\theta_R = 45°$ and 135°, the antenna is linearly polarized (LP) along the y-axis, same as that of the source antenna (the slot antenna). In assembling the PRMS antenna, the non-copper side of the MS is placed atop the slot antenna and is in direct contact with the feed-line (top side) of it as shown in Fig. 4. This leads to a very compact and low profile structure. An SMA connector is used to feed to the feed-line through the ground plane and the substrate material of the slot antenna. The dimensions of the final design are listed in Table 2.

2.3. Radiation Pattern Reconfigurable Antenna

The pattern reconfigurable metasurfaced antenna (PaRMS) is composed of a simple circular patch antenna and a semicircular MS with the same diameter, as shown in Figs. 5 and 6. The MS consists of small square patches used as the unit cells. Due to the semicircular structure of the MS, the

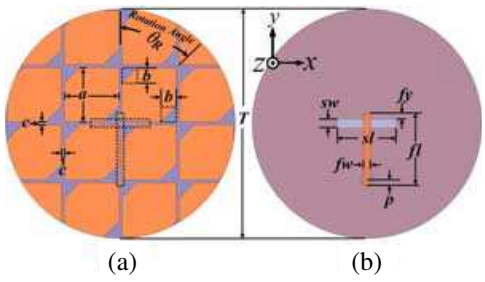

Figure 3: Geometries of (a) MS and (b) slot antenna.

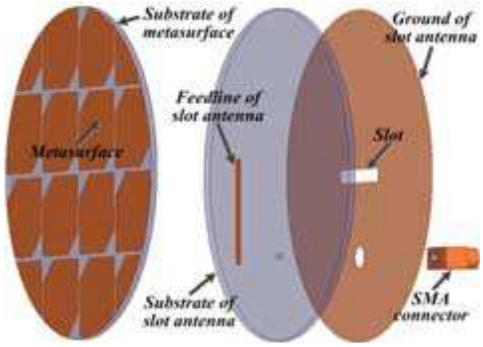

Figure 4: Assembly schematic of PRMS antenna.

integrated antenna will generate a tilted beam, making an angle of 30° with the boresight direction. By rotating the MS around the center of the antenna, the tilted beam can be steered to different directions. As the source antenna is circular and fed by a SMA connector at the center, the S_{11} of the PaRMS antenna is unchanged in rotation, thus simplifying the optimization work of the antenna significantly. The dimensions of the final design are listed in Table 3.

Table 2: Dimensions of PRMS antenna (Unit: mm).

a	b	c	sw	sl	fw	fl	fy	p	T
18.5	5.3	1	3	20	2.5	24.5	2	2	78

Table 3: Dimensions of PaRMS antenna (Unit: mm).

a	G	P_r	T
6	0.3	18	70

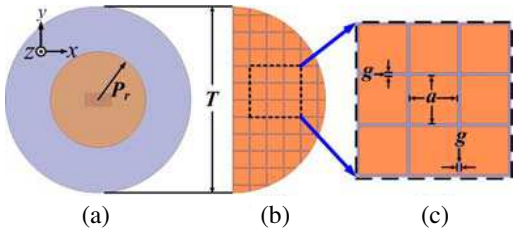

Figure 5: Geometries of (a) patch antenna, (b) MS and (c) unit cell.

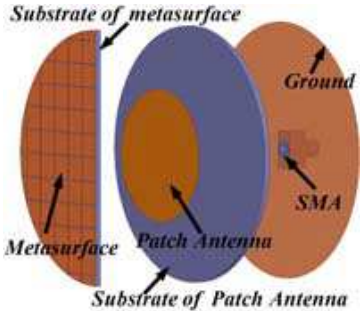

Figure 6: Assembly schematic of PaRMS antenna.

3. SIMULATION AND MEASUREMENT RESULTS

3.1. Frequency Reconfigurable Antenna

The frequency reconfigurability of the FRMS antenna is studied using reflection coefficient S_{11}. The simulated and measured S_{11} of the antenna with different rotation angles θ_R are shown in Fig. 7. The resonant frequency is proportional to the rotation angle. As the rotation angle increases from 10° to 25°, 35°, 55° and 80°, the resonant frequency shifts up from 4.77 GHz to 4.9, 5.07, 5.31 and 5.51 GHz, respectively, with a fractional tuning range of 14.6%. The simulated and measured efficiencies are shown in Fig. 8. It can be seen that the simulated and measured efficiencies are above 80% at the resonant frequencies.

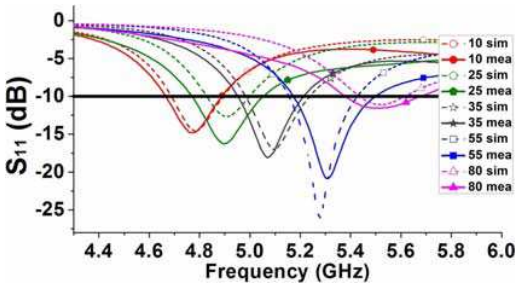

Figure 7: Simulated and measured S_{11} of FRMS antenna with different rotation angles.

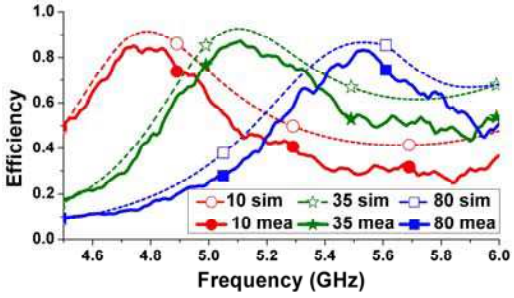

Figure 8: Simulated and measured efficiencies of FRMS antenna.

3.2. Polarization Reconfigurable Antenna

The simulated and measured S_{11} of the PRMS antenna with different rotation angles θ_R are shown in Fig. 9. The impedance bandwidth (for $S_{11} < -10$ dB) in LHCP ($\theta_R = 90°$) and RHCP ($\theta_R = 90°$) are more than from 3–4 GHz as shown in Figs. 9(a) and (c), respectively. In LP, i.e., $\theta_R = 45°$, Fig. 9(b) shows that the simulated and measured frequency bands shift down slightly to 2.82–3.7 GHz and 2.8–3.7 GHz, respectively. However, at $\theta_R = 135°$, Fig. 9(d) shows that the simulated and measured frequency bands shift up slightly to 3.28–4.08 GHz and 3.3–4.05 GHz, respectively.

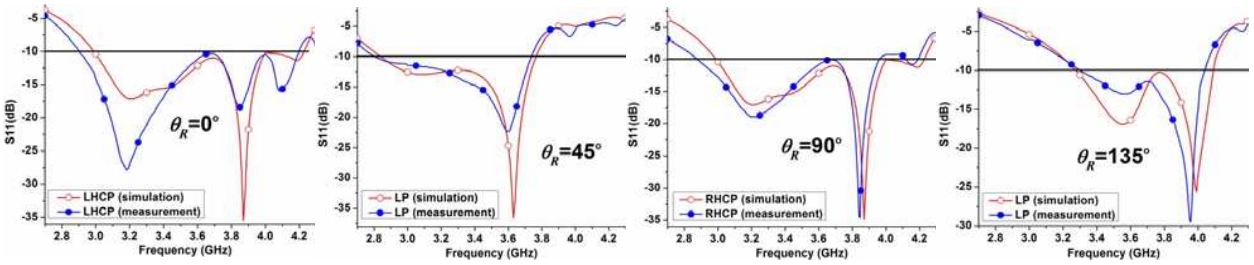

Figure 9: Simulated and measured S_{11} of PRMS antenna for (a) $\theta_R = 0°$, (b) $\theta_R = 45°$, (c) $\theta_R = 90°$ and (b) $\theta_R = 135°$.

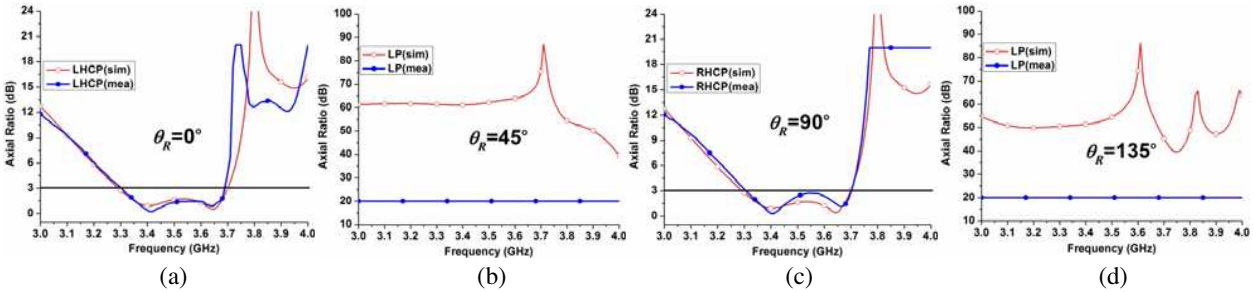

Figure 10: Simulated and measured ARs for different rotation angles.

The simulated and measured axial ratios (ARs) in the boresight of the PRMS antennas (along the $+z$ axis as shown in Fig. 3) are shown in Fig. 10. The simulated and measured ARs are less than 3 dB from 3.3–3.7 GHz for both LHCP and RHCP, with an axial ration bandwidth (ARBW) of 400 MHz (or a fractional bandwidth of 11.4%) as shown in Figs. 10(a) and (c), respectively. With $\theta_R = 45°$ and 135° when the antenna is operated in LP, Figs. 10(b) and (d) show that the simulated ARs are larger than 40 dB from 3–4 GHz, indicating very high linear polarization purity. Since the antenna measurement equipment, Satimo Starlab System, can measure the AR of CP antennas only up to 20 dB, the measured result is therefore a horizontal straight line at 20 dB in Figs. 10(b) and (d).

3.3. Radiation Pattern Reconfigurable Antenna

The simulated S_{11} of the PaRMS antenna is shown as the red line in Fig. 11. Due to the symmetrical antenna structure and the unchanged feeding position, the S_{11} does not vary with the rotation angle. The peak directivity and realized gain are shown in the same figure by the blue lines for the convenience of viewing the operating bandwidth. It can be seen that in the operating bandwidth from 5.48–5.7 GHz (4%), the peak realized gain is above 7 dBi with a peak of 7.7 dBi at 5.6 GHz, where the directivity can reach up to 8.2 dBi. The radiation pattern of the antenna at 5.6 GHz is

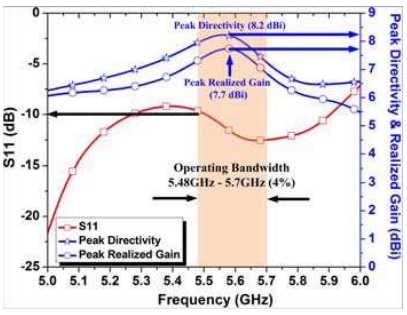

Figure 11: Final operating bandwidth.

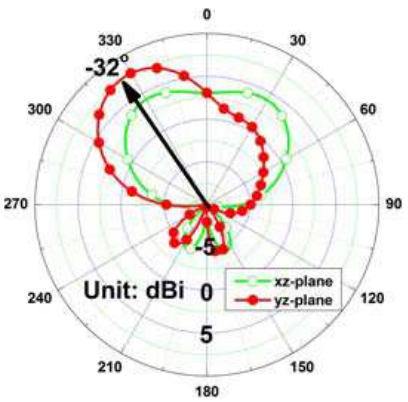

Figure 12: 2D radiation pattern.

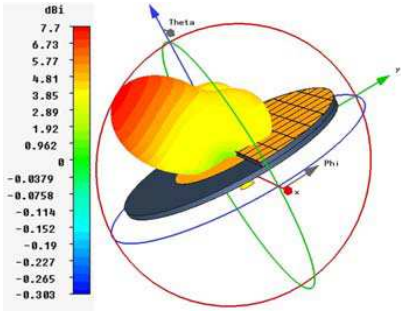

Figure 13: 3D radiation pattern.

shown in Fig. 12. It can be seen that the main beam makes an angle of 32° with the boresight direction. The 3D radiation pattern is plotted in Fig. 13. It can be seen that the main beam is tilted towards to the opposite side of the MS. Thus, the main beam can be steered continuously by rotating the MS around the center of the antenna.

4. CONCLUSIONS

Three different types of reconfigurable antennas, namely, frequency, polarization and pattern configurations, designed using matesurfaces have been presented. The source antennas of these reconfigurable antennas have circular shapes. Results have shown that, by using different MSs underneath the source antennas, the operating frequency, polarization and radiation pattern of the source antennas can be reconfigured by simply rotating the MS around the center of the source antenna.

REFERENCES

1. Sun, X. L., S. W. Cheung, and T. I. Yuk, "Dual-band monopole antenna with frequency-tunable feature for WiMAX applications," *IEEE Antennas and Wireless Propagation Letters*, Vol. 12, 100–103, 2013.
2. Bernhard, J. T., E. Kiely, and G. Washington, "A smart mechanically actuated two-layer electromagnetically coupled microstrip antenna with variable frequency, bandwidth, and antenna gain," *IEEE Transactions on Antennas and Propagation*, Vol. 49, 597–601, 2001.
3. Holloway, C. L., E. F. Kuester, J. A. Gordon, J. O'Hara, J. Booth, and D. R. Smith, "An overview of the theory and applications of metasurfaces: The two-dimensional equivalents of metamaterials," *IEEE Antennas and Propagation Magazine*, Vol. 54, 10–35, 2012.
4. Zhu, H. L., S. W. Cheung, K. L. Chung, and T. I. Yuk, "Linear-to-circular polarization conversion using metasurface," *IEEE Transactions on Antennas and Propagation*, Vol. 61, 4615–4623, 2013.
5. Zhu, H. L., K. L. Chung, X. L. Sun, S. W. Cheung, and T. I. Yuk, "CP metasurfaced antennas excited by LP sources," *2012 IEEE Antennas and Propagation Society International Symposium (APSURSI)*, 1–2, 2012.
6. Zhu, H., S. Cheung, X. Liu, and T. Yuk, "Design of polarization reconfigurable antenna using metasurface," *IEEE Transactions on Antennas and Propagation*, Vol. PP, No. 99, 1 (pages), 2014.
7. Zhu, H. L., X. H. Liu, S. W. Cheung, and T. I. Yuk, "Frequency-reconfigurable antenna using metasurface," *IEEE Transactions on Antennas and Propagation*, Vol. 62, 80–85, 2014.

Metamaterial Surfaces for Integrated Multiband Horn Applications

J. (Yiannis) C. Vardaxoglou
School of Electronic, Electrical and Systems Engineering
Loughborough University, Loughborough, LE11 3TU, UK

Abstract— Novel (Integrated Multiband Horn) IMH antenna designs using artificial metamaterial surfaces (FSS, EBG) are presented. A 'horn within a horn' concept is introduced whereby miniaturised metamaterial surfaces (of double ring elements) are embedded in the IMH.

1. INTRODUCTION

For some time now Electromagnetic Band Gap (EBG) properties of passive metallodielectric arrays or Frequency Selective Surfaces (FSS) have been studied [1, 2]. Metallic EBG (MEBG) structures have been used for the performance enhancement of mictrostrip antennas and circuits. Element miniaturisation also allows the unitisation these structures in realistic antenna applications [3]. This is only valid when the unit cell of the array smaller ($< \lambda/7$) than the wavelength. Here, we introduce a concept that utilises such structures to invoke a four band horn antenna. Each array was made from concentric ring elements and tested over a range of angles of incidence and polarisation prior to inserting them in the horn. Measured results are shown of the outer horn incorporating the high frequency horns.

2. INTEGRATED MULTIBAND HORN (IMH) CONCEPT

The main requirement was to produce a multiband antenna, with an overall volume and weight less than that made up of discrete antennas, operating at 2.4 GHz (E-band) 5.0 GHz (G-band) 10.5 GHz (J-band) 28.0 GHz (K-band). Fig. 1 shows two possible solutions for IMH, an embedded IMH where FSS form partial wall and a demultiplexer design, whereby the FSS/MEBG used as passive filters. The antennas are proposed to be mounted within the same overall physical housing, where there will be a trade-off physical size (environmentally/aesthetically pleasing mechanically robust design) against RF performance. Here the former was chosen for simplicity of use.

The EBG properties of periodic loading of concentric circular ring elements were assessed experimentally in a plane wave chamber. The unit cell is hexagonal. Fig. 2 shows the measured TE bandgaps for the arrays which are stable for up to 80° angle of incidence.

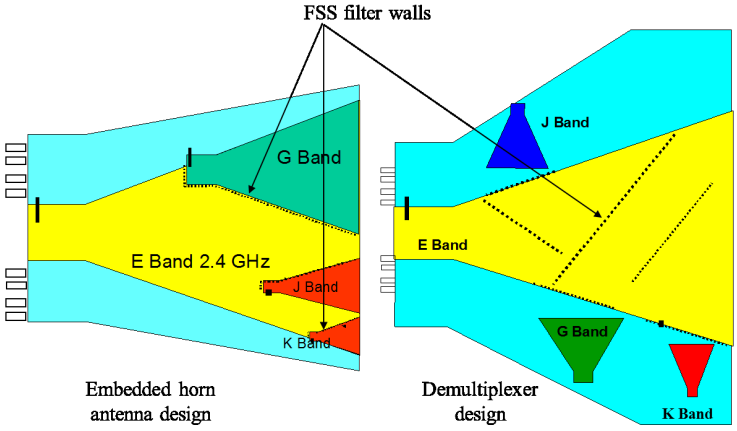

Figure 1: Two IMH concepts for G, E, J and K bands.

3. PROTOTYPES

The dimensions of the prototype built were as follows:

Table 1: The dimensions of individual horns chosen.

	E-band	G-band	J-band	K-band
a_1 (mm)	156.25	69.59	37.33	15
b_1 (mm)	265.62	118.29	63.46	45
d_1 (mm)	400	178.12	95.56	90

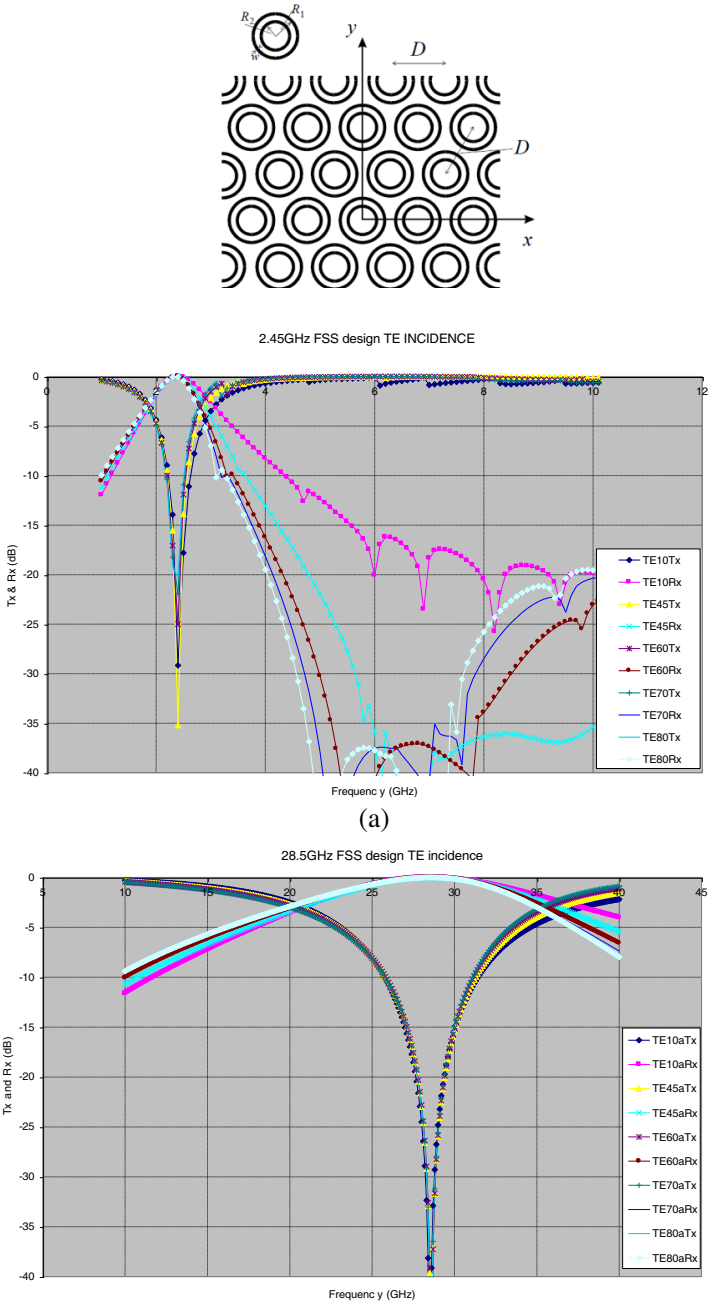

Figure 2: Plane wave of ring FSS Tx/Rx response of (a) E band and (b) K band.

4. RESULTS

4.1. E Band Horn

Average gain was 10 dB (worst 9 dB: best 11.06 dB) and the S_{11} was worst — 7.54 dB at 2.4 GHz (covered 8.32% @15 dB level), Fig. 3. The required BW of 4% was achieved. The probe diameter could be increased to improve the BW. The elevation plane pattern was slightly wider due to the

FSS horns worst case X polar -13.6 dB, Fig. 4. The azimuth patterns were narrower and the worst case X polar -16.8 dB was measured.

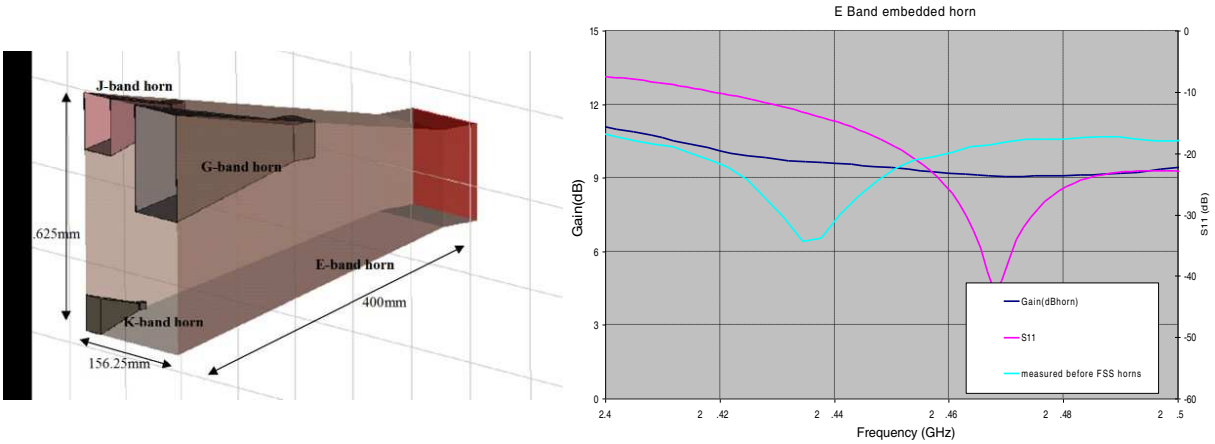

Figure 3: CAD model and gain of the E-band IMH.

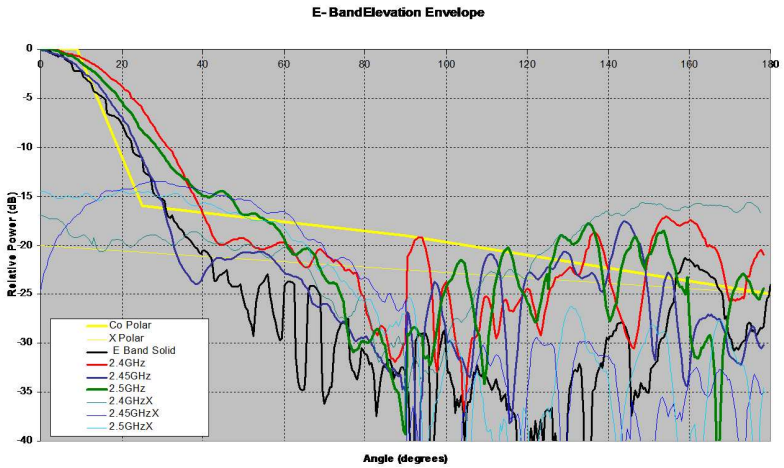

Figure 4: Elevation envelope of E-band horn.

4.2. G Band Horn

Average gain of the horn: 10.45 dB (worst 9.27 dB: best 11.68 dB), S_{11} worst — 5.32 dB at 5.1 GHz (covered 11.48% @10 dB level), BW 14.54% @15 dB, elevation plane pattern slightly wider than envelopes, worst case X polar -17.36 dB, azimuth patterns narrower than specified worst case X polar -15.53 dB.

4.3. J Band Horn

Average gain of the horn: 9.8 dB (worst 7.73 dB: best 11.66 dB), S_{11} worst — 10.08 dB at 10.28 GHz (covered band @10 dB level), BW 4.878%, elevation plane pattern wider than envelope, high side lobes worst case X polar -15.45 dB, a Azimuth patterns narrower than specified worst case X polar -17.84 dB.

4.4. K Band Horn

Average gain of the horn: 14.43 dB (worst 11.08 dB: best 16.08 dB), S_{11} worst — 4.44 dB at 27.5 GHz (covered 2% @10 dB level) Required BW 7%. Elevation plane pattern slightly wider than envelopes, azimuth patterns narrower than specified.

5. CONCLUSIONS

Results from the embedded IMH concept indicate that the utilization of FSS/EBG structures is a good prospect in a constrained illumination and polarization environment. The IMH did not suffer for undue inter scattering effects and produced moderate gain and bandwidth. The IMH horn used conventional coax-waveguide transformers and it is suggested that, for a more targeted design, these transformers to be specifically designed to meet the frequency bandwidth requirements.

REFERENCES

1. Vardaxoglou, J. C., *Frequency Selective Surfaces: Analysis and Design*, Research Studies Press, Somerset, UK; Wiley, New York, 1997.
2. De Maagt, P., R. Gonzalo, J. C. Vardaxoglou, and J. M. Baracco, "Photonic bandgap antennas and components for microwave and (sub)millimetre wave applications," *Special issue on Metamaterials, IEEE Trans. on Antennas and Propagation*, Vol. 51, No. 10, 2667–2677, Oct. 2003.
3. Capolino, F., *Applications of Metamaterials*, CRC Press, 2011.

Nonlinear Optical Properties of Gold Nanorods (GNRs) under FS Laser Excitation near the Third Optical Tissue Window and Application for Multichannel Cellular Imaging

Yalun Wang, Kanghui Li, Zhenfeng Zhu, and Jun Qian
Centre for Optical and Electromagnetic Research
Zhejiang University, Zijingang Campus, Hangzhou 310058, China

Abstract— Gold nanorod (GNR) was a promising bioimaging probe in the third optical tissue window (1600–1800 nm). In this paper, hydrophilic GNRs with proper dimensions were synthesized according to the classical seed mediated method. Their nanostructures were taken with a transmission electron microscope and their extinction spectra were recorded on a UV-vis scanning spectrophotometer. Their nonlinear optical features were recorded by a home built measurement system, under the femtosecond (fs) laser excitation of 1580 nm, which was selected as the demonstration of the third optical tissue window. A sharp third harmonic generation (THG) signal and a mild three photon luminescence (3PL) signal could be clearly distinguished. These signals could be utilized for multichannel nonlinear bioimaging in the third optical tissue window.

Negatively charged polystyrene sulfonate (PSS) and positively charged polyallylamine hydrochloride (PAH) were separately coated onto the positively charged GNRs through electrostatic adherence. The PAH-PSS coated GNRs were added in the culture medium of HeLa cells. Multichannel nonlinear optical imaging of cancer cells stained with GNRs was performed with a 1580 nm fs laser coupled scanning microscope. The signals were filtered by a 665 nm dichroic mirror, and then splitted by another 560 nm dichroic mirror into the green and red imaging channels. HeLa cells can be clearly visualized in both green and red channels with good contrast. For HeLa cells without GNRs treatment, there were no such signals detected in these channels.

This was a pioneer work of the multichannel nonlinear bioimaging in the third optical tissue window with GNRs and would be helpful for our further studies on in vivo bioimaging in this window with deeper penetration.

1. INTRODUCTION

Gold nanorod (GNR) is a type of metal nanoparticle of tens of nanometers in cylinder cap shape, with a transversal surface plasma resonance peak at around 520 nm and a tunable longitudinal surface plasma resonance (LSPR) peak. It had wide applications in bioimaging and biosensors, and some related studies have been performed in our group [1, 2]. Besides, GNR is appropriate for nonlinear (e.g., two-photon luminescence) bioimaging [3, 4].

Three-photon luminescence (3PL) is a process in which one single molecule absorbs three photons and emits one new photon with higher frequency. As the 3PL signal had a cubic power dependence on the input laser excitation, there would be a rather small focus on the sample, and photobleaching out of focus can be excluded in bioimaging [5]. Together with near infrared (NIR) excitation, the autofluorescence and photodamage towards biosamples were very small, as the energy of photon was small when its wavelength was long. As the excitation wavelength was far from the absorption of the nanoparticles, the photobleach was greatly reduced. In third harmonic generation (THG), three incident photons combine to generate a photon with tripled frequency/energy. In addition to the advantages of 3PL, THG produces no photodamage or photobleach in bioimaging as it is a thermal-free parametric process [6].

In this paper, we studied various nonlinear optical effects (3PL, SHG, THG) of GNRs, with the fs laser excitation from 1500 nm to 1600 nm, which was near the third optical tissue window (1600–1800 nm). In this window, scattering loss of light is very small and the absorption loss of light is not so distinct. Thus, nonlinear optical bioimaging can achieve very deep imaging depth, if fs-excitation with its wavelength in this optical window is adopted [7]. We further performed multichannel (3PL and THG) nonlinear optical imaging of cancer cells stained with GNRs, with a 1580 nm-fs laser coupled scanning microscope. The results would be very helpful to our further studies on applying GNRs in deeper nonlinear optical (THG and 3PL) *in vivo* bioimaging.

2. EXPERIMENTS

The gold nanorods used in our experiments were synthesized according to the seed mediated method suggested by Nikoobakht et al. with minor modifications [8, 9]. The extinction spectra of GNRs were recorded on a UV-vis scanning spectrophotometer (UV-2550, Shimadzu), and the nanostructures were taken with a transmission electron microscope (TEM, JEM-1200EX, Jeol).

The nonlinear optical features of GNRs were recorded by a home built measurement system (As shown in Fig. 1(a)). An optical parametrical oscillator (OPO) pumped by a mode-locked Ti: sapphire fs laser (200 fs, 76 MHz) was used as the excitation source, with output wavelength ranging from 1200 nm to 1600 nm. The linearly polarized near infrared (NIR) laser light was filtered by a 1000 nm long pass filter (Thorlabs), and was converted to be a circularly polarized light by a quarter-wave plate (Union Optic) to suppress the THG signals from the glass slide surface [6]. The laser beam was then directed into a microscope structure and focused onto the sample by a $10\times/0.25$ NA lens (Nikon). The signal was collected along the forward direction through a $40\times/0.75$ NA object lens (Nikon) and coupled into a fiber, which was connected to a spectrometer (PG2000, Ideaoptics Instruments). The as synthesized GNRs were uniformly dropped onto a glass slide and dried for the measurement.

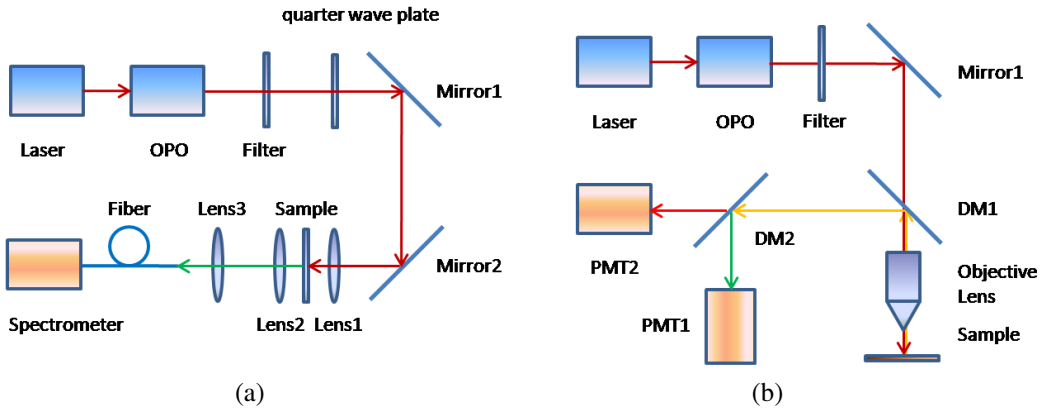

Figure 1: Schematic illustration of (a) the setup for nonlinear optical spectra measurements and (b) the fs laser coupled scanning microscope.

The multichannel nonlinear optical imaging of cells was taken by a scanning microscope (MPM 200, Thorlabs) coupled with the aforementioned fs OPO (as shown in Fig. 1(b)). In the microscope, the fs laser beam (1580 nm) was reflected), focused onto the sample by a $25\times/1.05$ NA objective lens (Olympus). The signal from the sample was epi-collected with the same objective lens, filtered by the 665 nm dichroic mirror, and was splitted by another 560 nm dichroic mirror (DM2, 560–850 nm long-pass, FF560-Di03-25 × 36, Semrock). The optical signals in different imaging channels (green imaging channel: < 560 nm; red imaging channel: $560 \sim 665$ nm) were collected by two separate photomultiplier tubes (PMTs, H7422-40, Hamamatsu). For the bright field image, the sample was illuminated by a halogen lamp and the photos were taken with a charge coupled device (CCD) equipped on the microscope.

Positively charged GNRs were encapsulated with polystyrene sulfonate (PSS, negative charge) and polyallylamine hydrochloride (PAH, positive charge) separately through electrostatic adherence [10]. HeLa cells were cultivated in Dulbecco minimum essential media (DMEM) with 10% fetal bovine serum (FBS), 1% penicillin, and 1% amphotericin B, at 37°C and 5% CO_2. The PAH-PSS-coated GNRs were added in the culture medium. After incubation, the cells were gently washed thrice by phosphate buffered saline (PBS, pH = 7.4, 10 mM) and imaged by the aforementioned scanning microscope.

3. RESULTS AND DISCUSSION

The extinction spectrum and TEM image of as-synthesized GNRs were shown in Fig. 2. They were monodispersed and had a cylinder cap shape, with a dimension of 65×25 nm. The LSPR peak of the GNRs was at 614.5 nm.

Due to the wavelength limitation of the OPO output ($1200 \sim 1600$ nm), 1580 nm was selected as the demonstration wavelength of the third optical tissue window. The nonlinear emission spectrum

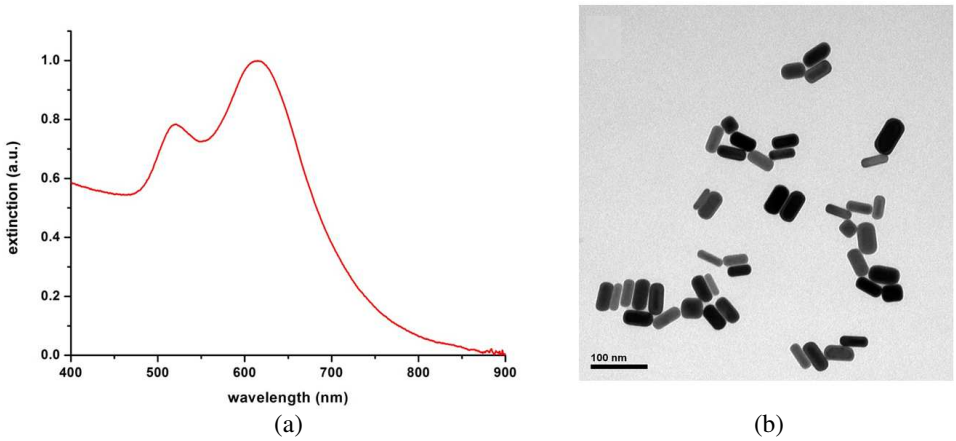

Figure 2: (a) The extinction spectrum and (b) TEM image of GNRs.

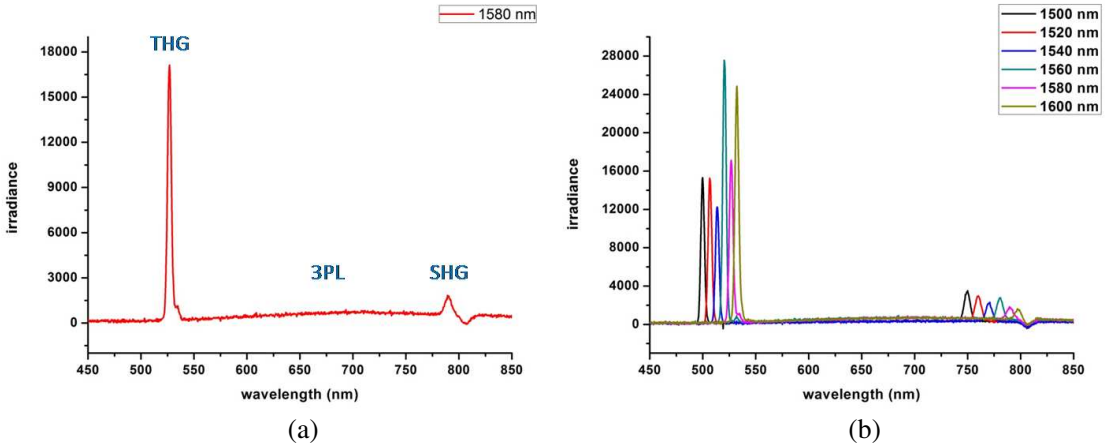

Figure 3: The nonlinear emission spectra of GNRs excited at (a) 1580 nm and (b) 1500–1600 nm.

of GNRs excited at 1580 nm was shown in Fig. 3(a). A sharp THG (at 527 nm) and a relatively weaker SHG (at 790 nm) can be easily discriminated from the spectra. 3PL was recognized by the slight apophysis between THG and SHG signals, and the lower intensity was partially due to the insufficient collection of the objective in the forward direction. The nonlinear optical spectra of GNRs under the fs excitation with various wavelengths were shown in Fig. 3(b). Tunable THG (from 500 nm to 533 nm) and SHG (from 750 nm to 800 nm) signals could be clearly observed, while the envelops of 3PL spectra were almost the same.

Nonlinear optical images of HeLa cells (stained with GNRs) were performed with the 1580 nm-fs laser coupled scanning microscope. HeLa cells can be clearly visualized with good contrast in both green (Fig. 4(a)) and red channels (Fig. 4(b)), and they matched perfectly in the merged image (Fig. 4(c)). There were no optical signals detected in these channels for HeLa cells without GNRs treatment. As SHG at 790 nm was out of the detected wavelength range of the red channel (560 $\sim$ 665 nm), it did not contribute any signals to Fig. 4(b). Thus, the contrast in Fig. 4(b) should be completely from the 3PL of GNRs, according to the spectrum in Fig. 3(a). THG and very small part of 3PL of GNRs contributed to the contrast in the green channel (Fig. 4(a)). As the signal in the green channel was stronger than that in the red channel, it indicated THG signal was stronger than 3PL and it was the main contribution for the green channel. Fig. 4(d) was the bright field image of the rectangle in Fig. 4(c). As we can see, they coincided very well. In our further study, we will apply GNRs in deeper nonlinear optical *in vivo* bioimaging, with the fs laser excitation in the third optical tissue window (1600–1800 nm), where light experiences less attenuation in biological tissues.

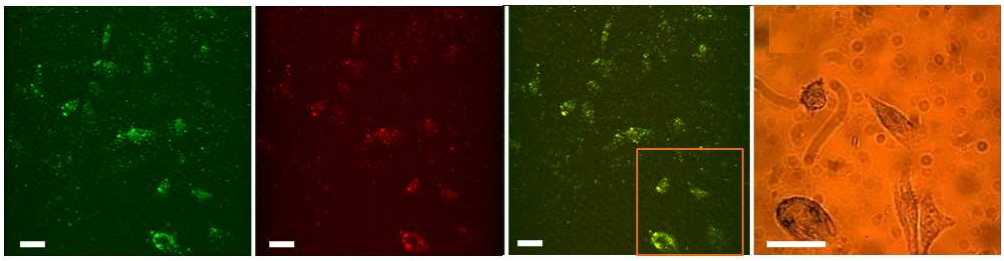

Figure 4: (a)–(c) The nonlinear optical images and (d) bright field of HeLa cells. The scale bar is 20 μm.

4. CONCLUSION

The nonlinear optical responses of GNRs near the third optical tissue window were studied, and THG and 3PL were found to be available. Multichannel (THG and 3PL) nonlinear optical imaging of cancer cells stained by GNRs was firstly demonstrated. The results would be helpful in our further studies on *in vivo* bioimaging in the third optical tissue window.

ACKNOWLEDGMENT

This work was partially supported by the National Basic Research Program (973) of China (2011CB 503700), the Ministry of Science and Technology of China (973 Program; 2013CB834704), the National Science Foundation of China (61275190).

REFERENCES

1. Zhang, Y., et al., "Multifunctional gold nanorods with ultrahigh stability and tunability for in vivo fluorescence imaging, sers detection, and photodynamic therapy," *Angewandte Chemie-International Edition*, Vol. 52, No. 4, 1148–1151, 2013.
2. Qian, J., et al., "Fluorescence-surface enhanced Raman scattering co-functionalized gold nanorods as near-infrared probes for purely optical in vivo imaging," *Biomaterials*, Vol. 32, No. 6, 1601–1610, 2011.
3. Durr, N. J., et al., "Two-photon luminescence imaging of cancer cells using molecularly targeted gold nanorods," *Nano Letters*, Vol. 7, No. 4, 941–945, 2007.
4. Cao, C. J., et al., "Multimodal optical microscopy in combination with gold nanorods for cancer cell imaging," *Journal of Biomedical Optics*, Vol. 17, No. 12, 2012.
5. Yu, J. H., et al., "High-resolution three-photon biomedical imaging using doped ZnS nanocrystals," *Nature Materials*, Vol. 12, No. 4, 359–366, 2013.
6. Schwartz, O. and D. Oron, "Background-free third harmonic imaging of gold nanorods," *Nano Letters*, Vol. 9, No. 12, 4093–4097, 2009.
7. Horton, N. G., et al., "In vivo three-photon microscopy of subcortical structures within an intact mouse brain," *Nature Photonics*, Vol. 7, No. 3, 205–209, 2013.
8. Nikoobakht, B. and M. A. El-Sayed, "Preparation and growth mechanism of gold nanorods (NRs) using seed-mediated growth method," *Chemistry of Materials*, Vol. 15, No. 10, 1957–1962, 2003.
9. Li, X., J. Qian, and S. L. He, "Impact of the self-assembly of multilayer polyelectrolyte functionalized gold nanorods and its application to biosensing," *Nanotechnology*, Vol. 19, No. 35, 2008.
10. Chen, L. L., et al., "Multilayered polyelectrolyte-coated gold nanorods as multifunctional optical contrast agents for cancer cell imaging," *Journal of Zhejiang University-Science B*, Vol. 11, No. 6, 417–422, 2010.

Near-infrared Fluorophore-doped Nanoparticles for *in vitro* and *in vivo* Bioimaging

Liliang Chu[1], **Shaowei Wang**[1], **Kanghui Li**[1], **Wang Xi**[2], **and Jun Qian**[1]

[1]Centre for Optical and Electromagnetic Research, Zhejiang University, China
[2]Department of Neurobiology, School of Medicine
Zhejiang University, Hangzhou, Zhejiang 310058, China

Abstract— Near-infrared (NIR) imaging technology has been widely used for bioimaging, since it can achieve deep penetration in biological tissues due to less absorption and scattering of NIR light. In our study, we reported the application of a kind of NIR fluorophore-doped nanoparticles for *in vitro* and *in vivo* microscopic bioimaging. Cellular imaging without autofluorescence, as well as vascular imaging of the mouse ear was obtained. The results of our experiments demonstrated NIR fluorophore-doped nanoparticles can be utilized as optical probes for high-contrast and deep-tissue functional bioimaging.

1. INTRODUCTION

Recently, optical imaging techniques have drawn great attention, due to their potentials for non-invasive study of living animals. Compared with visible light, near-infrared (NIR) light locating in "optical tissue window" (700–900 nm) [1] has less loss of light intensity and deeper tissue penetration capability. Thus, NIR imaging is a very powerful tool for deep-tissue in vivo bioapplications [2–4].

NIR fluorescent probes with high fluorescence efficiency, high chemical stability and less cytotoxicity are required in NIR imaging [5–9]. In our research, a typical type of NIR fluorophore, which is called IR-820, was adopted for NIR bioimaging. IR-820 doped organically modified silica (ORMOSIL) nanoparticles, as well as IR-820 doped polymer nanoparticles were synthesized, respectively. The nanoparticles have many advantages, such as relatively high fluorescence quantum yield, high stability in biological environment, facile surface functionalization and bio-compatibility, and they were further used for high-contrast *in vitro* cell imaging and deep-tissue *in vivo* animal imaging, separately.

2. EXPERIMENTAL SECTION

IR-820 doped ORMOSIL nanoparticles were synthesized according to the method previously reported [10]. 300 mg of Aerosol OT and 400 µl of 1-butanol were dissolved in 10 mL of DI water by vigorous magnetic stirring until the Aerosol OT was totally dissolved. 400 µl of the IR-820 in DMSO (0.5 mM) was then added to the solution. 20 minutes later, 100 µl of neat VETS was added into the mixture. After one hour, 15 µl of APTES was added to the solution. All the processes were under magnetic stirring for about 20 h. Aerosol-OT, 1-butanol, residual VTES and APTES were removed by dialyzing for at least 50 h. The dialyzed solution could be used for *in vitro* cell imaging after being filtered.

IR-820 doped polymer nanoparticles were prepared with the following method. 800 µl of DSPE-$mPEG_{5000}$ in chloroform (10 mg/mL) was mixed with 200 µl of IR-820 in ethanol (1 mM). The mixture was sonicated for several minutes to form a homogeneous solution and dried under vacuum in a rotary evaporator at 70°C. 250 µl of phosphate buffered saline (PBS, 10x) was added into the flask and the solution was sonicated for 2 minutes. Subsequently, an optically clear suspension containing IR-820 doped polymer nanoparticles was prepared, which can be used for further *in vivo* bioimaging.

HeLa cells were used for *in vitro* imaging, and nude mice were utilized for *in vivo* blood vessel imaging.

3. RESULTS AND DISCUSSION

A typical TEM picture (Figure 1) shows that IR-820 doped ORMOSIL nanoparticles were spherical, and have an average size of about 40 nm.

The absorption and fluorescence spectra of IR-820 doped ORMOSIL nanoparticles were shown in Figure 2. Their peak wavelengths are 835 nm and 850 nm respectively, which are located in a

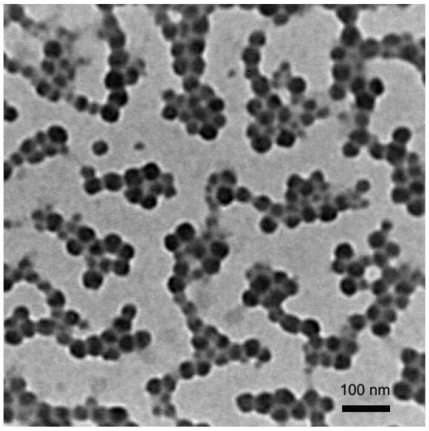

Figure 1: A TEM image of IR-820 doped ORMOSIL nanoparticles.

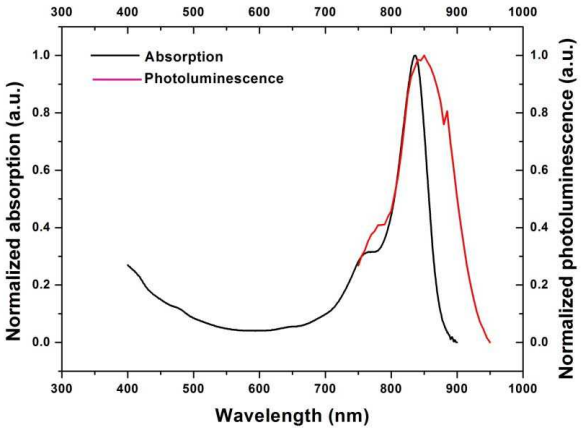

Figure 2: Normalized absorption and fluorescence spectra of IR-820 doped ORMOSIL nanoparticles.

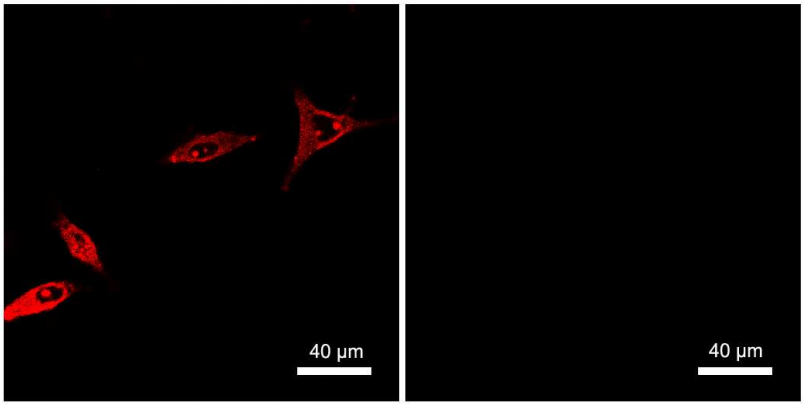

Figure 3: Fluorescence images of HeLa cells treated (a) with IR-820 doped ORMOSIL nanoparticles and (b) without IR-820 doped ORMOSIL nanoparticles (excitation wavelength: 635 nm).

NIR optical tissue window (700–900 nm), indicating that they can be applied in deep bioimaging with less absorption and scattering attenuation.

HeLa cells were cultivated for *in vitro* bioimaging and a 635 nm laser in an upright laser scanning confocal microscope (Olympus FV1000) was adopted as the excitation light source. Figure 3(a) is a high-contrast fluorescent image of HeLa cells, which were treated with IR-820 doped ORMOSIL nanoparticles for two hours. Due to bright fluorescence of IR-820 dyes under the 635 nm-excitation, as well as uniform staining of nanoparticles on cells, the morphologies of HeLa cells could be easily discriminated. For cells without the treatment of IR-820 doped ORMOSIL nanoparticles, nothing could be observed (Figure 3(b)), since the autofluorescence of HeLa cells was negligible under 635 nm-excitation.

Moreover, IR-820 doped polymer nanoparticles were utilized as optical contrast agents for *in vivo* bioimaging, due to their excellent photostability in animal body. The nanoparticles were intravenously injected into a nude mouse via the tail vein. The aforementioned upright laser scanning confocal microscope was used to perform *in vivo* imaging (excitation wavelength: 635 nm). Figures 4(a)–(h) show the images of blood vessels in the ear of the mouse at various vertical depths. Due to bright fluorescence of IR-820 and low background of tissue, the signal to noise ratio of all the images were very high, and even at 150 μm depth, the structure of blood vessels could still be observed very clearly. Furthermore, Figure 4(i) shows a 3D stack image (taken with 1 μm depth increment) of the NIR fluorescent nanoparticles in the blood vessels was reconstructed. Since the NIR fluorescence of the IR-820 was very distinct, the intravenously injected IR-820 doped polymer nanoparticles could reveal the vascular architecture very vividly. The experimental results

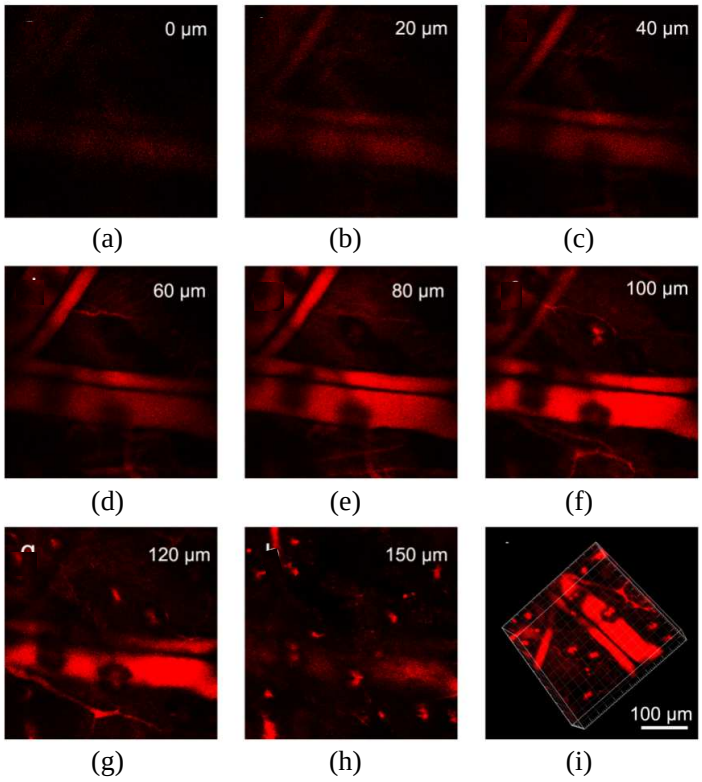

Figure 4: Images of blood vessels in the ear of a nude mouse at various vertical depths ((a) 0 μm, (b) 20 μm, (c) 40 μm, (d) 60 μm, (e) 80 μm, (f) 100 μm, (g) 120 μm, (h) 150 μm) and a three-dimensional reconstructive image (i) showing the distribution of the IR-820 doped polymer nanoparticles in the blood vessels of mouse ear.

illustrated that NIR fluorophore-doped nanoparticles have great potentials for high-contrast and deep-tissue *in vivo* functional bioimaging.

4. CONCLUSIONS

We demonstrated the applications of IR-820-doped nanoparticles as contrast agents for NIR optical imaging. High contrast living cells images, as well as deep-tissue (∼157 μm) vascular imaging in the ear of a mouse were obtained. Our study illustrated that NIR fluorophore-doped nanoparticles have great potentials for various *in vivo* functional bioimaging in the future.

REFERENCES

1. Anderson, R. and J. A. Parrish, "The optics of human skin," *J. Invest. Dermatol.*, Vol. 77, 13–19, 1981.
2. Weissleder, R., "A clearer vision for in vivo imaging," *Nat. Biotechnol.*, Vol. 19, 316–317, 2001.
3. Sevick-Muraca, E. M., J. P. Houston, and M. Gurfinkel, "Fluorescence-enhanced, near infrared diagnostic imaging with contrast agents," *Curr. Opin. Chem. Biol.*, Vol. 6, 642–650, 2002.
4. Geng, J. L., Z. S. Zhu, W. Qin, L. Ma, Y. Hu, G. G. Gurzadyan, B. Z. Tang, and B. Liu, "Near-infrared fluorescence amplified organic nanoparticles with aggregation-induced emission characteristics for in vivo imaging," *Nanoscale*, Vol. 6, 939–945, 2014.
5. Frangioni, J. V., "In vivo near-infrared fluorescence imaging," *Curr. Opin. Chem. Biol.*, Vol. 7, 626–634, 2003.
6. He, X. X., K. M. Wang, and Z. Cheng, "In vivo near-infrared fluorescence imaging of cancer with nanoparticle-based probes," *Wiley Interdiscip. Rev.: Nanomed. Nanobiotechnol.*, Vol. 2, 349–366, 2010.
7. Geng, J. L., K. Li, K. Y. Pu, D. Ding, and B. Liu, "Conjugated polymer and gold nanoparticle co-loaded PLGA nanocomposites with eccentric internal nanostructure for dual-modal targeted cellular imaging," *Small.*, Vol. 8, 2421–2429, 2012.

8. Ghoroghchian, P. P., P. R. Frail, K. Susumu, D. Blessington, A. K. Brannan, F. S. Bates, B. Chance, D. A. Hammer, and M. J. Therien, "Near-infrared-emissive polymersomes: Self-assembled soft matter for in vivo optical imaging," *Proc. Natl. Acad. Sci.*, Vol. 102, 2922–2927, USA, 2005.
9. Liu, J., J. L. Geng, L. D. Liao, N. Thakor, X. H. Gao, and B. Liu, "Conjugated polymer nanoparticles for photoacoustic vascular imaging," *Polym. Chem.*, Vol. 5, 2854–2862, 2014.
10. Qian, J., D. Wang, F. H. Cai, Q. Q. Zhan, Y. L. Wang, and S. L. He, "Photosensitizer encapsulated organically modified silica nanoparticles for direct two-photon photodynamic therapy and In Vivo functional imaging," *Biomaterials*, Vol. 33, 4851–4860, 2012.

A Photostable AIE Luminogen for Multifunctional Three-photon Bioimaging

Zhenfeng Zhu[1], **Chris Wai Tung Leung**[2], **and Xinyuan Zhao**[3]

[1]Centre for Optical and Electromagnetic Research
Zhejiang Provincial Key Laboratory for Sensing Technologies
Zhejiang University, Hangzhou 310058, China
[2]Department of Chemistry, The Hong Kong University of Science and Technology
Clear Water Bay, Kowloon, Hong Kong, China
[3]Bioelectromagnetics Laboratory, School of Medicine
Zhejiang University, Zijingang Campus, Hangzhou 310058, China

Abstract— In this study we realized multiphoton bioimaging, by utilizing a kind of fluorescent agent with aggregation induced emission (AIE) feature. The luminogen is called tetraphenylethene-triphenylphosphonium (TPETPP), and it is a highly specific mitochondria tracker. We studied its photostability under three-photon excitation, and found that even under long-term excitation, the three-photon fluorescence signals of TPETPP in the cells still kept very bright. Furthermore, under the same 1020 nm femtosecond excitation, TPETPP assisted three-photon imaging has higher spatial resolution than two-photon imaging of MitoTracker red FM (MT), which is a commercially available mitochondria imaging agent.

1. INTRODUCTION

With the advantages of sensitivity, selectivity, and biocompatibility, fluorescent probes have been a powerful tool for bioimaging and biosensing [1–4].

Multiphoton luminescence imaging, which takes the advantages of high spatial resolution, as well as large *in vivo* imaging depth [5], is playing an important role in both preclinical research and clinical diagnostic applications[6]. Multiphoton absorption/luminescence is a high order nonlinear optical process, which is closely related with the wavelength and intensity of the excitation light, as well as the luminescent efficiency of the fluorophore. Furthermore, fluorophore sample with high concentration can achieve nonlinear optical process more easily than that with low concentration.

However, most commercial organic fluorophores, which are highly emissive in solution, show weak or no emission in the solid state or aggregated state. This phenomenon is notoriously known as aggregation-caused quenching (ACQ) [7]. ACQ effect limits the applications of many fluorescent probes in high concentration. In 2001, a new phenomenon, which is opposite to ACQ effect and named as aggregation-induced emission (AIE), was discovered by Tang's group [8, 9]. In AIE system, the fluorescence of dye increased with the aggregation of the molecules instead of quenching.

Fluorescent probes which can specifically target to specific organelles are of significance. Very recently, Tang's group reported a type of AIE luminogen named tetraphenylethene-triphenylphosphonium (TPETPP), which is an excellent mitochondria tracker [10]. However, the absorption peak of TPETPP is around 320 nm, which is in ultraviolet spectral range. Excitation light with a wavelength in this range has high energy and may produce damage towards cells.

In this paper, we realized multiphoton fluorescence imaging of tumor cells, which were stained with TPPTPP, and further studied its photostability under three-photon excitation. Furthermore, under a 1020 nm-femtosecond laser excitation, three-photon imaging of TPETPP showed higher resolution than two-photon imaging of MitoTracker red FM (MT), which is a commercially available mitochondria targeting agent [11, 12]. We here demonstrate that TPETPP can light up mitochondria specifically with 1020 nm femtosecond laser in live cells with superior photostability as well as high spatial resolution, enabling the observation of mitochondrial morphological changes and study of these processes.

2. EXPERIMENTAL

2.1. Materials and Instruments

TPETPP is a tipical dye with AIE feature and was kindly provided by Prof. Tang's group [10]. Dimethylsulfoxide (DMSO) was purchased from Aldrich. Dulbecco Minimum essential medium

(MEM), fetal bovine serum (FBS), penicillin and streptomycin and MitoTracker Red FM were purchased from Invitrogen.

A Shimadzu 2550 UV-vis scanningspectrophotometer and a HITACHI F-2500 fluorescence spectrophotometer were used to measure the absorption and photoluminescence (PL) spectra of samples, respectively. An Olympus laser scanning confocal microscope (FV1000) equipped with various laser sources (e.g., CW laser, femtosecond laser) was used for one-photon and multiphoton imaging function.

2.2. Cell Culture

HeLa cells were cultivated in Dulbecco minimum essential media (DMEM) with 10% fetal bovine serum (FBS), 1% penicillin, and 1% amphotericin B, at 37°C and 5% CO_2. After 24 h, the TPETPP or MT dissolved in DMSO solution was used to treat the HeLa cells. The working concentrations of TPE-TPP and MT in our experiments were 250 µM and 50 nM, respectively. After incubation, the cells were gently washed thrice by phosphate buffered saline (PBS, pH = 7.4, 10 mM) and imaged by the Olympus laser scanning confocal microscope.

3. RESULTS AND DISCUSSION

Figure 1(a) shows the chemical structure of TPETPP. It includes the group of TPE with AIE feature and the function group of TPP for the targeting of mitochondrial. Figure 1(b) is the absorption of TPETPP in DMSO solution, the absorption peak located around 320 nm.

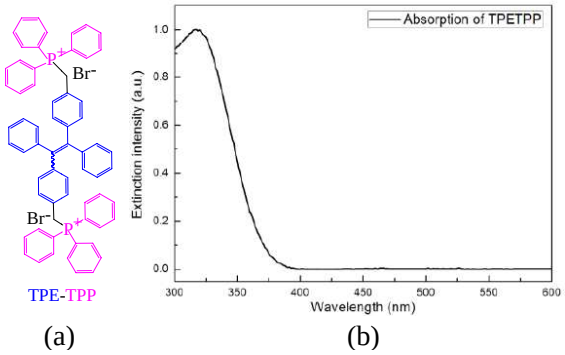

Figure 1: (a) Chemical structure of TPE-TPP, and (b) the absorption spectrum of TPETPP in DMSO.

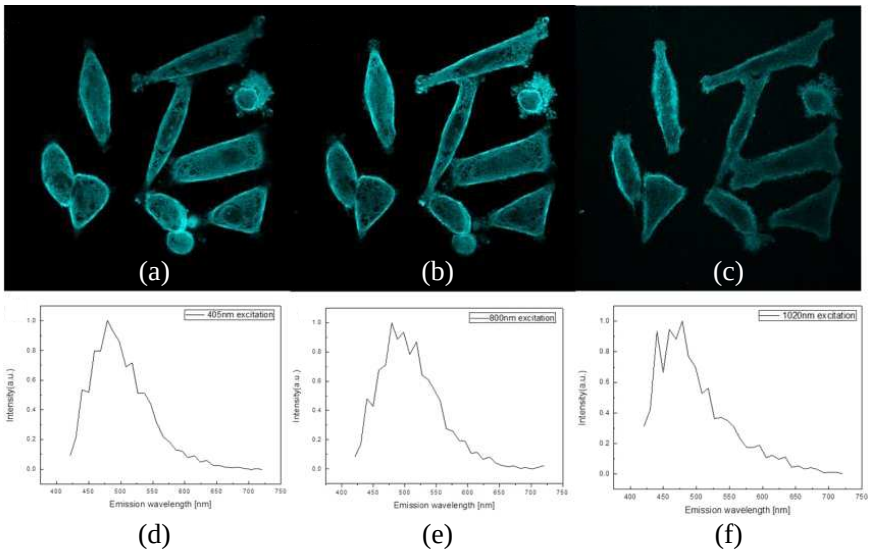

Figure 2: (a) One-photon, (b) two-photon and (c) three-photon fluorescence imaging of HeLa cell treated with TPETPP, and the excitation were (a) 405 nm CW laser, (b) 810 nm femtosecond laser, (c) 1020 nm femtosecond laser, respectively. The statistic (d) one-photon, (e) two-photon and (f) three-photon fluorescence spectra in the cells were shown accordingly.

Figures 2(a), (b), (c) show the one-photon, two-photon and three-photon fluorescence imaging of HeLa cells treated with TPETPP. Figures (d), (e), (f), show the statistic fluorescence spectra in the cells. They all have a luminescence spectrum in the range of 425–600 nm (with the maximum locating at 470 nm), and the envelopes of all the three spectra are very similar). It means under one-photon, two-photon and three-photon absorption, the excited TPETPP nanoparticles were finally relaxed to the same lowest excited electronic-vibrational state, from which the luminescence emission occurred. When the TPETPP sample was stimulated by 810 nm femtosecond laser, it needs to absorb two photons at the same time to get excited, and when the TPETPP sample was stimulated by 1020 nm femtosecond laser, it needs to absorb three photons at the same time to get excited.

Photostability is one of the most important requirements for fluorescence imaging. Tang's group have proved that in one-photon fluorescence imaging, TPETPP takes an obvious advantage over MT in photostability [10]. We then explore this property under three-photon excitation (by using a 1020 nm-femtosecond laser). Here, we still took MT as control. The initial three-photon fluorescence intensity referring to the first scan of TPE-TPP and MT stained cells was used for normalization, and the percentage of signal loss after each additional scan was calculated. As shown in Figure 3(c), under the excitation of 1020 nm laser, during 50 scans with total irradiation time of about 5 mins, the signal loss of TPETPP was less than 15%, and no significant difference was observed between the first and the 50th scan (Figure 3(a)). In contrast, the fluorescence signals of MT almost disappeared after 50 scans, with $< 40\%$ signal intensity remaining (Figure 3(b)).

The reason why TPETPP possesses high photostability under three-photon excitation can be explained as following. Due to the AIE feature, the nanoaggregates of TPETPP are much brighter emitters than its single molecular form, and in the mitochondrial, the TPE-TPP are in the state of aggregation. When exposed to excitation light, the outermost layer of the nanoaggregates may be photobleached. However, the condensed particles can prevent further photobleaching and photo-oxidation by avoiding oxygen diffusion into the particles. For MT, the low working concentration makes it present as an individual molecule which will be destroyed with ease by the strong excitation light.

High spatial resolution is another advantage of TPE-TPP-assisted three-photon bioimaging. Theoretically, under the same excitation wavelength, three-photon imaging is expected to achieve higher spatial resolution ($\lambda/2\sqrt{3}NA$) compared with one-photon imaging ($\lambda/2NA$) and two-photon imaging ($\lambda/2\sqrt{2}NA$). Here, we used the 1020 nm-femtosecond laser to excite TPETPP for three-photon fluorescence imaging and MT for two-photon fluorescence imaging. For MT, the theoretical spatial resolution under two-photon excitation is $1020/2\sqrt{2}NA = 360NA$. However, for TPETPP, the theoretical spatial resolution under three-photon excitation is $1020/3\sqrt{2}NA = 240NA$, which is higher than that of MT. Our experiments results further proved it. The areas of the multiphoton images of cells are magnified by 20 times, as shown in Figure 4. According to the multiphoton fluorescence signal in two different channels (cyan for TPETPP and red for MT) of the same part of the cell, we find that the spatial FWHM (full width at half maximum) in the cyan channel

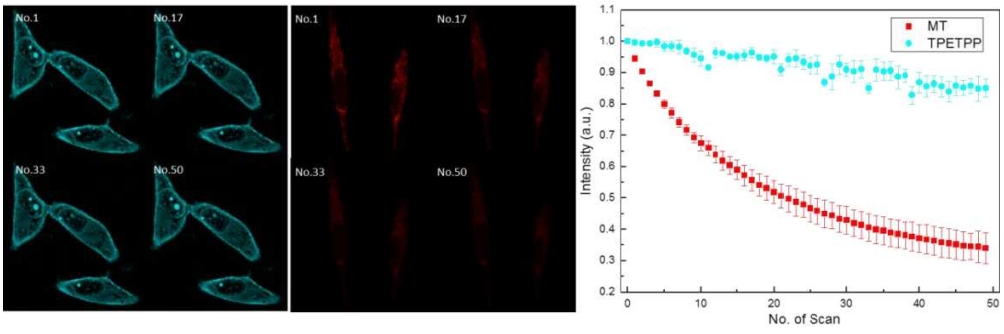

(a) (b) (c)

Figure 3: Three-photon fluorescence images of living HeLa cells stained with (a) TPETPP (cyan cell) and (b) MT (red cell) with increasing number of scans (1–50 scans; the number of scans shown in upper left corner), (c) three-photon fluorescence loss (%) of TPE-TPP (cyan) and MT (red) in HeLa cells with increasing number of scans. Excitation source: 1020 nm femtosecond laser filter: 449–520 nm (for TPE-TPP) and 581–688 nm (for MT).

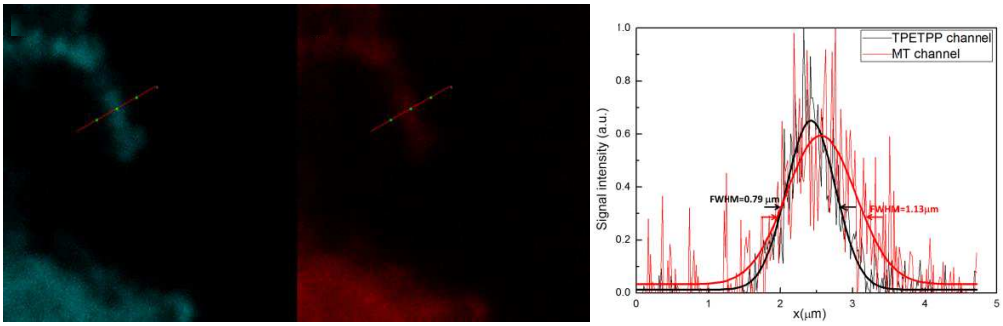

Figure 4: In vitro imaging of HeLa cells targeted by both TPETPP and MT, excitation wavelength:1020 nm, (a) channel 1 for the imaging of TPETPP, (b) channel 2 for MT, (c) line profile of the signal intensityfrom a (black), b (red line). Gaussianfits (smoothed line) are shown for clarity.

(0.79 μm) is narrower than that in the red one (1.13 μm), which illustrated TPETPP assisted three-photon imaging has higher spatial resolution than MT assisted two-photon imaging.

4. CONCLUSIONS

We studied multiphoton bioimaging, by utilizing TPETPP with AIE feature. Under the excitation of 1020 nm femtosecond laser, TPETPP achieved three-photon imaging and showed better photostability than a commercially available mitochondria tracker named MT. Besides, due to higher order nonlinear optical effect of TPETPP under 1020 nm excitation, TPETPP exhibited a higher spatial resolution than MT. TPETPP assisted three-photon bioimaging may have many promising biomedical applications in the future.

REFERENCES

1. Wang, Y., J. Y. J. Shyy, and S. Chien, "Fluorescence proteins, live-cell imaging, and mechanobiology: Seeing is believing," *Ann. Rev. Biomed. Eng.*, Vol. 10, 1–38, 2008.
2. VanEngelenburg, S. B. and A. E. Palmer, "Fluorescent biosensors of protein function," *Curr. Opin. Chem. Biol.*, Vol. 12, 60–65, 2008.
3. Borisov, S. M. and O. S. Wolfbeis, "Optical biosensors," *Chem. Rev.*, Vol. 108, 423–461, 2008.
4. Domaille, D. W., E. L. Que, and C. J. Chang, "Synthetic fluorescent sensors for studying the cell biology of metals," *Nat. Chem. Biol.*, Vol. 4, 168–175, 2008.
5. Zipfel, W. R., R. M. Williams, and W. W. Webb, "Nonlinear magic: Multiphotonmicroscopy in the biosciences," *Nature Biotechnol.* Vol. 21, 1369–1377, 2003.
6. Weissleder, R. and M. J. Pittet, "Imaging in the era of molecular oncology," *Nature*, Vol. 452, 580–589, 2008.
7. Birks, J. B., *Photophysics of Aromatic Molecules*, Wiley-Interscience, 1970.
8. Luo, J., Z. Xie, J. W. Y. Lam, L. Cheng, H. Chen, C. Qiu, H. S. Kwok, X. Zhan, Y. Liu, D. Zhu, and B. Z. Tang, *Chem. Commun.*, 1740, 2001.
9. Tang, B. Z., X. Zhan, G. Yu, P. P. S. Lee, Y. Liu, and D. Zhu, *J. Mater. Chem.*, Vol. 11, 2974, 2001.
10. Leung, C. W. T., Y. Hong, S. Chen, and B. Z. Tang, "A photostable AIE luminogen for specific mitochondrial imaging and tracking," *Journal of the American Chemical Society*, Vol. 135, 62–65, 2012.
11. Dong, L. F., V. J. A. Jameson, D. Tilly, L. Prochazka, J. Rohlena, K. Valis, J. Truksa, R. Zobalova, E. Mahdavian, K. Kluckova, M. Stantic, J. Stursa, R. Freeman, P. K. Witting, E. Norberg, J. Goodwin, B. A. Salvatore, J. Novotna, J. Turanek, M. Ledvina, P. Hozak, B. Zhivotovsky, M. J. Coster, S. J. Ralph, R. A. J. Smith, and J. Neuzil, "Mitochondrial targeting of α-tocopheryl succinate enhances its pro-apoptotic efficacy: A new paradigm for effective cancer therapy," *Free Radical Biol. Med.*, Vol. 50, 1546, 2011.
12. Yang, G., L. Liu, Q. Yang, F. Lv, and S. Wang, "A multifunctional cationic pentathiophene: Synthesis, organelle-selective imaging, and anticancer activity," *Adv. Funct. Mater.*, Vol. 22, 736, 2012.

Tuned Window for Standing Wave Linear Accelerators

Alberto Leggieri[1, 2], **Alessia Ciccotelli**[2], **Giuseppe Felici**[2], **Leonardo Zappelli**[3], **Davide Passi**[1], **and Franco Di Paolo**[1]

[1]Dipartimento di Ingegneria Elettronica, Università degli Studi di Roma "Tor Vergata"
Via del Politecnico, 1, Roma 00133, Italy
[2]S.I.T. — Sordina IORT Technologies, S.p.A., Via dell'Industria, 1A, Aprilia, LT 04011, Italy
[3]Dipartimento di Ingegneria dell'Informazione, Università Politecnica delle Marche
Via Brecce Bianche, Ancona 60131, Italy

Abstract— This paper proposes a dielectric window for Standing Wave Linear Accelerators (LINAC's) which can be tuned after brazing and welding, in order to compensate the electromagnetic alteration due to these production processes. This study investigates the in-frequency return loss behavior of the LINAC, in order to improve matching and transmitting conditions while maintaining the optimum coupling between LINAC and High Power Microwave (HPMW) source. Device design is single-frequency based and considers the dielectric window interface as an Input Matching Network (IMN) at the LINAC normal mode working frequency. Thus, design formulas are provided and Computer Aided Design techniques are proposed. A prototype has been made and tested by performing cold S-parameter measurements of a LINAC with the proposed dielectric window and with a traditional dielectric window. The proposed device offers more energy transport attitude over the traditional dielectric window, as shown by a return loss increase of 167% of the complete system.

1. INTRODUCTION

Dielectric windows are microwave devices which separates Ultra High Vacuum (UHV) inside vacuum devices (as vacuum tubes or LINAC) to the normal atmosphere in the transport waveguide (which connects the HPMW source), ensuring the microwave power transmission. These windows are made by a waveguide section, in which a dielectric plate is inserted. Typically, energy transport systems are based on rectangular waveguide (RWg) and, due to technological reason; dielectric windows are based on circular waveguide (CWg) sections. For these reasons, the most common kind of window is the pill-box type which consists of a CWg section, at which centre a dielectric (typically ceramic) cylindrical plate is enclosed. CWg section terminates on both sides to two CWg to RWg transitions. Vacuum windows also enable the RWg to be filled with SF6 for high-power transmission [1].

Several technological solutions can be adopted, as for example long pill-box type windows, with a very long longitudinal size [2], or with oversized diameter [3]. Usually, design of Radiofrequency (RF) structure can be achieved by using a circuit model and in all cases RF analysis, using high-frequency simulation codes, allows to optimize properties of the RF structure [2, 3]. For high power transfer, oversized circular plates are sometimes employed in order to reduce the RF field strength on the ceramic surface by increasing the diameter of its ceramic part compared to an ordinary pill-box type window [3]. Clearly this solution may result in an unwanted encumbrance.

This paper shows the design of a dielectric window for a Standing Wave LINAC to be employed in a medical mobile electron LINAC, dedicated to intra operative radiation therapy (IORT). The whole medical device is required to be as small and light as possible: Therefore, oversized and long structures are preferably avoided. After the manufacturing process, every LINAC may present a degradation of its electromagnetic characteristics, which inter alia may results in an increase of its reflection coefficient. By connecting to the LINAC input port a dielectric window made with a high insertion loss, these reflections reduce, but transmission efficiency decrease. Choosing a low insertion loss one, the transmission increases but multipath reflections through the LINAC may increase with respect to using a high insertion loss medium. In this paper, we propose a design technique to reduce these reflections. The Tuned Window consists of a low insertion loss pill-box type vacuum window with alumina ceramics connected to an input matching network (IMN).

In this paper a new formula for the calculation of the Pill-box radius is proposed and other formulas, taken from literature, are reported. In the LINAC technological production process, dielectric window is brazed or welded to the LINAC power coupler (LPC). During this factory step, the input characteristics of the system can be modified. In this paper, we propose to compensate such alteration by inserting a reactive IMN at the low pressure interface of the dielectric window.

Since the IMN is placed in the low pressure section and it can be inserted by screws without vacuum loss, it can be sized basing on the effective measured input parameters of the LINAC at the resonance. A design technique for the Tuned Window and a numerical method for optimization are proposed. Finally, a prototype is described.

2. THE TUNED WINDOW PRINCIPLE

Due to manufacturing production process, every LINAC has a proper normal mode working frequency, typically different to the others (up to 0.03% in band, respect to the design frequency). This phenomenon is due principally to the LINAC first brazing process, during which a very little, but not fully controllable, quantity of brazing alloy can penetrate into the resonant cavities. After the first brazing process, the LINAC is tuned. Such issue results in a LINAC own normal mode resonant frequency. However, global characteristics can be further degraded by following brazing or welding processes, as for example the dielectric window welding.

At the normal mode frequency of resonance, without the window, the LPC shows the external reflection coefficient ρ_{Ext} to the outside; ρ_{Ext} consists of the LINAC reflections coefficient ρ, transformed by the LPC. A pill-box dielectric window is connected to the LPC and ρ_{Ext} is transformed to ρ'_{in} by the window. This connection is performed by a brazing process.

After brazing, ρ'_{in} can be measured and an opportune IMN can be designed, to provide the right matching condition between the LPC and the HPMW source and ensuring the optimum reflection coefficient ρ_{Opt} shown by the LPC to the LINAC (Fig. 1).

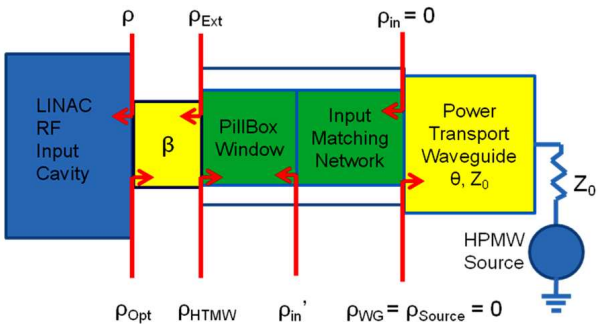

Figure 1: Devices disposition and reflections coefficients at the interfaces.

Due to technological production process, circular pill-box window has been chosen: A circular ceramic-disk was chosen for easy machining and brazing [3]. This dielectric plate, which has a metallization across its border, has been brazed to the waveguide section. The brazing process of the dielectric window is carried inside a vacuum oven with a maximum temperature of 780°C in which the component materials are welded by a CUSIL alloy of 28% Cu and 72% Ag. This temperature may deform the interface between the guide and the dielectric plate. Therefore, during this process, equally distributed forces have to be applied to the interface. The described operation is easier to perform, by using circular symmetry, then using a rectangular one. From an analysis on commercial available dielectric materials, the Alumina Al_2O_3 97.6% has been chosen, which provides the high transparency to the microwave in order to obtain very low insertion loss and great stress resistance.

After building and brazing or welding the pill-box window section to the LPC, reflection coefficient ρ'_{in} can be measured and the opportune values of the matching elements can be obtained. For this reason, the IMN has been made by an iris loaded waveguide, which is easily realizable, perfectly according to the exact normal mode working frequency of the brazed LINAC, on which the Tuned Window will be mounted. We show the design of the waveguide section and capacitive iris, a field simulation and a system optimization. After all, scattering parameters, cross sectional electric fields, transmitted and reflected waves are shown.

3. TUNED WINDOW DESIGN

Pill-box dielectric window was widely analyzed as a typical problem of waveguide junctions in microwave circuit in [1] and compact design formulas are described in [4] which can be employed to quickly design an initial dielectric window that can be optimized by adopting numerical codes. In

this work we propose a design technique for a Pill-box dielectric window with good electromagnetic performance and the IMN for matching the LINAC. Such whole system is the Tuned Window.

3.1. Circular Waveguide Cross Section

Pill-box dielectric window consists principally of a RWg to CWg mirrored transitions [1]. Each discontinuity may insert mathematically infinite modes, but only the modes over cut off can propagate in the adjacent spaces. Other modes (evanescent modes) may store and release reactive energy. This phenomenon considerably reduces transmitting and reflecting performances. Such behavior can be avoided if, at the desired frequency, the wave does not view the discontinuity, so that the fundamental mode of the RWg leads only the fundamental mode of the CWg. The discontinuity will result locally in-frequency invisible to the wave, if the fundamental mode wavelength propagating into the RWg will remain the same in the CWg. The fundamental propagating mode in a RWg is the TE_{10} and into a CWg is the TE_{11}. Fundamental mode wavelengths into the RWg and the CWg are respectively expressed in (1) and (2) [5].

$$\lambda_{gR} = \frac{\lambda_0}{\sqrt{\epsilon_r - \frac{\lambda_0^2}{\lambda_{cR}^2}}}, \tag{1}$$

$$\lambda_{gC} = \frac{\lambda_0}{\sqrt{\epsilon_r - \frac{\lambda_0^2}{\lambda_{cC}^2}}} \tag{2}$$

where

$$\lambda_{cR} = 2a\sqrt{\varepsilon_r \mu_r}, \tag{3}$$

$$\lambda_{cC} = \frac{2\pi r}{p'_{11}\sqrt{\varepsilon_r \mu_r}} \tag{4}$$

and

$$\lambda_0 = \frac{c_0}{f} \tag{5}$$

is the wavelength on free space, ε_r is the dielectric constant and μ_r the magnetic permittivity of the medium which fills the waveguides, a is the long side of the RWg and r is the radius of the CWg. p'_{11} is the first zero of the one order Bessel function derivative ($p'_{11} = 1.841$), f the normal mode resonant frequency of the LINAC and c_0 is the speed of the light in the vacuum.

The pill-box window consists of a CWg section of length L, at which centre a dielectric disk is inserted and at which ends CWg to RWg transitions are placed. One RWg face is connected to the LINAC and the other is connected to the HPMW source. The CWg subsection on the LINAC side is in an UHV atmosphere and the subsection on the HPMW side is filled by dry air or SF6 at the typical pressure of about 2 Bar. Due to the similarity of the dielectric constants of vacuum, air and SF6, for simplicity we can approximate the two CWg sectors as filled by the same dielectric. Since the CWg is partially filled with alumina ceramic, this may be treated as equivalent to the CWg filled uniformly with a dielectric having effective relative permittivity ε'_r. For most of the high power pill-box windows, the value of ε'_r will vary between 1.0 and 2.0. A value of 1.5 is reasonable for ε'_r [4]. Magnetic permeability of these mediums has been considered as 1. Since the power transport system is based on RWg, we can consider λ_{gR} as a known value. By substituting (4) in (2), setting $\lambda_{gR} = \lambda_{gC}$ and replacing ε_r with ε'_r, we obtain the value of the CWg radius which ensures the local transparency of the discontinuity. The proposed formula is expressed in (6):

$$r = \frac{\lambda_0 p'_{11}}{2\pi\sqrt{1 - \frac{\lambda_0^2}{\varepsilon'_r \lambda_{gR}^2}}} \tag{6}$$

3.2. Dielectric Disk

In order to have high electromagnetic transmission by minimize the wave scattering due to the crystal atoms, high purity alumina can be employed as the dielectric medium for the disk interposed between the two CWg subsections.

Such disk should be designed at least with the minimum thickness which ensures the structural capacity to endure the direct stress σ applied from the atmosphere normal force F_n, avoiding

breakdowns or significant deformations. According to [6], this direct stress corresponds to the pressure P which the dielectric cylindrical disk experiences on its area in contact to the UHV.

$$\sigma = \frac{F_n}{\pi r^2} = P \tag{7}$$

Dielectric medium mechanical characteristics are to be provided by the vendor and optimized according to the brazing facility expertise. Thickness t of the dielectric plate is to be optimized by using computer-aided design tool in order to maximize the microwave transmission efficiency of the dielectric window. Due to the waveguide pressurization adopted, the maximum pressure on the plate can be assumed to be less than 2 Bar. As high transparency medium for the dielectric plate, we have chosen alumina WESGO Ceramics type AL300, which is an Al_2O_3 97.6%. In order to employ a plate radius of about 30–40 mm, a good thickness in the above condition, should be around 2.5 mm.

3.3. Circular Waveguide Length

In order to transfer maximum of microwave power from rectangular to circular and then vice-versa for downward transmission, it is required that at the junction, impedance of the rectangular waveguide should match with the impedance of circular waveguide both in the input & output side. The junction is placed at the half of the CWg. From the junction, we can consider two CWg subsections of length L' given by (8). By considering the effective permittivity $\varepsilon'_r = 1.5$, according to [4], for impedance matching of rectangular and circular waveguide, we need to set wavelength of a single CWg section, loaded with this effective dielectric constant, to an opportune value, given by (9) in which a and b are respectively the long and the short side of the RWg cross section. Using standard transmission line theory on quarter wave length transformer for matching the length of the CWg subsections, L' can be written as in the (10) [4]:

$$L' = L/2 \tag{8}$$

$$\lambda'_{gC} = \frac{b}{0.816a}\lambda_{gR} \tag{9}$$

$$L' = \lambda'_{gC}/4 \tag{10}$$

3.4. Dimensioning and Numerical Optimization

For an S-Band LINAC operating at $f = 2998$ MHz and driven through a RWg WR284, which have $a = 72.14$ mm and $b = 34.04$ mm, by applying the (1) with $\varepsilon'_r = 1$ we obtain $\lambda_{gR} = 138.72$ mm and from the (5) we have $\lambda_0 = 100$ mm. From the (9) results that $\lambda'_{gC} = 80.17$ mm and by the (10) $L' = 20.04$ mm, so from the (8) the total length of the CWg is $L = 40.08$ mm. By applying (6) with $\varepsilon'_r = 1.5$ results in $r = 36$ mm.

The analytical design procedure, is a simplification of the real dimensioning problem, in which we have more difficulties given mostly from spatial distribution and complex value of dielectric constant. In fact, effective dielectric constant depends by the length of the CWg, resulting in a recursive problem, thus we need to set a value of ε'_r, and a numeric optimization is mandatory. Length L of circular waveguide sections as well as thickness t of dielectric plate can be optimized by an electromagnetic (EM) simulation. For this operation we have chosen Comsol Multiphysics® (Version 4.0), which is based on the Finite Element Method (FEM). By using this software, the simulation can be extended to a Thermo-structural analysis, in order to compute the electromagnetic behavior modifications due to the thermo mechanical induced conditions, as described in [7].

The aim of the simulation is to search the optimum values of L and t which provide the minimum reflection parameter and the maximum transmission parameter at the two ports of the Pill-box Window. The EM simulation has been performed setting two vacuum circular sections of radius r and variable length L, which enclose the dielectric plate, as previously defined. Two standard RWg WR284 sections are connected at the open faces of the CWg section. All the waveguide boundaries are made of copper with an Impedance Boundary Condition which considers the field penetration inside the conductor, according to its skin depth. At the RWg's external faces, TE ports are placed. The solution is computed by a Stationary solver at the normal mode LINAC operative frequency f, by sweeping the length L and the thickness t and calculating the scattering parameters at two ports. The simulation has been initially set with the dielectric window values analytically calculated above, and an Al_2O_3 97.6% plate of thickness $t = 2.5$ mm. This Alumina presents a dielectric constant of $\varepsilon_r = 9.0$ in S band, which in the simplified analytical dimensioning

has not been considered properly. By introducing this value in a numeric computation, we obtained an accurate dimensioning of the structure.

The optimization has shown an optimum length of the circular sections $L = 27\,\text{mm}$ and optimal dielectric plate thickness $t = 2.4\,\text{mm}$. With such values, an EM simulation has been performed in the operative range of the HPMW source, according to the normal mode operative frequency variation due to the LINAC cavities variable thermal conditions, which are in the range of 2993–3003 MHz. In this range, scattering parameters have been evaluated: The maximum reflection parameter is $|S_{11}|_{\text{dB}} = -34.5\,\text{dB}$ and the minimum transmission parameter is $|S_{21}|_{\text{dB}} = -0.0044\,\text{dB}$. As we expects, by exciting the TE_{10} mode of the RWg, in the cylindrical section the propagating mode is the TE_{11} of the CWg, as shown in Fig. 2.

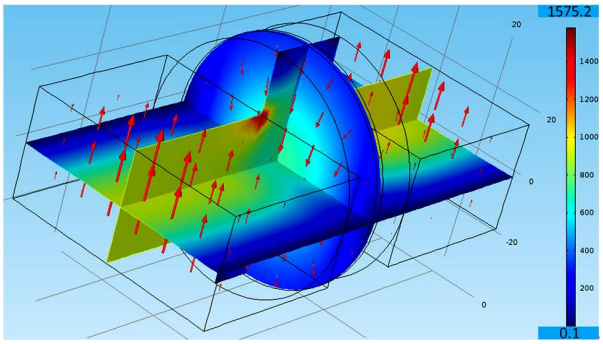

Figure 2: Geometry and electric field (V/m) distribution in the RWg and dielectric window on bisecting planes @ 2998 MHz (RWg TE_{10} and CWg TE_{11}) for $L = 27\,\text{mm}$ with $t = 2.4\,\text{mm}$.

3.5. Input Matching Network

The aim of inserting this network is to compensate the various alterations of the electromagnetic device characteristics due to the brazing and welding fabrication processes. Various matching strategies for microwave devices are available in literature and can be applied to such design [8]. This network will be realized through a RWg section loaded by an iris element earned in a flanged parker gasket. Such IMN can be inserted in the normal atmosphere interface of the window, between the RWg flanges of the dielectric window and the flanges of the power WG.

In order to physically realize the dielectric window, the CWg sections are welded at both the two interfaces: one (at the UHV side) welded to the LINAC and the other (at the normal atmosphere side) to a RWg flange. At this flange the transport RWg will be connected by screws and the reflection coefficient ρ'_{in} can be measured at the normal mode resonant frequency of the LINAC. In order to match the entire structure, a capacitive/inductive window can be placed at the input section of the structure.

Unfortunately, the complexity of the structure produces a coupling between the evanescent and propagating modes that makes very difficult to obtain a simple formula for the choice of the geometry of the window, like those discussed in [9]. Hence, more complex models based on equivalent circuits that take into account the presence of evanescent accessible modes [10, 11] must be used. The matching window has been implemented by a capacitive iris (see Fig. 3) realized in a Parker gasket with $d = 21.7\,\text{mm}$ and $t = 3.3\,\text{mm}$ (see Fig. 4).

4. PROTOTYPE MEASUREMENTS AND COMPARISONS

The Tuned Window has been simulated in the Department of Electronic Engineering of the University of Rome "Tor Vergata", realized in T.S.C. S.r.l. factory and gently tested in the RF department of S.I.T. S.p.A.

The circular section of the window is inserted between two steel slabs. Each slab has, at the center, a rectangular hole of $72.14\,\text{mm} \times 34.04\,\text{mm}$ which represents the CWg to RWg transition. Due to technological production reasons, the steel slab in the UHV side has 6 mm of thickness and the other one, on the normal pressure side, is 16 mm deep, at which end the iris has been inserted. The iris has been realized in the internal profile of a RWg WR284 Parker gasket with 3 mm of thickness. Iris is connected to the remaining structure by the typical ten WR284's screws. This solution allows to insert the iris after brazing or welding the UHV side of the window without any other welding process.

The LINAC reflection coefficient, moved by the window, ρ'_{in} has been measured by considering the modification due to the welding process. The Tuned Window prototype is made using the following materials: Oxygen Free High Conductivity (OFHC) 99.99% copper for the circular waveguide section and iris, AISI316L steel for the CWg to RWg transitions and WESGO Ceramics AL300® 97.6% Alumina for the dielectric disk. The prototype of the Pill-box Window without IMN has been tested using an Agilent E5071B VNA in the operative range of 2993–3003 MHz. Setup is depicted in Fig. 5. Measured and simulated scattering parameters are reported in Fig. 6. In this range, the maximum measured reflection parameter have $|S_{11}|_{\text{dB}} = -35.2$ dB and the average transmission parameter is $|S_{21}|_{\text{dB}} = -0.003$ dB. Such window will operate in transmitting a pulsed power of 2.5 MW with pulse duration of 4 µs and repetition frequency of 5 Hz.

The Pill-box window shown in this paper is a traditional dielectric window with high trans-

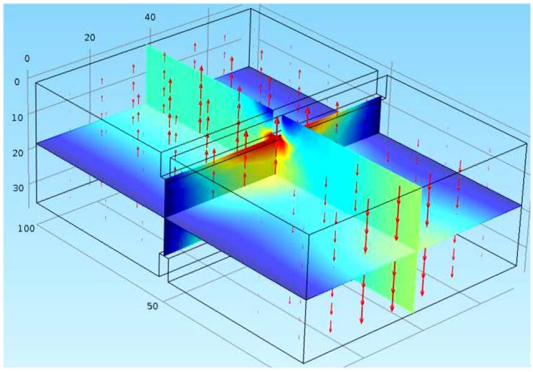

Figure 3: Capacitive iris structure on the RWg sector and fundamental mode (TE_{10}) electric field distribution on bisecting planes at 2998 MHz.

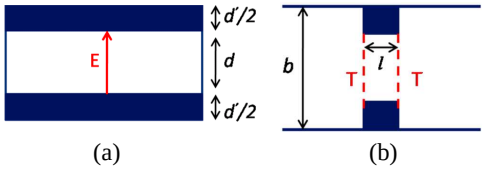

Figure 4: Capacitive iris: (a) longitudinal section, and (b) front views.

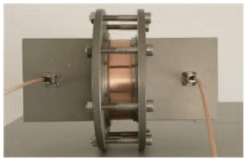

Figure 5: The pill-box window under test between two RWg launchers.

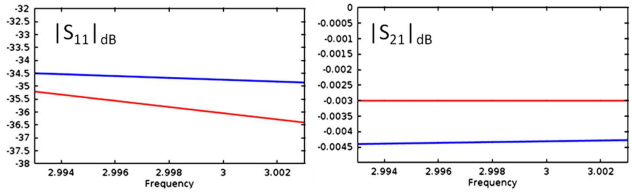

Figure 6: Simulated (blue) and measured (red) scattering parameters of the designed pill-box window without IMN. S_{11} and S_{21} in dB (vertical axis), versus frequency in GHz (horizontal axis).

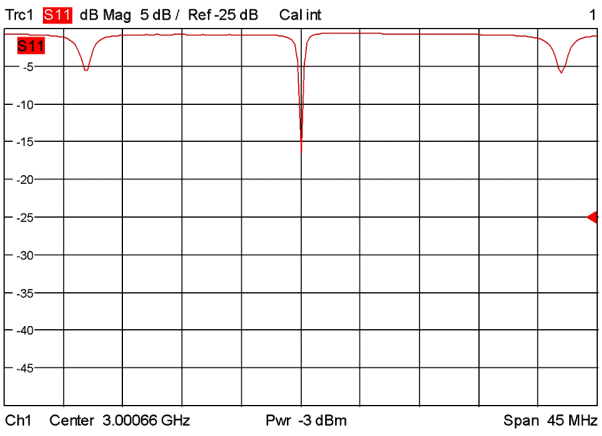

Figure 7: Measured reflection scattering parameter of the LINAC with only the traditional pill-box window. $|S_{11}|$ dB (vertical axis) versus frequency (horizontal axis) from 2.978 GHz to 3.023 GHz: The return loss is 16.5 dB.

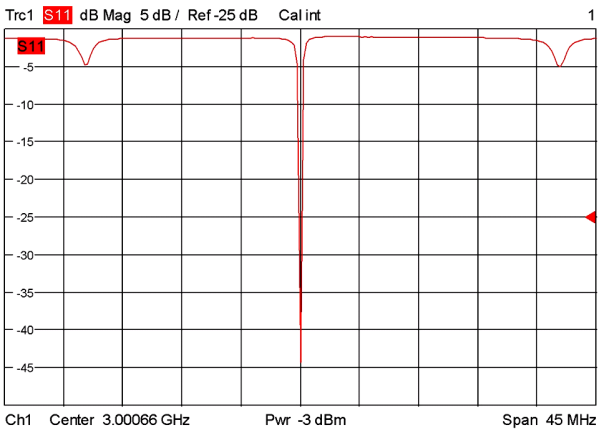

Figure 8: Measured reflection scattering parameter of the LINAC with the whole tuned window. $|S_{11}|$ dB (vertical axis) versus frequency (horizontal axis) from 2.978 GHz to 3.023 GHz: The return loss is 44 dB.

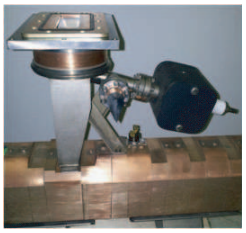

Figure 9: Side view of the tuned window on the LINAC.

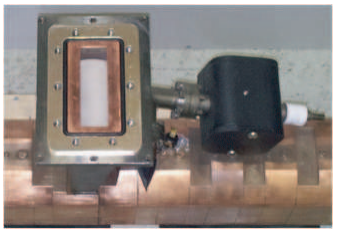

Figure 10: Top view of the tuned window on the LINAC.

parency performances, comparable to the windows described in the already present literature [2, 4].

The Tuned Window prototype has been designed for an R.F. standing wave side coupled LINAC of the IORT dedicated mobile accelerator NOVAC 111®, described in [12], working a 2.998 MHz in $\pi/2$ mode. Cold Measurements of the prototype have been performed by using a Rhode & Swartz ZVL VNA. The input characteristic of this LINAC has been measured without dielectric window in normal atmosphere and with the only traditional pill-box dielectric window in UHV. In both cases, with negligible differences, it has shown quality factor $Q_0 = 12200$, a Coupling Factor $k = 1.35$ and a return loss of 16.5 dB, as described in Fig. 7. By using the complete Tuned Window we have obtained a return loss of 44.0 dB, as shown in Fig. 8, while maintaining a good value of $Q_0 = 12140$ and improving $k = 0.99$. The Tuned Window, inserted on the NOVAC 11® LINAC, is shown in Figs. 9 and 10.

5. CONCLUSIONS

LINAC input characteristic has been investigated, in particular with the need to separate UHV inside the accelerating structure to the normal atmosphere in the transport waveguide, while maintaining the better transparency to electromagnetic waves. In order to ensure vacuum shielding and transparency to the microwave, an useful solution has been found. A particular dielectric window which includes a waveguide iris-based matching network has been designed and built. Design formulas have been provided and computer aided design techniques have been proposed.

An after brazing global improvement of the accelerator figures of merit is possible by employing the proposed device.

With the Tuned Window inserted on a standing wave electron LINAC we have obtained several advantages over the traditional dielectric window, as it has been documented by several measurements on the NOVAC 11® LINAC.

Measurements of the reflection parameter at the LINAC input port, with the Tuned Window, have shown a return loss increase of 167%, from a return loss of 16.5 dB to a return loss of 44.0 dB over the LINAC with a traditional dielectric window. Such resulting structure is much better matched and coupled to the generator, with respect to the LINAC with a traditional window. This improvement is possible since the iris was designed for the specific LINAC, by considering its reflection coefficient at the working frequency measured after the brazing processes. However, we noted that the same iris can be employed to match several other similar LINACs with good results. This improvement allows to use lighter and cheaper insulators or circulators in the Radiofrequency power transmission chain, and a bit lower power sources. This solution can offer a decrease of power line size, weight and cost.

REFERENCES

1. Arai, H., et al., "An analysis of a vacuum window for lower hybrid heating," *IEEE Transactions on Plasma Science*, Vol. 14, No. 6, 947–954, December 1986.
2. Hirano, K., et al., "Development of a high power 1.2 MW CW L-band klystron," *Proc. of Particle Accelerator Conference*, 1539–1541, Dallas, TX, 1995.
3. Otake, Y., et al., "Design and high-power test of a TE11-mode X-band RF window with taper transitions," *Proc. of Particle Accelerator Conference*, 1590–1592, Dallas, TX, 1995.
4. Lamba, O. S., et al., "Design and optimization of asymmetric RF window for 6 MW pulse power S-band Klystron," *Proc. of International Conference on Recent Advances in Microwave Theory and Applications*, 44–46, Jaipur, India, 2008.

5. Ramo, S., J. R. Whinnery, and T. Van Duzer, "Characteristics of common waveguides," *Fields and Waves in Communication Electronics*, 3rd Edition, 429–437, John Wiley & Sons, New York, 1994.
6. Ugural, A. C., "Stress and strain," *Mechanical Design: An Integrated Approach*, 1st Edition, 72–73, McGraw-Hill, New York, 2003.
7. Leggieri, A., D. Passi, and F. Di Paolo, "Multiphysics modeling based design of a key-holes magnetron," *Proc. of IEEE International Conference on Numerical Electromagnetic Modeling and Optimization*, Pavia, Italia, 2014.
8. Di Paolo, F., "Fundamental theory of transmission lines," *Networks and Devices Using Planar Transmission Lines*, 1st Edition, 19–81, CRC Press LLC, Boca Raton, FL, 2000.
9. Marcuvitz, N., Sec., "Capacitive obstacles of finite thickness" of Chap. "Four terminal structures," *Waveguide Handbook*, 1st Edition, 248–257, McGraw-Hill, New York, 1951.
10. Zappelli, L., "An equivalent circuit for discontinuities exciting evanescent accessible modes," *IEEE Transactions on Microwave Theory and Techniques*, Vol. 60, No. 5, 1197–1209, May 2012.
11. Zappelli, L., "An equivalent circuit for thick centered irises in rectangular waveguide," *Proc. of IEEE International Conference on Numerical Electromagnetic Modeling and Optimization*, Pavia, Italia, 2014.
12. S.I.T. S.p.A., NOVAC 11® product description, Italy, 2013, Available: http://soiort.com/en/solutions-eng/novac-11-eng/.

Simulation and Design of Monolithically Integrated Tunable Wavelength Converter Based on V-cavity Laser and Delayed Mach-Zehnder Interferometer

Yingchen Wu and Jian-Jun He
State Key Laboratory of Modern Optical Instrumentation, Centre for Integrated Optoelectronics
Department of Optical Engineering, Zhejiang University, Hangzhou 310027, China

Abstract— In this paper, we present the design and simulation results of a much simpler monolithically integrated wavelength converter based on a V-cavity laser (VCL) and delayed Mach-Zehnder interferometer (DMZI) with semiconductor optical amplifiers (SOAs). The dynamic characteristics of the wavelength converter are investigated using the large-signal dynamic model of semiconductor optical amplifier (SOA) with time-dependent transfer matrix method (TD-TMM). A 10 Gb/s return-to-zero (RZ) tunable all-optical wavelength converter is achieved with a large extinction ratio for both frequency up and down conversions.

1. INTRODUCTION

The rapid growth of internet and internet-related services calls for large-capacity and high-speed data networking. Optical networking allows for data reconfiguration directly in the optical layer rather than electrical layer. Since little electronic processing involved, the electronic bottle-neck can be avoided. The key to making optical packet routing (OPR) practical and cost-effective is in realizing the full potential of photonic integrated circuits. OPR technologies hold promise to provide the largest granularity with more efficient power and footprint scaling [1].

A variety of optical routing technologies have been proposed for use in OPR, which can be divided into two categories: space-switch-only [2–4] and wavelength-reconfigurable-routing [5, 6]. The later technique is more promising due to its flexibility and high scalability for larger throughput. However, it usually involves multi-epitaxial regrowth and some other complicated fabrication techniques. Tunable wavelength converters are very useful for realizing reconfigurable wavelength routers.

The focus of this paper is the simulation and design of a 10 Gb/s return-to-zero (RZ) tunable all-optical wavelength converter for use in OPR. The device is based on monolithically integration of a V-cavity laser and delayed Mach-Zehnder interferometer (DMZI) with semiconductor optical amplifiers (SOAs). Only one epitaxial regrowth is needed to realize the offset quantum-well integration platform, and no grating structure is required in the design, which leads to a much simpler device processing routine.

2. DEVICE INTEGRATION ARCHITECTURE

The device requires a single-input a single-output fiber. Figure 1 is the schematic of the wavelength converter. The device consists of a widely-tunable V-cavity laser (VCL), a delay waveguide, a differential MZI-SOA wavelength converter, and pre-amplifies SOAs. The on-chip VCL, which consists of two Fabry-Perot cavities coupled through a half-wave coupler, offers simple and efficient wavelength switching with 100 GHz ITU channel spacing in C band [7]. The on-chip VCL with deep-etched trenches as partially reflecting elements, is designed to provide a wavelength tuning over 20 nm at 20°C [8]. Probe light emitting out of both branches of V-cavity laser is coupled to MZI-SOAs through deep trenches. Deep-etched passive waveguides with big confinement factor are used for the delay waveguide.

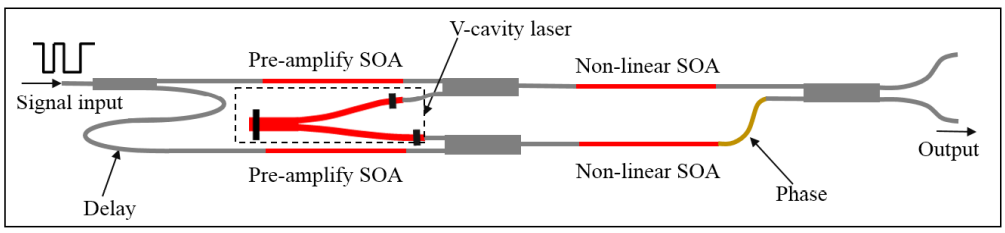

Figure 1: Schematic diagram of the monolithic wavelength converter showing the functional elements.

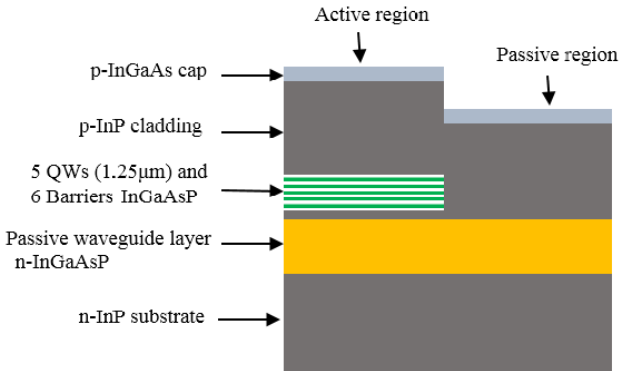

Figure 2: Cross-sectional view of the epitaxial layer structure for the offset quantum well integration platform.

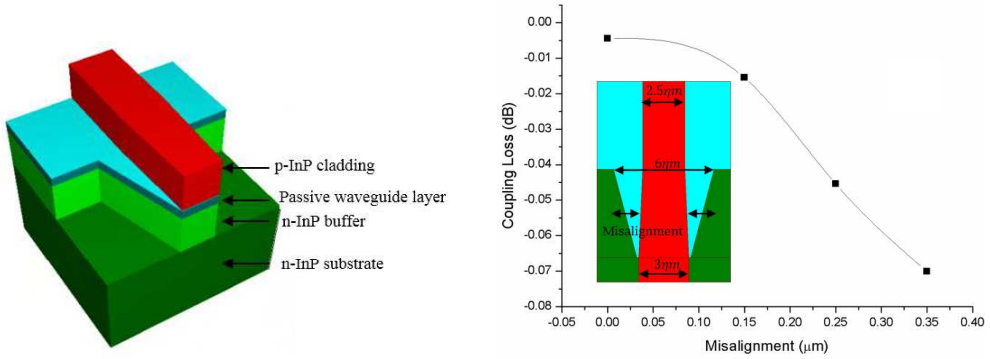

Figure 3: (a) Structure of taper between surface and deep-etch ridge waveguide. (b) Loss effect of the misalignment.

Figure 2 shows a cross-sectional view of the epitaxial layer structure for the offset quantum well integration platform. Figure 3(a) is the structure chart of the taper, which connect deep-etched passive waveguide and shallow-etched passive waveguide, can ensure coupling loss under 0.1 dB with a center misalignment tolerance of 0.5 μm as shown in Figure 3(b). The deep-etched waveguide is set 3 μm wide to reduce scattering loss of fundamental-mode on sidewall.

3. DYNAMIC SIMULATION RESULTS

DMZI structure is adopted in this design. The dynamic characteristics of the wavelength converter including optical pulse patterns, frequency chirp are investigated using the large-signal dynamic model of SOA with time-dependent transfer matrix method (TD-TMM). TD-TMM is carried out directly in time domain [10], so that it is more appropriate for dynamic characteristics simulation in a certain device than transfer matrix method (TMM) combined with multimode rate equations which is carried out in frequency domain [11].

The evolution of the slow-varying amplitude envelope $A_w\,(z,\,t)$ inside SOA's is governed by the pulse propagation equation [12, 13]

$$\frac{\partial A_w(z,t)}{\partial z}+\frac{1}{v_g}\frac{\partial A_w(z,t)}{\partial t}=-\frac{i}{2}\alpha\Gamma g_{m_w}A_w(z,t)+\frac{1}{2}(g_{m_w}-l)A_w(z,t)+\mu_w(z,t) \tag{1}$$

where w refers to different optical input signals, $A_w(z,t)$ is the pulse amplitude envelope function, α is the linewidth enhancement factor, v_g is the group velocity, Γ is the confinement factor, g_{m_w} is the material gain approximated by Equation (2) instead of Lorentzian curve in order to realise the asymmetric gain spectrum [14], l is loss constant.

$$g_{m_w}(N_i)=\frac{a_0(N_i-N_0)-a_1(\lambda_w-\lambda_p)^2+a_2(\lambda_w-\lambda_p)^3}{1+\varepsilon(D_1+D_2)} \tag{2}$$

where a_0, a_1, a_2 are gain constants, λ_p is the gain peak wavelength (assumed to shift linearly with carrier density), ε is the nonlinear gain coefficient, D_1, D_2 is the photon density for signal light and probe light respectively.

The amplified spontaneous emission (ASE) noise is represented by two statistically independent Gaussian distributed random process for $\mu_w(z,t)$ [12] that satisfies Equation (3).

$$\langle \mu_w(z,t)\mu_w^*(z',t')\rangle = \beta\Gamma R_{sp}\,\delta(t-t')\delta(z-z') \times (v_g E_w A_{cross}) \tag{3}$$

where β is the spontaneous coupling factor, R_{sp} is the spontaneous emission rate, $\delta(x)$ is δ function, E_w is the photon energy, A_{cross} is the cross-sectional area of the active layer.

The relation between carrier density $N$and photon density D represented by the flowing equation:

$$\frac{\partial N}{\partial t} = \frac{I}{qV} - AN - BN^2 - CN^3 - \sum_{w=1,2} v_g \Gamma g_{m_w} D_w \tag{4}$$

where I is the injection current, q is the electronic charge, V is the volume of active area, A, B, C are nonradiative recombination coefficient, bimolecular recombination coefficient and auger recombination coefficient, respectively. The change of effective refractive index is given by $\Delta n = \Gamma \frac{dn}{dN} N$.

Figure 4 shows the schematic of the TD-TMM SOA model with reflectional facet. The SOA is divided into small sections, and the amplitudes F and R of the counter propagating optical waves update in both time and space domain using the following transfer matrix [15]:

$$\left(\frac{1}{v_g}\frac{\partial}{\partial t} \pm \frac{\partial}{\partial z}\right)\begin{bmatrix} F(z,t) \\ B(z,t) \end{bmatrix} = \begin{bmatrix} A_{11} & 0 \\ 0 & A_{22} \end{bmatrix}\begin{bmatrix} F(z,t) \\ B(z,t) \end{bmatrix} + \begin{bmatrix} S_F \\ S_B \end{bmatrix} \tag{5}$$

where A_{11}, A_{22} is self-coupling coefficients for forward and backward-going waves respectively, cross-coupling coefficients between the waves are ignored because they are much smaller comparing with self-coupling coefficients, S_F, S_B are the ASE noises coupled into the forward and backward waves.

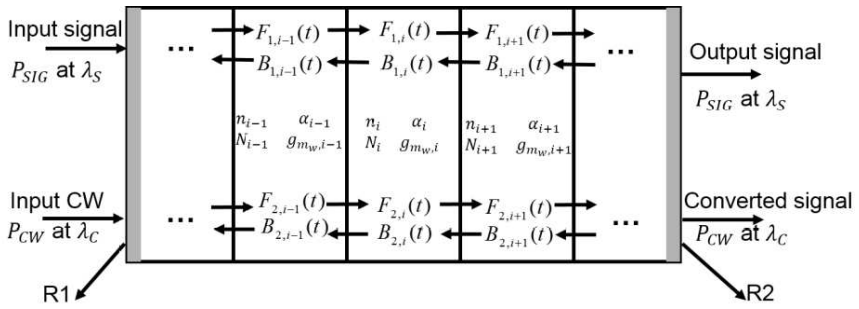

Figure 4: Schematic illustration of the TD-TMM SOA model.

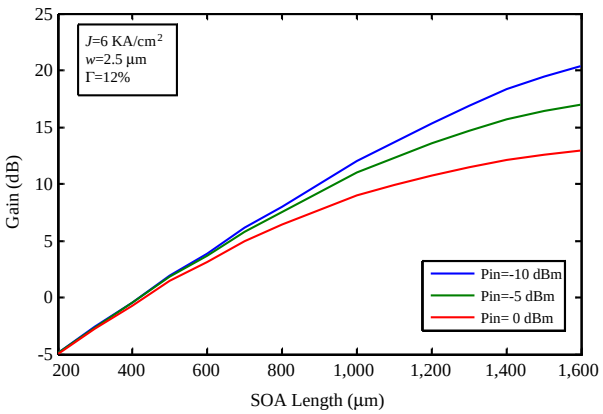

Figure 5: Simulated SOA gain versus SOA length for different input signal powers under constant current density.

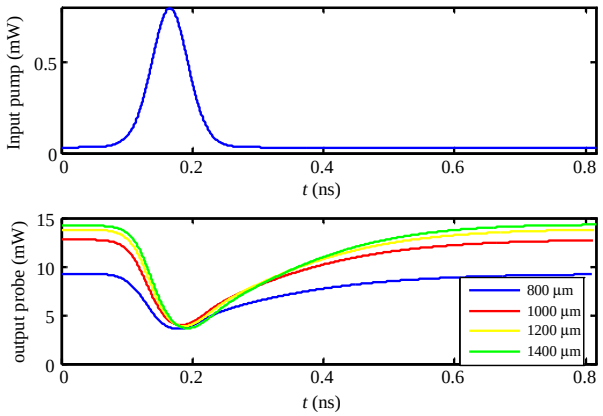

Figure 6: Simulated SOA gain recovery dynamics for different SOA length at 260 mA current injection with the input pump wavelength at 1550 nm, and the output probe at 1560 nm.

Stimulated gain versus SOA length under same current injection density for different input power levels are shown in Figure 5. Considering the coupling loss and loss of deep-etched delay waveguide, the input signal is expected under −10 dBm. Pre-amplify SOA is set 800 μm long and 2.5 μm width, with 120 mA current injection; it can offer 15 dB linear amplification.

Nolinear MZI SOAs are most important for operation of wavelength converter. When the pulse enters the upper arm, the phase of probe light changes due to carrier depletion induced by the pulse, which is a very fast process. The phase recovers slowly after the pulse has passed because of the relatively long carrier lifetime for a 10 GHz bitrate. The output of the MZI is controlled by the phase difference between the two arms. To reach a in-phase conversion, the MZI is set closed at static state, the phase shift in the first arm opens the MZI, and after the delay the other arm

Table 1: Parameters used in this simulation.

Symbol	Description	Value	Unit
Γ	Confinement factor	0.12	-
w	Waveguide width	2.5	μm
d	Thickness of active area	87.5	nm
β	Spontaneous emission coupling factor	2	-
v_g	Group velosity	8.34×10^7	m/s
A	Nonradiative recombination coefficient	1×10^8	s^{-1}
B	Bimolecular recombination coefficient	1×10^{-10}	cm^3/s
C	Active auger recombination coefficient	3.5×10^{-29}	cm^6/s
a_0	Material gain constant	2.5×10^{-20}	m^2
a_1		4.2×10^{18}	m^{-3}
a_2		5.7×10^{25}	m^{-4}
N_0	Transparent carrier density	1.4×10^{24}	m^{-3}
l	Carrier loss constant	2×10^4	m^{-1}
λ_P	Peak wavelength of material gain spectrum	1.55	μm
ε	Nonlinear gain coefficient	5×10^{-23}	m^3
α	Linewidth enhancement factor	3	
dn/dN	Index derivative wrt carrier density	-1.2×10^{-26}	m^3

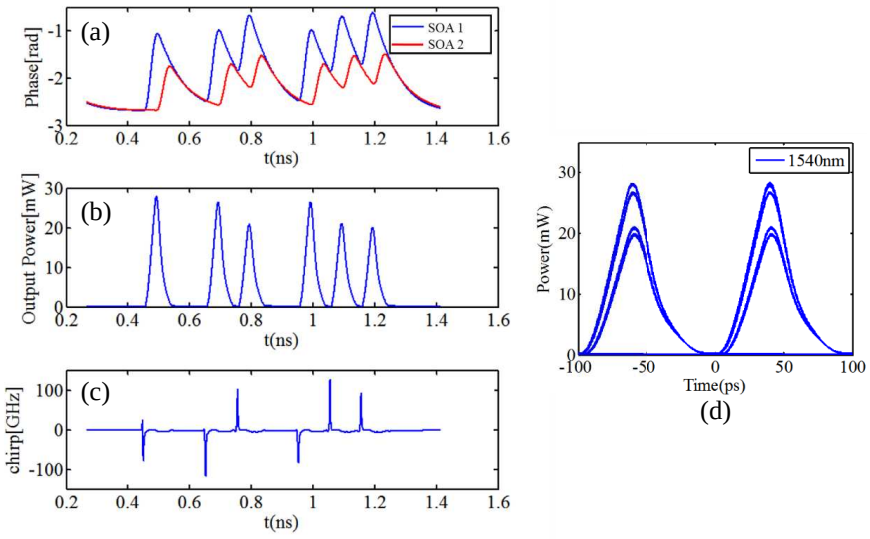

Figure 7: A simulation of (a) phase evolution, (b) output probe power, (c) frequency chirp of converted signal, (d) output eye diagram of the wavelength converter. The input pump wavelength at 1550 nm, and the output converted signal at 1540 nm.

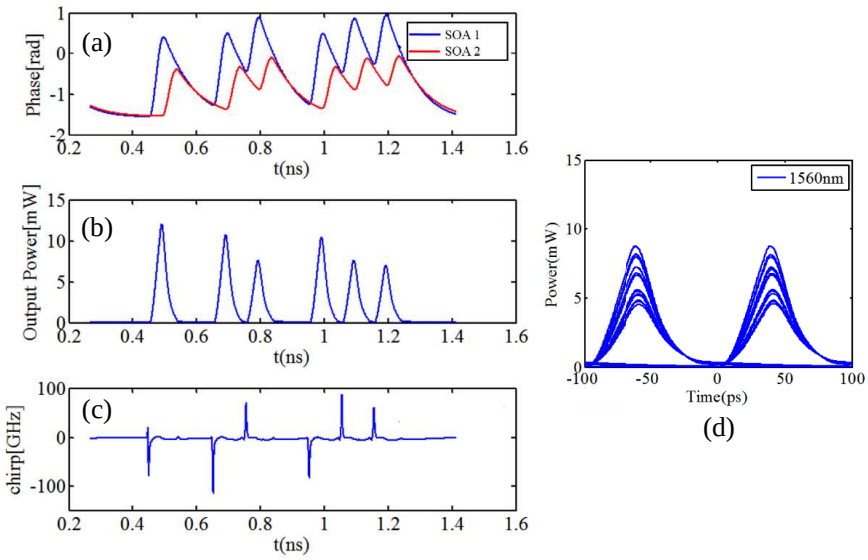

Figure 8: A simulation of (a) phase evolution, (b) output probe power, (c) frequency chirp of converted signal, (d) output eye diagram of the wavelength converter. The input pump wavelength at 1550 nm, and the output converted signal at 1560 nm.

got the same phase shift closes it. The independent control of phase change in both arms of DMZI structure makes it easier to have better performance than DISC structure [9].

With 260 mA current injection, the gain recovery phenomenon in SOA is shown in Figure 6. As it is shown, the recovery time decreases with the length of SOA increases, and become stable when longer than 1200 µm. The nonlinear-SOA is set 1200 µm long and the ridge is 2 µm wide, the recovery time is about 0.2 ns. Figure 7 and Figure 8 show the simulation results for up-conversion and down-conversion respectively. The phase change in the delayed arm is made slightly smaller to match the first one by reducing the input signal power or adjusting the current of phase section in the delayed arm. In-phase up-conversion always has lager extinction ratio and frequency chirp than down-conversion.

4. CONCLUSION

We present the design of a 10 Gb/s RZ wavelength converter based on VCL and DMZI requires very simple process technique, and give the dynamic characteristic simulation result based on SOA large-signal model with TD-TMM.

ACKNOWLEDGMENT

This work was supported by the National High-Tech R&D Program of China (grant No. 2013AA01-4401).

REFERENCES

1. Gripp, J., et al., "IRIS optical packet router," *Journal of Optical Networking*, Vol. 5, No. 8, 589–597, 2006.
2. Gripp, J., et al. "Optical switch fabrics for ultra-high-capacity IP routers," *Journal of Lightwave Technology*, Vol. 21, No. 11, 2839, 2003.
3. Stabile, R., A. Albores-Meija, and K. A. Williams, "Dynamic multi-path routing in a monolithic active-passive 16×16 optoelectronic switch," *Optical Fiber Communication Conference, Optical Society of America*, 2013.
4. Kamei, S., et al., "$N \times N$ cyclic-frequency router with improved performance based on arrayed-waveguide grating," *Journal of Lightwave Technology*, Vol. 27, No. 18, 4097–4104, 2009.
5. Segawa, T., et al., "A monolithic wavelength-routing switch using double-ring-resonator-coupled tunable lasers with highly reflective mirrors," *IEEE 2010 International Conference on Indium Phosphide & Related Materials (IPRM)*, 2010.

6. Mashanovitch, M., et al., "Photonic integrated circuits for optical routing and switching applications," *Optical Fiber Communication Conference, Optical Society of America*, 2011.
7. He, J.-J. and D. Liu, "Wavelength switchable semiconductor laser using half-wave V-coupled cavities," *Optics Express*, Vol. 16, No. 6, 3896–3911, 2008.
8. Zhang, S., et al., "Simple and compact V-cavity semiconductor laser with 50×100 GHz wavelength tuning," *Optics Express*, Vol. 21, No. 11, 13564–13571, 2013.
9. Ueno, Y., et al., "3.8-THz wavelength conversion of picosecond pulses using a semiconductor delayed-interference signal-wavelength converter (DISC)," *IEEE Photonics Technology Letters*, Vol. 10, No. 3, 346–348, 1998.
10. Lee, H., et al., "Theoretical study of frequency chirping and extinction ratio of wavelength-converted optical signals by XGM and XPM using SOA's," *IEEE Journal of Quantum Electronics*, Vol. 35, No. 8, 1213–1219, 1999.
11. Davis, M. G. and R. F. O'Dowd, "A transfer matrix method based large-signal dynamic model for multielectrode DFB lasers," *IEEE J. Quantum Electron.*, Vol. 30, No. 11, 2458–2466, Nov. 1994.
12. Zhang, L. M., S. F. Yu, M. C. Nowell, D. D. Marcenac, J. E. Carroll, and R. G. S. Plumb, "Dynamic analysis of radiation and side-mode suppression in a second-order DFB laser using time-domain large-signal traveling wave model," *IEEE J. Quantum Electron.*, Vol. 30, 1389–1395, 1994.
13. Agrawal, G. P. and N. A. Olsson, "Self-phase modulation and spectral broadening of optical pulses in semiconductor laser amplifiers," *IEEE J. Quantum Electron.*, Vol. 25, 2297–2306, Nov. 1989.
14. Willner, A. E. and W. Shieh, "Optimal spectral and power parameters for all optical wavelength shifting: Single stage, fanout, and cascadability," *J. Lightwave Technol.*, Vol. 13, 771–781, May 1995.
15. Li, X., *Optoelectronic Devices: Design, Modeling, and Simulation,* 184–185, Cambridge University Press, 2009.

Bandgap Engineering of InGaAsP/InP Multiple Quantum Well Structure by Dielectric Sputtering

Hongli Zhu, Yuan Zhuang, Xin Zhang, and Jian-Jun He
Centre for Integrated Optoelectronics, State Key Laboratory of Modern Optical Instrumentation
Department of Optical Engineering, Zhejiang University, Hangzhou 310027, China

Abstract— This paper investigates a method of Si_3N_4 sputtering and annealing on quantum well intermixing for bandgap engineering of InGaAsP/InP multiple quantum well structure. A bandgap blueshift of about 90 nm is obtained. At the same time, the PL peak width becomes narrower, and the intensity is slightly increased. The waveguide losses at the absorption edge of the waveguide with and without QWI are about 27 dB/cm and 39 dB/cm, respectively. The results indicate the good quality of the MQW material after the bandgap engineering by dielectric sputtering and annealing.

1. INTRODUCTION

The InGaAsP/InP multiple quantum well (MQW) heterostructure is a widely used material system for 1.55 μm optical communication lasers. Recently, photonic integrated circuit (PIC) has attracted more and more attention for its high-functionality, low-cost, and low-power-consumption [1]. A key issue in the fabrication of PICs is the bandgap engineering of the MQW wafer in order to monolithically integrate active and passive devices. Quantum well intermixing (QWI) is a promising method that can selectively shift the bandgap post-growth with simple process [2]. In this paper, we present our recent work on QWI by dielectric sputtering method [3, 4].

2. EXPERIMENTS

The sample is a 1.2% compressive strained laser structure containing five $In_{0.8}Ga_{0.2}As_{0.8}P_{0.2}$ QWs with 1.25Q InGaAsP barriers, with the emission wavelength around 1.54 μm. From the surface, the layers are a 0.5 μm Zn-doped (10^{18} cm^{-3}) InP sacrificial layer, 0.2 μm Zn-doped (10^{19} cm^{-3}) $In_{0.53}Ga_{0.47}As$ cap, 1.5 μm Zn-doped (10^{18} cm^{-3}) InP upper cladding, 0.004 μm Zn-doped (4×10^{17} cm^{-3}) l.3Q InGaAsP etch-stop layer, five repeats of l0 nm undoped $In_{0.8}Ga_{0.2}As_{0.8}P_{0.2}$QW and 5.5 nm undoped InGaAsP QW which is sandwiched by two 0.06 μm InGaAsP step-graded index confining layers, and 1.5 μm Si-doped (2×10^{18} cm^{-3}) InP buffer on Si-doped (4×10^{18} cm^{-3}) InP substrate. All the layers are grown by MOCVD.

Samples with and without QWI processing were fabricated on a monolithic chip. To compare the difference between them, a patterned layer of photoresist of 1.6 μm thick was used to protect the no-QWI region. The sample was first pre-processed with argon plasma for a very short time. The plasma source used in the experiment is Oxford Plasmalab System 100. The ICP chamber was set to 20 sccm Ar flow rate and 4 mTorr pressure. The RF power and ICP power were 500 W both, with a DC bias of 741 V. After being exposed under Ar plasma in the ICP chamber for 10 seconds, a dielectric layer of Si_3N_4 was deposited by sputtering method. The deposition was carried out at a RF power of 200 W with DC bias of 482 V and a chamber pressure of 20 mTorr with a chamber temperature of 20°C. Then the photoresist was removed by acetone. After that, the sample was annealed at 750°C for 120 seconds in a flowing nitrogen atmosphere using a rapid thermal anneal (RTA). Silicon caps were used during the RTA process to prevent phosphorus out-diffusion. At last, the sample was wet etched by hydrochloric acid solution for 45 seconds to remove the Si_3N_4 by lift-off of sacrificial layer. Photoluminescence (PL) measurement was then carried out at room temperature to assess the bandgap shift.

To evaluate the influence of the QWI process, waveguide loss measurement by Fabry-Perot fringe technique was performed. Straight ridge waveguides were fabricated with 2.5 μm width and 1.6 μm height by the standard dry-etch technology. The sample was then cleaved to form a 900-μm-long Fabry-Perot cavity. A tunable laser (1.46–1.64 μm) was used as the input light source. The light was coupled into the waveguide through a polarization preserving lens fiber in TE mode. The output light was coupled by a lens fiber into an InGaAs detector.

3. RESULTS AND DISCUSSION

Figure 1 shows the measured PL map of the sample for peak wavelength (a), peak intensity (b), and full-width-at-half-maximum (FWHM) (c). A comparison table is given in (d). The peak wavelength is about 1536 nm for the protected region, and is blue shifted to 1446 nm for the QWI region. The intensity of the QWI region is increased by about 30% while the FWHM is reduced from 125 nm to 92 nm. The wavelength blue shift of about 90 nm shows the effectiveness of the QWI based on Si_3N_4 sputtering. The slightly enhanced peak intensity and narrowed FWHM indicate that this method has the ability to maintain or improve the property of the QWs.

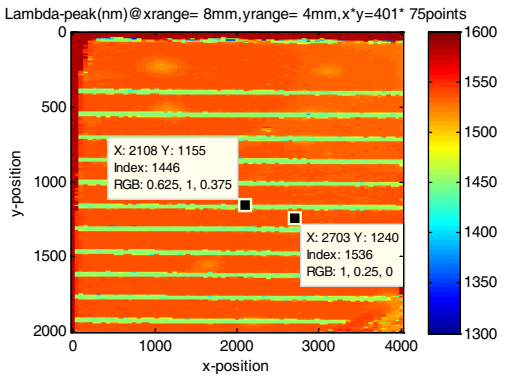

(a)

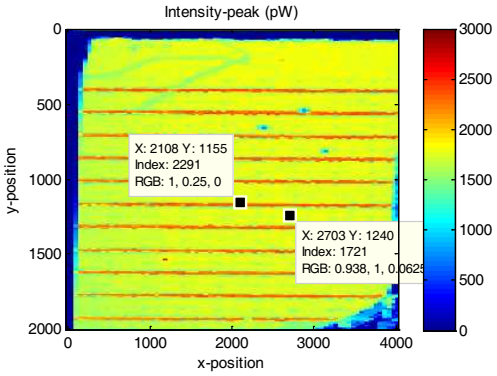

(b)

	with_QWI	without_QWI	difference
peak-wavelength(nm)	1446	1536	-90
peak-intensity(a.u.)	2291	1721	+33%
FWHM(nm)	92	125	-33

(c)

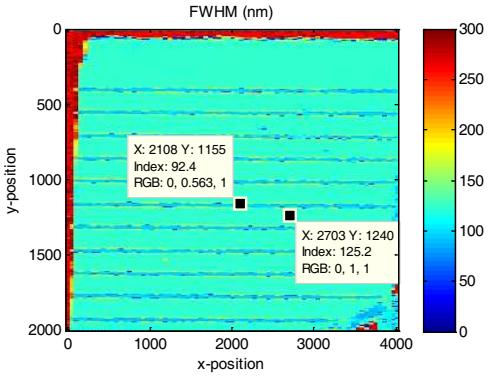

(d)

Figure 1: (a) Peak wavelength, (b) peak intensity, (c) FWHM of PL spectrum respectively for the same sample, and (d) the comparison table.

Figure 2 shows the measured transmission spectra of with and without QWI waveguides. {Red line refers to without QWI waveguide, and blue line refers to with QWI waveguide, respectively.} From the band edges of the two spectra, we can derive a net blue shift of about 85 nm with the QWI, which is consistent with the peak wavelength shift of the PL measurement in Figure 1(a). The Fabry-Perot interference fringe is generated due to the multiple reflectance of the two cleaved facets. Its contrast is related to the loss constant of the waveguide. We can therefore derive the loss coefficients of the waveguides as a function of the wavelength. It should be noted that, for wavelength shorter than the bandgap, the Fabry-Perot fringes disappear due to high absorption, and therefore another method based on the relative transmission intensity is used [5–7].

Figure 3 compares the loss coefficients derived from the measured transmission spectra for the waveguides with and without QWI. For wavelength slightly longer than the absorption edge, the measured loss is about 27 dB/cm at 1635 nm for the sample without QWI, while it is reduced to 20 dB/cm at 1550 nm for the sample with QWI. The loss further decreases to 18 dB/cm at 1635 nm for the intermixed waveguide. It should be noted that the loss in the QWI waveguide appears to be lower than that of the sample without QWI, even after considering the 85 nm difference in bandgaps. This indicates that no excess loss results from the QWI process, which is consistent with the slightly increased peak intensity of the PL measurement in Figure 1(b).

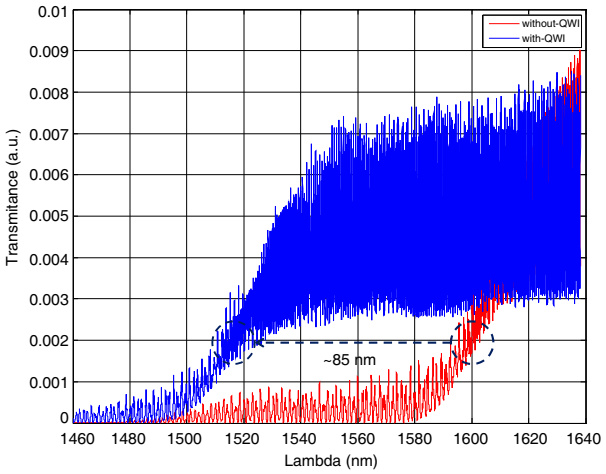

Figure 2: Measured transmission spectra of waveguides with and without QWI.

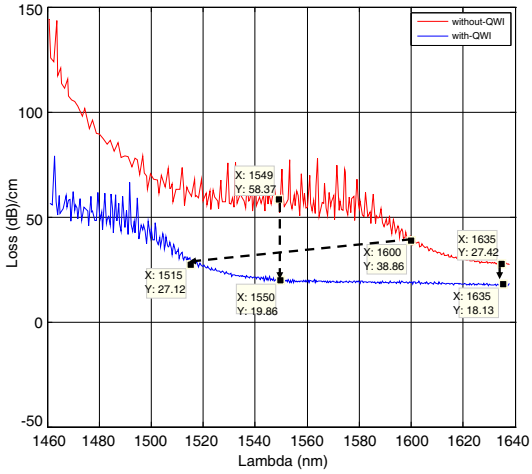

Figure 3: Loss coefficients derived from the measured transmission spectra of waveguides with and without QWI.

4. CONCLUSION

We have reported the experimental results on QWI experiment using Si_3N_4 sputtering and annealing. A maximum blue-shift of 90 nm has been achieved with a PL intensity enhancement and linewidth reduction. The waveguide loss measurement shows a reduced loss after the QWI process from 27 dB/cm to 18 dB/cm in the transparent region near the absorption edge. The technique is therefore suitable for active-passive integration in PIC applications.

ACKNOWLEDGMENT

This work was supported by the National High-Tech R&D Program of China (grant No. 2011AA010305), and the National Natural Science Foundation of China (grant No. 61377038).

REFERENCES

1. Raring, J. W. and L. A. Coldren, "40 Gbps widely tunable transceivers," *IEEE J. Sel. Topics Quantum Electron.*, Vol. 13, No. 1, 3–14, 2007.
2. Parker, J. S., J. S. Parker, A. Sivananthan, E. Norberg, and L. A. Coldren, "Regrowth-free high-gain InGaAsP-InP active-passive platform via ion implantation," *Optics Express*, Vol. 20, No. 18, 19947–19955, 2012.
3. Kowalski, O. P., C. J. Hamilton, S. D. McDougall, J. H. Marsh, A. C. Bryce, R. M. De La Rue, B. Vogele, and C. R. Stanley, "A universal damage induced technique for quantum well intermixing," *Applied Physics Letters*, Vol. 72, No. 5, 581–583, 1998.
4. McDougall, S. D., O. P. Kowalski, C. J. Hamilton, F. Camacho, B. Qiu, M. Ke, R. M. De La Rue, A. C. Bryce, and J. H. Marsh, "Monolithic integration via a universal damage enhanced quantum well intermixing technique," *IEEE J. Sel. Topics Quantum Electron.*, Vol. 4, No. 4, 636–646, 1998.
5. He, J. J., Y. Feng, E. S. Koteles, J. P. Poole, M. Davis, M. Dion, R. Goldberg, I. Mitchell, and S. Charbonneau, "Bandgap shifted InGaAsP/InP quantum well waveguides using MeV ion implantation," *Electronics Letters*, Vol. 31, No. 24, 2094–2095, 1995.
6. Charbonneau, S., E. S. Koteles, P. J. Poole, J. J. He, G. C. Aers, J. Haysom, M. Buchanan, Y. Feng, A. Delage, F. Yang, M. Davies, R. D. Goldberg, P. G. Piva, and I. V. Mitchell, "Photonic integrated circuits fabricated using ion implantation," *IEEE J. Sel. Topics Quantum Electron.*, Vol. 4, No. 4, 772–793, 1998.
7. Zhang, X. and J. J. He, "Optical loss of bandgap shifted lnGaAsP/lnP waveguide using argon plasma-enhanced quantum well intermixing," *Advances in Optoelectronics and Micro/Nano-Optics*, 2010.

High Stable Exciton Emission from SnO_2 Quantum Dots Grown via a Facile "Top-down" Strategy

Shu Sheng Pan[1], **Wei Lu**[2, 3], **Zhao Qin Chu**[1], **Si Chao Xu**[1], **Yun Xia Zhang**[1], **Yuan Yuan Luo**[1], **and Guang Hai Li**[1]

[1]Key Laboratory of Materials Physics, Anhui Key Laboratory of Nanomaterials and Nanostructures
Institute of Solid State Physics, Chinese Academy of Sciences, Hefei, Anhui 230031, China
[2]Department of Applied Physics, The Hong Kong Polytechnic University
Hung Hom, Kowloon, Hong Kong, China
[3]Materials Research Centre, The Hong Kong Polytechnic University
Hung Hom, Kowloon, Hong Kong, China

Abstract— SnO_2 is a promising wide band gap semiconductor for next generation ultraviolet (UV) non-polar optoelectronic devices applications. The development of SnO_2-based optoelectronic devices is obsessed by its low exciton emission efficiency. In this study, quantum confined SnO_2 nanocrystals have been facilely fabricated via pulsed laser ablation in liquid. The intensity of exciton emission from SnO_2 quantum dots (QDs) was stable for at least two years. The SnO_2 QDs possess high thermal stable exciton emission at 300 nm in water. Therefore, we have shown that SnO_2 QDs can be a potential luminescent material suitable for the realization of ultraviolet B non-polar light emitting devices and lasing devices.

The research on ultraviolet (UV) light emitting devices is enormously stimulated by the demand of full solid state lightning, integrated photonics, environmental circulation and biomedical diagnostics, and et al. [1]. Tin oxide (SnO_2) is an IV-VI semiconductors with wide direct band gap of 3.6 eV (3.2 eV for ZnO), high exciton binding energy of 130 meV (60 meV or ZnO), and exotic electrical characteristics (e.g., electron mobility: $\sim$250 cm^2/Vs, concentration: $\sim10^{19}/cm^3$), supreme chemical and physical stability [2, 3]. Moreover, SnO_2 and other IV-VI semiconductors have weak ionicity of chemical bond, and the p-type doping, which have greatly obsess the progress of ZnO-based light emitting devices, can be more facilely realized.

The SnO_2-based light emitting devices with different structures have been demonstrated [1, 4–6]. The main difficulty that cumbers the development of SnO_2-based light emitting devices is its weak exciton emission efficiency. Most of the UV luminescence from SnO_2 nanowires, films, or single crystal is believed to originate from the defects or unidentified impurities rather than the free exciton emission [7–10]. The valence band and the conduction band of the SnO_2 have same parity symmetry, and the dipole transition probability between the conduction and valence band is quite low [11]. As a result, the exciton or band-to-band emission can hardly be obtained in SnO_2 films or bulk. For quantum materials, the band structures of semiconductors will be modified due to the quantum confinement effect, and exciton emission is anticipated to be realized in quantum confined SnO_2 nanocrystals. At the same time, the intensity of exciton emission will dramatically increase with size decreasing according to the theoretical calculation [12]. In this study, we report on the thermal stability of exciton emission from high quality SnO_2 QDs grown by PLAL technique, a "top-down" strategy. The resultant SnO_2 QDs exhibit extra-high performance exciton emission properties at $\sim$300 nm, which may be applied for UV-B QDs light emitting devices.

Figure 1(b) indicates the typical photoluminescence (PL) spectra and the thermal stability of SnO_2 QDs in water in the wavelength range of 275 nm$\sim$460 nm. There are two emission peaks observed from the PL spectrum of the SnO_2 QDs: the dominant exciton emission peak at wavelength of $\sim$300 nm and weak defects-related emission peak at $\sim$404 nm. The detailed fabrication process can be found in our previous investigation [13]. The origination of the above two peaks has been demonstrated in our previous report [13]. It should be noted that the room temperature exciton emission intensity increases with storage time interval increasing at ambient temperature or high temperature at 90°C in a sealed bottle, as shown in Figure 1(b). There are some defects existed on the surface of as-prepared SnO_2 QDs, the crystal quality may be enhanced for long time storage, and defects will decrease after storage. This is consistent with the PL spectrum results, i.e., the ratio of exciton-to-defects intensity gradually increased with storage time. At the same time, the exciton emission peak slightly red shift with storage time increasing, which may be due to the SnO_2 QDs particle size grows up during storage. It should be pointed out that the exciton

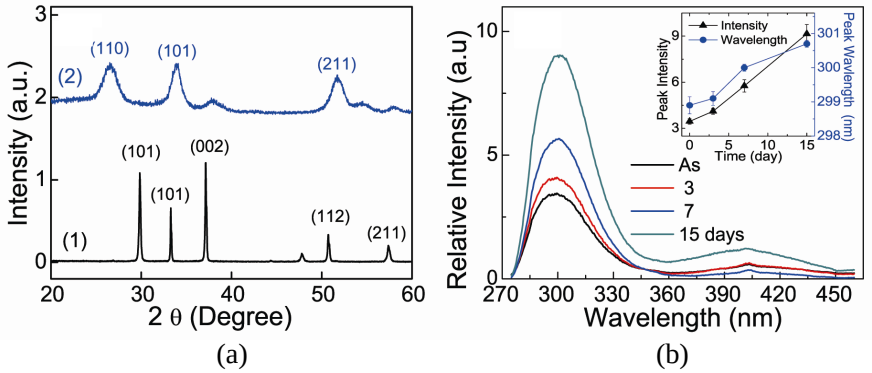

Figure 1: (a) X-ray diffraction (XRD) of (1) SnO starting material and (2) as-prepared SnO_2 nanoparticles by ns pulsed laser ablation. (b) PL Stability of SnO_2 QDs after different storage time interval at 90°C.

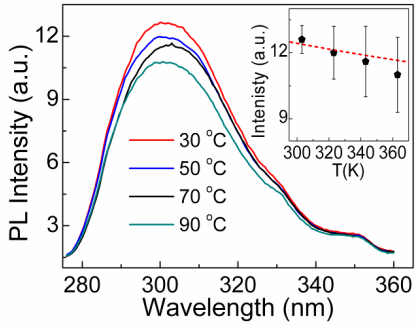

Figure 2: Thermal stability of exciton emission from SnO_2 QDs. inset, variation of peak intensity with temperature, redline: fitting curve, error bar: standard deviation.

emission intensity of SnO_2 QDs did not show any decrease even storage in ambient temperature for more than 24 months.

SnO_2 has supreme physical and chemical stability, which has been applied for chemical sensors, photocatalysis and solar cells. The SnO_2 nanocrystals exhibit high stable photoluminescence properties in several solvents, such as ethanol, acetone, and toluene [1]. For actual light emitting devices applications, the SnO_2 QDs need suffer from the increased temperature due to device resistance-induced heat. In order to understand the thermal stability of exciton emission, the PL spectrum of SnO_2 QDs in water at different temperature (30°C to 90 °C) was *in situ* investigated, as shown in Figure 2. The exciton emission of SnO_2 QDs exhibits high thermal stability; and the intensity only slightly decreases (∼9%) with temperature increasing from room temperature to 90°C.

In the intermediate temperature range, the variation in PL intensity mainly can be attributed to partial thermal dissociation of excitons. The temperature dependence of the exciton intensity can therefore be modeled by [14],

$$I_{FX}(T) = \frac{A}{1 + Be^{-\frac{E_b}{k_B T}}} \tag{1}$$

where E_g is the exciton binding energy, k_B is the Boltzmann constant. The temperature dependence of the exciton peak intensity is plotted in inset in Fig. 2. The results can be well described by the Eq. (1), and the fitted value of E_b is 140.9 meV, which is well consistent with the SnO_2 QDs exciton binding energy of 147 meV deduced from the optical absorption spectra [13].

In summary, the quantum confined SnO_2 nanocrystals have been facilely fabricated by nanosecond laser ablation of SnO in liquid. The SnO_2 QDs exhibit high performance exciton emission at 300 nm. The exciton emission manifests high thermal and time stability. The resultant SnO_2 QDs has strong enough exciton emission efficiency and thermal stability for development of ultraviolet-B band light emitting devices and laser devices.

ACKNOWLEDGMENT

This work was financial supported by the National Natural Science Foundation of China (Grant Nos. 11004197, 11374309, 11104270), China Postdoctoral Science Foundation funded project (Grant No. 2013M541847), "Hong Kong Scholars Program" (Grant Nos. XJ2011039, 201104336).

REFERENCES

1. Brovelli, S., N. Chiodini, R. Lorenzi, A. Lauria, M. Romagnoli, and A. Paleari, *Nat. Commun.*, Vol. 3, 690, 2012.
2. Yu, B., C. Zhu, and F. Gan, *Optical Materials*, Vol. 7, 15–20, 1997.
3. Pan, S. S. and G. H. Li, *Recent Pat. Nanotech.*, Vol. 5, 138–161, 2011.
4. Li, Y. F., W. J. Yin, R. Deng, R. Chen, J. Chen, Q. Y. Yan, B. Yao, H. D. Sun, S. H. Wei, and T. Wu, *Npg Asia Materials*, Vol. 4, e30, 2012.
5. Yang, H. Y., S. F. Yu, H. K. Liang, S. P. Lau, S. S. Pramana, C. Ferraris, C. W. Cheng, and H. J. Fan, *ACS Appl. Mater. Interfaces*, Vol. 2, 1191–1194, 2010.
6. Min, K. W., Y. K. Kim, G. Shin, S. Jang, M. Han, J. Huh, G. T. Kim, and J. S. Ha, *Adv. Funct. Mater.*, Vol. 21, 119–124, 2010.
7. Blattner, G., C. Klingshirn, and R. Helbig, *Solid State Commun.*, Vol. 33, 341–344, 1980.
8. Jeong, J., S. P. Choi, C. I. Chang, D. C. Shin, J. S. Park, B. T. Lee, Y. J. Park, and H. J. Song, *Solid State Commun.*, Vol. 127, 595–597, 2003.
9. Kar, A., M. A. Stroscio, M. Dutta, J. Kumari, and M. Meyyappan, *Appl. Phys. Lett.*, Vol. 94, 101905, 2009.
10. Chen, R., G. Z. Xing, J. Gao, Z. Zhang, T. Wu, and H. D. Sun, *Appl. Phys. Lett.*, Vol. 95, 061908-3, 2009.
11. Arlinghaus, F. J., *J. Phys. Chem. Solids*, Vol. 35, 931–935, 1974.
12. Pan, S. S., S. F. Yu, Y. X. Zhang, Y. Y. Luo, S. Wang, J. M. Xu, and G. H. Li, *J. Appl. Phys.*, Vol. 113, 143104, 2013.
13. Pan, S. S., S. F. Yu, W. F. Zhang, H. Zhu, W. Lu, and L. M. Jin, *Nanoscale*, Vol. 5, 11561–11567, 2013.
14. Černe, J., A. G. Markelz, M. S. Sherwin, S. J. Allen, M. Sundaram, A. C. Gossard, P. C. V. Son, D. Bimberg, *Phys. Rev. B*, Vol. 51, 5253, 1995.

Design and Simulation of 450 nm GaN-based Multiple-quantum-well Tunable V-cavity Laser

Zhipeng Hu, Jianjun Meng, Lin Wu, and Jian-Jun He
State Key Laboratory of Modern Optical Instrumentation, Centre for Integrated Optoelectronics
Department of Optical Engineering, Zhejiang University, Hangzhou 310027, China

Abstract— We present the design and simulation of a 450 nm GaN-based V-cavity tunable laser without grating and epitaxial regrowth. Quantum well structure has been optimized to realize good optical confinement. The simulation results show that 20 channels with 300 GHz spacing can be achieved, with a tuning range of 4.1 nm and high high side-mode suppression ratio (SMSR) over 30 dB.

1. INTRODUCTION

Tunable blue laser diodes based on gallium nitride (GaN) are of great interest for high resolution spectroscopy, such as gas analysis [1], industrial process monitoring [2], and combustion diagnostics [3], and bio-medical analysis. At present, GaN-based blue light sources are mainly on light emitting diodes (LED) or multimode Fabry-Perot lasers, which has poor spectral identity and tunability. Tunable blue laser diodes based on external cavity grating structure has recently been reported with narrow linewidth and wide tunable range [4–6], but it requires precise mechanics and alignment, complex structure, bulky and expensive systems. While for monolithic GaN laser, the complex gratings such as SG-DBRs used in telecom tunable lasers is difficult to fabricate for blue light, because the period of the gratings needed for blue light is too small. Recently, a compact tunable V-cavity laser (VCL) was proposed and wavelength tuning of up to 50 channels with 100 GHz spacing around 1550 nm was demonstrated experimentally with excellent side-mode suppression ratio (SMSR) in InP based material system [7]. Unlike those grating based tunable lasers, the longitudinal mode selection mechanism of the V-cavity laser has no limitation of such small period. By emplying this V-cavity laser structure, we designed a compact GaN-based V-cavity tunable laser with wide tuning range.

2. DEVICE DESIGN AND SIMULATION

Figure 1(a) shows the schematic diagram of a V cavity laser. It consists of a fixed gain cavity and a channel selector cavity with different optical path lengths, which are coupled through a 2×2 half-wave coupler.The half-wave coupler has been discussed in [8]. Since backside contacts are not available with the sapphire substrate, the device geometry is designed to use coplanar electrodes with shallow etched waveguide and deep etched mesa. Three positive electrodes and one negative electrodes are used. The coupler electrode is used for providing gain and small phase adjustment. In order to achieve good single mode operation and wide range tuning, the Vernier effect is used between the two cavities. The cross-section layer structure is shown in Figure 1(b). The active region consists of a three period MQW with 3 nm $In_{0.2}Ga_{0.8}N$ well and 15 nm GaN barrier. Since the mobility of electrons are much higher than holes, a typical 15 nm electron blocking layer (EBL)

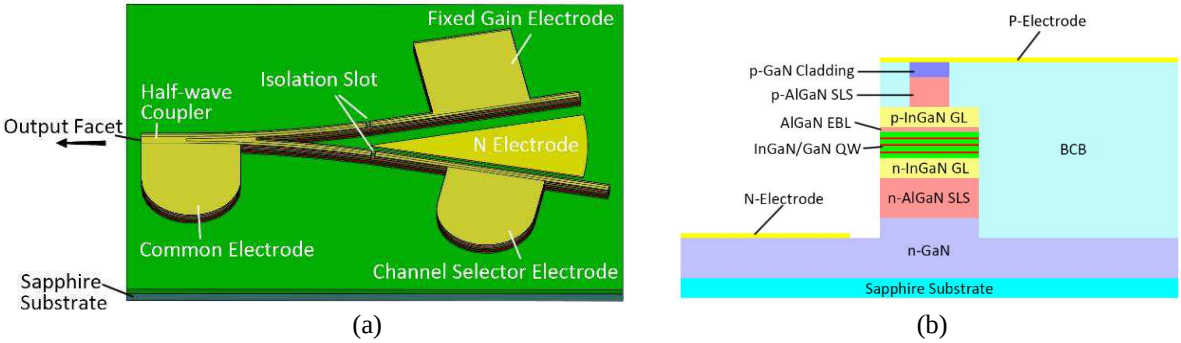

Figure 1: (a) Schematic diagram of a V cavity laser and (b) its layer structure.

of $Al_{0.2}Ga_{0.8}N$ is used to prevent the electrons from flowing into the p-type region. For nonpolar or semi-polar GaN laser diodes, high Al composition cladding layers are often used for large optical confinement, which causes macroscopic cracking [9]. It also brings some further drawbacks from the material perspective as discussed in [10]. Therefore, we adopt multiple periods of 2 nm/2 nm $Al_{0.3}Ga_{0.7}N$/GaN superlattice structure (SLS) layer, and use relatively high indium composition guiding layers (GLs) to realize high confinement factor. The thicknesses of the p-SLS and n-SLS layers are 400 nm and 600 nm respectively.

Figure 2(a) shows the vertical optical mode and refractive index profile along the growth direction of the layer structure, which was calculated by transfer matrix method (TMM) [11]. Large confinement factor $\Gamma(= 0.1813)$ is realized with high indium content InGaN GLs and high aluminum content AlGaN/GaN SLSs. The low reflective index of p-AlGaN EBL shifts the peak of the optical mode from the center of the active region toward the n-side layers, which results in asymmetric mode profiles and slightly lower [12]. Figure 2(b) shows that a slight resonance of the waveguide mode appears in the n-GaN layer which forms a resonator between the n-SLS and the substrate. It can be reduced by increasing the thickness or aluminum content of the n-SLS, which will also cause macroscopic cracking from the processing perspective. There is therefore a trade-off between high optical confinement and processing tradition. Figure 2(c) shows the dependence of optical confinement factor Γ on the indium composition of the InGaNGLs for different aluminum composition of the AlGaN/GaN SLSs. Γ increases as the indium composition in the GLs and aluminum composition in SLSs increases. Higher indium and aluminum content leads to a larger refractive index difference Δn between the GLs and SLS cladding layers, which results in a higher Γ. At low indium composition, there is insufficient confinement for $Al_{0.05}Ga_{0.95}N$ and $Al_{0.1}Ga_{0.9}N$ SLS layer structure. Γ increases to saturation when indium composition is greater than 0.04. When aluminum composition of SLS layer reaches 0.15, the SLS layer itself can get enough Δn to confine the optical mode in active region even with low indium composition guiding layer.

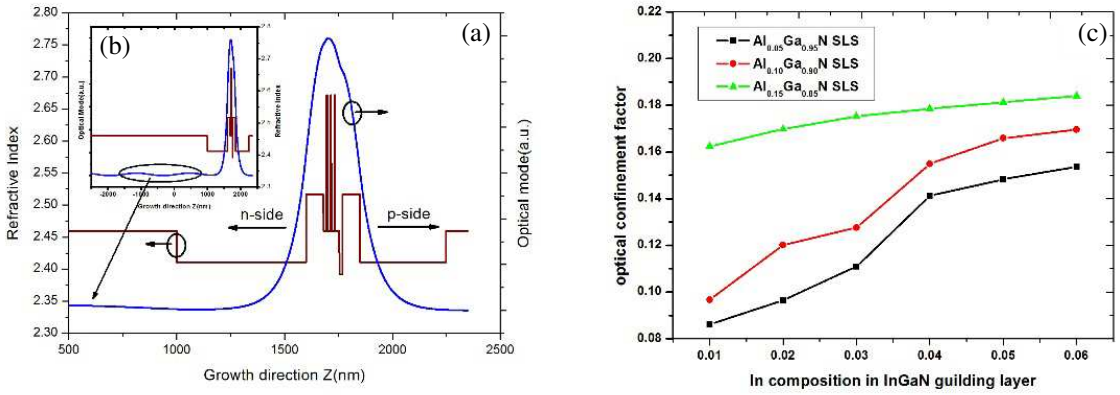

Figure 2: (a) Optical mode profile and refractive index on the growth direction Z of the layer structure and (b) anti-guide behavior of the n-GaN layer, (c) confinement factor (Γ) of various SLS structures versus In composition of the InGaN GLs.

Detailed theory, design principle and numerical results of the V-coupled cavity laser based on InP material system has been described in [8]. The device based on GaN was simulated using the same method. We set the length of the fixed gain cavity to 200 µm and calculated the threshold gain, SMSR and free spectral range (FSR) for GaN-based VCL with 2.5%, 5%, 10%, 15% cavity length difference, respectively. The switchable wavelength range is greatly increased by using Vernier effect, where the FSR of the combined cavity is determined by

$$\Delta f_c = \frac{\Delta f \Delta f'}{|\Delta f - \Delta f'|} \tag{1}$$

where Δf and $\Delta f'$ are the resonance frequency interval for the fixed gain cavity and channel selector cavity, respectively. We define bar-coupling coefficient as C_{11} and cross-coupling coefficients as C_{21}, and they have a relative phase difference $\phi = m\pi$ $(m = 0, \pm 1, \ldots)$ between them. For optimal

operation of the V-coupled cavity laser, half-wave coupler should satisfy $|C_{11}| + |C_{21}| = 1$. The threshold gain (in intensity) ΔG can be calculated by

$$\Delta G = -10\log_{10}\left(|C_{11}|^2 + |C_{21}|^2 + 2|C_{11}|\,|C_{21}|\cos\phi\right)/(8.686L). \tag{2}$$

and SMSR is calculated using the equation in [13].

Figure 3(a) shows the threshold gain difference and corresponding SMSR as a function of the bar-coupling coefficient C_{11} for a cavity length difference of 5%, maximal SMSR of 31.3 dB is obtained with the corresponding threshold gain difference among the longitudinal modes is 3.38 cm^{-1}. Figure 3(b) shows the variations of SMSR and FSR versus the cavity length difference, we can see that the SMSR increases with the cavity length difference while FSR decreases with it, so we have to trade-off between these two factors.

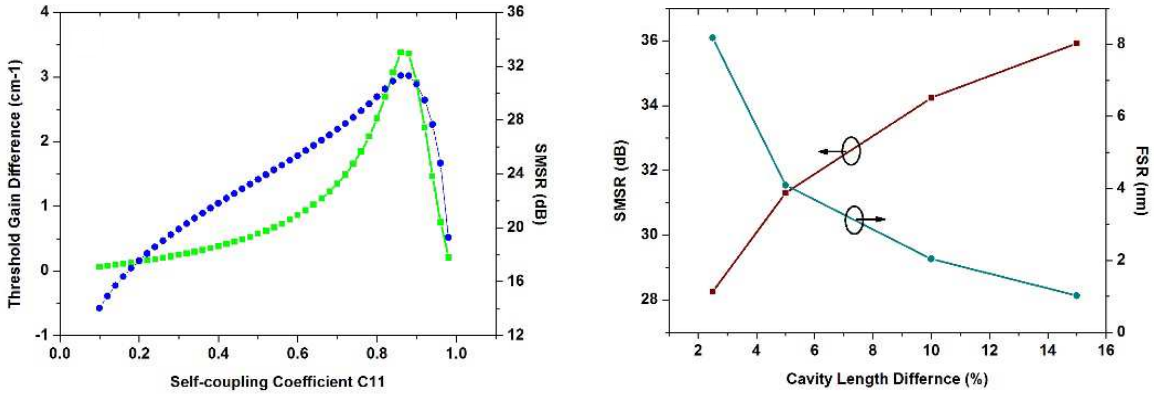

Figure 3: (a) Threshold gain difference and corresponding SMSR as a function of the self-coupling coefficient for a cavity length difference of 5%, (b) variations of SMSR and FSR versus the cavity length difference between fixed gain cavity and channel selector cavity.

Since the SMSR greater than 30 dB is acceptable for GaN laser diodes, to get a broader FSR we choose 5% cavity length difference, which can realize an FSR of 4.09 nm, or ~ 6 THz. The channel spacing can be calculated by $\Delta f = c/(2n_g L)$, which corresponds to 300 GHz. Therefore, we can obtain about 20 channels within an FSR.

3. CONCLUSIONS

In conclusion, we have presented the design and simulation of a GaN-based MQW tunable V-cavity laser with a reflective 2×2 half-wave optical coupler. Vertical optical mode profile are calculated by TMM method. With considering the material properties and processing conditions, we obtain large confinement factor $\Gamma(= 0.1813)$ with relative high indium doped InGaN GLs and aluminum doped AlGaN SLSs. Threshold gain, SMSR and FSR are also calculated for different structural parameters. With 5% cavity length difference, 20 channels with 300 GHz spacing within the free spectral range of 4.1 nm and high SMSR over 30 dB are achieved.

ACKNOWLEDGMENT

This work was supported by the National High-Tech R&D Program of China (grant No. 2014AA06A 504).

REFERENCES

1. Werle, P. W., P. Mazzinghi, F. D'Amato, M. De Rosa, K. Maurer, and F. Slemr, "Signal processing and calibration procedures for in situ diode-laser absorption spectroscopy," *Spectrochimica Acta Part A: Molecular and Biomolecular Spectroscopy*, Vol. 60, No. 8, 1685–1705, 2004.
2. Schlosser, E., J. Wolfrum, L. Hildebrandt, H. Seifert, B. Oser, and V. Ebert, "Diode laser based in-situ detection of alkali atoms: Development of a new method for determination of residence-time distribution in combustion plants," *Appl. Phys. B*, Vol. 75, No. 2–3, 237–247, 2002.

3. Allen, M. G., "Diode laser absorption sensors for gas-dynamic and combustion flows," *Meas. Sci. Technol.*, Vol. 9, No. 4, 545–562, 1998.
4. Hult, J., I. S. Burns, and C. F. Kaminski, "Wide-bandwidth mode-hop-free tuning of extended-cavity GaN diode lasers," *Applied Optics*, Vol. 44, No. 18, 3675–3685, 2005.
5. Komorowska, K., et al., "Tunable broad-area InGaN laser diodes in external cavity," *Integrated Optoelectronic Devices*, International Society for Optics and Photonics, 2007.
6. Omori, M., N. Mori, and N. Dejima, "Tunable light source with GaN-based violet laser diode," *SPIE OPTO*, International Society for Optics and Photonics, 2013.
7. Zhang, S., et al., "Simple and compact V-cavity semiconductor laser with 50×100 GHz wavelength tuning," *Optics Express*, Vol. 21, No. 11, 13564–13571, 2013.
8. He, J. J. and D. Liu, "Wavelength switchable semiconductor laser using half-wave V-coupled cavities," *Optics Express*, Vol. 16, No. 6, 3896–3911, 2008.
9. Okamoto, K., et al., "Pure blue laser diodes based on nonpolar m-plane gallium nitride with InGaN waveguiding layers," *Japanese Journal of Applied Physics*, Vol. 46, No. 9L, L820, 2007.
10. Lee, S.-N., et al., "Growth and characterization of the AlInGaN quaternary protective layer to suppress the thermal damage of InGaN multiple quantum wells," *Journal of Crystal Growth*, Vol. 310, No. 16, 3881–3883, 2008.
11. Bergmann, M. J. and H. C. Casey, "Optical-field calculations for lossy multiple-layer $Al_xGa_{1-x}N/In_xGa_{1-x}N$ laser diodes," *Journal of Applied Physics*, Vol. 84, No. 3, 1196–1203, 1998.
12. Lin, Y.-D., et al., "m-plane pure blue laser diodes with p-GaN/n-AlGaN-based asymmetric cladding and InGaN-based wave-guiding layers," *Applied Physics Letters*, Vol. 95, No. 8, 081110–081110, 2009.
13. Koch, T. L. and U. Koren, "Semiconductor lasers for coherent optical fiber communications," *Journal of Lightwave Technology*, Vol. 8, No. 3, 274–293, 1990.

Shaping the CPML Absorbing Boundary Condition to Eliminate Impinging Light at a Specific Position inside Electromagnetic Simulations

Sergio Cantero, Shuai-Hsun Lee, and Snow H. Tseng
Graduate Institute of Photonics and Optoelectronics
National Taiwan University, Taipei 10617, Taiwan

Abstract— In this research we explore the possibility to implement an optical target that eliminates incoming wave in finite-different time-domain (FDTD) simulations. This is achieved by a modified morphology of an absorbing boundary condition (ABC). In particular, our model is based on convolutional perfectly matched layers (CPML) ABC. To validate this method, a cylindrical CPML region is constructed as artificial absorbing material and simulated using a two-dimensional FDTD algorithm. Its performance is analyzed for focused beam wave source conditions. Varying the spatial size of the circular CPML, we compute the absorption efficiency for a wide range of applications and demonstrate its performance as a numerical optical target in FDTD simulations. We demonstrate that the reported simulation construct can effectively eliminate impinging light wave for a macroscopic light scattering simulation.

1. INTRODUCTION

The Finite-difference time-domain (FDTD) algorithm is widely used for electromagnetic wave propagation and light scattering problems. Based upon numerical solutions of Maxwell's equations, the electromagnetic wave characteristics can be accurately analyzed. This is of particular interest in modeling macroscopic scattering media, due to the difficulty to find analytical solutions [1]. The complexity of the problem relies on the large number of variables and the inhomogeneity of the material properties, such as index of refraction. To model light propagation through a macroscopic scattering medium to a target position, an absorber is required to eliminate impinging light. In modeling a physical problem in open space, absorbing boundary conditions (ABC) are applied to terminate the computational grid. ABCs are designed to absorb outgoing electromagnetic energy, allowing modeling an optical system isolated in free space with limited computation memory. The introduction in 1994 by Berenger of perfectly matched layers (PML) ABC effectively reduces the artificial numerical error caused by the simulation boundary [2].

Several modifications of the original PML formulation have been developed since its introduction. The numerical model presented utilizes convolutional perfectly matched layers (CPML) to efficiently embed the electromagnetic loss defined in a PML medium into the FDTD algorithm [3]. The advantage of CPML over other formulations is its independency on the host medium. For this reason, a CPML medium can be delimited in a defined region of interest within the simulation grid, allowing faster computations and less memory storage; as well as utilizing different boundary conditions, if necessary. Furthermore, no modification of the CPML algorithm is required due to the complexity of the medium, which is particularly useful in highly scattering media. In this research we construct a numerical tool capable to absorb light with efficacy in FDTD simulations.

2. NUMERICAL METHODS

A more detailed explanation of the CPML formulation can be found elsewhere [3] and therefore will not be discussed here. In a perfectly-matched medium as ABC the electric and magnetic conductivities, which are responsible for the energy losses, are increased across the boundary layers for effective absorption. Likewise in a cylindrical model, the conductivities are tapered down from the center of the target to the interface with the medium. Note that a different geometry can be formulated, as long as the conductivity is smoothly staggered from the boundary with the medium. In general, a given node within the PML has assigned a conductivity:

$$\begin{cases} \sigma(x,y,z) = \sigma_0 \left(\frac{L_{\max} - L(x,y,z)}{L_{\max}}\right)^m \\ \sigma_0 = 0.8\frac{m+1}{\eta\Delta} \end{cases} \tag{1}$$

Each node (x, y, z) of the FDTD grid is associated to a certain layer, with index L, depending on the morphology of the CPML region $L_{\max}$ is therefore the number of layers in the CPML construct

and $L = L_{\max}$ at the interface with the rest of the simulation region: Inner boundary if the CPML is the absorbing boundary condition or outer boundary if it is placed within the simulation. For a circular geometry, $L_{\max}$ is simply the radius of the region and $L(r)$ is the distance of the layer to the outer boundary. The parameters m and σ are the slope and maximum of the conductivity staggering. In PML formulations, m typically varies between 3 and 4 and σ is function of m, the wave impedance η, and the grid size Δ. Spatially sampling a circular shaped object into a rectangular grid is cause of numerical errors. Therefore a validation of the model was extensively discussed in previous research using two dimensional FDTD simulations [4]. Error analysis of the absorption efficiency compared the optical target under cylindrical incident source with external ABC, and to a planar-geometry target using Gaussian beam incidence. In this research, two applications of the optical target as numerical tool for scattering simulations are introduced. The model is presented first, as a method to eliminate light within the simulation and second, as an ideal absorber in modeling of optical imaging techniques.

3. SIMULATION RESULTS

In this research we first complement previous results with an evaluation of the near-field scattering distribution from the cylindrical optical target. An incident continuous-wave (cw) Gausian beam with wavelength 638.32 nm is embedded as soft source [2]. The FDTD grid resolution used for this simulation setup is 15.8×15.8 nm. After the incident beam is scattered by the target, the E_z distribution is stored at an equidistant contour from the target. The decrease in reflection of a Gaussian beam from targets with increasing radius is shown in Figure 1. Results show that the energy is mostly diffracted by small-sized absorbers (dotted lines). For effective absorption, the cross-section of the target must be increased. Approximately -80 dB and -100 dB maximal scattered amplitude can be achieved with radii three and four times the beam waist respectively (dashed lines). The limit is observed in larger absorbers (solid lines), in which the back-scattered energy is larger than the energy in the forward direction, meaning that the behavior is closer to the planar CPML behavior. For effective light absorption in simulations of scattering through macroscopic random media, the target should cover as much portion of the beam as possible, if additional scattering from the target should not affect the remaining field.

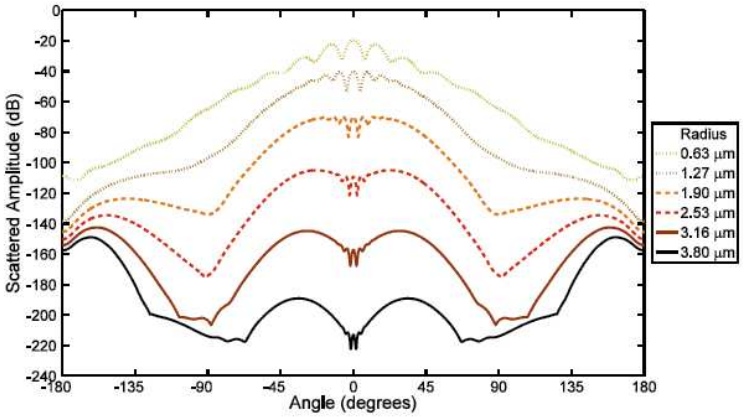

Figure 1: Angular distribution of a Gaussiam beam with 1.27 μm waist scattered by an optical target with different sizes. 0° corresponds to forward propagation in the z-axis and 180° to back-reflections.

An immediate application of the proposed model is to extract and isolate portions of this scattered field. To illustrate the problem, let us consider the light scattered by a known object, a small optical target (Figure 1). Note that due to a beam waist is larger than the object, it presents low absorption is low and can be contemplated as a strong scatterer. The E_z amplitude of this object after the incident source is in a steady state is shown in Figure 2(a). On the left side the Gaussian beam is incident and the scattered field propagates on the right side. In Figure 2(b), the same source is eliminated by a target large enough to cover most of the impinging energy. This data is subtracted to (a) in order to obtain Figure 2(c).

The concept is similar to the total-field/scattered-field (TF/SF) formulation, typically used to implement plane wave source conditions into electromagnetic FDTD simulations. The TF/SF main advantage is the possibility to separate the scattered field from the incident source, which is

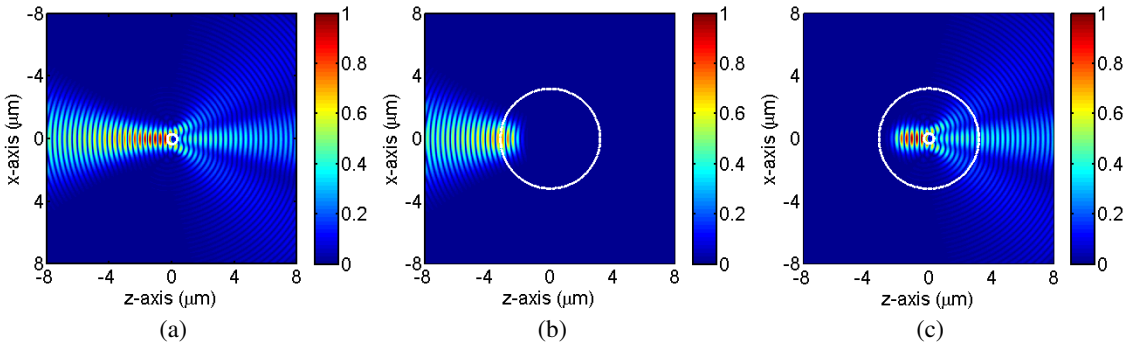

Figure 2: (a) Near-field computation of a Gaussian beam impinging a strongly scattering object: a 0.63 nm diameter CPML absorber. (b) Source eliminated by an optical target. (c) E_z field in (a) minus E_z field in (b).

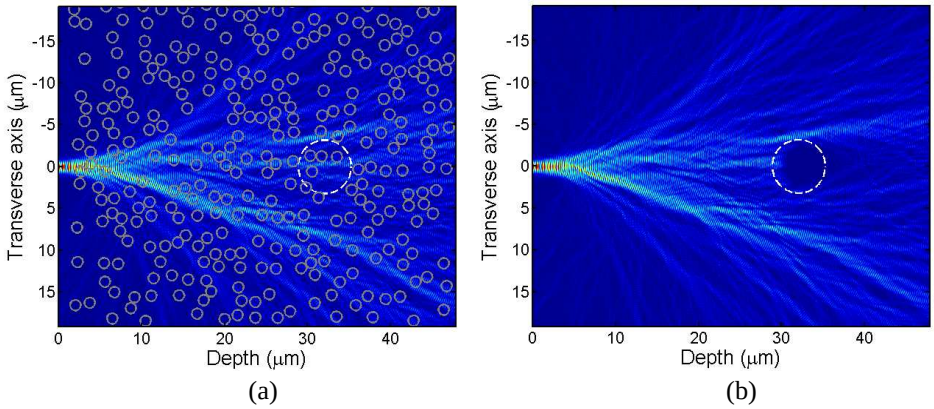

Figure 3: (a) Propagated light through a medium composed of a random aggregate of scattering cylinders. (b) Placement of an optical target inside the medium, centered at $z = 32.64\,\mu$m with radius 3.19 μm.

useful for retrieving properties of the problem object, such as its scattering cross-section. However, it expects the incident source to be known, and errors arise when the known source does not match plane wave propagation [5]. The optical target, on the other hand, can be applied to an arbitrary incident source, and its exact formulation is not necessary. The only requirement is the additional computation of the same medium with the optical target covering the incidence area. The equivalence of the suggested method with the TF/SF formulation is shown in Figure 2: The inner region of the optical target in (c), *total-field* includes both the incident field, computed in (b), and the scattered field; while at the external, *scattered-field*, region the source (b) is effectively subtracted.

In addition to the application of the presented numerical construct to extract portions of the electromagnetic energy within the problem, the proposed method can be used to model an absorbing object in FDTD simulations. Note that not only perfectly-matched conductivities can be implemented with the CPML formulation, but more general conductivity profiles are allowed, permitting different absorbing media to be modeled. For this purpose, the optical target is placed under a simple source-detector scheme. Figure 3 shows the placement of an optical target in a highly scattering medium. The medium consists of 300 randomly placed scatterers with index of refraction 1.44 and diameter 1.28 μm on a background homogeneous medium with index of refraction 1.33. An incident source of wavelength 638.32 nm is applied on a $38.3 \times 47.9\,\mu$m region with resolution 31.9×31.9 nm. As expected, strong scattering defocuses the electromagnetic energy at the random medium. At the same time, strongly focused paths materialize as previously studied by [6]. In Figure 3(b) the optical paths formed by the propagated light are ostensibly deformed after inserting an absorber.

To confirm the detectability of the target within the medium, a detector is placed along the

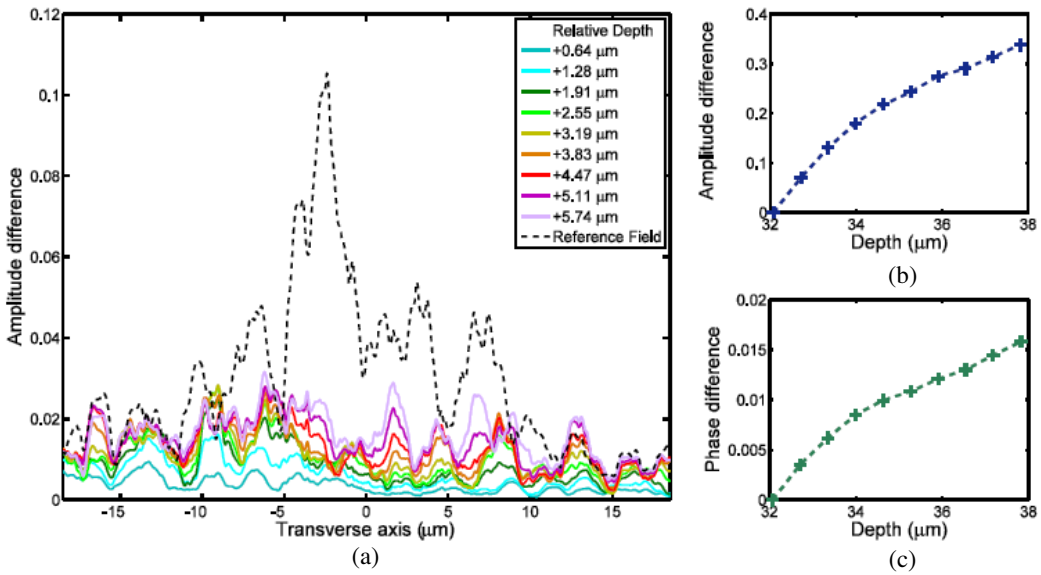

Figure 4: Amplitude difference at the detector, relative to the initial position ($z = 32.64\,\mu\text{m}$, $x = 0$). To smoothen the peaks, a local average is numerically integrated over the 40 nearest points. The difference between the field without absorber and the initial position in dashed line. Average difference in (b) amplitude and (c) phase at every point of the detector array.

side opposite to the source. The amplitude and phase of the electric field is then measured at the detector points. The difference in amplitude and phase of a moving target with respect to an initial position is presented in Figure 4. As we can observe, the differences are scattered through the medium and spread along the detector. However, as the target shifts its position from the original placement, the differences increase. Figure 4 shows the increasing average deviation in both amplitude (b) and phase (c) as the target moves towards the detector.

4. CONCLUSION

In summary, the possibility to shape the CPML ABC formulation to design an optical absorber within the simulation region is demonstrated. Instead of a planar geometry such as implemented in the boundary condition, a circular CPML with radial dependency is constructed. Results show reduction of the spurious scattering with increasing sizes up to the accuracy of CPML ABC. To determine the feasibility of the model, we introduced two applications under both focused light and omnidirectional light incidence. First, a method to extract scattered and incident field from a region is provided. Unlike other approaches, the mathematical formulation is not subject to the incident source formulation. And second, we confirm detection and tracking of a CPML target utilizing a very simple source-detector scheme.

Additionally, the CPML formulation is equally valid for a different value of the conductivity, not only perfectly matched layers. In large scale FDTD simulations, the computation time plays an important role and resolution and size are strongly limited. For this reason, the CPML absorber model reported in this manuscript presents the possibility to integrate absorption loss at specific regions of the simulation. This is possible without defining the electric or magnetic conductivity in every single grid point and thus reducing the computation time and memory resources required. An ideal absorber is of interest for scattering simulations in biomedical applications as tool to design and validate future and current biomedical optical techniques, such as in medical diagnosis. Scattering simulations confirm the effective light elimination by the optical target model.

REFERENCES

1. Tsai, C.-H., S.-H. Chang, and S. H. Tseng, "Applying the optical theorem in a finite-difference time-domain simulation of light scattering," *IEEE Trans. Antennas Propag.*, Vol. 58, 3091–3094, 2010.
2. Taflove, A. and S. C. Hagness, *Computational Electrodynamics: The Finite-difference Time-domain Method*, 3rd Edition, Artech House, 2005.

3. Roden, J. A. and S. D. Gedney, "Convolution PML (CPML): An efficient FDTD implementation of the CFS-PML for arbitrary media," *Microw. Opt. Tech. Lett.*, Vol. 27, 334–339, 2000.
4. Cantero, S., Y. Huang, and S. H. Tseng, "FDTD simulation of an optical absorber based on CPML absorbing boundary condition," 2014.
5. Çapoğlu, L. R., A. Taflove, and V. Backman, "Computation of tightly-focused laser beams in the FDTD method," *Optics Express*, Vol. 21, 87–101, Jan. 14, 2013.
6. Choi, W., A. P. Mosk, Q. H. Park, and W. Choi, "Transmission eigenchannels in a disordered medium," *Physical Review B*, Vol. 83, 134207, Apr. 27, 2011.

Optical Investigation of Nd^{3+}-sensitized Upconversion Nanoparticles for Damage-free *in vivo* Deep Imaging and *in vitro* Microscopy

Yuxiang Zhao and Qiuqiang Zhan*
Centre for Optical and Electromagnetic Research, South China Academy of Advanced Optoelectronics
South China Normal University (SCNU), Guangzhou 510006, China

Abstract— We firstly set up two optical models and investigated the upconverting excitation process of novel 795-nm excited Nd^{3+}-sensitized upconversion nanoparticles. Simulation results proved the novel UCNPs has the potential to show excellent *in vivo* deep imaging and damage-free *in vivo*, *in vitro* imaging ability under high power 795 nm laser excitation.

1. INTRODUCTION

Upconversion nanoparticles (UCNPs) have been demonstrated as the hot nanoprobes in the biophotonics research [1]. Superior to the conventional biological labels such as organic dyes and quantum dots UCNPs exhibit the unique properties of autofluorescence-free bioimaging under near-infrared light excitation Due to series of advantages such as large anti-Stokes shifts no photobleaching, no blinking, low cytotoxicity, deep imaging ability and high resolution UCNPs have attracted huge attention and interests in the biomedical and biotherapy in recent years [2]. However, traditional Yb^{3+}-sensitized UCNPs have been proved to reduce the overheating effect under high power 975 nm laser excitation [3]. Recently, Nd^{3+}-sensitized UCNPs have emerged as a candidate to replace traditional ones due to the minimized heating effect under 795 nm laser excitation [4]. Some groups have presented the synthesis and potential applications of Nd^{3+}-sensitized UCNPs which were still lack of optical investigation [5–7]. In this work, we optically modeled for Nd^{3+}-sensitized UCNPs-based bio-applications and showed the damage-free imaging ability using 795 nm laser exciting. Meanwhile, the Nd^{3+} to Yb^{3+} energy transfer efficiency was discussed to study the impact on deep imaging ability.

2. MODELING AND THEORETICAL METHODS

2.1. Optical Models

Two different optical models of UCNPs-based biomedical applications were constructed to investigate the Nd^{3+}-sensitized UCNPs: one is a cell-in-celldish model for *in vitro* microscopy; the other is a pork tissue model for *in vivo* deep tissue imaging.

2.1.1. Cell-in-celldish Model

As shown in Fig. 1(a) a cylinder area (diameter: 35 mm depth: 3 mm) was set up as PBS solution in cell-in-celldish for the investigation of *in vitro* microscopy while the UCNPs-labeled cells were adherent on the bottom. We simulated it on an inverted microscope with 100 mW high power CW laser exciting after focused by a 1.35 NA objective.

2.1.2. Pork Tissue Model

As described in Fig. 1(b), we selected the three layers (2.5 mm skin, 12.5 mm fat and 30 mm muscle) cylinder pork tissue model as its similar tissue optical properties with human beings, which acted as the part of tissue being irradiated by circle area (radius: 25 mm) CW laser source (power density: 500 mW/cm^2). A UCNPs-labeled tumor (radius: 2.5 mm) was in this tissue model at different depth from 5 mm to 42.5 mm.

2.2. Theoretical Methods

The theoretical methods of these two models are based on three different ones: diffusion equation heat transport equation and cell damage model, each of which is described as below and the parameters used are set as typical values [3, 8–13].

*Corresponding author: Qiuqiang Zhan (qiuqiang.zhan@coer-scnu.org).

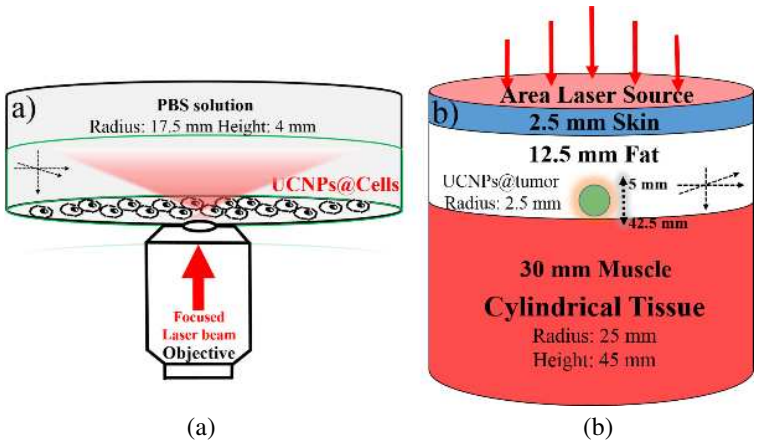

(a) (b)

Figure 1: Schematics of (a) *in vitro* cell-in-celldish model and (b) *in vivo* Pork Tissue model.

2.2.1. Diffusion Equation

Fluorescence diffusing imaging can be described as two equations: one is the excitation light Equation (1) and the other is the fluorescence emission Equation (2). In the steady state, we can describe them as [8]:

$$-\nabla(D_{ex}\nabla\varphi_{ex}) + \mu_a^{ex}\varphi_{ex}(r) = S(r) \tag{1}$$

$$-\nabla(D_{em}\nabla\varphi_{em}) + \mu_a^{em}\varphi_{em}(r) = \eta\mu_{ex}[\varphi_{ex}(r)]^2 \quad \text{for 975 nm laser} \tag{2a}$$

$$-\nabla(D_{em}\nabla\varphi_{em}) + \mu_a^{em}\varphi_{em}(r) = \eta\mu_{ex}[Y\varphi_{ex}(r)]^2 \quad \text{for 795 nm laser} \tag{2b}$$

where μ_a, μ_s', and $D_{ex/em} = 1/(3*(\mu_a^{ex/em} + \mu_s^{'ex/em}))$ denotes the absorption coefficient, reduced scattering coefficient and diffusion coefficient of excitation or emission light; Y is the energy transfer efficient from Nd^{3+} to Yb^{3+}, $\varphi_{ex/em}$ is the photon fluence rate of excitation and emission light and η is the power-related quantum yield coefficient of UCNPs For the side boundary and interface between 3 layers, we regard them as continuous conditions. Neumann boundary condition is used that accounts for the refractive index mismatch between tissue ($n_{tissue} \sim 1.4$) and air ($n_{air} \sim 1$) as: $n \cdot (D\nabla\varphi(r,t)) + \varphi(r,t)/2A = 0$, where A is 2.74 in this investigation.

2.2.2. Heat Transfer Equation

The spatiotemporal temperature distribution for two models are based on the Pennes' bioheat transfer equation with an additional term Q [14, 15]:

$$\rho c(dT/dt) = (kT) + Q \tag{3}$$

where the first term on the right side is heat conduction. The second term heat source Q absorbed can be obtained according to the lambert-Beer law for the *in vitro* model and calculated as $Q = \mu_a^{ex}\varphi_{ex}(r)$ from Equation (1) for the *in vivo* model. Regarding the boundary conditions, a heat flux condition was used combined with Newton's law of cooling to describe a convection process as: K $(\mathrm{d}T/\mathrm{d}n) = h(T - T_0)$ where $h_{air} = 25\,\mathrm{W/(m^2 \cdot K)}$, $h_{wall} = 5\,\mathrm{W/(m^2 \cdot K)}$

2.2.3. Cell/Tissue Damage Model

Here we predict this cell/tissue damage by using the Arrhenius injury model. The cells/tissue that are damaged over time is given by [12, 15]:

$$F_D = 1 - e^{-\Omega} = 1 - e^{-\int k dt} = 1 - e^{-\int Ae - Ea/(RT)dt} \tag{4}$$

where Ω is the damage index E_a is the activation energy, R is the universal gas constant, T is the temperature changed with time, and A is a scaling factor. Here we define healthy cell has $F_D = 0$, and $F_D = 0.6$ means the time cell begin to be damaged.

3. RESULTS AND DISCUSSION

3.1. Damage-free *in vitro* Microscopy with Nd^{3+}-sensitized UCNPs

In this simulation, 100 mW (focal plane power) CW laser beam was used [16]. In the *in vitro* microscopy, heating effect was primarily due to the absorption of exciting laser. As shown in Figs. 2(a)–(d), the spatiotemporal temperature distribution changed very little under 795 nm excitation, whereas under the 975 nm excitation the temperature had a huge raising after 20 minutes. After 30 s of irradiation, it didn't reach the apoptosis temperature under either 795 nm or 975 nm laser excitation. After 20 minutes-irradiation, the temperature increased to 46°C and most cells were damaged in the case of 975 nm laser in Fig. 2(h). On the contrary, almost all the cells were still healthy under high power 795 nm excitation after 20 minutes in Fig. 2(f), which was attributed to the minimized heating effect of Nd^{3+}-sensitized UCNPs.

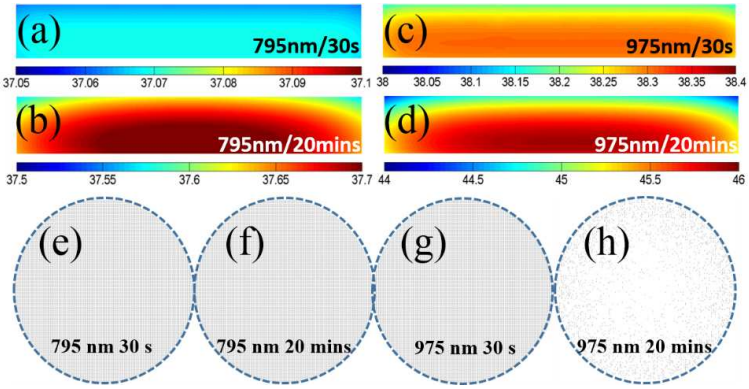

Figure 2: Simulated spatiotemporal temperature distributions of cell-in-celldish model under (a) 30 s, (b) 20 mins 795 nm laser excitation and (c) 30 s, (d) 10 mins 975 nm laser excitation (focal plane power: 100 mW). Cell viability predictions under (e) 1 min, (f) 20 mins 975 nm laser irradiation and (g) 1 min, (h) 20 mins 795 nm laser irradiation.

3.2. Damage-free *in vivo* Tissue Imaging with Nd^{3+}-sensitized UCNPs

500 mW/cm^2 circle area CW laser was selected in our simulation which had been proved to reduce the overheating effect in skin surface under 975 nm laser excitation [3]. Compared to the results in Fig. 3(a), each corresponding pictures in Fig. 3(b) showed a much higher temperature. After 3 minutes of 975 nm laser irradiation, temperature raised above 45°C and the inner part of skin was almost damaged in Fig. 3(e). After irradiated by high power 975 nm laser for 10 minutes, the damage condition in tissue was extremely severe as the temperature was up to 60°C. On the contrary, under high power 795 nm laser excitation the temperature had not reached 40°C and the

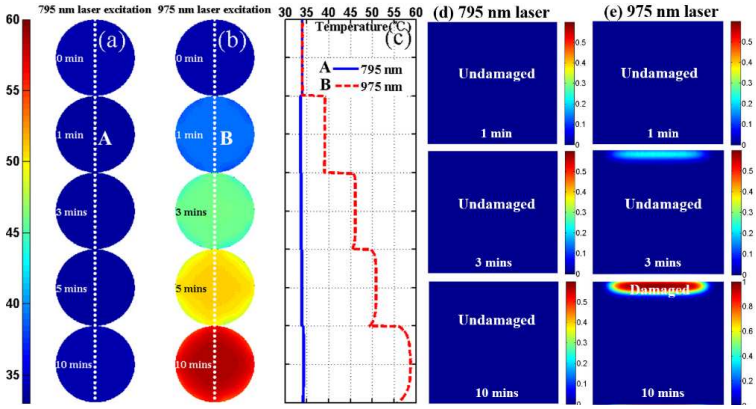

Figure 3: Simulated temperature distributions after different irradiation times of pork tissue model surface under (a) 795 nm, (b) 975 nm laser irradiation and (c) the corresponding temperature line. Simulated normalized tissue damage index distributions of pork tissue model after different time irradiation of (d) 795 nm and (e) 975 nm laser.

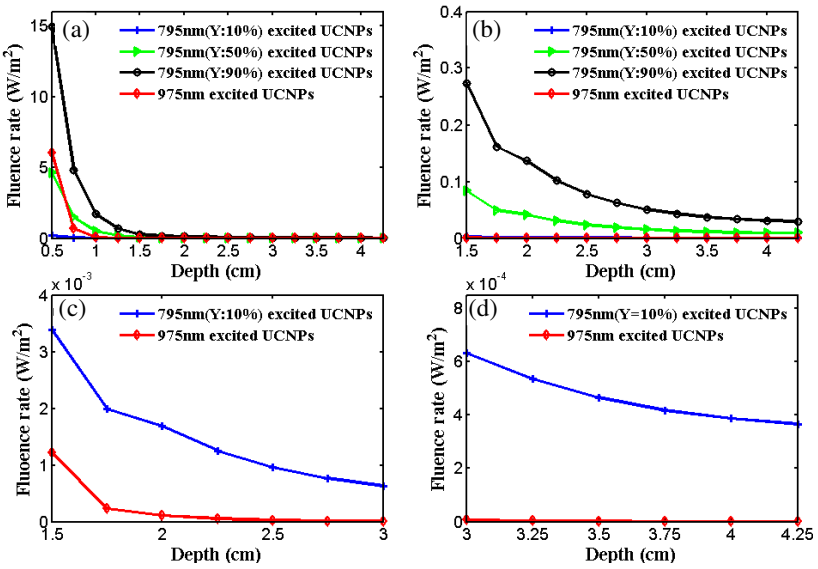

Figure 4: Stimulated UC PL fluence rate at detector point for different tumor depth (from 0.5 cm to 4.25 cm) of 500 mW/m^2 975 nm laser and 795 nm laser with different energy transfer efficient Y (10%, 50%, 90%) from $Nd^{3+}Yb^{3+}$.

whole tissue still kept undamaged even after 1 minutes of irradiation. Simulation results proved that the Nd^{3+}-sensitized UCNPs completely exhibit the damage-free *in vivo* deep imaging ability.

3.3. Nd^{3+} to Yb^{3+} Energy Transfer Efficiency (ETE) Dependent Deep *in vivo* Tissue Imaging

The upconversion (UC) photoluminescence (PL) process of Nd^{3+}-sensitized UCNPs is based on the energy transfer bridge Yb^{3+} (Nd^{3+}-Yb^{3+}-Ln^{3+}), which should be considered into deep tissue imaging application. In this simulation, 795-nm excited Nd^{3+}-sensitized UCNPs with 650 nm emission and 975 nm excited UCNPs with 800 nm emission were used to investigate the impact of ETE on the imaging depth. As shown in Fig. 4, the intensities of 800 nm UC emission (under 975 nm excitation) and 650 nm UC emission (under 795 nm excitation with different Y from 10% to 90%) on the surface were showed at different tumor depths from 0.5 cm to 4.25 cm. The surface UC PL intensity decreased rapidly with exciting depth increased because the much higher scattering and absorption in deep tissue. The 795 nm excited UCNPs ($Y \geq 50\%$) with 650 nm emission has a better deep (≥ 0.75 cm) imaging ability than 975-nm-excited ones. In the deep (≥ 1.5 cm) region showed in Figs. 4(d) and (e), Nd^{3+}-sensitized UCNPs ($Y = 10\%$) can replace the Yb^{3+}-sensitized ones which indicated the high deep imaging of the 795-nm-excited ones.

4. CONCLUSION

For the first time both *in vitro* cell microscopy and *in vivo* 3-layers pork tissue have been optically modeled systematically to give a new perspective to the study of Nd^{3+}-sensitized UCNPs. With two optical models, the spatiotemporal temperature and damage distribution have been investigated as the complementary research of Nd^{3+}-sensitized UCNPs. We have calculated and presented this novel UCNPs as the damage-free nanoprobes in both *in vitro* and *in vivo* imaging under high power laser irradiation by shifting the exciting wavelength from 975 nm to 795 nm. Simulation results of deep tissue imaging have exhibited the novel UCNPs with higher ($\geq 5\%$) Nd^{3+} to Yb^{3+} energy transfer efficiency are worth to be synthesized for *in vivo* deep tissue bio-applications.

ACKNOWLEDGMENT

This work was supported by Guangdong Innovative Research Team Program (No. 201001D01047993 18), the Natural Science Foundation of Guangdong province (No. S2013040014211), the Postdoctoral Science Foundation of China (No. 2013M530368), the Discipline and Specialty Construction Fundation of Colleges and Univerisities of Guangdong Province (No. 2013LYM_0017), the Young Faculty Academic Training Foundation of SCNU (No. 2012KJ017), and the Student Extracurricular Scientific Research Key Project of SCNU (No. 13GDKC02).

REFERENCES

1. Liu, Y., et al., "Lanthanide-doped luminescent nanoprobes: Controlled synthesis, optical spectroscopy, and bioapplications," *Chemical Society Reviews*, Vol. 16, 6924–6958, 2013.
2. Xu, C. T., et al., "Upconverting nanoparticles for pre-clinical diffuse optical imaging, microscopy and sensing: Current trends and future challenges," *Laser & Photonics Reviews*, Vol. 5, 663–697, 2013.
3. Zhan, Q., et al., "Using 915 nm laser excited $Tm^{3+}/Er^{3+}/Ho^{3+}$-doped NaYbF4 upconversion nanoparticles for in vitro and deeper in vivo bioimaging without overheating irradiation," *ACS Nano*, Vol. 5, 3744–3757, 2011.
4. Wang, Y.-F., et al., "Nd^{3+}-sensitized upconversion nanophosphors: Efficient in vivo bioimaging probes with minimized heating effect," *ACS Nano*, Vol. 8, 7200–7206, 2013.
5. Li, X., et al., "Nd^{3+} sensitized up/down converting dual-mode nanomaterials for efficient in-vitro and in-vivo bioimaging excited at 800 nm," *Sci. Rep.*, 2013.
6. Xie, X., et al., "Mechanistic investigation of photon upconversion in Nd^{3+}-sensitized core-shell nanoparticles," *Journal of the American Chemical Society*, Vol. 34, 12608–12611, 2013.
7. Zhong, Y., et al., "Elimination of photon quenching by a transition layer to fabricate a quenching-shield sandwich structure for 800 nm excited upconversion luminescence of Nd^{3+}-sensitized nanoparticles," *Advanced Materials*, Vol. n/a–n/a, 2013.
8. Xu, C. T., J. Axelsson, and S. Andersson-Engels, "Fluorescence diffuse optical tomography using upconverting nanoparticles," *Applied Physics Letters*, Vol. 25, 2009.
9. Zhan, Q., et al., "Optimization of optical excitation of upconversion nanoparticles for rapid microscopy and deeper tissue imaging with higher quantum yield," *Theranostics*, Vol. 5, 306, 2013.
10. George, A., R. R. Fernando, and F. C. Arion, "Tomographic bioluminescence imaging by use of a combined optical-PET (OPET) system: A computer simulation feasibility study," *Physics in Medicine and Biology*, Vol. 17, 4225, 2005.
11. Rylander, M. N., et al., "Optimizing heat shock protein expression induced by prostate cancer laser therapy through predictive computational models," *Journal of Biomedical Optics*, Vol. 4, 041113-041113–16, 2006.
12. Henriques, F. C., "Studies of thermal injury; the predictability and the significance of thermally induced rate processes leading to irreversible epidermal injury," *Archives of Pathology*, Vol. 5, 489–502, 1947.
13. Cohen, M. L., "Measurement of the thermal properties of human skin. A review," *Journal of Investigative Dermatology*, Vol. 3, 333–338, 1977.
14. Pennes, H. H., "Analysis of tissue and arterial blood temperatures in the resting human forearm," *Journal of Applied Physiology*, Vol. 2, 93–122, 1948.
15. Rylander, M. N., et al., "Heat shock protein expression and injury optimization for laser therapy design," *Lasers in Surgery and Medicine*, Vol. 9, 731–746, 2007.
16. Liu, Q., et al., "Upconversion luminescence imaging of cells and small animals," *Nat. Protocols*, Vol. 10, 2033–2044, 2013.

Tradeoff Study of Microwave Imaging Based on Frequency Considerations

Dau-Chyrh Chang[1], **Yau-Jyun Tsai**[1], **Chih-Hung Lee**[2, 3], **and Chang-Hsuan Kao**[1]

[1]Oriental Institute of Technology, CRC, OIT, Taiwan
[2]Yuan Ze University, Taiwan
[3]Electronics Testing Center, Taiwan

Abstract— The quality of image includes the resolution of pixel and contrast of the pixel. The better the quality of microwave image is with higher the resolution of image pixel and larger the image contrast. The contrast depends on the signal to noise ratio of the radar receiver. The resolution of pixel depends on the radar frequency. The higher the frequency the better the resolution of pixel will be. Unfortunately, the higher the frequency the smaller the signal to noise ratio will be. The phenomenon will cause the lower image contrast. In this paper, the formulation of microwave imaging, quality of radar image with various frequencies and number of transceivers are detail discussed. In order to obtain the better quality of image, a new technique with multiple frequencies is developed. The results of microwave image with better resolution and higher contrast by both simulation and measurement are agreed.

1. INTRODUCTION

Images are very useful for nowadays applications in medical and industries. The quality of images should include the image resolution, image contrast, and less false alarm image. The sensors of image include x-ray, acoustic, MRI, and microwave. The advantages and disadvantages of these sensors with image quality are discussed in many literatures. Traditional microwave image will have lower resolution, lower contrast, and many false alarm images with higher contrast. In the paper microwave image with higher image resolution and higher contrast with lower false alarm images will be discussed.

2. FORMULATION OF MICROWAVE IMAGING

All the formulation of coordination in the following is rectangular coordination. If the target image with rotation center at $(0, 0, 0)$ and image region $X_m/2 \geq x \geq -X_m/2$, $Y_m/2 \geq y \geq -Y_m/2$, $Z_m/2 \geq z \geq -Z_m/2$ is interested. The microwave image region is consisted of infinite scatter points $\sigma(x, y, z)$ with RCS (radar cross section area) magnitude σ at pixel (x, y, z). In order to reduce the coupling between transmitter and receiver, the location of bistatic transmitter and receiver are $T_x(x_t, y_t, z_t)$ and $R_x(x_r, y_r, z_r)$ respectively. The detail geometry is shown in Fig. 1.

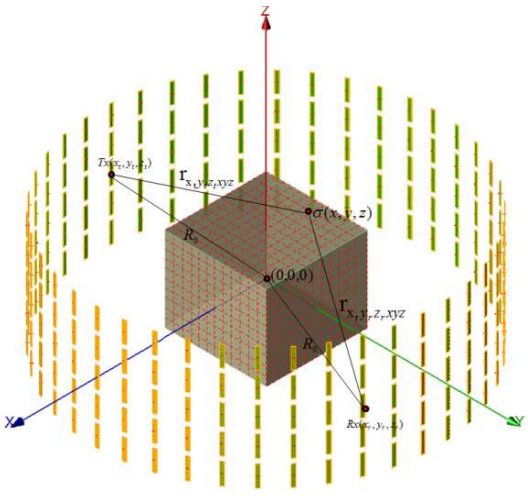

Figure 1: Geometry of microwave imaging.

2.1. Preliminary Image Construction

The geometry of image pixel $\sigma(x, y, z)$, transmitter and receiver will be formulated in this section.

The distance between transmitter and $\sigma(x, y, z)$ is as shown in Eq. (1),

$$r_{x_t y_t z_t xyz} = \sqrt{[(x_t - x)^2 + (y_t - y)^2 + (z_t - z)^2]} \tag{1}$$

The distance between receiver and $\sigma(x, y, z)$ is as shown in Eq. (2),

$$r_{x_r y_r z_r xyz} = \sqrt{[(x_r - x)^2 + (y_r - y)^2 + (z_r - z)^2]} \tag{2}$$

For the isotropic antenna radiation pattern, the spherical wave incident at $\sigma(x, y, z)$ and reflected by $\sigma(x, y, z)$ is shown in Eq. (3),

$$S = \frac{\sqrt{\sigma} e^{-jkr_{x_t y_t z_t xyz}}}{r_{x_t y_t z_t xyz}} \tag{3}$$

where the propagation constant, k, is function of guide wavelength λ_g, guide velocity v_g, and frequency. The propagation constant k is expressed as in Eq. (4),

$$k = 2\pi/\lambda_g = \omega/v_g \tag{4}$$

The signal received at the microwave receiver (ϕ_r, z_r) or (x_r, y_r, z_r) with isotropic antenna pattern for giving propagation constant k is shown in Eq. (5),

$$V_{\phi_b z_b} = \sum_{x=-X_m/2}^{x=+X_m/2} \sum_{y=-Y_m/2}^{y=+Y_m/2} \sum_{z=-Z_m/2}^{z=+Z_m/2} \frac{\sqrt{\sigma_{xyz}}}{(r_{x_t y_t z_t xyz})(r_{x_r y_r z_r xyz})} e^{-jk(r_{x_t y_t z_t xyz} + r_{x_r y_r z_r xyz})} \tag{5}$$

Then the target image $\sigma(x, y, z)$ can be constructed for giving simulated or measured data $V_{\phi_b z_b}$ in cylindrical coordination $2\pi \geq \phi_b \geq 0$ and $z_m \geq z_b \geq -z_m$. The number of received signal in ϕ and z are M and N respectively. The constructed of image from the M by N received data points for given propagation constant k or frequency f is given by Eq. (6),

$$\sigma_{xyzf} = \left| \frac{1}{MN} \sum_{z=z_i}^{z=z_f} \sum_{\phi=\phi_i}^{\phi=\phi_f} a_{\phi_b z_b} (r_{x_t y_t z_t xyz})(r_{x_b y_b z_b xyz})\ V_{\phi_b z_b} e^{-jk(r_{x_b y_b z_b xyz} + r_{x_t y_t z_t xyz})} \right|^2 \tag{6}$$

The three dimensional image for $X_m/2 \geq x \geq -X_m/2,\ Y_m/2 \geq y \geq -Y_m/2,\ Z_m/2 \geq z \geq -Z_m/2$ can be constructed by Eq. (6) for fixed frequency f. The mutual coupling between transmitter and receiver will degrade the small signal detection. In order to reduce the mutual coupling between transmitter and receiver, the bistatcic angle α for the same z value is included during measurement.

2.2. Fine Image Construction

The quality of image will be degraded from the low resolution pixel which due to the longer wavelength at lower frequency, lower image contrast due to the higher propagation loss at higher frequency, and false alarm image pixels due to the diffraction and reflection of wave propagation. By using the multiple frequencies or frequency agility technique, the final value of image is the average of image for total frequency points L and frequency increment Δf as shown in Eqs. (7) & (8),

$$\sigma_{xyz} = \frac{1}{L} \sum_{f_{lower}}^{f_{higher}} \sigma_{xyzf} \tag{7}$$

$$\Delta f = (f_{higher} - f_{lower})/L \tag{8}$$

3. RESULTS OF MEASUREMENT

In order to verify the proposed algorithm, two identical spherical metal targets $\sigma_1(x_1, y_y, 0)$ and $\sigma_2(x_2, y_2, 0)$ with radius 2.7 cm are arranged in Fig. 2. The RCS value of the metal sphere is -26.4 dBsm. In order to reduce the mutual coupling between transmitter at $(-129.2, 28.6, 0)$ and receiver $(-129.2, -28.6, 0)$, the bistatic angle is 25° which is corresponding the distance between

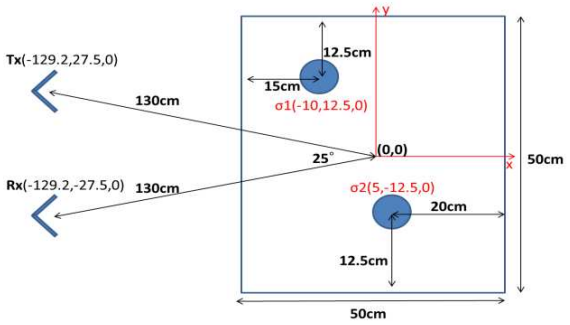

Figure 2: Geometry of arrangement.

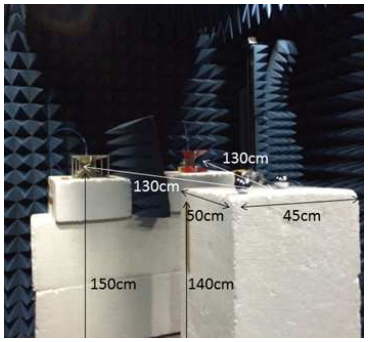

Figure 3: Measurement in anechoic chamber.

transmitter and receiver is 56 cm. The radius of transmitter (receiver) to the rotation center of target is about 130 cm. The antenna for both transmitter and receiver is wideband double ridge horn with bandwidth 700 MHz $\sim$ 18 GHz. In order to simply the structure of data acquisition, targets are rotate along the rotation center. This is similar to that of the bistatic radar with movement along the locus of radius 130 cm. In order to consider the quality of image at highest frequency, there are 501 data points received from 360°.

There are 15 images for frequency from 1 GHz to 15 GHz with frequency interval 1 GHz. Figs. 4 $\sim$ 6 are the examples of images at 1 GHz, 5 GHz, 10 GHz. From these figures, the lower the frequency is the lower the resolution will be. Except for the lower resolution at lower frequency, many false alarm targets are generated. For higher frequency, the signal to noise ratio will be lower due to the RF cable loss for VNA to transmitter and receiver and propagation loss. Although the resolution of image will be better for higher frequency, the contrast of image pixel will be lower. In order to compromise the resolution and contrast, Fig. 7 is the average summation of the image for frequency from 1 GHz to 15 GHz with frequency interval 1 GHz. The image of two metal spheres are clear with higher contrast and better resolution.

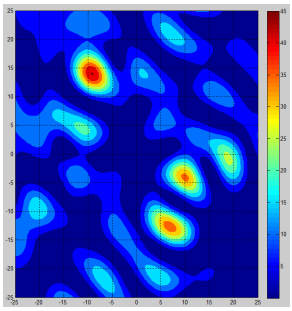

Figure 4: Image at 1 GHz.

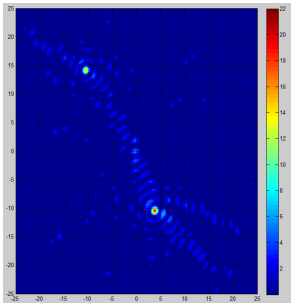

Figure 5: Image at 5 GHz.

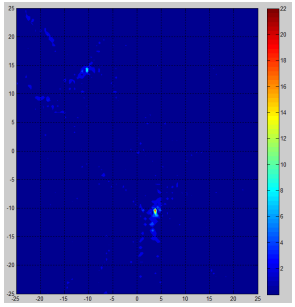

Figure 6: Image at 10 GHz.

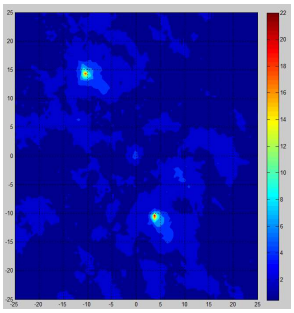

Figure 7: Final image with 15 frequencies.

4. CONCLUSION

The resolution of image will be lower for lower frequency and higher for higher frequency. Unfortunately, the contrast of image will be higher for lower frequency and lower for higher frequency. Except for the resolution and contrast of image quality, false alarm pixel may happen inside image in frequency domain. The formulation of radar image with compromise resolution and contrast is developed in this paper. The measurement results show that this technique is another approach for high quality radar image.

REFERENCES

1. Chang, D.-C. and H.-C. Lee, "Radar image of corner reflector," *IEEE AP-S International Symposium and USNC/CNC/URSI National Radio Science Meeting*, 2003.
2. Qi, Y. L., X. L. Yang, W. X. Tan, Y. P. Wang, and W. Hong, "Research on the microwave snapshot imaging radar based on antenna array," *IET International Radar Conference*, 2013.

Study on the Scattering Properties of an Artificial Electromagnetic Hard Surface

Xingxing Huang, Peiheng Zhou, Haiyan Chen, Mangui Han, and Longjiang Deng
National Engineering Research Center of Electromagnetic Radiation Control Materials
State Key Laboratory of Electronic Thin Film and Integrated Devices
University of Electronic Science and Technology of China, Chengdu 610054, China

Abstract— An artificial electromagnetic hard surface realized by the longitudinally oriented metal strips loaded on a grounded dielectric substrate is proposed. Electromagnetic scattering properties of the proposed structure are analyzed for both transverse magnetic (TM) polarization and transverse electric (TE) polarization, where TM polarization is defined by the polarized direction of the incidence electric field E parallel with the metal strips. The scattering properties of a high impedance surface (HIS) with similar structure are also proposed for comparison. In the case of the HIS, radar cross section (RCS) reduction over broad angles can be obtained for TE polarization, but get worse for TM polarization. While in the case of the hard surface, RCS reduction at the whole considered angles can be obtained for TE polarization, and almost invariable for TM polarization, which has the potential advantages in antenna design and stealth technique. To explain this phenomenon, the bistatic RCS are also analyzed. And the scattering reduction is estimated by comparing the mono- and bistatic scattering patterns of the hard surface loaded and unloaded metal cube.

1. INTRODUCTION

The concepts of artificially soft and hard surfaces were introduced to characterize the general way certain surfaces interact with electromagnetic waves [1]. The surface is direction dependent and polarization independent. These surfaces act upon on EM wave as a perfect electric conductor (PEC) for one linear polarization and a perfect magnetic conductor (PMC) for the other [2]. A widely known soft surface is the quarter-wavelength deep transversely corrugated surface used in hybrid-mode feed horns and the typical feature of this surface is that the wave no matter how polarized can't propagate along the surface [3]. Correspondingly the typical feature of an ideal hard surface is that a wave of any polarization is allowed to propagate along the surface [3]. Hard surface mainly have two important applications. One important applications of hard surface is in horns with low cross polarization and high aperture efficiency [3–8]. Another is the reduction of unwanted scattering from certain structures like struts [9] and axial supports of rear-radiating feeds [10] in prime-focus reflector antennas [3].

In this paper, we introduce a method for reducing RCS over a wide range of incident angles based on the characteristic of the hard surface. We use a simple hard surface structure which is a surface with longitudinally oriented metal strips on a grounded dielectric substrate. As we known, the PEC only support the wave which is vertical polarization (i.e., TM-case) along the surface, however the hard surface support the wave both vertical polarization and horizontal polarization (i.e., TE-case). The hard boundary can be used to obtain strong radiation fields along the surface for any polarization [11]. So, when the wave incident on the hard surface, radiation along the hard surface is stronger than that along the PEC. And the hard surface structure is lossless, so some of the incident energy is transformed to the surface that the RCS is reduced.

2. HARD SURFACE DESIGN

The proposed hard surface is based on the unit cell described in [12]. It is shown in Fig. 1(a). A grounded dielectric substrate, with relative dielectric permittivity $\varepsilon_r = 10.2$ and a thickness of $h = 2\,\text{mm}$ is used. The width of the strip is $w = 20\,\text{mm}$, and the width of the gap is $g = 0.8\,\text{mm}$. For this structure, the reflection phases for both TE and TM polarization over different incidence angles are given in Fig. 1(b). For TM polarization, the metal strips provide a hard boundary and the reflection phase is 180 degree. For TE polarization, this structure provides a hard boundary and the reflection phase is 0 degree around 2 GHz over different incident angles, and can be widely considered as artificial magnetic conductor (AMC) [13]. The basic property of the soft and hard surface (SHS) boundary is: a plane wave field is reflected from the generalized SHS plane so that its TE (linearly polarized E-field parallel along the surface y-axis) component is reflected as from a

PMC plane while its TM component is reflected as from a PEC plane [14]. Finally we can achieve the hard surface.

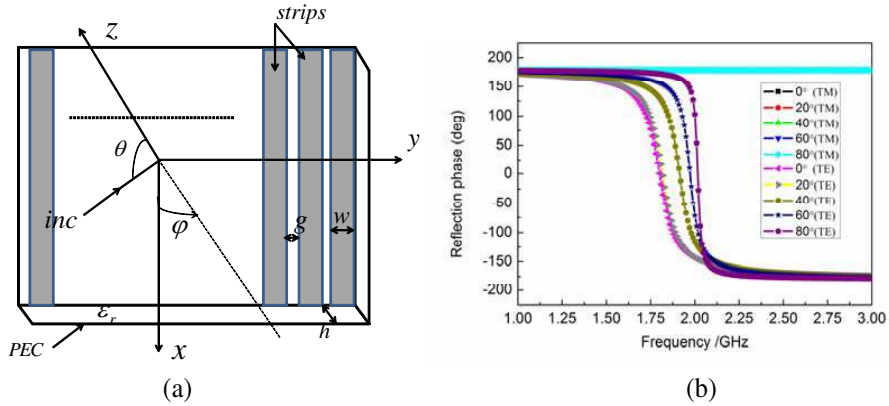

(a) (b)

Figure 1: (a) 3D schematic diagram of the hard surface. (b) Reflection phase of the hard surface with different incidence angles for TM and TE polarized case.

3. ANALYSIS OF MONOSTATIC AND BISTATIC RCS

A hard surface 624×624 mm with 30 unites is used for RCS discussion. Both TM and TE polarization incident wave are considered, and incidence angle θ starts from $-90°$ to $90°$ in the plane of φ=0°. Then the monostatic RCS of a metal cube (the height $h' = 2$ mm) with hard surface is calculated. A PEC metal cube ($h' = 2$ mm) of the same size, i.e., 624×624 mm, is calculated under the same conditions as above for comparison. For TE-polarization, the input impedance of the square patches HIS equals to that of the hard surface [15]. So, RCS of a square patches HIS (Fig. 2) with the same parameters under the same conditions is also presented for comparison (Fig. 3).

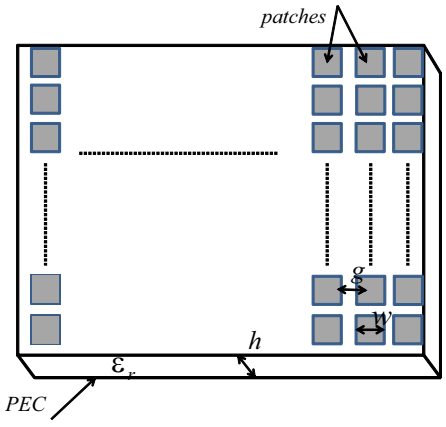

Figure 2: 3D schematic diagram of the square patches HIS.

It can be seen from Fig. 3 that in the case of the HIS, RCS reduction at broad angles can be obtained for TE polarization, but get worse for TM polarization. While in the case of the hard surface, RCS reduction at the whole considered angles can be obtained for TE polarization, and almost invariable for TM polarization. This can be explained given that both AMC (square patches HIS at 2 GHz) and hard surface support the TE polarization wave along the surface. While for TM polarization, the square patches HIS acts like AMC (at about 2 GHz) which not support the TM polarization wave along the surface and the hard surface acts like PEC.

For analyzing monostatic RCS reduction, the bistatic case is investigated next. Fig. 4 is the bistatic RCS of the hard surface at frequency 2 GHz under TE polarization, incidence wave angles at θ=45°, φ=0°. In Fig. 4(a), bistatic angles phi at 0°, it corresponds to the monostatic RCS when bistatic angles theta at 45° and the monostatic RCS have about 25 dB reduction. From Figs. 4(b), (c), (d) it can be seen that when incidence wave angles fixed and bistatic angles phi at 75°, 100°,

275°, the RCS of hard surface is higher than the metal about 10dB when bistatic theta is at 90°. We also can find that at many other bistatic angles phi (data not shown) the RCS of hard surface is higher than the metal when bistatic theta is at 90°. While at other bistatic angles theta, the RCS of hard surface is almost equal to metal. So, we obtain strong radiation fields along hard surface and it can deduce that the reduction of the energy at bistatic θ=45° is transformed to bistatic θ=90°, i.e., the surface.

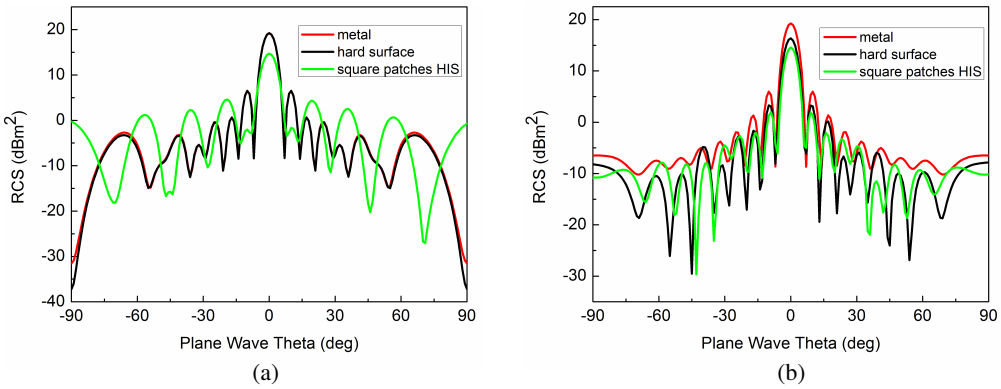

Figure 3: Monostatic RCS amplitude as a function of incidence angles theta. (a) The RCS of TM polarization for metal, hard surface and square patches HIS at 2 GHz. (b) The RCS of TE polarization for metal, hard surface and square patches HIS at 2 GHz.

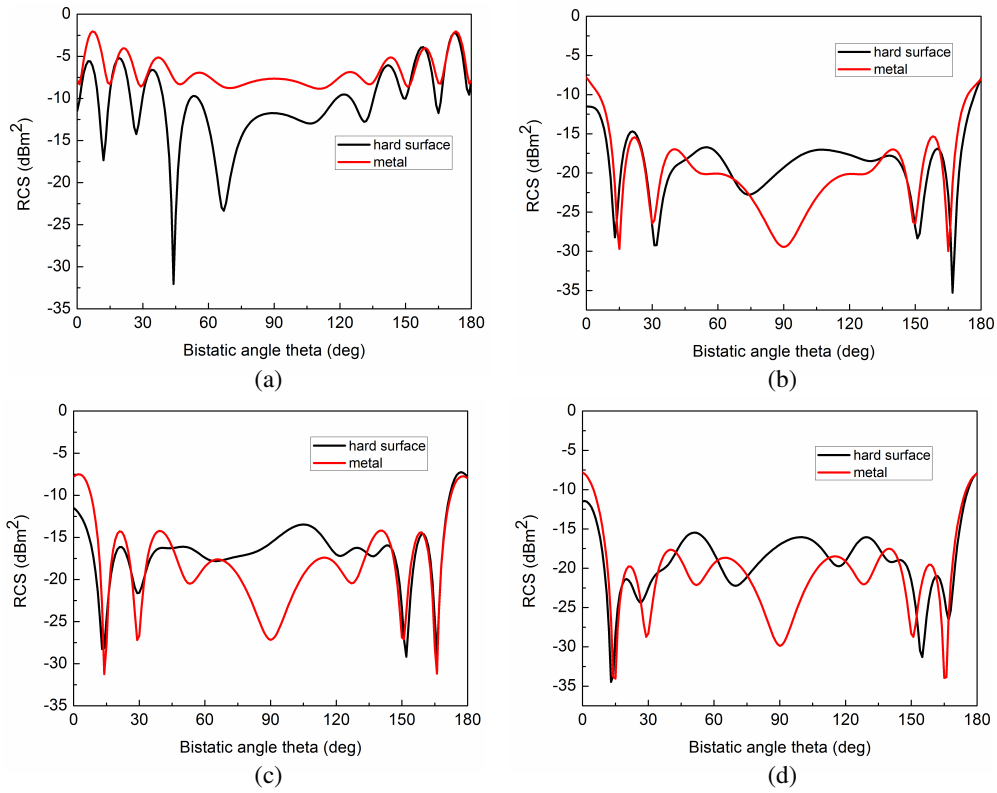

Figure 4: Bistatic RCS amplitude as a function of Bistatic angles theta. (a) Bistatic angles phi at 0°. (b) Bistatic angles phi at 75°. (c) Bistatic angles phi at 100°. (d) Bistatic angles phi at 275°.

4. CONCLUSIONS

The scattering properties of an artificial electromagnetic hard surface and a square patch HIS have been investigated. The basic properties have been derived by studying the RCS varies with polarization and incidence angle. When the plane of the incident wave is paralleled to the strips and

for TE polarization, the hard surface has almost all direction RCS reduction. It can be concluded that radiation fields along the hard surface is stronger than metal by analyzing the bistatic RCS. Some energy of incident wave is transformed to the surface. While for TM polarized incident wavethe RCS almost have no change. It corresponds to the characterization of hard surface. Thus the simple hard surface structure proposed could be used in stealth technique.

ACKNOWLEDGMENT

This research was partially supported by the National Natural Science Foundation of China (Grant No. 51025208, and Grant No. 51301031) and the fundamental research funds (Project No. ZYGX201 3J029).

REFERENCES

1. Kildal, P.-S., "Definition of artificially soft and hard surfaces for electromagnetic waves," *Electron. Lett.*, Vol. 24, No. 3, 168–170, Feb. 1988.
2. Maci, S. and P.-S. Kildal, "Hard and soft gangbuster surface," *Proc. URSI Int. Symp. Electromagnetic Theory*, 290–292, Pisa, Italy, May 2004.
3. Aas, J.-A., "Plane-wave reflection properties of two artificially hard surfaces," *IEEE Trans. Antennas and Prop.*, Vol. 39, No. 5, 651–656, May 1991.
4. Aly, M. S. and S. F. Mahmoud, "Propagation and radiation behavior of a longitudinally slotted horn with dielectric-filled slots," *Proc. Inst. Elec. Eng.*, Vol. 132, Pt. H, No. 7, 477–479, Dec. 1985.
5. Lier, E. and P.-S. Kildal, "A novel type of high-gain horn antennas," *Proc. 5th Int. Conf. Antennas Prop.*, 431–433, York, Mar.–Apr. 1987.
6. Lier, E., "Hard waveguide feeds with circular symmetry for aperture efficiency enhancement," *Electron. Lett.*, Vol. 24, No. 3, 166–167, Feb. 1988.
7. Kildal, P.-S. and E. Lier, "Hard horns improve cluster feeds of satellite antennas," *Electron. Lett.*, Vol. 24, No. 8, 491–492, Apr. 1988
8. Lier, E. and P.-S. Lildal, "Soft and hard horn antennas," *IEEE Trans. Antennas Prop.*, Vol. 36, 1152–1157, Aug. 1988.
9. Aas, J. A. and P.-S. Kildal, "Reduction of forward scattering from struts in reflector antennas," *Proc. 18th European Microwave Conf.*, 494–499, Stockholm, Sept. 1988.
10. Ulversoy, T. and P.-S. Kildal, "Radiation from slots in artificially soft and hard cylinders," *IEEE Trans. Antennas Prop.*, Vol. 36, 147–151, Jan. 1988.
11. Kildal, P.-S., "Artificially soft and hard surfaces in electromagnetics," *IEEE Trans. Antennas Prop.*, Vol. 38, No. 10, 1537–1544, Oct. 1990.
12. Chen, S., M. Ando, and N. Goto, "Frequency characteristics and bandwidth enhancement of artificially soft and hard surface," *Proc. Inst. Elect. Eng. Microw. Antenna Propag.*, Vol. 142, No. 4, 289–294, Aug. 1995.
13. Foroozesh, A. and L. Shafai, "Electromagnetic scattering by periodic conducting strip grating on grounded dielectric slab: Study of the angular and polarization dependence in different incident planes," *14th Int. Symp. On Antenna Technology and Applied Electromagnetics the American Electromagnetics Conf. (ANTEM-AMEREM)*, presented, Ottawa, July 2010.
14. Lindell, I. V., "Generalized soft-and-hard surface," *IEEE Trans. Antennas Prop.*, Vol. 50, No. 7, 926–929, Jul. 2002.
15. Luukkonen, O., C. Simovski, G. Granet, G. Goussetis, D. Lioubtchenko, A. V. Räisänen, and S. A. Tretyakov, "Simple and accurate analytical model of planar grids and high-impedance surfaces comprising metal strips or patches," *IEEE Trans. Antennas Prop.*, Vol. 56, No. 6, 1624–1632, Jun. 2008.

A Realization Compact Pseudo Chebyshev Low Pass Filters for UHF Band Using RF MEMS Technology

H. F. Liew[1], **S. I. S. Hassan**[2], **M. F. Malek**[2], **Y. Wahab**[1], **M. M. Nurhakimah**[2], **H. Nornikman**[3], **M. Mazlee**[1], **M. Ghauth Sazali**[1], **and S. S. Nadia**[1]

[1]School of Microelectronic, University Malaysia Perlis, Perlis, Malaysia
[2]School of Electrical System, University Malaysia Perlis, Perlis, Malaysia
[3]Faculty of Electronics and Computer Engineering, University Teknikal Malaysia, Melaka, Malaysia

Abstract— This paper describes the development compact Chebyshev microstrip filter is fabricated by using RF MEMS technology, which laser micromachining techniques are selected. The 5th order Chebyshev low pass filter operating within UHF range have been designed, simulated, fabricated, tested, investigated and implemented on silicon substrate with a band pass ripple of 0.01 dB. The design of lumped element and microstrip circuit filters are simulated and implemented by using Advanced Design System. The simulation and measurement results of microstrip low pass filter have been compared and excellent agreement is observed. Laser micromachining can lead to finer finishes, improved accuracy and less process overhead. The purpose for this work has been focus on laser micromachining into develop compact microstrip circuit. To satisfy these challenging in terms of geometry, machining accuracy, surface finish or processing speed, laser micromachining with diffraction limited beam quality offer many benefits such as small spot size, high power density, enhanced processing speeds, reduced heat affected zone for a range of micromachining applications. Laser micromachining has become a great prospective as a MEMS (micro-electro-mechanical systems) fabrication technique in ever-continuing trend of miniaturization in microelectronics, micro-optics and micromechanics for wireless communication system.

1. INTRODUCTION

The low-pass filters are often employed in many communication systems to eliminate harmonics and spurious signals with demand of compact size, low pass band insertion loss, and high attenuation. Filters can be realized in lumped type or microstrip line type. The lumped-element filter design generally works well at low frequencies, but two problems arise at microwave frequencies. First, lumped elements such as inductors and capacitors are generally available only for limited range of values and are difficult to implement at microwave frequencies, but must be approximated with distributed components. Furthermore, the normal lumped inductors and capacitor components introduce stray capacitance and inductance from leads. The conventional filter design method such as open-stub low-pass filters and stepped impedance low-pass filters are unable to meet the requirements for modern communication systems because of some drawbacks [1]. For low frequency applications large inductors and capacitors are needed causing a bulky system, which is often discouraged. The important of microstrip line has advantages of low cost, compact size, light weight, planar structure and easy integration with other components on a single board.

In literature, many design methodologies have been suggested to improve the low-pass filter's performance is normally not used now a days due to inherited deficiencies like slow roll off in the stop band, poor frequency response in the pass band, narrow stop band, large size [2, 3]. The miniaturizations of low pass filter circuit size are become advance in RF microwave communication applications, and it is accomplished in variety of method design. It was noticed that microwave filer circuit can be design in compact size and also will influence by wisely method technology of fabrication, such as thin film technology and defected ground structure. The new microstrip MEMS technology studied in laboratory looks promising for many reasons: first, the low cost of the substrates, standard silicon and glass, second, the simple technological process, and third the expected good performances. By using the MEMS fabrication, this low pass filter circuit can reduce to be smaller compare to previous. When the size of circuit are been reduced and increase the operating frequency and lumped element can be replaced by disturbed element, in order to help improve the simulation result performance. MEMS design technology is an extended form of traditional microelectronic IC fabrication techniques. They are fabricated using integrated circuit (IC) batch processing techniques and can range in size from a few micrometers to millimetres.

There are several methods to reduce the size of microstrip low pass filters which have been reported [3–9]. One of the effective methods of size reduction is to introduce slow wave structure

either in the main line [4, 5] or on the ground plane [4–6]. In [10, 14] a spiral resonator is used to replace the stepped impedance ladder network in the conventional design. The unsymmetrical stubs have also been used in [9] to design a compact filter. These methods increase the circuit complexity. The slow wave effect on the ground plane can be introduced by using the defective ground structures (DGS) [15]. The overall inductance and capacitance of the resonators can be increased using DGS and thus the compact circuit size can be achieved. The defects on the ground plane may cause unwanted radiation and it is difficult to integrate with other microwave components. To get wide stopband and sharp roll-off responses, many new methods have been proposed, such as defected ground structure (DGS) [11–13] and electromagnetic band-gap (EBG) [7, 8, 16]. In general, the etched ground of the DGS and periodic character of the EBG will cause radiation and larger size problems, respectively.

This paper is emphasized with applications of lasers in MEMS manufacture for fabricate of micorstrip low pass filter. Laser processing specifically for MEMS is currently a relatively small-scale activity and able to make the circuit size become compact.

2. MICROSTRIP LINE DESIGN TECHNIQUES

In order to design transformation to microstrip low pass filters [19], the transformations of the low pass prototype filters with normalized cut-off frequency, $W_c' = 1$ and having the source and load resistances of 1ohm are made into the desired type with the details of required source and load impedances using frequency and impedance transformations can be refer [17–20].

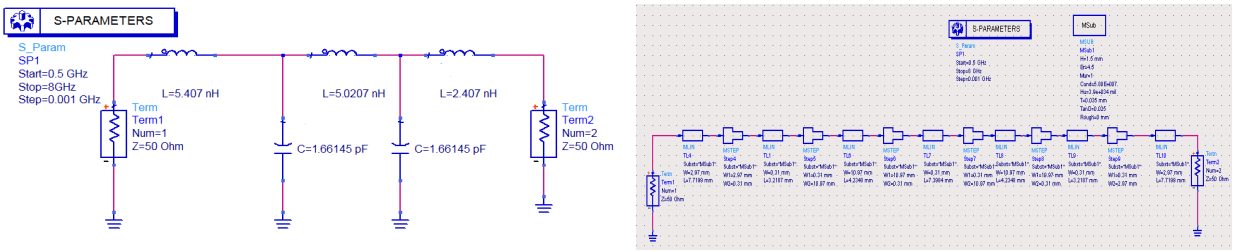

Figure 1: (a) ADS schematic design of lumped elements Chebyshev filter. (b) Schematic microstrip circuit Chebyshev low pass filters.

Table 1: The transmitter and receiver S-parameter specification value.

Operating frequency	0.5–8 GHz
Return loss $\lvert S_{11}\rvert$	> 20 dB
Insertion loss $\lvert S_{21}\rvert$	< 1 dB
Stopband attenuation	> 40 dB
cut off frequency (-3 dB)	2.5 GHz

3. METHODOLOGY

3.1. Fabrication on MEMS Technology-Laser Micromachining

The following sections contain an overview of these processes [21–26], together with a brief discussion of some other processes of potential importance to MEMS.

A scheme of the process flow is described in Figure 2. The fabrication process starts with the realization of a layer consisting of 1-02 µm of silicon oxide grown by wet thermal oxidation at 1000°C. The charges trapped at the silicon-oxide interface can induce a conductive channel that increase the losses on the substrates by capacitive coupling; at annealing 1000°C for 420 min in nitrogen atmosphere is performed in order to reduce the. A 1–2 µm thick layer of aluminum is then deposited by thermal evaporator at melting Point 660.37°C or boiling point 2467°C. Direct write laser micromachining, makes use of a laser beam tightly focused to a small spot which is moved over the surface of the wafer during machining. Typically direct write machining uses a laser with good beam profile and allow the beam to be focused to a small spot using simple microwave chip components and to give beam fluency at focus that is above the ablation threshold of the silicon

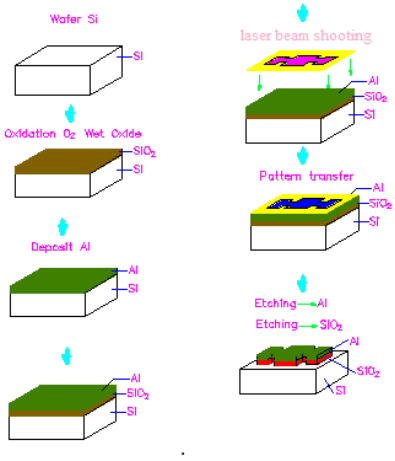

Figure 2: Laser micromachining process flow.

material. Accurate laser micromachining tends to use pulsed lasers at wavelengths where heating and melting-based surface disruption is minimal. By controlling the number of laser pulses [24, 27], and hence the total incident radiation, precise machining depths can be achieved while minimal thermal distortion occurs at the edge of the exposed region. The last process step is the release of suspended structures by removal of sacrificial resist with laser beam shooting (Figure 2). The etching process and parameters were optimized in order to remove the unwanted aluminum and oxide layer.

3.2. Process of Laser Micromachining

The setup is very simple. The laser and a detector (for measuring the intensity) set on an optical breadboard. The few attachments like a disperser and a small aperture cap which can be fixed on the detector. Firstly, the circuit can be implemented with AutoCAD software and after finish drawing, using alignment of the laser beam. This procedure can be slowly adjusting the laser in its support while checking the intensity pattern along two virtual horizontal lines at different heights on the beam cross-section. After this is done, the distance are be fixed for the detector and take intensity measurements of the beam along a horizontal line passing the point with the maximum intensity. This can be repeated with variants like with disperser alone, with cap alone, with disperser and cap. Similar readings can be taken for the vertical orientation of the laser beam too [28–30]. For calculating the beam divergence, calculate the maximum intensity of the beam, which helps in calculating the beam spot size, at different distances from the laser with the help of the optical breadboard. These can also be tabulated and the resulting calculations lead to the necessary results.

4. ADS RESULT AND SIMULATIONS

To validate whether this method was satisfactory, simulated the chebyshev microstrip circuit and measure the prototype circuit by using network analyzer and implemented on silicon substrate that had a dieletric constant of 11.9 and a thickness of 550 µm. The lumped element and microstrip line are designed by using ADS software and operating at the cut off frequency 2.5 GHz of the filter, which fulfill the design specification.

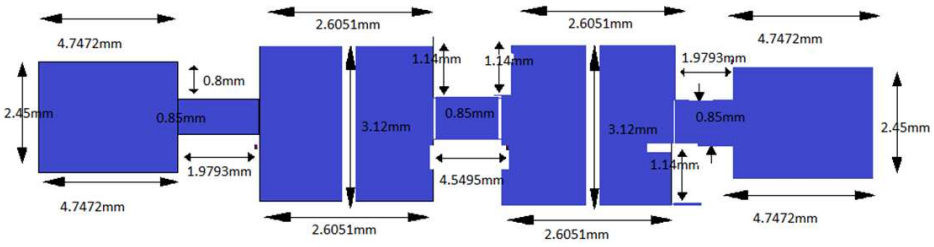

Figure 3: Schematic dimension of microstrip Chebyshev low pass filters.

Table 2: Dimension of Chebyshev microstrip low pass filter.

Section-Chebyshev-N_5	Z_c & Z_L	W (mm)	L (mm)
L_1	100	0.85	1.9793
C_2	20	3.12	2.6051
L_3	100	0.85	4.5495
C_4	20	3.12	2.6051
L_5	100	0.85	1.9793

4.1. Chebyshev LPF Simulation and Measurement Result

To verify this approach whether it is feasible or not, lumped elements of all types low pass filter with 3 dB cut off frequency set at 2.5 GHz were simulated. Number of order for Chebyshev were chosen to be $N = 5$. Based on comparison between simulation and measurement as below Figure 4, the results of pratical measure and simulation have been a fairly good agreement together. Improvement can be seen in the frequency reponses of the microstrip circuit as compared to an ideal lumped element filters. It is observed that the cut off frequency are close to 2.5 GHz, meausred and simulated of low pass filters are found to be similar. The improvement in the frequency response is achieved by fabricated by using laser micromachining without changing any specifications parameters.

5. ANALYSIS AND DISCUSSION

Table 3 represent the simulation result obtain from lumped elements of Chebyshev LPF by using silicon substrate. The ripples values amplitude of Chebsyev lumped element is same and located at specifications cut off point of 2.5 GHz. The return loss matching and second attenuation performances seem improves and the more unwanted frequency can be eliminated. The ripples values amplitude of all microstrip Chebsyev circuit performance is almost same and located at specifications cut off point of 2.5 GHz.

For Chebyshev microstrip Line presented that stopband attenuation frequency is seemed good where the amplitude is fall close to −40 dB. This means the attenuation are still consider enough to suppress the unwanted frequency signal. And also for the return loss matching performance

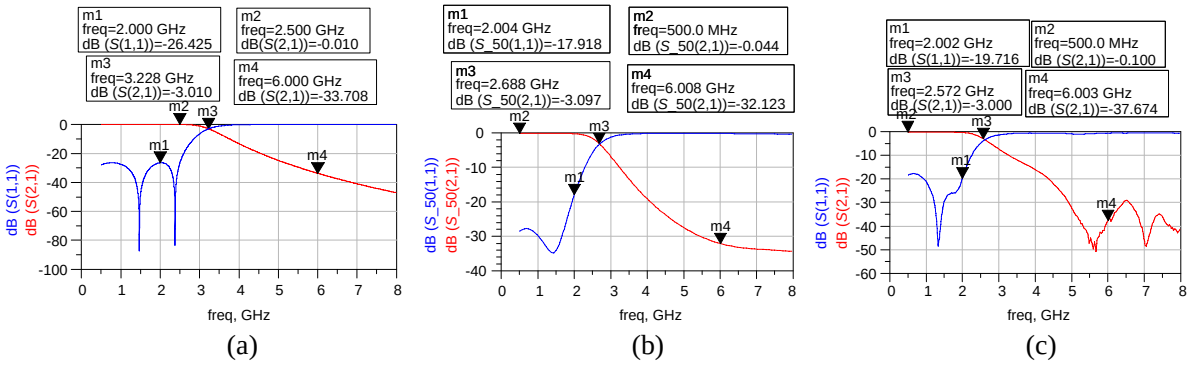

Figure 4: (a) Chebyshev 5^{th} order lumped element simulation result. (b) Simulation result of Chebyshev 5th order microstrip line filters. (c) Measurement result of Chebyshev 5th order microstrip line filters.

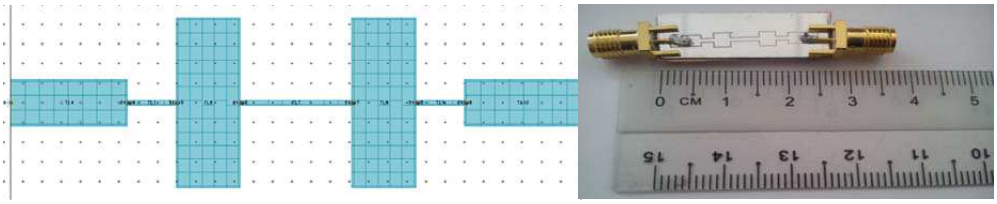

Figure 5: (a).Layout of Chebsyhev microstrip low pass filter. (b) Prototype of Chebsyhev microstrip low pass filter.

Table 3: Simulation result of composite filter in ADS.

Frequency	Lumped element	Microstrip line (Simulations)	Microstrip line (Measurement)
S_{11}-return loss 20 dB	26.425 dB	17.918 dB	19.716 dB
S_{21}-insertion loss 0.5 GHz	0.010 dB	0.041 dB	0.100 dB
Cut off Frequency −3 dB (2.5 GHz)	3.228 GHz	2.688 GHz	2.572 GHz
Stopband attenuation (40 GHz)	33.708 dB	32.123 dB	37.674 dB

are close to −20 dB and means power transmitter signal able delivery to receiver. Whereas for Chebyshev microstrip line have cut off frequency close to specifications of cutoff frequency 2.5 GHz which respect to the interest frequency.

6. CONCLUSION

The microfabricated microstrip filters components presented here demonstrate the flexibility of laser micromachining for the development of microwave devices. The simulated and measured results are in reasonable agreement. The design of lumped element circuit and microstrip filter with the fringing correction factor and prototype make S-parameter cut off frequency are closed to 2.5 GHz and miniaturization of circuit are achieved. Once the microstrip circuits are fabricated by MEMS technology, size of circuit is reduced and the exact components value can be realized. The processing used in this work has made use of the unique machining properties of controlling the laser beam pulses into produce components of an integrated device. While other manufacturing processes may be used to create parts of the devices, only laser micromachining has the ability to produce all components described here. Laser micromachining has been established to operate with a broad range of materials and has the ability to cope with changes in component materials. The high quality of direct writing laser micromachining has also been validated to produce surface qualities suitable for microwave components. The method of laser micromachining of directly write structures at high speed with laser micromachining allows it to be used as a cost effective microfabrication tool are accomplished of all stages of fabrication from prototype development to large scale production. The lowpass filter will be appropriate in many RF microwave system applications because of its compactness and high performance.

ACKNOWLEDGMENT

The authors acknowledge University Malaysia Perlis and the Malaysian Ministry of Higher Education for providing the Fundamental Research Grant Scheme (FRGS Grant No. 9011-00017), which made it possible to conduct and publish this research.

REFERENCES

1. Zhang, S., C. Zhu, J. K. O. Sin, and P. K. T. Mok, "A novel ultrathin elevated channel low-temperature poly-Si TFT," *IEEE Electron Device Letter*, Vol. 20 569–571, Nov. 1999.
2. Metev, S. M. and V. P. Veiko, *Laser Assisted Microtechnology*, 2nd Edition, R. M. Osgood, Jr., Ed., Springer-Verlag, Berlin, Germany, 1998.
3. Breckling, J., Ed., "The analysis of directional time series: Applications to wind speed and direction," *Ser. Lecture Notes in Statistics*, Vol. 61, Springer, Berlin, Germany, 1989.
4. Lim, J.-S., C.-S. Kim, D. Ahn, Y.-C. Jeong, and S. W. Nam, "Design of low-pass filters using defected ground structure," *IEEE Transactions on Microwave Theory and Techniques*, Vol. 53, No. 8, 2539–2545, 2005.
5. Boutejdar, A., A. Elsherbini, A. Balalem, J. Machac, and A. Omar, "Design of new DGS hairpin microstrip bandpass filter using coupling matrix method," *PIERS Proceedings*, 261–265, Prague, Czech Republic, Aug. 27–30, 2007.
6. Abdel-Rahman, A., A. R. Ali, S. Amari, and A. S. Omar, "Compact bandpass filters using defected ground structure (DGS) coupled resonators," *IEEE Conference International Microwave Symposium Digest, MTT-S*, 1–4, 2005.
7. Zhurbenko, V., V. Krozer, and P. Meincke, "Miniature microwave bandpass filter based on EBG structures," *Proceedings of the 36th European Microwave Conference*, 792–794, 2006.

8. Shaban, H. F., H. A. Elmikaty, and A. A. Shaalan, "Study the effects of electromagnetic bandgap (EBG) substrate on two patch microstrip antenna," *Progress In Electromagnetics Research B*, Vol. 10, 55–74, 2008.
9. Kim, I. S. and S.-W. Yun, "Compact LPF using asymmetrical microstrip step discontinuity for harmonic suppression," *IET Journals & Magazines, Electronics Letters*, Vol. 41, No. 16, 41–42, 2005.
10. Dai, G.-L. and M.-Y. Xia, "Novel miniaturized bandpass filters using spiral-shaped resonators and window feed structure," *Progress In Electromagnetics Research*, Vol. 100, 235–243, 2010.
11. Kumar, D. and A. De, "Parallel coupled microstrip filter design using electromagnetic bandgap structure," *International Journal of Contemporary Research in Engneering and Technology*, Vol. 1, No. 1, 37–40, 2010.
12. Ahn, D., J.-S. Park, C.-S. Kim, J. Kim, Y. Qian, and T. Itoh, "A design of the low-pass filter using the novel microstrip defected ground structure," *IEEE Transactions on Microwave Theory and Techniques*, Vol. 49, No. 1, 86-93, 2001.
13. Kumar, P., R. Mahmood, R. Gowri, and A. Kumar, "Design of microstrip low pass filter with sharp transition and improved Q-factors using hexagonal DGS," *Proceedings of National Conference on RTMMWT*, 92–94, 2010.
14. Akkaraekthalin, P. and J. Jantree, "Microstrip slow-wave open-loop resonator filters with reduced size and improved stopband characteristics," *Journal Electronics and Telecommunications Research Institute, ETRI*, Vol. 28, No. 5, 607–614, 2006.
15. Kumar, D. and A. De, "Low pass filter design by using the ladder network of DGS," *Journal of Communication and Computer*, Vol. 8, 276–278, 2010.
16. Yang, L., M. Fan, F.Chen, J. She, and Z. Feng, "A novel compact electromagnetic-bandgap (EBG) structure and its applications for microwave circuits," *IEEE Transactions on Microwave Theory and Techniques* Vol. 53, No. 1, 183–190, 2005.
17. Tan, Z. D., J. S. Mandeep, S. I. S. Hassan, and M. F. Ain, "Composite low pass filter design with T and π Network on microstrip line," Final Year Thesis, University Sains Malaysia, Malaysia, 2007.
18. Pozar, D. M., "Microwave filters," *Microwave Engineering*, 2nd Edition, Chapter 8, Charity Robey, 1998.
19. Fang, H. L. and S. I. S. Hassan, M. Fareq Abd. Malek, W. Yufridin, and S. Norshafinash, "New approach of transforming lumped element circuit of high-order chebyshev low pass filter into microstrip line form," *International Journal of Electrical & Computer Sciences (IJECS/IJENS)*, Vol. 13, No. 3, 21–30, 2013.
20. Levy, R., R. V. Snyder, and G. Matthaei, "Design of microwave filters," *IEEE Transactions on Microwave Theory and Techniques*, Vol. 50, No. 3, 783–793, 2002.
21. Fedder, G. K., "MEMS fabrication," *IEEE Proceedings International Test Conference, ITC*, Vol. 1, 691–698, 2003.
22. Islam, F., M. A. M. Ali, B. Y. Majlis, and N. Amin, "RF MEMS tunable filter: Design, simulation and fabrication process," *IEEE International Conference Electrical and Computer Engineering, ICECE*, 247–250, 2008.
23. Martoglio, L., E. Richalot, O. Picon, G. Issorgues-Bazin, and C. Vasseure, "Low-loss microstrip MEMS technology for RF passive components," *IEEE 31st European Microwave Conference*, 1–4, 2001.
24. Koul, S. K., "Design and development of passive and active RF components using MEMS technology," *IEEE International Workshop on Physics of Semiconductor Devices, IWPSD*, 670–675, 2007.
25. Giacomozzi, F., V. Mulloni, S. Colpo, J. Iannacci, B. Margesin, and A. Faes, "A flexible fabrication process for RF MEMS device," *Romanian Journal of Information Science and Technology,* Vol. 14, No. 3, 259–268, 2011.
26. Hayati, M., H. A.-D. Memari, and H. Abbasi, "Compat microstrip lowpass filetr with sharp roll-off and wide stopand using semicircle ended stub resonator," *Progress In Electromagnetics Research Letters*, Vol. 35, 73–81, 2012.
27. Ostendorf, A., "The use of vacuum UV wavelengths and ultrashort pulses for machining of dielectrics," *Proc. ICALEO 2000 Laser Microfabrication Conference*, A1-10, 2000.
28. Gower, M. C., "Excimer lasers: Principles of operation and equipment," *Laser Processing in Manufacturing*, R. C. Crafer and P. J. Oakley, Eds., Chapman & Hall, 1994.

29. Renn, M. J. and B. H. King, "Laser guided direct writing of electronic components," *Proc. ICALEO 2000 Laser Microfabrication Conference*, 46–50, 2000.
30. Holmes, A. S. and S. M. Saidam, "Sacrificial layer process with laser-driven release for batch assembly operations," *IEEE/ASME J. Micro-electromechanical System*, Vol. 7, 416–422, 1998.

Miniaturized Microscript Bandpass Filter Based on the Twist Split Ring Resonators

Jian Li, **Guangjun Wen**, **Yongjun Huang**, **Kaimin Wu**, **and Weijian Chen**
Centre for RFIC and System Technology, School of Communication and Information Engineering
University of Electronic Science and Technology of China, Chengdu, China

Abstract— In this paper, a novel design for miniaturized microscript bandpass filter based on the twist split ring resonators (TSRRs) is analyzed systematically. The proposed TSRRs printed on the conventional dielectric substrate with full size ground plane exhibit two resonance states separated each others. And the two resonance frequencies can be tuned by changing the distance between the two single split ring resonators. We first discuss the resonance characteristics and optimize the designed filter with finite element method based simulator (Ansoft HFSS V14). Then the designed microscript bandpass filter is fabricated by standard printed circuit board techniques. Finally, the proposed filters are numerically and experimentally discussed in details, including the passband, out-of-band suppression, and higher order properties. Both results show that the proposed filter exhibits a compact size and well passband characteristics, which can be used in radio frequency/microwave integrated circuits.

1. INTRODUCTION

In the pase decade, artificial designer materials consisting of sub-wavelength-size periodic inclusions have attracted exciting attention since the first experimental realizations of such composite structure [1, 2]. Researchers called the composed structures as metamaterials [3] to reveal their unique electromagnetic properties, e.g., negative refraction [4], reversals of both Doppler shift and Cherenkov radiation [5], enhancement of evanescent wave and super-resolution imaging [6–8]. Recent years, thanks for the breakthroughes of the designs and characterizations of metamaterials and also the nano fabrications, it has found plentiful and important applications for the metamaterials in various areas with operating frequencies covering a wide spectra ranged from low-frequency (acoustic) and microwave through terahertz to even optical ranges [9–15]. Most of the applications, e.g., focused lens [9], absorbers/reflectors [10–13], cloaks [14] and sensing [15], are based on the macroscopic properties of bulk metamaterial configurations, such as negative refractions.

On the other hand, it has observed that metamaterial unit cells can also be used for some miniature applications requirements. Specifically, due to the resonance nature of most metamaterial unit cells, one can achieve miniaturized microwave components, e.g., the compact bandpass/notch filters [16–19] and antennas [20, 21]. However, most of the reported metamaterials inspired bandpass filters (we main discuss the novel filter application of metamaterials in this paper) as mentioned above still suffer from large inclusion sizes and complex configurations, which restrict the practical bulk RF/microwave circuit integration applications.

In this paper, based on the motivation of simplifying filter designs and fabrications, we propose a novel design for the miniaturized microscript bandpass filter by using the twist split ring resonators (TSRRs), which previously discussed at terahertz band and can possess magnetoinductive coupling effects. The magnetoinductive coupling effects can result in both magnetic and electronic resonances [22]. Here the TSRRs are designed on a conventional substrate and two metallic holes are used to connect the TSSRs with ground plane to achieve a miniaturized microscript bandpass filter. It will be seen that the proposed filter in this paper has a very simple inclusion and exhibits very will frequency selection characteristics.

2. RESONANCE CHARACTERISTICS

The configuration of the TSRRs used to characterize the resonances is shown in Fig. 1(a). Two metallic SRRs with 90° twist angle and closer arrangement are printed on the Rogers Ro4003 dielectric substrate (the relative dielectric constant is $\epsilon_r = 3.55$ and loss tangent is $\tan\delta = 0.0027$, and the thickness is 0.8 mm). The extend lines within the conventional SRRs connected with the ground plane through metallic holes are used to control the impedance when design the microscript fed filter. The backside of the substrate is full-sized metallic ground plane and the thicknesses of both the TSRRs and ground plane are 0.017 mm. As shown in Fig. 1(a), one gap is presented between each SRR and microscript feed line to show the coupling effects from microscript feed line

to the twist SRR, so that the resonance characteristics of the TSRRs can be clearly obtained and analyzed [16].

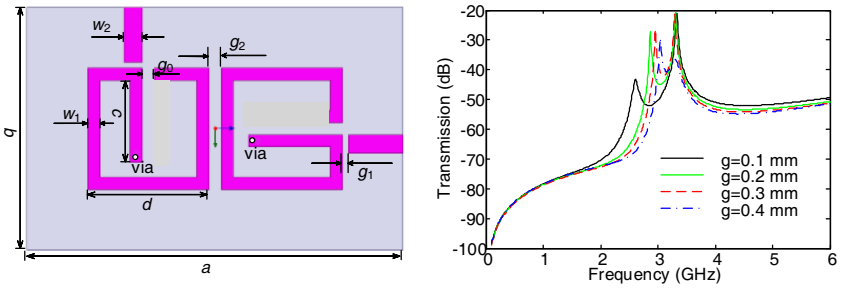

Figure 1: (a) Schematic representation of the TSRRs resonator, and (b) simulated transmission properties at different space values.

The resonance characteristics of the proposed configuration are demonstrated by numerical simulations through ANSYS High Frequency Structure Simulator (HFSS) V14.0. To obtain the resonance frequencies within the S-band and based on above mentioned material parameter values, we get the following dimensional parameter values for the TSRRs, in millimeter: $a = 12.4$, $b = 8.0$, $c = 2.7$, $d = 4.0$, $w_1 = 0.4$, $w_2 = 0.6$, $g_0 = 0.4$, and $g_1 = 0.2$. To discuss the effect on the resonance frequency shift, we change the space values g_2 between the two twist SRRs from 0.1 mm to 0.4 mm. The simulated results are shown in Fig. 1(b). It clearly shows that for one of the space condition (for example, $g_2 = 0.4$ mm), there are two distinct transmission peaks corresponding to two different resonance states. As shown in Fig. 2, the surface current density characteristics at such two resonance frequencies indicate quite different orientations. For specifically, the current densities at the surface of the twist SRRs for first resonance frequency are the same orientations relating to magnetic resonance, and contrarily for the second resonance frequency opposite current orientations appears at the twist SRRs corresponding to electronic resonance. These results are similar to the reference [22].

Moreover, when decrease the space g_2 from 0.4 mm to 0.1 mm, the first resonance frequency shifts downward sharply and the second frequency shifts upward slightly. Therefore, to obtain a wide passband one should narrow the space between the twist SRRs. It should be noted that when further narrow the gap between the twist SRRs (or connect directly with each other), the two resonance frequencies will be separated far from each other and therefore the insert loss of the filter will be enlarged.

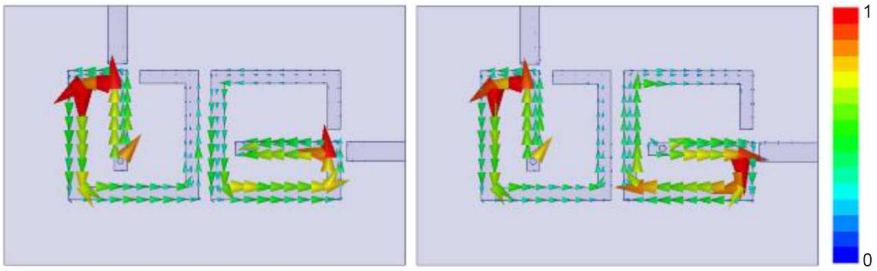

Figure 2: Simulated current density characteristics at two resonance states.

3. FILTER FABRICATION AND CHARACTERISTICS

Based on the above analysis, the proposed miniaturized microscript bandpass filter configuration is shown Fig. 3(a) with dimensional parameters in millimeter. The microscript feed lines are directly connected with the TSRRs (the only difference compared with previous numerical investigations). Finally, the designed filter is fabricated by standard printed circuit board fabrication techniques, and two 50 Ohm micro-miniature coaxial connectors (operated from DC to 6 GHz) are soldered to the two feed lines of the compact filter, as shown in Fig. 3(b).

The transmission and reflection properties of the proposed miniaturized microscript bandpass filter are then demonstrated numerically and experimentally. As shown in Fig. 4(a), the simulated

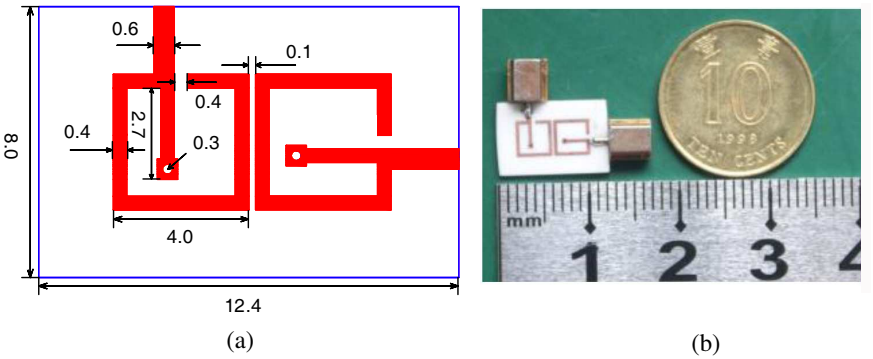

(a) (b)

Figure 3: (a) Designed filter configuration with dimensional parameters in millimeter and (b) the fabricated sample.

and measured results are agreed with each other quite well, which demonstrate the validities for both results. There is a wide passband with measured 3-dB bandwidth of 0.65 GHz (from 3.0 GHz to 3.65 GHz) centered at 3.325 GHz. This result indicates a very small electric size of about 0.13λ, where λ is the center operating wavelength. The measured insert loss is about 1.4 dB and return loss is larger than 10 dB within the whole passband. And the peak transmission is -1.37 dB at 3.27 GHz, as shown in the inset of Fig. 4(a). There are also two transmission dips near below and upper the passband, so that this filter possesses well frequency selection properties. Moreover, further simulation shows that the suppression apart center frequency up to 8 GHz is larger than 20 dB and the first higher order passband is located near 10 GHz, as shown in Fig. 4(b). Therefore, this filter has a well out-of-band harmonic suppression characteristics.

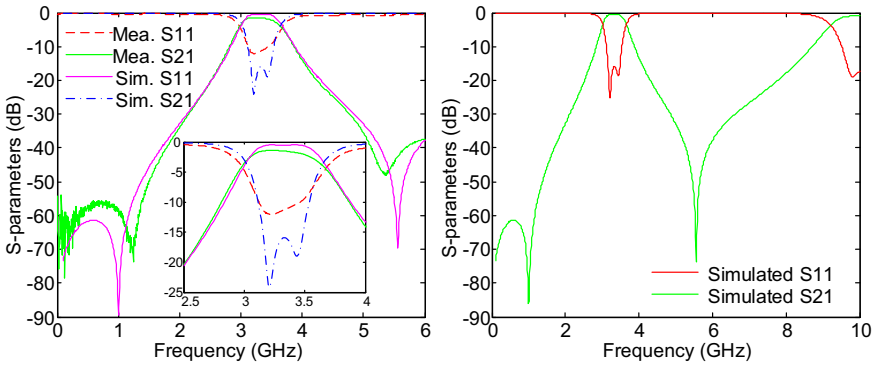

(a) (b)

Figure 4: (a) Measured and simulated transmission and reflection properties of the miniaturized microscript bandpass filter, and (b) simulated transmission and reflection properties of the compact filter in a wide frequency range.

4. CONCLUSION

In this paper, a novel miniaturized microscript wideband bandpass filter is discussed by using the TSRRs configuration as resonator. Both numerical and experimental results demonstrate the proposed filter exhibits pretty well passband and out-of-band harmonic suppression characteristics. Such kind of filter configuration can be widely used for miniature radio frequency/microwave integrated circuits applications.

ACKNOWLEDGMENT

This work was partially supported by the National Natural Science Foundation of China (Grant No. 61371047), the Research Fund for the Doctoral Program of Higher Education of China (Grant No. 20110185110014), and the Fundamental Research Funds for the Central Universities (Grant No. E022050205).

REFERENCES

1. Smith, D. R., W. Padilla, D. C. Vier, S. C. Nemat-Nasser, and S. Schultz, "Composite medium with simultaneously negative permeability and permittivity," *Phys. Rev. Lett.*, Vol. 84, No. 18, 4184–4187, 2000.
2. Shelby, R. A., D. R. Smith, and S. Schultz, "Experimental verification of a negative index of refraction," *Science*, Vol. 292, 77–79, 2001.
3. Engheta, N. and R. W. Ziolkowski, *Metamaterials: Physics and Engineering Explorations*, Wiley, New York, 2006.
4. Argyropoulos, C., N. M. Estakhri, F. Monticone, and A. Alù, "Negative refraction, gain and nonlinear effects in hyperbolic metamaterial," *Opt. Express*, Vol. 21, 15037–15047, 2013.
5. Duan, Z., C. Guo, and M. Chen, "Enhanced reversed Cherenkov radiation in a waveguide with double-negative metamaterials," *Opt. Express*, Vol. 19, 13825–13830, 2011.
6. Cui, T. J., X. Q. Lin, Q. Cheng, H. F. Ma, and X. M. Yang, "Experiments on evanescent-wave amplification and transmission using metamaterial structures," *Phys. Rev. B*, Vol. 73, 245119, 2006.
7. Zhang, X. and Z. Liu, "Superlenses to overcome the diffraction limit," *Nature Materials*, Vol. 7, 435–441, 2008.
8. Dong, H. Y., J. Wang, K. H. Fung, and T. J. Cui, "Super-resolution image transfer by a vortex-like metamaterial," *Opt. Express*, Vol. 21, 9407–9413, 2013.
9. Kundtz, N. and D. R. Smith, "Extreme-angle broadband metamaterial lens," *Nature Materials*, Vol. 9, 129–132, 2010.
10. Mei, J., G. Ma, M. Yang, Z. Yang, W. Wen, and P. Sheng, "Dark acoustic metamaterials as super absorbers for low-frequency sound," *Nature Communications*, Vol. 3, 756, 2012.
11. Xiong, X., Z.-H. Xue, C. Meng, S.-C. Jiang, Y.-H. Hu, R.-W. Peng, and M. Wang, "Polarization-dependent perfect absorbers/reflectors based on a three-dimensional metamaterial," *Phys. Rev. B*, Vol. 88, 115105, 2013.
12. Hao, J., J. Wang, X. Liu, W.J. Padilla, L. Zhou, and M. Qiu, "High performance optical absorber based on a plasmonic metamaterial," *Appl. Phys. Lett.*, Vol. 96, 251104, 2010.
13. Zhong, J., Y. Huang, G. Wen, H. Sun, P. Wang, and O. Gordon, "Single-/dual-band metamaterial absorber based on cross-circular-loop resonator with shorted stubs," *Appl. Phys. A*, Vol. 108, 329–335, 2012.
14. Landy, N. and D. R. Smith, "A full-parameter unidirectional metamaterial cloak for microwaves," *Nature Materials*, Vol. 12, 25–28, 2013.
15. Wu, X., X. Pan, B. Quan, X. Xu, C. Gu, and L. Wang, "Self-referenced sensing based on terahertz metamaterial for aqueous solutions," *Appl. Phys. Lett.*, Vol. 102, 151109, 2013.
16. Wu, B., X. Lai, T. Su, and C.-H. Liang, "Wideband cross coupled filter using split-ring resonator defected ground structure" *Journal of Electromagnetic Waves and Applications*, Vol. 22, No. 11/12, 1631–1638, 2008.
17. Fu, S.-H., C.-M. Tong, X.-M. Li, and M. Zhou, "Novel dual-mode square patch bandpass filter using slot-type SRR perturbation for mode splitting" *Microwave and Optical Tech. Lett.*, Vol. 53, 1703–1706, 2011.
18. Gupta, M. and J. Saxena, "Microstrip filter designing by SRR metamaterial" *Wireless Pers. Commun*, Vol. 71, 3011–3022, 2013.
19. Liu, Y., X. Tang, Z. Zhang, and X. Huang, "Novel nested split-ring-resonator (SRR) for compact filter application," *Progress In Electromagnetics Research*, Vol. 136, 765–773, 2013.
20. Si, L. M., W. Zhu, and H. J. Sun, "A compact, planar, and CPW-fed metamaterial-inspired dual-band antenna," *IEEE Antennas Wirel. Propag. Lett.*, Vol. 12, 305–308, 2013.
21. Wen, R., "Compact planar triple-band monopole antennas based on a single-loop resonator," *Electro. Lett.*, Vol. 49, 916–918, 2013.
22. Liu, N., S. Kaiser, and H. Giessen, "Magnetoinductive and electroinductive coupling in plasmonic metamaterial molecules" *Adv. Mater.*, Vol. 20, 4521–4525, 2008.

Improvement of Oblique Incidence Performance for a Microwave Absorber Based on Magnetic Polymer Composites

Linbo Zhang, Nan Zhang, Peiheng Zhou, Yangqiu Xu, Haiyan Chen, Jianliang Xie, and Longjiang Deng
National Engineering Research Center of Electromagnetic Radiation Control Materials
State Key Laboratory of Electronic Thin Film and Integrated Devices
University of Electronic Science and Technology of China, Chengdu 610054, China

Abstract— This paper presents a microwave absorber combining together the frequency selective surfaces (FSSs) and magnetic absorbing sheet for stable absorption under both TE and TM polarizations. The proposed absorber is constructed of magnetic absorbing substrate embedded with a periodic array of cross pattern composing a series of circular-metal-disks, and a bottom metal plane. The absorption characteristics of the magnetic absorbing substrate under both TE and TM polarizations are tuned and improved by introducing the circular-metal-disks. After optimizing the dimensions of the circular-metal-disks, the absorber with a thickness of 2.4 mm achieves a reflection coefficient less than −10 dB from 4.8 GHz to 11.0 GHz with a stable frequency response up to 30° for both polarizations. Meanwhile, the absorber has a wide bandwidth of 10.8 GHz with the incidence angle from 45° to 60° under TM polarization. The study of the current indicates that the improvement of the absorption characteristics is due to both the electric resonance and magnetic resonance.

1. INTRODUCTION

In recent years, there has been an increasing interest in the application of metamaterial absorbers. Most investigations of absorbers like Jaumann and circuit analog absorbers consider normal angle of incidence only [1]. There are a few of published information on oblique incidence performance of absorbers. However, the demand of good oblique incidence performance for various kinds of absorbers with emphasis on the applications in solving electromagnetic pollution problems such as electromagnetic interference (EMI) and electromagnetic compatibility (EMC) has been an increasing concern. Absorbers with good performance at oblique incidence for both transverse electric (TE) and transverse magnetic (TM) polarizations are badly needed.

Previous methods [2–7] have been proposed to enhance the oblique incidence performance. In Ref. [2], high permittivity dielectric layers are essential for frequency stability and increase of bandwidth. This design method can improve oblique incidence performance significant but is limited to Jaumann absorber. A. Kazemzadeh et al. have developed a design procedure for multilayered Jaumann absorbers with a stable frequency response up to 45° incidence for TE and TM polarizations and an ultrawide bandwidth [3]. However, the thickness of EM absorbers is greatly increased. Refs. [4–7] have introduced high-impedance surfaces to create electrically thin electromagnetic absorbers to improve oblique incidence performance, but the improvement is limited to TM polarization.

In this paper, a broadband magnetic MA is designed by embedding circular-metal-disks into magnetic absorbing sheet. Numerical computations show that the proposed absorber achieves a reflection coefficient less than −10 dB from 4.8 GHz to 11.0 GHz with a stable frequency response up to 30° for both polarizations. Meanwhile, the absorber has a wide bandwidth of 10.8 GHz with the incidence angle from 45° to 60° under TM polarization. Finally, the impedance characteristic and the current indicate that the improvement of the absorption characteristics is due to both the electric resonance and magnetic resonance.

2. METHODOLOGY

As shown in Figs. 1(a) and (b), the proposed absorber consists of a 2-D periodic array of circular-metal-disks embedded in a magnetic sheet. An electric conductor plat is placed at the bottom of the absorber. The magnetic sheet was prepared on the basis of polymer composite filled with FeCo alloy powder described in Ref. [8] and [9] at the weight ratio of 1:3. The relative permittivity and relative permeability of the magnetic sheet material are shown in Fig. 2.

We used the finite difference time domain (FDTD) solver CST Microwave Studio to mimic the problem shown in Fig. 1(a). The program simulated a single unit cell with appropriate boundary

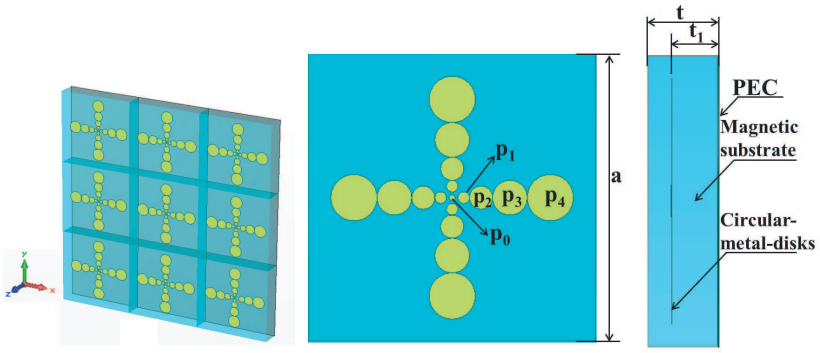

Figure 1: Geometry of the radar absorber based on a magnetic substrate with circular-metal-disks. (a) Perspective picture of MA. (b) Front view of the structure (p_0, p_1, p_2, p_3, and p_4 represent diameter of the disks, respectively. $p_0 = 0.2\,\text{mm}$, $p_1 = 0.4\,\text{mm}$, $p_2 = 0.8\,\text{mm}$, $p_3 = 1.2\,\text{mm}, p_4 = 1.6\,\text{mm}$.). (c) Cross section schematic of the fundamental structure. a is the period of MA, t is the thickness of the magnetic substrate, and t_1 is the position of the circular-metal-disks.

conditions, as perfect electric conductor (PEC) boundary on two opposite sides and perfect magnetic conductor (PMC) boundary on the other two opposite sides. A linearly polarized plane wave was incident on the surface of the magnetic absorbing sheets with either TE or TM polarization, as shown in Fig. 3. In the simulation, the material settings of the aluminum patches and the metal plane were lossy metal with an electrical conductivity of $3.72 \times 107\,\text{S/m}$ and PEC, respectively. Note that, there is not transmission because the bottom of the absorber is a PEC plate.

For oblique incidence, frequency stability and reflection coefficient are necessary for both TE and TM polarizations. The reflection coefficient, based on the transmission line theory [10], is calculated as a function of input impedance of MAs. According to Ref. [16], the input impedance of MAs for both polarizations at oblique incidence can be calculated by a recurrence formula.

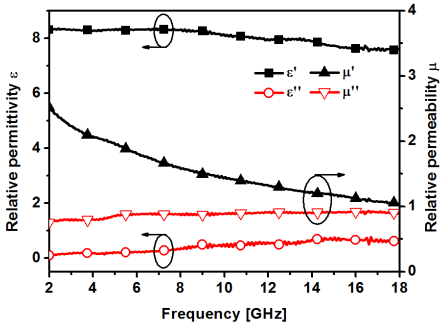

Figure 2: Relative permittivity (ε) and permeability (μ) of the magnetic absorbing sheet material as a function of frequency.

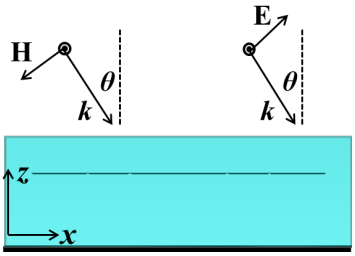

Figure 3: TE and TM plane wave incident on the MA. The electric (magnetic) field of the TE-polarized (TM-polarized) incident wave is along y-axis, and θ is the incidence angle.

$$Z_{in(\text{TE})} = Z_{(\text{TE})} \tanh(\nu_2 \cdot d) \tag{1}$$

$$Z_{in(\text{TM})} = Z_{(\text{TM})} \tanh(\nu_2 \cdot d) \tag{2}$$

$$Z_{(\text{TE})} = \frac{\eta\sqrt{\mu_r/\varepsilon_r}}{\cos(\theta_2)} \tag{3}$$

$$Z_{(\text{TM})} = \eta\sqrt{\mu_r/\varepsilon_r} \cdot \cos(\theta_2) \tag{4}$$

where $Z_{(\text{TE})}$, $Z_{(\text{TM})}$ are the characteristic impedance of absorbing layer for TE and TM polarization, respectively. $\eta \approx 377\,\Omega$ is the wave impedance of the free space, $\nu_0$is the propagation constant of

the free space, θ_2 represents the angle of transmission in the magnetic composite sheet, $\nu_2 = \nu_0\sqrt{\mu_r/\varepsilon_r}\cdot\cos(\theta_2)$ is the propagation constant along the plane normal of the substrate layer. The value of $\cos(\theta_2)$ is given by Snell's law:

$$\cos(\theta_2) = \sqrt{1 - \frac{\sin^2(\theta_1)}{\mu_r\varepsilon_r}} \tag{5}$$

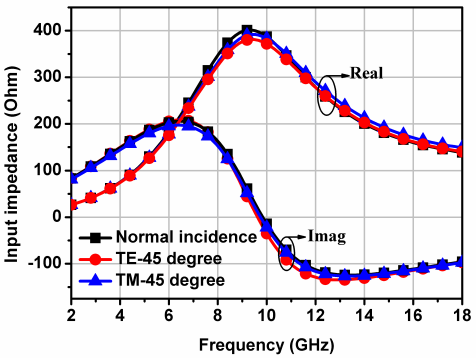

Figure 4: The input impedance of the MA without circular-metal-disks for the incidence angle of 0° and 45° under TE and TM polarization.

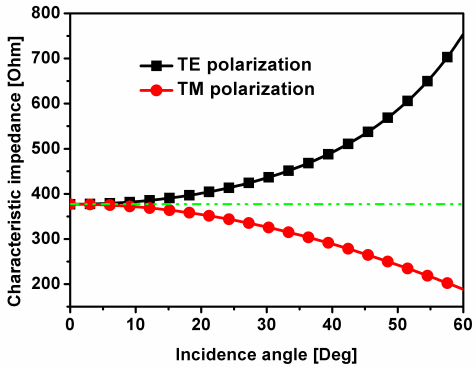

Figure 5: The variation of impedance of free space with angle of incidence at both TE and TM polarizations.

According to above formulas, the input impedance of the magnetic absorber is calculated and shown in Fig. 4. It is obtained that the input impedances vary slightly with oblique incidence angles compared to that at normal incidence. Therefore, the input impedance for different incidence angles can appropriate that for normal incidence angle as follows:

$$Z_{in} = Z_{(TE)} = Z_{(TM)} = \eta\sqrt{\mu_r/\varepsilon_r}\tanh(\nu_0\sqrt{\mu_r/\varepsilon_r}) \tag{6}$$

Then, the reflection coefficient with oblique incidence of plane wave at the angle of θ_1 for both polarizations can be calculated as [11]:

$$\Gamma(\text{TE}) = \frac{Zin - \eta/\cos(\theta_1)}{Zin + \eta/\cos(\theta_1)} \tag{7}$$

$$\Gamma(\text{TM}) = \frac{Z_{in} - \eta\cdot\cos(\theta_1)}{Z_{in} + \eta\cdot\cos(\theta_1)} \tag{8}$$

The characteristic impedance of free space [see in Fig. 5] can be expressed by $\eta/\cos(\theta_1)$ Ohm and $\eta\cdot\cos(\theta_1)$ Ohm for TE and TM polarization, respectively [12]. It is obtained that the totally different changing trends of characteristic impedance of free space inevitably leads to the case, that once the oblique incidence performance for MA in one polarization is good then another is bad [13–15]. It is difficult to simultaneously improve the oblique incidence performance of an absorber under both polarizations. Therefore, the introduction of the circular-metal-disks can be better to improve the oblique incidence performance.

3. NUMERICAL RESULTS AND DISCUSSIONS

Figure 6 shows the reflection coefficient of the absorber with and without circular-metal-disks. Figs. 6(a) and 6(b) demonstrates very stable operation frequency with incidence angle increases, and this performance remains even by embedding circular-metal-disks into MA [see in Figs. 6(c) and 6(d)]. In the case of TE polarization, −10 dB absorption bandwidth of the proposed MA is increased at least by 5.7% compared that of MA without circular-metal-disks from the incidence angle of 0° to 30°. In the case of TM polarization, −10 dB absorption bandwidth of the proposed MA is increased by 17%, 36% and 168% for the incidence angle of 30°, 45°, and 60°, respectively.

We now give an investigation into the physical origin of the absorption peaks at both TE and TM polarization. Figs. 7(a) and 7(b) show the normal incidence surface current distributions of

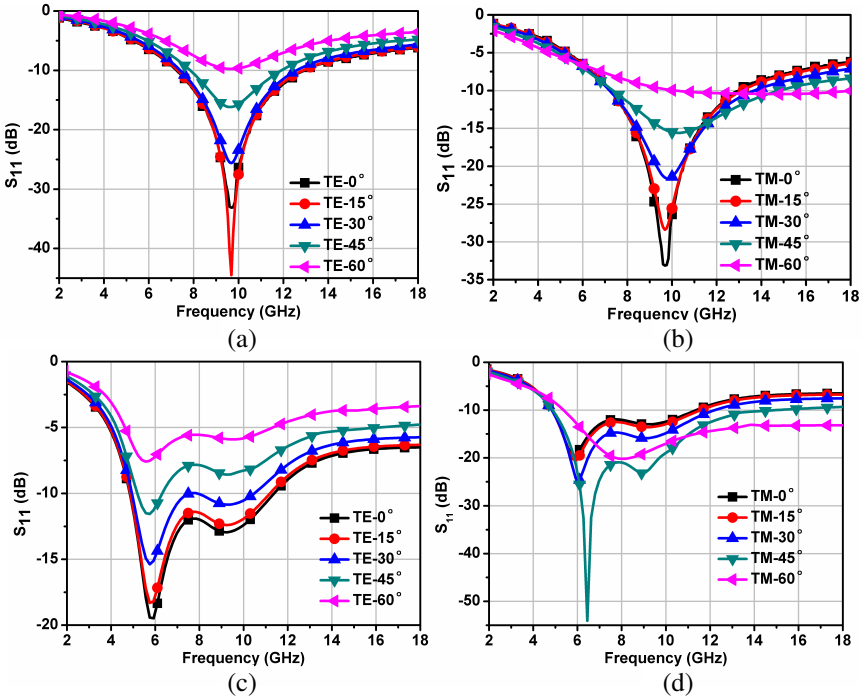

Figure 6: Simulated reflection coefficient of the proposed MAs for TE and TM polarizations: (a) MA without circular-metal-disks for TE-polarized wave, (b) MA without circular-metal-disks for TM-polarized wave, (c) MA with circular-metal-disks for TE-polarized wave, (d) MA with circular-metal-disks for TM-polarized wave.

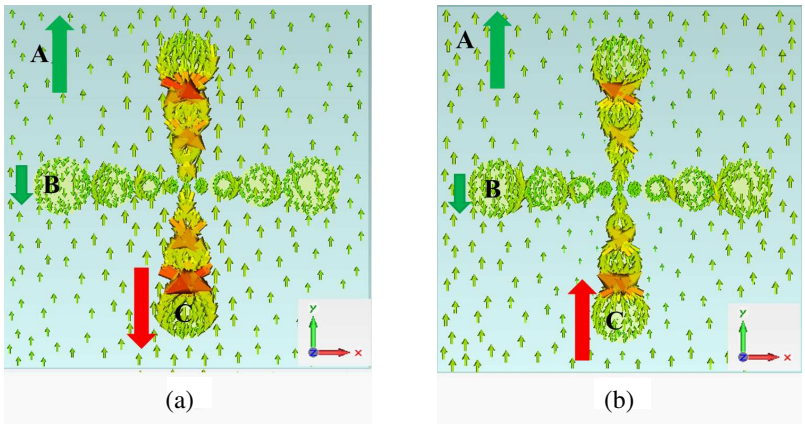

Figure 7: Surface current distributions (the electric field of the incident wave is along y-axis) of the MA with circular-metal-disks at two resonance frequencies for normal incidence (A, B, and C respect the current of different region of PEC, circular-metal-disks along x-axis, and circular-metal-disks along y-axis.). (a) 6.0GHz, (b) 9.5 GHz.

the proposed MA at two absorption frequencies of 6.0 GHz and 9.5 GHz, respectively. From the result in Fig. 5(a), only magnetic resonance can be at the absorption peak of 6.0 GHz. However, with regard to the other absorption peak at 9.5 GHz, both magnetic and electric resonances can be observed. For the magnetic resonance, the backed metal layer and the circular-metal-disks along x-axis carry electrical charges with opposite signs leading to a circulating current, which creates the magnetic flux coupling with the incidence magnetic field. At the electrical resonance, the induced current flows through the circular-metal-disks along y-axis parallel to the incidence field. Therefore, these two absorption peaks relies on the magnetic and electrical resonances.

4. CONCLUSION

A broadband magnetic absorber for realizing stable absorption under both TE and TM polarizations has been presented. By introducing circular-metal-disks, we improve the oblique incidence performance of the MA. Simulated results demonstrate that the optimized MA with a thickness of 2.4 mm exhibits good oblique incidence performance for both TE and TM polarization and a broadened −10 absorption bandwidth. By analyzing the distribution of the surface current of the proposed MA, it is found that this feature is mainly related to the magnetic and electric resonance.

REFERENCES

1. Salisbury, W. W., "Absorbent body of electromagnetic waves," U. S. Patent 2,599,944, Jun. 10, 1952.
2. Munk, B. A., P. Munk, and J. Pryor, "On designing Jaumann and circuit analog absorbers for oblique angle of incidence," *IEEE Trans. Antennas Propag.*, Vol. 55, No. 1, 186–192, Jan. 2007.
3. Munk, B., *Metamaterials: Critique and Alternatives*, Wiley, New York, 2009.
4. Tretyakov, S. A., *Analytical Modeling in Applied Electromagnetic*, Artech House, Boston, MA, 2003.
5. Tretyakov, S. A. and S. I. Maslovski, "Thin absorber structure for all incidence angles based on the use of a high-impedance surface," *Microw. Opt. Techn. Let.*, Vol. 38, No. 3, 175–178, Aug. 5, 2003.
6. Padooru, Y. R., A. B. Yakovlev, C. S. R. Kaipa, G. W. Hanson, F. Medina, F. Mesa, and A. W. Glisson, "New absorbing boundary conditions and analytical model for multilayered mushroom-type metamaterial: Applications to wideband absorbers," *IEEE Trans. Antennas Propag.*, Vol. 60, No. 12, 5727–5742, Dec. 2012.
7. Luukkonen, O., F. Costa, C. R. Simovski, A. Monorchio, and S. A. Tretyakov, "A thin electromagnetic absorber for wide incidence angles and both polarizations," *IEEE Trans. Antennas Propag.*, Vol. 57, No. 10, 3119–3125, Oct. 2009.
8. Zhou, P. H., L. J. Deng, J. L. Xie, et al., "Effects of particle morphology and crystal structure on the microwave properties of flake-like nano-crystalline Fe_3Co_2 particles," *Journal of Alloys and Compounds*, Vol. 448, No. 1, 303–307, 2008.
9. Liu, T., P. H. Zhou, J. L. Xie, et al., "Extrinsic permeability of Fe-based flake composites from intrinsic parameters: A comparison between the aligned and random cases," *Journal of Magnetism and Magnetic Materials*, Vol. 324, No. 4, 519–523, 2012.
10. Pozar, D. M., *Microwave Engineering*, John Wiley & Sons, Inc., 2012.
11. Kong, J. A., *Electromagnetic Wave Theory*, John Wiley & Sons, Inc., 1986.
12. Chambers, B. and A. Tennant, "Design of wideband Jaumann radar absorbers with optimum oblique incidence performance," *Electron. Lett.*, Vol. 30, No. 18, 1530–1532, Sep. 1994.
13. Balanis, C. A., *Advanced Engineering Electromagnetics*, Wiley, New York, 1989.
14. Munk, B. A., *Frequency Selective Surfaces: Theory and Design*, John Wiley & Sons, 2005.
15. Kazantsev, Y. N., A. V. Lopatin, N. E. Kazantseva, et al., "Broadening of operating frequency band of magnetic-type radio absorbers by FSS incorporation," *IEEE Trans. Antennas Propag.*, Vol. 58, No. 4, 1227–1235, Apr. 2010.

Metamaterial Based Patch Antenna with Broad Bandwidth and Simple Structures

X. S. Li[1], **F. M. Lin**[2], **and D. L. Wu**[2]

[1]School of Automation, Guangdong University of Technology, China
[2]School of Physics and Optoelectronic Engineering
Guangdong University of Technology, China

Abstract— A patch antenna based on metamaterials of composite split-ring-resonators (CSRRs) and strip gaps is presented. The antenna is constructed by using CSRR structures in forms of circular rings on the patch and employing strip gaps on the ground plane. The signal is fed by a common microstrip line that connects the patch and the input port. The antenna is based on a simple structure of an only one-layer substrate. Rogers RO4350 ($\varepsilon_r = 3.66$) is preferred as the dielectric material of the substrate. The antenna has a compact footprint that is only $0.408\lambda_0 \times 0.357\lambda_0$ at the lowest operating frequency of 1.7 GHz. The antenna could operate over two bands that are from 1.70 GHz to 2.98 GHz and from 3.99 GHz to 5.34 GHz. The CSRR and strip gaps are combined with the patch and ground to broaden its operating frequencies as well as to enhance its radiation performance via their coupling with the substrate in a different way. The measured impedance of the antenna shows a smooth variation in the vicinity of 50 Ω over the operating bands. This smooth variation enables the antenna to have broad bandwidth. Additionally, its radiation performance is kept favorable with a peak gain of 6.04 dB. The performances of the antenna were characterized computationally and verified experimentally. Good agreements between the simulations and measurements were observed convincing that the antenna could operate over wide bandwidths and radiate effectively with its simple structure and compact size. The presented design is favorable for its broadband as well as good radiation performance with a simple structure that is comprised of only one layer substrate. The antenna is promising for broadband applications that require the operating bands of WCDMA (1920–2170 MHz), WiMAX (2500–2690 MHz), Bluetooth (2400–2480 MHz) or Wibro (2300–2390 MHz).

1. INTRODUCTION

The metamaterial inspired patch antenna is a promising field of research for its favorable characteristics like multi-band operation, miniaturization, controllable radiation properties, etc.. Base on these advantages, metamaterial antennas have found their applications in a wide spectrum of industries, such as the WCDMA operating at 1.92–2.17 GHz, the WiMAX operating at 3.30–3.70 GHz, the Bluetooth operating at 2.40–2.48 GHz and the wireless broadband (Wibro) operating at 2.30–2.39 GHz [1, 2]. However, there are still several aspects of metamaterial antennas that need to be improved, such as their relatively complicated structures and low antenna gain.

To improve the performance of metamaterial antennas, several novel structures of metamaterials, like the CSRR, the reactive impedance surface (RIS), the partial reflective surface (PRS), the mushroom like electromagnetic band-gap (EBG) structures etc., are emerging in recent years [3–7]. The CSRR structures etched on the patch along with the substrate and the ground plane can be modeled as a LC circuit with left-handed material (LHM) properties. They could resonant at lower frequencies leading to effects of miniaturization and multi-band operation [3]. In order to further enhance the gain and extend the bandwidth of metamaterial antennas, the RIS structure embedded in the substrate or the chiral patterns placed over the patch were proposed [4, 8]. In the recently published works on metamaterial antennas, a RIS like pattern was etched on the ground with a only one-layer substrate and metamaterial inspired structures were being etched on the patch of the same antenna [9–12]. This type of metamaterial inspired antennas gave out a good example of extending the bandwidth while keeping the radiation performance acceptable. Something worth to be improved might be that the operation frequencies of these antennas are relatively high (all above 3 GHz). This is not so favorable for applications at lower frequencies, like WCDMA, Bluetooth, or Wibro.

From a practical point of view, it might be desirable to shift the operating frequency of the antenna in [9] to a lower band while keeping its broadband and favorable radiation performances. In this letter, a metamaterial inspired antenna is presented with the desirable characteristics aforementioned. It was constructed by using the CSRR structure in forms of circular rings on the patch

and employing the strip gaps on the ground plane. The antenna is broadband at lower frequencies and has a simple structure with a one-layer substrate. The radiation performances of the antenna are also kept desirable over its operating bands.

2. STRUCTURES AND RESULTS

The antenna based on LHM patterns is proposed. To achieve broadband and simple-structure properties, the configuration of the two antennas is based on an original one-layer patch antenna. It was constructed by employing CSRRs on the patch and etching strip gaps on the ground. The antenna is excited by a microstrip that connects the patch and the input port. The LHM patterns of CSRR and strip gaps are combined with the patch and ground to broaden its operating frequencies as well as enhance its radiation performance via their coupling with the substrate in a different way. The left-handed properties of these patterns have been verified in [12] and thus will not be further discussed. Their performances are characterized computationally and verified experimentally. Their broadband and simple-structure characteristics will be demonstrated as follows.

The structure of the antenna is shown in Fig. 1. In order to extend the operating frequencies, several metamaterial inspired patterns, the CSRRs, were arranged and etched on the patch. Another kind of metamaterial inspired structure, the strip gaps, was also employed on the ground plane to enhance the radiation performance as well as broaden the bandwidth of the antenna. It should be noted that there are some main differences between the antenna presented here and the one in [9]. Firstly, the dimensions of the patch were adjusted larger and then optimized so that the operating band could be shifted towards lower frequencies than those in [9] (above 5.3 GHz). In addition, the metamaterial structures employed on the patch are changed from periodic gaps to CSRRs of circular shapes. The unit cell of the CSRR is shown in Fig. 1(a). It is formed by two isolated concentric circular slots oppositely oriented. The fabricated antenna is shown in Fig. 1(c). The permittivity of the substrate is $\varepsilon_r = 3.66$ (Rogers RO4350). The thickness of the substrate is chosen to be as small as 1.524 mm. The overall antenna volume is only $0.408\lambda_0 \times 0.357\lambda_0 \times 0.0086\lambda_0$ at the lowest operating frequency of 1.7 GHz.

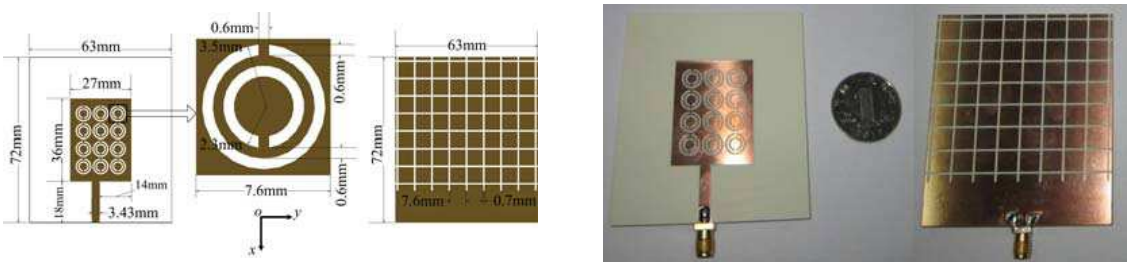

(a) Top view (b) Bottom view (c) Fabricated antenna

Figure 1: Structure of the antenna.

The reflection coefficient of the antenna is shown in Fig. 2. It can be seen that the two main bandwidths where the reflection coefficients are below −10 dB are located from 1.70 GHz to 2.98 GHz and from 3.99 GHz to 5.34 GHz. The corresponding two relative bandwidths are 75% at 1.70 GHz and 34% at 3.99 GHz, respectively. The reflection coefficient is also compared with that of the original antenna with the same dimensions excepting that the patch and ground are intact. The reflection coefficient performance of the proposed antenna is significantly improved according to Fig. 2. This demonstrates that the CSRRs and strip gaps employed here can affect the resonance of the antenna and extend its bandwidth by a large scale.

The impedance characteristics of the antenna are also shown in Fig. 3. According to the figure, there are several resonant frequencies where the imaginary part of the impedance is crossing zero. This has an effect of maintaining the real part of the impedance close to 50 Ω at the same frequencies. The operating bands of the metamaterial inspired antenna are thus successfully extended by introducing these resonant frequencies.

The radiation property of the antenna was measured in terms of its radiation patterns. Two frequencies, 1.8 GHz and 4.2 GHz, were randomly chosen to verify the radiation performance of the antenna. The three-dimensional gain patterns are shown in Fig. 4(a) and Fig. 4(b) in the dB scale. The patterns of the XOY and XOZ planes at 1.8 GHz and 4.2 GHz are also plotted in Fig. 4(c) and Fig. 4(d) in the dB scale, respectively. It should be noted that the antenna tends to radiate in

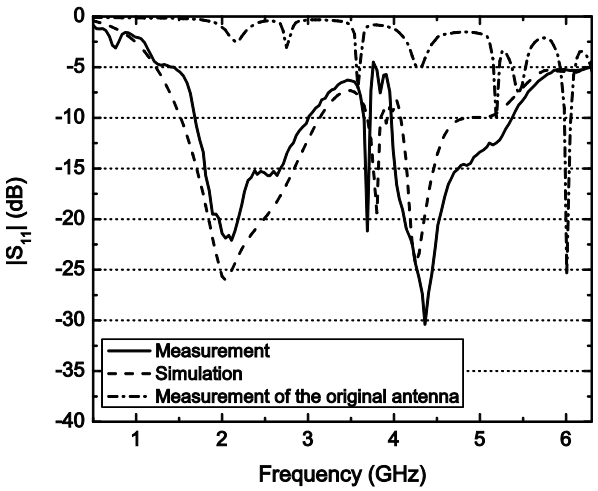

Figure 2: Reflection coefficients.

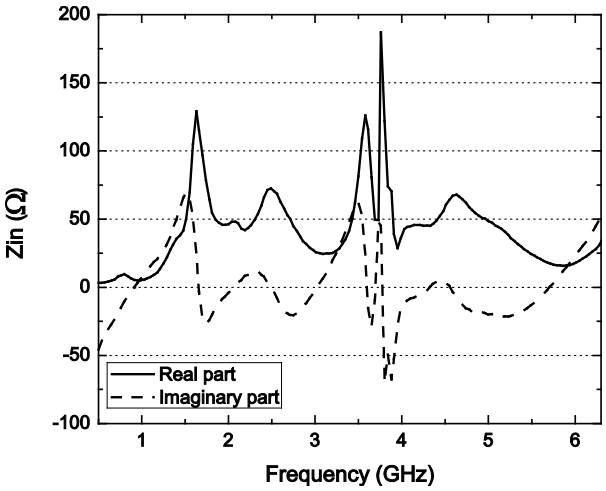

Figure 3: Measured impedance.

the vertical direction of the antenna at 1.8 GHz, which is similar to a dipole antenna that is placed along the x axis. The radiation pattern at 4.2 GHz has two main lobs in the XOY plane and one main lobe in the XOZ plane. This demonstrates that the metamaterial structure employed on the ground is capable of changing the radiation pattern of the patch. The position of the antenna could be adjusted so that the antenna is feasible for radiating or receiving signals in the desired direction.

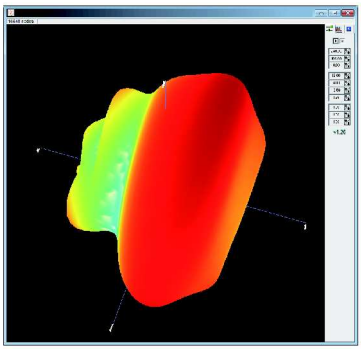

(a) 3D gain pattern at 1.8 GHz

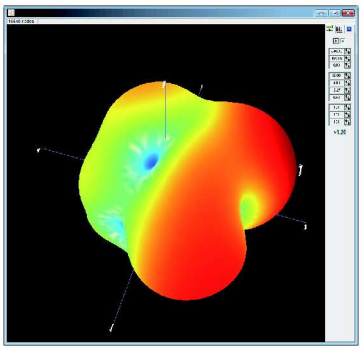

(b) 3D gain pattern at 4.2 GHz

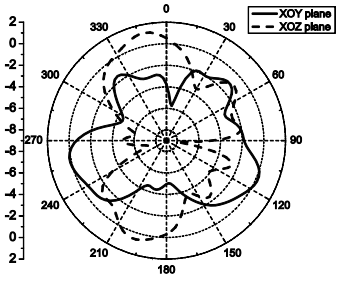

(c) *XOY* and *XOZ* planes at 1.8 GHz

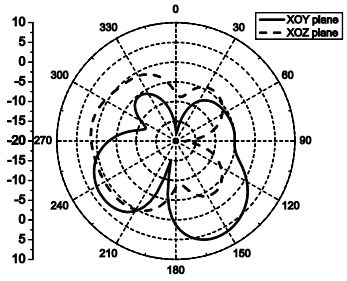

(d) *XOY* and *XOZ* planes at 4.2 GHz

Figure 4: Measured radiation patterns.

The radiation gain of the antenna was simulated and shown in Fig. 5. It can be seen that the antenna has a peak gain of 6.04 dB at 3.58 GHz. In Fig. 5, it could also be observed that the gain is above 2 dB over the frequency range of 1.7 GHz–5.8 GHz. However, the gain value below 3 GHz is lower than that above 3 GHz. This gain degradation may be due to a stronger ohmic loss of the

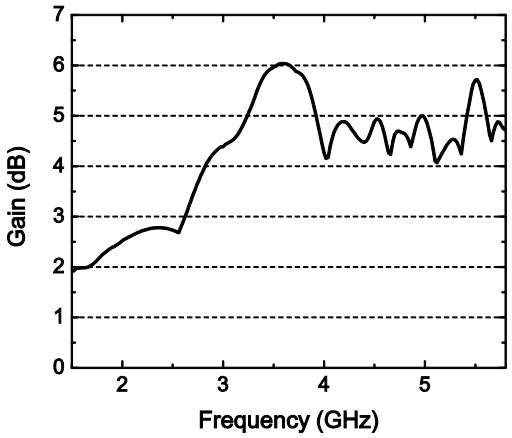

Figure 5: Simulated maximum gain.

antenna below 3 GHz. Nevertheless, Fig. 5 demonstrates that the antenna could radiate effectively over a wide band. This is quite favorable for such a patch antenna with broadband and simple structure characteristics.

3. CONCLUSION

The metamaterial inspired antenna with broadband and simple-structure characteristics is presented in this paper. The configuration of the antenna are based on the one-layer patch antenna with a compact footprint of $0.408\lambda_0 \times 0.357\lambda_0$ at the lowest operating frequency of 1.7 GHz. The CSRRs were employed on the patch and the strip gaps were etched on the ground. The dimension and substrate parameters of the antenna were adjusted and optimized to shift the operating frequencies towards relatively low bands that are from 1.70 GHz to 2.98 GHz and from 3.99 GHz to 5.34 GHz. The relative bandwidths of the antenna are 75% at 1.70 GHz and 34% at 3.99 GHz, respectively. The radiation gain is favorable over the operating bands with a simulated peak gain of 6.04 dB at 3.58 GHz. We find out that the antenna keeps the radiation performance favorable with such simple structures and compact sizes. The newly designed antenna is applicable for a wide spectrum of applications like WCDMA, WiMAX, Bluetooth and Wibro.

ACKNOWLEDGMENT

This work is supported by the Guangdong Natural Science Foundation under Grant S2011040003958, the Starting Funding of Doctors of Guangdong University of Technology under Grant 405115008, and the Youth Science Funds of Guangdong University of Technology under Grant 13QNYB004.

REFERENCES

1. Kim, J. and J. Choi, "Design of a multiantenna structure for WCDMA and Wibro MIMO systems using ENG-ZOR unit cells," *Microwave and Optical Technology Letters,* Vol. 52, No. 1, 13–17, 2010.
2. Li, W. T., Y. Q. Hei, W. Feng, and X. W. Shi, "Planar antenna for 3G/bluetooth/WiMAX and UWB applications with dual band-notched characteristics," *IEEE Antennas and Wireless Propagation Letters,* Vol. 11, 61–64, 2012.
3. Dong, Y. D., H. Toyao, and T. Itoh, "Design and characterization of miniaturized patch antennas loaded with complementary split-ring resonators," *IEEE Transactions on Antennas and Propagation,* Vol. 60, No. 2, 772–785, 2012.
4. Agarwal, K., Nasimuddin, and A. Alphones, "RIS-based compact circularly polarized microstrip antennas," *IEEE Transactions on Antennas and Propagation,* Vol. 61, No. 2, 547–554, 2013.
5. Ge, Y. H., K. P. Esselle, and T. S. Bird, "The use of simple thin partially reflective surfaces with positive reflection phase gradients to design wideband, low-profile EBG resonator antennas," *IEEE Transactions on Antennas and Propagation,* Vol. 60, No. 2, 743–750, 2012.
6. Cao, W. Q., B. N. Zhang, A. J. Liu, D. S. Guo, T. B. Yu, and Y. Wei, "A dual-band microstrip antenna with omnidirectional circularly polarized and unidirectional linearly polar-

ized characteristics based on metamaterial structure," *Journal of Electromagnetic Waves and Applications,* Vol. 26, No. 1, 274–283, 2012.

7. Ouedraogo, R. O., E. J. Rothwell, A. R. Diaz, K. Fuchi, and A. Temme, "Miniaturization of patch antennas using a metamaterial-inspired technique," *IEEE Transactions on Antennas and Propagation,* Vol. 60, No. 5, 2175–2182, 2012.
8. Liu, Y. H., K. Song, Y. Qi, S. Gu, and X. P. Zhao, "Investigation of circularly polarized patch antenna with chiral metamaterial," *IEEE Antennas and Wireless Propagation Letters,* Vol. 12, 1359–1362, 2013.
9. Li, L. W., Y. N. Li, T. S. Yeo, J. R. Mosig, and O. J. F. Martin, "A broadband and high-gain metamaterial microstrip antenna," *Applied Physics Letters,* Vol. 96, No. 16, 164101-1–3, 2010.
10. Liu, T., X. Y. Cao, J. Gao, Q. Yang, and W. Q. Li, "Design of miniaturized broadband and high gain metamaterial patch antenna," *Microwave and Optical Technology Letters,* Vol. 53, No. 12, 2858–2861, 2011.
11. Xiong, H., J. S. Hong, and Y. H. Peng, "Impedance bandwidth and gain improvement for microstrip antenna using metamaterials," *Radioengineering,* Vol. 21, No. 4, 993–998, 2012.
12. Guo, L. Y., H. L. Yang, M. H. Li, C. S. Gao, and Y. Tian, "A mircostrip antenna with single square ring structured left-handed metamaterial," *Acta Physica Sinica,* Vol. 61, No. 1, 014102-1–5, 2012.

Coherent Beam Combining of Two Tm-doped Fiber MOPAs with Output Power of 50 W

Xiaoxi Jin, **Xiong Wang**, **Xiaolin Wang**, **Yanxing Ma**, **and Pu Zhou**
College of Optoelectronic Science and Engineering
National University of Defense Technology, Changsha 410073, China

Abstract— Thulium-doped fiber lasers operating at $\sim 2\,\mu m$ band have significant application prospects in fields such as eye-safe lidar, remote sensing, medical care and nonlinear frequency conversion. However, due to thermal damage, mode instability and nonlinear effects, the output power level of single Tm-doped fiber laser was limited, which confined the development of Tm-doped fiber laser. Coherent beam combining (CBC) is an effective method to improve power level of fiber lasers. In this paper, we demonstrated CBC of two Tm-doped fiber master oscillator power amplifiers (MOPAs) with total output power reaching 50 W. The output powers of the both MOPAs can reach ~ 25 W when the pump power of each MOPA was ~ 55 W. Single frequency dithering technique was used to implement active phase locking in feedback loop of the CBC system. When the feedback loop was implemented, phase noises below 700 Hz in the system were compensated effectively, and the far field intensity patterns were highly stable compared with the fluctuating patterns obtained when the feedback loop did not work. The fringe contrast was increased from ~ 0.34 in open loop to ~ 0.90 in closed-loop. These results indicate that the system we presented is a promising way to increase the output power of Tm-doped fiber lasers. Since the output power of the system is pump-limited, it's reasonable to believe that higher output power at $\sim 2\,\mu m$ could be obtained via CBC, if more channels are combined together and/or the power of each channel is further scaled up.

1. INTRODUCTION

In recent years, thulium-doped fiber lasers (Tm-doped fiber lasers, TFLs) operating at $\sim 2\,\mu m$ have attracted researchers' interests. With many unique advantages [1, 2], such as eye-safe, higher nonlinear threshold and wide tunable range, lasers operating at $\sim 2\,\mu m$ have significant application prospects in eye-safe lidar, remote sensing, medical care, nonlinear frequency conversion and other fields [3].

However, the output power of single mode Tm-doped fiber laser is limited due to thermal effect, mode instability, nonlinear effect and the brightness of pump source [4], which confines the development of Tm-doped fiber in various application prospects. Coherent beam combining (CBC) of fiber lasers can increase the output power while simultaneously maintain good beam quality. There have existed several approaches for CBC, including passive phasing techniques (such as self-organized laser array [5–8], self-imaging resonator technique [9], self-Fourier laser cavity [10]), and active phasing techniques based on stochastic parallel gradient descent (SPGD) algorithm [11], multi-dithering technique [12] and single frequency dithering technique [13]. Although the configuration of passive CBC system is simple and there is no need of feedback loops to control and compensate phase noises, the number of combined lasers is limited due to the decrease of combination efficiency [14].

In the previous studies on CBC of Tm-doped fiber lasers, the output power was below several tens of watts. In 2013, 20 W passive CBC of two TFLs was reported [15], which is the highest power level of TFLs' CBC as far as we know.

In this paper, we demonstrated CBC with the output power of 50 W from two Tm-doped fiber master oscillator power amplifiers (MOPAs), which significantly increased the output power of TFL at $\sim 2\,\mu m$. The CBC was realized by active phase locking using single frequency dithering technique [13] in feedback loop.

2. EXPERIMENTAL SETUP

The experimental setup of the CBC of two Tm-doped fiber MOPAs is shown in Fig. 1.

Two MOPAs consisted of seed laser (SL), pre-amplifiers (PA and amplifiers (Amplifier 1, Amplifier 2). A single frequency fiber laser, whose center wavelength was 1971.5 nm, served as the seed laser. The output power of seed laser was 7.5 mW. Then the output power of seed laser was pre-amplified to 316 mW via PA, which consisted of a 1550 nm fiber laser, a 1550/2000 nm wavelength division multiplexer and 2.5 m single cladding Tm-doped fiber (6/125 μm). The output laser of PA was divided into two parts by a 10/90 coupler. The 10% part (29.6 mW) served as signal

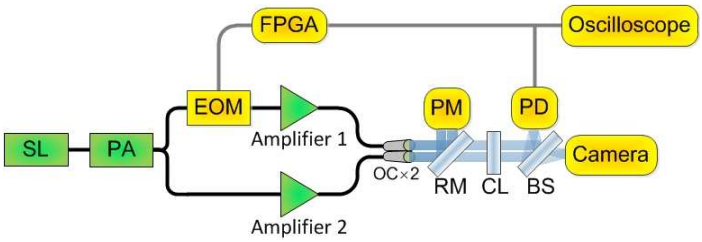

Figure 1: (Color online) Experimental setup of CBC of two Tm-doped fiber amplifiers in MOPA configuration. SL: seed laser; PA: pre-amplifier; EOM: electro-optical modulator; OC: optical collimator; RM: reflect mirror; PM: power meter; CL: convex lens; BS: beam splitter; PD: photodetector with pinhole; FPGA: field programmable gate array.

laser in one channel, which contained an electro-optical modulator (EOM) and Amplifier 1. And the 90% part (274 mW) served as signal laser in the other channel, which contained Amplifier 2. The bandwidth of EOM was 100 MHz at 2 μm. Two amplifiers (Amplifier 1 and Amplifier 2) were both made up of two 793 nm LDs, a $(6+1)\times 1$ signal pump combiner and 3.4 m double cladding Tm-doped fiber (25/250 μm). Thus, two MOPAs can output 25.0 W and 23.9 W via amplifiers, respectively.

And the output laser beams were collimated by two optical collimators (OC). A high reflectivity mirror (RM, $\sim$ 99%) and a power meter (PM) were used to measure the output power from two collimators. Only a small amount of power could be transmitted through reflect mirror, which was employed to detect the far field intensity patterns and control the feedback loop. Convex lens (CL) and beam splitter (BS) were used to obtain far field intensity patterns and cast them into camera and the pinhole of photodetector (PD). The camera recorded far field intensity patterns. And photodetector transformed optical intensity signal into electric signal to drive field programmable gate array (FPGA) and control electro-optical modulator (EOM). Field programmable gate array employed in our experiment was based on single frequency dithering technique to realize phase locking of two MOPAs. There existed optical isolators after each seed laser, pre-amplifiers and amplifiers in MOPAs to protect system.

3. RESULTS AND DISCUSSION

Based on experimental setup in Fig. 1, we measured the output power of two MOPAs separately via power meter. And experimental results were shown in Fig. 2. Output power of both MOPAs can reach to $\sim$ 25 W when pump power was $\sim$ 55 W. therefore, the combined output power can reach up to $\sim$ 50 W.

An optical spectrum analyzer (OSA, 0.05 nm resolution) was used to measure the spectrum of output laser. As shown in Fig. 3, the spectrum of output laser centered at $\sim$ 1971.5 nm.

After each MOPA's output power and their combined spectrum characteristics obtained, we confirmed that the output laser beams of these two MOPAs could be coherently combined and the output power would be $\sim$ 50 W. In this experiment, coherent beam combing was realized by active

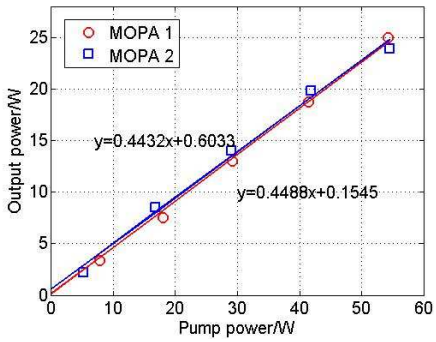

Figure 2: (Color online) Characteristics of each MOPA's output power.

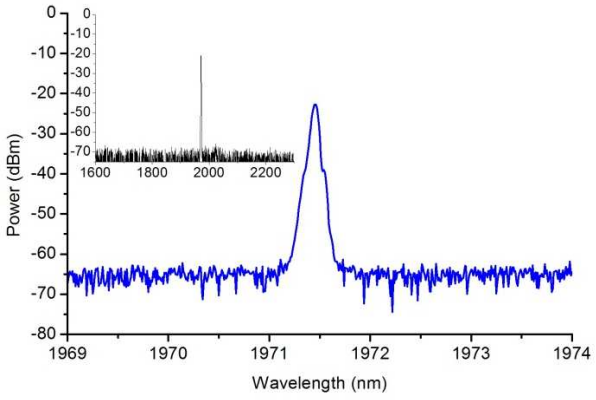

Figure 3: (Color online) Spectrum of output laser.

phase locking of two MOPAs using single frequency dithering technique. Field programmable gate array was employed to implement active phase locking by accepting signals from photodetector and controlling electro-optical modulator, which formed a feedback loop as shown in Fig. 1. Then we studied the changes of far field output patterns by switching the state of feedback control circuit. When system was in the open-loop state, the far field output patterns observed was like the one shown in Fig. 4(a), whose intensity was fluctuating all the time. While the patterns in closed-loop state was shown in Fig. 4(b), whose intensity concentrated in the center and was highly stable. The fringe contrast was increased from ~ 0.34 in open loop state to ~ 0.90 in closed-loop state. Thus, it can be concluded that the intensity of output coherently combined power could be increased and centered using active phase locking technique.

According to Fig. 5, phase noises below 700 Hz were compensated when system was in closed-loop state, which suggested that the output power in the center of laser beam increased significantly.

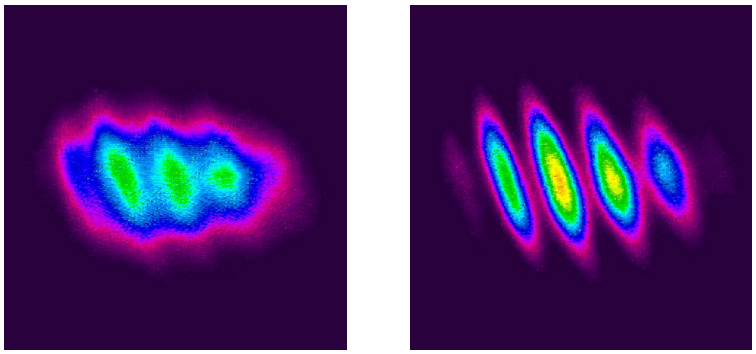

(a) open-loop (b) closed-loop

Figure 4: (Color online) Far field output patterns in (a) open and (b) closed state of feedback loop.

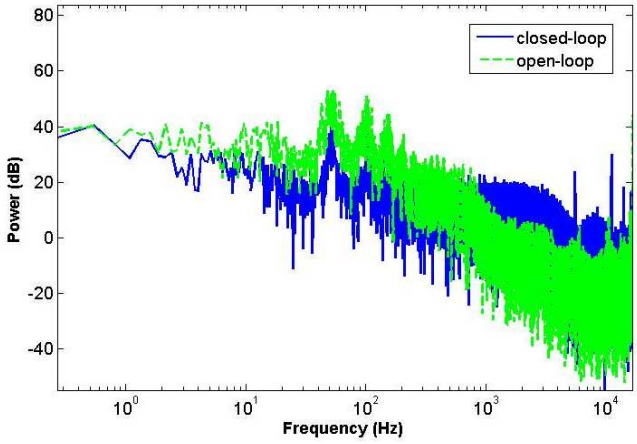

Figure 5: (Color online) Spectral density of output power. Green dotted line: open-loop; blue solid line: closed-loop.

4. CONCLUSIONS

In this paper, we presented CBC of 50 W at 1971.5 nm obtained from two Tm-doped fiber MOPAs using single frequency dithering technique for active phase locking. Phase noises below 700 Hz in the system were compensated effectively, and the fringe contrast was increased from ~ 0.34 to ~ 0.90.

Since the output power of the system is pump-limited, it's reasonable to believe that higher output power of Tm-doped fiber lasers could be obtained in the CBC system we presented, if more channels are combined together and/or the power of each channel is further scaled up.

REFERENCES

1. Jackson, S. D., "Towards high-power mid-infrared emission from a fibre laser," *Nature Photonics*, Vol. 6, 423–431, 2012.
2. Richardson, D. J., J. Nilsson, and W. A. Clarkson, "High power fiber lasers: Current status and future perspectives," *J. Opt. Soc. Am. B*, Vol. 27, B63–B92, 2010.
3. Jackson, S. D., A. Sabella, and D. G. Lancaster, "Application and development of high-power and highly efficient silica-based fiber lasers operating at 2 μm," *IEEE Journal of Selected Topics in Quantum Electronics*, Vol. 13, 567–572, 2007.
4. Zhu, J., W. Du, P. Zhou, X. Xu, and Z. Liu, "Numerical study on power limit of single-mode fiber lasers," *Acta Phys. Sin.*, Vol. 61, 259–265, 2012.
5. Bruesselbach, H., M. Minden, J. L. Rogers, D. C. Jones, and M. S. Mangir, "200 W self-organized coherent fiber arrays," *Conference on Lasers and Electro-Optics, (CLEO), IEEE*, 532–534, 2005.
6. Chen, Z., J. Hou, P. Zhou, and Z. Jiang, "Mutual injection-locking and coherent combining of two individual fiber lasers," *IEEE Journal of Quantum Electronics*, Vol. 44, 515–519, 2008.
7. Kurtz, R. M., R. D. Pradhan, N. Tun, T. M. Aye, G. D. Savant, T. P. Jannson, and L. G. DeShazer, "Mutual injection locking: A new architecture for high-power solid-state laser arrays," *IEEE Journal of Selected Topics in Quantum Electronics*, Vol. 11, 578–586, 2005.
8. Oka, M., H. Masuda, Y. Kaneda, and S. Kubota, "Laser-diode-pumped phase-locked Nd:YAG laser arrays," *IEEE Journal of Quantum Electronics*, Vol. 28, 1142–1147, 1992.
9. He, B., Q. Lou, J. Zhou, Y. Zheng, D. Xue, J. Dong, Y. Wei, F. Zhang, Y. Qi, and J. Zhu, "113-W in-phase mode output from two ytterbium-doped large-core double-cladding fiber lasers," *Chinese Optics Letters*, Vol. 5, 412–414, 2007.
10. Corcoran, C. J. and K. A. Pasch, "Modal analysis of a self-Fourier laser cavity," *Journal of Optics A: Pure and Applied Optics*, Vol. 7, L1, 2005.
11. Wang, X. L., Y. X. Ma, P. Zhou, H. T. Ma, X. Li, X. X. Xu, and Z. J. Liu, "Coherent beam combining of two W-level fiber amplifiers in turbulence atmospheric environment based on stochastic parallel gradient descent algorithm," *Laser Phys.*, Vol. 19, 984–988, 2009.
12. Shay, T. M., "Theory of electronically phased coherent beam combination without a reference beam," *Optics Express*, Vol. 14, 12188–12195, 2006.
13. Ma, Y., X. Wang, J. Leng, H. Xiao, X. Dong, J. Zhu, W. Du, P. Zhou, X. Xu, L. Si, Z. Liu, and Y. Zhao, "Coherent beam combination of 1.08 kW fiber amplifier array using single frequency dithering technique," *Optics Letters*, Vol. 36, 951–953, 2011.
14. Kouznetsov, D., J. Bisson, A. Shirakawa, and K. Ueda, "Limits of coherent addition of lasers: Simple estimate," *Opt. Rev.*, Vol. 12, 445–447, 2005.
15. Honzatko, P., Y. Baravets, F. Todorov, P. Peterka, and M. Becker, "Coherently combined power of 20 W at 2000 nm from a pair of thulium-doped fiber lasers," *Laser Physics Letters*, Vol. 10, 95104, 2013.

Numerical Investigation of a Novel Two-stage Structure to Compress Spectrum and Suppress Pedestal Employing a DIF Interconnected with a HNLF-NOLM

Ying Chen[1, 2], **Yu Guo**[3], **Bing Liu**[1], **Fan Yang**[2], **Xiaojun Zhou**[2], **Yong Liu**[2], **and Xiangning Chen**[1]

[1]Department of Optoelectronics, Academy of Equipment, Beijing 101416, China
[2]State Key Laboratory of Electronic Thin Films and Integrated Devices
School of Optoelectronic Information
University of Electronic Science and Technology of China, Chengdu 610054, China
[3]Air Force 95806 Unit, 100076, China

Abstract— A novel all-fiber spectral compression scheme is proposed and demonstrated, which is based on a two-stage structure employing a dispersion increasing fiber interconnected with a nonlinear optical loop mirror. Five sorts of DIF with different distribution of dispersion coefficient is analyzed one by one in the two-stage scheme. Numerical simulation result shows Logarithmic DIF is suitable for the two-stage scheme, obtain a SCR as high as 10.93 without a Raman self-frequency soliton shift under the condition of soliton number is equal to 1.4.

1. INTRODUCTION

All-optical analog-to-digital conversion (ADC) is the key technique to convert optical analog signals into optical digital ones, in which the whole process is realized in the optical domain. In an all-optical ADC based on Raman self-frequency shift quantization scheme, the resolution, one of the vital factors, can be effectively enhanced by compressing the spectrum after SSFS [1]. The basis of the spectral compression in an optical fiber is the compensation between the initial negative chirp of an optical pulse and the positive chirp introduced by the self phase modulation (SPM) effect. Spectral compression, a common technology in the passive picosecond pulse shaping [2], can be achieved through passing an initially highly negative-chirped optical pulse through an optical fiber [3, 4]. It can also be realized through passing a transform-limited optical pulse (or an optical pulse with a low chirp) through an anomalous dispersion fiber [5, 6].

In this paper, a novel two-stage architecture, employing a DIF as the first stage and an NOLM composed of an HNLF in the loop as the second stage, is introduced. The first DIF achieves the spectral compression, while the nonlinear optical loop mirror (NOLM) consisting of a high-nonlinear fiber (HNLF), HNLF-NOLM for short, is proposed for pedestal elimination due to the chirp-related intensity filtering effect of NOLM. Spectral compression with a large compression ratio is achieved in a two-stage structure composed of DIF concatenating a feed through HNLF-NOLM.

2. OPERATION PRINCIPLE

Figure 1 shows the configuration of the proposed two-stage scheme based on the interconnection between DIF and HNLF-NOLM. HNLF-NOLM is composed of a DIF and an optical coupler with a power-coupling ratio of $\alpha : 1 - \alpha$ ($\alpha \neq 0.5$). The spectral compression principle is analyzed as follow. The SMF is used to pre-chirp the input pulse, the two-stage structure of DIF and HNLF-NOLM is employed to compensate the negative chirp through the SPM effect, providing two-stage spectral compression. The spectral pedestal after compression is eliminated by the chirp-related intensity filtering effect of the NOLM architecture [7], the dispersion-induced chirp is linear and negative, the SPM-induced chirp is nearly linear and positive, which is mainly distributed around the center of pulse ($-0.5T_0 < T < 0.5T_0$). The origin of the spectral pedestal is the insufficient compensation of the nonlinear chirp at the leading and trailing edge of the optical pulse, which correspond to low-power chirp-related edges of the pulse in the time domain. Therefore, it can be efficiently filtered out in NOLM architecture which has a well-known intensity filtering effect [7].

3. SIMULATION

Simulation setup is shown in the Figure 2. A 20 m-long single-mode fiber with a GVD value of 15 ps/nm/km, which induce a linear negative chirp, is connected with the DIF. The output of DIF

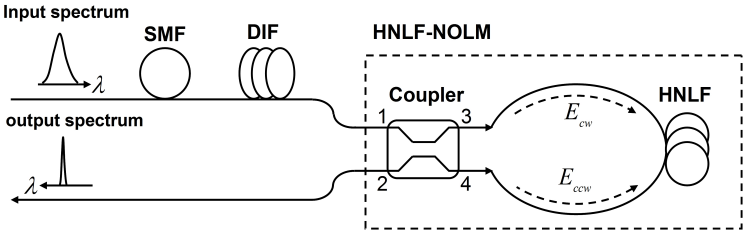

Figure 1: Configuration of the two-stage scheme.

is involved in the port 1 of the HNLF-NOLM. The HNLF-NOLM is composed of a coupler with a coupling ratio of 60/40 and the HNLF whose nonlinear coefficient, loss coefficient and length are $27\,\mathrm{W^{-1}km^{-1}}$, 0.939 dB/km and 1000 m, respectively. A chirp-free hyperbolic-secant pulse, with a central wavelength of 1560 nm, a duration of 300 fs (FWHM) and a peak power of 6.667 W, is used as the input.

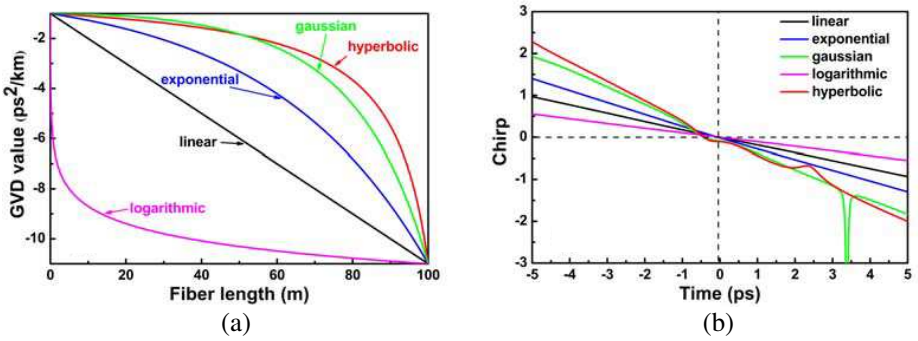

Figure 2: (a) Five sorts of DIF with different distribution of dispersion coefficient. (b) The chirp after pulse propagation in five kinds of DIF.

The propagation of a single optical pulse in a SMF or/and DIF is described by the GNLS equation [19]. The evolution of the two counter propagating pulses in the HNLF-NOLM is described by the coupled generalized nonlinear Schrödinger equations [19] (GNLS). Both GNLS and coupled GNLS equations are solved by using the split-step Fourier method for simulating the spectral compression procedure in the two-stage structure. Spectral compression ratio (SCR), defined as the ratio of the input to the output spectral width (FWHM), is used to evaluate the spectral compression performance. There are five sorts of DIF differentiated with the distribution of dispersion coefficient (β_2). Figures 2(a) and (b) illustrate distribution of five different GVD values of DIF and the pulse chirp after the propagation in the DIF (pulse peak power = 80 W), respectively. With varied soliton number by changing the input pulse peak power (10 W, 40 W and 80 W, corresponding to $N = 0.5$, 1, 1.4), spectral compression is numeric simulated under the condition of five different DIF one by one.

3.1. Linear DIF

Figure 3(a) represent spectrum evolution of two-stage spectral compression structure with the input peak powers of 10 W, 40 W and 80 W, which correspond to the soliton number N of 0.5, 1 and 1.4, respectively. The black line is the input spectrum, the red line is the spectrum outputted when $N = 0.5$, the green line is the output spectrum when $N = 1$, and the blue line is the output spectrum when $N = 1.4$, respectively. Figure 3(b) illustrates the SCR with the different input peak powers. The simulated result show that a higher soliton number leads to a better spectral compression ratio. But a 1.4 nm frequency shift to "red band" when $N = 1.4$ according to the Raman soliton self-frequency shift effect caused by the high enough pulse power.

3.2. Hyperbolic DIF

Figure 4(a) represent spectrum evolution of two-stage spectral compression structure with the input peak powers of 10 W, 40 W and 80 W, which correspond to the soliton number N of 0.5, 1 and 1.4, respectively. The black line is the input spectrum, the red line is the spectrum outputted when $N = 0.5$, the green line is the output spectrum when $N = 1$, and the blue line is the output

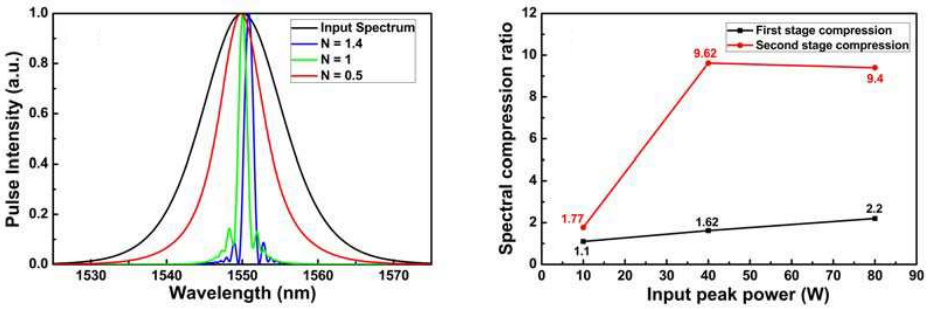

(a) (b)

Figure 3: (a) Spectrum evolution of two-stage spectral compression structure employed a linear DIF with the input peak powers of 10 W, 40 W and 80 W (red line, $N = 0.5$; green line, $N = 1$; blue line, $N = 1.4$, respectively). (b) SCR with the different input peak powers.

spectrum when $N = 1.4$, respectively. Figure 4(b) illustrates the SCR with the different input peak powers. The result shows that a higher spectral compression ratio is provided when soliton number is equal to 1, increasing SCR from 1.67 of first stage compression to 9.31 of second stage compression. However, it is obvious that more pedestal is raised simultaneously. A 3.25 nm Raman soliton self-frequency shift is also existed when soliton number is 1.4.

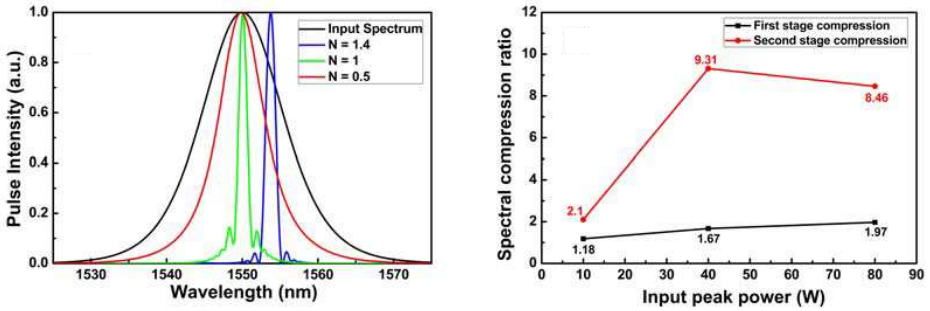

(a) (b)

Figure 4: (a) Spectrum evolution of two-stage spectral compression structure employed a hyperbolic DIF with the input peak powers of 10 W, 40 W and 80 W (red line, $N = 0.5$; green line, $N = 1$; blue line, $N = 1.4$, respectively). (b) SCR with the different input peak powers.

3.3. Exponential DIF

Figure 5(a) represent spectrum evolution of two-stage spectral compression structure with the input peak powers of 10 W, 40 W and 80 W, which correspond to the soliton number N of 0.5, 1 and 1.4, respectively. Figure 5(b) shows the SCR with the different input peak powers. It is implied that a higher SCR of 10.25 is obtained when N is equal to 1, but the side-lobe component level is larger at the same time. A 3.1 nm Raman soliton self-frequency shift is accompanied with spectral compression when N is equal to 1.4.

3.4. Gaussian DIF

Figure 6(a) represent spectrum evolution of two-stage spectral compression structure with the input peak powers of 10 W, 40 W and 80 W, which correspond to the soliton number N of 0.5, 1 and 1.4, respectively. Figure 6(b) displays the SCR with the different input peak powers. Similar conclusion can be arrived as described above. It should be noted that 5 nm Raman self-frequency shift is existed which is the longest shift in simulation.

3.5. Logarithmic DIF

Figure 7(a) represent spectrum evolution of two-stage spectral compression structure with the input peak powers of 10 W, 40 W and 80 W, which correspond to the soliton number N of 0.5, 1 and 1.4, respectively. Figure 7(b) displays the SCR with the different input peak powers. Different with other four kinds of DIF, a better SCR is achieved under condition of soliton number is 1.4, along with a bigger pedestal and a higher side-lobe component which may degrade the system

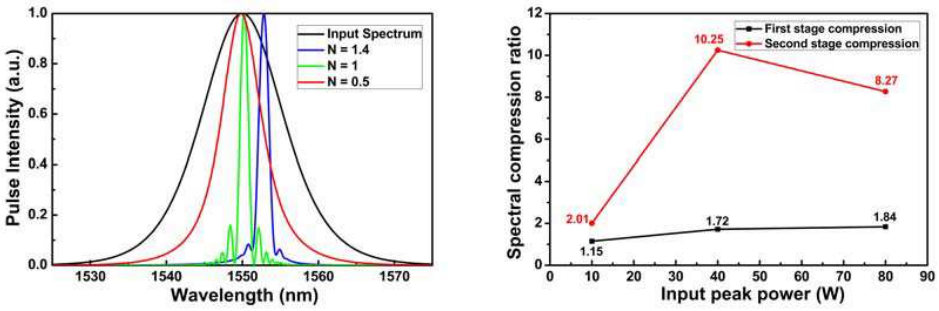

(a) (b)

Figure 5: (a) Spectrum evolution of two-stage spectral compression structure employed a exponential DIF with the input peak powers of 10 W, 40 W and 80 W (red line, $N = 0.5$; green line, $N = 1$; blue line, $N = 1.4$, respectively). (b) SCR with the different input peak powers.

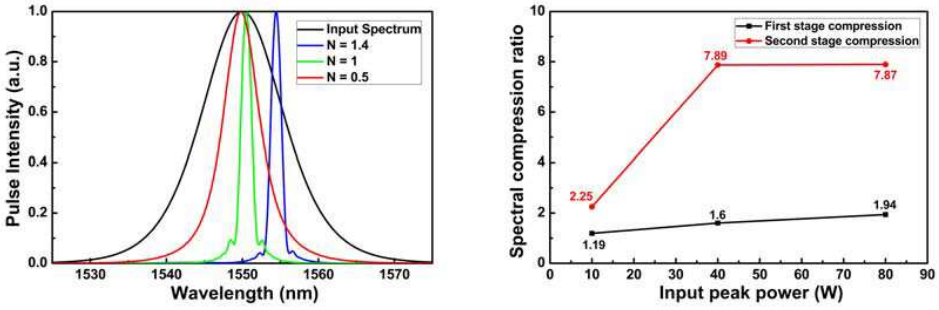

(a) (b)

Figure 6: (a) Spectrum evolution of two-stage spectral compression structure employed a Gaussian DIF with the input peak powers of 10 W, 40 W and 80 W (red line, $N = 0.5$; green line, $N = 1$; blue line, $N = 1.4$, respectively). (b) SCR with the different input peak powers.

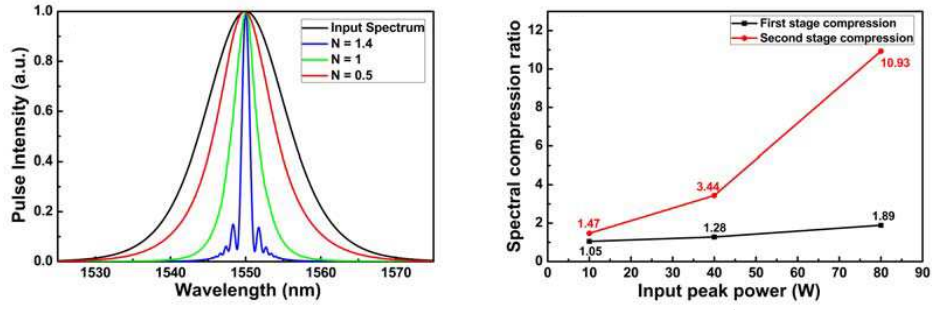

(a) (b)

Figure 7: (a) Spectrum evolution of two-stage spectral compression structure employed a logarithmic DIF with the input peak powers of 10 W, 40 W and 80 W (red line, $N = 0.5$; green line, $N = 1$; blue line, $N = 1.4$, respectively). (b) SCR with the different input peak powers.

performance. Moreover, there is no Raman soliton self-frequency shift which is the key for the spectral compression and the resolution improvement of all-optical quantization.

4. CONCLUSION

In a conclusion, a novel two-stage spectral compression structure is presented, employed a DIF as the first stage and an NOLM composed of an HNLF in the loop as the second stage. Five sorts of DIF with different distribution of dispersion coefficient is analyzed one by one in the two-stage scheme. Spectral compression ratio, which is defined as the ratio of the input to the output spectral width (FWHM), is used to describe the performance scheme. Numerical simulation result shows Logarithmic DIF is suitable for the two-stage scheme, obtain a SCR as high as 10.93 without a Raman self-frequency soliton shift under the condition of soliton number is equal to 1.4.

ACKNOWLEDGMENT

This work is partially supported by Chinese 973 Program under Grant No. 2012CB315701, National Nature Science Foundation of China (No. 61205109), Science and Technology Innovation Team of Sichuan Province (No. 2011JTD0001).

REFERENCES

1. Nishitani, T., K. Tsuyoshi, and I. Kazuyoshi, "Resolution improvement of all-optical analog-to-digital conversion employing self-frequency shift and self-phase-modulation-induced spectral compression," *IEEE Journal of Selected Topics in Quantum Electronics*, Vol. 14, No. 3, 724–732, 2008.
2. Sauteret, C., M. Novaro, and O. Martin, "Passive pulse shaping by spectral narrowing of picosecond pulses," *Applied Optics*, Vol. 20, No. 8, 1487–1490, 1981.
3. Oberthaler, M. and R. A. Höpfel, "Special narrowing of ultrashort laser pulses by self-phase modulation in optical fibers," *Applied Physics Letters*, Vol. 63, No. 8, 1017–1019, 1993.
4. Planas, S. A., M. N. L. Pires, C. C. H. Brito, et al., "Spectral narrowing in the propagation of chirped pulses in single-mode fibers," *Optics Letters*, Vol. 18, No. 9, 699–701, 1993.
5. Washburn, B. R., J. A. Buck, and S. E. Ralph, "Transform-limited spectral compression due to self-phase modulation in fibers," *Optics Letters*, Vol. 25, No. 7, 445–447, 2000.
6. Andresen, E. R., J. Thøgersen, and S. R. Keiding, "Spectral compression of femtosecond pulses in photonic crystal fibers," *Optics Letters*, Vol. 30, No. 15, 2025–2027, 2005.
7. Doran, N. J. and D. Wood, "Nonlinear-optical loop mirror," *Optics Letters*, Vol. 13, No. 1, 56–58, 1988.

Cr^{2+}: ZnSe Crystal Based High Power Passively Q-switched Tm-doped Fiber Laser

Yulian He, **Zhuo Li**, **Hongyu Luo**, **Lele Wang**, **Lian Han**, **and Jianfeng Li**
State Key Laboratory of Electronic Thin Films and Integrated Devices
School of Optoelectronic Information
University of Electronic Science and Technology of China (UESTC)
Chengdu 610054, China

Abstract— We presented a passively Q-switched Tm^{3+}-doped fiber laser using Cr^{2+} : ZnSe crystal as saturable absorber. By employing a crystal with 70% initial transmission, stable Q-switched pulses with a repetition rate of 150.7 kHz and pulse duration of 160 ns were achieved at the maximum pump power of 7.13 W. The obtained maximum output power of 1.32 W was also the reported highest level from the Cr^{2+} : ZnSe crystal based passively Q-switched Tm^{3+}-doped fiber lasers. Moreover, an 80% initial transmission Cr^{2+} : ZnSe crystal was also employed to compare. Stable Q-switched pulses with maximum output power of 0.96 W at a repetition rate of 138.1 kHz and pulse duration of 352 ns were obtained at the launched pump power of 4.19 W. Further increasing of the pump power will lead to the unstable Q-switching regime.

1. INTRODUCTION

Pulsed lasers operating at 2 μm eye safe wavelength region have attracted substantial attention owing to their widespread applications in metrology, remote sensing, free-space communication, time-resolved molecular spectroscopy, and mid-IR supercontinuum generation. Comparing to mode-locking, Q-switching provided the potential of delivering high power and high energy pulses, and more compact and flexible scheme would also be obtained if combining the preferred passively Q-switching and the fiber laser. Until now, a variety of passively Q-switched fiber lasers around 2 μm have been reported employing various saturable absorbers (SAs), e.g., semiconductor saturable absorber (SESAM) [2], graphene [3–5] and Cr^{2+} : ZnSe crystal [6–8]. In contrast to the other SAs, Cr^{2+} : ZnSe crystal was more favored in high power and high energy pulsed fiber lasers because of its large damage threshold of 2.8 J/cm^2 [9]. J. K. Sahu et al. demonstrated a passively Q-switched Tm^{3+}-doped fiber laser with pulse energy and duration of 12 μJ and 16 ns at 1822 nm, respectively [6]. F. Z. Qamar et al. realized a 1.9 μm single-clad passively Q-switched Tm^{3+}-doped fiber laser producing pulse duration of 330 ns and peak power of 15 W [7]. Y. Tang et al. achieved stable 2 μm passively Q-switching using a short double-clad Tm^{3+}-doped fiber, pulse energy of over 14 μJ and pulse duration of 120 ns at a repetition rate of 53 kHz were obtained.

In this paper, we demonstrated a passively Q-switched Tm^{3+}-doped fiber laser with Cr^{2+} : ZnSe crystals as the SA. Stable Q-switching regimes were both achieved using 70% and 80% initial transmission Cr^{2+} : ZnSe crystals, respectively. In the former case, maximum Q-switched pulse power of 1.32 W with pulse energy and duration of 8.74 μJ and 160 ns at a repetition of 150.7 kHz were achieved. In the latter case, the stable Q-switching was finally terminated at the launched pump power of 4.19 W yielding maximum output power of 0.96 W but free from crystal damage.

2. EXPERIMENTAL SYSTEM

The schematic diagram of Cr^{2+} : ZnSe crystal passively Q-switched Tm^{3+}-doped fiber laser was shown in Figure 1. Two 793 nm diode lasers were used to pump the active fiber through a $(2+1)\times 1$ pump combiner (ITF Canada). One signal port of the pump combiner was perpendicularly cleaved to provide 4% feedback by Fresnel reflection and act as the output coupler. The other signal port was spliced to a 3 m double-clad Tm^{3+}-doped active fiber (Coractive, DCF-TM-6/125) which had a hexagonal shaped inner cladding with a diameter of 125 μm and a numerical aperture (NA) of > 0.45. The core diameter and NA were 6 μm and 0.23, respectively. The pump absorption coefficient at 790 nm was 1.4 ± 0.3 dB/m. In order to avoid the parasitic lasing, the other end of the Tm^{3+}-doped fiber was cleaved at an angle of 8^0. The laser beam from angle cleaved end was collimated via an anti-reflection coated ZnSe objective lens and finally terminated by a broadband Au-coated mirror. A confocal scheme including two same anti-reflection coated plano-covex CaF_2 lens with focal length of 40 mm was inserted between the objective lens and the Au-coated mirror along the light path. Then 70% and 80% initial transmission Cr^{2+} : ZnSe crystals fabricated by

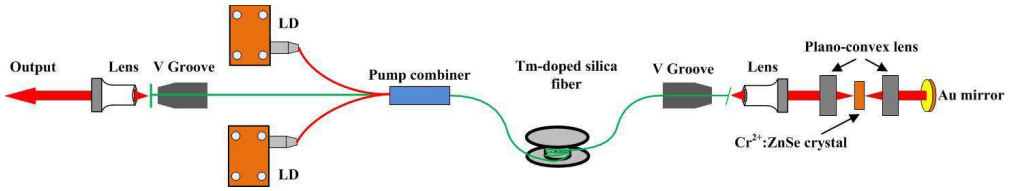

Figure 1: Experimental setup of Cr^{2+} : ZnSe crystal passively Q-switched Tm^{3+}-doped fiber laser.

post-growth thermal diffusion of iron in polycrystalline ZnSe were introduced into the confocal scheme, respectively. At the output end, another objective lens was employed to collimate the output laser and a 2 µm bandpass filter was used to block the residual pump. An InGaAs detector (Photonic Solution ET-5000F) with response time of approximately 28 ps connected with a 500 MHz bandwidth digital oscilloscope was used to monitor the pulse train. An RF spectrum analyzer (Advantest R3267) with resolution bandwidth of 10 Hz to 100 MHz was used to measure the signal-to-noise ratio (SNR) of the pulses. A monochromator with scanning resolution of 0.005 nm (Princeton instrument Acton SP2300) was used to measure the laser spectrum.

3. RESULTS AND DISCUSSION

Firstly, the Cr^{2+} : ZnSe crystal with 70% initial transmission was employed. The oscillator started to operate at continuous wave (CW) regime after reaching the launched pump power of 0.81 W. As the pump power was increased to 1.5 W, stable Q-switched pulses were achieved with corresponding pulse train and envelope shown in Figures 2(a) and (c), respectively. In this case, the obtained pulse width and repetition rate were 198 ns and 21.4 kHz, respectively. The stable Q-switching regime can be maintained to the maximum pump power of 7.13 W as shown in Figures 2(b) and (c), with an increasing repetition rate of 150.7 kHz and decreasing pulse duration of 160 ns. Figure 3(a) shows the measured spectrum of Q-switched pulses at the maximum launched pump power of 7.13 W. The center wavelength and FWHM bandwidth were 1985 nm and 15.3 nm, respectively. Figure 3(b) shows the measured radio frequency (RF) spectrum of the pulse train at a scanning span of 140 kHz and a resolution of 100 Hz. Such high SNR of 56 dB indicated the stable Q-switched operation of this laser.

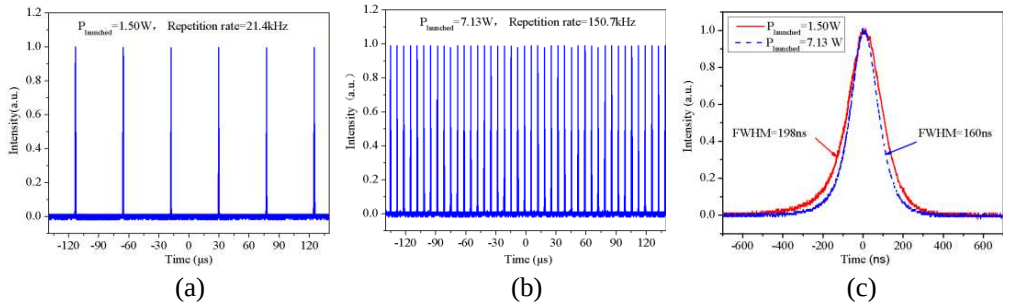

Figure 2: Q-switched pulse train at the launched pump power of (a) 1.5 W, (b) 7.13 W, and (c) their single pulse envelopes.

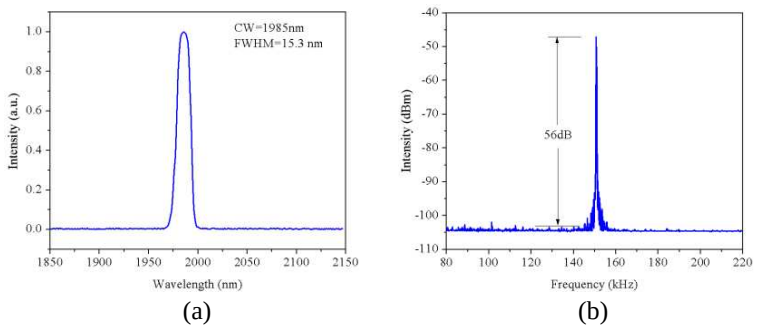

Figure 3: (a) Measured optical spectrum and (b) RF spectrum at the launched pump power of 7.13 W.

The measured repetition rate and pulse duration as a function of launched pump power were shown in Figure 4(a). It is observed that the repetition rate increased almost linearly from 21.4 kHz to 150.7 kHz as the launched pump power increased from 1.5 W to the maximum of 7.13 W. On contrary, the pulse duration decreased as the increased pump power as a result of strengthened cavity net gain which matched well with the typical Q-switched pulses evolution [10–12]. However, the speed of pulse narrowing was dramatically slowed down after arriving at the pump power of ∼4 W due mainly to the fully saturable Cr^{2+} : ZnSe crystal hence the dependence of the duration on the pump was weakened. Figure 4(b) shows the pulse power and energy as a function of the launched pump power. It was observed that the pulse power increased near linearly as the pump power and maximum output power of 1.32 W was achieved at a slope efficiency of 20.1%. The pulse energy also increased near linearly with pump power at the beginning, and then tended to saturate once the pump power was larger than ∼4 W as a result of full saturation of the Cr^{2+} : ZnSe crystal. During the available pump range, the pulse energy increased from 7.58 μJ to 8.74 μJ as the launched pump power was increased from 1.5 W to 7.13 W. Note that the saturation energy of the active fiber was calculated to be 15.7 μJ according to the saturable energy formula which was far beyond the measured value in this case. It indicated that the pulse energy was only limited by the Cr^{2+} : ZnSe crystal and further energy improvement was also expected if Cr^{2+} : ZnSe crystal of higher concentration was employed.

Then, an 80% initial transmission Cr^{2+} : ZnSe crystal was employed to replace the previous one in order to further increase the pulse power as a result of lower cavity insertion loss. The similar pulse evolution as the pump power as before was observed. However, after the pump exceeding the launched pump power of 4.19 W, the stable Q-switched pulses in this case tended to become unstable as shown in Figure 5 until the maximum launched pump power of 7.13 W. If re-adjusting the pump power down to 4.19 W, stable Q-switching re-appeared indicating the Cr^{2+} : ZnSe crystal was free from damage. At this launched pump power, broader pulse duration of 352 ns, higher repetition rate of 138.1 kHz, lower pulse energy of 6.92 μJ with respect to that employing 70% initial transmission Cr^{2+} : ZnSe crystal at the same pump level were achieved with maximum pulse power of 0.96 W at a slope efficiency of 25.8%.

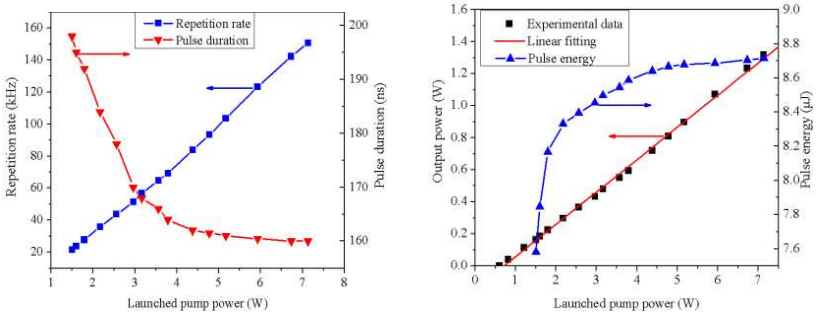

Figure 4: (a) The repetition rate and pulse duration, and (b) the output power and pulse energy of the Q-switched Tm^{3+}-doped fiber laser as a function of the launched pump power.

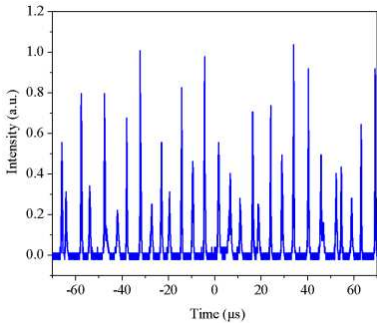

Figure 5: The unstable Q-switched pulse train after the launched pump power of 4.19 W.

4. CONCLUSIONS

In conclusion, we have realized passively Q-switched Tm^{3+}-doped fiber lasers employing 70% and 80% initial transmission Cr^{2+} : ZnSe crystals as the saturable absorber, respectively. In the former case, the pulse duration of 160 ns, pulse energy of 8.74 µJ, repetition rate of 150.7 kHz were achieved at the maximum launched pump power of 7.13 W. The obtained slope efficiency and largest output power were 20.1 % and 1.32 W which was also the highest level generating from the Cr^{2+} : ZnSe crystal based passively Q-switched Tm^{3+}-doped fiber lasers. In the latter case, though stable Q-switching was terminated at the launched pump power of 4.19 W, broader pulse duration, lower pulse energy, higher repetition rate, higher output power and slope efficiency were gained compared to that using the 70% initial transmission Cr^{2+} : ZnSe crystal at the same pump level. Thus if Q-switched pulses of higher output power and slope efficiency were expected, higher initial transmission Cr^{2+} : ZnSe crystal though not benefitting the initiation of Q-switching was preferred. On contrary, lower initial transmission Cr^{2+} : ZnSe crystal was recommended in order to obtain narrower and higher energy Q-switched pulses. Moreover, further pulse narrowing was also possible if shorter cavity was selected, and improved ion concentration of the active fiber was necessary in order to provide enough total cavity gain. The above conclusions can be shifted to crystal-based passively Q-switched fiber lasers operating at other wavelength regions as well, e.g., Co^{2+} : ZnSe crystal based Er^{3+}-doped silica fiber lasers, Fe^{2+} : ZnSe crystal based Ho^{3+}- or Er^{3+}-doped ZBLAN fiber lasers, etc..

ACKNOWLEDGMENT

This work was supported by National Nature Science Foundation of China (Grant Nos. 61377042, 6-1107037 and 61327004), and European Commission's Marie Curie International Incoming Fellowship (Grant No. 911333).

REFERENCES

1. Svelto, O., *Principles of Lasers*, Springer, New York, 2010.
2. Kivistö, S., R. Koskinen, J. Paajaste, S. D. Jackson, M. Guina, and O. G. Okhotnikov, "Passively Q-switched Tm^{3+}, Ho^{3+}-doped silica fiber laser using a highly nonlinear saturable absorber and dynamic gain pulse compression," *Opt. Commun.*, Vol. 16, No. 26, 22058–22063, 2008.
3. Liu, J., J. Xu, and P. Wang, "Graphene-based passively Q-switched 2 µm thulium-doped fiber laser," *Opt. Commun.*, Vol. 284, No. 24, 5319–5322, 2012.
4. Wang, F., F. Torrisi, Z. Jiang, D. Popa, T. Hasan, Z. Sun, W. Cho, and A. C. Ferrari, "Graphene passively Q-switched two-micron fiber lasers," *CLEO Technical Digest*, JW2A.72, San Jose, USA, May 2012.
5. Tang, Y. L., X. C. Yu, X. H. Li, Z. Y. Yan, and Q. J. Wang, "High-power thulium fiber laser Q switched with single-layer grapheme," *Opt. Lett.*, Vol. 39, No. 3, 614–617, 2014.
6. Sahu, J., V. Philippov, J. Kim, C. Codemard, P. Dupriez, J. Nilsson, A. Abdolvand, and N. V. Kuleshov, "Passively Q-switched thulium-doped silica fiber laser," *Conference on Lasers and Electro-Optics*, CThGG7, San Francisco, USA, May 2004.
7. Fadi, Q. Z. and K. A. Terence, "Passive Q-switching of the Tm-silica fibre laser near 2 µm by a Cr^{2+} : ZnSe saturable absorber crystal," *Opt. Commun.*, Vol. 248, No. 4, 501–508, 2005.
8. Tang, Y., Y. Yang, J. Xu, and Y. Hang, "Passive Q-switching of short-length Tm^{3+}-doped silica fiber lasers by polycrystalline Cr^{2+} : ZnSe microchips," *Opt. Commun.*, Vol. 281, No. 22, 5588–5591, 2008.
9. Fedorov, V. V., I. S. Moskalev, S. B. Mirov, T. J. Wagner, M. J. Bohn, P. A. Berry, and K. L. Schepler, "Energy scaling of nanosecond gain-switched Cr^{2+} : ZnSe lasers," *SPIE LASE*, 79121E–79121E-7, San Francisco, USA, Jan. 2011.
10. Li, J. F., H. Y. Luo, Y. L. He, et al., "Semiconductor saturable absorber mirror passively Q-switched 2.97 µm fluoride fiber laser," *Laser Phys. Lett.*, Vol. 11, No. 6, 065102, 2014.
11. Liu, C., C. Ye, Z. Luo, H. Cheng, D. Wu, Y. Zheng, Z. Liu, and B. Qu, "High-energy passively Q-switched 2 µm Tm^{3+}-doped double-clad fiber laser using grapheme-oxide-deposited fiber taper," *Opt. Express*, Vol. 21, No. 1, 204–209, 2013.
12. Laroche, M., A. M. Chardon, J. Nilsson, D. P. Shepherd, W. A. Clarkson, S. Girard, and R. Moncorge, "Compact diode-pumped passively Q-switched tunable Er-Yb double-clad fiber laser," *Opt. Lett.*, Vol. 27, No. 22, 1980–1982, 2002.

Through-Silicon-Via Pairs Modelling via Compressed Sensing

Tao Wang, Jun Fan, Yiyu Shi, and Boping Wu
Missouri University of Science and Technology, USA

Abstract— Through-Silicon-Vias (TSVs) are the critical enabling technique for three-dimensional integrated circuits (3D ICs). While there are a few existing works in literature to model the electrical performance of TSVs, they are either for fixed geometry or in lack of accuracy. In this paper, we use compressed sensing technique to model the electrical performance of TSV pairs. Experimental results indicate that with an exceptionally small number of samples, our model has a maximum relative error of 3.70% compared with full-wave simulations over a wide range of geometry parameters and frequencies.

1. INTRODUCTION

System-in-Package (SiP) technology is widely used today in high-density and small mobile devices such as smart phones, digital cameras, media players, and so on. Three-dimensional Integrated Circuits (3D ICs) technology is being considered as a real breakthrough along this direction, which can be used to achieve higher integration density and higher performance by vertically stacking ICs. Through-Silicon-Via (TSV) is the most critical enabling technique in 3D ICs, which routes the electrical path through all stacked chips. TSV shortens the connection between vertical stacking chips which leads to better electrical performance and more compact size of the system [1–4]. A typical TSV structure can be found in Figure 1.

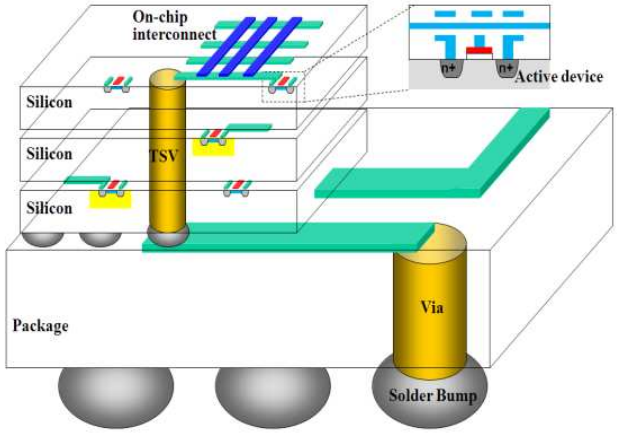

Figure 1: TSV structure in SiP.

It is important to model the TSV structure to estimate the delay, coupling noise and many other electrical performance metrics. In literature, this has been done analytically and numerically. A three dimensional full-wave solver can be used to analyse the TSV structure, but it takes a considerable amount of simulation time for each different geometrical dimension and frequency. In addition, it cannot produce a parameterized model which is desired for design optimization. Towards this, physics-based analytical models have also been developed (e.g., [4, 5]). However, the TSVs are embedded in the semi-conductive silicon substrate, so the behaviour of wave transmission is quite different from that in typical waveguide structures. Also, the properties of semiconductor devices make the rigorous analytical approach even more difficult. Accordingly, the physics-based circuit models proposed are only approximate, and are not quite accurate in a wide range of TSV geometries and frequencies.

A straightforward approach for analytical modeling of TSVs might be to build a look-up-table based on the samples with different geometry parameters and frequencies. However, the full wave simulation to obtain one sample takes a long time. Accordingly, it is not possible to build a model based on a large number of samples. With limited samples, the accuracy of the look-up-table approach is questionable.

In this paper, we propose to build the analytical model for a TSV pair based on compressed sensing technique. Compressed sensing is a recently developed technique to recover signals with randomly distributed samples. It is fast, stable and yields high reconstruction accuracy using an exceptionally small number of samples. Experimental results show that our model has a maximum relative error of 3.70% compared with full-wave simulations over a wide range of geometry parameters and frequencies.

The remainder of the paper is organized as follows: we briefly review the physics-based models in Section 2. Section 3 gives a brief review of the compressed sensing techniques and adapts the technique to the electrical modelling of TSV pairs. Experimental results are presented in Section 4 and concluding remarks are given in Section 5.

2. REVIEW OF PHYSICS-BASED MODEL (PHYSICAL BASED MODELS IS A BETTER NAME. PLEASE MAKE CORRECTIONS IN THE REMAINING OF THE PAPER)

In this paper, we focus on the structure of a pair of signal and ground TSVs, as shown in Figure 2(a). Previously, such a structure inside a lightly-doped silicon substrate has been investigated and a lumped circuit has been proposed, as shown in Figure 2(b) [5].

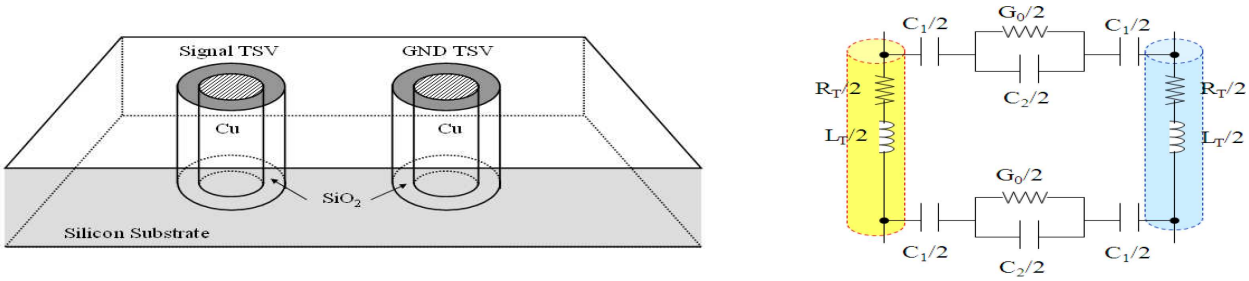

Figure 2: (a) A pair of signal and ground TSVs in a silicon substrate. (b) Lumped circuit model of the TSVs for lightly-doped case.

This structure was modeled with a 3D full-wave simulator, and the E-field distribution was analyzed to investigate a physics-based circuit model. In the model of Figure 2(b), the equations for C_1, C_2, G_0, R_T, and L_T have been derived as

$$C_1 = \frac{2\pi\varepsilon_{\mathrm{SiO_2}}T_L}{\ln\left(\frac{T_D+2T_T}{T_D}\right)}, \tag{1}$$

$$C_2 = \frac{\varepsilon_{Si}\pi T_L}{\ln\left(\frac{T_P}{T_D}+\sqrt{\left(\frac{T_P}{T_D}\right)^2-1}\right)}, \quad \text{and} \tag{2}$$

$$G_0 = \frac{\sigma_{Si}C_2}{\varepsilon_{Si}}, \tag{3}$$

$$R_T = R_{dc}+R_{ac}, \quad \text{and} \tag{4}$$

$$L_T = L_{ext}+2L_{\mathrm{int}}, \tag{5}$$

where $R_{dc}=\frac{2T_L}{\sigma_{Cu}\pi(T_D/2)^2}$, $R_{ac}=\frac{2T_L\sqrt{\pi\mu_0\sigma_{Cu}f}}{\sigma_{Cu}\pi T_D}$ and $L_{ext}=\frac{\mu_0 T_L}{\pi\cosh^{-1}(T_P/T_D)}$, $L_{\mathrm{int}}=\frac{T_L}{2\pi T_D}\sqrt{\frac{\mu_0}{\pi\sigma_{Cu}f}}$.

The above equations were extracted from a TSV structure, where the pitch between the two TSVs (T_P) is 20 µm, the TSV length (T_L) is 20 µm, the TSV diameter (T_D) is 10 µm, and the thickness of SiO_2 (T_T) is 0.2 µm.

For this given TSV geometry, the S-parameters extracted from the circuit model agree well with those obtained from the full-wave simulation up to 20 GHz. However, we notice that the difference becomes quite large (up to about 30%) when the TSV geometries deviates significantly from the settings listed above, or at high frequencies.

3. COMPRESSIVE SENSING BASED MODELS

3.1. Overview of Compressed Sensing

Compressed sensing is a recently developed technique in the field of signal processing. Its key idea is to use an exceptionally small number of samples to recover a desired signal, under the assumption that the signal has sparse representation in certain basis functions. In this section, we will use a one-dimensional signal to briefly review the technique.

Consider a signal $f(t)$ in the t-domain, which can be represented as

$$f(t) = \sum_{i=1}^{N} \psi_i \alpha_i \tag{6}$$

where ψ_i $(i = 1, \ldots, N)$ are the basis functions in a Hilbert space. α_i are the coefficients and can be calculated as

$$\alpha_i = \langle f, \psi_i \rangle, \quad i - 1, \ldots, N \tag{7}$$

where $\langle\rangle$ operation is the inner product defined in the space spanned by the basis functions. If the basis functions are chosen properly, many of the coefficients can be zero. Specifically, if the vector $\boldsymbol{\alpha}$ ($\boldsymbol{\alpha} \in \mathbb{R}^N$) formed by the coefficients has at most k non-zero entries, we call it k-sparse.

Under the assumption that we are able to find a set of basis functions to represent $f(t)$ with k-sparse coefficients, compressed sensing enables us to accurately recover f with $M = O(k \log(N/k))$ samples, when the sampling are "random" enough to follow certain properties.

There are many different ways to choose the basis functions and to reconstruct the signal. In Section 3, we will describe one that best fits the electrical performance of TSV pairs. A more detailed description of the compressed sensing techniques, including these conditions required to apply the technique, is beyond the scope of the paper. Interested readers are referred to [6, 7] for more details.

3.2. Application to Electrical Modeling of TSV Pairs

To apply the compressed sensing technique to the electrical modelling of TSV pairs, we will first need to select a proper set of basis functions such that the S parameter, as a function of T_P, T_L, T_D, T_T and f has a sparse representation. While there are many possible candidates such as wavelet functions and polynomials, in our experiments we find that discrete cosine functions offer the best sparsity and accuracy.

In this section, we use bold to indicate a vector (e.g., $\mathbf{f}$), bold capitalization to indicate a matrix (e.g., $\mathbf{A}$), and subscript to denote the element-wise index (e.g., $\mathbf{f}_i$).

Without loss of generosity, we discretize the range of interest for T_P, T_L, T_D, T_T and f and label them in integers, i.e., $T_P = \{1, 2, \ldots, P\}$, $T_L = \{1, 2, \ldots, L\}$, $T_D = \{1, 2, \ldots, D\}$, $T_T = \{1, 2, \ldots, T\}$ and $f = \{1, 2, \ldots, F\}$. As such, the basis functions we selected are

$$g_{i,j,k,l,m}(T_P, T_L, T_D, T_T, f) = \cos\left(\frac{\pi(2T_p - 1)(i-1)}{2T}\right) \ldots \cos\left(\frac{\pi(2f-1)(m-1)}{2F}\right)$$

where $1 \le i \le P$, $1 \le j \le L$, $1 \le k \le D$, $1 \le l \le T$, $1 \le m \le F$.

These basis functions need some constant coefficients to normalize, but omitting them does not affect our algorithm. The S parameter function $f(T_P, T_L, T_D, T_T, f)$ can be represented using these basis functions as

$$\begin{aligned} f\left(T_P, T_L, T_D, T_T, f\right) \;=\; & \sum_{i=1}^{P} \sum_{j=1}^{L} \sum_{k=1}^{D} \sum_{l=1}^{T} \sum_{m=1}^{F} \alpha(i,j,k,l,m) g_{i,j,k,l,m} \\ & (T_P, T_L, T_D, T_T, f) \end{aligned} \tag{8}$$

where $\alpha(i, j, k, l, m)$ are the coefficients. (8) it is in fact the discrete cosine transform (DCT).

Next, we randomly select M ($M \ll PLDTF$) samples with geometry parameters ($T_{P_u}, T_{L_u}, T_{D_u}$, T_{T_u}, f_u) $(u = 1, 2, \ldots, M)$ and measure the corresponding crosstalk f_u. As such, we can obtain a set of equations based on these sampling points, i.e.,

$$\begin{aligned} f_u\left(T_P, T_L, T_D, T_T, f\right) \;=\; & \sum_{i=1}^{P} \sum_{j=1}^{L} \sum_{k=1}^{D} \sum_{l=1}^{T} \sum_{m=1}^{F} \alpha(i,j,k,l,m) g_{i,j,k,l,m} \\ & (T_{P_u}, T_{L_u}, T_{D_u}, T_{T_u}, f_u) \end{aligned} \tag{9}$$

It is worthwhile to note here, that in (4), the only unknowns are the coefficients $\alpha(i, j, k, l, m)$. And we can re-cast it in a compact form as

$$\mathbf{f} = \mathbf{A}\boldsymbol{\alpha} \tag{10}$$

where $\mathbf{A}$ is a constant matrix formed by $g_{i,j,k,l,m}(T_{P_u}, T_{L_u}, T_{D_u}, T_{T_u}, f_u)$. $\boldsymbol{\alpha}$ is a vector formed by $\alpha(i, j, k, l, m)$. And $\mathbf{f}$ is a vector formed by f_u.

If we can get the coefficients by directly solving (10), and insert them back to (8), we will have an analytical expression for the crosstalk estimation. Unfortunately, we will not be able to do so, because the number of equations (M), which is equal to the number of samples available, is much smaller than the number of variables ($N = PLDTF$). In other words, (10) is an underdetermined equation.

With the assumption that the coefficients $\alpha(i, j, k, l, m)$ are sparse, however, we can *approximately* solve it using an optimization. Specifically, we can solve

$$\min_\alpha \|\boldsymbol{\alpha}\|_0 \quad \text{subject to } \mathbf{f} = \mathbf{A}\boldsymbol{\alpha} \tag{11}$$

where $\|\boldsymbol{\alpha}\|_0$ is the zero norm (the number of non-zeros in $\boldsymbol{\alpha}$). The meaning of such an optimization is to minimize the non-zeros in the coefficients subject to the measurement data available.

Zero-norm is a nonlinear function, and thus (11) is still very difficult to solve. Accordingly, we resort to an approximate version of (11), by replacing the zero-norm with one-norm, i.e.,

$$\min_\alpha \|\boldsymbol{\alpha}\|_1 \quad \text{subject to } \mathbf{f} = \mathbf{A}\boldsymbol{\alpha} \tag{12}$$

It is well established in literature that the optimal solution (12) is also sparse.

It is obvious that the quality of the compressed sensing algorithm depends on how to efficiently solve (12). While many different methods can be used such as the interior point methods [8] and the homotopy method [9], in this paper we choose to use the iteratively-weighted least squares (IRLS) method [10], as in the experiments we find that it leads to the most accurate results, with a minimum runtime.

Finally, we would like to present an extra benefit of our method. With the analytical expression (8), we are able to easily calculate the sensitivity information with respect to each geometry parameters accurately. Such information is extremely valuable to guide the design optimization.

4. EXPERIENTIAL RESULTS

To verify how the above discussed compressed sensing technique works in the electrical modelling of TSV pairs, we randomly select 400 samples in the range of interest as summarized in Table 1. HFSS is used to conduct full-wave simulation for those samples [11] to obtain the S-parameters. We then randomly select 380 of them to build the model using compressed sensing, and reserve the remaining 20 to verify the model accuracy.

Table 1: Range of the 400 samples.

Parameter		Range
T_P	TSV pitch	5 µm ∼ 25 µm
T_L	TSV length	10 µm ∼ 100 µm
T_D	TSV diameter	5 µm ∼ 25 µm
T_T	SiO_2 thickness	0.1 µm ∼ 1 µm
f	frequency	1 GHz ∼ 20 GHz

We first verify that the basis functions (DCT) we used actually lead to a sparse representation of the S parameter. For this purpose, we construct a model for the magnitude of S_{11} based on the 380 sampling points, and calculate the coefficients by solving the one-norm problem (12). The results are depicted in Figure 3. This indicates that the problem is indeed suitable for our compressed sensing based technique.

To visualize where these non-zero coefficients are in the DCT basis, we fix T_D, T_T and f, and plot the coefficients with various T_P and T_L in Figure 4. As we can see from the figure, many of the non-zero coefficients are clustered near the low frequency region (close to zero), with only a few in the high-frequency region. This reflects that the function is smooth and has little sharp transitions.

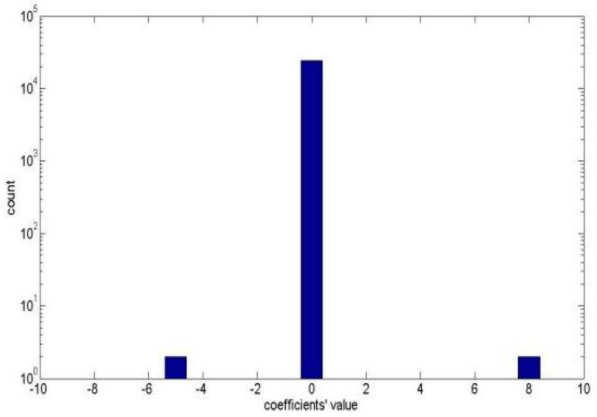

Figure 3: Histogram of the coefficients $\alpha(i, j, k, l, m)$. Note that log-scale is used for y-axis.

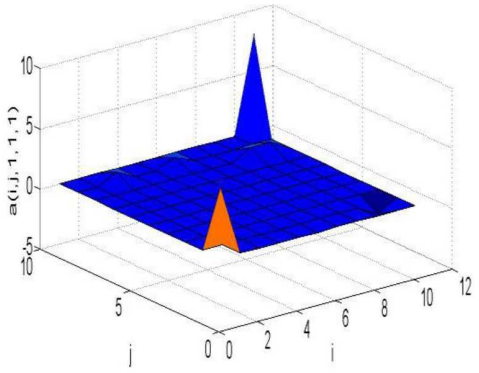

Figure 4: Plot of the coefficients $\alpha(i, j, 1, 1, 1)$.

In addition, we verify the accuracy of our model (CS) and compare it with the physics-based models [5] on the 20 reserved samples. The results are shown in Table 2. From the table we can see that the S-parameters predicted by our model closely match the results from HFSS, with an average error of 0.25% and maximum error of 0.83%, while that from [5] has an average error of 11.2% and maximum error of 29.93%.

Finally, we compare the phase and magnitude of S_{11}, S_{21} and S_{22} from our model and from the full-wave simulations. From the table we can see that our method has a maximum error of 3.94% over the 20 samples. In addition, it is also interesting to note that in general our model results in more error in phase than in magnitude. This is probably due to the existence of sharper transitions in the phase of those S-parameters.

Table 2: Accuracy verification (S_{11}(mag)).

Parameters					**HFSS**	**[5]**		**CS**	
T_T (μm)	T_D (μm)	T_P (μm)	T_L (μm)	f (μm)	S_{11}(mag)	S_{11}(mag)	relative error	S_{11}(mag)	relative error
0.8	23	9	90	3.0	0.0599	0.0542	9.48%	0.0597	0.26%
0.7	17	9	30	6.0	0.009	0.0092	1.95%	0.0090	0.09%
0.9	9	5	20	7.0	0.0047	0.004	15.04%	0.0047	0.09%
0.3	25	21	70	8.0	0.0379	0.0389	2.74%	0.0378	0.29%
1	9	5	40	9.0	0.0167	0.012	28.00%	0.0166	0.25%
0.7	25	11	60	10.0	0.0354	0.0363	2.66%	0.0352	0.40%
0.4	7	7	100	11.0	0.0328	0.0345	5.13%	0.0327	0.32%
0.9	13	17	20	12.0	0.0063	0.0066	4.31%	0.0064	0.80%
0.6	19	5	70	13.0	0.0503	0.0491	2.35%	0.0503	0.02%
0.9	13	17	20	14.0	0.0071	0.0069	2.86%	0.0071	0.11%
0.6	15	7	70	15.0	0.0437	0.0392	10.24%	0.0437	0.03%
0.8	23	9	90	17.0	0.0658	0.0565	14.09%	0.0656	0.31%
0.7	11	15	30	19.0	0.0107	0.0107	0.07%	0.0107	0.05%
1	9	5	40	20.0	0.0157	0.0117	25.48%	0.0157	0.02%
0.2	17	23	80	15.0	0.0387	0.0406	4.82%	0.0387	0.02%
0.3	5	11	40	13.0	0.016	0.0114	28.96%	0.0160	0.17%
0.1	15	25	50	19.0	0.0303	0.025	17.46%	0.0303	0.19%
0.9	13	17	20	7.0	0.0091	0.0076	16.66%	0.0091	0.12%
0.4	11	21	40	13.0	0.0231	0.0162	29.93%	0.0230	0.68%
0.9	13	17	20	17.0	0.0066	0.0067	1.78%	0.0066	0.83%

Table 3: Relative error (CS compared to HFSS).

	Minimum	**average**	**maximum**
S_{11} (mag)	0.02%	0.25%	0.83%
S_{11} (phase)	0.09%	0.78%	2.44%
S_{21} (mag)	0.04%	0.15%	0.73%
S_{21} (phase)	0.01%	0.76%	3.70%
S_{22} (mag)	0.00%	0.40%	1.97%
S_{22} (phase)	0.03%	1.13%	3.94%

5. CONCLUSION

In this paper, a compressed sensing based model is established to predict the S parameter of TSV pairs, as a function of the pitch of two TSVs, TSV length , TSV diameter, the thickness of SiO_2 and the frequency. It only requires a small number of samples, yet it has a maximum error of 3.70% over a wide range of geometry parameters and frequencies.

ACKNOWLEDGMENT

This paper is partially supported by the University of Missouri Research Board (UMRB). Address comments to Prof. Yiyu Shi (yshi@mst.edu).

REFERENCES

1. Jang, D. M., C. Ryu, K. Y. Lee, B. H. Cho, J. Kim, T. S. Oh, W. J. Lee, and J. Yu, "Development and evaluation of 3-D SiP with vertically interconnected Through Silicon Vias (TSV)," *57th Proceedings Electronic Components and Technology Conference, ECTC'07*, 847–852, May 29–Jun. 1, 2007.
2. Yoon, K., G. Kim, W. Lee, T. Song, J. Lee, H. B. Lee, K. Park, and J. Kim, "Modeling and analysis of coupling between TSVs, metal, and RDL interconnects in TSV-based 3D IC with silicon interposer," *11th Electronics Packaging Technology Conference, EPTC'09*, 702–706, Dec. 9–11, 2009.
3. Knickerbocker, J. U., P. S. Andry, B. Dang, R. R. Horton, M. J. Interrante, C. S. Patel, R. J. Polastre, K. Sakuma, R. Sirdeshmukh, E. J. Sprogis, S. M. Sri-Jayantha, A. M. Stephens, A. W. Topol, C. K. Tsang, B. C. Webb, and S. L. Wright, "Three-dimensional silicon integration," *IBM Journal of Research and Development*, Vol. 52, No. 6, 553–569, Nov. 2008.
4. Pak, J. S., J. Cho, J. Kim, J. Lee, H. Lee, K. Park, and J. Kim, "Slow wave and dielectric quasi-TEM modes of Metal-Insulator-Semiconductor (MIS) structure Through Silicon Via (TSV) in signal propagation and power delivery in 3D chip package," *2010 Proceedings 60th Electronic Components and Technology Conference (ECTC)*, 667–672, Jun. 1–4, 2010.
5. Wang, H., J. Kim, Y. Shi, and J. Fan, "The effects of substrate doping density on the electrical performance of Through-SIlicon Vias," *Proc. of Asia-Pacific EMC Symposium*, Jeju Island, Korea, 2011.
6. Tsaig, Y. and D. L. Donoho, "Extensions of compressed sensing," *Signal Processing*, Vol. 86, No. 3, 549–571, 2006.
7. Donoho, D. L., "Compressed sensing," *IEEE Trans. Inf. Theory*, Vol. 52, No. 4, 1289–1306, 2006.
8. Nesterov, Y. and A. Nemirovskii, "Interior-point polynomial algorithms in convex programming," *SIAM Studies in Applied Mathematics*, Vol. 13, Society for Industrial and Applied Mathematics (SIAM), Philadelphia, PA, 1994.
9. Osborne, M., B. Presnell, and B. Turlach, "On the LASSO and its dual," *J. Comput. Graph. Statist.*, Vol. 9, No. 2, 319–337, 2000.
10. Daubechies, M. I., R. DeVore, M. Fornasier, and C. Gunturk, "Iteratively re-weighted least squares minimization for sparse recovery," *Comm. Pure Appl. Math.*, Vol. 63, No. 1, 1–38, 2010.
11. *High Frequency Structure Simulator*, Ansoft.

Method to Reduce Coupon Lengths for Transmission Line *S*-parameter Measurements through Elimination of Guided-wave Multiple Reflections

Shaowu Huang, Jeff Loyer, Richard Kunze, and Boping Wu
Intel Corporation, 2800 Center Dr, DuPont, WA 98327, USA

Abstract— A new approach is proposed to reduce the length requirements for the measurement of transmission line S-parameters in printed circuit boards (PCBs). In addition, the approach improves the accuracy of measurements. We demonstrate that guided-wave multiple reflections of the transmission lines in the signal propagation direction limits use of short transmission lines samples. The elimination of the guided-wave multiple reflections is introduced to overcome the coupon length limit for accurate measurements of transmission lines S-parameters. We introduce implementations of the proposed approach in the time and frequency domains. For time-domain measurements, we do corrections to remove the reflection noise signals from received signals: the first is the waveform manipulation for removing the internal reflections, and the second is the novel manipulation of S-parameters to compensate for reflected and transmitted losses. For native frequency-domain measurements, that manipulation of the S-parameters is used as a de-embedding correction method to remove the reflected and transmitted signals' contributions from the S-parameters. Simulation results are presented to demonstrate the efficiency and accuracy of the new approach. Results show that the new approach can reduce the minimum length of high-speed transmission lines from 8 inches in traditional industry standards to only 0.5 inch for both 4-port TDR/VNA measurements and 2-port SET2DIL.

1. INTRODUCTION

The signal distortion and attenuation in transmission lines have been a key issue for printed circuit board (PCB) design and application. The issue escalates as the PCB operates at faster speed and higher frequency. Therefore, the PCB industry needs accurate and efficient methodologies to qualify and monitor the performance of PCB manufactured by the supply chains. This is extremely important in high volume manufacturing.There are several methodologies recommended by IPC specification [1], for example, the single-ended TDR/TDT to differential insertion loss (SET2DIL) method [2].

In existing methods, a trace length of 8 inches is typically chosen to achieve accurate measurements of S-parameters, particularly of insertion loss. For manufacturing, shorter coupons are desired, but two major effects require longer coupons: 1) limits of receiver sensitivity require insertion loss to be high enough to exceed the noise floor of the instrument, and 2) for non-50 ohm DUTs (or 100 ohms differential), return loss effects can cause errors in insertion loss measurements. A longer trace is chosen so that the effects of multiple reflections on the insertion loss measurements are negligible, compared to the insertion loss measured, and signal amplitude is sufficient for the instrument used.

In this work, we propose a new approach to reduce the length requirements for the measurement of transmission line S-parameters in printed circuit boards (PCBs). In addition, the approach improves the accuracy of measurements. In this work, we demonstrate that guided-wave multiple reflections of the transmission lines in the signal propagation direction limits use of short transmission lines samples. The reflections can be also interpreted as standing waves, waveguide modes, waveguide resonances, or layered medium multiple reflections. The elimination of the guided-wave multiple reflections is introduced to overcome the coupon length limit for accurate measurements of transmission lines S-parameters. We introduce implementations of the proposed approach in the time and frequency domains. For time-domain measurements, we do corrections to remove the reflection noise signals from received signals: the first is the waveform manipulation for removing the internal reflections, and the second is the novel manipulation of S-parameters to compensate for reflected and transmitted losses. For native frequency-domain measurements, that manipulation of the S-parameters is used as a de-embedding correction method to remove the reflected and transmitted signals' contributions from the S-parameters. Simulation results are presented to demonstrate the efficiency and accuracy of the new approach. Results show that the new approach can reduce the minimum length of high-speed transmission lines from 8 inches in traditional industry standards to only 0.5 inch for both 4-port TDR/VNA measurements and 2-port SET2DIL.

This can significantly reduce coupon area, allowing more compact PCB designs and enabling the ability to include coupons in the actual design, rather than as "outriggers" (dedicated portions of a PCB panel for manufacturing testing).

2. METHODOLOGY

2.1. Multiple Reflections of Transmission Lines with Finite Length

Figure 1 shows the diagram for a transmission line with length "d" and the signal propagation in z direction. For non-magnetic materials $\mu_1 = \mu_2 = \mu_3 = \mu_0$, $\varepsilon_1 = \varepsilon_{r1}\varepsilon_0$, $\varepsilon_2 = \varepsilon_{r2}\varepsilon_0$, $\varepsilon_3 = \varepsilon_{r3}\varepsilon_0$, with μ_0 and ε_0 as the free space permeability and permittivity respectively. The wave numbers are: $k_1 = k_0\sqrt{\varepsilon}_{r1}$, $k_2 = k_0\sqrt{\varepsilon}_{r2}$, and $k_3 = k_0\sqrt{\varepsilon}_{r3}$, where $k_0 = 2\pi f\sqrt{\mu_0\varepsilon_0}$ and f is a frequency of interest. In general transmission lines problems we can assume the wave propagation directions are same as the normal direction of the interfaces, which are the z direction. It is notable that different approaches can be used to describe the phenomena of the multiple reflections of transmission lines. In this section, we calculate the effects of the multiple reflections in term of varying dielectric materials in transmission lines. In the appendix, we show another way to evaluate the effects through using impedance discontinuities. Note that the analysis in terms of impedance will give same prediction if the loss/attenuation and phase is taken into account.

The total reflection coefficient from Region 1 to Region 2 for TM wave is [3]

$$R^{total} = \frac{R_{12} + R_{23}\exp\left(-2jk_2d\right)}{1 + R_{12}R_{23}\exp\left(-2jk_2d\right)} \tag{1}$$

And the total transmission coefficient from Region 1 to Region 3 for TM wave is

$$T^{total} = \frac{T_{12}T_{23}\exp\left(-jk_2d\right)\exp\left(jk_3d\right)}{1 + R_{12}R_{23}\exp\left(-2jk_2d\right)} \tag{2}$$

where R_{12} is the reflection coefficient from Region 1 to Region 2, R_{23} the reflection coefficient from Region 2 to Region 3, T_{12} the transmission coefficient from Region 1 to Region 2, and T_{23} the transmission coefficient from Region 2 to Region 3. Using Taylor series expansion, "$1/(1+x) = 1 - x + x^2 - x^3 + \ldots$", and truncating it up to first order, (1) and (2) can be casted to

$$R^{total} = R_{12} + R_{23}T_{12}T_{23}\exp\left(-2jk_2d\right) - R_{23}^2T_{12}T_{23}\exp\left(-4jk_2d\right) + \ldots \tag{3}$$

and

$$T^{total} = T_{12}T_{23}\exp\left(-jk_2d\right)\exp\left(jk_3d\right) - T_{12}T_{23}R_{12}R_{23}\exp\left(-3jk_2d\right)\exp\left(jk_3d\right) + \ldots \tag{4}$$

For the characterization of transmission lines, we represent the transmission lines as uniform and infinitely long in the propagation direction. Thus, we only need R_{12} as the reflection coefficient, and $T_{12}T_{23}\exp(-jk_2d)\exp(jk_3d)$ as the transmission coefficient. All other terms are noise signals, which exist due to the multiple reflections between the two interfaces. These noise signals will impair the accuracy of the measurements for s-parameters of a realistic (of finite length) transmission line. We further illuminate the problem using a ladder diagram showed in Figure 2.

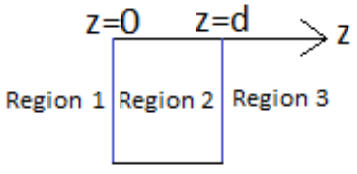

Figure 1: Diagram of a uniform transmission line with a finite length of d. The signal propagates in z direction. Region 1 has ε_1, μ_1, k_1, Region 2 has ε_2, μ_2, k_2, and Region 3 has ε_3, μ_3, k_3.

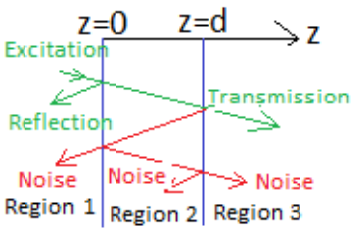

Figure 2: Ladder diagram for the measurement system of a uniform transmission line of finite length, including excitation signal, targeted reflection signal, targeted transmission signal, and noise signals due to the multiple reflections.

2.2. The Effects of Finite Length on the Characterization of Reflection Signals

Next, we will discuss the length effects on the measurements. The single interface reflection and transmission coefficients can be written as

$$R_{12} = \frac{\varepsilon_{r2}k_1 - \varepsilon_{r1}k_2}{\varepsilon_{r2}k_1 + \varepsilon_{r1}k_2} = \frac{\sqrt{\varepsilon}_{r2} - \sqrt{\varepsilon}_{r1}}{\sqrt{\varepsilon}_{r2} + \sqrt{\varepsilon}_{r1}} \tag{5a}$$

$$R_{23} = \frac{\varepsilon_{r3}k_2 - \varepsilon_{r2}k_3}{\varepsilon_{r3}k_2 + \varepsilon_{r2}k_3} = \frac{\sqrt{\varepsilon}_{r3} - \sqrt{\varepsilon}_{r2}}{\sqrt{\varepsilon}_{r3} + \sqrt{\varepsilon}_{r2}} \tag{5b}$$

$$T_{12} = 1 + R_{12} = \frac{2\sqrt{\varepsilon}_{r2}}{\sqrt{\varepsilon}_{r2} + \sqrt{\varepsilon}_{r1}} \tag{5c}$$

$$T_{23} = 1 + R_{23} = \frac{2\sqrt{\varepsilon}_{r3}}{\sqrt{\varepsilon}_{r3} + \sqrt{\varepsilon}_{r2}} \tag{5d}$$

Note, Equations 5(a)–5(d) indicate that the reflection and transmission coefficients are determined by the ratios of $\varepsilon_{r3}/\varepsilon_{r2}$ and $\varepsilon_{r1}/\varepsilon_{r2}$. Thus, in the modeling of multiple reflections, the Region 1 and Region 3 can be simplified as air as reference permittivity, which has $\varepsilon_{r1} = 1$ and $\varepsilon_{r3} = 1$. Then

$$R_{12} = \frac{\sqrt{\varepsilon}_{r2} - 1}{\sqrt{\varepsilon}_{r2} + 1} \tag{6a}$$

$$R_{23} = \frac{1 - \sqrt{\varepsilon}_{r2}}{1 + \sqrt{\varepsilon}_{r2}} = -R_{12} \tag{6b}$$

$$T_{12} = 1 + R_{12} = \frac{2\sqrt{\varepsilon}_{r2}}{\sqrt{\varepsilon}_{r2} + 1} \tag{6c}$$

$$T_{23} = 1 - R_{12} = \frac{2}{1 + \sqrt{\varepsilon}_{r2}} \tag{6d}$$

$$R^{total} = \frac{R_{12} - R_{12}\exp\left(-2jk_0d\right)}{1 - R_{12}^2\exp\left(-2jk_2d\right)} \tag{7}$$

Let's define the reflection signal-to-noise SNR_R, as the ratio of the first noise reflection signal to the targeted reflection signal,

$$SNR_R = \frac{R_{12}}{R_{23}T_{12}T_{23}\exp\left(-2jk_2d\right)} = -\exp\left(2jk_0\sqrt{\varepsilon}_{r2}d\right) \tag{8}$$

Examining the relative permittivity of region 2

$$\varepsilon_{r2} = \varepsilon'_{r2}\left(1 - j\tan\delta_2\right) \tag{9}$$

$$\sqrt{\varepsilon}_{r2} = \sqrt{\varepsilon'_{r2}\left(1 - j\tan\delta_2\right)} = \sqrt{\varepsilon'_{r2}}\sqrt{\left(1 - j\tan\delta_2\right)} \tag{10}$$

Since the loss tangent $\tan\delta_2 \ll 1$ (about $0.005 \sim 0.03$) for typical PCB dielectric materials, rewrite (10) using Taylor series expansion, "$\sqrt{1-x} = 1 - \frac{1}{2}x - \frac{1}{4}x^2 - \ldots$", and truncating it up to first order, we have

$$\sqrt{\varepsilon}_{r2} \approx \sqrt{\varepsilon'}_{r2}\left(1 - \frac{1}{2}j\tan\delta_2\right) \tag{11}$$

Substituting (10) into (8) yields

$$SNR_R = T_{12}T_{23}\exp\left(2jk_0\sqrt{\varepsilon'_{r2}}d\right)\exp\left(k_0\sqrt{\varepsilon'_{r2}}d\tan\delta_2\right) \tag{12}$$

The free space wave number $k_0 = \frac{2\pi}{\lambda_0}$, λ_0 is the free space wavelength. Then

$$SNR_R = T_{12}T_{23}\exp\left(4\pi j\sqrt{\varepsilon'_{r2}}\frac{d}{\lambda_0}\right)\exp\left(2\pi\sqrt{\varepsilon'_{r2}}\tan\delta_2\frac{d}{\lambda_0}\right) \tag{13}$$

The ratio of trace length to wavelength $\frac{d}{\lambda_0}$ depends on the frequency. $\frac{d}{\lambda_0}$ is small at low frequency while is large at high frequency. If we write SNR_R in dB scale we arrive at

$$20\log_{10}|SNR_R| = 20\log_{10}\exp\left(2\pi\sqrt{\varepsilon'_{r2}}\tan\delta_2\frac{d}{\lambda_0}\right) - 20\log_{10}|T_{12}T_{23}| \tag{14}$$

Thus,

$$20\log_{10}|SNR_R| \approx 289\cdot\sqrt{\varepsilon'_{r2}}\tan\delta_2\frac{d}{\lambda_0} - 20\log_{10}\left|\frac{4\sqrt{\varepsilon}_{r2}}{\left(\sqrt{\varepsilon}_{r2}+1\right)^2}\right| \tag{15}$$

SNR_R. The term $289\cdot\sqrt{\varepsilon'_{r2}}\tan\delta_2\frac{d}{\lambda_0}$ is the critical parameter, the loss of the transmission line. It increases with $\frac{d}{\lambda_0}$, (the electrical length of the trace). The term $-20\log_{10}|\frac{4\sqrt{\varepsilon}_{r2}}{(\sqrt{\varepsilon}_{r2}+1)^2}|$ is an inherent error term, a constant, and is due to the multiple reflections at the interfaces. In Table 1, we show the SNR_R for a typical PCB transmission lines of 8 inches and 1 inch at 4 GHz.

Table 1: SNR_R for differential transmission lines at 4 GHz: (a) length of transmission line = 8 inches; (b) length of transmission line = 1 inch.

Dielectric Material Types	ε'_{r2}	$\tan\delta_2$	d	λ_0 at 4 GHz	$289\cdot\sqrt{\varepsilon'_{r2}}\tan\delta_2\frac{d}{\lambda_0}$	$-20\log_{10}\left\|\frac{4\sqrt{\varepsilon}_{r2}}{(\sqrt{\varepsilon}_{r2}+1)^2}\right\|$	$20\log_{10}\|SNR_R\|$
Regular FR4	4	0.02	8 inches	2.953 inches	31.32 dB	1.02 dB	32.34 dB
Mid-loss	3.7	0.01	8 inches	2.953 inches	15.06 dB	0.91 dB	15.97 dB
Low-loss	3.5	0.005	8 inches	2.953 inches	7.32 dB	0.84 dB	8.16 dB

(a) 8 inches

Dielectric Material Types	ε'_{r2}	$\tan\delta_2$	d	λ_0 at 4 GHz	$289\cdot\sqrt{\varepsilon'_{r2}}\tan\delta_2\frac{d}{\lambda_0}$	$-20\log_{10}\left\|\frac{4\sqrt{\varepsilon}_{r2}}{(\sqrt{\varepsilon}_{r2}+1)^2}\right\|$	$20\log_{10}\|SNR_R\|$
Regular FR4	4	0.02	1 inches	2.953 inches	3.91 dB	1.02 dB	4.94 dB
Mid-loss	3.7	0.01	1 inches	2.953 inches	1.88 dB	0.91 dB	2.80 dB
Low-loss	3.5	0.005	1 inches	2.953 inches	0.92 dB	0.84 dB	1.75 dB

(b) 1 inch

2.3. The Effects of Finite Length on the Characterization of Transmission Signals

Similarly, let's define the transmission signal-to-noise SNR_T, as the ratio of the first noise transmission signal to the targeted transmission signal,

$$SNR_T = \frac{T_{12}T_{23}\exp(-jk_2d)\exp(jk_3d)}{-T_{12}T_{23}R_{12}R_{23}\exp(-3jk_2d)\exp(jk_3d)} = \frac{1}{R_{12}^2}\exp\left(2jk_0\sqrt{\varepsilon}_{r2}d\right) \tag{16}$$

thus

$$SNR_T = \frac{1}{R_{12}^2}\exp\left(2jk_0\sqrt{\varepsilon'_{r2}}d\right)\exp\left(k_0\sqrt{\varepsilon'_{r2}}d\tan\delta_2\right) \tag{17}$$

Then

$$SNR_T = \frac{1}{R_{12}^2}\exp\left(4\pi j\sqrt{\varepsilon'_{r2}}\frac{d}{\lambda_0}\right)\exp\left(2\pi\sqrt{\varepsilon'_{r2}}\tan\delta_2\frac{d}{\lambda_0}\right) \tag{18}$$

Write SNR_T in dB scale

$$20\log_{10}|SNR_T| = 20\log_{10}\exp\left(2\pi\sqrt{\varepsilon'_{r2}}\tan\delta_2\frac{d}{\lambda_0}\right) - 40\log_{10}(|R_{12}|) \tag{19}$$

then

$$20\log_{10}|SNR_T| \approx 289\cdot\sqrt{\varepsilon'_{r2}}\tan\delta_2\frac{d}{\lambda_0} - 40\log_{10}\left(\left|\frac{\sqrt{\varepsilon}_{r2}-1}{\sqrt{\varepsilon}_{r2}+1}\right|\right) \tag{20}$$

SNR_T has terms with identical properties as SNR_R: the critical term $289 \cdot \sqrt{\varepsilon'_{r2}} \tan\delta_2 \frac{d}{\lambda_0}$ due to the loss of transmission line and the constant, inherent error term $-40\log_{10}(|\frac{\sqrt{\varepsilon}_{r2}-1}{\sqrt{\varepsilon}_{r2}+1}|)$ due to the multiple reflections at the interfaces. In Table 2, we list the SNR_T for a typical PCB transmission lines of 8 inches and 1 inches at 4 GHz.

Table 2: SNR_T for differential transmission lines at 4 GHz: (a) length of transmission line = 8 inches; (b) length of transmission line = 1 inch.

Dielectric Material Types		ε'_{r2}	$\tan\delta_2$	d	λ_0 at 4 GHz	$\frac{289\cdot\sqrt{\varepsilon'_{r2}}}{\tan\delta_2 \frac{d}{\lambda_0}}$	$-40\log_{10}\left(\left\|\frac{\sqrt{\varepsilon}_{r2}-1}{\sqrt{\varepsilon}_{r2}+1}\right\|\right)$	$20\log_{10}\|SNR_R\|$
Regular FR4	FR4	4	0.02	8 inches	2.953 inches	31.32 dB	19.08 dB	50.40 dB
Mid-loss	IS-415	3.7	0.01	8 inches	2.953 inches	15.06 dB	20.02 dB	35.08 dB
Low-loss	IT-150DA	3.5	0.005	8 inches	2.953 inches	7.32 dB	20.72 dB	28.05 dB

(a) 8 inches

Dielectric Material Types		ε'_{r2}	$\tan\delta_2$	d	λ_0 at 4 GHz	$\frac{289\cdot\sqrt{\varepsilon'_{r2}}}{\tan\delta_2 \frac{d}{\lambda_0}}$	$-20\log_{10}\left\|\frac{4\sqrt{\varepsilon}_{r2}}{\left(\sqrt{\varepsilon}_{r2}+1\right)^2}\right\|$	$20\log_{10}\|SNR_R\|$
Regular FR4	FR4	4	0.02	1 inches	2.953 inches	3.91 dB	19.08 dB	23.00 dB
Mid-loss	IS-415	3.7	0.01	1 inches	2.953 inches	1.88 dB	20.02 dB	21.90 dB
Low-loss	IT-150DA	3.5	0.005	1 inches	2.953 inches	0.92 dB	20.72 dB	21.64 dB

(b) 1 inch

2.4. Compensation of Two Transmission Losses for Insertion Loss Measurements

Note that, in the measurement of single ended insertion loss (S_{21}) or differential insertion loss (Sdd21), the loss results S_{21} or Sdd21 need to comprehend the effects of T_{12} and T_{23} when short coupons ($< 8''$) are used. The waveform manipulation used in the current SET2DIL method only removes internal reflections, but does not compensate the two transmission losses, which is critical for shorter length coupons. As shown in Figure 1, because of the impedance mismatch, the transmission signal loses energy when propagating through the two interfaces: (1) the first interface from reference media (Region 1) to transmission line (Region 2), (2) the second interface from transmission line (Region 2) to reference media (Region 3).

Assuming the transmission line has the differential impedance Z_d, the two reference media have the same differential impedance Z_0, the total transmission coefficients $= T_1 * T_2 = (2 * Z_d/(Z_d + Z_0)) * (2 * Z_0/(Z_d + Z_0))$. The final SDD21 needs to be re-calculated as:

$$\text{Final SDD21} = [\text{SET2DIL SDD21 obtained with waveform manipulation}]/(T_1 * T_2). \quad (21)$$

In dB scale, it is:

$$\text{Final SDD21\_dB} = [\text{SET2DIL SDD21\_dB}] - 20 * \log 10(T_1 * T_2) \quad (22)$$

Normalized to unit inch length, then it is

$$\text{Final SDD21\_dB/inch} = [\text{SET2DIL SDD21\_dB/inch}] - 20 * \log 10(T_1 * T_2)/(\#\text{ of inches}) \quad (23)$$

Note, the term of $20 * \log 10(T_1 * T_2)/(\#$ of inches) is relatively small (compared to SDD21) for longer coupons (hence the choice of $8''$ for the original coupons), but it is significant for short coupons. For example, if $Z_d = 80$ ohms and $Z_0 = 100$ ohms, then $-20 * \log 10(T_1 * T_2) = 0.108$ dB. Then using different lengths of coupons, we have different amount of loss per inch, as shown in the following Table 3. We see it is only 0.013 dB/inch for 8 inch length coupons, however, it becomes 0.216 dB/inch for 0.5 inch coupons. It should be pointed out that this term is constant for all frequencies.

With the waveform manipulation for removing the internal reflections and the correction term to compensate the two transmission losses, weobtain the simulation results of 2-port SET2DILtime domain measurement and 4-port traditional scope time domain measurement, with 0.5 inch coupons.

They are in good agreement with all the simulation results of VNA frequency domain measurement results with three different lengths, 8 inches, 4 inches, and 0.5 inches. These results will be presented in Section 3.

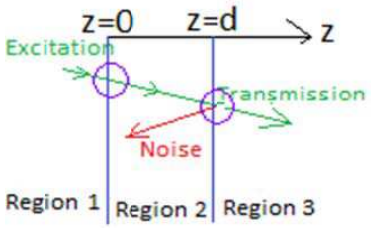

Figure 3: Diagram to show the two transmission losses, which are due to the two discontinuities (shown as two pink circles) in the interfaces between transmission line (Region 2) and reference media (Region 1 and Region 3).

Thus, for time domain measurements, either 2-port SET2DIL, or 4-port traditional scope, we need to do two corrections: to manipulate waveform for removing the internal reflections, and to compensate the two transmission losses. With these two corrections, we can use coupons much shorter than 8 inches to accurately measure the SDD21. In the Appendix, we also use simple circuit formula to further explain the error calculation.

Table 3: $-20 * \log 10(T_1 * T_2)/(\#$ of inches), for different coupon lengths, assuming $Z_d = 80$ ohms and $Z_0 = 100$ ohms.

	8 inches	4 inches	2 inches	1 inches	0.5 inches
$-20 * \log 10(T_1 * T_2)/(\#$ of inches)	0.013 dB	0.027 dB	0.054 dB	0.108 dB	0.216 dB

3. SIMULATIONS

Two different simulations, frequency domain simulation and time domain simulation, are performed to verify the proposed method for frequency domain measurement and time domain measurement, respectively.

In the frequency domain simulation, we use 3D full wave simulator HFSS to directly solve the S-parameters for two coupons, as showed in Figure 4. Figure 4(a) is a 4-port coupon, which is used in in characterization of differential transmission line. In the simulation, we used three different lengths; 0.5 inch, 2 inches, and 8 inches. Figure 4(b) is a 2-port SET2DIL coupon, which can be used for charactering differential loss. The simulation results are showed in Figure 5(a). The label "VNA" (Vector Network Analyzer) refers to results obtained directly from frequency domain simulation. Note, appropriate de-embedding have been done to the 0.5 inch and 2 inches S-parameters in Figure 5(a).

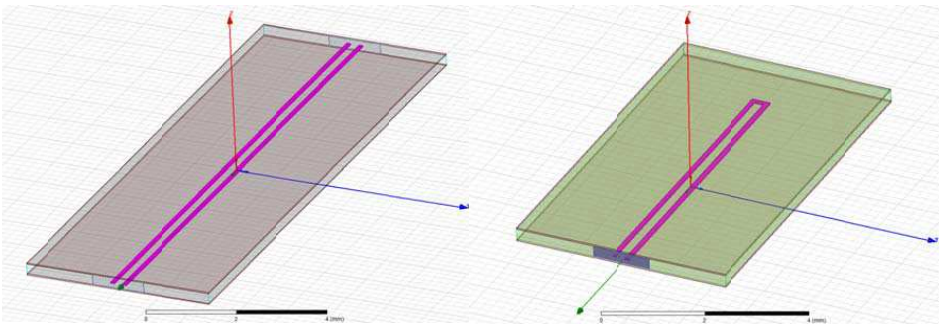

(a) (b)

Figure 4: 3D full wave simulation using HFSS: (a) a traditional 4-port coupon for characterizing two adjacent transmission lines; (b) SET2DIL coupon with 2 ports for characterizing a differential transmission line pair.

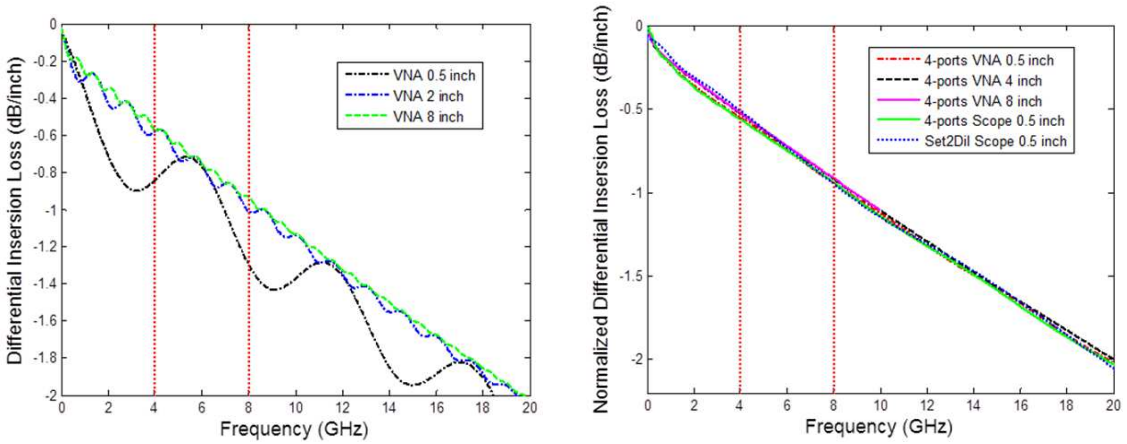

Figure 5: (a) Original Differential Insertion Loss obtained using frequency domain HFSS simulations. VNA" refers to the frequency results; (b) Frequency results obtained by using de-embedding(black, blue, and green curves), and time domain results obtained by removing the reflection signals. "Scope" (Oscilloscope) refers to the time domain results, while "VNA" refers to the frequency results.

In the time domain simulation, we obtain the step responses transformed from the frequency simulation S-parameter results. After removing the reflection signals, we transform the step response back to differential insertion loss in S-parameters. The results are shown as the curves in Figure 5(b). "Scope" (Oscilloscope) refers to the time domain results, while "VNA" refers to the frequency results. We see that time domain and frequency domain simulations are in good agreement. The results support the new approach, a trace as short as 0.5 inch can accurately give differential insertion loss.

4. CONCLUSION

A new approach is proposed to reduce the length requirements for the measurement of transmission line S-parameters in printed circuit boards (PCBs). The method also improves the accuracy of measurements. The proposed approach is implemented in the time and frequency domains. Simulations are performed to verify the **new** approach. Results show that the new approach can reduce the minimum length of high-speed transmission lines from 8 inches in traditional industry standards to only 0.5 inch for both 4-port TDR/VNA measurements and 2-port SET2DIL.

5. APPENDIX

In this section, we use simple circuit formula to estimate the errors due to the impedance discontinuities of first order reflection. In the Figure 6, the reflection coefficient due to the first impedance discontinuity is

$$\Gamma_1 = \frac{\mathrm{Z}_{DUT} - Z_{in}}{\mathrm{Z}_{DUT} + Z_{in}}$$

and transmission coefficient due to the first impedance discontinuity is

$$\mathrm{T}_1 = \frac{2\mathrm{Z}_{DUT}}{\mathrm{Z}_{DUT} + Z_{in}}$$

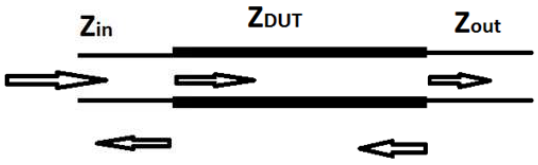

Figure 6: Diagram to show the impedance discontinuities.

And the reflection coefficient due to the second impedance discontinuity is

$$\Gamma_2 = \frac{\mathrm{Z}_{out} - Z_{DUT}}{\mathrm{Z}_{out} + Z_{DUT}}$$

the transmission coefficient due to the second impedance discontinuity is

$$\begin{aligned} \mathrm{T}_2 &= 1 + \Gamma_2 \\ \mathrm{T}_2 &= \frac{2\mathrm{Z}_{out}}{\mathrm{Z}_{DUT} + Z_{out}} \end{aligned}$$

The total error in the insertion loss measurement is

$$Error_T \cong \mathrm{T}_1\mathrm{T}_2$$

The total error in the return loss measurement is

$$Error_R \cong -\mathrm{T}_1\Gamma_2\mathrm{T}_1$$

The relative error in the return loss is

$$Error'_R \cong \frac{Error_R}{\Gamma_1}$$

In dB scale,

$$\begin{aligned} 20\log_{10}|Error_T| &\cong 20\log_{10}|\mathrm{T}_1\mathrm{T}_2| \\ 20\log_{10}\left|Error'_R\right| &\cong 20\log_{10}\left|\frac{\mathrm{T}_1\Gamma_2\mathrm{T}_1}{\Gamma_1}\right| \end{aligned}$$

Numerical results:

1. Assume the interconnect is for single end transmission line, $\mathrm{Z}_{DUT} = 40\,\mathrm{ohm}$, $Z_{in} = 50\,\mathrm{ohm}$, and $Z_{out} = 50\,\mathrm{ohm}$, then

$$\begin{aligned} \Gamma_1 &= \frac{80-100}{80+100} = -0.1111 \\ \mathrm{T}_1 &= 1 - 0.0526 = 0.8889 \\ \Gamma_2 &= \frac{50-45}{50+45} = 0.1111 \\ \mathrm{T}_2 &= 1 + 0.0526 = 1.1111 \\ 20\log_{10}|Error_T| &= -0.11\,\mathrm{dB} \\ 20\log_{10}\left|Error'_R\right| &= -2.05\,\mathrm{dB} \end{aligned}$$

1. Assume the interconnect is for differential transmission line, $\mathrm{Z}_{DUT} = 80\,\mathrm{ohm}$, $Z_{in} = 100\,\mathrm{ohm}$, and $Z_{out} = 100\,\mathrm{ohm}$, then

$$\begin{aligned} \Gamma_1 &= \frac{80-100}{80+100} = -0.1111 \\ \mathrm{T}_1 &= 1 - 0.0526 = 0.8889 \\ \Gamma_2 &= \frac{50-45}{50+45} = 0.1111 \\ \mathrm{T}_2 &= 1 + 0.0526 = 1.1111 \\ 20\log_{10}|Error_T| &= -0.11\,\mathrm{dB} \\ 20\log_{10}\left|Error'_R\right| &= -2.05\,\mathrm{dB} \end{aligned}$$

Note, for PCB transmission lines, the errors $Error_T$ and $Error'_R$ due to the impedance discontinuities are approximately constant (1) over different frequencies in frequency domain, and (2) for different lengths of DUT transmission lines.

REFERENCES

1. IPC-TM-650 Test Methods Manual, http://www.ipc.org/test-methods.aspx.
2. Loyer, J. and R. Kunze, "SET2DIL: Method to derive differential insertion loss from single-ended TDR/TDT measurements," *DesignCon*, 2010.
3. Chew, W. C., *Waves and Fields in Inhomogenous Media*, IEEE Press, 1995.

Performance Evaluation of an OFDM-based BPSK PLC System in an Impulsive Noise Environment

A. M. Nyete, T. J. O. Afullo, and I. Davidson
Discipline of Electrical, Electronic and Computer Engineering
University of KwaZulu-Natal, Durban, South Africa

Abstract— Power line carrier (PLC) communication provides a ready medium for broadband internet connectivity and as well as monitoring, control and automation functions for both industries and homes. In fact, the power line network is the most expansive network in the world reaching every room in every facility connected to the power grid. Thus, PLC technology is the most economical way to provide internet connectivity and home networking in rural/remote areas. However, the original design of power lines was not for communication purposes but electrical power transmission. Thus, PLC technology provides a readily available channel that is hostile when used for communication purposes. This hostility is due to the many problematic characteristics of the power line network from a communications perspective. They include reflections due to impedance mismatch, frequency varying attenuation, multipath due to the cable joints, as well as the different types of noise inherent in the channel. In this paper, we investigate the impact of impulse noise on the performance of an OFDM based BPSK PLC channel. This is motivated by the fact that the very characteristics of the impulse noise, namely; pulse width, amplitude and interarrival time, have not been studied at an elementary level in terms of their influence on the performance of the PLC channel. The mathematics behind the impulse function is utilized in an attempt to fully characterize the impulse noise for the PLC channel. The performance of the PLC system is compared in terms of the bit error rate (BER) characteristics for given signal to noise ratio (SNR) values for different impulsive noise parameters.

1. INTRODUCTION

PLC technology entails the utilization of the power grid for the transfer of information from the transmitter to the receiver. This technology is attractive due to the fact that no additional network layout is required to be able to send information; apart from terminal devices. PLC technologies are mainly classified into two; narrowband and broadband depending on the frequency band of operation. Broadband PLC operates in the frequency range between 1 MHz to 300 MHz. Narrowband PLC operates in the frequency range between 3 kHz to 500 kHz. Power lines terminate at almost every home and this enables the use of the low voltage network as a last mile and last inch access solution for communication purposes. PLC is useful in automation of meter reading services, pre-paid billing services, automation of fault detection, load management, high data rate internet access and home Television carrier services. PLC networks also form part of local area networking solutions [1, 2].

However, the PLC channel is a hostile environment for use as a communications media. This is primarily so because, the channel characteristics are highly varying with frequency, time, loads and topology. The channel is also plagued with different sources of noise which are difficult to effectively describe parametrically. The main noise types in PLC include background noise, narrowband interference and impulse noise. Also the signal is attenuated as it traverses the channel from the transmitter to the receiver. This attenuation is mainly dominated by frequency selective fading. The proper choice of modulation techniques, coding schemes, access techniques and error correction methods for the PLC channel is a thorny issue. This is primarily so because of the many characteristics of the PLC channel that have to be catered for. These would range from the different types of noise mentioned above, frequency selective fading, uncertainty of the channel transfer function, channel capacity constraints, bandwidth limitations, and the threshold bit error rate requirements [1–7]. The biggest threat to PLC performance is noise; and impulsive noise is the most dominant. This noise and its impact on the performance of an Orthogonal Frequency Division Multiplexing (OFDM) based Binary Phase Shift Keying (BPSK) system is the main focus of this paper.

2. IMPULSIVE NOISE

Impulsive noise is the most severe form of noise in PLC channels. It is mainly caused by the switching ON/OFF of electrical appliances or faults in the network. It is classified into three main categories [1, 8–10]:

1. Impulsive noise that is synchronous with the mains frequency and is periodic: This type of impulsive noise is cyclostationary and is synchronous with the mains frequency. It is generated by silicon controlled rectifiers in different power supplies.
2. Impulsive noise that is periodic but asynchronous with the mains frequency: This category of impulsive noise is generated by periodic impulses whose repetition rates are between 50 to 200 kHz.
3. Asynchronous impulsive noise: This kind of impulsive noise is very unpredictable and is the most dominant. It exhibits no regular occurrence and mainly arises from transients that originate from the connection or disconnection of electrical appliances from the power line network. The impulses can last for between some microseconds and a few milliseconds with a random occurrence. The power spectral density for this kind of noise can go as high as 50 dB above the background noise. It is also sometimes referred to as sporadic impulsive noise.

The four basic parameters that describe impulsive noise are the impulse width t_w, arrival time t_{arr}, interarrival time t_{IAT} or the impulse distance t_d and the impulse amplitude, A. The impulse width is the time duration that an impulse event lasts. The interarrival time is defined as the time difference between the start of two consecutive impulse events. The impulse distance is the time between the end of an impulsive event and the beginning of another. Thus, it defines the frequency of occurrence of the impulsive noise. The three basic impulsive event time parameters are related by the following expression [8, 10]:

$$t_{IAT} = t_w + t_d = t_{arr,i+1} - t_{arr,i} \tag{1}$$

And, using a general impulse function $imp(t)$ with unit amplitude and unit width, a train of impulses can be described by [10]:

$$n_{imptrain}(t) = \sum_{t=1}^{N} A_i \cdot imp\left(\frac{t - t_{arr,i}}{t_{w,i}}\right) \tag{2}$$

where $n_{imptrain}(t)$ is the train of impulses. The parameters A, t_w and t_{arr}, can be used to derive secondary parameters that are crucial in analysis of impulse noise and studying its behavioural characteristics over time. One of these secondary parameters is the impulse rate, given by [8]:

$$r_{imp} = \frac{N_{imp}}{T_{win}} \tag{3}$$

where N_{imp} is the number of impulses that occur within a given window of observation T_{win}. Another key aspect would be the actually disturbed time, which can be determined from the "disturbance ratio"; which by definition is the ratio of the sum of the widths of all impulses generated within a window of observation, and the length of the window, that is [8]:

$$disturbance\ ratio = \frac{\sum_{i=1}^{N_{imp}} t_{w,i}}{T_{win}} \tag{4}$$

3. OFDM BASED BPSK SYSTEM

OFDM modulation technique divides the coded information into blocks that are then transmitted using N subcarriers. These subcarriers are orthogonal to each other and this eliminates any interference between them. Thus, in practice some of the subcarriers are not affected by the impulsive noise. This is dependent on the moment at which the impulse occurs, and whether or not a particular subcarrier is negatively affected. Thus, OFDM, like many other multicarrier modulation schemes spreads the impulsive noise across all the subcarriers [11].

For an OFDM based BPSK system with N subcarriers, the symbol stream after the BPSK modulator is passed through a serial-to-parallel converter, whose output will be a set of N BPSK symbols denoted by $\{S_0, S_1, \ldots, S_{N-1}\}$ corresponding to the symbols transmitted over each carrier. For the generation of the transmitted signal, the inverse discrete Fourier transform (IDFT) is performed on the N symbols. N is chosen to be a power of 2 and the IDFT in this case is implemented using the inverse fast Fourier transform (IFFT) algorithm. The OFDM symbol that is produced by the IFFT is a sequence given by $\{S_0, S_1, \ldots, S_{N-1}\}$, whose length is N, where [12]:

$$s_k = \frac{1}{\sqrt{N}} \sum_{i=0}^{N-1} S_i^{j2\pi ki/N}, \quad 0 \le k \le N-1 \tag{5}$$

The symbols received after the filtering and sampling process, assuming that perfect synchronization and timing takes place, are expressed as follows:

$$r_k = s_k + n_k \quad 0 \leq k \leq N-1 \tag{6}$$

where n_k is the impulsive noise. At the receiver's side, an N-point fast Fourier transform (FFT) is performed on the received N sequence symbols $\{r_0, r_1, \ldots, r_{N-1}\}$ yielding:

$$R_k = \frac{1}{\sqrt{N}} \sum_{i=0}^{N-1} r_i^{-j2\pi ki}, \quad 0 \leq k \leq N-1 \tag{7}$$

4. SYSTEM PERFORMANCE EVALUATION

In this presentation, the amplitude of the noise impulses is assumed to be constant for ease of comparison. A constant impulse width of 50 µs is used while the interarrival time is varied between 100 µs and 10000 µs according to Equation (1). The channel gain is assumed to be random. The performance of the system as the interarrival time is varied is then determined in terms of the bit error rate and signal to noise ratio. The results for the three different values of the interarrival time considered are shown in Figure 1. From this graph, the performance of the system is best when $IAT = 10000$ µs while the worst performance is obtained when the $IAT = 100$ µs. This means that the impact of the impulsive noise on the system is least when the interarrival time is greatest at a constant pulse duration and constant pulse amplitude. The reverse is also true. For example, at a BER value of 10^{-3}, the SNR values for $IAT = 10000$ µs, 1000 µs and 100 µs are 15 dB, 19.5 dB and 21.5 dB respectively. Thus, a smaller value of interarrival time would translate to more frequent impulses and deteriorated system performance, and vice versa.

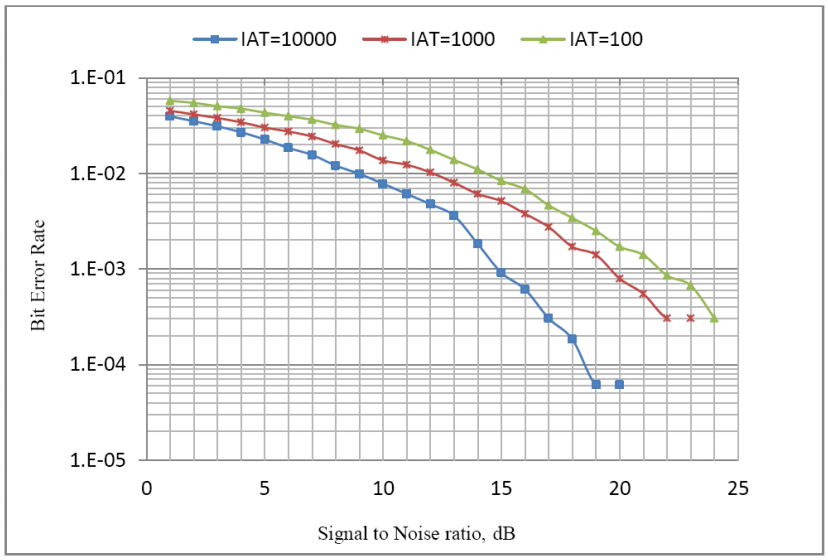

Figure 1: Performance characteristics for different noise interarrival time values.

5. CONCLUSION AND FUTURE WORK

In this paper, a simplistic approach has been presented that assesses the impact of impulsive noise on an OFDM based BPSK PLC system. The statistical properties of the impulsive noise have been utilized in their most basic form. The error statistics obtained show that the performance of the system is highly limited in the presence of the impulsive noise in the channel. We observe that a lower value of the IAT translates to more frequent impulses and this deteriorates the error performance of the system. This is explained by the fact the IAT and the impulse distance are directly related. Thus to improve on the system performance, modern digital signal processing techniques should be implemented on the channel. These techniques will be able to correct both bit and burst errors that occur due to the corruption of the signal by noise. The results presented here are based on hypothetical parameters of the impulsive noise and therefore our focus in future is to conduct extensive noise measurements that can then be used to model the noise and determine its actual impact on a real-time PLC channel.

ACKNOWLEDGMENT

The authors wish to acknowledge the funding support received from ESKOM through the EPPEI program.

REFERENCES

1. Berger, L. T, A. Schwager, and J. J. Escudero-Garzas, "Power line communications for smart grid applications," *Journal of Electrical and Computer Engineering*, Vol. 2013, Article 712376, 16 pages, 2013.
2. Ferreira, H. C., et al., "Power line communications: An overview," *IEEE AFRICON 1996*, 558–563, Stellenbosch, September 24–27, 1996.
3. Zwane, F. and T. J. O. Afullo, "An alternative approach in power line communication channel modelling," *Progress In Electromagnetics Research C*, Vol. 47, 85–93, 2014.
4. Lazaropoulos, A. G., "Broadband transmission characteristics of overhead high-voltage power line communication channels," *Progress In Electromagnetics Research B*, Vol. 36, 373–398, 2012.
5. Zimmermann, M. and K. Dostert, "A multipath model for the power line channel," *IEEE Transactions on Communications*, Vol. 50, No. 4, 553–559, April 2002.
6. Mulangu, C. T., T. J. Afullo, and N. M. Ijumba, "Modelling of broadband powerline communication channels," *SAIEE,* Vol. 102, No. 4, 107–112, December 2011.
7. Mulangu, C. T., T. J. O. Afullo, and N. M. Ijumba, "Estimation of specific attenuation due to scattering points for broadband PLC channels," *PIERS Proceedings*, Kuala Lumpur, Malaysia, 92–96, March 27–30, 2012.
8. Zimmermann, M. and K. Dostert, "Analysis and modeling of impulsive noise in broad-band powerline pommunications," *IEEE Transactions on Electromagnetic Compatibility*, Vol. 44, No. 1, 249–258, November 2002.
9. Bert, L. D., P. Caldera, D. Schwingshackl, and A. M Tonello, "On noise modeling for power line communications," *Proc. of ISPLC*, 283–288, 2011.
10. Zimmermann, M. and K. Dostert, "Analysis of the broadband noise scenario in powerline networks," *Proc. of ISPLC,* 131–138, 2000.
11. Bingham, J., "Multicarrier modulation for data transmission: An idea whose time has come," *IEEE Communications Magazine*, Vol. 28, 5–14, May 1990.
12. Zhidkov, S. V., "Analysis and comparison of several simple noise mitigation schemes for OFDM receivers," *IEEE Transactions on Communications*, Vol. 56, No. 1, 5–9, January 2008.

Effects of Focusing on Scintillations of Higher Order Laser Modes in Non-Kolmogorov Turbulence

Yahya Baykal
Department of Electronic and Communication Engineering, Çankaya University
Yukarıyurtçu Mah., Mimar Sinan Cad., No. 4, 06790 Etimesgut Ankara, Turkey

Abstract— The scintillation index of focused higher order laser beam propagating in non-Kolmogorov atmospheric turbulence is formulated by employing the Rytov method and the equivalence of the structure constant. Our evaluations are performed for even modes. The equivalence formula for the structure constant is extracted from our earlier work in which the equivalence is obtained by equating the scintillation indices found in the Kolmogorov and the non-Kolmogorov turbulence. If not specified otherwise, the focused beam is defined when the focal length is equal to the link length. For the focused higher order laser beams, as the power law exponent of the non-Kolmogorov spectrum decreases, the scintillations decrease. At any power law exponent, the scintillations tend to become larger when the mode order of the focused beam becomes larger, i.e., the focused Gaussian beam is advantageous over the focused higher order laser beams for any realization of the non-Kolmogorov turbulence. Again being valid for any power law exponent, increase in the source size is found to decrease the intensity fluctuations of all the focused higher order mode scintillations. Especially for the larger order beams, focusing the higher order beam at a distance smaller than the link length results in a change in the behaviour of the scintillation index versus the power law exponent. In such cases, the scintillations are observed to increase. Comparison of the focused higher order beam scintillations with the previously obtained collimated higher order beam scintillations yields that the focused higher order beam scintillations are lower. Collimated higher order beams exhibit lower scintillations than the collimated Gaussian beams whereas this is reversed in the focused case. Another observation in such comparison shows that the difference of the intensity fluctuations between the Gaussian and the higher order beams are much larger in the focused case, especially at larger power law exponent values.

1. INTRODUCTION

The intensity fluctuations occurring in atmospheric turbulence are studied for many different incidences. Among these incidences, higher order mode operation of laser, forms one set. As known, the radiation originating from a laser resonator together with external configurations can yield single mode field distributions other than the widely used TEM_{00} (Gaussian) field which are referred as the higher order modes. These types of modes can be operated in collimated or focused forms. The scintillations of collimated higher order modes are evaluated in both Kolmogorov [1, 2] and non-Kolmogorov turbulence [3]. Focusing of a beam in atmospheric turbulence results in completely different intensity fluctuations [4–6]. Atmospheric turbulence deviating from the Kolmogorov spectrum also varies the scintillation behaviour of the beams when compared to the scintillation behaviour in Kolmogorov turbulence [7–10].

In this paper, the scintillation index in non-Kolmogorov turbulence is evaluated when the excitation is a focused higher order laser beam.

2. FORMULATION

In Rytov method, the scintillation index is given by $m^2 = 4B_\chi(L)$ where $B_\chi(L)$ is the correlation of the log-amplitude which is previously reported in [11] for a general type optical beam and L is the propagation distance. In the $B_\chi(L)$ solution provided in [11], we employ the focused higher order mode field as the incident beam, which is expressed by $u_s(s_x, s_y) = H_n(s_x/\alpha_s)H_m(s_y/\alpha_s)\exp\{-[0.5k\beta(s_x^2 + s_y^2)]\}$ where $k = 2\pi/\lambda$, λ is the wavelength, H_n is the Hermite polynomial of order n, (s_x, s_y) is the transverse source coordinate, α_s is the source size, $\beta = 1/(k\alpha_s^2) + (i/F)$, F is the focal length. This will yield the scintillations as

$$m^2 = \frac{4\pi}{\left[H_n(0)\,H_m(0)\right]^2}\mathrm{Re}\left\{\int_0^L d\eta \int_0^\infty \kappa d\kappa \int_0^{2\pi} d\theta \left[E(\eta,\kappa,\theta,L)\,E(\eta,-\kappa,\theta,L) + \left|E(\eta,\kappa,\theta,L)\right|^2\right]\Phi_n(\kappa)\right\}, \tag{1}$$

where $\kappa \exp(i\theta)$ is the two-dimensional spatial frequency in polar coordinates, η is the distance along the propagation axis,

$$E(\eta,\kappa,\theta,L) = ik\exp\left[-\frac{0.5i(L-\eta)(1+\beta i\eta)\kappa^2}{k(1+\beta iL)}\right] H_n\left(\frac{\eta-L}{k}\varsigma\kappa\cos\theta\right) H_m\left(\frac{\eta-L}{k}\varsigma\kappa\sin\theta\right),$$

$\varsigma = \{\alpha_s(1-i\beta L)^{1/2}[1-iL(\frac{2}{k\alpha_s^2}-\beta)]^{1/2}\}^{-1}$, and the spectrum in non-Kolmogorov turbulence is $\Phi_n(\kappa) = h(\alpha)\kappa^{-\alpha}$, $0 \le \kappa < \infty$, $3 < \alpha < 4$, with the equivalence of the structure functions involved [12], $h(\alpha) = -\Gamma(\alpha)(k/L)^{\alpha/2-11/6} C_n^2/\{8\pi^2\Gamma(1-0.5\alpha)[\Gamma(0.5\alpha)]^2 \sin(0.25\pi\alpha)\}$, $3 < \alpha < 4$, $\Gamma(.)$ is the gamma function, α is the power law exponent of the non-Kolmogorov spectrum, $i = (-1)^{1/2}$. Note that Eq. (1) is valid for even order modes.

3. RESULTS

All the figures show the variation of the scintillation index versus the power law exponent of the non-Kolmogorov spectrum, α for various source and medium parameters. If not indicated, the higher order beam is focused at the propagation distance, i.e., $F = L$. From Fig. 1, it is seen that higher α values yield higher scintillations for all higher order modes and at the same, the scintillations become large as the mode order increases. It is not presented here but found that the increase in the source size decreases the scintillations of the focused higher order beams in non-Kolmogorov medium. Fig. 2 is plotted for the same modes as in Fig. 1 but with different source size, structure constant and wavelength. Change in the parameters naturally changes the scintillation index values, however the trend versus α remains the same. From Figs. 1 and 2, it is concluded that the scintillation index of the focused Gaussian beam is smaller than the scintillation index of the focused higher order laser beams for any α.

Figure 3 reflects the effect of the focal length on the scintillations of the given higher order modes if the focal length is different than $F = L$. The observation is that when the higher orders beams are focused at a distance before the receiver, the scintillations of all the even higher order modes attain closer values at all power law exponent. We additionally report, without presenting the results in a figure, that for the larger order beams, focusing the higher order beam at a distance

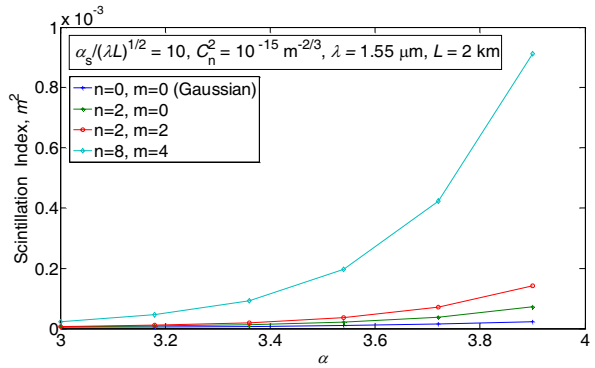

Figure 1: m^2 versus α for the indicated modes and parameters.

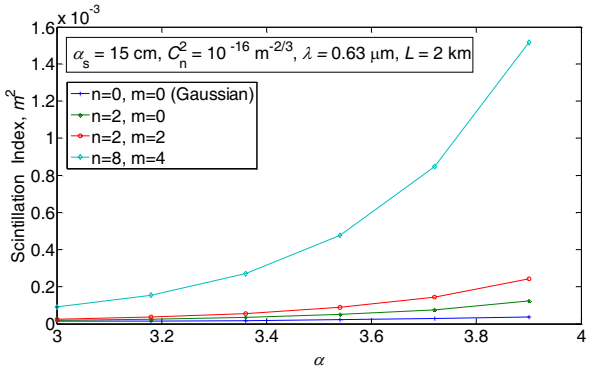

Figure 2: m^2 versus α for the same modes as in Fig. 1 but at different parameters.

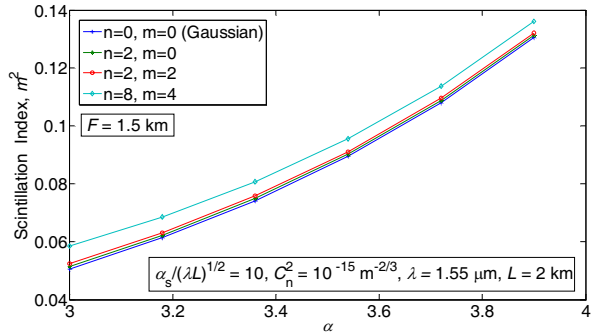

Figure 3: m^2 versus α for the same modes and parameters as in Fig. 1 but at $F = 1.5$ km.

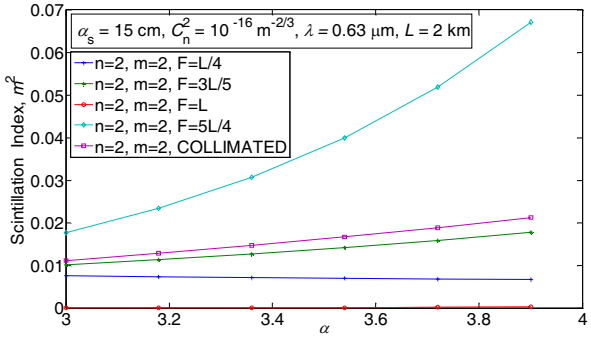

Figure 4: Comparison of m^2 at different focal lengths.

smaller than the link length will vary the behaviour of the scintillations versus α. In Fig. 4, the effect of the focal length on the scintillation index of the same higher order mode is examined as the power law exponent is varied. It is observed that depending on the chosen mode order and the source and medium parameters, the scintillations will show different variations, but the focused beam ($F = L$) will exhibit the smallest intensity fluctuations for all the power law exponent values of the non-Kolmogorov turbulence. This trend was found to be the opposite for collimated Gaussian beams in non-Kolmogorov turbulence [3].

4. CONCLUSION

Focused higher order mode scintillations are investigated in non-Kolmogorov atmospheric turbulence. Being valid for all the focused higher order modes, the scintillations become larger as the power law exponent and the mode order increase. Change in the source and medium parameters vary the scintillations, however, the trend versus α remains unchanged. When the higher orders modes are focused at a distance different than the propagation distance, the behaviour of the intensity fluctuations varies based on the chosen mode order, source and medium parameters where the minimum scintillations occurs at $F = L$ for any power law exponent of the non-Kolmogorov spectrum.

ACKNOWLEDGMENT

Yahya Baykal gratefully acknowledges the support given by Çankaya University and the ICT COST Action IC1101 entitled "Optical Wireless Communications — An Emerging Technology".

REFERENCES

1. Baykal, Y., "Intensity fluctuations due to higher-order Gaussian laser modes in weak atmospheric turbulence," *Opt. Commun.*, Vol. 57, No. 5, 311–313, 1986.
2. Arpali, S. A., H. T. Eyyuboğlu, and Y. Baykal, "Scintillation index of higher order cos-Gaussian, cosh-Gaussian and annular beams," *J. Mod. Opt.*, Vol. 55, No. 2, 227–239, 2008.
3. Baykal, Y., "Scintillations of higher order laser beams in non-Kolmogorov medium," *Opt. Lett.*, Vol. 39, No. 7, 2160–2163, 2014.
4. Andrews, L. C., R. L. Phillips, R. J. Sasiela, and R. Parenti, "Beam wander effects on the scintillation index of a focused beam," *Proceedings of SPIE*, Vol. 5793, 28–37, Orlando, USA, March 2005.
5. Charnotskii, M. and G. J. Baker, "Long- and short-term scintillation of the focused beams and point spread functions in turbulent atmosphere," *Proceedings of SPIE*, Vol. 8517, 85170G, San Diego, USA, August 2012.
6. Recolons, J., L. C. Andrews, and R. L. Phillips, "Analysis of beam wander effects for a horizontal-path propagating Gaussian-beam wave: Focused beam case," *Opt. Eng.*, Vol. 46, No 8, 086002, 2007.
7. Toselli, I., L. C. Andrews, R. L. Phillips, and V. Ferrero, "Scintillation index of optical plane wave propagating through non Kolmogorov moderate-strong turbulence," *Proceedings of SPIE*, Vol. 6747, 67470B, Florence, Italy, September 2007.
8. Gerçekcioğlu, H. and Y. Baykal, "Intensity fluctuations of flat-topped beam in non-Kolmogorov weak turbulence," *J. Opt. Soc. Am. A*, Vol. 29, No. 2, 169–173, 2012.
9. Gerçekcioğlu, H. and Y. Baykal, "Annular beam scintillations in non-Kolmogorov weak turbulence," *Appl. Phys. B*, Vol. 106, No. 4, 933–937, 2012.
10. Cui, L., B. Xue, L. Cao, S. Zheng, W. Xue, X. Bai, X. Cao, and F. Zhou, "Irradiance scintillation for Gaussian-beam wave propagating through weak non-Kolmogorov turbulence," *Opt. Express*, Vol. 19, No. 18, 16872–16884, 2011.
11. Baykal, Y., "Formulation of correlations for general-type beams in atmospheric turbulence," *J. Opt. Soc. Am. A*, Vol. 23, No. 4, 889–893, 2006.
12. Baykal, Y. and H. Gerçekcioğlu, "Equivalence of structure constants in non-Kolmogorov and Kolmogorov spectra," *Opt. Lett.* Vol. 36, No. 23, 4554–4556, 2011.

Nonparaxial Propagation of Complex Variable Function Cosh-Gaussian Beams

Dongmei Deng[1, 2], **Chidao Chen**[1], **Yushan Zheng**[3], **Xi Peng**[1], **Bo Chen**[1], **Yulian Peng**[1], **and Meiling Zhou**[1]

[1]Laboratory of Nanophotonic Functional Materials and Devices
South China Normal University, Guangzhou 510631, China
[2]CAS Key Laboratory of Geospace Environment
University of Science and Technology of China, Chinese Academy of Sciences, Hefei 230026, China
[3]Shenzhen Entry-exit Inspection and Quarantine Bureau, Shenzhen 518045, China

Abstract— By applying the superposition of beams, we obtain a group of virtual sources for a complex variable function (CVF) Cosh-Gaussian wave. We also derive a closed-form expression for the CVF-Cosh-Gaussian wave that in the appropriate limit yielding the paraxial CVF-Cosh-Gaussian beam. From the spectral representation of the CVF-Cosh-Gaussian waves, we derive the jth-order nonparaxial corrections for the corresponding paraxial CVF-Cosh-Gaussian beam analytically. The angular velocity of the nonparaxial CVF-Cosh-Gaussian beams decreases with the transmission distance increasing.

1. INTRODUCTION

In recent years, the study of spiral light beams [1–8] has drawn much attention is due to their potential application in different optic technologies including the laser manipulation [6]. The spiral beams [4–11] which have singularities and are characterized by a non-zero orbital momentum, their structure of the intensity distribution are rotated during propagation.

In 1971, Deschamps [12] has presented the virtual source method. In 1976 and 1977, Felsen and his collaborators [13, 14] have systematically developed this method. By using this method, Seshadri [15–17] has derived the virtual sources of Bessel-Gaussian, elegant Hermite-Gaussian, and cylindrical symmetric elegant Laguerre-Gaussian waves. Bandres et al. [18] have introduced the higher-order complex source that generates elegant Laguerre-Gaussian waves with radial mode number n and angular mode number m in 2004. In 2007, Zhang et al. [19] have employed this method to study the propagation properties of cosh-Gaussian beams in and beyond the paraxial regime. We have obtained the virtual sources of Elegant Hermite-Laguerrel Gaussian beam [20], Hollow gaussian beam [21], and Pearcey beam [22]. In 2012, Yan et al. [23] have studied the virtual source for an Airy beam. However, the virtual sources of the complex variable function (CVF) Cosh-Gaussian beams [10, 11] have not been reported.

In this paper, based on the superposition of beams, a group of virtual sources that generate the scalar CVF-Cosh-Gaussian wave are identified. The integral and the differential representation for the CVF-Cosh-Gaussian waves have been derived. From the spectral representation of the CVF-Cosh-Gaussian waves, we obtain the exact nonparaxial solution and the nth-order nonparaxial corrections for the corresponding paraxial CVF-Cosh-Gaussian beams analytically.

2. VIRTUAL SOURCE OF CVF-COSH-GAUSSIAN BEAMS

Suppose $E(r, z)$ be a monochromatic scalar wave function that describes a CVF-Cosh-Gaussian wave propagating along the positive z axis. Function $E(r, z)$ satisfies the homogeneous Helmholtz equation for $z > 0$. The CVF-Cosh-Gaussian field is assumed to have the general form

$$E(x, y, z) = q_0/q(z)\cosh(\zeta_\pm)\exp(ikz)\exp(v_1), \tag{1}$$

where $q(z) = z - iz_R$, $q_0 = -iz_R$, $\zeta_\pm = (x \pm iy)/(b\,w(z))\exp[-i\vartheta(z)]$, $w(z) = w_0\sqrt{1 + z^2/z_R^2}$, $\vartheta(z) = \pm\arctan(z/z_R)$, $v_1 = ik(x^2 + y^2)/(2q(z))$, $\sigma = (kw_0)^{-1}$, $q_\pm(z) = \pm z - iz_R$. The CVF-Cosh-Gaussian beam is generated by a group of sources of strength $S_{\rm cs}$ situated at $r = 0$ and $z = z_{\rm cs}$. Proper choice of $S_{\rm cs}$ and $z_{\rm cs}$ yields the desired beam. The wave function $E(x, y, z)$ satisfies the inhomogeneous Helmholtz equation

$$\Big(\frac{\partial^2}{\partial x^2} + \frac{\partial^2}{\partial y^2} + \frac{\partial^2}{\partial z^2} + k^2\Big)E(x, y, z) = -S_{cs}[\delta(x - iw_0/(2b))\delta(y \pm w_0/(2b)) + \delta(x - iw_0/(2b))\delta(y \mp w_0/(2b))]\delta(z - z_{\rm cs}), \tag{2}$$

Applying the Fourier transform pairs,

$$E(x,y,z) = \frac{1}{2\pi}\int_{-\infty}^{+\infty}\int_{-\infty}^{+\infty}\tilde{E}(f_x,f_y,z)\exp(iu_1)df_xf_y, \tag{3}$$

$$\tilde{E}(f_x,f_y,z) = \frac{1}{2\pi}\int_{-\infty}^{+\infty}\int_{-\infty}^{+\infty}E(x,y,z)\exp(-iu_1)dxdy, \tag{4}$$

where f_x and f_y are the spatial frequencies in the x and y directions, $u_1 = f_xx + f_yy$. From Eq. (2), $\tilde{E}(f_x,f_y,z)$ is obtained and substituted into Eq. (3), one can find that,

$$\begin{aligned}E(x,y,z) = {} & \frac{i}{4\pi}\int_{-\infty}^{+\infty}\int_{-\infty}^{+\infty}df_xdf_yS_{\rm cs}/\zeta[\exp(-i(if_xw_0/(2b) \mp f_yw_0/(2b)) \\ & + \exp(i(if_xw_0/(2b) \mp f_yw_0/(2b))]\exp[i\zeta(z-z_{\rm cs})]\exp(iu_1),\end{aligned} \tag{5}$$

where $\mathrm{Re}(z - z_{\rm cs}) > 0$, $\zeta = (k^2 - (f_x^2 + f_y^2))^{1/2}$. Expanding ζ into series and keeping the first and second terms, we obtain $\zeta = k(1 - (f_x^2 + f_y^2)/(2k^2))$. Under paraxial approximation, i.e., $k^2 \gg (f_x^2 + f_y^2)$, we replace ζ of the exponential part in Eq. (5) with the approximation and the other terms with k, Eq. (5) simplifies to

$$\begin{aligned}E_p(x,y,z) = {} & \frac{iS_{\rm cs}}{4\pi k}\exp[ik(z-z_{\rm cs})]\int_{-\infty}^{+\infty}\int_{-\infty}^{+\infty}df_xdf_y[\exp(-i(if_xw_0/(2b) \mp f_yw_0/(2b)) \\ & + \exp(i(if_xw_0/(2b) \mp f_yw_0/(2b))]\exp[-i(f_x^2+f_y^2)(z-z_{\rm cs})/(2k)]\exp(iu_1).\end{aligned} \tag{6}$$

The additional subscript p in $E_p(x,y,z)$ means the paraxial approximation. By using the relation

$$\int_{-\infty}^{+\infty}\exp(-ax^2+bx)dx = \sqrt{\frac{\pi}{a}}\exp\left(-\frac{b^2}{4a}\right), \tag{7}$$

one can obtain the integral of Eq. (6),

$$E_p(x,y,z) = \frac{S_{\rm cs}}{2(z-z_{\rm cs})}\exp[ik(z-z_{\rm cs})]\exp\left[\frac{ikr^2}{2(z-z_{\rm cs})}\right]\cosh\left[\frac{kw_0(x\pm iy)}{2b(z-z_{\rm cs})}\right]. \tag{8}$$

In order to obtain the CVF-Cosh-Gaussian beam for $z > 0$, we suppose the input paraxial approximation distribution is given by Eq. (1) for $z = 0$. By comparing Eq. (8) and Eq. (1) at $z = 0$, the parameters S_{cs} and z_{cs} can be given as

$$z_{\rm cs} = ikw_0^2/2 = iz_R, S_{\rm cs} = 2iz_R\exp(-kz_R). \tag{9}$$

Substituting Eq. (9), into (5), one can obtain the exact integral expression for $E(x,y,z)$

$$\begin{aligned}E(x,y,z) = {} & -\frac{z_R}{2\pi}\exp(-kz_R)\int_{-\infty}^{+\infty}\int_{-\infty}^{+\infty}df_xdf_y1/\zeta[\exp(-i(if_xw_0/(2b) \mp f_yw_0/(2b)) \\ & + \exp(i(if_xw_0/(2b) \mp f_yw_0/(2b))]\exp[i\zeta(z-iz_{\rm R})]\exp(iu_1).\end{aligned} \tag{10}$$

From Eq. (9), the source in Eq. (2) lies external to $z > 0$, and the solution given by Eq. (10) is the exact solution to the homogeneous Helmholtz equation.

3. EXACT NONPARAXIAL PROPAGATION OF A COMPLEX VARIABLE FUNCTION COSH-GAUSSIAN BEAM

Making use of the Green-function approach, we can obtain the differential representation of the CVF-Cosh-Gaussian waves. The solution of the differential equation

$$\left(\nabla_r^2 + \frac{\partial^2}{\partial z^2} + k^2\right)G(r,z) = -S_{\rm cs}/(2\pi)\left(\frac{\delta(r_1)}{r_1} + \frac{\delta(r_2)}{r_2})\delta(z-z_{\rm cs}\right), \tag{11}$$

is given by [16–18] $G(r,z) = S_{\rm cs}\exp(ikR)/(4\pi R)$, where $r_1 = \sqrt{\begin{array}{l}(x - iw_0/(2b))^2 + (y \pm w_0/(2b))^2 \\ +(z - iz_{\rm R})^2\end{array}}$, $r_2 = \sqrt{(x + iw_0/(2b))^2 + (y \mp w_0/(2b))^2 + (z - iz_{\rm R})^2}$. $R = [x^2 + y^2 + (z - iz_R)^2]^{1/2}$. Comparing Eq. (11) and Eq. (2) and applying Eq. (9), the differential or multipole representation of the CVF-Cosh-Gaussian waves is found to be

$$E(x,y,z) = \frac{iz_R}{2}\exp(-kz_R)\left[\frac{\exp(ikr_1)}{r_1} + \frac{\exp(ikr_2)}{r_2}\right]. \tag{12}$$

From Eq. (12), we see that CVF-Cosh-Gaussian modes can be generated by superposing two complex-source-point spherical wave $S_{\rm cs}\exp(ikR)/(4\pi R)$ corresponding to the paraxial Gaussian beam.

By using the power expansion $1/\zeta$ and $\exp[i\zeta(z - z_{\rm cs})]$ in Eq. (5) and keeping the product of both series terms up to order $\sigma^{2j}(\sigma = 1/(kw_0))$, we can obtain the jth-order corrections

$$\begin{aligned} E^{(0)}(x,y,z) &= E_1^{(0)}(x,y,z) + E_2^{(0)}(x,y,z) = -\frac{i}{4}Q\exp(ikz) \\ &\quad \times \exp[iQ(x^2+y^2)/w_0^2]\cosh\left[w_0Q(x \pm iy)/b\right], \qquad (13) \\ E^{(2j)}(x,y,z) &= (-1)^j\left[(Q\rho_1)^{2j}L_j^j(-iQ\rho_1^2)E_1^{(0)}(x,y,z)\right. \\ &\quad \left.+(Q\rho_2)^{2j}L_j^j(-iQ\rho_2^2)E_2^{(0)}(x,y,z)\right], \qquad (14) \end{aligned}$$

where $E^{(0)}(x,y,z)$ is the paraxial CVF-Cosh-Gaussian beam, $E^{(2j)}(x,y,z)$ is denoting the jth-order correction to the CVF-Cosh-Gaussian beam, $Q = (z/z_R - i)^{-1}$, $E_1^{(0)}(x,y,z) = -\frac{i}{4}Q\exp(iQ\rho_1^2)$, $E_2^{(0)}(x,y,z) = -\frac{i}{4}Q\exp(iQ\rho_2^2)$, $\rho_1 = \sqrt{(x - iw_0/(2b))^2 + (y \pm w_0/(2b))^2}/w_0$, $\rho_2 = \sqrt{\begin{array}{l}(x + iw_0/(2b))^2 \\ +(y \mp w_0/(2b))^2\end{array}}/w_0$, and $L_j^j(\cdot)$ is the associated Laguerre polynomial of order j and degree j. It is easy to find that Eq. (13) is the same as Eq. (1). Eq. (14) is the nonparaxial expression of the CVF-Cosh-Gaussian beams for the jth nonparaxial corrections. We can find that the nonparaxial solution approaches the exact solution Eq. (12) with the increase of the parameter j. In particular, when j becomes infinite, the nonparaxial solution becomes the exact solution.

4. CONCLUSION

In conclusion, a group of complex sources that generate the CVF-Cosh-Gaussian waves has been presented. We have obtained the integral and the differential representation for the CVF-Cosh-Gaussian waves. From the integral representation of the CVF-Cosh-Gaussian waves, we derive the first three orders of nonparaxial corrections for the corresponding paraxial CVF-Cosh-Gaussian beams analytically and numerically. The angular velocity of the paraxial and nonparaxial CVF-Cosh-Gaussian beams decreases with z increasing.

ACKNOWLEDGMENT

This research was supported by the National Natural Science Foundation of China (11374108, 11374107, 10904041), the Foundation for the Author of Guangdong Province Excellent Doctoral Dissertation (SYBZZXM201227), and the Foundation of Cultivating Outstanding Young Scholars ("Thousand, Hundred, Ten" Program) of Guangdong Province in China.

REFERENCES

1. Abramochkin, E. G. and V. G. Volostnikov, *Opt. Commun.*, Vol. 102, 336, 1993.
2. Abramochkin, E. G. and V. G. Volostnikov, *Opt. Commun.*, Vol. 125, 302, 1996.
3. Abramochkin, E., N. Losevsky, and V. Volostnikov, *Opt. Commun.*, Vol. 141, 59, 1997.
4. Berry, M., *Proc. SPIE*, Vol. 3487, 6, 1998.
5. Skryabin, D. V., J. M. McSloy, and W. J. Firth, *Phys. Rev. E*, Vol. 66, 055602(R), 2002.
6. Afanasiev, K. N., S. P. Kotova, A. M. Mayorova, and V. G. Volostnikov, *SPIE*, Vol. 6054, 60540U-1, 2005.
7. Izdebskaya, Y., V. Shvedov, and A. Volyar, *J. Opt. Soc. Am. A*, Vol. 2, 171, 2008.

8. Bekshaev, A. Y. and M. S. Soskin, *J. Opt. A: Pure Appl. Opt.*, Vol. 6, S170, 2004.
9. Bekshaev, A. Y., M. S. Soskin, and M. V. Vasnetsov, *Opt. Lett.*, Vol. 31, 694, 2006.
10. Bekshaev, A. Y. and M. S. Soskin, *Opt. Lett.*, Vol. 31, 2199, 2006.
11. Deng, D. M., Q. Guo, and W. Hu, *Phys. Rev. A*, Vol. 79, 023803, 2009.
12. Deng, D. M., Q. Guo, and W. Hu, *Opt. Lett.*, Vol. 34, 43–45, 2009.
13. Deschamps, G. A., *Electron. Lett.*, Vol. 7, 684–685, 1971.
14. Felsen, L. B., *J. Opt. Soc. Am.*, Vol. 66, 751–760, 1976.
15. Shin, S. Y. and L. B. Felsen, *J. Opt. Soc. Am.*, Vol. 67, 699–700, 1977.
16. Seshadri, S. R., *Opt. Lett.* Vol. 27, 998, 2002.
17. Seshadri, S. R., *Opt. Lett.*, Vol. 27, 1872, 2002.
18. Seshadri, S. R., *Opt. Lett.*, Vol. 28, 595 2003.
19. Bandres, M. A. and J. C. Gutiérrez-Vega, *Opt. Lett.*, Vol. 29, 2213–2215, 2004.
20. Zhang, Y. C., Y. J. Song, Z. R. Chen, J. H. Ji, and Z. X. Shi, *Opt. Lett.*, Vol. 32, 292–294, 2007.
21. Deng, D. M. and Q. Guo, *Opt. Lett.*, Vol. 33, 1225, 2008.
22. Deng, D. M. and Q. Guo, *J. Opt. Soc. Am. B*, Vol. 26, 2044–2049, 2009.
23. Deng, D. M., C. D. Chen, X. Zhao, B. Chen, X. Peng, and Y. S. Zheng, *Opt. Lett.* Vol. 39, 2703–2706, 2014.
24. Yan, S. H., B. L. Yao, M. Lei, D. Dan, Y. L. Yang, and P. Gao, *Opt. Lett.*, Vol. 37, 4774, 2012.

M^2-factor for the Partially Coherent Elegant Laguerre-Gaussian Beam Propagating through the Turbulent Ocean

B. Wang, Y. S. Yuan, Z. F. Cui, and J. Qu
Department of Physics, Anhui Normal University, Wuhu 241000, China

Abstract— On account of the extended Huygens-Fresnel principle and the second order moments of the Wigner distribution function, the analytical expression of the beam propagation factor (M^2-factor) for partially coherent elegant Laguerre-Gaussian (PCELG) beam has been theoretically derived. The corresponding analysis and discussions reveal that the M^2-factor of the PCELG beam in oceanic turbulence vary with changes in parameters of the beam and the oceanic turbulence. The acquired results may have some certain reference value for laser tracking, remote sensing and optical communication under the water.

1. INTRODUCTION

In the last decades, the propagation properties of beams in free space, an arbitrary medium and atmosphere have been theoretically and experimentally studied by many scholars [1–5]. As an extension of the standard Laguerre-Gaussian beam, the elegant Laguerre-Gaussian beam with a more symmetrical form is proposed [6]. Since then, some researchers have paid their attention to the propagation properties of the PCELG beam through the turbulent atmosphere and obtained a lot of achievements [7, 8].

Recently, the new power spectrum for the turbulent ocean, considering the temperature and salinity fluctuations, has been used to investigate the propagation properties of beams in oceanic turbulence. N. Farwell et al. use the new spectrum to deal with the intensity and coherence properties of a Gaussian beam propagating in the clear water turbulent ocean [9]. Chen et al. obtain the evolution of propagation quality factor for partially coherence Hermite-Gaussian beams traveling through the turbulent ocean [10]. Zhao et al. focus on the polarization degree of an anisotropic electromagnetic Gaussian Schell-model beam propagating in the clear-water turbulent ocean [11]. Besides, Fu et al. have revealed how the average intensity, polarization degree and the coherence degree for the partially coherent radially polarized doughnut beam in oceanic turbulence are affected by the parameters of the light source and turbulent ocean [12].

This paper aims to specifically investigate the M^2-factor of the PCELG beam through the oceanic turbulence. By applying the deduced analytical expressions, corresponding numerical calculations and discussions have been carried out.

2. THEORETICAL MODEL

For dealing with the M^2-factor of the PCELG beam through the turbulent ocean, we take the power spectrum of the refractive index fluctuations in ocean water, specifically for isotropic and homogeneous oceanic turbulence, nearly introduced in Ref. [11]. Here, ignoring the scattering and absorption by some possible suspended particles and supposing the eddy thermal diffusivity and the diffusion of the salt equal in value, the power spectrum takes the following form

$$\phi_n(\kappa) = 0.388 \times 10^{-8} \varepsilon^{-1/3} \kappa^{-11/3} \left[1 + 2.35\,(\kappa\eta)^{2/3}\right] f(\kappa, \zeta, \chi_T) \tag{1}$$

where ε denotes the rate of dissipation of turbulent kinetic energy per unit mass of fluid, ranging from $10^{-4}\,\mathrm{m^2/s^3}$ to $10^{-10}\,\mathrm{m^2/s^3}$, $\eta = 10^3\,\mathrm{m}$ describing the Kolmogorov micro scale (inner scale), with [11]:

$$f(\kappa, \zeta, \chi_T) = \frac{\chi_T}{v^2}\left[\zeta^2 \exp(-A_T\delta) + \exp(-A_S\delta) - 2\zeta\exp(-A_{TS}\delta)\right]$$

With x_T indicating the rate of dissipation of mean-square temperature, varying in the range from $10^{-4}\,\mathrm{K^2/s}$ to $10^{-10}\,\mathrm{K^2/s}$, other parameters are set as $A_T = 1.863 \times 10^{-2}$, $A_S = 1.9 \times 10^{-4}$, $A_{TS} = 9.41 \times 10^{-3}$, and $\delta = 8.284(\kappa\eta)^{(4/3)} + 12.978(\kappa\eta)^2$, ζ showing the relative strength of temperature and salinity fluctuations, which in the ocean water can vary in the interval $[-5; 0]$, combining with the maximum value 0 corresponding to the case under the domination of temperature-driven turbulence, the minimum value -5 corresponding to the situation that salinity-driven turbulence

gains the upper hand. It is necessary to note here, if $\phi_n(\kappa) = 0$, the condition is namely for propagation in free space.

Assuming that a PCELG beam propagates along z axis in the positive direction, into the half-space of $z \geq 0$, the electric field at the source plane in the rectangular coordinate system can be expressed as

$$E^{(0)}(\boldsymbol{\rho}, 0) = R\frac{(-1)^n}{2^{2n+m} \cdot n!} \sum_{t=0}^{n} \sum_{s=0}^{m} i^s \binom{n}{t} \binom{m}{s} H_{2t+m-s}\left(\frac{x}{w_0}\right) H_{2n-2t+s}\left(\frac{y}{w_0}\right) \exp\left(-\frac{x^2+y^2}{w_0^2}\right) \tag{2}$$

where $\boldsymbol{\rho} = (x, y)$ representing the transverse coordinates in the source plane, associated with $\boldsymbol{\rho}^2 = x^2 + y^2$, R standing for a positive constant, w_0 being the beam width of the PCELG beam at the source plane. $H(x)$ indicating an Hermite polynomial, m and n meaning the orders of the PCELG beam. As $m = n = 0$, it reduces to the electric field of the well known fundamental Gaussian beam.

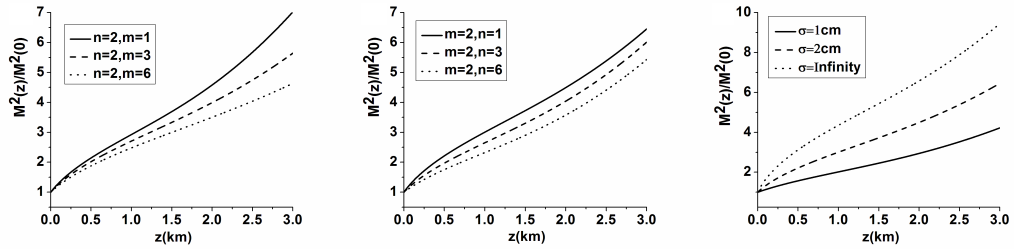

Figure 1: Propagation factor of PCELG beams $M^2(z)/M^2(0)$ versus propagation distance z through the oceanic turbulence for different beam parameters: (a) $\sigma = 2\,\mathrm{cm}$, $m = 2$, $n = 1$, 3, 6; (b) $\sigma = 2\,\mathrm{cm}$, $n = 2$, $m = 1$, 3, 6; (c) $m = 2$, $n = 1$, $\sigma = 1\,\mathrm{cm}$, $2\,\mathrm{cm}$, infinity.

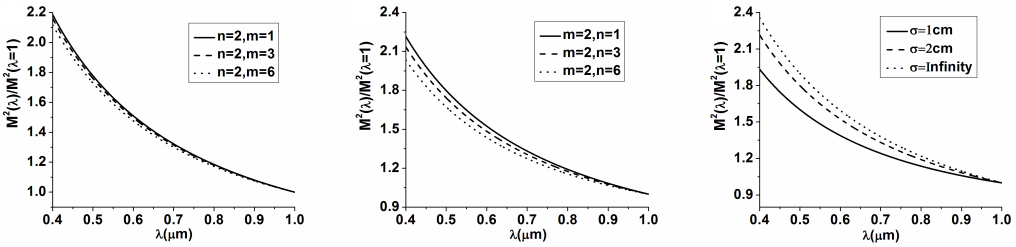

Figure 2: A comparison between propagation factor of PCELG beams $M^2(z)/M^2(0)$ in oceanic turbulence with different parameters and in free space: (a) $\varepsilon = 10^{-4}\,\mathrm{m^2\,s^{-3}}$, $\zeta = -2.5$, $\chi_T = 10^{-10}$, $10^{-9}\,\mathrm{K^2\,s^{-1}}$, in free space; (b) $\chi_T = 10^{-10}\,\mathrm{K^2\,s^{-1}}$, $\zeta = -2.5$, $\varepsilon = 10^{-8}, 10^{-7}\,\mathrm{m^2\,s^{-3}}$, in free space; (c) $\chi_T = 10^{-9}\,\mathrm{K^2\,s^{-1}}$, $\varepsilon = 10^{-4}$, $\zeta = -5$, -3, in free space.

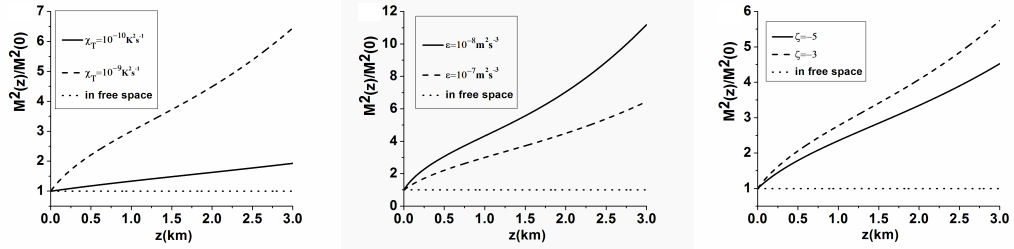

Figure 3: Propagation factor of PCELG beams $M^2(\lambda)/M^2(\lambda = 1)$ versus wavelength λ through the oceanic turbulence for different beam parameters: (a) $\sigma = 2\,\mathrm{cm}$, $m = 2$, $n = 1$, 3, 6; (b) $\sigma = 2\,\mathrm{cm}$, $n = 2$, $m = 1$, 3, 6; (c) $m = 2$, $n = 1$, $\sigma = 1\,\mathrm{cm}$, $2\,\mathrm{cm}$, infinity.

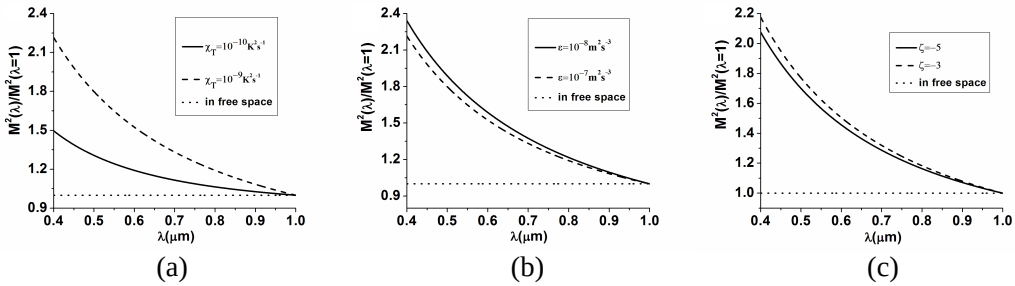

Figure 4: Propagation factor for PCELG beams $M^2(\lambda)/M^2(\lambda=1)$ in oceanic turbulence with different parameters and in free space: (a) $\varepsilon = 10^{-4}\,\mathrm{m^2\,s^{-3}}$, $\zeta = -2.5$, $\chi_T = 10^{-10}$, $10^{-9}\,\mathrm{K^2\,s^{-1}}$, in free space; (b) $\chi_T = 10^{-10}\,\mathrm{K^2 s^{-1}}$, $\zeta = -2.5$, $\varepsilon = 10^{-8}$, $10^{-7}\,\mathrm{m^2\,s^{-3}}$, in free space; (c) $\chi_T = 10^{-9}\,\mathrm{K^2 s^{-1}}$, $\varepsilon = 10^{-4}$, $\zeta = -5$, -3, in free space.

The M^2-factor for the PCELG beam through the oceanic turbulence takes the following form

$$M^2(z) = k\left[\left(\left\langle x^2\right\rangle + \left\langle y^2\right\rangle\right)\left(\left\langle \theta_x^2\right\rangle + \left\langle \theta_y^2\right\rangle\right) - \left(\langle x\theta_x\rangle + \langle y\theta_y\rangle\right)^2\right]^{1/2} \tag{3}$$

3. NUMERICAL CALCULATIONS

Corresponding numerical calculations have been illustrated, for discussing effects of parameters of beam and the oceanic turbulence on the M^2-factor for the PCELG beam in the turbulent ocean. It is of necessity to note that the beam width w_0 is set to be 5 cm.

4. CONCLUSIONS

In this paper, the analytical formula for the M^2-factor of the PCELG beam in oceanic turbulence is theoretically deduced and corresponding numerical calculations and analysis have been accomplished. The obtained results indicate that the M^2-factor of the PCELG beam with lower beam orders, larger initial coherence length, bigger χ_T and ζ or smaller ε is more influenced by turbulent ocean and the poorer beam quality is acquired whether for increasing in propagation distance or the wave length. Particularly, in free space, as the propagation distance or wave length varies, the M^2-factor always stay the same. Above all, the results may be of some significance for underwater laser tracking, remote sensing and optical communication.

ACKNOWLEDGMENT

Jun Qu acknowledges the support by the National Natural Science Foundation of China (NSFC) under Grant No. 11374015, Yangsheng Yuan acknowledges the support by Anhui Provincial Natural Science Foundation of China under Grant No. 1408085QF112.

REFERENCES

1. Eyyuboglu, H. T. and Y. K. Baykal, "Flat topped beams and their characteristics in turbulent media," *Optics Express*, Vol. 14, No. 10, 4196–4207, 2006.
2. Ponomarenko, S. A., J. J. Greffet, and E. Wolf, "The diffusion of partially coherent beams in turbulent media," *Optics Communications*, Vol. 208, No. 1, 1–8, 2002.
3. Roychowdhury, H., S. A. Ponomarenko, and E. Wolf, "Change in the polarization of partially coherent electromagnetic beams propagating through the turbulent atmosphere," *Journal of Modern Optics*, Vol. 52, No. 11, 1611–1618, 2005.
4. Ghafary, B. and M. Alavinejad, "Changes in the state of polarization of partially coherent flat-topped beam in turbulent atmosphere for different source conditions," *Applied Physics B*, Vol. 102, No. 4, 945–952, 2011.
5. Taherabadi, G., M. Alavynejad, F. D. Kashani, et al., "Changes in the spectral degree of polarization of a partially coherent dark hollow beam in the turbulent atmosphere for on-axis and off-axis propagation point," *Optics Communications*, Vol. 285, No. 8, 2017–2021, 2012.
6. Takenaka, T., M. Yokota, and O. Fukumitsu, "Propagation of light beams beyond the paraxial approximation," *JOSA A*, Vol. 2, No. 6, 826–829, 1985.

7. Mei, Z. and J. Gu, "Comparative studies of paraxial and nonparaxial vectorial elegant Laguerre-Gaussian beams," *Optics Express*, Vol. 17, No. 17, 14865–14871, 2009.
8. Wang, F., Y. Cai, and O. Korotkova, "Partially coherent standard and elegant Laguerre-Gaussian beams of all orders," *Optics Express*, Vol. 17, No. 25, 22366–22379, 2009.
9. Farwell, N. and O. Korotkova, "Intensity and coherence properties of light in oceanic turbulence," *Optics Communications*, Vol. 285, No. 6, 872–875, 2012.
10. Chen, F., Y. Chen, and Q. Zhao, "Change of propagation quality factor of partially coherence hermite-gaussian beams traveling through oceanic turbulence," *Chinese Journal of Lasers*, Vol. 40, No. 4, 0413002-1–0413002-7, 2013.
11. Tang, M. and D. Zhao, "Spectral changes in stochastic anisotropic electromagnetic beams propagating through turbulent ocean," *Optics Communications*, Vol. 312, 89–93, 2014.
12. Fu, W. and H. Zhang, "Propagation properties of partially coherent radially polarized doughnut beam in turbulent ocean," *Optics Communications*, Vol. 304, 11–18, 2013.

Microstrip Diplexer Design Using Three EBG

Ursula Martinez-Iranzo[1], **Bahareh Moradi**[1], **Eva Arasa**[2], **Julian Alonso**[2], **and Joan Garcia-Garcia**[1]

[1]Grupo de Aplicaciones Electromagnéticas Industriales — GAEMI
Electronic Engineering Department, Universidad Autónoma de Barcelona, Campus de Bellaterra
08208 Cerdanyola del Vallès, Barcelona, Spain
[2]Grupo de Sensores y Biosensores, Analytical Chemistry Department
Universidad Autónoma de Barcelona, Campus de Bellaterra, 08208 Cerdanyola del Vallès, Barcelona, Spain

Abstract— A novel diplexer design by combining of three electromagnetic band gap (EBG) structures is presented in this paper. The diplexer is constructed by combining an EBG at the input port with two different EBG at the output ports. The proposed diplexer is configured with filter in each arm to reject unwanted signals. The first or the second bandpass falls into the stop-band and can be suppressed by EBG structures as well as band pass is controlled directly by EBG structure. Further the EBG structure demonstrates a good performance to improve the mutual coupling. Practical applications of EBG structure usually have difficulty in accommodating its physical size, because the period of EBG lattices has to be a half-waveleng that the band-gap frequency. The proposed design has been implemented in a 25 mil thick Rogers RO301 0substrate. It provides a new idea for designing more efficient structures for microwave circuit applications, such as filters, diplexer, and other passive circuits. This research is only the first step for the feasibility study of the diplexer design by using EBG technology, which can be modified to the other desired frequency bands. The proposed diplexer is simple to fabricate, as it is designed using microstrip technology, and presents compact dimensions, making use of a low number of elements. The excellent simulation results of transmission, reflexion and isolation magnitudes are an excellent starting point to develop a robust design methodology.

1. INTRODUCTION

EBG structures exhibit unique characteristics to guide, filter or collimate electromagnetic waves and have attracted a lot of interest from the research community in recent years. EBG structure is a periodically loaded structure with reactive elements, whose cells provide a wide stop-band [1]. Due to this, they have been widely applied in designs of planar filters to optimize their performance and to minimize their circuits. These periodic structures were originally proposed at optical frequencies and are known as a photonic bandgap (PBG) structure or photonic crystal (PC) [2]. Recently, there has been considerable research effort in EBG structures because the interaction of electromagnetic waves with them generated phenomena like metasurfaces and enhanced transmission [3], and other advances in filters design [4].

It has been designed a mainly EBG with two frequency bands, that will be used to design a diplexer. The diplexer is one of the key components in a transceiver which greatly affects system performance that it also a current research due to theneed to improve its design features as high isolation, low insertion loss and high selectivity [5, 6]. In [7] has been designed a diplexer based on complementary split-ring resonators (CSRRs) with comparable characteristics to our diplexer, but on the other hand, a complicated fabrication with metalized vias. In [5] is designed a complicated fabricated diplexer with metallic vias to the ground and lower isolation values.

EBG structures have been designed in a RO3010 25 mil Rogers substrate characterized by a loss tangent $\delta = 0.0022$ and $\varepsilon_r = 10.2$, and simulations have been done using ADS 2013.06 simulation software in Agilent.

2. EBG STRUCTURES

EBG structures are relatively simple periodic structures, and can be analysed as infinite periodic structures. Conceptually, EBG can be defined as a loaded line, namely, each unit cell of the line consists of a length d of transmission line with a shunt susceptance across the midpoint of the line. Accordingly, the unit cell that defines a section can be defined as:

$$\begin{bmatrix} A & B \\ C & D \end{bmatrix} = \begin{bmatrix} \cos\frac{\theta}{2} & j\sin\frac{\theta}{2} \\ j\sin\frac{\theta}{2} & \cos\frac{\theta}{2} \end{bmatrix} \begin{bmatrix} 1 & 0 \\ jb & 1 \end{bmatrix} \begin{bmatrix} \cos\frac{\theta}{2} & j\sin\frac{\theta}{2} \\ j\sin\frac{\theta}{2} & \cos\frac{\theta}{2} \end{bmatrix} \tag{1}$$

Developing the unit cell matrix (1) we obtain the Equation (2) for reciprocal networks. If Equation (3) is defined, we can obtain a pass-band filter (if $\alpha = 0$, $\beta \neq 0$) and stop-band filter (if $\alpha \neq 0$, $\beta = 0$). Therefore, for the matrix that defines EBG loads have been designed two EBG at the output ports that suppress the desired frequency band.

$$\cosh\gamma d = \frac{A+D}{2} = \cos\theta - \frac{b}{2}\sin\theta \tag{2}$$

$$\gamma = \alpha + j\beta \tag{3}$$

Figure 1 shows the main EBG layout, in which the dark grey parts denote conductor strip and two sides are connected with a 50 Ω microstrip line, and simulated-S parameters in which we can observe two clear frequency bands at 4 and 6.8 GHz. The losses in the band-pass oscillate between −0.2 dB and −1.2 dB, being compatible with the typical values of the ohmic losses in microstrip filters. Return losses are below to −10 dB, also necessary to filters design. L_1 and L_2 can be modified to vary central frequency of each frequency bands, thus providing great flexibility to diplexers design. A line to basic cell coupling has been incorporated to maximize coupling between microstrip line and EBG structure.

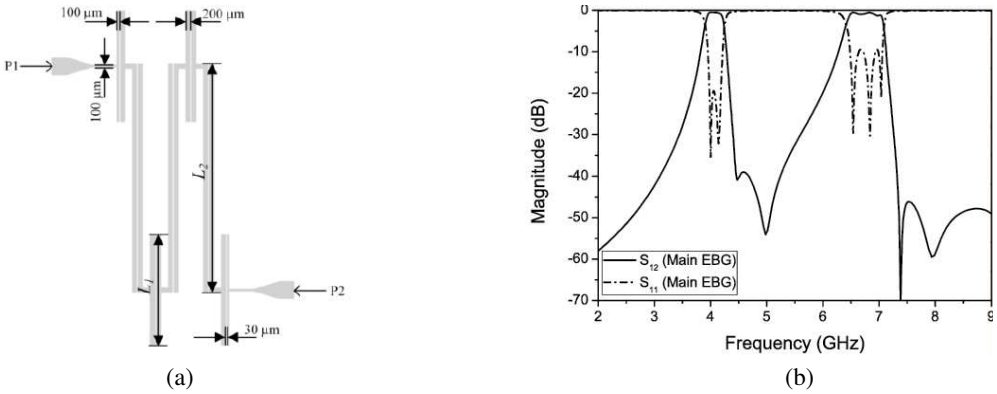

(a) (b)

Figure 1: Layout of the proposed main EBG with (a) two frequency bands and (b) simulated S-parameters. $P1$ is the input port, $P2$ is the output port and geometric values correspond to $L_1 = 9$ mm and $L_2 = 4.4$ mm.

Figure 2 shows the layout of the proposed low-pass EBG and S-parameters overlap of main EBG and low-pass EBG that suppress second frequency band at 6.8 GHz. Low-pass EBG has been designed to have the maximum impedance matching (50 Ω) at first bandat 4 GHz and a top cut-off frequency of 5.1 GHz. Layout of the proposed high-pass EBG and S-parameters superposition of main EBG and high-pass EBG has been shown in Figure 3. In this case, the maximum impedance matching (50 Ω) has been designed in second band at 6.8 GHz and lower cut-off frequency at 5.7 GHz. In all layouts, the dark grey parts denote conductor strip and two sides are connected with a 50 Ω microstrip line.

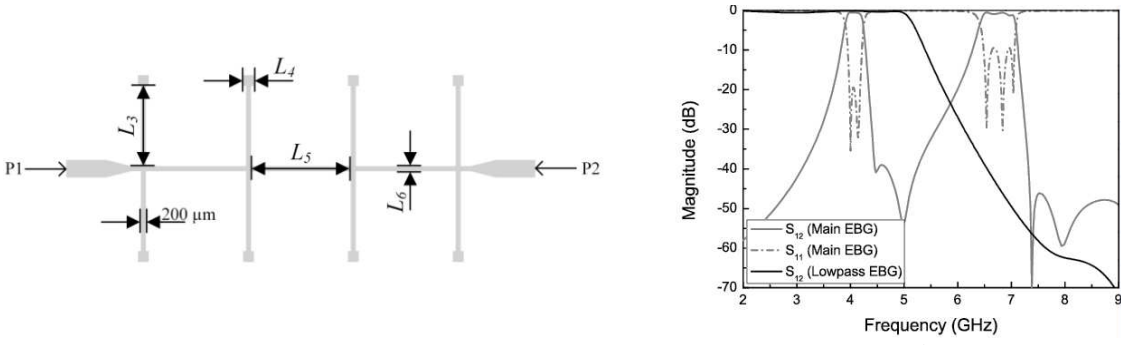

(a) (b)

Figure 2: Layout of (a) the proposed low-pass EBG and (b) simulated S-parameters. $P1$ is the input port, $P2$ is the output port and geometric values correspond to $L_3 = 9$ mm, $L_4 = 4.4$ mm, $L_5 = 4.4$ mm and $L_6 = 200$ µm.

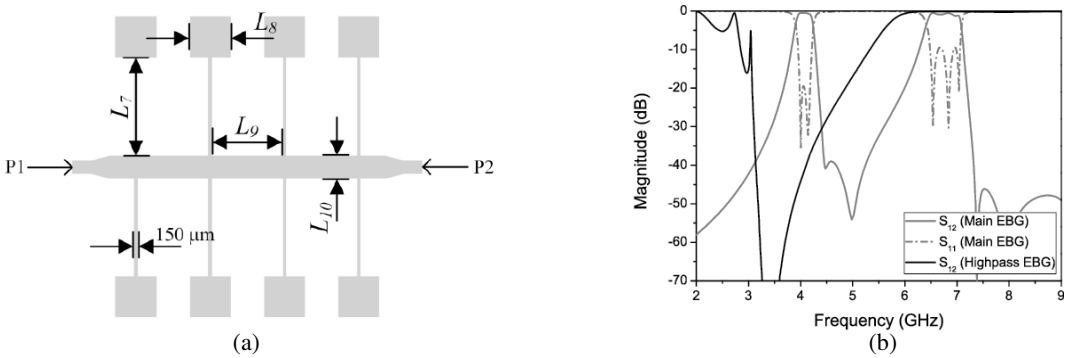

Figure 3: Layout of (a) the proposed high-pass EBG and (b) simulated S-parameters. $P1$ is the input port, $P2$ is the output port and geometric values correspond to $L_7 = 4.2\,\text{mm}$, $L_8 = 1.73\,\text{mm}$, $L_9 = 4\,\text{mm}$ and $L_{10} = 1\,\text{mm}$.

To EBG filters design, L_3, L_4, L_5, L_7, L_8 and L_9 provide the value of susceptance for which we define the cut-off frequencies, while L_6 and L_{10} allow maximum impedance matching ($50\,\Omega$) at the first or the second band as required. Therefore, this design has great flexibility because we can choose the desired bands and designing EBG filters for each case. Starting and ending frequencies of the band gap generated by both EBG filters are approximated by:

$$f_{low} = \frac{1}{\pi\sqrt{C_p\,(L_p + L_b)}} \tag{4}$$

$$f_{high} = \frac{c_0}{2b\sqrt{\varepsilon_r}} \tag{5}$$

where C_p and L_p are inductance and capacitance values for equivalent LC series circuit of squares and L_b inductance of bridges, c_0 is speed of light, b is L_5 or L_9, and ε_r is relative epsilon from substrate.

3. PROPOSED DESIGN

Figure 4 shows the layout of the diplexer prototype and S-parameters of transmission, reflexion and isolation magnitudes. At 4 GHz, port 3 is through, $S_{13} = -1.1\,\text{dB}$, while port 2 is isolated, $S_{12} = -40.1\,\text{dB}$. At 6.8 GHz, port 2 is through, $S_{12} = -0.8\,\text{dB}$, while port 3 is isolated, $S_{13} = -54.4\,\text{dB}$. At 4 and 6.8 GHz $S_{23} = -44.9\,\text{dB}$ and $-54.7\,\text{dB}$ respectively. Its size is about $0.26\lambda_g \times 0.42\lambda_g \times 0.008\lambda_g$, where λ_g is the wavelength of the first channel center frequency. Two channels have a fractional bandwidth (FBW) of 8% approximately.

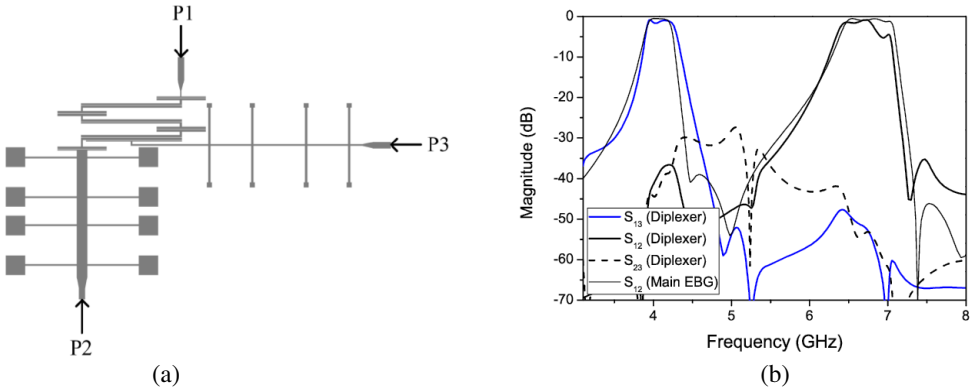

Figure 4: Layout of (a) the diplexer prototype and (b) simulated S-parameters. $P1$ is the input port, $P2$ is the output channel 1 and $P3$ is the output channel 3.

Table 1 shows the performance comparison of the proposed diplexer simulated results in this work with other diplexers. The suppression of S_{21} or S_{31} is much wider than those of previously reported diplexers, and isolation and size are quite similar. Moreover, diplexer of this work has an

Table 1: Comparison between the proposed diplexer and the references.

Ref.	3D Size	$\|S_{21}\|$or $\|S_{31}\|$(Insertion loss)		$\|S_{21}\|$or $\|S_{31}\|$(Suppression)		$\|S_{32}\|$ (Isolation)
		Channel 1	Channel 2	Channel 1	Channel 2	
This work	$0.26\lambda_g \times 0.42\lambda_g \times 0.008\lambda_g$	0.2 dB	1.2 dB	40 dB	54 dB	30 dB
[5]	$0.26\lambda_g \times 0.45\lambda_g \times 0.0016\lambda_g$	1.4 dB	1.6 dB	39 dB	40 dB	25 dB
[6]	$0.58\lambda_g \times 0.40\lambda_g \times 0.017\lambda_g$	1.9 dB	2.0 dB	27 dB	23 dB	26 dB
[7]	$0.27\lambda_g \times 0.23\lambda_g \times 0.008\lambda_g$	1.6 dB	2.3 dB	43 dB	28 dB	32 dB

easy fabrication without vias to the ground or without etched ground plane. Due to the positive results of the simulation with respect to previous works, work is in progress to improve compaction of the three EBG to obtain similar transmission results to main EBG and measure fabricated results.

4. CONCLUSION

This paper designs a planar diplexer based on three EBG. This new configuration of diplexer shows advantages of low loss, high isolation, easy fabrication, compact size and design flexibility. The diplexer performance, in terms of the simulated insertion loss (approximately 0.2 dB and 1.2 dB for the two channels), and isolation (better than 40 dB), is good. Therefore, the proposed diplexer is desirable for microwave transceiver systems.

ACKNOWLEDGMENT

This work has been supported by Ministerio de Ciencia y Educación of the Spanish government under the project TEC2010-16060.

REFERENCES

1. Pozar, D. M., *Microwave Engineering*, John Wiley & Sons, Inc., New York, 1998.
2. Rahmat-Samii, Y. and H. Mosallaci, "Electromagnetic bang-gap structures: classification, characterization and applications," *Proc. Inst. Elect. Eng-ICAP Symp.*, 560–564, Manchester, United Kingdom, 2001.
3. Navarro, M., M. Beruete, F. Falcone, and M. Sorolla, "EBG and metamaterial devices and phenomena in planar volumetric configurations," *Int. Symp. Ant. Tech. Appl. Elect.-ANTEM Symp.*, 1–4, Ottawa, Canada, July 2010.
4. Quevedo-Teruel, O., L. Inclán-Sanchez, J. L. Vazquez-Roy, and E. Rajo-Iglesias, "Compact reconfigurable planar EBGs based on short-circuited hairpin resonators," *IEEE Microw. Wireless Comp. Lett.*, Vol. 23, No. 9, 462–464, 2013.
5. Qin, W. and Q. Xue, "Design of a planar diplexer based on complementary compact microstrip resonant cell," *Proceedings of APMC*, 4–7, Kaohsiung, Taiwan, December 2012.
6. Zeng, H. Y., G. M. Wang, D. Z. Wei, and Y. W. Wang, "Planar diplexer using composite right-left-handed transmission line under balanced condition," *Elect. Lett.*, Vol. 48, No. 2, 104–106, 2012.
7. Dong, Y. and T. Itoh, "Substrate integrated waveguide loaded by complementary split-ring resonators for miniaturized diplexer design," *IEEE Microw. Wireless Comp. Lett.*, Vol. 21, No. 1, 10–12, 2011.

Wide-stopband Millimeter-wave BPF on GaN MMIC Using Asymmetric Feeding Structure

Jin Xu Xu, Xiu Yin Zhang, and Xiao Feng Liu
School of Electronic and Information Engineering
South China University of Technology, Guangzhou 510640, China

Abstract— This paper presents a novel compact bandpass filter for 30 GHz millimeter-wave applications in Monolithic Microwave Integrated Circuit (MMIC). The proposed circuit consists of two symmetrical coupled quarter-wavelength transmission-line resonators and two coupled transmission-line feeding structures. Two feeding lines are designed as asymmetrical structures, which are utilized not only to cause mismatch at the third harmonic frequency between the resonator and feeding lines so that the third harmonic can be suppressed but also to provide source-loaded to generate two transmission zeros near the passband, resulting in high selectivity. To verify the proposed idea, an experiment filter has been implemented. High skirt selectivity and wide stopband are observed in the results.

1. INTRODUCTION

Filters are key elements in modern wireless and mobile communication systems. They are widely used in many aspects. Since most electronic devices become compact, it is important to decrease the size of bandpass filter. In response to this requirement, much research has been carried out and there are various methods proposed [1–6]. One of the method is using a compact quarter-wavelength resonators. For example, the dumb-bell-shaped slot resonator in [1], the microstrip net-type resonators in [2], the octagonal hairpin resonators in [3] as well as the parallel-coupled-line filters in [4]. In another method, dual-mode resonators is also used to reduce the circuit size [5]. Beside miniaturized size, high-selectivity and harmonic suppression are two important topics in filter design. In general, the selectivity can be improved by introducing transmission zeros near the passband. To suppress spurious responses, it is feasible to introduce transmission zeros in the spurious frequency [6] or move the spurious frequency to a higher frequency using stepped impedance resonators (SIRs) [7].

In recent years, with the development of IC industry and the operating frequency in wireless communication system shifting to higher frequency, more and more bandpass filters have been complemented at such high frequency. For instance, a 4-stage on-chip open loop resonators band pass filter which operate at 60 GHz is proposed in [8]. A 70-GHz Millimeter-Wave compact bandpass filter fabricated using standard 0.18-µm CMOS technology is designed in [9]. At such high frequency,the characteristic of miniaturized size, high-selectivity and harmonic suppression are also required in the bandpass filter of millimeter-wave applications.

In this paper, a wide stop-band BPF is designed on GaN MMIC with good performance. The circuit consists of two symmetrical coupled quarter-wavelength transmission-line resonators and two coupled transmission-line feeding structures. The asymmetric feeding structures are utilized to suppress the third harmonic, whereas the fundamental one can pass with less influence. Source-load coupling is introduced to generate two transmission zero near the passband. Thus, both wide-stop band and high-selectivity is achieved in this design. Base on the proposed idea, a bandpass filter with wide stop-band at the operating frequency of 30 GHz has been implemented. The design methodology and experimental results are also presented.

2. FILTER DESIGNED ON GAN MMIC

The configuration of the proposed bandpass filter is shown in Fig. 1. Two folded symmetrical coupled quarter-wavelength transmission-line resonators and two coupled transmission-line feeding structures are used to make up the circuit. By using this structures, miniaturized circuit size is achieved. The resonators and feeding line are connected by the via, thus both electrical and magnetic coupling are realized. The asymmetrical structures of the feeding line are used not only to cause mismatch at the third harmonic frequency between the resonators and the feeding line but also to provide source-loaded coupling to generate two transmission zeros near the passband, resulting in both wide stop-band and high selectivity.

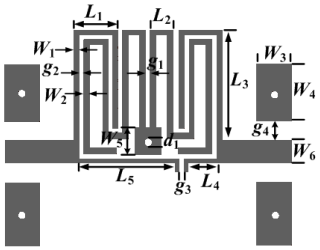

Figure 1: The configuration of the proposed circuit.

In this design, the harmonic suppression is obtained by the novel asymmetric feeding structure. One end of the feeding line is embedded in the gap of the resonators while the other end is put asymmetrical outside the resonator. The length of L_4 and L_5 is the length of each feeding lines which is put outside the resonators. Fig. 2 shows the simulated current distributions at 80 GHz with different L_4 and L_5. It is known that the asymmetric feeding structure caused by the unequal value of L_4 and L_5 will influence the asymmetric voltage distribution on the feeding line. Thus the external quality factor named Q_{e3} at the third harmonic frequency can be controlled by altering the value of L_4 and L_5. It is found that when L_4 and L_5 equal to 60 µm and 254 µm, the Q_{e3} approaches infinite. Therefore the mismatch between the resonator and feeding line can be caused, resulting in harmonic suppression. What's more, the end of the feeding line is extended in another direction to realize source-load coupling which can generate two transmission zero near the passband.

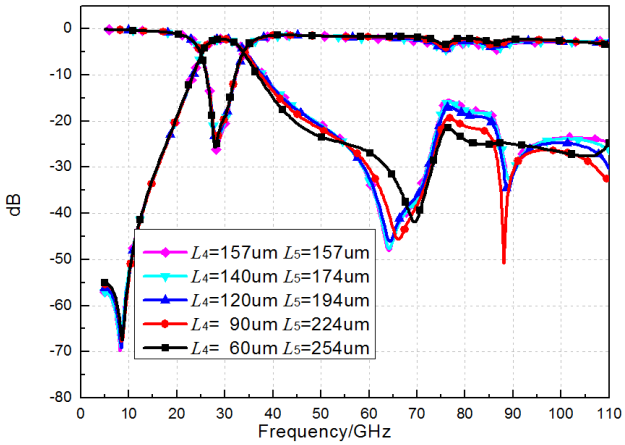

Figure 2: The simulated current distributions at 80 GHz with different L_4 and L_5.

3. EXPERIMENT

Based on the analysis above, the design procedures of the proposed filter are introduced as follows. The first step is to obtain the required operating frequency by determining the length of the resonators which have the electric length of quarter-wavelength. The second step is to obtain the required coupling coefficient k and external quality factor Q_e at the passband. In this design, a two-pole Chebyshev lowpass prototype with 0.5 dB passband ripple is chosen, the lumped circuit element values of the prototype filter are selected to be: $g_0 = 1$, $g_1 = 1.4029$, $g_2 = 0.7071$, $g_3 = 1.9841$. The proposed filter has a 3-dB bandwidth of 23%. Accordingly, the k and Q_e can be calculated by the equation below:

$$k_{12} = k_{13} = \frac{\text{FBW}}{\sqrt{g_1 g_2}} = 0.23 \tag{1}$$

$$Q_e = \frac{g_0 g_1}{\text{FBW}} = 6.1 \tag{2}$$

In this design, the gap g_1 can be adjusted to obtain the desirable k. As for Q_e at the passband, it is mainly determined by the position of the 50-ohm ports. In this design, we can alter the length

L_3, the width of the feeding line W_1 and the gap between the feeding line and the resonator g_2. The third step is to adjust L_4 and L_5 to get appropriate value to suppress the third harmonic.

For demonstration, a novel compact bandpass filter for 30 GHz millimeter-wave applications in Monolithic Microwave Integrated Circuit (MMIC) is designed. The dimensions are chosen as follows: (all in μm): $L_1 = 115$, $L_2 = 60$, $L_3 = 270$, $L_4 = 60$, $L_5 = 254$, $W_1 = 14$, $W_2 = 16$, $W_3 = 90$, $W_4 = 150$, $W_5 = 70$, $W_6 = 150$, $g_1 = 13$, $g_2 = 13$, $g_3 = 12$, $g_4 = 50$. The overall size of the fabricated filter is 7.9 mm × 5.4 mm or $0.1\lambda g \times 0.079\lambda g$. Fig. 3 shows the substrate structure of the MMIC filter. There are three layers of substrates in this design. They are SiN, GaN and Silicon from top to bottom with the relative dielectric constant of 6.5, 9, 11.9 and dielectric loss tangent of 0.09, 0.09, 0.01, respectively. And the thicknesses of each substrate are 0.15 μm, 6.28 μm and 93.57 μm. The material of the microstrip lines is gold, with a thickness of 2.15 μm.

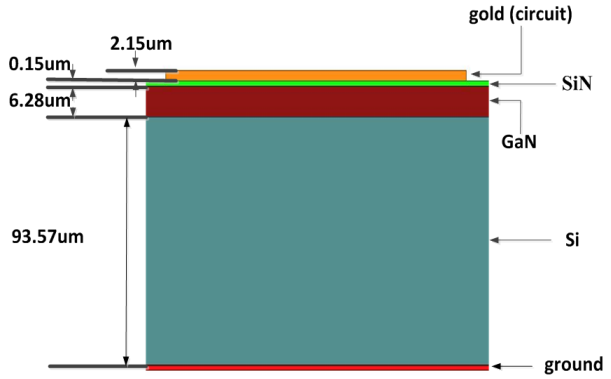

Figure 3: The substrate structure of the MMIC filter.

Figure 4 shows S-parameters of the proposed filter. The filter has a 3-dB bandwidth of about 6.8 GHz at the center frequency of 30 GHz. The insertion loss of the passband is about 3 dB and return loss is better than 15 dB at the center frequency. Also, four transmission zeros appear at the frequency of 10 GHz, 46 GHz, 75 GHz and 85 GHz, which help achieve the wide stopband and high skirt selectivity. The rejection level is more than 25 dB within the frequency range from 41 GHz to 110 GHz. The area of the filter is only 400 μm × 310 μm ($0.092\lambda g \times 0.069\lambda g$), where λg is the guided wavelength at the operating frequency of 30 GHz.

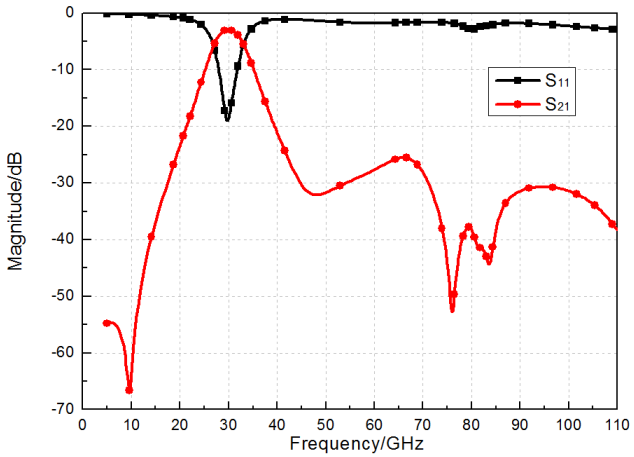

Figure 4: The S-parameters of the proposed filter.

4. CONCLUSION

A wide-stopband millimeter-wave BPF on GaN MMIC using asymmetric feeding structure has been proposed in this paper. The design methodology and experimental results have been presented. Due to the MMIC technology and its compact structure, the filter is only 400 μm × 310 μm ($0.092\lambda g \times 0.069\lambda g$) and a wide stopband response is realized by the novel feeding structure. Two transmission

zeros are realized near the passband edges by introducing the source-load coupling to this design which can help to achieve high selectivity. The BPF works at the frequncy of 30 GHz. The compact size as well as wide stopband makes it attractive for many millimeter-wave applications.

REFERENCES

1. Jung, D., J. Hansen, and K. Chang, "Miniaturised bandpass filter using dumb-bell-shaped slot resonator," *Electronics Letters*, Vol. 48, No. 22, 100–102, 2012.
2. Chen, C.-F., T.-Y. Huang, and R.-B. Wu, "Novel compact net-type resonators and their applications to microstrip bandpass filter," *IEEE Trans. Microw. Theory Tech.*, Vol. 54, No. 2, 755–762, 2006.
3. Liu, H. W. and W. M. Li, "Miniaturised microstrip bandpass filter using octagonal hairpin resonators with side-coupled technique," *Electronics Letters*, Vol. 44, No. 24, 1410–1411, 2008.
4. Park, J.-H., S. K. Lee, and Y. S. Lee, "Extremely miniaturized bandpass filter based on asymmetric coupled lines with equal reactance," *IEEE Trans. Microw. Theory Tech.*, Vol. 60, No. 2, 261–269, 2012.
5. Wang, J. P., J.-L. Li, J. Ni, S. S. Zhang, W. Wu, and D. G. Fang, "Design of miniaturized microstrip dual-mode filter with source-load coupling," *IEEE Microw. Wireless Compon. Lett.*, Vol. 20, No. 6, 319–321, 2010.
6. Gao, J. and L. Zhu, "Asymmetric parallel-coupled CPW stages for harmonic suppressed $\lambda/4$ bandpass filters," *Electronics Letters*, Vol. 40, No. 18, 1122–1123, Sep. 2004.
7. Chan, H. K. and K. Chang, "Wide-stopband bandpass filters using asymmetric stepped-impedance resonator," *IEEE Microw. Wireless Compon. Lett.*, Vol. 23, No. 2, 69–71, Feb. 2013.
8. Pokharel, R. K., X. Liu, R. Dong, A. B. A. Dayang, H. Kanaya, and K. Yoshida, "A high selectivity, low insertion loss 60 GHz-band on-chip 4-pole band pass filter for millimeter wave CMOS SoC," *Proceedings of the 6th European Microwave Integrated Circuits Conference*, 660–663, Oct. 2011.
9. Hsu, C. Y., Y. S. Lin, C. Y. Chen, et al., A 70-GHz millimeter-wave compact bandpass filter fabricated using standard 0.18-µm CMOS technology," *38th European IEEE Microwave Conference, EuMC*, 215–217, 2008.

Substrate Integrated Waveguide Frequency Reconfigurable Filter Controlled by Magnetic Field

Qiu Dong Huang, Xiao Liang Liu, and Yu Jian Cheng
University of Electronic Science and Technology of China, China

Abstract— In this work, a novel upper and lower sideband tunable SIW bandpass ferrite filter is presented. With the application of an external magnetic bias on the ferrite slabs, the lower sideband of the filter can be adjusted from 8.8 GHz to 10.7 GHz and the upper sideband can be tuned from 9.3 GHz to 12.0 GHz. Compared to previously reported frequency tunable SIW filters, the proposed filter offers a relatively wide tuning range and flexibly reconfigurable abilities while dramatically reducing the complexity of external control circuit.

1. INTRODUCTION

Frequency tunable/reconfigurable filters have special significance in future smart and miniaturized wireless systems [1, 2]. The currently popular substrate integrated waveguide (SIW) technique [3] combines the best and complementary features of both planar transmission lines and non-planar waveguides. Thus it is found very appropriate in microwave and millimeter-wave tunable filter applications. Researchers try to realize some SIW reconfigurable filters by use of PIN diodes [4, 5] and varactors [6, 7]. Unlike those conventional planar transmission lines, such as the microstrip line, the SIW is a uniconductor guided-wave structure and has the same electric potential for each metallic surface. Therefore, some difficulties exist in electronically tunable SIW designs. Besides, complex DC bias circuits may lead to unwanted leakage and interference. Tuning operation characteristics of SIW components by magnetic field is another possible way of avoiding these problems.

In this paper, a tunable bandpass filter is designed with YIG ferrite employed in. Both lower sideband and upper sideband of the filter can be adjusted separately. This ferrite-loaded SIW filter can be considered as two sub-components. Design principles of these two sub-components are based on isolator and switch respectively. Up to now most reconfigurable SIW bandpass filters are achieved by resonant cavity [8–11]. In [12] circulators/isolators are used as tunable bandpass filter. However no publication is found to use isolator and switch to achieve reconfigurable bandpass filter.

2. FILTER IMPLEMENTATION

This ferrite bandpass filter is proposed of a reconfigurable highpass filter, which is based upon ferrite switches, and a tunable broadband isolator can be viewed as a bandstop filter. In this section, these two sub-components are designed respectively. At last, the SIW frequency reconfigurable filter is proposed. The substrate used is 0.508 mm thick Rogers6010 substrate. Its permittivity and loss tangent are 10.2 and 0.0023, respectively. YIG ferrite is employed in this design. Its saturation magnetization value is 1850 Gs, relative dielectric constant is 14.5, and 3 dB line width is 20 Oe. All ferrite slabs used in this design is as thick as the substrate.

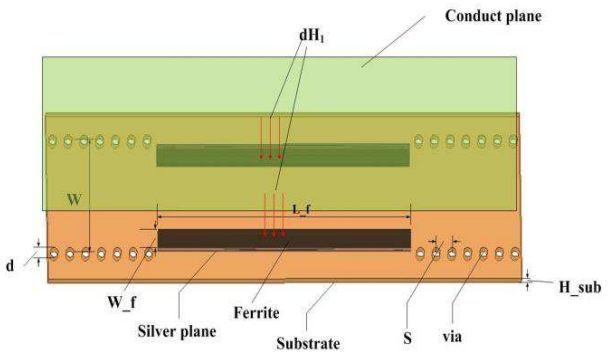

Figure 1: Structure of the highpass filter.

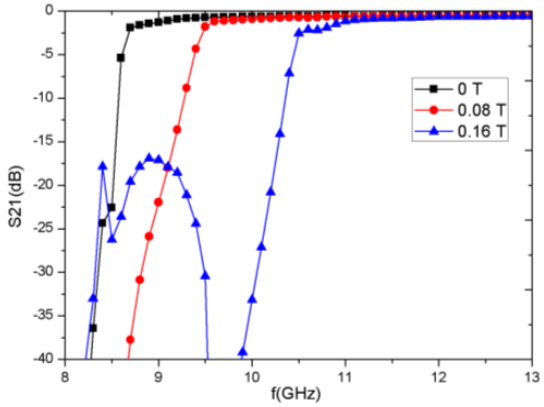

Figure 2: S_{21} in different dH_1.

2.1. Highpass Filter

In this part a highpass filter is employed to form the lower sideband of the reconfigurable bandpass filter. According to [13, 14] proper SIW dimension is chosen firstly. As shown in Fig. 1, the actual SIW width (W) is 6.1 mm, the distance between adjacent metallic vias (S) is 1.2 mm, and the diameter of vias (d) is 0.6 mm. After Full-wave EM simulations were performed with the help of *ANSYS* HFSS, $L\_f = 16$ mm and $W\_f = 1$ mm are obtained.

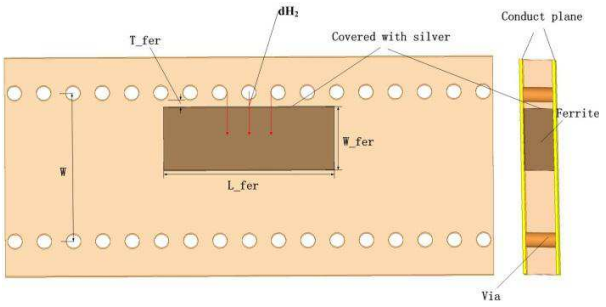

Figure 3: Configuration of the isolator.

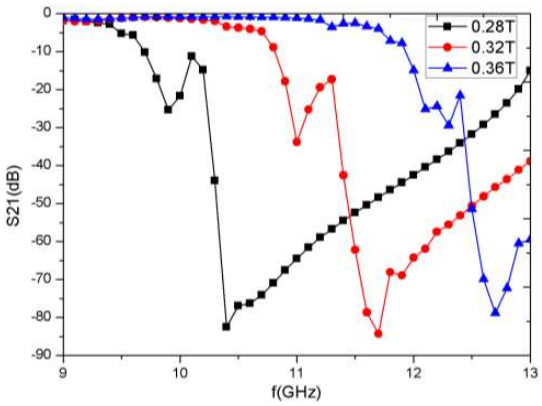

Figure 4: S_{21} response when dH_2 changes.

With the application of an external magnetic bias (dH_1) on the ferrite slabs, the cutoff frequency of the SIW is changed [15], thereby making the highpass filter tunable. Fig. 2 shows the highpass filter can be adjusted from 8.8 GHz to 10.7 GHz with about 1.5 dB insertion.

2.2. Isolator

The second component, which is associated with a wide ferrite slab in a SIW with the magnetic field perpendicular to the direction of propagation, employs the edge-mode effect [16] to achieve the bandstop phenomenon and then form the upper sideband of the SIW filter. As shown in Fig. 3, the wide ferrite slab, one of its surface is covered with silver, is inserted in the substrate. The silver plane acts as a short plane and EM wave will be absorbed in the ferrite slab when external magnetic bias (dH_2) is applied. The dimension of the ferrite is obtained by simulation and parameter optimization by Ansoft HFSS: $T\_fer = 1.25$ mm, $W\_fer = 2$ mm, $L\_fer = 8$ mm.

As shown in Fig. 4, the achieved upper sideband of the SIW filter is increased as dH_2 increases from 0.28 T to 0.36 T.

2.3. Tunable Bandpass Filter

As Fig. 5(a) shows, the isolator and the highpass filter are connected in this section and microstrip to SIW transition structure [17, 18] is added. By HFSS optimization simulation, the following parameter values are obtained: $W_1 = 0.45$ mm, $W_2 = 2.8$ mm, $L_1 = 3.3$ mm, $L_2 = 6.2$ mm, $L_3 = 3.6$ mm, $L\_sub = 64$ mm, $W\_sub = 16$ mm. When $dH_1 = 0$ and $dH_2 = 0.28$ T is applied to the ferrite slabs about 10 dB return loss is achieved as shown in Fig. 5(b). As shown in Fig. 5(c), the lower sideband of the filter can be adjusted from 8.8 GHz to 10.7 GHz. As shown in Fig. 5(d), the upper sideband can be tuned from 9.3 GHz to 12.0 GHz. Furthermore, a filter whose operating

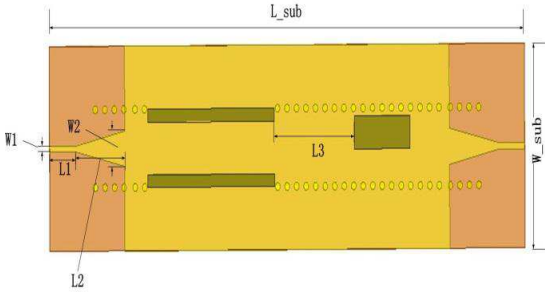

(a)

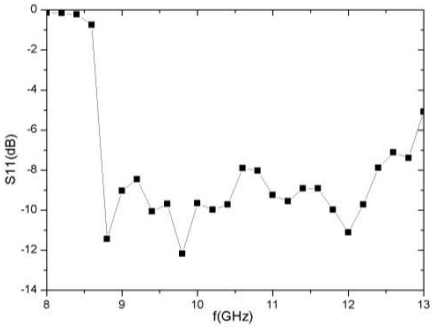

(b)

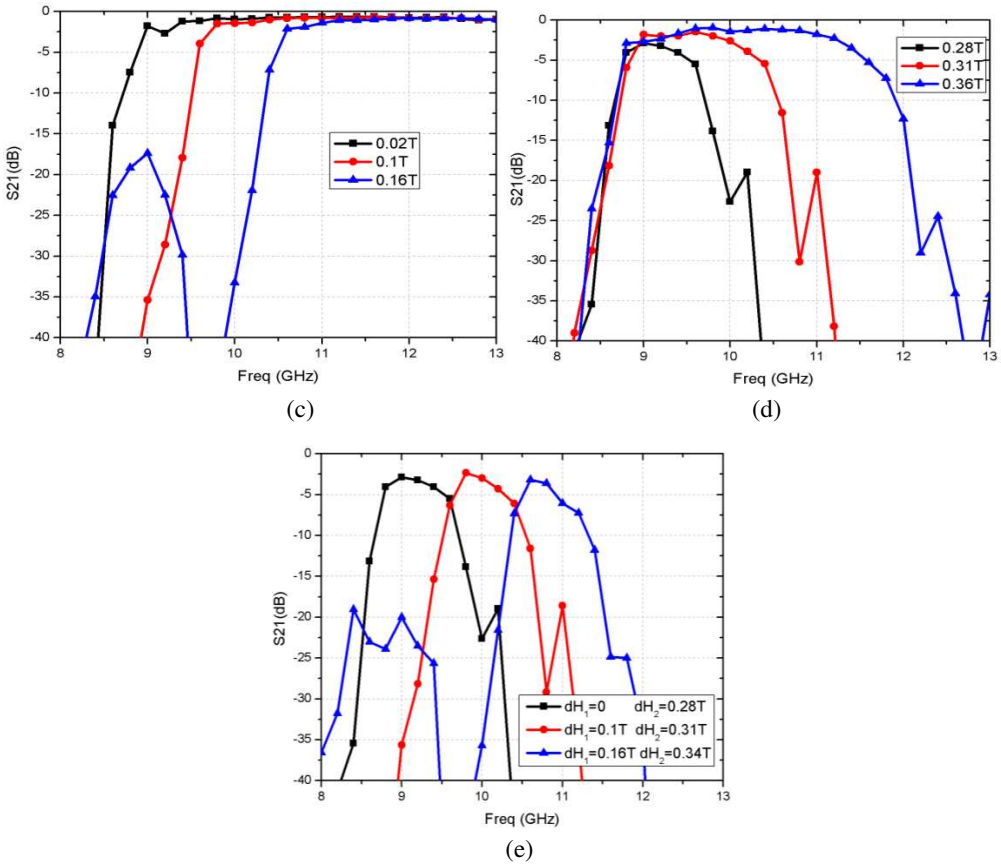

Figure 5: Geometry and variation of the passband center frequency with the applied magnetization field of the SIW filter: (a) Scheme of the SIW filter; (b) S_{11} response; (c) Variation of lower bandside with dH_1 changes; (d) Variation of lower bandside with dH_2 changes; (e) Variation of the passband with the applied magnetization field's increasing.

band can be adjusted from 8.8 GHz to 12 GHz is achieved with approximately 2.5 dB insertion loss as shown in Fig. 5(e).

3. CONCLUSION

A novel frequency reconfigurable SIW bandpass filter is presented in this paper. The bandpass of the proposed filters can be reconfigured by adjusting the dc-magnetic bias applied to the ferrite slabs located at an SIW structure. With the employment of the ferrite material, the proposed bandpass filter can realize upper sideband and lower sideband's tunable severally while dramatically reducing the complexity of external control circuit compared to traditional electronic control methodologies.

ACKNOWLEDGMENT

This work is supported in part by the China Postdoctoral Science Foundation under grant 2013T608 46 and 2012M511918.

REFERENCES

1. Berezdivin, R., et al., "Next-generation wireless communications concepts and technologies," *IEEE Communications Magazine*, Vol. 40, 108–116, 2006.
2. Velazquez-Ahumada, M. D. C., J. Martel-Villagr, F. Medina, and F. Mesa, "Design of bandpass filters using stepped impedance resonators with floating conductors," *Progress In Electromagnetics Research*, Vol. 105, 31–48, 2010.
3. Cheng, Y. J., "Substrate integrated waveguide frequency-agile slot antenna and its multibeam application," *Progress In Electromagnetics Research*, Vol. 130, 153–168, 2012.
4. Cheng, Y. J., Y. X. Guo, X. Y. Bao, and K. B. Ng, "Millimeter-wave low temperature cofired ceramic leaky-wave antenna and array based on the substrate integrated image guide technology," *IEEE Trans. Antennas Propag.*, Vol. 62, No. 2, 669–676, 2014.

5. Armendariz, M., V. Sekar, and K. Entesari, "Tunable SIW bandpass filters with PIN diodes," *IEEE Microwave Conference (EuMC)*, 2010.
6. Sirci, S., J. D. Martinez, M. Taroncher, et al., "Varactor-loaded continuously tunable SIW resonator for reconfigurable filter design," *IEEE 41st European Microwave Conference (EuMC)*, 436–439, 2011.
7. He, F. F., K. Wu, W. Hong, et al., "A low phase-noise VCO using an electronically tunable substrate integrated waveguide resonator," *IEEE Transactions on Microwave Theory and Techniques*, Vol. 58, No. 12, 3452–3458, 2010.
8. Zheng, Y., M. Sazegar, H. Maune, et al., "Compact substrate integrated waveguide tunable filter based on ferroelectric ceramics," *IEEE Microwave and Wireless Components Letters*, Vol. 21, No. 9, 477–479, 2011.
9. Cheng, Y. J. and C. A. Zhang, "Miniaturized half mode substrate integrated waveguide cavity resonator and filter with good spurious suppression," *Journal of Electromagnetic Waves and Applications*, Vol. 27, No. 3, 396–404, 2013.
10. Adhikari, S., A. Ghiotto, and K. Wu, "Simultaneous electric and magnetic two-dimensionally tuned parameter-agile SIW devices," *IEEE Transactions on Microwave Theory and Techniques*, Vol. 61, No. 1, 423–435, 2013.
11. Tetz, K., C. H. Chen, W. Nakagawa, et al., "Design, fabrication and characterization of narrowband angularly-insensitive resonant cavity filter," *IEEE the 15th Annual Meeting on Lasers and Electro-optics Society*, Vol. 2, 449–450, 2002.
12. Almalkawi, M., L. Zhu, and V. Devabhaktuni, "Magnetically tunable substrate integrated waveguide bandpass filters employing ferrites," *IEEE 36th International Conference on Millimeter and Terahertz Waves (IRMMW-THz)*, 1–2, 2011.
13. Cheng, Y., X. Bao, and Y. Guo, "60-GHz LTCC miniaturized substrate integrated multibeam array antenna with multiple polarizations," *IEEE Trans. Antennas Propag.*, Vol. 61, No. 12, 5958–5967, 2013.
14. Cheng, Y. J., W. Hong, and K. Wu, "Design of a substrate integrated waveguide modified R-KR lens for millimetre-wave application," *IET Microwaves, Antennas & Propagation*, Vol. 4, No. 4, 484–491, 2010.
15. Ghiotto, A., S. Adhikari, and K. Wu, "Ferrite-loaded substrate integrated waveguide switch," *IEEE Microwave and Wireless Components Letters*, Vol. 22, No. 3, 120–122, 2012.
16. Fesharaki, F., C. Akyel, and K. Wu, "Broadband substrate integrated waveguide edge-guided mode isolator," *Electronics Letters*, Vol. 49, No. 4, 269–271, 2013.
17. Cheng, Y. J., W. Hong, and K. Wu, "Millimeter-wave multibeam antenna based on eight-port hybrid," *IEEE Microw. Wireless Compon. Lett.*, Vol. 19, No. 4, 212–214, 2009.
18. Cheng, Y., H. Xu, D. Ma, et al., "Millimeter-wave shaped-beam substrate integrated conformal array antenna," *IEEE Trans. Antennas Propag.*, Vol. 61, No. 9, 4558–4566, 2013.

Additional Cross Coupling Coefficient Used as Matching Ladder Network in Coupled Based Band Pass Filters

B. Moradi, U. Martinez, and J. J. García-García
Electrical Engineering Department GAEMI
Universitat Autonoma de Barcelona, Cerdanyola Del Valles, Spain

Abstract— A coupling coefficient based filter is presented in this paper. The novelty of the proposed design is the introduction of a cross coupling interaction that allows to match the impedance achieving excellent performance, in the transmission and reflection response. Equivalent circuit model is discussed. Clear relation between each component and physical dimensions of the proposed design are established. Measured of a 19.4% band pas filter at 1.6 GHz is reported and compared with EM simulation and equivalent circuit model showing an excellent agreement.

1. INTRODUCTION

Coupling coefficient based design filter is an easy way to synthesize standard filter response [1]. In the design process of this kind of filters it is necessary to use electromagnetic simulators to optimize the filter performance in order to fit the specifications. The designs based on the coupling coefficient exhibit an inherent limitation fixed by the minimal distance allowed by the technology between adjacent resonators. The interaction between resonators and, specially, the interaction between the input-output ports introduces loads in the resonators that affects to the fundamental resonant frequencies as well as to the matching impedance. Therefore, to obtain a good performance it is necessary to go through some optimization process in which the design physical dimensions are modified to balance the resonators resonant frequencies and to achieve the best impedance matching [2]. However, even after this optimization process there is a big gap between the perfect impedance match and the optimized structure. In this paper we propose a small modification of the layout that introduces a cross coupling that can be interpreted as an additional matching ladder network. The proposed equivalent circuit model fits the measured and EM simulated responses. Since it is possible to set up direct relation between the equivalent circuit model parameters and the physical layout parameters, the equivalent circuit model becomes a very useful tool in the optimization stage of the filter design.

2. LAYOUT OF THE PROPOSED DESIGN

Figure 1 shows the layout dimensions of the proposed filter. It has been implemented in a Rogers RO3010 substrate using a laser milling machine. The minimal distance between the resonators is 0.2 mm and the distance between the port line extension and the resonators has been fixed to 0.15 mm which is the more critical distance of the design.

The ports feed the resonators through a capacitive coupling which intensity depends of the proximity to the extreme resonators (1.5 mm). The square shape of the resonators has been chosen to maximize the inter-resonator capacitance coupling, resulting in a final thickness of 3.1 mm, and to maximize the coupling between resonators according with the previous experience with this kind of design [3, 5]. The input and output ports are 50 Ω microstrip lines that, in this substrate correspond to 1.6 mm thick microstrip. Extensions of the ports with a 90° angle following the square resonator profile have been included in order to maximize the coupling with the side resonators.

3. EQUIVALENT CIRCUIT MODEL

The equivalent circuit model of a filter helps to understand the behavior of the design. In this case a clear relationship between the equivalent circuit model and the layout physical dimensions can be set. Fig. 2 shows the equivalent circuit model of the proposed filter. Basically it is composed by three LC tanks which have been modeled as three open rings, and a set of Π model for capacitive coupling networks sketched as the different couplings.

The coupling between resonators is a consequence of the electromagnetic interchange between resonators.

Geometry symmetries are able to force the predominance of one of both magnetic and electric coupling [5]. In our case there are three different kinds of electric coupling, characterized by the

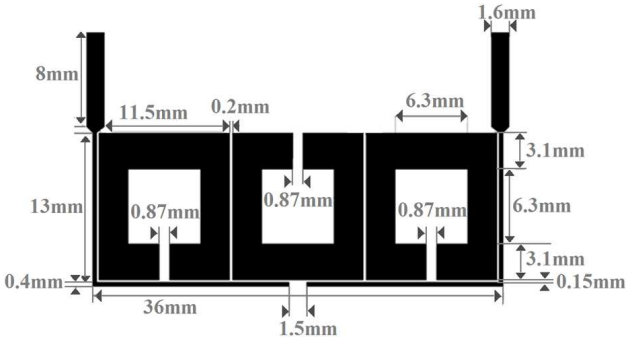

Figure 1: Layout of the proposed coupling coefficient based Chebyshev filter implementation.

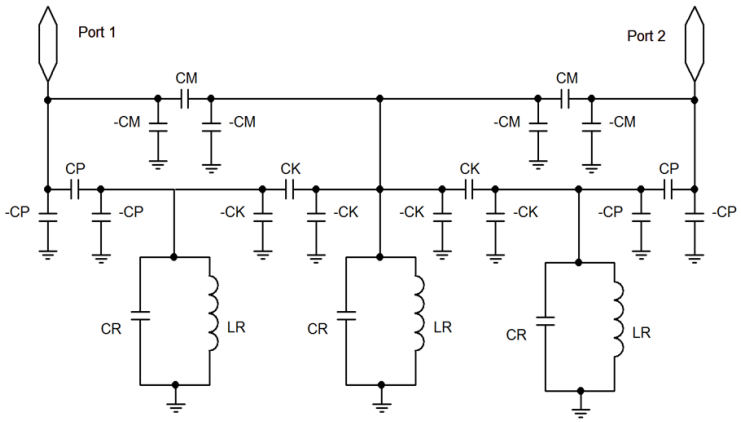

Figure 2: Equivalent circuit model of the proposed filter.

parameters C_P, C_M and C_K. C_P is modeling the coupling between the port extensions and the extern resonators. The value of this parameter can be modified in the layout altering the horizontal distance between the port extension and the adjacent resonator. Also, there is a dependence of this parameter with the side of the adjacent resonator, being possible to modify this coupling using rectangular shape resonators. The C_K parameter models the coupling between adjacent resonators and can be controlled directly with the distance between the resonators. The maximum value of this capacitance is fixed by the minimal distance between metallic layers that the fabrication technology allows. The maximum bandwidth of the filters is bounded to the maximum coupling coefficient [1], and this is the importance of this value. Finally, C_M represents the cross coupling coefficient that represent the novelty of the proposed design. The equivalent circuit model of the capacitive coupling is a Π circuit with two negative capacitors in the parallel branches. Interpreting the negative capacitors as inductors, the structure can be thought as L-C-L matching ladder. Since the value of the C_M can be controlled with the variation of the overlap between the port extension and the central square resonator. This matching ladder can be tuned in a certain range of values. The values of the different parameters can be initially estimated from the physical dimensions, but at the end there will be necessary to optimize them to fit the measured response. Table 1 shows a summary of the equivalent circuit model parameters for the best fit. Work is in progress to improve this fitting and to extend these relations to functions that can link the filter specifications with physical parameters in a useful range for the design process.

4. MEASURED RESULTS

Measures of the fabricated prototype depicted in Fig. 3 shows a band pass between 1.44 GHz and 1.75 GHz performing a 19.4% fractional bandwidth. The return losses are below the −10 dB in all the band pass and the insertion losses oscillate between −1.98 dB and −0.79 dB. The outsideband transmission level stays below −30 dB. The band-pass exhibits a non-symmetrical shape being sharper for the low frequency flank.

As can be seen in Fig. 3, the measured shows excellent agreement with the electromagnetic simulations and the equivalent circuit response. It is a privileged starting point to develop a robust

Table 1: Summary of equivalent circuit model parameters and geometrical parameters.

Equivalent Circuit parameter	Value		Layout dimensions
Resonant Tank	LR	6.5e-5 nH	External Ring perimeter: 48.13 mm
	CR	219000 pF	Ring: 48.13 mm
			Ring Thickness: 3.1 mm
Coupling	CP	296 pF	Overlap length between Port extension and resonant ring: 23.63 mm
			Distance between port extension and extreme rings: 150 µm
	CK	36505 pF	Distance between adjacent rings: 200 µm
			Side of the rings: 13 mm
	CM	55 pF	Overlap length between port extension and the central ring: 5 mm
			Distance between port extension and central ring: 150 µm

design methodology.

Further work is under development to improve the utilization of designs with small modifications can be extended to wideband-pass filters.

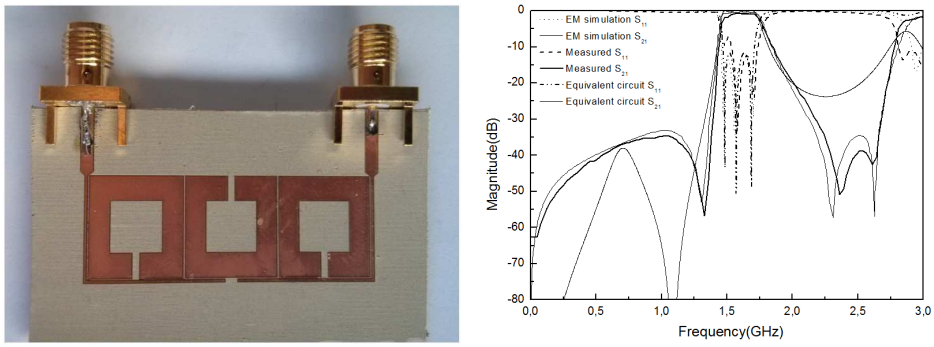

(a) (b)

Figure 3: (a) Picture of the fabricated prototype. (b) Comparison between S_{11}, and S_{21}, measured, electromagnetically simulated and equivalent circuit response.

5. CONCLUSION

The inclusion of the cross coupling in the standard Chebyshev filter supplies an additional matching ladder allowing to match the impedance of the design. The proposed equivalent circuit model based on the capacitance coupling transmission line lets to establish a clear relation between the equivalent circuit model and the layout physical dimensions, therefore establishing a link between the filter specifications and the layout physical dimensions. The designed filter using this cross coupling coefficient has been fabricated and tested. The measured shows and excellent agreement with the electromagnetic simulations and the equivalent circuit response. Work is in progress to extend the technique to match wide band filters through ladder networks with coupling interaction to other filters.

ACKNOWLEDGMENT

This work has been supported by Ministerio de Ciencia y Educación of the Spanish government under the project TEC2010-16060.

REFERENCES

1. Hong, J. and M. L. Lancaster, *Microstrip Filters for RF/Microwave Applications*, John Willey & Sons, Inc., New York, 2001.

2. Pozar, D. M., *Microwave Engineering*, John Willey & Sons, Inc., New York, 1998.
3. García-García, J., J. Bonache, I. Gil, F. Martín, M. C. Velazquez-Ahumada, and J. Martel, "Miniaturized microstrip and CPW filters using coupled metamaterial resonators," *IEEE Transactions on Microwave Theory and Techniques*, Vol. 54, No. 6, 2628–2635, 2006.
4. García-García, J., J. Bonache, I. Gil, F. Martín, R. Marqués, F. Falcone, T. Lopetegi, M. A. G. Laso, and M. Sorolla, "Comparison of electromagnetic band gap and split-rings resonators microstrip lines as stop band structures," *Microwave and Optical Technology Letters*, Vol. 44, No. 4, 376–379, 2005.
5. García-García, J., F. Martín, F. Falcone, J. Bonache, I. Gil, E. Amat, T. Lopetegi, M. A. G. Laso, J. A. M. Iturmendi, M. Sorolla, and R. Marqués, "Microwave Filters with Improved Stopband based on Sub-wavelength Resonators," *IEEE Transactions on Microwave Theory and Techniques*, Vol. 53, No. 6, 1997–2006, 2005.

High Efficiency TM_{01}-mode Cylindrical Waveguide Microwave Reactor for Microwave Material Continuing Processing

Yi-Chen Zhong, Wei-Na Huang, and Yu-Jian Cheng
University of Electronic Science and Technology of China, Chengdu, China

Abstract— A cylindrical waveguide microwave reactor is proposed for microwave material continuing processing. This traveling-wave type chemical reactor could be used in food processing, microwave chemistry, coal desulfurization, etc.. The new structure is designed in order to support the reactants at the central of the reactor to achieve the highest efficiency. Compared with the existing microwave reactors, such as rectangular waveguide types and ridge waveguide types, our structure has considerable advantages in the distribution of the field strength, reaction effect, lack and energy consumption on processing reactants.

1. INTRODUCTION

Nowadays, more microwave energy has been used in different areas of its unique effects such as food processing, machining, environmental protection, development of new materials, chemical synthesis, etc. [1]. The industrial application of microwave energy for continuous high-power microwave reactor raised higher requirements while the traditional box-type reaction chambers are not suitable to the assembly line in the factory anymore [2]. Previous researchers have done fruitful research in the continuous microwave reactor and various forms were invented [2, 3], such as rectangular waveguide types, ridge waveguide types, and folded waveguide types. They focused mainly in the distribution of the field strength, reaction effect, and energy consumption but it has not been satisfactorily resolved [4].

However, the application of the circular waveguide type microwave reactor is relatively uncommon while circular waveguide is widely used in other fields [2]. Because 1) it is difficult to transport sample in a circular waveguide reactants without wheels, which would seriously destroy the original distribution of field inside so that the efficiency and power capacity would drastically reduce [4]. 2) The dominant mode of circular waveguide (TE_{11} mode) has polarization degeneracy phenomenon, which will greatly reduce the microwave absorption efficiency. Therefore, high-order mode circular waveguide reactor is needed to improve the efficiency of it. In this paper, a cylindrical waveguide microwave reactor, as shown in Fig. 1, is proposed for microwave material continuing processing. This traveling-wave type chemical reactor compared with the existing microwave reactor, such as rectangular waveguide types, ridge waveguide types, has obvious advantages in the distribution of the field strength, reaction effect, and energy consumption.

2. MICROWAVE REACTOR DESIGN

As shown in Fig. 1, a cylindrical waveguide microwave reactor with two axial slits is demonstrated in this paper. It operates with TM_{01} mode, i.e., the first high-order mode. In this configuration, the electric field is concentrated on the axis of the cylindrical waveguide as shown in Fig. 2, which indicates that the field reduces significantly due to the strong interaction between the microwave and samples. Thus the sample is located in this region and carried by the low-loss conveyor belt. In this case, the electric field sufficiently react with the samples, thereby enhancing the absorption of the microwave power of the sample to accelerate the reaction (the absorbed power $P = 56.62 \times 10^{-12} f E^2 \varepsilon''$ is proportional to electric field strength) [5]. Two axial slits are cut out from the conductor wall of the cylindrical waveguide in order to fix the conveyor belt, which goes through the two slits, is connected to the wheels outside to support the sample and the absorbing materials are placed around the slots. However, the two axial slits will not influence the field in the reactor because currents on the wall of circular waveguide only have axial component, which means only a very small part of the electromagnetic waves will radiate from the slot [6]. We use the simulation software Ansoft HFSS 13.0 for modeling & simulation while C8 standard circular waveguide, which was shown in Fig. 3 with $L = 30$ mm, was chosen to find out the radiation loss ratio of TM_{01} mode at 915 MHz. The result is shown in Fig. 4 and it indicates that the width of slots should be no more than 20 mm, which is wide enough to fix a thicker conveyor belt [7]. The total radiation loss of a reactor within one meter long will be less than 0.06% of the power being inputted, which is less enough to be absorbed by absorbing materials.

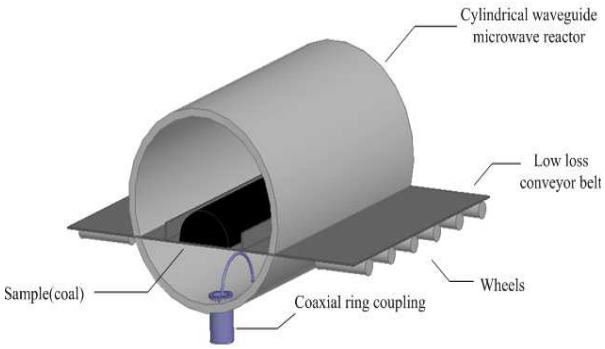

Figure 1: Pulverized coal desulfurization reaction.

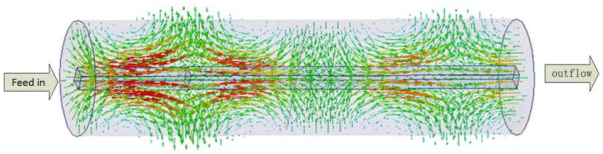

Figure 2: Distribution of electric fields in part of reactor.

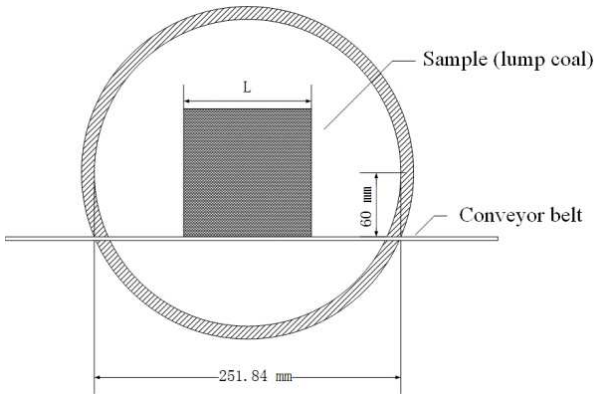

Figure 3: Axial view of the reactor.

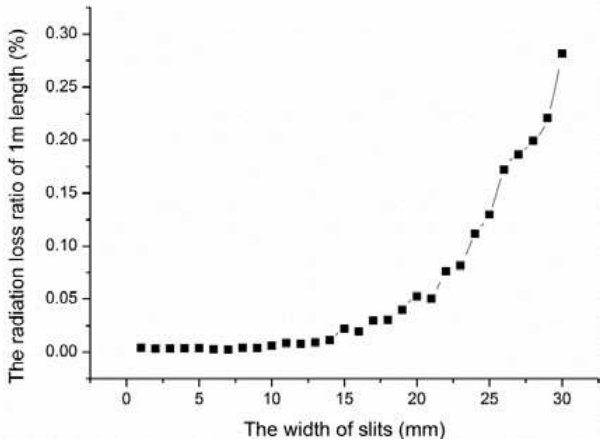

Figure 4: Radiation loss ratio.

However, the TM_{01} mode microwave in the reactor may be converted into the TE_{11} mode [6], i.e., the dominant mode of cylindrical waveguide, due to the discontinuity of the waveguide and the sample. It should be noted that the conversion will no always happen due to the orthogonally between the electric fields of these two mode [6]. Furthermore, the slits that wrapped by absorbing material outside could inhibit the appearance of the TE_{11} mode by cutting radially current on the inner surface.

The coaxial ring coupling feeding method is employed to excite the TM_{01} mode. Depending on the size of sample, reactor can be fed from beneath, as shown in Fig. 2, or above of the conveyor belt. Considering the versatility and power capacity, coaxial line Model 50-16 was chosen to feed the reactor. The feeding method is to connect the outer conductor of the coaxial line with the inner wall of the reactor, then wound the inner conductor into a semi-circle, the radius of 89.07 cm, and connect it to the inner wall too. Considering the impedance of microwave reactor is depending on type and quantity of samples, it is necessary to change the depth of insertion depending on reflection coefficient of the coaxial to get the best match. As shown in Fig. 5, twice small rectangular waveguides at both sides of reactor are used to transmit the reactant and block the microwave from leaking. Simulation results show that the ratio of power been leaked from both sides will be less than 0.02%.

3. COMPARISON AND RESULTS

Before compared with the other widely used reactors [3, 8], we must first establish a unified criteria. Although there have many different criteria for different types of samples and needs, we still can find some common standards such as efficiency, processing speed, uniformity of field, cost, etc. [9]. We selected others and ignored speed and cost because they are hard to compare between different reactors for different materials and applications. Two kinds of standard reactors which are widely used: rectangular waveguide reactor and ridge waveguide reactor working at 915 MHz will be compared with the reactor shown in this paper. They will be modeled and simulated in Ansoft

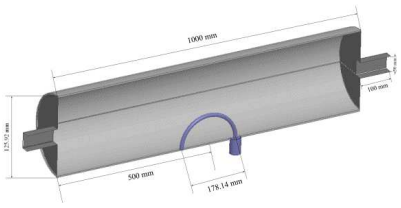

Figure 5: Feed and baffles of the reactor.

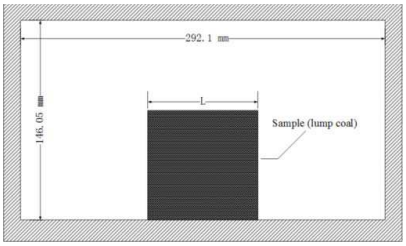

Figure 6: Rectangular type reactor.

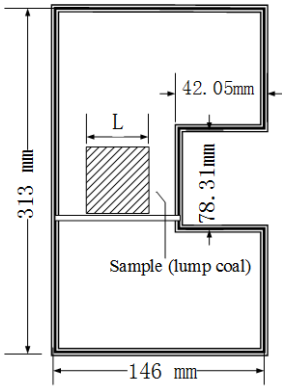

Figure 7: Single ridge type reactor.

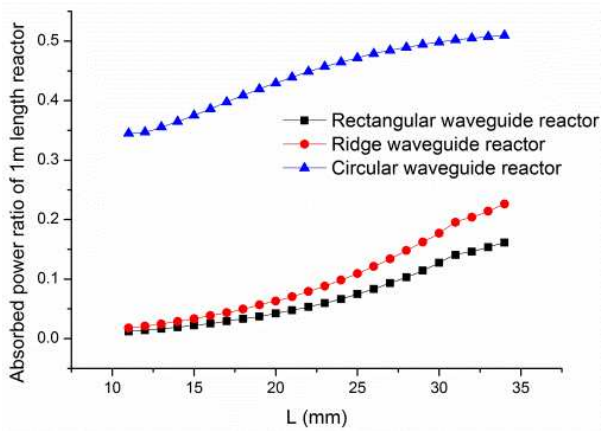

Figure 8: Absorbed power ratio of the three reactors.

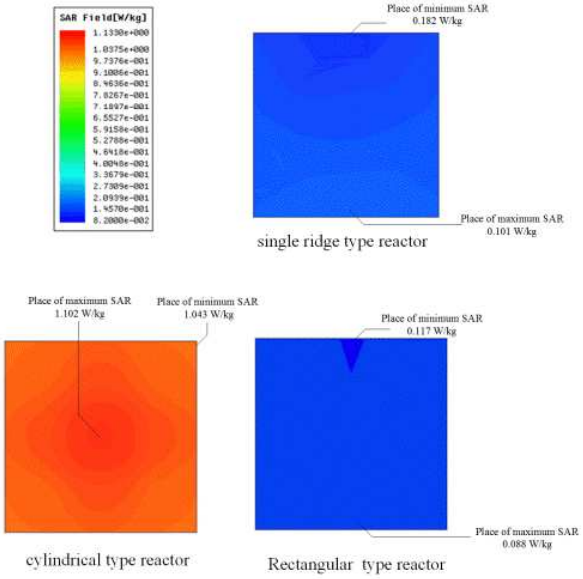

Figure 9: SAR of cross section of the three reactors.

HFSS 13.0 and the mismatch loss of feed will not be considered due to fair comparison.

The standard rectangular waveguide R8 and single ridge waveguide 24JD420 were selected as two comparison microwave reactors which are shown in Fig. 5 and Fig. 6. They are widely used as TE_{10} mode chemical reactor at 915 MHz for microwave material continuing processing [3]. The sample was put on the moving conveyor which goes along the central axis of the rectangular waveguide and the ridge waveguide reactors. We used square coal ($\varepsilon' = 4.88$, $\tan\delta = 0.3$) in long strip as samples because the thermal effects of microwave energy is widely used in removing sulfur of the coal [10], which is becoming an increasingly important environmental issues in China [10, 12].

Efficiency is nearly the most important factors to consider in microwave reactors [3, 12]. We compared the efficiency of these three kinds of reactor by putting the same sides of square coal in long strip into reactors continuously. The results shown in Fig. 8 indicated that more power will be absorbed if the bigger reactants were inputted [13] and the absorption efficiency of cylinder type reactor is considerable higher than the other twice with the same sides of reactants inputted. Specific Absorption Rate (SRA) is a measure of the rate at which energy is absorbed by the human body or the materials. We measured the SAR of the cross section of the square coal to compare the effect and uniformity of microwave heating. Fig. 9 shows the SARs (W/kg) of the cross sections of the square coal ($L = 20$ mm) which were in three different reactors feeding by coaxial line of 1 W inputted. The result indicates that compared with some traditional reactors, the reactor designed in this paper has much higher SAR ($6 \sim 12$ times) in reactants, which means the microwave energy has been fully utilized and the heating efficiency has been greatly improved.

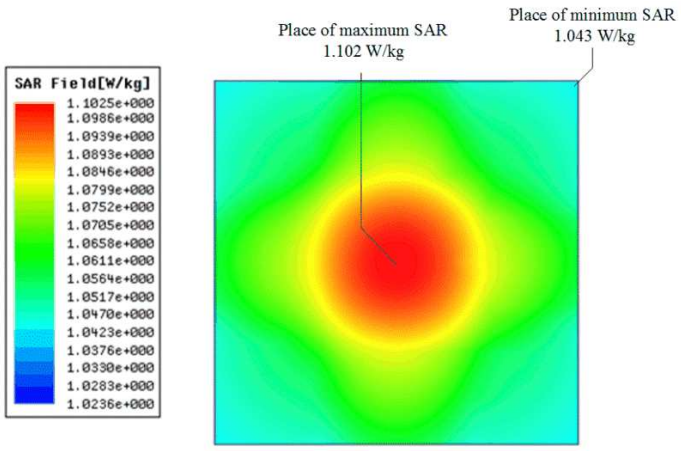

Figure 10: SAR of cross section of cylindrical reactor.

Another important factor of reactors is the uniformity of SAR, which means the inner and surface of the reactants should be uniformly heated at the same time. The picture of cylindrical type reactor in Fig. 9 was redrawn in Fig. 10 with a sparser scale to illustrate the SAR in the different parts of coal clearly. Fig. 10 indicates that the minimum SAR takes place at the corner of the square sample and it is just 5.45% lower than maximum SAR at the center. Compared with other reactors in Fig. 10, the cylindrical type reactor has the best uniformity of SAR.

4. CONCLUSION

A traveling-wave cylindrical waveguide microwave reactor is proposed for microwave material continuing processing. The new structure was designed in order to support the reactants at the central of the reactor to achieve the highest efficiency. Simulation results show that only very few microwave energy could be lacks from slots and both ends of reactor and it will be absorbed by the absorbing material. Compared with the existing microwave reactor, such as rectangular waveguide type reactor and ridge waveguide type reactor; our structure has considerable advantages in the distribution of the field strength, reaction effect, and energy consumption on processing reactants.

ACKNOWLEDGMENT

This work is supported by National Basic Research Program of China under Grant No. 2012CB214900.

REFERENCES

1. Ford, J. D. and D. C. T. Pei, "High temperature chemical processing via microwave absorption," *Journal of Microwave Power and Electromagnetic Energy*, 61–64, 1967.
2. Jing, Q. H., *Microwave Chemistry*, Science Press, Beijing, 2001.
3. Yu, V. B., K. I. Rybakov, and E. Semenov, "High-temperature microwave processing materials," *Journal of Physics D: Applied Physics*, Vol. 34, No. 13, 55–75, 2001.
4. Tinga, W. R. and W. A. G. Voss, *Microwave Power Engineering*, Vol. 2, Academic, New York, 1968.
5. Kappe, C. O., A. Stadler, and D. Dallinger, *Microwaves in Organic and Medicinal Chemistry*, 2nd Edition, Wiley-VCH, Weinheim, 2012.
6. Pozar, D. M., *Microwave Engineering*, John Wiley & Sons, 2009.
7. Larhed, M. and K. Olofsson, *Microwave Methods in Organic Synthesis*, Springer, Berlin, 2006.
8. Haque, K. Z., "Microwave energy for mineral treatment processes: A brief review," *International Journal of Mineral Processing*, Vol. 57, No. 1, 1–24, 1999.
9. Kingman, S. W. and N. A. Rowoson, "Microwave treatment of minerals: A review," *Minerals Engineering*, Vol. 11, No. 11, 1081–1087, 1998.
10. Cheng, Y. J., Z. X. Xia, and Y. Fan, "A frequency reconfigurable experimental microwave device of coal desulfurization," *Journal of University of Electronic Science and Technology of China*, Vol. 41, No. 1, 31–35, 2014.
11. Yi, Y. B., "Microwave desulfurization in coal," *Coal Technology*, Vol. 4, 54–55, 2003.

12. Xia, Z. X., Y. J. Cheng, and Y. Fan, "Frequency-reconfigurable TM_{010}-mode reentrant cylindrical cavity for microwave material processing," *Journal of Electromagnetic Waves and Applications*, Vol. 27, No. 5, 605–614, 2013.
13. Wang, L., Z. X. Xia, Y. J. Cheng, and Y. Fan, "A frequency reconfigurable microwave reaction cavity based on a quarter-wave coaxial cavity resonator," *10th International Symposium on Antennas, Propagation, and EM Theory*, Xi'an, China, Oct. 2012.

A Double Ended Active Electrode Using SiP with DC and 50 Hz Rejection

Linping Gao, Nikolas Gaio, Jinyong Zhang, and Lei Wang
Shenzhen Institutes of Advanced Technology, Chinese Academy of Sciences, China

Abstract— Active electrode is considered an extremely effective structure for capturing human bio-potential signals when compared with the traditional Ag/AgCl electrodes. This work presents a new configuration for a double ended active electrode included in a System-in-Package (SiP) solution. The chip overcomes the traditional problems of relatively large area and slow time response, and it demonstrates the characteristics of low power consumption, DC and 50 Hz rejection. It has a 2.1 kHz bandwidth with a 40 dB gain, and it reaches the extremely low cut-off frequency of 7.9 MHz. The working voltage is 1.8 V, and the power consumption of per channel is 6.7 µW. This chip has been fabricated with 0.18 µm 1P6M CMOS Process and then inserted in a SiP.

1. INTRODUCTION

In order to measure and record biological potential or current, there should be an "interface" between the body and the measuring instruments; this converts body current into circuits current. Electrode attributes to the interfaces, which not only works as simple contact point, but it also plays a significant part in the process of detection of a signal. The performance of the electrodes affects the inspection results of various biological signals such as EEG, EKG, EMG and ECG, to some extent [1]. As the resistance of the body surface is extremely high, conductive paste is applied on traditional electrodes. However, this solution presents several problems. For example, the chemical paste might damage the skin and induce uncomfortable feelings to patients. The preparation time is normally long and this structure cannot be utilized for a long-term test. Moreover, the bio-potential signal is extremely small and the leads are very susceptible to outside influences [2–4].

To solve these problems, new dry alternatives have been studied; among these, active electrode can be considered one of the most successful designs [4]. With this technology, amplifiers are directly integrated on the electrodes for ECG measurements. With active electrodes, conductive paste is not required and the preparation time will be drastically reduced. The most significant advantage of active electrode is that, compared to standard electrodes, it presents a more enhanced ability of anti-interference of physiological signals. The main objective of active electrode is to amplify small ECG signals and eliminate DC off-set voltages at different testing points. In as much as the low cut-off frequency of ECG is around 0.05 Hz, it is complicated to resolve the large reaction time and chip area aroused by ultra-low cutoff frequency [4, 5].

In this letter, a new active electrode design, which minimizes the problems listed above, is implemented. Additionally, pseudo resistances and de-blocking [6] technologies are applied in the circuit to reduce the large RC time constant. The active electrode chip shows the attributes of high input resistance, low output resistance and low-power consumptions. Moreover, the active electrode performance is guaranteed by inserting the active electrode system in a SiP; this is a quite new technology considered an attractive alternative to System-on-Circuit (SoC). In a SiP system, active and passive components are included on a single package substrate; on the contrary, in the SoC system, they are completely integrated in a silicon die [7–9].

The letter is organized as follows. In Section 2, the schematic structures are presented. In Section 3, the simulation and experimental results of active electrode are shown. Then conclusions are drawn in Section 4.

2. DESIGN

In order to get the inhibition of DC-off voltages coming from the skin, previous works have taken use of AC-coupled circuit [10]. The input resistance of traditional circuits is smaller than the one presented in this letter. In this letter, a chopper structure is bestowed as the main filter, and another amplifier is availed in a negative feedback circuit. The main amplifier is a differential circuit whose input is fed with the bio-potential signal at two testing points. It is illustrated in Figure 1 that bio-potential signal is pushed into a high resistance grid electrode whose resistance is extremely high. As the frequency bandwidth spectrum of ECG signal ranges from 0.05 Hz up to

350 Hz, it will be complicated to trade-off between the chip area and the time response based on the high-pass frequency. The amplifier structure is designed as a band-pass filter from 7.9 MHz to 2.1 kHz, and traditional resistance is replaced by pseudo resistor, shown as M_1 and M_2.

The transfer function of the double ended amplifier has been approximately calculated and shown in Equation (1), where A_d is magnification as 100, R is the equivalent value of pseudo resistor; τ_1 and τ_2 are time constants for the two amplifiers, respectively. In order to minimize the response time, a de-block technology [6] has been applied. In this design, one MOS transistor is employed as a switch for pseudo resistors and the gate voltage of this transistor is controlled by two comparators:

$$H(s) = A_d \frac{sR_0C_0}{(1+sR_0C_0)\left(1+s\frac{A_d\tau_1}{A_1}\right)\left(1+s\frac{\tau_2}{A_2}\right)} \tag{1}$$

The chopper structure: Figure 2 displays the schematic structure of chopper amplifier which is controlled by a bidirectional non-overlapping clock. The structure of this clock is illustrated in Figure 3.

It is necessary to have low output resistance because of the impendence feedback in the circuit; guaranteeing a low output resistance the noise introduced from outside interferences can be reduced.

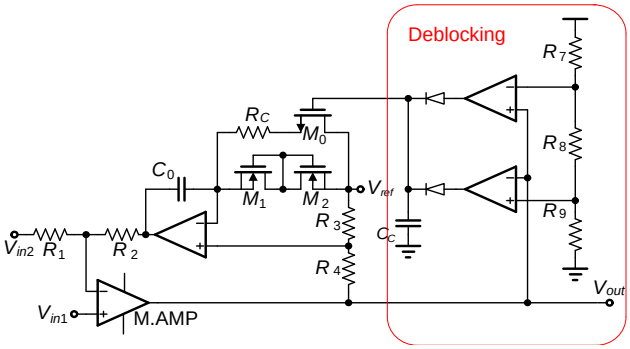

Figure 1: Schematic of the double ended amplifier

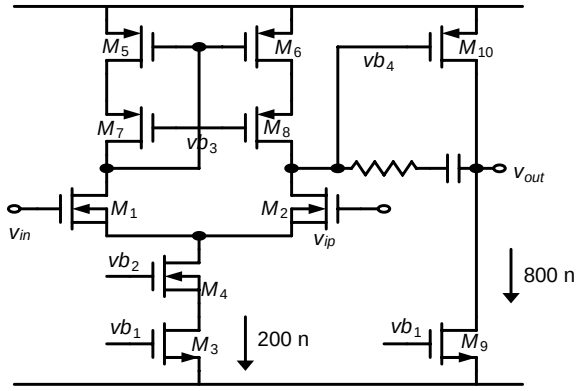

Figure 2: Schematic of the main amplifier.

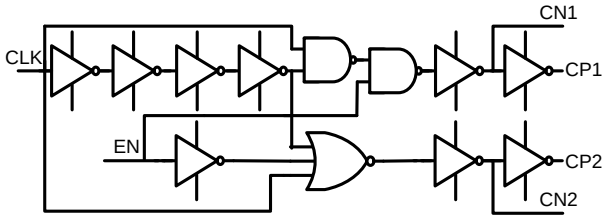

Figure 3: Logical diagram of the bidirectional non-overlapping clock.

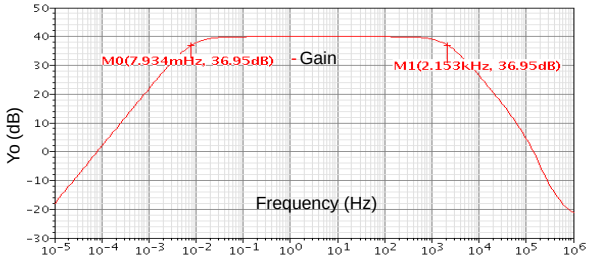

Figure 4: Closed loop gain of the main amplifier.

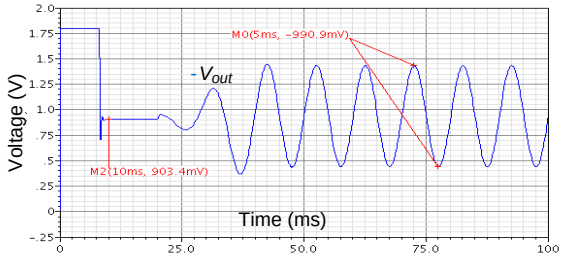

Figure 5: Transient response.

A single stage amplifier cannot achieve sufficient common mode rejection ratio and power supply rejection ratio. Thus a relatively large gain of 40 dB is anticipated in our circuit, so the two-stage structure is designed, and the bandwidth of chopper amplifier is supposed to be larger than 100 kHz. In virtue of the low-pass frequency of 2.1 kHz, it is only necessary to focus on the circuit flicker noise; for reducing it, gate areas have been increased, however, this choice made the parasitic capacitances increase leading to lower input resistance. In order to counter this effect, the substrate and source of each input component are connected together [11].

Auxiliary circuits have been included in SiP; this package improves the functions of the double ended amplifier. Working voltage of the amplifier goes from 0 V to 1.8 V; for this reason, a level-shifting circuit has been placed at the chip input to raise the voltages of bio-potential signal up to 900 mV. The bandwidth of the amplifier covers the majority of biological signals in human body, consequently, a filter is placed in the SiP to obtain a specific bandwidth for different types of signals. Since one of the advantages of SIP technology is to provide a quick and low-cost solution, the separation of amplifier and band-pass filter designs in SiP will enable the whole SiP system to be more flexible for different applications [12].

3. SIMULATION RESULTS

The frequency response is illustrated in Figure 4, this demonstrates that the low cut-off frequency is about 7.9 MHz. And, the transient response is simulated in Figure 5; the input signal is a mixture of AC and DC, and it only takes 10 µs to be DC stable.

4. EXPERIMENTAL RESULTS

The testing PCB board including the SiP is shown in Figure 6. In order to demonstrate the good functioning of the chip, the amplifier input has been fed with an ECG signal simulation generated by an IBUSS (p-type) analog meter. The TEKtronix AFG3102 has been employed as oscilloscope during the test and the Agilent E36020A has been used as the power supply. The minimum possible power supply value is 1.5 V; this is based on the feedback circuit. In addition, a LDO circuit converts the supply voltage to a relatively stable value of 1.8 V.

Figure 6 illustrates the SiP, the testing PCB and their dimensions. Even ifthe dimensions of this SiP have been determined, taking in account the necessity of soldering by hand, the package sizes obtained employing this technology can reach smaller values than those obtained with traditional packaging technologies. Based on this, the size of the testing PCB board could reach even smaller dimension. The ECG signal, created by the analog meter and detected by the active electrode is shown in Figure 7, the yellow line is the output of ECG signal. And this chip can work in good condition after 48 hours testing in this lab.

The experimental results demonstrate the amplification and filtering functions of this chip; Figure 7 shows the good quality of ECG signal and no significant noise effects (especially the 50 Hz noise). Moreover, the active electrode has also shown the characteristics of continuity and stability over a long time.

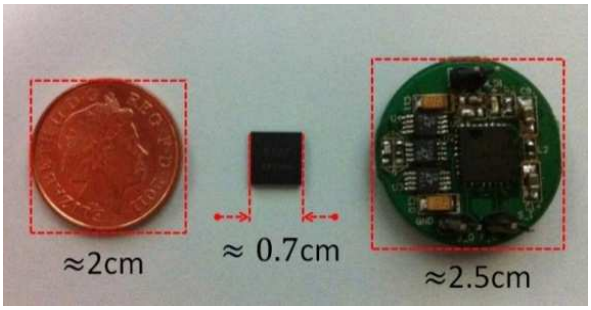

Figure 6: The chip and PCB are compared with one penny.

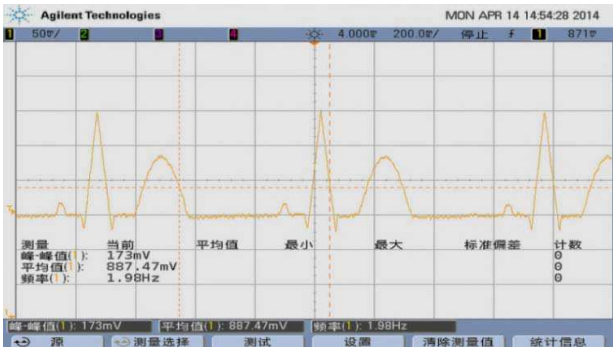

Figure 7: Timing waveform of the ECG.

5. CONCLUSIONS

In this letter, the structure of a double ended active electrode which had DC and 50 Hz rejection was presented. In this structure, pseudo resistances and de-blocking technology were firstly combined to decrease the chip area and response time. This chip was successfully fabricated using SMIC 0.18 µm process. It achieved the characteristics of low power consumption of 6.7 µW, extremely low cut-off frequency of 7.9 MHz and high input impedance. Since the bandwidth was large enough, and the encapsulation technology of SiP was applied, they would ensure the chip was multipurpose for different kinds of biological signals.

ACKNOWLEDGMENT

This study was financed partially by the 'One-hundred Talent' and the 'Low-cost Healthcare' Programs of the Chinese Academy of Sciences, the project of science and technology of Guangdong Province (2010A030500014).

REFERENCES

1. Xu, J. and R. F. Yazicioglu, "A 160 µW 8-channel active electrode system for EEG monitoring," *IEEE Trans. Biomed. Circuits Syst.*, Vol. 5, No. 6, 555–567, Dec. 2011.
2. Fonseca, C., J. P. S. Cunha, et al., "A novel dry active electrode for eeg recording," *IEEE Trans. Biomed. Eng.*, Vol. 54, No. 1, 162–165, Jan. 2007.
3. Ko, W. H., "Active electrodes for eeg and evoked potential," *IEEE Engineering in Medicine and Biology Society, Proc. 20th Annu. Int. Conf.*, Vol. 20, No. 4, 2221–2224, 1998.
4. Gargiulo, G., P. Bifulco, M. Cesarelli, M. Ruffo, M. Romano, R. A. Calvo, C. Jin, and A. van Schaik, "An ultra-high input impedance ECG amplifier for long-term monitoring of athletes," *Medical Devices*, Vol. 3, 1, Auckland, NZ, 2010.
5. Yoo, J., L. Yan, S. Lee, H. Kim, and H.-J. Yoo, "A wearable ECG acquisition system with compact planar-fashionable circuit board-based shirt," *IEEE Transactions on Information Technology in Biomedicine*, Vol. 13, No. 6, 897–902, 2009.
6. Grimbergen, C. A. and A. C. MettingVanRijn, "DC rejection and deblocking in multichannel bioelectric recordings," *Proc.17th Annu. Int. Conf. IEEE Engineering in Medicine and Biology Society*, Vol. 20, 1665–1666, 1995.
7. Lim, S. K., "Physical design for 3D system on package," *IEEE Design & Test of Computers*, Vol. 22, No. 6, 532–539, 2005.
8. Tummala, R. R. and V. K. Madisetti, "System on chip or system on package," *IEEE Design & Test of Computers*, Vol. 16, No. 2, 48–56, 1999.
9. Gershenson, J., G. Prasad, and Y. Zhang, "Product modularity: Definitions and benefits," *Journal of Engineering Design*, Vol. 14, No. 3, 295–313, 2003.
10. Wattanapanitch, W., M. Fee, and R. Sarpeshkar, "An energy-efficient micropower neural recording amplifier," *IEEE Trans. Biomed. Circuits Syst.*, Vol. 1, 136–147, 2007.
11. Chi, Y. M., "Ultra-high input impedance, low noise integrated amplifier for noncontact biopotential sensing," *IEEE Emerging and Selected Topics in Circuits and Systems*, Vol. 1, 526–535, Dec. 2011,
12. He, L., S. Elassaad, Y. Shi, Y. Hu, and W. Yao, *System-in-package: Electrical and Layout Perspectives,* Now Publishers Inc., 2011.

Simulation of a High-convergence Electron Optics System for an X-band High-impedance Relativistic Klystron

Danni Zhu, **Jun Zhang**, **Zumin Qi**, **and Wei Li**
College of Optoelectric Science and Engineering
National University of Defense Technology, Changsha 410073, China

Abstract— The high-impedance relativistic klystron based on the hot cathode, of high power, long pulse, high efficiency and stable amplitude and phase, is one of the promising candidates for the high-power microwave coherent power combing. As a high-quality, small radius electron beam plays a crucial role in an effective beam-wave interaction, a high-convergence electron optics system is required for an 11.424 GHz high-impedance relativistic klystron, with an output power of 105 MW. In the design, to alleviate the cathode loading due to high-convergence, the uniformity of the cathode emittance and the laminarity of beam are both sacrificed. Then serious space charge effect is likely to occur with a rather high current density. To minimize the scalloping, it is difficult to provide the best overlap of the beam trajectories and magnetic force lines with priority to the amplitude of magnetic flux at the cathode. With the synthesis of Pierce's electron gun and the cylindrical focusing electrode, a particle in cell model of the electron gun is constructed to obtain the electrostatic characteristics of the electron beam. Based on the electrostatic beam trajectories, a beam-focusing system is designed, with which electron beam can be well focused by adjusting the magnetic field profile especially in the transient region. The PIC simulation results indicate that the balance radius of the reasonably fluctuated beam is about 3 mm ,with a fine laminarity, and the transmission, the perveance and the area convergence are 100%, 0.9 μP and 97 : 1 respectively, which satisfy the requirement of the 11.424 GHz high-impedance relativistic klystron. Moreover, with the comparison between thermionic emission and explosive emission in PIC code, the micro-characteristics of beam shows the latter is tend to be more reliable.

1. INTRODUCTION

The 11.424 GHz klystron is under development as an alternative RF source for a next electron-positron linear collider by SLAC, KEK and BINP, with the highest output power of 75 MW [1, 2]. Moreover, the high-impedance relativistic klystron based on the hot cathode, owing to its high power, long pulse, high efficiency and stable amplitude and phase, becomes one of the promising candidates for the high-power microwave (HPM) coherent power combing. An effective beam-wave interaction in a high power X-band klystron requires a high-quality electron beam with small radius so that the electron optics system plays a crucial role in the performance of the device [3]. Although the 11.424 GHz klystron has been fabricated in SLAC, KEK and BINP, but discussions on simulation of a high-convergence electron optics system are scanty. However, in terms of time and funds, the simulation is an efficient way to ensure a satisfying performance of the beam-stick test in advance. Besides, there are several issues deserving deliberate consideration. Firstly, to alleviate the cathode loading due to high-convergence, the uniformity of the cathode emittance and the laminarity of beam are both sacrificed. Secondly, serious space charge effect is likely to occur with a rather high current density. Thirdly, to minimize the scalloping, it is difficult to provide the best overlap of the beam trajectories and magnetic force lines with priority to the amplitude of magnetic flux at the cathode.

This paper presents the design of a high-convergence electron optics system for an X-band high-impedance relativistic klystron by PIC simulation. In Section 2, the detailed design and optimization of electron gun are described and the electrostatic characteristics of beam is presented. In Section 3, a beam-focusing system well matched with the above beam is designed by a high-frequency structure simulator, and the typical particle-in-cell (PIC) simulation results indicate that the balance radius of the reasonably fluctuated beam is about 3 mm, and the beam voltage and current are 525 kV, 328 A respectively. Finally, a discussion on two cathode emission methods and a conclusion are given in Section 4.

2. ELECTRON GUN ELECTROSTATIC DESIGN

As the optimized parameters of the beam-wave interaction system are summarized in Table 1, the 11.424 GHz high-impedance relativistic klystron with power of 105 MW is already achieved in

PIC simulation [4]. It shows the target performance of the electron optics system that the beam voltage and current are 525 kV and 458 A respectively. Thus, the initial velocity due to the thermal emittance can be ignored under a high voltage. Fig. 1 indicates the best balance radius should be compressed to 3 mm. The average cathode loading over cathode is 13.5 A/cm^2 according to XB72K in KEK [5], implying the convergence of the cathode is as high as 117.

Table 1: Simulation parameters of the beam-wave interaction system.

Beam voltage	Beam current	Beam radius (mean)	Drift tube radius	Perveance	Output Power	Gain	Efficiency
525 kV	458 A	3.0 mm	4.6 mm	1.2 μP	105 MW	50 dB	43.5 %

The initial geometrical parameters are obtained from the synthesis method of the Pierce gun developed by Vaughan [6]. Since it doesn't take the anode hole aberrations into account, a cylindrical focusing electrode [7] is used to compensate as illustrated in Fig. 2. Furthermore, the synthesis method of the Pierce gun usually applying to convergence below 40 provides a rather rough geometric layout, which means special emphasis should be taken on the optimum gun geometry.

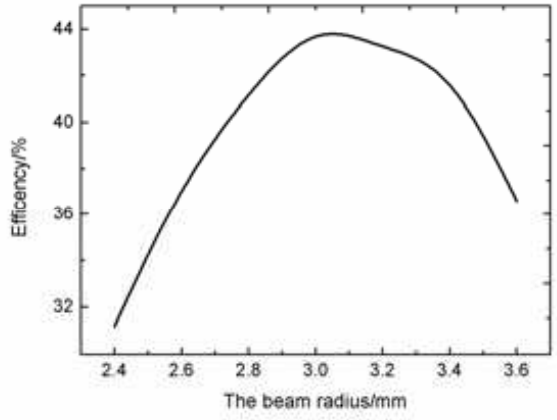

Figure 1: Extraction efficiency versus beam radius.

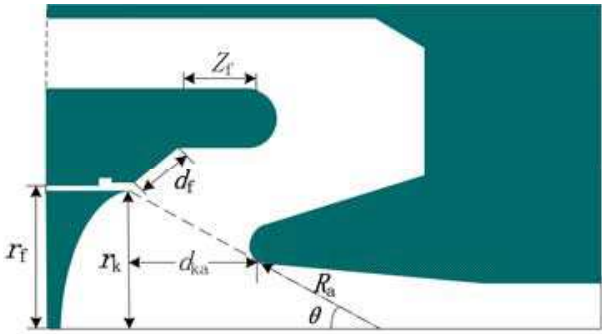

Figure 2: Electron gun model with cylindrical focusing electrode.

In order to realize a desirable high-convergence electron gun, the optimization routine is scheduled. Firstly, a suitable electric field contour distribution should be ensured as the beam trajectories always follow the magnetic force lines. Secondly, beam should be converged at least making the radius smaller than that of drift tube initially to avoid beam interception, and then by monitoring the beam current on different axial position the transmission of 100% through a drift tube is verified later. Thirdly, the target perveance and the beam radius are well worth considering, while the laminarity being kept as good as possible. Table 2 shows the main optimum gun geometric parameters.

Table 2: Main parameters of the electron gun.

r_k/mm	r_f/mm	Z_f/mm	d_f/mm	θ/°	R_a/mm	d_{ka}/mm
31	33	10	20	28	28.5	48

In the optimization, it finds that the beam radius is mainly influenced by the geometric layout and position of the cylindrical focusing electrode, the perveance is sensitive to the position of anode so that it is adjusted by changing the gap between the cathode and the anode, and the laminarity of beam can be improved by decreasing the radius of cathode in small scale. According to Fig. 3(a), the length of focus electron should be long enough to strengthen the shielding for the cathode and depress the cathode edge loading, and the electrostatic force increases at the same time. Therefore, the beam trajectories are converged with the beam radius decreasing so that the space charge effect is enhanced with the beam current reducing gradually. On the other hand, the position of inner top section of the focusing electrode also plays a key role on the beam radius. As d_f is

increased, it results in both raising and extending the focusing electrode. In Fig. 3(b), when d_f is below 20 mm the extension prevails so that the shielding is enhanced and hence the beam radius decreases. When d_f is over 20 mm the raise prevails so that the shielding is weaken and hence the beam radius increases, and the space charge effect is weaken leading to the beam current rising.

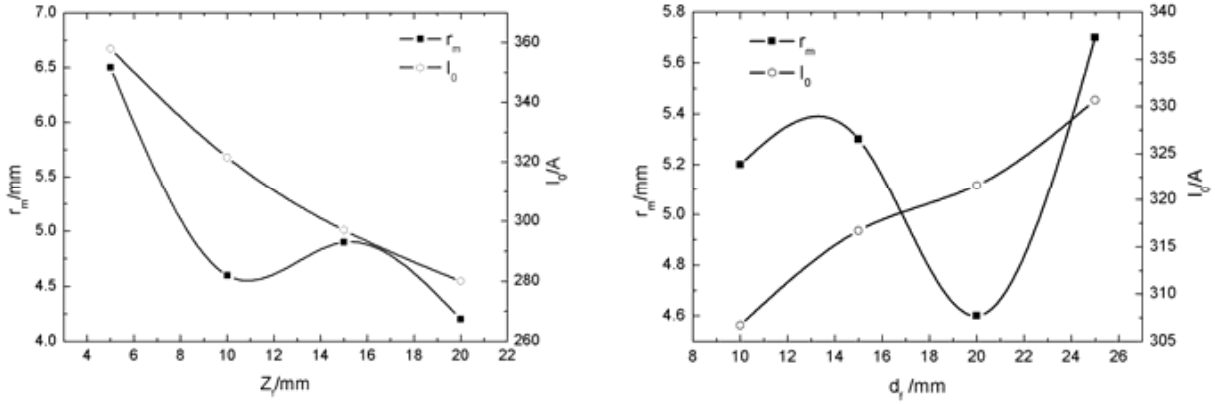

Figure 3: Beam radius r_m and the beam current I_0 versus the different structure. (a) Length Z_f of focus electron. (b) Position d_f of inner top section of the focusing electrode.

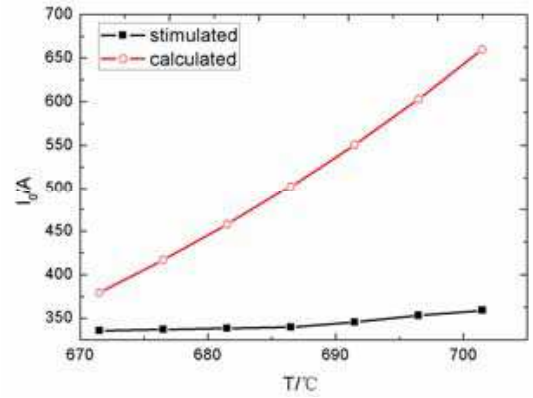

Figure 4: Beam current as a function of temperature in PIC simulation and theory.

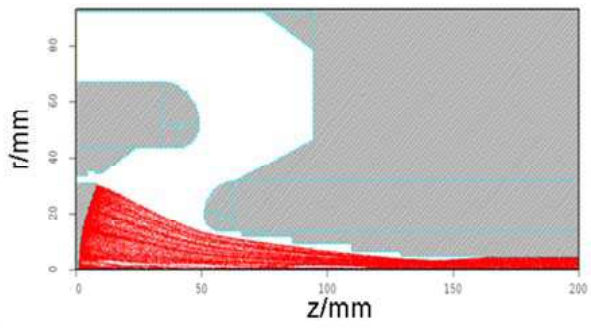

Figure 5: Final beam trajectories without magnetic field.

Under a high operating voltage, the voltage gradient in the electron gun becomes a critical issue. And the maximum gradient occurs at the top of the focusing electrode or the anode. In order to decrease the high-voltage gradient to a reliable level and confine the dimension of the gun, only the radius of the outer top section of the focusing electrode and anode are augmented to 15 mm and 12 mm respectively [8]. Further calculation indicates that the maximum gradient decreased to 360 kV/cm. For low operating temperature, the electron gun is a typical Pierce type with an oxide cathode. Based on Richardson-Dushman equation [9]

$$j_e = AT^2 e^{-\frac{e\phi}{KT}} \quad \left(\mathrm{A/cm^2}\right) \tag{1}$$

where k is the Boltzmann constant, A_0 is the Dushman parameter, and ϕ is the work function according to the material. In Fig. 4, as a function of temperature in both PIC simulation and Richardson-Dushman equation, the beam current is growing with the temperature rising whereas the growing rate is much smaller in simulation than that in theory. Therefore we can come into a conclusion that increasing the temperature does improve the cathode emittance ability in theory but the actual beam current is usually seriously limited by the space charge effect. Unfortunately, Richardson-Dushman equation is without taking this limitation into account.

The PIC simulation results of the gun without magnetic focusing are illustrated in Table 3, indicating the beam radius is compressed to 3.3 mm and the beam current is 328 A. The final beam trajectories are presented in Fig. 5, showing the beam transmission nearly of 100% and good laminarity. It can be seen that the beam-focusing system is indispensable to confine the scattered electrons intercepted by the tube through the drift region when the electrostatic focusing force vanished.

Table 3: Simulation results in electrostatic beam.

r_m/mm	I/A	j_k/(A·cm^{-2})	P/μP	M^2	Z_m/mm	E/(kV·cm^{-1})
3.3	328	10.9	0.9	88:1	85	360

3. MAGNETIC CIRCUIT AND BEAM OPTICS

The beam-focusing system is a space-charge balanced flow type with a solenoidal field. The correlative magnetic flux densities are illustrated in Eq. (2) ∼ Eq. (4), including the Brillouin value B_b, one at the beam drift region B_0, and one at the cathode B_k, where I and U are current beam and voltage respectively, r_0 is the beam balance radius and K is the shielding factor [10].

$$B_b = \frac{830}{r_0}\frac{I_0^{1/2}}{V_0^{1/4}}(Gs) \tag{2}$$

$$B_0 = B_b \Big/ \sqrt{1-K^2} \tag{3}$$

$$B_k = KB_0\left(\frac{r_0}{r_k}\right)^2 \tag{4}$$

Substitute $V_0 = 525$ kV, $I_0 = 328$ A, $r_0 = 3$ mm into the above equations when K is set to be 0.9, then $B_0 = 4270$ Gs, $B_k = 36$ Gs are obtained. This indicates the magnetic flux density at the beam drift region is 2.3 times as large as the Brillouin value. The geometric layout of the solenoidal magnet structure is presented in Fig. 6, containing six magnet coils and a solenoid yoke. On the outside of the front wall of the solenoid yoke, a trim coil marked coil1is set to tune the magnetic field near the cathode.

The arrangement for beam matching with the beam-focusing system is crucial to obtain perfect focusing beam characteristics, especially for the magnetic flux densities at the cathode and the entrance of the drift tube named transition region. The following basic guidelines to optimize the distribution of the magnetic flux are laid. On the one hand, the magnetic flux density at the cathode and one at the beam drift region should be approximate to B_k and B_0. On the other hand, the best overlap of the initial beam trajectories and magnetic force lines specially in gun and anode hole regions should be achieved [6].

In the optimization process we also find several disciplines described below.

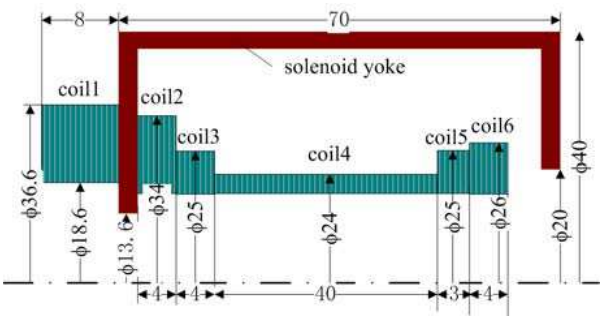

Figure 6: Diagram of the beam-focusing system (whose units are centimeters).

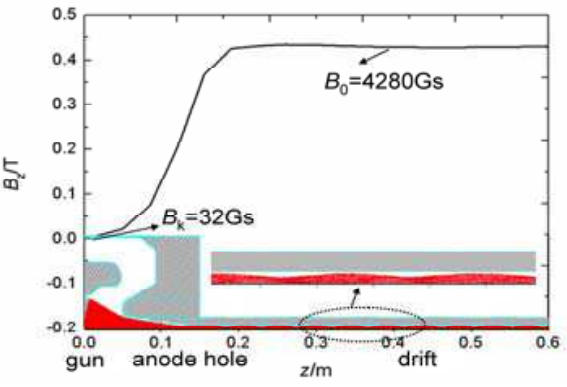

Figure 7: Magnetic profile and beam trajectories in the beam-focusing system.

1) Because the beam trajectories in whole region are sensitive to the magnetic flux density at the cathode, make priority to comply with the first principle.
2) Once the magnetic flux density at the cathode is too large, the beam is likely to be intercepted by the anode. Moreover, the low magnetic flux density just behind the anode hole in the transition region leads to the beam intercepted by the inner section of the anode.
3) In front of the drift tube of the transition region, the magnetic flux density should be $0.8B_0 \sim 0.9B_0$ to ensure the beam transmission 100% in this section.
4) After the perfect beam transmission is achieved, the stronger B_k is, the larger the balance radius of beam is with lower beam ripple.
5) It is shown that the magnetic flux density behind the entrance of the drift region should be increased to B_0 in the transition region as soon as possible, or the laminarity of beam goes poor.

The magnetic flux density in the transition region is dependent on the aperture of the solenoid yoke and the main magnet coils. Through enlarging the aperture of the front-wall in the solenoid yoke, the magnetic flux density behind the anode hole in the transition region can be improved. And the magnetic flux density in the whole transition region can be enhanced by a large aperture of the back-wall. Notably, the decrease of magnetic field at the end of solenoid is essential to collect the scattered beam for high efficiency.

The relative location of the beam-focusing system respect to the electron gun also influences the beam balance radius, transmission, fluctuation and laminarity, which also needs to be optimized. If remove the beam-focusing system back 45 mm, the magnetic field profile just satisfies the above disciplines as shown in Fig. 7, which indicates that the magnetic field at the cathode is 32 Gs, and the longitudinal magnetic field in the interaction region is about 4280 Gs. With magnetic field profile introduced, the beam trajectories were carried out with the PIC code in Fig. 7, showing the beam transmission is about 100% with good laminarity and low ripple. The beam trajectories in drift region in detail shows the balance radius has reached 3.15 mm and hence the convergence is improved to 97 thanks to the secondary compression from the magnetic field.

Although the perveance is still 0.9 μP as the result without magnetic focusing, the simulation result of the beam-wave interaction system based on the final beam parameters with the obtained beam-focusing system shows the output power reaches 79 MW, with efficiency of 44.5% and gain of 49 dB.

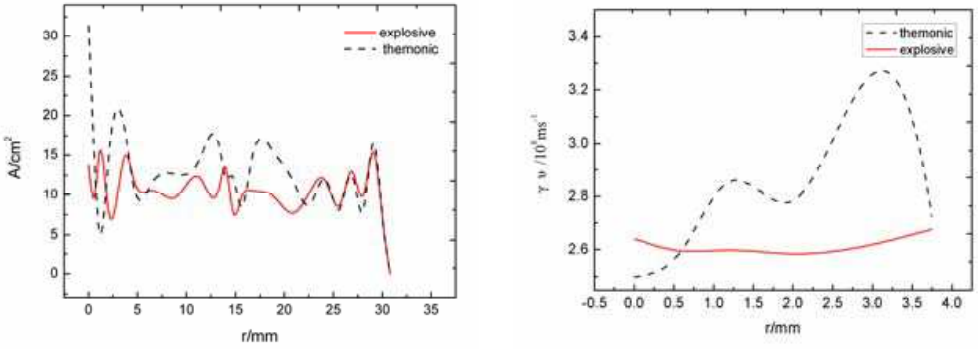

(a) current density distribution (b) electrons velocity distribution

Figure 8: Micro-characteristics of the beam distribution along the cathode radius.

4. DISCUSSION AND CONCLUSION

The above simulation is based on thermionic emission in PIC code, however the actual cathode emittance can also be simulated by explosive emission. Comparing the simulation results of these two cathode emission methods, the characteristics of beam are almost the same apart from the micro-characteristics as illustrated in Fig. 8. The current density distribution along the cathode radius is shown in Fig. 8(a). With a high-convergence, the cathode loading should not only be limited to a reasonable level but also have good uniformity. Therefore the simulation result by explosive emission is overwhelm the other one on the two points, whose average cathode loading

is about $10\,A/cm^2$, lower than that by thermionic emission. Distribution of the electrons velocity across the beam are presented in Fig. 8(b), which is more homogeneous by explosive emission.

To summarize, the design of a high-convergence electron optics system for an X-band high-impedance relativistic klystron by PIC simulation is presented in this paper. The static electricity characteristic of the gun is optimized by the big curvature radius focusing electrode and anode to reduce the electric field. A match magnetic focus system is designed, with which the electron beam can be well focused. A solid beam is obtained with a radius of 3 mm, and the beam voltage and current are 525 kV and 328 A. The fluctuation on the beam is small with favorable laminar flow characteristic, and the transmission, the perveance and the area compression are 100%, 0.9 μP and 97, respectively. With the comparison between thermionic emission and explosive emission in PIC code, the micro-characteristic of beams shows the latter is tend to be more reliable.

ACKNOWLEDGMENT

The authors would like to express their gratitude to the reviewer of this paper for his valuable comments and suggestions. The authors wish to express gratitude to Dr. X. J. Ge for his help in revising the English writing.

REFERENCES

1. Matsumoto, S., S. Fukuda, and S. Kazakov, "Development of PPM-focused X-band pulse klystron," *Proceedings of the 2nd Annual Meeting of Particle Accelerator Society of Japan and the 30th Linear Accelerator Meeting*, 345–366, Tosu, Japan, Jul. 2005.
2. Sprehn, D., G. Caryotakis, and A. Haase, "Latest results in SLAC 75 MW PPM klystrons," *Proceedings of SPIE*, 85–90, Florida, America, Apr. 2000.
3. Wang, S., Y. Wang, J. Yang, et al., "The optics system for sheet beam of klystron with uniform magnetic focusing field," *Chinese Journal of Vacuum Science and Technology*, Vol. 27, 226, 2007.
4. Zhu, D., J. Zhang, W. Li, and Z. Qi, "Simulation study of an X-band high power relative klystron amplifier," *Laser Part. Beams*, Vol. 26, 505, 2014.
5. Chin, Y. H., K. Takata, S. Fukuda, H. Mizuno, S. Michizono, et al., "The 120 MW X-band klystron development at KEK," *Proc. of EPAC98*, 1894–1896, 1998.
6. Electronic Tube Design Handbook Editorial Committee, *The Optics System for Microwave Tube Design Handbook*, National Defense Industry Press, Beijing, 2010.
7. Zhao, G., W. Wang, and Y. Gong, "Design of the electron gun for S-band high power TWT," *Vacuum Electronics*, Vol. 5, 1921, 2006.
8. Zhang, R. and Y. Wang, "Design simulation of electron optics system for 100 megawatt klystron" *Chinese Journal of Vacumm Science and Technology*, Vol. 5, No. 29, 499–503, 2009.
9. Ding, Y., *Design, Manufacture and Application of High Power Klystron*, National Defense Industry Press, Beijing, 2010.
10. Feng, H., "The study of electron optics system for X-band klystron," 6, University of Electronic Science and Technology of China, Chendu, 2012.

The Metamaterial Technology Applied to Planar Antennas

E. F. Guelber[1], **A. V. Cardoso**[1], **C. E. Capovilla**[2], **and H. X. Araujo**[1]

[1]Universidade Federal de São João Del Rei — UFSJ, Brazil
[2]Universidade Federal do ABC — UFABC, Brazil

Abstract— In this work, metamaterials structures are applied to electromagnetic devices in order to improve its performance, in terms of gain, bandwidth and resonance. Basically, three topologies are used (fractal, Jerusalem cross pair and tripole array), in two different planar antennas: Yagi-Uda and Quasi-Yagi. The obtained results show the expected changes on the behavior of the analyzed devices, in order to prove the metamaterial efficiency in high frequencies applications.

1. INTRODUCTION

Actually, metamaterial is a macroscopic composite of periodic or non-periodic structure, whose function is due to both the cellular architecture and the chemical composition [1]. Therefore, the behavior of a material, in the presence of an electric field, is determined by the macroscopic parameters, permittivity ε and permeability μ. Several metamaterial structures have been investigated along the last years. In particular, ones those are capable to provide artificial magnetic responses and electric walls.

The artificial magnetic conductors can be obtained when a plane wave focus on the capacitive gap, while the artificial electric conductor is obtained through the opposite way.

In fact, the metamaterial pattern is applied to physical devices aiming to obtain specific responses. In [2] a CSRR structure is employed to a UWB antenna in order to provide a rejection characteristic in a desired frequency. On the other hand, in [3] metamaterial structures are applied to an UHF antenna and a better gain is obtained, while in [4] the periodic is structures are applied to the septum of a GTEM — Gigahertz Transverse Electromagnetic chamber, expecting a shift on the resonance frequencies.

In this context, to improve the performance in terms of gain, bandwidth and resonance, of planar antennas, four different topologies are employed.

2. METAMATERIAL TECHNOLOGY

The electrical and magnetic properties of materials in relation to the electromagnetic field are characterized by the constitutive parameters permittivity (ε) and magnetic permeability (μ), respectively. Together, these two parameters determine the response of a material in the presence of an electromagnetic radiation [5]. In common materials found in nature, both parameters assume positive values. However, in metamaterials both ε as μ are negative and thus take a class called DNG (Double Negative). Therefore, the metamaterial technology is represented by periodic structures that are implemented with different shapes and sizes in order to attend several applications.

The fractal topology is one of the most known metamaterial pattern. Its unitary cell has the H format as its main characteristic, and have four levels of branching, being the fractal pattern generated by a main line, as can be seen in Fig. 1(a). The main advantages of fractal cell are its sub-wavelength properties, simple architecture and its wide application. The sub-wavelength allows the system to have a smaller size when compared with the wavelength along all resonance directions. Thus, the cell can behave as a compact reflector.

On the other hand, the JCP pattern consists of periodic structures where its unit cells are based on the concept of a pair of crossed wires in a cross shape as shown in Fig. 1(b). Thus, such structures are applied in strategic positions in order to act in devices that operate in the microwave and optical bands. This configuration shows modes of electric and magnetic resonance with negative permittivity and permeability, and thus negative refraction as expected metamaterials [6]. This pattern consists of sets of pairs of Jerusalem crosses coupled, so that, due such symmetry these structures show an isotropic response for any incident wave.

Thus, for any orientation of the incident magnetic field, an induced loop current comes near the displacement current at the external arms, because the perpendicular component of the field in relation to the area between the central arms of the crosses of Jerusalem. Although the JCP unitary cell be symmetrical, the surface current in the two conductors is asymmetrical [3], thus generating

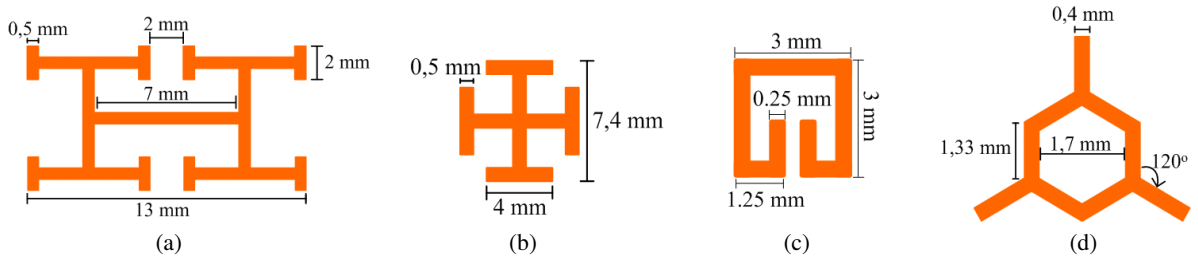

Figure 1: (a) Unitary fractal cell, (b) unitary JCP cell, (c) unitary CLL cell, (d) tripole array.

a current loop that can be represented by an equivalent magnetic dipole. With this magnetic moment is expected a negative resonance effect, which indeed proves the artificial behavior of such structure.

The CLL structure can be defined as a simplification of the SRR (*Split Ring Ressonator*), where its main characteristics is it behaviors as magnetic or electric conductor, depending on the direction of the incident wave. When the incident wave achieves its unitary cell at the gap, its response assumes an artificial magnetic conductor behavior, while at the opposite side an artificial electric conductor is observed. This phenomenon occurs due the gap at the front size of the unitary cell act as a capacitor, while in the back size, distributed inductance and resistance are present. It's shape and dimensions are shown in Fig. 1(c).

The tripole array, Fig. 1(c), is generally developed for mobile applications which require small and thin structures. The set of tripoles is arranged in two layers, so that its grouping is modeled in the hexagonal shape. The symmetry of the tripole provides an isotropic response to any incident wave, and it can be expected that this transmission property, in somehow, be preserved when the incident wave is tilted away from the normal incidence [5]. In this work, the dimensions of the adopted unitary cells are presented in [3, 4].

3. PATCH ANTENNAS

The planar Yagi-Uda antenna shows good characteristics as high gain and simple shape. In Fig. 2(a) is shown the Yagi-Uda antenna designed in this work, with seven elements and a feed line. The antenna consists of a rectangular drive, four directors and two reflectors placed near the feed line [7].

The driver is the radiating element and is connected to the feed line. On the other hand, the reflectors and directors, play the role of parasite elements, due they are not connected to the feed line, allowing the improvement of gain. The antenna was designed over the 5880 Rogers Duroid, with dielectric constant around 2.2 and 1.5 mm of thickness.

The metamaterials topologies, CLL and JCP were applied making holes on the four reflectors of the Yagi-Uda antenna, as seen in Fig. 2(b) and Fig. 2(c). Both implementation changed the resonance frequency for 10.5 GHz and increased the gain on this frequency, but the first with CLL cells, Fig. 3(a), presented a better result than the second with JCP cells, Fig. 3(b).

The second analyzed antenna was the Quasi-Yagi — QY, which is widely used in microwave systems. Its geometry has the advantages of planar antennas and the main characteristics of the

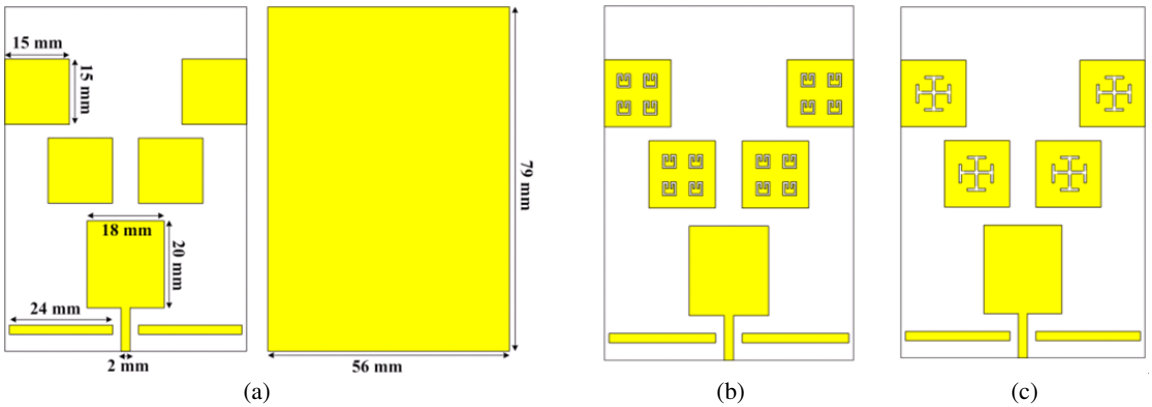

Figure 2: (a) Yagi-Uda dimensions. (b) Yagi-Uda with CLL cells. (c) Yagi-Uda with JCP cells.

Yagi-Uda as drivers. Furthermore, the QY antenna has a truncated ground plane which acts as a reflector, making it unnecessary the use of a separate dipole. Generally, the QY is built on substrates with $\varepsilon_r \geq 4$, in order to reduce its overall size, making it smaller than half wavelength. The analyzed antenna was built on a glass substrate with $\varepsilon_r = 4.82$ and a thickness of 0.8 mm. In Fig. 2(a) is shown the QY dimensions.

In the QY antenna, the JCP pattern was applied on the top of the substrate with the same thickness of the antenna, Fig. 2(b). The cells are placed on the upper side of the antenna, in arrays composed by four cell, which are located at 4.7 mm from the lateral border and 4.35 mm from the upper border. From Fig. 3(a), the resonance in 5.6 GHz and 9.6 GHz, was improved, around 25 dB and 10 dB, respectively. On the other hand, the fractal pattern was applied to the QY antenna on the ground plane, Fig. 2(b). The periodic structures were placed at 7.5 mm from the lateral border and 3.8 mm to the upper border. This configuration results on a wide rejected band, from 0 to 8 GHz, with resonance only in 8.3 GHz, as can be seen in Fig. 3(a).

The tripole array was applied to the antenna throughout all ground plane, as can be seen in Fig. 2(c). In Fig. 3(c), it can be observed resonances in 3.4 GHz, 4.7 GHz, 7.5 GHz and 8 GHz, and a shift from 6.5 GHz to approximately 5.8 GHz. It also can be observed a rejected band from 8.1 GHz to 10 GHz.

Therefore, it is clearly the influence of the metamaterial structures on the behavior of the QY antenna. Various configurations were performed, but no contributions on the antenna performance were found. Furthermore, each pattern, and its positioning, can improve or not the gain, bandwidth and resonance and even create a rejected band.

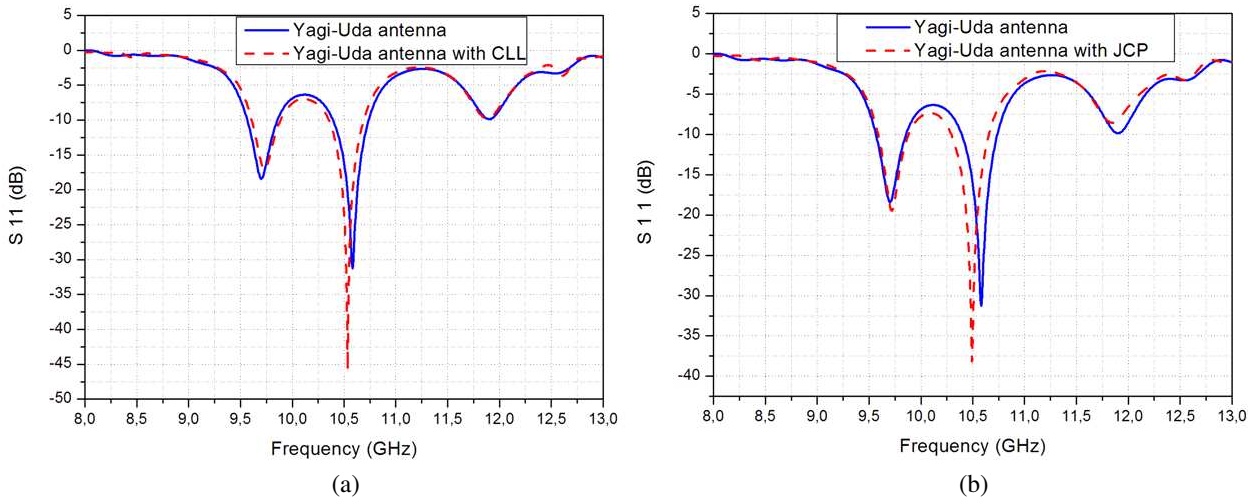

Figure 3: (a) S_{11} parameter of Yagi-Uda antenna with CLL pattern. (b) S_{11} parameter of Yagi-Uda antenna with JCP pattern.

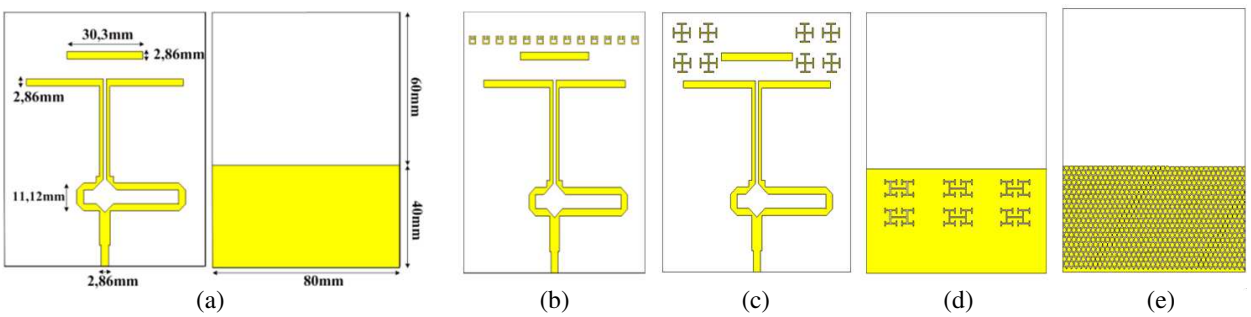

Figure 4: (a) QY dimensions; (b) QY with CLL cells on the top; (c) QY with JCP cells on the top; (d) QY with fractal cells on the ground plane; (e) QY with tripole array on the ground plane.

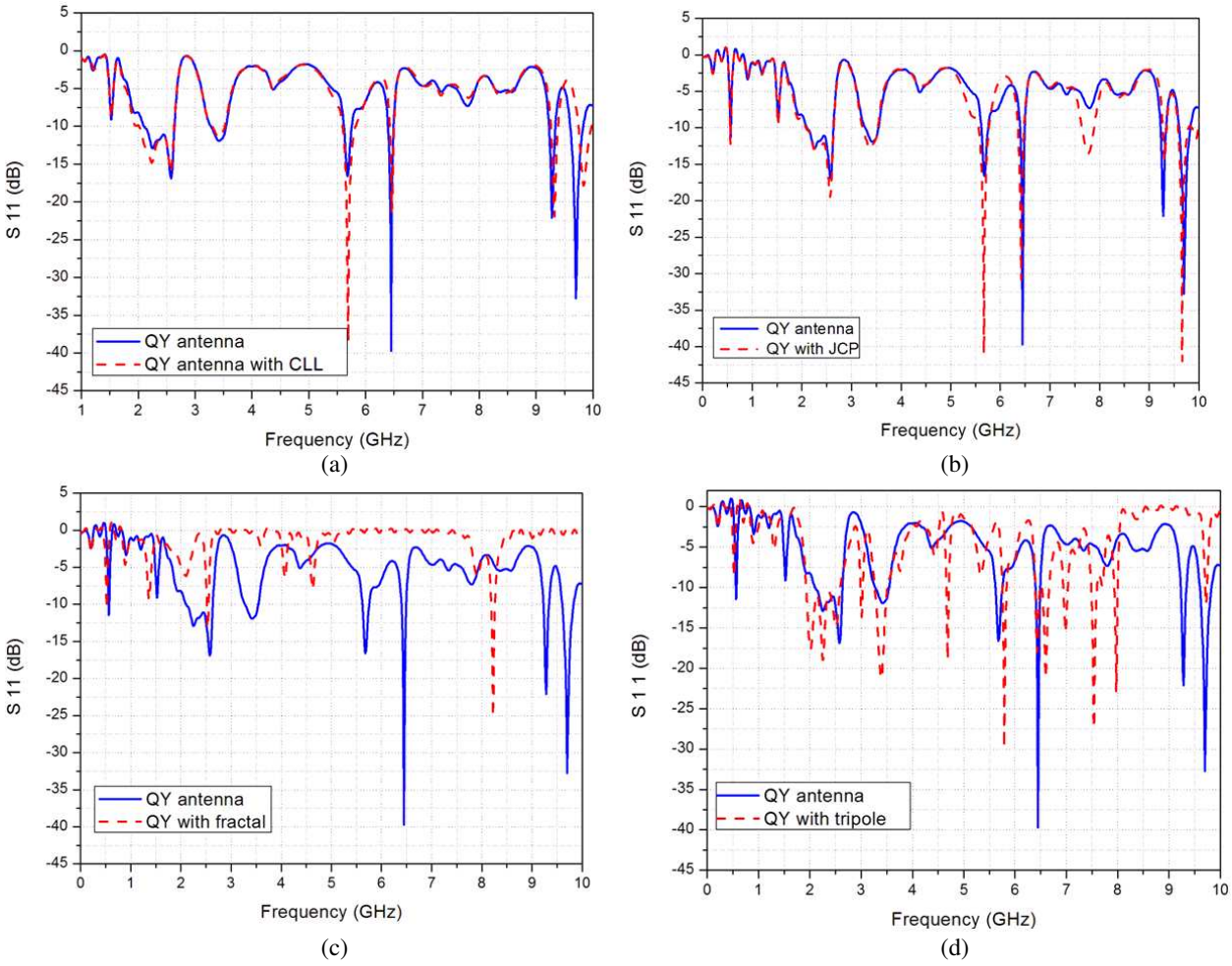

Figure 5: (a) S_{11} parameter of QY antenna with CLL pattern; (b) S_{11} parameter of QY antenna with JCP pattern; (c) S_{11} parameter of QY antenna with fractal pattern; (d) S_{11} parameter of QY antenna with tripole array.

4. CONCLUSIONS

Periodic structures are widely used in order to provide different behavior on devices that operate in high frequencies. Some of them, are capable to change the constitutive parameters ε and μ, so that, the incident wave can assume a different behavior. As soon as the constitutive parameters are not positive anymore, this materials are known as metamaterials.

In this work four metamaterial structures, fractal, CLL, JCP and tripole array, were applied in planar antennas. The S_{11} parameter was analyzed for all structures, where it was clearly observed the appearance of new resonant frequencies, bands of rejection and gain increasing.

ACKNOWLEDGMENT

The authors would like to thank CAPES for the partial financial support.

REFERENCES

1. Cui, T. J., "Electromagnetic metamaterials: Recent advances on the theory, experiments, and applications," *IEEE Antennas Propag. Mag.*, 2008.
2. Jo, N.-I, D.-O. Kim, and C.-Y. Kim, "A compact band notched UWB antenna for mobile applications," *PIERS Online*, Vol. 6, No. 2, 177–180, 2010.
3. Araujo, H. X., S. E. Barbin, and L. C. Kretly, "Metamaterial cell patterns applied to Quasi-Yagi antenna for RFID applications," *Radio and Wireless Symposium — RWS*, Santa Clara, USA, 2012.

4. De Araujo, H. X. and L. C. Kretly, "The effect of metamaterial patterning to improve the septum GTEM chamber performance," *PIERS Proceedings*, 1224–1228, Marrakesh, Morocco, March 20–23, 2011.
5. Capolino, F., *Metamaterials Handbook: Applications of Metamaterials*, 20-1–21-12, CRC Press, 2009.
6. Capolino, F., *Metamaterials Handbook: Theory and Phenomena of Metamaterials*, 19-1–19-28, CRC Press, 2009.

Analysis and Design of the Switched-beam Antenna Array for Automotive Radar Applications

Jau-Jr Lin
Department of Electrical Engineering, National Changhua University of Education
No. 2, Shi-Da Road, Changhua City, Taiwan, R.O.C.

Abstract— More and more vehicles equip with millimeter-wave radar systems to improve the driving safety. Usually, multiple antenna arrays are used to cover different horizontal field of view (FOV) for most models. Integration is one way to make the automotive radar system more compact and more affordable. A three-mode antenna array is designed to cover narrow ($-8°$ to $+8°$), wide ($-45°$ to $+45°$), and two-direction ($-75°$ to $-45°$ and from $+45°$ to $+75°$) FOV scenarios. The horizontal FOVs of a typical long-range radar (LRR) and short-range radar (SRR) cover from $-8°$ to $+8°$, and from $-45°$ to $+45°$, respectively. For the front-end blind side detection, the two-direction FOV covers from $-75°$ to $-45°$ and from $+45°$ to $+75°$, which are often blocked by the vehicle front pillars. Thus, this system can provide a total 150° FOV coverage. Based on these FOV requirements, a switch-beam antenna array is proposed, which is based on the minimum variance distortion less response (MVDR) beamforming algorithm. The simulation demonstrates this antenna array can operate not only over the narrow, wide, and two-direction FOV scenarios, but also wide bandwidth (76 to 81 GHz).

1. INTRODUCTION

In recent years, more and more high-end or safety-oriented automobiles equip with the millimeter-wave (mm-wave) automotive radar systems as a standard safety feature. The automotive radar systems can provide various active and passive safety features, such as adaptive cruise control (ACC), blind side detection, and pre-crash sensing and so on [1–3]. These automotive radar systems can alert and assist drivers to avoid possible impacts and stay away from the potential dangers, and some systems even response automatically to dangerous situations in a short time. If all cars equipped with automotive radar systems, this could reduce traffic accidents, which are due to drivers' errors, misjudgments, and bad driving behaviors. This will not only enhance drivers' and passengers' safety, but also improve road safety for all road users. However, the price of the automotive is still not affordable for every model and everyone. If a car buyer wants to enjoy all possible safety benefits as mentioned in [1–3], he will need multiple automotive radar modules to have a 360° radar protection, as shown in Fig. 1. This will cost the vehicle consumer even more.

To make the automotive radar modules affordable, one way is to use less separated modules, and do more integrations. This paper will analyze the automotive radar system first to understand the limitations, and discuss the possible strategies to integrate more modes. Finally, a three-mode switched-beam antenna array will be proposed to cover the narrow, wide, and two-direction field-of-view (FOV) objectives, and also 77/79 GHz automotive radar bands.

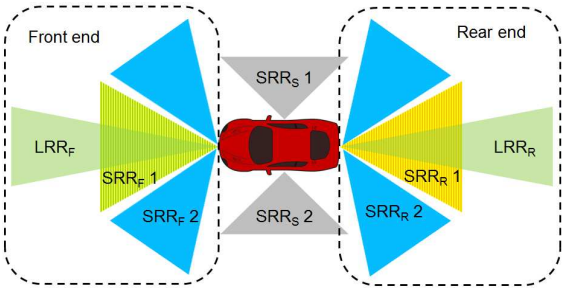

Figure 1: A 360° radar protection with LRRs and SRRs.

2. SYSTEM ANALYSIS

A typical FMCW (frequency-modulation continuous wave) automotive radar system is shown in Fig. 2. The advantages of FMCW radars in comparison to pulse radars are the low measurement

time and low peak-to-average power ratio. Note that low measurement time is the key to integrate more radar modes together and this will be discussed later. The system usually consists of 1-transmitter and N-receivers [3–5]. Note that N is the number of the radar receiver chains. The N-receivers make the target angle detection possible through the spatial signal processing. The baseband signal processor controls the PLL/synthesizer and VCO to generator desired FMCW waveforms, and the signals will be amplified by PA and transmitted through the antenna.

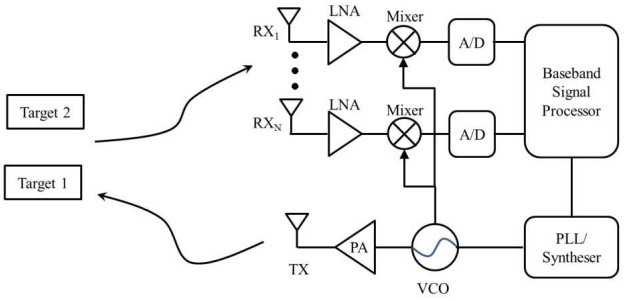

Figure 2: A typical FMCW automotive radar system.

The proposed 360° radar protection with LRRs (long-range radars) and SRRs (short-range radars) is shown in Fig. 1. There are one LRR ($\mathrm{LRR_F}$) and two SRR ($\mathrm{SRR_F}1$ and $\mathrm{SRR_F}2$) for front-end detections, and these can also be applied for the rear-end detections. Moreover, there could be some (SRRS1 and SRRS2) for side detections. The LRR operates at 76–77 GHz and detects the range up to $200 \sim 250$ meters. A SRR operates at 77–81 GHz. A SRR provides wider coverage and higher range resolution than a LRR [1–3]. Many papers and products have talked about integration of $\mathrm{LRR_F}$ and $\mathrm{SRR_F}1$. This paper focuses on a three-mode ($\mathrm{LRR_F}$, $\mathrm{SRR_F}1$ and $\mathrm{SRR_F}2$) automotive radar system for a total 150o front-end protection. $\mathrm{SRR_F}2$ is very important for the front-end blind side detections, which are often blocked by the vehicle front pillars. This is extremely helpful for the driving situations like leaving the perpendicular parking spots, exiting the narrow streets, and driving in the winding mountain roads, etc.

For RF circuits (LNAs, VCO, PAs, mixers, etc.), many researchers make the RF circuits feasible to work well over the operation band (76–81 GHz) [3–5]. For antenna designs, the challenges are not only to cover the wide operation frequency, but also the different horizontal FOV requirements, as shown in Fig. 1. In compared to a wide operation frequency, it is more challenge to design multiple FOV modes. Thus, there are usually two specific antennas for LRR and SRR applications, respectively. Some are even applied a lens antenna to achieve a narrow FOV requirement for a LRR [3, 6]. However, the temperature variations could have a big impact on the lens antenna characteristics. If one array is able to generate multiple FOVs, it will not only avoid extra packages, such as dielectric lens, but also reduce the module size. This will make the automotive radar more affordable.

Assume that a FMCW radar system is applied. Because LRR and SRR share the same RF circuits (Fig. 2), each possible radar operation mode should run in sequence. Thus, the total observation and processing time of all radar operation modes should be much less than the human's potential brake response time (PBRT) [10]. According to [7, 8], the transmitted FMCW signal $S_T(t)$ can be modeled as

$$S_T(t) = A_T \cos\left(2\pi f_c t + 2\pi \int_0^t f_T(\tau) d\tau\right). \tag{1}$$

where $f_T(\tau) = \frac{B}{T} \cdot \tau$ is the transmit frequency as a function of time, f_c is the carrier frequency, B is the bandwidth, A_T represents the transmitted signal amplitude, and T is the time duration. From [8] and [9], the bandwidth B is related to the given range resolution ΔR and can be formulated as

$$B = \frac{c}{2\Delta R}. \tag{2}$$

Similarly, the observation time T is related to the velocity resolution Δv and can be expressed as

$$T = \frac{c}{2f_c \Delta v}. \tag{3}$$

From Equation (3) and [9], the total period of operation modes will be tradeoffs among a velocity resolution, a radar waveform design, the capability of a baseband processor, the number of possible operation modes, etc. As mentioned earlier, in compared to pulse radar, the low measurement time of FMCW radar could accommodate more radar modes in the same period. Since the number of radar operation modes, which run in sequence, is limited, one possible solution is to divide modes for different driving situations. For example, if cars are running in the high way, the $\mathrm{LRR_F}$ and $\mathrm{SRR_F}1$ modes will be activated; if cars are running in the community, mountain road or parking lot, the $\mathrm{SRR_F}1$ and $\mathrm{SRR_F}2$ modes will be activated. This will allow more integration in a system.

3. BEAMFORMING ALGORITHM AND SIMULATION RESULTS

Here, the minimum variance distortionless response (MVDR) beamforming algorithm [10] is applied. For this automotive radar system, the horizontal FOV of $\mathrm{LRR_F}$ is $-8°$ to $+8°$, the horizontal FOV of $\mathrm{SRR_F}1$ is $-45°$ to $+45°$, the two-direction FOV of $\mathrm{SRR_F}2$ is $-75°$ to $-45°$ and $+45°$ to $+75°$, respectively. The several characteristics of MVDR will be utilized to obtain the array weights for different scenarios. Assume that a six-element uniform linear array (ULA) is applied. Six-element array matches to the receiver chain design in [4]. The separation of each element is $\lambda/2$ at 79 GHz and this will make the 77–81 GHz design easier. The radiation pattern of each array element is assumed as $|\cos(\theta)|$, which is close to a typical patch antenna [11]. When the radar system switches modes, the number of array elements will be selected, and the pre-derived beamforming weights will be employed. The broadside is 0o, and the endfire is $\pm 90°$.

MVDR is well-known that it can suppress the uncorrelated interference well [10]. This will be applied to narrow the mainlobe to meet the small FOV requirement of LRR. Assume that the desired signal is at $0°$ and two interferences are at $-15°$ and $+15°$, respectively. Fig. 3 is shown the normalized pattern at 76 and 77 GHz, respectively. The 3-dB mainlobe is well confined between $\pm 8°$, and the sidelobes are less than -13 dB.

MVDR is also well-known that it cannot suppress the correlated interference [10]. Thus, assume that the desired signal and the correlated signal are at $-15°$ and $+15°$, respectively. The angles can be tuned around to meet the wideband operation. Fig. 4 shows the normalized pattern of $\mathrm{SRR_F}1$

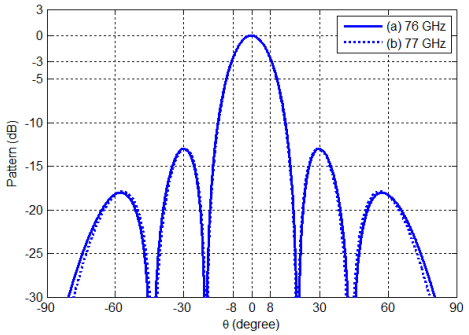

Figure 3: Horizontal pattern for the LRR application.

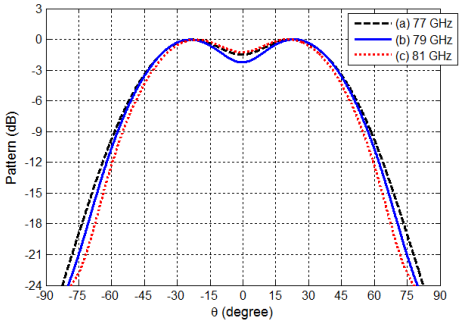

Figure 4: Horizontal pattern for the $\mathrm{SRR_F}1$ application.

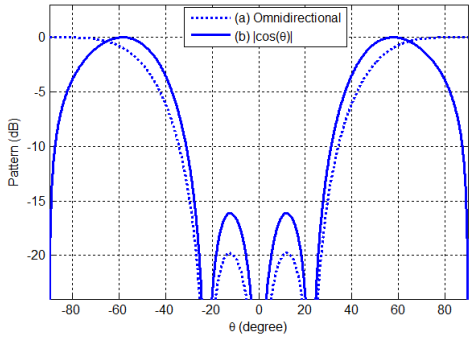

Figure 5: Horizontal pattern for the $\mathrm{SRR_F}2$ application with omnidirectional and $|\cos(\theta)|$ element patterns.

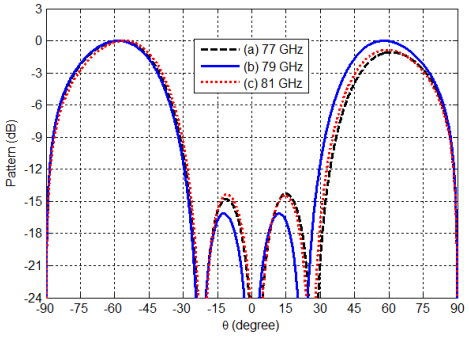

Figure 6: Horizontal pattern for the $\mathrm{SRR_F}2$ application.

application at 77, 79 and 81 GHz, respectively. The 3-dB beamwidths are all between ±45°. Here, the number of array elements is three to have a wider beamwidth by utilizing less array elements.

While the beam is steered to around the endfire, the beam broadening effect will be seen [11]. If the omnidirectional pattern of each array element is applied, the pattern will be like the dash line in Fig. 5. Because the pattern of each array element is assumed as $|\cos(\theta)|$, the overall beam pattern [11] will be shaped as the solid line in Fig. 5. This makes it possible to generate two mainbeams close to endfire. Assume that the desired signal are at +90°. To suppress the sidelobes, two interferences are set at −20° and + − 20°. Fig. 6 shows the normalized pattern of $\mathrm{SRR_F}2$ application at 77, 79 and 81 GHz, respectively. The 3-dB patterns are all between about −75° to −45° and +45° to +75°, and all sidelobes are less than −15 dB. Here, the number of array elements is four.

4. CONCLUSIONS

The proposed three-mode automotive radar system is intent to cover narrow (−8° to +8°), wide (−45° to +45°), and two-direction (−75° to −45° and from +45° to +75°) FOV scenarios. Instead of applying complex multi-beam beamforming algorithms, several properties of MVDR beamforming are utilized to narrow the mainlobe beamwidth, broaden the mainlobe beamwidth, and even create two mainlobes. The simulation results demonstrate that the three-mode automotive radar system is able to cover the desired FOVs and 77/79-GHz radar bands. Only one set of antenna array and one set of RF circuits are needed for this system. This highly integrated system will not only lower the cost, but also provide more added value for auto customers.

ACKNOWLEDGMENT

This work was supported by the Ministry of Economic Affairs, Taiwan, R.O.C., under contract number 100-EC-17-A-03-S1-195. We are also grateful to the National Center for High-performance Computing for providing computer time and facilities.

REFERENCES

1. Wenger, J., "Automotive radar-status and perspectives," *2005 IEEE CSIC*, 21–24, 2005.
2. Murad, M., J. Nickolaou, G. Raz, J. S. Colburn, and K. Geary, "Next generation short range radar (SRR) for automotive applications," *2012 IEEE Radar Conference (RADAR)*, 0214–0219, 2012.
3. Hasch, J., E. Topak, R. Schnabel, T. Zwick, R. Weigel, and C. Waldschmidt, "Millimeter-wave technology for automotive radar sensors in the 77 GHz frequency band," *IEEE Transactions on Microwave Theory and Techniques*, Vol. 60, 845–860, 2012.
4. Trotta, S., B. Dehlink, R. Reuter, Y. Yin, J. John, J. Kirchgessner, et al., "A multi-channel Rx for 76.5 GHz automotive radar applications with 55 dB IF channel-to-channel isolation," *2009 EuMIC*, 192–195, 2009.
5. Li, Y.-A., M.-H. Hung, S.-J. Huang, and J. Lee, "A fully integrated 77 GHz FMCW radar system in 65 nm CMOS," *2010 IEEE ISSCC*, 216–217, 2010.
6. Wang, H.-N., Y.-T. Huang, and S.-J. Chung, "A dielectric lens antenna feeding with microstrip patch antennas for 77 GHz long range radar application," *2012 APMC*, 412–414, 2012.
7. Komarov, I. and S. Smolskiy, *Fundamental of Short-range FM Radar*, 1st Edition, Artech House, 2003.
8. Lin, J.-J., Y.-P. Li, W.-C. Hsu, and T.-S. Lee, "Design of an FMCW radar baseband signal processing system for automotive application," submitted for review.
9. Ray, E., M. Nekoui, H. Pishro-Nik, "Real-time estimation of the distribution of brake response times for an individual driver," Technical Report, University of Massachusetts Amherst, 2012.
10. Van Veen, B. and K. Buckley, "Beamforming: A versatile approach to spatial filtering," *IEEE ASSP Mag.*, 4–24, 1988.
11. Balanis, C. A., *Antenna Theory: Analysis and Design*, Wiley, 1997.

Compact Printed Ultra-wide Band Antenna with Band-notched Characteristics

Chongzhi Han, Jiaran Qi, and Jinghui Qiu
Department of Microwave Engineering, School of Electronics and Information Engineering
Harbin Institute of Technology, Harbin, Heilongjiang, China

Abstract— In 2002, the Federal Communication Commission (FCC) set the frequency band of 3.1–10.6 GHz as the operating bandwidth of high-precision distance measurement, metal detection, and wireless communication systems. From then on, ultra-wide band (UWB) antennas have attracted more and more attention. In this paper, a novel low profile compact UWB microstrip antenna was proposed for UWB communication applications. It is shown both numerically and experimentally that the bandwidth of the antenna is wide enough to cover 3.1–10.6 GHz. Moreover, utilizing parasitic strips and gap structures, the characteristic of dual band suppression has been achieved rejecting the frequency band of 5.15–5.825 GHz and that of 3.3–3.8 GHz, in order to exclude the operating bandwidth of wireless local area network (WLAN) and worldwide interoperability for microwave access (WiMAX).

1. INTRODUCTION

Since the Federal Communication Commission (FCC) approved the frequency band of 3.1–10.6 GHz for the commercial use of ultra-wideband (UWB) communication in 2002 [1–4], the research on UWB antennas has attracted more and more attention for its inherent advantages, such as high data rate, low power consumption and low cost. Nowadays, considerable amounts of UWB antennas have been proposed, covering the bandwidth of 3.1–10.6 GHz [5–8]. Yet, most of them cannot achieve band-notched characteristics. As commonly known, the antenna with band-notched characteristics can reduce the interference between different systems such as WLAN (5.125–5.825 GHz) and WiMAX (3.3–3.8 GHz) [9, 11].

In order to solve the problem above mentioned, a new UWB microstrip antenna was proposed in this paper, which covers the bandwidth of 3.1–10.8 GHz with band-notched characteristics of 5.125–5.825 GHz and 3.3–3.8 GHz, respectively. The radiation part of the antennas consists of a hyperbolic plane fed by a coplanar waveguide structure (CPW) [5]. By adjusting its dimensions, the desired impedance bandwidth of the antenna is achieved. Two U-Shaped slots are etched on the hyperbolic plane, which provide the demanded band-notched characteristics, respectively. Furthermore, we optimize the structure of the antenna by CST Microwave Studio. Finally, CPW with rounded corners provides better impedance performance for the proposed antenna.

2. STRUCTURE OF THE ANTENNA

Figure 1 describes the geometry of the proposed antenna. It is fabricated on a FR4 substrate, with a total area of $30 \times 30 \times 1.1\,\text{mm}^3$, relative dielectric constant of 4.4, and loss tangent of 0.02. The antenna is composed of a hyperbolic plane radiator, fed by CPW, which realizes the UWB characteristics by generating more resonance frequencies. Additionally, two U-shape slots are etched on the radiator providing band-notched properties by destroying the original distribution of the surface currents. Moreover, the rounded corners of the CPW decrease the discontinuities of the antenna structure, which can thus broaden the operating bandwidth of the proposed antenna. The functions of the structure mentioned above will be discussed in detail in Section 3. As shown in Fig. 1, the optimized dimensions are achieved using CST Microwave Studio, and listed as follows: $W_1 = 10$, $W_2 = 8$, $W_3 = 10$, $W_4 = 24$, $W_5 = 27$, $W_6 = 7$, $W_7 = 8.8$, $W_8 = 2.66$, $W_9 = 9.3$, $g_1 = 0.16$, $g_2 = 0.5$, $g = 1$, $R_1 = 2$, and $R_2 = 3$ (all in millimeters).

3. RESULTS AND DISCUSSION

In order to get a better impedance bandwidth performance, several aspects should be taken in to consideration. Firstly, the structure of the CPW should be adjusted strictly, including dimensions of the rounded corners and gaps between the ground plane. Through simulations, we find that when $R_1 = 2$, $R_2 = 3$, $W_2 = 8$, and $g = 1$, the antenna can match well with the $50\,\Omega$ feeding line. Secondly, the shape of the radiator affects the bandwidth performance as well. As it is known,

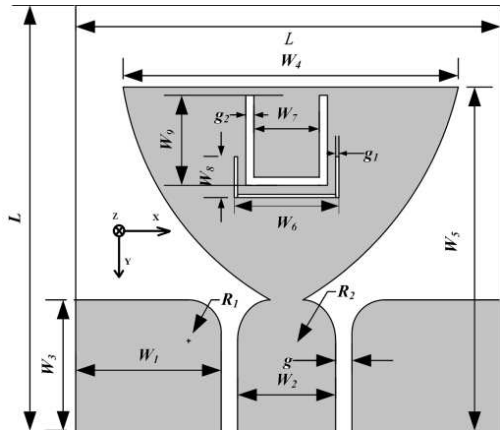

Figure 1: Configuration of the antenna.

it is better to choose curvatures without abrupt discontinuities as the shape of the antenna radiator to achieve a good impedance bandwidth. As we can see in Fig. 1, the radiator is a kind of curved surface based on the hyperbolic function, which is $x^2 = 2py$ ($p = 4$). The reason we choose the hyperbolic curve is that the antenna can cover a wider impedance bandwidth, which is 2.5–14.43 GHz. It should be noted that a smaller p makes a better impedance performance at low frequencies. However, a smaller p will unfortunately make the antenna size larger. Therefore, a suitable value of the parameter p should be chosen by compromising between the antenna compactness and the broadband requirements. With the aid of simulation, we set the value of p as 4. The effects of the parameter p on return-loss can be seen in Fig. 2.

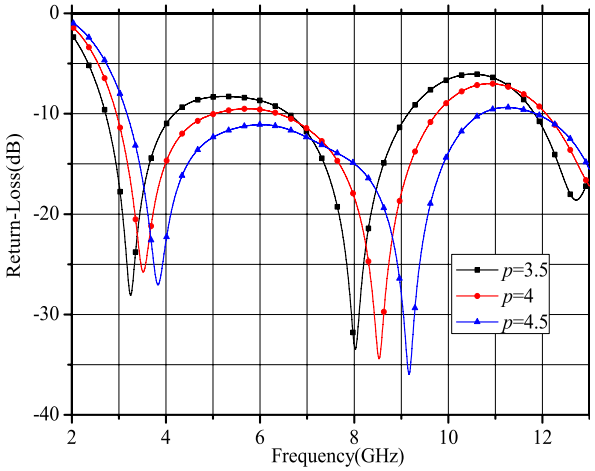

Figure 2: Simulated return-loss with different p.

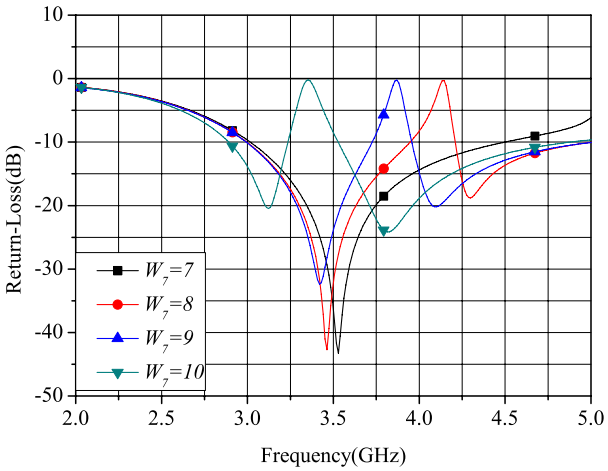

Figure 3: Simulated return-loss with different W_7.

Thirdly, as its most important property, we concentrate on the band-notched characteristics of the antenna. For the proposed antenna, two U-shaped slots are constructed to inhibit electromagnetic waves of specific frequency ranges by disturbing the surface current distribution. The suppressed frequency band has a close relationship with the length and the width of the slot. The length of the slot follows the function:

$$w = \frac{c}{f_r}\sqrt{\frac{2}{\varepsilon_r + 1}}, \tag{1}$$

where c is the free space light speed, f_r is the center operating frequency, and ε_r is the relative dielectric constant of the substrate [12]. In order to keep the antenna dimension unchanged, a straight slot can be bended to a U-shape with the same effective length.

We construct a larger U-shape slot on the antenna and adjust slot length and position to produce a notched-band with the center frequency at 3.55 GHz. The relationship between the slot length

and the center frequency of the notched band is shown in Fig. 3. Another U-shape slot is etched on the radiator in order to produce the other notched-band with the center frequency at 5.475 GHz according to Equation (1). What we should notice is that two slots may have mutual coupling effects on each other. As a result, the parameters of these two U-shaped slots need to be adjusted slightly through simulation.

To better understand the relationship between the shape of the antenna and its impedance bandwidth. Surface current distributions on the radiator and the ground plane of the proposed antenna were simulated by CST. Fig. 4 shows that the surface current at 3.1 GHz, 6.7 GHz, and 10.6 GHz. It is shown that currents on the bottom of the radiator contribute to the low frequency part of the bandwidth, while those on the top of the radiator contribute to that of high frequencies. These can also guide us to find the optimal position to etch the slot in order to achieve specific band-notched characteristics.

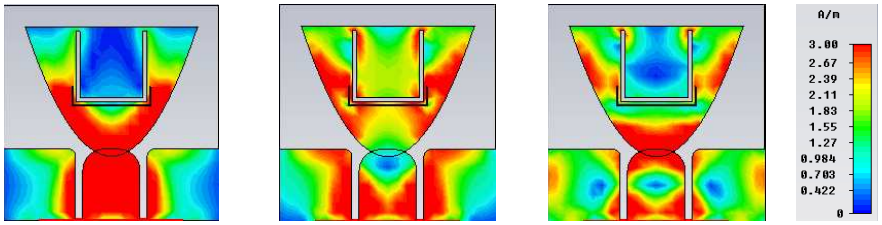

Figure 4: Surface current distributions of the proposed antenna.

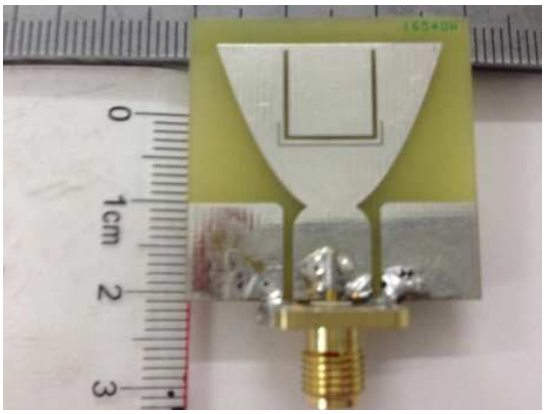

Figure 5: Photography of the UWB antenna.

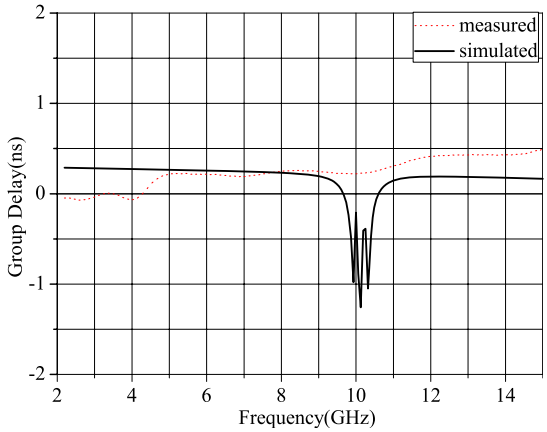

Figure 6: Simulated and measured group delay.

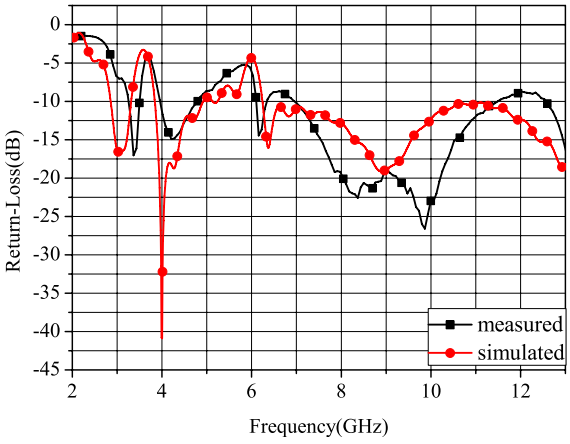

Figure 7: Simulated and measured return-loss of the proposed antenna.

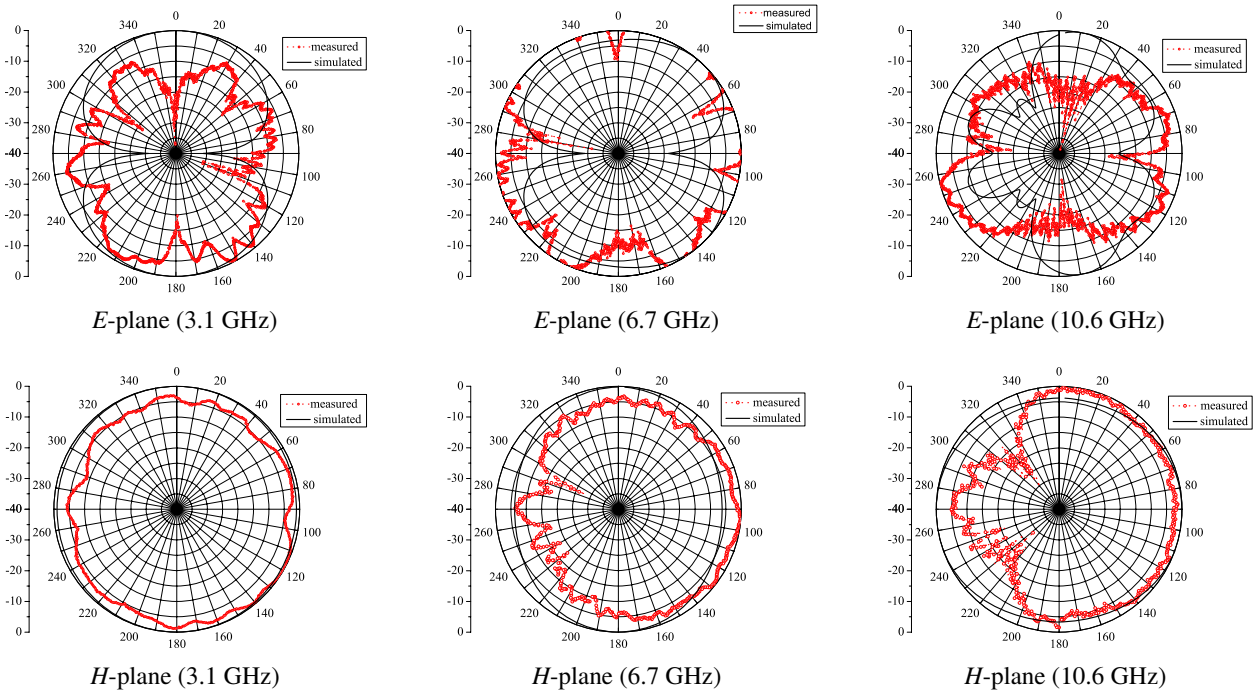

Figure 8: Simulated and measured radiation patterns.

4. EXPERIMENTAL RESULTS AND ANALYSIS

The prototype of the proposed printed compact UWB antenna is shown in Fig. 5. Fig. 6 presents the simulated and the measured results of its group delay. We can see that the group delay of the antenna over the operating bandwidth fluctuates smoothly, smaller than 1 µs. It indicates that the antenna has a good time domain performance, and is capable of transmitting and receiving broadband signals without distortion.

The impedance bandwidth of the proposed antenna is measured by Aglient network analyzer. Fig. 7 compares the simulated and the measured return-loss of the antenna. As indicated in Fig. 7, the measured return-loss has a good agreement with the simulation results. The antenna has a measured impedance bandwidth from 3.1 to 10.6 GHz (return loss < -10 dB), except for the frequency band from 3.3 to 3.8 GHz and that from 4.8 to 6.2 GHz.

Figure 8 shows the radiation patterns at 3.1, 6.7, and 10.6 GHz. It is demonstrated that stable omni-directional H-plane radiation patterns are achieved in the whole operating frequency band. It should be noticed that the radiation patterns in E-plane become imbalanced as frequency increases. The differences between the measured results and the simulation ones may cause by the fabrication and the measurement errors. The imbalanced radiation pattern is attributed to the imbalance of the current distribution at the high frequency.

5. CONCLUSION

In this paper, a novel compact UWB antenna with improved dual band-notched characteristics is proposed. Two U-shape slots are imported to realize the dual band-notched characteristics, covering the WLAN and the WiMAX bandwidth. The area of the antenna is $30 \times 30 \times 1.1\,\text{mm}^3$, with $S_{11} \leq -10$ dB and stable omni-directional H-plane radiation in the frequency band from 2.5 to 14.625 GHz. Good time domain performance is achieved in the whole operating frequency band, enabling the proposed antenna a good candidate for UWB wireless communication applications.

REFERENCES

1. Lin, Y. C. and K. J. Hung, "Compact ultrawideband rectangular aperture antenna and band-notched designs," *IEEE Transactions on Antennas and Propagation*, Vol. 54, 3075–3081, 2006.
2. Su, S. W., K. L. Wong, and F. S. Chang, "Compact printed ultrawideband slot antenna with a band notched operation," *Microwave and Optical Technology Letters*, Vol. 45, 128–130, 2005.

3. Nguyen, T. D., D. H. Lee, and H. C. Park, "Design and analysis of compact printed triple band-notched UWB antenna," *IEEE Antennas and Wireless Propagation Letters*, Vol. 10, 403–406, 2011.
4. Li, C. M. and L. H. Ye, "Improved dual band-notched UWB slot antenna with controllable notched bandwidths," *Progress In Electromagnetics Research*, Vol. 115, 477–493, 2011.
5. Chu, Q., C. X. Mao, and H. Zhu, "A compact notched band UWB slot antenna with sharp selectivity and controllable bandwidth," *IEEE Transactions on Antennas and Propagation*, Vol. 61, 3961–3966, 2013.
6. Lin, D. B., I. Tang, and Y. J. Wei, "Compact dual bandnotched CPW fed wide slot antenna for WLAN and WiMAX applications," *Microwave and Optical Technology Letters*, Vol. 53, No. 7, 1496–1501, 2011.
7. Ryu, K. S. and A. K. Ahmed, "UWB dielectric resonator antenna having consistent omnidirectional pattern and low cross-polarization characteristics," *IEEE Transactions on Antennas and Propagation*, Vol. 59, No. 4, 1403–1408, 2011.
8. Shilpa, J. and M. Kumar, "Compact planar UWB patch antenna with integrated bandpass filter & band notched characteristics," *IEEE International Conference on Communication Systems and Network Technologies*, Rajkot, India, 2012.
9. Rezaul, A., M. T. Islam, and A. T. Mobashsher, "Design of a dual band-notch UWB slot antenna by means of simple parasitic slits," *IEEE Antennas and Wireless Propagation Letters*, Vol. 12, 1412–1415, 2013.
10. Hong, C.-Y., C.-W. Ling, I-Y. Tarn, and S.-J. Chung, "Design of a planar ultrawideband antenna with a new band-notch structure," *IEEE Transactions on Antennas and Propagation*, Vol. 55, 3391–3397, 2007.
11. Peng, G., S. He, X. Wei, Z. Xu, N. Wang, and Y. Zheng, "Compact printed UWB diversity slot antenna with 5.5-GHz-band-notched characteristics," *IEEE Antenna and Wireless Propagation Letters*, Vol. 13, 376–379, 2014.

A Triangular Antenna with Spiral Slot Arrays for Beidou Navigation

Jianhua Zhou, Kaishuang Zhang, and Baiqiang You
Department of Electronic Engineering, Xiamen University, Xiamen, Fujian, China

Abstract— A dual-band triangular microstrip antenna is presented for Beidou navigation, applying spiral-slot arrays coupling technique. The antenna's radiation patch is designed on a single layer of medium loaded with 6-elements feed coupling slot arrays. Thus, the actual current path could be controlled and the size of the proposed antenna is reduced effectively. Dual-band radiation is realized by introducing two triangular vortex rings coupled with 6 meandering slots, covering 1.616 GHz and 2.492 GHz. The three meandering slots are introduced on the ground plane to improve the antenna performance further. The simulation results show that the 10 dB impedance working bandwidths are 17 MHz and 35 MHz respectively for lower and higher frequencies of Beidou navigation, with quite good radiation stability and high gain performances.

1. INTRODUCTION

Rapid development in the field of Beidou Navigation technology demands multiband and wideband antenna, primarily to achieve high data rate transmission function in CNSS (Compass navigation Satellite System). Rectangular and circular microstrip patches are widely applied in antenna design for low profile, simplification and light weight. In addition to the above advantages, triangular patch is a better choice for wideband radiation performance in dual-band antenna [1, 2]. For much higher gain and better directivity of an antenna, Y. S. H. Khraisat and M. M. Olaimat used a triangular patch antenna array to achieve better suppression for side lobe level compared with using a rectangular one [3]. By introducing some specific slots in antenna design, the corresponding resonant frequencies can be excited simultaneously [4, 5]. However, several slots introduced solely, that is equivalent to a load capacitance, are not sufficient to reach the desired frequency and also there would be a drawback of narrow bandwidth. Loading some modified slots or inverting the corresponding conductor on the ground plane of an antenna gives a simple tuning mechanism for the frequency bands and band spacing [6–9]. Furthermore, some improved structures were applied in multiband microstrip antennas, such as a spiral slot antenna [10–12]. A novel triangular split-ring resonator antenna was realized, measured and analyzed in Ref. [13].

In this paper, a triangular antenna loading with a spiral slot array on the radiation patch and ground plane respectively is proposed. The coupled inner and outer spiral slots are nested with each other. Meanwhile, the folded structure can be introduced in the triangular surface while other slots are in the clipped area with a self-similarity of resonator. Thus, the multiband radiation is expected with a good matching performance and bandwidth.

2. ANTENNA DESIGN AND CONFIGURATION

The configuration of the proposed triangular antenna loading with spiral slot arrays is shown in Fig. 1. On the top layer, a triangular patch, a self-similar pair of triangular slots is introduced parallel to the patch sides and each other, to increase energy coupling and realize dual-band radiation. The substrate is a triangular CER-10 (Taconic), with thickness of 3 mm and dielectric permittivity ε_r of 10 respectively. The thickness h of the triangular radiating patch is 0.0035 mm, so the actual height of the antenna will be the summation of the patch thickness h and the substrate thickness. The ground plane is modified by introducing three meandering slots to tune the frequency bands and bandwidth on the bottom layer. As shown in the figure, the main optimal dimensions of the designed antenna are as follows
$S_1 = 49.6\,\text{mm}$, $S_2 = 37.7\,\text{mm}$, $L_1 = 26.8\,\text{mm}$, $L_2 = 15.6\,\text{mm}$, $W = 0.9\,\text{mm}$, $d_0 = 1.8\,\text{mm}$, $d = 2.5\,\text{mm}$, $d_1 = 10.7\,\text{mm}$, $D = 3\,\text{mm}$, $L_\text{s} = 15.5\,\text{mm}$, $W_\text{s} = 1.1\,\text{mm}$.

The top layer of the designed antenna is supported by six meandering slots, comprising internal and external triangular ring respectively. The two triangular rings have similar geometric structures and are coupled to be as vortex slot ring arrays. A lower frequency band is realized through three large meandering slots, which are coupled to be an external triangular ring with each other arranged according to 60 degrees. While three small meandering slots are inserted into the external slots by 60 degrees and coupled to be an internal triangular ring, through which a higher resonant frequency band is generated. As depicted in Fig. 1, the two coupled triangular slot rings are obviously self-similar in structure so that the coupling effect of electromagnetic fields can be also enhanced after

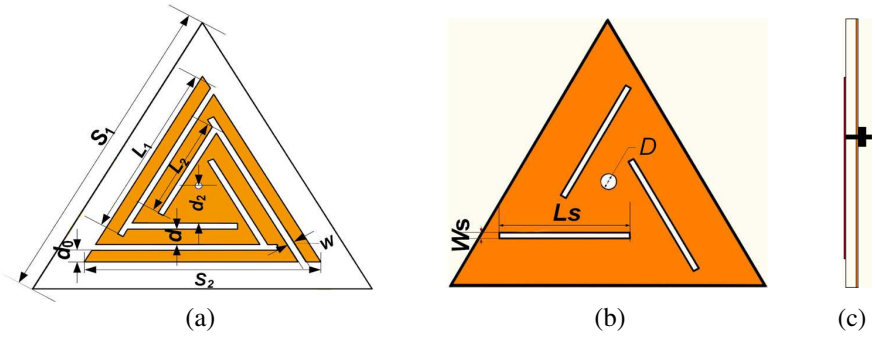

Figure 1: Configuration of the proposed antenna. (a) Top view. (b) Bottom view. (c) Side view.

optimization for the distribution feeding match. Both the bandwidth and return loss level of the antenna are improved significantly. Due to the loading of spiral slot arrays, further miniaturization would be expected.

However, conventional slot patch antenna usually has no good matching impedance in the return loss curve with narrow bandwidth. Based on ground plane technique, some modified slots are considered for improving the performance of antenna. For instance, when three meandering slots are mutually staggered on the ground plane, the resonant frequency band with good matching condition will be achieved and thus the bandwidth and the return loss curve can be improved.

3. RESULTS AND DISCUSSIONS

As in Fig. 2, the variation of the return loss S_{11} values at dual-bands with the lengths of the external spiral slots and internal spiral slots are illustrated. As expected, the desired frequencies are reached by introducing the triangular spiral slot arrays. It is also clear from the figure that the dual frequency bands decrease with the length of the spiral slot increasing. Furthermore, the slot lengths corresponding to the best return loss curves are $L_1 = 26.8\,\text{mm}$ at the lower band and $L_2 = 15.6\,\text{mm}$ at the higher band separately.

Considering the influence of the slot ring width and the distance between the external and internal slots at dual-bands on the performance of the antenna, Fig. 3 illustrates the variation of the return loss. Through the contrast of Fig. 3 with Fig. 2, it is obvious that the effect of the slot length is more than that of the slot ring width and distance. As the width and distance of the spiral slots increase, the relative current path at the edge of the triangular antenna patch will be reduced so that the lower frequency band will shift to the much lower. However, the distance from the internal spiral slot ring to the patch center is decreased in contrast so that the current path at the higher band decreases. Consequently, the higher frequency band increases with the width of the spiral slot as shown in the figure.

According to the analysis as above, it can be concluded that the designed antenna realize dual frequency bands with good matching condition. Furthermore, the simulated radiation patterns on XZ-plane and YZ-plane at 1.616 GHz and 2.492 GHz present all-direction radiation, as shown in Figs. 4(a) and (b) respectively. In addition, according to the formula for the bandwidth BW as

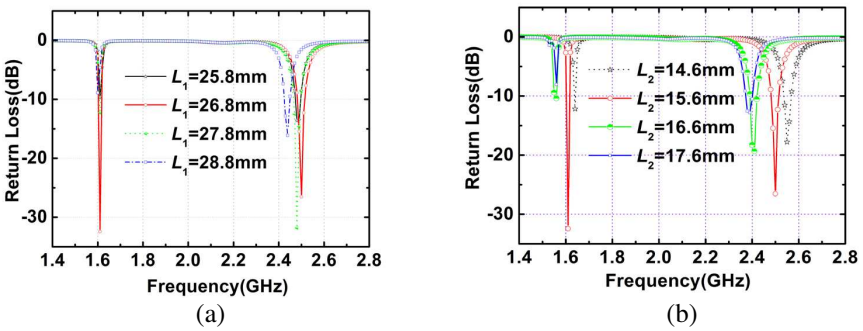

Figure 2: Profile optimization analyses: effects of the slot lengths on the return loss of the designed antenna. (a) The external spiral slot at lower band. (b) The internal spiral slot at higher band.

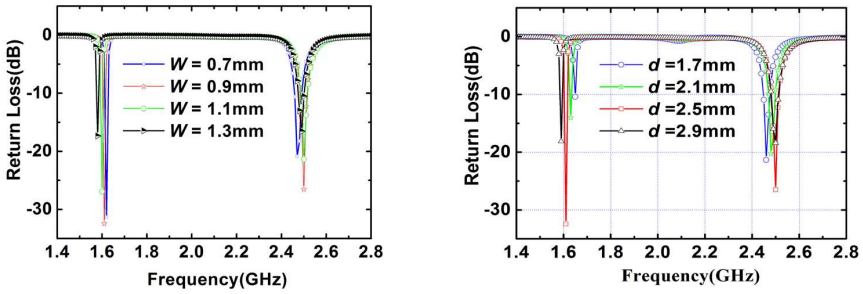

Figure 3: Effects and optimization on the return loss (S_{11}) for the proposed antenna at dual bands. (a) Optimization analyses of slot width. (b) Optimization analyses of the distance between slots.

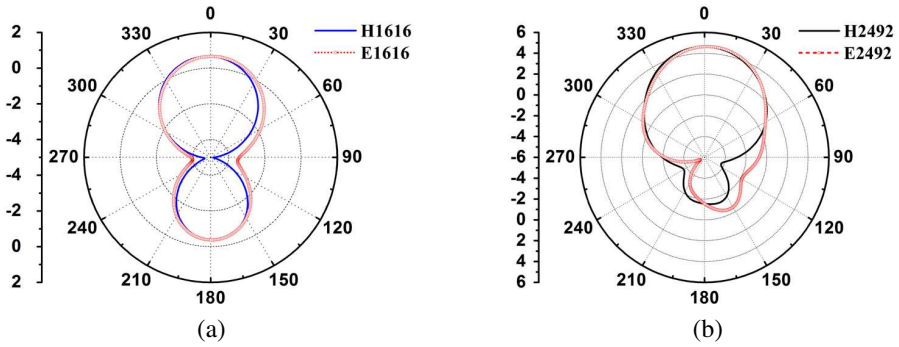

Figure 4: Simulated radiation patterns of the proposed antenna, (a) in lower band, (b) in higher band.

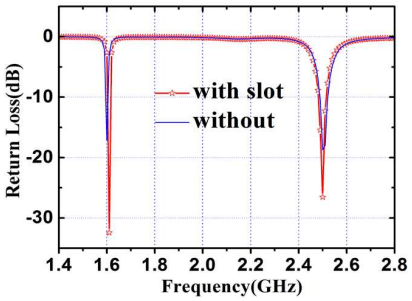

Figure 5: Simulated return losses of the proposed antenna with slots and without any slot.

follows

$$BW = (S-1)\Big/ Q_T\sqrt{S} \tag{1}$$

where S and Q_T are the standing wave ratio and quality factor respectively. The bandwidth of dual-band can be effectively improved by introducing modified slots on the ground plane. As illustrated in Fig. 5, if there is no slot in the ground plane, the return loss of the antenna without any slot introduced is more than -20 dB in the range from 1.6 GHz to 2.4 GHz. On the contrary, the dual frequency bands of the antenna with some suitable slots employed on the ground plane have a good performance in the return loss curve, due to the good matching condition achieved.

A fabricated model of the proposed antenna is shown in Fig. 6(a), and also the measured and simulated return losses of the proposed antenna are illustrated in Fig. 6(b). It can be observed that the measured results agree quite well with the simulated results. The measured 10 dB impedance working bandwidths are 17 MHz and 35 MHz respectively for the lower and higher frequencies, corresponding to the fractional bandwidth of 2.75% and 1.40% respectively. The major reason for the deviation in the higher frequency band is that the dimension of the fabricated antenna is small so as to generate carving errors during the processing.

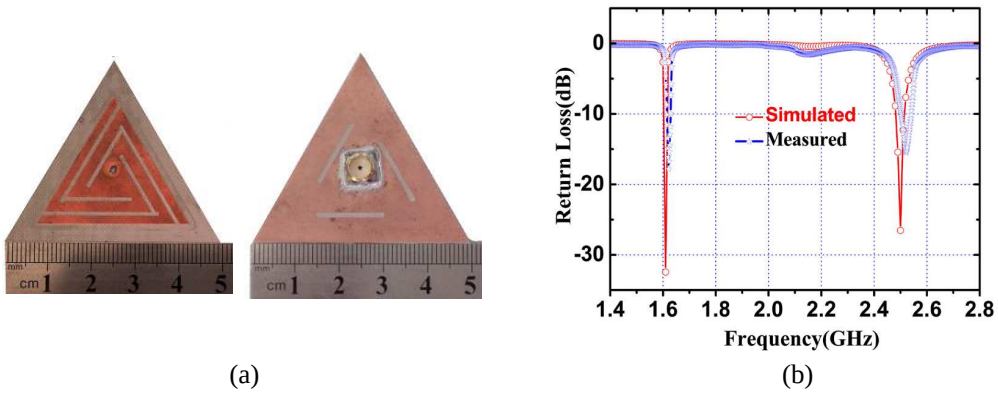

Figure 6: The outlook and properties of the fabricated prototype of the designed antenna. (a) Top & bottom view. (b) Comparison of simulated and measured return losses.

4. CONCLUSION

A triangular antenna loaded by spiral slot arrays with distribution feeding match to realize dual frequency bands is presented for Beidou navigation applications in this letter. Compared with the antennas with conventional slots, the frequency ratios of the proposed antenna can be effectively controlled through two self-similar spiral slot ring coupled strongly. By properly folding the spiral slots and tuning the coupled location, the multiband radiation can be achieved with the miniaturization of the antenna. Furthermore, the spiral slots on the ground plane are modified to enhance the bandwidth in dual frequency bands for the performance improvement of the designed antenna. The proposed antenna is easy to be fabricated for its simple configuration, and the measured results agree well with the simulated results.

ACKNOWLEDGMENT

This work is supported by Fujian Provincial Key Sci-Tech Project (2013HZ0002-1) of China. We thank the staff members of Microwave Library for helpful supports.

REFERENCES

1. Row, J. S. and K. W. Lin, "Low-profile design of dual-frequency and dual-polarised triangular microstrip antennas," *Electronics Letters*, Vol. 40, No. 3, 156–157, 2004.
2. Deshmukh, A. A., A. R. Jain, and K. P. Ray, "Analysis of broadband pair of slot cut equilateral triangular microstrip antenna," *Proc. IEEE Int. Conf. on Advances in Technology and Engineering (ICATE)*, 1–6, 2013.
3. Khraisat, Y. S. H. and M. M. Olaimat, "Comparison between rectangular and triangular patch antennas array," *Proc. IEEE Int. Conf. on Telecommunications (ICT)*, 1–5, 2012.
4. Singh, N., D. P. Yadav, S. Singh, et al., "Compact corner truncated triangular patch antenna for WiMAX application," *Proc. IEEE Microwave Symposium (MMS)*, 163–165, 2010.
5. Lin, S., J. Qiu, H. Ren, et al., "Simulation research of a novel multi-band fractal triangle antenna," *Proc. IEEE Microwave Conference, Asia-Pacific (APMC)*, 1–4, 2007.
6. Liu, L., S. Zhu, and R. Langley, "Dual-band triangular patch antenna with modified ground plane," *Electronics Letters*, Vol. 43, No. 3, 140–141, 2007.
7. Gemio, J., J. P. Granados, and J. S. Castany, "Dual-band antenna with fractal-based ground plane for WLAN applications," *IEEE Antennas and Wireless Propagation Letters*, Vol. 8, 748–751, 2009.
8. Han, L., W. Zhang, J. Zuo, et al., "Novel differential dual frequency antenna for wireless communication," *Proc. IEEE Microwave Conference, China-Japan Joint*, 154–156, 2008.
9. Ojaroudi, M. and N. Ojaroudi, "Ultra-wideband small rectangular slot antenna with variable band-stop function," *IEEE Transactions on Antennas and Propagation*, Vol. 62, No. 1, 490–494, 2014.
10. Bao, X. L. and M. J. Ammann, "Monofilar spiral slot antenna for dual-frequency dual-sense circular polarization," *IEEE Transactions on Antennas and Propagation*, Vol. 59, No. 8, 3061–3065, 2011.

11. Zou, M., J. Pan, Z. Nie, et al., "A wideband circularly polarized rectangular dielectric resonator antenna excited by a lumped resistively loaded monofilar-spiral-slot," *IEEE Antennas and Wireless Propagation Letters*, Vol. 12, 1646–1649, 2013.
12. Cao, W., A. Liu, B. Zhang, et al., "Dual-band spiral patch-slot antenna with omnidirectional CP and unidirectional CP properties," *IEEE Transactions on Antennas and Propagation*, Vol. 61, No. 4, 2286–2289, 2013.
13. Yang, K., H. Wang, Z. Lei, et al., "CPW-fed slot antenna with triangular SRR terminated feedline for WLAN/WiMAX applications," *Electronics Letters*, Vol. 47, No. 12, 685–686, 2011.

A New Spiral Antenna with Improved Axial Ratio and Shorted Arm Length

Huifen Huang and Zonglin Lv
School of Electronic and Information Engineering, South China University of Technology, China

Abstract— A new spiral antenna is proposed in this paper. The developed antenna has improved axial ratio (AR) and shorted arm length. The developed spiral antenna combines the low frequency characteristic of power spiral antenna and high frequency characteristic of Archimedean spiral antenna. The results reveal that the developed spiral antenna has noticeable improved axial ratio at low frequencies compared with Archimedean spiral antenna, and the problem of axial ratio degradation of power spiral antenna is also solved. The arm length is shorted by 46.4% than conventional Archimedean spiral antenna, and 63.5% than power spiral antenna.

1. INTRODUCTION

Among all frequency-independent antennas, Archimedean spiral antenna can be a good choice in ultra-wideband systems because of its great performance on circular polarization and maintaining consistent gain and input impedance. The radiation mechanism based on the current band theory is shown in [1]. Many efforts have been made to improve radiation characteristics without enlarging the size of the antenna.

Absorbing material that exhibit dielectric or magnetic loss tangents is placed under the antenna [2]. Electromagnetic band gap (EGB) reflector is used [3]. Spiral surrounded with a metallic ring is analyzed in [4].

Power spiral antenna [5] achieves noticeable improvement in axial ratio at low frequencies, but axial ratio degrades at high frequencies. Archimedean spiral antenna and power spiral antenna are combined to achieve good AR at both low and high frequencies [5]. But the antenna is not a self-complementary structure, and the arm length inevitably becomes longer.

In many occasions, short arm length is necessary. In recent studies, spiral antennas with planar feeding structure achieved more attraction. Feeding the equiangular spiral with a transmission line that follows the metal layer beneath the spiral to the center point is proposed [6], and the vertical balun is replaced by parallel-plane feeding structure and the overall size of the antenna is largely reduced. But it is impossible to feed Archimedean spiral antenna the same way because of the long and thin arm. However, Archimedean spiral antenna has a noticeable advantage at axial ratio bandwidth over its equiangular counterpart. On this condition, improving radiation characteristics as well as reducing the arm length is necessary.

2. ANTENNA DESIGN

Figure 1 shows the geometry of the spiral antennas which will be discussed in this paper. These three antennas are defined by the formulas below:

$$r(\varphi) = r_0 + A_1 * \varphi \tag{1}$$

$$r(\varphi) = r_0 * [A_2 * \varphi + 1]^{B_2} \tag{2}$$

$$r(\varphi) = r_0 * A_3 * \left[\frac{\arctan(\varphi - B_3)}{C_3} + D_3\right] \tag{3}$$

where r is radial distance, φ is the winding angle. The inner and outer radius is defined by r_0 and r_1. The start and end of the winding angle is defined by φ_0 and φ_1. A_1, A_2, A_3, B_2, B_3, C_3, D_3 are constants related to the defining geometrical parameters of the antennas.

In typical Archimedean spiral antenna, coils are equally distributed. As shown in Figure 2, the growth rate of r is a constant. The defining formula is (1), and the antenna is shown in Figure 1(a). As presented in [5], Figure 1(b) shows power spiral antenna, in which coils are not equally distributed. The defining formula is (2).

The new spiral antenna has similar structure at outer coils with power spiral antenna but wrapped tighter in the inner coils. The new antenna is shown in Figure 1(c). The defining formula is (3).

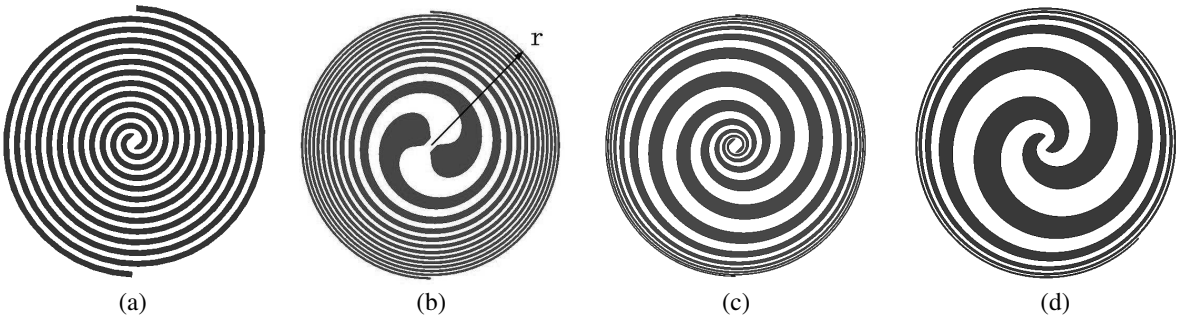

Figure 1: The antennas discussed in this paper. (a) Archimedean spiral, (b) power spiral, (c) new spiral, (d) shorted new spiral.

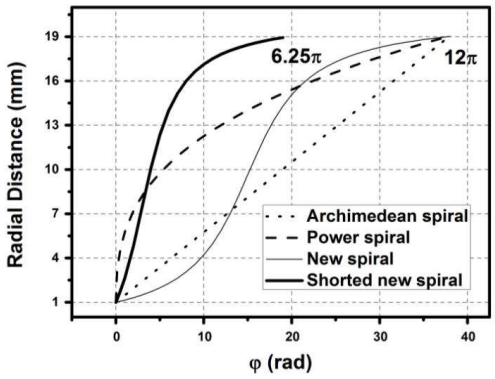

Figure 2: The relationship between r and φ.

Table 1: Parameters of the antennas.

A_1	A_2	B_2	A_3	B_3	C_3	D_3
0.475	485.5	0.3	8.27	3	3	0.906

Table 2: Arm length of the antennas (unit: mm).

Archimedean spiral	Power spiral	Shorted new spiral antenna
375	551	201

To reduce the arm length, we reduce the winding angle of the antenna, and it is found that the good axial ratio caused by the tight wrapping at the outer circles is not missing as long as we choose the suitable parameters. The end of the winding angle is reduced from 12π to 6.25π.

The defining geometrical parameters of the antennas are illustrated in Table 1. The arm length can be approximately seen as the length of the first edge.

The calculated results of the three antennas are shown in Table 2. The arm length of the new spiral antenna is 201 mm, 46.4% shorter than the conventional Archimedean spiral antenna, and 63.5% shorter than power spiral antenna.

3. SIMULATION AND MEASUREMENTS

These antennas are simulated by the HFSS software. All the antennas are fabricated on the 0.8 mm thick F4B ($\varepsilon_r = 2.2$) substrate. And all antennas are surrounded with a metallic ring as described in [5].

In the initial simulations, no balun is used, and we have assumed matched conditions at the input port and excitation source impedance is set to 160 Ω in accordance with the simulated input resistance.

Figure 3 demonstrates the simulated axial ratio performance for the three antennas. At low frequencies, the axial ratio of new spiral and power spiral has an improvement caused by the relatively tighter wrapping than conventional Archimedean spiral. The tighter wrapping causes

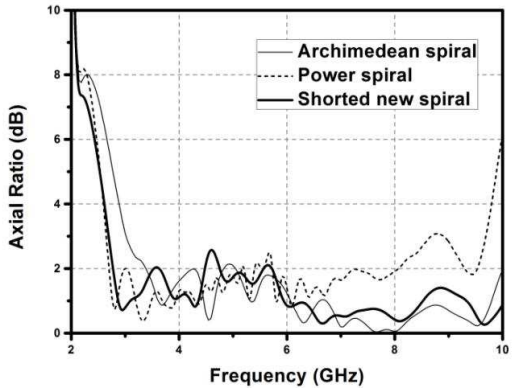

Figure 3: Simulated axial ratio for the three antennas at front side.

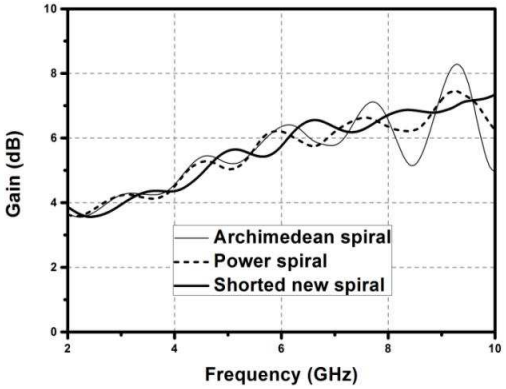

Figure 4: Simulated gain for the three antennas.

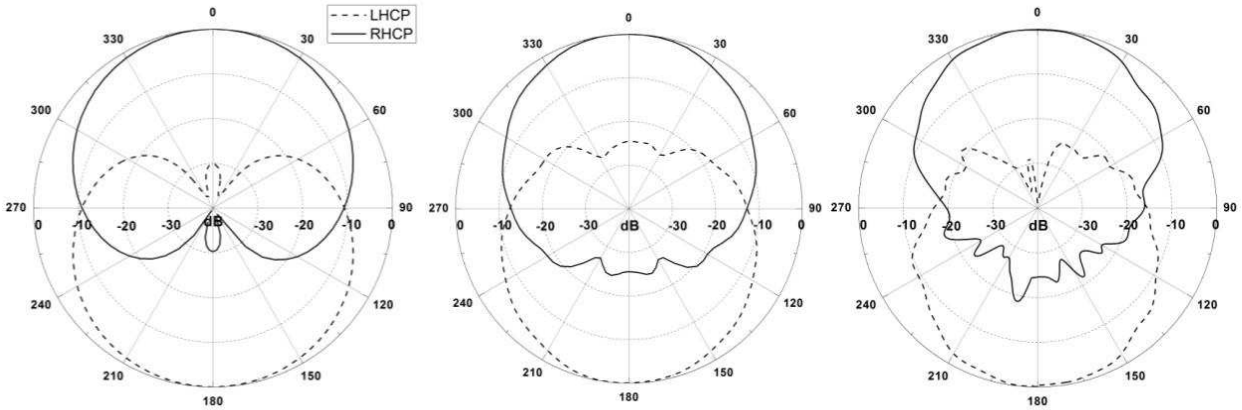

(a) (b) (c)

Figure 5: Simulated radiation pattern. (a) 3 GHz, (b) 6 GHz, (c) 9 GHz.

increased coupling between the spiral arms in active region [5]. The increased coupling reduces the residual currents and reflected derivatives. At high frequencies, the axial ratio of power spiral degrades. But the good axial performance of Archimedean spiral is maintained by the new spiral because of the relatively tighter wrapping at the inner coils. Figure 4 shows the comparison of the three kinds of spiral antennas.

And Figure 5 shows normalized RHCP and LHCP radiation patterns of the new spiral antenna at 3 GHz, 6 GHz, and 9 GHz.

4. CONCLUSION

A new spiral antenna structure is proposed in this paper. The antenna has similar part at outer circles with power antenna but wraps tighter in the inner circles. The new spiral antenna has noticeable improvement in axial ratio at low frequencies and better performance in high frequencies than power spiral, and arm length is also largely shorted.

ACKNOWLEDGMENT

This work is supported by the National Natural Science Foundation of China under Grant 61071056.

REFERENCES

1. Kaiser, J. A., "The Archimedean two-wire spiral antenna," *IRE Trans. Antennas Propag.*, Vol. 8, No. 5, 312–323, May 1960.
2. Nakano, H., S. Sasaki, H. Oyanagi, and J. Yamauchi, "Cavity-backed Archimedean spiral antenna with strip absorber," *IET Proc. Microw. Antennas Propag.*, Vol. 2, No. 7, 725–730, October 2008.

3. Bell, J. M. and M. F. Iskander, "A low-profile Archimedean spiral antenna using an EBG ground plane," *IEEE Antennas Wireless Propagation Letters*, Vol. 3, 223–226, 2004.
4. Liu, Q., C.-L. Ruan, L. Peng, and W.-X. Wu, "A novel compact Archimedean spiral antenna with gap-loading," *Progress In Electromagnetics Research Letters*, Vol. 3, 169–177, 2008.
5. Elmansouri, M. A. and D. S. Filipovic, "Low-dispersion spiral antennas," *IEEE Transactions on Antennas and Propagation*, Vol. 60, No. 12, 5522–5530, December 2012.
6. Veysi, M. and M. Kamyab, "Bandwidth enhancement of low-profile PEC-backed equiangular spiral antennas incorporating metallic posts," *IEEE Transactions on Antennas and Propagation*, Vol. 59, No. 11, 4315–4318, 2011.

Tri-band Dual-polarized Multilayer SAR Microstrip Antenna

Hossam Hamza[1] **and Khaled Hussien**[2]

[1]Xidian University, Xi'an, China
[2]Military Technical College, Cairo, Egypt

Abstract— A novel tri-frequency (C, X and Ku) bands with dual-linear polarized each, multilayer microstrip antenna single element is proposed and presented. The triple band operation is obtained by using two antenna elements, one for a dual-band resonance at C and X bands with dual linear polarization and above is for the Ku band (also with dual linear polarized behavior). The feeding mechanism for the dual antenna element is an aperture coupling through cross shaped slot with different shaped feeding ports (to enhance isolation). The Ku band antenna element has an electromagnetically coupled microstrip T-junction feed for one polarization and a direct feeding for the orthogonal polarization. The multilayer microstrip element exhibits a selective frequency band of operation, good isolation among the different feeding ports, good directivity pattern and high gain for both polarizations at all frequency bands. The performance of the proposed antenna was simulated using a commercial software based on the Finite Element Method (FEM) algorithm. The proposed antenna is designed to meet the requirements of Synthetic Aperture Radar (SAR), where multiple frequency with dual linear polarization is needed.

1. INTRODUCTION

SAR operations mainly depend on synchronized measurements using different frequencies, preferably simultaneous dual polarized. Since the performance of a SAR system such as synthetic aperture length, PRF, slant range resolution and so on are directly dependent on the antenna design and since the reflection behavior of an object depends on the different incident frequency and polarization, hence, SAR antenna design should satisfy multi-band operation to provide more information such as object penetration depth, while the dual-polarization capability will provide additional information and hence enhance the probability of mapping and identification [1]. Many Dual-Band Dual-Polarization (DBDP) antenna designs have been presented to meet some requirements in this field, such as shared-aperture including perforated structure [2], interlaced structures [3] and overlapped layout [4]. A considerable number of feed methods, such as probe-feed [5], aperture-coupled [6], proximity-coupled [7] and L-shape feed [8] are proposed. Also, enhanced port isolation or cross-polarization performance were handled in [9]. Recent work extends the use of DBDP antennas to obtain TBDP where L/S and L/X DBDP subarrays and L-band sub-array are applied [10].

In this paper a novel TBDP shared aperture SAR antenna based on one C/X DBDP and single Ku band DP antenna is proposed and simulated.

2. ANTENNA DESIGN AND CONFIGURATION

During the design, it was noted that using dual offset feed line beside a single feed line to couple the aperture helped to reduce the mutual coupling. A section of the microstrip line was placed at the end of each feed line to facilitate the impedance matching between the microstrip feed and the aperture. The DBDP antenna layers are organized as follows, a dual offset feed line with unequal arms lengths alongside [11] is underneath a foam layer with $\varepsilon_r = 1.06$ and thickness 0.245 mm, above this layer is the orthogonal line feed. The ground plane having an equal arms cross shaped slot in center is over a two thin Rogers RT/Duroid 6006 with $\varepsilon_r = 6.15$ and thickness 0.245 mm. The antenna above is a slotted square patch to provide two center resonance frequencies 7 GHz and 11.5 GHz placed over a foam substrate of thickness 3.2 mm in order to fulfill the lightweight constraint of SAR systems. Another layer of foam of thickness 1.016 mm is placed above the dual-band antenna.

An easy feed method to get dual polarized patch is to directly connect two orthogonal microstrip ports to the horizontal and vertical side of the microstrip patch. But a main drawback of this type is the DC contact between ports through the patch, also, the resonant frequency can be changed easily according to the depth of the inset which has the role of impedance matching. In order to avoid the above mentioned problems, we propose an electromagnetically coupled microstrip T-junction adjusted in a gap truncated from the patch alongside [12], hence, no lumped capacitors for

blocking DC contact will be needed. The single Ku band DP antenna is a rectangular patch over a finite conductor with a direct inset line feed placed in the orthogonal side. This antenna is designed over Rogers RT/Duroid 5880 $\varepsilon_r = 2.2$ and thickness 0.508 mm and having a center frequency of 16.24 GHz. Figure 1 shows the configuration of the TBDP antenna, DBDP antenna and detailed structure of the Ku patch.

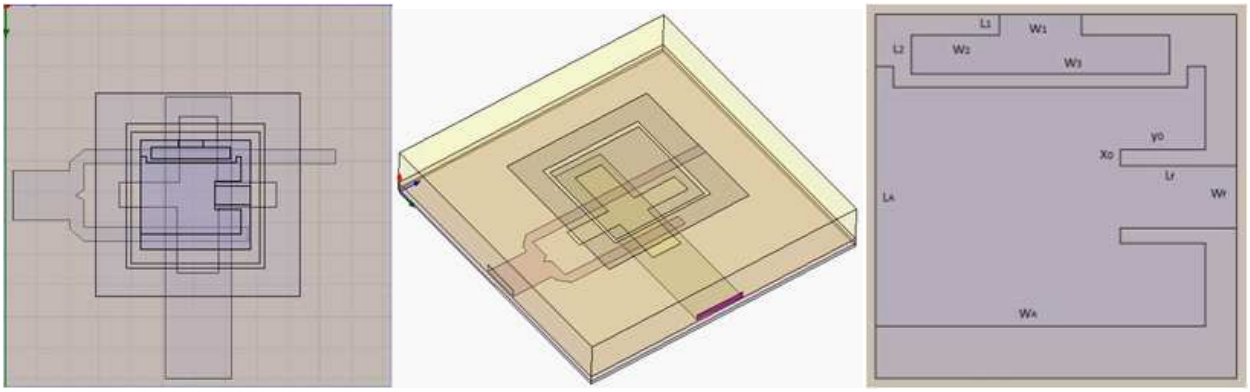

(a) (b) (c)

Figure 1: (a) Configuration of TBDP antenna top view, (b) DBDP antenna only, (c) detailed Ku patch showing the T-junction.

The geometrical dimensions of the proposed antenna is listed as follows, the C-band is a square patch of 13 mm edge length, the insider X-band is 8.4 mm by 8.5 mm rectangular patch, feed line of width equal to 4.2 mm and length 18.075 mm, the dual offset feed is two 100 Ω lines connected by a simple power divider to a 50 Ω line, the widths are 0.9 mm and 3.2 mm respectively and the Ku band DP patch antenna has $w_A = 6.4$ mm, $L_A = 5$ mm, T-junction $w_1 = 1.6$ mm, $L_1 = 0.4$ mm, $w_2 = 1.7$ mm, $L_2 = 0.75$ mm, $w_3 = 5$ mm, inset feed line $w_f = 1.2$ mm, $L_f = 2.25$ mm, $x_0 = 0.3$ mm and $y_0 = 1.65$ mm.

3. SIMULATIONS AND RESULTS

SAR missions may require single, dual or triple resonance operating frequency equipped with single or simultaneous linear polarization. The simulation of the proposed TBDP antenna is done to satisfy these requirements. The study includes each reflection coefficient and gain of a single feed in ON state (excited) while all other ports are OFF, then studying the reflection coefficient and isolation results when all ports are ON.

Figure 2 through Figure 5 show the return loss and E-plane co-polarized (solid) and cross-polarized (dashed) gain patterns at different ON states of the antenna, the C/X line feed and the Ku T-junction are named as the vertical polarization feeds, while C/X dual offset and Ku patch inset feed are the horizontal polarization feeds. The results are summarized in Table 1.

From the patterns above, it can be noted that the pattern radiated by the C/X dual-band antenna using line feed exhibits co-polarization gain level for C-band equal to 2.422 dB that is about 34 dB up in direction of maximum compared to the cross-polarization level, while the dual offset feed shows C-band co-polarization level 21.3 dB up compared to cross-polarization level. While the

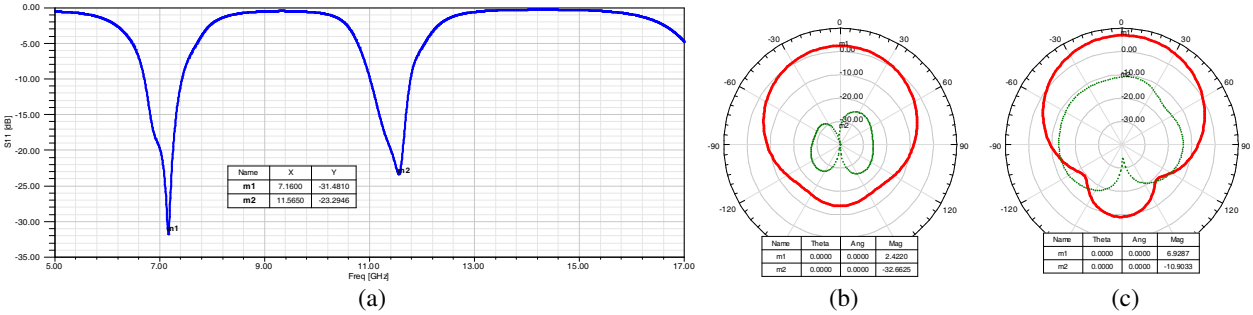

(a) (b) (c)

Figure 2: C/X Feed line. (a) Return loss [dB], (b) C-band Gain [dB], (c) X-band Gain [dB].

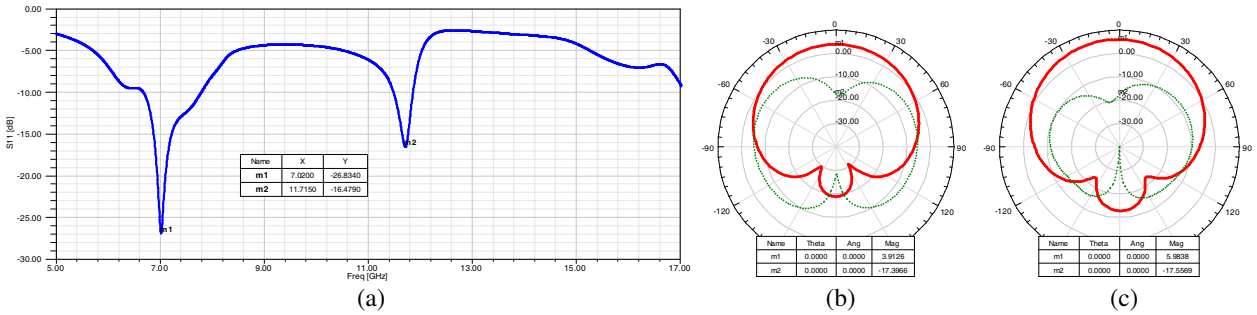

(a) (b) (c)

Figure 3: C/X dual offset feed. (a) Return loss [dB], (b) C-band Gain [dB], (c) X-band Gain [dB].

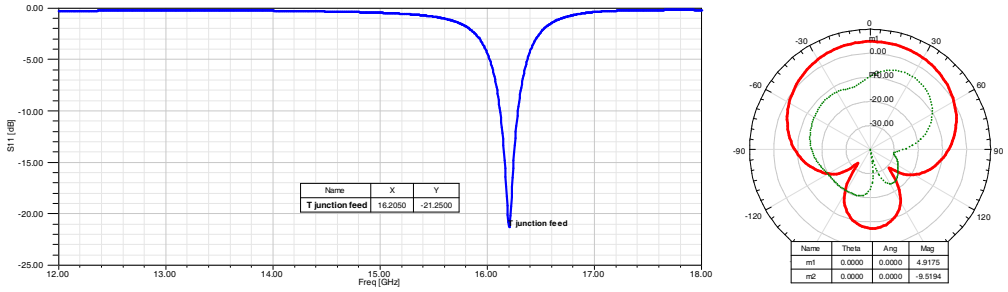

(a) (b)

Figure 4: Ku electromagnetically coupled T-junction feed. (a) Return loss [dB]. (b) Gain [dB].

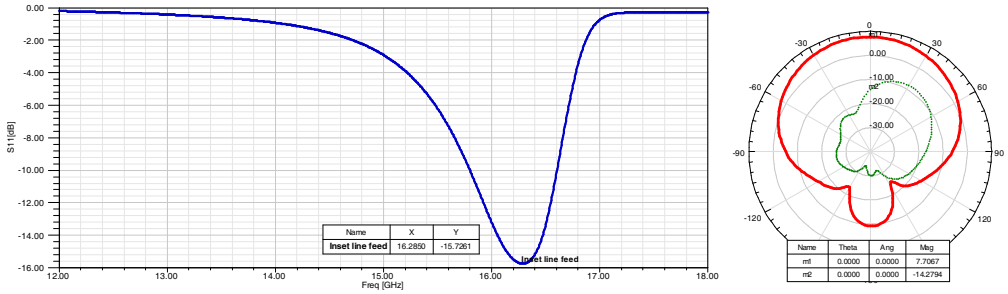

(a) (b)

Figure 5: Inset feed line. (a) Return loss [dB]. (b) Gain [dB].

Table 1: Return loss and gain of the proposed TBDP antenna one feed in ON state at a time.

	DBDP antenna				Ku band antenna	
Feeding port	Line Feed		Dual offset		T-junction	Inset Feed
Frequency [GHz]	7.16	11.565	7.02	11.715	16.205	16.285
Return loss [dB]	−31.481	−16.574	−26.834	−16.479	−21.25	−15.7261
Gain [dB]	2.422	6.9287	3.9126	5.9838	4.9175	7.7067

line feed exhibits a cross polarization −17.83 dB down the direction of maximum, whereas the dual offset feed cross-polarization drops to −23.54 dB compared to the co-polarized level. The antenna gains at Ku band are 4.9175 dB T-junction ON while other ports are OFF, and the co-polarized gain of the inset feed is 22 dB up the cross-polarized gain.

The case when all antenna ports are excited (ON state) is shown in Figure 6 below. The return loss shows the stability of resonance frequency of all ports regarding the state of other ports either ON or OFF. Hence, validate the structure and reveal that the isolation between different feeding ports for the same frequency band is less than −15 dB and less than −30 dB among different feeding ports for different frequency bands.

Another aspect to be considered is the bandwidth, for a SAR system to transmit or receive a HV/VH look, the proposed antenna provides 570 MHz intersecting BW in C-band between the horizontal and vertical polarizations, 380 MHz in X-band and 165 MHz in Ku band.

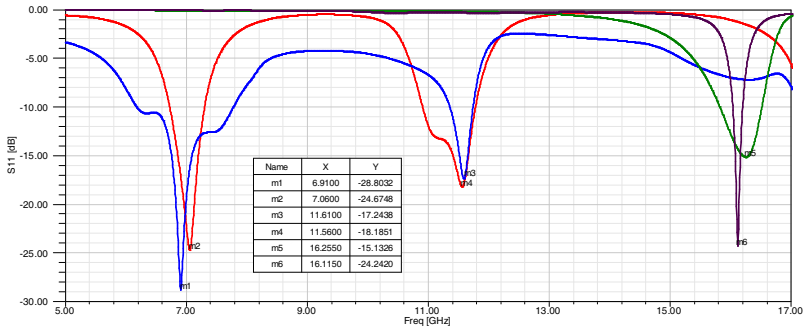

Figure 6: Return loss in [dB] for all TBDP antenna ports are excited.

4. CONCLUSION

A novel TBDP shared aperture microstrip antenna for the synthetic aperture radar (SAR) application is designed and simulated. The design based on sharing a single Ku band dual polarized patch on finite ground over a DBDP antenna. The dual polarizations are done by feeding the two antennas from two orthogonal directions by four different feeding lines. The proposed TBDP simulations included two steps, first step is studying the performance of each feed line for every antenna in ON state while all other ports are not excited. The second step is to introduce more than feeding port in ON state. The simulations results showed good return loss, gain, considerable high isolation and low cross polarization.

REFERENCES

1. Zhong, S.-S., *DBDP SAR Microstrip Array Technology*, edited by N. Nasimuddin, California, 2011.
2. Pozar, D. M. and S. D. Targonski, "A shared-aperture dual-band dual-polarized microstrip array," *IEEE Trans. Antennas Propagat.*, Vol. 49, No. 2, 150–157, Feb. 2001.
3. Pokuls, R., J. Uher, and D. M. Pozar, "Microstrip antennas for SAR applications," *IEEE Trans. Antennas Propagat.*, Vol. 46, No. 9, 1289–1296, 1998.
4. Li, P., K. M. Luk, and K. L. Lau, "A Dual-feed dual-band L-probe patch antenna," *IEEE Trans. Antennas Propagat.*, Vol. 53, No. 7, 2321–2323, Jul. 2005.
5. Waterhouse, R. B., "Design of probe-fed stacked patches," *IEEE Trans. Antennas Propagat.*, Vol. 47, No. 12, 1780–1784, Dec. 1999.
6. Gao, S. C., L. W. Li, M. S. Leong, and T. S. Yeo, "Dual-polarized slot-coupled planar antenna with wide bandwidth," *IEEE Trans. Antennas Propagat.*, Vol. 51, No. 3, 441–448, Mar. 2003.
7. Gao, S. and A. Sambell, "Dual-polarized broad-band microstrip antennas fed by proximity coupling," *IEEE Trans. Antennas Propagat.*, Vol. 53, No. 1, 526–530, Jan. 2005.
8. Wong H., K.-L. Lau, and K. M. Luk, "Design of dual-polarized L-probe patch antenna arrays with high isolation," *IEEE Trans. Antennas Propagat.*, Vol. 52, No. 1, 45–52, Jan. 2004.
9. Sun, Z., S. S. Zhong, X. R. Tang, and J. J. Liu, "C-band dual-polarized stacked patch antenna with low cross-polarization and high isolation," *Proceedings of EuCAP*, 2994–2997, Berlin, Germany, Mar. 2009.
10. Zhong, S. S., Z. Sun, L. B. Kong, C. Gao, W. Wang, and M. P. Jin, "Design of TBDP shared-aperture SAR array," *IEEE Microwave Conference Proceedings (APMC) Asia-Pacific*, 159–162, 2011.
11. Smith, C. B., "Wideband dual-linear polarized microstrip patch antenna," Doctoral Dissertation," Texas A&M University, 2008.
12. Choi, D. H. and S. O. Park, "Dual-band and dual-polarization patch antenna with high isolation characteristic," *IEEE Microwave Conference Proceedings (APMC) Asia-Pacific*, 2014–2016, 2006.

A Multiple-notch UWB Printed Slot Antenna with CNSS Enhanced

Baiqiang You, Tao Zhou, and Jianhua Zhou
Department of Electronic Engineering, Xiamen University, Xiamen, Fujian, China

Abstract— This paper is focused on the design of a printed slot antenna with multiple-notch function for ultra-wideband applications, accompanied with enhanced gain for Compass Navigation Satellite Systems. The proposed antenna consists of a curved radiation patch with an arc gradient microstrip line configuration and a class octagonal-shaped wide slot on a rectangular ground plane, supporting a much wider impedance bandwidth. With a class C-shaped slot on the patch and a class L-shaped strip attached on the ground, the multiple-notch function could be achieved to cover all of the 5.2/5.8 GHz WLAN, 3.5 GHz WiMAX and 4 GHz C-bands. By introducing a third-order stepping strip at the upper part of the wide slot on the ground, an additional operating frequency at 2.492 GHz of CNSS band can also be realized. The simulation results show that the designed antenna is with a small size and relative bandwidth larger than 122% in the band of $3.10 \sim 12.99$ GHz. The radiation patterns and current distributions are also analyzed respectively for the performance improvement.

1. INTRODUCTION

Since the Federal Communications Commission (FCC) released the frequency range from 3.1 GHz to 10.6 GHz for ultra-wideband (UWB) communication systems, the research work for UWB applications has received universal attention. With the development of ultra wideband technology, the UWB antennas, as one of crucial components for UWB communication and radar systems, have been studied for many years. Hence, a lot of printed microstrip slot, monopole, and CPW-fed UWB antennas with different geometries were investigated to obtain a broad impedance bandwidth [1–3].

Some wireless communication systems work in the frequency range of UWB systems, such as the wireless local area network (WLAN) operating at $5.15 \sim 5.35$ GHz and $5.725 \sim 5.825$ GHz, the worldwide inter operability for microwave access (WiMAX) operating at 3.5 GHz and C-band of satellite communication operating at $3.7 \sim 4.2$ GHz. Consequently, the multiple band-notch performances are required for UWB antennas to reject these existing wireless frequency bands.

More and more prototypes of compact UWB antennas with band-notch function have been carried out recently. Generally, the existing techniques for band notched use can be classified into the following two categories: embedded diverse slots, including U-shaped slot [4], arc-shaped slot [5], pi-shaped slot [6], V-shaped slot [7], T-shaped slot [8] and complementary SRR- shaped slot [9] etc.; loading various parasitic elements on the antennas, including strip near patch [10], strip near ground [11], Split ring resonators (SRRs) [12] and stepped impedance resonators (SIRs) near feed-line [13] etc.. However, only a few papers have been reported to study the integration of the UWB bands with other wireless system bands. In Ref. [14], by adding three narrow symmetrical L-shaped strips to the ground of a printed slot UWB antenna, extra Bluetooth, GSM and GPS bands were created, but no band-notch characteristics. In Ref. [15], three narrow a symmetrical U-shaped stubs were attached on the ground of a printed slot UWB antenna to support extra Bluetooth band and two notched band.

Here, a multiple-notch UWB printed slot antenna with CNSS enhanced is proposed. The multiple notched bands centered at 3.5 GHz WiMAX, 4 GHz C-bands and 5.2/5.8 GHz WLAN are produced with a class C-shaped slot embedded on the patch and a class L-shaped strip attached on the ground. The extra band with CNSS enhanced is centered at 2.492 GHz by applying a third-order stepping strip.

2. ANTENNA DESIGN

As shown in Fig. 1, an UWB printed slot antenna (named as Antenna I) consists of a curved radiation patch with an arc gradient microstrip line configuration and a class octagonal-shaped wide slot (with beveled bottom edges and stepped top edges) on a rectangular ground plane. The proposed antenna is designed to be printed on a FR4 substrate with an area size of $29 \times 23\,\text{mm}^2$ and thickness of 1 mm, relative permittivity of 4.4, and loss tangent of 0.02. The class C-shaped slot on the radiation patch and the class L-shaped stub on the ground act as a quarter-wave resonant structure at the required notch center frequency respectively, perturbing the resonant response. A third-order stepping strip is introduced at the upper part of the wide slot on the ground to create

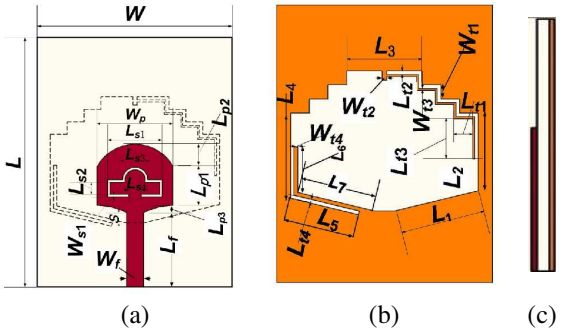

Figure 1: Configuration of the proposed antenna, Antenna I. (a) Top view. (b) Bottom view. (c) Side view.

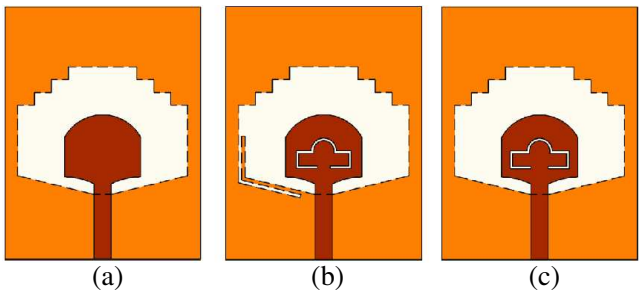

Figure 2: Configurations of the proposed UWB antennas. (a) Antenna II: base antenna. (b) Antenna III: with a class C-shaped slot. (c) Antenna IV: with a class C-shaped antenna and a class L-shaped stub.

an extra frequency. The optimal dimensions of the designed antenna are as follows: $W = 23.1\,\text{mm}$, $L = 29.7\,\text{mm}$, $W_f = 2\,\text{mm}$, $L_f = 8.9\,\text{mm}$, $S = 1.2\,\text{mm}$, $W_p = 9\,\text{mm}$, $L_{p1} = 4.7\,\text{mm}$, $L_{p2} = 2.7\,\text{mm}$, $L_{p3} = 0.8\,\text{mm}$, $W_{s1} = 0.3\,\text{mm}$, $L_{s1} = 6.5\,\text{mm}$, $L_{s2} = 2\,\text{mm}$, $L_{s3} = 2.4\,\text{mm}$, $L_{s4} = 1.5\,\text{mm}$, $L_1 = 9.3\,\text{mm}$, $L_2 = 8.2\,\text{mm}$, $L_3 = 8.1\,\text{mm}$, $L_4 = 9\,\text{mm}$, $L_5 = 7.5\,\text{mm}$, $L_6 = 4.8\,\text{mm}$, $L_7 = 8.5\,\text{mm}$, $W_{t1} = 1.5\,\text{mm}$, $L_{t1} = 2\,\text{mm}$, $W_{t2} = 0.5\,\text{mm}$, $L_{t2} = 0.4\,\text{mm}$, $W_{t3} = 0.2\,\text{mm}$, $L_{t3} = 4.4\,\text{mm}$, $W_{t4} = 0.4\,\text{mm}$, $L_{t4} = 0.5\,\text{mm}$.

A base UWB antenna, named as Antenna II, is depicted in Fig. 2(a), consisting of a curved radiation patch with a microstrip transmission line and a class octagonal-shaped wide slot on a rectangular ground plane. For a better impendence matching over the whole of UWB band, the patch is fed through an arc gradient 50-Ω microstrip line. To create multiband-notch function within the UWB, a class L-shaped stub of quarter-wavelength and a class C-shaped slot of half-wavelength can be considered to be introduced on the proposed antenna. For the frequency rejection of 5.2/5.8 GHz WLAN bands, a class C-shaped slot with a length L slot of 21.58 mm and a width of 0.3 mm is applied on the patch, referred to Antenna III as shown in Fig. 2(b). Similarly, for the frequency rejection of 3.5 GHz WiMAX and 4 GHz C-bands, a class L-shaped stub with a length L stub of 12.3 mm and a width of 0.4 mm is applied on the bottom of the slot ground, referred to Antenna IV as shown in Fig. 2(c). An additional resonance can be produced for the proposed UWB antenna by attaching a resonant strip of appropriate length to the ground. Exactly to have the 2.492 GHz CNSS band, a narrow third-order stepping strip of18.45 mm length and 0.2 mm width is attached to the top of the slot ground for Antenna I.

Each of the rejected or extra resonances takes place when the length of the strip, stub or the slot is equal to $\lambda_g/4$ or $\lambda_g/2$, in which λ_g is the guided wavelength at the desired frequency. Thus, the length L_G of each strip or stub located on the slot ground and the length L_P of each slot introduced on the patch can be obtained approximately from the following formula

$$L_G = \frac{c}{4f\sqrt{(\varepsilon_r+1)/2}}, L_P = \frac{c}{2f\sqrt{(\varepsilon_r+1)/2}} \tag{1}$$

where ε_r, c, and f are the relative dielectric constant of the substrate, the light velocity in free space, and the desired center frequency, respectively.

3. RESULTS AND DISCUSSION

The simulate reflection coefficients of Antennas I, II, III and IV are given in Fig. 3. It can be seen that Antenna I covers the whole UWB band (3.1 ∼ 10.6 GHz), with multiple notch-bands and an extra band. By comparing all the antennas, it is obvious that the base antenna without slots, strips and stubs provides an impedance bandwidth covering 3.1 ∼ 10.6 GHz. While the class C-shaped slot on the patch creates a notch band in 5.2 ∼ 5.8 GHz, and the class L-shaped stub on the ground creates a notch band in 3.5 ∼ 4 GHz. In addition, an extra band at 2.492 GHz is introduced to the initial UWB through the attachment of the third-order stepping strip to the ground. The simulated results confirm that the introduced slots and stubs or strips operate independently and have little effect on each other.

The simulated current distributions for the proposed antenna at the notched frequencies of

3.5 GHz, 4 GHz, 5.2 GHz and 5.8 GHz as well as the extra resonance frequency of 2.492 GHz are presented in Figs. 4(a)–(e), respectively. It can be observed that the current distributions at 3.5 GHz and 4 GHz concentrate mainly on the edges of the class L-shaped stub, and also the current distributions at 5.2 GHz and 5.8 GHz concentrate on the edges of the class C-shaped slot. In addition, the current distribution at 2.492 GHz is primarily decided by the third-order stepping strip structure. It can also be seen that, at some desired frequency, only the corresponding structure is active while the others are inactive, confirming the independence of the frequency bands. The directions of the current vectors in the stepping strip for extra band are the same as that in the radiation patch, while the directions of the current vectors in the class C-shaped slot and the class L-shaped stub are opposite to that in the radiation patch, resulting in shorting out the radiation patch at the relevant notch frequency.

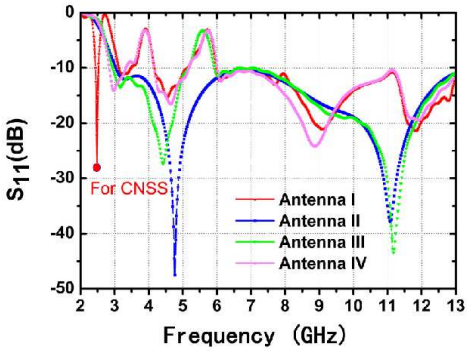

Figure 3: Simulated reflection coefficients of Antenna I, Antenna II, Antenna III and Antenna IV.

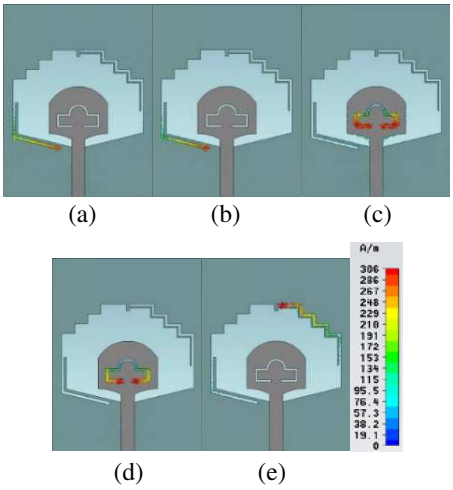

Figure 4: Simulated current distributions of Antenna I at frequencies of (a) 3.5 G, (b) 4 G, (c) 5.2 G, (d) 5.8 G, and (e) 2.492 G.

Figs. 5(a)–(c) show the simulated reflection coefficients vs different structure lengths for the proposed antenna with L-shaped stub in the notched band of 3.5 GHz ∼ 4 GHz), class C-shaped slot in the notched bands of 5.2 GHz ∼ 5.8 GHz) and third-order stepping strip in the extra band of 2.492 GHz respectively. It can be seen that an increase in some structure length results in a drop in the extra resonance frequency of CNSS, and vice versa. This confirms the validity of Eq. (1) and proves that the introduction of such slots, stubs and strips to the initial UWB slot antenna can lead to tunable notched bands and extra resonance bands.

According to the simulated E-plane and H-plane radiation patterns of the proposed antenna at three pass band frequencies of 2.492 GHz, 4.5 GHz and 9 GHz as presented in Fig. 6, the radiation features are all nearly omnidirectional for these three frequencies. For a prototype of the proposed antenna as shown in Fig. 7(a), the measured reflection coefficient is presented in Fig. 7(b) along

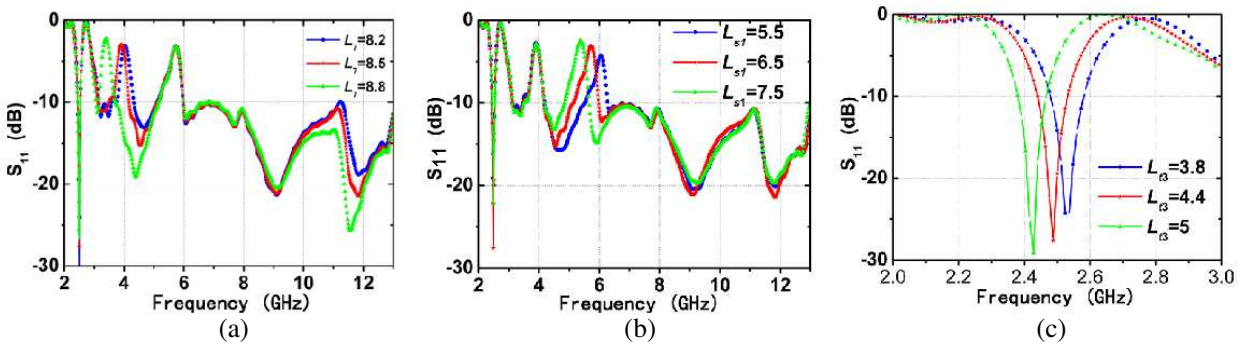

Figure 5: Simulated reflection coefficients vs different lengths for Antenna I with (a) class L-shaped stub, (b) class of C-shaped slot, and (c) third-order stepping strip. All dimensions are millimeters.

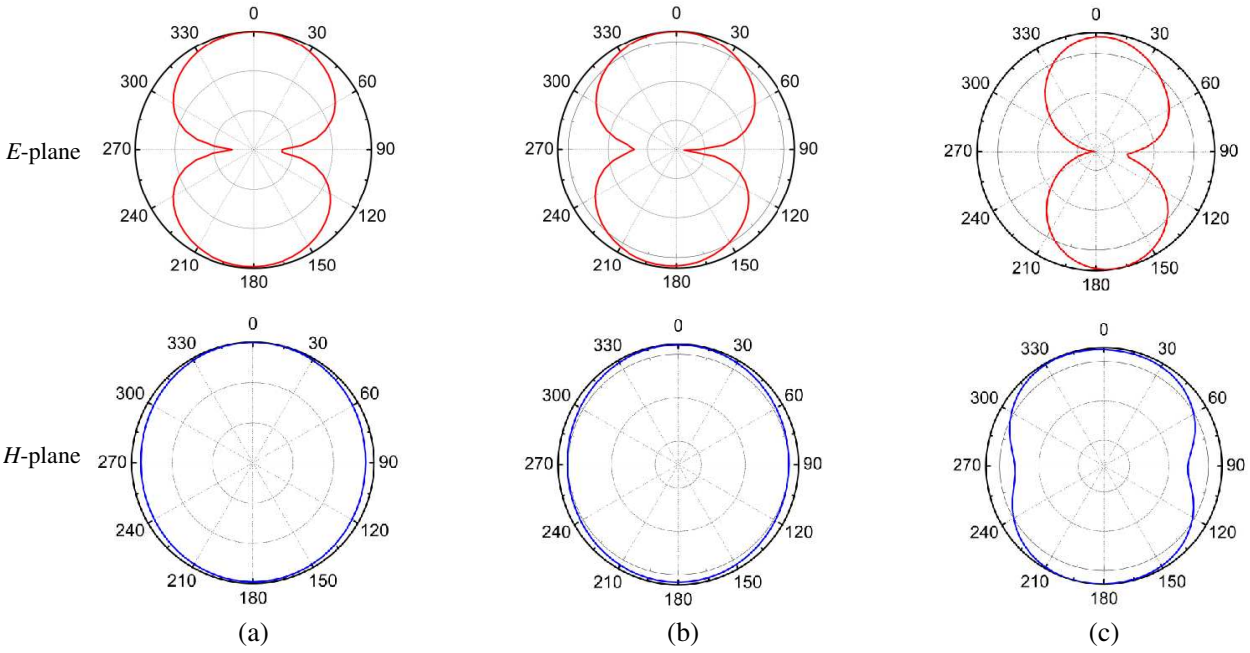

Figure 6: Simulated E-plane and H-plane radiation patterns of the proposed antenna at 2.492 G, (b) 4.5 G, and (c) 9 G.

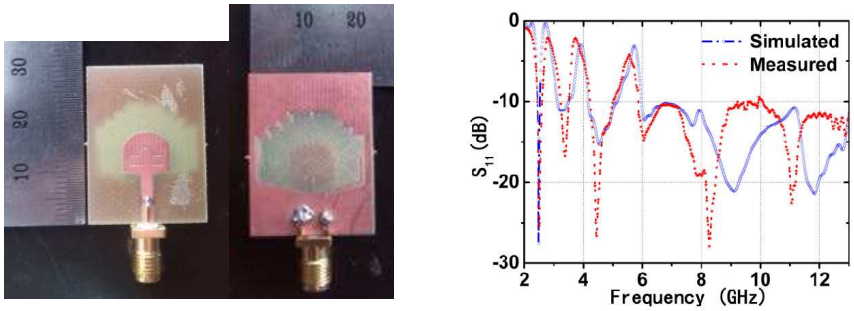

Figure 7: Prototype of the proposed antenna and the contrast of simulation and measurement.

with the simulated one. Most of the measurement agrees well with the simulation, specifically for lower frequency band.

4. CONCLUSION

In this letter, a printed slot antenna with multiple-notch function for UWB applications and also enhanced gain for CNSS is proposed. The multiple-notch performance is implemented by introducing a class C-shaped slot and a class L-shaped stub to the proposed antenna, and also an additional resonant frequency of CNSS is excited by attaching a third-order stepping strip. The designed antenna with optimized dimensions can operate in the frequency range from 3.10 GHz to 12.99 GHz, with multiple rejection bands around 3.15 $\sim$ 4.16 GHz and 5.15 $\sim$ 5.98 GHz. The simulation and measurement show that the proposed antenna could be a good candidate for UWB applications.

ACKNOWLEDGMENT

This work is supported by Fujian Provincial Key Sci-Tech Project (2013HZ0002-1) of China. We thank the staff members of Microwave Library for helpful supports.

REFERENCES

1. Ahmed, O. and A. R. Sebak, "A printed monopole antenna with two steps and a circular slot for UWB applications," *IEEE Antennas Wireless Propag. Lett.*, Vol. 7, 411–413, 2008.

2. Cheng, S., P. Hallbjorner, and A. Rydberg, "Printed slot planar inverted cone antenna for ultrawideband applications," *IEEE Antennas Wireless Propag. Lett.*, Vol. 7, 18–21, 2008.
3. Denidni, T. A. and M. A. Habib, "Broadband printed CPW-fed circular slot antenna," *Electron. Lett.*, Vol. 42, No. 3, 135–136, 2006.
4. Lee, W. S., D. Z. Kim, K. J. Kim, and J. W. Yu, "Wideband planar monopole antennas with dual band-notched characteristics," *IEEE Trans. Microw. Theory Tech.*, Vol. 54, No. 6, 2800–2806, 2006.
5. Hong, S. J., J. W. Shin, H. Park, and J. H. Choi, "Analysis of the band-stop techniques for ultrawideband antenna," *Microw. Opt. Technol. Lett.*, Vol. 49, No. 5, 1058–1062, 2007.
6. Zhao, Y. L., Y. C. Jiao, G. Zhao, L. Zhang, Y. Song, and Z. B. Wong, "Compact planar monopole UWB antenna with band-notched characteristic," *Microw. Opt. Technol. Lett.*, Vol. 50, No. 10, 2656–2658, 2008.
7. Rostamzade, M., S. Mohamadi, C. Ghobadi, J. Nourinia, and M. Ojaroudi, "Square monopole antenna for UWB applications with novel rod-shaped parasitic structures and novel V-shaped slots in the ground plane," *IEEE Antennas Wireless Propag. Lett.*, Vol. 11, 446–449, 2012.
8. Ojaroudi, N. and M. Ojaroudi, "Novel design of dual band-notched monopole antenna with bandwidth enhancement for UWB applications," *IEEE Antennas Wireless Propag. Lett.*, Vol. 12, 698–701, 2013.
9. Kim, J., C. S. Cho, and J. W. Lee, "5.2 GHz notched ultra-wideband antenna using slot-type SRR," *Electron. Lett.*, Vol. 42, No. 6, Mar. 2006.
10. Mishra, S. K., R. K. Gupta, A. Vaidya, and J. Mukherjee, "A compact dual-band fork-shaped monopole antenna for Bluetooth and UWB applications," *IEEE Antennas Wireless Propag. Lett.*, Vol. 10, 627–630, 2011.
11. Samadi Taheri, M. M., H. R. Hassani, and M. A. Nezhad, "UWB printed slot antenna with Bluetooth and dual notch bands," *IEEE Antennas Wireless Propag. Lett.*, Vol. 10, 255–258, 2011.
12. Zhang, Y., W. Hong, C. Yu, Z. Kuai, Y. Don, and J. Zhou, "Planar ultra wideband antennas with multiple notched bands based on etched slots on the patch and/or split ring resonators on the feed line," *IEEE Trans. Antennas Propag.*, Vol. 56, No. 9, 3063–3068, Sep. 2008.
13. Zhang, Y., W. Hong, C. Yu, J. Zhou, and Z. Kuai, "Design and implementation of planar ultra-wideband antennas with multiple notched bands based on stepped impedance resonators," *IET Microw. Antennas Propag.*, Vol. 3, No. 7, 1051–1059, 2009.
14. Bod, M., H. R. Hassani, and M. M. Samadi Taheri, "Compact UWB printed slot antenna with extra bluetooth, GSM, and GPS bands," *IEEE Antennas Wireless Propag. Lett.*, Vol. 11, 531–534, 2012.
15. Taheri, S., M. Mehdi, H. R. Hassani, et al., "UWB printed slot antenna with Bluetooth and dual notch bands," *IEEE Antennas Wireless Propag. Lett.*, Vol. 10, 255–258, 2011.

Active Phased Array Radars as an Effective ECCM systems

Faran Awais Butt, Ahmed Malik, and Madiha Jalil
School of Engineering, University of Management and Technology (UMT), Lahore, Pakistan

Abstract— Phased Array Radars have started to regain some serious attention over the past few decades owing to its high accuracy, efficiency and less susceptible characteristics. The most basic requirement that one could wish for in a good modern radar is its beam agility, low distribution loss, maximum bandwidth, lower cost, maximum efficiency and effective resource management. Modern phased array radars can be best utilized to achieve characteristics of an effective radar system with minimum tradeoffs. The most basic thing that it can achieve is, that the antennas can be arranged to get the desired radiation pattern. The characteristics and detection abilities of active phased array radar systems are discussed. Moreover, the paper suggests that active phased array radar can be best suited as an electronic counter-counter measure system.

1. INTRODUCTION

Most recently aircrafts have been developing in higher detection capabilities are getting better in efficiency. Moreover, aircrafts and missiles are getting better in mobility and RCS reduction, therefore higher search and tracking is required for a better air defense system and there is a need for advances in the existing radar technologies [9]. Active phased array radars can be a very good solution for radar designers to overcome various issues faced during the designing. In active phased array antennas, transmission and reception is performed using transmit/receive modules which are known as T/R modules.

Phased array radars can be broadly categorized into passive phased array and active phased array radar system. In a passive phased array radar, the microwave feed network in the backside of the antenna is powered by a single radio frequency source, which send its source into phased shift modules which are fed to the emitting elements whereas in the active phased array there is a radiating source for each element. The significance of active phased array radar is the use of T/R module for each radiating element [1].

In this paper, we have presented an analysis of modern active phased array radar systems which are not only efficient but are also best suited to cope up the threats of electronic countermeasure system and hence fulfill the requirements of modern air defense system. Section 2 explains few notable characteristics of active phased array systems and Section 3 presents simulations highlighting the detection abilities of the phased array system.

2. CHARACTERISTICS OF AN ACTIVE PHASED ARRAY RADAR

2.1. Graceful Degradation

Most of the radars stop functioning in case there is an issue with the radiating element or the antenna. Phased array radars have multiple antennas and radiating element, so they overcome this issue. Active phased array radars provide graceful degradation so that many transmit receive modules may fail and radar would still not stop functioning.

2.2. Data Rate

High data rate is required for detection of fast moving aircrafts. Phased array radars are most suitable for such aircrafts as they can be expected to optimize energy beam adaptively to individual surveillance region in response to a threat environment. The overall system of the radar can be maneuvered with ease. Specifically, it can be expected to adaptively optimize energy, beam and time assignment to individual surveillance region in response to any external threat [9]. The beam agility of phased arrays causes fast time sharing between search, acquisition and tracking stage for radars in a diversified environment [10].

2.3. Maintenance and Flexibility

Owing to the advancement in the existing circuit technology, very small size and light weight modules can be mounted on the phased array system [2]. These modules are known as transmit receive modules. These T/R modules can provide tractability to the overall system. The modules can provide flexibility in the overall working of the system according to the nature of the target threat. If any module stops functioning owing to any reason, it can be disconnected and replaced

quickly without affecting much the performance of the entire system. Antenna performance is improved by the use of T/R modules and such a system also provides a great amount of improvement in the choice of array architecture [11].

2.4. Power Management

Active array system also provides a great amount of improvement in the areas of power management and efficiency [3]. Power is radiated directly into space with minimum power loss and also power consumption cost is reduced. The usage is controlled by the managing radar waveforms and the corresponding beams energy. By doing this, the probability of target detection is also maximized. In addition to the reduction in transmission and reception losses, active arrays can provide wide instantaneous bandwidth and higher average radiated power [11].

2.5. Anti Jamming Capabilities and Polarization

Modern phased array radars are under a complicated electromagnetic surrounding, so they should have high resolution anti jamming potentialities. Jammers can be very effective if they can use the same polarization as that of the radar using DRFM (digital radio frequency memory). This can be overcome if the antenna elements have two orthogonal polarization channels and can receive dual polarization echo signals [6].

3. DETECTION ABILTIY OF MODERN PHASED ARRAY RADAR SYSTEM

Phased array radars have discovered many capabilities that were not present only a few years ago [7]. With the enhancement of microwave and signal processing technology, phased array radars have been designed and used in many areas of research [4, 5]. Since phased array antennas have higher cost, there use is cost effective only if they would handle multifunctional capabilities like search and multi target tracking. There saturation is also better than other radars against multiple targets [8]. Now we are going to present few simulations highlighting the detection abilities of active phased array system.

Figure 1 shows the normalized pattern of a 2d array with 10 elements on x axis and 100 elements on y axis, where as Figure 2 shows the normalized pattern with 100 elements on x axis and 100 elements on y axis. Clearly we can see that the side lobes amplitudes have decreased considerably. So by this, jamming can also be countered and more power can be concentrated in particular direction of interest. Figures 3 and 4 show the normalized pattern for different spacing between elements. Number of elements are 10 on both x and y axis. The spacing between elements in the Figure 3 is 1 and spacing between elements in Figure 4 is 0.5. Simulations in Figure 3 and Figure 4 show that spacing between the elements also affects the pattern and hence it needs to be taken into account while designing an effective ECCM system.

Now we will investigate the effect of squinting on the total electric field of the phased array system. Equation (1) shows the function of electric field that will be used in remaining simulations.

$$E_T(\theta, \Phi) = \sum_{n=1}^{N} A_n F_n(\theta_n, \phi_n) e^{-j(k|r_n|+\beta_n)} \tag{1}$$

where E_T is the total electric field in linear volts for N elements and F is the element pattern function for the nth element in linear form, 'A' refers to the amplitude of element in volts, 'R' is

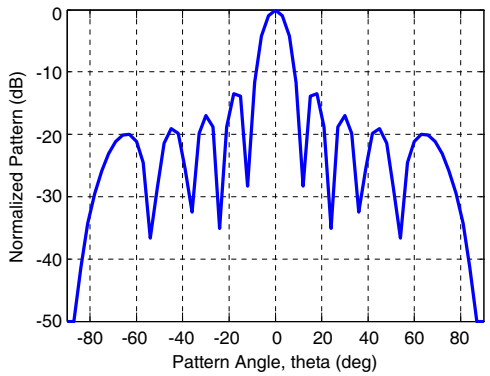

Figure 1: Normalized pattern vs. pattern angle for 10 elements on x axis.

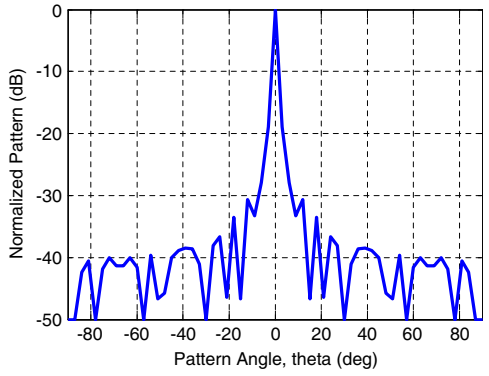

Figure 2: Normalized pattern vs. pattern angle for 100 elements on x axis.

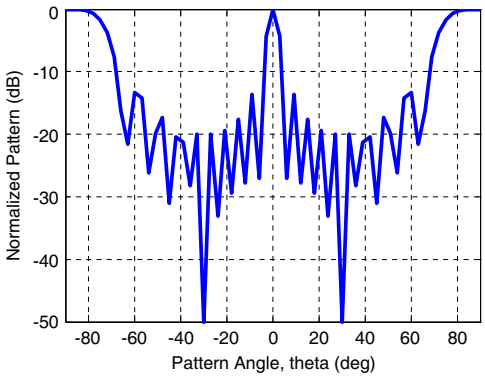

Figure 3: Normalized pattern vs. pattern angle for spacing of 1 between elements.

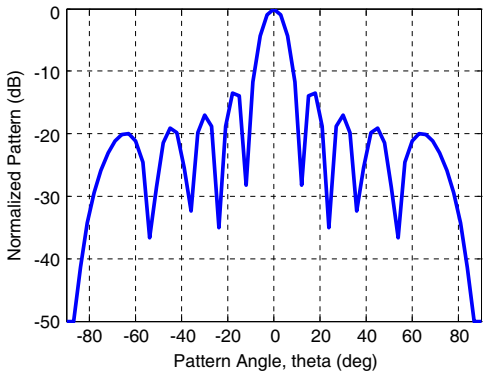

Figure 4: Normalized pattern vs. pattern angle for spacing of 0.5 between elements.

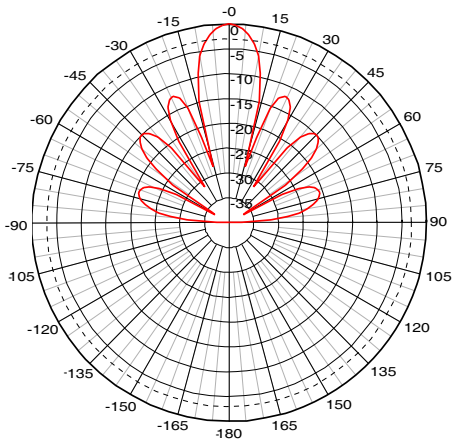

Figure 5: Electric field pattern for 5 elements.

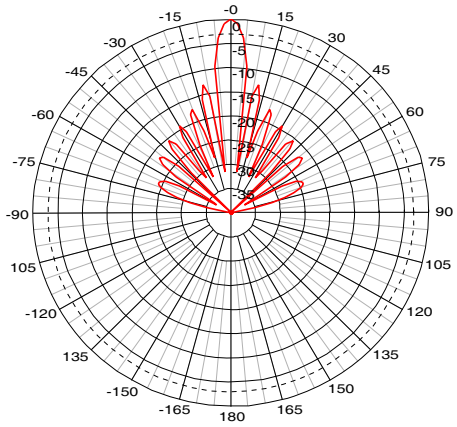

Figure 6: Electric field pattern for 10 elements.

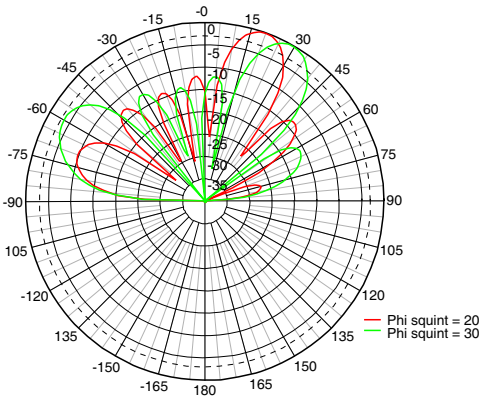

Figure 7: Electric field pattern for azimuth squint of 20° and 30°.

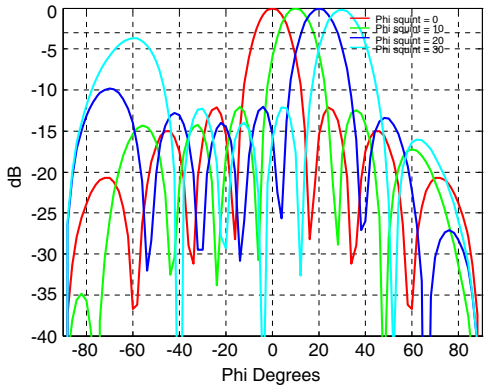

Figure 8: Pattern cuts for azimuth squint of 0°, 10°, 20° and 30°.

the distance from the element and 'B' is the phase of element in radians [12]. Figure 5 shows the pattern for 5 elements each on x and y axis and Figure 6 shows the corresponding pattern for 10 elements. These simulations are performed for operating frequency of 5 GHz. The results show that increasing number of elements is narrowing the lobe for each element. These properties also become useful while considering sidelobe blanking for overcoming the sidelobe jamming and hence proving an effective ECCM system.

Figure 7 is highlighting the pattern for phi squints of 20 and 30 degrees and Figure 8 is showing the power corresponding to various values of squint angles. The corresponding phi squints give the maximum peak at these values. Taking into consideration different T/R modules, we can also have an effect of a MIMO system and overall system can be able to transmit while having frequency diversity, different polarization and sidelobe blanking. The results shows that offsetting

the transmission angle of different radiating elements of active phased array radar can give us a desired radiation pattern and hence can be very useful as it can overcome the effects of various forms of jamming.

The figures show that at specified phi squints, corresponding power is 0 dB. Such a system can be very effective against barrage,sweep and spot jamming. An active phased array tracking system is quite immune to ECM effects because they can quickly scan an area randomly and are not bound to scan its radar beam in a particular method as it is done in conventional radars. The irregular position of the beam would make it difficult for the opposing ECM system when and where to send false signals. If we have active phased array antennas depending upon the target threat, the TR modules at undesired directions can be silenced to get all power concentrated at focused direction, where the target threat is expected.

4. CONCLUSION

Modern active phased arrays radars can be exploited to have all properties that one could wish for in good military based radar. They provide an overall improvement in radar functionality and performance. They also provide improved anti-jamming ability, fast beam scanning and ability to track multiple targets at a time. The benefit we can extract from the active nature of the arrays is the modifications of TR modules which are independent of other TR modules. Hence active phased array radar can be casted by the user according to the demands of the situation. In future, modern phased array systems with MIMO functionality can make an ideal ECCM system. The benefit of active phased array would be the vigilance to approaching threats all across azimuth and elevation angles.

REFERENCES

1. Agarwal, A. K. and E. L. Holzman, "Beamformer architectures for active phased-array radar antennas," *IEEE Transactions on Antennas and Propagation*, Vol. 47, 1999.
2. Kiuchi, E. and I. Ueda, "Tactical cylindrical active phased array radar," *IEEE International Symposium on Phased Array Systems and Technology*, 1996.
3. Tahim, R. S., J. Fishee, and K. Chang, "Multi band antenna technology," *IEEE International Symposium on Antennas and Propagation Society*, Vol. 4, 2004.
4. Xing, S., "Millimeter-wave phased-array radar and its application," *Progress Telecommunication Engineering*, Vol. 48, No. 1, 6–12, 2008.
5. Wang, D.-C., "System analysis of wideband phased array radar," *Modern Radar*, Vol. 30, No. 3, 1–6, 2008.
6. Song, L.-Z. and X.-L. Qiao, "A kind of signal processing method for the polarization phased array radar," *5th International Conference on Wireless Communications, Networking and Mobile Computing, 2009, WiCom 2009*, 2009.
7. Brookner, E., "Phased-array and radar breakthroughs," *IEEE Radar Conference*, 2007.
8. Farina, A. and P. Neri, "Multitarget interleaved tracking for phased-array radar," *IEEE Proceedings — Communications, Radar and Signal Processing*, Vol. 127.
9. Kiuchi, E. and I. Ueda, "Tactical cylindrical active phased array radar," *IEEE International Symposium on Phased Array Systems and Technology*, 1996.
10. Colin, J.-M., "Phased array radars in France: Present and future," *IEEE International Symposium on Phased Array Systems and Technology*, 1996.
11. Agrawal, A. K. and E. L. Holzman, "Beamformer architectures for active phased-array radar antennas," *IEEE Transactions on Antennas and Propagation*, Vol. 47, No. 3, 432–442, 1999.
12. Tucker, N., "Phased array design toolbox V2. 3 for matlab," Technical Report, 2009.

Design and Implementation of a New Missile-borne Conical Conformal Antenna

Ming Li, **Liang Xu**, **Wen Bin Zeng**, **and Guo Liu**
The Institute of Radio Wave Propagation, Xidian University, Xi'an, Shaanxi 710071, China

Abstract— In this paper, a conical missile-borne conformal antenna is proposed to meet a specific application. To achieve good omnidirectional circularly polarized (CP) radiation, the proposed antenna array is consisted of four identical CP microstrip antennas, which are distributed around the projectile. Shifter network and optimized patch is used to get CP performance for each antenna. The measured results are in good agreement with the simulation one. The experimental results show that the axial ratio (AR) of element antenna is less than 3 dB and omni-axis ratio is less than 6 dB. The pattern of antenna in the horizontal direction is circular, with un-roundness less than 2 dB and the vertical pattern is "8".

1. INTRODUCTION

Since microstrip antenna with small size, light weight, and low cross-section, in recent years has been widely applied to missiles, aircraft, rockets, satellites and other spacecraft. In engineering applications, microstrip antenna is often conformal with the rotating projectile [1]. Traditional missile conformal microstrip antenna is usually used the patch as a unit to achieve the circular array, but the number of units increases the array size and has a great effect on the aircraft. This is only based on the cylindrical conformal, not suitable for conical one [2, 3]. In telemetry system, in order to avoid the emergency of the phenomenon cannot receive the signal caused by the influence of the flight trajectory and attitude to antenna, we often want to antennas in the horizontal direction is omnidirectional, as compared with its vertical "8" font when mounted on the aircraft [4]. Literature [5] designs a cross dipole antenna, the antenna in the horizontal plane has realized the omnidirectional circular polarized radiation. The literature [6] presents a missile-borne conformal multi-polarization antenna to achieve the request of low elevation gain to missile-borne antenna.

This paper put forward a kind of beidou navigation missile-borne conformal microstrip antenna, for a right-handed circularly polarization, the center frequency of 1.268 GHz. Existing conformal microstrip array antenna are mostly cylindrical conformal microstrip arrays, polarization is vertical polarization. Compared with linear polarization antenna, circular polarization antenna can better accept to wave, reducing polarization loss.

2. ANTENNA DESIGN

The antenna consists of four identical microstrip antenna spacing in projectile around, fed by a four power splitters. Shifter network and optimized patch is used to get CP performance for each antenna.

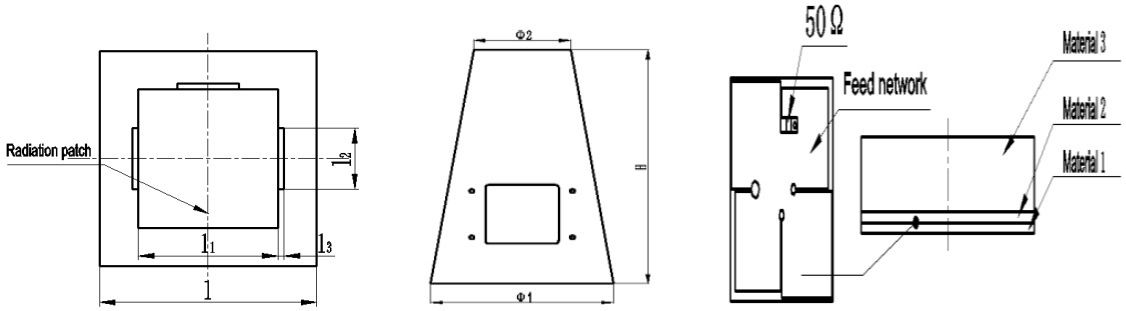

Figure 1: The schematic structure of the antenna.

Specific structure of antenna is shown in Figure 1, open four slots on conical shell, loading a same curvature metal copper on the inner wall, antenna is fixed on the metal copper. As the thickness

of the ceramic sheet is large and not easily bent, unlike the conventional conformal antenna is attached directly to the outer wall above the projectile. Bottom diameter of projectile is ϕ_1, the bottom one is ϕ_2, vertebral height is h_1. The antenna section in sequence from the bottom to top as the ground plate, the medium 1, the feed network, the medium 2, the ground plate, medium 3, and the radiating patch. Relative dielectric constant substrate from bottom to top, in turn, is 4.5, 5, 20, height of h_2, h_3, h_4, width of l. Microstrip patch is composed of a square patch and the rectangular patch, the square patch width is l_1, the rectangular patch length is l_2, width is l_3. The specific dimensions are given in Table 1.

Figure 2 shows the influence of the antenna axial ratio when loaded metal projectile. As can be seen from the diagram, when the antenna with metal body conformal, antenna axis ratio change obviously. This is due to the metal projectile are connected to the ground plate, introduces a kind of asymmetry, and worsen the axis ratio. Through simulation optimization, we add a rectangular patch on the surrounding square patch to improve the axial ratio of the antenna. Figure 3 is the optimized axis ratio of antenna. The results show that the optimized axis ratio is less than 3 dB and meet the design requirements.

From the Figure 4 we can see that, 3 dB beam width of a single antenna is 100°, to achieve the omni-directional circularly polarized antenna needs at least 4 element microstrip antenna array.

Table 1: The size parameters.

Parameters	ϕ_1	ϕ_2	h_1	h_2	h_3
Value (mm)	107.7	65.8	110	1	1
Parameters	h_4	l	l_1	l_2	l_3
Value (mm)	7	35	11.6	5.4	2

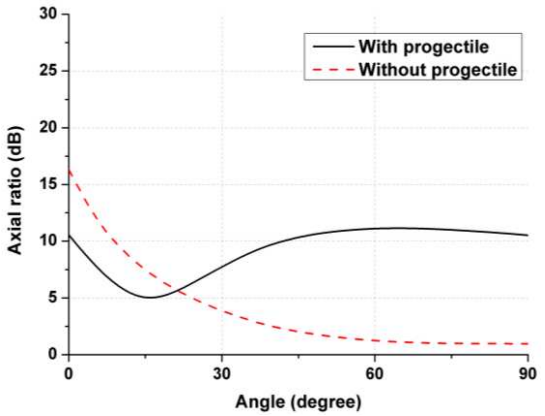

Figure 2: Projectile impact on antenna.

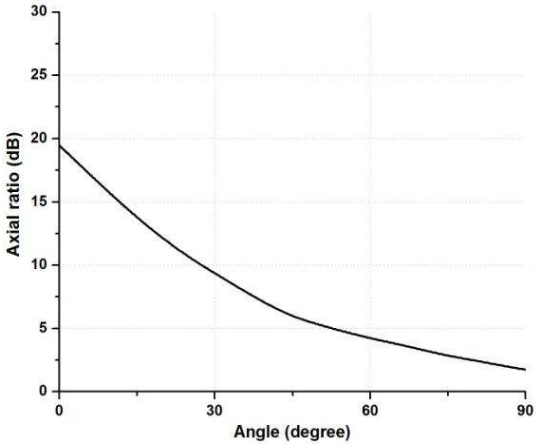

Figure 3: The optimized axial ratio.

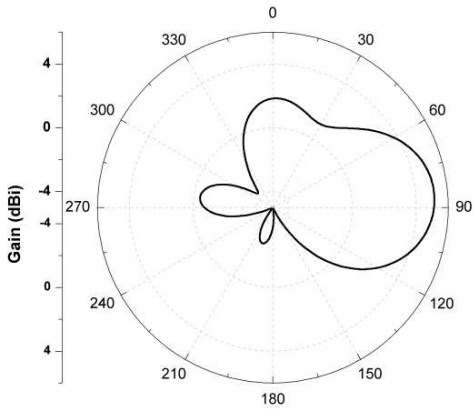

Figure 4: Single antenna horizontal pattern.

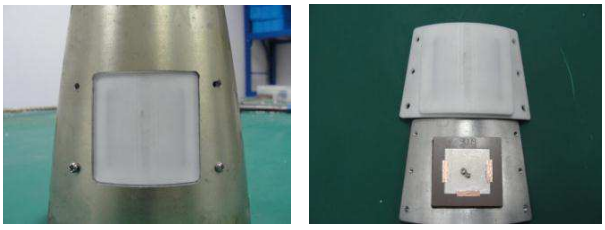

Figure 5: Physical picture of antenna.

3. RESULTS AND DISCUSSIONS

Through the above theoretical analysis, produced a physical antenna, shown in Figure 5.

Measured the antenna VSWR by vector network analyzer, The simulation and experimental results is shown in Figure 6. The isolation resistor in the feed network has broadened the Measured the antenna VSWR by vector network analyzer, The simulation and experimental results is shown in Figure 6. The isolation resistor in the feed network has broadened the bandwidth of the antenna impedance. Measured results from the chart shows that the impedance bandwidth of the antenna for the 1.18 GHz $\sim$ 1.36 GHz, the relative bandwidth is 28.3%. Figure 7 shows antenna axial ratio in the horizontal plane with the direction change curve. We can learn from the diagram, antenna in the main direction of each axis ratio is smaller than 3 dB, Omni axial ratio is less than 6 dB, and the 3 dB axial ratio bandwidth is 1.257 $\sim$ 1.276 GHz, circular polarization performance is very good.

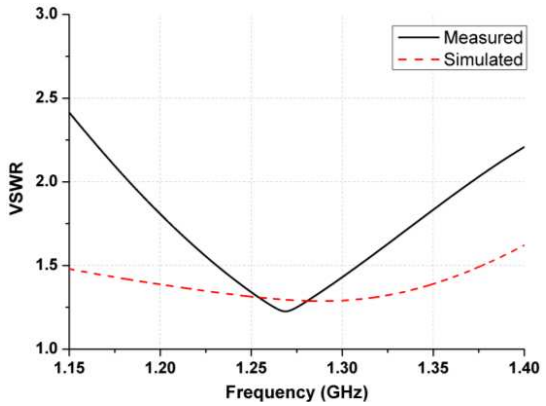

Figure 6: Measured chart of VSWR.

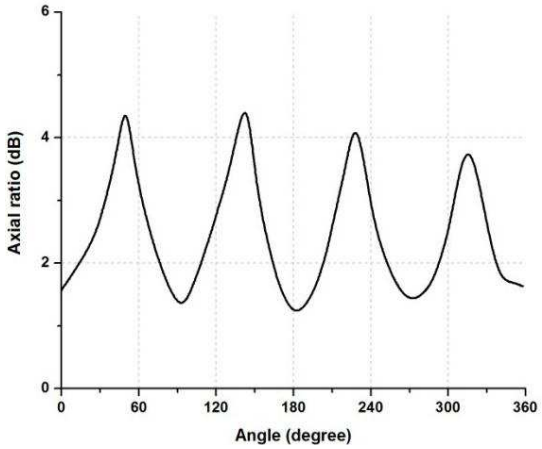

Figure 7: Measured chart of AR.

Figure 8 shows the simulation and measured antenna pattern in the E plane and H plane. As seen from Figures 8(a) and 8(b), antenna vertical pattern is "8", zero depth is about -20 dB, horizontal pattern un-roundness is less than 3 dB, achieved omnidirectional radiation.

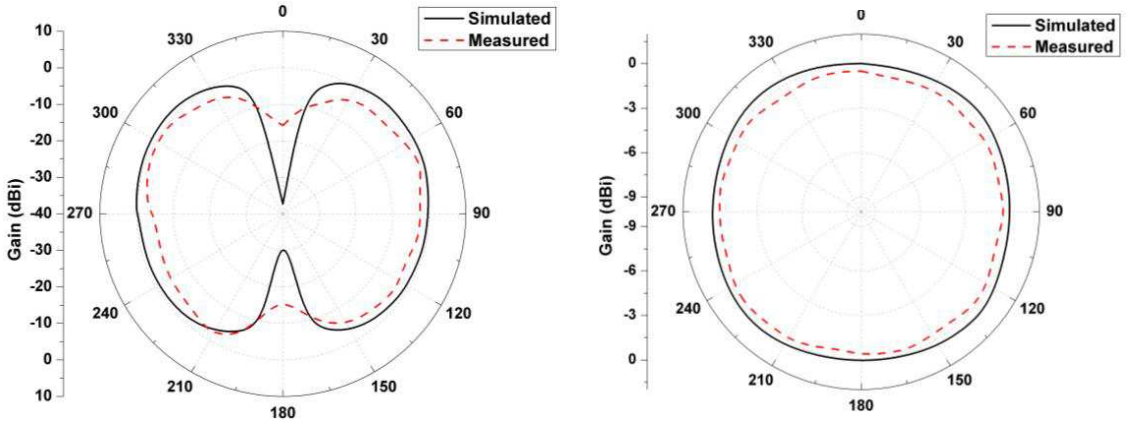

Figure 8: Comparison between simulated and measured patten. (a) Vertical pattern of antenna. (b) Horizontal pattern of antenna.

4. CONCLUSION

In this paper, we put forward a kind of beidou navigation missile cone conformal microstrip antenna, the antenna in the horizontal plane has realized the omnidirectional circular polarized radiation. Created object on the basis of simulation and measured results show that the antenna performance indicators in accordance with the simulation analysis. Good omnidirectional antenna radiation

characteristics ensure the projectile receive signal during the flight can be stabilized. The antenna structure is compact, low profile, good performance, has a broad application prospect in the field of engineering.

ACKNOWLEDGMENT

This work was supported by the National Natural Science Foundation of China under Grant 61179021.

REFERENCES

1. Sim, C. Y. D. and T. Y. Han, "GPS antenna design with slotted ground plane," *Microwave and Optical Technology Letters*, Vol. 50, No. 3, 2008.
2. Josefsson, L. and P. Persson, *Conformal Array Antenna Theory and Design*, Hoboken, New Jersey, 2006.
3. Barrie, D., "Conformal consensus," *Aviation Week & Space Technology*, Vol. 165, No. 17, 51, 2006.
4. Jayakunar, J., "A comformal cylindrical microstrip array for producing omnidirectional radiation pattern," *IEEE Trans. AP*, Vol. 34, 1258–1261, 1989.
5. Morrow, J. and D. Polarization, "Adjustable omnidirectional dipole array," *IEEE Antennas and Wireless Propagation Letters*, Vol. 2, 223–225, 2003.
6. Foschini, G. J. and M. J. Gans, "On limits of wireless communicationsin afading enviromnent when using multiple antennas," *Wireless Personal Comnmnicafions*, Vol. 6, No. 3, 311–355, 1998.

Absorption of 30 and 20 GHz Microwave Communication Signal as a Function of Rain Rate

Inderjit Singh Hudiara
Chitkara University, Chandigarh-Patiala National Highway, Rajpura, Punjab 140401, India

Abstract— The attenuation of Microwave communication signals operating at 30 GHz and 20 GHz has been measured as a function of rain rate. The line of sight distance between the transmitters and receivers was 2.3 km. It is experimentally observed that as the rain starts falling the signal received by the receivers at both the frequencies starts decreasing and as the rain rate starts increasing, the signals received by both the receivers starts decreasing and reaches to a minimum value when the rain rate is highest and as the rain rate starts decreasing the signal received at both the frequencies starts increasing and reaches the previous maximum value when the rain stops. This shows that microwave signal is absorbed by water contents of rain and we must transmit more power during rain to get the same power at the receiver. However, the increase in power at the transmitter end will depend on the rain rate. It is observed that the attenuation of microwave signal operating at 30 GHz and 20 GHz follow the same pattern. Line of sight path attenuation as a function of rain rate has also been experimentally measured at these frequencies. It is observed that the rain induced attenuation increases at both the frequencies as the rainfall rate increases. It is observed that the rain induced attenuation at 30 GHz is higher than at 20 GHz for the same rainfall rate. Specific rain induced attenuation has also been calculated using Medhurst technique and compared with Marshal and Palmer and International Telecommunication Union Models.

Rain attenuation parameters as a function of rainfall rate obtained in this experimental study can be used for designing efficient and reliable terrestrial and satellite communication systems.

1. INTRODUCTION

Absorption of Microwave Communication signal is one of the most important constraints in the performance of microwave communication system. The knowledge of absorption of microwave signal at the operating frequency is very useful for designing of reliable communication system, particularly in tropical climates where high rainfall occurs. Microwave links operating above 10 GHz are severely impaired by the presence of rain on the path link. The absorption of signal also takes place by atmospheric gases, scattering, clouds and absorption and depolarization by rain. Out of all these factors, absorption by rain is the most dominant. The loss factor of water is very high and hence rain absorbs microwave signal. The signal is absorbed over the entire path link over which it is raining and the cumulative attenuation becomes quite significant and deteriorates the received signal. Hence it is highly desirable to experimentally measure the signal absorbed by rain as a function of rain rate, so that a signal fade margin can be added in the transmitter signal power.

2. EXPERIMENTAL SET UP

Two CW transmitters operating at 20 GHz and 30 GHz were installed in an air conditioned hut to maintain constant temperature. Two receivers corresponding to each transmitter and operating at 20 GHz and 30 GHz were installed in another air conditioned hut located at a distance of 2.3 km from the transmitters. These huts were made on the roofs of two houses, one window was made in the transmitter hut and another in the receiver hut. Both these windows were covered with perspex sheet 3 mm thick. The transmitter antennas and receiver antennas were placed behind these perspex sheets. The transmitter Antennas were facing the receiver antennas as shown in the Fig. 1.

The receivers were calibrated by standard signal sources. The received signal by the receivers were recorded on strip line chart as shown in Fig. 2 and further analyzed for excess attenuation due to rain.

3. RAIN DATA COLLECTION

The rain-rate data was collected using a tipping bucket rain gauge installed at the experimental site as shown in Fig. 3.

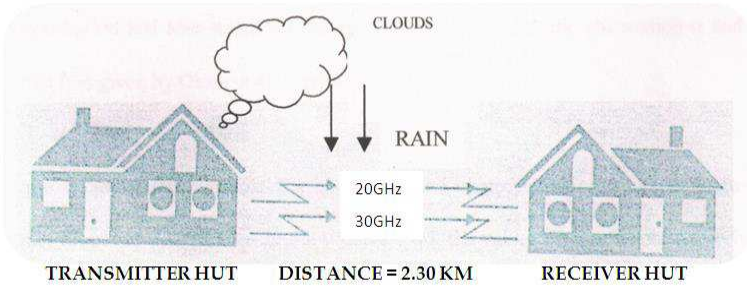

Figure 1: Line of sight link operating at 30 GHz and 20 GHz.

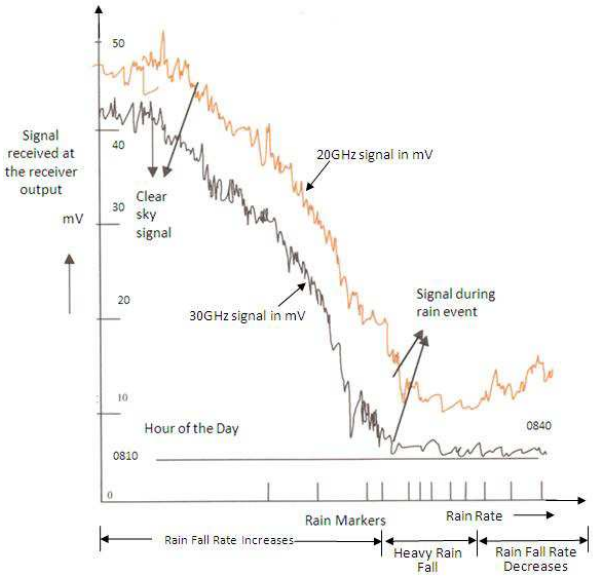

Figure 2: Signal output at 30 and 20 GHz as a function of rain rate.

Figure 3: Tipping bucket rain gauge.

The bucket is calibrated to mark one tip for each 0.254 mm of rainfall. The tipping event was recorded using strip line chart recorder as shown in Fig. 2. The rain rate (mm/hr) at a particular instant is calculated by measuring the distance between the two tips as follows:

$$R\,(\text{mm/hr}) = (0.254 * x)/d$$

where d is the distance between two tips in mm and x is the speed of the chart in mm per hour.

4. MEASUREMENT OF RAIN INDUCED ATTENUATION

The attenuation induced by rain on the microwave signal propagating at 20 GHz and 30 GHz over 2.30 km line of sight link was measured as a function of rainfall rate. The rain induced attenuation continuously increased at both the frequencies as the rainfall rate increased. Fig. 4 shows a plot of rain attenuation versus rate of rainfall at 20 GHz and 30 GHz together with the best-fit curve equation as given below:

$$A_{20} = 1.0278R^{0.8556}\ \text{dB} \quad (1)$$

$$A_{30} = 2.9006R^{0.6149}\ \text{dB} \quad (2)$$

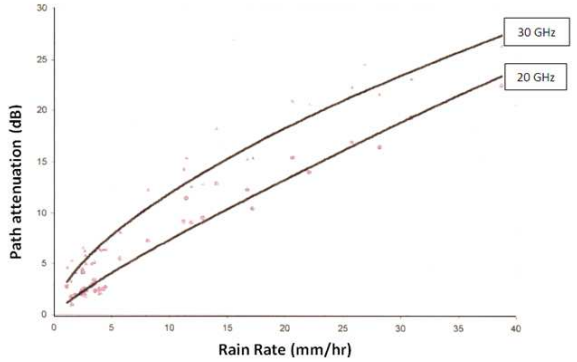

Figure 4: Plot of measured rain attenuation as a function of rainfall rate at 20 GHz and 30 GHz.

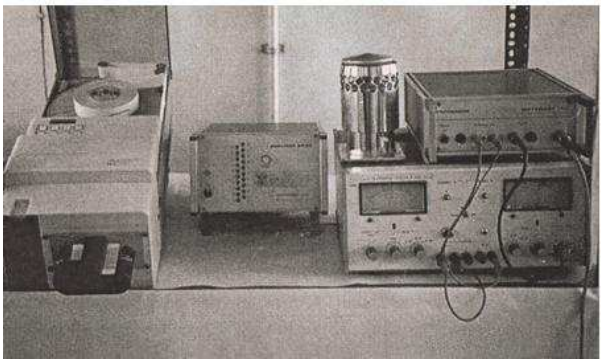

Figure 5: Experimental arrangement for measuring drop size distribution using disdrometer and paper tape puncher.

5. MEASUREMENT OF SPECIFIC ATTENUATION

It is the attenuation due to rain expressed in dB/km. Mathematically:

$$A = \int \alpha \mathrm{d}x \,\mathrm{dB} \tag{3}$$

where α is the specific attenuation of the rain volume expressed in dB/km and integration is taken along the extent of the propagation path from $x = 0$ to $x = L$. The Equation (1) can be written as:

$$A = \alpha L \,\mathrm{dB} \tag{4}$$

$$\alpha = \frac{A}{L} \,\mathrm{dB} \tag{5}$$

The specific attenuation α (dB/km) is a fundamental quantity in the calculation of rain attenuation for terrestrial path and can be calculated using rain drop size distribution (RDSD) and

Table 1: Comparison of coefficients a and b calculated as a function of Raindrop size distribution.

RDS Distribution	***a***		***b***	
	20 GHz	**30 GHz**	**20 GHz**	**30 GHz**
Experimental	0.071	0.186	1.31154	1.0478
MP RDSD	0.0751	0.191	1.103	1.032
ITU-R RDSD	0.0721	0.177	1.0827	1.01109

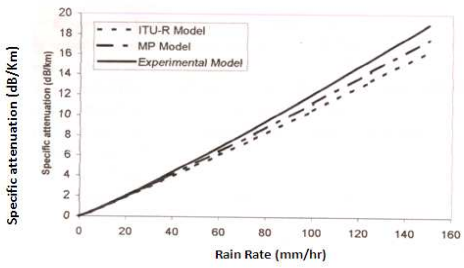

Figure 6: Comparison of specific attenuation at 20 GHz calculated by experimental model with existing models.

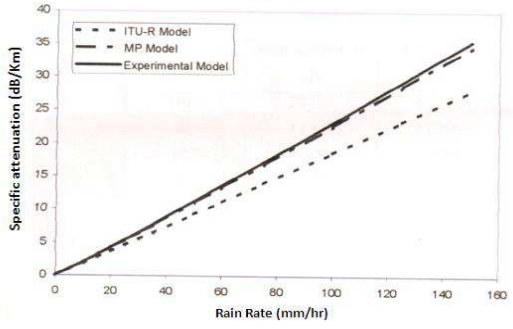

Figure 7: Comparision of specific attenuation at 30 GHz calculated by experimental model with existing models.

Mie-scattering theory. The relation of specific attenuation α and rain rate R is given by Olsen et al. [1] as

$$\alpha = aR^b \text{ dB/km} \tag{6}$$

The values of co-efficient a and b depend upon frequency, rain temperature and rain drop size distribution. In this present work the values of co-efficient a and b based on MP drop size distribution model as suggested by Olsen et al. [1] has been taken.

In the present study Medhurst [2] technique has been used for the evaluation of specific attenuation based on rain drop size data collected by disdrometer. The experimental arrangement made for measuring rain drop size distribution using disdromter and paper tape puncher is shown in the Fig. 5. The method is based on the proportion of the total volume of water reaching the ground which consists of drops of different diameters interval. Using this technique the specific attenuation at 20 and 30 GHz has been evaluated at different rain rates based on 1 minute integration time data collected by disdrometer. An empirical relation obtained from the regression analysis over specific attenuation values calculated at various rain rates has resulted in the following models:

$$\alpha_{20} = 0.071R^{1.1154} \tag{7}$$

$$\alpha_{30} = 0.186R^{1.0478} \tag{8}$$

The values of co-efficient a and b as obtained analytically [1] for various drop size distributions, are given in Table 1 along with our calculated values for comparison. The raindrop temperature was assumed to be 20°C. The values for refractive index required for calculations were also taken at temperature of 20°C.

Based on experimental models, the specific attenuation values at 20 and 30 GHz have been evaluated for different rain rates and compared with those based on LP-RDSD, adopted by CCIR and MP-RDSD given by Olsen et al. [1] as shown in Figs. 6 and 7.

6. CONCLUSION

It has been experimentally observed that the absorption of microwave communication signal depends on the rain rate and the operating microwave frequency. In the Fig. 2 it can be seen that in clear sky maximum signal is obtained by both the receivers, i.e., operating at 20 GHz and 30 GHz. However, as the rain starts, the signal received by both the receivers starts decreasing as shown in the Fig. 2. The absorption of microwave signal goes on increasing as the rainfall rate increases and reaches to a maximum when the rain rate is highest. As the rain rate starts decreasing the signal being received by the receivers again starts increasing and will attain the same value when rain stops and there is no moisture in the air and the sky is clear. Therefore for line of sight communication to remain uninterrupted during rain we should transmit higher signal corresponding to the signal absorbed by the rain. The results of these experimental measurements can be used for designing efficient and reliable terrestrial and satellite communication systems.

REFERENCES

1. Olsen, R. L., D. V. Rogers, and D. B. Hodge, "The aRb relation in the calculation of rain attenuation," *IEEE Trans. Antennas Propagation*, Vol. 26, 318–329, 1978.
2. Medhurst, R. G., "Rainfall attenuation of centimeter waves: Comparison of theory and measurement," *IEEE Trans. Antennas Propagation*, Vol. 13, 550–564, 1965.
3. Crane, R. K., "Prediction of the effects of rain on satellite communication systems," *Proc. IEEE*, Vol. 65, 456–474, 1977.
4. CCIR, "Propagation data and prediction methods required for terrestrial line of sight systems," *Reports and Recommendations of CCIR*, Reports 564-3, International Telecommunication Union, 1974–1986.
5. CCIR, "Propagation data and prediction methods required for terrestrial line of sight systems," *XVIII Plenary Assembly*, Vol. 5, Reports 338-6, 355–420, Geneva, 1990.
6. CCIR, "Propagation data and prediction methods required for terrestrial line of sight systems," *XVIII Plenary Assembly*, Vol. 5, Reports 564-4, 447–505, Geneva, 1990.
7. Macial, L. R. and M. S. Assis, "Tropical rainfall drop-size distribution," *International Journal of Satellite Communication*, Vol. 8, 181–186, UK, 1990.
8. Jassal, B. S., A. K. Verma, and L. Singh, "Rain drop size distribution and attenuation for Indian climate," *Ind. J. Radio & Space Phy.*, Vol. 23, 193–196, 1994.

9. ITU-R recommendation P. 838-3, "Specific attenuation model for rain for use in prediction method," 2001.
10. ITU-R recommendation P.83.7-3, "Characteristics of precipitation for propagation modelling," 2001.
11. ITU-R recommendation P.618-7, "Propagation data and prediction methods required for Earth-space telecommunication systems," 2001.
12. Ojo, J. S., M. O. Ajewole, and S. K. Sarkar, "Rain rate and rain attenuation prediction for satellite communication in KU and KA bands over Nigeria," *Progress In Electromagnetics Research B*, Vol. 5, 207–223, 2008.
13. Lakshmi, S., Y. H. Lee, and J. T. Ong, "Truncated gamma drop size distribution models for rain attenuation in Singapore," *IEEE Trans. Antennas and Propagation*, Vol. 58, No. 4, Apr. 2010.

On the Influence of the Electronic Structure of Atoms on the Behavior of Radiation Transition Probabilities in Alternating Electric Fields

E. V. Koryukina
National Research Tomsk State University, 36, Lenin Ave., Tomsk 634050, Russia

Abstract— In this work, it is shown that the behavior of transition probabilities in emission spectra of rare gases, induced by alternating circular electric field, is specified by the electronic structure of atomic states. The method of the energy matrix diagonalization for an atom in the electric field free from limitations of perturbation theory was used for our theoretical calculations. In the framework of this method, regularities in the behavior of transition probabilities in emission spectra of rare gas atoms were revealed. The found regularities have allowed us to classify the behavior of considered probabilities according to the electronic structure of the Stark states participating in the transition.

1. INTRODUCTION

A theoretical study of emission spectra of atoms in alternating electric fields is a topical problem of modern physics with a lot of practical applications. The behavior of spectra is characterized by the positions of the Stark components of spectral lines and transition probabilities between the Stark states. To calculate these spectral characteristics, a reliable and efficient method is required.

To calculate emission spectra of atoms excited by optical lasers, a theoretical method based on non-stationary perturbation theory was developed [1]. However, other excitation sources (electrodeless high-frequency lamps, light-emitting diodes, terahertz lasers, and so on) have appeared by the present time. These sources generate electric fields with parameters essentially different from electric field parameters of optical lasers. Non-stationary perturbation theory, by virtue of its limitations, is unsuitable for calculating emission spectra excited by such sources. This fact necessitates the creation of a new theoretical approach for calculating atomic emission spectra in alternating electric fields. Such approach was suggested and developed in [2, 3] for the case of a circularly polarized electric field. This method is free from limitations of perturbation theory and valid in a wide range of changes in the frequency and strength of the electric field.

In this work, regularities in the behavior of transition probabilities between the Stark states of atoms at changes in the frequency and strength of a circular electric field were investigated within the suggested method. Rare gas He, Ne, Ar, and Kr atoms were chosen as subjects for study, because these atoms are widely used in different excitation sources. The calculations have shown that the behavior of transition probabilities in emission spectra of considered atoms is specified by the electronic structure of atomic Stark states participating in the transition.

2. THEORETICAL METHOD

In a circularly polarized electric field, the non-stationary Schrödinger equation is written as

$$i\frac{\partial\psi_n(\vec{r},t)}{\partial t} = \left(\widehat{H}_0(\vec{r}) - F\left(x\cos\omega t \pm y\sin\omega t\right)\right)\psi_n(\vec{r},t), \tag{1}$$

where ψ_n is the wave function of the n-th state of the system, $\widehat{H}_0(\vec{r})$ is the unperturbed Hamiltonian, and the operator $-F(x\cos\omega t \pm y\sin\omega t)$ describes perturbation induced by the interaction of an atom with a circularly polarized field of frequency ω and strength F. The "+" and "−" signs correspond to the right and left polarization of the field, respectively. To go to the stationary Schrödinger equation, it is necessary to use the rotating-wave approximation [4]. In the framework of this approximation, the wave function in the coordinate system rotating around the Z-axis with the frequency ω, has the form

$$\varphi(\vec{r},t) = \exp\left(i\omega t\widehat{J}_z\right)\psi(\vec{r},t), \tag{2}$$

where $\widehat{J}_z$ is the z-component of the total angular momentum operator. On substituting Eq. (2) in Eq. (1), we get

$$i\frac{\partial\varphi(\vec{r},t)}{\partial t} = \widehat{Q}\varphi(\vec{r},t), \quad \widehat{Q} = \left(\widehat{H}_0 - \omega\widehat{J}_z \pm F\widehat{D}_x\right). \tag{3}$$

As seen from Eq. (3), the operator $\widehat{Q}$ is time-independent. Hence, in the rotating-wave approximation, it is possible to go from the non-stationary Schrödinger Eq. (1) to the stationary one, and we have

$$\widehat{Q}\varphi(\vec{r}) = \varepsilon\varphi(\vec{r}), \quad \varphi(\vec{r},t) = \exp(-i\varepsilon t)\varphi(\vec{r}) \tag{4}$$

where $\widehat{Q}$ is the operator of energy of an atom in the electric field, and ε and $\varphi(\vec{r},t)$ are the energy and wave function of an atom/ion in the electric field in the rotating coordinate system. Instead of solving the Schrödinger equation within perturbation theory, it is much more convenient to solve this equation by the method of the energy matrix diagonalization [2, 3]. It was shown in [3] that the wave functions and energies of the atom and ion, being solutions to the Schrödinger Eq. (4), are determined from diagonalization of the energy matrix with elements

$$Q_{mn} = E_n^{(0)}\delta_{mn} - \omega\left\langle\varphi_m^{(0)}(\vec{r})\left|\widehat{J}_z\right|\varphi_n^{(0)}(\vec{r})\right\rangle \pm F\left\langle\varphi_m^{(0)}\left|D_x\right|\varphi_n^{(0)}\right\rangle, \tag{5}$$

where $\varphi_n^{(0)}$ and $E_n^{(0)}$ are the wave function and energy of the n-th state of an atom in the absence of external electric field, and D_x is the x-component of the dipole transition operator. Diagonalization of the energy matrix with elements (5) gives a set of wave functions and an energy spectrum for the n-states of the atom in the electric field. Upon diagonalization of the energy matrix, we get the energies ε_n and wave functions as

$$\varphi_n(\vec{r},t) = e^{-i\varepsilon_n t}\sum_k C_{nk}\varphi_k^{(0)}(r) \tag{6}$$

for the n states of the atom/ion in the electric field in the rotating coordinate system. The coefficients C_{nk} in the wave functions (6) depend on the electric field frequency and strength. After averaging over the oscillation period, the average energy of the atom in the electric field in the initial coordinate system is written as

$$\bar{E}_n = \left\langle\psi_n(\vec{r},t)\left|H(\vec{r},t)\right|\psi_n(\vec{r},t)\right\rangle = \varepsilon_n + \omega\left\langle\varphi_n(\vec{r})\left|\widehat{J}_z\right|\varphi_n(\vec{r})\right\rangle. \tag{7}$$

It follows from Eq. (7) that $\bar{E}_n$ is time-independent. The matrix elements of the D_x operator in Eq. (5) are calculated as follows

$$\begin{aligned}\left\langle\varphi_m^{(0)}\left|D_x\right|\varphi_n^{(0)}\right\rangle &= \left\langle\gamma JM\left|D_x\right|\gamma' J'M'\right\rangle \\ &= \frac{(-1)^{J-M}}{\sqrt{2}}\left[\begin{pmatrix} J & 1 & J' \\ -M & -1 & M'\end{pmatrix} - \begin{pmatrix} J & 1 & J' \\ -M & 1 & M'\end{pmatrix}\right]\left\langle\gamma J\left\|D\right\|\gamma' J'\right\rangle\end{aligned} \tag{8}$$

where the reduced matrix elements $\langle\gamma J\|D\|\gamma' J'\rangle$ are calculated depending on a coupling scheme within the formalism of irreducible tensor operators. Details of calculating these matrix elements are reported in [3, 5].

As seen from the above reasoning, the proposed approach is free from limitations of perturbation theory, and it may be applied to calculations of spectral characteristics of any atom in a circularly polarized electric field of an arbitrary strength and frequency. The developed theoretical approach was implemented in a special software package StarkD written in FORTRAN.

3. RESULTS AND DISCUSSION

In the framework of the suggested approach, the calculations were performed within the *LS*-coupling scheme for the He atom, and within the *Jl*-coupling scheme for the rest rare gas atoms. A simulation of the behavior of transition probabilities in electric fields of different strengths and frequencies has allowed us to classify the behavior of these probabilities versus the transition type and the degree of energy state mixtures in the electric field. The type of the $JM \rightarrow J'M'$ transition is specified by the quantum numbers J and J', and the degree of the Stark state mixtures is determined by the quantum numbers n and l of the electron from the external electron shell. An analysis of wave functions has shown that a weak interaction of the Stark states is typical for low-lying atomic states (at small n). The degree of interaction of these states increases with n. As for the dependence of the degree of state mixtures on the quantum number l of the electron from the shell from which

the transition occurs, ns states practically do not mix even for the large principal quantum number n, and the Stark state interactions increase with l.

Based on the electronic structure of atomic states and the degree of the Stark state interactions, the following classification of the types of behavior for transition probabilities $A(JM \to J'M')$ with changes in the electric field F and electric field frequency ω has been established.

1) For weak mixture of the Stark states, all $M \to M'$ transitions are equiprobable (at $J, J' \leq 1$) and pairwise equiprobable (at $J, J' \geq 2$), and the transition probabilities decrease with increasing electric field strength (see Table 1). For strong interactions of states, all $M \to M'$ transitions are unequiprobable, and transition probabilities can either decrease or increase with increasing F (Figs. 1 and 2). The larger the quantum numbers n and l, the greater is the difference between probabilities of the $M \to M'$ transitions.

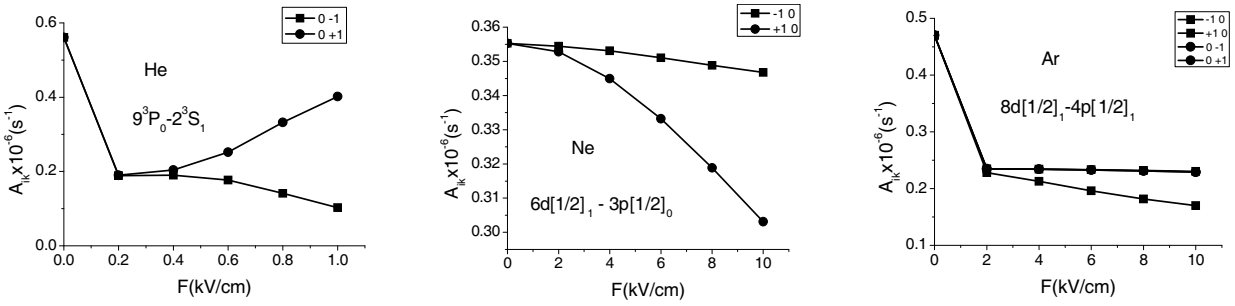

Figure 1: F-dependence of transition probabilities for states with $J,\ J' = 0,\ 1$ ($\omega = 100\,\mathrm{MHz}$).

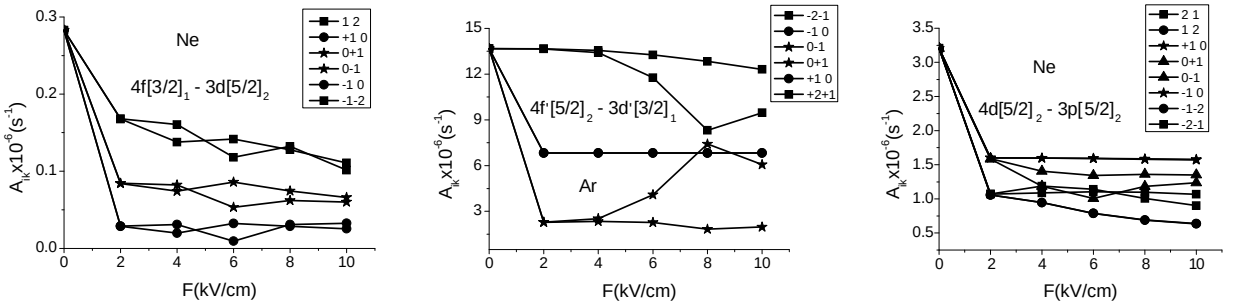

Figure 2: The F-dependence of transition probabilities for states with $J,\ J' = 1,\ 2$ ($\omega = 100\,\mathrm{MHz}$).

2) For weak mixture of the Stark states, the transition probabilities are practically indifferent to an increase in the electric field frequency. In particular, probabilities of the $5^3P_0(M = 0) - 2^3S_1(M' = \pm 1)$ transitions for the He atom are equal to $1.01 \cdot 10^6\,\mathrm{s}^{-1}$ at ω from 10^2 to $10^7\,\mathrm{MHz}$. Analogous results were obtained for other rare gas atoms. For strong state interactions, an increase in ω leads to the fact that unequiprobable $M \to M'$ transitions tend to become pairwise equiprobable (Fig. 3).

3) Both for weak and strong mixtures of states, the behavior of the $A(JM \to J'M')$ probabilities for $J \leq J'$ and $J > J'$ differs noticeably. If $J \leq J'$, then the probabilities of all transitions drastically diminish with switching on the electric field, and then they become practically insensitive to changes in the electric field strength. On the contrary, if $J > J'$, then at least one of all probabilities is practically independent of the electric field strength, whereas the remaining ones demonstrate the same behavior as that of the transition probabilities for $J \leq J'$ (see Table 1 and Figs. 1 and 2).

4) Both for weak and strong mixture of states, switching on the electric field leads to the M-ordered distribution of transition probabilities. As can be seen from Table 1 and Fig. 2, for the $J = 1 \to J' = 2$ transitions, the probabilities of the $\pm M \to \max|M'|$ transitions are maximal, and these probabilities decrease with M'. The same behavior is observed for the $J = 2 \to J' = 1$ transitions, namely, probabilities of the $\max|M| \to \pm M'$ transitions are maximal, and these probabilities decrease with M.

Thereby, the obtained results have allowed us to reveal the role of the electronic structure of

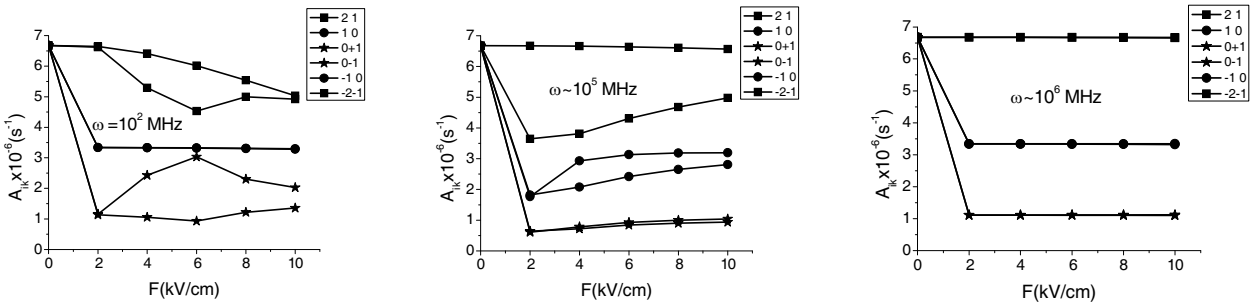

Figure 3: Ne atom. The ω-dependence for probabilities of the $4d[5/2]_2M$–$3p[3/2]_1M'$ transitions.

Table 1: Dependence of transition probabilities (in $10^6\,\mathrm{s}^{-1}$) on the electric field strength ($\omega = 100\,\mathrm{MHz}$).

Atom	Transition	λ (nm) (at $F=0$)	A_{ik} (at $F=0$)	$M \to M'$	A_{ik}	
					$F = 2\,\mathrm{kV/cm}$	$F = 10\,\mathrm{kV/cm}$
Ne	$9s'\ [1/2]_0$–$3p'[3/2]_1$	452.898	0.51	$0 \to \pm1$	0.17	0.17
Ar	$4p'[1/2]_1$–$4s'[1/2]_0$	772.663	12.51	$\pm1 \to 0$	12.50	12.50
Kr	$6p'\ [3/2]_1$–$5s'[1/2]_1$	430.170	1.57	$\pm1 \to 0$	1.57	1.57
				$0 \to \pm1$	1.57	1.57
Ne	$9s'[1/2]_1$–$3p'[3/2]_2$	454.577	0.436	$\pm1 \to \pm2$	0.173	0.131
				$\pm1 \to 0$	0.044	0.043
				$0 \to \pm1$	0.131	0.130
Ar	$4p[5/2]_2$–$4s[3/2]_1$	842.696	22.46	$\pm2 \to \pm1$	22.46	22.46
				$\pm1 \to 0$	11.23	11.23
				$0 \to \pm1$	3.75	3.75

atomic states in the behavior of transition probabilities in the electric field and to classify the behavior of transition probabilities according to the electronic structure of these states.

4. CONCLUSIONS

Based on our calculation results, the classification of the behavior of transition probabilities in emission spectra of rare gas atoms in an alternating circular electric field depending on the electronic structure of atomic states was established. The found classification gives a possibility to predict the behavior of spectral characteristics of atoms at changes in the electric field parameters.

These theoretical results obtained for the first time are interesting from the theoretical viewpoint and can be used for solving practical problems of plasma spectroscopy, gas discharge physics, and astrophysics.

REFERENCES

1. Delone, N. B. and V. P. Krainov, *Atoms in Strong Light Fields*, Atompress, Moscow, 1984.
2. Koryukina, E. V., "Calculation of the dynamic Stark effect in the many-level approximation," *Russ. Phys. J.*, Vol. 46, No. 11, 1071–1076, 2003.
3. Koryukina, E. V., "Modelling of the dynamic Stark effect and calculation of the transition probabilities for an Ar atom," *J. Phys. D: Appl. Phys.*, Vol. 38, No. 17, 3296–3303, 2005.
4. Bunkin, F. V. and A. M. Prohorov, "Excitation and ionization of atoms in a strong radiation field," *Zh. Eksp Teor. Fiz.*, Vol. 46, No. 3, 1090–1097, 1964 (in Russian).
5. Koryukina, E. V., "Calculation of the emission spectra of atoms and ions in the external electric field," *Russ. Phys. J.*, Vol. 49, No. 11, 104–107, 2006.

Higher-order Surface Modes in the Goubau Line

Ekaterina Kuzmina[1] **and Yury Shestopalov**[2]

[1]Moscow State Institute of Radio Engineering, Electronics, and Automation (Technical University)
pr. Vernadskogo 78, Moscow, Russia
[2]Department of Electronics, Mathematics and Natural Sciences
Faculty of Engineering and Sustainable Development, University of Gävle, Gävle SE-801 76, Sweden

Abstract— Existence of the higher-order surface waves of the Goubau line is proved and their structure is analyzed. An efficient computational approach is proposed based on numerical solution to initial-value problems obtained by the parameter differentiation. Several applications and further research directions are discussed.

1. INTRODUCTION

A significant amount of fundamental results of the mathematical theory of wave propagation in open and shielded metal-dielectric waveguides obtained recently [1, 2] open new possibilities for solving forward and inverse problems of electromagnetics. In particular, the description of the spectrum of normal waves is completed for a wide family of waveguides with dielectric inclusions (which actually envelopes all known types of basic guiding structures including slot and strip lines). It is shown that the spectrum is nonempty, forms a countable set of isolated points on the complex plane (there is no continuous spectrum), is located symmetrically in a certain band, and the spectral points enter the spectrum in fours. Consequently, the mathematical background and potential related to comprehensive mathematical modeling and analysis of more complicated structures increase. In this work, we apply some of these results to investigate higher-order surface modes propagating in an open metal-dielectric waveguide, the Goubau line (GL): a perfectly conducting cylinder of circular cross section covered by a concentric dielectric layer (see Fig. 1).

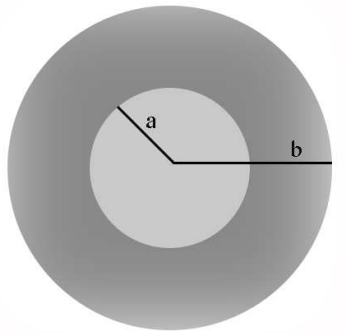

Figure 1: The Goubau line, where a and b are the radii of the internal (perfectly conducting) and external (dielectric) cylinders.

A. Sommerfeld predicted [3] existence of a wire wave propagating along a conducting cylinder. The similar type of wave is known for a GL introduced by Goubau [4]. This wave propagates outside a cylindrical conducting surface, which is possible if the surface has a coating, and is a surface mode; a thin dielectric cover plays the role of conductivity. A GL allows thus to transmit electromagnetic waves along a single wire when non-radiating surface waves are bound to the wire. Since the early 1950s, a big variety of studies and applications of GLs and covered cylindrical structures have been performed and published; one may find a comprehensive list of references, e.g., in [5–7]; many important applications, including the cloaking, are outlined in [7, 8]. However, rigorous proofs of the existence of surface waves and a satisfactory mathematical analysis of the GL multi-parameter dispersion equations (DEs) are absent, to the best of our knowledge. In particular, very little information is available concerning the existence, properties, and structure of higher-order surface waves in a GL.

In this paper, we show that analysis of the spectrum of higher-order surface modes reduces to the solution of specific families of Sturm-Liouville boundary eigenvalue problems with the boundary

operator depending on the spectral parameter. We prove the existence and analyze the spectrum of higher-order surface modes revealing some of their important properties that were not reported earlier. An efficient computational approach is proposed using numerical solution to the appropriate initial-value problems. A comparison with dielectric guides (fibers) shows advantages of GLs as transmission lines in certain frequency ranges. The developed techniques enable one to study conducting cylinders, complex waves, and multi-layer lossy dielectric covers.

2. STATEMENT

Consider the propagation of symmetric eigenwaves, described in terms of nontrivial solutions to homogeneous Maxwell's equations in the GL, in which a and b, $b > a$, are the radii of the internal (perfectly conducting) and external (dielectric) cylinders. We consider symmetric azimuthally-independent waves having the nonzero components

$$\mathbf{H} = [0, H_2(r,z), 0], \quad \mathbf{E} = [E_1(r,z), 0, E_3(r,z)], \tag{1}$$

$$E_1 = \phi(r)e^{-i\beta z}, \quad H_2 = -\frac{i\omega\epsilon}{k_s^2}\frac{d\phi}{dr}e^{-i\beta z}, \quad E_3 = -\frac{i\beta}{k_s^2}\frac{d\phi}{dr}e^{-i\beta z}, \tag{2}$$

where

$$k_s^2 = \begin{cases} k_0^2 - \beta^2, & r > b, \\ \epsilon k_0^2 - \beta^2, & a < r < b, \end{cases}$$

β is the wave propagation constant (spectral parameter), $\epsilon > 1$ is relative permittivity of the homogeneous dielectric, k_0 is the free-space wavenumber, and ϕ is a cylindrical function. Determination of surface waves (2) can be reduced to the following singular Sturm-Liouville boundary eigenvalue problems on the half-line with a discontinuous (piecewise constant) coefficient in the differential equation:

$$\mathcal{L}\phi \equiv \frac{1}{r}\frac{d}{dr}\left(r\frac{d\phi}{dr}\right) + k_s^2\phi = 0, \ r > a, \ \phi(a) = 0, \ [\phi]|_{r=b} = \left[\frac{d\phi}{dr}\right]\Big|_{r=b} = 0, \ \phi(r) \to 0, \ r \to \infty, \tag{3}$$

$$\phi \in C^1[a, +\infty) \cap C^2(a,b) \cap C^2(b, +\infty). \tag{4}$$

The conditions at infinity in (3) and the form (2) can be taken as a definition of symmetric (surface) waves in open waveguides under study. The surface waves are described in terms of real-valued quantities; in particular, the boundary operators in (3) is defined (as real-valued functions of a real variable γ or $\lambda = \gamma^2$) on a certain interval I. The spectrum of surface waves may be empty or consist of several (real) points located on this interval. For surface waves, potential function $\phi(r)$ can be represented, according to conditions at infinity, as

$$\phi(r) = \begin{cases} AK_0(\frac{r}{a}\sqrt{u^2 - x^2}), & r > b, \\ \frac{B}{Y_0(x)}\left[J_0(\frac{r}{a}x)Y_0(x) - Y_0(\frac{r}{a}x)J_0(x)\right], & a < r < b \end{cases} \tag{5}$$

Here,

$$\gamma = \frac{\beta}{k_0}, \ x = k_0 a\sqrt{\epsilon - \gamma^2}, \ u = k_0 a\sqrt{\epsilon - 1}, \ s = \frac{b}{a} > 1, \tag{6}$$

and $J_k(x)$, $Y_k(x)$, $K_0(x)$, and $K_1(x)$ denote, respectively, the Bessel and Neumann functions of the order $k = 0, 1$ and the McDonald functions.

3. ANALYSIS

Applying to (5) the transmission (continuity) condition we obtain the dispersion equation (DE) for surface waves

$$F_G(x,u,s) \equiv G_g(x,u,s) - F_g(x,s) = 0. \tag{7}$$

where

$$G_g(x,u,s) = \epsilon\sqrt{u^2 - x^2}\frac{K_0(s\sqrt{u^2 - x^2})}{K_1(s\sqrt{u^2 - x^2})}, \qquad F_g(x,s) = x\frac{\Phi_1(x,s)}{\Phi_2(x,s)}, \tag{8}$$

$$\Phi_1(x,s) = J_0(sx)Y_0(x) - J_0(x)Y_0(sx), \qquad \Phi_2(x,s) = J_0(x)Y_1(sx) - J_1(sx)Y_0(x).$$

Denote by $h_m^0(s)$, and $h_m^{10}(s)$ $(m = 1, 2, \dots)$ zeros of Φ_1 and Φ_2. For a fixed $s > 1$, all these zeros are real and simple points [2]; the sequences $\{h_m^0(s)\}$ and $\{h_m^{10}(s)\}$ are increasing w.r.t index m and alternate on the positive semi-axis. $h_m^{10}(s)$ are decreasing functions of $s > 1$. The domain of function $F_G(x, u, s)$ is

$$D_{F_G}(u,s) : \{x : \mid x \mid \leq u \setminus H_G(u,s), \quad u > 0, \quad s \geq 1, \}$$
$$H_G(u,s) = \left\{h_m^{01}(s) : 0 \leq h_m^{01}(s) \leq u, \ m = 1, 2, \dots N(u)\right\},$$
$$H_G(u,s) = \emptyset \ (N(u) = 0) \quad \text{if all } h_m^{01}(s) > u \quad (m = 1, 2, \dots N(u)).$$

According to the conditions on parameters we will consider $F_G(x, u, s)$ on the set

$$D_{F_G}^+(u,s) : \{(x,u,s) : 0 \leq x \leq u \setminus H_G(u,s), \ u > 0, \ s > 1\}.$$

Figure 2 illustrates the proof of existence of roots of DE (7).

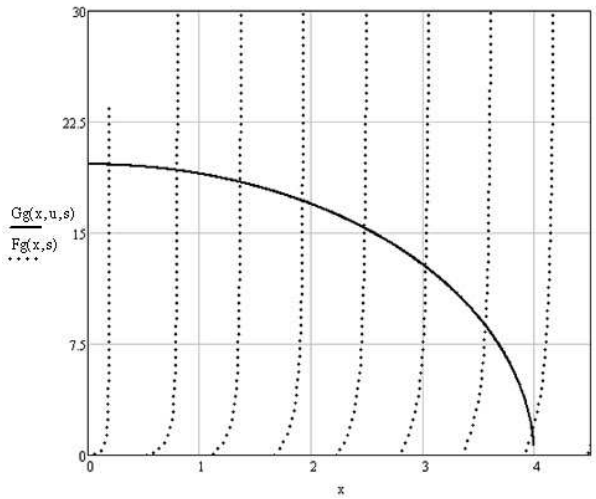

Figure 2: Behavior of functions $G_g(x; u)$ and $F_g(x)$ (8) for the Goubau line ($\epsilon = 5$) for $s = 6.615$.

Perform the analysis of higher-order surface waves using parameter-differentiation method and reduction to the solution of the Cauchy initial value problems. Note first that (i) for every $u > 0$ there exists a (minimal positive) zero $h_m^0(s)$ of function $\Phi_1(x, s)$ such that

$$u = h_m^0(s_m^0) \quad \text{for one and only one} \quad s = s_m^0 = s(u) > 1, \quad m = 1, 2, \dots; \tag{9}$$

(ii) according to the explicit form (7) of the DE $F_0(x = u, u, s_m^0) = 0$ for any $u > 0$ and $\frac{\partial F_0(u,u,s)}{\partial x} \neq 0$. Numbers s_m^0 can be determined, for every given $u > 0$, by solving numerically the equation $\Phi_1(u, s) = 0$. Thus $x = x^m(s) = x^m(s)$ can be determined as a regular perturbation of the value $x = h_m^0$ attained at $s = s_m^0$: for a fixed $u > 0$, find the implicit function $x^m = x^m(s)$ as a (real) solution to the Cauchy problem

$$\begin{cases} \frac{dx^m}{ds} = \tilde{F}_0(x, u, s), \quad s > s_m^0, \\ x^m(s_m^0) = h_m^0(s_m^0), \ m = 1, 2, \dots, N_0(u). \end{cases} \tag{10}$$

Note that $x^m(s)$ satisfies the condition

$$h_m^0(s) > x^m(s) > h_m^{01}(s), \quad m = 1, 2, \dots, N_0(u). \tag{11}$$

We prove that if a given $u = k_0 a\sqrt{\epsilon - 1}$ satisfies the condition

$$u = k_0 a\sqrt{\epsilon - 1} > h_m^0(s),$$

the Cauchy problem (10) is uniquely solvable. Thus, for arbitrary $s = b/a > 1$ that may be sufficiently close to unity, there exists a root $x^1 = x^1(s)$ of DE (7) [more exactly, implicit function

$x^1(s)$ specified by Equation (7) in the vicinity of point A_0^1]. In other words, for an arbitrarily thin dielectric layer there exists (at least one) surface wave propagating in the Goubau line under the condition

$$u = k_0 a\sqrt{\epsilon - 1} \geq h_1^0(s). \tag{12}$$

Relationship (12) is the necessary condition that provides the existence of at least one such wave. Taking into account the domain of function $F_0(x, u, s)$ and $\tilde{F}_0(x, u, s)$ we have the condition $x \in (0, k_0 a\sqrt{\epsilon})$.

4. STRUCTURE OF HIGHER-ORDER WAVES

The cross-sectional structure of the nth higher-order wave is characterized by the number of zeros (oscillations) of potential function $\phi_n(r)$ on (a, b); namely, $\phi_n(r)$ has exactly n zeros (see Fig. 3) and the intervals between two neighboring zeros contained in the interval tend to zero. We calculate normalized propagation constants γ of the fundamental (with no oscillations) and higher-order surface modes v.s. parameter s for different values of parameter u using numerical solution of (10). Cutoff values of s are determined by condition (2). The results are summarized in Fig. 4. The potential functions ϕ_n preserve their types (number n of zeros or oscillations) along the dispersion curves.

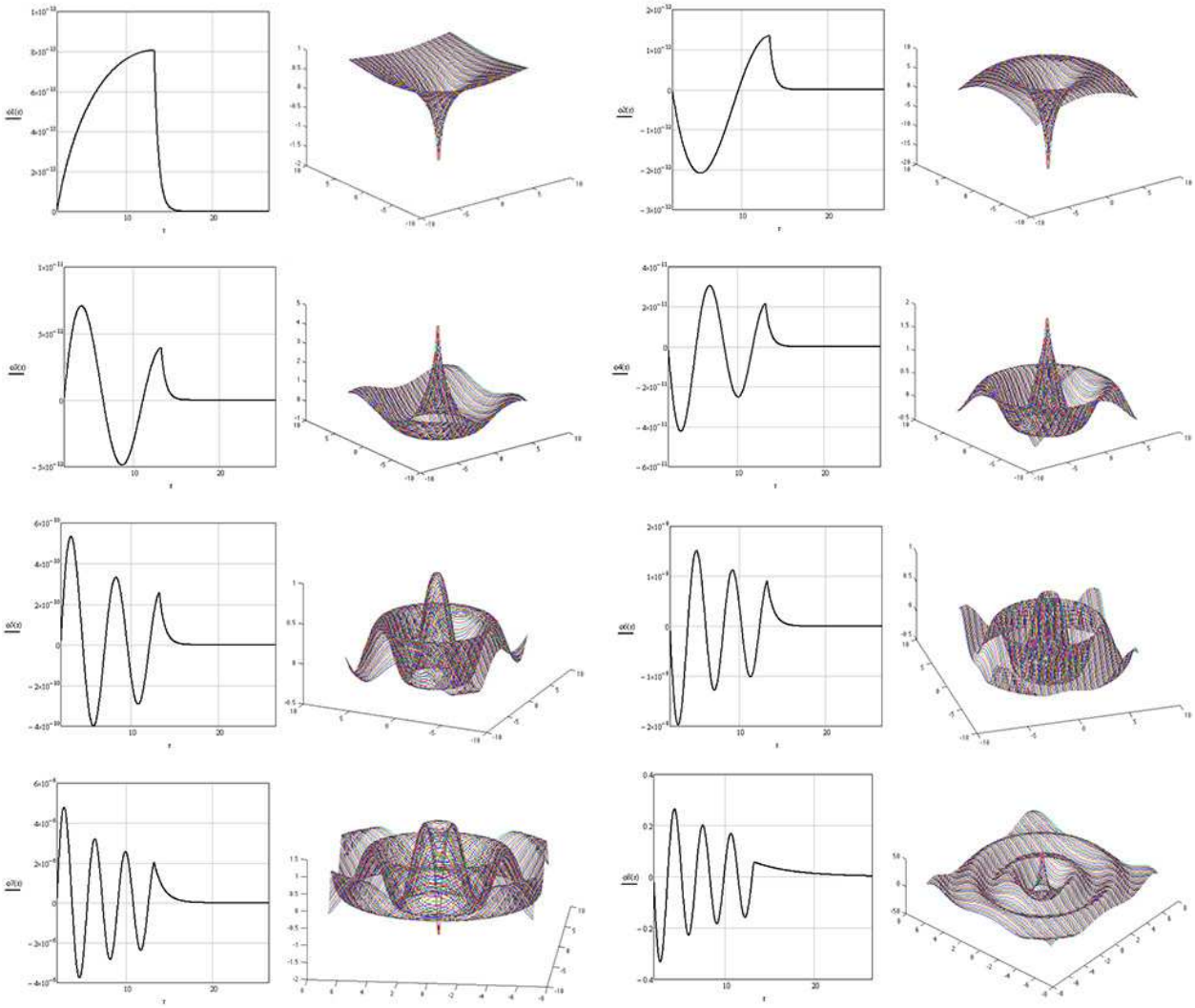

Figure 3: Potential function $\phi_n(r)$ (5) of the higher-order surface waves of the Goubau line calculated for different eigenvalue indices $n = 0, 1, \ldots, 7$ at $a = 2$, $b = 13.23$, and $\epsilon = 5$.

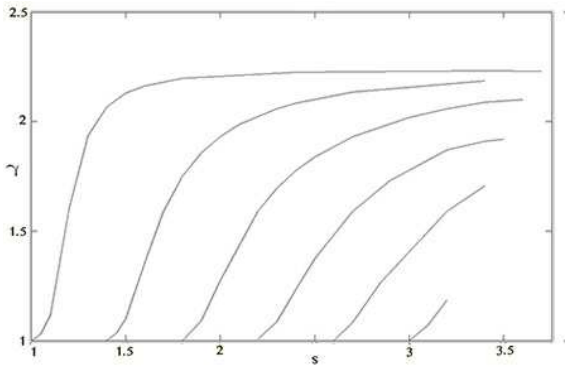

Figure 4: Normalized propagation constants γ (vertical axis) of the fundamental (with no oscillations) and higher-order surface modes of the Goubau line v.s. parameter s calculated for value $u = 8$.

5. CONCLUSION

We have shown that higher-order surface modes in the GL exist for arbitrarily thin dielectric coating if the electrical cross-sectional dimension is sufficiently large. We have determined the cutoff values and cross-sectional structure of the higher-order surface modes in the coating and have demonstrated that their spectrum can be efficiently calculated from the numerical solution of Cauchy initial value problems obtained using parameter differentiation. We have reduced the analysis of the spectrum of symmetric surface modes to singular and regular Sturm-Liouville boundary eigenvalue problems on the half-line and on the intervals. We have shown that the spectrum of surface waves of the Goubau line with an infinitely thin dielectric coating is a perturbed set of zeros of a well-defined function. The established properties of surface waves enable one to use GLs as near-field testing and sensor devices and for cloaking [7, 8].

REFERENCES

1. Shestopalov, Y. and Y. Smirnov, "Eigenwaves in waveguides with dielectric inclusions: Spectrum," *Applicable Analysis*, Vol. 93, No. 2, 408–427, 2014.
2. Shestopalov, Y., E. Kuzmina, and A. Samokhin, "On a mathematical theory of open metal-dielectric waveguides," *FERMAT*, 2014 (in Press).
3. Sommerfeld, A., "On the propagation of electrodynamic waves along the wire," *Ann. Physik*, Vol. 67, 673–682, 1899.
4. Goubau, G., "Surface waves and their application to transmission lines," *J. Appl. Phys.*, Vol. 21, 1119–1128, 1950.
5. Overfelt, P. L., K. Halterman, S. Feng, and D. R. Bowling, "Mode bifurcation and fold points of complex dispersion curves for the metamaterial goubau line," arXiv:0909-0535v1, 2009.
6. Rao, T. and M. Hamid, "Mode spectrum of the modified goubau line," *Proc. IEE*, Vol. 126, 1127–1232, 2005.
7. Fleury, R. and A. Alu, "Cloaking and invisibility: A review," *FERMAT*, 2014.
8. Stulle, F. and J. Bergoz, "The Goubau line surface waves for bench testing of beam instrumentation at high frequencies," *Proc. BIW2012*, *Newport News*, 146–148, VA, USA, 2011.

Inverse Problem Method for Permittivity Reconstruction of Two-layered Media: Numerical and Experimental Results

Yu. V. Shestopalov[1], **Yu. G. Smirnov**[2], **and E. D. Derevyanchuk**[2]

[1]University of Gävle, Sweden
[2]Penza State University, Russia

Abstract— This study employs the technique developed in [1–3] and deals with complex permittivity reconstruction of layered materials in the form of diaphragms (sections) in a single-mode waveguide of rectangular cross section from the transmission coefficient measured at different frequencies.

1. INTRODUCTION

Reconstruction of electromagnetic parameters of nanocomposite and artificial materials is an urgent problem. In practice, as a rule, these parameters cannot be directly measured [4–6]. Therefore, methods of mathematical modeling must be applied. This work is a continuation of the series of papers [1–3] devoted to the analysis of permittivity determination of layered materials. We set forth a specially developed mathematical and numerical technique that combines analytical and numerical approaches providing thus the results with guaranteed accuracy.

We consider complex permittivity reconstruction of layered materials in the form of diaphragms (sections) in a single-mode waveguide of rectangular cross section from the transmission coefficient measured at different frequencies. The developed numerical-analytical method guarantees accuracy of the result and can be implemented in practical measurements.

2. INVERSE PROBLEM

Assume that a waveguide $P = \{x\colon\ 0 < x_1 < a, 0 < x_2 < b, -\infty < x_3 < \infty\}$ with the perfectly conducting boundary surface ∂P is given in the cartesian coordinate system. A three-dimensional body Q $(Q \subset P)$ $Q = \{x\colon\ 0 < x_1 < a, 0 < x_2 < b, 0 < x_3 < l\}$ is placed in the waveguide; the body has the form of a diaphragm adjacent to the waveguide walls.

Domain $P\backslash\bar{Q}$ is filled with an isotropic and homogeneous layered medium having constant permeability $(\mu_0 > 0)$ and constant permittivity $(\varepsilon_0 > 0)$, each section of the diaphragm having constant permeability μ_0 and permittivity:

$$\varepsilon_j(\omega) = \varepsilon_j^1 + i\frac{\sigma_j}{\omega} \tag{1}$$

where ε_j^1 is real part of complex permittivity and σ_j is conductivity $(j = 1, 2, \ldots, n)$.

Length of each section l_j $(j = 1, 2, \ldots, n)$ of the diaphragm is known.

The electromagnetic field inside and outside the object in the waveguide is governed by Maxwell's equations

$$\begin{aligned} \mathrm{rot}\mathbf{H} &= -i\omega\varepsilon\mathbf{E} \\ \mathrm{rot}\mathbf{E} &= i\omega\mu_0\mathbf{H}, \end{aligned} \tag{2}$$

where $\mathbf{E}$ and $\mathbf{H}$ are the vectors of the electric and magnetic field intensity and ω is the circular frequency.

Assume that $\pi/a < k_0 < \pi/b$, where $k_0^2 = \omega^2\varepsilon_0\mu_0$ (a single-mode waveguide). The incident electrical field is

$$\mathbf{E}^0 = \mathbf{e}_2 A \sin\left(\frac{\pi x_1}{a}\right) e^{-i\gamma_0 x_3} \tag{3}$$

with a known A and $\gamma_0 = \sqrt{k_0^2 - \pi^2/a^2}$.

Solving the forward problem for Maxwell's equations with the aid of (1) we obtain explicit expressions for the field inside every section of diaphragm Q and outside the diaphragm:

$$\begin{aligned} E^{(0)} &= \sin\left(\frac{\pi x_1}{a}\right)\left(Ae^{-i\gamma_0 x_3} + Be^{i\gamma_0 x_3}\right), \\ E^{(j)} &= \sin\left(\frac{\pi x_1}{a}\right)\left(C_j e^{-i\gamma_j x_3} + D_j e^{i\gamma_j x_3}\right), \\ E^{(n+1)} &= \sin\left(\frac{\pi x_1}{a}\right) Fe^{-i\gamma_{n+1} x_3}, \quad \gamma_{n+1} = \gamma_0 \\ & j = (1, 2, \ldots, n) \end{aligned} \tag{4}$$

Substituting (4) into Maxwell's equations we have:

$$\gamma_j = \sqrt{\omega^2 \varepsilon_j^1 \mu_0 + \omega^2 \sigma_j \mu_0 - \frac{\pi^2}{a^2}} \tag{5}$$

From the conditions on the boundary surfaces $L := \{x_3 = 0, \ldots, x_j = l_j, \ldots, x_3 = l_n\}$ of the diaphragm sections

$$[E]|_L = 0, \qquad [H]|_L = 0, \tag{6}$$

where square brackets $[\cdot]$ denote the function jump over the boundary surfaces, applied to (3)–(5) we obtain using conditions (6) a system of equations for the unknown coefficients

$$\begin{cases} A + B = C_1 + D_1 \\ \gamma_0 (B - A) = \gamma_1 (D_1 - C_1) \\ C_j e^{-i\gamma_j l_j} + D_j e^{i\gamma_j l_j} = C_{j+1} e^{-i\gamma_{j+1} l_j} + D_{j+1} e^{i\gamma_{j+1} l_j} \\ \gamma_j \left(D_j e^{i\gamma_j l_j} - C_j e^{-i\gamma_j l_j}\right) = \gamma_{j+1} \left(D_{j+1} e^{i\gamma_{j+1} l_j} - C_{j+1} e^{-i\gamma_{j+1} l_j}\right), \end{cases} \tag{7}$$

where $C_{n+1} = F,\ D_{n+1} = 0$. In system (7) coefficients A, B, C_j, D_j are supposed to be complex.

Inverse problem P: *find the complex permittivity $\varepsilon_j^1 + i\frac{\sigma_j}{\omega}$ of each section j from the known amplitude A of the incident wave and transmission coefficient F at different frequencies.*

Expressing C_j, D_j via C_{j+1}, D_{j+1} we obtain a recurrent formula that couples amplitudes A and F:

$$A = \frac{1}{2\prod_{j=0}^{n} \gamma_j} (\gamma_n p_{n+1} + \gamma_0 q_{n+1}) F e^{-i\gamma_0 l_n}, \tag{8}$$

where

$$\begin{aligned} p_{j+1} &= \gamma_{j-1} p_j \cos\alpha_j + \gamma_j q_j i \sin\alpha_j, \quad p_1 := 1, \\ q_{j+1} &= \gamma_{j-1} p_j i \sin\alpha_j + \gamma_j q_j \cos\alpha_j, \quad q_1 := 1. \end{aligned} \tag{9}$$

Here $\alpha_j = \gamma_j (l_j - l_{j-1})$, $j = 1, \ldots, n$.

We solve the inverse problem under study assuming that permittivities are governed by (1).

Considering the last equation at different frequencies we obtain a system of n equations with n unknown permittivities; solving this system numerically we find all permittivities.

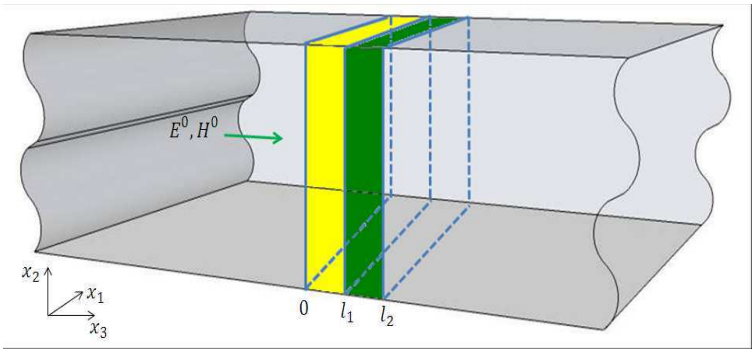

Figure 1: Two-sectional diaphragm in a waveguide.

3. TWO-SECTIONAL DIAPHRAGM

In the case of a two-sectional diaphragm, we obtain a system of 2 equations with 2 unknown permittivities by duplicating (7) at two different frequencies:

$$\begin{cases} \frac{A(\omega_1)}{F(\omega_1)} e^{i\gamma_0(\omega_1)l_2} = \frac{\gamma_2(\omega_1)p_3(\omega_1)}{2\gamma_0(\omega_1)\gamma_1(\omega_1)\gamma_2(\omega_1)} + \frac{\gamma_0(\omega_1)q_3(\omega_1)}{2\gamma_0(\omega_1)\gamma_1(\omega_1)\gamma_2(\omega_1)}, \\ \frac{A(\omega_2)}{F(\omega_2)} e^{i\gamma_0(\omega_2)l_2} = \frac{\gamma_2(\omega_2)p_3(\omega_2)}{2\gamma_0(\omega_2)\gamma_1(\omega_2)\gamma_2(\omega_2)} + \frac{\gamma_0(\omega_2)q_3(\omega_2)}{2\gamma_0(\omega_2)\gamma_1(\omega_2)\gamma_2(\omega_2)} \end{cases} \tag{10}$$

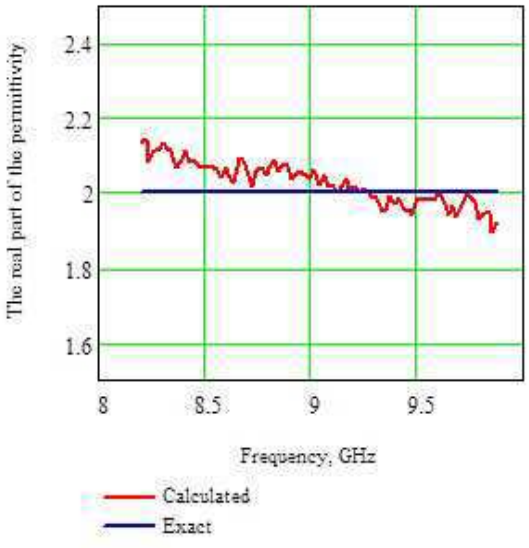

Figure 2: The real part of the permittivity of the first section ε_1^1. Blue and red lines denote, respectively, the permittivity values calculated by the present method and measured using experimental facilities.

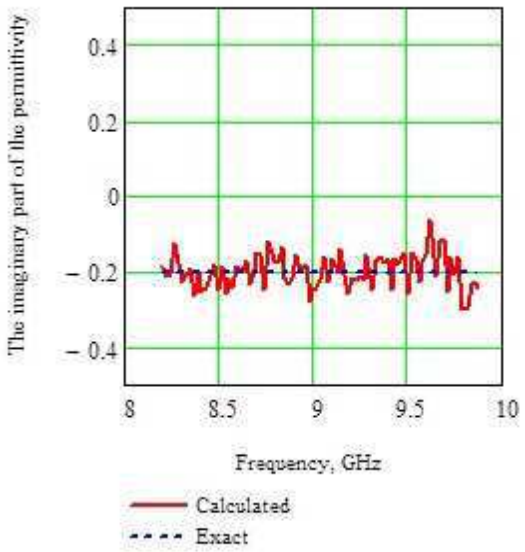

Figure 3: The conductivity of the first section σ_1. Blue and red lines denote, respectively, the permittivity values calculated by the present method and measured using experimental facilities.

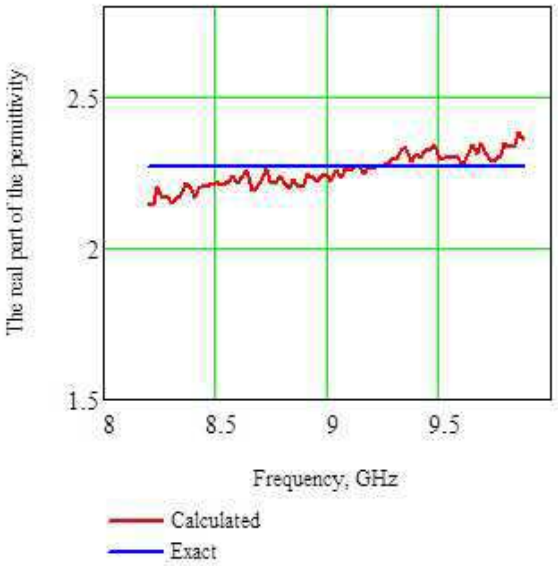

Figure 4: The real part of the permittivity of the first section ε_2^1. Blue and red lines denote, respectively, the permittivity values calculated by the present method and measured using experimental facilities.

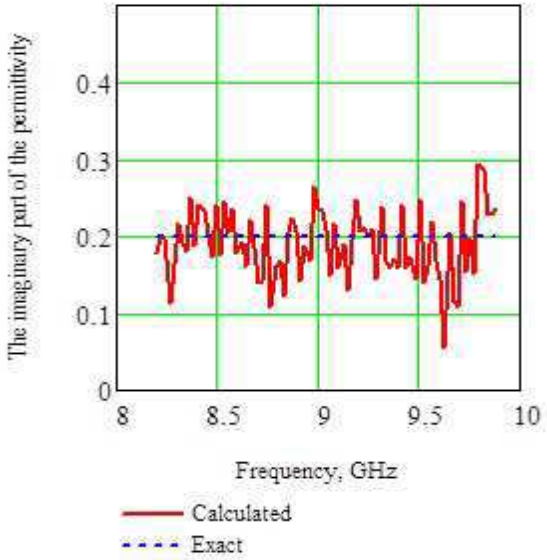

Figure 5: The conductivity of the second section σ_2. Blue and red lines denote, respectively, the conductivity values calculated by the present method and measured using experimental facilities.

where

$$\begin{aligned} p_3 &= \gamma_1 p_2 \cos(\alpha_2) + \gamma_2 q_2 i \sin(\alpha_2), \\ p_2 &= \gamma_0 p_1 \cos(\alpha_1) + \gamma_1 q_1 i \sin(\alpha_1), \qquad p_1 = 1 \\ q_3 &= \gamma_1 p_2 i \sin(\alpha_2) + \gamma_2 q_2 \cos(\alpha_2), \\ q_2 &= \gamma_0 p_1 i \sin(\alpha_1) + \gamma_1 q_1 \cos(\alpha_1), \qquad q_1 = 1 \end{aligned} \tag{11}$$

$$\gamma_j(\omega) = \sqrt{\omega^2 \varepsilon_j^1 \mu_0 + \omega^2 \sigma_j \mu_0 - \frac{\pi^2}{a^2}}, \quad \alpha_j = \gamma_j (l_j - l_{j-1}), \quad j = 1, 2.$$

4. NUMERICAL RESULTS. TWO-SECTIONAL DIAPHRAGM

Parameters of the two-sectional diaphragm diaphragm are $a = 2.286\,\text{cm}$, $b = 1.02\,\text{cm}$, $c = 2\,\text{cm}$, $l_1 = 0.995\,\text{cm}$, $l_2 = 2.004\,\text{cm}$, and the excitation frequency is $f \in (8,2; 12,4)\,\text{GHz}$.

Numerical results confirm the efficiency of the method. In fact, the calculated permittivities coincide very well with the the statistical average (mean value) of the values obtained from the noisy measurement data, as it is illustrated by the Figures 1–5.

5. CONCLUSION

We have developed a numerical-analytical method of solution to the inverse problem of reconstructing permittivities of n-sectional diaphragms in a waveguide of rectangular cross-section. Comparison of numerical and experimental results validates the efficiency of the method.

ACKNOWLEDGMENT

We acknowledge the results of the series of measurements of the real and imaginary parts of the permitivity of teflon and quartz samples performed at the laboratory of the Kharkiv Institute of Radio Physics and Electronics of the National Academy of Sciences of Ukraine led by Prof. I. Ivanchenko and similar results presented by Prof. A. Vertiy.

REFERENCES

1. Smirnov, Y. G., Y. V. Shestopalov, and E. D. Derevyanchuk, "Permittivity reconstruction of layered dielectrics in a rectangular waveguide from the transmission coefficient at different frequencies," *Inverse Problems and Large-scale Computations, Series: Springer Proceedings in Mathematics & Statistics*, Vol. 52, XII, 169–181, 2013.
2. Smirnov, Y. G., Y. V. Shestopalov, and E. D. Derevyanchuk, "Permittivity determination of multi-sectional diaphragm with metamaterial layers in rectangular waveguide," *PIERS Proceedings*, 135–139, Taipei, Mar. 25–28, 2013.
3. Smirnov, Y. G., Y. V. Shestopalov, and E. D. Derevyanchuk, "Reconstruction of permittivity and permeability tensors of anisotropic materials in a rectangular waveguide from the reflection and transmission coefficients at different frequencies," *PIERS Proceedings*, 290–295, Stockholm, Sweden, Aug. 12–15, 2013.
4. Shestopalov, Y. V., Y. G. Smirnov, and V. V. Yakovlev, "Volume singular integral equations method for determination of effective permittivity of meta- and nanomaterials," *Progress In Electromagnetics Research Symposium Abstracts*, 291–292, Cambridge, USA, Jul. 2–6, 2008.
5. Solymar, L. and E. Shamonina, *Waves in Metamaterials*, Oxford University Press Inc., New York, 2009.
6. Usanov, D. A., A. V. Skripal, A. V. Abramov, and A. S. Bogolyubov, "Determination of the metal nanometer layer thicknesss and semiconductor conductivity in metal-semiconductor structures from electromagnetic reflection and transmission spectra," *Technical Physics*, Vol. 51, No. 5, 644–649, 2006.

Propagation of TM Waves in a Double-layer Nonlinear Inhomogeneous Cylindrical Waveguide

E. Yu. Smolkin and D. V. Valovik
Penza State University, Russia

Abstract— The paper focuses on the problem of electromagnetic TM wave propagation in a two-layered circular cylindrical dielectric waveguide (this is an example of Bragg's waveguide) with a inhomogeneous nonlinear permittivity inside one of its layers, the other layer has a constant permittivity. The physical problem is reduced to a nonlinear transmission eigenvalue problem for Maxwell's equations. Eigenvalues of the problem correspond to propagation constants of the waveguide. Existence of eigenvalues of the considered problem is stated. Numerical experiments are carried out for three types of nonlinearities. Comparisons with linear/nonlinear inhomogeneous cases are given.

1. INTRODUCTION

Investigation of the spectra of electromagnetic waveguide systems is still an urgent task (see, e.g., [1–4]). Analysis of electromagnetic wave propagation (TE or TM) in a plane layer or in a cylindrical waveguide filled with nonlinear homogeneous medium is of special interest. One of the simplest cases in these problems refers to a single-layer waveguide in which the dielectric permittivity is described by the Kerr law (see, e.g., [4, 5]). Some waveguide problems for cylindrical waveguides are solved by methods of the theory of integral equations (see, for example, [4, 5]). The multilayer inhomogeneous nonlinear waveguide structure in the case of TE waves is studied in [7, 8]; the case of TM waves is studied numerically in [6].

2. STATEMENT OF THE PROBLEM

Consider three-dimensional space $\mathbb{R}^3$ with cylindrical coordinate system $O\rho\varphi z$. The space is filled with isotropic medium with constant permittivity $\varepsilon = \varepsilon_0\varepsilon_3$, where $\varepsilon_0 > 0$ is the permittivity of free space. In this medium a circular cylindrical waveguide

$$\Sigma := \{(\rho, \varphi, z) : 0 \leqslant \rho < R_1,\, 0 \leqslant \varphi < 2\pi\} \cup \{(\rho, \varphi, z) : R_1 \leqslant \rho \leqslant R_2,\, 0 \leqslant \varphi < 2\pi\}$$

is placed; its generating line (the waveguide axis) is parallel to the axis Oz. The waveguide is filled with isotropic nonmagnetic medium. Throughout the paper we assume that $\mu = \mu_0$, where $\mu_0 > 0$ is the permeability of free space. The waveguide is unbounded in z direction (see Figure 1).

Consider the monochromatic TM waves $(\mathbf{E}, \mathbf{H})e^{-i\omega t}$, where $\mathbf{E} = (E_\rho, 0, E_z)^T$, $\mathbf{H} = (0, H_\varphi, 0)^T$, ω is the circular frequency, the quantities $\mathbf{E}$, $\mathbf{H}$ are called the complex amplitudes [1], $(\cdot)^T$ denotes the transpose operation, and components of the field $\mathbf{E}$, $\mathbf{H}$ do not depend on φ.

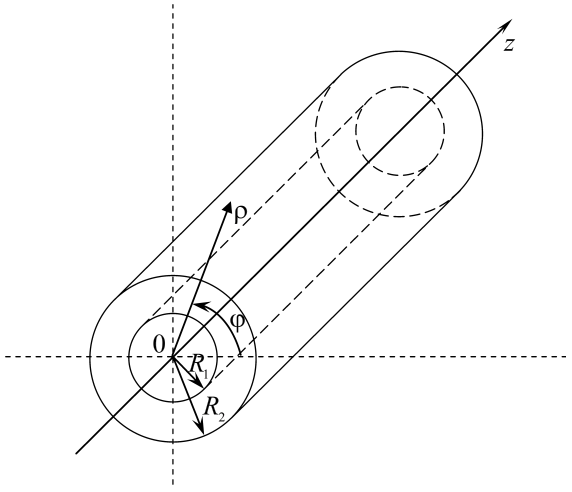

Figure 1: Geometry of the problem.

Complex amplitudes of the electromagnetic field $\mathbf{E}$, $\mathbf{H}$ satisfy stationary Maxwell's equations

$$\operatorname{rot}\mathbf{H} = -i\omega\varepsilon\mathbf{E}, \quad \operatorname{rot}\mathbf{E} = i\omega\mu\mathbf{H}, \tag{1}$$

the continuity condition for the tangential components on the media interfaces (on the boundaries of the waveguide) $\rho = R_1$, $\rho = R_2$, and the radiation condition at infinity: the electromagnetic field decays as $O(\rho^{-1})$ when $\rho \to \infty$. The solutions to Maxwell's equations are sought in the entire space.

The dielectric permittivity in the whole space has the form $\varepsilon = \tilde{\varepsilon}\varepsilon_0$, where

$$\tilde{\varepsilon} = \begin{cases} \varepsilon_1, & 0 \leqslant \rho < R_1, \\ \varepsilon_2(\rho) + \alpha f\left(|\mathbf{E}|^2\right), & R_1 \leqslant \rho \leqslant R_2, \ \} \\ \varepsilon_3, & \rho > R_2, \end{cases} \tag{2}$$

and $\min\{\varepsilon_1, \varepsilon_3\} \geqslant \varepsilon_0 > 0$, $\alpha > 0$ are real constants, $\varepsilon_2(\rho) \in C^1[R_1, R_2]$, $f(u) \in C[0, +\infty)$.

We assume that the surface waves propagating along the axis Oz of the waveguide Σ depend harmonically on z. Thus, the components have the form

$$E_\rho = \mathrm{E}_\rho(\rho)e^{i\gamma z}, \quad E_z = \mathrm{E}_z(\rho)e^{i\gamma z}, \quad H_\varphi = \mathrm{H}_\varphi(\rho)e^{i\gamma z}, \tag{3}$$

where γ is the (real) propagation constant (the spectral parameter of the problem).

Let $k_0^2 := \omega^2\mu_0\varepsilon_0$. Substituting the complex amplitudes $\mathbf{E}$ and $\mathbf{H}$ with components (3) into Equation (1) and introducing the notation $u_1(\rho;\gamma) := \mathrm{E}_\rho(\rho;\gamma)$, $u_2(\rho;\gamma) := i\mathrm{E}_z(\rho;\gamma)$ we obtain

$$\gamma u_2' + \left(\gamma^2 - k_0^2\tilde{\varepsilon}\right)u_1 = 0, \quad -\gamma\rho^{-1}(\rho u_1)' - \rho^{-1}\left(\rho u_2'\right)' - k_0^2\tilde{\varepsilon}u_2 = 0, \tag{4}$$

where u_1, u_2 are real functions and $\tilde{\varepsilon}$ is given by (2). Also we assume that the functions u_1, u_2 are sufficiently smooth.

Tangential components of electromagnetic field are known to be continuous at media interfaces. In this case the tangential components are E_z and H_φ. Taking into account that $H_\varphi(\rho) = \frac{1}{i\omega\mu}(i\gamma E_\rho(\rho) - E_z'(\rho))$, we obtain

$$[\gamma u_1 + u_2']\big|_{\rho=R_1} = 0, \quad [\gamma u_1 + u_2']\big|_{\rho=R_2} = 0, \quad [u_2]\big|_{\rho=R_1} = 0, \quad [u_2]\big|_{\rho=R_2} = 0, \tag{5}$$

where $[v]\big|_{\rho=s} = \lim_{\rho\to s-0} v(\rho) - \lim_{\rho\to s+0} v(\rho)$.

Problem P_M is to find quantities $\gamma = \widehat{\gamma}$ for which a non-trivial solution $u_1(\rho;\widehat{\gamma})$, $u_2(\rho;\widehat{\gamma})$ to (4)–(5) exists; this solutions has prescribed value $u_1(R_1)$, $u_2(R_1)$ (or $u_1(R_2)$, $u_2(R_2)$) and decays as $O(\rho^{-1})$ when $\rho \to \infty$. The quantities solving problem P_M are called eigenvalues, the corresponding functions $u_1(\rho;\widehat{\gamma})$, $u_2(\rho;\widehat{\gamma})$ are called eigenfunctions.

Statement 1. *Let $\min\{\varepsilon_1, \varepsilon_3\} \geqslant \varepsilon_0$, $\alpha > 0$ be real constants and the linear problem (Problem P_M for $\alpha = 0$) have $k \geqslant 1$ solutions $\tilde{\gamma}_i$, $i = \overline{1,k}$. Then there is a value $\alpha_0 > 0$ such that, for any $\alpha \leqslant \alpha_0$, problem P_M has at least one eigenvalue in the vicinity of each $\tilde{\gamma}_i$.*

It follows from this statement that there exist axial-symmetric TM-polarized waves propagating without attenuation in inhomogeneous cylindrical dielectric waveguides of circular cross section filled with non-magnetic isotropic inhomogeneous nonlinear medium.

3. NUMERICAL RESULTS

Numerical experiments are carried out for the following functions:

1. $\varepsilon = \varepsilon(\rho) + \alpha u^2$, $\alpha = 0.01$, where (a) $\varepsilon(\rho) = \varepsilon_2 + \rho^{-1}$, (b) $\varepsilon(\rho) = \varepsilon_2 + \rho$;
2. $\varepsilon = \varepsilon(\rho) + \frac{\alpha u^2}{1+\beta u^2}$, $\alpha = 0.01$, $\beta = 0.001$, where (a) $\varepsilon(\rho) = \varepsilon_2 + \rho^{-1}$, (b) $\varepsilon(\rho) = \varepsilon_2 + \rho$;
3. $\varepsilon = \varepsilon(\rho) + \alpha\left(1 - e^{-\beta u^2}\right)$, $\alpha = 5$, $\beta = 0.01$, where (a) $\varepsilon(\rho) = \varepsilon_2 + \rho^{-1}$, (b) $\varepsilon(\rho) = \varepsilon_2 + \rho$,

ε_2 is a positive real constant.

The following values of parameters are used for calculations given in Figures 2–19: $\varepsilon_1 = 4$, $\varepsilon_2 = 9$, $\varepsilon_3 = 1$, $R_1 = 2$, $2 < R_2 < 8$, $k_0 = 1$. Initial conditions for carrying out the calculations are defined in [6], here we also use $C_1 = 1$.

In this report the dependence $\gamma(\Delta R)$ is called a dispersion curve, where $\Delta R = R_2 - R_1$, R_1 is fixed, R_2 is varied. Dispersion curves for the cases 1(a) and 1(b), 2(a) and 2(b), and 3(a) and 3(b)

are shown in Figs. 2 and 3, 8 and 9, and 14 and 15, respectively. The vertical axis corresponds to $\gamma^2 > 4$ and the horizontal axis corresponds to the thickness $0 < \Delta R = R_2 - R_1 < 6$ of the outer cylindrical shell (see Figure 1). The dotted red curves correspond to the linear inhomogeneous case and the blue dotted curves correspond to the nonlinear inhomogeneous case (in the same figure the inhomogeneity is the same for both types of curves; red and blue curves differ in a nonlinear term only).

The vertical dashed lines in Figs. 2 and 8, 3 and 9, 14 and 15 correspond to $\Delta R = 1.5$, $\Delta R = 1.2$, $\Delta R = 1.242$ and $\Delta R = 1.075$, respectively. Eigenvalues of the problem are points of intersections of these dashed lines with the dispersion curves; first three points in Figures 2 and 3 are marked (the smallest value, red dot, corresponds to the linear case and the others two (green and black dots) correspond to the Kerr case); first four points in Figures 8, 9, 14, 15 are marked (the smallest value, red dot, corresponds to the linear case and the others three (green, blue and black dots) correspond to the case with saturated nonlinearity).

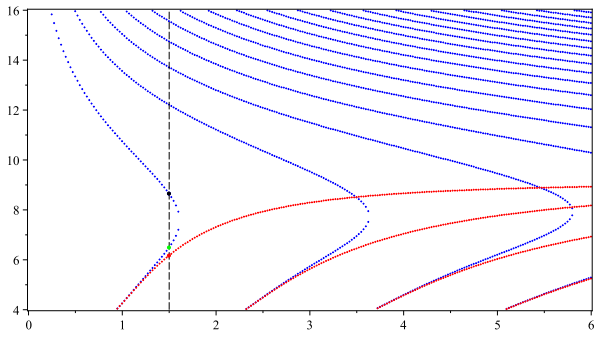

Figure 2: Case 1(a). Marked eigenvalues: $\gamma \approx 2.482$ (red dot), $\gamma \approx 2.546$ (green dot), and $\gamma \approx 2.940$ (black dot).

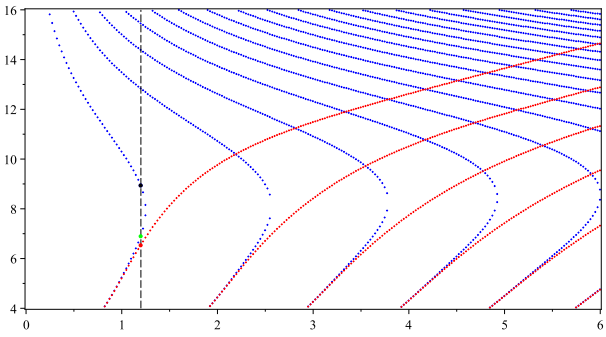

Figure 3: Case 1(b). Marked eigenvalues: $\gamma \approx 2.554$ (red dot), $\gamma \approx 2.624$ (green dot), and $\gamma \approx 3.988$ (black dot).

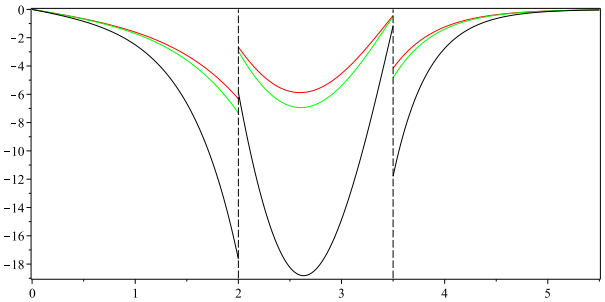

Figure 4: Eigenfunction $u_1(\rho)$ for the case 1(a): $R_2 = 3.5$; $\gamma \approx 2.482$ (red), $\gamma \approx 2.546$ (green), and $\gamma \approx 2.940$ (black).

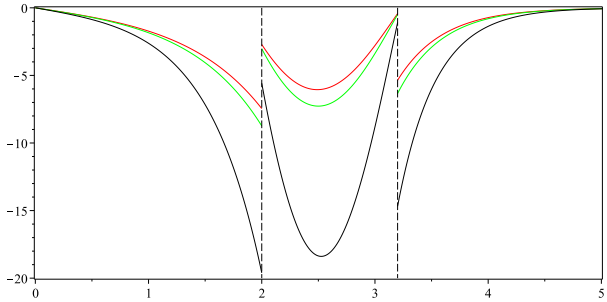

Figure 5: Eigenfunctions $u_1(\rho)$ for the case 1(b): $R_2 = 3.2$; $\gamma \approx 2.554$ (red), $\gamma \approx 2.624$ (green), and $\gamma \approx 2.988$ (black).

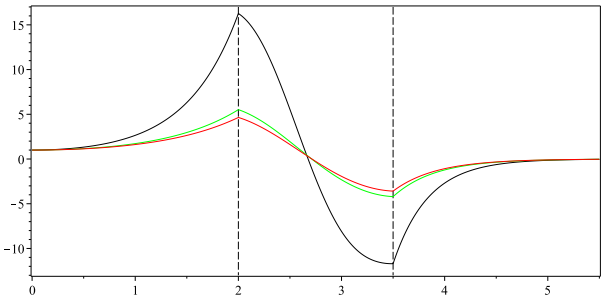

Figure 6: Eigenfunctions $u_2(\rho)$ for the case 1(a): $R_2 = 3.5$; $\gamma \approx 2.482$ (red), $\gamma \approx 2.546$ (green), and $\gamma \approx 2.940$ (black).

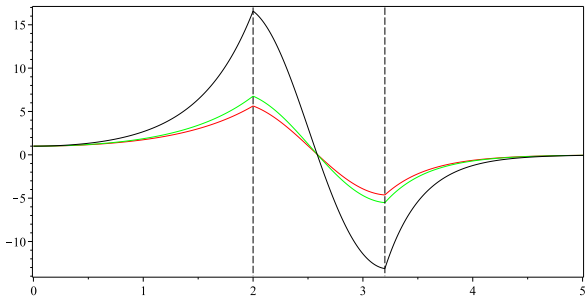

Figure 7: Eigenfunctions $u_2(\rho)$ for case 1(b): $R_2 = 3.2$; $\gamma \approx 2.554$ (red), $\gamma \approx 2.624$ (green), and $\gamma \approx 2.988$ (black).

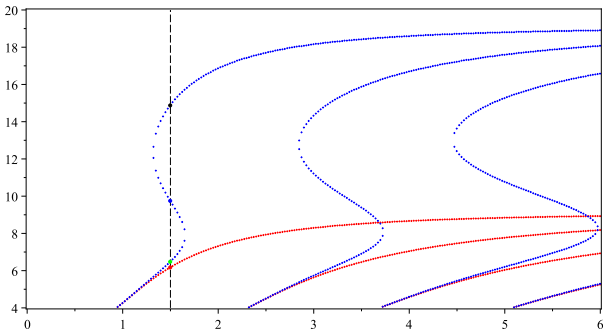

Figure 8: Case 2(a). Marked eigenvalues: $\gamma \approx 2.482$ (red dot), $\gamma \approx 2.5425$ (green dot), $\gamma \approx 3.12$ (blue dot), and $\gamma \approx 3.855$ (black dot).

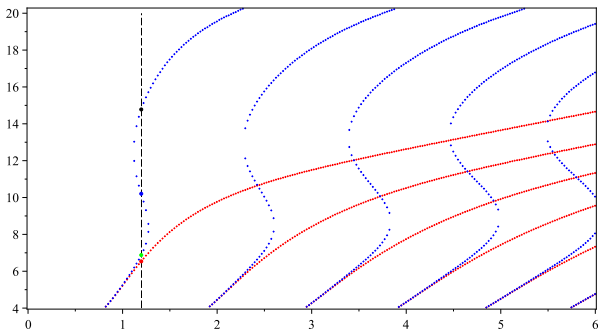

Figure 9: Case 2(b). Marked eigenvalues: $\gamma \approx 2.554$ (red dot), $\gamma \approx 2.62$ (green dot), $\gamma \approx 3.1925$ (blue dot), and $\gamma \approx 3.8425$ (black dot).

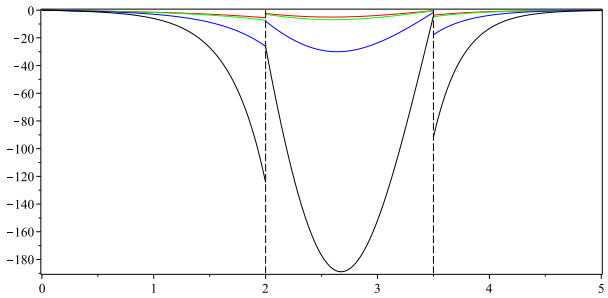

Figure 10: Eigenfunctions $u_1(\rho)$ for the case 2(a): $R_2 = 3.5$; $\gamma \approx 2.482$ (red), $\gamma \approx 2.5425$ (green), $\gamma \approx 3.12$ (blue), and $\gamma \approx 3.855$ (black).

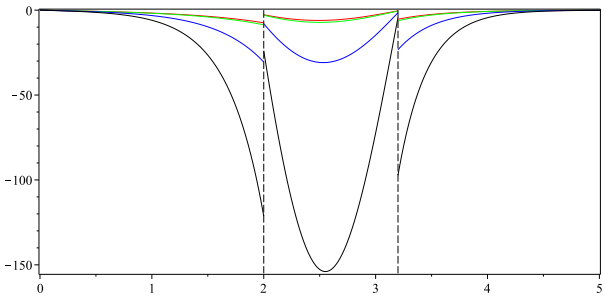

Figure 11: Eigenfunctions $u_1(\rho)$ for the case 2(b): $R_2 = 3.2$; $\gamma \approx 2.554$ (red), $\gamma \approx 2.62$ (green), $\gamma \approx 3.1925$ (blue), and $\gamma \approx 3.8425$ (black).

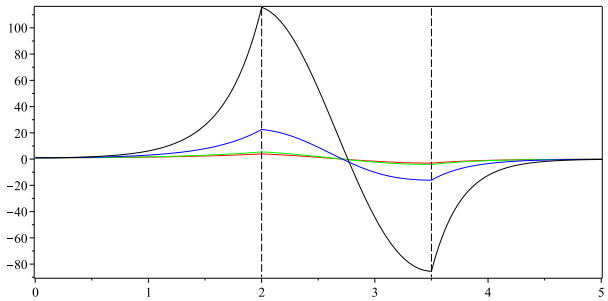

Figure 12: Eigenfunctions $u_2(\rho)$ for the case 2(a): $R_2 = 3.5$; $\gamma \approx 2.482$ (red), $\gamma \approx 2.5425$ (green), $\gamma \approx 3.12$ (blue), and $\gamma \approx 3.855$ (black).

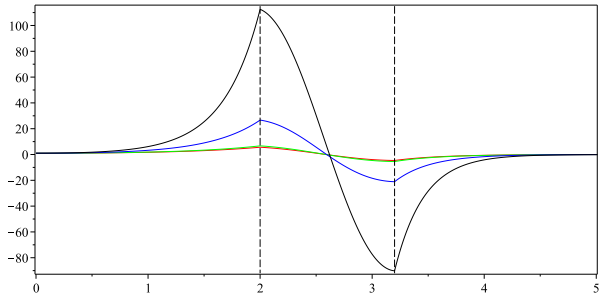

Figure 13: Eigenfunctions $u_2(\rho)$ for the case 2(b): $R_2 = 3.2$; $\gamma \approx 2.554$ (red), $\gamma \approx 2.62$ (green), $\gamma \approx 3.1925$ (blue), and $\gamma \approx 3.8425$ (black).

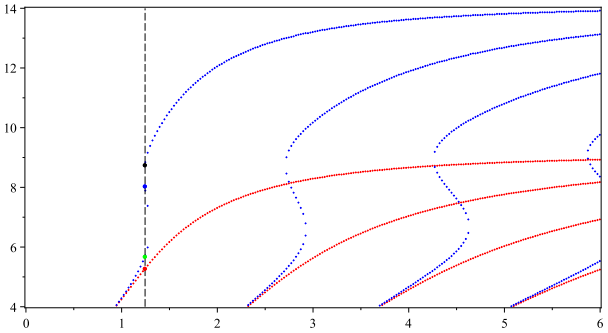

Figure 14: Case 3(a). Marked eigenvalues: $\gamma \approx 2.294$ (red dot), $\gamma \approx 2.38$ (green dot), $\gamma \approx 2.8325$ (blue dot), and $\gamma \approx 3.955$ (black dot).

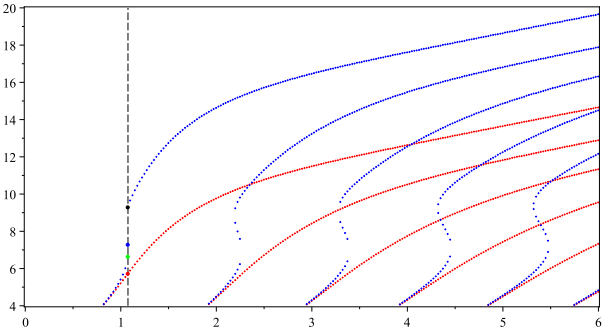

Figure 15: Case 3(b). Marked eigenvalues: $\gamma \approx 2.388$ (red dot), $\gamma \approx 2.5725$ (green), $\gamma \approx 2.695$ (blue), and $\gamma \approx 3.045$ (black dot).

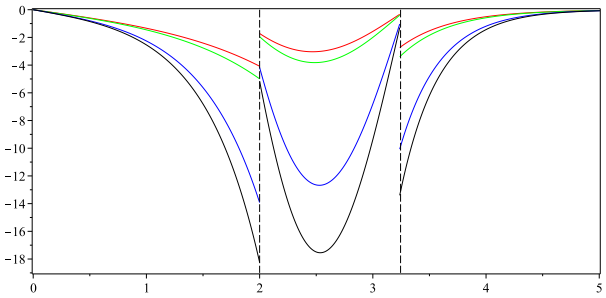

Figure 16: Eigenfunctions $u_1(\rho)$ for the case 3(a): $R_2 = 3.245$; $\gamma \approx 2.294$ (red), $\gamma \approx 2.38$ (green), $\gamma \approx 2.8325$ (blue), and $\gamma \approx 2.955$ (black).

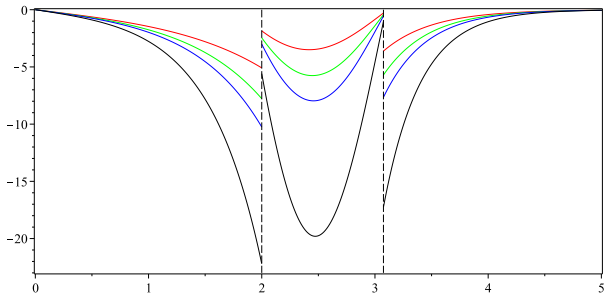

Figure 17: Eigenfunctions $u_1(\rho)$ for the case 3(b): $R_2 = 3.075$; $\gamma \approx 2.388$ (red), $\gamma \approx 2.5725$ (green), $\gamma \approx 2.695$ (blue), and $\gamma \approx 3.045$ (black).

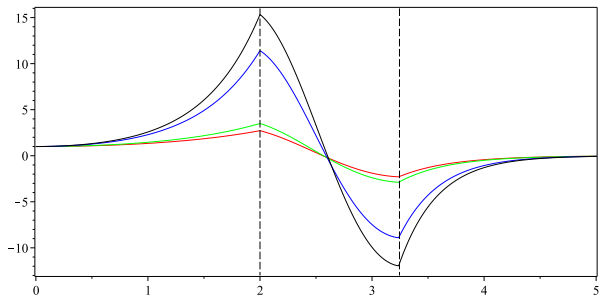

Figure 18: Eigenfunctions $u_2(\rho)$ for the case 3(a): $R_2 = 3.245$; $\gamma \approx 2.294$ (red), $\gamma \approx 2.38$ (green), $\gamma \approx 2.8325$ (blue), and $\gamma \approx 2.955$ (black).

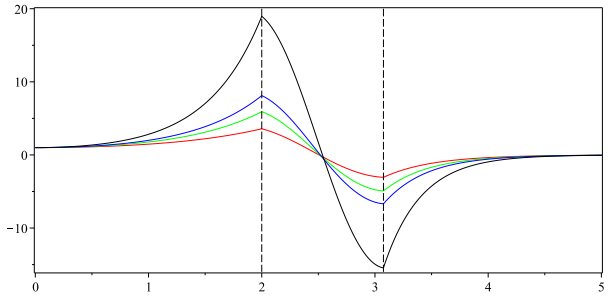

Figure 19: Eigenfunctions $u_2(\rho)$ for the case 3(b): $R_2 = 3.075$; $\gamma \approx 2.388$ (red), $\gamma \approx 2.5725$ (green), $\gamma \approx 2.695$ (blue), and $\gamma \approx 3.045$ (black).

In Figures 4–7, 10–13, and 16–19, eigenfunctions $u_1(\rho)$, $u_2(\rho)$ are plotted for the cases 1–3, respectively. The vertical axis corresponds to the value of the plotted functions $u_1(\rho)$, $u_2(\rho)$ and the horizontal axis corresponds to the value ρ.

ACKNOWLEDGMENT

The authors are grateful to Yu. G. Smirnov for useful discussions and attention to the study. The work is partly supported by the RFBR (No. 14-01-31234), the Russian Federation President Grant (No. MK-90.2014.1), and The Ministry of Education and Science of the Russian Federation (Goszadanie No. 2.1102.2014/K).

REFERENCES

1. Eleonskil, V. M., L. G. Oganesyants, and V. P. Silin, "Cylindrical nonlinear waveguides," *Journal of Experimental and Theoretical Physics*, Vol. 35, 44–47, 1972.
2. Eleonskil, V. M. and V. P. Silin, "Propagation of electromagnetic waves in an inhomogeneous nonlinear medium," *Journal of Experimental and Theoretical Physics*, Vol. 66, 146–153, 1974.
3. Akhmediev, N. N. and A. Ankevich, *Solitons, Nonlinear Pulses and Beams*, Chapman and Hall, London, UK, 1997.
4. Smirnov, Yu. G. and D. V. Valovik, *Electromagnetic Wave Propagation in Non-linear Layered Waveguide Structures*, Penza State University Press, Penza, Russia, 2011.
5. Schürmann, H. W., V. S. Serov, and Yu. V. Shestopalov, "*TE*-polarized waves guided by a lossless nonlinear three layer structure," *Physical Review E*, Vol. 58, 1040–1050, 1998.
6. Valovik, D. V. and E. Yu. Smolkin, "Calculation of the propagation constants of inhomogeneous nonlinear double-layer circular cylindrical waveguide by means of the Cauchy problem method," *Journal of Communications Technology and Electronics*, Vol. 58, 762–769, 2013.
7. Valovik, D. V., Yu. G. Smirnov, and E. Yu. Smolkin, "Nonlinear transmission eigenvalue problem describing TE wave propagation in two-layered cylindrical dielectric waveguides," *Computational Mathematics and Mathematical Physics*, Vol. 53, 973–983, 2013.
8. Smirnov, Yu. G., E. Yu. Smolkin, and D. V. Valovik, "Nonlinear double-layer Bragg waveguide: Analytical and numerical approaches to investigate waveguiding problems," *Advances in Numerical Analysis*, Vol. 53, 1–11, 2014.

Numerical Analyze of Waveguide Transmission Coefficient with Non-uniform Dielectric Slab

A. P. Smirnov[1], **A. N. Semenov**[1], **and Y. V. Shestoplalov**[2]

[1]Lomonosov Moscow State University, Moscow, Russia
[2]University of Gavle, Gavle, Sweden

Abstract— Propagation in the time domain of electromagnetic waves in a rectangular waveguide with a non-uniform dielectric slab is considered. Electromagnetic field components are computed and investigation of energy transport in the guide is performed by using Finite Difference Time Domain (FDTD) method in different frequency ranges. Parallel high performance FDTD solver, based on Maxwell equations approximation in integral form on Yee lattice and developed by the paper authors is used. A method for calculating the transmission coefficient with respect to all the problem parameters is proposed. The method is based on the analysis of the amplitude of the scattered wave derived from FDTD numerical solution. The pure scattered field method is proposed to specify the waveguide mode with respect to numerical dispersion. Computations for nonstationary Maxwell equations system are performed for the H_{10}-mode scattering from a dielectric slab placed in the waveguide. Multiple numerical computations for the corresponding large-scale problems have been performed on Lomonosov Moscow State University IBM BlueGene/P supercomputer. Using the methods described above, we compute the values of the waveguide transmission, attenuation and propagation factors in a wide range of permittivity and different positions of the dielectric slab inclusions. Continuous curves on the complex plane describing the dependence of the transmission coefficient on the dielectric constant are obtained. The comparison of the transmission coefficient calculated by the present approach and the volume integral equation method is performed.

1. INTRODUCTION

Investigation of electromagnetic waves scattering on dielectric bodies that have complicated geometry or structure is an important problem when composite or artificial materials and media are used as elements of various devices. However, the solution usually cannot be obtained directly, because of composite character of the material and small size of samples, which leads to the necessity of applying methods of mathematical modeling and numerical solution of the corresponding electromagnetic problems [1].

In this work we are using 3-dimensional FDTD solver EMWSolver3D [2]. Based on Maxwell equations approximation in integral form on Yee lattice, it provides numerical solution in time domain. EMWSolver3D supports multi-core single processors machines and provides hybrid MPI/ OpenMP support for IBM BlueGene/P series.

Pure scattered field method is used to specify waveguide mode with respect to numerical dispersion [3].

This work aims at propagation factors estimation of filters created on the basis of single-layered parallel-plane dielectric diaphragms in waveguides of rectangular cross section with dielectric inclusions. This topic is interesting for the possibility of design of specific frequency selective filters. For instance, such filters can suppress a desired band of frequencies. The proposed method can be used for benchmark problems where electromagnetic parameters of materials obtained analytically or numerically reconstructed from inverse problem [5].

2. INHOMOGENEOUS ONE-SECTIONAL DIAPHRAGM

Lets consider geometry of the problem at Figure 1. Assume that a waveguide $P = \{x : 0 < x < a,\ 0 < y < b,\ -\infty < z < \infty\}$ of rectangular cross-section with the perfectly conducting boundary surface ∂P is given in the Cartesian coordinate system (see figure).

A three-dimensional body Q ($Q \subset P$ is a domain) with a constant magnetic permeability μ_0 and variable permittivity $\varepsilon_r(\vec{r})$ is placed in the waveguide. Function $\varepsilon(\vec{r})$ is bounded in $\bar{Q}$, $\varepsilon_r \in L_\infty(Q)$, and $\varepsilon_r^{-1} \in L_\infty(Q)$. The boundary ∂Q of domain Q is piecewise smooth. In the provided numerical experiment electric permittivity $\varepsilon_r(\vec{r})$ was set constant.

We assume that the electromagnetic field $\mathbf{E_t} = \mathbf{E_s} + \mathbf{E_{inc}}$, $\mathbf{H_t} = \mathbf{H_s} + \mathbf{H_{inc}}$ in the waveguide is excited by an external field with E_{inc}, H_{inc} the time dependence functions $e^{-i\omega t}$ and where E_s and H_s are scattered field components obtained from FDTD numerical scheme [1].

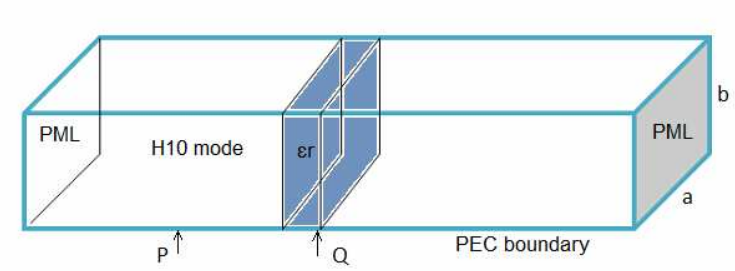

Figure 1: Geometry of the problem.

Choose the waveguide parameters so that $\pi/a < k_0 < \pi/b$, where k_0 is the free-space wave number, $k_0^2 = \omega^2\varepsilon_0\mu_0$, and ω is the circular frequency. In this case, only one mode propagates in the waveguide (namely, the principal $\mathbf{H}_{10}$ mode), and all other modes are evanescent (decaying).So let $a = 2b = 0,625\lambda$. It suits the condition that $\Lambda < \dfrac{2}{\sqrt{\frac{1}{a^2} + \frac{1}{b^2}}}$, where λ wavelength in cubic waveguide.

According to the work [3] transmission coefficient F can be obtained from exact solution of finite-difference problem and E_ω field in frequency domain that is calculated using Fourier transform from time domain solution.

3. NUMERICAL MODELLING

Lets consider domain Q ($Q \subset P$ — domain) with constant magnetic permeability μ_0 and varying permittivity $\varepsilon_r(\vec{r})$ located inside waveguide. Function $\varepsilon_r(\vec{r})$ is bounded in $\bar{Q}$, $\varepsilon_r \in L_\infty(Q)$, and $\varepsilon_r^{-1} \in L_\infty(Q)$. Boundary ∂Q of domain Q is piecewise smooth. Dielectric permittivity $\varepsilon_r(\vec{r})$ is piecewise function, that describes Q_1 ($Q1 \subset Q$ — domain, which have cube shape ($Q_1 = \{x : 0 < x_1 \le x \le x_2 < a,\ 0 < y_1 \le y \le y_2 < b,\ z_1 \le z \le z_2\}$) located inside Q (see Figure 2).

The thickness of diaphragm Q $l_1 = \lambda$. The numerical FDTD parameters: $\Delta x = \Delta y = \Delta z = \lambda/120$. The size of inhomogeneity $x_2 - x_1 = y_2 - y_1 = z_2 - z_1 = \lambda/10$. Simulation is performed for three locations $d = z_2 - z_0 = \lambda/12,\ \lambda/2,\ \lambda$ of inhomogeneity $Q1$ related to z-axis. Dielectric permittivity $\varepsilon_1 = 1.9$ of diaphragm Q is constant, while permittivity of inhomogeneity is varying $\varepsilon_2 = 1.9 \ldots 15.9$ with step 1. For each simulation transmission coefficient F is calculated. Figure 3 illustrates graph of transmission coefficient F on complex plane. Dielectric permittivity can be uniquely determined from the transmission coefficient F relying on the absence of the curves intersection on in the graph.

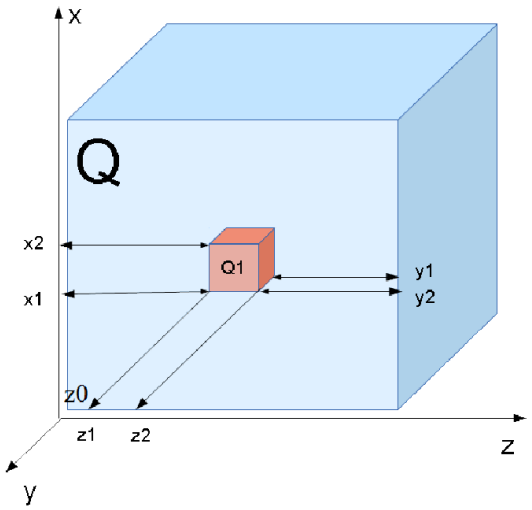

Figure 2: Geometry and location of inhomogeneity Q_1 inside dielectric diaphragm Q.

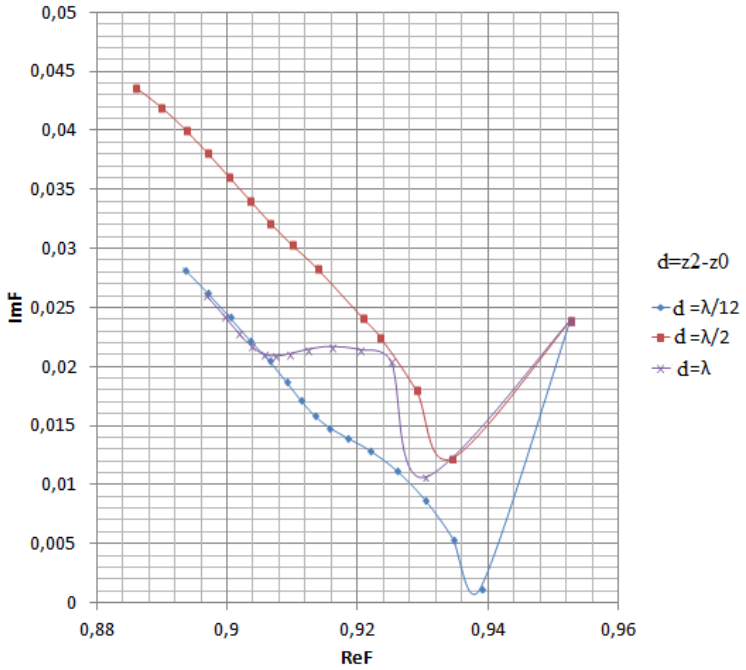

Figure 3: Transmission coefficient F on complex plane for three locations $d = z_2 - z_0 = \lambda/12,\ \lambda/2,\ \lambda$ of inhomogeneity $Q1$ related to z-axis for $\varepsilon_2 = 1.9 \ldots 15.9$ with step 1.

4. CONCLUSION

Scattering in the time domain of electromagnetic waves in the waveguide of rectangular cross section with inhomogeneous single-layered parallel-plane dielectric diaphragm is considered. Electromagnetic field components are computed and investigation of energy transport in the guide is effected by using Finite Difference Time Domain (FDTD) method for different positions of cubic inhomogeneity. Computation for the nonstationary Maxwell equation system is performed by efficient 3D FDTD solver EMWSolver3D created by authors of this paper. Simulation is performed for the H10-mode scattering from dielectric slab inclusions. Numerical computations for solving large-scale problems have been implemented on IBM BlueGene/P. Continuous curves on the complex plane describing the dependence of the transmission coefficient on the dielectric constant are obtained.

ACKNOWLEDGMENT

This work is supported by Russian Foundation for Basic Research (RFFI grant 14-01-00337).

REFERENCES

1. Taflove, A. and S. C. Hagness, *Computational Electrodynamics: The Finite Difference Time-domain Method*, Norwood, 2000.
2. Smirnov, A. P. and A. N. Semenov, "Full wave Maxwell's equations solver EMWSolver3D," *PIERS Proceedings*, 252–255, Moscow, Russia, August 19–23, 2012.
3. Smirnov A., A. Semenov, and Y. Shestopalov, "FDTD simulation of waveguide with non-uniform dielectric slab," *PIERS Proceedings*, 76–78, Stockholm, Sweden, August 12–15, 2013.
4. Gedney, S. D., *IEEE Trans. Antennas Prop.*, Vol. 44, 1630–1639, 1996.
5. Smirnov, Y. G., Y. V. Shestopalov, and E. D. Derevyanchuk, "Permittivity reconstruction of layered dielectrics in a rectangular waveguide from the transmission coefficients at different frequencies," *Inverse Problems Workshop*, Karlstad, Sweden, May 2012.

Efficient Method for Field Coupling to Nonuniform Transmission Line Using Cascaded SPICE Model

Haiyan Xie[1], **Jianguo Wang**[2], **Yong Li**[1], **Hongfu Xia**[1], **and Chun Xuan**[1]

[1]Northwest Institute of Nuclear Technology, P. O. Box 69-12, Xi'an, Shaanxi 710024, China
[2]Northwest Institute of Nuclear Technology, P. O. Box 69-1, Xi'an, Shaanxi 710024, China

Abstract— This paper presents a method of equivalent cascaded SPICE model for external field coupling with nonuniform transmission line. Two nonuniform transmission lines excited by an external EMP with different incidences have been studied to validate its accuracy and efficiency. The results show that the induced voltages obtained by the proposed method agree well with those via the software CST even when the segment number is up to three and the proposed method has higher efficiency. Due to the application of SPICE model and directly computation in the time domain, this method allows for the analysis of nonuniform transmission line terminated with nonlinear loads and integrated circuits.

1. INTRODUCTION

External field coupling through wires or cables is an important coupling path for external field interaction with electronic systems and has attracted many attentions [1, 2].

Due to the fact that many transmission lines are nonuniform, fields coupling to nonuniform transmission lines should be studied. External field coupling with nonuniform transmission lines has been studied by some researchers in the frequency domain, where the method of equivalent cascaded network chain [3], the electromagnetic topology method [4], and transmission-line super theory [5] have been applied. These methods are the frequency-domain method and are not suitable for nonuniform transmission line with nonlinear loads. Three dimensional (3D) numerical method, such as finite-difference time-domain (FDTD) method [6], has been employed to compute lightning-induced voltages on an overhead line [7]. The FDTD method can be applied to compute field coupling with nonuniform transmission line with nonlinear loads. However, the meshes are determined by the minimum size of the line and thus this method is inefficient. To analyze field coupling with transmission lines efficiently in the time domain directly, some SPICE models for external field coupling with transmission lines have been developed [2, 8, 9]. However, these SPICE models are only suitable for uniform transmission lines and nonuniform transmission lines have not been considered.

This paper presents a method of equivalent cascaded SPICE model for external field coupling with nonuniform transmission lines. The accuracy and the efficiency of the proposed method are validated by comparing with the commercial software CST. Due to the direct computation in time domain, this method can be used for the analysis of nonuniform transmission line with nonlinear loads. Moreover, this method allows the analysis of nonuniform transmission line loaded by integrated circuit due to the application of SPICE model.

2. METHOD OF EQUIVALENT CASCADED SPICE MODEL

For transmission line with weak nonuniformity, the coupling with external field can be described by

$$\begin{aligned} \frac{\partial}{\partial z}\mathbf{V}(z,t) + \mathbf{L}(z)\frac{\partial}{\partial t}\mathbf{I}(z,t) &= \mathbf{V}_F(z,t) \\ \frac{\partial}{\partial z}\mathbf{I}(z,t) + \mathbf{C}(z)\frac{\partial}{\partial t}\mathbf{V}(z,t) &= \mathbf{I}_F(z,t) \end{aligned} \quad . \tag{1}$$

Here $\mathbf{V}(z)$ and $\mathbf{I}(z)$ are the line voltage vector and the line current vector, respectively. $\mathbf{L}(z)$ and $\mathbf{C}(z)$ are the per-unit-length (p.u.l.) inductance and capacitance matrices of the line, which are not constant but the functions of the z axis. $\mathbf{V}_F$ and $\mathbf{I}_F$ are distributed voltage and current source vectors which denote the effect of the external fields.

Because $\mathbf{L}(z)$ and $\mathbf{C}(z)$ are the functions of the z axis, (1) can not be decoupled by similarity transformation for general configurations of nonuniform transmission line but only for some certain

configurations of nonuniform transmission line [11]. As a result, different modes are coupled together on nonuniform transmission line and the SPICE model for general nonuniform transmission line can not be derived directly from (1).

Because transmission line equation can not be decoupled by similarity transformation for general configurations, we divide nonuniform transmission lines into several sections and each section are approximated by a uniform transmission line, as shown in Figure 1. Consequently, the nonuniform line can be seen as cascaded series of segments of uniform lines.

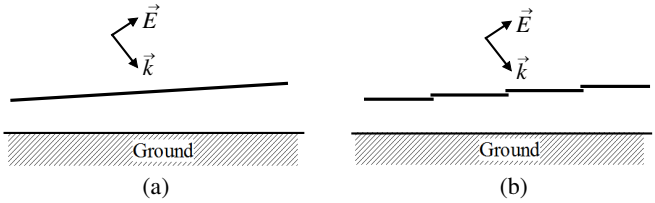

Figure 1: Nonuniform transmission line approximated by cascaded series of many short sections of uniform lines. (a) Nonuniform transmission line. (b) Cascaded series of segments of uniform lines.

The equation for the nth section of uniform line can be written as

$$\begin{aligned} &\frac{\partial}{\partial z}\mathbf{V}_n(z,t) + \mathbf{L}_n\frac{\partial}{\partial t}\mathbf{I}_n(z,t) = \mathbf{V}_{Fn}(z,t) \\ &\frac{\partial}{\partial z}\mathbf{I}_n(z,t) + \mathbf{C}_n\frac{\partial}{\partial t}\mathbf{V}_n(z,t) = \mathbf{I}_{Fn}(z,t) \qquad (n=1,\ldots,N) \end{aligned} . \tag{2}$$

$\mathbf{L}_n$ and $\mathbf{C}_n$ are the inductance and capacitance matrices of nth section and they are constant. N is the number of the sections. For this segment of uniform line, a similar transformation can be applied to decouple the Equation (2) to mode quantities as

$$\begin{aligned} \mathbf{V}_n(z,t) &= \mathbf{T}_{Vn}\mathbf{V}_{mn}(z,t) \\ \mathbf{I}_n(z,t) &= \mathbf{T}_{\mathrm{I}n}\mathbf{I}_{mn}(z,t) \end{aligned} . \tag{3}$$

Then the relation between the terminal mode voltages and currents of the nth section of uniform line can be written as

$$\begin{aligned} \left[\mathbf{V}_{mn}(0,t) - \mathbf{Z}_{Cmn}\mathbf{I}_{mn}(0,t)\right]_i &= \left[\mathbf{V}_{mn}(l_n, t-T_{in}) - \mathbf{Z}_{Cmn}\mathbf{I}_{mn}(l_n, t-T_{ni})\right]_i + \left[\mathbf{V}_{0n}(t)\right]_i \\ \left[\mathbf{V}_{mn}(l_n,t) + \mathbf{Z}_{Cmn}\mathbf{I}_{mn}(l_n,t)\right]_i &= \left[\mathbf{V}_{mn}(0, t-T_{in}) + \mathbf{Z}_{Cmn}\mathbf{I}_{mn}(0, t-T_{ni})\right]_i + \left[\mathbf{V}_{ln}(t)\right]_i \end{aligned} . \tag{4}$$

Here l_n is the length of the nth section of uniform line. $\mathbf{Z}_{Cmn}$ is the mode characteristic impedance diagonal matrix. T_{ni} is the one-way time delay of the ith modal line of the nth section. $\mathbf{V}_{0n}$ and $\mathbf{V}_{ln}$ are the additional source due to external excitation field, which can be realized through delay lines and controlled sources for plane-wave excitation [2] and should be computed numerically for nonuniform-field excitation [8]. Then the SPICE model for the nth segment of uniform line can be developed and is shown in Figure 1.

Because these uniform segments are cascaded to approximate nonuniform transmission line. The voltages and currents at the node, which connects two adjacent segments of uniform line, and terminals satisfy the relation defined by

$$\begin{aligned} &\mathbf{V}_{n-1}(l_{n-1}) = \mathbf{V}_n(0), \quad &&\mathbf{I}_{n-1}(l_{n-1}) = \mathbf{I}_n(0) \\ &\mathbf{V}_1(0) = \mathbf{V}(0), &&\mathbf{I}_1(0) = \mathbf{I}(0) \\ &\mathbf{V}_N(l_N) = \mathbf{V}(l), &&\mathbf{I}_N(l_N) = \mathbf{I}(l) \end{aligned} , \tag{5}$$

where l is the length of the nonuniform transmission line. As a result, the equivalent cascaded SPICE model for nonuniform transmission line is given in Figure 1.

The segment number N is an important parameter for this method, which determines the accuracy and efficiency of this method. Enough sections should be divided to ensure the good approximation of the nonuniform transmission line. However, some researches do not show that the more segments the better [12]. Too much segments will increase the computation complexity and numerical faults. Thus an appropriate segment number N should be chosen to ensure the accuracy

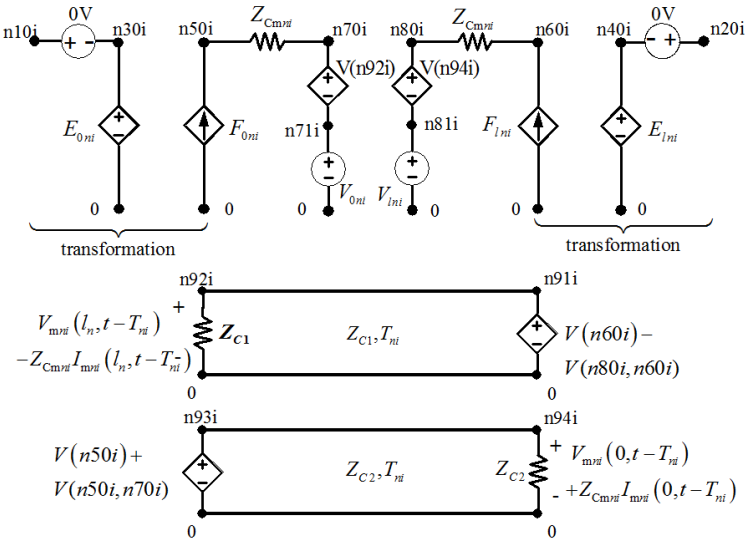

Figure 2: SPICE model for nth section of uniform line.

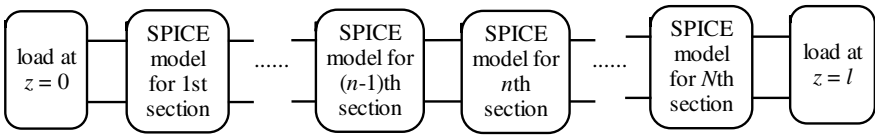

Figure 3: Cascaded SPICE model for nonuniform transmission line.

and efficiency. In this paper, the self-adapting method is applied to determine the segment number N.

After the equivalent cascaded SPICE model for nonuniform transmission line is developed and the terminal connections are defined, a SPICE software can be employed to obtain the voltages induced on the loads by an external field.

3. NUMERICAL VALIDATION

Nonuniform single-conductor and multiconductor transmission lines excited by an external electromagnetic pulse (EMP) have been studied by using the proposed method. The external EMP is a bi-exponential pulse and defined by $E(t) = kE_0[\exp(-\beta t) - \exp(-\alpha t)]$, where $k = 1.3$, $E_0 = 50\,\mathrm{kV/m}$, $\alpha = 6.0 \times 10^8\,\mathrm{s}^{-1}$, and $\beta = 4.0 \times 10^7\,\mathrm{s}^{-1}$. In order to validate the accuracy and efficiency of the proposed method, the results of different segment numbers are compared with those via the microwave studio of CST. All the computations are carried out on a personal desktop.

A nonuniform single-conductor transmission line with the radius of 1 mm and the length of 1 m excited by the EMP with a perpendicular incidence is shown in Figure 4. The heights of the line over the ground at the near and far ends are $h_1 = 0.5\,\mathrm{cm}$ and $h_2 = 3.5\,\mathrm{cm}$, respectively. The terminal loads R_1 and R_2 are $50\,\Omega$.

Figure 1 shows the induced voltages at R_1 and R_2 obtained by the cascaded SPICE model when the segment number N equals 1, 3, and 5, comparing with those via the software CST. When the segment number $N = 1$, the whole nonuniform line is considered as a uniform transmission line. The results show that the induced voltages at R_1 and R_2 obtained by the proposed method are in

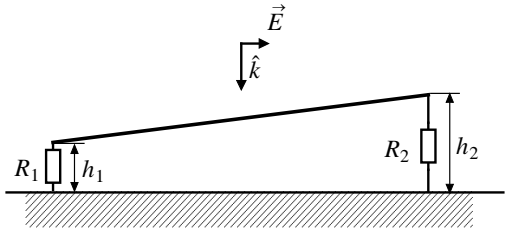

Figure 4: Nonuniform single-conductor transmission line excited by an EMP with perpendicular incidence.

a good agreement with those via CST even when the segment number N equals 3 and the results when $N = 3$ have little difference with those when $N = 5$. This implies that the approximation of three segments of uniform line is sufficient for this nonuniform line.

The time taken by the proposed method and CST is compared in Table 1. The cost time of the proposed method when $N = 3$ and $N = 5$ are 1.92 s and 2.88 s, respectively, while the time taken by CST is 4.2 h, where the smallest mesh size is 2 mm and the number of mesh cells is 215,136. It can be concluded from these results that the proposed method has good accuracy and efficiency for the nonuniform single-conductor transmission line.

A nonuniform multiconductor transmission line excited by the EMP with a horizontal incidence, as shown in Figure 6, are also studied by using the proposed method to validate its ability for nonuniform multiconductor transmission line. The nonuniform multiconductor transmission line consists of two wires with the radius of 1 mm, the length l of 2 m, and the height h of 2 cm. The distances between the two wires at the near and far ends are $D_0 = 1$ cm and $D_l = 5$ cm, respectively. All the loads are 50 Ω.

Figure 7 shows the induced voltages at R_{01} and R_{l1} obtained by the cascaded SPICE model when the segment number N equals 1, 3, and 5, comparing with those via the software CST. The results show that the induced voltages at R_{01} and R_{l1} obtained by the proposed method when $N = 3$ have little difference with those when $N = 5$ and they agree well with those via the software CST.

The time taken by the two method are given in Table 2. The time taken by the proposed method when $N = 3$ and $N = 5$ are 3.91 s and 7.61 s, respectively, much shorter than 8.8 h taken by CST, where the smallest mesh size is 1 mm and the number of mesh cells is 257,040. It can be concluded from these results that the proposed method also has good accuracy and efficiency for the nonuniform multiconductor transmission line.

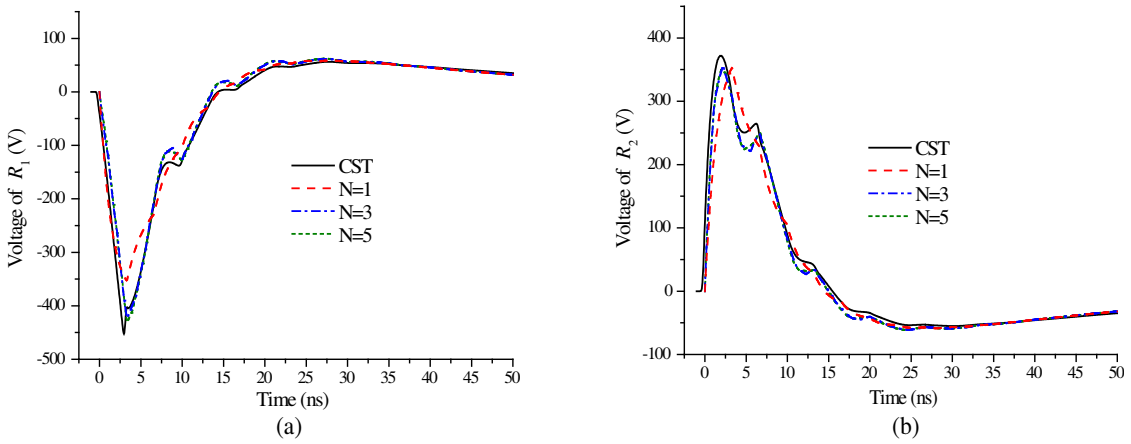

Figure 5: Induced voltages of nonuniform single-conductor transmission line when the EMP has a perpendicular incidence. (a) Voltage of R_1. (b) Voltage of R_2

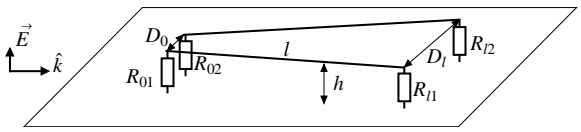

Figure 6: Nonuniform multiconductor transmission line excited by an EMP with horizontal incidence.

Table 1: Cost time of the proposed method and CST for nonuniform single-conductor transmission line.

	Cost time
Proposed method ($N = 3$)	1.92 s
Proposed method ($N = 5$)	2.88 s
CST	15061 s ≈ 4.2 h

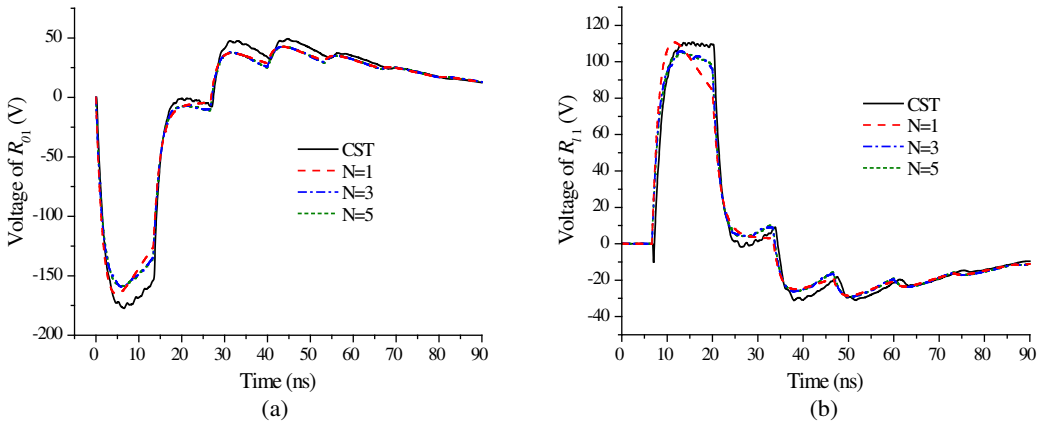

Figure 7: Induced voltages of nonuniform muticonductor transmission line when the EMP has a horizontal incidence. (a) Voltage of R_{01}. (b) Voltage of R_{l1}.

Table 2: Cost time of the proposed method and CST for nonuniform multiconductor transmission line.

	Cost time
Proposed method ($N = 3$)	3.91 s
Proposed method ($N = 5$)	7.61 s
CST	31514 s $\approx$ 8.8 h

4. SUMMARY AND CONCLUSION

A method of equivalent cascaded SPICE model has been presented for external field coupling to nonuniform transmission line. Nonuniform single-conductor and multiconductor transmission lines excited by an external EMP with different incidences have been studied by using this method. The results show that the induced voltages obtained by the proposed method are in a good agreement with those via the software CST even the segment number N is up to 3 and the proposed method is more efficient than CST. Due to the application of SPICE model, this method can be employed in time domain directly and allows for the analysis of nonuniform transmission line loaded with nonlinear loads and integrated circuits.

ACKNOWLEDGMENT

Acknowledgement is made to National Natural Science Foundation of China for the support of this research through Grant No. 61201090 and No. 61231003.

REFERENCES

1. Tesche, F. M., M. V. Ianoz, and T. Karlsson, *EMC Analysis Methods and Computational Models*, Wiley, New York, 1997.
2. Paul, C. R., *Analysis of Multiconductor Transmission Lines*, 2nd Edition, John Wiley & Sons, Inc., New Jersey, 2008.
3. Omid, M., Y. Kami, and M. Hayakawa, "Field coupling to nonuniform and uniform transmission lines," *IEEE Trans. Electromagn. Compat.*, Vol. 39, No. 3, 201–211, 1997.
4. Besnier, P. and P. Degauque, "Electromagnetic topology: Investigations of nonuniform transmission line networks," *IEEE Trans. Electromagn. Compat.*, Vol. 37, No. 2, 227–233, 1995.
5. Haase, H., T. Steinmetz, and J. Nitsch, "New propagation models for electromagnetic waves along uniform and nonuniform cables," *IEEE Trans. Electromagn. Compat.*, Vol. 46, No. 3, 345–352, 2004.
6. Taflove, A., *Computational Electrodynamics, The Finite Difference Time-domain Method*, Artech House, Boston, 1995.
7. Sumitani, H., T. Takeshima, Y. Baba, et al., "3-D FDTD computation of lightning-induced voltages on an overhead two-wire distribution line," *IEEE Trans. Electromagn. Compat.*, Vol. 54, No. 5, 1161–1168, 2012.

8. Xie, H., J. Wang, R. Fan, and Y. Liu, "A hybrid FDTD-SPICE method for transmission lines excited by a nonuniform incident wave," *IEEE Trans. Electromagn. Compat.*, Vol. 51, No. 3, 811–817, 2009.
9. Xie, H., J. Wang, R. Fan, et al., "SPICE models to analyze radiated and conducted susceptibilities of shielded coaxial cables," *IEEE Trans. Electromagn. Compati.*, Vol. 52, No. 1, 215–222, 2010.
10. Baum, C. E., *Nonuniform Multiconductor Transmission Lines*, 516, Interaction Notes, 1996.
11. Nitsch, J., C. E. Baum, and R. Sturm, "Analytical treatment of circulant nonuniform multiconductor transmission line," *IEEE Trans. Electromagn. Compati.*, Vol. 34, No. 1, 28–38, 1992.
12. Zeng, Z., "Approximate series solutions of pulse waveforms and transmission efficiencies of exponential transmission line," *High Power Laser and Particle Beams*, Vol. 38, No. 8, 2247–2251, 2011.

Reduced Vlasov-Maxwell Modeling

P. Helluy[1], **M. Massaro**[2], **L. Navoret**[1], **N. Pham**[2], **and L. T. Strub**[3]

[1]University of Strasbourg & Inria Tonus, France
[2]University of Strasbourg, France
[3]AxesSim, France

Abstract— We describe CLAC (Conservation Laws Approximation on many Cores), a generic Discontinuous Galerkin (DG) solver for three-dimensional electromagnetic simulations. The solver runs on clusters of GPUs, it is based on hybrid parallelism using the OpenCL and MPI libraries. We explain how to solve the Vlasov-Maxwell equations with this tool. We present several numerical results.

1. INTRODUCTION

CLAC is a generic DG solver for conservation laws. The structure of the underlying hyperbolic system is described in an abstract manner. It can run on GPU clusters and it uses the MPI library for communications between GPUs in the cluster and OpenCL for driving the GPUs. The CLAC solver is very efficient for simulating industrial EM devices.

In plasma physics or beam physics applications, it is important to couple the Maxwell model with the Vlasov model, which describes the motions of charged particles. The unknown of the Vlasov equation is the distribution function of the charged particles, which depends on time and on a six-dimensional space-velocity variable.

In order to harness our multi-GPU solver we reduce the Vlasov equation to a space-only first order hyperbolic system compatible with the Maxwell model. We compute the coupled system with the generic DG solver.

We present two-dimensional and three-dimensional numerical simulations for the Maxwell or the Vlasov-Maxwell equations.

2. DG FOR CONSERVATION LAWS

2.1. Conservation Laws

We consider a very general system of conservation laws

$$\partial_t W + \partial_i F^i(W) = S(W). \tag{1}$$

In this system, the unknown is a vector of conservative variables $W(x,t) \in \mathbb{R}^m$ that depends on the space variable $x = (x_1, x_2, x_3) \in \mathbb{R}^3$ and on the time t. We use the convention of sum on repeated indices. The source term is denoted by S. For a vector $n = (n_1, n_2, n_3) \in \mathbb{R}^3$ we shall also define the flux function by

$$F(W, n) = F^i(W) n_i. \tag{2}$$

The Maxwell equations enter this framework. In dimensionless form, They read

$$\partial_t E - \nabla_x \times H = -J, \tag{3}$$
$$\partial_t H + \nabla_x \times E = 0, \tag{4}$$

where E is the electric field, H the magnetic field and J the electric current. If we set

$$W = \left(E^T, H^T\right)^T, \quad S = \left(-J^T, (0,0,0)^T\right)^T,$$

and

$$F(W, n) = \begin{bmatrix} 0 & -n\times \\ n\times & 0 \end{bmatrix} W,$$

then the Maxwell equations are a particular case of (1), with $m = 6$.

2.2. General DG Formalism

The DG approximation is defined on a mesh of the computational domain Ω. We consider a mesh made of a finite number of open cells. Let L and R be two neighbor cells. We denote by n_{LR} the unit normal vector on $\partial L \cap \partial R$ oriented from L to R.

In each cell L, we consider a basis of scalar function φ_i^L, $i = 1, \ldots, p_L$ with support in L. It is possible to take different approximation order p_L on different cells. In cell L, the solution of (1) is approximated by

$$W(x,t) = W_L(x,t) = W_L^j(t)\varphi_j^L(x) \quad X \in L. \tag{5}$$

The numerical solution satisfies the DG approximation scheme (see for instance [1–3] and included references)

$$\forall L, \forall i \quad \int_L \partial_t W \varphi_i^L - \int_L F\left(W, \nabla_x \varphi_i^L\right) + \int_{\partial L} F\left(W_L, W_R, n_{LR}\right) \varphi_i^L = \int_L S\varphi_i^L. \tag{6}$$

In practice the integrals on L or ∂L are perform numerically with Gauss-Legendre quadrature and the basis functions φ_i^L form an interpolation basis associated to the quadrature points in L.

Because W is discontinuous at the cell boundaries, it is not possible to define $F(W, n_{LR})$ on ∂L. Therefore, as in the finite volume method, we have to introduce a numerical flux $F(W_L, W_R, n_{LR})$. In practice, for stability reasons, we prefer an upwind numerical flux.

Introducing expansion (5) into (6) we obtain a system of ordinary differential equations satisfied by the basis coefficients $W_L^j(t)$. We solve the differential equations with a standard second order Runge-Kutta integrator.

3. REDUCED VLASOV-MAXWELL

In addition to the Maxwell equations, we can consider the motion of charged particles accelerated by the EM field. The distribution function $f(x,v,t)$ counts the particles at time t and position x having a velocity $v = (v^1, v^2, v^3)$. We denote by D the velocity domain, $v \in D$. The distribution function satisfies the Vlasov equation (written in dimensionless form)

$$\partial_t f + \nabla_x \cdot (fv) + \nabla_v \cdot (f(E + v \times H)) = 0. \tag{7}$$

The electric current J appearing in the Ampre equation is then given by

$$J = \int_{v \in \mathbb{R}^3} fv dv.$$

The difficulty is that the Vlasov Equation (7) is set in a six-dimensional space. We propose a simple reduction procedure that allows to rewrite the Vlasov-Maxwell system under a system of conservations laws in the standard physical three-dimensional space. In this way we can apply our generic DG solver.

For this purpose, we consider a finite number of continuous basis functions depending on the velocity v

$$\varphi_i(v), \quad i = 1, \ldots, P.$$

We assume that the velocity domain is large enough so that the basis functions vanish on the boundary of the velocity domain

$$v \in \partial D \Rightarrow \varphi_i(v) = 0.$$

We expand the distribution function in this basis

$$f(x,v,t) \simeq \sum_{j=1}^{P} f^j(x,t)\varphi_j(v) = f^j\varphi_j.$$

We insert this representation into the Vlasov Equation (7), multiply by φ_i and integrate on the velocity domain D.

Defining the following $P \times P$ matrices

$$M_{i,j} = \int_v \varphi_i\varphi_j, \quad A_{i,j}^k = \int_v \varphi_i\varphi_j v^k, \quad B_{i,j} = -\int_v (E + v \times H) \cdot \nabla_v \varphi_i \varphi_j, \tag{8}$$

the Vlasov equation can be rewritten in the reduced form

$$M\partial_t w + A^k \partial_k w + Bw = 0, \quad w = \left(f^1, \ldots, f^P\right)^T. \tag{9}$$

The form (9) is called the reduced Vlasov equation. It is a first order hyperbolic system of conservation laws [4] that can also be solved by the standard DG solver. For practical reasons it is important to provide an efficient choice of basis functions φ_i. A good choice ensures a small number of basis functions P and that the matrices M, A^k and B are sparse. In practice, we use an adequate choice of numerical quadrature that leads to diagonal matrices M and A^k [5].

4. HYBRID OPENCL/MPI PARALLELISM

4.1. OpenCL Parallelization

OpenCL library provides a model of parallel computing which can be used to drive GPUs and multicore accelerators. It is very similar to CUDA.

In this model, the memory is divided into global memory of some gigabytes with slow access and local cache memory of a few tens of kilobytes with quick access. Computations are performed by many "work-items" having access to all the global memory. The work-items are grouped into "work-groups" with common local memory.

All work-items execute the same program, called "kernel". Each work-item is identified by an index for parallelization.

The mesh is first split into several subdomains. Each subdomain is handled by one MPI node, associated to one GPU.

The OpenCL algorithm is divided into stages, each carried out by a specific kernel. These steps are (1) the calculation of the volume integral $\int_L F(W, \nabla\varphi_i^L)$ for each basis function φ_i^L, (2) the calculation of the surface integral $\int_{\partial L} F(W_L, W_R, n_{LR})\varphi_i^L$ for each basis function φ_i^L and (3) the Runge-Kutta step.

In the different OpenCL kernels participating to the element computations, the number of work-items depends on the degree of interpolation of the element.

A strategy for grouping elements of the same order into homogeneous zones is implemented. In this way the work-items of a same zone perform exactly the same operations, which improve the GPU efficiency.

4.2. MPI Parallelization

MPI allows us to parallelize computations on distributed memory architecture by launching multiple process which communicate between each others. We perform a subdivision of the mesh into sub-domains. During the simulation, the boundary cells data are exchanged between sub-domains thanks to MPI send and receive operations. Before the MPI exchanges, the boundary data have also to be copied between the GPU and the CPU, which increases the simulation cost compared to other MPI parallel algorithms.

In order to avoid performance waste, we have implemented an asynchronous task graph in CLAC. This graph task allows to computing the interior of the zones while the boundaries are exchanged between the MPI nodes.

5. NUMERICAL RESULTS

In this section, we present the results obtained with three test cases.

5.1. EM Simulation

The objective of this test case is to evaluate the MPI scalability of the computation.

We consider the mesh of a domain containing a generic airplane. The mesh is made of more than 3×10^6 hexaedrons with an second order approximation. This represents more than 10^9 degrees of freedom per time step. The airplane is illuminated by a plane wave with Gaussian profile polarized in E_y. The computational domain is surrounded by PML layers.

We use 8 NVIDIA K20 GPUs to perform the computation. The simulation does not fit into a single GPU memory. We obtain a time per iteration of 1.73 s, which represents 362 Gflops. In this test case, if we deactivate the asynchronous graph task, we spend about 30% of the computation time in the memory transfers between the CPU and the GPU and about 20% in the MPI communications.

We plot on Figure 1 the surface current $|n \times H|$ on the body of the airplane at time 51 ns.

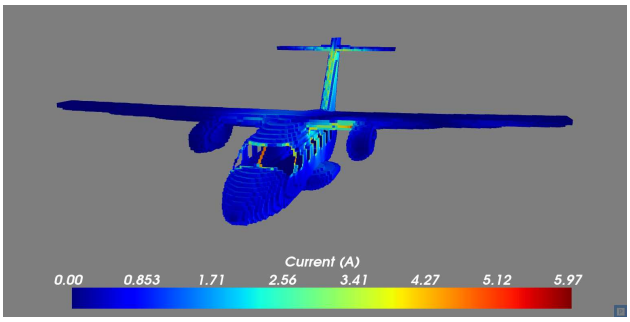

Figure 1: Generic airplane, current on the fuselage at time 51 ns.

5.2. Two-stream Instability

In this example we test the validity of the reduced Vlasov model in a simplified one-dimensional situation. The initial distribution function represents two Gaussian beams of charged particles moving in opposites directions. The distribution is a stationary solution of the Vlasov-Maxwell system. We add a small perturbation in order to trigger instability.

$$f_0(x,v) = (1+\epsilon\cos(kx_1))\frac{1}{2\sqrt{2\pi}}\left(e^{-\frac{(v_1-v_0)^2}{2}} + e^{-\frac{(v_1+v_0)^2}{2}}\right).$$

The value of parameters for this test case are $k = 0.2$, $\epsilon = 5\times10^{-3}$ and $v_0 = 3$. In the one-dimensional Maxwell equations, we consider a very large speed of light, which leads in practice to the resolution of the Poisson equation.

We compare our reduced Vlasov-Poisson method to a well-validated Particle-In-Cell (PIC) scheme [6]. The distribution function is plotted at time $t = 25$ and $t = 50$ in Figures 2. We observe an excellent agreement between the two approaches [4, 7].

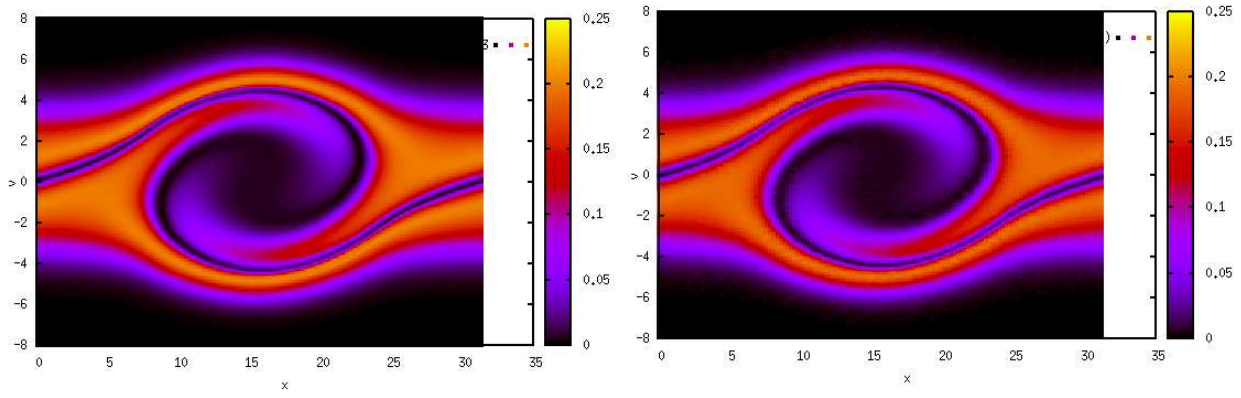

Figure 2: The distribution function of the two-stream test case at time $t = 25$. The first coordinate is the space coordinate x_1. The second coordinate is the velocity v_1. (a) Reduced Vlasov-Poisson method. (b) The PIC method.

5.3. Reduced Vlasov-Maxwell

In this section, we present preliminary Vlasov-Maxwell numerical results obtained with the reduced approach in two dimensions. We consider a cloud of charged particles in the center of a square domain Ω. Because the particles repel each other, the cloud expands with time. We plot the evolution of the total charge in the domain at different times. We also represent the distribution function in the velocity space at a given point $(x_1, x_2) = (0.37, 0.5)$. The initial distribution function is

$$f(x_1,x_2,v_1,v_2,0) = -q(x_1)q(x_2)q(v_1)q(v_2),$$

where the smooth function q has its support in $[-1/2, 1/2]$ and satisfies $\int_{r=-\infty}^{\infty} q(r)dr = 1$. On the boundary of Ω, we apply homogeneous Silver-Müller conditions. We use a mesh of Ω with

$8 \times 8 = 64$ cells. The velocity mesh is of order $d = 2$. It contains 305 Gauss-Lobatto nodes. We plot the charge evolution on Figure 3.

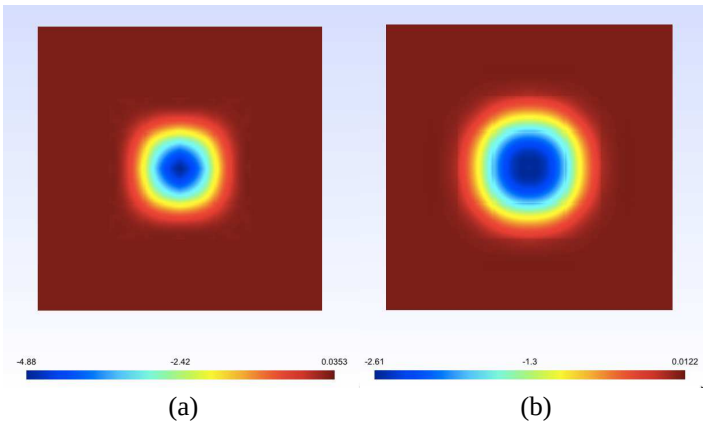

Figure 3: evolution of the charge in the computational domain, (a) $t = 0$, (b) $t = 0.5$.

It would be also possible to plot other quantities, such as the EM field or the dependance of the distribution in the velocity space

6. CONCLUSION

We have presented CLAC, an electromagnetic simulation tool. This tool is intended for industrial practical computations. It is accelerated by two parallelism technologies: MPI and OpenCL, which allows to run CLAC on GPU clusters.

The design of the software is generic, in such a way that it can potentially solve any non-linear hyperbolic system of conservation laws. We have then proposed a reduction technique that allows to rewriting the six-dimensional Vlasov equation as a three-dimensional hyperbolic system. We have presented preliminary one-dimensional and two-dimensional numerical results obtained with this reduction approach.

ACKNOWLEDGMENT

This work has benefited from several supports: from the french defense agency DGA, from the Labex ANR-11-LABX-0055-IRMIA and from the AxesSim company.

REFERENCES

1. Bourdel, F., P. A. Mazet, and P. Helluy, "Resolution of the non-stationary or harmonic Maxwell equations by a discontinuous finite element method. Application to an E.M.I. (electromagnetic impulse) case," *Proceedings of the 10th International Conference on Computing Methods in Applied Sciences and Engineering*, 405–422, 1992.
2. Cohen, G., X. Ferrieres, and S. Pernet, "A spatial high-order hexahedral discontinuous Galerkin method to solve Maxwell's equations in time domain," *Journal of Computational Physics*, Vol. 217, No. 2, 340–363, 2006.
3. Klöckner, A., T. Warburton, J. Bridge, and J. S. Hesthaven, "Nodal discontinuous Galerkin methods on graphics processors," *J. Comput. Phys.*, Vol. 228, No. 21, 7863–7882, 2009.
4. Helluy, P., N. Pham, and A. Crestetto, "Space-only hyperbolic approximation of the Vlasov equation," *ESAIM: Proceedings*, Vol. 43, 17–36, 2013.
5. Helluy, P., L. Navoret, N. Pham, and A. Crestetto, "Reduced Vlasov-Maxwell simulations," http://hal.archives-ouvertes.fr/hal-00957045, Mar. 2014.
6. Birdsall, C. K. and A. B. Langdon, "Plasma physics via computer simulation, institute of physics (IOP)," *Series in Plasma Physics*, 1991.
7. Helluy, P., N. Pham, and L. Navoret, "Hyperbolic approximation of the Fourier transformed Vlasov equation," 2014, http://hal.archives-ouvertes.fr/hal-00872972.

A Fast Algorithm for Calculating Complex Targets Near-field EM Scattering Characteristics

Yanjie Cui, Wenqiang Chen, Xiangyang Zhang, Jianping Zheng, and Bai Yang
Science and Technology on Electromagnetic Scattering Laboratory, Beijing 100854, China

Abstract— In order to meet the requirements of fuse's digital simulation and hard-ware-in-the-loop simulation, a fast algorithm based on the electromagnetic scattering modeling techniques of complex targets in the near field is proposed to calculate the echo power of fuse. The main research work in this paper involves the followings: (1) Considering the influence of antenna pattern and distance as well as spherical wave irradiation, a method established by the PO and PTD and GO methods is presented for electromagnetic scattering modeling of complex targets in the near field. (2) In the filed of EM scattering theory of complex targets for missile-target encounter, the EM scattering model of complex targets is introduced to missile-target encounter model. The relative system of coordinates is established to describe missile-target encounter with parallel track. The system of coordinates of a rocket and the system of coordinates of a target are established to describe polarization and antenna pattern located on the rocket. The system of coordinates of the elementary reflector coordinates is established to calculate EM scattering of the elementary reflector in the near field. The system of coordinates of the target is established to calculate EM scattering after transforming the movement parameter and electromagnetic parameter which are in others system of coordinates into the system of coordinates of the target. (3) A fast algorithm is put forward to calculate the echo power of fuse in the near-field. Numerical results prove its high efficiency and preciseness. The goal of this paper is to calculate EM scattering in any missile-target encounter conditions for fuse's digital simulation and hard-ware-in-the-loop simulation and the proposed method would be especially valuable in engineering application.

1. INTRODUCTION

The near-field characteristics of target echo of fuse are very important for fuse's digital simulation. Nowadays, domains of current domestic and overseas researchers have focused on the study of the near-field target characteristic of the fuse, including the study on measurement and algorithm for calculating echo power of fuse. The simulation algorithms are based on PO and PTD method to calculate the echo power of the geometrical elements which are illuminated by radar beam during missile target encounter [1]. But the methods mentioned above cost a lot of time for calculating just one trajectory of the target. However, we often need hundreds of simulation results of echo power under different trajectories for fuse's digital simulation. Inevitably there are serious specific problem. Therefore use of principles, methods should be improved to enhance the numeration efficiency.

This article investigates a new method by dividing the target into several independent cubes and using the PO and PTD and GO methods to calculate the RCS of each cube. Then calculate the echo power of fuse by integrating those of the geometrical elements which are illuminated by radar beam during missile target encounter. Because the RCS of the cubes can be calculated beforehand and store in the database, it would dramatically reduced the time expenses. At the same time, the RCS store in the database can be used in various of conditions of missile target encounter. And the emulation results show that the general time of calculation of echo power of fuse from fast algorithm on all trajectory of the target is less than 1 sec. And the proposed method would be especially valuable in engineering application.

2. METHOD OF MODELING OF NEAR-FIELD ELECTROMAGNETIC SCATTERING

We will introduce the basic principles of method of modeling of near-field electromagnetic scattering before the introduction of fast algorithm. The scattering field of facets and wedges is computed by Physical Optics (PO) and Physical Theory of Diffraction (PTD) and multi-scattering of facets and facets is calculated by Geometrical Optics (GO) and PO.

2.1. Calculation of the Scattering Field of Facets

At first we should divide the surface of the target into small plane triangular elements and make sure the maximal dimension should according to qualification of the PO method [2, 3] ($L_{\max} \leq \lambda/5$) and the criterion of a far zone [4] ($L_{\max} \leq \sqrt{R/2\lambda}$), where λ represents length of wave, $L_{\max}$ represents

the maximal dimension of triangular elements, R represents limiting distance between object and radar.

Referring to the methods of literature [5], the electric field of irradiating wave can be represented as

$$\mathbf{E}_i = \frac{\exp\left(i[\omega t + k\left(R_{im} + \rho \cdot \hat{\mathbf{r}}_i\right)]\right)}{R_{im}} \hat{\mathbf{e}}_i \tag{1}$$

where $k = 2\pi/\lambda$ — wave number, ρ — vector which has been directed from the beginning of coordinates of triangular element in one points on a surface of a triangle, R_{im} — distance from the beginning of system of coordinates of triangle up to the phase center of the transmitting antenna.

The electric field of scattering wave can be represented as:

$$\mathbf{E}_{po} = \frac{ik}{4\pi} \int\limits_S \mathbf{T} \frac{\exp\left(ik\left(R_{im} + R_{sm} - \mathbf{q} \cdot \rho\right)\right)}{R_{im} R_{sm}} dS \tag{2}$$

where $\mathbf{T} = (\hat{\mathbf{n}} \times \mathbf{H}_{\sum}) - [(\hat{\mathbf{n}} \times \mathbf{E}_{\sum}) \times \hat{\mathbf{r}}_{\mathbf{s}}]$, $\mathbf{E}_{\sum} = \mathbf{E}_i + \mathbf{E}_s$ represents sum of the electric field, $H_{\sum} = H_i + H_s$ represents sum of the magnetic field, $\mathbf{q} = \hat{\mathbf{r}}_{\mathbf{s}} - \hat{\mathbf{r}}_i$ represents incremental directed vector, ρ — vector directed from the beginning of coordinate system of triangle to point of surface of triangle, R_{sm} — distance from the beginning of system of coordinates of triangle up to the phase center of the receiving antenna, r_i represents the directing vector of the irradiating wave, r_s represents the directing vector of the reflection wave.

2.2. Calculation of the Scattering Field of Wedges

According to Physical Theory of Diffraction (PTD) [6], the scattering field of wedges can be represented as:

$$\mathbf{E}_d = \frac{\mathrm{j}k}{4\pi} \oint\limits_l \left\{ [\hat{\mathbf{r}}_s \times (\hat{\mathbf{r}}_s \times \mathbf{J}_e)] + ik(\hat{\mathbf{r}}_s \times \mathbf{J}_m) \right\} \varphi(\hat{\mathbf{r}}_s)\, \mathrm{d}l \tag{3}$$

$\mathbf{r}_s$ represents the directing vector of the reflection wave. $\mathbf{J}_e$, $\mathbf{J}_m$ are defined from the following formulas:

$$\mathbf{J}_e = -\frac{2F}{ik} \frac{\left(\mathbf{E}_i \cdot \hat{\mathbf{t}}\right) \cdot \hat{\mathbf{t}}}{\sin\gamma_i \sin\gamma_s}, \quad \mathbf{J}_m = -\frac{2G}{ik} \frac{\left(\mathbf{H}_i \cdot \hat{\mathbf{t}}\right) \cdot \hat{\mathbf{t}}}{\sin\gamma_i \sin\gamma_s} \tag{4}$$

where F, G — coefficients of diffraction of Ufimtsev, γ_i and γ_s, — spatial angle between directing vectors r_i and r_s and a vector $t = \{0, 0, 1\}$.

2.3. Calculation of the Multi-scattering Field of Facets and Facets

The problem of an estimation of contributions double reflections between triangles is solved on the basis of technology of the "Shooting and bouncing rays" (SBR). The physical sense of the theory consists that the field falling on some triangular element of a surface, does not scattering in surrounding space, but reflected by laws of GO in a direction of other triangular element and induced on it secondary electromagnetic waves. Thus reflection of waves between triangles is considered on the basis of plane equivalent apertures. As the aperture the plane triangle projected on a plane, orthogonal to mirror reflected ray is considered. The primary goal is definition of amplitude and polarization of an electromagnetic wave reflected from the first triangular element to the second. The integral of physical optics is calculated on the area of the second triangle accepting reflected wave, the multi-scattering field can be represented as:

$$\sigma = 4\pi R_{sm}^2 \frac{|\mathbf{E}_s|^2}{|\mathbf{E}_i|^2} \tag{5}$$

where σ represents RCS of multi-scattering field and $\mathbf{E}_i$ represents the transmitting electric field, and $\mathbf{E}_s$ represents the receiving electric field. And R_{sm} represents the distance from the beginning of system of coordinates of triangle up to the phase center of the receiving antenna.

2.4. Modeling of Near-field Electromagnetic Scattering in Missile-target Encounter

There are four systems of coordinates need to be found: system of coordinates of relative positioning of a rocket and the aerodynamic target, system of coordinates of the target and system of coordinates of the antenna and system of coordinates of the elementary reflector (ER) in The

trajectory of relative movement of the target represents the direct line. The relative system of coordinates is established to describe missile-target encounter with parallel track. In SCT calculation of intensity of a resulting field of scattering of object is carried out, and in system of coordinates of the antenna basis of the irradiating and reflected waves in a direction on ER are formed. In system of coordinates of ER calculation of intensity of a field of scattering of the reflector is carried out. For definition basis of the irradiating and reflected waves should be set in system of coordinates of ER. Then according to the formula (2) and formula (3) as well as formula (5), we can derive total near-field EM scattering characteristics in missile-target encounter.

3. FAST ALGORITHM FOR CALCULATING NEAR-FIELD EM SCATTERING CHARACTERISTICS

The method mentioned above cost a lot of time for calculating just one trajectory of the target. This article investigates a new method calculate the echo power of fuse.

We use multipoint model and the target is represented as a set of projective cubes, each of which limits the certain element of a surface of the target (Fig. 1). To each of cubes the local point is appointed. This point is formed as an average point of all triangular elements getting in limits of the given cube. In other words, representation of the purpose as a set of cubes corresponds to its representation as a set of local points $P_k,\ k = 1, \ldots, N_p$. The amount of cubes (local reflectors) is defined from a condition of maintenance of required resolution on any parameter of a signal and accuracy of operation of fuse. On Fig. 1, the model of airplane consisting of 20 cubes (local points) is shown. Thus the fuselage of the plane is submitted by set of 8 points laying on an axis of the plane, and each of wings — accordingly from 6 points. To each of cubes there corresponds a file of triangular elements and the sharp edges getting in area of the given cube.

After dividing the target into several independent cubes, then we use the PO and PTD and GO methods to calculate the RCS of each cube. Calculation of RCS is carried out for corners of an azimuth $\alpha_i = \{0^\circ \sim 360^\circ\}$ and corners of a vision $\beta_i = \{0^\circ \sim 360^\circ\}$ in local system of coordinates of a reflector for the set distance R from the antenna to a local reflector. In multipoint model for each local reflector the array of values of RCS in local system of coordinates $\sigma_{ij} = \sigma\ (\alpha_i,\ \beta_j)$ is formed. As shown in Fig. 3. According to representation of the target as a set of local reflectors

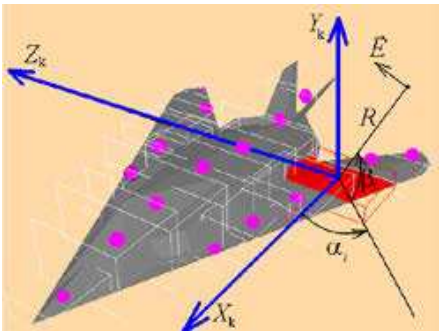

Figure 1: Formation of multipoint target on the base of its fast algorithm.

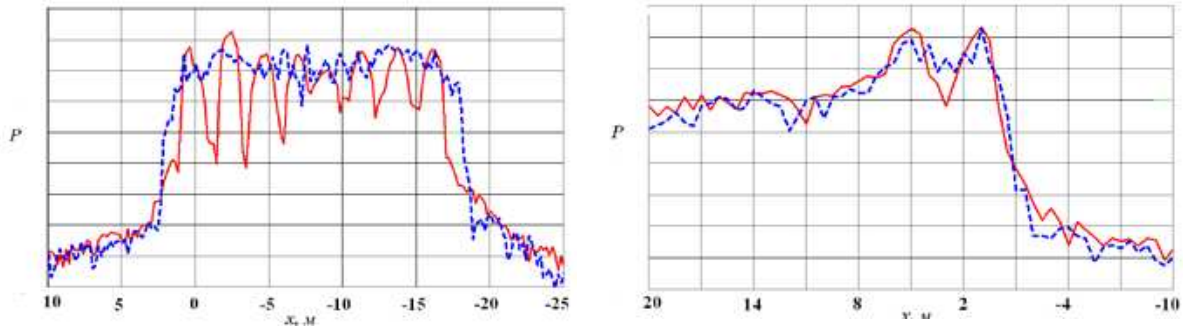

(a) Angel of the beams is 90°

(b) Angel of the beams is 45°

Figure 2: Power of fuse in dependence from coordinate X of airplane model (Continuous line — fast algorithm, Shaped line — traditional algorithm).

power of input signal of fuse we shall consider as:

$$P = \frac{P_i D_i D_s \lambda^2}{(4\pi)^2} \left| \sum_{m=1}^{N_p} \frac{F_{im} F_{sm} \sqrt{\frac{\sigma_m}{4\pi}} \exp(i\varphi_m)}{R_m^2} \right|^2 \tag{6}$$

where N_p — number of local points of the target, $\sigma_m = \sigma_{i,j}$ — the array of values of RCS of the multipoint model for each local reflector, F_{im}, F_{sm} — values of the normalized functions of direction of transmitting and reception aerials in a direction on local point, located on distance R_m from the conditional (phase) center of aerials.

Because the RCS of the cubes can be calculated beforehand and store in the database, the formula (6) leave out the process for calculating RCS of every facets of target in the real time and it would dramatically reduced the time expenses. At the same time, the RCS store in the database can be used in various of conditions of missile target encounter. And the emulation results show that the general time of calculation of echo power of fuse from fast algorithm on all trajectory of the target is less than 1 sec.

As an example on Fig. 2 results of calculation of power of fuse from airplane model are shown on the base of its tradition model and with use of fast model. On both figures the continuous line designates a curve calculated on fast algorithm, and by a shaped line — a curve calculated on the base of tradition algorithm. We can see that the emulation results calculated by fast algorithm are with a good agreement with tradition algorithm. At the same time, the emulation results show that the general time of calculation of echo power of fuse from fast algorithm on all trajectory of the target is less than 1 sec. And the proposed method would be especially valuable in engineering application.

4. CONCLUSION

In conclusion, the proposed method for calculating the echo power of fuse in this article is precise and useful. And the emulation results show that the general time of calculation of echo power of fuse from fast algorithm on all trajectory of the target is less than 1 sec. And the proposed method would be especially valuable in engineering application.

REFERENCES

1. Jeng, S.-K., "Near-field scattering by physical theory of diffraction and shooting and bouncing rays," *IEEE Trans. on Antennas and Propagation*, Vol. 46, No. 4, 551–558, 1998.
2. , ,, . , 2005.
3. Youssef, N. N., "Radar cross section of complex targets," *Proceeding of the IEEE*, Vol. 77, No. 5, May 1989.
4. Crispin, J. W. and K. M. Siegel, *Method of Radar Cross Section Analysis*, Academic Press, New York and London, 1968.
5. "SAF analysis of shipboard antenna performance, coupling, and radar in complex near-field scattering environments," *IEEE Antennas and Propagation Society International Symposium, AP-S. Digest*, 1995.
6. , (), , 1994.

Fast Iterative Computation of Internal Field Intensity for Cabin on HIRF Based on Energy Conservation Modification

Zichang Liang, Yi Liao, Pengcheng Gao, and Liangshuai Guo
Shanghai Key Laboratory of Electromagnetic Environmental Effects for Aerospace
Shanghai 200438, China

Abstract— Aiming at the requirements of internal field strength calculation of electrically large cabin under high intensity radiated field (HIRF), the sub-domain decomposition methods are used for accelerating the calculation of electromagnetic current iteration method. Moreover, multiple reflection field distribution with limited number of reflections are estimated and modified according to the energy conservation principle, as well as with the prior knowledge of reflection field random distribution. Therefore, fast computation of field intensity distribution of electrically large cabin can be realized. The results derived by the proposed method agree reasonably with the results obtained by using the numerical method. Finally, this fast iterative computation method is applied for electric field intensity analysis of oversized cabin with internal stirrer.

1. INTRODUCTION

In modern complicated electromagnetic environment, there are both natural electromagnetic interference sources (such as lightning and static electricity) and human interference sources (such as radar, radio communications, navigation, electronic warfare equipment, and microwave electromagnetic weapons). High intensity radiated fields (HIRF) is one of the major artificial EM interference. Meanwhile, aviation aircraft electronic devices, which have the features of high integrity, accuracy and complexity, are inherently operated in these complicated electromagnetic environments. Studies on HIRF effect are of great significance for the development of civil aircrafts, rockets and satellites.

However, the modeling and simulation for aerospace vehicles on HIRF are very complex. Both the external electromagnetic wave reflection and the internal wave propagation are needed to be considered. Besides, the scale of the calculated structure is usually larger due to the requirements of the largest HIRF effect analysis frequency up to 40 GHz, where the size of passenger cabin of airplane reached to thousands of wavelength. HIRF effect of electrically large structures attract increasing attention in the field of electromagnetic environment.

Time domain methods including FDTD and FIT were used to analyze the electric field distribution for small composite material aircraft below the frequency of 1 GHz [1]. MoM (moment of method) technique was also used for HIRF simulation of aircraft over the frequency range of 10 kHz $\sim$ 1 GHz [2]. In the European HIRF SE projects, many numerical method including MoM and multilevel domain differentiated (MDD) are utilized for HIRF simulation within the low frequency range [3]. While in the frequency range above 3 GHz, a called power balance method (PWB) was proposed for the solution of HIRF effects, but it only gives the mean power densities in the aircraft cabin [4].

In this paper, the sub-domain decomposition technique is investigated based on the electromagnetic current iteration method. The contribution of multiple reflections for field distribution can be rapidly pre-estimated according to the energy conservation principle, as well as the prior knowledge of random degree of multiple reflection fields. An aircraft cabin is utilized to validate the proposed method. Reasonable agreement is obtained by comparing the results from proposed method with those from numerical method. Moreover, the presented method is used for the analysis of field distribution for oversized cabin with internal stirrer.

2. FAST ITERATIVE CALCULATION METHOD FOR FIELD DISTRIBUTION OF CABIN

The solution of cabin structure is called "internal problem". The electromagnetic wave bounced back and forth multiple times in the cabin. The iterative calculation for total reflection is usually time-consuming. Moreover, the convergence of computation is poor. While the high order reflection of electromagnetic wave becomes isotropic after sufficient reflections, and it can be estimated efficiently by using the PWB method. In this paper, based on the electromagnetic current iteration method in [5], the fast calculation of electric field distribution for electrically large cabin structure is realized according to sub-domain decomposition and modification of energy conservation principle.

2.1. Sub-domain Decomposition Iteration Method

The cabin can be divided into many sub-regions according to geometric shape of the structures. The connections between adjacent sub-regions are treated with virtual surfaces. For the sake of realizing iteration acceleration, the ratio of area for virtual surface to area for cabin wall is required to be less than 0.5.

The electromagnetic current iterative method mainly based on Huygens principle, which gets the induced currents with the equivalent electromagnetic current on the connection faces, S_a. If we consider a metal cabin, the mth reflection magnetic field can be expressed as

$$\mathbf{H}_c^{(m)}(r_c) \approx \int_{S_a} \mathbf{J}_a^{(m)}(r_a) \times \nabla' g(r_c - r_a) dS_a + \frac{1}{\mathrm{j}kZ_0} \nabla \times \int_{S_a} \mathbf{M}_a^{(m)}(r_a) \times \nabla' g(r_c - r_a) dS_a, \quad (1)$$

where $\mathbf{J}_a^{(m)}(r_a) = \hat{n} \times \mathbf{H}_a^{(m)}(r_a)$, $\mathbf{M}_a^{(m)}(r_a) = E_a^{(m)}(r_a) \times \hat{n}$ are the equivalent electromagnetic current densities, respectively. $\hat{n}$ is the normal of connection face. $\vec{E}_a^{(m)}(r_a)$ and $\vec{H}_a^{(m)}(r_a)$ are the electric and magnetic fields at the location of r_a on the connection face of S_a, respectively. $\vec{H}_a^{(m)}(r_a)$ is approximated by

$$\mathbf{H}_a^{(m)}(r_a) \approx \int_{S_c} \mathbf{J}_c^{(m-1)}(r_c) \times \nabla' g(r_a - r_c) dS_c, \quad (2)$$

where $\mathbf{J}_c^{(m-1)}(r_c)$ is the induced current of cabin. The initial inwall induced current can be calculated with physical optics (PO).

$$\vec{J}_c^{(0)}(r_c) = 2\hat{n} \times \vec{H}_c^{(0)}(r_c) \quad (3)$$

When the whole cabin is divided into several sub-domains, a single iteration calculation contains positive and negative iterative processes. The positive process is to use equations from (1) to (3) for calculating the electromagnetic transmission and reflection in each sub-domain, while the negative process is to use equations from (3) to (1) inversely.

2.2. Modification with Energy Conservation

Observing iterative process of electromagnetic wave propagation and reflection, field intensity distribution in the cabin can be considered as the superposition of different reflection fields.

$$\mathbf{E}(r) = \mathbf{E}_f^{(m-1)}(r) + \mathbf{E}^{(m)}(r) + \mathbf{E}_z^{(m+1)}(r) \quad (4a)$$

$$\mathbf{E}_f^{(m-1)}(r) = \sum_{n=0}^{m-1} \mathbf{E}^{(n)}(r) \quad (4b)$$

$$\mathbf{E}_z^{(m+1)}(r) = \sum_{n=m+1}^{\infty} \mathbf{E}^{(n)}(r) \quad (4c)$$

where, $\mathbf{E}_f^{(m-1)}(r)$ is the sum of electric fields including the incident field, as well as first reflection field, second reflection field, and till to the $(m-1)$th reflection field. $\mathbf{E}^{(m)}(r)$ is the sum of electric field of the mth reflection and beyond. According to the energy conservation principle, EM powers which go into the cabin window, runoff the cabin window, and dissipate in the wall are balanced. The powers go into and runoff the window can be expressed by

$$P^{(mn)} = \int \mathbf{E}^{(m)} \times \mathbf{H}^{(n)} \cdot \mathrm{d}s \quad (4d)$$

The relations of energy balance can be obtained when lossless cabin walls are considered.

$$P_{in} = P_{out}^{(0\sim m)} + P_{out}^{(z)} + P_{out}^{(mz)}$$

where P_{in} is the power from which the incident field goes into the cabin. $P_{out}^{(0\sim m)}$ is the sum of powers including the incident field, as well as first reflection field, second reflection field, and till to the mth reflection field. $P_{out}^{(z)}$ is overall power of the mth reflection and beyond. $P_{out}^{(mz)}$ is the

coupling energy of $P_{out}^{(0\sim m)}$ and $P_{out}^{(z)}$, which is small due to the strong randomness of high order reflection field. The spurious wave electric field can be approximated by:

$$E_z^{(m+1)} \approx a\sqrt{\frac{P_{in} - P_{out}^{(0\sim m)}}{P^{(m)}}} E^{(m)} \tag{4e}$$

where, E_z is the magnitude of spurious wave. P_{in} is the incident power. $P^{(m)}$ is the power of mth reflection. $E^{(m)}$ is the magnitude of mth reflection wave. a is a correction factor which depends on the coupling energy between spurious wave and low-order reflection wave.

3. SIMULATION OF HIRF EFFECT FOR TYPICAL CABIN

3.1. Results Comparison

A rectangular box is used for ensuring the validation of the proposed method, as shown in Fig. 1. The dimensions are 2 m × 0.5 m × 0.5 m. The frequency is 10 GHz. Five orders reflection are taken into account with the iterative calculation method and the correction factor of 0.5 in (7) is selected. The obtained electric field results in an appointed plane are compared with the results by MoM. Table 1 lists all the mean electric fields, which shows good agreements.

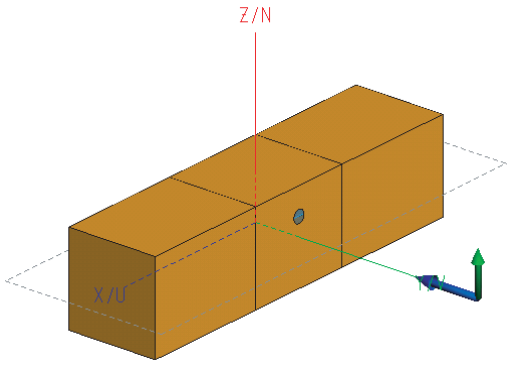

Figure 1: Simplified cabin model for validation.

Table 1: The comparison of electric field results.

The radius of aperture (mm)	Mean electric field inside the cabin (V/m)	
	Proposed method	MoM
15	0.12	0.12
25	0.21	0.18
35	0.23	0.22
45	0.28	0.28

3.2. Application for Cabin with Stirrer

Stirrers are often used inside the cabin to simulate the different electromagnetic wave propagation direction of incidence, especially for the high frequency cases. The stirrer could improve the efficiency of HIRF effects testing. In this paper, the proposed method is applied to EM computation for aircraft cabin with a length of 18 m. The cabin is decomposed to nine sub-domains with each length of 2 m, as shown in Fig. 2. The frequency of 10 GHz is considered again and 22 cores are configured for parallel computation. It only takes 10 minutes for electric field analysis on the whole solving process.

Figure 3 shows the electric field distribution inside the cabin. The results are given when azimuth angle are 30°, 40°, and 50° for stirrer. It can be seen that the beam of reflection wave changes with different azimuth angles and sweeps through the left side of cabin which is the area of smaller field intensity. These results also conform to the law of electromagnetic wave reflection.

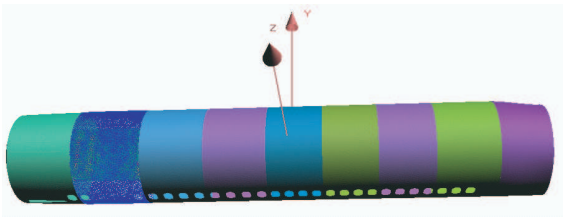

Figure 2: The decomposition of a typical cabin.

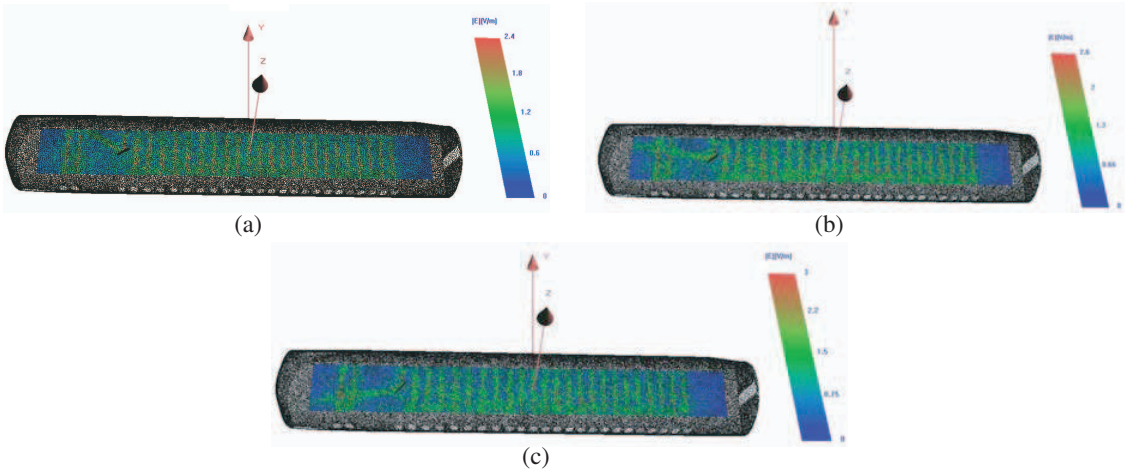

(a) (b) (c)

Figure 3: The electric field distribution of cabin with an internal stirrer. (a) Azimuth angle of 30°. (b) Azimuth angle of 40°. (c) Azimuth angle of 50°.

4. CONCLUSION

The sub-domain decomposition technique is investigated based on the electromagnetic current iteration method. The electric field distribution of cabin is approximated according to the energy conservation principle and could be rapidly pre-estimated. The proposed method is used for the analysis of field distribution for oversized cabin with internal stirrer and reasonable results are obtained.

ACKNOWLEDGMENT

This work was supported in part by the National Science Foundation of China (No. 61302036).

REFERENCES

1. Reznicek, Z., Z. Raida, and J. Jilkova, "Analyzing small aircraft model with homogeneous composite material substitutes on HIRF," *International Symposium on EMC Europe*, 1–4, Jun. 2009.
2. Bandinelli, M., R. Guidi, M. Bercigli, G. Vecchi, and F. Vipiana, "Advanced MoM techniques integrated into a single code to manage complex HIRF environments," *International Conference on Electromagnetics in Advanced Applications (ICEAA)*, 1117–1120, Sep. 2011.
3. Francavilla, M. A., F. Vipiana, S. Arianos, and G. Vecchi, "Multilevel domain differentiated analysis of large multi-scale structures inside the HIRF-SE framework," *International Conference on Electromagnetics in Advanced Applications (ICEAA)*, 944–946, Sep. 2011.
4. Junqua, I., J.-P. Parmantier, and M. Ridel, "Modeling of high frequency coupling inside oversized structures by asymptotic and PWB methods," *International Conference on Electromagnetics in Advanced Applications (ICEAA)*, 68–71, Sep. 2011.
5. Liang, Z., X. Wang, and H. Yu, "Iterative calculating the composite scattering between hedgehopping target and rough surface," *Guidance & Fuze*, Vol. 30, No. 2, 30–33, 2009 (in Chinese).

Dual Band Microstrip Antenna

Rafal Przesmycki and Paweł Skokowski
Faculty of Electronics, Military University of Technology
Gen. S. Kaliskiego 2 str., Warsaw 00-908, Poland

Abstract— In the article a structure of multilayer microstrip antenna operating at frequencies 2.4 GHz and 5.8 GHz have been presented. The antenna structure consists of three dielectric layers and two radiant elements; it is supplied by electromagnetic coupling. Moreover problems occurring in multilayer dual-frequency structures have been discussed in the article.

1. INTRODUCTION

Portable electronic devices more and more boldly enter the everyday life of a modern man. A society uses not only simple mobile phones but also multimedia equipment which makes constant access to the Internet and user's position by GPS system possible [5–9]. It can be assumed that it is transitional stage to integrate many electronic devices with clothes and build a system which will include a lot of elements enabling human contact with the entire world and unlimited access to any information but also monitoring his vital functions and alarming him and suitable services about potential dangers and threats [1, 2].

A fast development of technology of wireless Internet access and requirements of meeting norms imposed on WLAN, WiMAX and other wireless network technologies extort the demand for devices, which apart from reliability and functionality will be characterized by a small size [13, 14]. Since a necessary element of each wireless system is antenna, it forces also on these elements miniaturization as well as possibility of operation in more than one frequency band [3, 4, 11, 12]. Antennas which due to their properties best meet the above requirements are microstrip antennas. This article presents a multilayer microstrip antenna operating in two frequency ranges: 2.4 GHz and 5.8 GHz.

2. STRUCTURE OF ANTENNA

The antenna has two radiant patches located on separate dielectric layers. Each patch is responsible for operation in a different frequency range. Patch located on the middle layer (layer marked with 2) is responsible for operation at frequencies from the range 5.8 GHz, whereas patch placed on the upper layer (3) is responsible for operation of antenna within the frequency range 2.4 GHz. In Figure 1 graphic display of antenna model has been presented with indication of distribution of particular antenna elements.

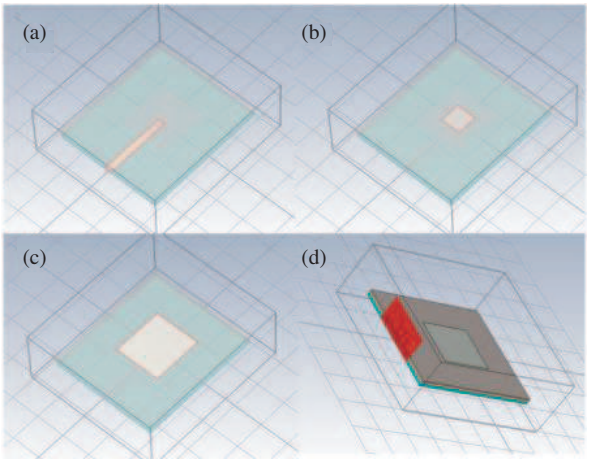

Figure 1: View of location of particular antenna elements: (a) layer 1 and feeder, (b) layer 2 with patch radiating at 5.8 GHz, (c) layer 3 with patch radiating at 2.4 GHz, (d) general view of the whole antenna with charging port.

Figure 2: Finished final antenna models.

For construction of an initial model the following dielectrics have been chosen:
– layer 1: ULTRALAM 2000 ($\varepsilon_r = 2.60$; $h = 1.524\,\text{mm}$),
– layer 2: ULTRALAM 2000 ($\varepsilon_r = 2.40$; $h = 1.524\,\text{mm}$),
– layer 3: Duroid 6202 or Duroid 6200 ($\varepsilon_r = 2.94$; $h = 0.762\,\text{mm}$).

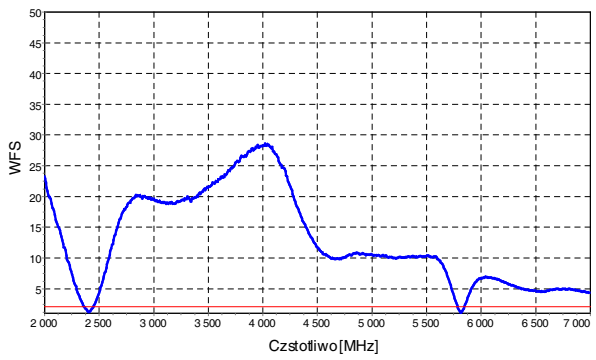

Figure 3: SWR of a single element.

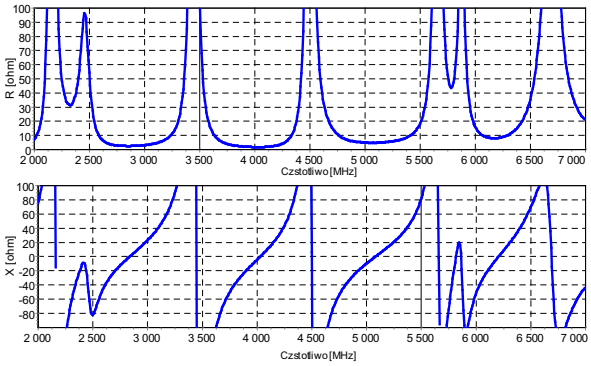

Figure 4: Resistance and input reactance of a single element — measurement result.

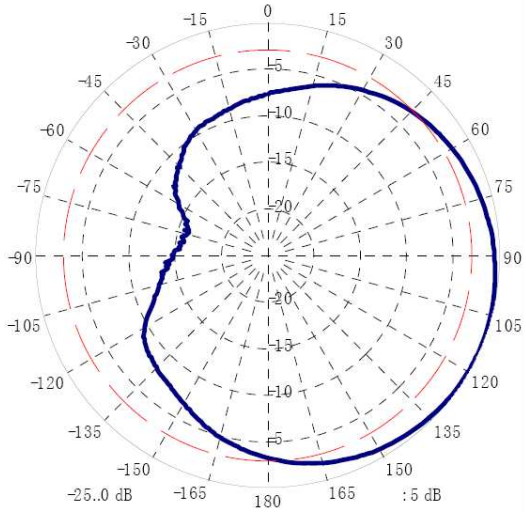

Figure 5: Measured normalized radiation pattern of single element antenna for frequency 2400 MHz.

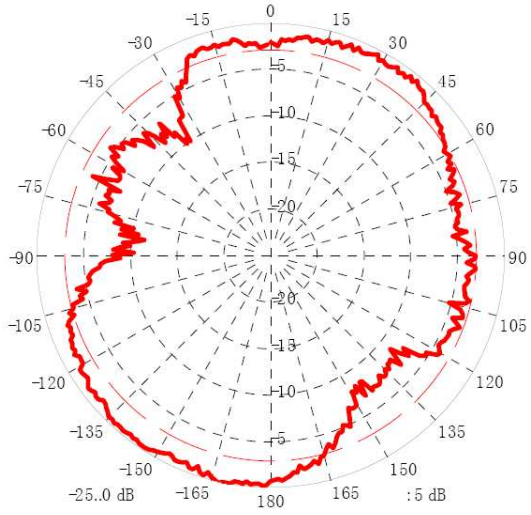

Figure 6: Measured normalized radiation pattern of single element antenna for frequency 5800 MHz.

A built model of microstrip antenna consists of three separate dielectric layers. In the antenna structure dielectrics with close electric and geometric parameters (thickness) have been used. The first layer is dielectric of 1.524 mm thickness and permittivity equal to $\varepsilon_r = 2.6$. In that layer shield was placed from below and feeder line from the top. The second layer is dielectric with the same electrical and geometrical parameters as layer 1. That layer contains radiant element with dimension $14 \times 14\,\text{mm}$ located at the top of dielectric. The third layer is dielectric of 0.762 mm thickness and permittivity equal to $\varepsilon_r = 2.94$, on which the second radiant patch with dimensions $35 \times 32\,\text{mm}$ is placed. It is placed in parallel towards the first radiant patch in layer two. External dimensions of all three layers are the same, respectively: width — 68 mm and length — 84 mm. Total thickness of the antenna is about 3.9 mm.

On the basis of the above presented antenna model two-element and four-element aerial arrays have been constructed. In order to protect the antenna against mechanical defects they have been covered with layer of foamed PVC.

3. MEASUREMENT RESULTS OF ELECTRIC PARAMETERS AND ANTENNA CHARACTERISTICS

In this item an analysis and juxtaposition of results of electric parameters and radiation characteristics of final antenna models have been presented.

For final models of dual-frequency microstrip antennas measurements of such electric parameters as: WFS, S_{11}, input resistance, input reactance and radiation characteristics at selected frequencies from antenna operation range have been conducted. In Figure 2 a view of final antenna models is shown.

The antenna obtains the value WFS $<$ 2 for the following frequency ranges: from 2360 to 2440 MHZ and from 5780 to 5840 MHz. In Figure 7 a built two-element microstrip antenna has been presented.

The antenna obtains the value WFS $<$ 2 for the following frequency ranges: from 2360 to 2530 MHZ and from 5700 to 5840 MHz.

The antenna obtains the value WFS $<$ 2 for the following frequency ranges: from 2340 to 2550 MHZ and from 5780 to 5840 MHz.

Finished dual-frequency microstrip antennas have common frequency ranges of operation (WFS $<$ 2) in particular ranges, respectively 2364–2445 MHz and 5780–5840 MHz. These are frequency subranges included in open-access ISM band. Increasing of the number of radiant elements has led to narrowing of radiation characteristics in V plane.

For the frequency 2340 MHz along with the increase of the number of elements an useful width of radiation beam at level -3 dB has been changing respectively: 125°, 80° and 45°. Whereas in plane H radiation characteristics of antennas, regardless of a number of elements, have not undergone significant changes and kept their shape [15–18].

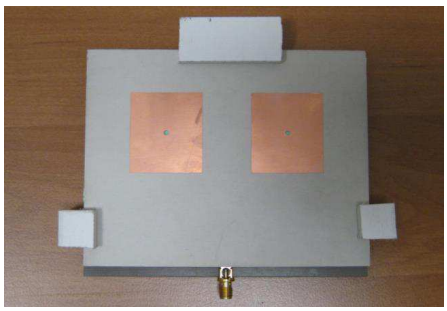

Figure 7: Finished 2×1 antenna models.

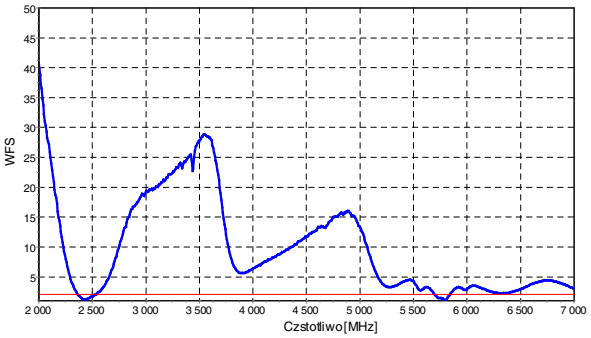

Figure 8: SWR of two-element antenna.

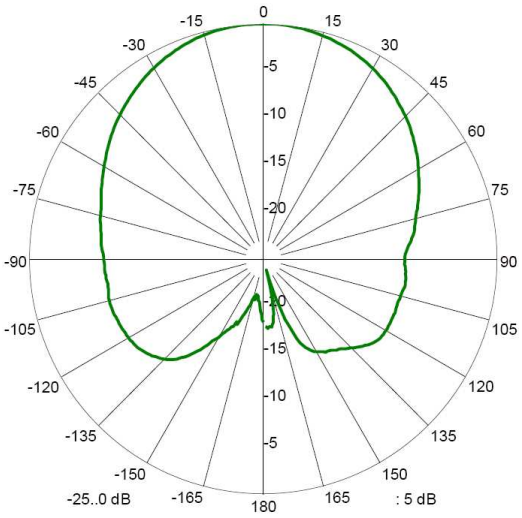

Figure 9: Measured normalized radiation pattern for frequency 2400 MHz (two elements).

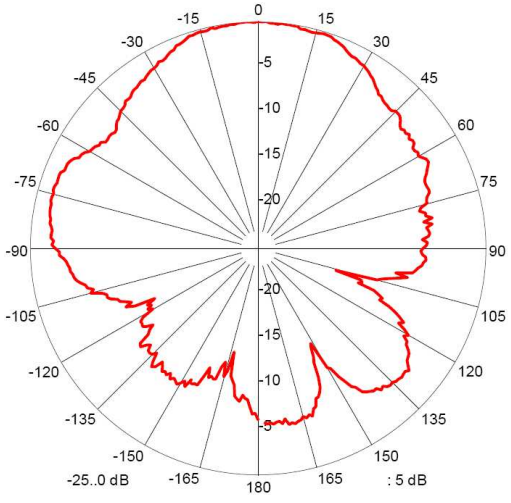

Figure 10: Measured normalized radiation pattern for frequency 5840 MHz (two elements).

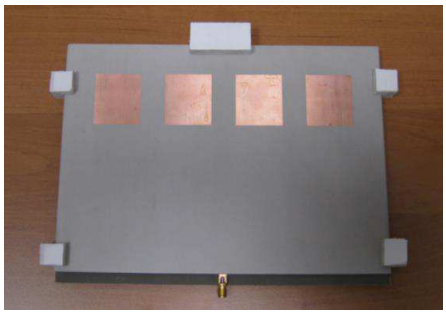

Figure 11: Finished 4×1 antenna model.

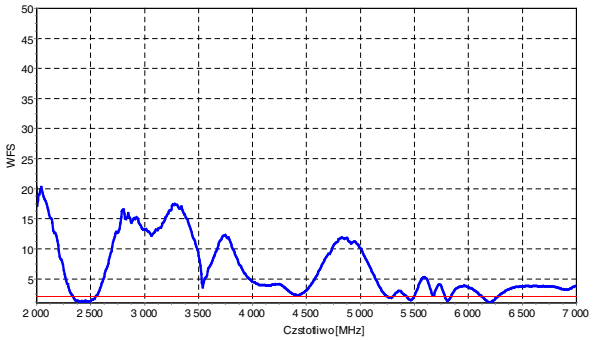

Figure 12: SWR of four-element antenna.

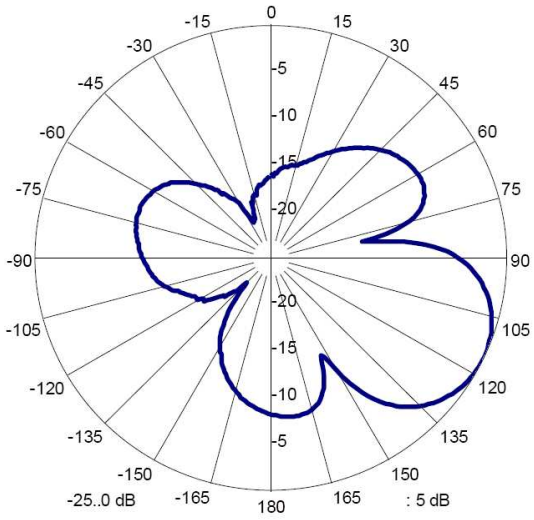

Figure 13: Measured normalized radiation pattern for frequency 2400 MHz (four elements).

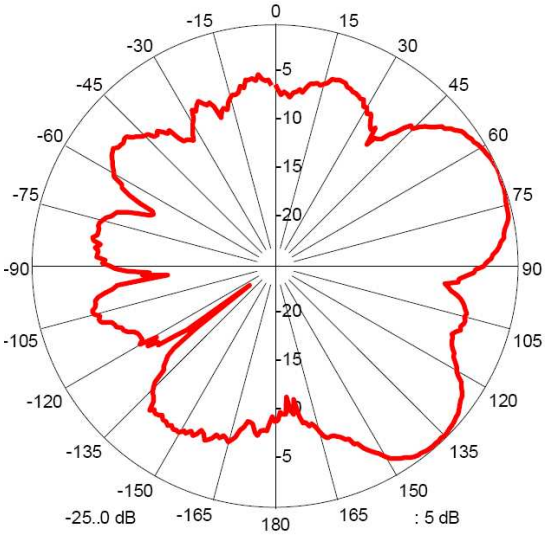

Figure 14: Measured normalized radiation pattern for frequency 5800 MHz (four elements).

4. CONCLUSIONS

While designing dual-frequency multilayer microstrip antennas a few important conditionings should be taken into account. The main condition of designing multi-range antennas is resonant frequency spacing between them. Designing multilayer microstrip dual-frequency antenna with an attempt of obtaining two frequencies, where one is over twice bigger than the other, we will encounter a series of design-construction problems. The first one will be the problem of stimulation of radiant patches for such diverse frequencies caused by significant differences in size of radiant patches. With two-fold frequency difference the surface of patches(radiant elements) will be even fourfold different (with the assumption of using dielectric of a similar value of permittivity in particular layers). Unfortunately it will cause undesirable distortions in radiation characteristics. In such cases, if we place the patch radiating electromagnetic wave of lower frequency over the patch radiating electromagnetic wave of higher frequency, then due to a significant size of the first one, it will be a form of 'shield' at the main direction of radiation causing distortion of radiation characteristics. If we place radiant patches in reverse order — i.e., the patch of a much smaller size is placed at the top, then we will encounter a problem consisting in difficulties with stimulation of this patch to radiate. In this case, the patch of a bigger size will rather effectively hinder stimulation of the patch situated over it to radiate electromagnetic waves.

REFERENCES

1. Gruszczynski, M., M. Wnuk, and L. Nowosielski, "Multisystem microstrip antenna for mobile communications," *2012 IEEE Antennas and Propagation Society International Symposium (APSURSI) Book Series: IEEE Antennas and Propagation Society International Symposium*, 2012.

2. Nowosielski, L., M. Wnuk, and C. Ziolkowski, "Interlaboratory tests in scope of measurement of radio disturbance," *2009 European Microwave Conference*, Vols. 1–3, 288–291, 2009.
3. Piotrowski, Z., L. Nowosielski, L. Zagozdzinski, and P. Gajewski, "Electromagnetic compatibility of the military handset with hidden authorization function based on MIL-STD-461D results," *PIERS Proceedings*, 116–120, Cambridge, USA, July 2–6, 2008.
4. Gajewski, P., J. Lopatka, L. Nowosielski, B. Uljasz, and Z. Piotrowski, "Multimedia transmission over HF links," *IEEE 21st Century Military Communications Conference Proceedings, Military Communications Conference*, Vols. 1 and 2, 45–47, 2000.
5. Bugaj, M. and M. Wnuk, "Optimization parameters of dielectric in aperture-coupled stacked patch antenna on bandwidth," *18th International Conference on Microwaves, Radar And Wireless Communications (MIKON-2010)*, Vols. 1 and 2, 2010.
6. Bugaj, M. and M. Wnuk, "Influence of parameters of dielectric in aperture-coupled stacked patch antenna on bandwidth," *Przeglad Elektrotechniczny*, Vol. 85, No. 9, 50–53, 2009.
7. Bugaj, M. and M. Wnuk, "The influence examination of dielectric parameters on bandwidth in multilayer aperture-coupled microstrip Antennas with utilization the FDTD method," *2008 MIKON Conference Proceedings*, Vols. 1 and 2, 708–711, 2008.
8. Wnuk, M. and M. Bugaj, "Analysis of radiating structures placed on multilayer dielectric," *Computational Methods and Experimental Measurements XIII Book Series: Wit Transactions on Modelling and Simulation*, Vol. 46, 747–755, 2007.
9. Wnuk, M., G. Rózanski, and M. Bugaj, "The analysis of microstrip antennas using the FDTD memod," *Computational Methods and Experimental Measurements XII Book Series: Wit Transactions on Modelling and Simulation*, Vol. 41, 611–620, 2005.
10. Kubacki, R., E. Cwalina, M. Kuchta, and A. Dukata, "Electromagnetic field distribution in the office room and computer enclosure evoked by electromagnetic high power pulses," *Przeglad Elektrotechniczny*, Vol. 88, No. 12B, 209–212, 2012.
11. Kubacki, R., M. Wnuk, and J. Kieliszek, "Fresnel approximations in mathematical expressions of the electric field for base station antennas," *Przeglad Elektrotechniczny*, Vol. 84, No. 12, 190–193, 2008.
12. Kubacki, R., "Biological interaction of pulse-modulated electromagnetic fields and protection of humans from exposure to fields emitted from radars," *2008 MIKON Conference Proceedings*, Vols. 1 and 2, 66–72, 2008.
13. Kubacki, R., J. Sobiech, and E. Sedek, "Model for investigation of microwave energy absorbed by young and mature living animals," *Electromagnetic Field, Health and Environment, Proceedings of EHE '07 Book Series: Studies in Applied*, Vol. 29, 126–132, 2008.
14. Kubacki, R., J. Kieliszek, and A. Krawczyk, "The investigation of influence of the electromagnetic fields emitted from short-wave diathermy to the pacemakers," *Przegląd Elektrotechniczny*, Vol. 83, No. 12, 105–107, 2007.
15. Kubacki, R., J. Sobiech, J. Kieliszek, and A. Krawczyk, "Comparison of numerical and measurement methods of SAR of ellipsoidal phantoms with muscle tissue electrical parameters," *COMPEL — The International Journal for Computation and Mathematics in Electrical and Electronic Engineering*, Vol. 25, No. 3, 691–704, 2006.
16. Dabrowski, M. P., W. Stankiewicz, R. Kubacki, E. Sobiczewska, and S. Szmigielski, "Immunotropic effects in cultured human blood mononuclear cells pre-exposed to low-level 1300 MHz pulse-modulated microwave field," *Electromagnetic Biology and Medicine*, Vol. 22, No. 1, 1–13, 2003.
17. Kubacki, R., M. Wnuk, W. Kolosowski, and J. Sobiech, "New approach to electromagnetic field calculations in the near-field of microwave antennas," *Computational Methods and Experimental Measurements XI Book Series: Computational Engineering*, Vol. 4, 413–422, 2003.
18. Kubacki, R., M. Krukowski, J. Kieliszek, and J. Sobiech, "New computational model of electromagnetic field distribution for predicting of the safety zones in the near-field of microwave antennas," *XIV International Conference on Microwaves, Radar and Wireless Communications, MIKON-2002*, Vols. 1–3, 902–905, 2002.

Wideband Microstrip Antenna

Rafal Przesmycki, Marek Bugaj, and Marian Wnuk
Faculty of Electronics, Military University of Technology
Gen. S. Kaliskiego 2 str., Warsaw 00-908, Poland

Abstract— The article concerns the issue of narrow-banding of microstrip antennas. In the article methods of increasing operation bandwidth of microstrip antennas have been presented and examples of the structure of microstrip antennas with significant working band have been shown. Results obtained during simulation and design of antennas have been confirmed through the measuring way.

1. INTRODUCTION

A fast development of technology of wireless Internet access and requirements of meeting norms imposed on WLAN, WiMAX and other wireless network technologies extort the demand for devices, which apart from reliability and functionality, will be characterized by a small size. Since a necessary element of each wireless system is antenna, it forces also on these elements miniaturization as well as possibility of operation in more than one frequency band. Antennas which due to their properties best meet the above requirements are microstrip antennas [4, 5].

Narrow band is the main defect of microstrip antennas. Typical working bandwidth of antenna is almost always too small. Currently wireless communication systems need antennas with broad frequency band. For instance, cellular telephony systems (GSM 900: range: 890–960 MHz) require band: 7.5%, for GSM 1800 (range: 1710–1880 MHz) band at the level 9.5% is necessary and for systems UMTS 12.2% [6, 7]. To meet these not easy requirements special methods have been designed for broadening frequency working band of microstrip antenna such as: increase of thickness of dielectric base, application of structures using electromagnetic coupling with an extra radiant patch or parasitic elements, two-layer configurations supplied by coupling with aperture, introduction of matching elements in the radiant patch supply system, e.g., supply by capacitance [1–3].

2. METHODS OF INCREASING WORKING BAND

One of basic problems connected with using planar antennas in radio communication links is their relatively narrow frequency working band, which has been mentioned in Introduction. Increase of frequency working band of planar antenna can be realized through using

- frequency-retuned planar radiators,
- dual-frequency radiators,
- multilayer structures [4];

The simplest way for broadening working band of microstrip antenna is conducting it on its thicker base under a radiant patch. Disadvantages of this method is the fact that thicker dielectric base decreases antenna efficiency and is conducive to occurrence of surface waves, thereby causing undesirable effects in radiation characteristics. Moreover along with the increase of base thickness problems with coaxial probe supply appear.

Retuning of antenna frequency band is obtained by change of resonant frequency of planar radiator, which with its determined dimensions depends on permittivity of dielectric base [4, 6]. There are three ways to change that permittivity. One of them is that varactor diodes are inserted into the dielectric area and they can be used to change value of its permittivity. In a similar way one can influence permittivity of dielectric base by placing pins in it which contain radiator and conductive base in selected points. Third method is that between dielectric layer and conductive base an air-gap is used which decreases effective permittivity of the area between radiator and that base [1, 8–10]. It should be stressed that in these cases we do not deal with actual broadening of working band but only with a possibility of retuning work frequency of such antennas.

Some variant of the described above frequency-retuned planar radiators are dual-frequency radiators which have two various resonant frequencies. It can be carried out with the use of planar radiator stimulated to work in properly selected two kinds of its stimulation with which such an antenna maintains the same or similar electric properties. The other way to obtain dual-frequency

work of planar radiator is its loading with reactance element in the form of shorted asymmetric strip line. A similar result can be obtained by using two-layer planar antenna [2, 3, 11, 12].

In the situation when retuned or dual-frequency planar antenna does not meet requirements for frequency working band resulting from the system needs, absolute broadening of its working band is necessary by using planar structures: two-layer with electromagnetic coupling, multilayer supplied by capacitance or multilayer with radiant elements coupled with aperture [13, 14].

A different unmentioned above method of increasing working band of planar antenna is using for building such an antenna dielectric base with properly large thickness. However this method has a number of drawbacks, e.g., it reduces efficiency of antenna radiation and is not recommended to be used in practice.

We can obtain the broadband character of antenna by using additional radiant patches coupled directly with radiant or non-radiant edges of rectangular microstrip antenna. In such configuration bandwidth can be even up to 5 times higher than in antenna with one rectangular radiator. Nevertheless broadening of antenna working band is obtained at the cost of increase of antenna dimensions. Moreover, by choosing radiators with slightly different resonant lengths we will induce modes at frequencies close to each other. Thus the band will be broadened more than in case of antenna with one extra radiator coupled directly.

In multilayer structures radiant elements supplied by capacitance provide significant broadening of frequency bandwidth of microstrip antennas. Typical values of bandwidth for such configurations comprise within the range from 15 to 60% [5].

3. BROAD-BAND MICROSTRIP ANTENNA WITH RECTANGULAR RADIATOR

The basic antenna structure consists of rectangular radiator supplied by symmetric microstrip line and shield.

The antenna was made on FR-4 basewith thickness of 1.6 mm and permittivity equal to 4.4 mm. Width of feeder is 2.5 mm.

Rectangular radiator with dimensions 16.6 mm × 12.4 mm was placed within the distance of 11.65 mm from the left base edge and within 11.75 mm from the right base edge. In the middle of the lower edge of radiator symmetric microstrip feeder was placed. It was 2.5 mm wide and 13.6 mm long and placed within the distances of 18.8 mm and 18.7 mm from the base edge. On the other side of the base shield with dimensions 40 mm × 12.5 mm was placed by the base lower edge. The whole metallization was made of copper of 0.4 mm thickness. The designed antenna is connected to 50 Ω SMA joint. The antenna was designed to work in frequency band from 4 GHz to 8 GHz. The model and dimensioning are presented in Figure 1.

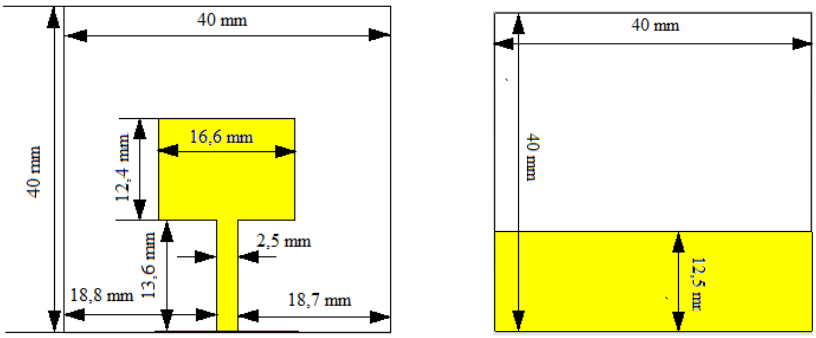

Figure 1: Structure of broad-band antenna with rectangular radiator.

To make an analysis and simulation of antennas the CST environment has been used.

4. BROAD-BAND MICROSTRIP ANTENNA WITH U-SHAPED RADIATOR

The second project presents configuration of broad-band microstrip antenna with U-shaped radiator. The antenna structure consists of U-shaped radiator, supplied by asymmetric microstrip line and shield. Asymmetric feeder means that it was placed asymmetrically towards the lower edge of radiator. That antenna, like the previous one, was made on FR-4 base with thickness of 1.6 mm and permittivity 4.4.

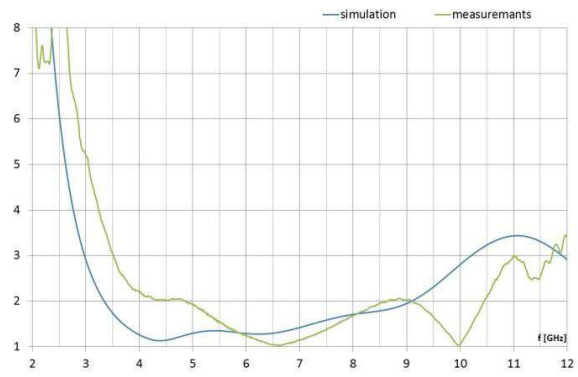

Figure 2: SWR of antenna with rectangular radiator.

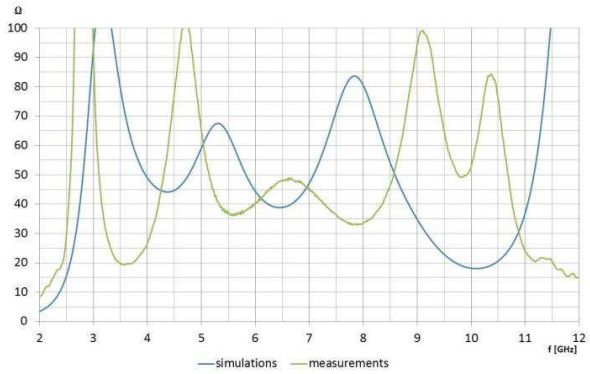

Figure 3: Input resistance of antenna with rectangular radi-ator.

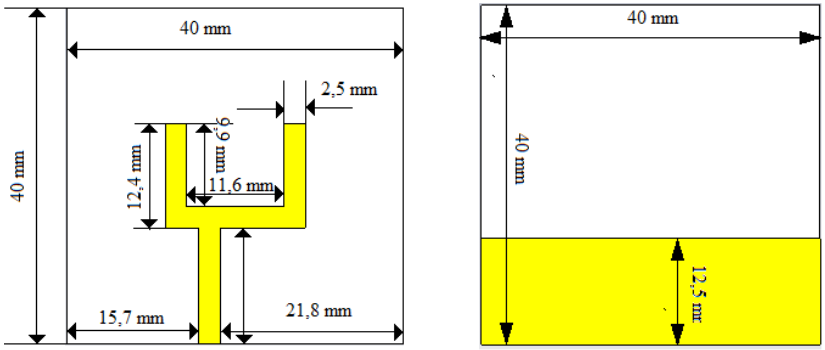

Figure 4: Structure of broad-band antenna with U-shaped radiator.

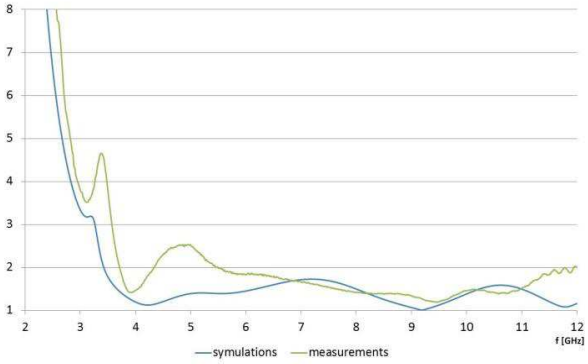

Figure 5: SWR of antenna with U-shaped radiator.

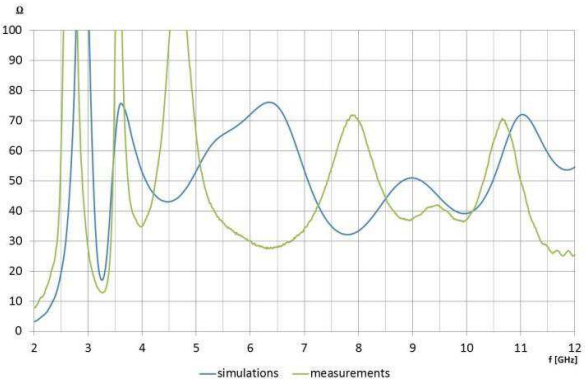

Figure 6: Input resistance of antenna with U-shaped radiator.

U-shaped radiator is 2.5 mm wide, lower edge is 16.6 mm, side edges are 12.4 mm, whereas 'incision' giving radiator the shape of letter U has dimensions: 11.6 mm × 9.9 mm. Asymmetric feeder with dimensions 13.6 mm × 2.5 mm was placed within the distance 15.7 mm from the base left edge. Back of the antenna looks the same as in the first project. The antenna was connected to 50 Ω SMA joint. Asymmetric feeder and U-shaped radiator allowed to broaden the band. An expected working band is 4 GHz to 10 GHz.

5. MEASUREMENTS OF RADIATION CHARACTERISTICS

In order to check correctness of the conducted in the previous chapter analysis and verification of parameters of the obtained final mathematical model of antenna, experimental measurements of radiation characteristics of physical model of antenna built on the basis of the results obtained

during the simulation process have been carried out.

In Figures 8–11, juxtapositions of radiation characteristics of the analysed antennas in planes V and H for three selected frequencies within antenna working band have been presented.

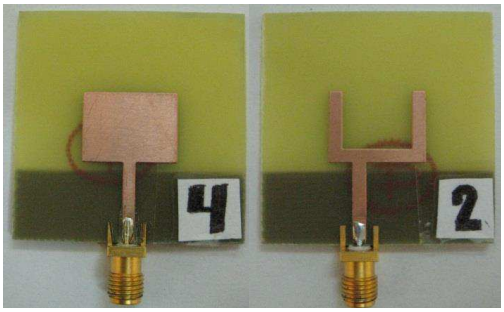

Figure 7: The look of tested antennas.

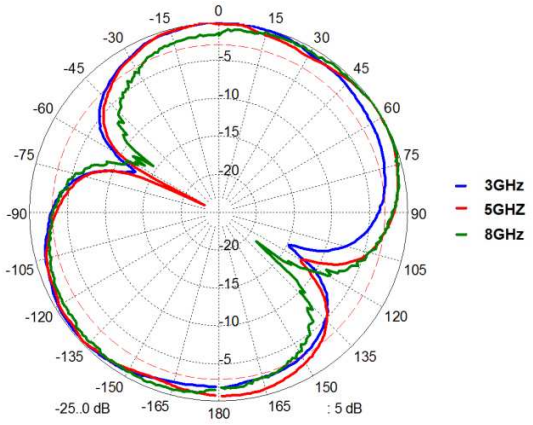

Figure 8: Juxtaposition of radiation characteristics of microstrip antenna with U-shaped radiator for different frequencies from working band in V polarization.

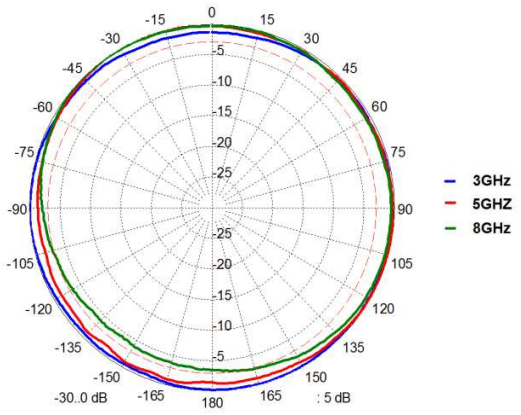

Figure 9: Juxtaposition of radiation characteristics of microstrip antenna with U-shaped radiator for different frequencies from working band in H polarization.

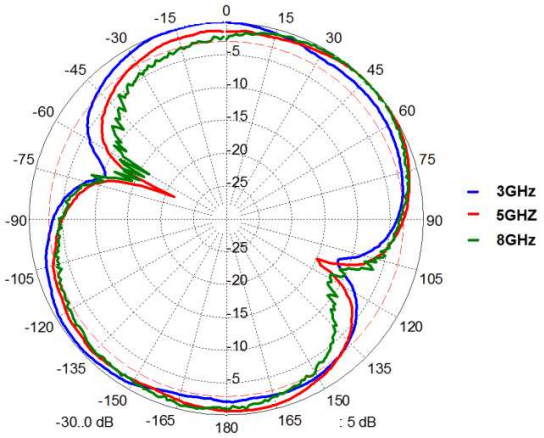

Figure 10: Juxtaposition of radiation characteristics of microstrip antenna with rectangular radiator for different frequencies from working band in V polarization.

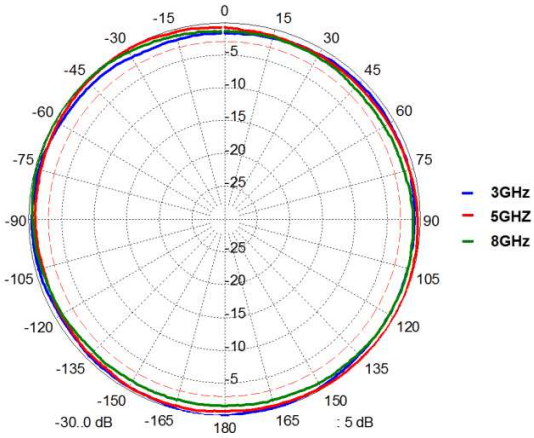

Figure 11: Juxtaposition of radiation characteristics of microstrip antenna with rectangular radiator for different frequencies from working band in H polarization.

6. CONCLUSIONS

The presented antenna models allow to use all current positive properties of planar antennas with simultaneous work in wide frequency range, which is most often the main reason for limitations in using microstrip antennas in many constructions. Taking into account tendencies for miniaturization of aerial devices and development of radio technologies and integrated systems the presented in the article structures seem to be very prospective. The structure of this antenna is a modern solution of aerial device with compact form, which is particularly important in situations of using it on movable objects. The designed antennas operate within the band 4 to 10 GHz and certainly they can be alternative to antennas which are currently used and operating in this band. The results of the conducted measurements fully confirm the possibility of designing planar antennas working in wide frequency range.

REFERENCES

1. Bahartia, I. B., R. Garg, and A. Ittipiboon, *Microstrip Antenna Design Handbook*, Artech House, Londyn, 2001.
2. Wong, K.-L., *Compact and Broadband Microstrip Antennas*, Jhon Wiley & Sons, New York, 2002.
3. Bahartia, P., I. Bahl, R. Garg, and A. Ittipiboon, *Microstrip Antenna Design Handbook*, Artech House, Londyn, 2001.
4. Katulski, R., "Analiza i badania anten do satelitarnej telekomunikacji morskiej," *Gdansk*, WAT wewn.2558/98, 1998.
5. Wnuk, M., G. Rozanski, and M. Bugaj, "The analysis of microstrip antennas using the FDTD method," *Computational Methods and Experimental Measurements XII Book Series: WIT Transactions on Modelling and Imulation*, Vol. 41, 611–620, 2005, ISBN: 1-84564-020-9, ISSN: 1746–4064
6. Piotrowski, Z., L. Nowosielski, L. Zagozdzinski, and P. Gajewski, "Electromagnetic compatibility of the military handset with hidden authorization function based on MIL-STD-461D results," *PIERS Proceedings*, 116–120, Cambridge, USA, Jul. 2–6, 2008.
7. Gajewski, P., J. Lopatka, L. Nowosielski, B. Uljasz, and Z. Piotrowski, "Multimedia transmission over HF links," *IEEE 21st Century Military Communications Conference Proceedings, Military Communications Conference*, Vols. 1 and 2, 45–47, 2000.
8. Kubacki, R., E. Cwalina, M. Kuchta, and A. Dukata, "Electromagnetic field distribution in the office room and computer enclosure evoked by electromagnetic high power pulses," *Przeglad Elektrotechniczny*, Vol. 88, No. 12B, 209–212, 2012.
9. Kubacki, R., "Biological interaction of pulse-modulated electromagnetic fields and protection of humans from exposure to fields emitted from radars," *2008 MIKON Conference Proceedings*, Vols. 1–2, 66–72, 2008.
10. Kubacki, R., J. Sobiech, and E. Sedek, "Model for investigation of microwave energy absorbed by young and mature living animals," *Electromagnetic Field, Health and Environment, Proceedings of EHE'07 Book Series: Studies in Applied*, Vol. 29, 126–132, 2008.
11. Kubacki, R., J. Kieliszek, and A. Krawczyk, "The investigation of influence of the electromagnetic fields emitted from short-wave diathermy to the pacemakers," *Przeglad Elektrotechniczny*, Vol. 83, No. 12, 105–107, 2007.
12. Kubacki, R., J. Sobiech, J. Kieliszek, and A. Krawczyk, "Comparison of numerical and measurement methods of SAR of ellipsoidal phantoms with muscle tissue electrical parameters," *COMPEL — The International Journal for Computation and Mathematics in Electrical and Electronic Engineering*, Vol. 25, No. 3, 691–704, 2006.
13. Dabrowski, M. P., W. Stankiewicz, R. Kubacki, E. Sobiczewska, and S. Szmigielski, "Immunotropic effects in cultured human blood mononuclear cells pre-exposed to low-level 1300 MHz pulse-modulated microwave field," *Electromagnetic Biology and Medicine*, Vol. 22, No. 1, 1–13, 2003.
14. Kubacki, R., M. Krukowski, J. Kieliszek, and J. Sobiech, "New computational model of electromagnetic field distribution for predicting of the safety zones in the near-field of microwave antennas," *XIV International Conference on Microwaves, Radar and Wireless Communications, MIKON-2002*, Vols. 1–3, 902–905, 2002.

Ultra-wideband Antenna with Metamaterial and Periodic Structure

Roman Kubacki, Salim Lamari, and Mirosław Czyżewski
Faculty of Electronics, Military University of Technology
Gen. S. Kaliski 2 Str., Warsaw 00-908, Poland

Abstract— In this article a compact ultra-wideband (UWB) microstrip antenna basing on the planar patterned array metamaterial concept has been presented. This latter consists of loading the ordinary rectangular microstrip antenna on its metallic parts with periodic shaped patterns. The antenna is $27.48\times31.74\times0.787\,\text{mm}^3$ dimensions. The antenna patch is etched out simply with an array of crosses, and the ground plane consists of small square patches separated by slots and loaded with slits on their angles. The substrate of the antenna is Rogers RT 5880 with $\varepsilon_r = 2.2$ and 0.787 mm thickness. This antenna after being designed, simulated and fabricated, showed enhancement in bandwidth. The measured bandwidth at the -10 dB return loss is 13.985 GHz, ranging from 4.389 GHz to 17.581 GHz, which represents 120% fractional bandwidth.

1. INTRODUCTION

Nowadays many applications due to their working environment, require integrated and miniaturized systems where the antenna should coexist with the transmitting and receiving modules. These latter have even seen their construction being miniaturized thanks to the recent development in solid state devices and MEMS. It remains only to the antenna to follow and render the system complete.

Among the antenna that received the greatest interest during the last decades we find the microstrip antenna. The microstrip antenna benefits from several advantages like simple structure, small size, low cost conformality and easy fabrication by means of lithographic technique. But suffers from a major handicap of narrow bandwidth. Several studies and tests were conducted to improve the bandwidth and the literature is prolific in this topic. Among the techniques used to overcome this obstacle we can find increasing the height of the substrate and/or decreasing its dielectric constant, dielectric substrates layering or stacking with different dielectric permittivity values, different feeding and coupling techniques, etc. [1–4, 20–24]. Unfortunately these ways were limited and achieved only small bandwidth enhancement and could not realize miniaturization.

Especially with the advent of the ultra-wideband technology, which the communication systems adopt more and more because of its many advantages like high bandwidth, high data rates, security, jamming and interference robustness, coexistence with other radio systems, thus avoiding more spectrum scarcity, etc. [5, 7–15]. Consequently this technology is found in many areas and found applications in vehicles and traffic regulation, ground penetrating radar and mine detection, "see through the wall" applications among which we find medical imaging, localization and detection of persons [16–18]. So the microstrip antenna has to be adapted to follow these developments and meet the requirements of the time to keep its place in the concert.

During the last decade new materials appeared, known as metamaterials because of their properties not found in nature like negative refractive index (NRI) implied by both negative permittivity and permeability, thus due to these characteristic they are also called left hand materials (LHM). The metamaterials are human engineered materials and were theoretically predicted forty years ago by Veselago [19]. Their properties were verified experimentally by many ways and gave rise to two main categories, the resonant and the non-resonant types. The resonant type is a composite of a meta-structure of electric and magnetic plasma like particles made by means of split ring resonators and metallic wires put on opposite sides. But this type as its name suggest is a resonating structure and seems of less practice interest because it shows low bandwidth and high losses. On the other side the non-resonant type, which is preferred in an application point of view because it can be engineered in planar configurations compatible with modern microwave integrated circuits, could be designed to exhibit low loss and high bandwidth. A similar structure was proposed in [6], it is a planar patterned configuration, which consists of arrays of different patterned cells arranged on both metallic sides of a substrate. This configuration was used and applied directly on an ordinary microstrip patch antenna in [27]. The antenna has the following dimensions $28 \times 32 \times 0.794\,\text{mm}^3$, with a feeding line of $8 \times 2.46\,\text{mm}^2$ dimensions, it achieved a -10 dB bandwidth of 3.2 GHz starting from 5.3 GHz to 8.5 GHz.

In this paper we propose a new antenna following the same philosophy basing on different patterns to enhance much further the bandwidth. The shapes of the patterns consist of simple

crosses put in a 3×4 array on the patch, and on the ground plane, they are small patches separated by crossing slots, the patches are forming a 7×6 cells array and loaded with small slits on their angles.

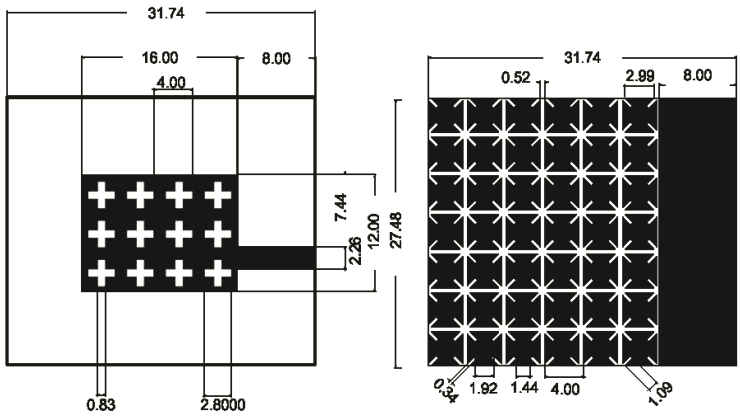

Figure 1: The antenna configuration.

2. ANTENNA CONSTRUCTION

For purposes of comparison, a conventional microstrip antenna was designed and simulated, and will hence serve as a reference. This antenna has the following overall dimensions $28 \times 32 \times 0.787\,\text{mm}^3$, a patch with $12 \times 16\,\text{mm}^2$ and a feeding line of $2.46 \times 8\,\text{mm}^2$. Our proposed antenna originates from the conventional antenna with slightly reduced dimensions of $27.48 \times 31.74 \times 0.787\,\text{mm}^3$, with the same patch dimensions and a reduced coupling line of $2.26 \times 8\,\text{mm}^2$. The substrate is the RT 5880 with 2.2 permittivity and 0.787 mm thickness. The metallic parts of the antenna were repetitively etched out with different patterns in such way they construct planar arrays respectively on both sides of the substrate. So on the patch, an array of 12 crosses arranged in 3×4 configuration. On the other side, i.e., the ground plane, the patterns are formed by small patches separated by crossing slots, the patches are loaded with small radial slits on their angles. The area in the ground plane under the feeding line was not etched out The antenna configuration is shown in Figure 1.

The whole structure made of planar patterns on both sides of the substrate incites the left handed characteristic by driving a coupling between the patch and the ground plane. Thus the characteristics of the antenna are enhanced. The design and the simulations were carried out in the CST MWS 2011 environment. The final configuration of antenna was obtained after a parameter sweeping of the dimensions of the main shapes for optimization and better enhancement of the characteristics.

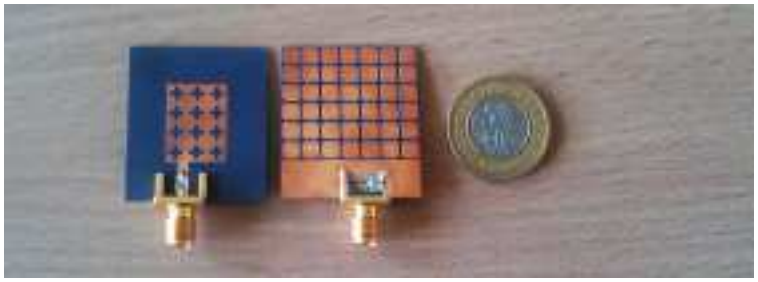

Figure 2: Picture of the fabricated antenna.

3. RESULTS AND DISCUSSION

As stated above in order to verify our approach, both antennas, after being designed and simulated, were fabricated, and their characteristics measured The picture of the proposed antenna is depicted in Figure 2. The dimensions of the antenna were continuously studied and submitted to parameter sweeping with the aim of obtaining better results. As we can notice that some dimensions in the

antenna were slightly reduced, like the overall dimensions of the antenna and those of the feeding line. In both antennas we observe, as shown in Figures 3 and 4, a good agreement between the results of the simulations and the measurements. Also the proposed antenna achieved a −10 dB bandwidth of 13.192 GHz, ranging from 4.389 GHz to 17.581 GHz, it is 58 times larger than that of the conventional antenna, which is 0.225 GHz only, so a 120% fractional bandwidth is realized. And it is more than 4 times larger than in the antenna in [14].

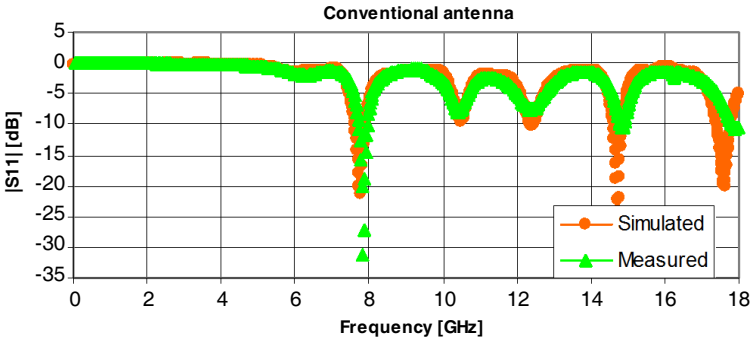

Figure 3: The results of simulation and measurement of the conventional antenna.

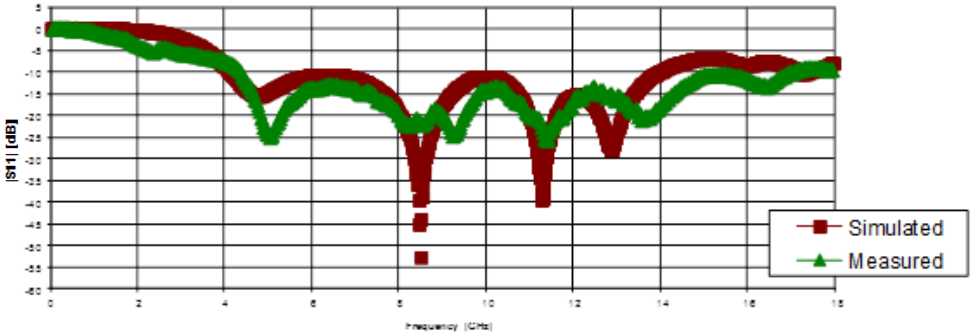

Figure 4: The results of simulation and measurement of the proposed antenna.

4. CONCLUSION

In this paper a compact ultra-wideband microstrip antenna is realized basing on the principle of planar patterned metamaterial. The metamaterials draw their properties rather from the structure than the contents, and confer special characteristics not found in natural materials. As it is noticed in the experiment shown in this paper, the structure applied here to the ordinary microstrip antenna has enhanced significantly its bandwidth, and transformed it from simple narrow bandwidth to an ultra-wideband antenna just by loading simply shaped patterns on its metallic parts.

ACKNOWLEDGMENT

The project was financed from NCBiR means within the Agreement No. DOBR-BIO4/016/13071/-2013 in the years 2013–2015.

REFERENCES

1. Bugaj, M., R. Przesmycki, M. Wnuk, and K. Piwowarczyk, "Analysis of methods measuring attenuation of RF line," *Przeglad Elektrotechniczny*, Vol. 88, No. 2, 17–19, 2012.
2. Bugaj, M. and M. Wnuk, "Influence of parameters of dielectric in aperture-coupled stacked patch antenna on bandwidth," *Przeglad Elektrotechniczny*, Vol. 85, No. 9, 50–53, 2009.
3. Bugaj, M. and M. Wnuk, "Optimization parameters of dielectric in aperture-coupled stacked patch antenna on bandwidth," *18th International Conference on Microwaves, Radar and Wireless Communications (MIKON-2010)*, Vols. 1 and 2, 2010.

4. Bugaj, M. and M. Wnuk, "The influence examination of dielectric parameters on bandwidth in multilayer aperture-coupled microstrip antennas with utilization the FDTD method," *2008 MIKON Conference Proceedings*, Vols. 1 and 2, 708–711, 2008.
5. Caloz, C. and T. Itoh, *Electromagnetic Metamaterial Transmission Line Theory and Microwave Applications, The Engineering Approach*, John Wiley and Sons, 2006.
6. Gajewski, P., J. Lopatka, L. Nowosielski, B. Uljasz, and Z. Piotrowski, "Multimedia transmission over HF links," *IEEE 21st Century Military Communications Conference Proceedings, Military Communications Conference*, Vols. 1 and 2, 45–47, 2000.
7. Garg, R., P. P. Bhartia, I. Bahl, and A. Ittipiboon, *Microstrip Antenna Design Handbook*, Artch House Inc., Noowood, 2001.
8. Ghavami, M., L. B. Michael, and R. Kohno, *Ultra Wideband Signals and Systems in Communication Engineering*, Wiley and Sons, Ltd., London, 2004.
9. Gruszczynski, M., M. Wnuk, and L. Nowosielski, "Multisystem microstrip antenna for mobile communications," *2012 IEEE Antennas and Propagation Society International Symposium (APSURSI)*, Book Series: *IEEE Antennas and Propagation Society International Symposium*, 2012.
10. Nowosielski, L., R. Przesmycki, and M. Wnuk, "The laboratory stand for conducted emissions measurement in accordance with the military standard," *2010 IEEE International Symposium on Electromagnetic Compatibility (EMC 2010)*, 275–278, 2010.
11. Nowosielski, L., R. Przesmycki, M. Wnuk, and J. Rychlica, "The methods of measuring attenuation of thin absorbent materials used for electromagnetic shielding," *PIERS Online*, Vol. 7, No. 3, 261–265, 2011.
12. Nowosielski, L., M. Wnuk, R. Przesmycki, K. Piwowarczyk, and M. Bugaj, "Coaxial cables shielding efficiency measuring methodology," *PIERS Proceedings*, 72–76, Kuala Lumpur, Malaysia, Mar. 27–30, 2012.
13. Nowosielski, L., M. Wnuk, and C. Ziolkowski, "Interlaboratory tests in scope of measurement of radio disturbance," *2009 European Microwave Conference*, Vols. 1–3, 288–291, 2009.
14. Piotrowski, Z., L. Nowosielski, L. Zagozdzinski, and P. Gajewski, "Electromagnetic compatibility of the military handset with hidden authorization function based on MIL-STD-461D results," *PIERS Online*, Vol. 4, No. 5, 566–570, 2008.
15. Piwowarczyk, K., R. Przesmycki, L. Nowosielski, and M. Wnuk, "The measurement of the immunity on the electric field about the radiofrequency within the range (80–1000) MHz," *Przeglad Elektrotechniczny*, Vol. 86, No. 3, 165–167, 2010.
16. Przesmycki, R., M. Wnuk, L. Nowosielski, K. Piwowarczyk, and M. Bugaj, "Analysis of the radiated emissions of IT equipment," *PIERS Proceedings*, 1419–1423, Moscow, Russia, Aug. 19–23, 2012.
17. Przesmycki, R., M. Wnuk, L. Nowosielski, K. Piwowarczyk, and M. Bugaj, "The conducted and radiated emission levels from IT devices," *PIERS Proceedings*, 77–81, Kuala Lumpur, Malaysia, Mar. 27–30, 2012.
18. Rahayu, Y., T. A. Rahman, R. Ngah, and P. S. Hall, "Ultra wideband technology and its applications," *5th International on Wireless and Optical Communications Networks, WOCN'08*, 1–5, 10.1109/WOCN.2008.4542537, 2008.
19. Shelby, R. A., D. R. Smith, and S. Schultz, "Experimental verification of a negative Index of Refraction," *Science Magazine*, Vol. 292, No. 5514, 77–79, 2001.
20. Takahara, H., K. Ohno, and M. Itami, "A study on UWB radar assisted by inter vehicle communication for safety applications," *IEEE International Conference on Vehicular Electronics and Safety (ICVES)*, 24–104, 2012.
21. Veselago, V. V., "The electrodynamics of substances with simultaneously negative values of ε and μ," *Sov. Phys. Uspekhi*, Vol. 10, No. 4, 509–514, 1968.
22. Wnuk, M. and M. Bugaj, "Analysis of radiating structures placed on multilayer dielectric," *Computational Methods and Experimental Measurements XIII*, Book Series: *WIT Transactions on Modelling and Simulation*, Vol. 46, 747–755, 2007.
23. Wnuk, M., M. Bugaj, R. Przesmycki, L. Nowosielski, and K. Piwowarczyk, "Wearable antenna constructed in microstrip technology," *PIERS Proceedings*, 67–71, Kuala Lumpur, Malaysia, Mar. 27–30, 2012.

24. Wnuk, M., G. Różański, and M. Bugaj, "The analysis of microstrip antennas using the FDTD method," *Computational Methods and Experimental Measurements XII*, Book Series: *WIT Transactions on Modelling and Simulation*, Vol. 41, 611–620, 2005.
25. Wong, K. L., *Comapct and Boradband Microstrip Antennas*, John Wiley and Sons, 2002.
26. Zilkowski, R. W., "Design, fabrication and testing of double negative metamaterials," *IEEE Trans. Antennas Propag.*, Vol. 51, No. 7, 1516–1529, 2003.
27. Li, L.-W., Y.-N. Li, T. S. Yeo, J. R. Mosig, and J. F. Olivier, "A broadband and high gain metamaterial microstrip antenna," *Appl. Phys. Lett.*, Vol. 96, 164101, 2010.

Identification of Interface in the Complex Systems Based on Radiated Emission of Mobile Computer

Rafal Przesmycki, Marian Wnuk, Pawel Skokowski, and Marek Bugaj
Faculty of Electronics, Military University of Technology
Gen. S. Kaliskiego 2 Str., Warsaw 00-908, Poland

Abstract— In the article structure of complex systems has been described and levels of radiated undesirable emissions deriving from contemporary IT equipment found on the European Union market have been defined and estimated. Moreover an analysis of radiated emission for particular equipment interfaces of a portable PC computer and results of identification of equipment interfaces for a portable device such as tablet characterized by increased radiated emission have been presented in the article.

1. INTRODUCTION

Generally, energy emitted by any source can depend on frequency (f), time (t) and direction (Φ). Its amount sent at the moment t towards Φ, with frequency f, falling to time unit, unitary solid angle and unitary frequency range (expressed in case of three-dimensional space in $[\mathrm{W}\cdot\mathrm{sr}^{-1}\cdot\mathrm{Hz}^{-1}]$), can be called source emissivity:

$$\varepsilon = f(\Phi, f, t). \tag{1}$$

Quantity ε can be found as operator describing conversion of energy released in source (which depends only on frequency and time) into space-time-frequency distribution of energy in medium surrounding source. If direction, frequency and time features of source are independent of each other, then its emissivity ε can be presented in the form of product of three functions representing separate characteristics describing frequency, direction and time selectivity of source [1, 2, 6].

2. COMPLEX SYSTEMS

Complex system is an internally compatible system. A set of electromagnetic signal sources and relations between them and their attributes can be called such a system. Relationship between sources are represented by their mutual interaction (internal interaction) and interaction towards surroundings (external interaction). An example of complex system is an IT device built from many electronic components with determined distinctive features. One of such features is spectrum of radiated emission being the mapping of emission of radiated disturbances. In case of complex system electronic devices cooperate with each other forming the whole system. So the example of complex system is central unit of PC computer or a portable device such as tablet which consists of many electronic components and equipment interfaces located in one casing forming the IT system as a whole [3–5].

3. THE LABORATORY STAND FOR MEASURING RADIATED EMISSION

Measurements of radiated disturbances emitted by IT devices have been conducted in accordance with the EN 55022 : 2011 standard. They consist in measurement of electromagnetic field intensity within the distance of 3 m from a device with the use of measurement antennas and measuring receiver within frequency range from 30 MHz to 6000 MHz. For automatic stimulation of operation of selected computer modules a program BurnInTest has been used. In the application BurnInTest we can select tests used for testing both software and hardware. Each test is assigned for testing various modules of computer system. Those tests can be conducted at the same time since each one has its own individual programs for testing particular components. There is also an opportunity to change load of specific interface into a particular cycle of processor clock through increase or decrease of the number of cycles for particular tests. On the tested portable computer ACER IconiaTab W700 it was necessary to install and activate the software BurnInTest, which allows to choose tests used during research.

Below in the next chapters selected settings and descriptions of tests used during testing the portable computer ACER IconiaTab W700 have been discussed and measurement results for such conducted tests have been presented [11–14].

4. TEST OF CPU AND RAM

This test allows to select a few subtests divided into two groups. The first one is 'Select Math Tests' and the second 'Select SIMD Math Tests'. In the first one there are two different tests: test on integers based on 32 bit table of random numbers from which numbers are processed with the use of mathematical operations. The second test is a test using floating-point numbers. Performed mathematical operations include: addition, subtraction, multiplication, division, addition and subtraction of floating-point numbers as well as multiplication and division of floating-point numbers. Each mathematical operation is performed twice and results are compared. If results obtained in two calculation differ, there is an error. For every test each mathematical operation lasts half second. This test allows to check RAM installed in a computer. It works in the way that standard is entered into RAM and next read out sequence numbers from RAM are verified. The formula changes automatically after transition of each cycle.

5. TEST OF GRAPHICS CARD

There is a possibility to choose one of a few available graphics tests: Local Video Memory Only: testing only local video memory. All Video Memory: testing total video memory, that is local video memory and other video memory such as RAM reserved for graphics. EMC Scrolling Characters: is used to test emissivity of monitors. Monitor and displayed image must be adjusted in such a way to maximize electromagnetic field at a monitor output (e.g., by selecting maximum brightness and white text against black background, letter H etc.). In each case, at first the test determines how much appropriate memory is free and then fills this memory with series of test formulas. Every test formula is entered into video memory and displayed in test window. After display data of test formula are read out again from video memory and verified.

6. TEST OF USB

This test allows to test USB ports. Two test versions are available in the test: USB1 (USB which 1. x transfer rate up to 12 Mb/s) and USB2 (USB 2.0 transfer rate 480 Mb/s). The number of operations in the performed test matches the number of bytes sent and received to and from interface load. Using versions USB1 or USB2 and the BurnInTest program it is possible to check: if USB port is turned ON, data which can be sent and are received by USB, USB error rates and transfer rate, if USB ports were correctly installed, USB cabling and a few USB ports simultaneously.

7. TEST HDD

This test contains series of operations which use a mass storage memory device (hard disk or other data carrier) connected to a computer. In the test we can connect to twenty drives which can be tested or checked at the same time. The drives can be connected via IDE, SATA, SCSI, USB, FireWire buses or any different method operated by the Windows system. User can select one of the following sequences or choose automatic switching between formulas. Available binary sequences in the test HDD are: cyclic data, data formula (0, 1, 2, ..., 255), random data contributing high or low level, binary data (10101010), binary data (01010101), binary data (00000000), binary data (11111111), pseudorandom binary data. During each test cycle a file is formed which is next verified on a tested HDD. The file size is equal to some percentage of disk capacity. All files are formed in main directory of selected disks. Default file size is 1.0% of disk size.

8. MEASUREMENT RESULTS

From among available tests the following ones have been selected: of processor, RAM, graphics card, USB and hard disks. During conducting emissivity tests three kinds of measurements have been made:

- all interfaces worked simultaneously,
- all interfaces were turned off. The computer worked with activated operation system in idle state. Thanks to that noise background for measuring environment was obtained,
- interfaces which at particular moment were tested have been turned on one by one: CPU and RAM, VGA, USB, Serial ATA IDE (HDD) [7–10].

In Figure 1 levels of electromagnetic field intensity have been presented in frequency function for noise background of measuring environment(blue colour) and portable computer with operation of all equipment interfaces (red colour). Presented in Figure 1 in blue colour noise background

(computer operation without extorting movement on interfaces) is reference diagram to which other frequency spectra of portable PC computer working under load of particular interfaces are

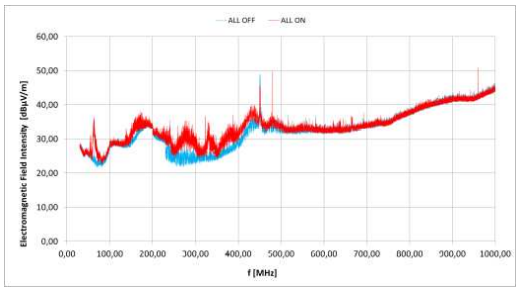

Figure 1: Levels of radiated emission of tablet with no load of equipment interfaces (blue colour) and with operation of all equipment interfaces (red colour).

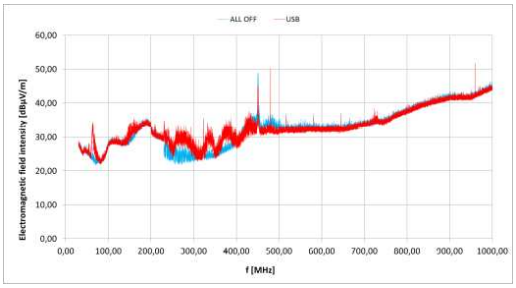

Figure 2: Levels of radiated emissions of tablet with no load of equipment interfaces (blue colour) and with operation of USB interface (red colour).

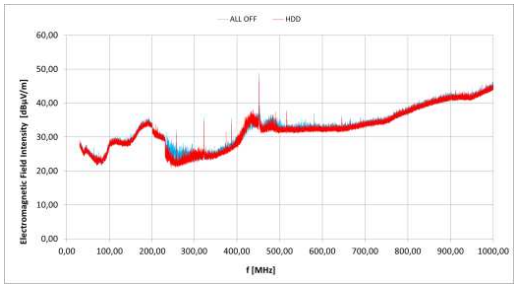

Figure 3: Levels of radiated emission of tablet with no load of equipment interfaces (blue colour) and with operation of HDD (red colour).

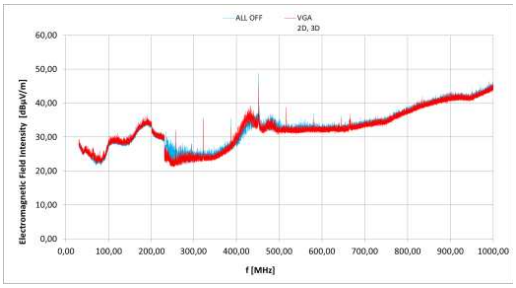

Figure 4: Levels of radiated emission of tablet with no load of equipment interfaces (blue colour) and with operation of VGA graphics (red colour).

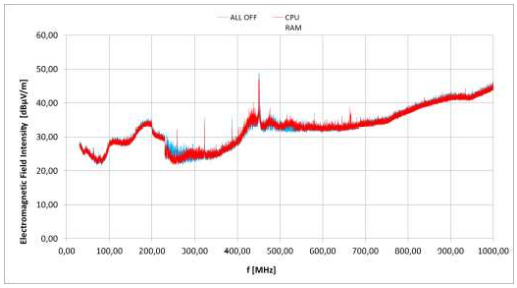

Figure 5: Levels of radiated emission of tablet with no load of equipment interfaces (blue colour) and with operation of CPU and RAM (red colour).

Table 1: Levels of EM field intensity from equipment interfaces situated in tablet ACER.

Device/kind of interface	f [MHz]	Emission level within the distance 3 m from tablet ACER IconiaTab W700 [dBµV/m]		Device/ kind of interface	f [MHz]	Emission level within the distance 3 m from tablet ACER IconiaTab W700 [dBµV/m]	
		With work of Interface	Without work of interface			With work of Interface	Without work of interface
USB	62–70	33,67	24,50	VGA	417–421	43,08	28,67
USB	140–160	33,18	28,79	USB	480,00	50,28	34,14
VGA	153,00	37,22	28,92	VGA	511–514	38,42	32,61
USB	260–290	31,05	24,30	CPU, RAM	663–666	36,89	33,04
VGA	288,00	41,98	34,55	HDD	680,00	46,91	40,02
HDD	374,00	31,56	28,01	VGA	820,00	46,71	38,84
VGA	382,00	43,46	35,10	USB	960,00	51,80	42,53

compared. In that way it will be possible to state if the emissivity increase occurred within a particular frequency range for tested interface. In Figures 2 to 5 measured values of the noise background level have been presented along with Values of electromagnetic field intensity radiated by tablet ACER IconiaTab W700 within the range from 30 MHz to 1000 MHz for various loads of the device. Load should be understood as activation of particular equipment interfaces of IT device.

On the basis of obtained measurement results one can state that there is a possibility to identify equipment interfaces of tablet which cause the increase of emissivity level. So, a distinctive feature of operation of specific interfaces is its work frequency and emissivity level allowing to identify a given equipment interface. The results of equipment interface identification have been collected in Table 1.

9. CONCLUSIONS

In the article levels of radiated undesirable emissions deriving from modern IT equipment present on the European Union market have been determined and estimated. Those emissions are by-products generated in unintentional way during realization of basic function of the device and therefore one should strive for as low their level as possible. Determined levels might be the basis at initial stages of designing electromagnetic safety of contemporary IT devices by striving for providing conformity with suitable norms effective in the European Union. Moreover due to identification of internal components of portable device causing increased emission there is a possibility of significant acceleration of the process of preparing the device for sale in case when its emissivity level is inconsistent with the norm. The collected within the study measurement results of radiated emission generated by particular components of the above mentioned devices have allowed to build data base which could be used for identification of components characterized by too high level of radiated emission.

ACKNOWLEDGMENT

The project is financed from NCBiR means within the Agreement No. 0024/R/ID2/2012/02 in the years 2012–2015.

REFERENCES

1. Piotrowski, Z., L. Nowosielski, L. Zagozdzinski, and P. Gajewski, "Electromagnetic compatibility of the military handset with hidden authorization function based on MIL-STD-461D results," *PIERS Online*, Vol. 4, No. 5, 566–570, 2008.
2. Gajewski, P., J. Lopatka, L. Nowosielski, B. Uljasz, and Z. Piotrowski, "Multimedia transmission over HF links," *IEEE 21st Century Military Communications Conference Proceedings, Military Communications Conference*, Vol. 1, 45–47, 2000.
3. Kubacki, R., J. Ferenc, and R. Przesmycki, "The measurements of the complex permittivity and permeability of powdered nanocrystalline Fe-Si-B-Cu-Nb ('finemet')," *Przeglad Elektrotechniczny*, Vol. 87, No. 12B, 92–95, 2011.
4. Kubacki, R., L. Nowosielski, and R. Przesmycki, "The improved technique of electric and magnetic parameters measurements of powdered materials," *Advances in Engineering Software*, Vol. 42, No. 11, 911–916, 2011.
5. Kubacki, R., L. Nowosielski, and R. Przesmycki, "Technique for the electric and magnetic parameter measurement of powdered materials," *Computational Methods and Experimental Measurements XIV Book Series: WIT Transactions on Modelling and Simulation*, Vol. 48, 241–250, 2009.
6. Kubacki, R., E. Cwalina, M. Kuchta, and A. Dukata, "Electromagnetic field distribution in the office room and computer enclosure evoked by electromagnetic high power pulses," *Przeglad Elektrotechniczny*, Vol. 88, No. 12B, 209–212, 2012.
7. Kubacki, R., M. Wnuk, and J. Kieliszek, "Fresnel approximations in mathematical expressions of the electric field for base station antennas," *Przeglad Elektrotechniczny*, Vol. 84, No. 12, 190–193, 2008.
8. Kubacki, R., "Biological interaction of pulse-modulated electromagnetic fields and protection of humans from exposure to fields emitted from radars," *17th International Conference on Microwaves, Radar and Wireless Communications, MIKON-2008*, 1–7, 2008.

9. Kubacki, R. S., J. Sobiech, and E. Sedek, "Model for investigation of microwave energy absorbed by young and mature living animals," *Electromagnetic Field, Health and Environment, Proceedings of EHE' 07 Book Series: Studies in Applied*, Vol. 29, 126–132, 2008.
10. Kubacki, R., J. Kieliszek, and A. Krawczyk, "The investigation of influence of the electromagnetic fields emitted from short-wave diathermy to the pacemakers," *Przeglad Elektrotechniczny*, Vol. 83, No. 12, 105–107, 2007.
11. Kubacki, R., J. Sobiech, J. Kieliszek, and A. Krawczyk, "Comparison of numerical and measurement methods of SAR of ellipsoidal phantoms with muscle tissue electrical parameters," *The International Journal for Computation and Mathematics in Electrical and Electronic Engineering*, Vol. 25 No. 3, 691–704, 2006.
12. Dabrowski, M. P., W. Stankiewicz, R. Kubacki, E. Sobiczewska, and S. Szmigielski, "Immunotropic effects in cultured human blood mononuclear cells pre-exposed to low-level 1300 MHz pulse-modulated microwave field," *Electromagnetic Biology and Medicine*, Vol. 22, No. 1, 1–13, 2003.
13. Kubacki, R., M. Wnuk, W. Kolosowski, and J. Sobiech, "New approach to electromagnetic field calculations in the near-field of microwave antennas," *Computational Methods and Experimental Measurements XI Book Series: Computational Engineering*, Vol. 4, 413–422, 2003.
14. Kubacki, R., M. Krukowski, J. Kieliszek, and J. Sobiech, "New computational model of electromagnetic field distribution for predicting of the safety zones in the near-field of microwave antennas," *14th International Conference on Microwaves, Radar and Wireless Communications, MIKON-2002*, Vol. 3, 902–905, 2002.

Measurement and Analysis of Compromising Emanation for Laser Printer

Rafal Przesmycki
Faculty of Electronics, Military University of Technology
Gen. S. Kaliskiego 2 Str., Warsaw 00-908, Poland

Abstract— The article concerns problems connected with electromagnetic compatibility and compromising emanation, i.e., information security. In the article channels of electromagnetic information permeability have been de-scribed and then there has been the focus on laser printers for which forcing signals used during measurements of compromising emanation have been presented and measurement results of compromising emanation deriving from laser printer have been described.

1. INTRODUCTION

Information security against electromagnetic permeability of devices and electromagnetic systems (IT) is of great importance. This problem increases with a higher and higher use of ICT devices for processing and transmitting information which should not fall into the wrong hands. It results from the fact that each electronic device is the source of undesirable (secondary) emission of electromagnetic energy induced in surrounding space and in all close conductors and metal structures.

When signals of undesirable emission are correlated with unclassified information, they can be used for reconstructing that information by intelligence services. The phenomenon of such undesirable emission is called compromising emanation and its use by intelligence-penetration or electromagnetic infiltration. Undertakings which aim is to hinder system recognition on the basis of compromising emanation are called information protection against electromagnetic penetration or emission safety.

Electromagnetic emissions with the feature of compromising emanation can arise at any stage of processing of encoded information in the form of electric current courses. There is also no possibility to conduct tests of the source itself and the channel of information permeability. However such tests can be conducted in laboratory conditions in which examined devices are introduced into operation mode allowing to learn their infiltration susceptibility. In this article an example of such experiments has been presented. It seems that most suitable for illustrating the issue of electromagnetic information permeability are devices or their components which process information in serial way and the rule of encoding is uncomplicated and well-known.

2. LASER PRINTER

Monochromatic laser printers are probably the most popular devices in our workplaces which allow to obtain perfect quality printouts at little cost. Just like in case of VGA monitors, the following features of information signal converted in that device prove the possibility of information interception from laser printer:

- information about the colour of each printout point is encoded in the form of rectangular pulses, high contents of harmonics increases probability of formation of electromagnetic emissions.
- data are encoded in analogue way through regulation of level of particular signals corresponding with two basic colours which makes easy information reconstruction possible
- data are sent in serial way.

3. MEASURING POSITION FOR MEASURING COMPROMISING EMANATION

In order to determine sources of compromising emanation deriving from laser printer it is necessary to estimate a contents degree of test signal intentionally generated by laser printer in the signal received by measuring position as radiated or conducted compromising emanation. Measuring position for conducting tests of determining sources of compromising emanations should make reception of generated test signal propagating as radiated or conducted compromising emanation possible. In this article attention has been paid to radiated compromising emanation. Printout

of selected images on paper sheets was used for laser printer as enforcement for compromising emanation. With the use of receiving antennas [5–9] signal received by antenna gets through commutator which switches antennas to FSET 22 broad-band receiver. In the receiver those signals are filtered and their conversion into lower frequency range takes place. Signal after detection is passed to VIDEO output in the receiver and then it is passed to input of external channel of oscilloscope on which there is a possibility of displaying received information in time domain [1–4].

4. MEASUREMENT RESULTS

Common observation of spectrum obtained during printer operation in the printing and stand-by mode does not give the answer about the possibility of occurrence of compromising emanations. Since it turns out that significant sources of electromagnetic emissions of laser printer are stepper motors and other electric elements which do not process signals carrying information about a printed document. Those elements are e.g., all kinds of paper end sensors, paper jam sensors, toner state etc.. Therefore during classification of printers from the perspective of levels of electromagnetic emissions correlated with classified information an evaluation method allowing to state presence of such emissions should be taken. One of the methods can be conducting measurements of radiated emissions from printer during printing documents significantly differing in contents.

In order to determine distinctive features for laser printer during operation reflected in components of frequency spectrum or in time domain test patterns used during tests conducted with printing operation of laser printer have been chosen. The following images have been chosen as test signals generated to the printout process by laser printer: White image on A4 sheet, A4 sheet filled with three lines placed in the middle of the sheet, A4 sheet filled with three lines placed outside the sheet, A4 sheet filled with eight lines placed in the middle of the sheet. The look of test patterns generated during printing by laser printer has been shown in Figure 1. Measurement results for the two mentioned test patterns (white image on A4 sheet and A4 sheet filled with three lines placed in the middle of the sheet) have been presented in Figures 2–4.

Very often evaluation of spectrum itself is insufficient due to difficulties resulting from rating of appearing signals at particular frequencies. Those signals often inform only about the moment of taking paper from sheet feed unit, heater operation or they are connected with work of elements demagnetizing roller. Because of that it is necessary to use other methods consisting in the use of more advanced measuring devices. Anyway in most cases qualification of emissions occurs with the use of visual method. It should be remembered though that in doubtful cases or in such ones where visual assessment is impossible evaluation methods based on digital methods of processing of recorded signals are used [10–13].

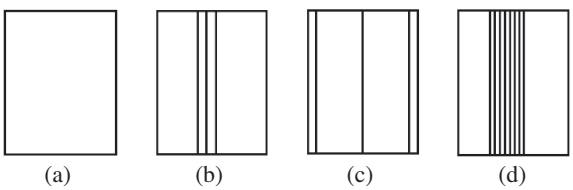

Figure 1: Test patterns used during tests of compromising emanation deriving from laser printer.

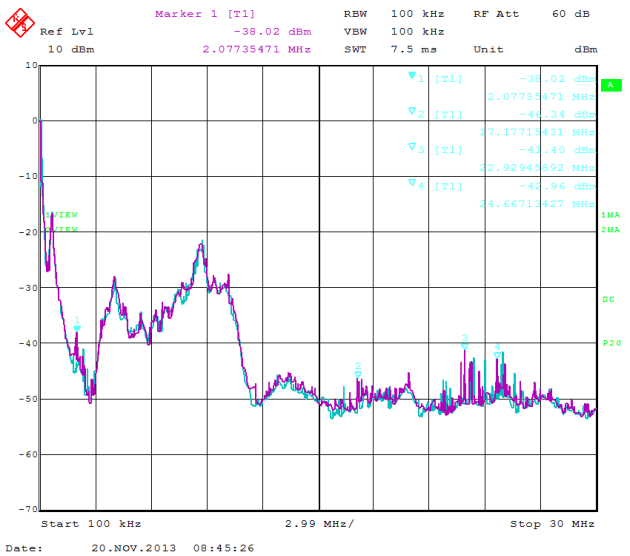

Figure 2: Radiated emissivity deriving from laser printer printing white image (blue colour) and test pattern (violet colour) within frequency range 100 kHz–30 MHz.

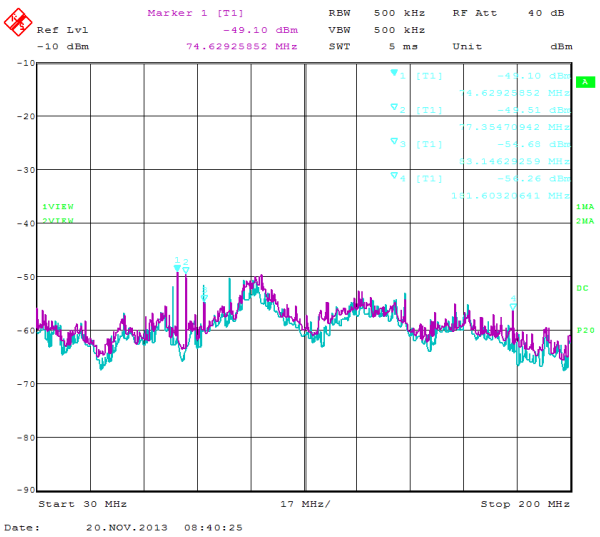

Figure 3: Radiated emissivity deriving from laser printer printing white image (blue colour) and test pattern (violet colour) within frequency range 30 MHz–200 MHz.

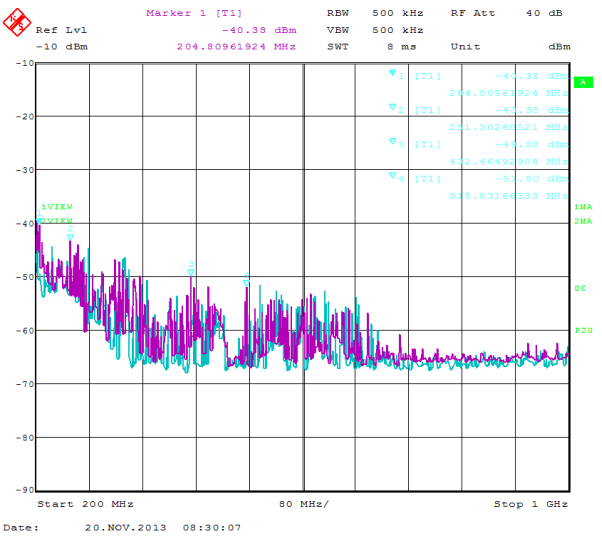

Figure 4: Radiated emissivity deriving from laser printer printing white image (blue colour) and test pattern (violet colour) within frequency range 200 MHz–1000 MHz.

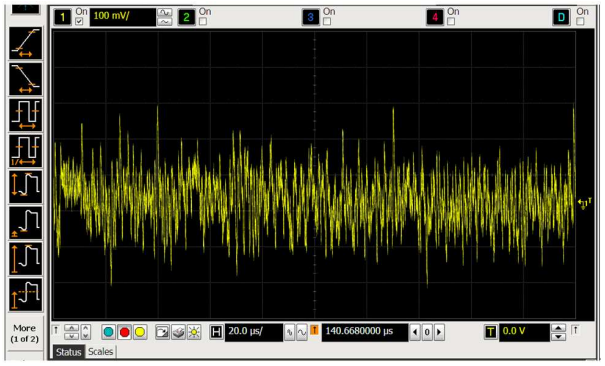

Figure 5: Oscillogram for laser printer connected to PC and printing test pattern a). The signal received by antenna for $f = 220$ MHz from VIDEO output of FSET22 receiver.

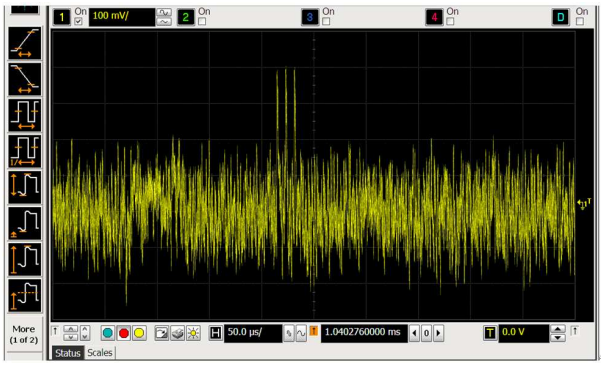

Figure 6: Oscillogram for laser printer connected to PC and printing test pattern b). The signal received by antenna for $f = 220$ MHz from VIDEO output of FSET22 receiver.

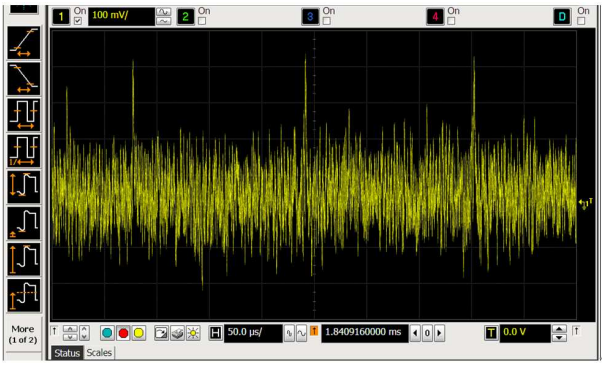

Figure 7: Oscillogram for laser printer connected to PC and printing test pattern c). The signal received by antenna for $f = 220$ MHz from VIDEO output of FSET22 receiver.

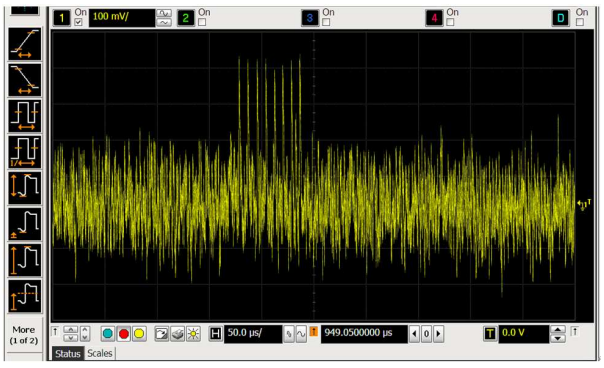

Figure 8: Oscillogram for laser printer to PC computer and printing test pattern d). The signal received by antenna for $f = 220$ MHz from VIDEO output of FSET22 receiver.

Identification is a process or a result of processes of identifying a particular object with other object. It may include distinguishing common features, capturing similarities between a tested

object and other objects of the same category, estimating values of observed parameters of a particular object. Using any methods of signal identification of compromising emanation [18] requires determination of distinctive features characteristic for model information signals and determination of a similarity degree of those features for analogous parameters of tested signals. On the basis of an analysis of radiated emission levels by laser printer probable signal reception frequencies of compromising emanation have been determined. To test whether radiated signals within that frequency range actually have the character of compromising emanation, a series of recordings of those signals has been made with the use of digital oscilloscope and analysed [14–17]. The measurements have been made while printing sheets containing particular content(number of vertical lines) for images defined in Figure 1. The sample results have been placed in Figures 5–8.

5. CONCLUSIONS

The presented above time courses of radiated emission signals by laser printer show clearly that those signals have an evident connection with contents of printed pages and thus they have the character of compromising emanation signals. Time courses directly identify the contents form of printed page. Of course it happens when a sheet with simple graphics in the form of vertical lines is printed. A number of 'pins' in time course informs about a number of lines in a document. However visual view from time course starts getting complicated when a printed page contains graphics or text. Then one can only distinguish printout of blank paper sheet from filled one. So the question arises: is it possible to reconstruct, with the use of electromagnetic emissions, contents of a printed document just like it is in case of information displayed on a computer monitor? It turns out to be possible and quality of reconstructed data is so high that it can be read out immediately.

ACKNOWLEDGMENT

The project is financed from the NCBiR means within the Agreement No. 0024/R/ID2/2012/02 in the years 2012–2015.

REFERENCES

1. Gruszczynski, M., M. Wnuk, and L. Nowosielski, "Multisystem microstrip antenna for mobile communications," *IEEE Antennas and Propagation Society International Symposium (APSURSI)*, Book Series: *IEEE Antennas and Propagation Society International Symposium*, 2012.
2. Nowosielski, L., M. Wnuk, and C. Ziolkowski, "Interlaboratory tests in scope of measurement of radio disturbance," *2009 European Microwave Conference*, Vol. 1–3, 288–291, 2009.
3. Piotrowski, Z., L. Nowosielski, L. Zagozdzinski, and P. Gajewski, "Electromagnetic compatibility of the military handset with hidden authorization function based on MIL-STD-461D results," *PIERS Online*, Vol. 4, No. 5, 566–570, 2008.
4. Gajewski, P., J. Lopatka, L. Nowosielski, B. Uljasz, and Z. Piotrowski, "Multimedia transmission over HF links," *IEEE 21st Century Military Communications Conference Proceedings, Military Communications Conference*, Vols. 1, 2, 45–47, 2000.
5. Bugaj, M. and M. Wnuk, "Optimization parameters of dielectric in aperture-coupled stacked patch antenna on bandwidth," *18th International Conference on Microwaves, Radar and Wireless Communications (MIKON-2010)*, Vols. 1, 2, 2010.
6. Bugaj, M. and M. Wnuk, "Influence of parameters of dielectric in aperture-coupled stacked patch antenna on bandwidth," *Przeglad Elektrotechniczny*, Vol. 85, No. 9, 50–53, 2009.
7. Bugaj, M. and M. Wnuk, "The influence examination of dielectric parameters on bandwidth in multilayer aperture-coupled microstrip Antennas with utilization the FDTD method," *MIKON Conference Proceedings*, Vols. 1, 2, 708–711, 2008.
8. Wnuk, M. and M. Bugaj, "Analysis of radiating structures placed on multilayer dielectric," *Computational Methods and Experimental Measurements XIII*, Book Series: *WIT Transactions on Modelling and Simulation*, Vol. 46, 747–755, 2007.
9. Wnuk, M., G. Rózanski, and M. Bugaj, "The analysis of microstrip antennas using the FDTD memod," *Computational Methods and Experimental Measurements XII*, Book Series: *WIT Transactions on Modelling and Simulation*, Vol. 41, 611–620, 2005.
10. Kubacki, R., E. Cwalina, M. Kuchta, and A. Dukata, "Electromagnetic field distribution in the office room and computer enclosure evoked by electromagnetic high power pulses," *Przeglad Elektrotechniczny*, Vol. 88, No. 12B, 209–212, 2012.

11. Kubacki, R., M. Wnuk, and J. Kieliszek, "Fresnel approximations in mathematical expressions of the electric field for base station antennas," *Przeglad Elektrotechniczny*, Vol. 84, No. 12, 190–193, 2008.
12. Kubacki, R., "Biological interaction of pulse-modulated electromagnetic fields and protection of humans from exposure to fields emitted from radars," *MIKON Conference Proceedings*, Vols. 1, 2, 66–72, 2008.
13. Kubacki, R., J. Sobiech, and E. Sedek, "Model for investigation of microwave energy absorbed by young and mature living animals," *Electromagnetic Field, Health and Environment, Proceedings of EHE '07*, Book Series: *Studies in Applied*, Vol. 29, 126–132, 2008.
14. Kubacki, R., J. Kieliszek, and A. Krawczyk, "The investigation of influence of the electromagnetic fields emitted from short-wave diathermy to the pacemakers," *Przeglad Elektrotechniczny*, Vol. 83, No. 12, 105–107, 2007.
15. Kubacki, R., J. Sobiech, J. Kieliszek, and A. Krawczyk, "Comparison of numerical and measurement methods of SAR of ellipsoidal phantoms with muscle tissue electrical parameters," *COMPEL — The International Journal for Computation and Mathematics in Electrical and Electronic Engineering*, Vol. 25, No. 3, 691–704, 2006.
16. Dabrowski, M. P., W. Stankiewicz, R. Kubacki, E. Sobiczewska, and S. Szmigielski, "Immunotropic effects in cultured human blood mononuclear cells pre-exposed to low-level 1300 MHz pulse-modulated microwave field," *Electromagnetic Biology and Medicine*, Vol. 22, No. 1, 1–13, 2003.
17. Kubacki, R., M. Wnuk, W. Kolosowski, and J. Sobiech, "New approach to electromagnetic field calculations in the near-field of microwave antennas," *Computational Methods and Experimental Measurements XI*, Book Series: *Computational Engineering*, Vol. 4, 413-422, 2003.
18. Kubacki, R., M. Krukowski, J. Kieliszek, and J. Sobiech, "New computational model of electromagnetic field distribution for predicting of the safety zones in the near-field of microwave antennas," *XIV International Conference on Microwaves, Radar and Wireless Communications, MIKON-2002*, Vols. 1–3, 902–905, 2002.

Compromising Emanations from USB 2 Interface

Leszek Nowosielski and Marian Wnuk
Faculty of Electronics, Military University of Technology
Gen. S. Kaliskiego 2 Str., Warsaw 00-908, Poland

Abstract— In the article assessment of the possibility of use and usability of USB 2.0 interface in IT devices used for classified information processing to minimize the risk of electromagnetic eavesdropping has been made. In those devices the aim is to minimize the level of radiated emissions via radio path, in which there is a high probability of interception by unauthorized persons and reproduction of conveyed information. The article has focused on revealing the possibility of eavesdropping of radiated compromising emanation during data transmission through USB 2.0 interface. For that purpose a comparative analysis of signal occurring directly on transmission line of USB 2.0 port has been made as well as its equivalent received by FSET 22 receiver as radiated emission. For the analysis signals generated by transmission lines of USB 2.0 port have been used. They were obtained as a result of measurements directly on transmission line and at the output of envelope detector of FSET 22 receiver received as radiated emission.

1. INTRODUCTION

Because of the fact that nowadays a big emphasis is put on classified information protection, modern IT devices and communication systems [10–13] are required not to pose a threat of interception of this kind of information. In this case loss of confidentiality might occur as a result of using electromagnetic emissions arising during operation of IT devices to intercept classified data. In this kind of devices a big emphasis is put on minimization of compromising emanation via radiated path. A particular threat of radiation of compromising signals via radio path is made by modern broad-band telecommunications interfaces such as: USB 2.0, USB 3.0, Ethernet etc.. In this study assessment of the possibility of use and usability of USB 2.0 interface in IT devices assigned for classified information processing has been made as well as a procedure of testing IT devices equipped with USB 2.0 interface has been suggested which aim is to assess the possibility of conducting electromagnetic eavesdropping of this type of devices.

2. OPTIMIZATION OF BINARY TESTING SEQUENCE FROM THE PERSPECTIVE OF MAXIMIZATION OF LEVEL OF RADIATED COMPROMISING EMANATION

A form of signal course directly on transmission line has a direct influence on the level of particular spectrum components of radiated emission from USB 2.0 received by eavesdropping receiver. That being so, for analyses aiming at assessment of the possibility of conducting electromagnetic eavesdropping, such a form of binary information sequences was selected which were generated by BTSG (binary testing sequence generator) transmission software operating at PC equipped with a tested USB 2.0 port, which results in maximization of a level of particular components of frequency spectrum of radiated emission. As a result of conducted tests and analyses it was determined that particular components of signal spectrum on USB 2.0 transmission line have maximal levels of particular spectrum components of radiated emission only for binary information sequences generated by BTSG, which after their processing by standard output systems of USB port generate periodic binary stream on transmission line. To force periodic binary stream on transmission line, BTSG should generate binary information sequence which after processing by standard output systems of USB 2.0 port will cause occurrence of periodic binary stream on transmission line.

Significant processes of signal processing in USB 2.0 interface, which have influence on a form of binary stream at its output include the process of bit stuffing and NRZI (non return to zero inverted) linear encoding. Taking into account the influence of the above methods of signal processing on the form of binary stream at output of USB 2.0 port, with the use of BTSG application it is necessary to transmit of the following binary information sequences through USB 2.0 interface:

- sequence of logic 0s: 000000000000000000...,
- sequence of logic 1s: 1111111111111111...,
- sequence of logic 1s and 0s: 010101010101010101....

3. DETERMINATION OF DISTINCTIVE FEATURES OF SIGNALS OF RADIATED COMPROMISING

In order to show the possibility of electromagnetic eavesdropping during data transmission through USB 2.0 interface, measurements of signal spectrum occurring directly on USB 2.0 transmission line during transmission of information data sequence generated by BTSG described in the previous item of this article have been conducted. The measurements were carried out with the use of laboratory stand, which block diagram is presented in Fig. 1. An analysis of frequency spectra corresponding to particular sequences of information data generated by BTSG has allowed to define distinctive features such as frequencies characteristic for radiated compromising emanations generated by USB 2.0 port. In Fig. 2 a sample signal spectrum of radiated emission generated by USB 2.0 interface during transmission of information data sequence consisting of logic zeroes is presented. The conclusion resulting from the above spectrogram is that radiated compromising emanation occurs at frequencies: 240 MHz, 480 MHz and 720 MHz.

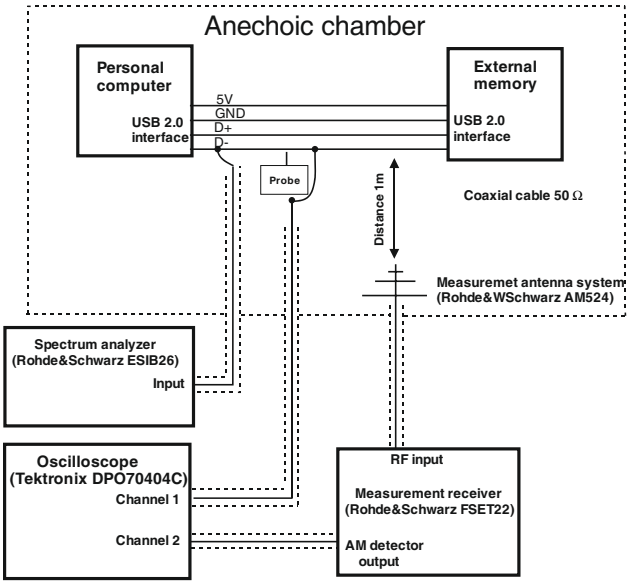

Figure 1: Block diagram of laboratory station for observation of signal occurring directly on transmission line of USB 2.0 port and its equivalent received by eavesdropping receiver as radiated emission.

In a further part of the experiment FSET 22 eavesdropping receiver was retuned to particular frequencies at which radiated compromising emanation occurs and then a comparative analysis of signal occurring directly on USB 2.0 transmission line and its equivalent received by eavesdropping receiver as radiated emission was made. For the comparative analysis signals generated by USB 2.0 port were used. They were received as a result of measurements directly on transmission line and at the output of envelope detector of FSET 22 receiver as radiated emission. A sample display of oscillograms matching information data sequence generated by BTSG consisting of logic zeroes is presented in Fig. 3. The analysed time courses and their spectra were obtained as a result of measurements conducted at measuring position, which block diagram is presented in Fig. 1. After an initial comparative analysis large similarity of signals recorded directly on transmission line of USB 2.0 port can be noticed (oscillogram of yellow colour in Fig. 3) as well as its equivalent received by eavesdropping receiver as radiated emission(oscillogram of green colour in Fig. 3). The result of the above observation proves the possibility of electromagnetic eavesdropping.

In Table 1 distinctive frequencies occurring during transmission of particular sequences of information data generated by BTSG was presented on which large correlation of signals occurring directly on USB 2.0 transmission line was found as well as at the output of envelope detector of FSET 22 receiver received as radiated emission.

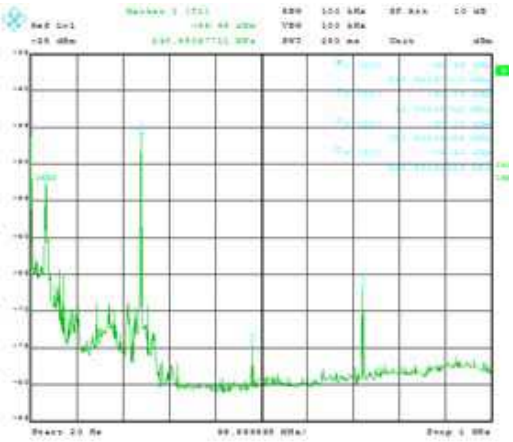

Figure 2: Frequency spectrum of signal during transmission of logic zeroes.

Figure 3: Oscillogram for USB 2.0 interface during transmission of information data sequence consisting of logic zeroes. Yellow colour — directly from interface transmission line. Green colour — signal at output of amplitude detector of eavesdropping receiver tuned to frequency $f = 240\,\text{MHz}$.

Table 1: Distinctive frequencies for compromising emanation generated by USB 2.0 port.

Information data sequence generated by FG	...111111...	...000000...	...010101...
Distinctive frequencies for compromising emanation generated by USB 2.0 port.	34.29 MHz, 68.58 MHz, 102.87 MHz	240 MHz, 480 MHz, 720 MHz	120 MHz, 240 MHz, 360 MHz,

4. ASSESSMENT OF DEGREE OF ELECTROMAGNETIC LEAKAGE FROM USB 2.0 INTERFACE

In order to assess a degree of electromagnetic leakage from USB 2.0 interface a degree of similarity between signal generated by USB 2.0 port received as a result of measurements directly on transmission line and at the output of envelope detector of FSET 22 receiver received as radiated emission was calculated. The degree of similarity was calculated for signals recorded during transmissions of particular test sequences of information data generated by BTSG discussed in the second item of this article. As a measure of the leakage degree correlation coefficient was used. On the basis of the studies it has been found that selection of an appropriate number of analysed signal samples for calculating correlation coefficient has a significant influence on their value. In Table 2 dependence of correlation coefficient value of signal recorded directly on transmission line of USB 2.0 interface has been presented as well as for signal recorded at the output of envelope detector of FSET 22 receiver received as radiated emission in the function of signal sample amount. For the analysed signals the biggest value of correlation coefficient was obtained for 8000 signal samples.

Table 2: Dependence of correlation coefficient value of signal recorded directly on transmission line of USB 2.0 interface and for signal recorded at the output of envelope detector of FSET 22 receiver received as compromising emanation in the function of signal sample amount.

Item no.	**Number of samples**	**Correlation coefficient**
1	500	0,6245
2	5000	0,6980
3	8000	0,6967

5. CONCLUSIONS

The article has focused on showing the possibility of electromagnetic eavesdropping during data transmission through USB 2.0 interface. For that purpose the comparative analysis of signal occurring directly on transmission line of USB 2.0 port has been made as well as its equivalent received by FSET 22 receiver as radiated emission. The conclusion from the conducted analyses is that:

- Using USB 2.0 interface for data transmission poses a threat of electromagnetic eavesdropping, which negates the possibility of its usability in IT devices used for classified information processing without using additional protections.
- A form of signal course directly on transmission line has a direct influence on the level of particular spectrum components of radiated emission from USB 2.0 port received by eavesdropping receiver. That being so, for testing IT devices equipped with USB 2.0 interface aiming at assessment of possibilities of conducting electromagnetic eavesdropping it is necessary to select such a form of binary information sequences generated by BTSG transmission software operating on PC equipped with a tested USB 2.0 port, which results in maximization of the level of particular components of frequency spectrum of radiated emission. Such sequences include binary sequences consisting of: logic zeroes, logic ones and alternate sequences of logic ones and zeroes.
- Binary information sequence generated by BTSG transmission line in the form of sequence of logic zeroes causes radiated emission with maximal levels of particular components of frequency spectrum.
- Correlation coefficient between signal recorded at the output of envelope detector of eavesdropping receiver FSET 22 as radiated emission and signal recorded directly on transmission line of USB 2.0 interface can be successfully used as similarity measures between the above mentioned signals during tests of IT devices equipped with USB 2.0 interface aiming at assessment of possibilities of conducting electromagnetic eavesdropping.
- The radio path attenuation have a big influence on the compromising emanation level. The attenuation can estimated using the radio-wave propagation modelling [1–9].

ACKNOWLEDGMENT

The project is financed from NCBiR means within the Agreement No. 0024/R/ID2/2012/02 in the years 2012–2015.

REFERENCES

1. Kubacki, R., J. Ferenc, and R. Przesmycki, "The measurements of the complex permittivity and permeability of powdered nanocrystalline Fe-Si-B-Cu-Nb ("Finemet")," *Przeglad Elektrotechniczny*, Vol. 87, No. 12B, 92–95, 2011.
2. Kubacki, R., E. Cwalina, M. Kuchta, and A. Dukata, "Electromagnetic field distribution in the office room and computer enclosure evoked by electromagnetic high power pulses," *Przeglad Elektrotechniczny*, Vol. 88, No. 12B, 209–212, 2012.
3. Kubacki, R., "Biological interaction of pulse-modulated electromagnetic fields and protection of humans from exposure to fields emitted from radars," *2008 MIKON Conference Proceedings*, Vol. 1 and 2, 66–72, 2008.
4. Kubacki, R., J. Sobiech, and E. Sedek, "Model for investigation of microwave energy absorbed by young and mature living animals," *Electromagnetic Field, Health and Environment, Proceedings of EHE'07*, *Studies in Applied*, Vol. 29, 126–132, 2008.
5. Kubacki, R., J. Kieliszek, and A. Krawczyk, "The investigation of influence of the electromagnetic fields emitted from short-wave diathermy to the pacemakers," *Przeglad Elektrotechniczny*, Vol. 83, No. 12, 105–107, 2007.
6. Kubacki, R., J. Sobiech, J. Kieliszek, and A. Krawczyk, "Comparison of numerical and measurement methods of SAR of ellipsoidal phantoms with muscle tissue electrical parameters," *COMPEL — The International Journal for Computation and Mathematics in Electrical and Electronic Engineering*, Vol. 25, No. 3, 691–704, 2006.
7. Dabrowski, M. P., W. Stankiewicz, R. Kubacki, E. Sobiczewska, and S. Szmigielski, "Immunotropic effects in cultured human blood mononuclear cells pre-exposed to low-level 1300 MHz pulse-modulated microwave field," *Electromagnetic Biology and Medicine*, Vol. 22, No. 1, 1–13, 2003.

8. Kubacki, R., M. Krukowski, J. Kieliszek, and J. Sobiech, "New computational model of electromagnetic field distribution for predicting of the safety zones in the near-field of microwave antennas," *XIV International Conference on Microwaves, Radar and Wireless Communications, MIKON-2002*, Vol. 1–3, 902–905, 2002.
9. Michalak, J. and B. Uljasz, "Relative efficiency of broadcasting in the cluster based network — Simulation results," *Military Communications and Information Systems Conference (MCC 2013)*, Francja, Saint-Malo, Jun. 10–Jul. 8, 2013, ISBN 978-83-62954.
10. Piotrowski, Z., "Angle phase drift correction method effectiveness," *Signal Processing Algorithms, Architectures, Arrangements, and Applications Conference Proceedings*, 82–86, 2009, ISBN: 978-83-62065-00-4.
11. Byłak, M. and D. Laskowski, "Assessment of network coding mechanism for the network protocol stack 802.15.4/6LoWPAN," *Advances in Intelligent Systems and Computing, Springer International Publishing AG*, Switzerland, Vol. 224, 75–82, 2013, ISSN: 2194–5357 (Print), 2194–5365 (Online).
12. Laskowski, D., P. Łubkowski, and M. Kwasniewski, "Identification of suitability services for wireless networks," *Przeglad Elektrotechniczny*, R. 89 9/2013, Sigma-Not, Warszawa, str. 128-132, 2013, ISSN 0033-2097.
13. Byłak, M. and D. Laskowski, "Diagnosis coding efficiency of network coding mechanism for wireless networks," *Przeglad Elektrotechniczny*, R. 89 9/2013, Sigma-Not, Warszawa, str. 133-138, 2013, ISSN 0033-2097.

Attenuation Measurements of Materials Used in Construction of Buildings

Marek Bugaj
Faculty of Electronics, Military University of Technology
Gen. S. Kaliskiego 2 Str., Warsaw 00-908, Poland

Abstract— In the article research methodology and measuring position for determining attenuation of materials used for building structures have been described. The discussed research methodology is based on microwave measuring set on the basis of coaxial line guaranteeing large bandwidth of realized measurements. In the article selected samples of materials used for building structures have been characterized as well as attenuation results of those materials have been presented.

1. INTRODUCTION

Attenuation of walls, ceilings or other building barriers depends — among other things — on permittivity of material the wall is made of, frequency of incident radiation and wall thickness. In order to determine attenuation of electromagnetic waves by wall, each wall should be measured individually to define what level of electromagnetic field intensity is attenuated by such a barrier. In order to determine attenuation of materials used for building structures it is necessary to perform analytical calculations of electric field attenuation or make a direct measurement on a natural sample of a particular material. For analytical calculation of electromagnetic field attenuation by shielding material it is necessary to determine electric and magnetic values of material a particular structural material is made of. Parameters which define the above mentioned properties are respectively permittivity ε and magnetic permeability μ of tested material. Due to the fact that building materials, particularly those based on natural raw materials(concrete, brick, plaster), are characterized by seldom repeatable composition, the only method of estimating their electric and magnetic properties is conducting laboratory measurements with the use of natural samples [3, 4, 7, 8, 10–12, 14].

2. MICROWAVE MEASURING SET FOR ATTENUATION TESTS BASED ON COAXIAL LINE

For conducting attenuation tests of materials used for building structures a microwave measuring set has been designed. With the use of the above mentioned set we can make measurement and determine values of combined coefficients of dispersion matrices which next can be used for calculation of attenuation coefficients and absorption of particular shielding material. The measuring set in current configuration makes measurements within the frequency range from 50 MHz to 6 GHz possible. Band limitations for this set are caused by the set structure on the basis of coaxial line, possessed measuring equipment and measuring software [2, 5, 6, 9, 13].

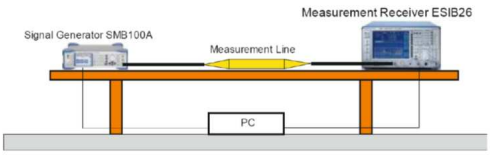

Figure 1: Block diagram of measuring position.

3. METHOD OF MEASURING ATTENUATION OF BUILDING MATERIALS

Measurement of attenuation of materials used for building structures was conducted with the use of measuring position which block diagram is presented in Figure 1. Measurements were divided in two stages. The first stage is reference measurement during which the signal level which directly crosses measuring line (without the placed tested material sample) is measured. The second stage is basic measurement in which the signal level crossing measuring line with the placed tested material

sample inside is measured. Due to obtained results from the two measuring stages it is possible to calculate attenuation of the tested sample of material A using the dependence:

$$A = E_1 - E_2, \tag{1}$$

where: E_1 — signal level at the output of measuring line without the material sample placed inside for a particular frequency, E_2 — signal level at the output of measuring line with the material sample placed inside for a particular frequency [19–21].

Measuring methodology is based on measurement of signal level at the output of measuring line without sample and with sample placed in microwave set for measuring attenuation. Test signal is generated by microwave generator in a given frequency range. Received signal at the output of measuring line is measured with the use of measuring receiver. The designed program allows to perform basic preparation activities automatically, carry out measurements themselves and make appropriate diagrams presenting the obtained results. The application allows to introduce initial and final frequency of measuring range and define measuring step and level of test signal deriving from signal generator [15–18].

4. SELECTED MATERIALS USED FOR BUILDING STRUCTURES

During conducted tests the study subject were selected samples of building materials with different thickness. The first sample was red brick commonly used for structure of building walls with three various thicknesses: 7.1 mm, 8.0 mm, 17.8 mm. The look of particular samples from red brick has been shown in Figure 2. The second studied sample was clinker brick commonly used for structure of walls inside buildings, chimneys etc. with three various thicknesses: 8.4 mm, 9.2 mm, 16.5 mm. The look of particular samples from clinker brick has been shown in Figure 3. The third selected studied sample was concrete commonly used for structure of ceilings, main walls inside buildings etc. with two various thicknesses: 9.0 mm, 17.2 mm. The look of particular samples from concrete has been shown in Figure 4. Another studied sample was cellular concrete (suporex) commonly used for structure of walls inside buildings with two various thicknesses: 8.3 mm, 16.8 mm. The look of particular samples from suporex has been shown in Figure 5. The last selected sample was cardboard gypsum commonly used for structure of partition walls inside buildings etc. with three various thicknesses: 11.25 mm, 22.50 mm, 33.75 mm. The look of particular samples from cardboard gypsum has been shown in Figure 6.

Figure 2: Look of samples — red brick

Figure 3: Look of samples — clinker brick

Figure 4: Look of samples — concrete.

Figure 5: Look of Samples — suporex.

Figure 6: Look of Samples — cardboard gypsum.

5. MEASUREMENT RESULTS

To present measuring possibilities of the described measuring method in Section 3 attenuation measurements of samples of building materials used for building structures within the frequency range from 10 kHz to 6000 MHz were conducted. The purpose of the presented and discussed below measurement results is to show the reader the method how to make the parameter analysis of building materials based on measurement results carried out in accordance with research methodologies described in the following study. In Figures from 7 to 11 measured attenuation values of particular samples characterized in Section 4 have been presented.

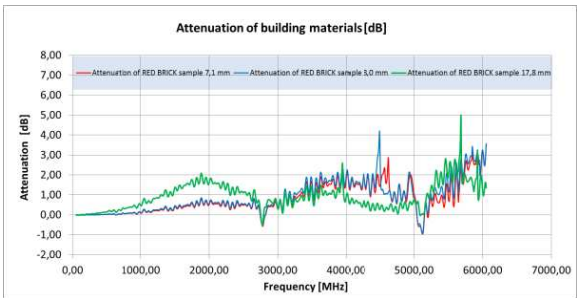

Figure 7: Diagrams of attenuation of red brick samples in frequency function.

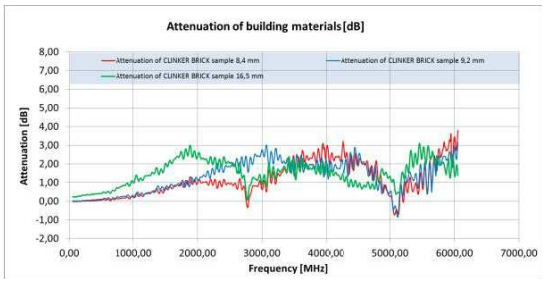

Figure 8: Diagrams of attenuation of clinker brick samples in frequency function.

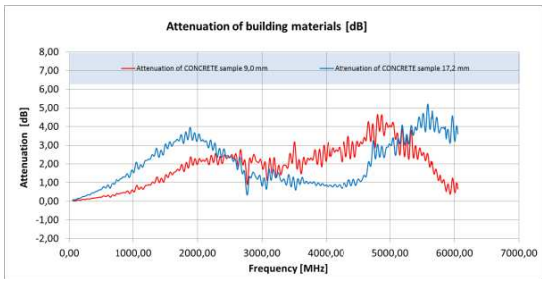

Figure 9: Diagrams of attenuation of concrete samples in frequency function.

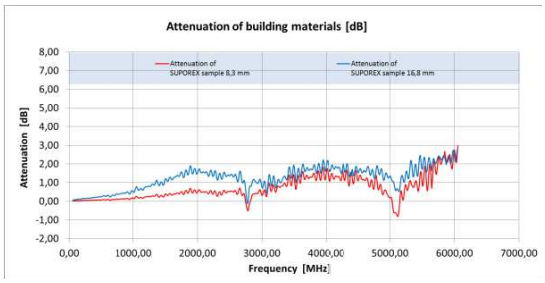

Figure 10: Diagrams of attenuation of cellular concrete (suporex) samples in frequency function.

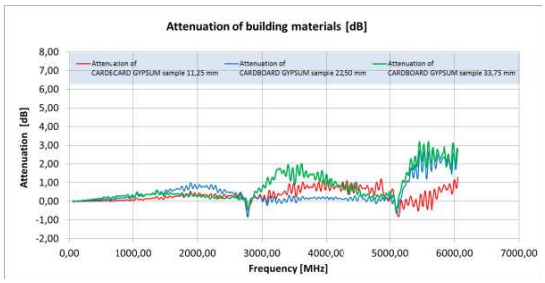

Figure 11: Diagrams of attenuation of cardboard gypsum samples in frequency function.

On the basis of the received results for selected samples of materials used for building structures it is clearly seen that the attenuation value practically does not depend on such little changes of material thickness. The obtained data show that within low frequencies (up to 1000 MHz) attenuation of selected material samples is characterized by low values and is lower than 1 dB. Increase of attenuation along with increase of test frequency can be seen. Within high frequencies (from 1 GHz to 6 GHz) such materials as red brick, clinker brick and concrete are characterized by high values of shielding efficiency and are higher than 3 dB. For samples made of suporex and cardboard gypsum it can be clearly seen that the attenuation value in the whole examined frequency range has low values (below 2 dB). So those materials are transparent for electromagnetic waves within that frequency range. It can be easily noticed that the sample made of concrete is characterized by the largest attenuation in the whole examined frequency range [1].

6. CONCLUSIONS

The whole gamut of building materials with various physical and electromagnetic properties is currently used. For electromagnetic field building materials mainly acquire significance during occurrence of the phenomenon of shielding and EM wave absorption. The used materials have diametrically opposed properties of reaction to EM field. Starting from metal (mainly aluminium) or metalized facades which have prevailing shielding properties and ending on traditional, based on mineral raw products (concrete, brick, plaster) with parameters directed towards field energy absorption. While materials like metal, glass, plastic have quite solid parameters during changes

of weather conditions, walls (facades) made of concrete, brick, plaster or gypsum are especially very susceptible to changes of humidity of surroundings. It causes that real attenuation of such materials can be determined only by measurements in natural or laboratory conditions with the use of natural samples. It is practically impossible to test all used materials due to their broad assortment gamut and seldom repeatable composition. Because of that there is no possibility of accurate determination of attenuation value of a particular wall (facade) or a simple, quick and direct method of making its measurement. So in the article attention was focused on a few selected kinds of materials used for building structure.

ACKNOWLEDGMENT

The project is financed from NCBiR means within the Agreement No. 0024/R/ID2/2012/02 in the years 2012–2015.

REFERENCES

1. Gruszczynski, M., M. Wnuk, and L. Nowosielski, "Multisystem microstrip antenna for mobile communications," *2012 IEEE Antennas and Propagation Society International Symposium (APSURSI) Book Series: IEEE Antennas and Propagation Society International Symposium*, 1–2, 2012.
2. Nowosielski, L., R. Przesmycki, and M. Wnuk, "The laboratory stand for conducted emissions measurement in accordance with the military standard," *2010 IEEE International Symposium on Electromagnetic Compatibility (EMC 2010)*, 275–278, 2010.
3. Piwowarczyk, K., R. Przesmycki, L. Nowosielski, and M. Wnuk, "The measurement of the immunity on the electric field about the radiofrequency within the range (80–1000) MHz," *Przeglad Elektrotechniczny*, Vol. 86, No. 3, 165–167, 2010.
4. Nowosielski, L., M. Wnuk, and C. Ziolkowski, "Interlaboratory tests in scope of measurement of radio disturbance," *2009 European Microwave Conference*, 288–291, 2009.
5. Piotrowski, Z., L. Nowosielski, L. Zagozdzinski, and P. Gajewski, "Electromagnetic compatibility of the military handset with hidden authorization function based on MIL-STD-461D results," *PIERS Online*, Vol. 4, No. 5, 566–570, 2008.
6. Gajewski, P., J. Lopatka, L. Nowosielski, B. Uljasz, and Z. Piotrowski, "Multimedia transmission over HF links," *IEEE 21st Century Military Communications Conference Proceedings, Military Communications Conference*, Vol. 1, 45–47, 2000.
7. Kubacki, R., J. Ferenc, R. Przesmycki, and M. Wnuk, "The nanocrystalline FeSiBCuNb finemet absorption properties at microwaves," *IEEE Transactions on Electromagnetic Compatibility*, Vol. 54, No. 1, 93–100, 2012.
8. Nowosielski, L., R. Przesmycki, M. Wnuk, and J. Rychlica, "The methods of measuring attenuation of thin absorbent materials used for electromagnetic shielding," *PIERS Online*, Vol. 7, No. 3, 261–265, 2011.
9. Przesmycki, R., M. Wnuk, L. Nowosielski, and K. Piwowarczyk, "Small chambers shielding efficiency measurements," *PIERS Online*, Vol. 7, No. 3, 256–260, 2011.
10. Kubacki, R., J. Ferenc, and R. Przesmycki, "The measurements of the complex permittivity and permeability of powdered nanocrystalline Fe-Si-B-Cu-Nb ('finemet')," *Przeglad Elektrotechniczny*, Vol. 87, No. 12B, 92–95, 2011.
11. Kubacki, R., L. Nowosielski, and R. Przesmycki, "The improved technique of electric and magnetic parameters measurements of powdered materials," *Advances in Engineering Software*, Vol. 42, No. 11, 911–916, 2011.
12. Kubacki, R., L. Nowosielski, and R. Przesmycki, "Technique for the electric and magnetic parameter measurement of powdered materials," *Computational Methods and Experimental Measurements XIV Book Series: WIT Transactions on Modelling and Simulation*, Vol. 48, 241–250, 2009.
13. Kubacki, R., E. Cwalina, M. Kuchta, and A. Dukata, "Electromagnetic field distribution in the office room and computer enclosure evoked by electromagnetic high power pulses," *Przeglad Elektrotechniczny*, Vol. 88, No. 12B, 209–212, 2012.
14. Kubacki, R., M. Wnuk, and J. Kieliszek, "Fresnel approximations in mathematical expressions of the electric field for base station antennas," *Przeglad Elektrotechniczny*, Vol. 84, No. 12, 190–193, 2008.

15. Kubacki, R., "Biological interaction of pulse-modulated electromagnetic fields and protection of humans from exposure to fields emitted from radars," *17th International Conference on Microwaves, Radar and Wireless Communications, MIKON 2008*, 1–7, 2008.
16. Kubacki, R., J. Sobiech, and E. Sedek, "Model for investigation of microwave energy absorbed by young and mature living animals," *Electromagnetic Field, Health and Environment, Proceedings of EHE' 07 Book Series: Studies in Applied*, Vol. 29, 126–132, 2008.
17. Kubacki, R., J. Kieliszek, and A. Krawczyk, "The investigation of influence of the electromagnetic fields emitted from short-wave diathermy to the pacemakers," *Przeglad Elektrotechniczny*, Vol. 83, No. 12 105–107, 2007.
18. Kubacki, R., J. Sobiech, J. Kieliszek, and A. Krawczyk, "Comparison of numerical and measurement methods of SAR of ellipsoidal phantoms with muscle tissue electrical parameters," *The International Journal for Computation and Mathematics in Electrical and Electronic Engineering*, Vol. 25, No. 3, 691–704, 2006.
19. Dabrowski, M. P., W. Stankiewicz, R. Kubacki, E. Sobiczewska, and S. Szmigielski, "Immunotropic effects in cultured human blood mononuclear cells pre-exposed to low-level 1300 MHz pulse-modulated microwave field," *Electromagnetic Biology and Medicine*, Vol. 22, No. 1, 1–13, 2003.
20. Kubacki, R., M. Wnuk, W. Kolosowski, and J. Sobiech, "New approach to electromagnetic field calculations in the near-field of microwave antennas," *Computational Methods and Experimental Measurements XI Book Series: Computational Engineering*, Vol. 4, 413–422, 2003.
21. Kubacki, R., M. Krukowski, J. Kieliszek, and J. Sobiech, "New computational model of electromagnetic field distribution for predicting of the safety zones in the near-field of microwave antennas," *XIV International Conference on Microwaves, Radar and Wireless Communications, MIKON-2002*, Vol. 3, 902–905, 2002

New Attempt to Building Materials Permittivity Measurements

Roman Kubacki
Faculty of Electronics, Military University of Technology
Gen. S. Kaliskiego 2 Str., Warsaw 00-908, Poland

Abstract— In the work, measured results of complex permittivity of some commonly used building materials have been presented. The relative permittivity was measured in the coaxial line with TEM fundamental mode. Such a measurement condition corresponds to the free-space test, with a planar incident wave. In the literature different techniques were presented for coaxial lines permittivity determination, basing on measurements of complex values of scattering parameters. In proposed attempt the only magnitude of reflection and transmission coefficients have been used for relative permittivity determination. The relationship for calculation of the relative permittivity and analysis concerning the algorithm convergence has been discussed. Proposed calculation method allows applying this method for measuring the electric field, neglecting the phase assessing. As an example of material measurement the relative of permittivity of two kinds of bricks, concrete and cellular concrete were presented.

1. INTRODUCTION

Information about the attenuation of various building materials is important for the study of radiofrequency (RF) signal propagation in either indoor and outdoor environments [6, 7, 9, 12, 14, 20, 21]. Many researchers published investigations and numerical calculations that predict wireless local area network performance claim regarding the propagation losses through the walls at higher frequency range [2, 10, 11, 19]. In addition, ultra-wideband (UWB) wireless communication became the subject of intensive investigation due to its potential applications in high rate transmission [3–5, 15–17]. Despite that many aspects of UWB-based communication systems have not been deeply revealed the propagation of such signals and mainly the degradation of these signals in indoor environment is important issue. The signal propagation through the wall for electromagnetic waves, is governed, among other, by the properties of material in the propagation medium. Therefore, the knowledge of electromagnetic properties of building materials would provide significant insights into the capabilities and limitation of RF technology indoor and outdoor applications. Different attempts have been presented to study the propagation of RF signals through the walls. Pena et al. presented the permittivity and conductivity of brick and doubly reinforced concrete walls for the 900 MHz band [13]. Another electric parameter such as penetration loss of concrete and plasterboard walls over the frequency from 900 till 18000 MHz was analyzed by Zhang et al. [22]. On the other hand Suzuki et al. [18] presented reflection coefficients in the frequency range from 1.9 to 4 GHz for walls made of limestone blocks, glass and brick. The investigated building materials can be divided into two groups, i.e., drywall, wooden wall and glass having uniform structures and the ones such a brick and concrete with non-uniform structures. Muqaibel reported that in the frequency range from 2 to 8 GHz, the electric constants of materials with uniform structures tend to decrease with frequency whereas this parameter of non-uniform structure materials shows a more complex behavior [8]. For UWB investigation the Fourier transforms is especially recommended. In this case, using a short-duration electromagnetic pulse, the time-domain radiated measurements are used [8]. The incident pulse is partially transmitted through the slab and is partially reflected, with multiple reflections occurring between the slab boundaries.

2. MEASUREMENT SYSTEM

The permittivity measurements of solid materials are commonly performed using coaxial fixtures. At microwaves, the coaxial line technique is especially recommended for broadband frequency measurements. The method of measurements of ε based on determining the scattering parameters (S_{ik}) of the measured sample is the most popular [1]. In this work the method of permittivity determination has been developed for measurement of the slab materials in the free-space condition and in the coaxial lines. The main consideration of the developed method is to use only amplitude of the transmission (S_{21}) and reflection (S_{11}) coefficients. This means that permittivity of material has been determined uniquely from the measurement of the amplitude without measuring the phases of these coefficients. Such a method can be especially dedicated for measurements when measuring device is equipped only with amplitude measuring sensor. In the paper, proposed method

is discussed for coaxial line technique with TEM mode. In such a case, the measured material completely fills the cross section of the holder.

For building material having grain-structure rather large samples are recommended for measurements to average out the fluctuation in the dielectric properties of the heterogeneous materials. This is why the coaxial lines (holder) should be enlarged to host large samples, Fig. 1. In the design of an enlarged measurement holder the outer conductor radius (b) is made larger but the inner conductor radius (a) should be adjusted for a characteristic impedance of 50 Ω. However, there is a restriction for the diameters due to possible higher-order propagating modes which can be induced at higher frequencies. In the investigation the following holder diameters have been taken into consideration $a = 24,1$ mm and $b = 10.5$ mm. With such a coaxial holder measurements have been realized in the frequency range from 50 MHz to 5 GHz.

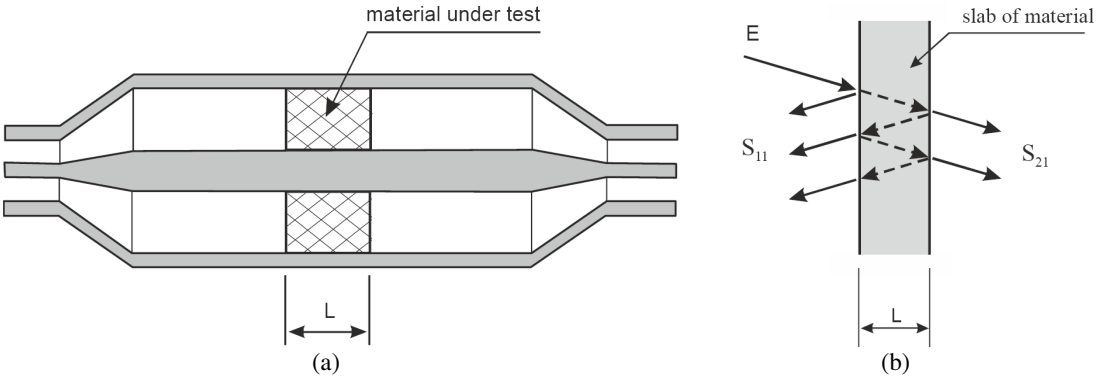

Figure 1: Schematic drawing of an enlarged coaxial line (holder), (a) longitudinal view, (b) multiple reflections in the sample of material.

The single-slab plane-wave model was developed to compute the relative permittivity of the measured material. The material is characterized by unknown complex relative electric permittivity $\varepsilon = \varepsilon' - j\varepsilon''$. The reflection and transmission S-parameters in coaxial line when the incident electromagnetic field is treated as plane wave can be interpreted as the infinite series of rays as a multiple reflections between the two surfaces of the sample — Fig. 1(b). The reflection and transmission of rays can be described according to the theory of optics [1] and the S-parameters are done in a complex forms.

In the presented method only magnitudes of S_{11} and S_{21} are available in the measurements, thus these equations cannot be solved in an analytical form. Zhihong et al. [23] discussed similar attempt but only samples with large attenuation were taking into consideration. In their case the multiple reflections in the sample were neglected, yielding to technique which was signifier simplification of the method. In this work no simplification was taken into account. Full model of multiple reflections allows to transformed equations based on multiple reflections into the following magnitude forms;

$$|S_{11}| = \left| \frac{\left(1 - E^2\right)\left(1 - e^{-2\gamma L}\right)}{(1+E)^2 - (1-E)^2 e^{-2\gamma L}} \right| \tag{1}$$

$$|S_{21}| = \left| \frac{4Ee^{-\gamma L}}{(1+E)^2 - (1-E)^2 e^{-2\gamma L}} \right| \tag{2}$$

where: $|S_{11}|$, $|S_{21}|$ — magnitudes of measured S-parameters,

$$E = E' + jE'' = \sqrt{\varepsilon' - j\varepsilon''}$$

$\gamma = j\omega\sqrt{\varepsilon_0\mu_0}\sqrt{\varepsilon}$ — propagation constant, L — thickness of the sample.

Two unknown values of permittivity (ε', ε'') can be solved iteratively form Equations (1) and (2). In this iterative approach the Newton's numerical method for root determination has been used. However, when solving such equations iteratively there is a problem with convergence and uniqueness of solution. The right side of Equations (1) and (2) are ambiguous functions of frequency. In fact, these relationships are also ambiguous functions of permittivity. From this point of view

the unique solution can be obtained when good initial guess is available. To determine unknown and changeable values of ε' and ε'' in function of frequency the additional techniques should be introduced to omit this ambiguities. In this approach the E' and E'' as unknown parameters have been solved iteratively form Equations (1) and (2) and the final data can be determined according the relationship $\varepsilon' - j\varepsilon'' = E^2$. Such attempt yields to much stable solution.

3. RESULTS

The measurement equipment includes a vector network analyzer and a coaxial line with enlarged holder and calibration kit. The measured samples were located in the holder. Measurements were carried out for 4 samples as representative of building materials, i.e., a brick, a clinker brick, a concrete, and a cellular concrete. The thicknesses of samples were as follows: a brick $L = 7.1$ mm, a clinker brick $L = 8.4$ mm, a concrete $L = 9$ mm, a cellular concrete $L = 8.3$ mm. The obtained results of real and imaginary permittivity in frequency range from 50 MHz to 5 GHz have been presented in Figures 2 and 3.

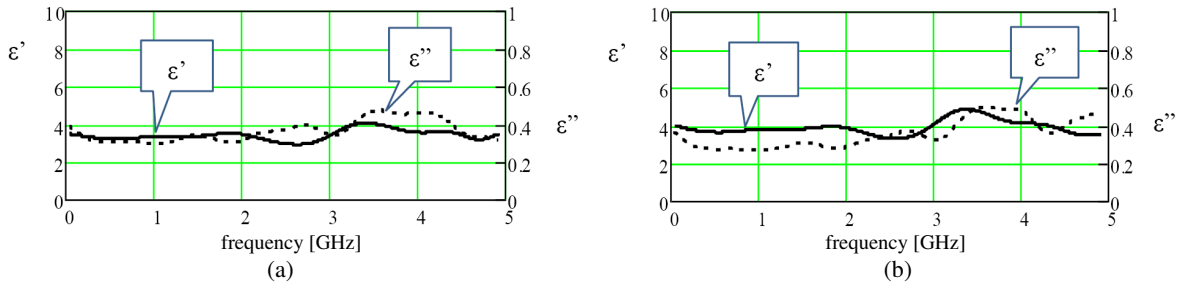

Figure 2: Real (ε') and imaginary (ε'') parts of the relative permittivity for: (a) brick, (b) clinker brick.

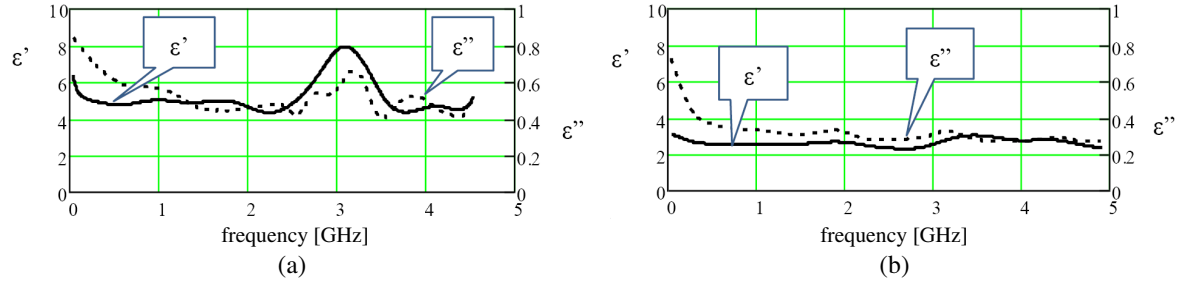

Figure 3: Real (ε') and imaginary (ε'') parts of the relative permittivity for: (a) concrete, (b) cellular concrete.

The relative permittivity of brick and clinker brick is quite similar in function of frequency and value of the real part is contained in between 3 and 5. The imaginary part value is in between 0.3 and 0.5. The highest values of permittivity were observed for concrete and for this building material real part is in between 5 to 8 and imaginary part is 0.4 to 0.65. On the other hand, the lowest value was measured for cellular concrete.

ACKNOWLEDGMENT

The project was financed from NCBiR means within the Agreement No. DOBR-BIO4/016/13071/2013 in the years 2013–2015.

REFERENCES

1. Baker-Jarvis, J., M. D. Janezic, B. F. Riddle, R. T. Johnj, P. Kabos, C. L. Holloway, and C. A. Grosvenor, "Measuring the permittivity and permeability of lossy materials: solids, liquids, metals, building materials and negative-index materials," *Natl. Inst. Stand. Technol., Technical Note, NIST*, 2005.
2. Bugaj, M., R. Przesmycki, M. Wnuk, and K. Piwowarczyk, "Analysis of methods measuring attenuation of RF line," *Przeglad Elektrotechniczny*, Vol. 88, No. 2, 17–19, 2012.

3. Bugaj, M. and M. Wnuk, "Influence of parameters of dielectric in aperture-coupled stacked patch antenna on bandwidth," *Przeglad Elektrotechniczny*, Vol. 85, No. 9, 50–53, 2009.
4. Bugaj, M. and M. Wnuk, "Optimization parameters of dielectric in aperture-coupled stacked patch antenna on bandwidth," *18th International Conference on Microwaves, Radar and Wireless Communications (MIKON-2010)*, Vols. 1 and 2, 2010.
5. Bugaj, M. and M. Wnuk, "The influence examination of dielectric parameters on bandwidth in multilayer aperture-coupled microstrip Antennas with utilization the FDTD method," *2008 MIKON Conference Proceedings*, Vols. 1 and 2, 708–711, 2008.
6. Gajewski, P., J. Lopatka, L. Nowosielski, B. Uljasz, and Z. Piotrowski, "Multimedia transmission over HF links," *IEEE 21st Century Military Communications Conference Proceedings, Military Communications Conference*, Vols. 1 and 2, 45–47, 2000.
7. Gruszczynski, M., M. Wnuk, and L. Nowosielski, "Multisystem microstrip antenna for mobile communications," *2012 IEEE Antennas and Propagation Society International Symposium (APSURSI)*, Book Series: *IEEE Antennas and Propagation Society International Symposium*, 2012.
8. Muqaibel, A. H. and A. Safaai-Jazi, "A new formulation for characterization of materials based on measured insertion transfer function," *IEEE Trans. Microw. Theory Tech.*, Vol. 51, No. 8, 1946–1951, 2003.
9. Nowosielski, L., R. Przesmycki, and M. Wnuk, "The laboratory stand for conducted emissions measurement in accordance with the military standard," *2010 IEEE International Symposium on Electromagnetic Compatibility (EMC 2010)*, 275–278, 2010.
10. Nowosielski, L., R. Przesmycki, M. Wnuk, and J. Rychlica, "The methods of measuring attenuation of thin absorbent materials used for electromagnetic shielding," *PIERS Online*, Vol. 7, No. 3, 261–265, 2011.
11. Nowosielski, L., M. Wnuk, R. Przesmycki, K. Piwowarczyk, and M. Bugaj, "Coaxial cables shielding efficiency measuring methodology," *PIERS Proceedings*, 72–76, Kuala Lumpur, Malaysia, Mar. 27–30, 2012.
12. Nowosielski, L., M. Wnuk, and C. Ziolkowski, "Interlaboratory tests in scope of measurement of radio disturbance," *2009 European Microwave Conference*, Vols. 1–3, 288–291, 2009.
13. Pena, D., R. Feick, H. D. Hristov, and W. Grote, "Measurement and modeling of propagation losses in brick and concrete walls for the 900-MHz band," *IEEE Trans. Antennas Propag.*, Vol. 51, No. 1, 31–39, 2003.
14. Piotrowski, Z., L. Nowosielski, L. Zagozdzinski, and P. Gajewski, "Electromagnetic compatibility of the military handset with hidden authorization function based on MIL-STD-461D results," *PIERS Online*, Vol. 4, No. 5, 566-570, 2008.
15. Piwowarczyk, K., R. Przesmycki, L. Nowosielski, and M. Wnuk, "The measurement of the immunity on the electric field about the radiofrequency within the range (80–1000) MHz," *Przeglad Elektrotechniczny*, Vol. 86, No. 3, 165–167, 2010.
16. Przesmycki, R., M. Wnuk, L. Nowosielski, K. Piwowarczyk, and M. Bugaj, "Analysis of the radiated emissions of IT equipment," *PIERS Proceedings*, 1419–1423, Moscow, Russia, Aug. 19–23, 2012.
17. Przesmycki, R., M. Wnuk, L. Nowosielski, K. Piwowarczyk, and M. Bugaj, "The conducted and radiated emission levels from IT devices," *PIERS Proceedings*, 77–81, Kuala Lumpur, Malaysia, Mar. 27–30, 2012.
18. Suzuki, H. and A. S. Mohan, "Measurement and prediction of high spatial resolution indoor channel characteristic map," *IEEE Trans. Veh. Technol.*, Vol. 49, No. 4, 1321–1333, 2000.
19. Wnuk, M. and M. Bugaj, "Analysis of radiating structures placed on multilayer dielectric," *Computational Methods and Experimental Measurements XIII*, Book Series: *WIT Transactions on Modelling and Simulation*, Vol. 46, 747–755, 2007.
20. Wnuk, M., M. Bugaj, R. Przesmycki, L. Nowosielski, and K. Piwowarczyk, "Wearable antenna constructed in microstrip technology," *PIERS Proceedings*, 67–71, Kuala Lumpur, Malaysia, Mar. 27–30, 2012.
21. Wnuk, M., G. Różański, and M. Bugaj, "The analysis of microstrip antennas using the FDTD method," *Computational Methods and Experimental Measurements XII*, Book Series: *WIT Transactions on Modelling and Simulation*, Vol. 41, 611–620, 2005.
22. Zhang, Y. P. and Y. Hwang, "Measurements of the characteristics of indoor penetration loss," *IEEE 44th Vehicular Technology Conf.*, Vol. 3, 1741–1744, 1994.

23. Zhihong, M. and S. Okamura, "Permittivity determination using amplitudes of transmission and reflection coefficients at microwave," *IEEE Trans on Microwave Theory and Tech.*, Vol. 47, No. 5, 546–550, 1999.

Measurements of Wall Attenuation in Closed Spaces inside a Building

Marek Bugaj
Faculty of Electronics, Military University of Technology
Gen. S. Kaliskiego 2 str., Warsaw 00-908, Poland

Abstract— Within this article the issue of measuring wall attenuation in closed spaces inside a building has been discussed. Measuring methodology and measurement results obtained while determining wall attenuation as well as other structural components in closed spaces inside a building have been presented.

1. INTRODUCTION

In order to measure values of wall attenuation in closed spaces a measuring set is required which includes transmitter of measuring signal and meter of electromagnetic field intensity. Particular parts of the measuring set might also include software which activated on an operating computer makes automation of measuring process possible [20, 21]. Within this article the principle of operation of measuring set without using operating software has been presented.

The suggested measuring method is a basic comparative method [17, 18]. On the basis of obtained measurement results it is possible to determine attenuation of elements inside a building such as walls, ceilings and other building structural components. For the discussed measuring method a few following principles should be met:

- transmitting and receiving antenna must be remote from a tested obstacle within the distance meeting the principles of far zone, i.e., wave incident on obstacle should have the nature of plane wave,
- in order to make measurements properly, antennas should be characterized with the same radiation characteristics [1–3].

Measurement of wall attenuation in closed spaces comes down to performance of two measurements of signal level at the receiver input for particular frequency. The first measurement is made as so called reference measurement. With a determined value of signal level generated by transmitter of measuring signal the level of electromagnetic field intensity is measured in the place of installation of receiving antenna of meter of electromagnetic field intensity [15, 16]. During standardization measurement transmitting antenna of measuring signal transmitter and receiving antenna of electromagnetic field intensity meter are placed close to one another in direct visibility. Measurements can be made at discrete frequencies or in a given band with determined step. Measured values of electromagnetic field intensity corresponding with particular measuring frequencies ought to be remembered [4–8].

2. MEASURING POSITION

Block diagram of measuring position for wall attenuation in closed spaces has been shown in Figs. 1 and 2. The position includes measuring signal transmitter and electromagnetic field intensity meter.

The suggested above measuring position for measuring wall attenuation in closed spaces consists of the following elements: signal generator, transmitting antennas, receiving antennas, measuring receiver, HF paths, power amplifier possible to use in transmitting path [9–12].

Measurements being reference measurement were made within the frequency range from 200 MHz to 6 GHz for four distances between measuring antennas (1 m, 2 m, 4 m, 6 m).

It can be easily noticed that along with moving away of measuring antennas from each other the nature of received courses more and more differs from linear (Fig. 3). Levels of received signal decrease along with moving away of measuring antennas from each other. Obtained reference courses along with results of basic measurements will serve to determine wall attenuation in closed spaces inside a building [13, 14, 19].

At a stage of conducting basic measurements, measurements of signal levels received by measuring antennas have been made in the configuration in which between measuring antennas there was a wall for which attenuation was determined. Measurements were conducted in accordance

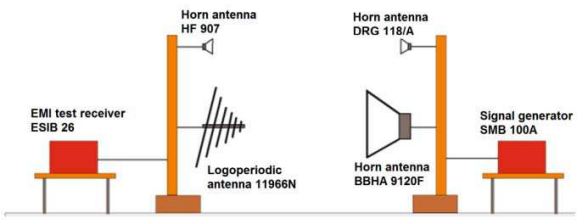

Figure 1: Block diagram of measuring position for wall attenuation in closed spaces in the configuration for reference measurement.

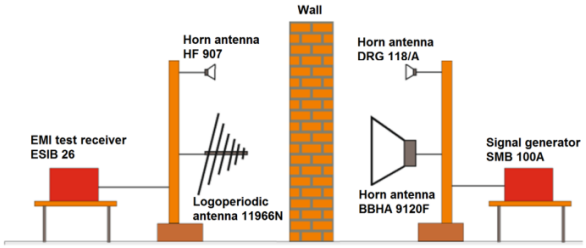

Figure 2: Block diagram of measuring position for wall attenuation in closed spaces in the configuration for basic measurement.

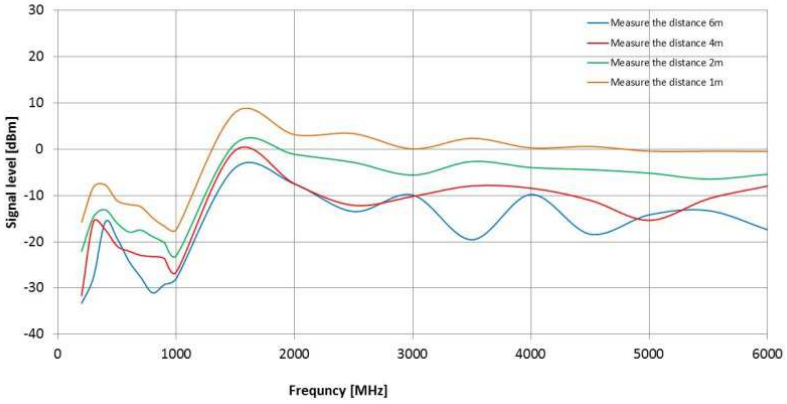

Figure 3: Diagrams of signal levels received by measuring antennas in the configuration of direct visibility of antennas for four distances between measuring antennas (1 m, 2 m, 4 m, 6 m).

Figure 4: View of measuring position while performing reference measurements.

with the above described methodology. Measurements being basic measurements were carried out within the frequency range from 200 MHz to 6 GHz for five scenarios of antenna arrangement:

a) reinforced concrete wall between corridor and room in which there is anechoic chamber, the distance between measuring antennas was 1 m, (Fig. 9),
b) gypsum-cardboard wall between corridor and lecturer's room, the distance between measuring antennas was 1 m, (Fig. 6),
c) gypsum-cardboard and wooden wardrobe wall between lecturer's room and other lecturer's room, the distance between measuring antennas was 2 m (Fig. 10),
d) wooden door between corridor and lecturer's room, the distance between measuring antennas was 1 m, (Fig. 3),
e) reinforced concrete ceiling between corridor on the ground floor and corridor on the first floor, the distance between measuring antennas was 4 m (Fig. 12).

3. MEASUREMENT RESULTS OF WALL ATTENUATION IN CLOSED SPACES INSIDE A BUILDING

To obtain wall attenuation it is necessary to use energy balance equation of radio link:

$$P_{odbmin}[\text{dBm}] = P_{nad}[\text{dBW}] + G_{nad}[\text{dB}] - L_{prop}[\text{dBm}] + G_{odb}[\text{dB}] \tag{1}$$

After transformations we receive attenuation dependence:

$$L_{prop}[\text{dBm}] = P_{nad}[\text{dBW}] - P_{odbmin}[\text{dBm}] + G_{nad}[\text{dB}] + G_{odb}[\text{dB}] \tag{2}$$

where:

P_{odbmin}[dBm] — minimal signal power received at the output of receiving antenna, expressed towards one watt, necessary for correct reception of radio signal,

p_{nad}[dBW] — power of signal transmitted at the input of transmitting antenna expressed towards one watt,
G_{nad}[dB] — gain of transmitting antenna,
L_{prop}[dBm] — attenuation of radio wave in propagation environment,
G_{odb}[dB] — gain of receiving antenna.

On the basis of reference and basic measurements we can determine attenuation of a selected wall in closed space according to the dependence:

$$L_{wall}[\text{dB}] = P_1[\text{dBm}] - P_2[\text{dBm}] \tag{3}$$

where:
P_1[dBm] — level of signal received by measuring antennas in reference measurement,
P_2[dBm] — level of signal received by measuring antennas in basic measurement,
P_2[dBm] — wall attenuation.

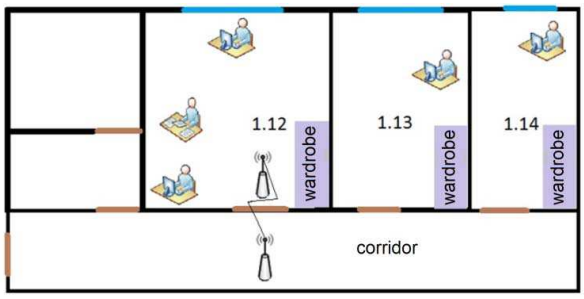

Figure 5: Section of building with the marked first measuring position. Measurement of attenuation between room 1.12 and corridor through closed door.

Figure 6: View of measuring position while performing basic measurements.

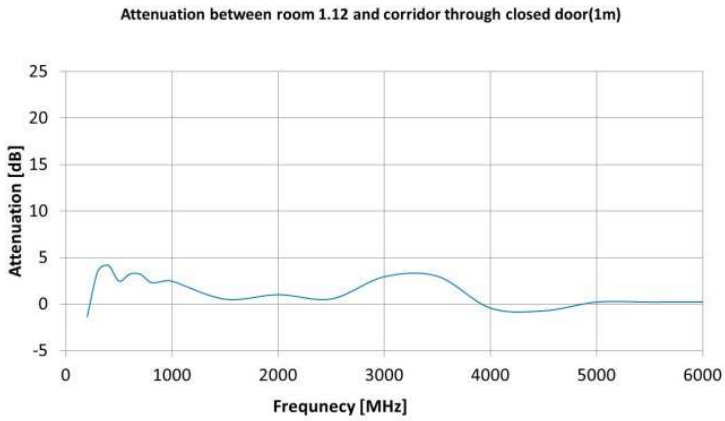

Figure 7: Attenuation received as a result of measurement through door between room 1.12 and corridor.

In Fig. 4, arrangement of measuring antennas while conducting measurement according to the scenario from Fig. 3 is presented. In that configuration a wave propagates mainly through door. In Fig. 5, juxtaposition of measurement results and attenuation results for the configuration from Fig. 3 obtained with the use of selected analytical models is shown.

In next figures measurement results for particular scenarios have been presented respectively.

As it can be noticed from the above presented attenuation results of selected walls in closed spaces, diagrams differ from each other in attenuation values. The wooden door fixed in gypsum-cardboard wall is characterized by the least attenuation. The attenuation value of the discussed door is about 2 dB in the entire frequency band from 200 MHz to 6000 MHz. Walls made of gypsum-cardboard are characterized by larger attenuation. The attenuation value of such walls fluctuates within the range from 5 dB to 10 dB depending on measuring frequency. Reinforced concrete walls have the biggest attenuation. Their attenuation, depending on measuring frequency, ranges from about 10 dB to even 40 dB in case of the ceiling between the floors of the building.

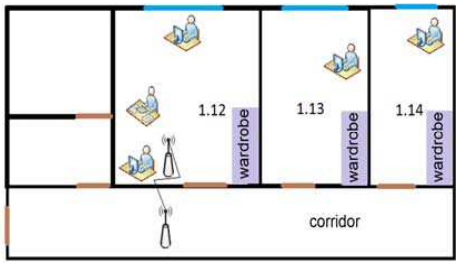

Figure 8: Section of building with the marked first measuring position. Measurement of attenuation between room

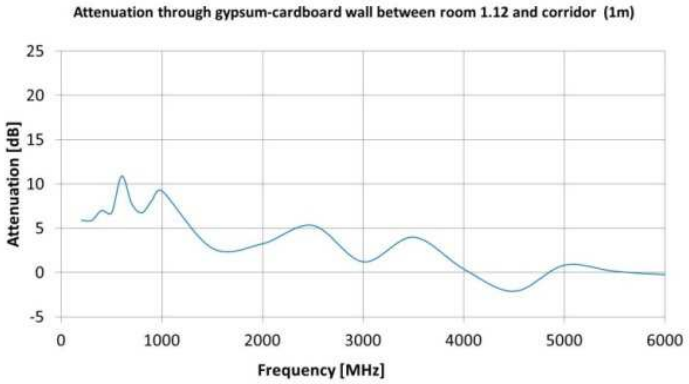

Figure 9: Attenuation received as a result of measurement through gypsum-cardboard wall between room 1.12 and corridor.

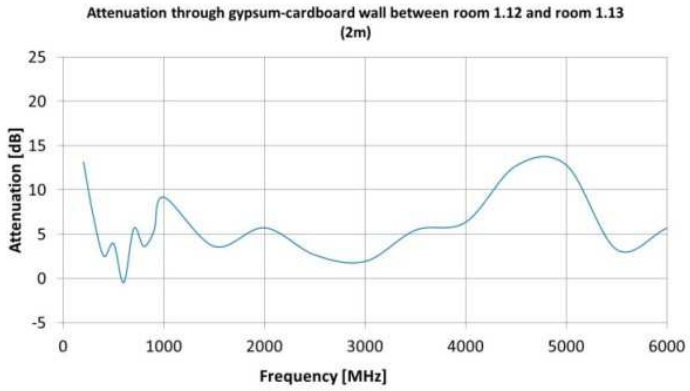

Figure 10: Attenuation received as a result of measurement through gypsum-cardboard wall between room 1.12 and room 1.13.

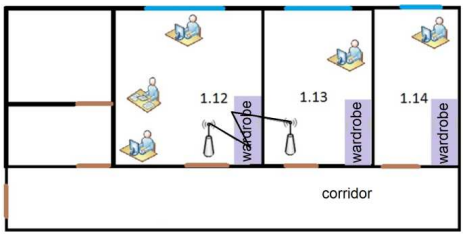

Figure 11: Section of building with the marked first measuring position. Measurement of attenuation between room 1.12 and room 1.13.

4. CONCLUSIONS

Measurement of wall attenuation and structural components in an already existing building is quite problematic. The main encountered problem is a possibility of providing the same measuring conditions while performing reference measurements like those occurring during basic measurement. Unfortunately while conducting measurements in closed space a problem of multipath and other phenomena accompanying wave propagation appears. It results in the fact that in specific situations for particular frequencies we can obtain a negative value of attenuation, i.e., reinforcement. It is an obvious influence of surroundings occurring around measuring equipment. Having measurement results we can also attempt to make an analysis and selection of most suitable propagation model for field prediction in a building.

ACKNOWLEDGMENT

The project is financed from the NCBiR means within Agreement No. 0024/R/ID2/2012/02 in the years 2012–2015.

REFERENCES

1. Gruszczynski, M., M. Wnuk, and L. Nowosielski, "Multisystem microstrip antenna for mobile communications," *2012 IEEE Antennas and Propagation Society International Symposium (APSURSI) Book Series: IEEE Antennas and Propagation Society International Symposium*, 2012.
2. Nowosielski, L., R. Przesmycki, and M. Wnuk, "The laboratory stand for conducted emissions measurement in accordance with the military standard," *2010 IEEE International Symposium on Electromagnetic Compatibility (EMC 2010)*, 275–278, 2010.

3. Piwowarczyk, K., R. Przesmycki, L. Nowosielski, and M. Wnuk, "The measurement of the immunity on the electric field about the radiofrequency within the range (80–1000) MHz," *Przegląd Elektrotechniczny*, Vol. 86, No. 3, 165–167, 2010.
4. Nowosielski, L., M. Wnuk, and C. Ziolkowski, "Interlaboratory tests in scope of measurement of radio disturbance," *2009 European Microwave Conference*, Vol. 1–3, 288–291, 2009.
5. Piotrowski, Z., L. Nowosielski, L. Zagozdzinski, and P. Gajewski, "Electromagnetic compatibility of the military handset with hidden authorization function based on MIL-STD-461D results," *PIERS Proceedings*, 116–120, Cambridge, USA, July 2–6, 2008.
6. Gajewski, P., J. Lopatka, L. Nowosielski, B. Uljasz, and Z. Piotrowski, "Multimedia transmission over HF links," *IEEE 21st Century Military Communications Conference Proceedings, Military Communications Conference*, Vols. 1 and 2, 45–47, 2000.
7. Kubacki, R., J. Ferenc, R. Przesmycki, and M. Wnuk, "The nanocrystalline FeSiBCuNb finemet absorption properties at microwaves," *IEEE Transactions on Electromagnetic Compatibility*, Vol. 54, No. 1, 93–100, 2012.
8. Nowosielski, L., R. Przesmycki, M. Wnuk, and J. Rychlica, "The methods of measuring attenuation of thin absorbent materials used for electromagnetic shielding," *PIERS Proceedings*, 870–874, Marrakesh, Morocco, March 20–23, 2011.
9. Przesmycki, R., M. Wnuk, L. Nowosielski, and K. Piwowarczyk, "Small chambers shielding efficiency measurements," *PIERS Proceedings*, 875–879, Marrakesh, Morocco, March 20–23, 2011.
10. Kubacki, R., J. Ferenc, and R. Przesmycki, "The measurements of the complex permittivity and permeability of powdered nanocrystalline Fe-Si-B-Cu-Nb ("Finemet")," *Przegląd Elektrotechniczny*, Vol. 87, No. 12B, 92–95, 2011.
11. Kubacki, R., L. Nowosielski, and R. Przesmycki, "The improved technique of electric and magnetic parameters measurements of powdered materials," *Advances in Engineering Software*, Vol. 42, No. 11, 911–916, 2011.
12. Kubacki, R., L. Nowosielski, and R. Przesmycki, "Technique for the electric and magnetic parameter measurement of powdered materials," *Computational Methods and Experimental Measurements XIV Book Series: WIT Transactions on Modelling and Simulation*, Vol. 48, 241–250, 2009.
13. Kubacki, R., E. Cwalina, M. Kuchta, and A. Dukata, "Electromagnetic field distribution in the office room and computer enclosure evoked by electromagnetic high power pulses," *Przegląd Elektrotechniczny*, Vol. 88, No. 12B, 209–212, 2012.
14. Kubacki, R., M. Wnuk, and J. Kieliszek, "Fresnel approximations in mathematical expressions of the electric field for base station antennas," *Przegląd Elektrotechniczny*, Vol. 84, No. 12, 190–193, 2008.
15. Kubacki, R., "Biological interaction of pulse-modulated electromagnetic fields and protection of humans from exposure to fields emitted from radars," *2008 MIKON Conference Proceedings*, Vols. 1 and 2, 66–72, 2008.
16. Kubacki, R., J. Sobiech, and E. Sedek, "Model for investigation of microwave energy absorbed by young and mature living animals," *Electromagnetic Field, Health and Environment, Proceedings of EHE '07 Book Series: Studies in Applied*, Vol. 29, 126–132, 2008.
17. Kubacki, R., J. Kieliszek, and A. Krawczyk, "The investigation of influence of the electromagnetic fields emitted from short-wave diathermy to the pacemakers," *Przegląd Elektrotechniczny*, Vol. 83, No. 12, 105–107, 2007.
18. Kubacki, R., J. Sobiech, J. Kieliszek, and A. Krawczyk, "Comparison of numerical and measurement methods of SAR of ellipsoidal phantoms with muscle tissue electrical parameters," *COMPEL — The International Journal for Computation and Mathematics in Electrical and Electronic Engineering*, Vol. 25, No. 3, 691–704, 2006.
19. Dabrowski, M. P., W. Stankiewicz, R. Kubacki, E. Sobiczewska, and S. Szmigielski, "Immunotropic effects in cultured human blood mononuclear cells pre-exposed to low-level 1300 MHz pulse-modulated microwave field," *Electromagnetic Biology and Medicine*, Vol. 22, No. 1, 1–13, 2003.
20. Kubacki, R., M. Wnuk, W. Kolosowski, and J. Sobiech, "New approach to electromagnetic field calculations in the near-field of microwave antennas," *Computational Methods and Experimental Measurements XI Book Series: Computational Engineering*, Vol. 4, 413–422, 2003.

21. Kubacki, R., M. Krukowski, J. Kieliszek, and J. Sobiech, "New computational model of electromagnetic field distribution for predicting of the safety zones in the near-field of microwave antennas," *XIV International Conference on Microwaves, Radar and Wireless Communications, MIKON-2002*, Vols. 1–3, 902–905, 2002.

Measurement of Shielding Effectiveness with the Method Using High Power Electromagnetic Pulse Generator

Leszek Nowosielski and Jerzy Lopatka
Faculty of Electronics, Military University of Technology
Gen. S. Kaliskiego 2 Str., Warsaw 00-908, Poland

Abstract— The new shielding effectiveness (SE) measurement methodology basing on HPEM-RF DS110 pulse generator is described. In order to conduct validation of research methodology the shielding effectiveness measurement results for selected enclosure are presented. During the measurement the worked out methodology was used. The obtained measurement results are compared to shielding efficiency measurement results which are obtained using standard measurement methodology basing on the selective measurement receiver and RF signal generator which is used as source of testing signal.

1. DESCRIPTION OF THE SHIELDING EFFECTIVENESS METHOD WITH THE USE OF HIGH POWER ELECTROMAGNETIC PULSE GENERATOR

One of the most innovative solutions of the problem of increasing measuring dynamics range of shielding effectiveness of small shielding chambers is using, as probing signal, high power pulses generated by Marx generator. As the source of test signal in the designed laboratory stand for measuring shielding effectiveness the high power pulse generator HPEM-RF DS110 was used. The shape of test signal generated by the above generator in the time function and its frequency spectrum were presented in Fig. 1. Due to significant levels of spectrum components of test pulse and its coverage in the frequency range it can be used as probing signal in the procedure of measuring shielding effectiveness of small shielding chambers within the frequency range from 10 MHz to 600 MHz.

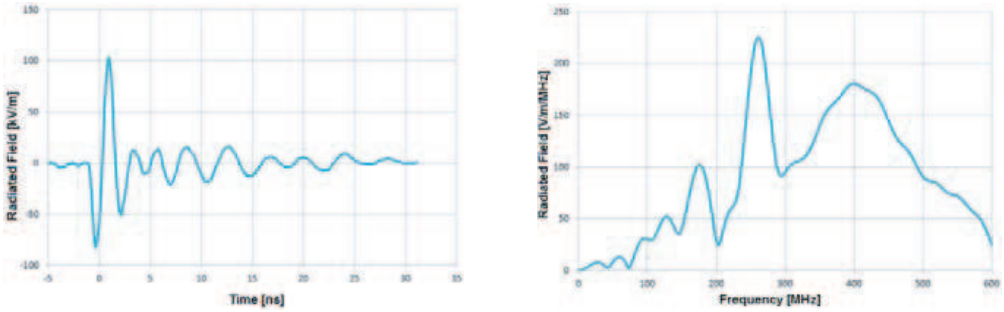

(a) (b)

Figure 1: Representation of high power pulse generated by HPEMRF DS110 generator in time and frequency domain.

In order to measure shielding effectiveness values of small shielding chambers with the method using high power pulse generator a measuring set is required which includes transmitter of measuring signal and meter of electric field strength. The transmitter of measuring signal consists of high power pulse generator HPEM-RF DS110 along with transmitting antenna. The task of the generator is to supply pulses with minimum value of electric field strength of several hundred thousand volts per meter with maximum duration of a single pulse not exceeding 5 ns. The effect of its action is obtaining high power pulse at the input of transmitting antenna of the order of several hundred thousand volts for a very short period of time.

The meter of electric field strength consists of: operating computer, oscilloscope with RF attenuators and sensor with matching block. Sensor with matching unit connected through RF attenuators to oscilloscope with the use of coaxial cable is used for monitoring generated electric field strength. Display of data collected from sensor in the time domain occurs in the oscilloscope. In order to guarantee correct measurement the oscilloscope must be placed in a special shielding casing protecting it from the high generated electric field strength level. Installed software of

the operating computer allows, on the basis of high power pulse recorded in the time domain, to determine the frequency spectrum with the use of FFT.

Measuring SE by the method using high power generator amounts to performance of two measurements of signal level at the input of sensor included in the meter of the high power pulse level. The first measurement is conducted as so called standardization measurement. Block diagram of the position for standardization measurement is presented in Fig. 2(a). Standardization measurement takes place for a particular value of signal level generated by high power pulse generator. The electric field strength level is measured in the place of installation of sensor along with matching block. Measured values of electric field strength matching particular measuring frequencies are remembered by a computer operating the measuring process.

After conducting standardization measurement basic measurement should be carried out during which sensor with matching block is placed in the examined small shielding chamber. Block diagram of the position for basic measurement is shown in Fig. 2(b). Basic measurement takes place for a particular value of signal level generated by high power pulse generator. The electric field strength level is measured in the place of installation of sensor along with matching unit. Measurements should be performed in the same way as during standardization measurement. Measured values of electric field strength corresponding with particular measuring frequencies ought to be remembered. After subtracting recorded field strength levels corresponding with particular measuring frequencies, during standardization ($E(f)_{stand}$) and basic ($E(f)_{basic}$) measurement, we will receive the difference of levels of received signals in [dB], which is the value of shielding effectiveness of the small shielding chamber casing defined in the fallowing way:

$$\mathrm{SE} = 20\log_{10} = (E(f)_{stand}/E(f)_{basic})\,[\mathrm{dB}]. \tag{1}$$

Measurements of shielding effectiveness should be conducted for each of the four sides of the tested casing. As the final result of shielding effectiveness results of shielding effectiveness measurements with the lowest value should be chosen from the set of four values corresponding with each side of the tested casing, for each frequency of test signal. The shielding effectiveness depend on the parameters of the material used for tested enclosure. The parameters of materials can be obtained by using measurement methodology described in literature items [1, 7, 8].

In order to conduct validation of research methodology based on the high power pulse generator described above, tests of a sample shielding chamber designed in the form of cube being closed by adding one wall were carried out (Fig. 3).

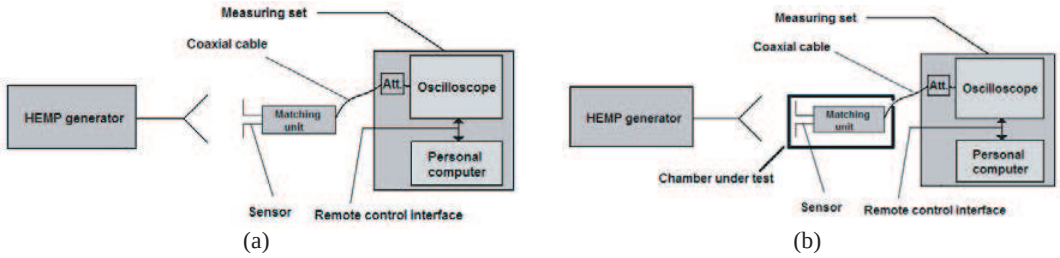

Figure 2: Block diagram of measuring position for (a) standardization and (b) basic measurement.

Figure 3: Measuring position for measuring shielding effectiveness with the use of high power generator: (a) standardization measurement, (b) basic measurement.

2. MEASUREMENT RESULTS

In order to conduct validation of the designed measuring methodology levels of shielding effectiveness obtained as a result of measurements carried out with the method using high power pulses with measurement results obtained with the use of a different measuring methodology were compared. For comparison a classic measuring methodology was used which uses selective measuring receiver and signal generator as the source of test signal. In Fig. 4(a) the final result of shielding effectiveness measurement corresponding with results of shielding effectiveness measurements of the lowest value was presented, from the set of four values matching each side of the tested casing and for each frequency of test signal.

Unfortunately due to physical limitations of measuring potentials used for validation of measuring methods, it is impossible to compare — in the full frequency range — results obtained with the method using high power pulse generator and the method using selective measuring receiver and RF signal generator as the source of test signal. The results of shielding effectiveness measurements shown in Fig. 4(a) obtained with the method using high power pulse generator and values of shielding effectiveness obtained with the method using the selective measuring receiver and RF signal generator presented in Fig. 4(b) can be compared only within the range of frequency from 100 MHz to 600 MHz. Limitation of measuring range of suggested method only up to 600 MHz results from the fact that the used for measurements high power pulse generator generates test signal with large enough spectral concentration up to 600 MHz (Fig. 1). Whereas limitation of measuring range of the method using the selective measuring receiver from 100 MHz results from the fact that small shielding chambers (dimensions smaller than 1 m × 1 m × 1 m) do not allow to place in their interior test antennas with dimensions large enough to effectively radiate test signal with frequency smaller than 100 MHz. As measurement antenna can be used optional antenna [2–6] tuned to the frequency of the test signal.

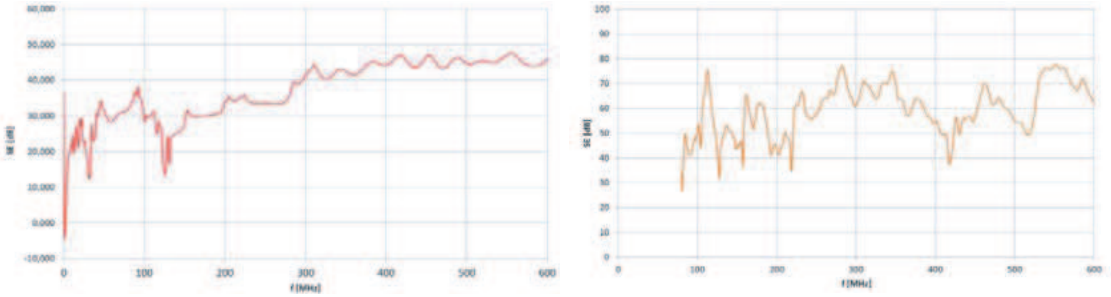

(a) (b)

Figure 4: The final result of shielding effectiveness for the examined shielding casing: (a) the method basing on HPEMRF DS110 pulse generator, (b) the method basing on selective measuring receiver and signal generator as the source of test signal.

3. CONCLUSIONS

The shielding effectiveness values obtained with the use of the method basing on high power pulse generator differ from the values measured with the use of the method using selective measuring receiver and signal generator in about 10 dB. The above difference results from a big influence of the difference of measuring probe location during standardization and basic measurement in both measuring methods. Difficulties with location of measuring probes in the same place inside and outside the tested shielding casing result from differences of dimensions of used measuring probes in both measuring procedures. The foregoing has the influence on uncertainty of measurement with both methods, which oscillates around the value 10 dB.

The described measuring method basing on high power pulse generator has many advantages such as:

- large dynamics range of shielding effectiveness measurement,
- large measurement rate in comparison with traditional methods of measuring casing shielding effectiveness,
- measuring probe dimensions allow to conduct measurements of shielding casings of small overall dimensions (smaller than 1 m × 1 m × 1 m).

The measured shielding effectiveness can be used in many applications where the electromagnetic field distribution is needed [9–22].

ACKNOWLEDGMENT

The project is financed from NCBiR means within the Agreement No. DOBR-BIO4/016/13071/2013 in the years 2013–2015.

REFERENCES

1. Bugaj, M., R. Przesmycki, M. Wnuk, and K. Piwowarczyk, "Analysis of methods measuring attenuation of RF line," *Przeglad Elektrotechniczny*, Vol. 88, No. 2, 17–19, 2012.
2. Bugaj, M. and M. Wnuk, "Optimization parameters of dielectric in aperture-coupled stacked patch antenna on bandwidth," *2010 MIKON Conference Proceedings*, 1–4, 2010.
3. Bugaj, M. and M. Wnuk, "Influence of parameters of dielectric in aperture-coupled stacked patch antenna on bandwidth," *Przeglad Elektrotechniczny*, Vol. 85, No. 9, 50–53, 2009.
4. Bugaj, M. and M. Wnuk, "The influence examination of dielectric parameters on bandwidth in multilayer aperture-coupled microstrip Antennas with utilization the FDTD method," *2008 MIKON Conference Proceedings*, 1–4, 2008.
5. Wnuk, M. and M. Bugaj, "Analysis of radiating structures placed on multilayer dielectric," *Computational Methods and Experimental Measurements XIII Book Series: WIT Transactions on Modelling and Simulation*, Vol. 46, 747–755, 2007.
6. Wnuk, M., G. Rózanski, and M. Bugaj, "The analysis of microstrip antennas using the FDTD memod," *Computational Methods and Experimental Measurements XII Book Series: WIT Transactions on Modelling and Simulation*, Vol. 41, 611–620, 2005.
7. Kubacki, R., J. Ferenc, R. Przesmycki, and M. Wnuk, "The nanocrystalline FeSiBCuNb finemet absorption properties at microwaves," *IEEE Transactions on Electromagnetic Compatibility*, Vol. 54, No. 1, 93–100, 2012.
8. Kubacki, R., J. Ferenc, and R. Przesmycki, "The measurements of the complex permittivity and permeability of powdered nanocrystalline Fe-Si-B-Cu-Nb ('finemet')," *Przeglad Elektrotechniczny*, Vol. 87, No. 12B, 92–95, 2011.
9. Kubacki, R., E. Cwalina, M. Kuchta, and A. Dukata, "Electromagnetic field distribution in the office room and computer enclosure evoked by electromagnetic high power pulses," *Przeglad Elektrotechniczny*, Vol. 88, No. 12B, 209–212, 2012.
10. Kubacki, R., M. Wnuk, and J. Kieliszek, "Fresnel approximations in mathematical expressions of the electric field for base station antennas," *Przeglad Elektrotechniczny*, Vol. 84, No. 12, 190–193, 2008.
11. Kubacki, R., "Biological interaction of pulse-modulated electromagnetic fields and protection of humans from exposure to fields emitted from radars," *2008 MIKON Conference Proceedings*, 1–7, 2008.
12. Kubacki, R. S. and J. Sobiech, "Model for investigation of microwave energy absorbed by young and mature living animals," *Electromagnetic Field, Health and Environment, Proceedings of EHE' 07 Book Series: Studies in Applied*, Vol. 29, 126–132, 2008.
13. Kubacki, R., J. Kieliszek, and A. Krawczyk, "The investigation of influence of the electromagnetic fields emitted from short-wave diathermy to the pacemakers," *Przeglad Elektrotechniczny*, Vol. 83, No. 12, 105–107, 2007.
14. Kubacki, R., J. Sobiech, J., Kieliszek, and A. Krawczyk, "Comparison of numerical and measurement methods of SAR of ellipsoidal phantoms with muscle tissue electrical parameters," *COMPEL — The International Journal for Computation and Mathematics in Electrical and Electronic Engineering*, Vol. 25, No. 3, 691–704, 2006.
15. Dabrowski, M. P., W. Stankiewicz, R. Kubacki, E. Sobiczewska, and S. Szmigielski, "Immunotropic effects in cultured human blood mononuclear cells pre-exposed to low-level 1300 MHz pulse-modulated microwave field," *Electromagnetic Biology and Medicine*, Vol. 22, No. 1, 1–13, 2003.
16. Kubacki, R., M. Wnuk, W. Kolosowski, and J. Sobiech, "New approach to electromagnetic field calculations in the near-field of microwave antennas," *Computational Methods and Experimental Measurements XI Book Series: Computational Engineering*, Vol. 4, 413–422, 2003.
17. Kubacki, R., M. Krukowski, J. Kieliszek, and J. Sobiech, "New computational model of electromagnetic field distribution for predicting of the safety zones in the near-field of microwave antennas," *2002 MIKON Conference Proceedings*, Vol. 3, 902–905, 2002.

18. Michalak, J. and B. Uljasz, "Relative efficiency of broadcasting in the cluster based network — Simulation results," *Military Communications and Information Systems Conference (MCC 2013)*, Francja, Saint-Malo, Oct. 7–8, 2013, ISBN 978-83-62954.
19. Piotrowski, Z., "Angle phase drift correction method effectiveness," *Signal Processing Algorithms, Architectures, Arrangements, and Applications Conference Proceedings*, 82–86, 2009, ISBN: 978-83-62065-00-4.
20. Bylak, M. and D. Laskowski, "Assessment of network coding mechanism for the network protocol stack 802.15.4/6LoWPAN," *Advances in Intelligent Systems and Computing*, Vol. 224, 75–82, Springer International Publishing AG, Switzerland, 2013, ISSN: 2194-5357 (Print), 2194-5365 (Online).
21. Laskowski, D., P. Lubkowski, and M. Kwasniewski, "Identification of suitability services for wireless networks," *Przeglad Elektrotechniczny*, R. 89, Sigma-Not., Warszawa, Str. 128-132, Sep. 2013, ISSN: 0033-2097.
22. Bylak, M. snd D. Laskowski, "Diagnosis coding efficiency of network coding mechanism for wireless networks," *Przeglad Elektrotechniczny*, R. 89, Sigma-Not., Warszawa, Str. 133-138, Sep. 2013, ISSN: 0033-2097.

Honeycomb Ventilation Grill Shielding Effectiveness Measuring Methodology

Leszek Nowosielski and Cezary Piotrowski
Faculty of Electronics, Military University of Technology
Gen. S. Kaliskiego 2 str., Warsaw 00-908, Poland

Abstract— In the article assessment methodology of shielding effectiveness of ventilation panels of small overall dimensions made in the form of honeycomb with the use of the computer simulation method has been presented. Methodology and description of simulation environment for measuring shielding effectiveness of ventilation panels by the method of computer simulation have been shown. Final effect of simulation software operation is characteristics of shielding effectiveness of a tested ventilation panel in the frequency function. In order to conduct validation of simulation software values of shielding effectiveness for a selected ventilation panel obtained by the computer simulation method have been compared with results obtained due to tests in real laboratory conditions.

1. INTRODUCTION

While designing small in dimension shielding casings assigned for shielding of electronic devices supplied by electric energy it is necessary to provide for this kind of constructions the required:

- shielding effectiveness of ventilation panels used for cooling electronics placed inside a casing,
- shielding effectiveness of shielding casing components, which provide access inside a casing (e.g., inspection doors and windows),
- attenuation of undesirable signals by power supply filters and telecommunication interface filters [1].

The above mentioned parameters of shielding casing components have a direct influence on resulting shielding effectiveness of the whole shielding casing. That being so, in the design and construction process of shielding casings it is necessary to have tools allowing to assess shielding effectiveness or attenuation of undesirable signals for particular casing components. In this article a tool for assessment of shielding effectiveness of ventilation panels of small overall dimensions made in the form of honeycomb has been suggested and discussed with the use of computer simulation method. Methodology of measuring shielding effectiveness and description of simulation environment have been presented. The final effect of computer simulation is characteristics of shielding effectiveness of ventilation panel in the frequency function. In order to conduct validation of simulation software, values of shielding effectiveness for a selected ventilation panel received by the computer simulation method were compared with results obtained from tests conducted in real laboratory conditions. The study object was a Tecknit ventilation panel of dimensions $152.4\,\text{cm} \times 152.4\,\text{cm}$.

The calculated shielding effectiveness can be used in many applications where the electromagnetic field distribution is needed [9–19].

2. CONCEPTION OF CALCULATION METHODOLOGY OF SHIELDING EFFECTIVENESS OF VENTILATION PANELS BY THE COMPUTER SIMULATION METHOD

At the first stage of suggested algorithm for calculating shielding effectiveness of ventilation panels it is necessary to model in computer simulation environment a tight shielding casing with an installed tested ventilation panel. The condition of obtaining proper results is providing large enough level of shielding effectiveness of walls of shielding casing in which a tested ventilation panel is installed. That level should exceed an expected value of shielding effectiveness of the tested ventilation panel. It can be achieved by selecting suitable parameters of materials describing shielding properties of modelled casing walls. The parameters of materials can be obtained by using measurement methodology described in literature items [7, 8].

Measurement of shielding effectiveness of ventilation panel comes down to making two measurements of electric field strength level at the input of meter of electric field strength for particular

frequencies. The first measurement is carried out as so called reference measurement. With a determined value of signal level generated by the test signal source, the level of electric field strength in the place of meter probe installation is measured within a particular distance from transmitting antenna of the test signal probe. After making reference measurement, basic measurement is performed during which a measuring probe is placed inside a modelled shielding casing with an installed ventilation panel. Measurements should be conducted in the same way as during reference measurement. After calculation of the difference of recorded levels of electric field strength corresponding to particular measuring frequencies during reference and basic measurements we will receive the value of shielding effectiveness of modelled shielding casing expressed in decibels. Because of the fact that casing walls are made of material providing much higher shielding effectiveness than shielding effectiveness of a tested ventilation panel, that being so, the received calculation results will match shielding effectiveness of the tested ventilation panel. A simplified block diagram of measuring position for shielding effectiveness of ventilation panels of small overall dimensions is presented in Fig. 1.

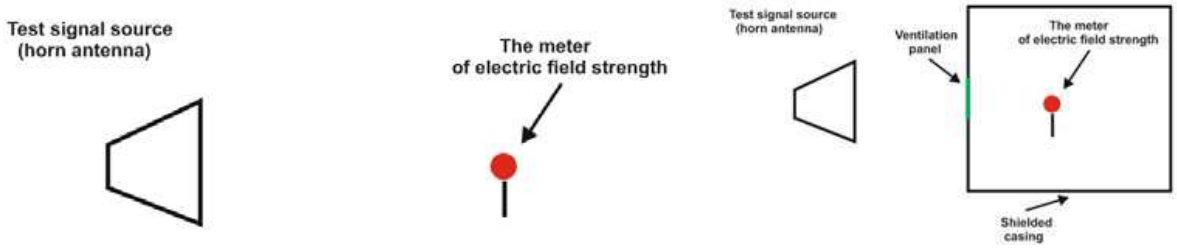

Figure 1: Block diagram of position for measuring shielding effectiveness of ventilation panels of small overall dimensions by the computer simulation method: (a) reference measurement, (b) basic measurement.

Software algorithm for assessment of shielding effectiveness of ventilation panels by the computer simulation method is based on modelled in CST Microwave Studio simulation environment measuring position presented in Fig. 1 using retuned test signal source and meter of electric field strength. User's graphic interface of CST Microwave Studio environment of simulation model using horn transmitting antenna as the source of test signal is presented in Fig. 2.

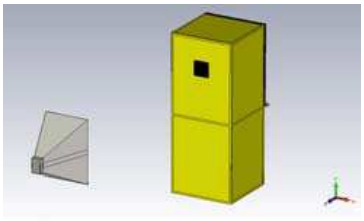

Figure 2: User's graphic interface of CST Microwave Studio environment of simulation model using horn transmitting antenna as the source of test signal.

Figure 3: Ventilation panel installed in the real shielding casing.

3. SOFTWARE VALIDATION FOR ASSESSMENT OF SHIELDING EFFECTIVENESS OF VENTILATION PANELS BY THE COMPUTER SIMULATION METHOD

In order to check correctness of simulation software operation for assessment of shielding effectiveness of ventilation panels, values of shielding effectiveness for a selected ventilation panel obtained by the computer simulation method have been compared with results obtained during laboratory tests with the use of real measuring position. The study object was the Tecknit ventilation panel of dimensions 152.4 cm × 152.4 cm. To conduct measurement of shielding effectiveness of the above ventilation panel in laboratory conditions it was installed in shielding casing which effectiveness is much higher than expected shielding effectiveness of the tested ventilation panel. Parameters of ventilation panel and shielding casing are equal to parameters of their computer models used

during tests with the computer simulation method. The view of physically made shielding casing with installed ventilation panel is presented in Fig. 3. The structure of measuring position and principle of shielding effectiveness measurement along with discussion of measurement results are shown below.

The algorithm idea of measuring shielding effectiveness of ventilation panels in real laboratory conditions comes down to performance of two measurements of electric field strength level at the input of meter of electric field strength for particular frequencies. The first measurement is made as so called reference measurement and is carried out with meter of electric field strength placed directly in front of test signal transmitting antenna. The second measurement, defined as basic, is made with meter of electric field strength, which probe is placed inside shielding casing with installed ventilation panel. After calculating the difference of recorded electric field strength levels corresponding to particular measuring frequencies during reference and basic measurements we will receive the value of shielding effectiveness of modelled shielding casing expressed in decibels. The above measurement algorithm coincides with methodology of calculating shielding effectiveness of ventilation panels by the computer simulation method described in chapter two of this article.

In Fig. 4, measurement results of shielding effectiveness of the Tecknit ventilation panel of dimensions 152.4 cm × 152.4 cm are presented. They were conducted with the laboratory method (green and black curve) and the computer simulation method with the use of horn transmitting antenna (blue curve). The results obtained by the laboratory measurement method coincide with the results received by the computer simulation method over test signal frequency equal to 1.3 GHz. Divergences of shielding effectiveness levels of ventilation panel below the frequency 1.3 GHz result first of all from using rod antenna as a measuring antenna of electric field strength. The used length of rod antenna does not correspond to frequency range of test signal below 1.3 GHz. During measurements a longer measuring antenna could not be used due to limited dimensions of the used shielding casing.

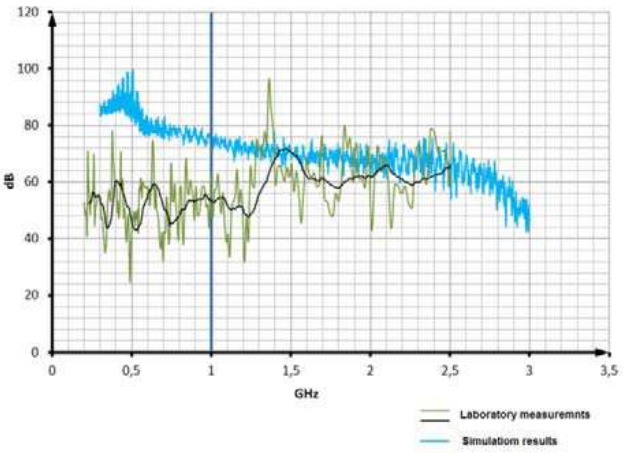

Figure 4: Values of the level of shielding effectiveness of ventilation panel received by the methods of laboratory tests and computer simulation.

Because of difficulties with selection of a type of measuring antenna and its size, measurement of shielding effectiveness with the laboratory test method has significant limitations particularly for lower frequency range. As measurement antenna can be used optional antenna [2–6] tuned to the frequency of the test signal. That being so, it seems appropriate to use laboratory measurements for higher frequencies of test signal and simulation tests for lower measurement frequencies.

The presented comparison of results of laboratory and simulation tests allows only to validate both methods of determining shielding effectiveness over the frequency 1.3 GHz for the applied measurement environment and study object.

4. CONCLUSIONS

In the article assessment methodology of shielding effectiveness by the method of computer simulation of ventilation panels of small overall dimensions made in the form of honeycomb was presented. The presented methodology of calculating shielding effectiveness by the computer simulation method seems appropriate for the whole frequency range, especially for low frequency range

where using measurements with real laboratory station is impossible due to inability of using measuring antennas of overall dimensions matched to wave length of test signal and enabling their installation inside the small tested shielding casing. Measuring antennas of large dimensions compared to overall dimensions of the tested ventilation panel corresponding to low frequencies are impossible to use in real laboratory station.

ACKNOWLEDGMENT

The project is financed from NCBiR means within the Agreement No. 0024/R/ID2/2012/02 in the years 2012–2015.

REFERENCES

1. Bugaj, M., R. Przesmycki, M. Wnuk, and K. Piwowarczyk, "Analysis of methods measuring attenuation of RF line," *Przeglad Elektrotechniczny*, Vol. 88, No. 2, 17–19, 2012.
2. Bugaj, M. and M. Wnuk, "Optimization parameters of dielectric in aperture-coupled stacked patch antenna on bandwidth," *18th International Conference on Microwaves, Radar and Wireless Communications (MIKON-2010)*, Vols. 1–2, 2010,
3. Bugaj, M. and M. Wnuk, "Influence of parameters of dielectric in aperture-coupled stacked patch antenna on bandwidth," *Przeglad Elektrotechniczny*, Vol. 85, No. 9, 50–53, 2009.
4. Bugaj, M. and M. Wnuk, "The influence examination of dielectric parameters on bandwidth in multilayer aperture-coupled microstrip antennas with utilization the FDTD method," *2008 MIKON Conference Proceedings*, Vols. 1–2, 708–711, 2008.
5. Wnuk, M. and M. Bugaj, "Analysis of radiating structures placed on multilayer dielectric," *Computational Methods and Experimental Measurements XIII Book Series: Wit Transactions on Modelling and Simulation*, Vol. 46, 747–755, 2007.
6. Wnuk, M., G. Rózanski, and M. Bugaj, "The analysis of microstrip antennas using the FDTD memod," *Computational Methods and Experimental Measurements XII Book Series: Wit Transactions on Modelling and Simulation*, Vol. 41, 611–620, 2005.
7. Kubacki, R., J. Ferenc, R. Przesmycki, and M. Wnuk, "The nanocrystalline FeSiBCuNb finemet absorption properties at microwaves," *IEEE Transactions on Electromagnetic Compatibility*, Vol. 54, No. 1, 93–100, 2012.
8. Kubacki, R., J. Ferenc, and R. Przesmycki, "The measurements of the complex permittivity and permeability of powdered nanocrystalline Fe-Si-B-Cu-Nb ('Finemet')," *Przeglad Elektrotechniczny*, Vol. 87, No. 12B, 92–95, 2011.
9. Kubacki, R., E. Cwalina, M. Kuchta, and A. Dukata, "Electromagnetic field distribution in the office room and computer enclosure evoked by electromagnetic high power pulses," *Przeglad Elektrotechniczny*, Vol. 88, No. 12B, 209–212, 2012.
10. Kubacki, R., M. Wnuk, and J. Kieliszek, "Fresnel approximations in mathematical expressions of the electric field for base station antennas," *Przeglad Elektrotechniczny*, Vol. 84, No. 12, 190–193, 2008.
11. Kubacki, R., "Biological interaction of pulse-modulated electromagnetic fields and protection of humans from exposure to fields emitted from radars," *2008 MIKON Conference Proceedings*, Vols. 1–2, 66–72, 2008.
12. Kubacki, R., J. Sobiech, and E. Sedek, "Model for investigation of microwave energy absorbed by young and mature living animals," *Electromagnetic Field, Health and Environment, Proceedings of EHE '07 Book Series: Studies in Applied*, Vol. 29, 126–132, 2008.
13. Kubacki, R., J. Kieliszek, and A. Krawczyk, "The investigation of influence of the electromagnetic fields emitted from short-wave diathermy to the pacemakers," *Przeglad Elektrotechniczny*, Vol. 83, No. 12, 105–107, 2007.
14. Kubacki, R., J. Sobiech, J. Kieliszek, and A. Krawczyk, "Comparison of numerical and measurement methods of SAR of ellipsoidal phantoms with muscle tissue electrical parameters," *COMPEL — The International Journal for Computation and Mathematics in Electrical and Electronic Engineering*, Vol. 25, No. 3, 691–704, 2006.
15. Dabrowski, M. P., W. Stankiewicz, R. Kubacki, E. Sobiczewska, and S. Szmigielski, "Immunotropic effects in cultured human blood mononuclear cells pre-exposed to low-level 1300 MHz pulse-modulated microwave field," *Electromagnetic Biology and Medicine*, Vol. 22, No. 1, 1–13, 2003.

16. Kubacki, R., M. Wnuk, W. Kolosowski, and J. Sobiech, "New approach to electromagnetic field calculations in the near-field of microwave antennas," *Computational Methods and Experimental Measurements XI Book Series: Computational Engineering*, Vol. 4, 413–422, 2003.
17. Kubacki, R., M. Krukowski, J. Kieliszek, and J. Sobiech, "New computational model of electromagnetic field distribution for predicting of the safety zones in the near-field of microwave antennas," *XIV International Conference on Microwaves, Radar and Wireless Communications, MIKON-2002*, Vols. 1–3, 902–905, 2002.
18. Michalak, J. and B. Uljasz, "Relative efficiency of broadcasting in the cluster based network — simulation results," *Military Communications and Information Systems Conference*, Francja, Saint-Malo, 07-08.10.2013, 2013, ISBN 978-83-62954.
19. Bylak, M. and D. Laskowski, "Assessment of network coding mechanism for the network protocol stack 802.15.4/6LoWPAN," *Advances in Intelligent Systems and Computing*, Springer International Publishing AG, Switzerland, Vol. 224, 75–82, ISSN: 2194–5357 (Print); 2194–5365 (Online), 2013.

Technique of High Power Microwave Pulses Dosimetry of Living Systems

Roman Kubacki and Salim Lamari
Faculty of Electronics, Military University of Technology
Gen. S. Kaliskiego 2 Str., Warsaw 00-908, Poland

Abstract— In order to investigate the biological effects evoked in the high power microwave fields, the numerical calculation of dosimetry for *in vitro* study has been carried out. The widely used 90 mm Petri dishes filled with human blood was planned to be exposed to high power microwave pulses. Electric and magnetic vectors of the incident field were parallel to the surface of Petri dishes. Taking into account that according to the actual safety standards the specific absorption rate (SAR) is a basic restriction parameter for protecting against thermal effects in the risk assessment study the numerical calculation has been performed to maintain the SAR distribution in the specimen. The novel attempt of the dosimetry takes into account the calculation of SAR of all frequency harmonics of the spectrum taking into consideration the function of permittivity of the medium (human blood) in the analyzed frequency range.

1. INTRODUCTION

Electromagnetic radiation emitted from HPM (High Power Microwaves) generators can be characterized by extremely high power in peak (mega or giga watts) and pulse duration less than 50 ns and they are called as e-bomb. Many reports demonstrated the destructive effects of e-bombs to electronics exposed to HPM's. Despite the fact that potential health hazard from HPM pulses is not broadly investigated, the generators emitting such HPM pulses have been called as non-lethal weapon. Electromagnetic radiation emitted from HPM generators can also be treated as ultra-wideband (UWB) signals. Such frequency range of radiation can be obtained with contemporary antennas [3, 4, 7, 8, 16–19] or microstrip antennas [5, 9, 20–22]. In addition, ultra-wideband (UWB) wireless communication became the subject of intensive investigation due to its potential applications in high rate transmission [2, 11–14].

The ultra-wideband signals have different forms of interaction with biological structures comparing with continuous signals because the frequency spectrum of harmonics of such radiation sometimes exceeds 500 MHz. This is why, for such signals the efficiency of electromagnetic absorption inside biological tissues cannot be investigated with the same methods as it was presented for monochromatic signals or for narrowband signals. The main parameter which differentiates the level of absorption in function of frequency is permittivity. However, the real and imaginary part of permittivity of biological tissues significantly changes in such broad frequency band [1, 7, 10]. From this point of view the level of absorbed electromagnetic energy by tissues depends on frequency.

According to the actual safety standards the specific absorption rate (SAR) is a basic restriction parameter for protecting against thermal effects in the risk assessment study. This parameter should be treated as a basic restriction for protecting against thermal effects from exposure to radiofrequency fields. The SAR is expressed by watt per kg of tissue mass, according to the following equation

$$\mathrm{SAR} = \frac{\sigma |E_{int}|^2}{\rho} \tag{1}$$

where: σ is the conductivity of the tissue in S/m, ρ is the mass density in kg/m^3, $|E_{int}|$ is the root-mean-square of the induced electric field in the medium in V/m.

Nevertheless, there is still an open question if specific absorption rate (SAR) is a suitable parameter to characterize the dose-effect dependence. The SAR has been effective parameter for continuous wave (CW) due to thermal effect. In case of HPM/UWB pulsed radiation, the value of SAR can be determined only for time duration of single pulse or for train of pulses. Between pulses the field does not affect the biological structures. For such radiation bioeffects of HPM/UWB signals could be different from CW.

The Petri dishes of different types are widely used in biological investigation to assess the microwave exposure level of cell cultures. An important requirement of the biological research is accurate field and/or dosimetry assessment. Biological effects should be related to the induced

internal electromagnetic field or energy rate absorbed by the biological specimen. At microwaves the dosimetry of exposure to very high power pulses of cells in a solid nutrient medium (agarose gel) was presented by Pakhomov et al. [15]. The carrier frequency was 9.3 GHz and the radiation was modulated by pulses of 0.5 µs duration and 10 Hz repetition. The simulation was made for setup based on waveguide and electric field strength of 1.57 MV/m. For this configuration the radiation was treated as a narrowband signal and the SAR of 650 MW/kg was obtained.

In the work, the novel technique was proposed to improve the dosimetry of living tissues exposed to high power microwaves radiation. In this method the incident signal has been presented as a series of frequency harmonics. Harmonic amplitudes were calculated using the Fourier transform. The SAR has been calculated for each harmonic taking into account value of blood permittivity, suitable for analyzed frequency.

In the exposure of cell cultures with Petri dishes an important task is polarization. Generally speaking, three polarizations can be used, yielding to a different coupling to the electromagnetic field and different SAR distribution inside the medium. The k polarization, used in this work, refers to the exposure in the free space when electric and magnetic vectors of incident field are parallel to the bottom surface of the specimen.

2. MATERIALS AND METHODS

The generation system has been based on DS110 RF Source (Diehl BGT Defence, Germany) [6]. The setup consists of a generator of HPM pulses equipped with reflector. Generated signal (pulses) consists of the main part of the pulse of 4 ns time duration and 30 ns of the remaining part as presented in Figure 1(a). Maximum value of the pulse is 240 kV/m. The remaining part of the pulse reaches value of 70 kV/m.

Using DS110 RF Source (Diehl BGT Defence, Germany) it is possible to emit single pulse or a train of pulses with 5 Hz repetition. Signal, as presented in Figure 1(a), has a broadband spectrum frequency of harmonics.The frequency spectrum of signal presented in Figure 1(a) covers the frequency bandwidth of 500 MHz, from 150 MHz to 650 MHz. Such a RF source can be useful to investigate the biological effects of exposure to high power pulses as well as UWB signals.

The Petri dishes are intended to place 0.5 m above the DS110 RF Source (Diehl BGT Defence, Germany). All elements will be installed in an anechoic chamber providing the free space condition of exposure. For such case the electromagnetic field incidents on the bottom of Petri dish surface. This configuration provides the TEM type field with k polarization — vectors E and H are parallel to the surface of specimen (Figure 1(b)). In the investigation the standard 90 mm Petri dishes have been performed with the internal diameter of 86.5 mm (radius of 43.25 mm). Dishes were filled with 4 ml of human blood as specimen. This corresponds to medium height of 0.68 mm of the medium.

Presented in this paper, the HPM pulses as a ultra wideband signal covers a broad frequency range from 150 MHz to 650 MHz. For such a broad frequency range relative complex permittivity of investigated medium changes significantly. For further study the SAR for each harmonic was numerically calculated taking into account suitable amplitude of harmonic and permittivity for its frequency. To model the SAR distribution in the specimen, the three-dimensional model accounting both dielectric materials, i.e., human blood as a medium and supporting plastic part (Petri dish) has been developed. The coordinate system has been placed in the dish bottom with the origin

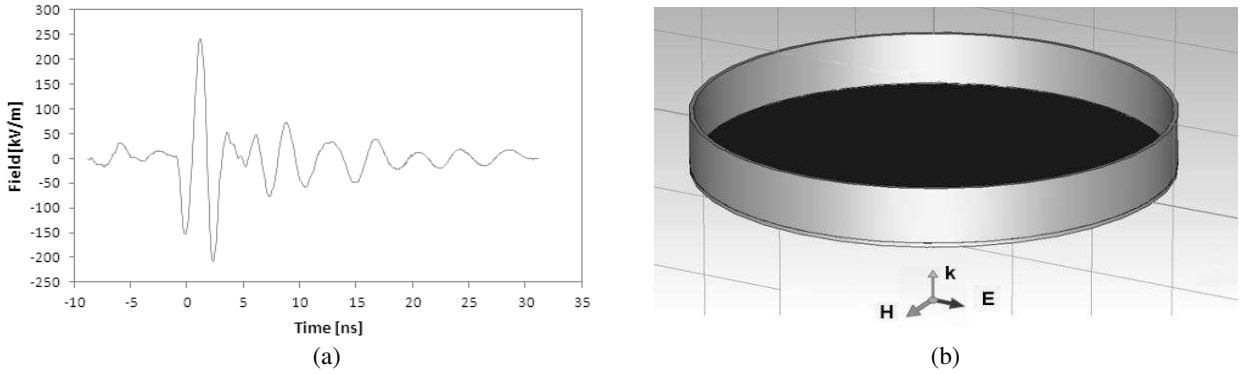

(a) (b)

Figure 1: (a) HPM pulse in function of time, (b) 90 mm Petri dish filled with blood and electromagnetic field configuration showing the k, E, H directions.

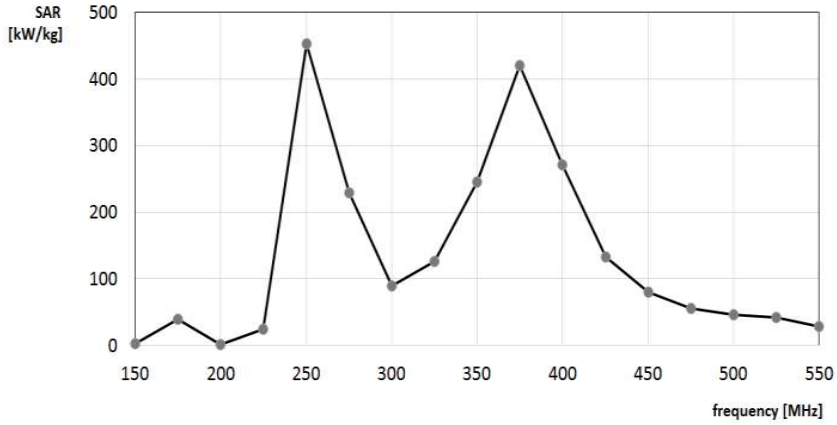

Figure 2: Function of maximum values of SAR in function of harmonic frequencies.

of coordinate centered in the middle of circular layer of dish bottom. The dish thickness of the side and the bottom of 1 mm and relative permittivity of 2.5 and conductivity of 0.02 S/m were considered in the calculation. The maximum values of SAR of all harmonics were presented in Figure 2. Presented values have been determined at the middle point of horizontal layer located 0.3 mm above the specimen bottom.

In the Figure 2 the SAR values for all harmonics within analyzed frequency range have been determined. The discussed exposure to HPM/UWB can also be treated as 17 plane waves having SARs as presented in the picture. It is easy to notice that assessing such exposure, according existing methods, using only one value of SAR is too large simplification of the problem. Figure 2 shows that for incident pulsed field used in this investigation two SAR maxima appear in function of frequency — 250 and 375 MHz, achieving values of 450 and 420 kW/kg. For other frequencies SAR have significantly lower values.

Presented data for HPM/UWB signals open the question if the SAR as the basic restriction factor should be predicted only for one frequency as is defined in guidelines or for all representative harmonics as is underlined in this work. According to the general statement on safety factors limitations the establishing data should be provided for the whole frequency range, thus the assessing of SAR for only one frequency, for example for carrying frequency, is insufficient. As the minimum approach the SAR should be assessed at specific frequencies where they reach maximum values.

3. CONCLUSIONS

In the paper the study describing the exposure system and dosimetry evaluation have been proposed for high power microwave pulses (HPM) as well as for ultra-wideband (UWB) signals. In order to investigate the biological effects the numerical simulation for in vitro has been carried out for the widely used 90 mm Petri dish filled with human blood exposed to high power microwaves (HPM) with the free space condition. The incident electromagnetic field was with the k polarization. The simulation has been performed to maintain uniformity of the specific absorption rate (SAR) distribution in the specimen. According to the actual safety standards the SAR is a basic restriction parameter for protecting against thermal effect in the risk assessment study. The novel attempt at the dosimetry takes into account calculation of SAR of all frequency harmonics of the spectrum of incident signal with regard to permittivity of the medium in the analyzed frequency range.

ACKNOWLEDGMENT

The project was financed from NCBiR means within the Agreement No. DOBR-BIO4/016/13071-/2013 in the years 2013–2015.

REFERENCES

1. Alison, J. M. and R. J. Sheppard, "Dielectric properties of human blood at microwave frequencies," *Phys. in Medicine and Biology*, Vol. 38, 971–979, 1993.
2. Bugaj, M., R. Przesmycki, M. Wnuk, and K. Piwowarczyk, "Analysis of methods measuring attenuation of RF line," *Przeglad Elektrotechniczny*, Vol. 88, No. 2, 17–19, 2012.

3. Bugaj, M. and M. Wnuk, "Influence of parameters of dielectric in aperture-coupled stacked patch antenna on bandwidth," *Przeglad Elektrotechniczny*, Vol. 85, No. 9, 50–53, 2009.
4. Bugaj, M. and M. Wnuk, "Optimization parameters of dielectric in aperture-coupled stacked patch antenna on bandwidth," *18th International Conference on Microwaves, Radar and Wireless Communications (MIKON-2010)*, Vols. 1 and 2, 2010.
5. Bugaj, M. and M. Wnuk, "The influence examination of dielectric parameters on bandwidth in multilayer aperture-coupled microstrip antennas with utilization the FDTD method," *2008 MIKON Conference Proceedings*, Vols. 1 and 2, 708–711, 2008.
6. Catalogue, Technical Details, DIEHL BGT Defence, 2008.
7. Gabriel, C., S. Gabriel, and E. Corthout, "The dielectric properties of biological tissues," *Phys. in Medicine and Biology*, Vol. 41, 2231–2249, 1996.
8. Gajewski, P., J. Lopatka, L. Nowosielski, B. Uljasz, and Z. Piotrowski, "Multimedia transmission over HF links," *IEEE 21st Century Military Communications Conference Proceedings, Military Communications Conference*, Vols. 1 and 2, 45–47, 2000.
9. Gruszczynski, M., M. Wnuk, and L. Nowosielski, "Multisystem microstrip antenna for mobile communications," *2012 IEEE Antennas and Propagation Society International Symposium (APSURSI)*, Book Series: *IEEE Antennas and Propagation Society International Symposium*, 2012.
10. Jaspard, F. and M. Nadi, "Dielectric properties of blood: An investigation of temperature dependence," *Physiological Measurement*, Vol. 23, 547–549, 2002.
11. Nowosielski, L., R. Przesmycki, and M. Wnuk, "The laboratory stand for conducted emissions measurement in accordance with the military standard," *2010 IEEE International Symposium on Electromagnetic Compatibility (EMC 2010)*, 275–278, 2010.
12. Nowosielski, L., R. Przesmycki, M. Wnuk, and J. Rychlica, "The methods of measuring attenuation of thin absorbent materials used for electromagnetic shielding," *PIERS Online*, Vol. 7, No. 3, 261–265, 2011.
13. Nowosielski, L., M. Wnuk, R. Przesmycki, K. Piwowarczyk, and M. Bugaj, "Coaxial cables shielding efficiency measuring methodology," *PIERS Proceedings*, 72–76, Kuala Lumpur, Malaysia, Mar. 27–30, 2012.
14. Nowosielski, L., M. Wnuk, and C. Ziolkowski, "Interlaboratory tests in scope of measurement of radio disturbance," *2009 European Microwave Conference*, Vols. 1–3, 288–291, 2009.
15. Pakhomov, A. G., P. Gajsek, L. Allen, B. E. Stuck, and M. R. Murphy, "Comparison of dose dependences for bioeffects of continuous-wave and high-peak power microwave emission using gel-suspended cell cultures," *Bioelectromagnetics*, Vol. 23, 158–167, 2002.
16. Piotrowski, Z., L. Nowosielski, L. Zagozdzinski, and P. Gajewski, "Electromagnetic compatibility of the military handset with hidden authorization function based on MIL-STD-461D results," *PIERS Online*, Vol. 4, No. 5, 566-570, 2008.
17. Piwowarczyk, K., R. Przesmycki, L. Nowosielski, and M. Wnuk, "The measurement of the immunity on the electric field about the radiofrequency within the range (80–1000) MHz," *Przeglad Elektrotechniczny*, Vol. 86, No. 3, 165–167, 2010.
18. Przesmycki, R., M. Wnuk, L. Nowosielski, K. Piwowarczyk, and M. Bugaj, "Analysis of the radiated emissions of IT equipment," *PIERS Proceedings*, 1419–1423, Moscow, Russia, Aug. 19–23, 2012.
19. Przesmycki, R., M. Wnuk, L. Nowosielski, K. Piwowarczyk, and M. Bugaj, "The conducted and radiated emission levels from IT devices," *PIERS Proceedings*, 77–81, Kuala Lumpur, Malaysia, Mar. 27–30, 2012.
20. Wnuk, M. and M. Bugaj, "Analysis of radiating structures placed on multilayer dielectric," *Computational Methods and Experimental Measurements XIII*, Book Series: *WIT Transactions on Modelling and Simulation*, Vol. 46, 747–755, 2007.
21. Wnuk, M., M. Bugaj, R. Przesmycki, L. Nowosielski, and K. Piwowarczyk, "Wearable antenna constructed in microstrip technology," *PIERS Proceedings*, 67–71, Kuala Lumpur, Malaysia, Mar. 27–30, 2012.
22. Wnuk, M., G. Różański, and M. Bugaj, "The analysis of microstrip antennas using the FDTD method," *Computational Methods and Experimental Measurements XII*, Book Series: *WIT Transactions on Modelling and Simulation*, Vol. 41, 611–620, 2005.

Modelling of Electromagnetic Wave Propagation with the Use of the Ray-tracing Method

Leszek Nowosielski, Jerzy Łopatka, and Michał Siłaczuk
Faculty of Electronics, Military University of Technology
Gen. S. Kaliskiego 2 Str., Warsaw 00-908, Poland

Abstract— The article concerns problems of electromagnetic wave propagation in semi-anechoic chambers. Electromagnetic wave propagation modelling using ray-tracing methodology is described. The analytical equations which are used in ray-tracing methodology are presented. The elaborated program algorithm basing on presented analytical equations is described. The worked out software application basing on the described algorithm is presented. The validation results of elaborated software are presented too.

1. INTRODUCTION

In widely available literature concerning methods of radio-wave propagation modelling [11, 12, 18–24] one can find a series of solutions different from each other in:

- modelled propagation environment (open space, urbanized area, building interior),
- dimensionality (two-dimensional, three-dimensional),
- possible to obtain calculation accuracy.

Only a few of them can be used for modelling of radio-wave propagation in semi-anechoic chambers. Despite the development of numerical methods used for solving electromagnetic problems (method of moments, FDTD) writing a program application implementing specific radio-wave propagation models is still very difficult and sometimes even impossible. We can distinguish a group of methods of radio-wave propagation modelling due to which, after some simplifications, it is possible to obtain simulation results with permissible accuracy in its acceptable duration. This group includes the ray tracing method [1, 2].

2. DESCRIPTION OF THE RAY-TRACING METHOD

The ray-tracing method for electric field strength of i-ray calculation in a particular point use the following dependence:

$$E_i = E_o L_i(d) f_{ti} f_{ri} \Pi_j \Gamma(\theta_{ji}) \Pi_k T(\theta_{ki}) e^{-jkd}, \tag{1}$$

where:
E_i — electric field strength from next ray (V/m),
E_o — electric field strength within the distance of 1 (m) from the source (V/m),
d — length of radio channel (m),
$L_i(d)$ — losses at distance d (channel length),
$\Gamma(\theta_{ji})$ — reflection coefficient,
$T(\theta_{ki})$ — transmission coefficient,
e^{-jkd} — phase shift at length d,
k — wave number ($2\pi/\lambda$),
f_{ti} — distribution of electric field strength of transmitting antenna,
f_{ri} — distribution of electric field strength of receiving antenna.

Total electric field strength in a particular point is vector superposition of fields deriving from particular rays and is expressed as:

$$E = \Sigma_1^i E_i \tag{2}$$

Occurring in Formula (1) coefficient of channel losses is calculated in the following way:

$$L(d) = -10 \log \left(\frac{G_t G_r \lambda^2}{(4\pi)^2 d_o^2} \right) + 10n \log \left(\frac{d}{d_0} \right), \tag{3}$$

where:
G_t, G_r — transmitting and receiving antenna gain,
λ — wave length (m),
d_o — reference distance, usually 1 (m),
d — channel length (total ray path) (m),
n — coefficient dependent on environment, in free space $n = 2$.

3. ASSUMPTIONS FOR MODELLING OF RADIO-WAVE PROPAGATION IN SEMI-ANECHOIC CHAMBERS

During working out the algorithm it was assumed that distribution of electric field strength would be determined in two dimensions. Propagation environment will be semi-anechoic chamber with length 5 (m) and height 3 (m). Ceiling and walls of the chamber are covered with a material absorbing energy of electromagnetic waves in the form of ferrite plates and graphitoidal absorbers. The chamber floor along the entire length is tiled only with ferrite plates and is the plane reflecting electromagnetic waves. Between transmitting and receiving antenna, which for the need of simulation will be represented as single surface points, there are no extra objects (obstacles). As input data for the algorithm application user must introduce: length of wave λ (m) generated by transmitter, height of transmitting antenna position h_1 (m), transmitting antenna gain G_t, relative ground permittivity ε, electric field strength E_o (V/m) within the distance of 1 (m) from transmitting antenna, polarization of generated radio wave (vertical, horizontal). Relative ground permittivity ε can be obtained by using measurement methodology described in literature items [9, 10, 13–17].

As a simulation model two-dimensional implementation of ray-tracing was chosen. Using reciprocity principle allows to determine resultant of electric field strength in the receiving point. For each space point two rays are traced:
- direct,
- reflected from ground.

4. ALGORITHM OF RADIO-WAVE PROPAGATION MODELLING

In Fig. 1 the algorithm of calculation of electric field strength distribution has been presented. Analysing the below algorithm one should bear in mind that variable y represents the height of receiving antenna suspension in centimetres and variable x — the distance (in straight line)

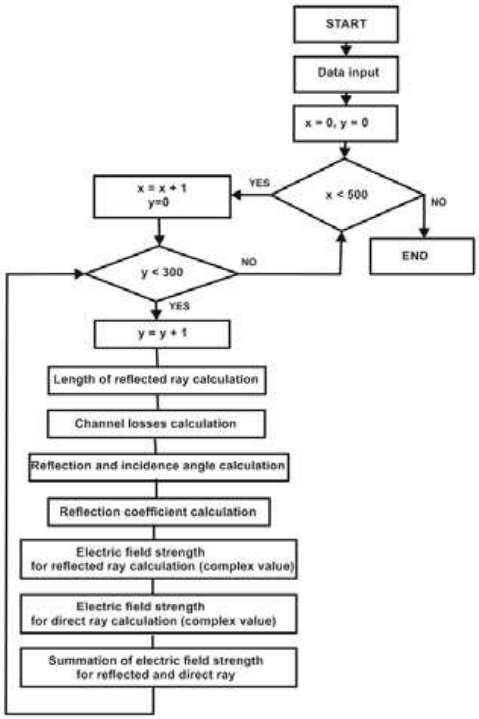

Figure 1: Algorithm calculating electric field strength — implementation of two-dimensional ray-tracing method.

of receiving antenna from transmitting antenna in centimentres. Software modelling radio-wave propagation and implementing the ray-tracing method was conducted on the platform JavaFX in Java language.

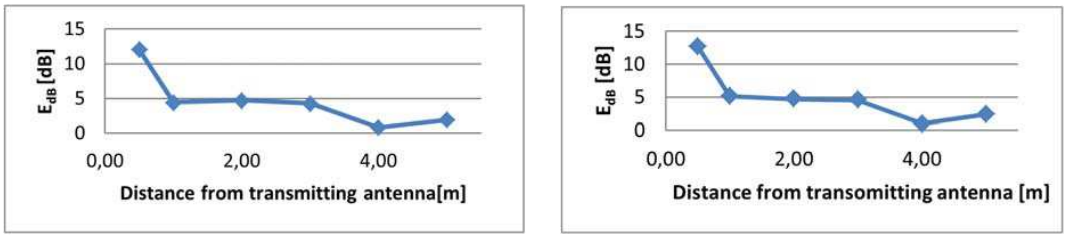

(a) (b)

Figure 2: Accuracy of simulation results for HPEM generator (a) without reflector and (b) with reflector.

5. VALIDATION OF SIMULATION SOFTWARE

In order to verify the designed simulation software levels of electric field strength obtained with the computer simulation method were compared with results received from measurements conducted in semi-anechoic chamber. As the source of test signal the generator HPEM DS-110 was used. Two range measurements of the HPEM generator were conducted. The first measurement was carried out for the HPEM generator without reflector, the second for the HPEM generator with reflector. The measurements were conducted at frequency $f = 350\,\mathrm{MHz}$, vertical electric field polarization and along direct ray. Both transmitting and receiving antennas were located at height $h = 1\,(\mathrm{m})$. As receiving antenna can be used optional antenna [3–8] tuned to the frequency of the test signal. During computer simulations environment close to the environment in semi-anechoic chamber was simulated. The measurement results were compared with results obtained with the use of designed simulation software. Two test scenarios simulating range measurement of the HPEM generator were conducted. In the first one measurement without aerial reflector was simulated, in the second — measurement with reflector.

Each value obtained as a result of simulation E_{sim} was compared with corresponding measurement result E_{meas} according to the below dependence:

$$E = |10\log(E_{sim}/E_{meas})|, \tag{4}$$

6. CONCLUSIONS

In the above presented Fig. 2 we can notice that for measuring points placed within the distance bigger than one meter from transmitting antenna, the obtained simulation results differ from the measurement results in not more than 5 (dB). The obtained differences between simulated and measured values fall into ranges published in specialist literature obtained for models of simulated channel according to models: Seidel and Rapaport, Holt, Pahlavan and Lee and McKown.

Moreover those differences do not depend on the structure of transmitting antenna — value $E\,(\mathrm{dB})$ is approximately the same for both tested scenarios. Thus we can assume that implementation of the ray-tracing method was performed correctly. It is worth noticing that along with increase of the distance from transmitting antenna the designed implementation of ray-tracing allows to obtain results closer to measured values.

ACKNOWLEDGMENT

The project is financed from NCBiR means within the Agreement No. 0024/R/ID2/2012/02 in the years 2012–2015.

REFERENCES

1. Yang, C.-F., B.-C. Wu, and C.-J. Ko, "A ray-tracing method for modeling indoor wave propagation and penetration," *IEEE Transactions on Antennas and Propagation*, Vol. 46, No. 6, 907–919, 1998.
2. Liang, G. and H. L. Bertoni, "A new approach to 3-D ray tracing for propagation prediction in cities," *IEEE Transactions on Antennas and Propagation*, Vol. 46, No. 6, 853–863, 1998.

3. Bugaj, M., R. Przesmycki, M. Wnuk, and K. Piwowarczyk, "Analysis of methods measuring attenuation of RF line," *Przeglad Elektrotechniczny*, Vol. 88, No. 2, 17–19, 2012.
4. Bugaj, M. and M. Wnuk, "Optimization parameters of dielectric in aperture-coupled stacked patch antenna on bandwidth," *2010 MIKON Conference Proceedings*, 1–4, 2010.
5. Bugaj, M. and M. Wnuk, "Influence of parameters of dielectric in aperture-coupled stacked patch antenna on bandwidth," *Przeglad Elektrotechniczny*, Vol. 85, No. 9, 50–53, 2009.
6. Bugaj, M. and M. Wnuk, "The influence examination of dielectric parameters on bandwidth in multilayer aperture-coupled microstrip Antennas with utilization the FDTD method," *2008 MIKON Conference Proceedings*, 1–4, 2008.
7. Wnuk, M. and M. Bugaj, "Analysis of radiating structures placed on multilayer dielectric," *Computational Methods and Experimental Measurements XIII Book Series: WIT Transactions on Modelling and Simulation*, Vol. 46, 747–755, 2007.
8. Wnuk, M., G. Rózanski, and M. Bugaj, "The analysis of microstrip antennas using the FDTD memod," *Computational Methods and Experimental Measurements XII Book Series: WIT Transactions on Modelling and Simulation*, Vol. 41, 611–620, 2005.
9. Kubacki, R., J. Ferenc, R. Przesmycki, and M. Wnuk, "The nanocrystalline FeSiBCuNb finemet absorption properties at microwaves," *IEEE Transactions on Electromagnetic Compatibility*, Vol. 54, No. 1, 93–100, 2012.
10. Kubacki, R., J. Ferenc, and R. Przesmycki, "The measurements of the complex permittivity and permeability of powdered nanocrystalline Fe-Si-B-Cu-Nb ('finemet')," *Przeglad Elektrotechniczny*, Vol. 87, No. 12B, 92–95, 2011.
11. Kubacki, R., E. Cwalina, M. Kuchta, and A. Dukata, "Electromagnetic field distribution in the office room and computer enclosure evoked by electromagnetic high power pulses," *Przeglad Elektrotechniczny*, Vol. 88, No. 12B, 209–212, 2012.
12. Kubacki, R., M. Wnuk, and J. Kieliszek, "Fresnel approximations in mathematical expressions of the electric field for base station antennas," *Przeglad Elektrotechniczny*, Vol. 84, No. 12, 190–193, 2008.
13. Kubacki, R., "Biological interaction of pulse-modulated electromagnetic fields and protection of humans from exposure to fields emitted from radars," *2008 MIKON Conference Proceedings*, 1–7, 2008.
14. Kubacki, R. S. and J. Sobiech, "Model for investigation of microwave energy absorbed by young and mature living animals," *Electromagnetic Field, Health and Environment, Proceedings of EHE' 07 Book Series: Studies in Applied*, Vol. 29, 126–132, 2008.
15. Kubacki, R., J. Kieliszek, and A. Krawczyk, "The investigation of influence of the electromagnetic fields emitted from short-wave diathermy to the pacemakers," *Przeglad Elektrotechniczny*, Vol. 83, No. 12, 105–107, 2007.
16. Kubacki, R., J. Sobiech, J., Kieliszek, and A. Krawczyk, "Comparison of numerical and measurement methods of SAR of ellipsoidal phantoms with muscle tissue electrical parameters," *COMPEL — The International Journal for Computation and Mathematics in Electrical and Electronic Engineering*, Vol. 25, No. 3, 691–704, 2006.
17. Dabrowski, M. P., W. Stankiewicz, R. Kubacki, E. Sobiczewska, and S. Szmigielski, "Immunotropic effects in cultured human blood mononuclear cells pre-exposed to low-level 1300 MHz pulse-modulated microwave field," *Electromagnetic Biology and Medicine*, Vol. 22, No. 1, 1–13, 2003.
18. Kubacki, R., M. Wnuk, W. Kolosowski, and J. Sobiech, "New approach to electromagnetic field calculations in the near-field of microwave antennas," *Computational Methods and Experimental Measurements XI Book Series: Computational Engineering*, Vol. 4, 413–422, 2003.
19. Kubacki, R., M. Krukowski, J. Kieliszek, and J. Sobiech, "New computational model of electromagnetic field distribution for predicting of the safety zones in the near-field of microwave antennas," *2002 MIKON Conference Proceedings*, Vol. 3, 902–905, 2002.
20. Michalak, J. and B. Uljasz, "Relative efficiency of broadcasting in the cluster based network — Simulation results," *Military Communications and Information Systems Conference (MCC 2013)*, Francja, Saint-Malo, Oct. 7–8, 2013, ISBN 978-83-62954.
21. Piotrowski, Z., "Angle phase drift correction method effectiveness," *Signal Processing Algorithms, Architectures, Arrangements, and Applications Conference Proceedings*, 82–86, 2009, ISBN: 978-83-62065-00-4.

22. Bylak, M. and D. Laskowski, "Assessment of network coding mechanism for the network protocol stack 802.15.4/6LoWPAN," *Advances in Intelligent Systems and Computing*, Vol. 224, 75–82, Springer International Publishing AG, Switzerland, 2013, ISSN: 2194-5357 (Print), 2194-5365 (Online).
23. Laskowski, D., P. Lubkowski, and M. Kwasniewski, "Identification of suitability services for wireless networks," *Przeglad Elektrotechniczny*, R. 89, Sigma-Not., Warszawa, Str. 128-132, Sep. 2013, ISSN: 0033-2097.
24. Bylak, M. snd D. Laskowski, "Diagnosis coding efficiency of network coding mechanism for wireless networks," *Przeglad Elektrotechniczny*, R. 89, Sigma-Not., Warszawa, Str. 133-138, Sep. 2013, ISSN: 0033-2097.

Electromagnetically Shielded Real-time MANET Testbed

Anna Kaszuba, Radoslaw Checinski, Michal Kryk, Jerzy Lopatka, and Leszek Nowosielski
Faculty of Electronics, Military University of Technology,
Gen. S. Kaliskiego 2 Str., Warsaw 00-908, Poland

Abstract— Mobile ad-hoc networks (MANETs) are fast growing methods of efficient wireless communications in highly mobile environment. Such networks can be designed using software simulators, that allow users to design, test and analyze new solutions at a low cost. These tools enable also an analysis of network configuration and protocol used for optimizing radio resources and performing the best Quality of Service (throughput, delays, etc.). However the simulators cause approximations of results due to simplification of EM compatibility issues and propagation phenomena in the electromagnetic environment. Furthermore the most common simulators do not allow the simulation in a real time, that causes long simulation. This problem can be solved using real time test beds, containing SDR (Software Defined Radio) base solutions. The most popular device based on this technology is USRP (Universal Soft-ware Radio Peripheral), that is widely used by researchers to study various transmission protocols or create real-time applications like OpenBTS or MIMO links.

1. INTRODUCTION

Mobile wireless networks offer a wide set of wideband services in different environments, and they can be used as a cost-effective mechanism for supporting communication. To provide reliable communications such networks should contain mechanisms for link quality monitoring, adaptive routing and interference avoidance. Proper operation of such mechanisms needs distributed algorithms, enabling joint configuration of whole network, that require exchange al lot of control data, so their efficiency is one of the most critical parameters of the network, and it should be thoroughly designed and tested. The most researches in the mobile ad-hoc rely on computer simulation and there are many commercial and open source programs that help to build communication models. However, these models do not fully reflect radio propagation phenomena and other electromagnetic dependencies. From the other side, experiments performed in a real environment are expensive; require a large number of testers and work coordination over a large geographic area [1]. Even with careful choreography, such experiments are only marginally reproducible, making testing and debugging difficult. Therefore, to minimize time, costs and human resources, tests can be performed in laboratory-based wire testbed, using devices that emulate wireless channels [2].

This article describes a real-time testbed for MANET, where each radio node is represented by one USRP. Electromagnetic environment emulation is performed by RF switch matrix, providing attenuation of RF signals. The work presents also the software architecture of radio nodes including implemented physical layer based on OFDM (Orthogonal Frequency-Division Multi-plexing) modulation and MAC (Media Access Control) layer based on TDMA (Time Division Multiple Access) radio access. Next, control process of whole test bed and RF switch matrix is described. The obtained results show performance of the testbed.

2. HARDWARE ARCHITECTURE

The overall concept of the wired testbed for wireless MANET is shown in Figure 1.

The laboratory-based ad-hoc network model consists of: RF switch matrix, RF-shielded enclosures, source of interferences, monitoring devices, clock signals distribution box, user computers, control computer.

This MANET testbed can be used for tests of up to 8 nodes using static and dynamic scenarios. Radio situation can be monitored and recorded for further analysis, using wideband receiver connected also to RF-switch matrix.

Additionally, in order to simulate scenarios with external interfaces, the arbitrary generator can be used.

The unit that control all these elements is the control computer, that manages each device using the Ethernet interface and multi IO card.

The testbed contains also clock signals distribution box, which delivers reference signals (10 MHz and PPS) to all radios, to enable tests with ideal synchronisation.

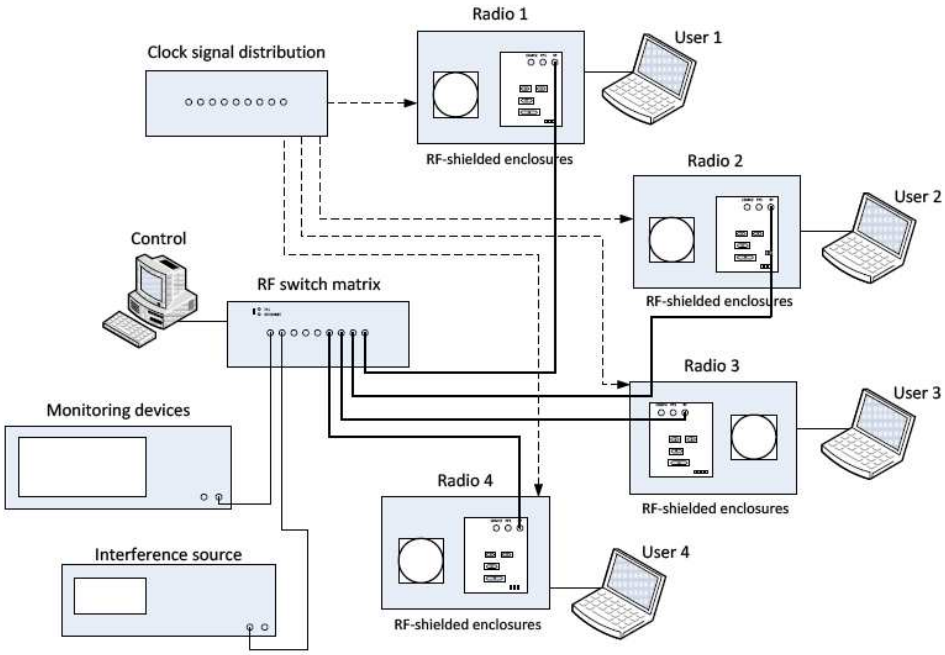

Figure 1: Concept of the MANET testbed.

2.1. RF Switch Matrix

This device emulates the telecommunication channels by adjusting attenuation in specific paths. It has the ability to connect up to 9 nodes with possible frequency range from 30 MHz to 3 GHz (Figure 2). The RF switch matrix consists of 36 programmable attenuators and 9 RF power divider/combiners [3].

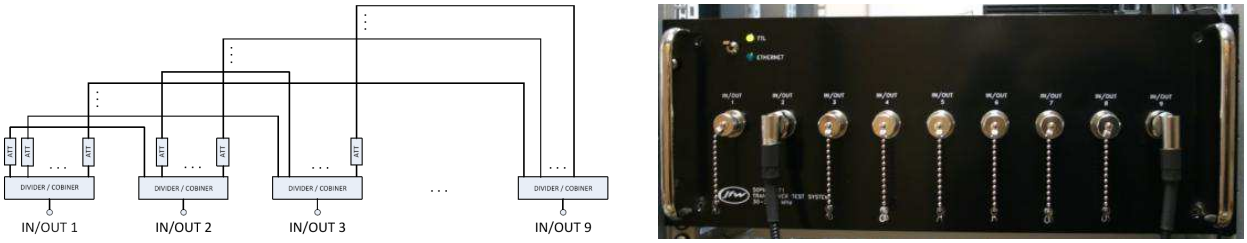

Figure 2: RF switch matrix.

This device can be controlled using LAN port or by parallel interface with electric signals in TTL standard. Attenuation switching time is up to 2 µs, therefore the RF switch matrix can create fast and slow fading, shadowing and nodes movements. The RF switch matrix can also set high attenuation between radios to block the communication, because the maximum attenuation between particular inputs/outputs is equal to 128 dB.

2.2. Radio Nodes

2.2.1. Universal Software Radio Peripheral

The USRP is a low cost software defined radio platform. It converts radio signal between baseband domain and high frequency domain and vice versa. In case of USRP Newtork Series the signal processing on baseband domain is performed by software at the host computer.

Architecture of USRP N210 consists of Ethernet interface controller, FPGA, dual ADC and DAC, RF daughter board [4]. It has the following external interfaces:

- Gigabit Ethernet — used for communication between host computer and the USRP,
- MIMO Expansion — to provide communication between two USRPs for MIMO systems,
- 1 PPS and 10 MHz inputs to synchronize the device.

2.2.2. RF-shielded Enclosures

During the MANET testbed operation, defined attenuation between nodes is required, whereas for USRP a significant crosstalk level of RF signal to the power circuits was observed [5].

Based on these results, RF-shielded enclosures (Figure 3) were designed as containers for tested RF devices that ensure an appropriate level of attenuation, to minimize radiated and conducted RF leakage between tested devices, and to provide separation of individual transceiver blocks.

The electromagnetic compatibility (EMC) measurements show that the level of attenuation for a single box does not exceed 50 dB for radiated disturbances in the frequency range from 80 MHz to 2.5 GHz. Characteristics of shielding efficiency, made in anechoic chamber are shown in (Figure 4).

Figure 3: RF-shielded enclosure.

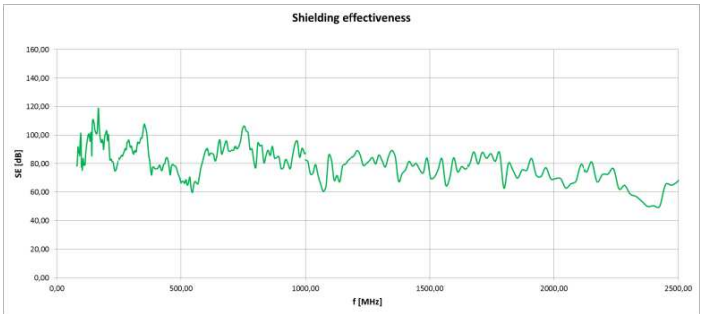

Figure 4: Shielding effectiveness in the range of 80 MHz to 2500 MHz.

3. SOFTWARE ARCHITECTURE OF RADIO NODE

This chapter presents short overview of software implementation of physical and Medium Access Control layer of each node used in the testbed.

3.1. PHY Layer

Physical layer bases on OFDM modulation. Figure 5 presents block diagram of transmitter and receiver part.

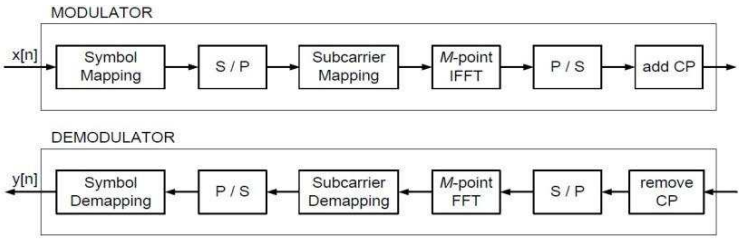

Figure 5: Block diagram of OFDM transmitter and receiver.

Physical layer is responsible for communication between host PC and the USRP, to enable transmission of modulated signals in proper time slots of TDMA frame. This feature is supported by UHD (USRP Hardware Driver) driver, that allows the user to send data with timestamp information, describing the time when the data should be transmitted. This time is synchronized with the USRP time. It can be set to time defined by user, or to the current UTC time, if the device is equipped with GPSDO sensor [6]. More information about frequency and time synchronization can be found in [7].

3.2. MAC Layer

MAC layer has been developed to perform hierarchical network organization, containing many clusters. Each cluster has 3 types of nodes: Cluster Heads, Regular nodes and Gateways. *Cluster Head* is the main node, which realizes radio resource allocation in the cluster. *Gateways* are responsible for communication between clusters and *Regular nodes* work as typical network users. MAC layer consists of three main parts: SAR (Segmentation and Reassembly) layer, queuing layer and TDMA scheduling.

MAC layer also provides other functionalities: dynamic cluster building [8], dynamic resource allocation, cluster graph colouring (determination of center frequencies for each cluster), neighbourhood discovery and maintenance.

4. TESTBED MANAGMENT

4.1. Control Application

The testbed contains devices controlled by one main computer with dedicated software. This software includes 2 components: for scenarios management and metrics display from all network nodes.

Scenario manager (Figure 6) enables loading scenarios from *xml* files, setting attenuations between all nodes, loading scenario map and setting all devices. Each radio node receives settings for physical, MAC and application layer. Data from attenuations data base are converted to set attenuator in RF switch matrix in specific time during scenario realization.

Result display component is presented on Figure 7. It contains the scenario map with marked position of each node and attenuations between all nodes. In the bottom right corner there is a tool for metrics display.

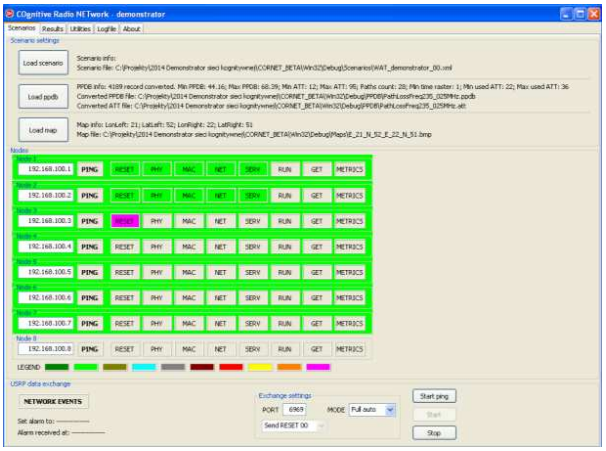

Figure 6: Scenario component view.

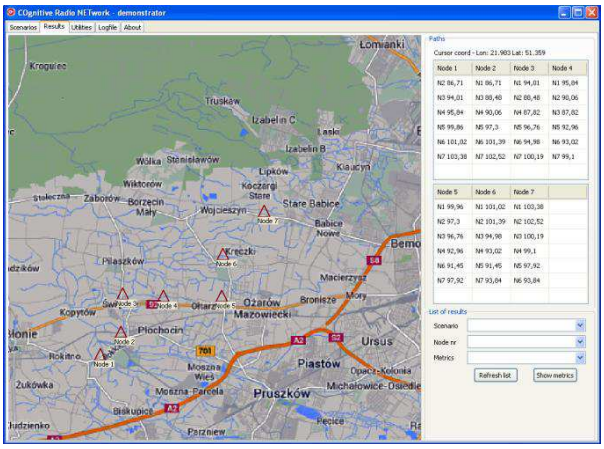

Figure 7: Results component view.

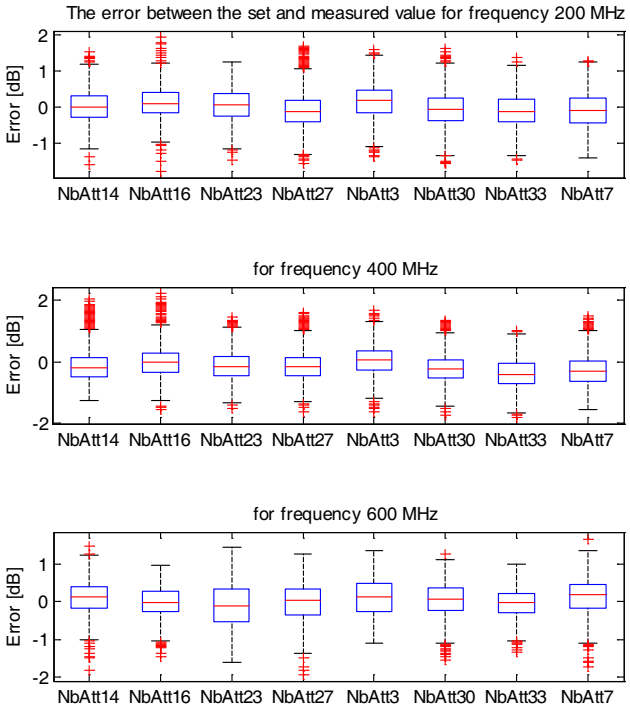

Figure 8: Accuracy of the RF switch matrix control.

5. TEST RESULTS

5.1. Accuracy of the RF Switch Matrix Control

To verify the accuracy of the RF switch matrix control, a one thousand different test sequences for nine input matrix have been performed. Nodes were placed at random positions in flat area and attenuations between them were calculated using free-space path loss model.

The results of the accuracy of the RF switch matrix control are shown in Figure 8.

Measurements are made for three different frequencies and for eight randomly selected paths in the RF switch matrix. The calculated error is the difference between the defined and measured attenuation.

5.2. Scenario Test Results

The testbed enables collection of metrics from physical and MAC layers, for example: RSSI, CFO, number of valid packets, data link layer throughput, MAC layer delay, MAC frame loss rate, MAC frame error rate. Figure 9 and Figure 10 present sample metrics collected during tests.

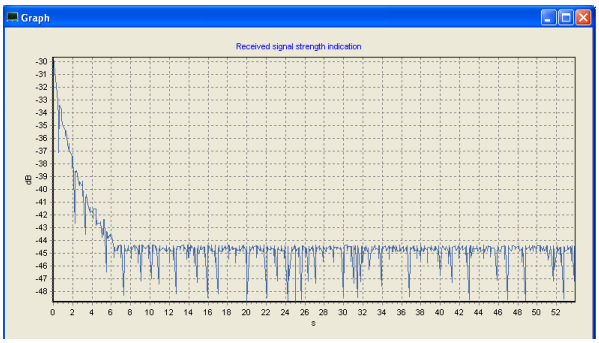

Figure 9: Received signal strength indication from node 1.

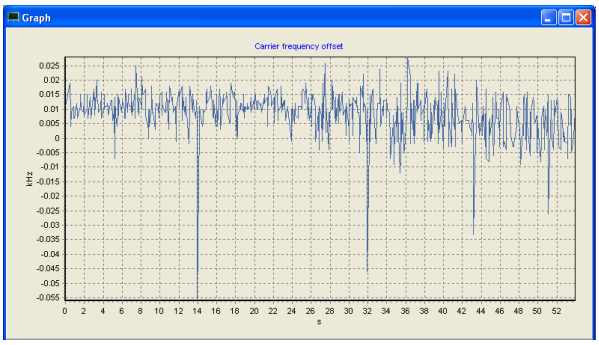

Figure 10: Carrier frequency offset for node 1.

6. SUMMARY

This article presents a laboratory testbed, using RF switch matrix for wire-based measurements of the MANET parameters, according to predefined scenario. The matrix inserts a programmable attenuation between selected RF nodes, to simulate a large-scale RF attenuation. All USRPs, creating MANET network are placed in RF shielded enclosures to minimize RF leakage. Collected metrics allow to estimate quality of links between RF nodes.

Achieved results show, that developed testbed is a reliable base for implementation of cognitive MANET with mechanisms for situation awareness and self-organization.

REFERENCES

1. Seastrom, J. and B. Walker, "Addressing scalability in a laboratory-based multihop wireless testbed," *Mobile Networks and Applications*, Vol. 15, No. 3, 435–445, 2010.
2. Clancy, T. C. and B. D. Walker, "MeshTest: Laboratory-based wireless testbed for large topologies," *3rd International Conference on Testbeds and Research Infrastructures for the Development of Networks and Communities*, Lake Buena Vista, 2007.
3. JFW Industries, Available: http://www.jfwindustries.com/products/50PMA_033_Transceiver_Test_System_from_JFW_Industries-1290-137.html.
4. Research, E., "USRP N200/N210 networked series datasheet," 2012.
5. Kryk, M., A. Kaszuba, R. Chęciński, and K. Malon, "Laboratory-based Ad hoc network model," *SECON*, Warsaw, 2013.
6. Ettus Research, "GPSDO kit datasheet," 2012.
7. Research, E., "UHD — Synchronization application notes," 2012.
8. Bednarczyk, W. and P. Gajewski, "An enhanced algorithm for MANET clustering based on weighted parameters," *Universal Journal of Communications and Network*, Vol. 1, No. 3, 88–94, 2013.

Lidar Monitoring of Atmospheric Atomic Mercury and Sulfur Dioxide in Guangzhou, China

Guangyu Zhao[1], **Xiuxiang Wu**[1], **Ming Lian**[1], **and Sune Svanberg**[1, 2]

[1]Center for Optics and Electromagnetic Research
South Normal China University City Campus, Guangzhou 51006, China
[2]Department of Physics, Lund University, Lund SE-221 00, Sweden

Abstract— A Differential Absorption Lidar (DIAL) system based on a dye laser pumped by a 20 Hz Nd:YAG laser was constructed and used for range-resolved atomic mercury and sulfur dioxide monitoring. These gases are both severe pollutants in China, and there is a considerable interest to map such gases. Measurements were performed from a fixed laboratory, with the eye-safe laser beam pointing upwards at a 15° angle, to assess the vertical distribution of the gases. Long term quasi-continuous monitoring of background mercury and sulfur dioxide concentrations is presented. In particular, the influence of weather conditions was studied during prolonged measurement sequences. We have now studied prominent wash-out effects on mercury due to rainfall. For sulfur dioxide, a pollutant that causes acid rain quite high concentrations measured in Guangzhou were observed to fall drastically at rainfall due to wash-out.

1. INTRODUCTION

Today, due to the Chinese rapid industrialization and urbanization, one area of growing concern is the mercury emissions, and the adverse effect of mercury on human health and the ecosystem is well-known. Man-made mercury emissions are the main cause of global mercury pollution [1]. Waste incineration, coal-fired power plants, and other industrial processes which are powered with fossil fuels such as cement plants and metallurgic industries are the important sources of global man-made mercury pollution [2]. Mercury is a high abundance and widespread element in the earth crust. Mercury mostly exists as cinnabar, HgS. Volcanic, geothermal, and other geogas emissions cause gaseous mercury release. For example; geogas emissions cause the abnormally high soil mercury concentrations in the Chengdu area of the Sichuan province, China [3]. Mercury is also an important tracing gas in geophysics with potential for prospecting [4].

Acid rain is mainly due to dilute sulfuric acid and dilute nitric acid formation. The combustion of fossil fuels produces oxides of sulfur and nitrogen which are released to the atmosphere. Sulfur dioxide reacts with water to generate sulfuric acid [5]. Acid rain is a severe environmental issue with impact on human health, soil acidification, buildings and statues. According to estimates, the annual mean concentration of SO_2 in major Chinese cities was 60 $\mu g/m^3$ in 1993 [6].

Differential Absorption Lidar (DIAL) applied in remote sensing of atmospheric gaseous pollutants has been an effective method to acquire range-resolved concentration information in real-time measurement (see, e.g., [7]). A first version of a DIAL system constructed by our group is described in [8], where also initial studies of atomic mercury (the only air pollutant present in atomic form) are reported. The system is constructed with a 30 cm diameter receiving telescope and is equipped with a narrow-band dye laser pumped by a 20 Hz Nd:YAG laser. We now describe further measurements of background atomic mercury and also sulfur dioxide measurements, as well as the concentration reduction at rainfall due to wash-out. The results were performed with the DIAL system located at the South China Normal University, University City Campus in Guangzhou, China.

2. MERCURY MONITORING

The DIAL technique uses pulsed laser emission at on- and off-wavelengths matched to a peak of an absorption line and slightly off the absorption peak of the gas interest, respectively. The slope of the ratio of the recorded on-wavelength and off-wavelength lidar signal intensities gives information on the gas concentration. We have [7]:

$$\frac{I(\lambda_{on}, R)}{I(\lambda_{off}, R)} = \exp\left\{-2\int_0^R N_{(r)}\left[\sigma\left(\lambda_{on}\right) - \sigma\left(\lambda_{off}\right)\right]dr\right\} \tag{1}$$

Here $I(\lambda_{on}, R)$ and $I(\lambda_{off}, R)$ are the backscattering light intensities for the on- and off-wavelengths, respectively; $\sigma(\lambda_{on})$ and $\sigma(\lambda_{off})$ are the absorption cross-sections for the on- and off-wavelengths, respectively; $N(r)$ is the gas concentration at distance r, and R is the detection distance. The absorption line parameters of the gas of interest can generally be found from HITRAN [9].

The on- and off-wavelengths of mercury, as employed in our study are 253.729 nm and 253.744 nm (vacuum), respectively. The dye laser is set around 5 mJ per pulse. Figure 1 shows the variation of the background mercury concentration for a period of quasi-continuous monitoring, from 00 : 00, November 5th, 2013 to 9 : 00, November 6th, 2013. There was rainfall from 7 : 35 until 10 : 00, November 4th, 2013 with an integrated rain level is 3.8 mm. The mean temperature during the monitoring period was 20 ± 1°C; the mean temperature when it was raining was about 1°C lower than when it was not raining. The figure shows a 60–110 m altitude measurement which resulted in an average mercury concentration of 6 ± 1 ng/m^3 from 0 : 00 to 7 : 00, November 5th, 2013. From 8 : 00 to 10 : 00 on the 5th the average mercury concentration is 1 ± 1 ng/m^3. Generally speaking, for this period sometimes the mercury concentration is lower than the DIAL system resolution. We note that there is a prominent wash-out effect on mercury due to the rainfall with strong reduction of the background concentration. The mercury concentrations are also sensitive to temperature, especially in industrial areas with deposited mercury, since the metal is very volatile. Since the variation of temperature between the period of rainfall and no rain is only slight; the reduction of mercury concentration is mainly caused by the rainfall effect. The average mercury concentration from 12 : 00 in 5th to 9 : 00 in 6th is 4 ± 1 ng/m^3. It indicates that the mercury concentration rises again quite rapidly after the rainfall.

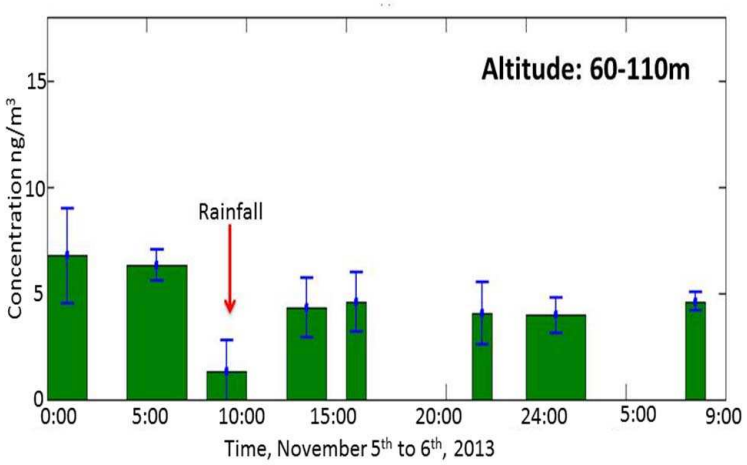

Figure 1: A 35-hour quasi-continuous mercury concentration measurement; the error bars give the evaluated errors of the mercury concentrations; Rain was falling from 7 : 35 until 10 : 00; during this time the rainfall was 3.8 mm.

3. SULFUR DIOXIDE MONITORING

The on- and off-wavelengths for sulfur dioxide are 300.03 nm and 299.3 nm (vacuum), respectively. Compared to mercury, sulfur dioxide measurements are less demanding due to broader absorptive features. The dye laser is set around 5 mJ/pulse. Figure 2 gives a typical DIAL curve of sulfur dioxide monitoring; the insert figure is the curve of the backscattering signal of on- and off- wavelengths, also showing the interception of a cloud by the beam. The figure shows obvious sulfur dioxide absorption from 150 m up to 1500 m, corresponding to the altitude interval from 50 m to 40 m. We could observe that the ratio is almost flat from 150 m to 2000 m corresponding to the altitude between 400 m and 550 m, which indicates that the concentration is much lower at high altitude. For sulfur dioxide around 300 nm, longer measurement ranges than for mercury, up to 3 km, are possible, related to reduced atmospheric scattering and higher available output pulse energies. In our experiments, the cloud base frequently limited the measurement range.

Figure 3 gives the concentration distribution for different altitudes (50–10 m, 10–20 m, 200–400 m and 400–550 m). In Figure 3, the white areas represent absence of data due to weather conditions and low-lying clouds. For the 50–100 m altitude, the highest concentration (203 µg/m^3) is obtained around 18 : 00. From 18 : 00 to 19 : 00, the concentration of SO_2 remains high; the

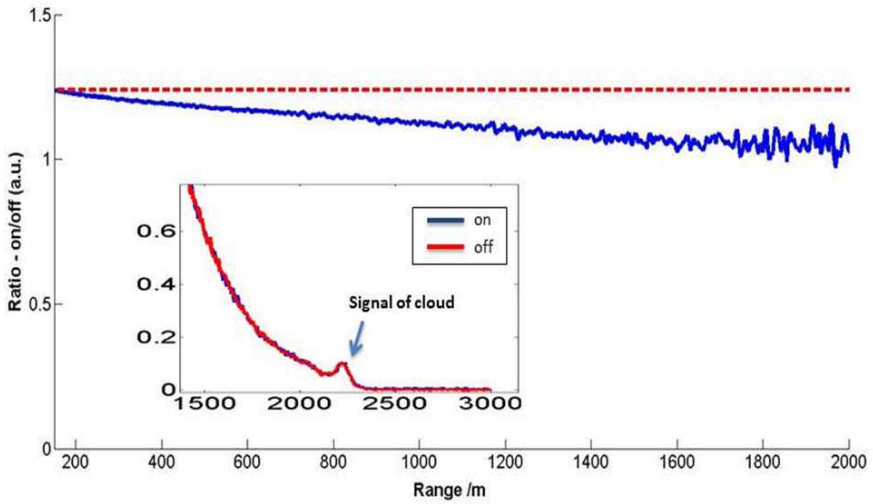

Figure 2: Differential absorption curve of sulfur dioxide. The insert figure shows the curves for on- and off-wavelengths, with termination in a cloud at 2200 m range.

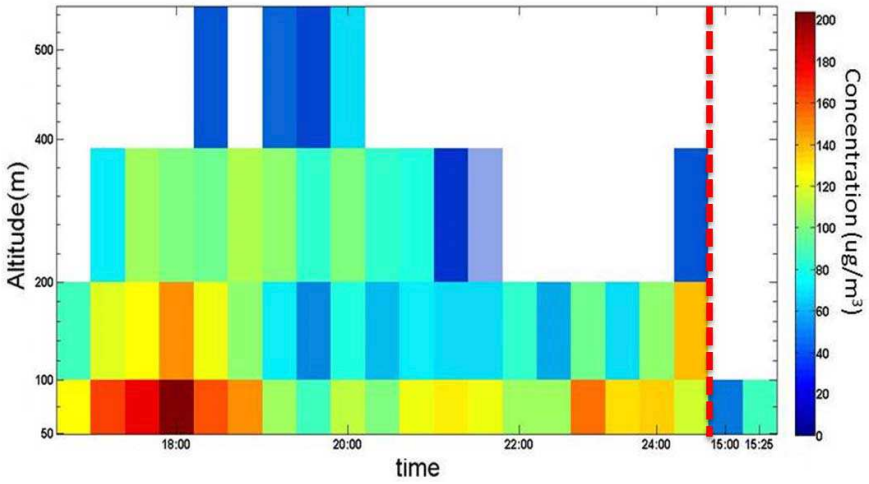

Figure 3: Sulfur dioxide data from 24 hours of DIAL measurements, from 16 : 15, March 5th, 2014 to 15 : 25, March 6th, 2014.

average concentration is 177 $\mu g/m^3$. From 100 m up to 200 m, the concentration distribution is similar as for 50–100 m, but showed a trend of decrease. For the higher altitude (200–400 m), the concentration continues to decline. For the 400–550 m altitude, the average concentration from 19 : 00 to 20 : 30 is 41 $\mu g/m^3$. Measurements were performed quasi-continuously under dry weather conditions until shortly after midnight. Then, during the night it started to rain, with an integrated rainfall for March 6 of 4.5 mm. Measurements were then resumed in the afternoon. As show in the figure (15 : 00–15 : 25) the observed SO_2 concentrations and also the measurement range are much lower than before. We observe drastic SO_2 wash-out due to the rainfall.

4. CONCLUSIONS

A 35-hour quasi-continuous DIAL mercury concentration measurement and a 24-hours quasi-continuous measurement for sulfur dioxide were performed in Guangzhou, China. The wash-out effects on mercury due to rainfall have been studied. Likewise, the concentration of SO_2 falls drastically at rainfall due to wash-out and associated acid rain formation. Our lidar system is now being integrated into a fully mobile facility, capable to be deployed into the field for remote sensing measurements in the atmospheric, aquatic, agricultural and cultural heritage sectors. Besides DIAL, fluorescence and Raman lidar, remote laser-induced break-down spectroscopy (LIBS) lidar studies will be pursued.

ACKNOWLEDGMENT

The authors are very grateful for the valuable contributions by Liang Mei and for support from Prof. Sailing He. This work was financially supported by the Guangdong Innovative Research Team Program (Grant 201001D0104799318).

REFERENCES

1. Lindqvist, O. and H. Rodhe, "Atmospheric mercury — A review," *Tellus*, Vol. 37B, No. 3, 136–159, 1985.
2. Dang, M. T. and J. Liu, "Current situation and solutions to Chinese mercury pollution," *Applied Chemical Industry*, Vol. 34, No. 7, 394–396, 2005.
3. Yao, X. L. and D. F. Yang, "A discussion on mercury pollution source on the Chengdu plain," *Acta Geological Sichuan*, Vol. 20, No. 2, 130–135, 2000.
4. Kovalevskii, A. L., "Mercury-biogeochemical exploration for mineral deposits," *Biogeochemistry*, Vol. 2, 211–220, 1986.
5. Driscoll, C. T., et al., "Acidic deposition in the Northeastern U.S.: Sources and inputs, ecosystem effects, and management strategies," *BioScience*, Vol. 51, 180–198, 2001.
6. Xu, H. Y., "The state of air pollution in China and its influence on human health," *Climatic and Environment Research*, Vol. 4, No. 1, 1999.
7. Svanberg, S., "LIDAR," *Springer Handbook of Lasers and Optics*, F. Träger, Ed., 1031–1052, Springer, Heidelberg, 2007.
8. Mei, L., G. Y. Zhao, and S. Svanberg, "Differential absorption lidarsystem employed forbackground atomic mercury vertical profiling in South China," *Opt. Lasers Eng.*, Vol. 55, 128–135, 2014.
9. Rothman, L. S., I. E. Gordon, Y. Babikov, A. Barbe, D. Chris Benner, P. F. Bernathand, G. Wagner, et al., "The HITRAN2012 molecular spectroscopic database," *Journal of Quantitative Spectroscopy and Radiative Transfer*, Vol. 130, 4–50, 2013.

Development of 3D Anisotropic Artificial Dielectric Metamaterial for THz Frequency Range

E. A. Gurvitz, S. A. Andronaki, S. I. Gusev,
V. Y. Soboleva, Y. D. Nazarov, and M. K. Khodzitsky
Saint-Petersburg National Research University of Informational Technologies, Mechanics and Optics
ITMO University, Russia

Abstract— The paper is devoted to development of 3D anisotropic dielectric artificial structure. The proposed structure was simulated by CST Microwave studio and the tensors of refractive index were obtained. The dielectric structure was made by 3D printer. The trasmission spectra were obtained using the time domain spectrometry technique and the tensors of permittivity and the refractive index dispersion were calculated. The simulation and experimental results are presented and analyzed in the frequency range of 0.1–2 THz.

1. INTRODUCTION

Nowadays, the metamaterials [1] and their applications challenge the customary view on the physics of optics and photonics. Since the works of Veselago, Pendry and Yablonovich [2–4] the metamaterials find their applications in the fields of satellites communications, data transfer and processing systems, solar energy technology and cloaking. It can be explained by unusual properties of artificial structures for example: negative refraction index, extremely values of permittivity and permeability, superresolution effect, invisibility, tunability of constitutive parameters [5–10].

The most important property of metamaterials is capability to scale their sizes from centimeters to nanometers. Such property allows to use the well-known effects in any frequency range. The scale factor and quality of the structure are limited only by possibility of used fabrication technology. Always, metamaterials are composite structures, which consist of unit cells. Sizes of unit cell strongly depend on wavelength, hence the sizes of unit cell are also limited by resolution of fabrication device as noted before.

The development of dielectric metamaterials can find their niche and they can fast, easy and inexpensively be done by the 3D printer technologies of the local facilities everywhere. In contrast to the metallic composite structures [11], the dielectrics metamaterials are predominantly 3D structures and, of course, they can be reduced to 2D or 1D designs [12]. However, capabilities of dielectric metamaterials are limited by resolution of 3D printing devices about hundred of micrometers. We suggest the method of fabrication of 3D anisotropic dielectric structure for terahertz frequency range.

In this paper we propose model of dielectric anisotropic metamaterial structure. The suggested model has very simple geometry parameters and it possesses anisotropy if the radiation is directed along the different sides of the model. The anisotropy of the proposed design was obtained by FDTD numerical simulation method in CST Microwave Studio and it was experimentally confirmed by the refractive index dispersion obtained from the transmission spectra by the time domain spectroscopy. The potential applications of anisotropic dielectric metamaterial are optical elements, such as polarizer, prisms, waveplates, microlenses arrays metamaterial devices such as cloaks, beam splitters and combiners, filters and etc..

2. SIMULATION RESULTS

At this moment, most of 3D printers work with high precision resolution, because the structures need more than ten microns resolution for terahertz frequency range. Therefore, the simple geometry of cubic structure with square holes was chosen. The projection of the structure on XY plane is presented in Fig. 1(a), the upper left corner of the figure demonstrates the unit cell highlighted by red color. The full structure is shown in Fig. 1(b). For more matching of the numerical simulation model to the experimental dielectric material, the refractive index dispersion extracted from the transmission spectra Fig. 1(c) was included in the model.

The simulations were performed by the time domain solver for the pulse duration of 3.75 ps. The anisotropy of the investigated structure was shown by analysis of refractive index for the different position of radiation sources, when the wave-vector is directed along y and z axes.

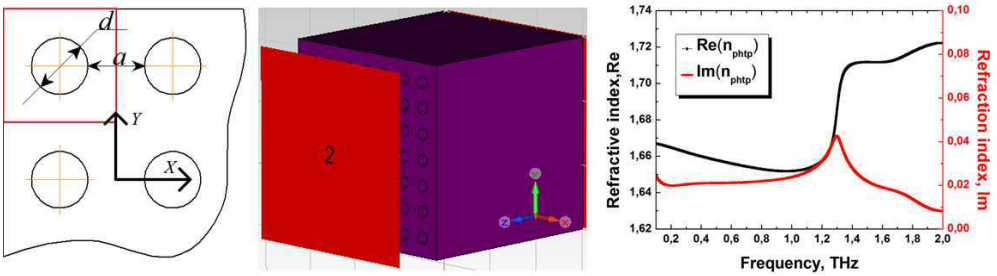

Figure 1: (a) The scheme of the structure projected on the XY plane (the side of circular hole with diameter of $d = 200\,\mu\text{m}$, the period the structure of $400\,\mu\text{m}$ $(a+d)$). (b) The simulated structure with the side length of $3000\,\mu\text{m}$. (c) The dispersion of imaginary and real parts of photopolymer refractive index used for the simulation.

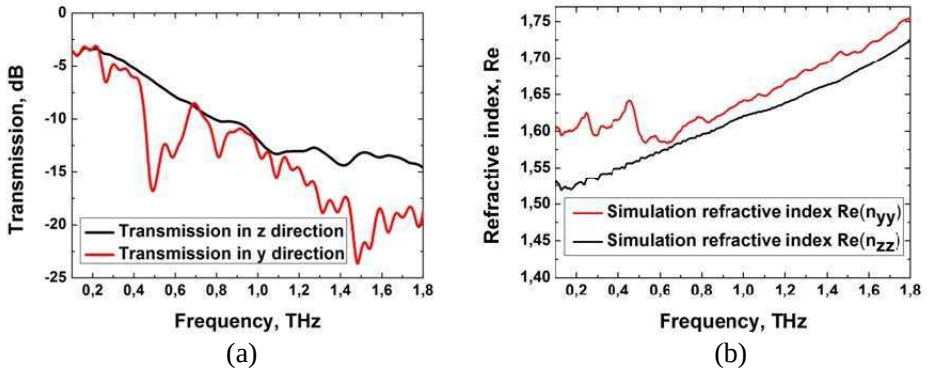

Figure 2: The transmission spectra (a) of structure along y and z axes. (b) The real parts of $\hat{n}_{yy}$ and $\hat{n}_{zz}$ refractive indices components extracted from the simulated transmission spectra.

The complex refractive index is presented as the diagonal matrix (1) with the following elements:

$$\hat{\mathbf{n}} = \begin{pmatrix} \hat{n}_{xx} & 0 & 0 \\ 0 & \hat{n}_{yy} & 0 \\ 0 & 0 & \hat{n}_{zz} \end{pmatrix} \tag{1}$$

The elements $\hat{n}_{xx}$ and $\hat{n}_{yy}$ are equivalent due to the tetrad symmetry of the structure, but $\hat{n}_{zz}$ element will be obvious differ from the $\hat{n}_{xx}$ and $\hat{n}_{yy}$ due to the chosen model geometry.

Let's consider the characteristic dimensions of the structure under study. It is clear that not for every frequency in the signal the proposed design will obey the model of effective medium. Since in the frequency range of 0.1–0.3 THz the wavelength inside the metamaterial is in five times larger of the unit cell size, the structure may work as effective medium. For the highest THz frequencies the anisotropic dielectric structure may be represented as photonic crystal if the radiation propagates along of y or x axes and therefore in the transmission spectra may be observed the stop band gaps in transmission spectrum Fig. 2(a). In the case of the THz wave propagation along of z axis, the structure still works as effective medium. The real part of refraction index spectrum of the structure were extracted from the reference and sample transmission spectra using the following formula [13] and shown in Fig. 2(b):

$$n_{smpl}(f) = 1 + \frac{c}{(2\pi f d)} \left(\phi_{smpl}(f) - \phi_{ref}(f)\right), \tag{2}$$

where $n_{smpl}(f)$ is the real part of refractive index of the investigated structure, c is the speed of light, f is the frequency, d is the sample thickness, ϕ_{smpl} and ϕ_{ref} are the phases of the complex amplitudes of the sample and the reference transmission spectra.

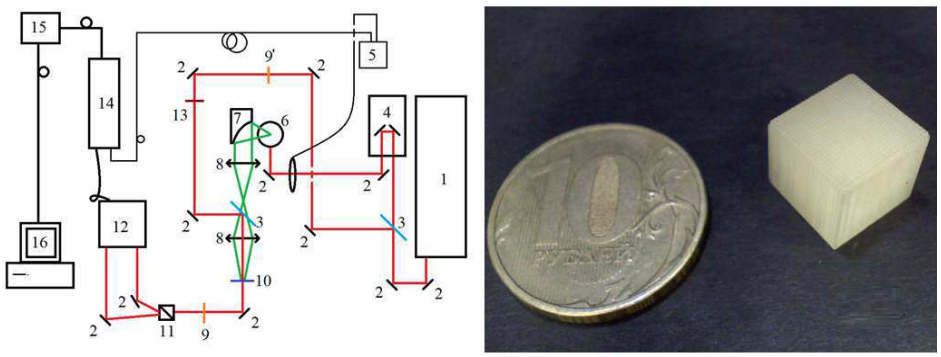

Figure 3: The experimental setup scheme (a): IR Yb:KYW laser ($\lambda = 1040\,\text{nm}$, $\tau = 200\,\text{fs}$) (1), mirrors (2), beam splitters (3), delay line (4), chopper (5), GaAs crystal of the magnetic field of 2.4 T (6), parabolic mirror (7), terahertz lenses (8), wave plates $\lambda/4$ and $\lambda/2$ (9, 9′), CdTe crystal (10), Wollaston prism (11), balance detector (12), Glan-Taylor prism (13), lock-in-amplifier (14), analog to digital converter (ADC) (15), personal computer (PC) (16) and sample (s). (b) Photo of experimental anisotropic dielectric metamaterial sample with 200 µm holes.

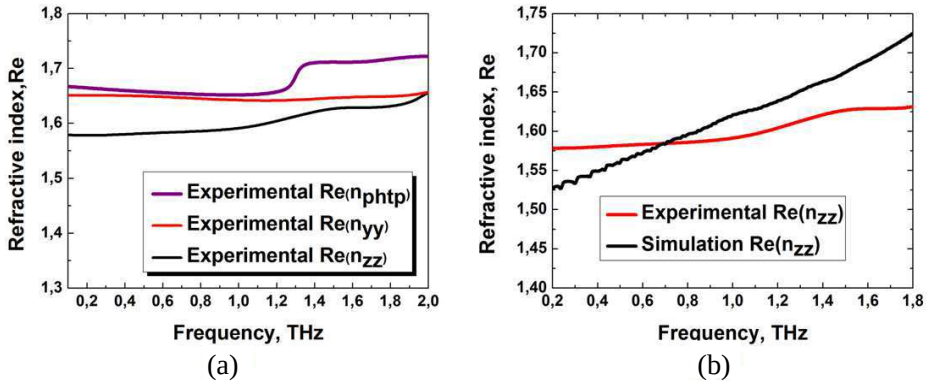

Figure 4: (a) The experimental dispersion of the refractive index components $\hat{n}_{yy}$, $\hat{n}_{zz}$ of investigated structure and the dispersion of the refractive index of the photopolymer. (b) The comparison of the experimental and the simulated $\hat{n}_{zz}$ refractive index component.

3. EXPERIMENTAL RESULTS

The experimental setup of THz time domain spectrometry for the experimental verification of the simulated results was used (see Fig. 3). The Yb:KYW laser pumps semiconductor crystal GaAs for THz radiation emission. Further, THz radiation is focused on the CdTe crystal and it induces the anisotropy in the crystal increasing the difference of s and p polarizations that can be easy detected with Wollaston prism. Changing the probe beam optical path, THz pulse is indirectly detected by balance detectors and registered by lock-in-amplifier and ADC. The sample was placed at the focus of THz lenses and the transmission spectra were obtained for two sides of the anisotropic dielectric metamaterial sample.

The components of refractive index tensor of the structure are less than photopolymer refractive index because of the holes. Thereby, the anisotropy of the refractive index dispersion was shown by the numerical simulation of the structure for the excitation pulse propagation along y and z axis by FDTD method in CST Microwave Studio. The obtained real parts of $\hat{n}_{zz}$ and $\hat{n}_{yy}$ refractive index components are shown in Fig. 4(a). The refractive index components of the structure are less than the photopolymer refractive index. Fig. 4(a) demonstrates the anisotropy confirmed by the experimental and the numerical simulation of the structure. As seen from the figure, the simulation and the experimental data demonstrate the same behavior.

4. CONCLUSIONS

The new approach of the development of anisotropic dielectric metamaterials based on 3D printer technologies was proposed for the frequency range of 0.1–2 THz. The anisotropic metamaterial

model was made of the photopolymer with resolution of 25 micrometers. The dispersion of the refractive index tensor components ($\hat{n}_{xx} = \hat{n}_{yy} \neq \hat{n}_{zz}$) was shown numerically and by the time domain spectroscopy method. The experimental values of the real part ($\hat{n}_{zz}$) are changed from 1.57 to 1.656 in the frequency range of 0.1–2 THz. The experimental values of the real part $\hat{n}_{xx}$ and $\hat{n}_{yy}$ are changed from 1.570 to 1.656 in the frequency range of 0.1–2 THz. The proposed anisotropic structure can be used for development of wave plates, beam splitters, invisibility cloaks, etc. for THz frequencies.

ACKNOWLEDGMENT

This work was financially supported by Government of Russian Federation, Grant 074-U01.

REFERENCES

1. Capolino, F., *Theory and Phenomena of Metamaterials*, CRC Press, New York, 2009.
2. Veselago, V., "The electrodynamics of substances with simultaneously negative values of [permittivity] and [permeability]," *SPU*, Vol. 10, No. 4, 509–514, 1968.
3. Yablonovitch, E., "Inhibited spontaneous emission in solid-state physics and electronics," *Phys. Rev. Lett.*, Vol. 58, No. 20, 2059–2062, 1987.
4. Pendry, J. B., "Negative refraction makes a perfect lens," *Phys. Rev. Lett.*, Vol. 85, No. 1, 3966–3969, 2000.
5. Khodzitsky, M., A. Kharchenko, A. Strashevskyi, and S. Tarapov, "Left-handed properties of metal-ferrite composites placed into waveguide in millimetric wave range," *Telecommunications and Radio Engineering*, Vol. 68, No 7, 561–566, 2009.
6. Smith, D., W. Padilla, D. Vier, S. Nemat-Nasser, and S. Schultz, "Composite medium with simultaneously negative permeability and permittivity," *Phys. Rev. Lett.*, Vol. 84, 4184, 2000.
7. Schurig, D., J. Mock, B. Justice, S. Cummer, J. Pendry, A. Starr, and D. Smith, "Metamaterial electromagnetic cloak at microwave frequencies," *Science*, Vol. 314, No. 5801, 977–980, 2006.
8. Gurvitz, E., E. Sedykh, and M. Khodzitskiy, "Nonlinear cloaking at microwave frequencies," *Proc. SPIE 8455, Metamaterials: Fundamentals and Applications V*, 845532, 2012.
9. Silveirinha, M. and N. Engheta, "Design of matched zero-index metamaterials using nonmagnetic inclusions in epsilon-near-zero media," *Phys. Rev. B*, Vol. 75, 075119, 2007.
10. Alu, A., M. Silveirinha, A. Salandrino, and N. Engheta, "Epsilon-near-zero metamaterials and electromagnetic sources: Tailoring the radiation phase pattern," *Phys. Rev. B*, Vol. 75, 155410, 2007.
11. Yury, E. T., M. K. Khodzitskiy, G. V. Belokopytov, Y. V. Grachev, X.-C. Zhang, and E. A. Sedykh, "The influence of period between U-shaped resonators on metasurface response at terahertz frequency range," *Proc. SPIE 8806, Metamaterials: Fundamentals and Applications VI*, 88062Q, 2013.
12. Vendik, I., et al., "Tunable metamaterials for controlling THz radiation," *IEEE Transactions on Terahertz Science and Technology*, Vol. 2, No. 5, 2012.
13. Zhang, X.-C. and J. Xu, *Introduction to THz Wave Photonics*, Springer, New York, 2010.

SSBI Cancellation Method for IMDD-OFDM System with a Single Photodiode

Xuebing Zhang, Jianping Li, and Zhaohui Li
Institute of Photonics Technology, Jinan University, Guangzhou, Guangdong 510632, China

Abstract— A novel SSBI cancellation approach is proposed for IMDD-OFDM system by using only asinglephotodiode (PD). Simulation results indicate that the proposed approach can cancel the SSBI effectively and also achieve 3.2 dB improvement of power efficiency compared with the conventional IMDD-OFDM.

1. INTRODUCTION

Coherent detection has achieved dramatic success to provide excellent solutions for high-speed and long-haul transmission in the past few years [1–4]. The optical research has turn to seek for the solution of cost-sensitive short-reach high-speed communication. Direct-detection orthogonal frequency-division multiplexing (OFDM) as a promising candidate technology has been widely invested. The simple signal-to-signal beat interference (SSBI) cancellation receiver based on balanced detection for a single sideband optical OFDM signal with a reduced guard band has been proposed [5]. However, the generation of the optical single sideband OFDM signal is complex and balanced detection is used at the receiver. The direct detection optical OFDM transmission using beat interference cancellation receiver is demonstrated. But the balanced detection of this method is also complex [6]. Most recently, a cost-effective 61 Gbits/s direct-detection optical OFDM based on block-wise signal phase switching with signal-to-signal beat noise cancellation is proposed. However, the algorithm requires high optical signal-to-noise power ratio (OSNR) and has high complexity for SSBI cancellation [7].

In this paper, we proposed a novel approach to cancel SSBI for IMDD-OFDM system using 16 quadrature amplitude modulation (16 QAM) formats with only a single photodiode. In this method, 2 intensity modulators (IMs) are used to generate dual-polarization OFDM signal which is detected by a single photodiode. In order to recover the OFDM signal without SSBI, the specially designed OFDM signal of transmitter is needed. Simulation results show that the proposed method can successfully cancel the SSBI and can also achieve 3.2 dB improvement of power efficiency compared with conventional IMDD-OFDM. Although the frequency efficiency decreases by one-third, the carrier signal power ratio (CSPR) could be greatly reduced and more optical power is accommodated to signal.

2. PRINCIPLE AND SIMULATION SETUP

The principle of the proposed SSBI cancellation approach for IMDD-OFDM system is illustrated in Fig. 1. We first generate the optical OFDM signal with real component (I) and imagine component (Q) on two orthogonal polarizations by using two independent IMs, then only one photodiode is used to detect the OFDM signals as shown in Fig. 1(a). As there are no polarization crosstalk terms in the beating results when detected by the PD due to the assumed perfect orthogonality of the two polarization components, the corresponding photocurrent is the addition of the independently detected X- and Y-polarization components. After detection, the photo currents for the double-polarization signal is given by

$$\begin{aligned} I &= |E_{x,0} + E_{x,s}|^2 + |E_{y,0} + E_{y,s}|^2 \\ &= |E_{x,0}|^2 + 2\mathrm{Re}\left\{E_{x,0}E_{x,s}^*\right\} + |E_{x,s}|^2 + |E_{y,0}|^2 + 2\mathrm{Re}\left\{E_{y,0}E_{y,s}^*\right\} + |E_{y,s}|^2 \end{aligned} \quad (1)$$

where, $E_{x,0}$ is the main carrier and $E_{x,s}$ is the OFDM signal on x-polarization. $E_{y,0}$ and $E_{y,s}$ are the respective main carrier and OFDM signal on y-polarization. Fig. 1(b) shows the main concept of the SSBI cancellation on time domain. One frame contains three symbols which are dual-polarization signal. For the three symbols of signal, we respectively transmit I and Q, I and -Q, -I and -Q of the OFDM signals on x and y polarizations. The spectrum of the three symbols of OFDM signals are illustrated in Fig. 1(c). Then the three photocurrents I_1, I_2 and I_3 are descripted

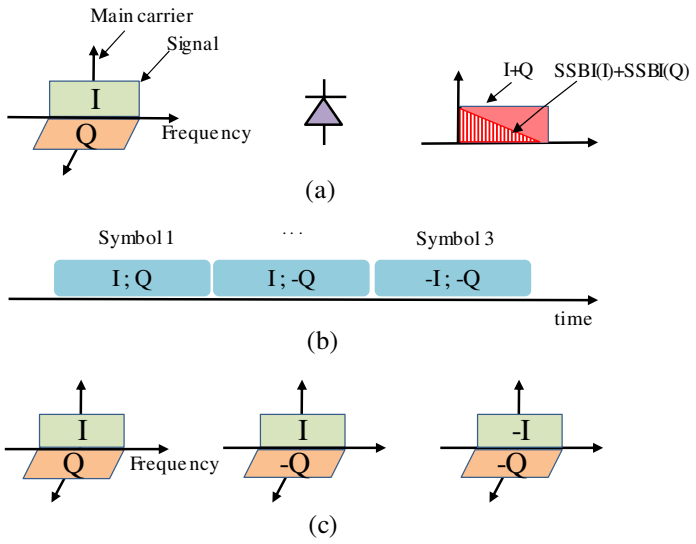

Figure 1: Principle of SSBI cancellation approach.

as

$$I_1 = |I|^2 + |Q|^2 + 2\mathrm{Re}\left\{I \cdot E_{x,0}^*\right\} + 2\mathrm{Re}\left\{Q \cdot E_{x,0}^*\right\} + |E_{x,0}|^2 + |E_{y,0}|^2 \quad (2)$$

$$I_2 = |I|^2 + |Q|^2 + 2\mathrm{Re}\left\{I \cdot E_{x,0}^*\right\} + 2\mathrm{Re}\left\{-Q \cdot E_{x,0}^*\right\} + |E_{x,0}|^2 + |E_{y,0}|^2 \quad (3)$$

$$I_3 = |I|^2 + |Q|^2 + 2\mathrm{Re}\left\{-I \cdot E_{x,0}^*\right\} + 2\mathrm{Re}\left\{-Q \cdot E_{x,0}^*\right\} + |E_{x,0}|^2 + |E_{y,0}|^2 \quad (4)$$

where I (x-pol.) and Q (y-pol.) are real and imagine components of the complex signal. $|I|^2$ and $|Q|^2$ are the SSBIs to be cancelled. $E_{x,0}$ and $E_{y,0}$ are the main carriers on x and y polarizations, respectively. From equation (2), (3) and (4), the recovered signal is written as

$$S = (I_2 - I_3) + j \cdot (I_1 - I_2) = 4\mathrm{Re}\left\{I \cdot E_{x,0}^*\right\} + j \cdot 4\mathrm{Re}\left\{Q \cdot E_{y,0}^*\right\} \quad (5)$$

The simulation setup is depicted in Fig. 2. At the transmitter, the optical source at 1550 nm with 100 kHz line-with is firstly split into two parts. Then the upper path is fed into an IM, which is driven by the real component of the complex electrical OFDM signal. The OFDM generator is used to produce complex OFDM-16QAM radio frequency (RF) signal. The baseband signal is comprised of 64 subcarriers. The FFT size is 256. The center one subcarrier is unloaded to avoid the DC influence. In the lower path, the imagine component of the complex electrical OFDM signal is modulated onto optical carrier by another IM. Then the two parts of optical OFDM signals combine by a polarization beam coupler (PBC) to generate the dual-polarization OFDM signal. At the receiver, only one photodiode is used to detect the optical OFDM signals. Then we compare the proposed SSBI cancellation scheme with the conventional IMDD-OFDM scheme. To ensure the two systems have the same net bit rate, the SSBI cancellation scheme uses three times bit rate over the conventional IMDD-OFDM to transmit the signals.

3. RESULTS AND DISCUSSION

We first measure the Q factor as a function of carrier to signal power ratio (CSPR) at back-to-back. Here, the Q factor is defined as the signal-to-noise ratio of the OFDM signals. In order to

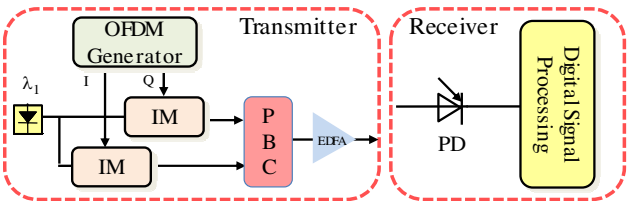

Figure 2: Simulation setup of the SSBI cancellation system. IM: Intensity modulator; PBC: polarization beam coupler; PD: photodiode.

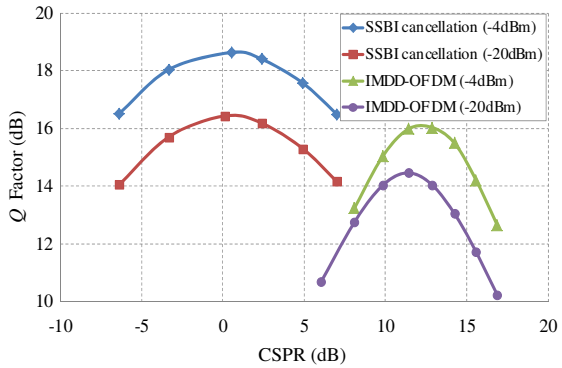

Figure 3: Q factoras a function of CSPR with different received power at back-to-back.

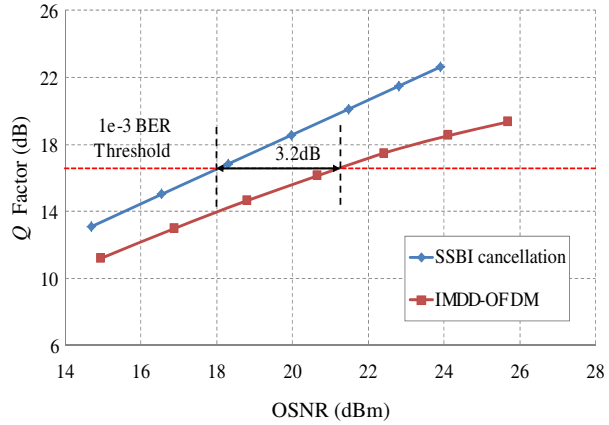

Figure 4: Q factor versus OSNR at back-to-back.

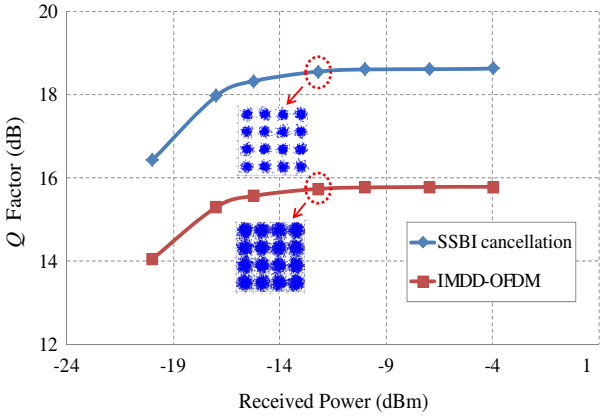

Figure 5: SNR versus received optical power at back-to-back.

compare the performance of the two schemes, the OSNRs of the schemes are set to be the same value ($\sim$ 20.6 dB). Here, the OSNR is denoted as the ratio of the whole optical power including main carrier and OFDM signal to the optical noise power in 12.5 GHz optical band-with. The measured SNR versus CSPR are shown in Fig. 3. The optimum CSPRs of the proposed approach are the same value of 1.2 dB when the received optical power are -20 dBm and -4 dBm. But the optimum CSPR of the conventional IMDD-OFDM are 11.5 dB and 12.5 dB with the corresponding received optical powers. The optimum CSPR of the proposed scheme has greatly decreased and thus more optical power is assigned to the signal. Therefore, the proposed SSBI cancellation scheme has batter Q factor preference compared with the conventional IMDD-OFDM.

Figure 4 illustrates the Q factor versus OSNR performance of the two systems which are measured at optical back-to-back with -4 dBm received optical power. From the analysis before, the

optimum CSPRs of the two systems are set as 0.56 dB and 12.5 dB, respectively. The power efficiency of the proposed scheme has 3.2 dB improvement at the 1e-3 BER threshold (Q factor = 16.52 dB for 16QAM modulation format) compared with the conventional IMDD-OFDM transmission scheme.

Under the optimum CSPRs and the designed OSNR condition (CSPR of 0.56 dB and 12.52 dB, OSNR of 20.6 dB), the Q factor versus received optical power at optical back-to-back is shown in Fig. 5. The Q factor performance improves along with the received optical power increasing. It can be seen that the almost −15 dBm optical power is adequate for both the SSBI cancellation and conventional IMDD-OFDM schemes in the simulation because the Q factor performance is barely improved beyond −16 dBm. The constellations of recovered 16QAM are shown in the inserts.

4. CONCLUSIONS

In this paper, we propose a novel approach to cancel SSBI for IMDD-OFDM signal with only a single photodiode. In this method, 2 intensity modulators (IMs) are used to generate dual-polarization OFDM signal which is detected by a single photodiode. Simulation results show that the approach successfully cancels the SSBI and has 3.2 dB power efficiency improvement compared with the conventional IMDD-OFDM scheme at the 1e-3 BER threshold.

REFERENCES

1. Savory, S. J., G. Gavioli, R. I. Killey, and P. Bayvel, "Electronic compensation of chromatic dispersion using a digital coherent receiver," *Opt. Express*, Vol. 15, No. 5, 2120–2126, 2007.
2. Fludger, C. R. S., T. Duthel, D. van den Borne, C. Schulien, E. D. Schmidt, T. Wuth, J. Geyer, E. de Man, G.-D. Khoeand, and H. de Waardt, "Coherent equalization and POLMUX-RZ-DQPSK for robust 100-GE transmission," *J. Lightwave Technol.*, Vol. 26, No. 1, 64–72, 2008.
3. Shieh, W. and C. Athaudage, "Coherent optical orthogonal frequency division multiplexing," *Electron. Lett.*, Vol. 42, No. 10, 587–589, 2006.
4. Liu, X., F. Buchali, and R. W. Tkach, "Improving the nonlinear tolerance of polarization-division-multiplexed CO-OFDM in long-haul fiber transmission," *J. Lightwave Technol.*, Vol. 27, No. 16, 3632–3640, 2009.
5. Ma, J. X., "Simple signal-to-signal beat interference cancellation receiver based on balanced detection for a single-sideband optical OFDM signal with a reduced guard band," *Opt. Lett.*, Vol. 38, No. 21, 4335–4338, 2013.
6. Nezamalhosseini, S. A., L. R. Chen, Q. Zhuge, M. Malekiha, F. Marvastiand, and D. V. Plant, "The oretical and experimental investigation of direct detection optical OFDM transmission using beat interference cancellation receiver," *Optics Express*, Vol. 21, No. 13, 15237–15246, 2013.
7. Li, A., D. Che, X. Chen, Q. Hu, Y. F. Wang, and W. Shieh, "61 Gbits/s direct-detection optical OFDM based on blockwise signal phase switching with signal-to-signal beat noise cancellation," *Optics Letters*, Vol. 38, No. 14, 2614–2616, 2013.

Microwave Plasma Reactor Based on Microwave Oven

R. Pongsopon, T. Chim-Oye, and M. Fuangfoong
Department of Physics, Faculty of Science and Technology
Thammasat University, Rangsit Center, Pathum Thani 12120, Thailand

Abstract— In this paper, a simple compact size microwave plasma reactor (MPR) based on 2.45 GHz 700 W home used microwave oven has been design and constructed for use in laboratory. Main design criteria were low cost and available of parts and components in home country, in order to make it easy to use, to repair, to move and no leak of microwave radiation. This system consist of reactor vessel, mini air pump and solution container with heater. The reactor vessel is made from 800 ml Pyrex beaker with two pipes mounted on the aluminum cover plate of vessel for injection and exhaust gas. The quarter wavelength electrode unit consisting of five tungsten rods is placed on a circular aluminum plate with diameter $\lambda/2$ for used to generating plasma. Currently the microwave plasma reactor built is being used to be microwave plasma chemical vapor deposition system (MPCVD). However, such a system can easily be adapted to serve as surface cleaner of substrate. The fabricated system is used to test the produce carbon nanoparticle from ethanol vapor and treatment of hydrophobic glass by measuring in contact angle with water drops.

1. INTRODUCTION

Currently, plasma technologies are being widely used in the field of medical, material, agriculture and environment processing. There are many methods for generating plasma such as by using AC, DC high voltage, radio frequency and method that use microwave. Atmospheric pressure microwave plasma has been developed in this work. The objective of this work was design and constructs a microwave plasma reactor at atmospheric pressure base on 2.45 GHz 700 W home used microwave oven for education and research. Main design criteria were:

- Low cost,
- Using available materials and possible to reproduce,
- Easy to operate and maintenance,
- No leak of microwave radiation,
- Easy to move.

Currently the microwave plasma systems built is being used to plasma treat the glass surface and produce the carbon nanoparticle from vapor ethanol. However, a system can easily be adapted to be microwave plasma CVD in the further.

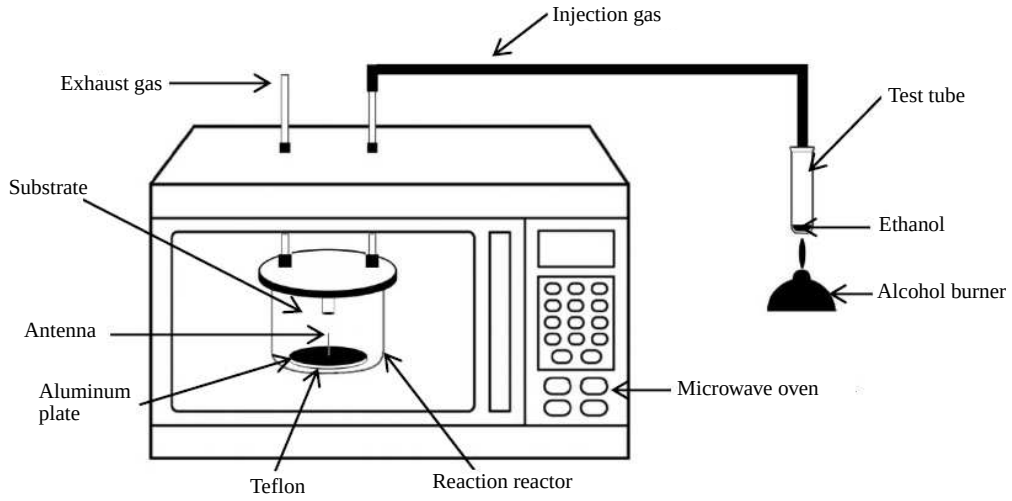

Figure 1: Configuration of experimental setup.

2. EXPERIMENTAL SETUP AND METHOD

The experimental setup is shown in Figure 1. The system includes a microwave oven, plasma reactor, mini air pump and solution container with heater.

The length of receiving antenna or electrode (L) can be calculated by using the following formula.

$$L = \frac{C}{4f\sqrt{\mu_r \varepsilon_r}}$$

where, c is the speed of electromagnetic wave is (2.997×10^8 m/s), f is the frequency of microwave (2.45 GHz), μ_r and ε_r are relative permittivity and permeability of the medium (air), respectively. When the relative permittivity and permeability of air equal 1, approximately, so the length of antenna is about 30 mm. Figure 3 is shown the arrangement of an electrode for investigation of efficiency of plasma generating.

Figure 2: Photo of microwave reactor.

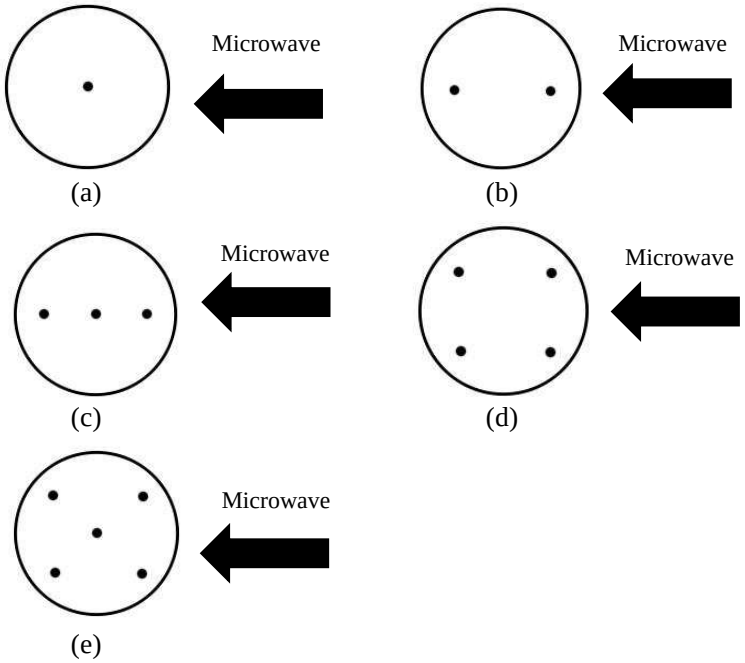

Figure 3: Arrangement of an electrode.

Figure 4 is a photograph of it generating plasma in ethanol vapor with one electrode. The electrode is placed on a circular aluminum plate with diameter 80 mm and install on a Teflon base so that the reactor vessel will not be damaged by the heat when the plasma is being generated. The substrate is place in position at 30 mm above the tip of electrode.

3. RESULTS

During plasma process, the carbon particles are deposited at the surface of the glass substrate. Figure 5 shows a SEM image of carbon nanoparticle on the substrate.

Figure 6 is an example of surface modified with the plasma and the change in hydrophobicity of the surface was investigated. The water contact angle on untreated glass plate was 41.7° whereas it reduced to zero after 60 seconds of treatment.

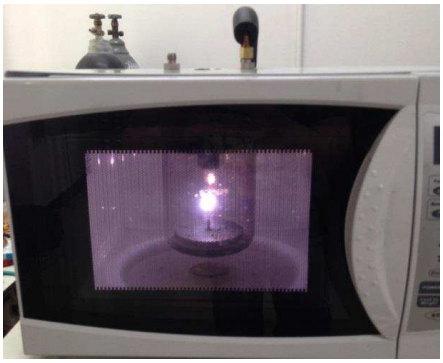

Figure 4: Photograph of plasma generation in ethanol vapor.

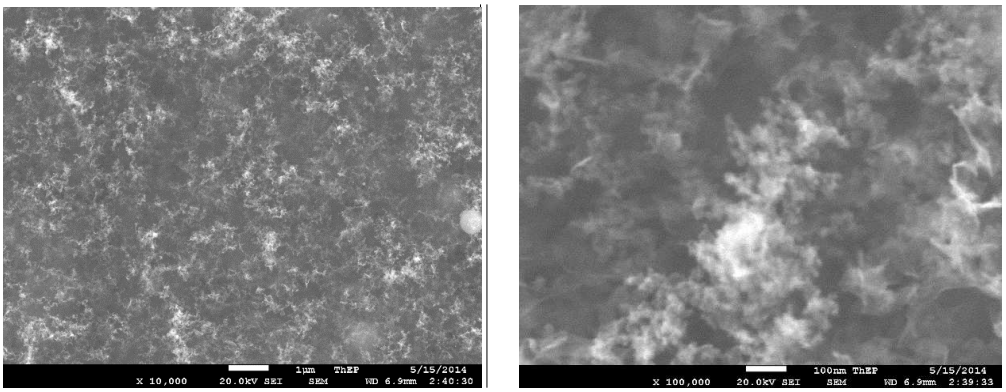

Figure 5: SEM photograph of the film created.

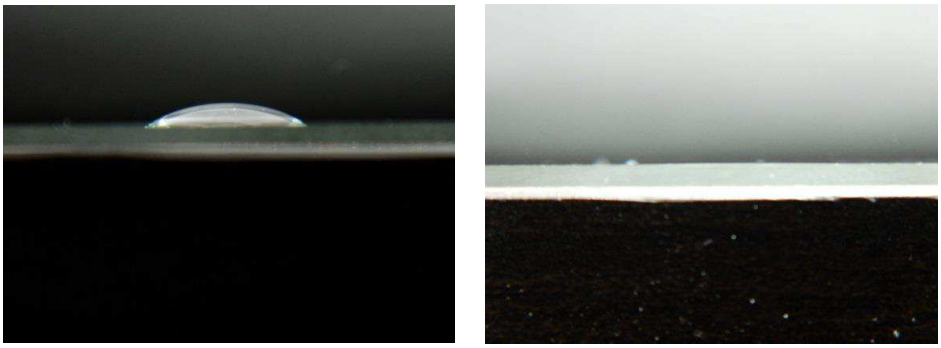

Figure 6: Image of water drop on untreated and plasma treated glass plate sample. (a) Before treatment. (b) After treatment.

4. CONCLUSIONS

In this research a method for generating plasma inside a plasma reactor base on microwave oven was investigated and an electrode suitable for generating plasma was fabricated. By using experiments in decomposing ethanol using plasma and through detailed investigation into the length of the electrode used, it was confirmed that the quarter wavelength was optimal for the generation of plasma. It is possible to increase the efficiency of decomposing ethanol by increasing the number of electrodes. Tests were conducted into creating carbon nanoparticles by using these electrodes in reactor vessel. We were found that at 5 electrodes, the efficiency of plasma generation bester than 1, 2, 3 and 4 electrodes. Carbon nanoparticles were successfully created inside reactor vessel by using the vapor from ethanol. For an example of surface modified with the plasma and the change in hydrophobicity of the surface was investigated. The water contact angle on untreated glass plate was more than 40° whereas it reduced to zero after 60 seconds of treatment.

ACKNOWLEDGMENT

The authors would like to thank Thammasat University for proving necessary facilities to carry out this research study.

REFERENCES

1. Nomura, S., et al., "Production of hydrogen in a conventional microwave oven," *J. Appl. Phys.*, Vol. 106, 073306, 2009.
2. Nomura, S., et al., "Simultaneous production of hydrogen and carbon nanotubes in a conventional microwave oven," *International Symposium on Plasma Chemistry (ISPC19)*, 65, 2009.
3. Khongkrapan, P., et al., "Thermochemical conversion of waste papers to fuel gas in a microwave plasma reactor," *Journal of Clean Energy Technologies*, Vol. 1, No. 2, Apr. 2013.
4. Khongkrapan, P., et al., "Fuel gas and char from pyrolysis of waste paper in a microwave plasma reactor," *International Journal of Energy and Environment*, Vol. 4, No. 6, 969–974, 2013.
5. Toyota, H., et al., "A practical electrode for microwave plasma processes," *International Journal of Materials Science and Applications*, Vol. 2, No. 3, 83–88, 2103.

An Experimental Investigation of the Concentration of KCl in Liquid Electrode of Atmospheric Pressure DBD

F. Manu[1], **C. Tawee**[1], **F. Pollawat**[2], **and F. Wasana**[3]

[1]Department of Physics, Faculty of Science and Technology
Thammasat University, Rangsit Center, Thailand
[2]Sirinthorn International Institute of Technology
Thammasat University, Rangsit Center, Thailand
[3]Faculty of Science and Technology
Thammasat University, Rangsit Center, Thailand

Abstract— In this paper, the high voltage power supply for dielectric barrier discharge (DBD) have been design and constructed by using a function generator, power amplifier and twin car's ignition coil. Three different types of electrode configurations namely, cylindrical-cylindrical, cylindrical-plate and parallel-parallel were used in the experiment. The air discharge gap between the dielectric layers was fixed at 3 mm. The main objective of this study is to study the effect of the concentration of potassium chloride (KCl) in liquid electrode of the DBD at atmospheric pressure on the uniform discharge and number of electrode on the discharge voltage. Finally, we investigate the usage of DBD system with cylindrical-cylindrical electrode for waste water treatment.

1. INTRODUCTION

The atmospheric pressure plasma is non-equilibrium plasma produced by the dielectric barrier. The non-equilibrium atmospheric pressure plasma has been used in many areas, such as surface treatment, surface modification, waste water treatment, air flow control, agriculture and medical field. The dielectric barrier discharge (DBD) is one of a method of an atmospheric pressure generation. Basically, the DBD device consists of a pair of electrodes covered with dielectric material and a high voltage alternating current or high voltage pulse power supply. The DBD plasma can be easily obtained in atmospheric pressure by using simple equipment and an arbitrary geometry electrode. An experimental device for DBD generally consists of two electrodes separated by thin dielectric layer. An AC voltage is applied to the electrodes at a frequency of several hundred hertz to few hundred kilo hertz. A breakdown occurs in the gap between the two electrodes at a sufficiently high voltage enough to ionize the media around. The purpose of the dielectric barrier is to limit the electron current between the electrodes. The DBD devices can be made in many configurations, three different types of electrode configurations namely, cylindrical-cylindrical, cylindrical-plate and parallel plate were used in the experiment. In this work, the simple high voltage pulse power supply for DBD system and liquid electrode DBD atmospheric pressure have constructed. The air discharge gap between the dielectric layers was fixed at 2 mm.

2. MATERIALS AND METHODS

Figure 1 shows the block diagram of simple high voltage power supply. The sine wave from function generator fed to input of power amplifier and produced high voltage output by using 2 car's ignition coil, which is used to power the DBD plasma system.

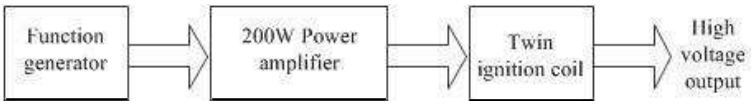

Figure 1: Block diagram of pulse high voltage power supply.

The schematic diagram of liquid cylindrical-cylindrical electrode is shown in Figure 2. It consists of two test tubes and there are some liquid of potassium chloride in two test tubes. To generate the volumetric DBD plasma, we have developed 4×4 cylindrical electrodes as shown in Figure 3. The parallel electrode system made from glass plate with thickness 2 mm. The dimension of parallel electrode is $25 \times 130 \times 130$ mm ($W \times L \times H$). The air discharge gap between the dielectric layers for

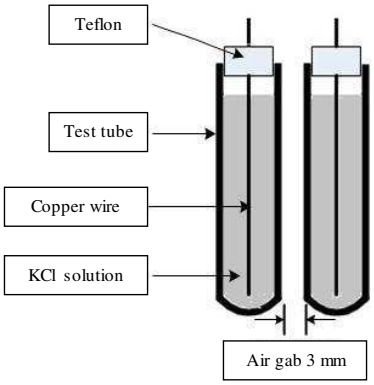

Figure 2: Schematic diagram of liquid cylindrical-cylindrical electrode.

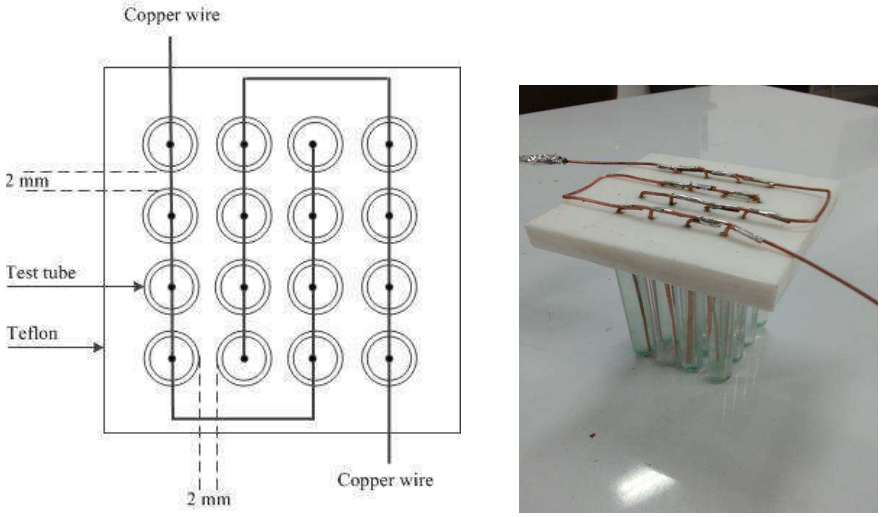

(a) Top view (b)

Figure 3: (a) Schematic arrangement, (b) photo of 4×4 cylindrical electrodes.

all type electrodes were fixed at 2 mm. The concentration of potassium chloride solution is varying by 5, 10, 15, 20, 25 and 30 percent. The discharge current and voltage across the gab are measured by digital oscilloscope. The image of the discharge was captured by a digital camera.

2.1. Ozone Reactor with Cylindrical Electrode Configuration

The ozone generator for waste water treatment is designed by using two cylindrical electrodes as shown in Figure 4. The plasma chamber is shape cylinder, which made from acrylic material. Based on the process of testing an ozone generator is in the process color fading of waste water, taken 3 cycle process, where each cycle has an average duration process 20 minutes.

3. RESULTS

(a) High voltage power supply

We have successfully developed the high voltage power supply and applied it to produce atmospheric pressure plasma system. The output voltage from this power supply depends on frequency and can be up to ~ 19.9 kV.

(b) Atmospheric pressure plasma

To obtain a homogeneous discharge, the voltage and frequency were carefully adjust. Uniform discharge was observed throughout the inter-electrode space only at particular values of voltage and frequency. These values were measured for the three type of electrode as shown in Table 1.

In Figure 5 there were three different discharge processes with three different voltages of

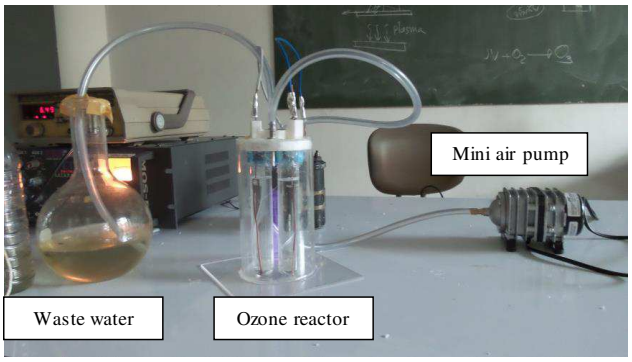

Figure 4: Schematic diagram and photo of ozone generator for waste water treatment.

Table 1: Voltage and frequency of uniform discharge in different of the concentration of KCl.

Concentration of KCl	Voltage (kV)	Frequency (kHz)
5%	19.88	5.43
10%	16.57	4.94
15%	16.90	4.91
20%	16.57	4.91
25%	16.57	4.91

all type electrode, uniformly and intensity of violet blue light gradually increase with apply voltage and frequency. In Figures 5(a) and (b), the discharge was not uniform.

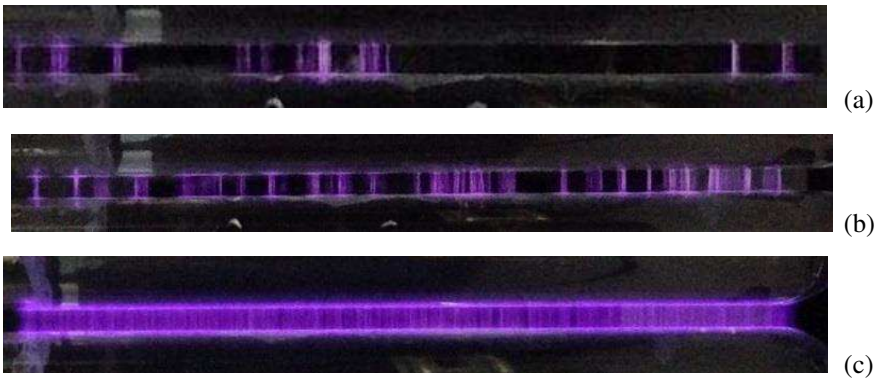

Figure 5: Image of three different discharge at (a) 13.58 kV, 1.9 kHz (b) 14.25 kV, 2 kHz and (c) 16.57 kV, 4.9 kHz.

Figure 6: Waste water after treatment.

(c) Waste water treatment

The test result of waste water after the treatment using ozone generator is physical changes on the waste water, which is obtained the fading color in the waste water that is more clearly compared with the color of initial waste water.

4. CONCLUSION

We have successfully developed the high voltage power supply for plasma DBD. The atmospheric pressure plasma by using liquid electrode was developed and produced by applying 1.9–4.94 kHz, 13.58–16.57 kV. Uniform discharge was observed throughout length of inter-electrode space when the voltage across the electrode was about 16.57 kV and frequency 4.91 kHz. The discharge does not depend on the concentration of potassium chloride and the large volumetric plasma could be increased by more electrodes. For ozone generator with two liquid electrodes has been applied to industrial waste water treatment.

ACKNOWLEDGMENT

The authors would like to thank Thammasat University for proving necessary facilities to carry out this research study.

REFERENCES

1. Zhang, G.-Q., et al., "Characterization of a dielectric barrier plasma gun discharging at atmospheric pressure," *Chin. Phys. Lett.*, Vol. 2, No. 1, 23–27, 2004.
2. Li, G., et al., "Measurement of plasma density produced in dielectric barrier discharge for active aerodynamic control with interferometer," *Chin. Phys. Lett.*, Vol. 26, No. 10, 10522-1–4, 2009.
3. Zhou, Z., Y. Huang, S. Yang, and W. Cheu, "Introduction of a new atmospheric pressure plasma device and application on tomato seeds," *Agriculture Science*, Vol. 2, No. 1, 23–27, 2011.
4. Agung, et al., "An ozone reactor design with various electrical configurations," *International Journal of Electrical and Computer Engineering (IJECE)*, Vol. 1, No. 2, 93–10, 2011.
5. Nafarizal, N., et al., "Development and application of in-house high voltage power supply for atmospheric pressure plasma treatment system," *ICSE2012 Proc.*, 2012.

An Optimal Match between the Ground-based Laser and a Relay Mirror System

Lipeng Luo, Yongte Jiang, Haiqiang Tong,
Chunmei Chai, Chunnan Zhang, and Xiuxiang Chu
School of Sciences, Zhejiang Forestry University, Lin'an 311300, China

Abstract— Based on the application of a relay mirror system, we study the intensity distribution and receiving efficiency of laser beams through a relay mirror system. When Fresnel number is big, this studies shows that the coupling efficiency of power between ground-based telescope and relay mirror is high for collimated beams. Due to small spot and high intensity concentrated on central obscuration, beams focusing to relay mirror is not suitable. For the reason that the distance between the laser source and relay mirror is fixed, and the distance from the relay mirror to a target is various, the intensity distribution is changed with different target. It is impossible to keep in high coupling efficiency when beams focus to target directly through a relay mirror system.

1. INTRODUCTION

With the use of a relay mirror system, the effects of atmosphere on the propagation of laser beams can be significantly reduced. Meanwhile, the obscurations at the propagation path, such as buildings, mountains can be avoided. In military, a relay mirror system can be not only used as a ballistic missile defense system to attack the air and ground targets, but also used for the space surveillance and space control [1–5]. In optical communication, the propagation distance can be significantly enhanced with the help of a relay mirror system [6].

There are many factors that will affect on the propagation of a laser beam through a relay mirror system, such as diffraction, turbulent atmosphere [7–9], thermal blooming [10, 11], different types laser beams [12–14] and its focal length. In this paper we will study the optimal match between ground-based telescope and receiver of relay mirror for flattened beams with different focal length.

2. THEORY STUDY

In the absence of atmosphere, the propagation of laser beams through a relay mirror system can be shown as Figure 1. A laser beam is projected by a Cassegrain telescope from a ground-based laser source. A relay mirror system with two-Cassegrain telescope receives the beam and focuses it on a target [15]. z_1 denotes the distance between laser source and the relay mirror. z_2 is the distance from the relay mirror to a target.

In practice, the propagation of beams in a relay mirror system without correction can be treated with geometry optics. Therefore, the propagation in Figure 1 can be simplified into three cases. The first one is focus transmitting, shown as Figure 2. Namely, the based-ground telescope focuses the beam to the relay mirror. The second one is collimated transmitting, see Figure 3. The based-ground telescope project a collimated beam to relay mirror. The third one is directed transmitting, illuminated as Figure 4. The based-ground telescope focuses a beam to a target through a relay mirror directly.

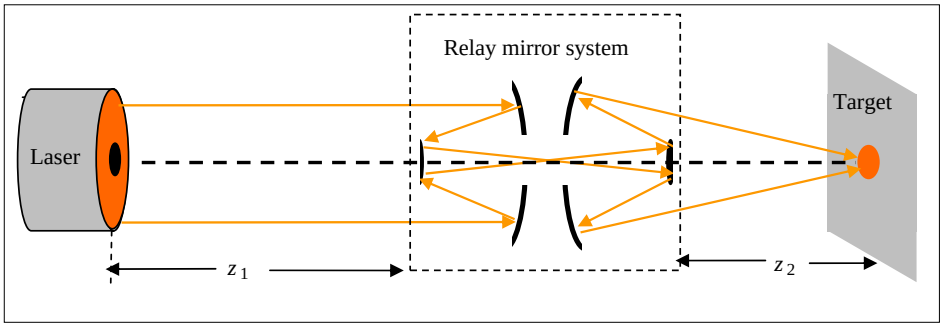

Figure 1: Configuration for beams through a relay mirror system.

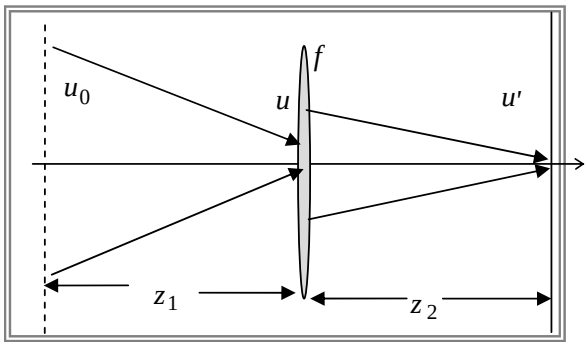

Figure 2: Laser beam focusing to relay mirror.

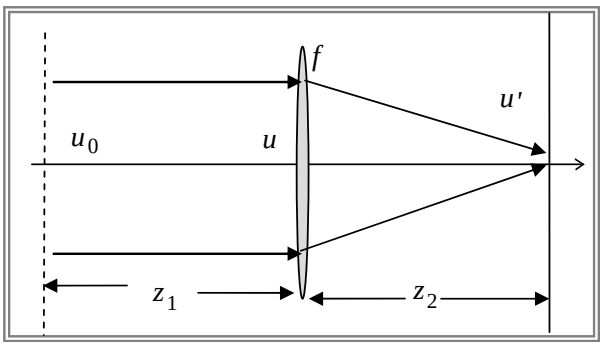

Figure 3: Propagation of collimated beams through relay mirror system.

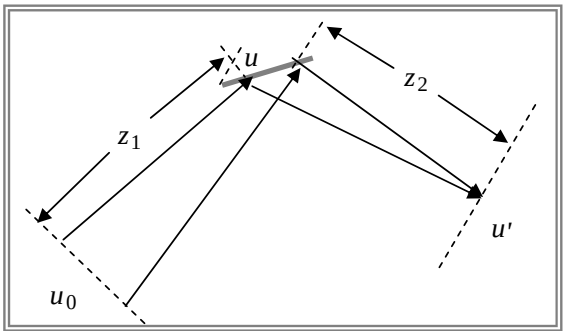

Figure 4: Laser beam focusing to target directly through relay mirror system.

In Figures 2–4, u_0, u and u' denote the optical field at the source plane, relay mirror and target, respectively. We assume that a laser source is located at the plane ($z = 0$) and propagates along z-axis in a cylindrical coordinates system. r_0 and r are the radial coordinates at source plane ($z = 0$) and receiver plane ($z = z_1$), respectively. $\rho_0 = r_0/a$, $\rho = r/a$ are the normalized transverse coordinates. a and ε are the radius and obscuration ratio of the transmitter aperture. The optical field of high power laser projected by ground-based telescope is chosen as the form:

$$u_0(\rho_0) = \begin{cases} A_0 & \varepsilon^2 \le \rho_0^2 \le 1 \\ 0 & \text{others} \end{cases} \tag{1}$$

where A_0 is the amplitude. Therefore, with the use of Fresnel diffraction integration, the optical field at z_1 plane can be expressed as

$$u(\rho, N_F) = -iA_0 N_F \exp\left(iN_F\rho^2/2\right) \int_\varepsilon^1 J_0\left(N_F\rho\rho_0\right) \exp\left[iN_F\rho_0^2\left(1-1/\delta\right)/2\right] \rho_0 d\rho_0 \tag{2}$$

where $N_F = ka^2/z_1$ is Fresnel number, $k = 2\pi/\lambda$ is wave number, λ is wavelength, $\delta = f/z_1$, f is the focal length. For the case that the beams focusing to the relay mirror ($\delta = 1$), the field at z_1-plane can be expressed as

$$u(\rho, N_F) = \frac{1}{i\rho} A_0 \exp\left(iN_F\rho^2/2\right) \left[J_1\left(N_F\rho\right) - \varepsilon J_1\left(N_F\varepsilon\rho\right)\right] \tag{3}$$

The intensity is

$$I(\rho, N_F) = A_0^2 \left[J_1\left(N_F\rho\right) - \varepsilon J_1\left(N_F\varepsilon\rho\right)\right]^2 / \rho^2 \tag{4}$$

If $\varepsilon = 0.25$, from Eq. (4) we can obtain that the 84% encircled power is concentrated on the aperture with $3.83/N_{F1}$ normalized radius. Therefore, the loss of power due to central obscuration is big in the near field. For example, $a = 0.5\,\text{m}$, $\lambda = 1.06\,\mu\text{m}$ and $z_1 = 30\,\text{km}$, the normalized radius is 0.13. So concentrated laser beam not only cause big loss of laser energy due to central obscuration, but also destroy the secondary mirror. From the studies above we can see that to focus a beam to a relay mirror is not suitable when the Fresnel number is big.

If a collimated beams ($\delta \to \infty$) are projected to relay mirror, from Eq. (2) the intensity distribution with different Fresnel number can be calculated numerically (see Figure 5). I_n in Figure 5 denotes the intensity divided by A_0^2.

Figure 5 shows that when $N_{F1}(1-\varepsilon^2) = 4n\pi$ (n is integer), the on-axis intensity is equal to $4A_0^2$ when $N_{F1}(1-\varepsilon^2) = (2n+1)2\pi$ (n is integer), the on-axis intensity is equal to zero. The on-axis intensity can be expressed in the form

$$I(0, N_F) = 4A_0^2 \sin^2\left[\frac{1}{4}N_F\left(1-\varepsilon^2\right)\right] \tag{5}$$

If the radius and obscuration ratio of receiver telescope is as the same as the ground-based telescope, the receiving efficiency with different Fresnel number are listed in Table 1.

From Table 1 we can see that the receiving efficiency is high when the Fresnel number is big. With Fresnel number degreasing, the receiving efficiency degreases.

Figure 6 shows the intensity profiles for the case that the beam focus to a target directly through a relay mirror, i.e., the relay mirror is equal to a reflective mirror. For the reason that the distance between the laser source and relay mirror is fixed, and the distance from the relay mirror to a target is various, the intensity distribution is changed with different target. Namely, the coupling efficiency is different with different target (see Table 2). In Table 2, we also assume that the radius and obscuration ratio of receiver telescope is as the same as the ground-based telescope. Therefore,

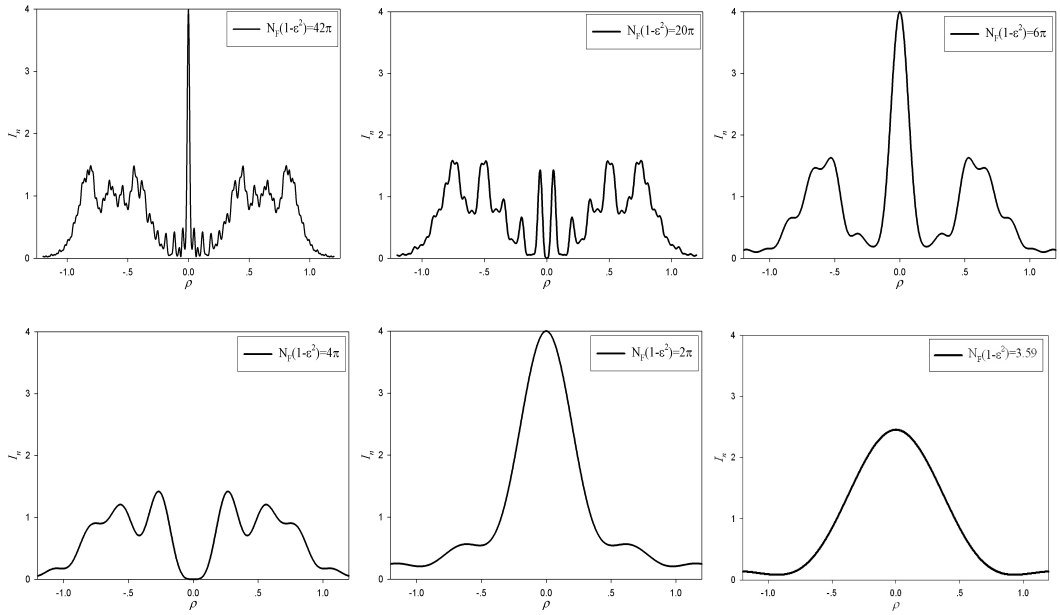

Figure 5: Intensity distribution of collimated beams with different Fresnel number.

Table 1: Receiving efficiency with different Fresnel number.

$N_{F1}\ (1-\varepsilon^2)$	42π	20π	6π	4π	2π	3.59
Encircled power (%)	93.0	87.5	86.0	83.2	67.5	62.9
Loss due to obscuration (%)	1.4	3.0	4.5	4.9	18.6	18.7
receiver efficiency (%)	91.6	84.5	81.5	78.3	48.9	44.2

Table 2: Receiving efficiency with different δ.

δ	1.25	1.5	1.75	2
Encircled power (%)	94.2	93.4	92.9	92.4
Loss due to obscuration (%)	84.6	59.7	27.7	15.1
receiver efficiency (%)	9.6	33.7	65.2	77.3

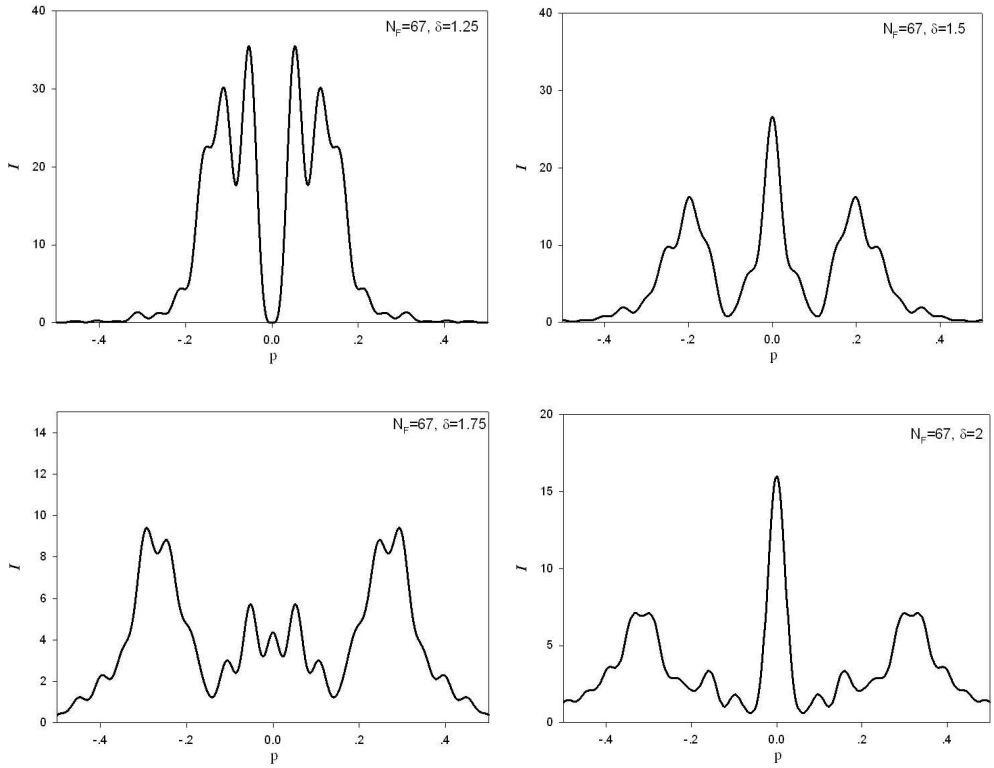

Figure 6: Variations of intensity profiles with different δ.

it is impossible to keep in high coupling efficiency when beams focus to target through relay mirror directly.

From the studies we can see that the coupling efficiency is high when a collimated beam is projected to a relay mirror.

REFERENCES

1. Hartman, M., S. Restaino, J. Baker, D. Payne, and J. Bukley, "EAGLE/relay mirror technology development," *Proc. of SPIE*, Vol. 4724, 2002.
2. Dierks, J., S. Ross, and P. Kervin, "Relay mirror experiment overview: A GBL pointing and tracking demonstration," *Proc. of SPIE*, Vol. 1482, 1991.
3. Sydney, P., M. Dillow, J. Anspach, P. Kervin, and T. Lee, "Relay mirror experiment scoring-analysis and the effects of atmospheric turbulence," *Proc. of SPIE*, Vol. 1482, 1991.
4. Duff, E. A. and D. C. Washburn, "The magic of relay mirrors," *Proc. of SPIE*, Vol. 5413, 2004.
5. Spencer, M. G., B. N. Agrawal, and M. Romano, "Acquisition, tracking, pointing, and line-of-sight control laboratory experiments for a space-based bifocal relay mirror," *Proc. of SPIE*, Vol. 4714, 2002.
6. Armstrong, J. W., C. Yeh, and K. E. Wilson, "Earth-to-deep-space optical communications system with adaptive tilt and scintillation correction by use of near-Earth relay mirrors," *Optics Letter*, Vol. 23, 1087–1089, 1998.
7. Andrews, L. C., R. L. Phillips, R. J. Sasiela, and R. R. Parenti, "Beam wander effects on the scintillation index of a focused beam," *Proc. of SPIE*, Vol. 5793, 28–37, 2005.
8. Eyyuboğlu, H. T., C. Arpali, and Y. Baykal, "Flat topped beams and their characteristics in turbulent media," *Opt. Express*, Vol. 14, 4196–4207, 2006.
9. Cai, Y. and S. He, "Propagation of various dark hollow beams in turbulent atmosphere," *Opt. Express*, Vol. 14, 1353–1367, 2006.
10. Gebhardt, F. G., "High power laser propagation," *Appl. Opt.*, Vol. 15, 1976.
11. Gebhardt, F. G., "Twenty-five years of thermal blooming," *Proc. of SPIE*, Vol. 1221, 1990.
12. Chu, X., Z. Liu, and Y. Wu, "Propagation of a general multi-Gaussian beam in turbulent atmosphere in a slant path," *J. Opt. Soc. Am. A*, Vol. 25, 74–79, 2008.

13. Cai, Y. and S. He, "Propagation of various dark hollow beams in turbulent atmosphere," *Opt. Express*, Vol. 14, 1353–1367, 2006.
14. Eyyuboğlu, H. T. and Y. Baykal, "Reciprocity of cos-Gaussian and cosh-Gaussian laser beams in turbulent atmosphere," *Opt. Express*, Vol. 12, 4659–4674, 2004.
15. Chu, X. and G. Zhou, "Power coupling of a two-Cassegrain telescope system in turbulent atmosphere in a slant path," *Opt. Express*, Vol. 15, 7697–7707, 2007.

Sub-5 nm Lanthanide Doped ZrO_2 Upconversion Nanoparticle for Protein Targeted Biomaging

Jing Liu and Qiuqiang Zhan*
Centre for Optical and Electromagnetic Research, South China Normal University
Guangzhou 510006, China

Abstract— Lanthanide-doped upconversion nanoparticles (UCNPs) are a promising new generation of imaging agents for bioimaging due to no auto-fluorescence, large penetration depth and non-blinking. In this paper an efficient ultra-small core-shell UCNP was synthesized using a hydrothermal method and a thermal decomposition procedure. A new inorganic host — ZrO_2 was used for its low phonon energy and high absorption coefficient [1]. The as-synthesized core-shell nanoparticles has a diameter smaller than 5 nm. An aptamer was employed as a recognizer for protein recognition to implement the bioimaging. Therefore, the small and efficient core-shell nanoparticles was fabricated to achieve the single-proteins-targeted imaging.

1. INTRODUCTION

Photoluminescence (PL) imaging is a powerful tool for life science studies and biological medical applications due to its high resolution and sensitivity. However, most biological molecules don't have spontaneous fluorescence when excited by light. Thus the molecules of interest need to be labeled by extraneous light-emitting probes for studies. Generally speaking, the cell components and other biological molecules are in a nanoscale size, mainly sub-5-nm. Considering such an ultra-small size, it is necessary to utilize a comparable nanoparticle to label these biological molecules to avoid external interference [2]. But it has been challenging to find probes that are bright enough for imaging and not too large to disrupt the protein's function.

Fluorescent organic dye molecules and most semiconductor quantum dots meet the size requirements but impose other limitations, such as light stability and cytotoxicity. As an alternative, lanthanide-doped upconversion nanoparticles (UCNPs) have been considered as a new choice of luminance probe for biological applications [3–5]. UCNPs utilize sequential absorption of multiple photons through real ladder-like energy levels of trivalent lanthanide ions (Ln^{3+}) which were embedded in an appropriate inorganic host lattice to produce higher energy anti-Stokes luminescence. The excitation light-NIR light has a deeper penetration and also less damage to living body. Compared with traditional luminance probes, UNCPs have many advantages, like deep penetration, autofluorescence free, high resolution, photo-bleaching free, continuous emission and low phototoxicity [6]. These lead UCNPs to attract remarkable *in vitro* and *in vivo* applications including optical bioimaging [7–9] high-sensitive biosensing [10], multimodal imaging [11–13] as well as *in vivo* animal theranostics.

However, the size of commonly used UCNPs is tens of nanometer in diameter, which is not suitable for the single molecules imaging. Although sub-10-nm UCNPs have recently been synthesized, the size is still relatively large for bio-probe [14, 15]. In all, the tradeoff between small size and high luminance still exists. Therefore a sub-5-nm bright probe is in urgent need. We proposed to design lanthanide-doped zirconium oxide (ZrO_2-Ln^{3+}) upconversion nanoparticles (UCNPs). Particularly, ZrO_2 crystal has low phonon energy and high host absorption coefficient [16, 17]. It can be synthesized through a modified solvothermal procedure which results in an ultra-small size (sub-5 nm) [18]. To the best of our knowledge, there are seldom UCNPs based on ZrO_2, neither such small, uniform and monodisperse NPs [19–22].

2. SYNTHESIS AND CHARACTORIZATION

We designed and synthesized an efficient core-shell structure. The uniform and monodisperse ZrO_2:20%Yb^{3+}, 2%Er^{3+} core was synthesized according to a modified solvothermal procedure reported in the literature [23]. This prepared NPs are hydrophobic, because of capped with organic ligand (benzyl alcohol), and dispersed in chloroform to form a clear colloidal solution (Fig. 2(b)). The size and morphology were characterized by transmission electronic microscopy (TEM), which shows uniform spherical NPs with an average diameter of 3.5 nm (Fig. 1(a)). The shell $NaYF_4$:2%Yb^{3+}

*Corresponding author: Qiuqiang Zhan (qiuqiang.zhan@coer-scnu.org).

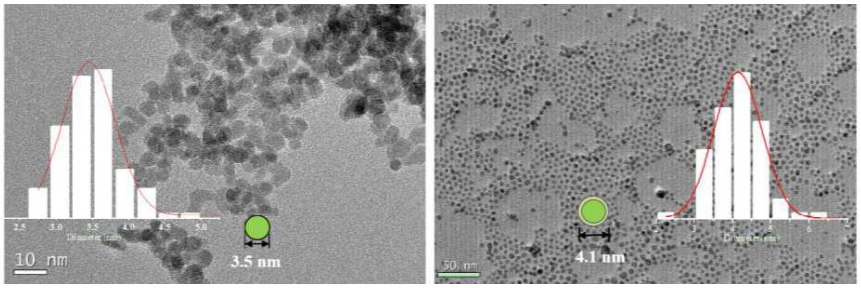

Figure 1: (a) TEM of ZrO_2:20%Yb^{3+}, 2%Er^{3+} (core) and histogram of the size distribution (inset); (b) TEM of ZrO_2:20%Yb^{3+}, 2%Er^{3+}@$NaYF_4$:2%Yb^{3+} (core-shell) and histogram of the size distribution (inset).

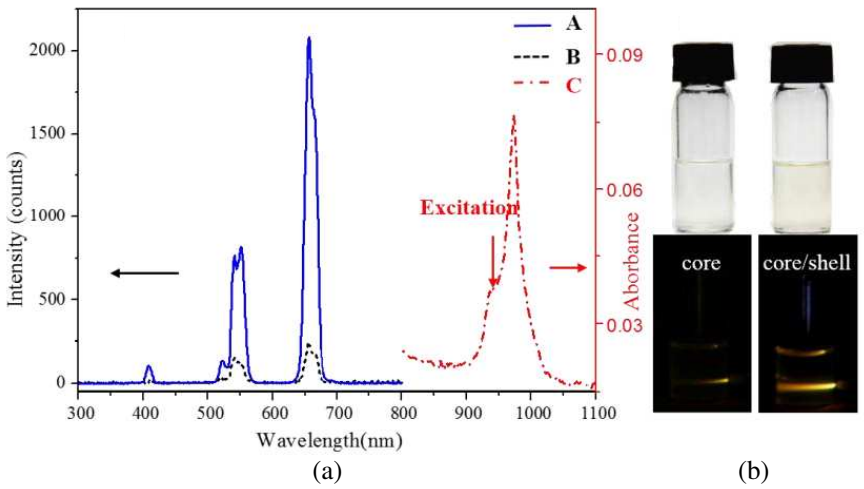

Figure 2: (a) PL emission (left) when excited at 925 nm (red arrow) and PL excitation (right) spectra forZrO_2-Ln^{3+} NPs. A is core/shell NPs PL emission (blue dash dot) and B is core NPs PL emission (black solid line); (b) ZrO_2-Ln^{3+} core NPs (upper left) and core/shell NPs (upper right) dispersed in hexane and luminance photographs were taken with a 2 W laser.

was synthesized through a thermal decomposition procedure which was modified from the procedure of shell of $NaYF_4$ [24]. We controlled the mole ratio of Zr and Y to achieve a thin shell which is about 0.6 nm. The as-prepared core-shell UCNPs was dispersed in organic solvents, like cyclohexane or chloroform, also to form a clear colloidal solution (Fig. 2(b)), which was a little yellowing than the core solution because of the oleic acid (OA). TEM also shows the uniform spherical NDs with an average diameter of 4.1 nm.

3. PL SPECTRA OF CORE AND CORE-SHELL NPS

The UC PL spectra of core and core-shell NPs were measured respectively via the microscope and spectrograph. We use diluted solutions to spin UCNPs onto the coverslips, which can form dispersive particles on the coverslips. A 925-nm laser beam was chosen as the excitation light because of less absorption by water reducing the heating effect when cell and animal experiments were taken [25]. The confocal luminescence images of core and core-shell UCNPs were taken respectively, and single particle was found to implement spot scanning to achieve the corresponding PL spectra. The UC PL of core and core-shell were compared and shown in Fig. 2(a), and obviously the core-shell PL intensity is of one order of magnitude than the core. This is also demonstrated in the luminance photographs (Fig. 2(b)), that the core-shell luminesce is much lighter than the core. Although the core is enough bright, the large surface-to-volume ratios and poor crystallinity that produce many defects which lead to serious energy quenching. A high thermal oil environment can not only produce a thin shell, but also make the crystallinity better.

4. SURFACE MODIFIED AND PROTEIN-TARGETED BIOIMAING

Before biological application, the UCNPs must be transformed into hydrophilia. The scheme below demonstrates the whole process (Scheme 1). The nitrite $NOBF_4$ were used to get rid of the OA capped on the NPs, which rendered the NPs surface positively charged [26]. Then the hydrophilic NPs was capped with water soluble polymers by a layer-by-layer method. The negatively charged PAA was used to encapsulate the hydrophilic UCNPs, which facilitated the successive coating of the positively charged PAH. All the surface zeta potentials were measured by a Zeta-Plus and the results are shown in Fig. 3(b). Surface modification of the nanoparticles was further confirmed by fourier-transform infrared (FTIR) spectroscopy. In the FTIR spectrum of OA-UCNPs (Fig. 3(a)-A), the peak at 3371 cm^{-1} was attributed to the O-H strong wide peak, and peaks at approximately 2923 and 2853 cm^{-1} were attributed to the asymmetric and symmetric stretching vibrations of methylene (CH_2) in the long alkyl chain, indicating the presence of OA on the surface of the nanoparticles (Fig. 3(a)). To be contrastive, peaks at approximately 2926 and 2855 cm^{-1} cannot be obviously observed in the spectrum of the UCNPs free of OA (Fig. 3(a)-B). The peak at 1687 cm^{-1} and 1642 cm^{-1} as well as the inconspicuous peak located around 744 cm^{-1} indicated the existence of additional N-H bonds (Fig. 3(a)-C).

There are many proteins in cell membrane, such as nucleolin or prion protein (PrPC) [27], which can be targeted by the specific aptamer functionalized UCNPs. And the ultra-small UCNPs is suitable to mark single proteins. Considering this, the streptavidin (SA) was linked to the surface of NPs after modified by polymers which was used to specific recognition with the aptamer. We can find there is a high specificity that most cell membranes were marked by the UCNPs when excited under a 925 nm CW (continuous wave) laser in the microscope (Fig. 4(c)). In the control group, when the UCNPs was not cultivated with SA, there were seldom UCNPs labeling the cell membranes (Fig. 4(b)).

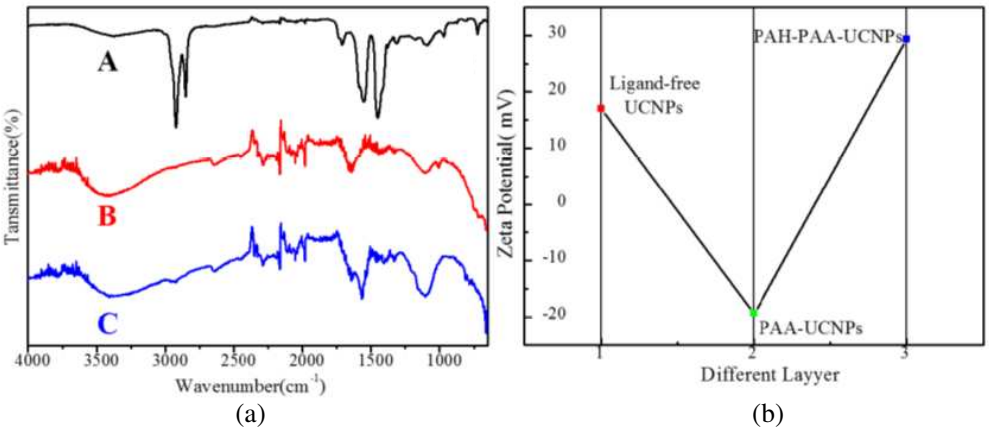

Figure 3: (a) FTIR spectra of (A) OA-UCNPs, (B) ligand-free UCNPs, (C) PAH-UCNPs. (b) Zeta potential data of different layers on UCNPs.

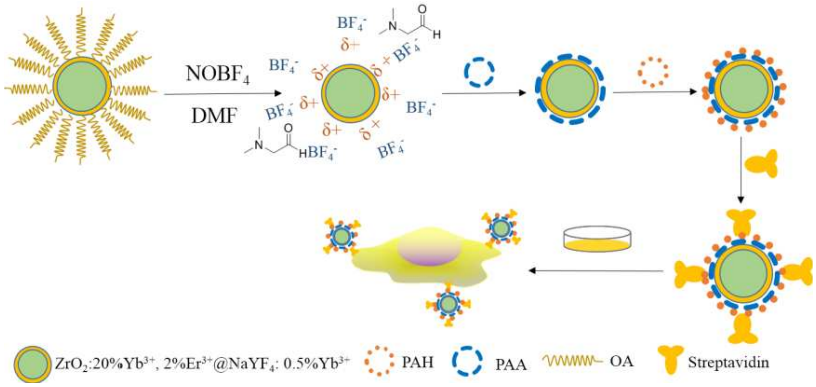

Figure 4: Scheme 1. Schematic illustration showing the hydrophilization and coating of PAA and PAH, the bioconjugation between PAA-PAH-UCNPs, and the incubation of SA-UCNPs with Hepatoma cells.

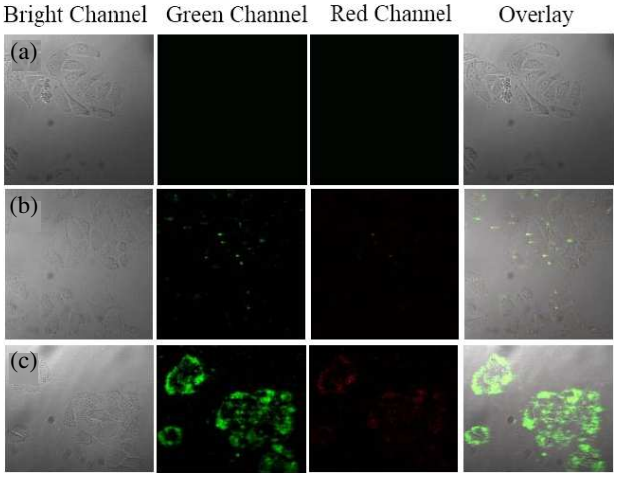

Figure 5: In vitro cancer cell imaging (right) using 925 nm laser excited UCNPs: images of Hepatoma cells separately incubated with (a) nothing as blank, (b) bio-aptamer pre-incubated and then PAH-ZrO_2-Ln^{3+}@ $NaYF_4$:Yb^{3+}, (c) bio-aptamer pre-incubated and then SA-ZrO_2-Ln^{3+}@ $NaYF_4$:Yb^{3+}. Bright channel (first column), green channel (second column), red channel (third column) and overlay image.

5. CONCLUSION

A type of 4-nm lanthanide-doped core-shell UCNPs was designed and sythnsized. Owing to the efficient host and shell, it has a remarkable brighter luminance. This small as well as brilliant UCNPs has a significant application in bioimaging. It would contribute a lot in the single-molecules imaging, which has become increasingly important because it can greatly help the researchers to understand the activities of human cells at the molecular level.

ACKNOWLEDGMENT

This work was supported by Guangdong Innovative Research Team Program (No. 201001D0104799318), the Natural Science Foundation of Guangdong Province (No. S2013040014211), the Postdoctoral Science Foundation of China (No. 2013M530368), the Discipline and Specialty Construction Fundation of Colleges and Univerisities of Guangdong Province (No. 2013LYM_0017), the Young Faculty Academic Training Foundation of SCNU (No. 2012KJ017), and the Student Extracurricular Scientific Research Key Project of SCNU (No. 13GDKC02). J. L. is grateful to Yuxiang Zhao for help in terms of optical system and also to Nana Li for help of cultivating cancer cell.

REFERENCES

1. Liu, Y., S. Zhou, D. Tu, Z. Chen, M. Huang, H. Zhu, E. Ma, and X. Chen, *Journal of the American Chemical Society*, Vol. 134, 15083–15090, 2012.
2. Whitesides, G. M., *Nature Biotechnology*, Vol. 21, 1161–1165, 2003.
3. Gorris, H. H. and O. S. Wolfbeis, *Angewandte Chemie International Edition*, Vol. 52, 3584–3600, 2013.
4. Zhou, J., Z. Liu, and F. Li, *Chemical Society Reviews*, Vol. 41, 1323–1349, 2012.
5. Chen, G., H. Qiu, P. N. Prasad, and X. Chen, *Chemical Reviews*, 2014.
6. Hilderbrand, S. A. and R. Weissleder, *Current Opinion in Chemical Biology*, Vol. 14, 71–79, 2010.
7. Nyk, M., R. Kumar, T. Y. Ohulchanskyy, E. J. Bergey, and P. N. Prasad, *Nano Letters*, Vol. 8, 3834–3838, 2008.
8. Wang, F., D. Banerjee, Y. Liu, X. Chen, and X. Liu, *Analyst*, Vol. 135, 1839–1854, 2010.
9. Zhou, J., Z. Liu, and F. Li, *Chemical Society Reviews*, Vol. 41, 1323–1349, 2012.
10. Kumar, M. and P. Zhang, *Langmuir*, Vol. 25, 6024–6027, 2009.
11. Xing, H., W. Bu, S. Zhang, X. Zheng, M. Li, F. Chen, Q. He, L. Zhou, W. Peng, and Y. Hua, *Biomaterials*, Vol. 33, 1079–1089, 2012.
12. Liu, Q., M. Chen, Y. Sun, G. Chen, T. Yang, Y. Gao, X. Zhang, and F. Li, *Biomaterials*, Vol. 32, 8243–8253, 2011.

13. Chen, F., W. Bu, S. Zhang, X. Liu, J. Liu, H. Xing, Q. Xiao, L. Zhou, W. Peng, and L. Wang, *Advanced Functional Materials*, Vol. 21, 4285–4294, 2011.
14. Ostrowski, A. D., E. M. Chan, D. J. Gargas, E. M. Katz, G. Han, P. J. Schuck, D. J. Milliron, and B. E. Cohen, *ACS Nano*, Vol. 6, 2686–2692, 2012.
15. Liu, Q., Y. Sun, T. Yang, W. Feng, C. Li, and F. Li, *Journal of the American Chemical Society*, Vol. 133, 17122–17125, 2011.
16. Sato, K., H. Abe, and S. Ohara, *Journal of the American Chemical Society*, Vol. 132, 2538–2539, 2010.
17. Joo, J., H. B. Na, T. Yu, J. H. Yu, Y. W. Kim, F. Wu, J. Z. Zhang, and T. Hyeon, *Journal of the American Chemical Society*, Vol. 125, 11100–11105, 2003.
18. Ninjbadgar, T., G. Garnweitner, A. Börger, L. M. Goldenberg, O. V. Sakhno, and J. Stumpe, *Advanced Functional Materials*, Vol. 19, 1819–1825, 2009.
19. Liu, Y., S. Zhou, D. Tu, Z. Chen, M. Huang, H. Zhu, E. Ma, and X. Chen, *Journal of the American Chemical Society*, Vol. 134, 15083–15090, 2012.
20. Bai, X., A. Pucci, V. T. Freitas, R. A. Ferreira, and N. Pinna, *Advanced Functional Materials*, Vol. 22, 4275–4283, 2012.
21. Lü, Q., F. Guo, L. Sun, A. Li, and L. Zhao, *The Journal of Physical Chemistry C*, Vol. 112, 2836–2844, 2008.
22. Chen, G., Y. Zhang, G. Somesfalean, Z. Zhang, Q. Sun, and F. Wang, *Applied Physics Letters*, Vol. 89, 163105-163105–163103, 2006.
23. Ninjbadgar, T., G. Garnweitner, A. Börger, L. M. Goldenberg, O. V. Sakhno, and J. Stumpe, *Advanced Functional Materials*, Vol. 19, 1819–1825, 2009.
24. Ostrowski, A. D., E. M. Chan, D. J. Gargas, E. M. Katz, G. Han, P. J. Schuck, D. J. Milliron, and B. E. Cohen, *ACS Nano*, Vol. 6, 2686–2692, 2012.
25. Zhan, Q., J. Qian, H. Liang, G. Somesfalean, D. Wang, S. He, Z. Zhang, and S. Andersson-Engels, *ACS Nano*, Vol. 5, 3744–3757, 2011.
26. Dong, A., X. Ye, J. Chen, Y. Kang, T. Gordon, J. M. Kikkawa, and C. B. Murray, *Journal of the American Chemical Society*, Vol. 133, 998–1006, 2010.
27. Chen, L. Q., S. J. Xiao, P. P. Hu, L. Peng, J. Ma, L. F. Luo, Y. F. Li, and C. Z. Huang, *Analytical Chemistry*, Vol. 84, 3099–3110, 2012.

Applicator for Superficial Microwave Hyperthermia Filled with Anisotropic Dielectric Media: Numerical Investigation of Design Degrees of Freedom

J. Vrba, Jr.[1], **D. Vrba**[1], **M. Wiewegh**[1], **and J. Vrba**[2]

[1]Faculty of Biomedical Engineering, Czech Technical University in Prague, Czech Republic
[2]Faculty of Electrical Engineering, Czech Technical University in Prague, Czech Republic

Abstract— In this paper properties of an rectangular-waveguide applicator (test applicator) for superficial microwave hyperthermia filled with stratified isotropic and/or anisotropic dielectric media are discussed. Man-made biaxial anisotropic material is considered here. Electric field distributions in a cross-section of the test applicator filled with anisotropic material are compared with the test applicator filled completely with water and with the one partially filled with water and partially with high permittivity materials. Furthermore, for some applicators power loss densities in the virtual phantom of muscle tissue are numerically estimated.

1. INTRODUCTION

From all applicators for superficial microwave hyperthermia proposed in the past and used now in the field of RF/microwave hyperthermia rectangular-waveguide applicators excels, in comparison to planar applicators, in

1. homogeneity of the SAR distribution created in the treated biological tissue,
2. low leaked electromagnetic fields, due to closed metallic walls around the applicator aperture.

On the other hand, the main drawbacks of these applicators are that they are fairly bulky and heavy. Often, in order to decrease the dimensions of these applicators/decrease their working frequency they are completely filled with water that makes them even weightier.

In the past the effective aperture of the rectangular-waveguide applicator with TE_{10} mode was improved using side dielectric slabs of titanium dioxide which shows high relative electric permittivity. The rest of these modified applicators is filled with water.

The numerical investigation performed and presented in this paper is motivated by expectation that by filling a rectangular waveguide with anisotropic media the number of degrees of freedom for the applicator design will increase. The parameters like power loss distribution produced in the treated area as well as electric field distribution in the applicator cross-section are the main investigated properties in this paper.

The proposed rectangular-waveguide applicator is compared with a rectangular waveguide applicator filled completely with water and with the one partially filled with water and partially with titanium dioxide slabs.

The numerical simulations are performed using a full-wave well-proven commercial electromagnetic field simulator COMSOL Multiphysics [1].

2. BIAXIAL DIELECTRIC MATERIAL

In the presented analysis the problem is considered to be loss-less and the anisotropic dielectric material is a composite of two materials. The material which forms a continuous phase is loss-less and shows permittivity ε_c. The other material is considered as perfect electric conductor (PEC) and it is dispersed in the continuous phase in a form of mono-spheres (all spheres have the same radius r) in a rectangular lattice with lattice parameters a_x, a_y and a_z in x-, y- and z-direction. The considered anisotropic material has lattice parameters $a_x = a_z \neq a_y$, which in crystallography corresponds to tetragonal $a_x = a_z \neq a_y$ crystal system). Such material belongs to a class of so called biaxial [2] materials. This means that the permittivity can be written in a Cartesian coordinates as diagonal matrix and permittivity in x- and z-directions have to be the same

$$\bar{\bar{\varepsilon}} = \begin{pmatrix} \varepsilon_x & 0 & 0 \\ 0 & \varepsilon_y & 0 \\ 0 & 0 & \varepsilon_x \end{pmatrix}.$$

Design of the anisotropic material is not the goal of the presented study. The geometry of such material is in Fig. 1.

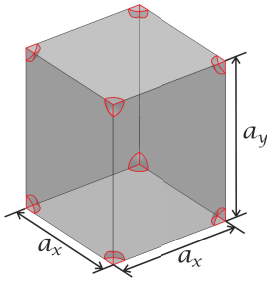

Figure 1: 3D view of a unit cell with 1 sphere of radius r. The is geometry periodical with a spatial period in all three dimensions equal to the corresponding unit cell edge length a_x, a_y and a_z.

3. FIELD DISTRIBUTION INSIDE APPLICATORS FILLED WITH ISOTROPIC MATERIAL

The geometries of rectangular waveguides considered here are depicted in Fig. 2. For the rectangular waveguide filled completely with an isotropic material, in this case water, the dominant mode is TE_{10} [3].

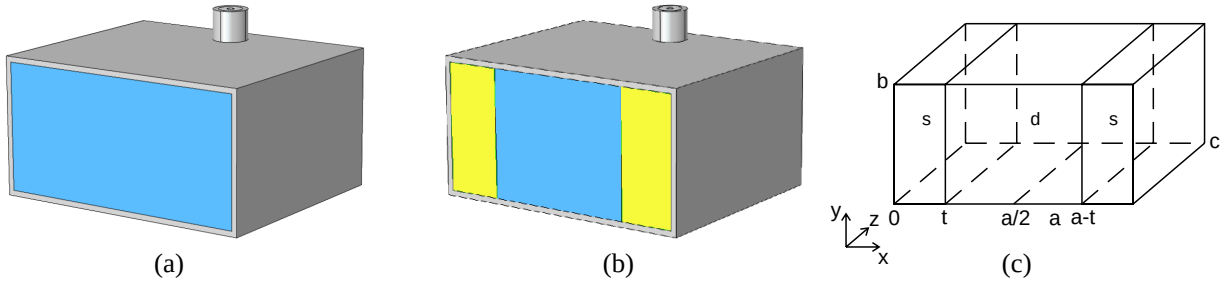

Figure 2: Geometries of the considered rectangular-waveguide applicators: (a) applicator completely filled with water (depicted in blue), (b) applicator partially filled with dielectric isotropic/anisotropic material (depicted in yellow). (c) Rectangular waveguide dimensions and orientation. $a = 70\,\mathrm{mm}$, $b = 35\,\mathrm{mm}$ and $c = 60\,\mathrm{mm}$. Thickeness of the slabs is denoted as t.

The dominant mode of the rectangular-waveguide applicator filled with stratified media as depicted in Fig. 2 is a slightly modified TE_{10}. Basic properties of the rectangular waveguide filled with three layers of isotropic material, e.g., cut-off frequency of the dominant mode, phase constant in propagation direction β_z, EM field distribution, were evaluated using a well-known theory [4]. One of the steps necessary to evaluate the basic properties is to numerically solve following transcendental equation

$$\begin{aligned} &\left(\omega^2\varepsilon_d\mu - \beta_z^2\right)\sqrt{\omega^2\varepsilon_s\mu - \beta_z^2}\,\tan\left(\sqrt{\omega^2\varepsilon_s\mu - \beta_z^2}t\right) \\ =\ &\left(\omega^2\varepsilon_s\mu - \beta_z^2\right)\sqrt{\omega^2\varepsilon_d\mu - \beta_z^2}\,\cot\left(\sqrt{\omega^2\varepsilon_d\mu - \beta_z^2}\left(\frac{a}{2} - t\right)\right), \end{aligned} \tag{1}$$

where ε_d, ε_s are permittivity of inner region and slabs, respectively. The ability of an applicator to homogeneously irradiate the treated area can be estimated by computation of power loss density. Biological tissues show negligible magnetic loss and for homogeneous phantom considered here the power loss density is proportional to $|E|^2$. The field distribution in the waveguide will be plotted for the dominant electric field component E_y.

4. NUMERICAL MODEL

The numerical model is based on a simple rectangular waveguide applicator feeded with a coaxial port.

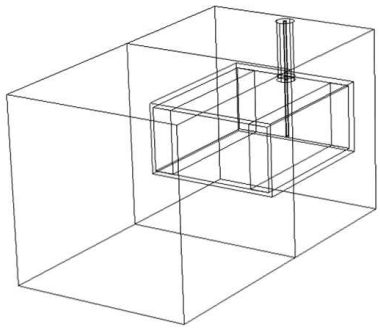

Figure 3: Numerical model of the applicator virtually irradiating a muscle tissue phantom.

It is basically an adapter between coaxial and rectangular waveguide technology where the rectangular waveguide aperture lay on a patient to be treated (mostly there is a water bolus between patient and the applicator, the water bolus is for simplicity omitted here). In this numerical model the tested applicator virtually irradiates phantom of a muscle tissue. Dielectric properties of muscle tissue at the working frequency can be found in [5].

5. RESULTS

Field distribution $|E_y|^2$ of the dominant TE_{10} mode in the rectangular waveguide filled with homogeneous (Fig. 2(a) [4]) and stratified isotropic media (for modified TE_{10} mode, Figs. 2(b) and (c) [4] and Eq. (1)) has been found, respectively and they are plotted in Fig. 4.

Relative permittivity of water and TiO_2 in the evaluated field distribution is consider 80.1 and 100, respectively. For an microwave applicator, effective treatment is considered in a region of treated patient, where power loss density induced with the applicator falls to 50% of its maximum. This region is proportional to the length ℓ of an aperture in x-direction plotted in Fig. 4. For two combinations of permittivities (water/TiO_2 and water/$\varepsilon_r = 300$) field distribution was optimized by varying thickness t of the slabs. Two 2.9 cm thick TiO_2 slabs improve the homogeneity of the

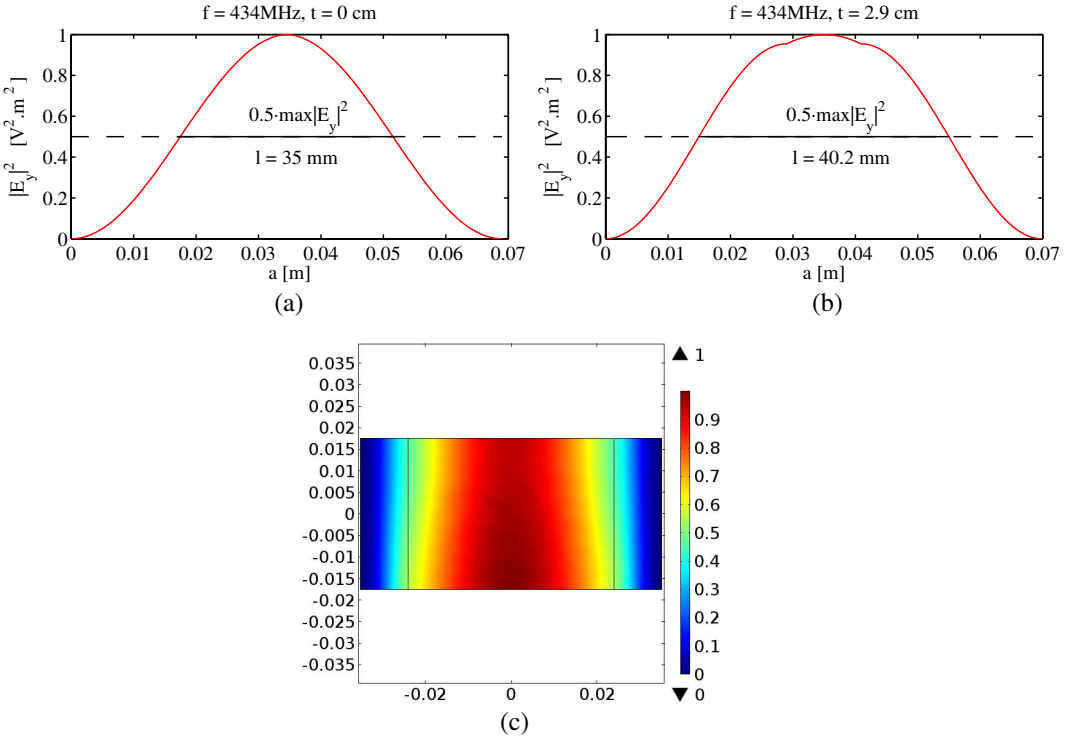

Figure 4: (a) Electric field distribution $|E_y|^2$ in rectangular waveguide filled with water only, (b) partially with water and partially with TiO_2 and (c) partially with water and partially with an isotropic material with $\varepsilon_r = 300$.

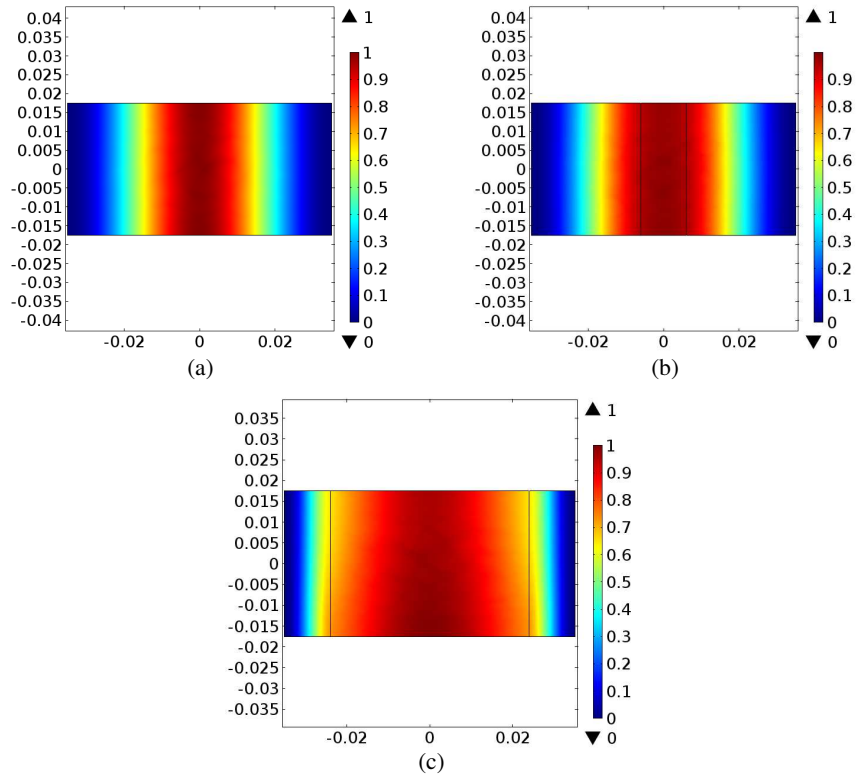

Figure 5: (a) Electric field distribution $|E_y|^2$ in rectangular waveguide filled with water only, (b) partially with water and partially with TiO_2 and (c) partially with water and partially with an isotropic material with $\varepsilon_r = 300$.

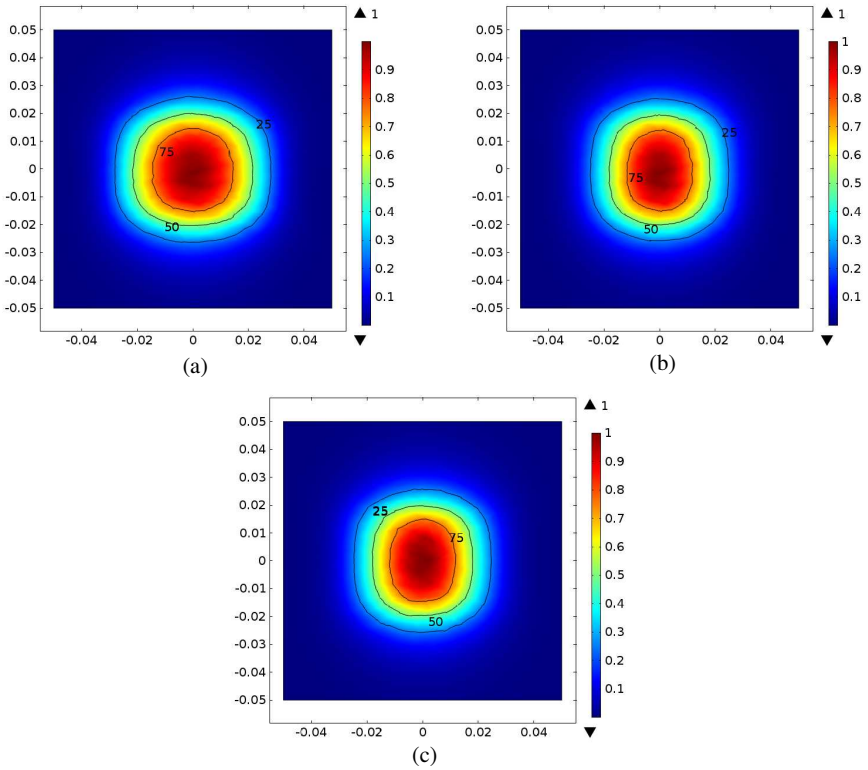

Figure 6: (a) Power loss distribution (1 cm bellow the surface of the phantom) produced by the rectangular waveguide applicator filled partially with water and partially with an isotropic material with $\varepsilon_r = 300$ and (b) by the rectangular waveguide filled partially with water and partially with an anisotropic material with $\varepsilon_{rx} = \varepsilon_{rz} = 300$ and $\varepsilon_{ry} = 80$. (c) By the rectangular waveguide filled partially with water and partially with an anisotropic material with $\varepsilon_{rx} = 300$ and $\varepsilon_{ry} = \varepsilon_{rz} = 80$.

field distribution in the waveguide cross-section by a factor of $A = 40.2/35 = 1.15$ (relative to homogeneously filed applicator). Using high-permittivity ($\varepsilon_r = 300$) dielectric slabs with slabs of $t = 1.1$ cm yields $A = 1.62$. There is a danger of excitation of higher-order modes (excitation of higher order modes is tested numerically). in this paper the possibility to suppress higher-order modes using anisotropic materials is investigated.

In Fig. 5 numerically estimated electric field distribution $|E_y|^2$ in rectangular waveguides filled with water only (a), partially with water and partially with TiO_2 (b) and partially with water and partially with an isotropic material with $\varepsilon_r = 300$ (c) are plotted. For the last case the field distribution shows certain dependency in y-direction. This dependency in y-direction may degrade ability of the applicator homogeneously irradiate a treated area.

If the permittivity of slabs was considered anisotropic (analysis was performed for following cases $\varepsilon_{rx} = \varepsilon_{rz} = 300$ and $\varepsilon_{ry} = 80$, $\varepsilon_{rx} = \varepsilon_{rz} = 300$ and $\varepsilon_{ry} = 250$, $\varepsilon_{rx} = 300$ and $\varepsilon_{ry} = \varepsilon_{rz} = 80$) the numerically estimated field distribution in the applicator cross-section showed narrower pattern than for the applicator with slabs of isotropic material with $\varepsilon_r = 300$. Instead of plotting the field distributions we have decided to plot power loss densities produced by applicators 1 cm under the surface of the phantom. Numerically estimated power loss density produced by applicators filled with isotropic and anisotropic slabs is plotted in Figs. 6(a) and (b), (c), respectively. Again, the power loss densities for the applicator with anisotropic materials (b), (c) show narrower pattern than the applicator with isotropic materials.

6. CONCLUSIONS

Evaluated field distribution fits very well the one numerically estimated using COMSOL Multiphysics. Homogeneity of field distribution was expected to be further improved using anisotropic materials but this has not been proven in this study.

ACKNOWLEDGMENT

This research has been supported by the research program of the Grant Agency of the Czech Republic, Project No. 14-00386P Study of Thermal and Nonthermal Effects of High-Power EM Field Structure of Matter and Project No. 13-29857P Human Body Interactions with EM Field Radiated by Metamaterial Structures.

REFERENCES

1. *COMSOL Multiphysics User's Guide*, 4th Edition, COMSOL AB, October 2010.
2. Sihvola, A., *Electromagnetic Mixing Formulae and Applications*, The Institution of Engineering and Technology, May 2000.
3. Pozar, D. M., *Microwave Engineering*, 2nd Edition, John Wiley and Sons, New York, 1998.
4. Balanis, C. A., *Advanced Engineering Electromagnetics*, Solution Manual ed., Wiley, May 1989.
5. Andreuccetti, D., R. Fossi, and C. Petruccim, "An internet resource for the calculation of the dielectric properties of body tissues in the frequency range 10 Hz–100 GHz," March 2013, [Online] Available: http://niremf.ifac.cnr.it/tissprop/.

Measurement of Temperature Increase of Metal Hip Replacements During Magnetic Resonance Imaging

M. Wiewegh[1] and J. Vrba[2]

[1]Faculty of Biomedical Engineering, Czech Technical University in Prague, Czech Republic
[2]Faculty of Electrical Engineering, Czech Technical University in Prague, Czech Republic

Abstract— In this paper measurements of temperature increase of three different hip replacements during MRI were carried out. The hip replacements were embedded in an agar phantom which mimics dielectric properties of muscle tissue and were placed into a MRI system with the static magnetic field intensity of $B_0 = 1.5\,\mathrm{T}$. The MRI of the samples took in total 20 minutes. Thermograms of the hip replacements were taken with a thermographic camera in two different time instances.

1. INTRODUCTION

With the increasing number of magnetic resonance (MR) systems and the growing number of patients with joint replacements, the question of safety of these patients during magnetic resonance imaging (MRI) arises.

There are many contraindications for MRI of patients with metal implants like stents, clamps, bolts and joint replacements [1]. This paper is focused on measurement of effect on hip replacement in MRI during diagnostics. For measurements were selected type of hip replacement, whose material properties are listed in Table 1.

Table 1: Material properties of hip replacement [4–6].

Material	Electrical conductivity $[\mathrm{S}\cdot\mathrm{m}^{-1}]$	Thermal conductivity $[\mathrm{W}\cdot\mathrm{K}^{-1}\cdot\mathrm{m}^{-1}]$	Specific heat $[\mathrm{kJ}\cdot\mathrm{K}^{-1}\cdot\mathrm{kg}^{-1}]$	Relative permeability μ_r $[-]$	Density ρ_t $[\mathrm{kg}\cdot\mathrm{m}^{-3}]$
AISI 316L	135.135	16.3	0.5	1.08	8000
$Co_{35}Ni_{20}Cr_{10}Mo$	96.81	11.2	0.5	1	8430
Ti_6Al_4V	56.18	6.7	0.5263	1	4430
Polyethylen	0.0005	0.38	1.9	1	930

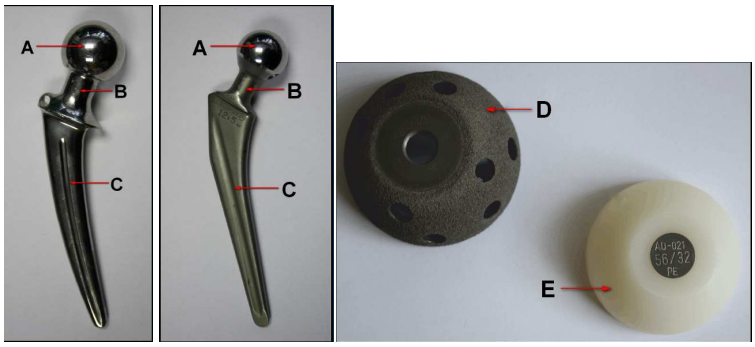

(a) (b) (c)

Figure 1: (a) and (b) describe stainless steel and cobalt alloy hip replacement, respectively. There is femoral head A, neck B and stem C. In (c) there is metal shell D and polyethylene liner E.

Effect of electromagnetic and magnetic field on metals can be depending on material properties dual. One is induced heating [1, 2] and second is movement. Given the value of the permeability (see Table 1) all joint replacements are not expected to shift in the patient.

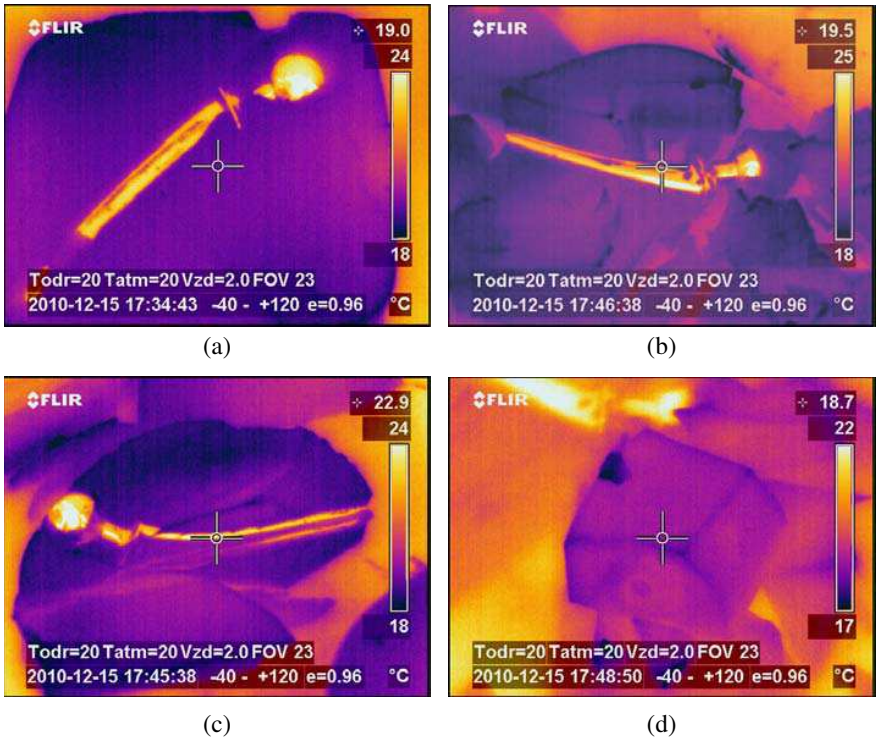

Figure 2: (a) shows the thermogram of stainless steel hip replacement measured after 10 minutes, maximum temperature rise appears in the region of the head (ball) A. (b) shows the thermogram of stainless steel hip replacement with polyethylene liner and (c) shows the thermogram of the cobalt alloy after 20 minutes of heating, where the maximum temperature rise appears in the region of femoral head A, neck B and the narrow edges of the stem C. In (d) there is the thermogram of metal shell after 20 minutes of MRI.

The observed effect was temperature rising during MRI due to radiated electromagnetic field at radiofrequency coils of Larmor frequency ω_0 [3], which is for the 1.5 T MR system used here approximately 64 MHz.

In this paper measurements of temperature increase of three different hip replacements during MRI were carried out. The hip replacements were embedded in an agar phantom which mimics dielectric properties of muscle tissue and were placed into a MRI system. The MRI of the samples took in total 20 minutes. Thermograms of the hip replacements were taken with a thermographic camera.

Temperature was measured in two different time instances, after ten and twenty minutes of MRI, respectively. After first ten minutes temperature of the stainless steel without the acetabular component. After twenty minutes, the temperature of stainless steel with the acetabular component and of the cobalt alloy.

2. METHOD

In order not to influence the EM fields in the MRI system during experiments, e.g., by metalic temperature sensors, the temperature was measured using thermographic camera. The accuracy of the measured temperature distribution by the thermographic camera is affected by the time interval between the end of MRI procedure and the temperature measurement. Therefore it was necessary to perform the temperature measurements of all parts of the prosthesis immediately after completion of the diagnostic procedure.

In a living tissue an excessive heat dissipation can be reduced by the bloodstream. The method used here did not take into account the bloodstream.

An important step was selection of a suitable environment in which the implant was located during the MRI procedure. Measurements on dead animals, which would be implanted joint replacement, would not significantly (not affected) increase the accuracy of measurement results. On the contrary, it would be necessary to remove the implant from the body and thus increase the cooling time. Agar phantom could be divided before the MRI procedure and could be very easily

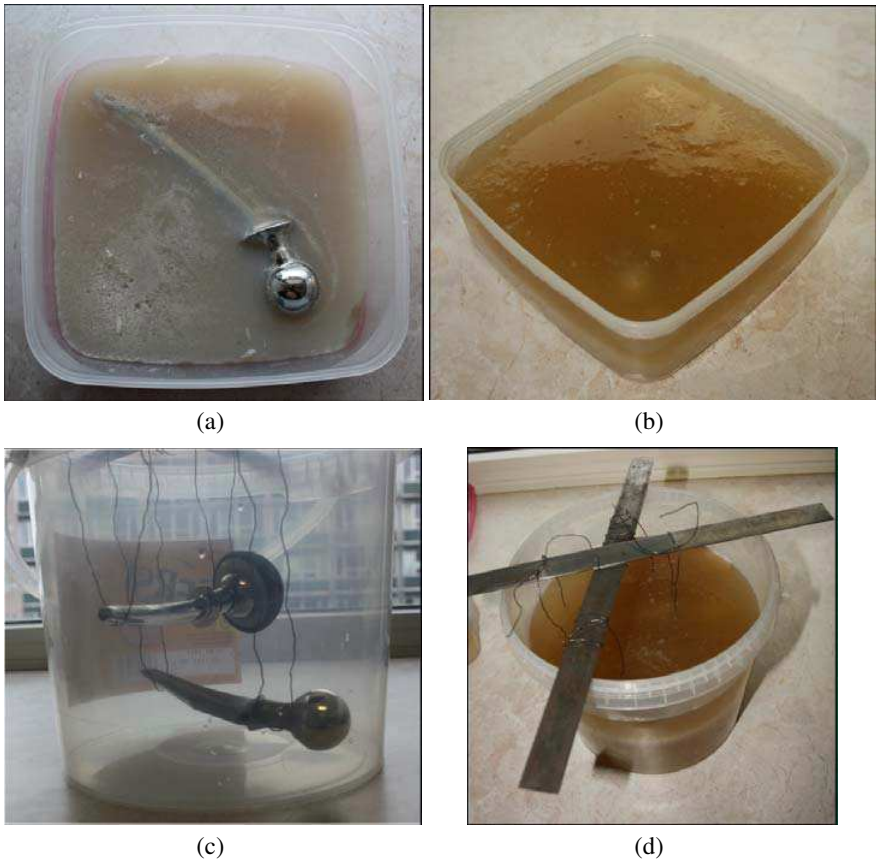

Figure 3: (a) and (b) show stainless steel hip replacement, which was used for measurement after ten minutes. In (c), (d) there is spatial arrangement of stainless steel with the acetabular cup and cobalt alloy hip replacement, which were used for measurement after twenty minutes.

and quickly opened before the temperature measurement. For this reason the agar phantom was chosen.

The considered three hip replacements vary in material and/or in geometry. Two of them were made of stainless steel (AISI 316L) and the third one of cobalt alloy (Co_{35} Ni_{20} Cr_{10} Mo). One stainless steel hip replacement was complete, i.e., with an acetabular component. The acetabular component consists of polyethylen liner and metal shell of titan alloy (Ti_6 Al_4 V). The other stainless steel hip replacement was heated with the MR system without the acetabular component.

3. RESULTS

Temperature was measured in two different time instances, after ten and twenty minutes of MRI, respectively. After first ten minutes temperature of the stainless steel without the acetabular component rose about 5 to 6°C. After twenty minutes, the temperature of stainless steel with the acetabular component and of the cobalt alloy rose about 7°C and 6°C, respectively. The temperature of the titan alloy rose about 2°C.

4. CONCLUSION

After verification of magnetic properties of implants materials the observed increased temperature could be attributed to surface electric currents induced by the RF EM fields.

In the performed experiments biological tissues were represented by a solid agar phantom with no blood vessels taken into account. Due to the absence of the bloodstream it can be assumed that the measured temperatures are higher than those which would be achieved in the living tissue.

For all tested implants a temperature increase was observed. In the case of stainless steel and cobalt alloys the temperature increase could cause, particularly in susceptible patients, burning sensation. For titanium alloys the temperature increase is rather low to be recognized by the patient. None of the measured temperature increase should not pose a safety hazard.

ACKNOWLEDGMENT

I would like to thank the management of the University Hospital for access to MRI and also the head of radiology and radiology staff for cooperation. I would like to thank Mrs. Karolina Veverkova, PhDr. and the Department of Mechanics, Biomechanics and Mechatronics at the Faculty of Mechanical Engineering for lending hips replacements.

This work was supported by the Grant Agency of the Czech Technical University in Prague, grant No. SGS14/217/OHK4/3T/17.

REFERENCES

1. Formica, D. and S. Silvestri, *BioMedical Engineering OnLine*, Vol. 3, No. 1, 11, DOI: 10.1186/1475-925X-3-11, Available from: http://www.biomedical-engineering-online.com/content/3/1/11.
2. Moshin, S. A., N. M. Sheikh, and U. Saeed, "MRI induced heating of deep brain stimulation leads: Effect of the air-tissue interface," *Progress In Electromagnetics Research*, Vol. 83, 81–91, 2008.
3. Blumer, P., *Spatially Resolved Magnetic Resonance: Methods, Materials, Medicine, Biology, Rheology, Geology, Ecology, Hardware*, 760 P., Wiley-VCH, New York, 1998, ISBN 35-272-9637-9.
4. Walter, A. S., *Prvodn List Sfrick Jamky*, Praha, 2000.
5. Matweb, *316 Stainless St., Annealed Sheet*, http://www.matweb.com/search/DataSheet.aspx?MatGUID=1336be6d0c594b55afb5ca8bf1f3e04 2&ckck=1, 200-.
6. Matbase, *Titanium: TiAl6V4*, http://www.matbase.com/material/non-ferrous-metals/titanium/tial6v4/properties, valid to Jan. 1, 2011.

Zeroth-order Mode Resonator Metamaterial Applicators for Superficial and Deep Local Microwave Hyperthermia

D. Vrba[1], **J. Vrba, Jr.**[1], **M. Wiewegh**[1], **and J. Vrba**[2]

[1]Department of Biomedical Technology, Faculty of Biomedical Engineering
Czech Technical University in Prague, Kladno, Czech Republic
[2]Department of Electromagnetic Field, Faculty of Electrical Engineering
Czech Technical University in Prague, Zikova 4, Prague 166 36, Czech Republic

Abstract— Paper deals with our new results in the field of applicators used for microwave regional thermotherapy, like, e.g., cancer treatment, physiotherapy, etc.. New type of applicator based on Metamaterial technology especially with zeroth order resonances will be introduced. The main aim of this work is to verify whether EM wave penetrating into the biological tissue can have good SAR homogeneity and depth of penetration approaching to theoretical limit.

1. INTRODUCTION

Aim of this paper is to verify whether a metamaterial structure can be used as applicator for hyperthermia treatment. For this experiment antenna is adapted from [1] with respect to required quality. Applicators for hyperthermia treatment have to be design in such a way they produce suitable shape of radiated electromagnetic wave. For local and deep local treatment electromagnetic plane wave can would by suitable because it ensures:

- the best penetrating depth,
- the best homogeneity of SAR.

2. DESIGN OF THE APPLICATOR

The applicator is proposed (shown in Fig. 1) is based on microstrip technology which allows very thin and low profile applicator construction. The input impedance of this structure at the operating frequency is approx. 5 ohms [2, 3]. To improve applicator reflection coefficient, a $\lambda/4$ impedance transformer is used. The length of the impedance transformer is 107 mm. The impedance transformer increases the applicator overall dimensions from 80 mm (without the impedance transformer) to 187 mm (the impedance transformer included). The longitudinal dimension of the applicator can be decreased by using a double layered dielectric substrate with the impedance transformer on the other side. The inductive microstrips are grounded by capacitors. The interdigital capacitor for this design consists of four fingers. The length of each finger is $L_f = 18$ mm, length of the inductive part is $L_{ind} = 41$ mm, length of the unit cell $L = 22$ mm, and dimensions of grounded capacitor are $16 \times 13\,\text{mm}^2$.

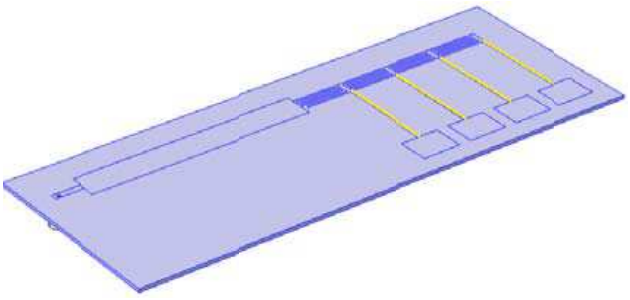

Figure 1: Aperture view of Applicator 2 based on microstrip technology. Applicator dimensions are $187 \times 56\,\text{mm}^2$ for a substrate thickness of 1.5 mm.

Table 2 lists the effective field size (EFS) for three different depths in muscle tissue-equivalent phantom. EFS (Active Element) is defined as irradiated area/active element area and EFS (Applicator) irradiated area/ground plane area. EFS is numerically estimated for three different levels of SAR, namely 25%, 50% and 75%. All SAR levels are normalized to the maximum SAR in the 1 cm deep plane.

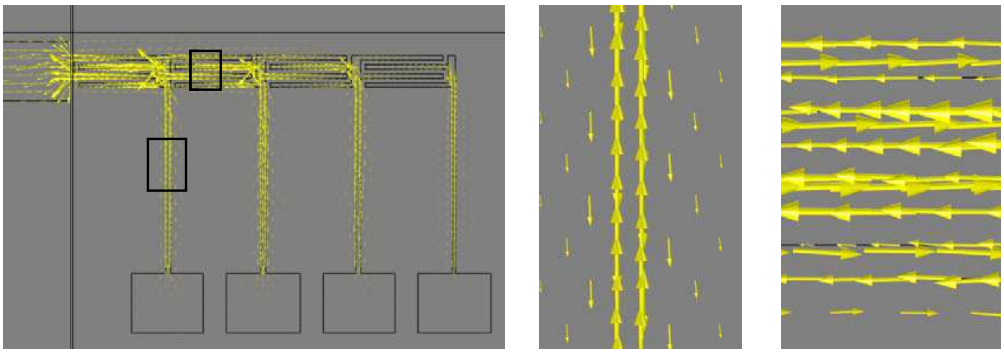

Figure 2: (a) Surface current density (at some time instant) represented by yellow arrows on the surface of metallic parts of Applicator. (b) Currents flowing from bottom to top are on the antenna structure whereas currents with the opposite orientation are currents on the ground plane underlying the 1.5 mm thick substrate. (c) Detail of one interdigital capacitor where currents flowing from right to left are currents on the interdigital capacitors and the current flowing from left to right are the currents on the ground plane.

Table 1: Dielectric properties (@434 MHz) of materials considered in numerical models.

Material	FR4 [5]	De-ionized water (20°C) [6]	Muscle tissue [4]
Relative permittivity ε_r [-]	4.2	80.1	57
Equivalent conductivity σ_e [S/m]	0.0016	0.047	0.81

Table 2: Dependence of effective field surface and depth.

Penetration depth in muscle tissue (cm)	Level of SAR (%)	Irradiated area $\geq$ SAR% (cm^2)	EFS (Radiating element) (%)	EFS (Applicator) (%)
1	75	16	33	24
	50	37	77	55
	25	64	133	95
2	50	1	2	1
	25	31	64	46
3	25	3	6	4

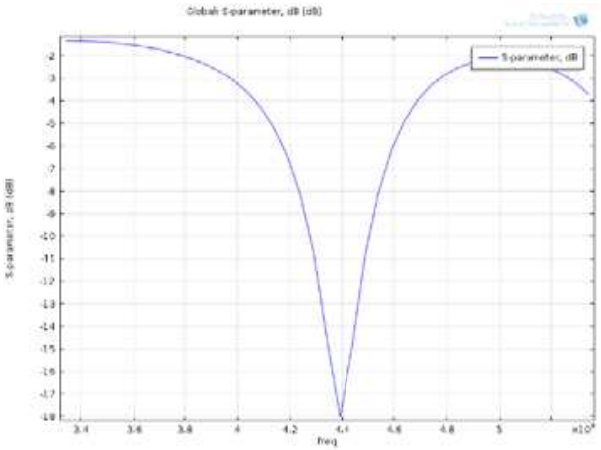

Figure 3: Reflection coefficient of Applicator which is matched by the impedance transformer.

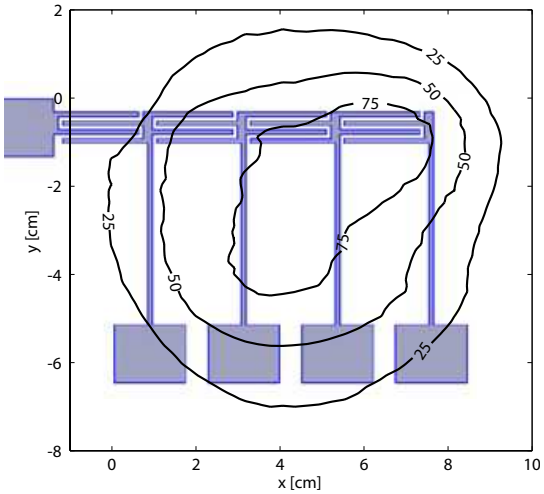

Figure 4: Power deposition pattern 1 cm deep in muscle phantom from Applicator 2 prototype.

3. CONCLUSIONS

New MTM structures with capability of creating plane wave to be radiated into the biological tissue were introduced in this paper. It has been demonstrated here that EM wave penetrating into the biological tissue had very good SAR homogeneity and depth of penetration approaching theoretical limit. Our future plans will be to do an experiment with this structure and verify the promising simulation results experimentally.

ACKNOWLEDGMENT

This work was supported by the Grant Agency of the Czech Technical University in Prague, grant No. SGS14/217/OHK4/3T/17.

REFERENCES

1. Vrba, D. and J. Vrba, "Novel applicators for local microwave hyperthermia based on zeroth-order mode resonator metamaterial," *International Journal of Antennas and Propagation*, Vol. 2014, Apr. 2014.
2. Sanada, A., M. Kimura, I. Awai, C. Caloz, and T. Itoh, "A planar zeroth-order resonator antenna using a left-handed transmission line," *34th European Microwave Conference, 2004*, Vol. 3, 1341–1344, 2004.
3. Polivka, M. and D. Vrba, "Input resistance of electrically short not-too-closely spaced multielement monopoles with uniform current distribution," *IEEE Antennas and Wireless Propagation Letters*, Vol. 11, No. 1, 1592–1595, 2012.
4. Hasgall, P., E. Neufeld, M. Gosselin, A. Klingenböck, and N. Kuster, "IT'IS database for thermal and electromagnetic parameters of biological tissues," [Online], available: www.itis.ethz.ch/database, 2011.
5. ISOLA, ISOLA 370HR datasheet, [Online], available: www.isola-group.com/products/370hr/, 2014.
6. Ellison, W. J., "Permittivity of pure water, at standard atmospheric pressure, over the frequency range 0–25 THz and the temperature range 0–100°C," *Journal of Physical and Chemical Reference Data*, Vol. 36, No. 1, 1–18, 2007.

Design and Implementation of Printed Monopole Antenna for Portable Devices

Jamal Nasir[1], **Mohd. H. Jamaluddin**[1], **Imdad Khan**[2], **Muhammad R. Kamarudin**[1], **and Muzammil Hussain**[2]

[1]Wireless Communication Center (WCC), Universiti Teknologi Malaysia, Malaysia
[2]Department of Electrical Engineering
COMSATS Institute of Information Technology, Abbottabad, Pakistan

Abstract— Ultra-wideband (UWB) has been identified as the future technology. Mostly, bandwidth critical applications such as sensor data collection and location tracking can benefit from the advantageous, highly wide bandwidth of the UWB technology. It is very challenging for the antenna engineers to reduce the size of the antenna while maintaining the performance parameters such as low voltage standing wave ratio (VSWR), wide bandwidth and symmetric radiation patterns. In this paper, a novel, compact printed monopole antenna has been proposed for the portable wireless communication devices. The operating frequency range of the proposed antenna spans from 3–12 GHz, covering the entire frequency range of the UWB spectrum whose range is from 3.1–10.6 GHz. The simulated results of proposed antenna shows good conformity with measured results. The antenna has been etched out in the middle of the radiating patch to form a slot. Moreover, the size of the ground plane has also been reduced. These techniques have been effective to widen the bandwidth of this compact antenna for UWB operation.

1. INTRODUCTION

The Federal Communication Commission (FCC) in 2002 allocated the frequency band from 3.1 to 10.6 GHz to Ultra-wide Band wireless communication [1]. This allocation motivated both the industrial and academic communities to develop compact antennas for UWB communication. The revolution of Wireless technology has changed our life for the last few decades. Today, people are using cell phones providing more freedom to communicate anywhere at any time. Internet by using Wireless Technology provided an opportunity to interconnect computers with each other without any cable.

Presently, a lot of research is being done on wireless personal area network (WPAN) throughout the world. Within a limited range, WPAN provides a consistent wireless connection between portable devices like laptops, computers and other electronic gadgets. In order, to have a reliable communication, fast exchange of data and storage is required between these devices.

The UWB antenna design requires extensive work in miniaturization with high efficiency and large impedance bandwidth. In order to reduce the size of UWB antenna three dimensional radiators have been replaced by planar versions given in [2, 3]. Printed antennas on PCB is a good option for portable devices because it can be easily embedded into wireless devices or integrated with many other RF circuits.

One of the drawbacks of microstrip patch antenna is their inherited narrow bandwidth. A lot of research has been carried out to increase the impedance bandwidth of patch antennas. Like, in [4] a ring shaped slot has been introduced to increase the bandwidth. While, in [5] a slot with a U-shape has been etched on the radiating patch for bandwidth enhancement.

Different techniques have been used to fabricate UWB antenna having small size, omni directional radiation and high efficiency. In [13] compact triple band planar monopole antenna has been proposed for WLAN and WiMAX applications. Similarly, printed UWB antenna has been proposed in [4] having frequency range of 3.1 GHz–5 GHz. Another printed antenna for portable devices is proposed in [5] having dimension of 50×100 mm. Similarly, other design with reduced size has been proposed in [6–10].

In this paper a new printed monopole design has been proposed for UWB portable device application. The design has been simulated in HFSS and its results have been tested experimentally. Maximum gain of 2.5 dBi has been achieved at 8.5 GHz and radiation efficiency of 85%–98% has been achieved throughout UWB range. By using partial ground plane and using slot in radiating plane overall size has been reduced with good radiating efficiency throughout UWB range. The overall antenna size of the proposed antenna is 27.5 mm $\times$ 29.5 mm. The outline of the paper is as follows. Section 2 describes the antenna design; Section 3 describes the results, and Section 4 summarizes the conclusion.

2. ANTENNA DESIGN

Figure 1 shows the geometry of proposed printed monopole antenna. Which is printed on FR4 substrate printed circuit board therefore it is easy to fabricate different RF circuits on the same substrate. Overall dimension of antenna is 27.5 mm × 29.5 mm. Thickness of substrate is 1.6 mm with relative permittivity of 4.8.

The antenna consists of a rectangular radiating element and a rectangular slot with width 2 mm and length 10 mm is cut inside radiating element for impedance matching. In order to increase impedance bandwidth partial ground plane has been used to achieve the complete UWB range. The length of the ground plane L_G is 8.9 mm. The radiating element is excited by 50 Ω coaxial probe at the end of micro stripfeed line of width 2.8 mm. The dimensions of radiating element and ground plane are given in Table 1.

Table 1: Parameters of the antenna.

Basic configuration	Variable	Dimensions (mm)
Substrate	W	**29.5**
	L	**27.5**
Patch Antenna	W_P	**14**
	L_P	**16**
	S_W	**10**
	S_L	**2**
	L_F	**9.5**
	W_F	**2.8**
Ground Plane	L_G	**8.9**

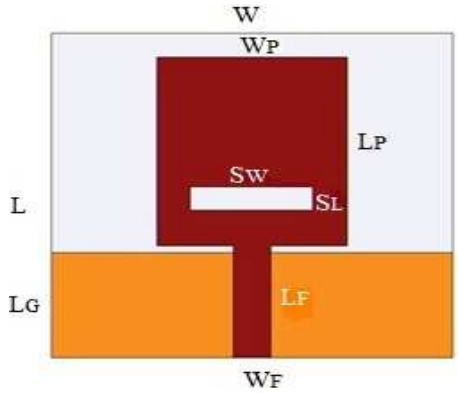

Figure 1: Geometry of patch antenna and ground plane.

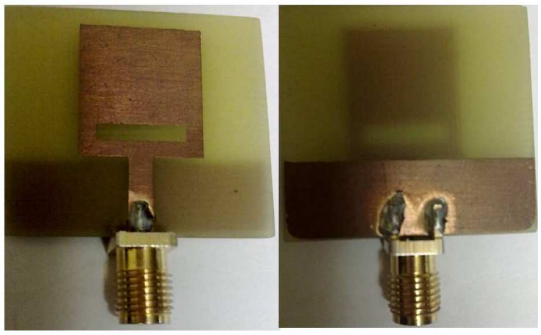

Figure 2: Prototype of the proposed antenna.

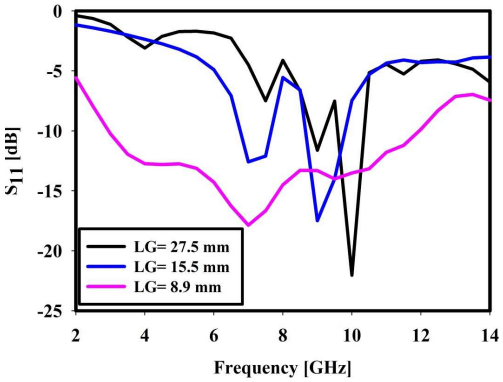

Figure 3: Parametric study of the reflection coefficient magnitudes over the length of the ground plane.

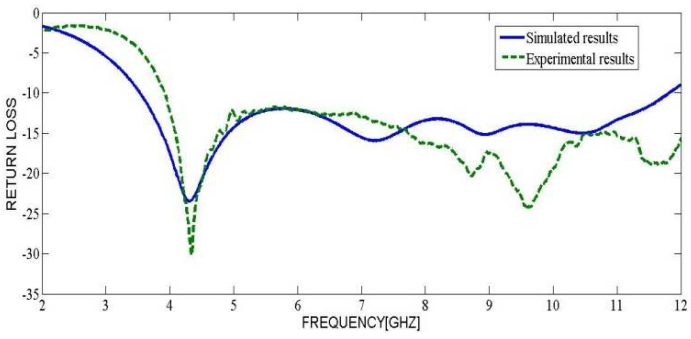

Figure 4: Simulated and measured reflection coefficient magnitudes.

3. RESULTS AND DISCUSSIONS

Based on the dimensions given in Section 2, the antenna is simulated and then the antenna prototype has been fabricated as shown in Figure 2.

3.1. Parametric Study

In order to optimize the antenna design, parametric study has been conducted. The parametric study is important as it helps in giving an approximation measure before the antenna is fabricated. The Figure 3 shows the antenna reflection coefficient plotted against various values of ground length L_G. As clear from Figure 3 that for $L_G = 27.5\,\text{mm}$ the antenna is able to operate only over a narrow band. As the length of the ground is decreased the bandwidth improves and a best result is obtained when the length of the ground L_G becomes 8.9 mm.

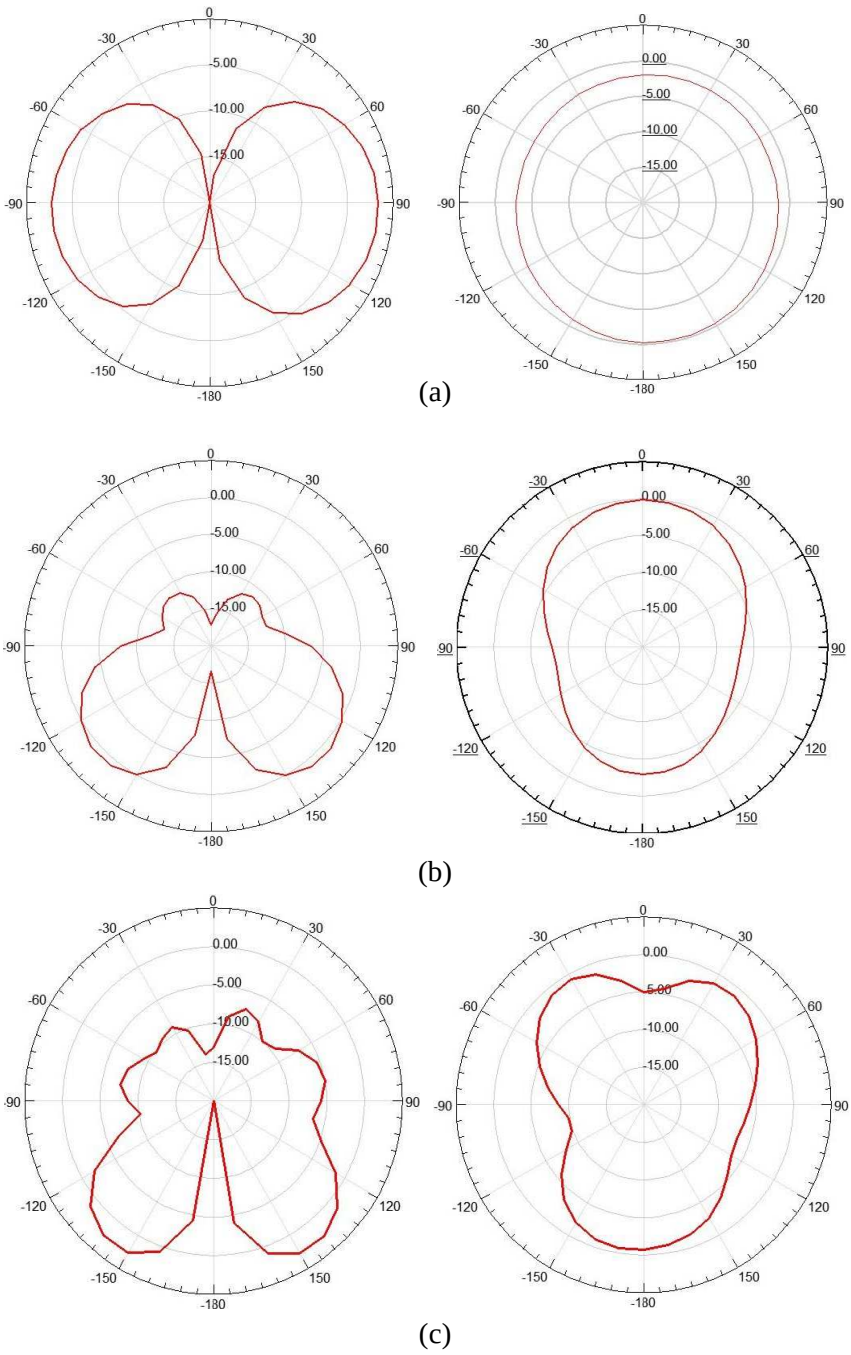

Figure 5: Simulated radiation pattern. (a) E-plane and H-plane pattern at 4 GHz. (b) E-plane and H-plane pattern at 7.5 GHz. (c) E-plane and H-plane pattern at 10 GHz.

3.2. Study of Input Performances

The proposed antenna has been simulated in HFSS V.14 and based upon its simulation results the antenna is optimized which leads to the development of its prototype which is then tested using network analyzer. Figure 4 shows the comparison of simulated and measured reflection coefficient magnitude $|S_{11}|$. It is observed from the figure that the impedance bandwidth is from 3.9 GHz to 12 GHz and the simulated and measured results shows close conformity with each other.

In [11] it is shown that the creation of a rectangular slot on the active zone of the patch increases the bandwidth of the antenna. The introduction of the slot on the patch has created a capacitive reactance that cancels out the inductive reactance of the feed line [12].

3.3. Radiation Pattern

The radiation patterns, both E and H plane of the proposed antenna are shown in Figure 5 at 4.5 GHz, 7 GHz and 10 GHz respectively.

It can be observed from the Figure 5 that the radiation pattern at 7 GHz in x-y plane is like donut shape while at 10 GHz donut shape gets many side lobes. Similarly the radiation pattern at 4 GHz in H-plane is omnidirectional as compared to the radiation pattern at 10 GHz which is more like directional. It is observed that the radiation pattern shows good performance in impedance bandwidth.

3.4. Simulated Gain and Efficiency

The simulated results show that average antenna gain is above 2 dB between 3.5 GHz to 6 GHz. Which shows uniform gain in this frequency range, whereas antenna gain decreases below 2 dB from 6 GHz to 7.2 GHz and gradually increases from 2 dB to 2.5 dB at 8.5 GHz frequency. It is observed that the maximum gain of antenna is 2.5 dB at 8.5 GHz frequency. The maximum simulated efficiency of the antenna is 95% at 3.2 GHz and the lowest efficiency is 88% at 9 GHz.

4. CONCLUSION

In this paper, a new design of printed monopole antenna has been proposed for portable devices. The design has been simulated in HFSS version 14 and the results have been analyzed. The proposed model has been fabricated and S_{11} parameter has been measured experimentally. The maximum gain of antenna is about 2.5 dB and the bandwidth of the proposed antenna is between 3.9 GHz to 11 GHz. It can be used for ultra wide band applications and printed structure is suitable for portable applications. The maximum efficiency of 95% has been achieved for the proposed design. The total size of antenna is 27.5 mm × 29.5 mm.

ACKNOWLEDGMENT

The authors would like to thank the Ministry of Science, Technology and Innovation (MOSTI) under Science Fund (Vote 4S056), Ministry of Higher Education (MOHE) and UTM for funding this project under GUP Grant (Vote 04H36 and 05H62) and FRGS (Vote 4F283). We would also like to appreciate the members of WCC UTM for their useful helps and technical advices.

REFERENCES

1. "FCC report and order for Part 15 acceptance of ultra wideband (UWB) systems from 3.1–10.6 GHz," FCC, Washington, DC, 2002.
2. Wu, X. H. and Z. N. Chen, "Comparison of planer dipoles in UWB applications," *IEEE Trans. Antennas Propagation*, Vol. 53, 1973–1983, 2005.
3. Rahim, S. A., S. Danesh, U. A. Okonkwo, M. Sabran, and M. Khalily, "UWB monople antennawith cirular polarization," *Microwave and Optical Technology Letters*, Vol. 54, No. 4, 949–953, 2012.
4. See, S. P. and Z. N. Chen, "A small UWB antenna for wireless USB," *ICUWB Conference*, 198–203, Nov. 2007.
5. Kaivanto, E., "Printed UWB antenna for portable devices," *IEEE Antennas and Propagation Society International Symposium*, 1–4, 2008.
6. Chen, Z. N., T. S. P. See, and X. Qing, "Small printed ultrawideband antenna with reduce ground plane effect," *IEEE Trans. Antennas Propagation*, Vol. 55, 383–388, 2007.
7. Sadat, S., M. Fardis, F. G. Gharakhili, and G. R. Dadashzade, "A compact microstrip square-ring slot antenna for UWB applications," *Progress In Electromagnetics Research*, Vol. 67, 173–179, 2007.

8. Lee, K. F., K. M. Luk, K. F. Tong, S. M. Shum, T. Huyn, and R. Q. Lee, "Experimental and simulation studies of the coaxially fed U-slot rectangular patch," *IEEE Proceedings of Microwave Antennas Propagation*, Vol. 144, No. 5, 354–358, 1997.
9. Jusoh, M., M. F. Jamlos, M. R. Kamarudin, F. Malek, M. H. Mat, and M. A. Jamlos, "A novel compact tree-design antenna (NCTA) with high gain enhancement for UWB aplication," *Journal of Electromagnetic Waves and Applications*, Vol. 25, Nos. 17–18, 2474–2486, 2011.
10. Jusoh, M., M. F. Jamlos, M. R. Kamarudin, Z. A. Ahmad, M. A. Romli, and S. H. Ronald, "A UWB MIMO spatial design effect on radiation patten," *PIERS Proceedings*, 1510–1513, Kuala Lumpur, Malaysia, Mar. 27–30, 2012.
11. Pele, I., Y. Mahe, A. Chousseaud, S. Toutain, and P. Y. Garel, "Antenna design with control of radiation pattern and frequency bandwidth," *IEEE Antennas and Propagation Society International Symposium*, Vol. 1, 783–786, 2004.
12. Huynh, T. and K. F. Lee, "Single-layer single-patch wideband microstrip antenna," *Electronics Letters*, Vol. 31, No. 16, 1310–1312, 1995.
13. Iddi, H. U., M. R. Kamarudin, T. A. Rahman, A. Y. Abdulrahman, M. Khalily, and M. F. Jamlos, "Triple-band CPW-fed planar monopole antenna for WLAN/WiMAX applications," *Microwave and Optical Technology Letters*, Vol. 55, No. 9, 2209–2214, 2013.

Study of the Precursor Aspects of Earthquakes Suing InSAR Case Study L'Aquila Earthquake

Kamel Hasni, **Jie Chen**, **and Nabil Hamdadou**
School of Electronics and Information Engineering, Beihang University, Beijing 100191, China

Abstract— In this work, we are trying to assess the feasibility of the detection of small deformation of the crust, just few weeks before an earthquake using InSAR. The SAR data made available by the European Space Agency (ESA) after the L'Aquila earthquake (06 April 2009) Mw 6.3, was used for this purpose. Two tracks 079 (descending), 401 (ascending) of Envisat satellite were used. An anomaly in the topography was revealed in the interferograms generated for the period of one month before the earthquake. This anomaly quantified as half fringe = 1.4 cm in both ascending and descending couples. This anomaly was not present in the previous interferograms. The change in the instability of the ionosphere few days before the earthquake, leaded to a big difference in the value of the TEC between the acquisitions, and integrated a delay in the SAR signal.

1. INTRODUCTION

The interaction of powerful processes, which take place in the Earth crust, e.g., earthquakes (EQs), volcanoes, etc., with neutral and charged components of the atmosphere (ionosphere) is one of the most important problems of our environment. Evidences for ionospheric disturbances emerging days before the strong EQ shocks are widely considered in the literature. Data from a number of vertical sounding ionosondes have been analyzed for a thorough study of the F2 region ionosphere behavior. Ionospheric disturbances in F2 region have been shown to appear generally 1–7 days before the EQ event [2, 3, 5]. At heights of the maximum of the F2 region, the corresponding critical frequency (foF2) is strongly influenced by EQ preparation processes. Then the variations from its median values can exceed twice the standard deviation. Moreover, their localization is found to be centered at or near the epicenter of the forthcoming EQ (Liu et al., 2001, 2006). Analysis of GPS total electron content (TEC) data within the area affected by the EQ has revealed a systematic ionospheric variability several days before the seismic shock as shown for instance by (Liu et al., 2004, 2006) who observed a TEC variation up to 40TEC units.

Disturbances affecting the E and D ionospheric regions days before strong EQs have also been observed. First experimental evidences concerning the D region disturbances during the EQ preparation period are changes of the characteristics of VLF signals received by ground-based receivers from remote transmitters (Gokhberg et al., 1987, 1989). As for EQ-related disturbances in the E region there is a row of cases and statistical studies. The most frequent feature characterizing the E region is the appearance several days before of strong Es layers over the zone affected by the EQ (Ondoh and Hayakawa, 1999; Liperovsky et al., 2000; Pulinets et al., 2000; Chuo et al., 2002).

2. IONOSPHERIC EFFECT ON INTERFEROMETRIC SAR

The ionosphere is a region of the earth's extending from an altitude of about 50–1000 km where solar radiation ionizes atmospheric gases. For the purposes of SAR, it is sufficient to model the ionosphere as a thin layer, at an effective ionospheric height of 400 km. During its 2-way passage through the dispersive ionosphere, a SAR signal experiences a group delay and phase advance which are inversely proportional to frequency squared:

$$-\tau_{phase} = \tau_{group} = 2K_0 STEC/f^2 \tag{1}$$

where $K_0 = 40.28\,\mathrm{m^2 s^{-2}}$ and STEC is the Stant range TEC. TEC refers to the zenith value, the density of free electrons contained in a cylinder with unit area passing through the atmosphere in the direction of nadir. STEC is proportional to TEC through one over the cosine of the zenith angle. For interferometry, only the phase delay is of interest. The corresponding influence on a repeat-pass interferogram is obtained by replacing STEC in (Eq. (1)) with $\Delta STEC$, the difference in $\Delta STEC$ values between the master and the slave acquisitions, giving an Interferometric phase delay at the carrier frequency f_c of:

$$\phi_0^{iono} = -\frac{2K_0 \Delta STEC}{c f_c}(cycles) \tag{2}$$

The Interferometric phase at the carrier frequency is comprised of a topographic component due to the differential range between the master and the slave and an ionospheric component due to the differential phase advance.

$$\phi_0 = 2f_c\Delta R/c - 2K_0\Delta STEC/(cf_c) \tag{3}$$

These two components can be separated because of their different behavior (frequency) (B. Ramon et al., 2010).

3. DATA ANALYSIS

We used five Envisat images covering the period before the L'Aquila Earthquake (06 April 2009). Three ascending (Track 401) and two descending (Track 079).

Table 1: Envisat data used in this study.

Date	Track	orbit
19/01/2009	401	asc
23/02/009	401	asc
30/03/2009	401	asc
01/02/2009	079	desc
08/03/2009	079	desc

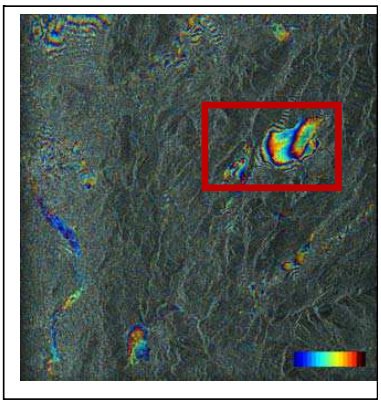

Figure 1: Couple 20090119–20090223.

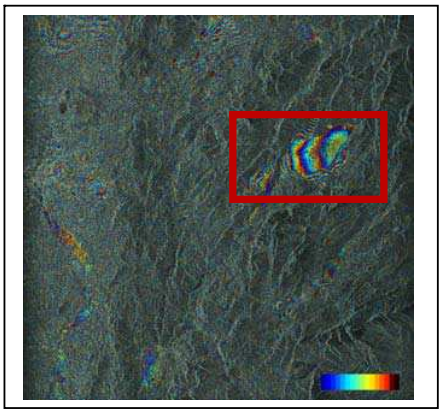

Figure 2: 20090223–20090330.

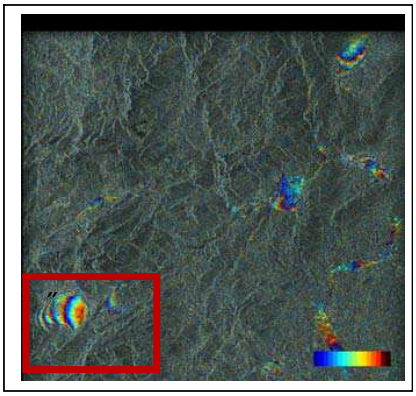

Figure 3: 20090201–20090308.

The area delimited by red rectangles, represent the city of L'Aquila (Italy) where the Earthquake of magnitude 6.3, occurred on 06 April 2009. In the interferograms 20090223–20090330 and 20090201–20090308 we can see that there is an extra 1/4 fringe added to the topographic phase comparing to the Interferogram of the couple 20090119–20090223. The first guess would be a bad corregistration of the images. But since all the interferograms was coregisterred the same way and with the same parameters. This leads to an external source of bias.

[1] used data from Rome and Sofia Ionospheric stations, to study the period of earthquake activity for earthquakes of magnitude (M) between 5 and 6 in central Italy. They found that several ionospheric disturbances occurred in the intermediate E–F region before the earthquake shock.

Another study, [4] of earthquakes of magnitude between 5.5 and 6. Observed in Italy for the period 1979–2009 including 06 April 2009 L'Aquila earthquake. They also used the ionospheric station situated in Rome. The precursor identification for L'Aquila earthquake, used the observed $\Delta h'Es$, $\delta f_0 Es$, and $\delta f_0 F2$. The study of these parameters helped to understand the empirical dependencies for the seismo-ionospheric disturbances relating the earthquake magnitude and the epicenter distance.

Another study [7], was dedicated to the use of Demeter satellite that gives the VLF measurements data and GPS observations that used to compute the TEC. In normal cases, the TEC values are correlated to the geomagnetic variations and the ACE data, because all of them are triggered by solar events. However, they find that before the L'Aquila earthquake occurrence the TEC increased but the other parameters didn't show similar variations. So, it is supposed that the electron number enhancement must have another source than the sun and might be a regional phenomenon related to earthquake.

The use of TEC maps in [7], revealed that there was an increase in the values of the TEC starting from 30 March which corresponds to the date of acquisition of the third image in Table 1 (track 401). This image is heavily affected by ionospheric effect due to the variation of TEC in that day, thing that affected all the interferograms generated using this image.

4. CONCLUSION

The analysis of the interferograms related to the period preceding L'Aquila earthquake, within few days. Revealed the precursor feasibility of SAR interferometry for the study of earthquakes.

REFERENCES

1. Nenovski, P., C. Spassov, M. Pezzopane, U. Villante, M. Vellante, and M. Serafimova, "Ionospheric transcients observed at mid-latitudes prior to earthquake activity in Central Italy," *Nat. Hazards Syst. Sci.*, Vol. 10, 1197–1208, 2010.
2. Hayakawa, M., "Atmospheric and ionospheric electromagnetic phenomena associated with earthquakes," *TERRAPUB*, Tokyo, 1999.
3. Hayakawa, M. and O. A. Molchanov, "Seismo electromagnetics lithosphere-atmosphere-ionosphere coupling," *TERRAPUB*, Tokyo, ISBN: 4-88704-130-6, 2002.
4. Perrone L., L. P. Korsunova, and A. V. Mikhailov, "Ionospheric precursors for crustal earthquakes in Italy," *Ann. Geophys.*, Vol. 28, 941–950, 2010.
5. Pulinets, S. A., J. Y. Liu, and I. A. Safronova, "Interpretation of results of statistical analysis of critical frequency foF2 variations before earthquakes after Chung-Li ionospheric station data (Taiwan)," *Geomagn, Aeronomy*, Vol. 44, 102–106, 2004, (translated from *Geomagnetizm I Aeronomiya*, Vol. 44, 113–118, 2004).
6. Brcic, R., A. Parizzi, M. Eineder, R. Bamler, and F. Meyer, "Estimation and compensation of Ionospheric delay for SAR interferometry," *Proc. IGARSS*, Jul. 2010.
7. Stangl, G., M. Y. Boudjada, P. F. Biagi, S. Krauss, A. Maier, K. Schwingenschuh, E. Al-Haddad, M. Parrot, and W. Voller, "Investigation of TEC and VLF space measurements associated to L'Aquila (Italy) earthquakes," *Nat. Hazards Earth Syst. Sci.*, Vol. 11, 1019–1024, 2011.

A Dual Band Center-fed Sleeve Dipole Array for IEEE 802.11a/b Application

Dau-Chyrh Chang[1], **Yi-Ci Su**[1], **Chih-Hung Lee**[2], **and Chang-Hsuan Kao**[1]

[1]Oriental Institute of Technology, CRC, Taiwan
[2]Electronics Testing Center, Yuan Ze University, Taiwan

Abstract— Traditional end-fed sleeve dipole array antenna will cause the current distribution to attenuate gradually along the antenna array. This phenomenon not only causes the lower aperture efficiency but also with frequency scan. Lower aperture efficiency and frequency scanning will degrade the antenna performance. In order to solve the lower aperture efficiency and frequency scan characteristics of the end-fed sleeve dipole array, a dual bands three elements printed sleeve dipole antenna array with beam direction at boresight direction has been developed for the application of IEEE 802.11 a/b/g. The size of sleeve dipole antenna array is 220 mm in length, 8 mm in width, and 0.4 mm in thickness The beam direction always points at the boresight direction even if for various frequency operation.

1. INTRODUCTION

The end-fed sleeve dipole array antennas are most used in traditional communication system for its easy fabrication. Due to the power radiation continuous along the antenna dipole array, the current distribution will attenuate gradually along the sleeve dipole array. Since the current distribution is triangular asymmetry shape instead of uniform shape along the array, the aperture efficiency of the array will be seriously degraded. Except for the current distribution decreased along the sleeve array, the antenna beam will also scan in the E-plane for the operating bandwidth. The higher the frequency is the larger the scan angle will be. Usually, the amount of scan angle is about percent of bandwidth. For example, the bandwidth of IEEE 11a is about 600 MHz (5.2 GHz $\sim$ 5.8 GHz) with fractional bandwidth about 12%. The amount of scan angle for this sleeve dipole array antenna is 12 degrees in the E-plane. If the E-plane antenna half power beamwidth is 12 degrees, the antenna gain will degrade 3 dB with maximum center frequency 5.5 GHz at broadside direction.

The current distribution of can be triangular symmetry or uniform distribution for the centerfed of the sleeve dipole array. The aperture efficiency of the sleeve dipole array with center-fed is improved if compared with that of end-fed. The amount of beam scan angle will be cancelled out even for larger frequency scan angle by using the center-fed of the array. The beam direction of the sleeve dipole array will always point at the boresight direction even if the frequency is changed. In order to solve the above two disadvantages of the end-fed sleeve dipole array, dual bands (2.4 GHz $\sim$ 2.5 GHz and 5.2 GHz $\sim$ 5.8 GHz) with high aperture efficiency and without frequency scanning center-fed sleeve dipole array antenna, is developed.

2. ARRAY SIMULATION AND MEASUREMENT

In order to have higher aperture efficiency, the sleeve dipole array with center fed IEEE 802.11a/b/g is designed and implemented. The sleeve dipole array with three dipole elements operates simulta-

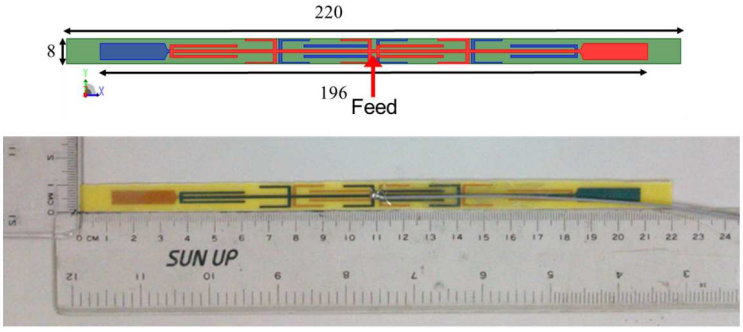

Figure 1: Simulation model and implemented of sleeve dipole array.

neous at 2.4 GHz and 5.5 GHz. The size of sleeve dipole array as shown in Fig. 1, printed on FR4 substrate, is with 22 cm in length 0.8 cm in width and 0.04 cm in thickness.

The simulated and measured return loss for dual bands is shown Fig. 2. The return loss for simulation is less than 10 dB for frequency in 2.4 ∼ 2.5 GHz and 3 dB for frequency in 5.2 ∼ 5.8 GHz.

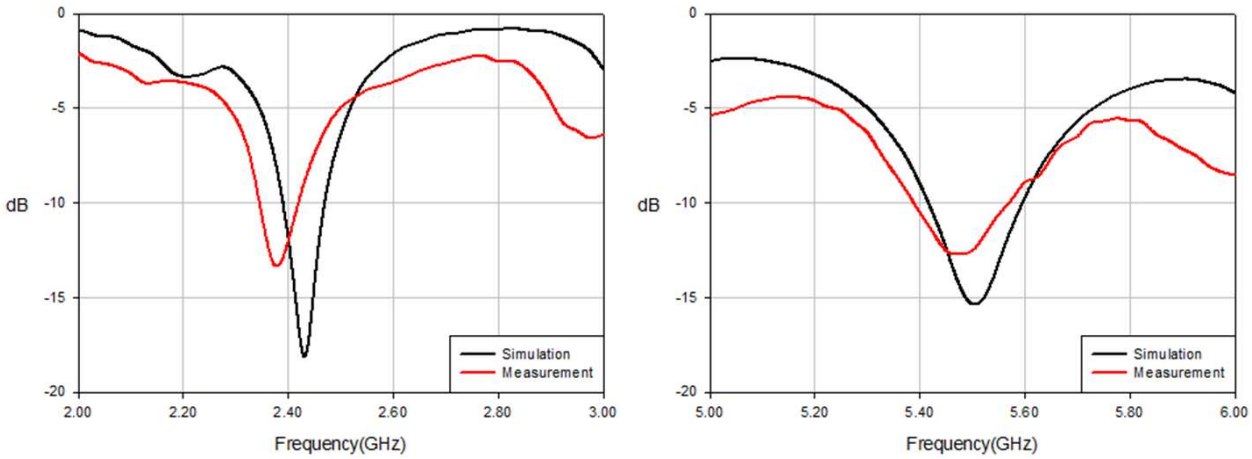

Figure 2: Simulated and measured return loss. (a) 2.4 GHz band, (b) 5.5 GHz band.

Figure 3 is the simulated and measured directivity for the two bands. Fig. 4 is the E-plane simulation E-plane pattern for different frequencies. The E-plane plane is composed of two sleeve dipole arrays with center fed. The E-plane beam direction will opposite for the sleeve dipole arrays with center fed. The final E-plane beam patterns are at boresight direction for all frequencies. At 5.2 GHz, the beamwidth is narrow and point at borsignt direction. Unfortunately, the beamwidth is wider at 5.5 GHz and 5.8 GHz. This is due to the beam scan angel is large for higher frequency. Fig. 5 is the H-plane patterns. The H-plane pattern is almost omnidirectional. Figs. 6 and 7 are the measured and simulated E-plane and H-plane patterns at 2.45 GHz and 5.2 GHz. The gain difference for measurement and simulation is due to the 1.13 mm mini coaxial cable and connector. It is supposed for the extra loss is 2 dB for measurement.

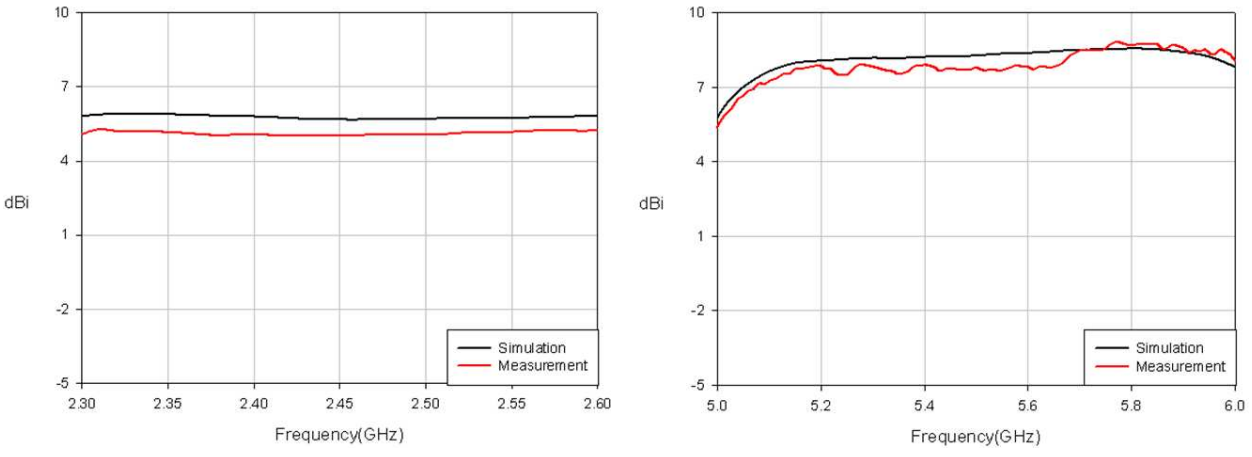

Figure 3: Directivity for simulation and measurement. (a) 2.4 GHz band, (b) 5.5 GHz band.

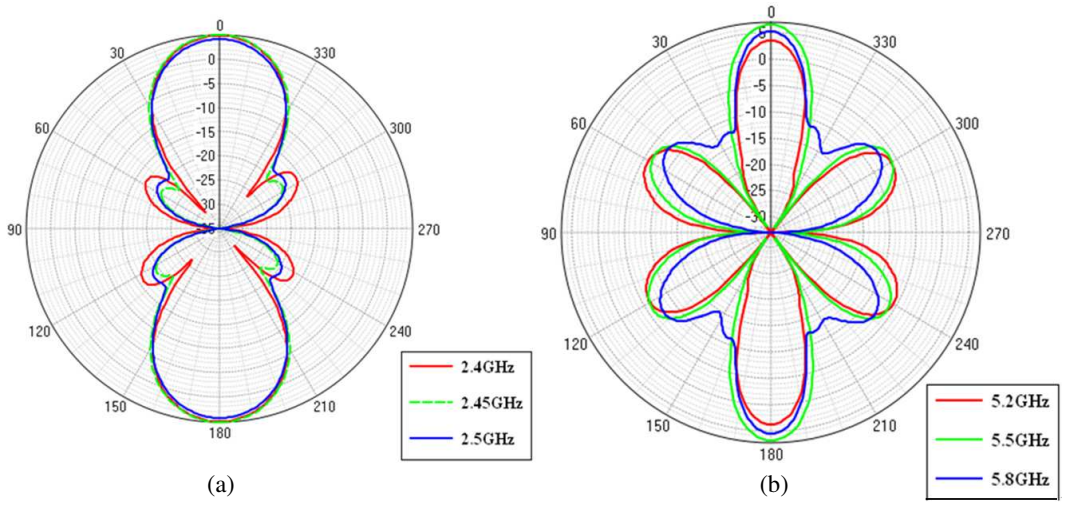

Figure 4: Simulated E-plane patterns for different band. (a) 2.4 GHz band, (b) 5.5 GHz band.

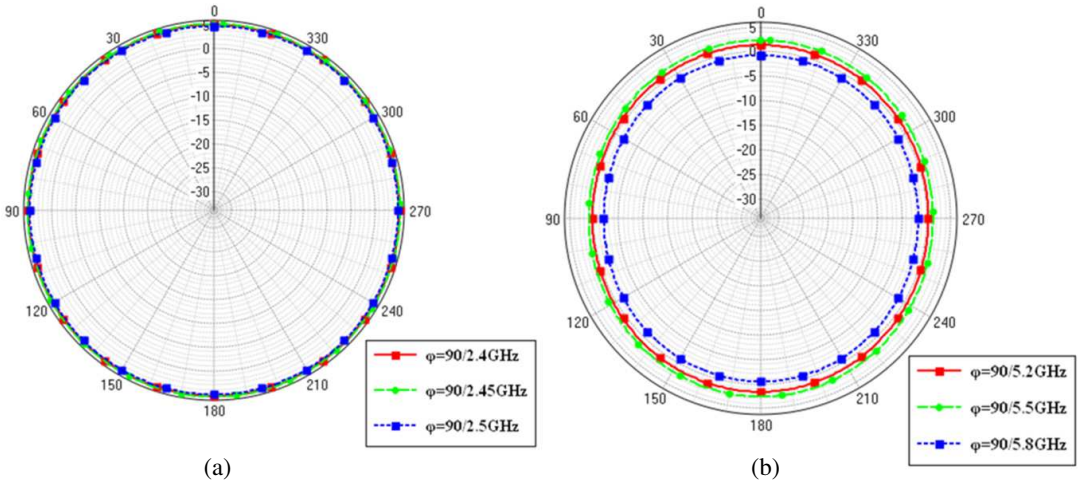

Figure 5: Simulated H-plane patterns for different band. (a) 2.4 GHz band, (b) 5.5 GHz band.

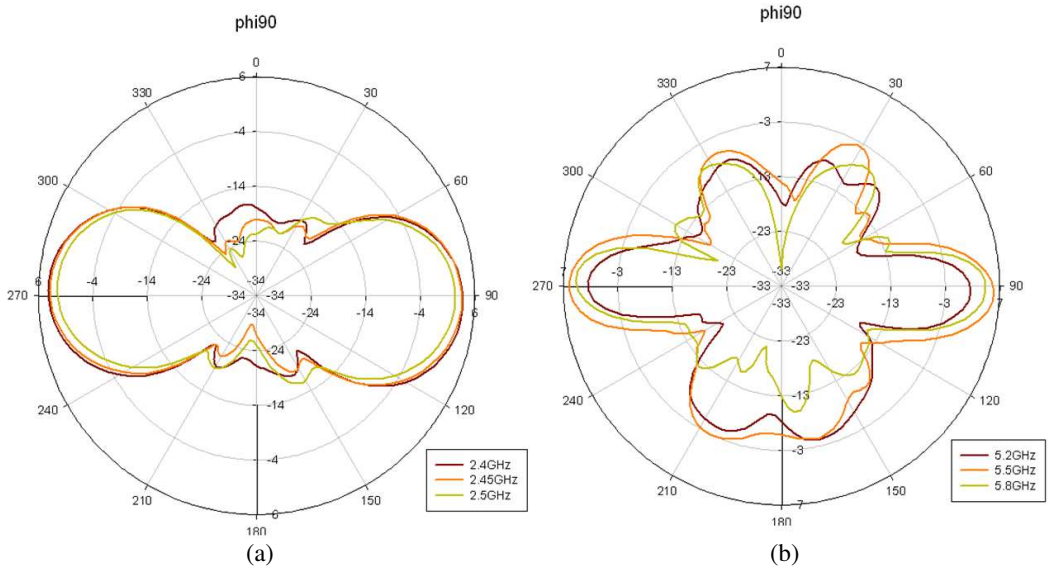

Figure 6: Measured E-plane patterns at 2.4 GHz and 5.5 GHz bands. (a) 2.45 GHz, (b) 5.5 GHz.

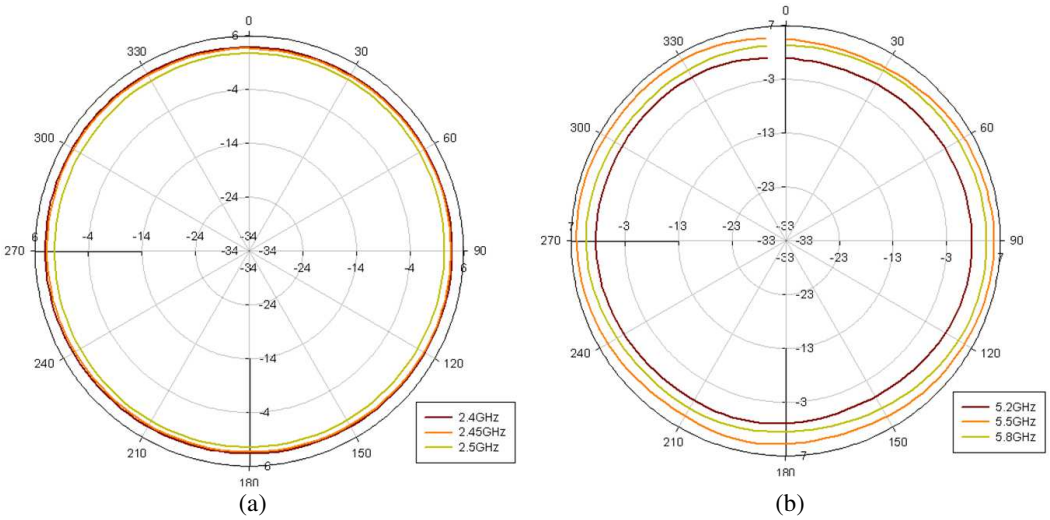

(a) (b)

Figure 7: Measured H-plane patterns at 2.4 GHz and 5.5 GHz bands. (a) 2.45 GHz, (b) 5.5 GHz.

3. CONCLUSION

High aperture efficiency of sleeve dipole array with three elements for 2.4 GHz and 5.5 GHz are designed and implementation. The simulated directivity for three elements array is 5.6 dBi for 2.4 GHz and 8.3 dBi for 5.5 GHz band. The E-plane beam direction will not be tilted off boresight direction for the band. Detail results will be presented. The measured efficiency, directivity, and gain are 76.7%, 5.01 dBi and 3.87 dBi at 2.45 GHz respectively. And measured efficiency, directivity, and gain are 67.4%, 7.78 dBi, and 5.95 dBi at 5.5 GHz.

REFERENCES

1. GEMS, "3-D high performance parallel EM simulation software," www.2comu.com.
2. Elliott, R. S., "On the design of traveling-wave-fed longitudinal shunt slot arrays," *IEEE Transactions on Antenna and Propagation*, Vol. 27, No. 5, September 1979.
3. Chang, D.-C. and C.-C. Chen, "Optimization of directivity for sleeve dipole array," Oriental Institute of Technology, 2011.